STATE OF THE CLIMATE IN 2023

Special Supplement to the
Bulletin of the American Meteorological Society
Vol. 105 No. 8, August 2024

Cover Credit:
Ice Worm Glacier in the North Cascade mountains of Washington, United States, which was under continuous annual monitoring from 1984 onward and disappeared in 2023. Large photo: The location of former Ice Worm Glacier in 2023. Inset photo: Ice Worm Glacier in 1986. Photo credits Mauri Pelto. 13 August 2023 is the date for the main photo. 16 August 1986 is the date for the inset photo.

How to cite this document:
Special Supplement to the Bulletin of the American Meteorological Society, Vol. 105, No. 8, August 2024 https://doi.org/10.1175/2024BAMSStateoftheClimate.1. Compiled by NOAA's National Centers for Environmental Information, *State of the Climate in 2023* is based on contributions from scientists from around the world. It provides a detailed update on global climate indicators, notable weather events, and other data collected by environmental monitoring stations and instruments located on land, water, ice, and in space.

Citing the complete report:
Blunden, J. and T. Boyer, Eds., 2024: "State of the Climate in 2023". Bull. Amer. Meteor. Soc., 105 (8), Si–S484 https://doi.org/10.1175/2024BAMSStateoftheClimate.1.

Corresponding author: Full Report: Jessica Blunden / jessica.blunden@noaa.gov

©2024 American Meteorological Society
For information regarding reuse of this content and general copyright information, consult the AMS Copyright Policy.

STATE OF THE CLIMATE IN 2023

Table of Contents

Abstract ..... Siii

1. Introduction S1

2. Global Climate S12

3. Global Oceans S156

4. The Tropics S214

5. The Arctic S277

6. Antarctica and the Southern Ocean S331

7. Regional Climates S371

Abstract

—J. BLUNDEN AND T. BOYER

In 2023, La Niña conditions that generally prevailed in the eastern Pacific Ocean from mid-2020 into early 2023 gave way to a strong El Niño by October. Atmospheric concentrations of Earth's major greenhouse gases—carbon dioxide, methane, and nitrous oxide—all increased to record-high levels. The annual global average carbon dioxide concentration in the atmosphere rose to 419.3±0.1 ppm, which is 50% greater than the pre-industrial level. The growth from 2022 to 2023 was 2.8 ppm, the fourth highest in the record since the 1960s.

The combined short-term effects of El Niño and the long-term effects of increasing levels of heat-trapping gases in the atmosphere contributed to new records for many essential climate variables reported here. The annual global temperature across land and oceans was the highest in records dating as far back as 1850, with the last seven months (June–December) having each been record warm. Over land, the globally averaged temperature was also record high. Dozens of countries reported record or near-record warmth for the year, including China and continental Europe as a whole (warmest on record), India and Russia (second warmest), and Canada (third warmest). Intense and widespread heatwaves were reported around the world. In Vietnam, an all-time national maximum temperature record of 44.2°C was observed at Tuong Duong on 7 May, surpassing the previous record of 43.4°C at Huong Khe on 20 April 2019. In Brazil, the air temperature reached 44.8°C in Araçuaí in Minas Gerais on 20 November, potentially a new national record and 12.8°C above normal.

The effect of rising temperatures was apparent in the cryosphere, where snow cover extent by June 2023 was the smallest in the 56-year record for North America and seventh smallest for the Northern Hemisphere overall. Heatwaves contributed to the greatest average mass balance loss for Alpine glaciers around the world since the start of the record in 1970. Due to rapid volume loss beginning in 2021, St. Anna Glacier in Switzerland and Ice Worm Glacier in the United States disappeared completely. In August, as a direct result of glacial thinning over the past 20 years, a glacial lake on a tributary of the Mendenhall Glacier in Alaska burst through its ice dam and caused unprecedented flooding on Mendenhall River near Juneau.

Across the Arctic, the annual surface air temperature was the fourth highest in the 124-year record, and summer (July–September) was record warm. Smaller-than-normal snow cover extent in May and June contributed to the third-highest average peak tundra greenness in the 24-year record. In September, Arctic minimum sea ice extent was the fifth smallest in the 45-year satellite record. The 17 lowest September extents have all occurred in the last 17 years.

In Antarctica, temperatures for much of the year were up to 6°C above average over the Weddell Sea and along coastal Dronning Maud Land. The Antarctic Peninsula also experienced well-above-average temperatures during the 2022/23 melt season, which contributed to its fourth consecutive summer of above-average surface melt. On 21 February, Antarctic sea ice extent and sea ice area both reached all-time lows, surpassing records set just a year earlier. Over the course of the year, new daily record-low sea ice extents were set on 278 days. In some instances, these daily records were set by a large margin, for example, the extent on 6 July was 1.8 million km^2 lower than the previous record low for that day.

Across the global oceans, the annual sea surface temperature was the highest in the 170-year record, far surpassing the previous record of 2016 by 0.13°C. Daily and monthly records were set from March onward, including an historic-high daily global mean sea surface temperature of 18.99°C recorded on 22 August. Approximately 94% of the ocean surface experienced at least one marine heatwave in 2023, while 27% experienced at least one cold spell. Globally averaged ocean heat content from the surface to 2000-m depth was record high in 2023, increasing at a rate equivalent to ~0.7 Watts per square meter of energy applied over Earth's surface. Global mean sea level was also record high for the 12th consecutive year, reaching 101.4 mm above the 1993 average when satellite measurements began, an increase of 8.1±1.5 mm over 2022 and the third highest year-over-year increase in the record.

A total of 82 named tropical storms were observed during the Northern and Southern Hemispheres' storm seasons, below the 1991–2020 average of 87. Hurricane Otis became the strongest landfalling hurricane on record for the west coast of Mexico at 140 kt (72 m s^{-1}), causing at least 52 fatalities and $12–16 billion U.S. dollars in damage. Freddy became the world's longest-lived tropical cyclones on record, developing into a tropical cyclone on 6 February and finally dissipating on 12 March. Freddy crossed the full width of the Indian Ocean and made one landfall in Madagascar and two in Mozambique. In the Mediterranean Sea—outside of traditional tropical cyclone basins—heavy rains and flooding from Storm Daniel killed more than 4300 people and left more than 8000 missing in Libya.

The record-warm temperatures in 2023 created conditions that helped intensify the hydrological cycle. Measurements of total-column water vapor in the atmosphere were the highest on record, while the fraction of cloud area in the sky was the lowest since records began in 1980. The annual global mean precipitation total over land surfaces for 2023 was among the

lowest since 1979, but global one-day maximum totals were close to average, indicating an increase in rainfall intensity.

In July, record-high areas of land across the globe (7.9%) experienced extreme drought, breaking the previous record of 6.2% in July 2022. Overall, 29.7% of land experienced moderate or worse categories of drought during the year, also a record. Mexico reported its driest (and hottest) year since the start of its record in 1950. In alignment with hot and prolonged dry conditions, Canada experienced its worst national wildfire season on record. Approximately 15 million hectares burned across the country, which was more than double the previous record from 1989. Smoke from the fires were transported far into the United States and even to western European countries. August to October 2023 was the driest three-month period in Australia in the 104-year record. Millions of hectares of bushfires burned for weeks in the Northern Territory. In South America, extreme drought developed in the latter half of the year through the Amazon basin. By the end of October, the Rio Negro at Manaus, a major tributary of the Amazon River, fell to its lowest water level since records began in 1902.

The transition from La Niña to El Niño helped bring relief to the prolonged drought conditions in equatorial eastern Africa. However, El Niño along with positive Indian Ocean dipole conditions also contributed to excessive rainfall that resulted in devastating floods over southeastern Ethiopia, Somalia, and Kenya during October to December that displaced around 1.5 million people. On 5 September, the town of Zagora, Greece, broke a national record for highest daily rainfall (754 mm in 21 hours, after which the station ceased reporting) due to Storm Daniel; this one-day accumulation was close to Zagora's normal annual total.

Editor and Author Affiliations (alphabetical by name)

Ades, Melanie, European Centre for Medium-Range Weather Forecasts, Reading, United Kingdom

Adler, Robert, University of Maryland, College Park, Maryland

Adusumilli, Susheel, Scripps Institution of Oceanography, University of California, San Diego, La Jolla, California

Agyakwah, W., NOAA/NWS National Centers for Environmental Prediction Climate Prediction Center, College Park, Maryland

Ahmadpour, Somayeh, Brandenburg University of Technology (BTU), Cottbus-Senftenberg, Germany

Aldeco, Laura S., Servicio Meteorológico Nacional, Buenos Aires, Argentina

Alexander, Michael A., NOAA/OAR Physical Sciences Laboratory, Boulder, Colorado

Alexe, Mihai, European Centre for Medium-Range Weather Forecasts, Bonn, Germany

Alfaro, Eric J., Center for Geophysical Research and School of Physics, University of Costa Rica, San José, Costa Rica

Allan, Richard P., Department of Meteorology and National Centre for Earth Observation, University of Reading, Reading, United Kingdom

Allgood, Adam, NOAA/NWS National Centers for Environmental Prediction Climate Prediction Center, College Park, Maryland

Alves, Lincoln M., Centro Nacional de Monitoramento e Alertas de Desastres Naturais CEMADEN, São Paulo, Brazil

Amador, Jorge A., Center for Geophysical Research and School of Physics, University of Costa Rica, San José, Costa Rica

Amaya, Dillon J., NOAA/OAR Physical Sciences Laboratory, Boulder, Colorado

Amory, Charles, Université Grenoble Alpes, Institut des Géosciences de l'Environnement, IRD, CNRS, Grenoble INP, Grenoble, France

Anderson, John, Hampton University, Hampton, Virginia

Andrade, B., Seychelles Meteorological Authority, Mahe, Seychelles

Andreassen, Liss Marie, Section for Glaciers, Ice and Snow, Norwegian Water Resources and Energy Directorate, Oslo, Norway

Anneville, Orlane, National Research Institute for Agriculture, Food and Environment (INRAE), CARRTEL, Université Savoie Mont Blanc, Thonon les Bains, France

Aono, Yasuyuki, Graduate School of Agriculture, Osaka Metropolitan University, Sakai, Japan

Arguez, Anthony, NOAA/NESDIS National Centers for Environmental Information, Asheville, North Carolina

Armenteras Pascual, Dolores, Science Faculty, Universidad Nacional de Colombia, Bogotá, Colombia

Arosio, Carlo, University of Bremen, Bremen, Germany

Asher, Elizabeth, NOAA Global Monitoring Laboratory, Boulder, Colorado

Augustine, John A., NOAA Global Monitoring Laboratory, Boulder, Colorado

Avalos, Grinia, Servicio Nacional de Meteorología e Hidrología del Perú, Lima, Perú

Azorin-Molina, Cesar, Centro de Investigaciones sobre Desertificación – Spanish National Research Council (CSIC-UV-GVA), Valencia, Spain

Baez-Villanueva, Oscar M., Hydro-Climate Extremes Lab (H-CEL), Ghent University, Ghent, Belgium

Baiman, Rebecca, Department of Atmospheric and Oceanic Sciences, University of Colorado Boulder, Boulder, Colorado

Ballinger, Thomas J., International Arctic Research Center, University of Alaska Fairbanks, Fairbanks, Alaska

Banwell, Alison F., Earth Science Observation Center, Cooperative Institute for Research in Environmental Sciences (ESOC/CIRES), University of Colorado Boulder, Boulder, Colorado

Bardin, M. Yu., Yu. A. Izrael Institute of Global Climate and Ecology, Institute of Geography, Russian Academy of Sciences, Moscow, Russia

Barichivich, J., Laboratoire des Sciences du Climat et de l'Environnement (LSCE), LSCE/IPSL, CEA-CNRS-UVSQ, Gif-sur-Yvette, France; Instituto de Geografía, Pontificia Universidad Católica de Valparaíso, Valparaíso, Chile

Barreira, Sandra, Argentine Naval Hydrographic Service, Buenos Aires, Argentina

Beadling, Rebecca L., Department of Earth and Environmental Science, Temple University, Philadelphia, Pennsylvania

Beauchemin, Marc, Environment and Climate Change Canada, Montreal, Canada

Beck, Hylke E., Physical Science and Engineering Division, King Abdullah University of Science and Technology, Thuwal, Saudi Arabia

Becker, Emily J., Rosenstiel School of Marine, Atmospheric, and Earth Science, University of Miami, Miami, Florida

Beckley, Brian, KBR, Inc., Greenbelt, Maryland; NASA Goddard Space Flight Center, Greenbelt, Maryland

Bekele, E., NOAA/NWS National Centers for Environmental Prediction Climate Prediction Center, College Park, Maryland

Bellouin, Nicolas, University of Reading, Reading, United Kingdom; Institute Pierre Simon Laplace (IPSL), Guyancourt, France

Benedetti, Angela, European Centre for Medium-Range Weather Forecasts, Reading, United Kingdom

Berne, Christine, Météo France, Toulouse, France

Berner, Logan T., School of Informatics, Computing, and Cyber Systems, Northern Arizona University, Flagstaff, Arizona

Bernhard, Germar H., Biospherical Instruments Inc., San Diego, California

Bhatt, Uma S., Geophysical Institute, University of Alaska Fairbanks, Fairbanks, Alaska

Bigalke, Siiri, Plant, Soils and Climate Department, Utah State University, Logan, Utah

Bissolli, Peter, Deutscher Wetterdienst, WMO RA VI Regional Climate Centre Network, Offenbach, Germany

Bjerke, Jarle W., Norwegian Institute for Nature Research, Trondheim, Norway; FRAM – High North Research Centre for Climate and the Environment, Tromsø, Norway

Blake, Eric S., NOAA/NWS National Hurricane Center, Miami, Florida

Blannin, Josh, Met Office Hadley Centre, Exeter, United Kingdom

Blenkinsop, Stephen, School of Engineering, Newcastle University, Newcastle-upon-Tyne, United Kingdom

Blunden, Jessica, NOAA/NESDIS National Centers for Environmental Information, Asheville, North Carolina

Bochníček, Oliver, Slovak Hydrometeorological Institute, Bratislava, Slovakia

Bock, Olivier, Université Paris Cité, Institut de physique du globe de Paris, CNRS, IGN, F-75005 Paris, France; Univ Gustave Eiffel, ENSG, IGN, F-77455 Marne-la-Vallée, France

Bodin, Xavier, Laboratoire EDYTEM, CNRS/Université Savoie Mont-Blanc, Le Bourget-du-Lac, France

Bonte, Olivier, Hydro-Climate Extremes Lab (H-CEL), Ghent University, Ghent, Belgium

Bosilovich, Michael G., Global Modeling and Assimilation Office, NASA Goddard Space Flight Center, Greenbelt, Maryland

Boucher, Olivier, Institute Pierre Simon Laplace (IPSL), Guyancourt, France

Box, Jason E., Geological Survey of Denmark and Greenland (GEUS), Copenhagen, Denmark

Boyer, Tim, NOAA/NESDIS National Centers for Environmental Information, Silver Spring, Maryland

Bozkurt, Deniz, Department of Meteorology, University of Valparaíso, Valparaíso, Chile; Center for Climate and Resilience Research (CR)2, Santiago, Chile

Brettschneider, Brian, NOAA/NWS Alaska Region, Anchorage, Alaska

Bringas, Francis G., NOAA/OAR Atlantic Oceanographic and Meteorological Laboratory, Miami, Florida

Brubaker, Mike, Alaska Native Tribal Health Consortium, Anchorage, Alaska

Buehler, Stefan A., Universität Hamburg, Hamburg, Germany

Bukunt, Brandon, NOAA/NWS Weather Forecast Office, Tiyan, Guam

Burgess, David, Geological Survey of Canada, Natural Resources Canada, Ottawa, Canada

Butler, Amy H., NOAA Chemical Sciences Laboratory, Boulder, Colorado

Byrne, Michael P., Climate Dynamics Lab, University of St Andrews, St Andrews, United Kingdom
Calderón, Blanca, Center for Geophysical Research, University of Costa Rica, San José, Costa Rica
Camargo, Suzana J., Lamont-Doherty Earth Observatory, Columbia University, Palisades, New York
Campbell, Jayaka, Department of Physics, The University of the West Indies, Kingston, Jamaica
Campos, Diego, Earth Sciences Department, Barcelona Supercomputing Center, Barcelona, Spain
Cappucci, Fabrizio, European Commission Joint Research Centre, Ispra, Italy
Carrea, Laura, University of Reading, Reading, United Kingdom
Carter, Brendan R., Cooperative Institute for Climate, Ocean, and Ecosystem Studies, University of Washington, Seattle, Washington; NOAA/OAR Pacific Marine Environmental Laboratory, Seattle, Washington
Cerveny, Randall, Department of Geography, Arizona State University, Tempe, Arizona
Cetinić, Ivona, NASA Goddard Space Flight Center, Greenbelt, Maryland; Universities Space Research Association, Columbia, Maryland
Chambers, Don P., College of Marine Science, University of South Florida, St. Petersburg, Florida
Chan, Duo, School of Ocean and Earth Science, University of Southampton, Southampton, United Kingdom
Chandler, Elise, Bureau of Meteorology, Melbourne, Australia
Chang, Kai-Lan, Cooperative Institute for Research in Environmental Sciences, University of Colorado Boulder, Boulder, Colorado; NOAA Chemical Sciences Laboratory, Boulder, Colorado
Charlton, Candice S., Department of Physics, The University of the West Indies, Kingston, Jamaica
Chen, Jack, Environment and Climate Change Canada, Ottawa, Canada
Chen, Lin, Institute for Climate and Application Research (ICAR)/KLME/ILCEC/CIC-FEMD, Nanjing University of Information Science and Technology, Nanjing, China
Cheng, Lijing, International Center for Climate and Environment Sciences, Institute of Atmospheric Physics, Chinese Academy of Sciences, Beijing, China
Cheng, Vincent Y. S., Environment and Climate Change Canada, Toronto, Canada
Chisholm, Lucy, Environment and Climate Change Canada, Halifax, Canada
Christiansen, Hanne H., Arctic Geophysics Department, University Centre in Svalbard, Longyearbyen, Norway; Geology Department, University Centre in Svalbard, Longyearben, Norway
Christy, John R., University of Alabama in Huntsville, Huntsville, Alabama
Chung, Eui-Seok, Korea Polar Research Institute, Incheon, South Korea
Ciasto, Laura M., NOAA/NWS National Centers for Environmental Prediction Climate Prediction Center, College Park, Maryland
Clarke, Leonardo, Department of Physics, The University of the West Indies, Kingston, Jamaica
Clem, Kyle R., School of Geography, Environment and Earth Sciences, Victoria University of Wellington, Wellington, New Zealand
Clingan, Scott, Cooperative Institute for Research in Earth Science, University of Colorado, Boulder, Colorado; NOAA Global Monitoring Laboratory, Boulder, Colorado
Coelho, Caio A.S., Centro de Previsão do Tempo e Estudos Climáticos/National Institute for Space Research, Center for Weather Forecasts and Climate Studies, Cachoeira Paulista, Brazil
Coldewey-Egbers, Melanie, German Aerospace Center (DLR), Oberpfaffenhofen, Germany
Colwell, Steve, British Antarctic Survey, Cambridge, United Kingdom
Cooper, Owen R., NOAA Chemical Sciences Laboratory, Boulder, Colorado
Cornes, Richard C., National Oceanography Centre, Southampton, United Kingdom
Correa, Kris, Servicio Nacional de Meteorología e Hidrología del Perú, Lima, Perú
Costa, Felipe, Centro Internacional para la Investigación del Fenómeno de El Niño (CIIFEN), Guayaquil, Ecuador
Covey, Curt, Lawrence Livermore National Laboratory, Livermore, California
Coy, Lawrence, Science Systems and Applications, Inc., Lanham, Maryland; NASA Goddard Space Flight Center, Greenbelt, Maryland
Crétaux, Jean-Francois, LEGOS (CNES/CNRS/IRD/UPS), Université de Toulouse, Toulouse, France
Crimmins, Theresa, USA National Phenology Network, School of Natural Resources and the Environment, University of Arizona, Tucson, Arizona.
Crotwell, Molly, Cooperative Institute for Research in Earth Science, University of Colorado, Boulder, Colorado; NOAA Global Monitoring Laboratory, Boulder, Colorado
Culpepper, Joshua, Department of Biology, York University, Toronto, Canada
Cunha, Ana P., Centro Nacional de Monitoramento e Alertas de Desastres Naturais CEMADEN, São Paulo, Brazil
Cusicanqui, Diego, Institut de Géosciences de l'Environnement (IGE), Université Grenoble Alpes, INRAE, CNRS, IRD, Grenoble INP, ISTerre, Grenoble, France
Datta, Rajashree T., Department of Atmospheric and Oceanic Sciences, University of Colorado Boulder, Boulder, Colorado
Davis, Sean, NOAA Chemical Sciences Laboratory, Boulder, Colorado
De Bock, Veerle, Royal Meteorological Institute, Ukkel, Belgium
de Jeu, Richard A. M., Planet Labs, Haarlem, The Netherlands
De Laat, Jos, Royal Netherlands Meteorological Institute (KNMI), DeBilt, The Netherlands
Deb, Pranab, Centre for Ocean, River, Atmosphere and Land Sciences (CORAL), Indian Institute of Technology Kharagpur, Kharagpur, India
Decharme, Bertrand, Centre National de Recherches Météorologiques, Météo-France/CNRS, Toulouse, France
Degenstein, Doug, University of Saskatchewan, Saskatoon, Canada
Delaloye, Reynald, Department of Geosciences, University of Fribourg, Fribourg, Switzerland
Derksen, Chris, Climate Research Division, Environment and Climate Change Canada, Toronto, Canada
Diamond, Howard J., NOAA/OAR Air Resources Laboratory, College Park, Maryland
DiGangi, Elizabeth, AEM R&D, Germantown, Maryland
Dindyal, S., Mauritius Meteorological Service, Vacoas, Mauritius
Divine, Dmitry, Norwegian Polar Institute, Fram Centre, Tromsø, Norway
Dokulil, Martin T., Research Institute for Limnology, University of Innsbruck, Mondsee, Austria
Donat, Markus G., Barcelona Supercomputing Center, Barcelona, Spain; Catalan Institution for Research and Advanced Studies (ICREA), Barcelona, Spain
Dong, Shenfu, NOAA/OAR Atlantic Oceanographic and Meteorological Laboratory, Miami, Florida
Dorigo, Wouter A., Department of Geodesy and Geoinformation, TU Wien, Vienna, Austria
Drost Jensen, Caroline, Danish Meteorological Institute, Copenhagen, Denmark
Druckenmiller, Matthew L., National Snow and Ice Data Center, Cooperative Institute for Research in Environmental Sciences, University of Colorado, Boulder, Boulder, Colorado
du Plessis, Marcel, Department of Marine Sciences, University of Gothenburg, Gothenburg, Sweden
Duchemin, Diane, CESBIO, Université de Toulouse, CNES/CNRS/INRAe/IRD/UPS, Toulouse, France
Dugan, Hilary, Department of Integrative Biology, University of Wisconsin-Madison, Madison, Wisconsin
Dulamsuren, Dashkhuu, Institute of Meteorology, Hydrology and Environment, National Agency for Meteorology, Ulaanbaatar, Mongolia
Dunn, Robert J. H., Met Office Hadley Centre, Exeter, United Kingdom
Durre, Imke, NOAA/NESDIS National Center for Environmental Information, Asheville, North Carolina

Dutton, Geoff, Cooperative Institute for Research in the Earth Sciences, NOAA Global Monitoring Laboratory, Boulder, Colorado
Duveiller, Gregory, Max Planck Institute for Biogeochemistry, Jena, Germany
Earl-Spurr, Craig, Bureau of Meteorology, Perth, Australia
Echeverría Garcés, Paola, Instituto Nacional de Meteorología e Hidrología de Ecuador (INAMHI), Quito, Ecuador
Ekici, Mithat, Turkish State Meteorological Service, Ankara, Türkiye
Elias Chereque, Alesksandra, Department of Physics, University of Toronto, Toronto, Canada
Elipot, Shane, Rosenstiel School of Marine, Atmospheric, and Earth Science, University of Miami, Miami, Florida
ElKharrim, M., General Directorate of Meteorology, Rabat, Morocco
Epstein, Howard E., Department of Environmental Sciences, University of Virginia, Charlottesville, Virginia
Espinoza, Jhan-Carlo, Université Grenoble Alpes, Institut des Géosciences de l'Environnement, IRD, CNRS, Grenoble INP, Grenoble, France
Estilow, Thomas W., Rutgers University, Piscataway, New Jersey
Estrella, Nicole, Ecoclimatology, Department of Life Science Systems, TUM School of Life Sciences, Technical University of Munich, Freising, Germany.
Farrell, Sinead, Department of Geographical Sciences, University of Maryland, College Park, Maryland
Fauchereau, Nicolas, National Institute of Water and Atmospheric Research (NIWA), Auckland, New Zealand
Fausto, Robert S., Geological Survey of Denmark and Greenland (GEUS), Copenhagen, Denmark
Feely, Richard A., NOAA/OAR Pacific Marine Environmental Laboratory, Seattle, Washington
Fenimore, Chris, NOAA/NESDIS National Centers for Environmental Information, Asheville, North Carolina
Fereday, David, Met Office Hadley Centre, Exeter, United Kingdom
Fernandez, Denise, National Institute of Water and Atmospheric Research (NIWA), Auckland, New Zealand
Fettweis, Xavier, University of Liège, Liège, Belgium
Fioletov, Vitali E., Environment and Climate Change Canada, Toronto, Canada
Flemming, Johannes, European Centre for Medium-Range Weather Forecasts, Bonn, Germany
Florentine, Caitlyn, Northern Rocky Mountain Science Center, U.S. Geological Survey, Bozeman, Montana
Fogarty, Chris, Canadian Hurricane Centre, Dartmouth, Canada
Fogt, Ryan L., Department of Geography, Ohio University, Athens, Ohio
Forbes, Bruce C., Arctic Centre, University of Lapland, Rovaniemi, Finland
Foster, Michael J., Cooperative Institute for Meteorological Satellite Studies, Space Science and Engineering Center, University of Wisconsin-Madison, Madison, Wisconsin
Franz, Bryan A., NASA Goddard Space Flight Center, Greenbelt, Maryland
Frederikse, Thomas, Planet Labs, Haarlem, The Netherlands
Fricker, Helen A., Scripps Institution of Oceanography, University of California, San Diego, La Jolla, California
Frith, Stacey M., Science Systems and Applications, Inc., Lanham, Maryland; NASA Goddard Space Flight Center, Greenbelt, Maryland
Froidevaux, Lucien, Jet Propulsion Laboratory, California Institute of Technology, Pasadena, California
Frost, Gerald V. (JJ), Alaska Biological Research, Inc., Fairbanks, Alaska
Fu, Shanshan, Nanjing University of Information Science and Technology, Nanjing, China
Fu, Yao, School of Earth and Atmospheric Sciences, Georgia Institute of Technology, Atlanta, Georgia
Füllekrug, Martin, University of Bath, Bath, United Kingdom
Ganter, Catherine, Bureau of Meteorology, Melbourne, Australia
Gao, Meng, NASA Goddard Space Flight Center, Greenbelt, Maryland; Science Systems and Applications Inc., Lanham, Maryland
Garforth, Judith, Woodland Trust, Grantham, United Kingdom.
Garg, Jay, ADNET Systems, Inc., Hampton, Virginia
Gerland, Sebastian, Norwegian Polar Institute, Fram Centre, Tromsø, Norway
Gevorgyan, Artur, Hydrometeorology and Monitoring Center, Yerevan, Armenia
Giglio, Donata, Department of Atmospheric and Oceanic Sciences, University of Colorado Boulder, Boulder, Colorado
Gille, Sarah T., Scripps Institution of Oceanography, University of California, San Diego, La Jolla, California
Gilson, John, Scripps Institution of Oceanography, University of California San Diego, La Jolla, California
Gleason, Karin, NOAA/NESDIS National Centers for Environmental Information, Asheville, North Carolina
Gobron, Nadine, European Commission Joint Research Centre, Ispra, Italy
Godin-Beekmann, Sophie, Laboratoire Atmosphères, Observations Spatiales (LATMOS), UVSQ, Sorbonne Université, CNRS, IPSL, Guyancourt, France
Goes, Marlos, Cooperative Institute for Marine and Atmospheric Studies, University of Miami, Miami, Florida; NOAA/OAR Atlantic Oceanographic and Meteorological Laboratory, Miami, Florida
Goldenberg, Stanley B., NOAA/OAR Atlantic Oceanographic and Meteorological Laboratory, Miami, Florida
Gómez Camacho, Julio, National Meteorological Service of Mexico, Mexico City, Mexico
González Hernández, Yolanda, Centro Internacional para la Investigación del Fenómeno de El Niño (CIIFEN), Guayaquil, Ecuador
Goodman, Steven, Thunderbolt Global Analytics, Huntsville, Alabama
Goto, Atsushi, World Meteorological Organization, Geneva, Switzerland
Graham, Garrett, Cooperative Institute for Satellite Earth System Studies, North Carolina State University, Asheville, North Carolina
Grimm, Alice, Federal University of Parana, Curitiba, Brazil
Grooß, Jens-Uwe, Forschungszentrum Jülich (IEK-7), Jülich, Germany
Gruber, Alexander, Department of Geodesy and Geoinformation, TU Wien, Vienna, Austria
Gu, Guojun, University of Maryland, College Park, Maryland
Guglielmin, Mauro, Department of Theoretical and Applied Sciences, Insubria University, Varese, Italy
Hahn, Sebastian, Department of Geodesy and Geoinformation, TU Wien, Vienna, Austria
Haimberger, Leopold, University of Vienna, Vienna, Austria
Hakmi, S., General Directorate of Meteorology, Rabat, Morocco
Hall, Brad D., NOAA Global Monitoring Laboratory, Boulder, Colorado
Hamlington, Benjamin D., Center for Coastal Physical Oceanography, Old Dominion University, Norfolk, Virginia
Hanna, Edward, Department of Geography and Lincoln Climate Research Group, Lincoln, United Kingdom
Hanssen-Bauer, Inger, Norwegian Meteorological Institute, Oslo, Norway
Harlan, Merritt E., U.S. Geological Survey, Denver, Colorado
Harnos, Daniel S., NOAA/NWS National Centers for Environmental Prediction Climate Prediction Center, College Park, Maryland
Harris, I., National Centre for Atmospheric Science (NCAS), University of East Anglia, Norwich, United Kingdom; Climatic Research Unit, School of Environmental Sciences, University of East Anglia, Norwich, United Kingdom
He, Qiong, Earth System Modeling Center, Nanjing University of Information Science and Technology, Nanjing, China
Heatta, Máret J., Saami Council, Kárášjohka, Norway
Heim, Richard R. Jr., NOAA/NESDIS National Centers for Environmental Information, Asheville, North Carolina

Hemming, Deborah L., Met Office Hadley Centre, Exeter, United Kingdom.; Birmingham Institute of Forest Research, Birmingham University, Birmingham, United Kingdom.

Hendricks, Stefan, Alfred Wegener Institute, Helmholtz Centre for Polar and Marine Research, Bremerhaven, Germany

Hicks, J., NOAA/NWS National Centers for Environmental Prediction Climate Prediction Center, College Park, Maryland

Hidalgo, Hugo G., Center for Geophysical Research and School of Physics, University of Costa Rica, San José, Costa Rica

Hirschi, Martin, Institute for Atmospheric and Climate Science, ETH Zurich, Zürich, Switzerland

Ho, Shu-peng (Ben), NOAA/NESDIS Center for Satellite Applications and Research, College Park, Maryland

Hobbs, Will, Australian Antarctic Program Partnership, Institute for Marine and Antarctic Studies; Australian Research Council Centre of Excellence for Climate Extremes, University of Tasmania, Hobart, Australia

Holzworth, Robert, University of Washington, Seattle, Washington

Horton, Radley M., Columbia Climate School, Columbia University, New York, New York

Hrbáček, Filip, Department of Geography, Masaryk University, Brno, Czech Republic

Hu, Guojie, Cryosphere Research Station on Qinghai-Tibet Plateau, Northwestern Institute of Eco-Environment and Resources, Chinese Academy of Sciences, Beijing, China

Hu, Zeng-Zhen, NOAA/NWS National Centers for Environmental Prediction Climate Prediction Center, College Park, Maryland

Huang, Boyin, NOAA/NESDIS National Centers for Environmental Information, Asheville, North Carolina

Huang, Hongjie, Nanjing University of Information Science and Technology, Nanjing, China

Hurst, Dale, NOAA Global Monitoring Laboratory, Boulder, Colorado

Ialongo, Iolanda, Finnish Meteorological Institute, Helsinki, Finland

Inness, Antje, European Centre for Medium-Range Weather Forecasts, Reading, United Kingdom

Isaksen, Ketil, Norwegian Meteorological Institute, Oslo, Norway

Ishii, Masayoshi, Department of Atmosphere, Ocean, and Earth System Modeling Research, Meteorological Research Institute, Japan Meteorological Agency, Tsukuba, Japan

Jacox, Michael G., NOAA/NMFS Southwest Fisheries Science Center, Monterey, California; NOAA/OAR Physical Sciences Laboratory, Boulder, Colorado

Jadra, Gerardo, Instituto Uruguayo de Meteorología, Montevideo, Uruguay

Jain, Piyush, Environment and Climate Change Canada, Edmonton, Canada

Jersild, Annika, Earth System Science Interdisciplinary Center/Cooperative Institute for Satellite Earth System Studies, University of Maryland, College Park, Maryland

Jeuring, Jelmer, Norwegian Meteorological Institute, Bergen, Norway

Jevrejeva, Svetlana, National Oceanography Centre, Liverpool, United Kingdom

Jia, Gensuo, Institute of Atmospheric Physics, Chinese Academy of Sciences, Beijing, China

John, Viju O., EUMETSAT, Darmstadt, Germany

Johns, William E., Rosenstiel School of Marine, Atmospheric, and Earth Science, University of Miami, Miami, Florida

Johnsen, Bjørn, Norwegian Radiation and Nuclear Safety Authority, Østerås, Norway

Johnson, Bryan, NOAA/OAR Earth System Research Laboratory, Global Monitoring Laboratory, Boulder, Colorado; University of Colorado Boulder, Boulder, Colorado

Johnson, Gregory C., NOAA/OAR Pacific Marine Environmental Laboratory, Seattle, Washington

Jones, P. D., Climatic Research Unit, School of Environmental Sciences, University of East Anglia, Norwich, United Kingdom

Josey, Simon A., Marine Systems Modelling, National Oceanography Center, Southampton, United Kingdom

Jumaux, G., Meteo France, Direction Interregionale Pour L'Ocean Indien, Reunion

Junod, Robert, Earth System Science Center, University of Alabama in Huntsville, Huntsville, Alabama

Kääb, Andreas, Department of Geosciences, University of Oslo, Norway

Kabidi, K., General Directorate of Meteorology, Rabat, Morocco

Kaiser, Johannes W., Norwegian Institute for Air Research (NILU), Kjeller, Norway

Kaleschke, Lars, Alfred Wegener Institute, Helmholtz Centre for Polar and Marine Research, Bremerhaven, Germany

Kaufmann, Viktor, Institute of Geodesy, Working Group Remote Sensing and Photogrammetry, Graz University of Technology, Graz, Austria

Kazemi, Amin Fazl, Iran National Meteorology Organization, Tehran, Iran

Keller, Linda M., Department of Atmospheric and Oceanic Sciences, University of Wisconsin-Madison, Madison, Wisconsin; Antarctic Meteorological Research and Data Center, Space Science and Engineering Center, University of Wisconsin-Madison, Madison, Wisconsin

Kellerer-Pirklbauer, Andreas, Institute of Geography and Regional Science, Cascade – The Mountain Processes and Mountain Hazards Group, University of Graz, Graz, Austria

Kendon, Michael, Met Office Hadley Centre, Exeter, United Kingdom

Kennedy, John, Independent Researcher, Verdun, France

Khalatyan, Yelena, Hydrometeorology and Monitoring Center, Yerevan, Armenia

Khan, Valentina, Hydrometeorological Centre of Russia, World Meteorological Organization (WMO) North EurAsia Climate Center, Moscow, Russia

Khaykin, Sergey, Laboratoire Atmosphères, Observations Spatiales (LATMOS), UVSQ, Sorbonne Université, CNRS, IPSL, Guyancourt, France

Khiem, Mai Van, National Center for Hydro-Meteorological Forecasting, Vietnam Meteorological and Hydrological Administration, Hanoi, Vietnam

Kidd, Richard, EODC GmbH, Vienna, Austria

Killick, Rachel E., Met Office Hadley Center, Exeter, United Kingdom

Kim, Seong-Joong, Korea Polar Research Institute, Incheon, South Korea

King, Tyler V., U.S. Geological Survey, Boise, Idaho

Kipling, Zak, European Centre for Medium-Range Weather Forecasts, Reading, United Kingdom

Kirchmeier-Young, Megan, Environment and Climate Change Canada, Toronto, Canada

Klotzbach, Philip J., Department of Atmospheric Science, Colorado State University, Fort Collins, Colorado

Knaff, John A., NOAA/NESDIS Center for Satellite Applications and Research, Fort Collins, Colorado

Kohler, Jack, Norwegian Polar Institute, Fram Centre, Tromsø, Norway

Koppa, Akash, Hydro-Climate Extremes Lab (H-CEL), Ghent University, Ghent, Belgium

Korshunova, Natalia N., All-Russia Research Institute of Hydrometeorological Information, World Data Center, Obninsk, Russia

Kraemer, Benjamin M., University of Freiburg, Freiburg, Germany

Kramarova, Natalya A., NASA Goddard Space Flight Center, Greenbelt, Maryland

Kromer, Jessica, Department of Geography, Pennsylvania State University, State College, Pennsylvania

Kruger, A. C., Climate Service, South African Weather Service, Pretoria, South Africa

Kumar, Arun, NOAA/NWS National Centers for Environmental Prediction Climate Prediction Center, College Park, Maryland

Kuusela, Mikael, Department of Statistics and Data Science, Carnegie Mellon University, Pittsburg, Pennsylvania

La Fuente, R. Sofia, Vrije Universiteit Brussel, Brussels, Belgium

Laas, Alo, Institute of Agricultural and Environmental Sciences, Estonian University of Life Sciences, Tartumaa, Estonia

Labe, Zachary, M., Atmospheric and Oceanic Sciences Program, Princeton University, Princeton, New Jersey

Editor and Author Affiliations (continued)

Lader, Rick, International Arctic Research Center, University of Alaska Fairbanks, Fairbanks, Alaska

Lait, Leslie, R., Science Systems and Applications, Inc., Lanham, Maryland; NASA Goddard Space Flight Center, Greenbelt, Maryland

Lakatos, Mónika, Climatology Unit, Hungarian Meteorological Service, Budapest, Hungary

Lakkala, Kaisa, Finnish Meteorological Institute, Sodankylä, Finland

Lam, Hoang Phuc, National Center for Hydro-Meteorological Forecasting, Vietnam Meteorological and Hydrological Administration, Hanoi, Vietnam

Lan, Xin, Cooperative Institute for Research in the Earth Sciences, NOAA Global Monitoring Laboratory, Boulder, Colorado; NOAA Global Monitoring Laboratory, Boulder, Colorado

Landschützer, Peter, Flanders Marine Institute, InnovOcean Campus, Ostend, Belgium

Landsea, Chris W., NOAA/NWS National Hurricane Center, Miami, Florida

Lantz, Kathleen O., NOAA Global Monitoring Laboratory, Boulder, Colorado

Lapierre, Jeff, AEM R&D, Germantown, Maryland

Lara, Mark J., Department of Plant Biology, University of Illinois, Urbana, Illinois; Department of Geography, University of Illinois, Urbana, Illinois

Lavado-Casimiro, Waldo, Servicio Nacional de Meteorología e Hidrología del Perú, Lima, Perú

Lavers, David A., European Centre for Medium-Range Weather Forecasts, Reading, United Kingdom

Lazzara, Matthew A., Department of Physical Sciences, School of Arts and Sciences, Madison Area Technical College, Madison, Wisconsin; Antarctic Meteorological Research and Data Center, Space Science and Engineering Center, University of Wisconsin-Madison, Madison, Wisconsin

Leblanc, Thierry, Jet Propulsion Laboratory, California Institute of Technology, Wrightwood, California

Lee, Simon H., Department of Applied Physics and Applied Mathematics, Columbia University, New York, New York

Lee, Tsz-Cheung, Hong Kong Observatory, Hong Kong, China

Leibensperger, Eric, Department of Physics and Astronomy, Ithaca College, Ithaca, New York

Lennard, Chris, Department of Environmental and Geographical Science, University of Cape Town, Cape Town, South Africa

Leuliette, Eric, NOAA/NWS NCWCP Laboratory for Satellite Altimetry, College Park, Maryland

L'Heureux, Michelle, NOAA/NWS National Centers for Environmental Prediction Climate Prediction Center, College Park, Maryland

Lieser, Jan L., Bureau of Meteorology, Melbourne, Australia; Institute for Marine and Antarctic Studies (IMAS), University of Tasmania, Hobart, Australia

Liley, Ben, National Institute of Water & Atmospheric Research (NIWA), Lauder, New Zealand

Lin, I-I, National Taiwan University, Taipei, Taiwan

Liu, Chao, Department of Physical Oceanography, Woods Hole Oceanographic Institution, Woods Hole, Massachusetts

Liu, Yakun, Massachusetts Institute of Technology, Cambridge, Massachusetts

Lo, Y. T. Eunice, Cabot Institute for the Environment, University of Bristol, Bristol, United Kingdom

Locarnini, Ricardo, NOAA/NESDIS National Centers for Environmental Information, Silver Spring, Maryland

Loeb, Norman G., NASA Langley Research Center, Hampton Virginia

Loomis, Bryant D., NASA Goddard Space Flight Center, Greenbelt, Maryland

Lopez, Hosmay, NOAA/OAR Atlantic Oceanographic and Meteorological Laboratory, Miami, Florida

Lorrey, Andrew M., National Institute of Water and Atmospheric Research (NIWA), Auckland, New Zealand

Loyola, Diego, German Aerospace Center (DLR), Oberpfaffenhofen, Germany

Lozier, Susan M., School of Earth and Atmospheric Sciences, Georgia Institute of Technology, Atlanta, Georgia

Lu, Rui, Nanjing University of Information Science and Technology, Nanjing, China

Luks, Bartłomiej, Institute of Geophysics, Polish Academy of Sciences, Warsaw, Poland

Lumpkin, Rick, NOAA/OAR Atlantic Oceanographic and Meteorological Laboratory, Miami, Florida

Luo, Jing-Jia, Institute for Climate and Application Research, (ICAR)/KLME/ILCEC/CIC-FEMD, Nanjing University of Information Science and Technology, Nanjing, China

Luojus, Kari, Arctic Research Centre, Finnish Meteorological Institute, Helsinki, Finland

Lyman, John M., Cooperative Institute for Marine and Atmospheric Research, University of Hawaii, Honolulu, Hawaii; NOAA/OAR Pacific Marine Environmental Laboratory, Seattle, Washington

Macander, Matthew J., Alaska Biological Research, Inc., Fairbanks, Alaska

MacFerrin, Michael, Earth Science and Observation Center, Cooperative Institute for Research in Environmental Sciences, University of Colorado, Boulder, Colorado

MacGilchrist, Graeme M., University of St. Andrews, St Andrews, United Kingdom

MacLennan, Michelle L., Department of Atmospheric and Oceanic Science, University of Colorado Boulder, Boulder, Colorado

Magee, Andrew D., Centre for Water, Climate and Land, School of Environmental and Life Sciences, University of Newcastle, Callaghan, Australia

Magnin, Florence, Laboratoire EDYTEM, CNRS/Université Savoie Mont-Blanc, Le Bourget-du-Lac, France

Magnússon, Rúna Í., Plant Ecology and Nature Conservation Group, Wageningen University & Research, Wageningen, The Netherlands

Mamen, Jostein, Climate Division, Norwegian Meteorological Institute, Oslo, Norway

Mankoff, Ken D., Business Integra, New York, New York; NASA Goddard Institute for Space Studies, New York, New York

Manney, Gloria, NorthWest Research Associates, Inc, Socorro, New Mexico; Department of Physics, New Mexico Institute of Mining and Technology, Socorro, New Mexico

Marengo, Jose A., Centro Nacional de Monitoramento e Alertas de Desastres Naturais CEMADEN, São Paulo, Brazil

Marjan, Mohammadi, Iran National Meteorology Organization, Tehran, Iran

Marouchos, Andreas, CSIRO Environment, Canberra, Australia

Martinez, Rodney, World Meteorological Organization, San Jose, Costa Rica

Massom, Robert A., Australian Antarctic Division, Australian Antarctic Program Partnership (AAPP) and Australian Centre for Excellence in Antarctic Science (ACEAS), Hobart, Australia

Matsuzaki, Shin-Ichiro, National Institute for Environmental Studies, Tsukuba, Japan

Matthews, Tom, Department of Geography, King's College London, London, United Kingdom

Mayer, Michael, University of Vienna, Vienna, Austria; European Centre for Medium-Range Weather Forecasts, Reading, United Kingdom

McBride, C., Climate Service, South African Weather Service, Pretoria, South Africa

McCarthy, Michael, University of Washington, Seattle, Washington

McMahon, Clive R., Sydney Institute of Marine Science, IMOS Animal Tagging, Mosman, Australia

McVicar, Tim R., CSIRO Environment, Canberra, Australian Capital Territory; Australian Research Council Centre of Excellence for Climate Extremes, Sydney, Australia

Mears, Carl A., Remote Sensing Systems, Santa Rosa, California

Medley, Brooke, Cryospheric Sciences Laboratory, NASA Goddard Space Flight Center, Greenbelt, Maryland

Meier, Walter N., National Snow and Ice Data Center, Cooperative Institute for Research in Environmental Sciences, University of Colorado, Boulder, Colorado

Mekonnen, Ademe, North Carolina A&T University, Greensboro, North Carolina
Menzel, Annette, Ecoclimatology, Department of Life Science Systems, TUM School of Life Sciences, Technical University of Munich, Freising, Germany; Institute for Advanced Study, Technical University of Munich, Garching, Germany
Merchant, Christopher J., University of Reading, Reading, United Kingdom
Merio, Leo-Juhani, Finnish Environment Institute (SYKE), Oulu, Finland
Merrifield, Mark A., Cooperative Institute for Marine and Atmospheric Research, University of Hawaii, Honolulu, Hawaii
Meyer, Michael F., U.S. Geological Survey, Madison, Wisconsin
Meyers, Tristan, National Institute of Water and Atmospheric Research (NIWA), Auckland, New Zealand
Mikolajczyk, David E., Antarctic Meteorological Research and Data Center, Space Science and Engineering Center, University of Wisconsin-Madison, Madison, Wisconsin
Miller, John B., NOAA Global Monitoring Laboratory, Boulder, Colorado
Minney, Caitlin, Bureau of Meteorology, Melbourne, Australia
Miralles, Diego G., Hydro-Climate Extremes Lab (H-CEL), Ghent University, Ghent, Belgium
Mishonov, Alexey, Earth System Science Interdisciplinary Center/Cooperative Institute for Satellite Earth System Studies, University of Maryland, College Park, Maryland; NOAA/NESDIS National Centers for Environmental Information, Silver Spring, Maryland
Mitchum, Gary T., College of Marine Science, University of South Florida, St. Petersburg, Florida
Moat, Ben I., National Oceanography Centre, Southampton, United Kingdom
Moise, Aurel, Centre for Climate Research Singapore, Meteorological Service Singapore, Singapore
Molina-Carpio, Jorge, Universidad Mayor de San Andrés, La Paz, Bolivia
Montesano, Paul M., NASA Goddard Space Flight Center, Greenbelt, Maryland
Montzka, Stephan A., NOAA Global Monitoring Laboratory, Boulder, Colorado
Moody, Ronald, Meteorological Service Jamaica, Kingston, Jamaica
Moon, Twila A., National Snow and Ice Data Center, Cooperative Institute for Research in Environmental Sciences, University of Colorado, Boulder, Colorado
Mora, Natali, Center for Geophysical Research, University of Costa Rica, San José, Costa Rica
Morice, Colin, Met Office Hadley Centre, Exeter, United Kingdom
Morino, Isamu, National Institute for Environmental Studies, Tsukuba, Japan
Mostafa, A. E., Department of Seasonal Forecast and Climate Research, Cairo Numerical Weather Prediction, Egyptian Meteorological Authority, Cairo, Egypt
Mote, Thomas L., Department of Geography, University of Georgia, Athens, Georgia
Mrekaj, Ivan, Technical University in Zvolen, Zvolen, Slovakia
Mudryk, Lawrence, Climate Research Division, Environment and Climate Change Canada, Toronto, Ontario, Canada
Muharsyah, Robi, Division of Climate Variability Analysis, Meteorological, Climatological, and Geophysical Agency, Jakarta, Indonesia
Mühle, Jens, Scripps Institution of Oceanography, University of California San Diego, La Jolla, California
Müller, Rolf, Forschungszentrum Jülich (IEK-7), Jülich, Germany
Nance, D., Cooperative Institute for Research in Earth Science, University of Colorado, Boulder, Colorado; NOAA Global Monitoring Laboratory, Boulder, Colorado
Neigh, Christopher S. R., NASA Goddard Space Flight Center, Greenbelt, Maryland
Nerem, R. Steven, Colorado Center for Astrodynamics Research, Cooperative Institute for Research in Environmental Sciences, University of Colorado Boulder, Boulder, Colorado
Newman, Paul A., NASA Goddard Space Flight Center, Greenbelt, Maryland
Nicolas, Julien P., European Centre for Medium-Range Weather Forecasts, Bonn, Germany
Noetzli, Jeannette, WSL Institute for Snow and Avalanche Research SLF Climate Change, Davos Dorf, Switzerland; Extremes and Natural Hazards in Alpine Regions Research Center CERC, Davos Dorf, Switzerland
Noll, Ben, National Institute of Water and Atmospheric Research (NIWA), Auckland, New Zealand
Norton, Taylor, Antarctic Meteorological Research and Data Center, Space Science and Engineering Center, University of Wisconsin-Madison, Madison, Wisconsin
Nyland, Kelsey E., Department of Geography, George Washington University, Washington, DC
O'Keefe, John, The Harvard Forest, Harvard University, Petersham, Massachusetts
Oe, Mitsuho, Japan Meteorological Agency, Tokyo, Japan
Okunaka, Yuka, Tokyo Climate Center, Japan Meteorological Agency, Tokyo, Japan
Orlik, Alexander, GeoSphere, Vienna, Austria
Osborn, Tim J., Climatic Research Unit, School of Environmental Sciences, University of East Anglia, Norwich, United Kingdom
Overland, James E., NOAA Pacific Marine Environmental Laboratory, Seattle, Washington
Pálsson, Finnur, Institute of Earth Sciences, University of Iceland, Reykjavík, Iceland
Parrington, Mark, European Centre for Medium-Range Weather Forecasts, Bonn, Germany
Pasch, Richard J., NOAA/NWS National Hurricane Center, Miami, Florida
Pascual Ramírez, Reynaldo, National Meteorological Service of Mexico, Mexico City, Mexico
Paterson, Linda, Bureau of Meteorology, Perth, Australia
Pellet, Cécile, Department of Geosciences, University of Fribourg, Fribourg, Switzerland
Pelto, Mauri S., Nichols College, Dudley, Massachusetts
Perez, Renellys C., NOAA/OAR Atlantic Oceanographic and Meteorological Laboratory, Miami, Florida
Perovich, Donald K., University of Dartmouth, Hanover, New Hampshire
Petersen, Kyle, Cooperative Institute for Research in Earth Science, University of Colorado, Boulder, Colorado; NOAA Global Monitoring Laboratory, Boulder, Colorado
Petropavlovskikh, Irina, NOAA/OAR Earth System Research Laboratory, Global Monitoring Laboratory, Boulder, Colorado; University of Colorado Boulder, Boulder, Colorado
Petty, Alek, NASA Goddard Space Flight Center, Greenbelt, Maryland
Pezza, Alexandre B., Greater Wellington Regional Council, Wellington, New Zealand
Pezzi, Luciano P., National Institute for Space Research (INPE), São José dos Campos, São Paulo, Brazil
Phillips, Coda, Cooperative Institute for Meteorological Satellite Studies, Space Science and Engineering Center, University of Wisconsin-Madison, Madison, Wisconsin
Phoenix, Gareth K., School of Biosciences, University of Sheffield, Sheffield, United Kingdom
Pierson, Don, Department of Ecology and Genetics, Uppsala University, Uppsala, Sweden
Pinto, Izidine, Royal Netherlands Meteorological Institute (KNMI), De Bilt, The Netherlands
Pita, Ivenis, Cooperative Institute for Marine and Atmospheric Studies, University of Miami, Miami, Florida; NOAA/OAR Atlantic Oceanographic and Meteorological Laboratory, Miami, Florida
Pitts, Michael, NASA Langley Research Center, Hampton, Virginia
Po-Chedley, Stephen, Lawrence Livermore National Laboratory, Livermore, California
Pogliotti, Paolo, Environmental Protection Agency of Valle d'Aosta, Saint Christophe, Italy
Poinar, Kristin, University at Buffalo, Buffalo, New York
Polvani, Lorenzo, Columbia University, New York, New York

Porat, Amos, Israel Meteorological Service, Bet Dagan, Israel
Preimesberger, Wolfgang, Department of Geodesy and Geoinformation, TU Wien, Vienna, Austria
Price, Colin, Tel Aviv University, Tel Aviv, Israel
Purkey, Sarah G., Scripps Institution of Oceanography, University of California San Diego, La Jolla, California
Quispe, Willy R., Servicio Nacional de Meteorología e Hidrología de Bolivia, La Paz, Bolivia
Ramos, Andrea M., Instituto Nacional de Meteorología, Brasilia, Brazil
Randel, William J., National Center for Atmospheric Research, Boulder, Colorado
Raphael, Marilyn N., Department of Geography, University of California, Los Angeles, Los Angeles, California
Raymond, Colin, University of California, Los Angeles, Los Angeles, California
Reagan, James, NOAA/NESDIS National Centers for Environmental Information, Silver Spring, Maryland
Reid, Phillip, Bureau of Meteorology, Melbourne, Australia; Australian Antarctic Program Partnership (AAPP), Hobart, Australia
Rémy, Samuel, HYGEOS, Lille, France
Ressl, Hans, GeoSphere, Vienna, Austria
Ricciardulli, Lucrezia, Remote Sensing Systems, Santa Rosa, California
Richardson, Andrew D., School of Informatics, Computing, and Cyber Systems, Northern Arizona University, Flagstaff, Arizona; Center for Ecosystem Science and Society, Northern Arizona University, Flagstaff, Arizona
Ricker, Robert, NORCE Norwegian Research Centre, Tromsø, Norway
Rivera, Patricia P., Servicio Nacional de Meteorología e Hidrología del Perú, Lima, Perú
Robinson, David A., Rutgers University, Piscataway, New Jersey
Robjhon, M., NOAA/NWS National Centers for Environmental Prediction Climate Prediction Center, College Park, Maryland
Rodell, Matthew, Earth Sciences Division, NASA Goddard Space Flight Center, Greenbelt, Maryland
Rodriguez Guisado, Esteban, Agencia Estatal de Meteorología, Madrid, Spain
Rodriguez-Fernandez, Nemesio, CESBIO, Université de Toulouse, CNES/CNRS/INRAe/IRD/UPS, Toulouse, France
Roebeling, Maarit, Deutscher Wetterdienst, WMO RA VI Regional Climate Centre Network, Offenbach, Germany
Rogers, Cassandra, D. W., Bureau of Meteorology, Melbourne, Australia
Rohini, P., India Meteorological Department, Ministry of Earth Sciences, Pune, India
Romanovsky, Vladimir E., Geophysical Institute, University of Alaska Fairbanks, Fairbanks, Alaska; Earth Cryosphere Institute, Tyumen Science Center, Tyumen, Russia
Ronchail, Josyane, Laboratoire LOCEAN-IPSL, Paris, France
Rosencrans, Matthew, NOAA/NWS National Centers for Environmental Prediction Climate Prediction Center, College Park, Maryland
Rosenlof, Karen, NOAA Chemical Sciences Laboratory, Boulder, Colorado
Rösner, Benjamin, Remote Sensing Section, Deutscher Wetterdienst, Offenbach, Germany
Rozanov, Alexei, University of Bremen, Bremen, Germany
Rozkošný, Jozef, Slovak Hydrometeorological Institute, Bratislava, Slovakia
Rusanovskaya, Olga O., Irkutsk State University, Institute of Biology, Irkutsk, Russia
Rutishauser, This, Swiss Academy of Sciences (SCNAT), Bern, Switzerland
Sabeerali, C. T., India Meteorological Department, Ministry of Earth Sciences, Pune, India
Said, Ryan, Vaisala R&D, Louisville, Colorado
Sakai, Tetsu, Meteorological Research Institute, Japan Meteorological Agency, Tsukuba, Japan
Salinas, Roberto, Direcciónde Meteorología e Hidrología / Dirección Nacional de Aeronáutica Civil, Asunción, Paraguay
Sánchez-Lugo, Ahira, NOAA/NESDIS National Centers for Environmental Information, Asheville, North Carolina
Santee, Michelle L., Jet Propulsion Laboratory, Pasadena, California
Sass, Louis, U.S. Geological Survey, Alaska Science Center, Anchorage, Alaska
Sato, Kanako, Japan Agency for Marine-Earth Science and Technology, Yokosuka, Japan
Sawaengphokhai, Parnchai, ADNET Systems, Inc., Hampton Virginia
Sayouri, A., General Directorate of Meteorology, Rabat, Morocco
Scambos, Theodore A., Cooperative Institute for Research in Environmental Sciences, University of Colorado Boulder, Boulder, Colorado
Scheller, Johan H., Department of Ecoscience, Arctic Research Centre Aarhus University, Roskilde, Denmark
Schenzinger, Verena, Medical University of Innsbruck, Innsbruck, Austria
Schlegel, Robert W., Laboratoire d'Océanographie de Villefranche, Sorbonne Université, Villefranche-sur-mer, France
Schmid, Claudia, NOAA/OAR Atlantic Oceanographic and Meteorological Laboratory, Miami, Florida
Schmid, Martin, Eawag, Department Surface Waters - Research and Management, Kastanienbaum, Switzerland
Schreck, Carl J., Cooperative Institute Satellite Earth System Studies, North Carolina State University, Asheville, North Carolina
Schulz, Cristina, Department of Marine and Environmental Sciences, Northeastern University, Massachusetts
Segele, Z. T., NOAA/NWS National Centers for Environmental Prediction Climate Prediction Center, College Park, Maryland
Seneviratne, Sonia I., ETH Zurich, Department of Environmental Systems Science, Zürich, Switzerland
Sensoy, Serhat, Turkish State Meteorological Service, Ankara, Türkiye
Seong, Ji-In, Climate Change Monitoring Division, Korea Meteorological Administration, Seoul, South Korea
Serna Cuenca, Julieta, Instituto de Hidrología, Meteorología y Estudios Ambientales de Colombia (IDEAM), Bogotá, Colombia
Serreze, Mark C., National Snow and Ice Data Center, Cooperative Institute for Research in Environmental Sciences, University of Colorado, Boulder, Colorado
Sezaki, Fumi, Japan Meteorological Agency, Tokyo, Japan
Shao, Xi, NOAA/NESDIS Center for Satellite Applications and Research, College Park, Maryland
Sharma, Sapna, Department of Biology, York University, Toronto, Canada
Shi, Jia-Rui, Woods Hole Oceanographic Institution, Woods Hole, Massachusetts
Shi, Lei, NOAA/NESDIS National Centers for Environmental Information, Asheville, North Carolina
Shiklomanov, Nikolay I., Department of Geography, George Washington University, Washington, DC
Shimaraeva, Svetlana V., Irkutsk State University, Institute of Biology, Irkutsk, Russia
Shinohara, Ryuichiro, Regional Environment Conservation Division, National Institute for Environmental Studies, Tsukuba, Japan
Shukla, R., ERT, Laurel, Maryland
Silow, Eugene A., Irkutsk State University, Institute of Biology, Irkutsk, Russia
Simmons, Adrian J., European Centre for Medium-Range Weather Forecasts, Reading, United Kingdom
Smeed, David A., National Oceanography Centre, Southampton, United Kingdom
Smith, Adam, NOAA/NESDIS National Centers for Environmental Information, Asheville, North Carolina
Smith, Benjamin E., Polar Science Center, Applied Physics Laboratory, University of Washington, Seattle, Washington
Smith, Ryan H., NOAA/OAR Atlantic Oceanographic and Meteorological Laboratory, Miami, Florida
Smith, Sharon L., Geological Survey of Canada, Natural Resources Canada, Ottawa, Canada
Soden, Brian J., University of Miami, Miami, Florida

Sofieva, Viktoria, Finnish Meteorological Institute, Helsinki, Finland
Soldo, Logan, Cooperative Institute for Research in the Environmental Sciences, University of Colorado, Boulder, Boulder, Colorado
Souza, Everaldo, Federal University of Pará (UFPA), Belém, Brazil
Spence-Hemmings, Jacqueline, Meteorological Service Jamaica, Kingston, Jamaica
Spillane, Sandra, Met Éireann, Dublin, Ireland
Sreejith, O. P., India Meteorological Department, Ministry of Earth Sciences, Pune, India
Srivastava, A. K., India Meteorological Department, Ministry of Earth Sciences, Pune, India
Stackhouse, Jr., Paul W., NASA Langley Research Center, Hampton, Virginia
Stammerjohn, Sharon, Institute of Arctic and Alpine Research, University of Colorado Boulder, Boulder, Colorado
Stauffer, Ryan, Atmospheric Chemistry and Dynamics Laboratory, NASA Goddard Space Flight Center, Greenbelt, Maryland
Steinbrecht, Wolfgang, Deutscher Wetterdienst, Hohenpeissenberg, Germany
Steiner, Andrea K., Wegener Center for Climate and Global Change, University of Graz, Graz, Austria
Stella, Jose L., Servicio Meteorológico Nacional, Buenos Aires, Argentina
Stephenson, Tannecia S., Department of Physics, The University of the West Indies, Kingston, Jamaica
Stevens, Laura, Cooperative Institute for Satellite Earth System Studies, North Carolina State University, Asheville, North Carolina
Stoy, Paul, C., Biological Systems Engineering, College of Agricultural and Life Sciences, University of Wisconsin-Madison, Madison, Wisconsin
Stradiotti, Pietro, Department of Geodesy and Geoinformation, TU Wien, Vienna, Austria
Streletskiy, Dmitry A., Department of Geography, George Washington University, Washington, DC
Sukianto, Thea, Department of Statistics and Data Science, Carnegie Mellon University, Pittsburg, Pennsylvania
Svendby, Tove, Norwegian Institute for Air Research (NILU), Kjeller, Norway
Sweet, William, NOAA/NOS Center for Operational Oceanographic Products and Services, Silver Spring, Maryland
Taha, Ghassan, Morgan State University, Baltimore, Maryland; NASA Goddard Flight Center, Greenbelt, Maryland
Takahashi, Kiyotoshi, Tokyo Climate Center, Japan Meteorological Agency, Tokyo, Japan
Takemura, Kazuto, Tokyo Climate Center, Japan Meteorological Agency, Tokyo, Japan
Taylor, Michael A., Department of Physics, The University of the West Indies, Kingston, Jamaica
Tedesco, Marco, Lamont-Doherty Earth Observatory, Columbia University, Palisades, New York; NASA Goddard Institute of Space Studies, New York, New York
Thackeray, Stephen J., United Kingdom Centre for Ecology & Hydrology, Lancaster, United Kingdom.
Thiaw, W. M., NOAA/NWS National Centers for Environmental Prediction Climate Prediction Center, College Park, Maryland
Thibert, Emmanuel, Institut de Géosciences de l'Environnement (IGE), Université Grenoble Alpes, INRAE, CNRS, IRD, Grenoble INP, ISTerre, Grenoble, France
Thomalla, Sandy, Southern Ocean Carbon-Climate Observatory, Council for Scientific and Industrial Research (CSIR), Pretoria, South Africa; Marine and Antarctic Research Centre for Innovation and Sustainability, Department of Oceanography, University of Cape Town, Cape Town, South Africa
Thoman, Richard L., International Arctic Research Center, University of Alaska Fairbanks, Fairbanks, Alaska
Thompson, Philip R., Cooperative Institute for Marine and Atmospheric Research, University of Hawaii, Honolulu, Hawaii
Thomson, Laura, Queen's University, Kingston, Ontario, Canada
Thorsteinsson, Thorsteinn, Icelandic Meteorological Office, Reykjavík, Iceland
Tian-Kunze, Xiangshan, Alfred Wegener Institute, Helmholtz Centre for Polar and Marine Research, Bremerhaven, Germany
Timmermans, Mary-Louise, Yale University, New Haven, Connecticut
Timofeyev, Maxim A., Institute of Biology, Irkutsk State University, Irkutsk, Russia
Tømmervik, Hans, Norwegian Institute for Nature Research, Trondheim, Norway; FRAM – High North Research Centre for Climate and the Environment, Tromsø, Norway
Tourpali, Kleareti, Aristotle University, Thessaloniki, Greece
Trachte, Katja, Brandenburg University of Technology (BTU), Cottbus-Senftenberg, Germany
Trewin, Blair C., Bureau of Meteorology, Melbourne, Australia
Triñanes, Joaquin A., Laboratory of Systems, Technological Research Institute, Universidad de Santiago de Compostela, Campus Universitario Sur, Santiago de Compostela, Spain; Cooperative Institute for Marine and Atmospheric Studies, Rosenstiel School of Marine, Atmospheric, and Earth Science, University of Miami, Miami, Florida; NOAA/OAR Atlantic Oceanographic and Meteorological Laboratory, Miami, Florida
Tripathy, Sarat Chandra, National Centre for Polar and Ocean Research, Vasco da Gama, India
Tronquo, Emma, Hydro-Climate Extremes Lab (H-CEL), Ghent University, Ghent, Belgium
Trotman, Adrian, Caribbean Institute for Meteorology and Hydrology, Bridgetown, Barbados
Truchelut, Ryan E., WeatherTiger, Tallahassee, Florida
Trusel, Luke D., Department of Geography, Pennsylvania State University, State College, Pennsylvania
Turner, Katherine, Department of Geosciences, University of Arizona, Tucson, Arizona; Geophysical Fluid Dynamics Laboratory, Princeton, New Jersey; Department of Atmospheric and Oceanic Sciences, Princeton University, Princeton, New Jersey
Tye, Mari R., National Center for Atmospheric Research, Boulder, Colorado
Uehling, John, Cooperative Institute Satellite Earth System Studies, North Carolina State University, Asheville, North Carolina
van der A, Ronald, Royal Netherlands Meteorological Institute (KNMI), De Bilt, The Netherlands
van der Linden, Roderick, Deutscher Wetterdienst, Offenbach, Germany
van der Schalie, Robin, Planet Labs, Haarlem, The Netherlands
van der Schrier, Gerard, Royal Netherlands Meteorological Institute (KNMI), De Bilt, The Netherlands
Van Meerbeeck, Cédric J., Caribbean Institute for Meteorology and Hydrology, Bridgetown, Barbados
van Vliet, Arnold J. H., Environmental Systems Analysis Group, Wageningen University & Research, The Netherlands
Vazife, Ahad, Iran National Meteorology Organization, Tehran, Iran
Verburg, Piet, National Institute of Water and Atmospheric Research (NIWA), Wellington, New Zealand
Vernier, Jean-Paul, NASA Langley Research Center, Hampton, Virginia
Vimont, Isaac J., NOAA Global Monitoring Laboratory, Boulder, Colorado
Virasami, R., Mauritius Meteorological Service, Vacoas, Mauritius
Virts, Katrina, University of Huntsville in Alabama, Huntsville, Alabama
Vivero, Sebastián, Department of Geosciences, University of Fribourg, Fribourg, Switzerland
Volkov, Denis L., Cooperative Institute for Marine and Atmospheric Studies, University of Miami, Miami, Florida; NOAA/OAR Atlantic Oceanographic and Meteorological Laboratory, Miami, Florida
Vömel, Holger, National Center for Atmospheric Research, Boulder, Colorado

Editor and Author Affiliations (continued)

Vose, Russell S., NOAA/NESDIS National Centers for Environmental Information, Asheville, North Carolina

Waigl, Christine F., Geophysical Institute, University of Alaska Fairbanks, Fairbanks, Alaska

Walker, Donald (Skip) A., Institute of Arctic Biology, University of Alaska Fairbanks, Fairbanks, Alaska

Walsh, John E., International Arctic Research Center, University of Alaska Fairbanks, Fairbanks, Alaska

Wang, Bin, School of Ocean and Earth Science and Technology, Department of Meteorology, University of Hawaii at Manoa, Honolulu, Hawaii; International Pacific Research Center, Honolulu, Hawaii

Wang, Hui, NOAA/NWS National Centers for Environmental Prediction Climate Prediction Center, College Park, Maryland

Wang, Muyin, NOAA Pacific Marine Environmental Laboratory, Seattle, Washington; Cooperative Institute for Climate, Ocean, and Ecosystem Studies, University of Washington, Seattle, Washington

Wang, Ray H. J., Georgia Institute of Technology, Atlanta, Georgia

Wanninkhof, Rik, NOAA/OAR Atlantic Oceanographic and Meteorological Laboratory, Miami, Florida

Warnock, Taran, University of Saskatchewan, Saskatoon, Canada

Weber, Mark, University of Bremen, Bremen, Germany

Webster, Melinda, Polar Science Center, Applied Physics Laboratory, University of Washington, Seattle, Washington

Wehrlé, Adrian, University of Zürich, Zürich, Switzerland

Weller, Robert A., Department of Physical Oceanography, Woods Hole Oceanographic Institution, Woods Hole, Massachusetts

Westberry, Toby K., Oregon State University, Corvallis, Oregon

Widlansky, Matthew J., Cooperative Institute for Marine and Atmospheric Research, University of Hawaii, Honolulu, Hawaii

Wiese, David N., Jet Propulsion Laboratory, California Institute of Technology, Pasadena, California

Wild, Jeannette D., Earth System Science Interdisciplinary Center, University of Maryland, College Park, Maryland; NOAA/NESDIS Center for Satellite Applications and Research, College Park, Maryland

Willems, An, Royal Meteorological Institute, Ukkel, Belgium

Willett, Kate M., Met Office Hadley Centre, Exeter, United Kingdom

Williams, Earle, Massachusetts Institute of Technology, Cambridge, Massachusetts

Willis, Josh K., Jet Propulsion Laboratory, California Institute of Technology, Pasadena, California

Wolken, Gabriel J., Alaska Division of Geological & Geophysical Surveys, Fairbanks, Alaska; University of Alaska Fairbanks, Fairbanks, Alaska

Wong, Takmeng, NASA Langley Research Center, Hampton, Virginia

Wood, Kimberly M., Department of Hydrology and Atmospheric Sciences, University of Arizona, Tucson, Arizona

Woolway, Richard Iestyn, School of Ocean Sciences, Bangor University, Bangor, United Kingdom

Wouters, Bert, Department of Geoscience & Remote Sensing, Delft University of Technology, Delft, The Netherlands

Wu, Francis, Environment and Climate Change Canada, Vancouver, Canada

Yang, Dedi, Environmental Sciences Division, Oak Ridge National Laboratory, Oak Ridge, Tennessee

Yin, Xungang, NOAA/NESDIS National Centers for Environmental Information, Asheville, North Carolina

Yin, Ziqi, Department of Atmospheric and Oceanic Sciences, University of Colorado Boulder, Boulder, Colorado

Yu, Lisan, Department of Physical Oceanography, Woods Hole Oceanographic Institution, Woods Hole, Massachusetts

Zeng, Zhenzhong, School of Environmental Science and Engineering, Southern University of Science and Technology, Shenzhen, China

Zhang, Huai-min, NOAA/NESDIS National Centers for Environmental Information, Asheville, North Carolina

Zhang, Peiqun, Beijing Climate Center, Beijing, China

Zhao, Lin, School of Geographical Sciences, Nanjing University of Information Science and Technology, Nanjing, China

Zhong, Feng, Hydro-Climate Extremes Lab (H-CEL), Ghent University, Ghent, Belgium

Zhu, Zhiwei, Nanjing University of Information Science and Technology, Nanjing, China

Ziemke, Jerry R., Goddard Earth Sciences Technology and Research, Morgan State University, Baltimore, Maryland; NASA Goddard Space Flight Center, Greenbelt, Maryland

Ziese, Markus, Global Precipitation Climatology Centre, Deutscher Wetterdienst, Offenbach, Germany

Zotta, Ruxandra M., TU Wien, Vienna, Austria

Zou, Cheng-Zhi, NOAA/NESDIS Center for Satellite Applications and Research, College Park, Maryland

Editorial and Production Team

Allen, Jessicca, Graphics Support, Cooperative Institute for Satellite Earth System Studies, North Carolina State University, Asheville, North Carolina

Camper, Amy V., Graphics Support, Innovative Consulting and Management Services, LLC, NOAA/NESDIS National Centers for Environmental Information, Asheville, North Carolina

Haley, Bridgette O., Graphics Support, NOAA/NESDIS National Centers for Environmental Information, Asheville, North Carolina

Hammer, Gregory, Content Team Lead, Communications and Outreach, NOAA/NESDIS National Centers for Environmental Information, Asheville, North Carolina

Love-Brotak, S. Elizabeth, Lead Graphics Production, NOAA/NESDIS National Centers for Environmental Information, Asheville, North Carolina

Ohlmann, Laura, Technical Editor, Innovative Consulting and Management Services, LLC, NOAA/NESDIS National Centers for Environmental Information, Asheville, North Carolina

Noguchi, Lukas, Technical Editor, Innovative Consulting and Management Services, LLC, NOAA/NESDIS National Centers for Environmental Information, Asheville, North Carolina

Riddle, Deborah B., Graphics Support, NOAA/NESDIS National Centers for Environmental Information, Asheville, North Carolina

Veasey, Sara W., Visual Communications Team Lead, Communications and Outreach, NOAA/NESDIS National Centers for Environmental Information, Asheville, North Carolina

STATE OF THE CLIMATE IN 2023

INTRODUCTION

T. Boyer, J. Blunden, and R. J. H. Dunn

Special Online Supplement to the *Bulletin of the American Meteorological Society* Vol. 105 No. 8, August, 2024

https://doi.org/10.1175/2024BAMSStateoftheClimate_Intro.1
Corresponding author: Jessica Blunden / jessica.blunden@noaa.gov
©2024 American Meteorological Society
For information regarding reuse of this content and general copyright information, consult the AMS Copyright Policy.

STATE OF THE CLIMATE IN 2023

Introduction

Editors

Jessica Blunden
Tim Boyer

Chapter Editors

Anthony Arguez
Josh Blannin
Peter Bissolli
Kyle R. Clem
Howard J. Diamond
Matthew L. Druckenmiller
Robert J. H. Dunn
Catherine Ganter
Nadine Gobron
Gregory C. Johnson
Rick Lumpkin
Rodney Martinez
Ademe Mekonnen
John B. Miller
Twila A. Moon
Marilyn N. Raphael
Carl J. Schreck III
Laura Stevens
Richard L. Thoman
Kate M. Willett
Zhiwei Zhu

Technical Editor

Lukas Noguchi

BAMS Special Editor for Climate

Timothy DelSole

American Meteorological Society

Cover Credit:
The port of the city of Tefé, Brazil along Lake Tefé during drought conditions in the Central Amazon (30 September 2023). Photo credit: Ayan Fleischmann, Mamirauá Institute for Sustainable Development.

How to cite this document:
Introduction is one chapter from the *State of the Climate in 2023* annual report and is available from https://doi.org/10.1175/2024BAMSStateoftheClimate_Intro.1. Compiled by NOAA's National Centers for Environmental Information, *State of the Climate in 2023* is based on contributions from scientists from around the world. It provides a detailed update on global climate indicators, notable weather events, and other data collected by environmental monitoring stations and instruments located on land, water, ice, and in space. The full report is available from https://doi.org/10.1175/2024BAMSStateoftheClimate.1.

Citing the complete report:
Blunden, J. and T. Boyer, Eds., 2024: "State of the Climate in 2023". Bull. Amer. Meteor. Soc., 105 (8), Si–S483 https://doi.org/10.1175/2024BAMSStateoftheClimate.1.

Citing this chapter:
Boyer, T., J. Blunden, and R J. H. Dunn, 2024: Introduction [in "State of the Climate in 2023"]. Bull. Amer. Meteor. Soc., 105 (8), S1–S11, https://doi.org/10.1175/2024BAMSStateoftheClimate_Intro.1.

Editor and Author Affiliations (alphabetical by name)

Blunden, Jessica, NOAA/NESDIS National Centers for Environmental Information, Asheville, North Carolina

Boyer, Tim, NOAA/NESDIS National Centers for Environmental Information, Silver Spring, Maryland

Dunn, Robert J. H., Met Office Hadley Centre, Exeter, United Kingdom

Editorial and Production Team

Allen, Jessicca, Graphics Support, Cooperative Institute for Satellite Earth System Studies, North Carolina State University, Asheville, North Carolina

Camper, Amy V., Graphics Support, Innovative Consulting and Management Services, LLC, NOAA/NESDIS National Centers for Environmental Information, Asheville, North Carolina

Haley, Bridgette O., Graphics Support, NOAA/NESDIS National Centers for Environmental Information, Asheville, North Carolina

Hammer, Gregory, Content Team Lead, Communications and Outreach, NOAA/NESDIS National Centers for Environmental Information, Asheville, North Carolina

Love-Brotak, S. Elizabeth, Lead Graphics Production, NOAA/NESDIS National Centers for Environmental Information, Asheville, North Carolina

Ohlmann, Laura, Technical Editor, Innovative Consulting and Management Services, LLC, NOAA/NESDIS National Centers for Environmental Information, Asheville, North Carolina

Noguchi, Lukas, Technical Editor, Innovative Consulting and Management Services, LLC, NOAA/NESDIS National Centers for Environmental Information, Asheville, North Carolina

Riddle, Deborah B., Graphics Support, NOAA/NESDIS National Centers for Environmental Information, Asheville, North Carolina

Veasey, Sara W., Visual Communications Team Lead, Communications and Outreach, NOAA/NESDIS National Centers for Environmental Information, Asheville, North Carolina

2. INTRODUCTION

T. Boyer, J. Blunden, and R. J. H. Dunn

The year 2023 was marked by the highest global mean surface temperature on record, exceeding the previous record-high year (2016) by a large margin of 0.13°C to 0.17°C, according to a range of scientific analyses presented in this report. This record high was evident in many other global climate indicators (Plate 1.1; Chapter 2, Global Climate). For example, humid-heat indices, which are relevant to human comfort and safety in ambient air temperature and humidity, were also record high in 2023, with humid-heat intensity (anomaly of maximum daily wet-bulb temperature) having doubled the value from the previous record year (1998). Sidebars 2.1, 3.1, and 5.2 detail the extreme heat observed across the globe in 2023 and its impacts across land, ocean, and ice-covered regions. Still, as is evident from the compendium of statistics, analyses, and events across this year's *State of the Climate* report, cause and effect of a changing climate are more complex than simply the measure of surface temperatures. The year 2023 began in the La Niña phase of the El Niño–Southern Oscillation, having been the prevalent phase over much of the previous three years. A transition occurred during the year that led to the establishment of an El Niño in April/May/June, which reached the threshold necessary to be classified as strong by August/September/October (Chapter 4; The Tropics). The El Niño–Southern Oscillation is a coupled atmosphere–ocean system where surface temperatures are not the only factor, though they are a distinct indicator of its state. For example, the Madden-Julian Oscillation (a transient rainfall suppression/enhancement atmospheric phenomenon) contributed to the westerly wind bursts that hastened the breakdown of the La Niña in the early part of the year and the buildup of the El Niño into June. The timing of the establishment and strengthening of El Niño atmospheric patterns was critical in 2023, as it roughly coincided with the Atlantic Hurricane season. Despite favorable ocean conditions over the Gulf of Mexico and much of the North Atlantic (i.e., tropical cyclone heat potential above the threshold conducive to hurricane generation), the Gulf of Mexico had a below-average year for tropical cyclone activity in 2023, which is typical during El Niño. Atypically, the whole North Atlantic basin had an above-average season for both number of cyclones and accumulated cyclone energy.

The Gulf of Mexico example shows the value of the *State of the Climate* report in bringing together information from different disciplines and across geographic scales from global to regional to local. Another example, the disappearance of Ice Worm Glacier in the Pacific Northwest region of the United States, is depicted on the cover of the report. For the first time, all reference glaciers of the World Glacier Monitoring Service lost mass in 2023. While Ice Worm Glacier was not a reference glacier, it had been monitored continuously for 40 years. Both Ice Worm Glacier and St. Anna Glacier (also known as St. Annafirn Glacier) in Switzerland, the other glacier which disappeared in 2023 (after having been monitored for 12 years), were very small glaciers (less than 0.5 km^2 area) when monitoring began, so their disappearance did not alter to any degree the global alpine glacier mass balance. However, these glacier disappearances are reflective of the global pattern of glacial mass loss. Within 10 km of Ice Worm Glacier, five other glaciers have disappeared since 2015. Local and regional events such as these emphasize the impacts of a changing climate at a scale, which makes it easier to understand the statistics and analyses of climate at the global scale. Chapter 7, Regional Climates, provides an exhaustive listing of air temperature, precipitation, and significant events in regions and subregions across the globe. It is here that local impacts, the statistics and analyses of events, and trends at larger scales are most minutely detailed. Moreover, pairing this regional/local information with the information from the other chapters of the *State of the Climate* can lead to a better understanding

of the complex factors that contribute to local conditions and events, and provides us with a clearer understanding of global climate. The cover of this chapter (Chapter 1; Introduction) shows satellite imagery of the Rio Negro River as it flows past Manaus, Brazil. In October 2023, the water level on the Rio Negro at the port of Manaus was at its lowest level since 1902. The factors that led to the low water level are the hydrological cycles affected by both the La Niña at the beginning of the year and the El Niño later in the year as well as record-high sea surface temperatures globally (Espinoza et al. 2024). There are numerous other details at the regional and local level in the *State of the Climate*—such as Hurricane Otis' unexpected intensification from Category 1 to Category 5 (Sidebar 4.1), the record extent of wildfires in Canada (Sidebar 7.1), the record-high temperatures in northern China (Sidebar 7.4), and the record-low sea ice extent in the Southern Ocean (section 6f)—from which we could extract or already have extracted a better understanding of the local and global climate system.

The compilation of the *State of the Climate* is possible due to the dedication of the chapter editors and 592 section authors from 59 countries. Plate 1.1 provides information for essential climate variables detailed in the report in the form of 36 time series, showing the climate variables for 2023 in the context of the long-term record. The sequence of the *State of the Climate in 2023* is similar to previous years: Chapter 1, Introduction (i.e., this chapter); Chapter 2, Global Climate; Chapter 3, Global Oceans; Chapter 4, The Tropics; Chapter 5, The Arctic; Chapter 6, Antarctica and the Southern Ocean; and Chapter 7, Regional Climates, which covers the seven regions of North America, Central America and the Caribbean, South America, Africa, Europe and the Middle East, Asia, and Oceania. In a notable change from previous years, Chapter 8, Relevant datasets and sources, has been removed. Instead, the datasets used in the *State of the Climate* are found in appendices at the ends of Chapters 2–6 and are separated by section. This is intended to make it easier for researchers to find and access the datasets used for the statistics and analysis in the individual sections, in the hope that they will utilize the datasets and the information provided in the *State of the Climate* to further understanding of Earth's climate system on global, regional, and local scales. Also new to this year's report are sections on humid-heat extremes over land (section 2d2), which were introduced last year as a sidebar and serve as a climate indicator more directly connected to human health as opposed to surface temperature. Another new addition is a section on stratospheric aerosols (section 2g5), an indicator that was introduced in the *State of the Climate in 2019* and is instrumental in tracking the ongoing effects of the Hunga Tonga–Hunga Ha'apai eruption of 2022. The section on lightning flashes has been replaced by a section on thunder hours, which is a proxy for lightning activity.

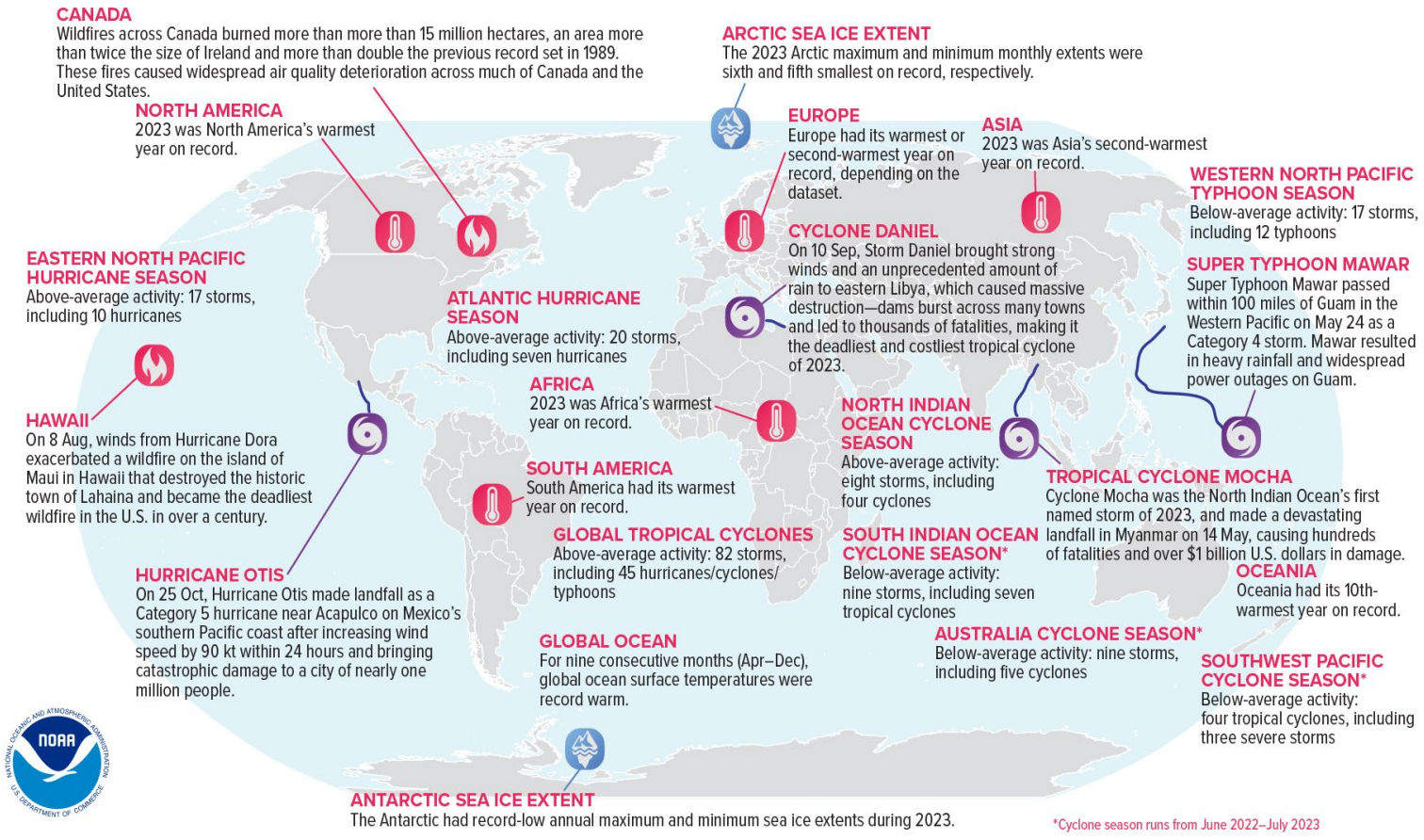

Fig. 1.1. Geographical distribution of selected notable climate anomalies and events in 2023.

Plate 1.1. (Next page.) Global (or representative) average time series for essential climate variables through 2023. Anomalies are shown relative to the base period in parentheses, although base periods used in other sections of the report may differ. The numbers in the parentheses in the lower left or right side of each panel indicate how many in situ (red), reanalysis (blue), and satellite (orange), datasets are used to create each time series in that order. (a) Northern Hemisphere (NH) polar stratospheric ozone (Mar); (b) Southern Hemisphere (SH) polar stratospheric ozone (Oct); (c) surface temperature; (d) night marine air temperature; (e) lower tropospheric temperature; (f) lower stratospheric temperature; (g) extremes (warm days [solid] and cool days [dotted]); (h) Arctic sea ice extent (max [solid]) and min [dotted]); (i) Antarctic sea ice extent (max [solid] and min [dotted]); (j) glacier cumulative mean specific balance; (k) NH snow cover extent; (l) NH lake ice duration; (m) Mauna Loa apparent transmission; (n) lower stratospheric water vapor; (o) global land evaporation; (p) total column water vapor – land; (q) total column water vapor – ocean; (r) upper tropospheric humidity; (s) specific humidity – land; (t) specific humidity – ocean; (u) relative humidity – land; (v) relative humidity – ocean; (w) precipitation – land; (x) precipitation – ocean; (y) ocean heat content (0–700 m); (z) sea level rise; (aa) tropospheric ozone; (ab) tropospheric wind speed at 850 hPa; (ac) land wind speed; (ad) ocean wind speed; (ae) biomass burning; (af) cloud radiative effect; (ag) soil moisture; (ah) terrestrial groundwater storage; (ai) fraction of absorbed photosynthetically active radiation (FAPAR); (aj) land surface albedo – visible (solid) and infrared (dotted).

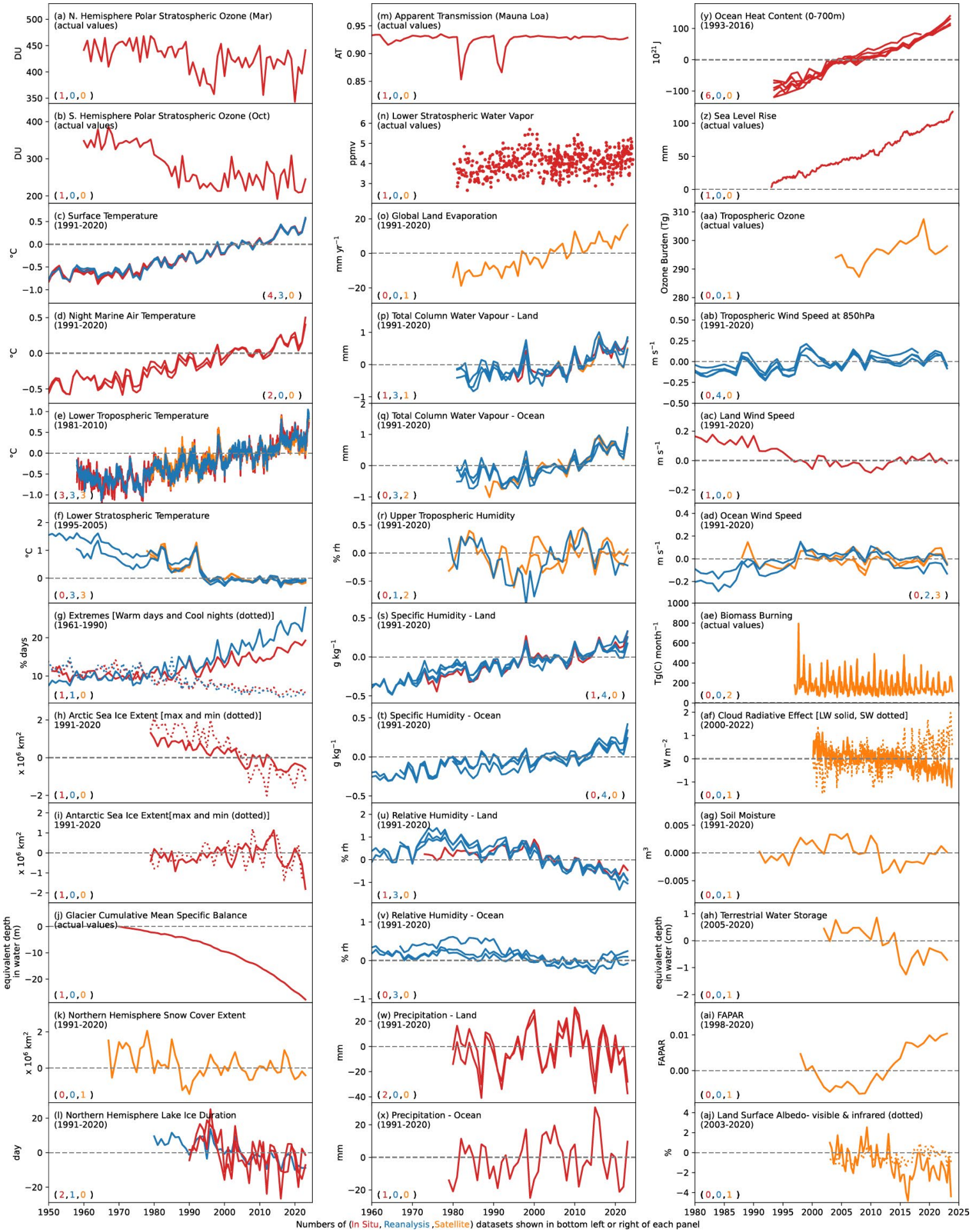

Numbers of (In Situ, Reanalysis ,Satellite) datasets shown in bottom left or right of each panel

Essential Climate Variables

J. BLUNDEN, T. BOYER, AND R. J. H. DUNN

The following variables are considered fully monitored in this report, in that there are sufficient spatial and temporal data, with peer-reviewed documentation to characterize them on a global scale:

- Surface atmosphere: air pressure, precipitation, temperature, water vapor, wind speed and direction
- Upper atmosphere: Earth radiation budget, temperature, water vapor, wind speed and direction
- Atmospheric composition: carbon dioxide, methane and other greenhouse gases, ozone
- Ocean physics: ocean surface heat flux, sea ice, sea level, surface salinity, sea surface temperature, subsurface salinity, subsurface temperature, surface currents, surface stress
- Ocean biogeochemistry: ocean color
- Ocean biogeosystems: plankton
- Land: albedo, river discharge, snow

The following variables are considered partially monitored, in that there is systematic, rigorous measurement found in this report, but some coverage of the variable in time and space is lacking due to observing limitations or availability of data or authors:

- Atmospheric composition: aerosols properties, cloud properties, precursors of aerosol and ozone
- Upper atmosphere: lightning
- Ocean physics: subsurface currents
- Ocean biogeochemistry: inorganic carbon
- Land: above-ground biomass, anthropogenic greenhouse gas fluxes, fire, fraction of absorbed photosynthetically active radiation, glaciers, groundwater, ice sheets and ice shelves, lakes, permafrost, soil moisture
- Surface atmosphere: surface radiation budget

The following variables are not yet covered in this report, or are outside the scope of it.

- Ocean physics: sea state
- Ocean biogeochemistry: nitrous oxide, nutrients, oxygen, transient tracers
- Ocean biogeosystems: marine habitat properties
- Land: anthropogenic water use, land cover, land surface temperature, latent and sensible heat fluxes, leaf area index, soil carbon

Acknowledgements

The editors thank the BAMS editorial staff, in particular Bryan Hanssen, who provided technical guidance and oversaw publication of the report; Andrea Herbst, who provided peer review support; and Nicole Rietmann, who oversaw the hundreds of citations and references this year; and the NCEI Graphics team for facilitating the construction of the report and executing the countless number of technical edits needed. We thank our technical editor Lukas Noguchi for his dedication and attention to detail. We also express our gratitude to Dr. Timothy DelSole, who served as the AMS special editor for this report. Finally, we thank all of the authors and chapter editors who provide these valuable contributions each year, always with an aim to improve and expand their analyses for the readers.

References

Espinoza, J. C., J. C. Jimenez, J. A. Marengo, J. Schongart, J. Ronchail, W. Lavado-Casimiro, and J. V. M. Ribeiro, 2024: The new record of drought and warmth in the Amazon in 2023 related to regional and global climatic features. *Sci. Rep.*, **14**, 8107, https://doi.org/10.1038/s41598-024-58782-5.

STATE OF THE CLIMATE IN 2023

GLOBAL CLIMATE

R. J. H. Dunn, J. Blannin, N. Gobron, J. B. Miller, and K. M. Willett, Eds.

Special Online Supplement to the *Bulletin of the American Meteorological Society* Vol. 105, No. 8, August, 2024

https://doi.org/10.1175/BAMS-D-24-0116.1

Corresponding author: Robert Dunn / robert.dunn@metoffice.gov.uk

©2024 American Meteorological Society
For information regarding reuse of this content and general copyright information, consult the AMS Copyright Policy.

STATE OF THE CLIMATE IN 2023
Global Climate

Editors

Jessica Blunden
Tim Boyer

Chapter Editors

Anthony Arguez
Josh Blannin
Peter Bissolli
Kyle R. Clem
Howard J. Diamond
Matthew L. Druckenmiller
Robert J. H. Dunn
Catherine Ganter
Nadine Gobron
Gregory C. Johnson
Rick Lumpkin
Rodney Martinez
Ademe Mekonnen
John B. Miller
Twila A. Moon
Marilyn N. Raphael
Carl J. Schreck III
Laura Stevens
Richard L. Thoman
Kate M. Willett
Zhiwei Zhu

Technical Editor

Lukas Noguchi

BAMS Special Editor for Climate

Timothy DelSole

American Meteorological Society

Cover Credit:
Aerial photo of smoke from wildfires in Alberta, Canada, on 5 May 2023. (Photo credit: Alberta Forestry and Parks)

How to cite this document:
Global Climate is one chapter from the *State of the Climate in 2023* annual report and is available from https://doi.org/10.1175/BAMS-D-24-0116.1. Compiled by NOAA's National Centers for Environmental Information, *State of the Climate in 2023* is based on contributions from scientists from around the world. It provides a detailed update on global climate indicators, notable weather events, and other data collected by environmental monitoring stations and instruments located on land, water, ice, and in space. The full report is available from https://doi.org/10.1175/2024BAMSStateoftheClimate.1.

Citing the complete report:
Blunden, J. and T. Boyer, Eds., 2024: "State of the Climate in 2023". Bull. Amer. Meteor. Soc., 105 (8), Si–S483 https://doi.org/10.1175/2024BAMSStateoftheClimate.1.

Citing this chapter:
Dunn, R. J. H., J. Blannin, N. Gobron, J. B Miller, and K. M. Willett, Eds., 2024: Global Climate [in "State of the Climate in 2023"]. Bull. Amer. Meteor. Soc., 105 (8), S12–S155, https://doi.org/10.1175/BAMS-D-24-0116.1.

Citing a section (example):
Azorin-Molina, C., R. J. H. Dunn, L. Ricciardulli, C. A. Mears, J. P. Nicolas, T. R. McVicar, Z. Zeng, and M. G. Bosilovich, 2024: Land and ocean surface winds [in "State of the Climate in 2023"]. Bull. Amer. Meteor. Soc., 105 (8), S76–S79, https://doi.org/10.1175/BAMS-D-24-0116.1.

Editor and Author Affiliations (alphabetical by name)

Ades, Melanie, European Centre for Medium-Range Weather Forecasts, Reading, United Kingdom

Adler, Robert, University of Maryland, College Park, Maryland

Alexe, Mihai, European Centre for Medium-Range Weather Forecasts, Bonn, Germany

Allan, Richard P., Department of Meteorology and National Centre for Earth Observation, University of Reading, Reading, United Kingdom

Anderson, John, Hampton University, Hampton, Virginia

Anneville, Orlane, National Research Institute for Agriculture, Food and Environment (INRAE), CARRTEL, Université Savoie Mont Blanc, Thonon les Bains, France

Aono, Yasuyuki, Graduate School of Agriculture, Osaka Metropolitan University, Sakai, Japan

Arguez, Anthony, NOAA/NESDIS National Centers for Environmental Information, Asheville, North Carolina

Armenteras Pascual, Dolores, Science Faculty, Universidad Nacional de Colombia, Bogotá, Colombia

Arosio, Carlo, University of Bremen, Bremen, Germany

Asher, Elizabeth, NOAA Global Monitoring Laboratory, Boulder, Colorado

Augustine, John A., NOAA Global Monitoring Laboratory, Boulder, Colorado

Azorin-Molina, Cesar, Centro de Investigaciones sobre Desertificación – Spanish National Research Council (CSIC-UV-GVA), Valencia, Spain

Baez-Villanueva, Oscar M., Hydro-Climate Extremes Lab (H-CEL), Ghent University, Ghent, Belgium

Barichivich, J., Laboratoire des Sciences du Climat et de l'Environnement (LSCE), LSCE/IPSL, CEA-CNRS-UVSQ, Gif-sur-Yvette, France; Instituto de Geografía, Pontificia Universidad Católica de Valparaíso, Valparaíso, Chile

Beck, Hylke E., Physical Science and Engineering Division, King Abdullah University of Science and Technology, Thuwal, Saudi Arabia

Bellouin, Nicolas, University of Reading, Reading, United Kingdom; Institute Pierre Simon Laplace (IPSL), Guyancourt, France

Benedetti, Angela, European Centre for Medium-Range Weather Forecasts, Reading, United Kingdom

Blannin, Josh, Met Office Hadley Centre, Exeter, United Kingdom

Blenkinsop, Stephen, School of Engineering, Newcastle University, Newcastle-upon-Tyne, United Kingdom

Bock, Olivier, Université Paris Cité, Institut de physique du globe de Paris, CNRS, IGN, F-75005 Paris, France; Univ Gustave Eiffel, ENSG, IGN, F-77455 Marne-la-Vallée, France

Bodin, Xavier, Laboratoire EDYTEM, CNRS/Université Savoie Mont-Blanc, Le Bourget-du-Lac, France

Bonte, Olivier, Hydro-Climate Extremes Lab (H-CEL), Ghent University, Ghent, Belgium

Bosilovich, Michael G., Global Modeling and Assimilation Office, NASA Goddard Space Flight Center, Greenbelt, Maryland

Boucher, Olivier, Institute Pierre Simon Laplace (IPSL), Guyancourt, France

Buehler, Stefan A., Universität Hamburg, Hamburg, Germany

Byrne, Michael P., Climate Dynamics Lab, University of St Andrews, St Andrews, United Kingdom

Campos, Diego, Earth Sciences Department, Barcelona Supercomputing Center, Barcelona, Spain

Cappucci, Fabrizio, European Commission Joint Research Centre, Ispra, Italy

Carrea, Laura, University of Reading, Reading, United Kingdom

Chang, Kai-Lan, Cooperative Institute for Research in Environmental Sciences, University of Colorado Boulder, Boulder, Colorado; NOAA Chemical Sciences Laboratory, Boulder, Colorado

Christiansen, Hanne H., Arctic Geophysics Department, University Centre in Svalbard, Longyearbyen, Norway; Geology Department, University Centre in Svalbard, Longyearben, Norway

Christy, John R., University of Alabama in Huntsville, Huntsville, Alabama

Chung, Eui-Seok, Korea Polar Research Institute, Incheon, South Korea

Ciasto, Laura M., NOAA/NWS National Centers for Environmental Prediction Climate Prediction Center, College Park, Maryland

Clingan, Scott, Cooperative Institute for Research in Earth Science, University of Colorado, Boulder, Colorado; NOAA Global Monitoring Laboratory, Boulder, Colorado

Coldewey-Egbers, Melanie, German Aerospace Center (DLR), Oberpfaffenhofen, Germany

Cooper, Owen R., NOAA Chemical Sciences Laboratory, Boulder, Colorado

Cornes, Richard C., National Oceanography Centre, Southampton, United Kingdom

Covey, Curt, Lawrence Livermore National Laboratory, Livermore, California

Crétaux, Jean-Francois, LEGOS (CNES/CNRS/IRD/UPS), Université de Toulouse, Toulouse, France

Crimmins, Theresa, USA National Phenology Network, School of Natural Resources and the Environment, University of Arizona, Tucson, Arizona.

Crotwell, Molly, Cooperative Institute for Research in Earth Science, University of Colorado, Boulder, Colorado; NOAA Global Monitoring Laboratory, Boulder, Colorado

Culpepper, Joshua, Department of Biology, York University, Toronto, Canada

Cusicanqui, Diego, Institut de Géosciences de l'Environnement (IGE), Université Grenoble Alpes, INRAE, CNRS, IRD, Grenoble INP, ISTerre, Grenoble, France

Davis, Sean, NOAA Chemical Sciences Laboratory, Boulder, Colorado

de Jeu, Richard A. M., Planet Labs, Haarlem, The Netherlands

Degenstein, Doug, University of Saskatchewan, Saskatoon, Canada

Delaloye, Reynald, Department of Geosciences, University of Fribourg, Fribourg, Switzerland

DiGangi, Elizabeth, AEM R&D, Germantown, Maryland

Dokulil, Martin T., Research Institute for Limnology, University of Innsbruck, Mondsee, Austria

Donat, Markus G., Barcelona Supercomputing Center, Barcelona, Spain; Catalan Institution for Research and Advanced Studies (ICREA), Barcelona, Spain

Dorigo, Wouter A., Department of Geodesy and Geoinformation, TU Wien, Vienna, Austria

Duchemin, Diane, CESBIO, Université de Toulouse, CNES/CNRS/INRAe/IRD/UPS, Toulouse, France

Dugan, Hilary, Department of Integrative Biology, University of Wisconsin-Madison, Madison, Wisconsin

Dunn, Robert J. H., Met Office Hadley Centre, Exeter, United Kingdom

Durre, Imke, NOAA/NESDIS National Center for Environmental Information, Asheville, North Carolina

Dutton, Geoff, Cooperative Institute for Research in the Earth Sciences, NOAA Global Monitoring Laboratory, Boulder, Colorado

Duveiller, Gregory, Max Planck Institute for Biogeochemistry, Jena, Germany

Estilow, Thomas W., Rutgers University, Piscataway, New Jersey

Estrella, Nicole, Ecoclimatology, Department of Life Science Systems, TUM School of Life Sciences, Technical University of Munich, Freising, Germany.

Fereday, David, Met Office Hadley Centre, Exeter, United Kingdom

Fioletov, Vitali E., Environment and Climate Change Canada, Toronto, Canada

Flemming, Johannes, European Centre for Medium-Range Weather Forecasts, Bonn, Germany

Foster, Michael J., Cooperative Institute for Meteorological Satellite Studies, Space Science and Engineering Center, University of Wisconsin-Madison, Madison, Wisconsin

Frederikse, Thomas, Planet Labs, Haarlem, The Netherlands

Frith, Stacey M., Science Systems and Applications, Inc., Lanham, Maryland; NASA Goddard Space Flight Center, Greenbelt, Maryland

Froidevaux, Lucien, Jet Propulsion Laboratory, California Institute of Technology, Pasadena, California

Füllekrug, Martin, University of Bath, Bath, United Kingdom

Garforth, Judith, Woodland Trust, Grantham, United Kingdom.

Garg, Jay, ADNET Systems, Inc., Hampton, Virginia
Gobron, Nadine, European Commission Joint Research Centre, Ispra, Italy
Godin-Beekmann, Sophie, Laboratoire Atmosphères, Observations Spatiales (LATMOS), UVSQ, Sorbonne Université, CNRS, IPSL, Guyancourt, France
Goodman, Steven, Thunderbolt Global Analytics, Huntsville, Alabama
Goto, Atsushi, World Meteorological Organization, Geneva, Switzerland
Grimm, Alice, Federal University of Parana, Curitiba, Brazil
Gruber, Alexander, Department of Geodesy and Geoinformation, TU Wien, Vienna, Austria
Gu, Guojun, University of Maryland, College Park, Maryland
Guglielmin, Mauro, Department of Theoretical and Applied Sciences, Insubria University, Varese, Italy
Hahn, Sebastian, Department of Geodesy and Geoinformation, TU Wien, Vienna, Austria
Haimberger, Leopold, University of Vienna, Vienna, Austria
Hall, Brad D., NOAA Global Monitoring Laboratory, Boulder, Colorado
Harlan, Merritt E., U.S. Geological Survey, Denver, Colorado
Harris, I., National Centre for Atmospheric Science (NCAS), University of East Anglia, Norwich, United Kingdom; Climatic Research Unit, School of Environmental Sciences, University of East Anglia, Norwich, United Kingdom
Hemming, Deborah L., Met Office Hadley Centre, Exeter, United Kingdom.; Birmingham Institute of Forest Research, Birmingham University, Birmingham, United Kingdom.
Hirschi, Martin, Institute for Atmospheric and Climate Science, ETH Zurich, Zürich, Switzerland
Ho, Shu-peng (Ben), NOAA/NESDIS Center for Satellite Applications and Research, College Park, Maryland
Holzworth, Robert, University of Washington, Seattle, Washington
Horton, Radley M., Columbia Climate School, Columbia University, New York, New York
Hrbáček, Filip, Department of Geography, Masaryk University, Brno, Czech Republic
Hu, Guojie, Cryosphere Research Station on Qinghai-Tibet Plateau, Northwestern Institute of Eco-Environment and Resources, CAS, Beijing, China
Hurst, Dale, NOAA Global Monitoring Laboratory, Boulder, Colorado
Inness, Antje, European Centre for Medium-Range Weather Forecasts, Reading, United Kingdom
Isaksen, Ketil, Norwegian Meteorological Institute, Oslo, Norway
John, Viju O., EUMETSAT, Darmstadt, Germany
Jones, P. D., Climatic Research Unit, School of Environmental Sciences, University of East Anglia, Norwich, United Kingdom
Junod, Robert, Earth System Science Center, University of Alabama in Huntsville, Huntsville, Alabama
Kääb, Andreas, Department of Geosciences, University of Oslo, Norway
Kaiser, Johannes W., Norwegian Institute for Air Research (NILU), Kjeller, Norway
Kaufmann, Viktor, Institute of Geodesy, Working Group Remote Sensing and Photogrammetry, Graz University of Technology, Graz, Austria
Kellerer-Pirklbauer, Andreas, Institute of Geography and Regional Science, Cascade – The Mountain Processes and Mountain Hazards Group, University of Graz, Graz, Austria
Khaykin, Sergey, Laboratoire Atmosphères, Observations Spatiales (LATMOS), UVSQ, Sorbonne Université, CNRS, IPSL, Guyancourt, France
Kidd, Richard, EODC GmbH, Vienna, Austria
King, Tyler V., U.S. Geological Survey, Boise, Idaho
Kipling, Zak, European Centre for Medium-Range Weather Forecasts, Reading, United Kingdom
Koppa, Akash, Hydro-Climate Extremes Lab (H-CEL), Ghent University, Ghent, Belgium
Kraemer, Benjamin M., University of Freiburg, Freiburg, Germany
La Fuente, R. Sofia, Vrije Universiteit Brussel, Brussels, Belgium
Laas, Alo, Institute of Agricultural and Environmental Sciences, Estonian University of Life Sciences, Tartumaa, Estonia
Lan, Xin, Cooperative Institute for Research in the Earth Sciences, NOAA Global Monitoring Laboratory, Boulder, Colorado; NOAA Global Monitoring Laboratory, Boulder, Colorado
Lantz, Kathleen O., NOAA Global Monitoring Laboratory, Boulder, Colorado
Lapierre, Jeff, AEM R&D, Germantown, Maryland
Lavers, David A., European Centre for Medium-Range Weather Forecasts, Reading, United Kingdom
Leblanc, Thierry, Jet Propulsion Laboratory, California Institute of Technology, Wrightwood, California
Leibensperger, Eric, Department of Physics and Astronomy, Ithaca College, Ithaca, New York
Lennard, Chris, Department of Environmental and Geographical Science, University of Cape Town, Cape Town, South Africa
Liley, Ben, National Institute of Water & Atmospheric Research (NIWA), Lauder, New Zealand
Liu, Yakun, Massachusetts Institute of Technology, Cambridge, Massachusetts
Lo, Y. T. Eunice, Cabot Institute for the Environment, University of Bristol, Bristol, United Kingdom
Loeb, Norman G., NASA Langley Research Center, Hampton Virginia
Loyola, Diego, German Aerospace Center (DLR), Oberpfaffenhofen, Germany
Magnin, Florence, Laboratoire EDYTEM, CNRS/Université Savoie Mont-Blanc, Le Bourget-du-Lac, France
Matsuzaki, Shin-Ichiro, National Institute for Environmental Studies, Tsukuba, Japan
Matthews, Tom, Department of Geography, King's College London, London, United Kingdom
Mayer, Michael, University of Vienna, Vienna, Austria; European Centre for Medium-Range Weather Forecasts, Reading, United Kingdom
McCarthy, Michael, University of Washington, Seattle, Washington
McVicar, Tim R., CSIRO Environment, Canberra, Australian Capital Territory; Australian Research Council Centre of Excellence for Climate Extremes, Sydney, Australia
Mears, Carl A., Remote Sensing Systems, Santa Rosa, California
Menzel, Annette, Ecoclimatology, Department of Life Science Systems, TUM School of Life Sciences, Technical University of Munich, Freising, Germany; Institute for Advanced Study, Technical University of Munich, Garching, Germany
Merchant, Christopher J., University of Reading, Reading, United Kingdom
Merio, Leo-Juhani, Finnish Environment Institute (SYKE), Oulu, Finland
Meyer, Michael F., U.S. Geological Survey, Madison, Wisconsin
Miller, John B., NOAA Global Monitoring Laboratory, Boulder, Colorado
Miralles, Diego G., Hydro-Climate Extremes Lab (H-CEL), Ghent University, Ghent, Belgium
Montzka, Stephan A., NOAA Global Monitoring Laboratory, Boulder, Colorado
Morice, Colin, Met Office Hadley Centre, Exeter, United Kingdom
Morino, Isamu, National Institute for Environmental Studies, Tsukuba, Japan
Mrekaj, Ivan, Technical University in Zvolen, Zvolen, Slovakia
Mühle, Jens, Scripps Institution of Oceanography, University of California San Diego, La Jolla, California
Nance, D., Cooperative Institute for Research in Earth Science, University of Colorado, Boulder, Colorado; NOAA Global Monitoring Laboratory, Boulder, Colorado
Nicolas, Julien P., European Centre for Medium-Range Weather Forecasts, Bonn, Germany
Noetzli, Jeannette, WSL Institute for Snow and Avalanche Research SLF Climate Change, Davos Dorf, Switzerland; Extremes and Natural Hazards in Alpine Regions Research Center CERC, Davos Dorf, Switzerland
Noll, Ben, National Institute of Water and Atmospheric Research (NIWA), Auckland, New Zealand

O'Keefe, John, The Harvard Forest, Harvard University, Petersham, Massachusetts
Osborn, Tim J., Climatic Research Unit, School of Environmental Sciences, University of East Anglia, Norwich, United Kingdom
Parrington, Mark, European Centre for Medium-Range Weather Forecasts, Bonn, Germany
Pellet, Cécile, Department of Geosciences, University of Fribourg, Fribourg, Switzerland
Pelto, Mauri S., Nichols College, Dudley, Massachusetts
Petersen, Kyle, Cooperative Institute for Research in Earth Science, University of Colorado, Boulder, Colorado; NOAA Global Monitoring Laboratory, Boulder, Colorado
Phillips, Coda, Cooperative Institute for Meteorological Satellite Studies, Space Science and Engineering Center, University of Wisconsin-Madison, Madison, Wisconsin
Pierson, Don, Department of Ecology and Genetics, Uppsala University, Uppsala, Sweden
Pinto, Izidine, Royal Netherlands Meteorological Institute (KNMI), De Bilt, The Netherlands
Po-Chedley, Stephen, Lawrence Livermore National Laboratory, Livermore, California
Pogliotti, Paolo, Environmental Protection Agency of Valle d'Aosta, Saint Christophe, Italy
Polvani, Lorenzo, Columbia University, New York, New York
Preimesberger, Wolfgang, Department of Geodesy and Geoinformation, TU Wien, Vienna, Austria
Price, Colin, Tel Aviv University, Tel Aviv, Israel
Randel, William J., National Center for Atmospheric Research, Boulder, Colorado
Raymond, Colin, University of California, Los Angeles, Los Angeles, California
Rémy, Samuel, HYGEOS, Lille, France
Ricciardulli, Lucrezia, Remote Sensing Systems, Santa Rosa, California
Richardson, Andrew D., School of Informatics, Computing, and Cyber Systems, Northern Arizona University, Flagstaff, Arizona; Center for Ecosystem Science and Society, Northern Arizona University, Flagstaff, Arizona
Robinson, David A., Rutgers University, Piscataway, New Jersey
Rodell, Matthew, Earth Sciences Division, NASA Goddard Space Flight Center, Greenbelt, Maryland
Rodriguez-Fernandez, Nemesio, CESBIO, Université de Toulouse, CNES/CNRS/INRAe/IRD/UPS, Toulouse, France
Rogers, Cassandra D. W., Bureau of Meteorology, Melbourne, Australia
Rohini, P., India Meteorological Department, Ministry of Earth Sciences, Pune, India
Rosenlof, Karen, NOAA Chemical Sciences Laboratory, Boulder, Colorado
Rozanov, Alexei, University of Bremen, Bremen, Germany
Rozkošný, Jozef, Slovak Hydrometeorological Institute, Bratislava, Slovakia
Rusanovskaya, Olga O., Irkutsk State University, Institute of Biology, Irkutsk, Russia
Rutishauser, This, Swiss Academy of Sciences (SCNAT), Bern, Switzerland
Sabeerali, C. T., India Meteorological Department, Ministry of Earth Sciences, Pune, India
Said, Ryan, Vaisala R&D, Louisville, Colorado
Sakai, Tetsu, Meteorological Research Institute, Japan Meteorological Agency, Tsukuba, Japan
Sánchez-Lugo, Ahira, NOAA/NESDIS National Centers for Environmental Information, Asheville, North Carolina
Sawaengphokhai, Parnchai, ADNET Systems, Inc., Hampton Virginia
Schenzinger, Verena, Medical University of Innsbruck, Innsbruck, Austria
Schlegel, Robert W., Laboratoire d'Océanographie de Villefranche, Sorbonne Université, Villefranche-sur-mer, France
Schmid, Martin, Eawag, Department Surface Waters - Research and Management, Kastanienbaum, Switzerland
Seneviratne, Sonia I., ETH Zurich, Department of Environmental Systems Science, Zürich, Switzerland
Sezaki, Fumi, Japan Meteorological Agency, Tokyo, Japan
Shao, Xi, NOAA/NESDIS Center for Satellite Applications and Research, College Park, Maryland
Sharma, Sapna, Department of Biology, York University, Toronto, Canada
Shi, Lei, NOAA/NESDIS National Centers for Environmental Information, Asheville, North Carolina
Shimaraeva, Svetlana V., Irkutsk State University, Institute of Biology, Irkutsk, Russia
Shinohara, Ryuichiro, Regional Environment Conservation Division, National Institute for Environmental Studies, Tsukuba, Japan
Silow, Eugene A., Irkutsk State University, Institute of Biology, Irkutsk, Russia
Simmons, Adrian J., European Centre for Medium-Range Weather Forecasts, Reading, United Kingdom
Smith, Sharon L., Geological Survey of Canada, Natural Resources Canada, Ottawa, Canada
Soden, Brian J., University of Miami, Miami, Florida
Sofieva, Viktoria, Finnish Meteorological Institute, Helsinki, Finland
Soldo, Logan, Cooperative Institute for Research in the Environmental Sciences, University of Colorado, Boulder, Boulder, Colorado
Sreejith, O. P., India Meteorological Department, Ministry of Earth Sciences, Pune, India
Stackhouse, Jr., Paul W., NASA Langley Research Center, Hampton, Virginia
Stauffer, Ryan, Atmospheric Chemistry and Dynamics Laboratory, NASA Goddard Space Flight Center, Greenbelt, Maryland
Steinbrecht, Wolfgang, Deutscher Wetterdienst, Hohenpeissenberg, Germany
Steiner, Andrea K., Wegener Center for Climate and Global Change, University of Graz, Graz, Austria
Stoy, Paul, C., Biological Systems Engineering, College of Agricultural and Life Sciences, University of Wisconsin-Madison, Madison, Wisconsin
Stradiotti, Pietro, Department of Geodesy and Geoinformation, TU Wien, Vienna, Austria
Streletskiy, Dmitry A., Department of Geography, George Washington University, Washington, DC
Taha, Ghassan, Morgan State University, Baltimore, Maryland; NASA Goddard Flight Center, Greenbelt, Maryland
Thackeray, Stephen J., United Kingdom Centre for Ecology & Hydrology, Lancaster, United Kingdom.
Thibert, Emmanuel, Institut de Géosciences de l'Environnement (IGE), Université Grenoble Alpes, INRAE, CNRS, IRD, Grenoble INP, ISTerre, Grenoble, France
Timofeyev, Maxim A., Institute of Biology, Irkutsk State University, Irkutsk, Russia
Tourpali, Kleareti, Aristotle University, Thessaloniki, Greece
Tronquo, Emma, Hydro-Climate Extremes Lab (H-CEL), Ghent University, Ghent, Belgium
Tye, Mari R., National Center for Atmospheric Research, Boulder, Colorado
van der A, Ronald, Royal Netherlands Meteorological Institute (KNMI), De Bilt, The Netherlands
van der Schalie, Robin, Planet Labs, Haarlem, The Netherlands
van der Schrier, Gerard, Royal Netherlands Meteorological Institute (KNMI), De Bilt, The Netherlands
van Vliet, Arnold J. H., Environmental Systems Analysis Group, Wageningen University & Research, The Netherlands
Verburg, Piet, National Institute of Water and Atmospheric Research (NIWA), Wellington, New Zealand
Vernier, Jean-Paul, NASA Langley Research Center, Hampton, Virginia
Vimont, Isaac J., NOAA Global Monitoring Laboratory, Boulder, Colorado
Virts, Katrina, University of Huntsville in Alabama, Huntsville, Alabama
Vivero, Sebastián, Department of Geosciences, University of Fribourg, Fribourg, Switzerland
Vömel, Holger, National Center for Atmospheric Research, Boulder, Colorado

Editor and Author Affiliations (continued)

Vose, Russell S., NOAA/NESDIS National Centers for Environmental Information, Asheville, North Carolina

Wang, Ray H. J., Georgia Institute of Technology, Atlanta, Georgia

Warnock, Taran, University of Saskatchewan, Saskatoon, Canada

Weber, Mark, University of Bremen, Bremen, Germany

Wiese, David N., Jet Propulsion Laboratory, California Institute of Technology, Pasadena, California

Wild, Jeannette D., Earth System Science Interdisciplinary Center, University of Maryland, College Park, Maryland; NOAA/NESDIS Center for Satellite Applications and Research, College Park, Maryland

Willett, Kate M., Met Office Hadley Centre, Exeter, United Kingdom

Williams, Earle, Massachusetts Institute of Technology, Cambridge, Massachusetts

Wong, Takmeng, NASA Langley Research Center, Hampton, Virginia

Woolway, Richard Iestyn, School of Ocean Sciences, Bangor University, Bangor, United Kingdom

Yin, Xungang, NOAA/NESDIS National Centers for Environmental Information, Asheville, North Carolina

Zeng, Zhenzhong, School of Environmental Science and Engineering, Southern University of Science and Technology, Shenzhen, China

Zhao, Lin, School of Geographical Sciences, Nanjing University of Information Science and Technology, Nanjing, China

Zhong, Feng, Hydro-Climate Extremes Lab (H-CEL), Ghent University, Ghent, Belgium

Ziemke, Jerry R., Goddard Earth Sciences Technology and Research, Morgan State University, Baltimore, Maryland; NASA Goddard Space Flight Center, Greenbelt, Maryland

Ziese, Markus, Global Precipitation Climatology Centre, Deutscher Wetterdienst, Offenbach, Germany

Zotta, Ruxandra M., TU Wien, Vienna, Austria

Zou, Cheng-Zhi, NOAA/NESDIS Center for Satellite Applications and Research, College Park, Maryland

Editorial and Production Team

Allen, Jessicca, Graphics Support, Cooperative Institute for Satellite Earth System Studies, North Carolina State University, Asheville, North Carolina

Camper, Amy V., Graphics Support, Innovative Consulting and Management Services, LLC, NOAA/NESDIS National Centers for Environmental Information, Asheville, North Carolina

Haley, Bridgette O., Graphics Support, NOAA/NESDIS National Centers for Environmental Information, Asheville, North Carolina

Hammer, Gregory, Content Team Lead, Communications and Outreach, NOAA/NESDIS National Centers for Environmental Information, Asheville, North Carolina

Love-Brotak, S. Elizabeth, Lead Graphics Production, NOAA/NESDIS National Centers for Environmental Information, Asheville, North Carolina

Ohlmann, Laura, Technical Editor, Innovative Consulting and Management Services, LLC, NOAA/NESDIS National Centers for Environmental Information, Asheville, North Carolina

Noguchi, Lukas, Technical Editor, Innovative Consulting and Management Services, LLC, NOAA/NESDIS National Centers for Environmental Information, Asheville, North Carolina

Riddle, Deborah B., Graphics Support, NOAA/NESDIS National Centers for Environmental Information, Asheville, North Carolina

Veasey, Sara W., Visual Communications Team Lead, Communications and Outreach, NOAA/NESDIS National Centers for Environmental Information, Asheville, North Carolina

2. Table of Contents

Authors and affiliations S15
a. Overview S21
Sidebar 2.1: Impacts of extreme global temperatures and events in 2023 ..... S22
b. Temperature S29
1. Global surface temperature S29
Sidebar 2.2: Near-surface equivalent temperature as a key climate change metric S30
2. Lake surface water temperature S33
3. Night marine air temperature S35
4. Surface temperature extremes S37
5. Tropospheric temperature S39
6. Stratospheric temperature S41
c. Cryosphere S43
1. Permafrost temperature and active-layer thickness S43
2. Rock glacier velocity S44
3. Alpine glaciers S46
4. Lake ice S48
5. Northern Hemisphere continental snow cover extent S50
d. Hydrological cycle—atmosphere S52
1. Surface humidity S52
2. Humid-heat extremes over land S55
3. Total column water vapor S57
4. Upper-tropospheric humidity S59
5. Precipitation S61
6. Land surface precipitation extremes S62
7. Cloudiness S63
8. Lake water storage S66
9. Groundwater and terrestrial water storage S67
10. Soil moisture S69
11. Monitoring global drought using the self-calibrating Palmer Drought Severity Index S70
12. Land evaporation S72
e. Atmospheric circulation S74
1. Mean sea level pressure and related modes of variability S74
2. Land and ocean surface winds S76
3. Upper air winds S79
4. Thunder hours S81
f. Earth radiation budget S83
1. Earth radiation budget at top-of-atmosphere S83
2. Mauna Loa apparent transmission record S85

2. Table of Contents

g. Atmospheric composition S87
1. Long-lived greenhouse gases S87
2. Ozone-depleting substances S90
3. Tropospheric aerosols S91
4. Tropospheric ozone S94
5. Stratospheric aerosols S96
6. Stratospheric ozone S99
7. Stratospheric water vapor S101
8. Carbon monoxide S103
h. Land surface properties S105
1. Terrestrial surface albedo dynamics S105
2. Terrestrial vegetation dynamics S106
3. Biomass burning S107
4. Phenology of primary producers S109
5. Vegetation optical depth S113
Acknowledgments S115
Appendix 1: Acronyms S120
Appendix 2: Datasets and sources S124
Appendix 3: Supplemental materials S135
References S141

2. GLOBAL CLIMATE

R. J. H. Dunn, J. Blannin, N. Gobron, J. B. Miller, and K. M. Willett, Eds.

a. Overview

—R. J. H. Dunn, J. Blannin, N. Gobron, J. B. Miller, and K. M. Willett

Globally, 2023 was the warmest year since records began in the mid-1800s to mid-1900s, according to all seven global temperature datasets. The prolonged La Niña that began in 2020 faded at the start of 2023 and was replaced by a strong El Niño by the end of the year. The change to El Niño conditions contributed to exceptionally high temperatures worldwide, especially in the latter part of the year as the El Niño strengthened. The pervasive warmth was highlighted by widespread and intense temperature extremes, with record numbers of warm days globally and the third-highest land fraction experiencing record numbers of warm days. Also, globally averaged lake surface temperatures in the warm season were the highest since records began in 1995. Over the oceans, night-time air temperatures likewise reached record values. Not only was the near-surface affected, but the lower troposphere average had record temperatures, with particularly exceptional values over the tropics in the latter part of the year. The stratosphere, which usually cools in response to anthropogenic carbon dioxide (CO_2) increases, also warmed this year, reflecting a recovery from the Hunga Tonga–Hunga Ha'apai (HTHH) eruption in 2022.

The unprecedented temperature anomalies over recent years and decades have had worldwide impacts on many essential climate variables covered in this chapter. A sidebar on these impacts in 2023 is included to link the sections and domains where the high global temperatures have driven important changes in Earth's climate system (Sidebar 2.1). The warm temperatures drove consistent changes in the hydrological cycle with greater quantities of water in the atmosphere but also record areas under extreme drought. Glaciers continued to lose mass for the 36th consecutive year, and land surface variables also showed substantial or record-breaking changes.

The fading La Niña in the early part of the year contributed to destructive flooding in New Zealand (e.g., post-Cyclone Gabrielle in February). Later on, the growing El Niño had regional impacts, with increased rainfall in South America leading to flooding in Chile in August, and, conversely, Australia experiencing its driest three-month period on record (August–October). Globally, upper-air winds were also reduced in the second half of the year in a manner typical of El Niño conditions. The impact of the El Niño can even be seen in the high number of thunder hours—a proxy for lightning activity, and which this year replaces the section on lightning flashes—across the eastern Pacific Ocean and southeastern South America.

Atmospheric composition changes both in 2023 and in general are characterized mainly by continued record-breaking atmospheric abundances of long-lived greenhouse gases (LLGHGs). These are the result of continued anthropogenic GHG emissions and year-to-year variability in short-lived species such as water vapor, aerosols, and carbon monoxide related to annual anomalies in emissions and circulation. Globally averaged atmospheric concentrations of CO_2, methane (CH_4), and nitrous oxide (N_2O) for 2023 each reached new annual record-high values of 419.3 ppm, 1922.6 ppb, and 336.7 ppb, respectively. The gases that destroy stratospheric ozone most effectively (i.e., chlorofluorocarbons [CFCs]) continue to decline, and their initial replacements (i.e., hydrochlorofluorocarbons [HCFCs]) may have peaked, although the current replacement compounds (i.e., hydrofluorocarbons [HFCs]) continue to increase, albeit with minimal impact on stratospheric ozone.

Large fires, especially those in eastern and western Canada, led to large anomalies in both carbon monoxide and tropospheric aerosols. In the stratosphere, the HTHH eruption that started in late 2021 still appeared to be impacting levels of water vapor, ozone, and aerosols in 2023. However, stratospheric ozone anomalies are mainly linked to circulation changes, including those related to the onset of El Niño in 2023; the long-term recovery of stratospheric ozone is consistent with model predictions given the decrease in CFCs and related compounds.

Earth's radiation budget at the top-of-atmosphere (approximately 20 km) continued to show a net imbalance. Anomalies for all components were greater than their interannual variability for the first time in the CERES (Clouds and the Earth's Radiant Energy System) record (starting March 2000). The Mauna Loa atmospheric transmission record resumed in July 2023, after being interrupted by the eruption of its volcano in late November 2022.

This year we welcome two new sections to the report: 1) Humid-heat extremes over land (previously introduced in Sidebar 2.1 in *State of the Climate* in 2022), a timely regular addition to the report closely linked to human heat health, and 2) Stratospheric aerosols (previously introduced in Sidebar 2.2 in *State of the Climate* in 2019), which shows the ongoing effects of the HTHH eruption in January 2022.

Another sidebar (Sidebar 2.2) this year discusses near-surface equivalent temperature as a metric to measure changes in the total energy content of the near-surface atmosphere, comprising sensible and latent heat components. A large fraction of the change in near-surface total energy content has been in the latent heat component, which is not captured when measuring surface air temperature. Using the equivalent temperature, this sidebar shows how near-surface atmospheric heating reached record levels in 2023.

As usual, Plate 2.1 shows maps of global annual anomalies for many of the variables and metrics presented herein. Many of these variables are also presented as time series in Plate 1.1. Many sections now use the 1991–2020 climatological reference period, in line with the World Meteorological Organization recommendations, although this newer reference period is not possible for all datasets, depending on their length of record or legacy processing methods.

Sidebar 2.1: **Impacts of extreme global temperatures and events in 2023**

—R. J. H. DUNN, N. GOBRON, AND K. M. WILLETT

The year 2023 saw record-breaking global surface temperatures (section 2b1), especially during the latter half of the calendar year. Record frequencies of extreme temperature days (e.g., by numbers of warm days [TX90p]) were experienced. Near-record spatial extents (in percent of land gridboxes) experienced record warm-day frequencies, while marine heatwaves (in sea-surface temperature) covered the largest total area (in percent of ocean gridboxes) on record (section 2b4). Although significant in its own right, this record warmth resulted in widespread impacts across the essential climate variables (GCOS 2022) presented in this chapter. And, despite being numerically exceptional, this warmth is consistent with globally increasing temperatures over the last decades that are unequivocally the result of human activities (IPCC 2021).

High temperatures and the transition from La Niña to El Niño conditions during 2023 resulted in large quantities of water in the atmospheric column. Evaporation over land reached record levels for the globe, dominated by record values for the Northern Hemisphere (section 2d12). The water vapor content of the near-surface atmosphere was record or near-record high globally, exceeding 2022 levels by a large margin (section 2d1). The energy contribution from the related latent heat component contributed to a record-high global anomaly in equivalent temperature, a measure of the total energy content of the atmosphere (Sidebar 2.2). It was also a record-breaking year for humid-heat indices, as humid-heat intensity doubled the previous record anomaly in 1998, reaching +0.6°C (section 2d2). Three datasets of total column water vapor showed the wettest year on record globally, as well as over the oceans, for all five datasets (section 2d3), with over 1 kg of water vapor extra per square meter across Earth's surface. Despite this increased moisture aloft, 2023 had the lowest cloud area fraction since records began in 1980 (section 2d7) with skies clearer globally. Consequently, the clouds reflected away to space a record small amount of shortwave radiation, but also blocked a record small amount of longwave radiation from leaving Earth. The overall effect was the weakest cooling effect of clouds on record. The clearer skies may have contributed to a lower global mean precipitation total over land surfaces for the year, with 2023 being one of the driest years since 1979 (section

2d5), but global one-day maximum accumulations (Rx1day) were close to average, demonstrating increased intensity of the rain that did fall (section 2d6), as expected under warmer conditions (e.g., Fowler et al. 2021). Global soil moisture, which on average has increased since around 2012, returned to 2020 levels. This return was due to a combination of little change in the Northern Hemisphere and a strong drying in the Southern Hemisphere, likely the result of the shift from La Niña to El Niño conditions (section 2d10). And overall, 2023 saw terrestrial water storage measures reach their second-lowest point since 2002 (section 2d9), leading to 7.9% of global land area being under extreme drought (self-calibrating Palmer Drought Severity Index, scPDSI ≤–4) in July, the first time 7% has been surpassed for this most-severe drought category (section 2d11).

The land surface responded to the elevated temperatures, with a near-record negative anomaly for the visible albedo in the Northern Hemisphere (section 2h1) as the surface darkened. The surface was notably darker for a substantial fraction of Earth's surface (17%), linked to rapid snowmelt in Canada and Siberia. The darkening was also linked to increased plant growth (which causes the absorption of radiation) in other parts of the world, and there were also record positive anomalies for the fraction of absorbed photosynthetically active radiation in the Northern Hemisphere (section 2h2). Plants directly responded to the warmth; early in the year, the full bloom for the cherry trees in the Arashiyama district of Kyoto, Japan, occurred on the earliest date in the over-1200-year-long record, and there was an early start of season in North America. In the latter half of the year, leaf fall in boreal autumn was delayed in North America and Europe as above-average temperatures prevailed (section 2h4).

Glaciers in mountainous regions have continued to lose mass, with the 36th consecutive year of global mass balance loss and the 15th with losses of more than 500-mm water equivalent. This year also marked the highest ratio of negative to positive mass balance observations of any year in the record. In the European Alps, a second consecutive very-warm summer resulted in a 10% decrease in remaining ice volume for Swiss glaciers since 2021 (GLAMOS 2023; WMO 2024; section 2c3). The effects of the warmth penetrated into the ground, with permafrost temperatures at record levels at 10-m and even 20-m depth in the same region. In the Arctic, permafrost temperatures were record high at 9 of the 17 reporting sites, and active-layer thicknesses (the layers in the ground which freeze and thaw each year) also set records for all sites in Svalbard, in some places by up to 5 m (section 2c1).

The exceptional wildfire season in Canada (see Sidebar 7.1 for details), where large-scale fires burned continually from May to September, consumed three times more biomass than the previous record and pushed the global emissions of carbon from biomass burning to the highest annual total since 2015 (section 2h3). Plumes of smoke from these fires elevated aerosol optical depth at 550 nm and increased particulate matter at 2.5 μm in diameter (PM2.5) across North America during 2023, dominating the number of days with extreme (>99.9th percentile) aerosol optical depth globally (section 2g3). Low precipitation amounts and the subsequent drought in central and southern Canada were also contributing factors to the wildfires in those areas (sections 2d5, 2d10). The warm, dry spring resulted in the lowest May snow cover in the satellite record for Canada, and also globally (section 2b5). And finally, above-average thunder hours in the western United States and Canada in 2023 contributed to a greater number of fires ignited by lightning during the year (section 2e4).

(a) Surface Temperature

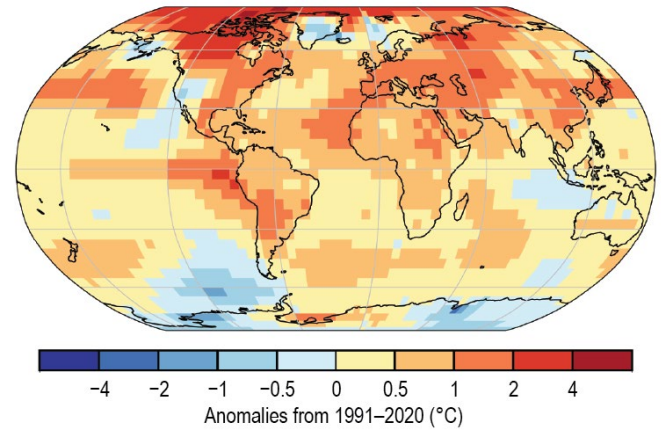

(b) Lake Temperature

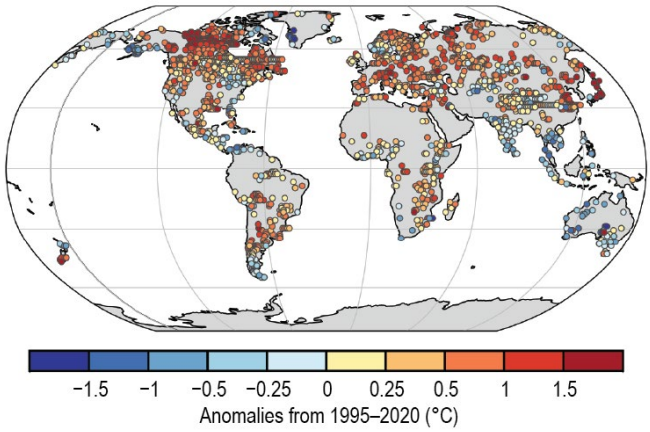

(c) Night Marine Air Temperature

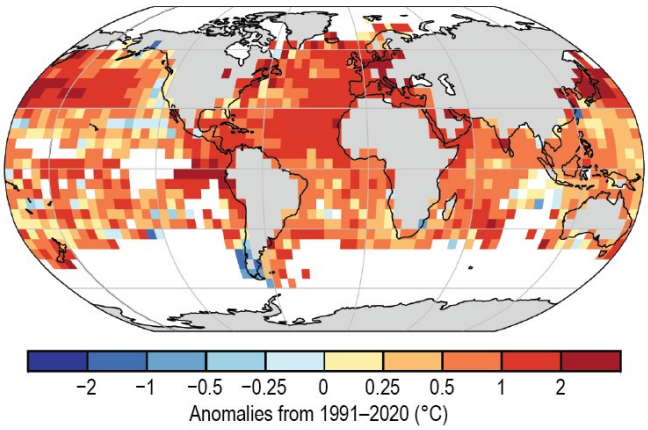

(d) Warm Days (TX90p)

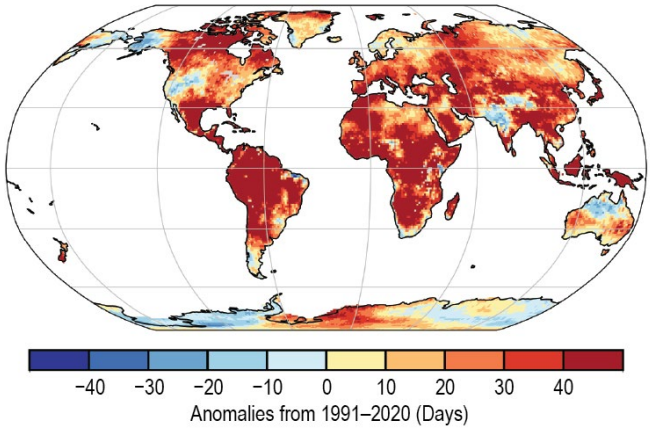

(e) Cool Nights (TX10p)

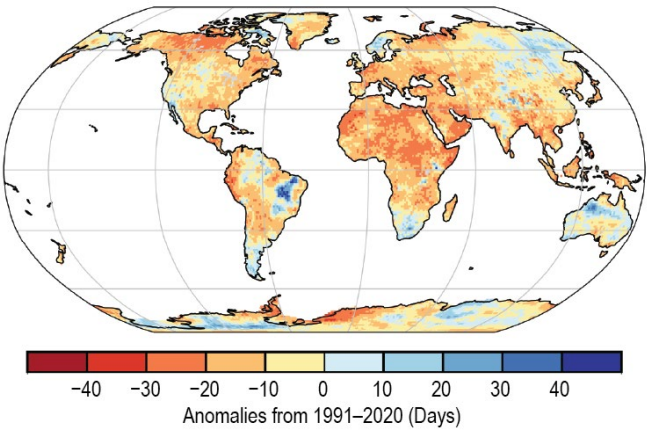

(f) Lower Tropospheric Temperature

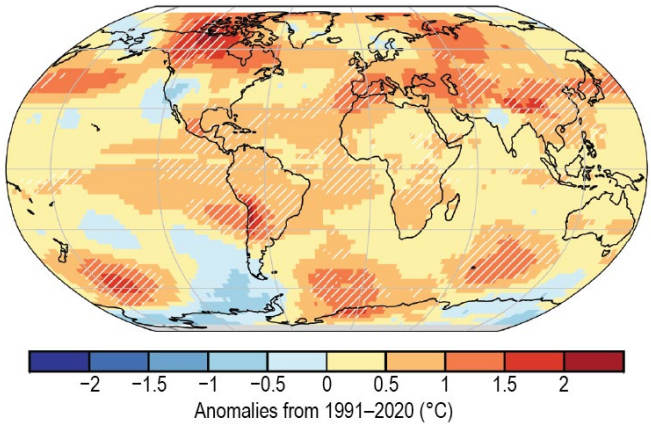

(g) Surface Specific Humidity

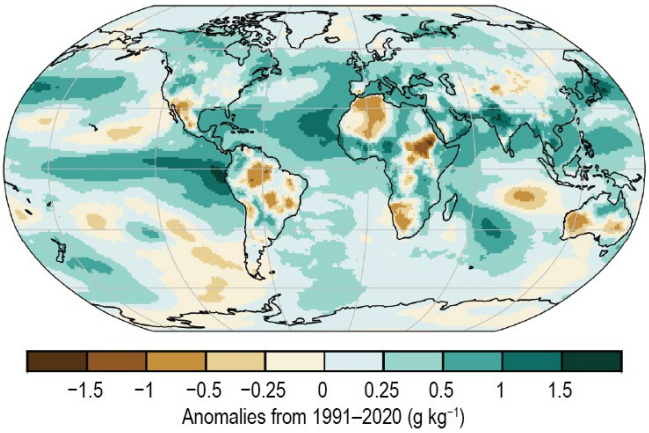

Plate 2.1. (a) NOAA NCEI Global land and ocean surface annual temperature anomalies (°C); (b) Satellite-derived lake surface water temperature anomalies, from European Space Agency (ESA) Climate Change Initiative (CCI) LAKES/ Copernicus Climate Change Service (C3S) /Earth Observation Climate Information Service (EOCIS) (°C); (c) CLASSnmat night marine air temperature annual average anomalies (°C); (d) ERA5 warm day threshold exceedance (TX90p); (e) ERA5 cool night threshold exceedance (TN10p); (f) Average of Remote Sensing Systems (RSS) and UAH lower tropospheric temperature anomalies (°C). Hatching denotes regions in which 2023 was the warmest year on record; (g) ERA5 surface specific humidity anomalies (g kg^{-1});

(h) Surface Relative Humidity

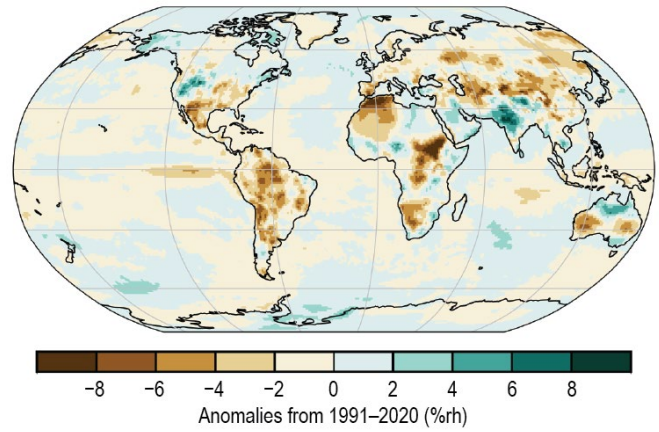

(i) Humid-heat days (TwX90p)

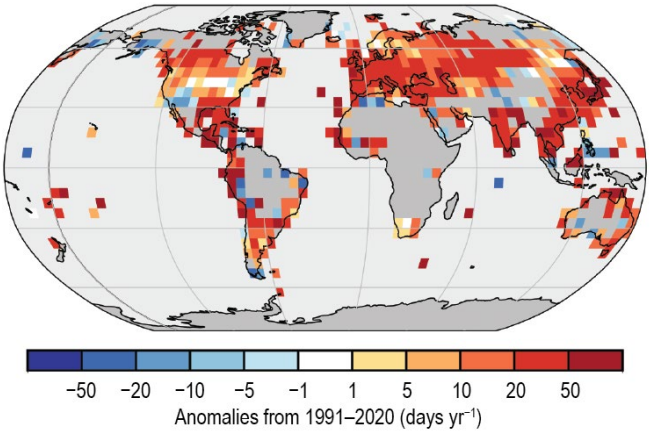

(j) Maximum T_{wet}

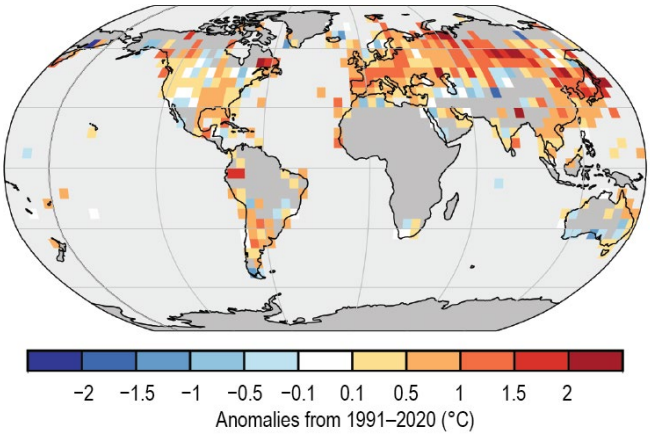

(k) Total Column Water Vapor

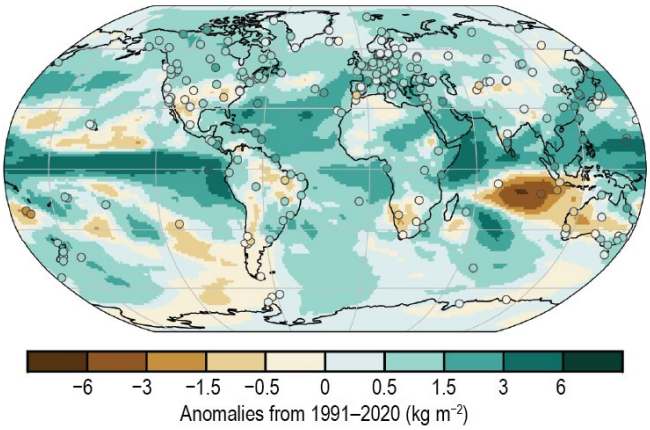

(l) Upper Tropospheric Humidity

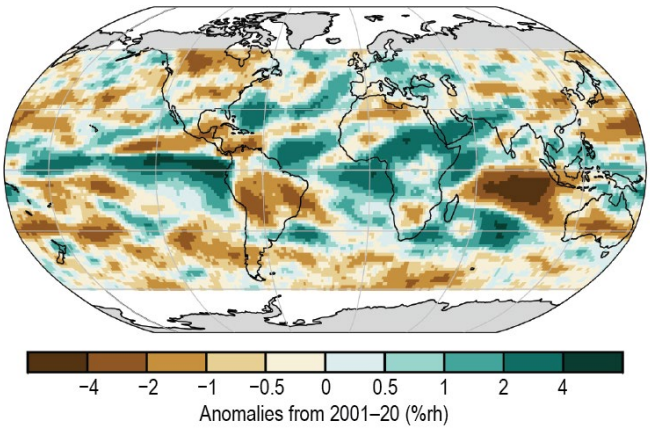

(m) Precipitation

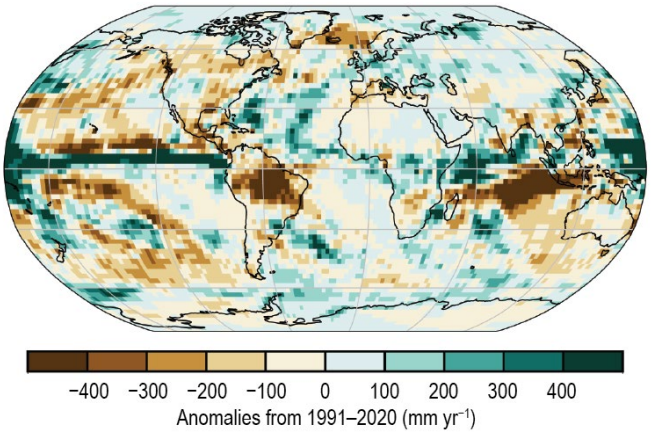

(n) Maximum 5 Day Precipitation Amount

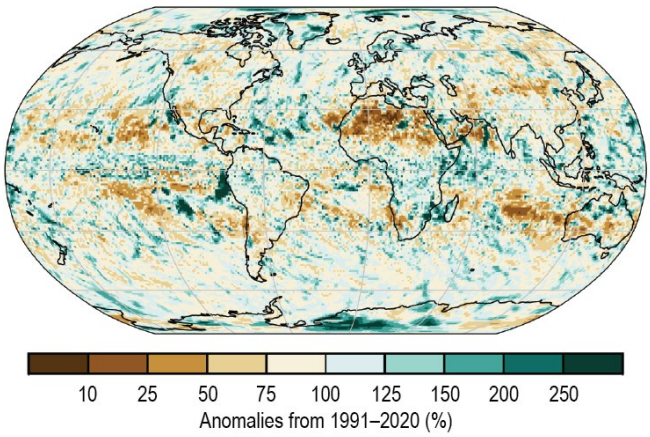

Plate 2.1 (cont.) (h) ERA5 surface relative humidity anomalies (%rh); (i) HadISDH.extremes humid heat frequency anomalies (T_wX90p), measured by the number of days where the daily maximum wet-bulb temperature exceeds the local daily 90th percentile (days yr^{-1}). White gridboxes (over land) represent regions with insufficient data.; (j) HadISDH. extremes humid heat intensity (T_wX), measured by the annual median anomaly of daily maximum wet-bulb temperature (°C). White gridboxes (over land) represent regions with insufficient data. (k) ERA5 TCWV anomalies (%). Data from GNSS stations are plotted as filled circles; (l) Annual microwave-based upper tropospheric humidity (UTH) anomalies (%rh); (m) GPCP v2.3 annual mean precipitation anomalies (mm yr^{-1}); (n) CHIRPS maximum 5-day (Rx5day) annual precipitation anomalies (mm);

(o) Cloudiness

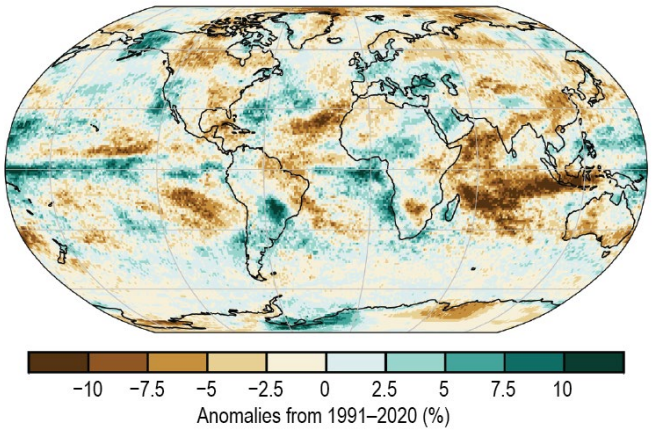

(p) Lake Water Level

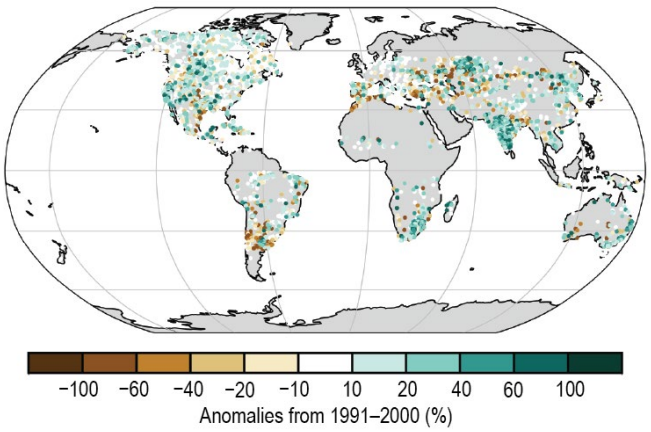

(q) Terrestrial Water Storage

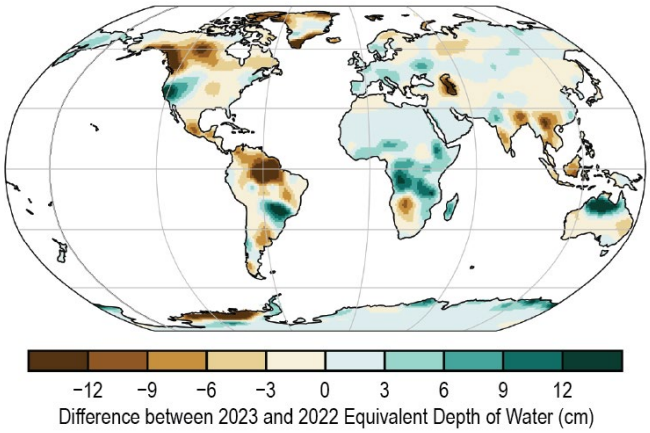

(r) Soil Moisture

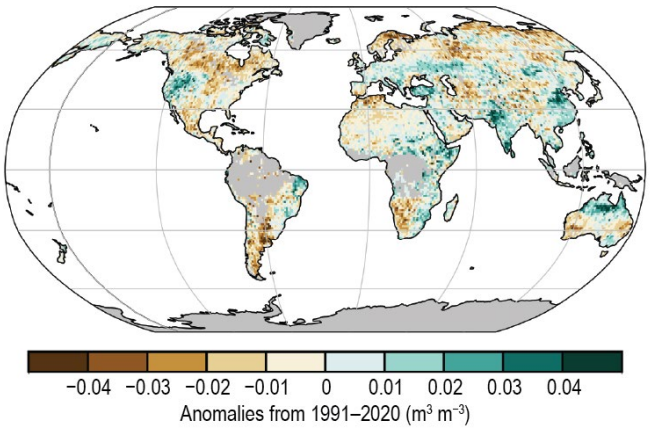

(s) Drought

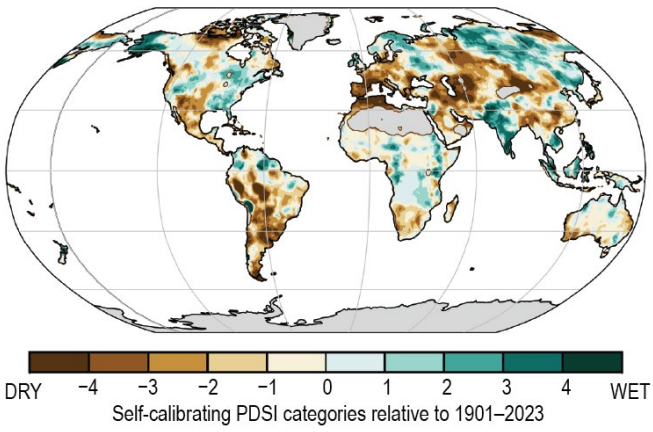

(t) Land Evaporation

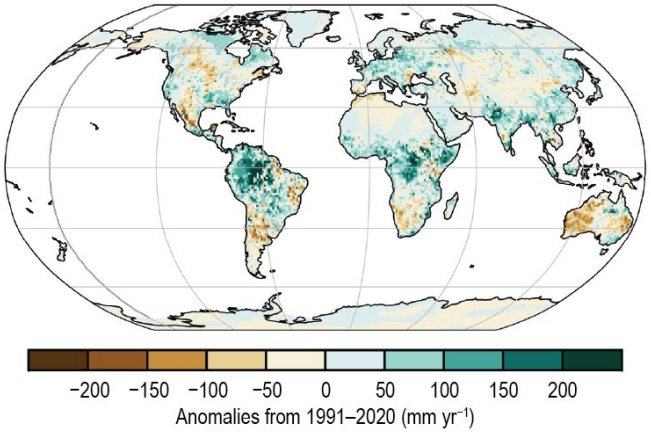

(u) Sea Level Pressure

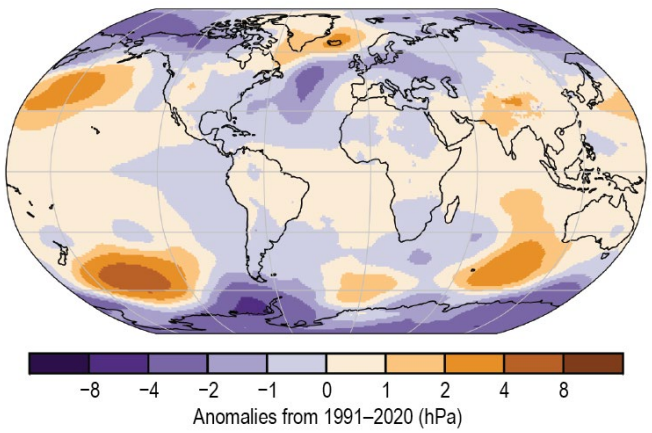

Plate 2.1 (cont.) (o) PATMOS-x 6.0 cloud fraction annual anomalies (%); (p) GloLakes lake water storage anomalies (%); (q) GRACE-FO difference in annual-mean terrestrial water storage between 2022 and 2023 (cm); (r) Copernicus Climate Change Service (C3S) average surface soil moisture anomalies (m3 m^{-3}). Data are masked where no retrieval is possible or where the quality is not assured and flagged, for example due to dense vegetation, frozen soil, or radio frequency interference; (s) Mean self-calibrating Palmer Drought Severity Index (scPDSI) for 2021. Droughts are indicated by negative values (brown), wet episodes by positive values (green). No calculation is made where a drought index is meaningless (gray areas: ice sheets or deserts with approximately zero mean precipitation); (t) GLEAM land evaporation anomalies (mm yr^{-1}); (u) ERA5 mean sea level pressure anomalies (hPa);

(v) Surface Winds

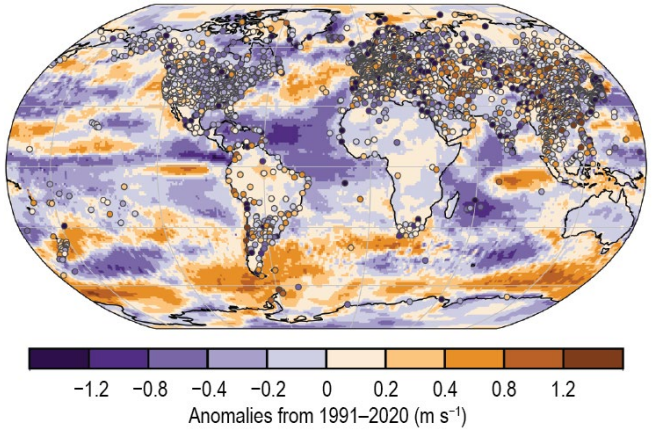

(w) Upper Air (850-hPa) Eastward Winds

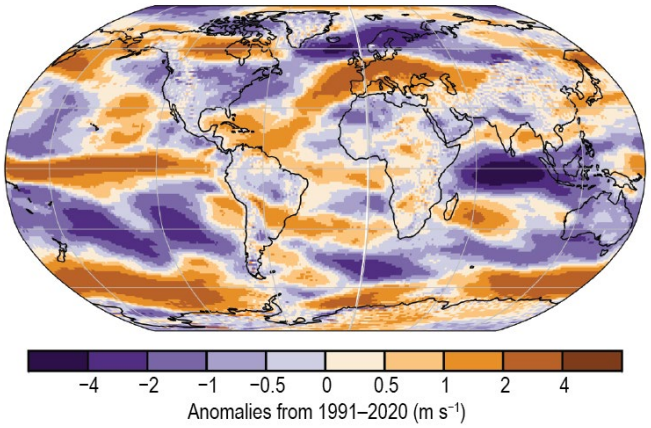

(x) Total Aerosol

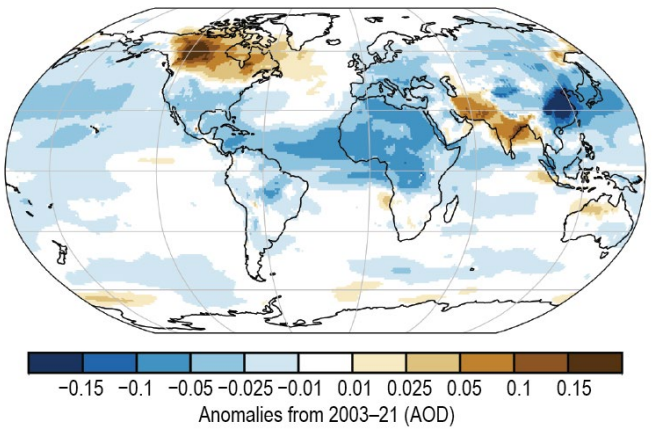

(y) PM25

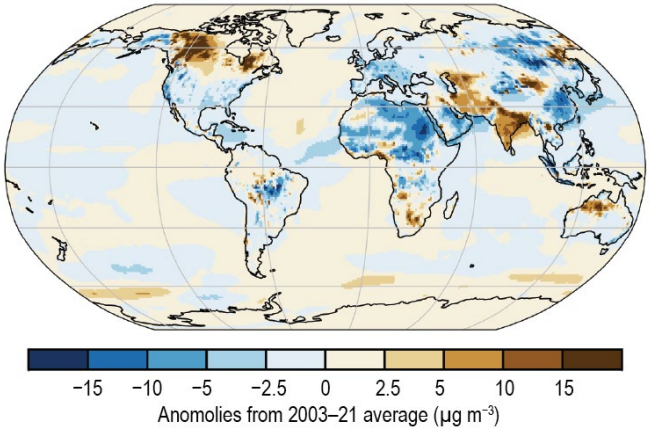

(z) Extreme Aerosol Days

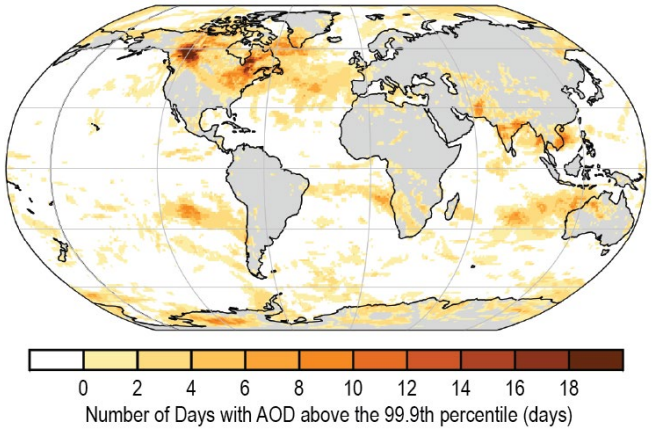

(aa) OMI/MLS Tropospheric Column Ozone

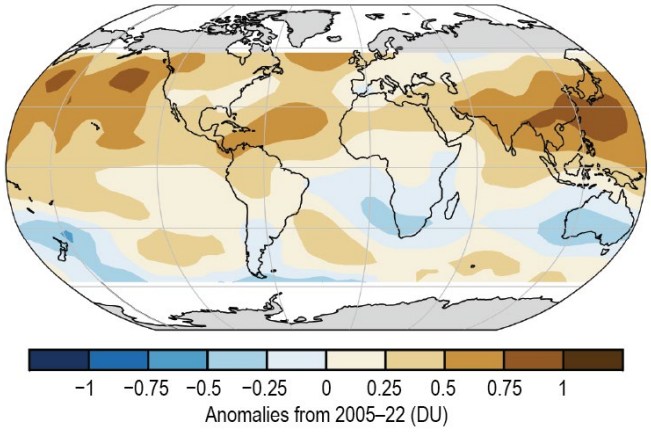

(ab) Stratospheric (Total Column) Ozone

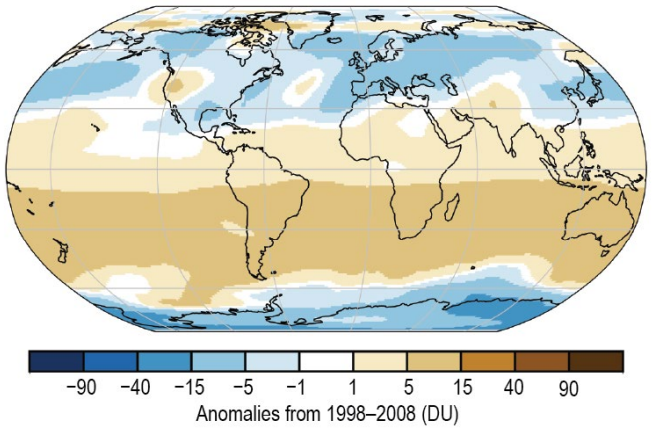

Plate 2.1 (cont.) (v) Surface wind speed anomalies (m s^{-1}) from the observational HadISD3 dataset (land, circles), the ERA5 reanalysis output (land, shaded areas), and Remote Sensing Satellite (RSS) satellite observations (ocean, shaded areas); (w) ERA5 850-hPa eastward wind speed anomalies for Sep–Dec (m s^{-1}); (x) CAMS reanalysis total aerosol optical depth (AOD) anomalies at 550 nm; (y) CAMS reanalysis PM2.5 anomalies (µg m^{-3}) ; (z) Number of days with AOD above the 99.9th percentile from CAMS reanalysis. Areas with zero days appear as the white/gray background; (aa) OMI/MLS tropospheric ozone column anomalies for 60°S–60°N (DU); (ab) total column ozone anomalies determined from TROPOMI aboard Sentinel-5 Precursor (S5P; DU);

(ac) Carbon Monoxide

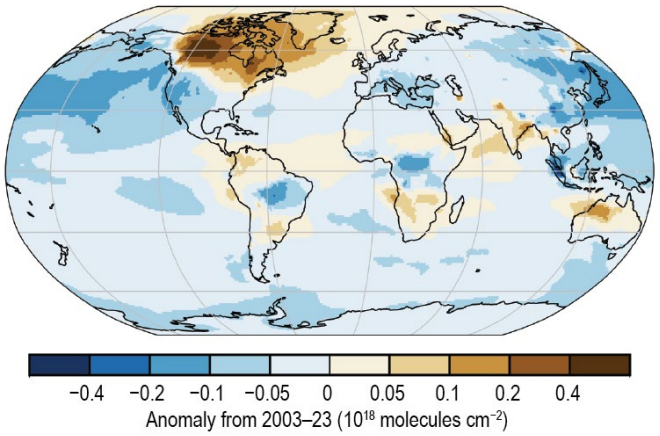

(ad) Land Surface Albedo in the Visible

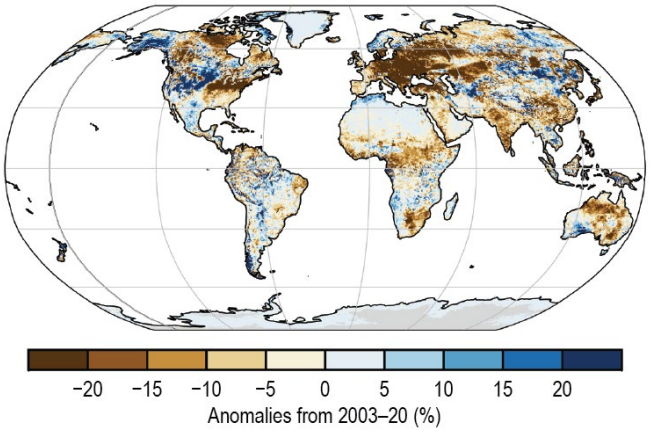

(ae) Land Surface Albedo in the Near-Infrared

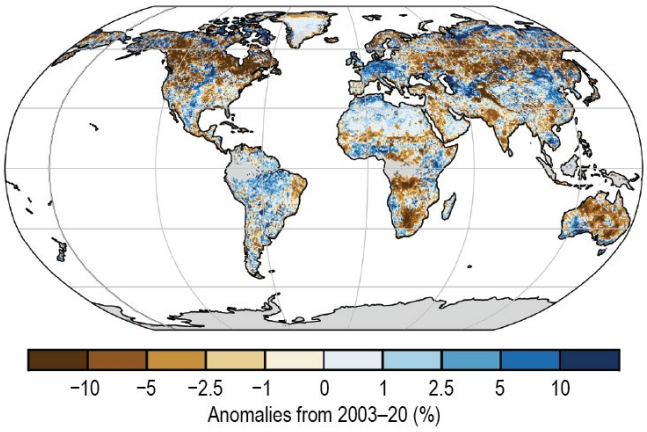

(af) Fraction of Absorbed Photosynthetically Active Radiation

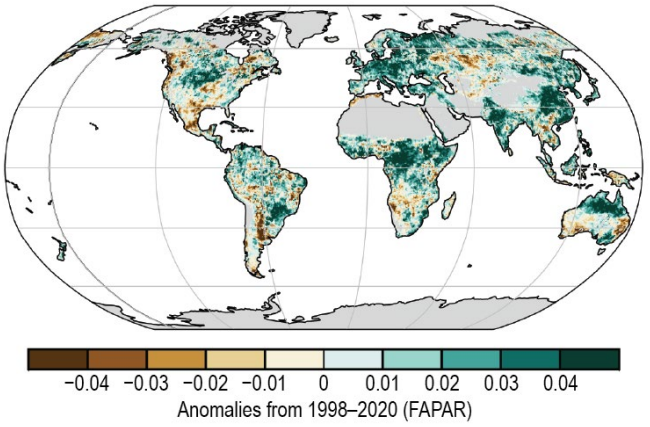

(ag) Carbon Emissions from Biomass Burning

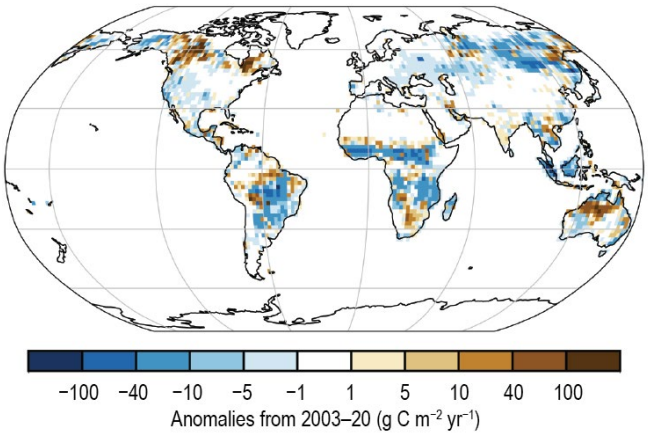

(ah) Vegetation Optical Depth

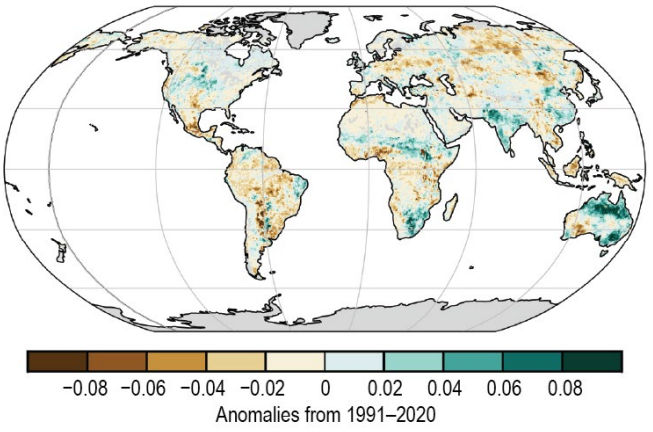

Plate 2.1 (cont.) (ac) CAMS reanalysis total column carbon monoxide anomalies (× 10^{18} molecules cm^{-2}); (ad) VIIRS land surface visible broadband albedo anomalies (%); (ae) VIIRS land surface near-infrared albedo anomalies (%); (af) FAPAR anomalies; (ag) GFASv1.4 carbonaceous emission anomalies (g C m^{-2} yr^{-1}) from biomass burning; (ah) VODCA CXKu-band VOD anomalies.

b. Temperature

1. GLOBAL SURFACE TEMPERATURE

—A. Sanchez-Lugo, C. Morice, J. P. Nicolas, A. Arguez, F. Sezaki, and A. Goto

The global surface temperature for 2023 was 0.55°C–0.60°C above the 1991–2020 average, according to seven global temperature datasets (Table 2.1; Fig. 2.1). This was the highest value since global records began in the mid-1800s to mid-1900s (with the length of record depending on the dataset), surpassing the previous warmest year on record in 2016 (equal with 2020 in the GISTEMP dataset) by a large margin (+0.13°C to +0.17°C). The datasets consist of four global in situ surface temperature analyses (GISTEMP, Lenssen et al. 2019; HadCRUT5, Morice et al. 2021; NOAAGlobalTemp, Vose et al. 2021; Berkeley Earth, Rhode and Hausfather 2020) and three global atmospheric reanalyses (ERA5, Hersbach et al. 2020; Bell et al. 2021; JRA-55, Kobayashi et al. 2015; JRA-3Q, Kosaka et al. 2024).

Table 2.1. Global temperature anomalies (°C; 1991–2020 base period) for 2023. Note that for the HadCRUT5 column, land values were computed using the CRUTEM.5.0.2.0 dataset (Osborn et al. 2021), ocean values were computed using the HadSST.4.0.1.0 dataset (Kennedy et al. 2019), and global land and ocean values were computed using the HadCRUT.5.0.2.0 dataset (Morice et al. 2021).

Global	NASA-GISTEMPv4	HadCRUT5	NOAA GlobalTemp	Berkeley Earth	ERA5	JRA-55	JRA-3Q
Land	+0.78	+0.73	+0.83	+0.73	+0.85	+0.76	+0.79
Ocean	+0.43	+0.47	+0.43	–	+0.50	+0.48	+0.50
Land and Ocean	+0.56	+0.56	+0.55	+0.57	+0.60	+0.56	+0.58

All seven datasets agree that the last nine years (2015–23) were the nine warmest years since global records began, and the global trends at the short-term (1981–2023; 0.19°C–0.20°C decade^{-1}) and long-term (1880–2023; 0.08°C–0.09°C decade^{-1}) periods for each dataset are comparable to one another. On a trend-adjusted basis, following the Arguez et al. (2020) approach, 2023 was well above the trend in all seven datasets, exceeding the 90th percentile in each. In fact, 2023 registered the highest departure above the trend line (computed for the period 1975–2023) in all four in-situ analyses and the second-highest departure in each reanalysis product, eclipsed only by 1981 in ERA5 and 2016 in JRA-55 and JRA-3Q.

The global surface temperature for 2023 was also 1.35°C–1.54°C above the 1850–1900 average (a period commonly used to represent pre-industrial conditions). The pre-industrial temperature anomaly range was computed using the three datasets that extend back to 1850 (NOAAGlobalTemp, HadCRUT5, Berkeley Earth) using each dataset's own 1850–1900 baseline. The year 2023 marked the ninth consecutive year with a temperature more than 1°C above this average.

After three consecutive years (mid-2020 to early 2023) of La Niña across the tropical

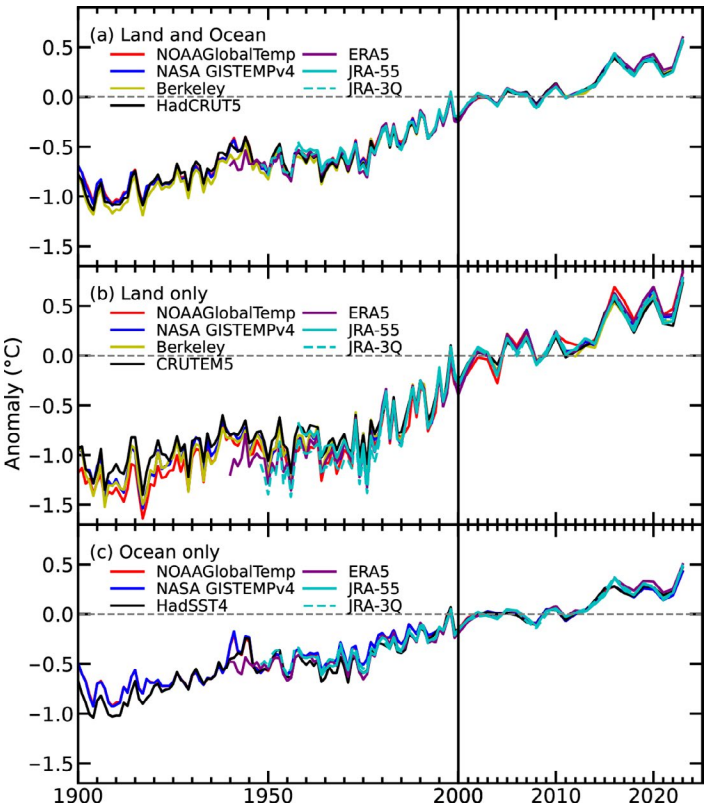

Fig. 2.1. Global average surface-air temperature anomalies (°C; 1991–2020 base period). In situ estimates are shown from NOAAGlobalTemp (Vose et al. 2021), NASA GISTEMPv4 (Lenssen et al. 2019), HadCRUT5 (Morice et al. 2021), CRUTEM5 (Osborn et al. 2021), HadSST4 (Kennedy et al. 2019), and Berkeley (Rhode and Hausfather 2020). Reanalysis estimates are shown from ERA5 (Hersbach et al. 2020; Bell et al. 2021), JRA-55 (Kobayashi et al. 2015), and JRA-3Q (Kosaka et al. 2024).

Pacific Ocean, 2023 quickly transitioned to ENSO-neutral and then to El Niño conditions by May. Monthly global ocean surface temperatures were unusually high (Plate 2.1a; Appendix Figs. A2.1–A2.5), with new global ocean temperature records set each month from June through December 2023. This sustained warmth resulted in a record-high annual global ocean surface temperature that was 0.43°C–0.50°C above the 1991–2020 average. The unusually warm oceans across many basins, along with the presence of El Niño and the long-term warming trend caused by anthropogenic greenhouse gas emissions, were key contributors to the high monthly global surface temperature records observed during the latter half of the year (see also section 3b and Sidebar 3.1 for details). The annual global land surface temperature was also record high, at 0.73°C–0.85°C above average.

Much-warmer-than-average conditions were observed across most of the world's surface, with the largest positive temperature anomalies occurring across parts of the higher northern latitudes (Plate 2.1a; Appendix Figs. A2.1–A2.5). Even with record warmth for the globe as a whole, below-average annual temperatures were observed across parts of Greenland, the southwestern contiguous United States, and parts of the Southern Ocean and Antarctica.

Sidebar 2.2: Near-surface equivalent temperature as a key climate change metric

—T. MATTHEWS, M. BYRNE, P. C. STOY, AND K. M. WILLETT

Only ~1% of the accumulating heat in Earth's system is being stored in the atmosphere (von Schuckmann et al. 2023) and heat has accumulated continuously over the past decades, warming the ocean, the land, the cryosphere, and the atmosphere. According to the Sixth Assessment Report by Working Group I of the Intergovernmental Panel on Climate Change, this planetary warming over multiple decades is human-driven and has resulted in unprecedented and committed changes to the Earth system, with adverse impacts for ecosystems and human systems. The Earth heat inventory provides a measure of the Earth energy imbalance (EEI), yet air temperature has been the de facto metric for communicating climate change. It has therefore been relatively straightforward to estimate global mean temperature change since the pre-industrial period (Hansen et al. 2010; Morice et al. 2021; Rohde and Hausfather 2020). Air temperature trends are also highly relevant to society, not least due to the universal temperature sensitivity observed in the biosphere (Gillooly et al. 2001) and because of the fundamental control of temperature on the hydrological cycle (Held and Soden 2006).

Air temperature alone, however, provides an incomplete perspective of atmospheric heat accumulation (Matthews et al. 2022; Pielke 2003). The total energy content (TEC) of the atmosphere is mostly comprised of sensible heat (~97%) with a minor contribution from latent heat (~3%; Peixoto and Oort 1992). In tracking sensible heat content, air temperature is therefore a good proxy for TEC; however, it is less appropriate for monitoring changes in TEC because almost half of the recent gain in global mean near-surface energy has been channeled into latent heat (Matthews et al. 2022; Stoy et al. 2022), exceeding 75% in some tropical regions. The potential for this increase to be "hidden" by air temperature trends is concerning, as latent heat plays a key role in determining maximum intensities for precipitation extremes (Ali et al. 2018; O'Gorman 2012; Song et al. 2022), near-surface air temperature, and human heat stress (Matthews 2018). Hotspots and hot moments of societally relevant heat accumulation are therefore at risk of being missed by using air temperature alone to track climate change. A metric proportional to TEC could also help constrain assessments of Earth's changing energy budget (von Schuckmann et al. 2023).

$$Teq = T + \frac{L_v}{c_p} q$$

In response to these concerns, the equivalent temperature (*Teq*) has been suggested as an important additional metric for use in climate communications (Matthews et al. 2022; Pielke 2003; Song et al. 2022): in which T is the (dry-bulb) air temperature, L_v is the latent heat of vaporization, c_p is the

specific heat capacity of air at constant pressure, and q is the specific humidity. *Teq* therefore tracks the sensible heat content through T and the latent heat through $L_v/c_p\ q$. It represents the air temperature that could be reached if all latent heat was converted to sensible heat. A related quantity—the equivalent potential temperature—is conserved under reversible moist adiabatic processes and has been used to explore the land–ocean warming contrast and to help understand the maximum possible intensity of heatwaves (Byrne and O'Gorman 2013; Zhang and Boos 2023).

T, *Teq*, and the "latent temperature" ($Tq = Teq - T$) were computed using near-surface air temperature, dewpoint, and surface pressure from ERA5 (Hersbach et al. 2020) following Raymond et al. (2021) to evaluate L_v and c_p. For comparison, *Teq* from the HadISDH near-surface in situ humidity product (land only; Willett et al. 2014, 2013) was also assessed, processing it from hourly observations through to the quality-controlled and homogenized monthly mean gridded fields. Note that both ERA5 and HadISDH data were assessed for the overlapping 1973–2023 period. The 1991–2020 ERA5 climatology illustrates that *Teq* is more variable over Earth's surface than *T*. Both share a minimum slightly below 220 K in Antarctica, while *Teq* climbs to more than 30 K above *T* in the tropics due to the much greater contribution from *Tq* at low latitudes (Figs. SB.2.1a–c). *Teq* therefore exhibits a much steeper poleward reduction (Fig. SB.2.1d).

The ERA5 trends in *T* highlight the familiar warming enhancement over land (Byrne and O'Gorman 2018) and in the Arctic (Figs. SB.2.2a,b). However, *Tq* trends are different, being generally greatest in the northern tropics and subtropics and more similar between land and ocean (Figs. SB.2.2c,d). The weaker trends over subtropical land agree with Simpson et al. (2024) and highlight that latent heat content can fall even as *T* (and hence saturation vapor pressure) climbs due to reductions in relative humidity. The *Teq* trends reflect the combined response of *T* and *Tq* (Figs. SB.2.2e,f), with perhaps the most significant difference from *T* being that Arctic amplification appears more subdued relative to the (densely populated) northern low latitudes. HadISDH agrees with this pattern but suggests even larger low-latitude trend amplification

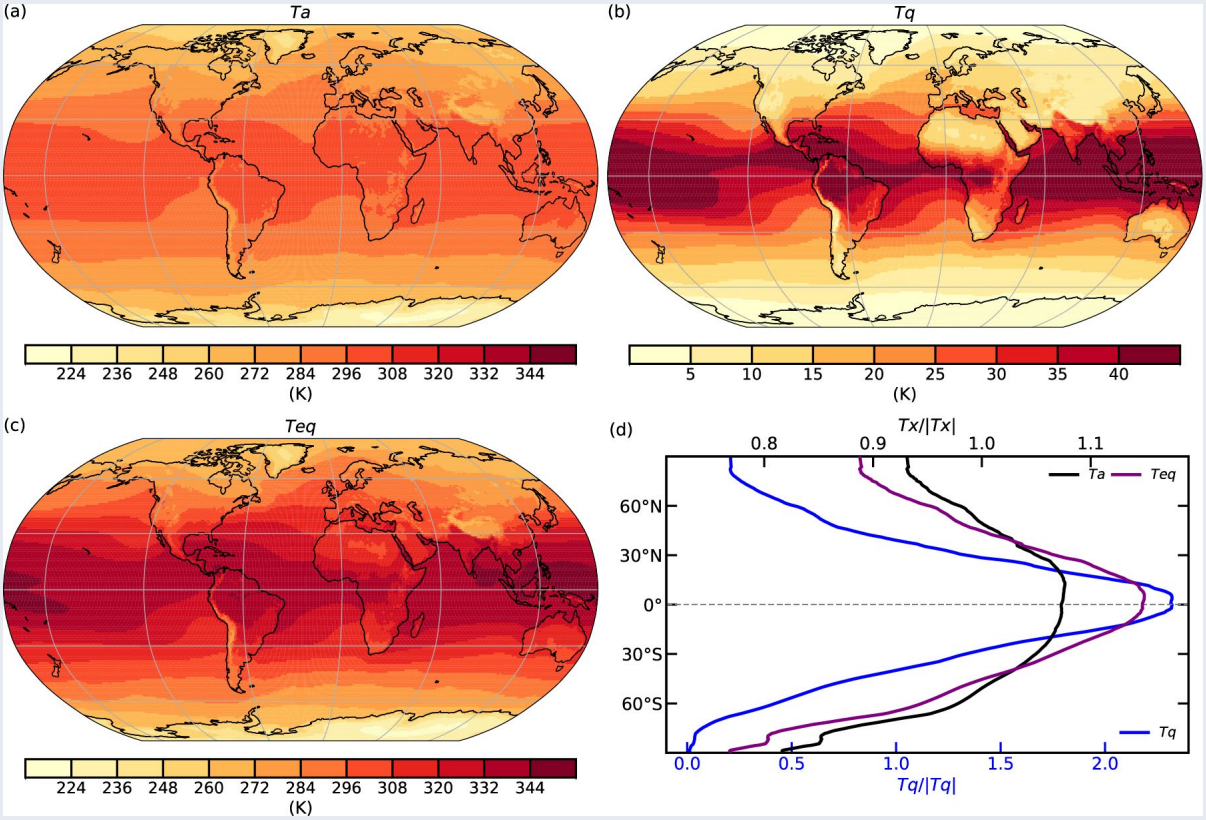

Fig. SB.2.1. The 1991–2020 ERA5 climatology for (a) air temperature (*Ta*), (b) latent temperature (*Tq* = *Teq* – *Ta*), and (c) equivalent temperature (*Teq*). (d) Zonal-mean profiles (*Tx*) normalized to the mean of each series plotted (|*Tx*|). Note that *Tq* is plotted on the bottom x-axis due to its greater variability.

(Fig. SB.2.2f), likely driven by undersampling in those tropical regions (e.g., East Africa) where ERA5 suggests lower *Teq* trends due to drying (Figs. SB.2.2c,e; see Willett et al. 2023).

The ERA5 trend (1973–2023) in global-mean near-surface *Teq* is 0.36±0.03 K decade^{-1} (Fig. SB.2.3). The comparison series from HadISDH indicates a larger trend of 0.55±0.03 K decade^{-1}, likely due to a combination of its land-only nature and incomplete spatial sampling. Disaggregating the *Teq* trend for ERA5 indicates that approximately 58% is explained by the *T* trend (0.21±0.01 K decade^{-1}) and 42% by *Tq* (0.15±0.02 K decade^{-1}). However, because climatological *Tq* is much lower than *T* (Fig. SB.2.1), the *Tq* trend represents a much more significant relative increase. This was well illustrated in 2023: the hottest year on record for *Teq* (in ERA5 and HadISDH:

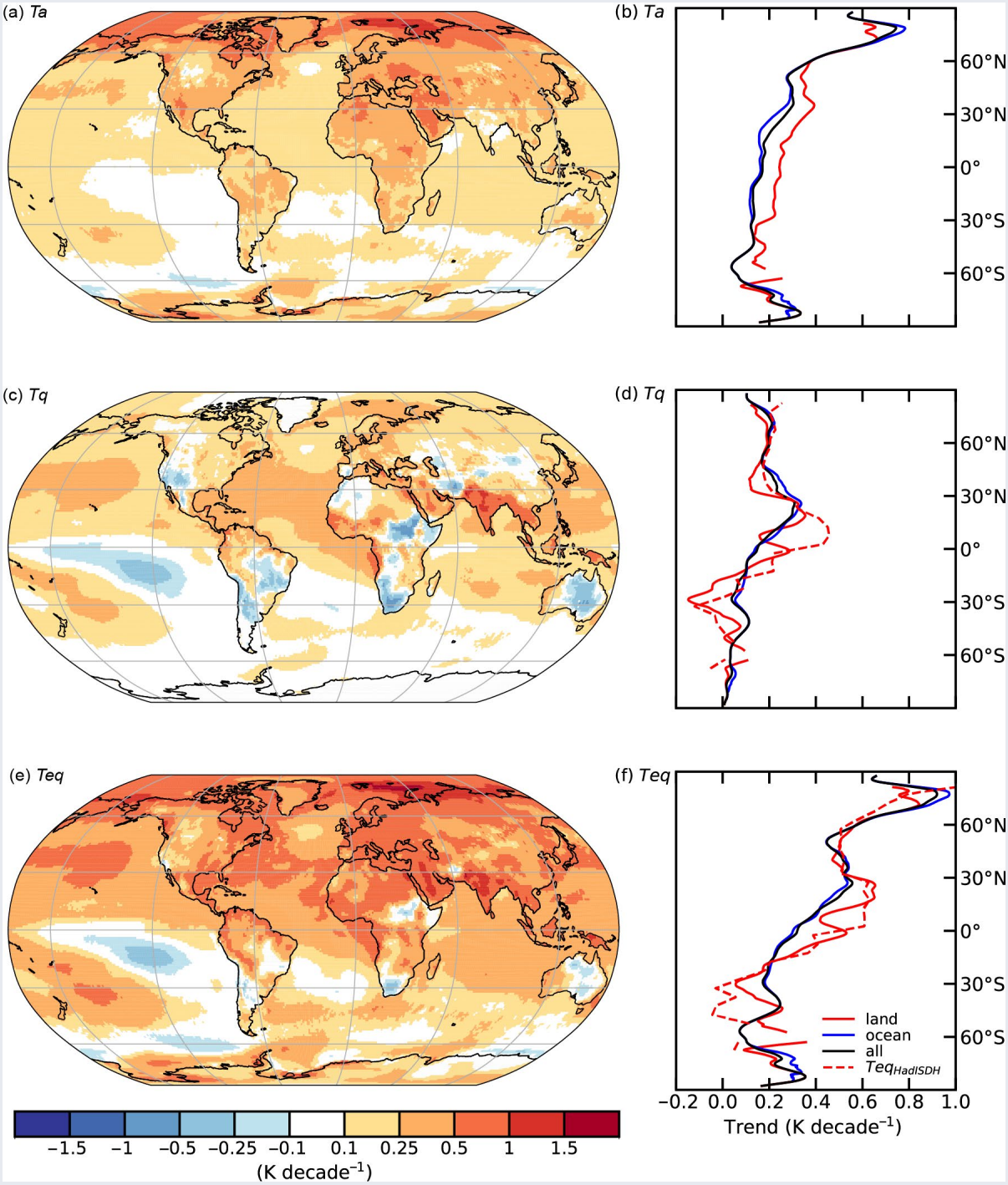

Fig. SB.2.2. The 1973–2023 ERA5 trends and their zonal means (K decade^{-1}; right-hand panels, smoothed with 5° running mean) in (a),(b) air temperature (*Ta*), (c),(d) latent temperature (*Tq* = *Teq* – *T*), and (e), (f) equivalent temperature (*Teq*). In panels (d),(f), (land only) zonal-mean trends for HadISDH are also shown as the dashed line.

Fig. SB.2.3) and for *Ta* and *Tq* individually (Table SB.2.1). The latter both recorded anomalies of 0.6 K relative to the 1991–2020 climatology (see sections 2b1, 2d), but the much lower baseline in *Tq* translates the 0.6 K anomaly to a relative increase of 2.5%—over an order of magnitude larger than for *T* (0.21%). This carries through to *Teq* to some extent, with the relative anomaly in 2023 of 1.2 K representing a rise of 0.38% (Table SB.2.1). As measured by *Teq*, the climate has therefore departed even further from the reference points of human history.

Although *Teq* is a complete physical descriptor of atmospheric heating, its unfamiliarity may present a challenge in climate communications, not least because its absolute values (Fig. SB.2.2) and its variability (Fig. SB.2.3) are much higher than for *T*. However, presenting relative changes as above may be a simple and intuitive solution for overcoming this communication barrier. Such efforts are worth pursuing, as *Teq* is a key indicator of changes to the atmospheric state that are of critical relevance to society.

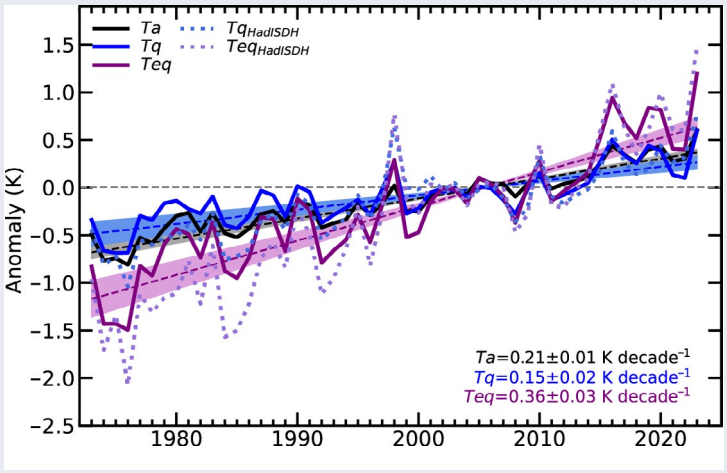

Fig. SB.2.3. 1973–2023 ERA5 and HadISDH trends in global mean air temperature (*Ta*; ERA5 only), latent temperature (*Tq* = *Teq* – *Ta*), and equivalent temperature (*Teq*). Trend lines were computed with simple linear regression, and shading spans 95% confidence intervals. The trends presented on the plot are for ERA5, with ±1 sigma standard error.

Table SB.2.1. Top-10 years for annual mean values in ERA5 (1973–2023). Note that relative anomalies are computed from the 1991–2020 baseline.

Rank	Ta year	Ta (K)	Ta (%)	Tq year	Tq (K)	Tq (%)	Teq year	Teq (K)	Teq (%)
1	2023	0.60	0.21	2023	0.60	2.51	2023	1.20	0.38
2	2016	0.44	0.15	2016	0.50	2.12	2016	0.94	0.30
3	2020	0.43	0.15	2019	0.44	1.85	2019	0.84	0.27
4	2019	0.40	0.14	2020	0.38	1.62	2020	0.82	0.26
5	2017	0.34	0.12	2017	0.34	1.41	2017	0.68	0.22
6	2022	0.30	0.10	1998	0.27	1.14	2015	0.52	0.17
7	2021	0.27	0.10	2015	0.27	1.13	2018	0.52	0.17
8	2018	0.26	0.09	2018	0.25	1.07	2021	0.41	0.13
9	2015	0.26	0.09	2010	0.15	0.63	2022	0.40	0.13
10	2010	0.13	0.05	2021	0.13	0.56	1998	0.29	0.09

2. LAKE SURFACE WATER TEMPERATURE

—L. Carrea, C. J. Merchant, R. I. Woolway, J.-F. Crétaux, T. M. Dokulil, H. Dugan, A. Laas, E. Leibensperger, S.-I. Matsuzaki, L. J. Merio, D. Pierson, O. O. Rusanovskaya, S. V. Shimaraeva, E. A. Silow, M. Schmid, M. A. Timofeyev, and P. Verburg

The globally averaged satellite-derived lake surface water temperature (LSWT) anomaly during the 2023 warm season was +0.46°C with respect to the 1995–2020 baseline, the highest since the record began in 1995 (Fig. 2.2a). The mean LSWT trend during 1995–2023 was 0.20±0.01°C decade^{-1}, broadly consistent with previous analyses even though the number of lakes analyzed has doubled since 2022 (Woolway et al. 2017, 2018; Carrea et al. 2019, 2020, 2021, 2022a; Fig. 2.2a). The 2023 warm-season anomalies for each lake are shown in Plate 2.1b; of the 1949 studied lakes that were not dry, 79% of these were warmer than average and 21% were colder. For 33 lakes, no anomalies could be computed since they were found to be dry.

Large coherent regions of high LSWT were identified in 2023, with 44% of all observed lakes experiencing LSWT anomalies in excess of +0.5°C (Plate 2.1b). The highest anomalies occurred

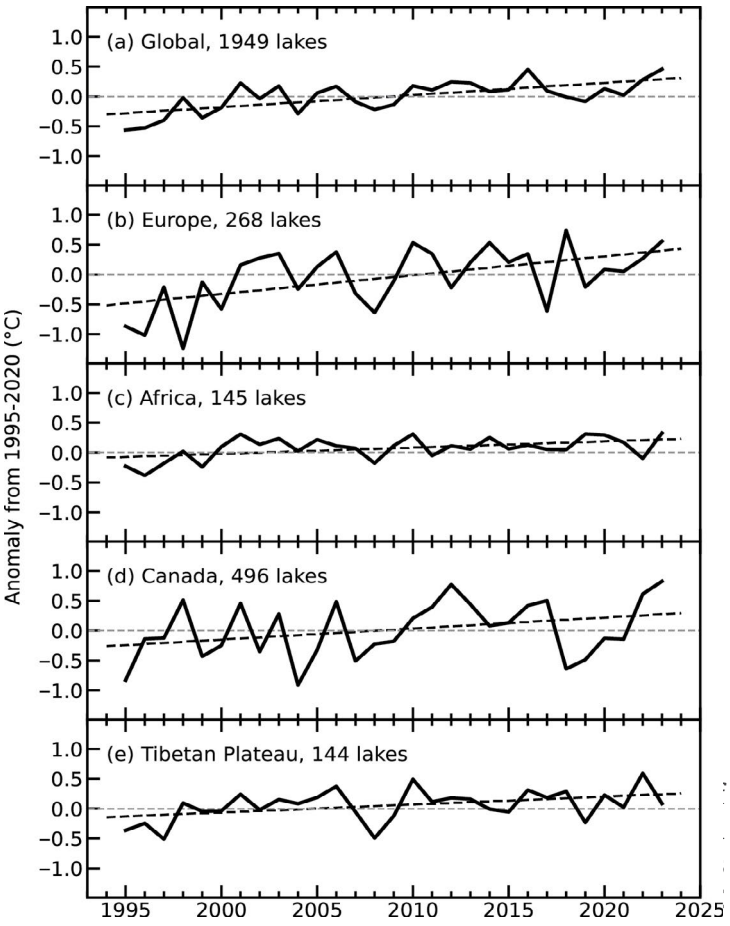

in lakes situated in northern Canada, eastern China, Japan, and Europe. Negative LSWT anomalies were consistently observed in Patagonia, Greenland, Alaska, Australia, northern South America, and southeast Asia.

Four regions were studied in more detail: Europe (number of lakes, n = 268, Figs. 2.2b, 2.3a), Canada (n = 496, Figs. 2.2d, 2.3c), Tibet (n = 144, Figs. 2.2e, 2.3d), and Africa (n = 145, Figs. 2.2c, 2.3b). In these regions, the warm-season LSWT anomalies are consistent with the corresponding air temperature anomalies, as compiled by NASA's Goddard Institute for Space Studies (GISS; Lenssen et al. 2019; GISTEMP Team 2023), with an average warming trend of +0.31±0.03°C decade^{-1} in Europe (Fig. 2.2b) and +0.18±0.03°C decade^{-1} in Canada (Fig. 2.2d). In Canada, where the mean LSWT anomaly was +0.83°C in 2023, 92% of observed lakes had positive anomalies. In Europe, the

Fig. 2.2. Annual time series of satellite-derived warm-season lake surface water temperature anomalies (°C; 1995–2020 base period) from 1995 to 2023 for lakes distributed (a) globally, and regionally in (b) Europe, (c) Africa, (d) Canada, and (e) the Tibetan Plateau.

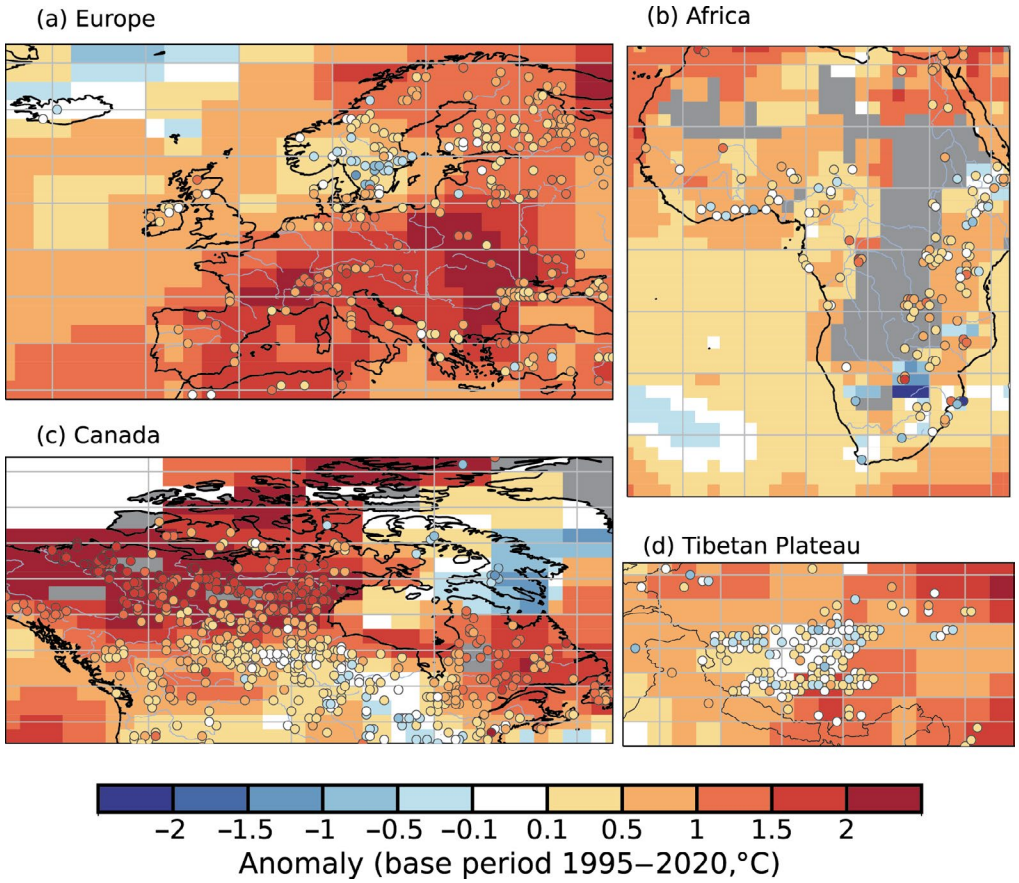

Fig. 2.3. Lake temperature anomalies (°C, colored dots) and 2-m air temperature anomalies (°C) in 2023 for lakes in (a) Europe, (b) Africa, (c) Canada, and (d) the Tibetan Plateau. These values were calculated for the warm season (Jul–Sep in the extratropical Northern Hemisphere; Jan–Mar in the extratropical Southern Hemisphere; Jan–Dec in the tropics) with reference to the 1995–2020 base period.

decade^{-1} and +0.10±0.02°C decade^{-1}, respectively (Figs. 2.2c,e). In Africa, 81% of the 145 lakes had positive LSWT anomalies, and the average anomaly in 2023 was +0.33°C. In Tibet, the average 2023 anomaly was +0.09°C, with 70% of the lakes experiencing positive anomalies.

In situ observations of (single-point) warm season temperature anomalies from 38 lakes are shown in Fig 2.4, 23 of which have measurements for the year 2023, with an average of +0.78°C. The anomalies calculated here differ from those derived from satellite data, which represent lake-wide averages. Five lakes experienced negative anomalies (average of −0.76°C) and 18 lakes had positive anomalies (average of +1.21°C) in 2023. The time series in Fig. 2.4 clearly show that lakes are warming.

The period 1995–2020 is used as a baseline for both in situ (unless no data were available) and satellite temperatures to compute anomalies. The warm-season averages for midlatitude lakes were computed for summers (July–September in the Northern Hemisphere and January–March in the Southern Hemisphere), and January–December averages are presented for tropical lakes (within 23.5° of the equator).

Lake surface water temperature time series were derived from the European Space Agency Climate Change Initiative (ESA CCI) LAKES/Copernicus Climate Change Service (C3S) /Earth Observation Climate Information Service (EOCIS) climate data record (Carrea et al. 2022b, 2023). The LSWT time series has been derived using ATSR2, AATSR, MODIS, AVHRR and SLSTR sensors. For 2023, satellite observations from SLSTR on Sentinel3A and 3B were used. The retrieval method of MacCallum and Merchant (2012) was applied on image pixels filled with water according to both the inland water dataset of Carrea et al. (2015) and a reflectance-based water detection scheme (Carrea et al. 2023).

The satellite-derived LSWT data are spatial averages for each of a total of 1949 lakes. The satellite-derived LSWT data were validated with in situ measurements with an average satellite-minus-in situ temperature difference of less than 0.5°C and standard deviation (robust) of less than 0.7°C (Carrea et al. 2023). Lake-wide average surface temperatures have been shown to give a more representative picture of LSWT responses to climate change compared to single-point measurements (Woolway and Merchant 2018).

The average surface air temperature was calculated from GHCN v4 (250-km smoothing radius) data of the NASA GISS surface temperature analysis (Lenssen et al. 2019; GISTEMP Team 2024).

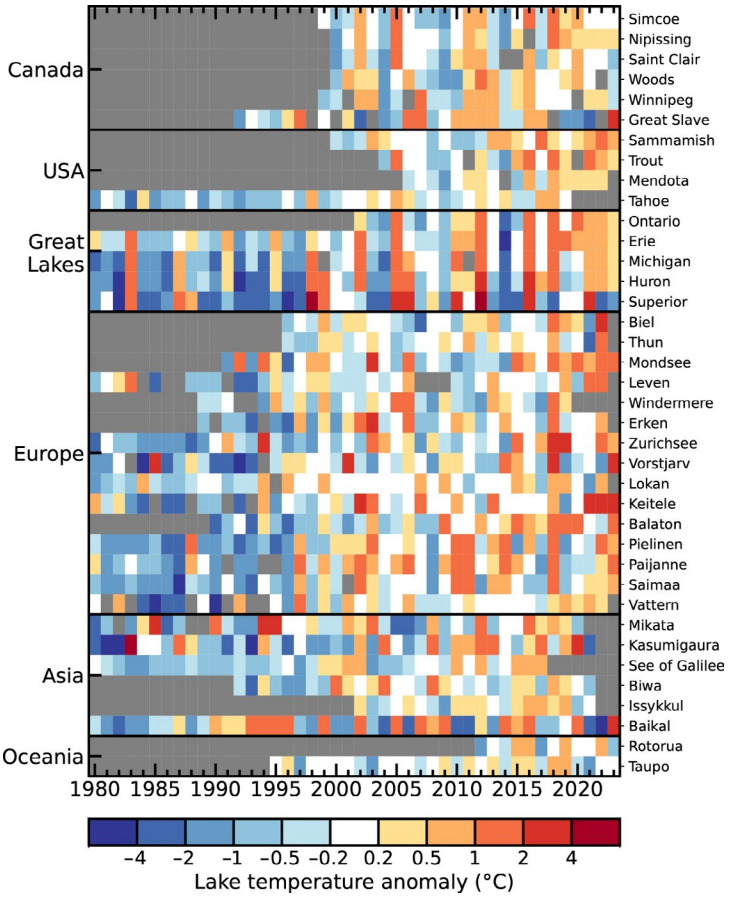

Fig. 2.4. In situ lake surface water temperature observations from 38 globally distributed lakes, showing the annually averaged warm season (Jul–Sep in the Northern Hemisphere; Jan–Mar in the Southern Hemisphere) anomalies (°C; 1995–2020 base period or the available base period).

3. NIGHT MARINE AIR TEMPERATURE

—R. C. Cornes and R. Junod

Two night marine air temperature (NMAT) datasets are routinely updated and used for analysis in this section: UAHNMAT (Junod and Christy 2020) and CLASSnmat (Cornes et al. 2020). These datasets are evaluated in combination with the HadSST4 dataset (Kennedy et al. 2019). Since these datasets are not spatially interpolated, they each have slightly different spatial coverage. In this evaluation the data have been masked to allow comparisons to be made over the common coverage areas, and to the common period of 1900–2023. NMAT and sea-surface temperature

(SST) data are expected to follow each other closely across large spatial scales and over longer time periods. As such, the NMAT data are used here to evaluate the more widely used SST data, which are considered in more detail in section 3b.

In all three datasets, 2023 was the warmest year in the series, with exceptional global annual average temperatures that were 0.50°C, 0.40°C, and 0.47°C above the 1991–2020 baseline in the CLASSnmat, UAHNMAT, and HadSST4 series, respectively (Fig. 2.5a). During the latter half of the year, consistent positive anomalies of >+0.5°C were recorded in the CLASSnmat and HadSST4 datasets (Fig. 2.6). The anomalies in the UAHNMAT were slightly lower, although global average anomalies were consistently above +0.4°C from June to December.

Large-scale averages of the NMAT/SST data are plotted in Figs. 2.5b–d. These results indicate that 2023 was the warmest year in each of the three regions. The largest anomalies were recorded in the northern extratropics (north of 30°N), with average annual anomalies of >+0.7°C in the CLASSnmat and HadSST4 datasets and +0.6°C in UAHNMAT. These results reflect the high frequency of marine heatwaves that occurred globally throughout 2023 (see sections 2b4, 3b, and Sidebar 3.1), although individual events are not evident in those results due to the consideration of annual averages. Examination of the grid-cell values (Plate 2.1c) indicates three areas of marked positive anomalies, which are also present in the UAHNMAT and HadSST data (not shown): the eastern tropical Pacific, the northern Pacific, and the North Atlantic. The pattern across the tropical Pacific reflects the strong El Niño that developed during the latter half of the year.

Marine air temperature data recorded on board ships have been used for many years for climate monitoring purposes and to evaluate land air temperature and SST datasets (Rayner et al. 2003). However, two main biases exist in these observations: artificial diurnal heating due to the superstructure of the ships (Cropper et al. 2023) and variable temperature observing heights (Kent et al. 2013). To reduce the effect of diurnal heating biases, the daytime observations are removed from the data, resulting in night marine air temperature data. As such, the processing is designed to remove this artefact from the data rather than for

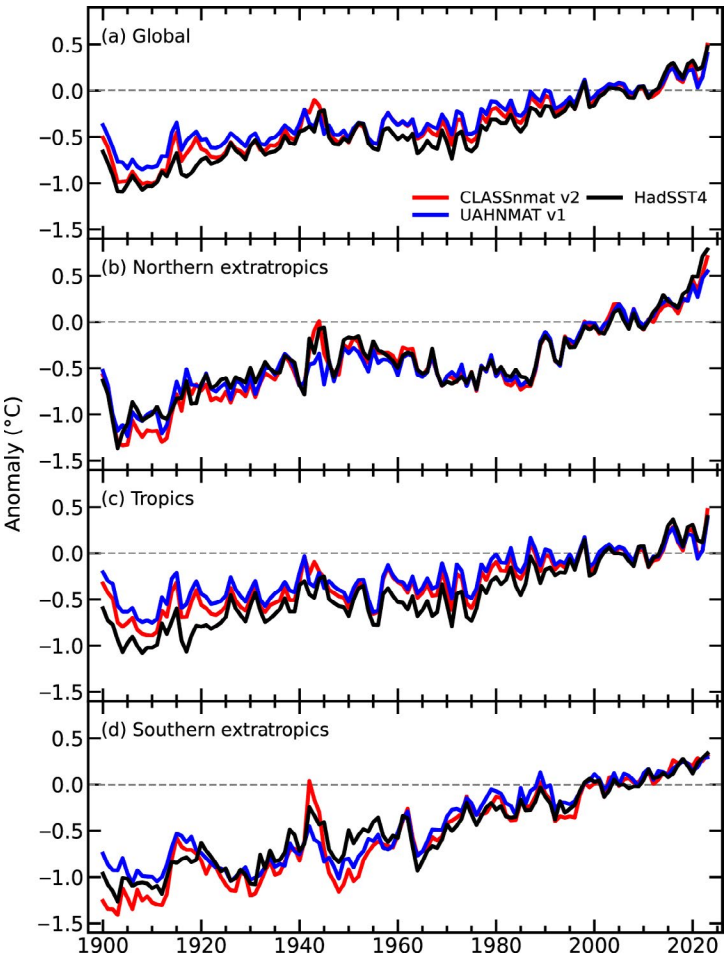

Fig. 2.5. Annual average marine temperature anomalies (°C; 1991–2020 base period) calculated from the CLASSnmat, UAHNMAT, and HadSST4 datasets averaged over the (a) globe, (b) northern extratropics, (c) tropics, and (d) southern extratropics. The tropics is defined as the latitude range 30°S–30°N and the northern (southern) extratropics as >30°N (<30°S). The averages only include values that are common to all three datasets for a given year; since UAHNMAT starts in 1900, only values for the period 1900–2023 are plotted.

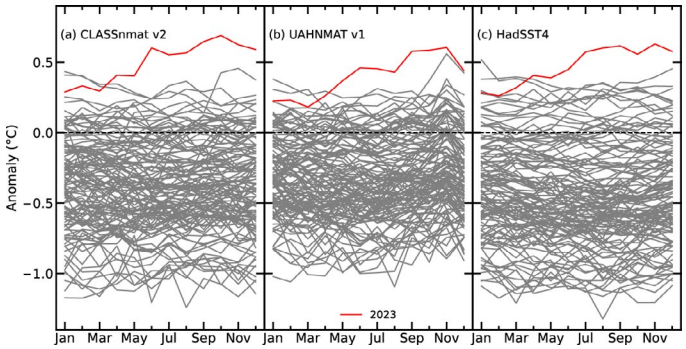

Fig. 2.6. Global monthly average marine temperature anomalies (°C; 1991–2020 base period) in the (a) CLASSnmat, (b) UAHNMAT, and (c) HadSST4 datasets. Each line represents a year of data, and the results for 2023 are shown in red.

quantifying night temperature per se (c.f. terrestrial nighttime temperature extremes in section 2b4). Inhomogeneities arising from changing observation height are removed by adjusting the temperature readings to a common reference height, which is typically 10 m above the sea surface. The UAHNMAT and CLASSnmat datasets examined in this section use different methods to implement the height correction, and they also differ in the quality-control of the data and the approach taken to addressing other biases in the data, notably for the warm bias that exists in the data during the World War II period (Cornes et al. 2020).

4. SURFACE TEMPERATURE EXTREMES

—R. J. H. Dunn, M. G. Donat, R. W. Schlegel, and M. G. Bosilovich

The record-breaking global surface temperatures of 2023 (section 2b1) also translated to record numbers of "warm days" (TX90p; Table 2.2) and, as in the last few years, well-below-average numbers of "cool nights" (TN10p; Table 2.2) over land.

The GHCNDEX dataset of gridded in situ observations (Donat et al. 2013) had a globally averaged number of warm days of 70±7. As this dataset has limited spatial coverage for 2023, several reanalysis products are used (ERA5, Hersbach et al. 2020; Bell et al. 2021; JRA-55, Kobayashi et al. 2015; MERRA-2, Gelaro et al. 2017) to give a globally complete assessment of the land surface extreme temperatures. As shown in Fig. 2.7c and Table 2.2, all reanalysis products reached record values in 2023 for the number of warm days, values which were substantially more than the previous record set in 2016. There is a wide spread in values from these globally complete products, from 70 to 81 warm days in the year (relative to the value over the 1981–2010 reference period of 36.5), with ERA5 showing greater warming than MERRA-2 and JRA-55.

Many areas of the world had their highest number of warm days on record in 2023 (Fig. 2.8a). Globally averaged, 2023 had the third-highest land fraction experiencing record numbers of warm days, following the strong El Niño years of 2010 and 1998 (Fig. 2.8b). Regionally, most of Canada had record numbers of warm days, with a large fraction of South America, and substantial areas of Africa, Europe, and Asia also showing record numbers of warm days (see Chapter 7 for details on regional temperatures). In contrast, Australia had almost no areas of record high values for TX90p (Plate 2.1d). A similar pattern is seen in the anomalies of cool nights (Plate 2.1e). Below-average numbers of warm days occurred in the western United States, Alaska, parts of the Indian subcontinent, and northern Australia.

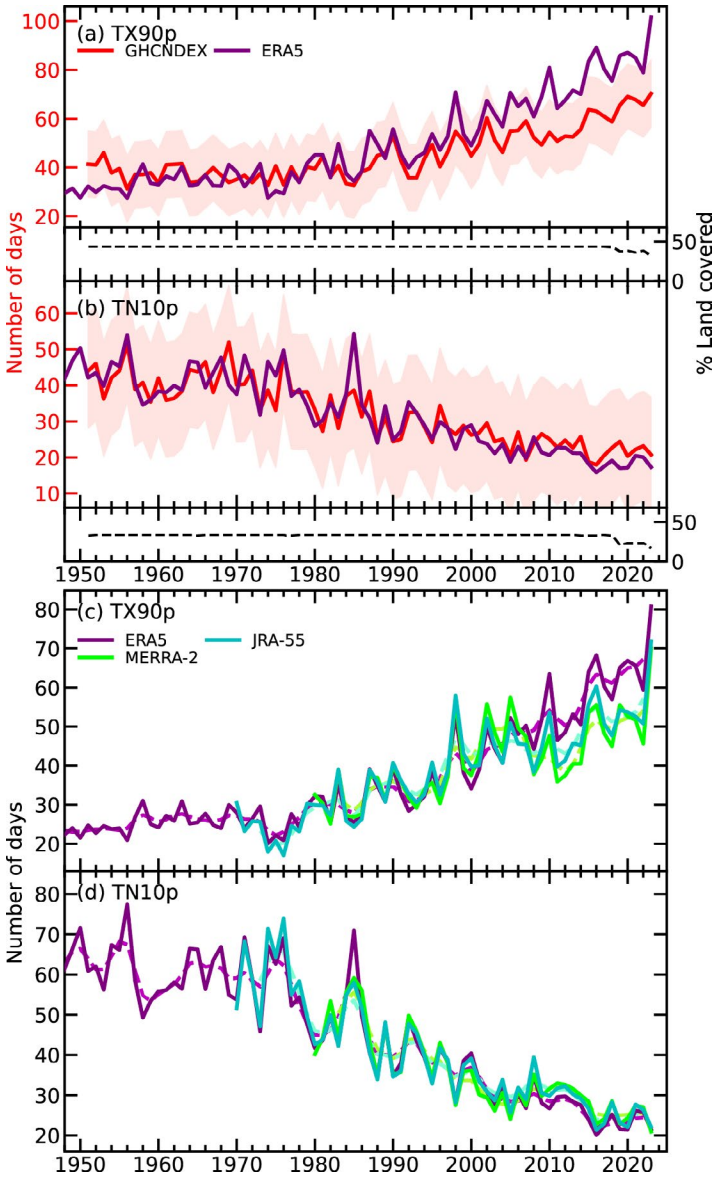

Fig. 2.7. (a),(b) Time series of the (a) annual number of warm days (TX90p) and (b) cool nights (TN10p) averaged over global land regions based on gridded station data from the GHCNDEX dataset (smoothed shown by dashed lines) and ERA5 using 1961–90 as the reference period. The spatial coverage in GHCNDEX is limited, the black dashed lines show the percentage of land area covered (right y-axis). The 2-σ coverage uncertainty (following Brohan et al. 2006; Dunn et al. 2020) is shown by the light red bands in (a),(b). (c),(d) As in (a),(b), for three atmospheric reanalyses (ERA5, MERRA-2, and JRA-55) using 1991–2020 as the reference period.

Table 2.2. Definitions of indices used for land surface temperature extremes, their globally averaged values (days) for 2023, and ranks from the four datasets. Coverage uncertainties are shown for GHCNDEX.

Index	Name	Definition	GHCNDEX (1951–2023) Value, [rank] Reference Period 1961–90	ERA5 (1940–2023) Value, [rank] Reference Period 1961–90	ERA5 (1940–2023) Value, [rank] Reference Period 1991–2020	MERRA-2 (1980–2023) Value, [rank] Reference Period 1991–2020	JRA-55 (1970–2023) Value, [rank] Reference Period 1991–2020
TX90p	Warm days	The annual count of days when the daily maximum temperature exceeds the 90th percentile	22 [third lowest]	102 [highest]	81 [highest]	70 [highest]	72 [highest]
TN10p	Cool nights	The annual count of nights when the daily minimum temperature falls below the 10th percentile	21±8 [seventh lowest]	17 [fourth lowest]	21 [third lowest]	21 [lowest]	--

Indices recommended by the former World Meteorological Organization Expert Team on Climate Change Detection and Indices (Zhang et al. 2011) characterize temperature extremes using observations of daily maximum and minimum temperatures. These indices are calculated from the daily maximum and minimum temperatures for stations in the GHCN-daily dataset (Menne et al. 2012) and interpolated on to a regular 2.5° grid to form GHCNDEX (Donat et al. 2013). As in previous years' assessments, spatial coverage falls off in recent years, so we use reanalysis products to provide globally complete fields for these indices. A recent comparison of reanalysis and observational products for these indices shows good agreement, especially for the indices presented here (Dunn et al. 2022). These indices use a fixed reference period (1961–90 for GHCNDEX and ERA5; 1991–2020 for ERA5, MERRA-2, and JRA-55), and intercomparison between these is not trivial (Dunn et al. 2020; Yosef et al. 2021; Dunn and Morice 2022).

A marine heatwave (MHW) is detected when five or more consecutive days of temperature are above a 90th-percentile daily climatology (Hobday et al. 2016). Marine heatwaves are categorized as moderate when the greatest temperature anomaly during the event is less than double the difference between the 90th percentile and the seasonal anomaly. When this value is more than double, triple, or quadruple the difference, the MHW is categorized as strong, severe, or extreme, respectively (see Fig. 2 in Hobday et al. 2018). The direct inverse is used to detect and categorize marine cold spells (MCSs; i.e., days below the 10th percentile). The baseline period used to detect events in this report is 1982–2011, because 1982 is the first full year of the NOAA OISST product (Huang et al. 2021).

The 2023 analysis of NOAA OISST daily v2.1 revealed that 94% of the global ocean surface experienced at least one marine heatwave (Hobday et al. 2016; Figs. 2.9a,b),

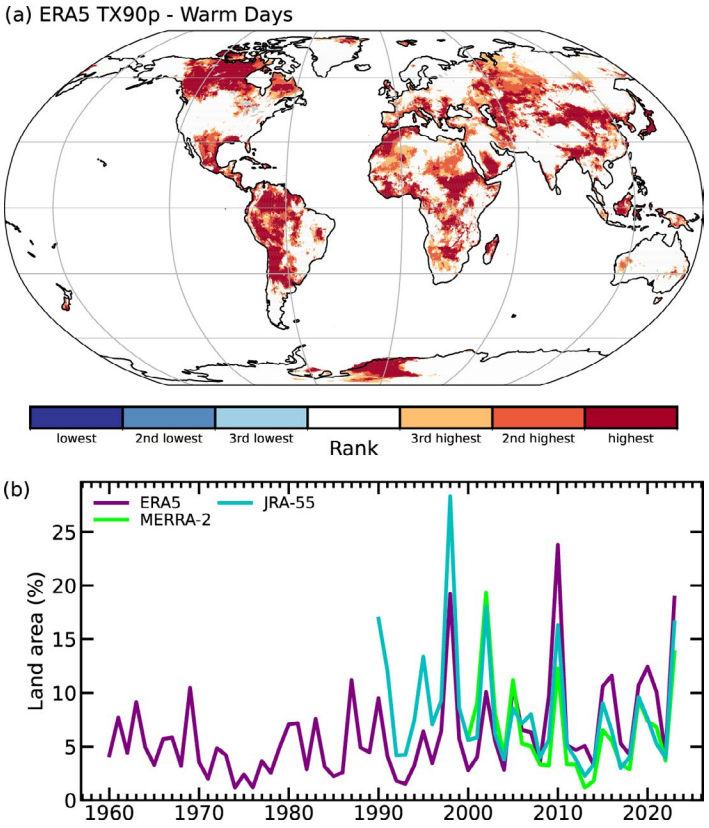

Fig. 2.8. (a) Map indicating grid cells where the warm day index (TX90p) for 2023 ranked in the three highest (orange to red) or three lowest (blue) values based on ERA5 since 1940 using the 1991–2020 reference period. (b) Time series of the percent of land area ranked as the highest value for TX90p in each year for ERA5 (from 1960), JRA-55 (from 1990), and MERRA-2 (from 2000). The ranks from the first 20 years of each reanalysis are not calculated.

and 27% experienced at least one MCS (Figs. 2.9c,d). The most common MHW category (Hobday et al. 2018) in 2023 was Category 2 Strong (49%), with the coverage of Category 3 Severe events reaching 10%. Category 1 Moderate MCSs have remained the most common (16%) cool events in all years since 1987. The ocean experienced a new global average record of 116 MHW days in 2023. This is far more than the 2016 MHW record of 86 days (Fig. 2.9a). This equates to a daily average MHW coverage of 32%. In 2023, the global ocean experienced 13 MCS days, far below the record of 37 days in 1982, equating to a daily average coverage of 4% (Fig. 2.9c).

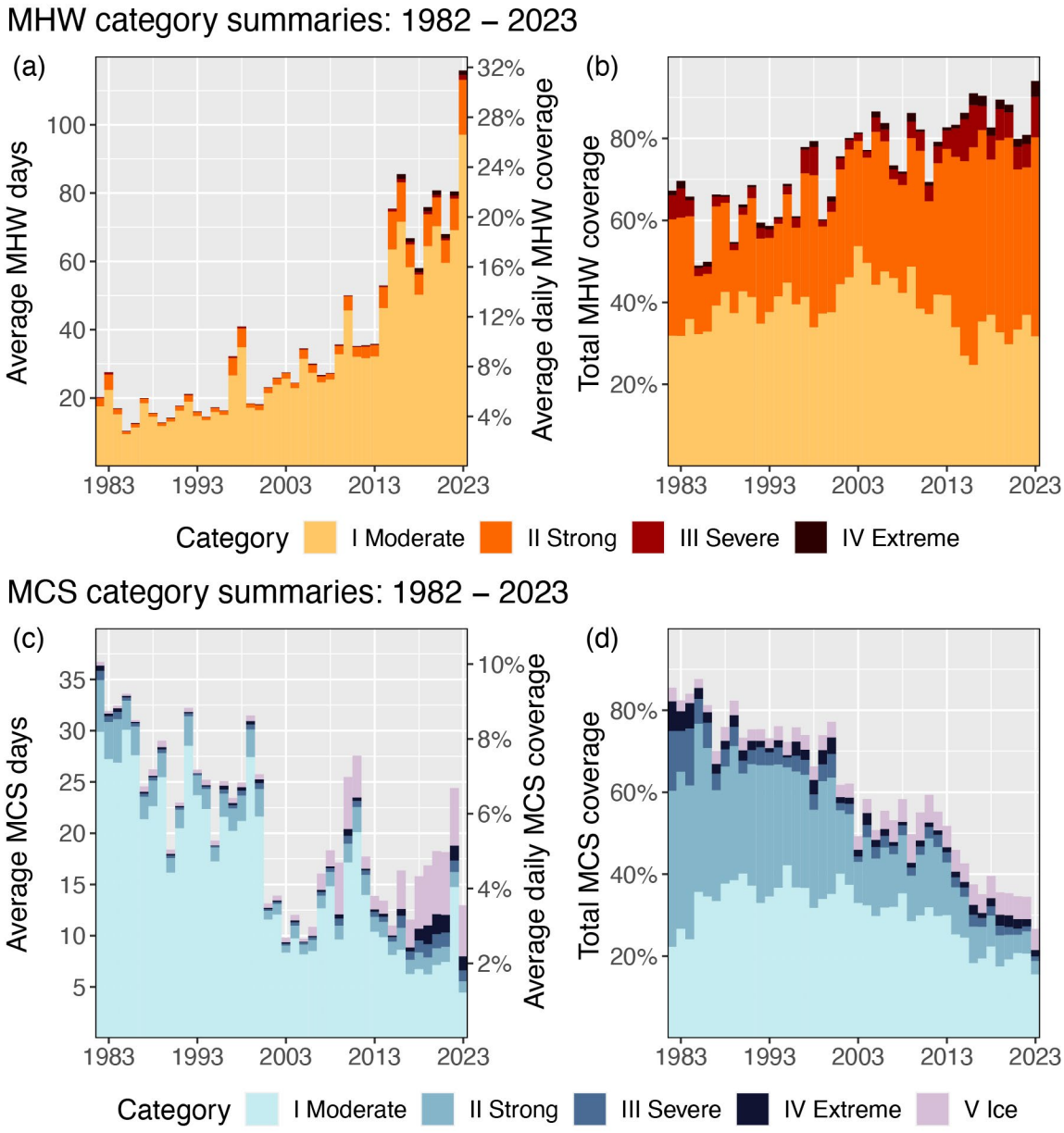

Fig. 2.9. Annual global marine heatwave (MHW; [a],[b]) and marine cold spell (MCS; [c],[d]) occurrence from NOAA OISST v2.1 using a climatology base period of 1982–2011. (a),(c) The average count of MHW/MCS days experienced over the surface of the ocean each year (left y-axis), also expressed as the percent of the surface of the ocean experiencing a MHW/MCS on any given day (right y-axis) of that year. (b),(d) Total percent of the surface area of the ocean that experienced an MHW/MCS at some point during the year. The values shown are for the highest category of MHW/MCS experienced at any point.

5. TROPOSPHERIC TEMPERATURE

—S. Po-Chedley, J. R. Christy, L. Haimberger, C. A. Mears, and C.-Z. Zou

The annual average lower tropospheric temperature (LTT) was record high for 2023, with particularly exceptional values in the tropics during the second half of the year (Fig. 2.10). The annual average LTT was 0.43°C–0.65°C above the 1991–2020 average, depending on the dataset (Fig. 2.11). In the annual average, LTT was above average over approximately 90% of Earth with

record-setting temperatures over 17%–20% of the globe (Plate 2.1d). While La Niña conditions during late 2022 into early 2023 depressed global LTT in the first half of the year, El Niño developed in May and strengthened through the year. The El Niño conditions, paired with the underlying global warming trend (Table 2.3), contributed to the record observed tropospheric warmth in 2023 (Fig. 2.10). Continued research is needed to quantify other factors that may have enhanced the exceptional global tropospheric warmth in 2023 (Perkins-Kirkpatrick et al. 2024; Rantanen and Laaksonen 2024; Schmidt 2024).

Long-term records of tropospheric temperature are derived from in situ balloon-borne radiosonde measurements, microwave measurements from satellites, and atmospheric reanalysis models. In this section, we focus on LTT, which represents a weighted vertical average of atmospheric temperature with weight concentrated in the lower troposphere (c.f., Fig. 1 in Christy et al. 2003). Other measures of tropospheric temperature yield broadly consistent results (Po-Chedley et al. 2023). Despite differences in geographic sampling and observation type, the records show excellent agreement on interannual timescales (the minimum correlation coefficient between pairs of annually averaged, global mean, detrended LTT time series is 0.84; Fig. 2.11). While global trend differences are non-negligible (approximately ±0.04°C per decade across datasets, depending on the start date), all datasets exhibit substantial lower tropospheric warming ranging from 0.14°C to 0.22°C per decade. Satellite and reanalysis datasets indicate that 2023 was the warmest year on record for global LTT. 2016 and 2023 were tied as the warmest year in the RATPAC-A radiosonde dataset, and 2023 ranked fourth in the RICH and RAOBCORE radiosonde datasets. Differences in the relative ordering of annual mean global LTT anomalies are due in part to sampling. For example, if we sample reanalysis and satellite LTT values to match RAOBCORE data availability, then 2023 falls behind 2016 as the warmest year on record.

Table 2.3. Global lower-tropospheric temperature (LTT) trends (°C decade^{-1}) over the periods 1958–2023 and 1979–2023. NASA MERRA-2 data begins in 1980 and NOAA STAR v5.0 begins in 1981.

Method	Source	Start Year 1958	Start Year 1979
Radiosonde	NOAA RATPAC vA2 (Free et al. 2005)	0.19	0.22
Radiosonde	RAOBCORE v1.9 (Haimberger et al. 2012)	0.16	0.18
Radiosonde	RICH v1.9 (Haimberger et al. 2012)	0.18	0.20
Satellite	UAH v6.0 (Spencer et al. 2017)	–	0.14[1]
Satellite	RSS v4.0 (Mears and Wentz 2016)	–	0.22
Satellite	NOAA STAR v5.0 (Zou et al. 2023)	–	0.14[1]
Reanalysis	ERA5 (Hersbach et al. 2020)	0.16	0.18
Reanalysis	JRA-55 (Kobayashi et al. 2015)	0.17	0.19
Reanalysis	NASA MERRA-2 (Gelaro et al. 2017)	–	0.20
Median	**N/A**	**0.17**	**0.19**

[1]The retrieval algorithm in UAH and STAR LTT is different from other datasets and results in vertical sampling that is slightly higher in the troposphere (Spencer et al. 2017). As a result, temperature trends are approximately 0.01°C decade^{-1} smaller in UAH and STAR LTT.

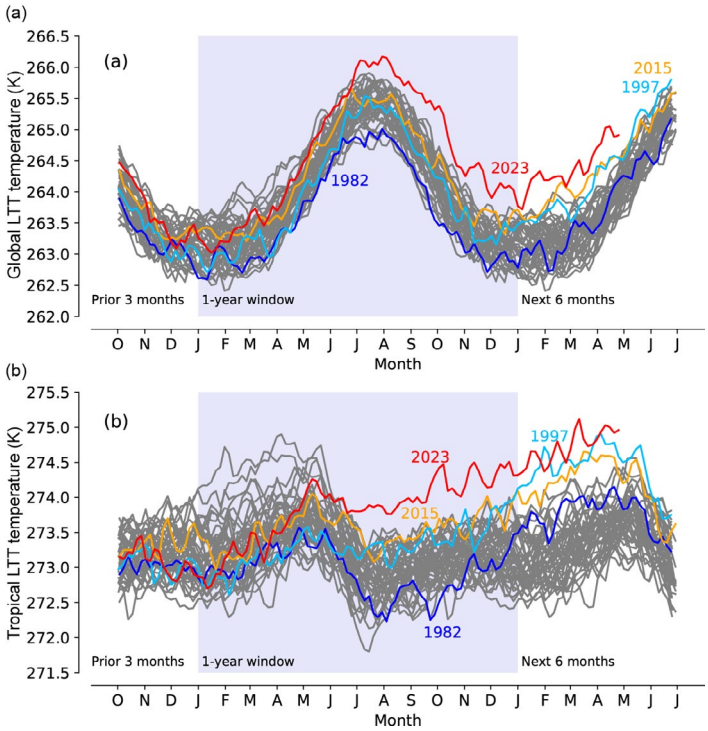

Fig. 2.10. Seasonal cycle of five-day average lower tropospheric temperature (LTT; K) for the (a) global and (b) tropical (20°S–20°N) mean. Each year (1979–2023) is plotted as a different gray line, except for select years that experienced the onset of El Niño (1982, 1997, 2015, and 2023 in blue, cyan, orange, and red, respectively). The full seasonal cycle is shown (shaded blue background) along with data from the preceding three months and following six months. Pentad values are from the UAH LTT dataset.

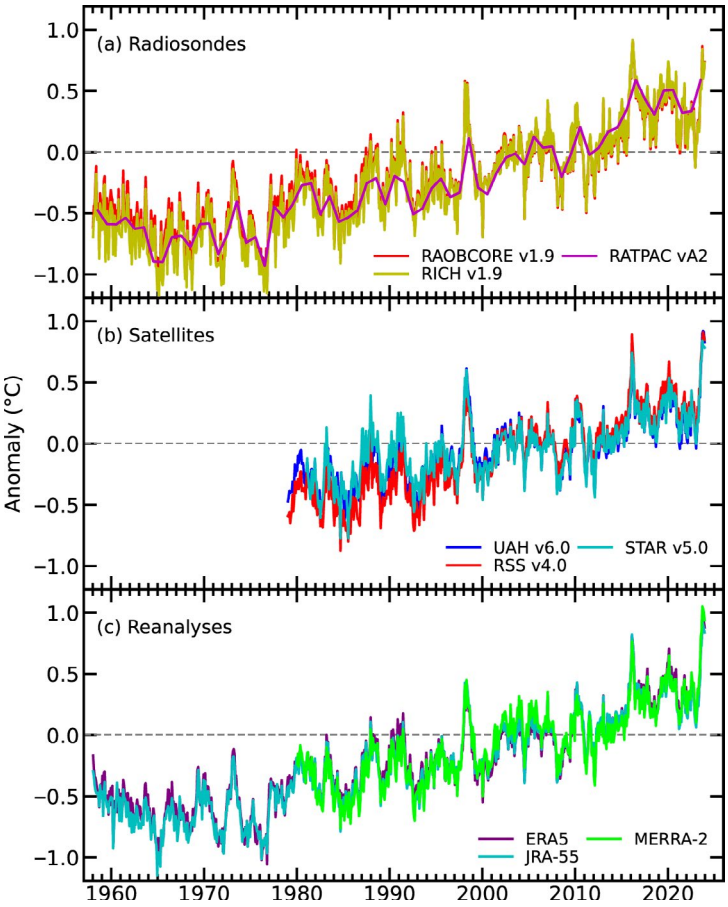

Fig. 2.11. Monthly average global lower tropospheric temperature (LTT) anomalies (°C) for (a) radiosonde, (b) satellite, and (c) reanalysis datasets. Annual averages are displayed for the RATPAC-A dataset. Anomalies are with respect to a 1991–2020 base period.

Over the Southern Hemisphere extratropics, record-high annual average LTT values were recorded over parts of the Southern Ocean into the South Atlantic, South Pacific, and South Indian Oceans. Over the Northern Hemisphere extratropics, record-high values occurred over northwest Canada into the Arctic Ocean, along the northwest coast of Africa and western Europe, and over Central and East Asia. In the tropics, all-time highs were concentrated over tropical South America, eastern Africa, and the tropical Atlantic and eastern tropical Pacific. Most of the tropics (20°S–20°N) set record-high LTT values for the months of July through December (not shown).

In some ways, 2023 appears to be following aspects of the 1997/98 El Niño event (Bell and Halpert 1998), which produced record-high tropospheric temperatures (Figs. 2.10, 2.11). Twenty-five years later, 1998 still ranks as one of the 10 warmest years in most tropospheric temperature datasets. In both 1997 and 2023, El Niño conditions were established by the early summer and strengthened through December. Since there is generally a three- to five-month lag between the warm sea-surface temperatures that accompany an El Niño event and tropical and global tropospheric temperature, record tropospheric warmth occurred in 1998 and, similarly, will likely continue to persist into 2024.

6. STRATOSPHERIC TEMPERATURE

—W. J. Randel, C. Covey, L. Polvani, and A. K. Steiner

Global mean temperatures in the lower, middle, and upper stratosphere increased slightly during 2023, mainly reflecting a recovery from anomalous cooling due to the Hunga Tonga–Hunga Ha'apai (HTHH) volcanic eruption in early 2022 (Davis et al. 2023). The long-term trends, however, show multi-decadal cooling of the stratosphere due to anthropogenic carbon dioxide (CO_2) increases and ozone (O_3) loss. The Arctic stratospheric polar vortex was disturbed by a major stratospheric warming in February 2023, while the Antarctic polar vortex was strong and persistent during the winter and

spring. The stratospheric quasi-biennial oscillation progressed normally in 2023, with equatorial easterly zonal wind shears and cold temperatures descending from the middle to lower stratosphere during the year.

Time series of global monthly temperature anomalies from the middle troposphere to the upper stratosphere based on satellite measurements are shown in Fig. 2.12. In addition to long-term stratospheric cooling and tropospheric warming due to greenhouse gas increases, transient variations arise from a variety of causes, including large volcanic eruptions (e.g., in 1982 and 1991), El Niño–Southern Oscillation (e.g., tropospheric warming events in 1997, 2016, and 2023), and large-scale wildfires (e.g., Australia in 2019/20). The middle stratosphere was anomalously cold in 2022 and early 2023 due to radiative effects of large water vapor (H_2O) anomalies injected by the January 2022 HTHH volcanic eruption (Millan et al. 2022; Wang et al. 2023; Davis et al. 2023; Flemming et al. 2024; Stocker et al. 2024). The HTHH stratospheric H_2O anomalies diffused and propagated upwards during 2023, resulting in smaller stratospheric radiative impacts and leading to a recovery from the anomalous cooling. The 11-year solar cycle was also increasing during 2023 (https://www.swpc.noaa.gov/products/solar-cycle-progression), which may contribute to slightly higher temperatures in the middle and upper stratosphere (Randel et al. 2009).

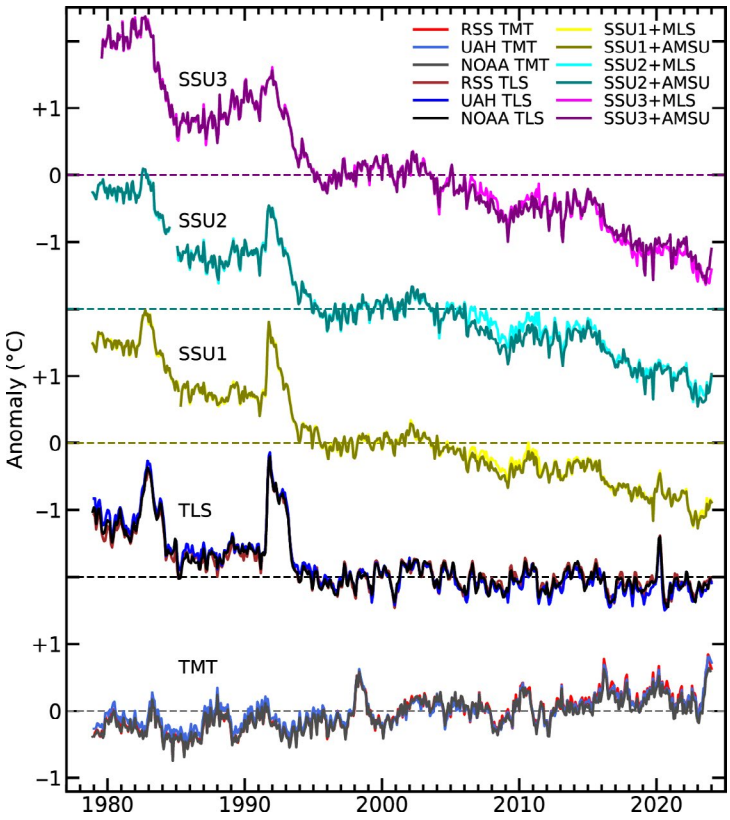

Fig. 2.12. Monthly global temperature anomalies (°C) from the middle troposphere to upper stratosphere (bottom to top). Middle and upper stratosphere data are from the Stratospheric Sounding Unit (SSU) updated with microwave measurements, representing thick-layer averages centered near 30 km, 38 km, and 45 km (SSU1, SSU2, and SSU3, respectively). Lower-stratosphere temperatures (TLS) are ~13-km–22-km layer averages from satellite microwave measurements. Middle troposphere (TMT) data are ~0-km–10-km layer averages and are included for comparison. Satellite data sources and details are discussed in Steiner et al. (2020). Each time series has been normalized to zero for the period 1995–2005, and curves are offset for clarity.

c. Cryosphere

1. PERMAFROST TEMPERATURE AND ACTIVE-LAYER THICKNESS

—J. Noetzli, H. H. Christiansen, M. Guglielmin, F. Hrbáček, G. Hu, K. Isaksen, F. Magnin, P. Pogliotti, S. L. Smith, L. Zhao, and D. A. Streletskiy

In recent decades, permafrost in cold regions worldwide have undergone widespread and persistent change, but the process is mostly slow and not directly visible. Permafrost is ground material with a maximum temperature of 0°C for at least two consecutive years. Its strongest warming was observed in cold high-latitude and high-elevation permafrost, where decadal rates of permafrost temperature increase by up to 1.0°C decade^{-1} at the depth of zero annual amplitude (DZAA, the depth where annual temperature fluctuations become negligible; e.g., Smith et al. 2023; Noetzli et al. 2021; Smith et al. 2022; Etzelmüller et al. 2023; Magnin et al. 2023; PERMOS 2023). In ice-bearing ground in warmer permafrost regions, latent heat effects due to phase change can significantly reduce temperature changes to below 0.1°C decade^{-1}. The layer above the permafrost that thaws during summer is called the active layer. Its annual thickness (active-layer thickness; ALT) has generally increased in all regions as a result of higher air temperatures. ALT increased by a few centimeters per decade in continuous permafrost in the Arctic in sediments and by decimeters per decade in discontinuous permafrost in bedrock in the Arctic, Antarctica, Scandinavia (e.g., Smith et al. 2022; Noetzli et al. 2023; section 5j), and the Qinghai-Tibet Plateau (QTP, Zhao 2024; Hu 2024). ALT changes of several meters were recorded during the past 20 years in the European Alps in bedrock as well as in degrading permafrost sites in talus slopes (e.g., PERMOS 2023, 2024; Magnin et al. 2023; Pogliotti et al. 2023).

Permafrost temperatures in 2023 were the highest on record for 9 of the 17 Arctic sites and higher than those in 2022 for most sites (see section 5j). However, for six sites in northwestern North America, permafrost temperatures were lower in 2023 compared to those in 2022, resulting from the delayed reaction at depth to the lower air temperatures during 2020–22. Similarly, the effect of higher air temperatures in 2023 is not yet observed at depths of 15 m–20 m. In the cold permafrost in Svalbard, the ground temperatures at 20 m were the fifth highest on record in 2023, based on measurements since 1999. Permafrost temperature at 10 m increased only slightly compared to 2022 and 2021 (Fig. 2.13, Janssonhaugen) and was still above the long-term average.

Active-layer thickness observed in 2023 in the Arctic differs between regions (Fig. 2.14; see section 5j): In high-Arctic Svalbard, record ALTs were documented after the record-warm summer of 2023 (see section 5b) for all sites, with values in bedrock of up to nearly 5 m in extreme cases. In 2023, above-average values were measured in Greenland and at sites from the Barents Sea region to West Siberia. In Central, East Siberia, and Chukotka in the Russian Arctic, in Arctic Alaska, western Alaska, and Northwest Canada (in 2022), ALT was close to the long-term average. In North America, the largest positive ALT anomaly in 2023 was observed in interior Alaska.

Mountain permafrost temperatures near the DZAA in mainland Norway were the highest on record in 2023, meaning reported warming continues (Noetzli et al. 2023; Etzelmüller et al. 2023). In the European Alps, permafrost temperatures at 10-m and 20-m depth were at record levels, particularly for bedrock sites, due to two consecutive hot summers in 2022 and 2023 (as yet, the full effect of the 2023 summer heat cannot be observed at greater depth). In contrast, permafrost temperatures decreased at 10-m depth for several rock glacier stations in

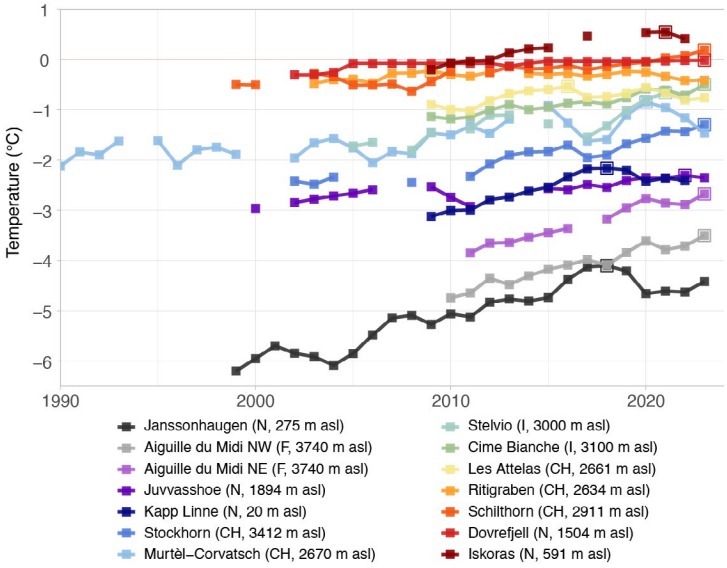

Fig. 2.13. Mean annual ground temperatures (°C) measured in European permafrost boreholes in the Alps, Scandinavia, and Svalbard at a depth of ca. 10 m. Maximum values for each time series are highlighted by a square. (Data sources: Norway: Norwegian Meteorological Institute and the Norwegian Permafrost Database [NORPERM]; Switzerland: Swiss Permafrost Monitoring Network [PERMOS]; France: Magnin et al. 2023; Italy: Pogliotti et al. 2023 and Guglielmin, M. unpublished data.)

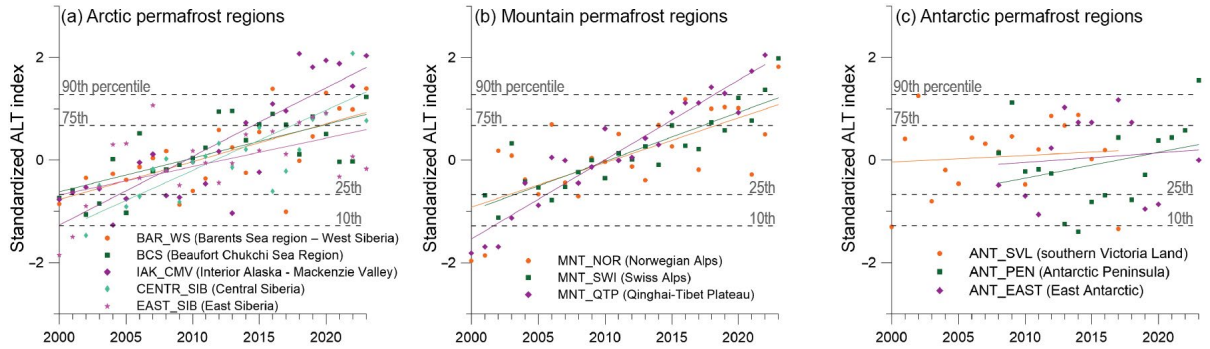

Fig. 2.14. Standardized active-layer thickness (ALT) index relative to 2000–20. (a) Arctic regions: Beaufort Chukchi Sea–Arctic Alaska and Mackenzie Delta region (BCS), Interior Alaska and central Mackenzie Valley, Northwest Territories (IAK_CMV), Barents Sea region–West Siberia (BAR_WS), Central Siberia (CENT_SIB), East Siberia (EAST_SIB); (b) Mountain regions: Norwegian mountains (MNT_NOR), Swiss Alps (MNT_SWI), Qinghai-Tibet Plateau (MNT_QTP); and (c) Antarctic: southern Victoria Land (ANT_SVL), Antarctic Peninsula (ANT_PEN), East Antarctic (ANT_EAST). (Source: Circumpolar Active Layer Monitoring [CALM].)

2023 after a snow-poor winter (Fig. 2.13; PERMOS 2024). The ALT for 2023 at the majority of sites in the Norwegian mountains and in the European Alps were at or close to their previous maximum, or set a new maximum (Fig. 2.14). Degraded permafrost in the upper part of the ground can be observed at several sites in Europe, e.g., by talik formation or active layers that no longer freeze during winter (Etzelmüller 2023; PERMOS 2023, 2024).

Permafrost temperatures at depths of 10 m and 20 m at six sites in the QTP in central Asia (Kunlun mountain pass to Liangdaohe) warmed significantly between 2005 and 2022, with many record values observed in 2021 (Fig. 2.15). For ALT in this region, a large increase was observed at 10 sites from 1981 to 2022 (Fig. 2.14), associated with a significant increase in air temperature.

Active-layer thickness in the Antarctic Peninsula region has increased since 2014, with the 2023 value being the maximum for 2006–23 (Fig. 2.14). Permafrost temperatures at DZAA at Rothera Station and Signy Island have remained stable since 2013 (Grifoni et al., accepted). In East Antarctica and Victoria Land, ALT remains relatively stable without clear detectable trends (Hrbáček et al. 2023).

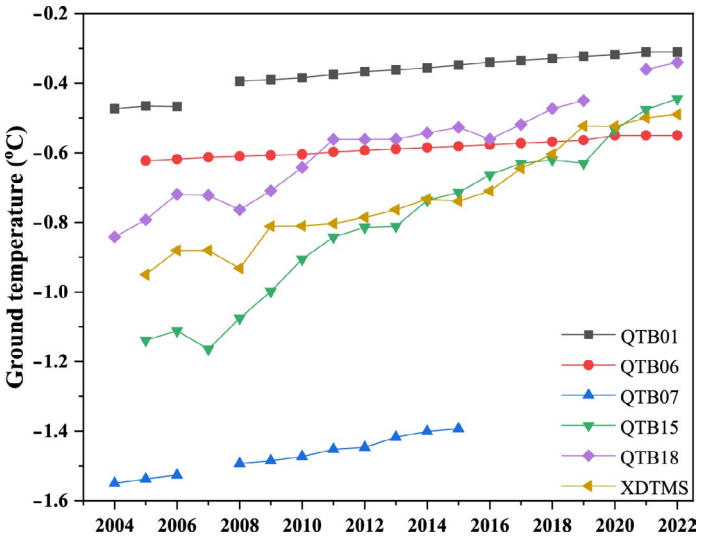

Fig. 2.15. Ground temperatures (°C) measured at 10-m depth in the Qinghai-Tibet Plateau during the period 2005–22. (Source: Cryosphere Research Station on Qinghai-Xizang Plateau, Chinese Academy of Sciences.)

Permafrost observation relies on field measurements at the national or institutional level and is globally collected in the framework of the Global Terrestrial Network for Permafrost (Streletskiy et al. 2021) as an essential climate variable of the Global Climate Observation System. The global coverage of permafrost monitoring sites is sparse and is mainly available in the Northern Hemisphere. Coverage is particularly limited in regions such as Siberia, central Canada, Antarctica, and the mountains in Central Asia, the Himalayas, and the Andes.

2. ROCK GLACIER VELOCITY

—C. Pellet, X. Bodin, D. Cusicanqui, R. Delaloye, A. Kääb, V. Kaufmann, E. Thibert, S. Vivero, and A. Kellerer-Pirklbauer

Rock glaciers are debris landforms generated by the creep of perennially frozen ground (permafrost) whose velocity changes are indicative of changes in the thermal state of permafrost and associated ground hydrological changes (i.e., increasing temperatures lead to increase in velocity and vice-versa; RGIK 2023a; Staub et al. 2016). Rock glacier velocity (RGV) is a time

series of annualized surface velocity values measured/computed on a rock glacier or a part of it (RGIK 2023b). Rock glacier velocities observed in different mountain ranges worldwide have been increasing since the 1950s, with large regional and inter-annual variability. These changes are consistent with the evolution of permafrost temperatures (section 2c1).

Although the hydrological year 2023 (October 2022 to September 2023) was the warmest on record in the European Alps (Fig. 2.16a), RGVs slightly increased in the western part of the Alps and continued to decrease in the east. Compared to 2022, velocity increased in the French Alps (+4% at Laurichard) and western Swiss Alps (+11% at Grosses Gufer and +15% at Gemmi/Furggentälti), whereas velocities continued to decrease in the Austrian Alps (–8% at Dösen and –22% at Hinteres Langtalkar; Fig. 2.16b). These regional evolutions are consistent with different snow conditions, namely exceptionally late onset of the snow cover and low snow depth in the east, which enabled marked cooling of the ground (as confirmed by the permafrost temperature decrease at 10-m depth observed on rock glacier Murtèl-Corvatsch in eastern Switzerland, Fig. 2.16). In the west, slightly later-than-average onset of the snow cover and slightly below-average snow depth were observed (PERMOS 2024). The reported RGV observations in 2023 in the European Alps are part of a general acceleration trend observed at all sites since the 1950s (Cusicanqui et al. 2021; Kellerer-Pirklbauer et al. 2024; PERMOS 2024).

In the Dry Andes in South America, RGVs reconstructed on three rock glaciers showed low velocities from 1950 to 2000, followed by a steady acceleration since the 2000s (Fig. 2.16c), consistent with the slight air temperature increase observed in the region since 1976 (Vivero et al. 2021). The potential effects of the above-average snow depth and longer snow cover duration in this region, associated with the strong El Niño event in 2023, have yet to be quantified.

Rock glacier velocities observed in Central Asia during the period of around 2018–23 show overall high values. Maximum velocities have been observed at Karakoram and Morenny, and

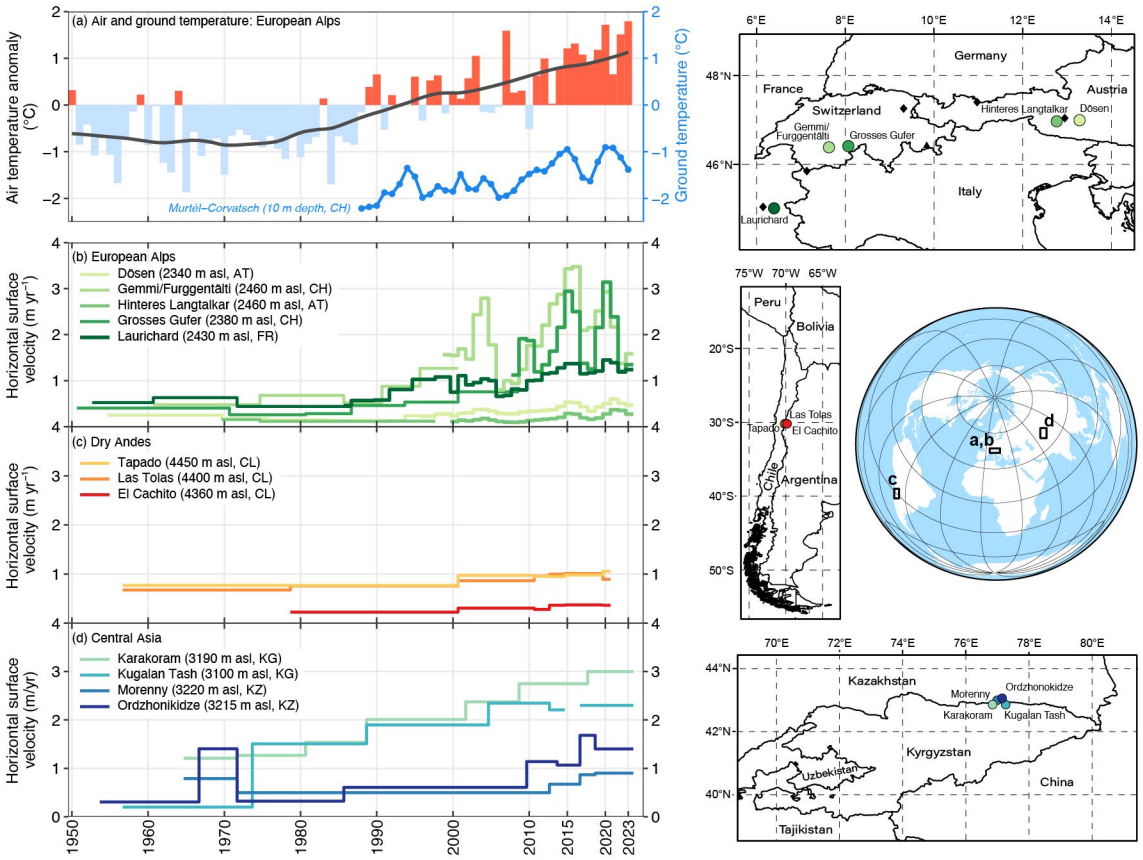

Fig. 2.16. Rock glacier velocity and climate: (a) air and ground temperature (°C) in the European Alps, (b)–(d) rock glacier velocities (m yr^{-1}) at selected sites in the (b) European Alps, (c) Dry Andes (updated from Vivero et al. 2021), and (d) Central Asia (updated from Kääb et al. 2021). Rock glacier velocities are based on in situ geodetic surveys or photogrammetry in the context of long-term monitoring. In situ hydrological mean annual permafrost temperature measured at 10-m depth (blue line) at Murtèl Corvatsch (black triangle on Europe map) and air temperature: composite anomaly to the 1981–2010 base period (bars) and composite 20-year running mean (solid line) at Besse (FR), Grand Saint-Bernard (CH), Saentis (CH), Sonnblick (AT), and Zugspitze (D, black diamonds on Europe map). (Sources: Météo-France, Deutscher Wetterdienst [DWD], MeteoSwiss, GeoSphere Austria, Swiss Permafrost Monitoring Network [PERMOS], University of Fribourg, University of Graz, Graz University of Technology, Université Grenoble Alpes [INRAE], University of Oslo.)

velocities on Kugalan Tash and Ordzhonikidze remain at a high level, although velocity slightly decreased at the latter (Fig. 2.16d; Kääb et al. 2021). This evolution is consistent with increasing air temperatures reported in the region since 1900 (Azisov et al. 2022; Sorg et al. 2015) and with the RGV evolution reported in the European Alps and Dry Andes.

Rock glacier velocity refers to velocities related to permafrost creep, which is a generic term referring to the combination of both internal deformation within the crystalline structure of the frozen ground (creep stricto sensu) and shearing in one or more discrete layers at depth (shear horizon; RGIK 2023b). RGVs are mostly related to the evolution of ground temperature and liquid water content between the upper surface of permafrost (i.e., permafrost table) and the layer at depth of the shear horizon (Cicoira et al. 2019; Frauenfelder et al. 2003; Kenner et al. 2017; Staub et al. 2016). Despite variable size, morphology, topographical and geological settings, and velocity ranges, consistent regional RGV evolutions have been highlighted in several studies (e.g., Pellet et al. 2023; Kellerer-Pirklbauer et al. 2024). Multi-annual long-term RGV time series are reconstructed using repeated aerial or optical satellite images. Horizontal displacements are computed based on cross-correlation feature tracking on multi-temporal ortho-images or digital elevation model matching (Kääb et al. 2021; Vivero et al. 2021). The resulting accuracy strongly depends on the spatial resolution of the images and on the image quality (i.e., presence of snow and shadows). Surface displacements are averaged for a cluster of points/pixels selected within areas considered as representative of the downslope movement of the rock glacier (RGIK 2023b). Annual rock glacier velocities are commonly measured using terrestrial geodetic surveys performed each year at the same time (usually at the end of summer). The positions of selected boulders (10–100 per landform) are measured with an average accuracy in the range of mm to cm (Lambiel and Delaloye 2004; Kellerer-Pirklbauer et al. 2024; PERMOS 2024; Thibert and Bodin 2022).

3. ALPINE GLACIERS

—M. S. Pelto

Mountain-region (i.e., alpine) glacier annual mass balance (sum of accumulation and ablation) observations are reported to the World Glacier Monitoring Service (WGMS). The WGMS reference glaciers each have at least 30 continuous years of mass balance observation, and benchmark glaciers have at least a 10-year mass balance record and are in regions that lack sufficient reference glaciers. In 2023, all 35 reporting reference glaciers had a negative balance, along with all 18 benchmark glaciers. This is the first year that all reference glaciers have had a negative balance. The 2023 dataset includes 109 glaciers from six continents, with 108 having a negative balance and 1 glacier reporting a positive mass balance. This makes 2023 the 36th consecutive year with a global alpine glacier mass balance loss, the 15th consecutive year with a mean global mass balance below –500 mm water equivalent (w.e.), and the year with the highest ratio of negative-to-positive mass balance observations of any year in the record (Fig. 2.17).

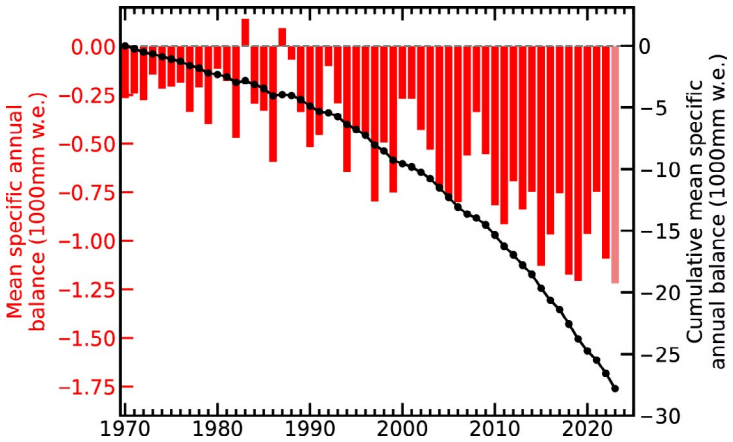

Fig. 2.17. Time series of global mean annual glacier mass balance (mm w.e.) of alpine glaciers from 1970 to 2023 as determined by the World Glacier Monitoring Service, using 19 regional averages from 53 glaciers in total.

The combination of benchmark and reference glaciers is used to generate regional averages (WGMS 2023). Global values are calculated using a single averaged value for each of 19 mountain regions, limiting bias towards well-observed regions (WGMS 2023). In 2023, the mean annual mass balance of the 35 reference glaciers was –1568 mm w.e., and –1590 mm w.e. for all 109 reporting glaciers regardless of record length. In a similar result, 2022 mean annual mass balance was –1475 mm w.e. for 37 reporting reference glaciers and –1568 mm w.e. for all 116 reporting glaciers. The regionally averaged global mass balance was –1090 mm w.e. in 2022; a final value for 2023 has not yet been determined, but the preliminary value is –1219 mm w.e.

The result of the melt in several regions has been an increasing complete loss of glaciers (see below; Huss and Fischer 2016; Fountain et al. 2023). This led to the Global Land Ice Measurements

from Space (GLIMS) initiative adding an extinct glacier layer to its Glacier Viewer in 2023 to indicate glaciers that have been lost (GLIMS 2023). The sustained mass balance loss this century is also reducing the drought-buffering capacity of alpine glaciers in most midlatitude mountain ranges (Ultee et al. 2022). In 2023, we continued to see many glaciers across the globe with minimal to no retained snow cover, leading to surface darkening and even greater mass losses (Fig. 2.18).

In the European Alps, all 21 reporting glaciers had annual mass balances below –1300 mm w.e., with an average of –2311 mm w.e. In the Pyrenees, mass balances were also strongly negative. The combination of a snow drought and warm summer temperatures led to this sharp loss in glacier volume.

In High Mountain Asia, 22 of 23 glaciers had negative mass balances across seven nations: China, India, Kazakhstan, Kyrgyzstan, Nepal, Tajikistan, and Uzbekistan. The mean annual mass balance was –1048 mm w.e.

In North America, all 16 glaciers outside of the Arctic had negative mass balances averaging –2700 mm w.e. The combination of limited winter snowpack and a prolonged ablation season across the Pacific Northwest was the most significant contributor to this loss.

In South America, all 10 glaciers had significant negative annual mass balance averaging –1715 mm w.e. Continued drought in the central Andes and a warm melt season across the entire region led to negative mass balances from Ecuador southward to Argentina and Chile. In the central Andes, many glaciers from 32°S to 36°S lost all snow cover.

In Sweden and Norway, all 14 glaciers had negative annual mass balances averaging –1364 mm w.e. Across the Arctic in the Canadian Arctic Islands, Iceland, and Svalbard, all 19 glaciers had negative mass balances averaging –976 mm w.e. (see section 5h).

The rapid volume loss from 2021 to 2023 led to the complete loss of two glaciers in the WGMS mass balance dataset: St. Anna Glacier, Switzerland (reported 2011–23), and Ice Worm Glacier in the United States (reported 1984–2023). These glaciers are indicative of the increasing rate of glacier disappearance.

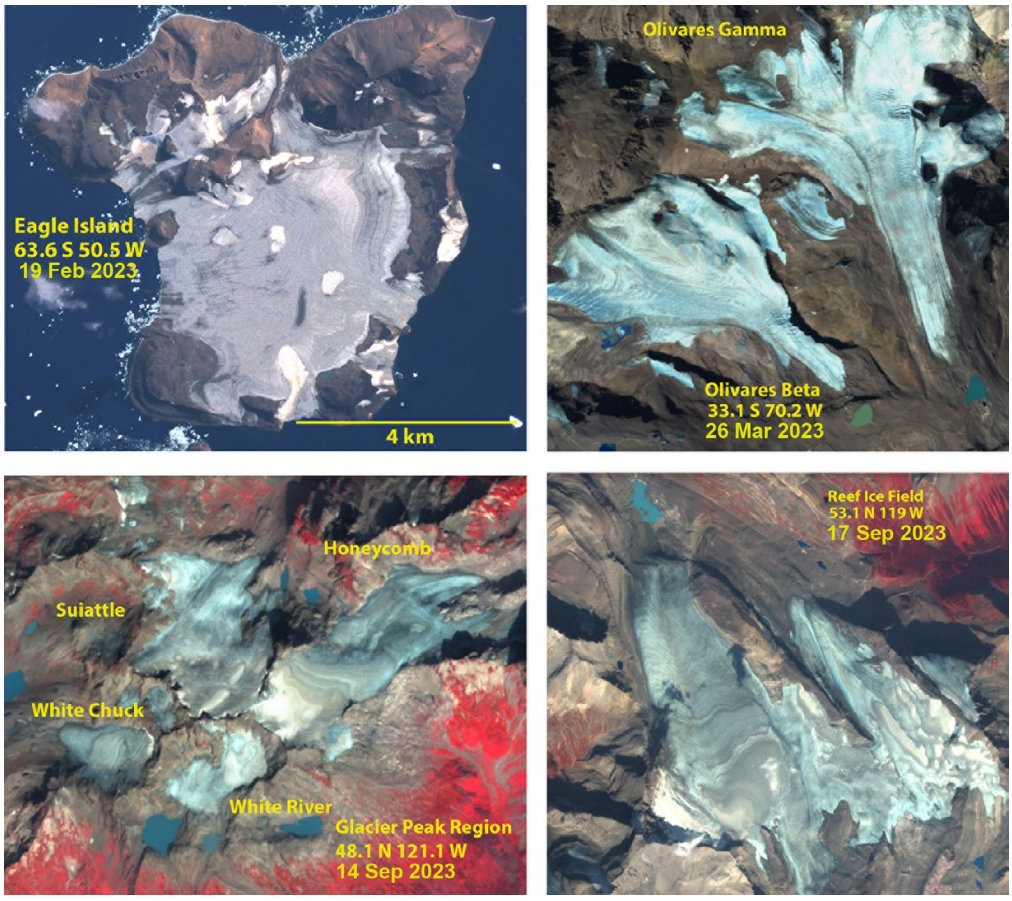

Fig. 2.18. Many alpine glaciers across the globe lost all or nearly all their snow cover in 2023, as illustrated by (a) the 63°S Antarctic Peninsula region, (b) the Andes, (c) North Cascades, and (d) 53°N in the Canadian Rockies. To be in equilibrium, a glacier needs to have at least 50% of its area snow covered throughout the year.

4. LAKE ICE

—S. Sharma, R. I. Woolway, and J. Culpepper

In the 2022/23 winter season (November 2022–April 2023), lake ice phenology (timing of ice-on and ice-off) across the Northern Hemisphere (NH) generally revealed that some lakes had later-than-normal ice-on dates and earlier-than-normal ice-off dates, although most lakes had shorter-than-normal seasonal ice cover. Notably, in situ phenological records revealed that ice-off dates were later for over half (55.8%) of the studied lakes, although the ice season remained shorter.

Across the NH, based on the ERA5 reanalysis data, lakes froze on average four days later and thawed five days earlier, with ice duration nine days shorter relative to the 1991–2020 base period (Fig. 2.19). The ice-on date was the third latest, the ice-off date was the third earliest, and the duration of lake ice cover was the fifth shortest since the start of the record in 1980.

Further, in situ lake ice observations from 157 lakes revealed that, on average, during the 2022/23 winter, ice-on was 2.1 days later, ice-off was 1.6 days later, and ice duration was 1.7 days

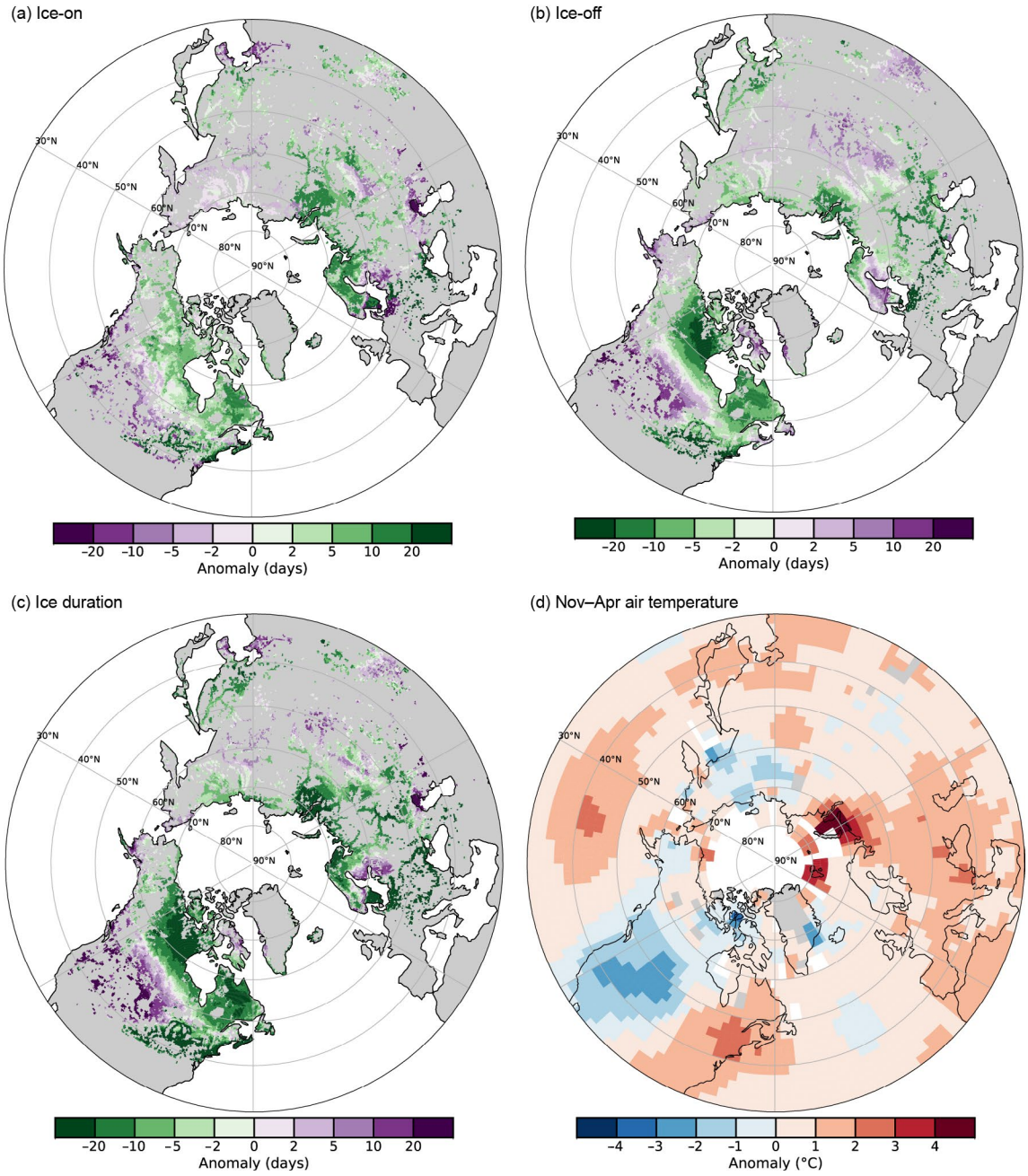

Fig. 2.19. Anomalies (days) for (a) the start of ice cover, (b) end of ice cover, and (c) duration of ice cover for lakes across the Northern Hemisphere (NH), with negative (positive) values being earlier (later) in the year. (d) Surface air temperature anomalies (°C) for the NH cold-season (Nov–Apr average) in 2023. The base period is 1991–2020. (Sources: ERA5, GISTEMPv4.)

shorter relative to the 1991–2020 base period (Fig. 2.20). Notably, Lake Suwa in Japan froze on 26 January 2023, marking the third year in a row this lake froze; three such consecutive freezes have not occurred in at least the past decade. In the last several decades, it has become increasingly rare for Lake Suwa to freeze.

Mountain lakes continue to be underrepresented in global studies of ice phenology (Christianson et al. 2021), owing to challenges in obtaining data and unsafe winter conditions (Block et al. 2019). During winter 2023, the 18 mountain lakes in our dataset (>1000 m a.s.l.) froze 7.8 days later and thawed 3.2 days later on average. Low-temperature anomalies during this winter likely led to later breakup (Fig. 2.20) as well as increased snowfall in the western United States from nine atmospheric rivers throughout December 2022 and January 2023 that impacted the area (NOAA/NCEI 2023c). Castle Lake in northern California, for example, broke up 34.4 days later than its 32-year mean. Despite the overall later breakup dates, ice cover duration continued to show signs of decline, with 10 mountain lakes having shorter ice duration and one lake having a near-zero anomaly. The continued decline in ice-cover duration suggests that generally later formation counteracts the later breakup date.

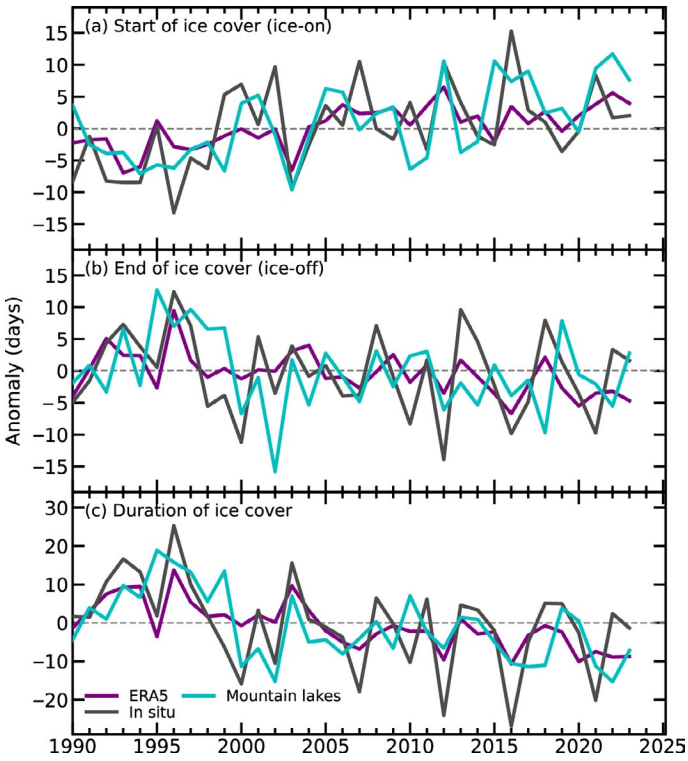

Fig. 2.20. Anomalies (days) in the timing of (a) ice-on, (b) ice-off, and (c) ice duration from 1980 to 2023 derived from ERA5 reanalysis, in situ observations, and mountain lakes. Base period is 1991–2020.

In North America, the Laurentian Great Lakes had 24.1% less maximal ice coverage during the 2022/23 winter, relative to the winters of 1991–2020. Both Lakes Erie and Superior had approximately 35% less ice coverage in 2023, followed by Lakes Huron (25.5%), Michigan (15%), and Ontario (9.8%; Fig. 2.21). Ice coverage was highest on 4 February—20 days earlier than average—across all of the Great Lakes.

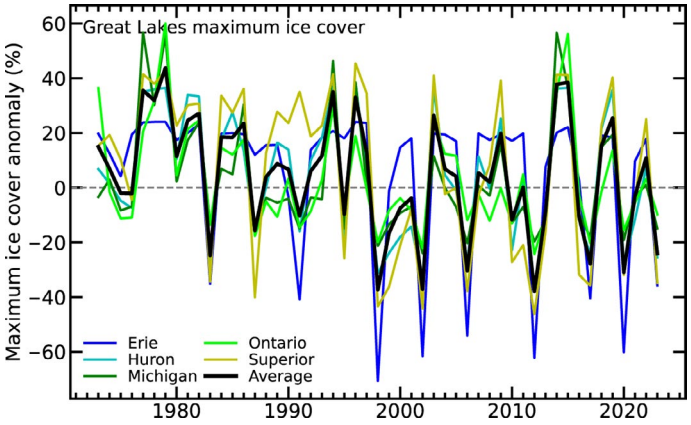

Fig. 2.21. Anomalies in the Laurentian Great Lakes maximum ice cover extent (%) for the period 1973–2023 (base period is 1991–2020) for individual lakes (Erie, Huron, Michigan, Ontario, Superior) and the Great Lakes average.

The ERA5 reanalysis product (Hersbach et al. 2020) was used to calculate ice-on and ice-off dates, in addition to ice-duration dates across NH lakes, following the methodology of Grant et al. (2021). Many citizen scientists, in addition to established monitoring networks, contributed in situ observations for 157 lakes across Canada, the United States, Norway, Finland, and Japan. Citizen scientist networks have been instrumental in sharing their local ice records and can offer extensive, efficient, and cost-effective local in situ environmental monitoring across vast spatial and temporal scales (Fritz et al. 2019; Lopez et al. in press). Furthermore, in situ ice phenology data for eight mountain lakes in the United States and 10 lakes in Europe were obtained and updated through personal correspondence with the data authors (Caine et al. 2023; Chandra et al. 2022; Kainz et al. 2017). Annual maximum ice coverage (%) data for each of the Laurentian Great Lakes were acquired for the period 1973–2023 from the NOAA Great Lakes Environmental Research Laboratory, in addition to the surface air temperature data for the NH cold season (November–April average) from the NASA Goddard Institute for Space Studies' surface temperature analysis (GISTEMP Team 2024). Anomalies for each of our ice metrics were calculated for the 2022/23 winter relative to the 1991–2020 normal base period.

5. NORTHERN HEMISPHERE CONTINENTAL SNOW COVER EXTENT

—D. A. Robinson and T. W. Estilow

Annual snow cover extent (SCE) over NH lands averaged 24.3 million km² in 2023. This was 0.8 million km² (3.2%) below the full period-of-record (November 1966–December 2023) mean, marking the seventh-least-extensive cover on record (Table 2.4; Fig. 2.22a). Monthly SCE in 2023 ranged from a maximum of 47.1 million km² in January to a minimum of 2.9 million km² in August.

Northern Hemisphere SCE in January and March ranked in the lower tercile of the 57-year record (1.8% and 2.8% below normal,

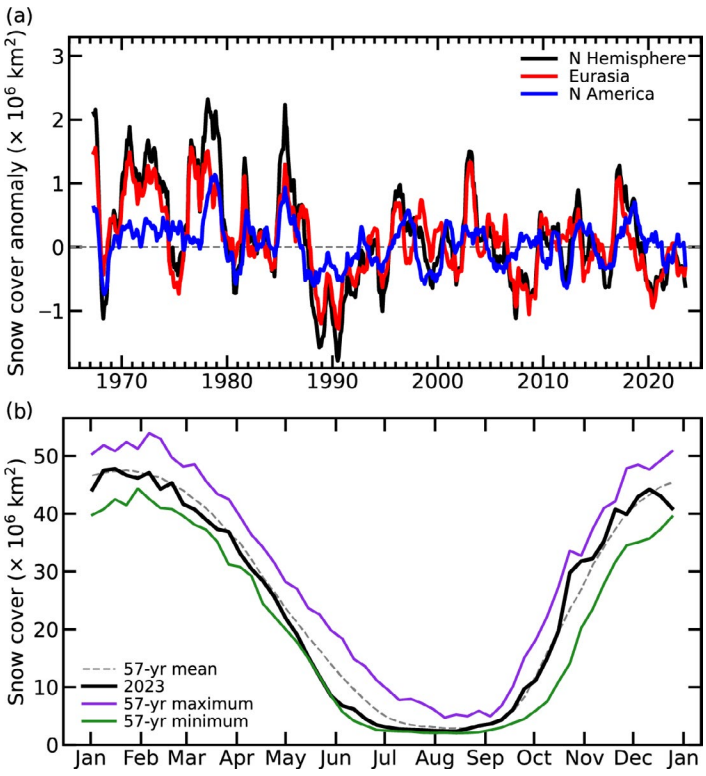

Fig. 2.22. (a) Twelve-month running anomalies of monthly snow cover extent (SCE; × 10⁶ km², or million km²) over Northern Hemisphere (NH, black) lands as a whole and Eurasia (red) and North America (blue) separately plotted on the seventh month using values from Nov 1966 to Dec 2023. Anomalies relative to the full period are calculated from NOAA snow maps. Mean NH SCE is 25.1 million km² for the full period of record. Monthly means for the period of record are used for nine missing months during 1968, 1969, and 1971 to create a continuous series of running means. Missing months fall between Jun and Oct. (b) Weekly NH SCE time series (× 10⁶ km²) for 2023 (black) plotted with the mean (gray dashed line), maximum (purple), and minimum (green) SCE for each week. Mean weekly SCE and extremes are calculated using the 57-year record from Jan 1967–Dec 2023. Weekly data granules represent SCE for each seven-day period ending on Monday.

Table 2.4. Monthly and annual climatological information on Northern Hemisphere (NH), Eurasia (EUR), and North America (NA) snow cover extent (SCE) between Nov 1966 and Dec 2023. Included are the numbers of years with data used in the calculations, NH anomalies, NH means (Nov 1966–Dec 2023), standard deviations (Nov 1966–Dec 2023), 2023 values, and rankings (highest and lowest). Areas are in millions (× 10⁶) of square kilometers (km²). The years 1968, 1969, and 1971 have one, five, and three missing months, respectively, thus are not included in the annual calculations. NA includes Greenland. Ranks are from most (1) to least extensive (least to most in parentheses)

Month	Yrs	2023 NH Anomaly (× 10⁶ km²)	NH Mean (× 10⁶ km²)	NH Std. Dev.	2023 NH rank	2023 EUR rank	2023 NA rank
Jan	57	–0.9	47.1	1.5	41 (17)	48 (10)	27 (31)
Feb	57	–0.4	45.9	1.8	32 (26)	37 (21)	24 (34)
Mar	57	–1.1	40.4	1.8	43 (15)	52 (6)	4 (54)
Apr	57	–0.2	30.5	1.6	28 (30)	43 (15)	16 (42)
May	57	–2.3	19.0	2.0	50 (8)	35 (23)	57 (1)
Jun	56	–3.3	9.3	2.5	50 (7)	46 (11)	53 (4)
Jul	54	–1.0	3.8	1.2	44 (11)	42 (13)	41 (14)
Aug	55	–0.4	2.9	0.7	39 (17)	39 (17)	29 (27)
Sep	55	–0.1	5.4	0.9	28 (28)	22 (34)	33 (23)
Oct	56	+0.2	18.6	2.6	25 (32)	24 (33)	28 (29)
Nov	58	+1.2	34.4	2.1	17 (42)	16 (43)	28 (31)
Dec	58	–1.2	43.7	1.8	48 (11)	18 (41)	56 (3)
Annual Calculations	**54**	**–0.8**	**25.1**	**0.8**	**48 (7)**	**45 (10)**	**45 (10)**

respectively; Fig. 2.22b), while February (–0.9%) and April (–0.7%) were in the middle. North America (NA) had more extensive snow cover compared to normal than Eurasia (EUR) during each of these four months. In particular, NA had its fourth-most-extensive SCE in March (+7.6%) and its 16th most extensive in April (+4.8%). Thereafter, melt quickly occurred across NA, with May having its least-extensive SCE of the satellite era (–19.5%). Both continents contributed to June having the sixth-least SCE across the NH (–35.6%; Fig 2.23). Across the NH, September and October began the new snow season with SCE in the middle tercile (–1.0% and +0.9%, respectively). SCE was above normal for both continents in November (+3.6%; Fig 2.23). While SCE remained above normal over EUR in December (+2.1%), SCE in NA declined to its third least extensive for the month (–10.8%), contributing to the seventh-least-extensive SCE overall for the NH (–2.8%).

The contiguous United States' (US) SCE (not shown) was close to normal at the beginning of 2023, then became well above normal in March (+45.6%; fourth most extensive) and April (+62.3%, seventh most extensive). In May, the US SCE was below average (–17.6%) while Canadian SCE (not shown) was the lowest on record (–30.7%). Autumn snow cover began early over the US and was the 11th most extensive on record for October (+68.6%), but for the remainder of the year, US SCE was below normal, with December having the sixth-least-extensive SCE on record (–43.4%).

SCE is calculated at the Rutgers Global Snow Lab (GSL) from daily SCE maps produced by meteorologists at the US National Ice Center, who rely primarily on visible satellite imagery to construct the maps (Estilow et al. 2015). Maps depicting daily, weekly, and monthly conditions, anomalies, and climatologies may be viewed at the GSL website (https://snowcover.org).

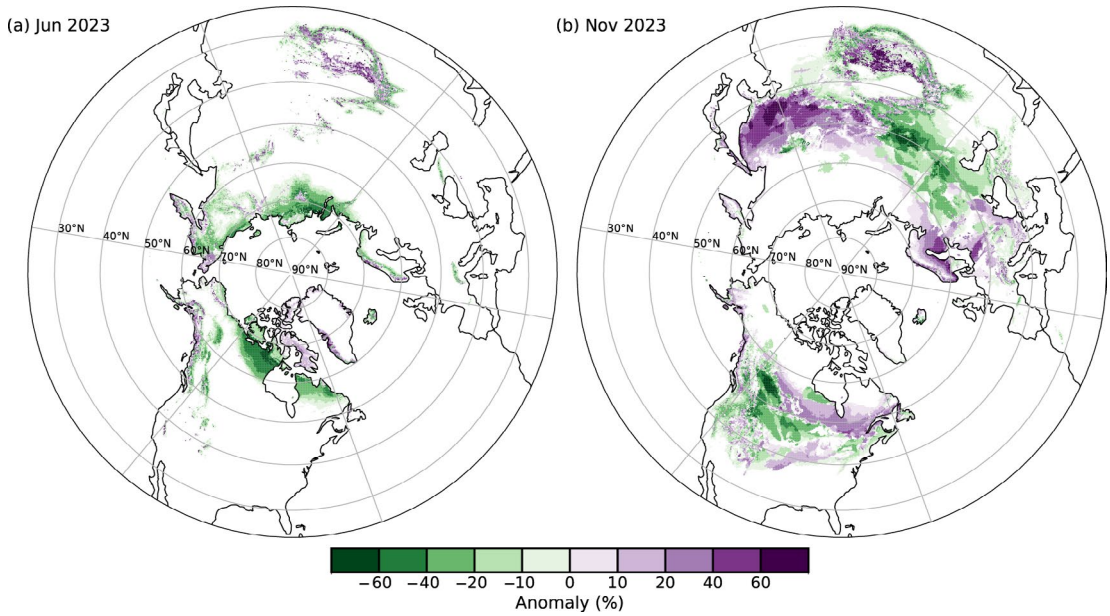

Fig. 2.23. Monthly snow cover extent (SCE) departure (%) maps for (a) Jun and (b) Nov 2023. Jun exhibited the lowest SCE anomaly (–2.17 million km²) during 2023, while Nov was the highest above normal (+0.53 million km²). Mean monthly SCE calculated using the 30-yr span from 1991–2020. Negative departures indicate less SCE than normal (green) with positive departures (purple) showing areas of SCE above the 30-yr mean.

d. Hydrological cycle—atmosphere

1. SURFACE HUMIDITY

—K. M. Willett, A. J. Simmons, M. Bosilovich, and D. A. Lavers

The near-surface atmosphere had record or near-record water vapor content for 2023, with global specific humidity (q) anomalies reaching 0.17 g kg^{-1}–0.42 g kg^{-1} across the various datasets (Figs. 2.24a–d; Table 2.5). These anomalies exceeded 2022 q levels by a large margin of 0.14 g kg^{-1} to 0.28 g kg^{-1}. As has been the case since 2011, saturation (relative humidity, RH) remained below average over land, being –0.46%rh to –1.05%rh across datasets. This decline reflects the fact that the temperature over land is rising so quickly that the water-holding capacity is outpacing the actual water vapor content, which is governed largely by local water availability and slower ocean warming rates. Relative humidity over oceans was close to average in 2023, within ±0.1%rh.

Global annual mean q anomalies (relative to 1991–2020; Figs. 2.24a–d; Table 2.5) from HadISDH, MERRA2, JRA-55, and the new JRA-3Q surpassed previous records, with HadISDH and MERRA2 reaching 0.33 g kg^{-1} over land and 0.4 g kg^{-1} and 0.42 g kg^{-1}, respectively, over ocean. Years of previous records differed among datasets. ERA5 had similarly large increases from 2022 (Table 2.5) and record-high q over ocean, reaching 0.24 g kg^{-1}. Masking to HadISDH coverage resulted in higher 2023 anomalies, especially over ocean where HadISDH spatial coverage is very limited. Global annual mean anomalies of RH (Figs. 2.24.e–h; Table 2.5) were lower than those of 2022 over land by between 0.12%rh for ERA5 to 0.32%rh for JRA-3Q. JRA-55 had 2023 as

Table 2.5. Global mean surface-specific (*q*) and relative humidity (RH) anomalies for 2023 and comparison with previous values. Note that no previous record is reported for ocean RH because a long-term trend has not been robustly established. RH values for MERRA-2 are not included in this report. Values in bold type identify new records.

Dataset	*q* (g kg^{-1}) 2023 global mean anomaly	*q* (g kg^{-1}) 2022 global mean anomaly	*q* (g kg^{-1}) Previous record high (year of previous record)	RH (%rh) 2023 global mean anomaly	RH (%rh) 2022 global mean anomaly	RH (%rh) Previous record low (year of previous record)
HadISDH.land	**0.33**	**0.14**	**0.27 (1998)**	–0.46	–0.24	–0.79 (2019)
ERA5 over land	0.17	–0.01	0.21 (2016)	–1.05	–0.93	–1.32 (2021)
ERA5 over land masked	0.22	0.02	0.25 (2016)	–1.01	–0.88	–1.28 (2021)
MERRA-2 over land	**0.33**	**0.19**	**0.27 (2020)**	--	--	--
JRA-55 over land	**0.25**	**0.06**	**0.21 (2016)**	**–0.87**	**–0.62**	**–0.83 (2021)**
JRA-3Q over land	**0.26**	**0.08**	**0.21 (1998/2016)**	–0.91	–0.59	–0.93 (2021)
HadISDH.marine	**0.4**	**0.12**	**0.27 (2020)**	0.06	–0.23	--
ERA5 over ocean	**0.24**	**0.03**	**0.20 (2019)**	–0.08	–0.12	--
ERA5 over ocean masked	**0.40**	**0.19**	**0.34 (2016)**	–0.12	–0.06	--
MERRA-2 over ocean	**0.42**	**0.18**	**0.25 (2019)**	--	--	--
JRA-55 over ocean	**0.34**	**0.09**	**0.19 (2016/2020)**	0.25	0.21	--
JRA-3Q over ocean	**0.34**	**0.09**	**0.19 (2020)**	0.10	0.10	--

record low for land RH but by a very small margin (0.04%rh). Over ocean, where agreement between datasets is much poorer, 2023 values were only slightly higher than in 2022 for ERA5 and JRA-55 (+0.04%rh and +0.03%rh), identical for JRA-3Q, and much larger for HadISDH.marine (+0.29%rh). ERA5 2023 anomalies were slightly drier than average (–0.08%rh) whereas the other datasets were above average (0.06%rh to 0.25%rh). Masking ERA5 to HadISDH coverage resulted in even drier anomalies.

The increases in q relative to 2022 were characteristic of El Niño—this can be seen clearly for 1998, 2010, and 2016 in Figs. 2.24a–d. The La Niña during 2021 and 2022 also likely contributed through its tendency to depress the near-surface water content. Plate 2.1g shows the largest positive q anomalies lying mostly within ±30° latitude over typical El Niño-related wet regions to a large degree. For example, the southern United States, northwestern and southeastern South America, east Africa, and eastern China are broadly positive; the January to December averaging likely dampens these seasonal-scale anomalies. India, Southeast Asia, and northern Australia also show strong positive q anomalies despite El Niño favoring dry conditions over these regions. Over oceans, strong positive q anomalies were present over the typical El Niño–Southern Oscillation (ENSO) region in the tropical Pacific and also over the North Pacific, tropical North Atlantic, and southern Indian Ocean. The latter is associated with the positive phase of the Indian Ocean dipole. These features correspond well to anomalously warm sea-surface temperatures (Plate 2.1a). Figure 2.25a shows that the temporal and latitudinal extent of positive q anomalies in 2023 were unusual in historical context. It also shows that although long-term trends (Fig. 2.25b) are positive over the entire Northern Hemisphere and tropics, there is considerable intra- and inter-annual variability in addition to latitudinal variability.

For RH, the fingerprint of ENSO was less clear in the global and latitudinal mean time series (Figs. 2.24e–h; 2.25c) and the 2023 annual anomaly map (Plate 2.1h). Dry anomalies dominated

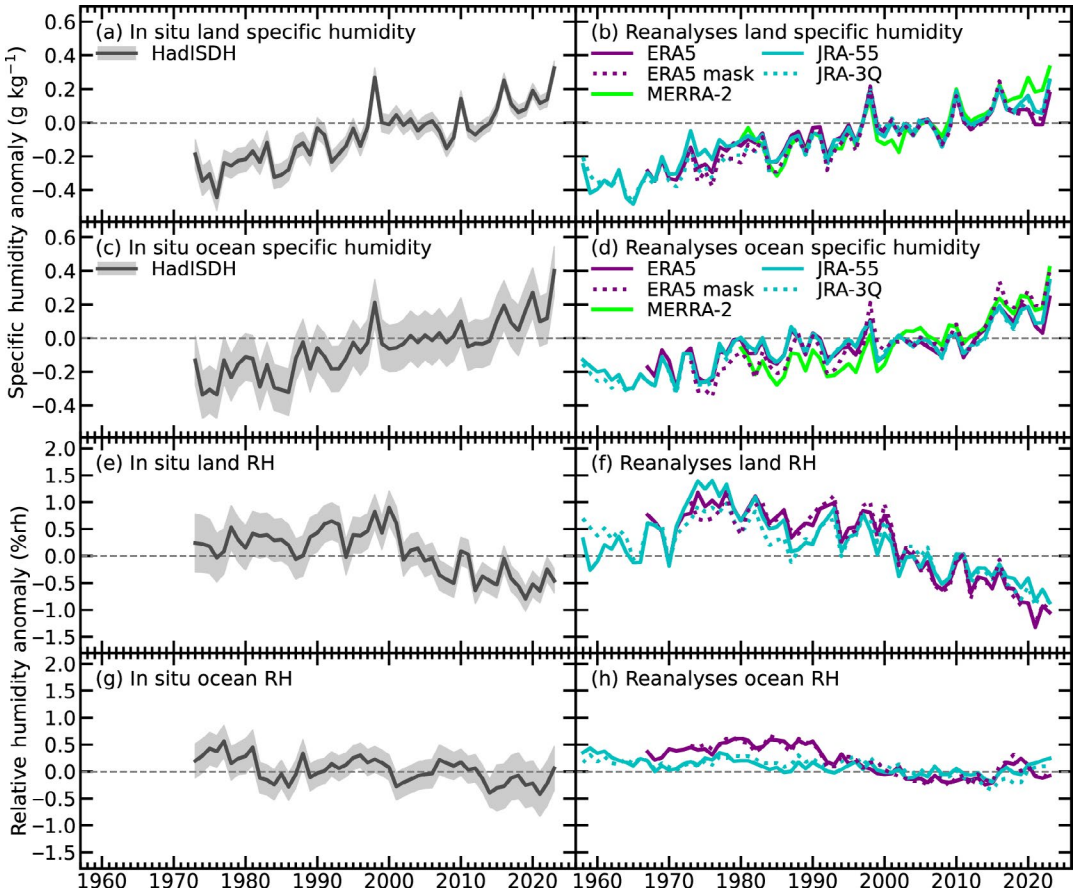

Fig. 2.24. Global average surface humidity annual anomalies (g kg^{-1} for [a]–[d] and %rh for [e]–[h]; 1991–2020 base period). For the in situ datasets, 2-m surface humidity is used over land and ~10-m surface humidity is used over the oceans. For the reanalysis, 2-m humidity is used over the whole globe. For ERA5, ocean series-only points over open sea are selected. ERA5 mask is a version of ERA5 limited to the spatial coverage of HadISDH. Two-sigma uncertainty is shown for HadISDH, capturing the observation, gridbox sampling, and spatial coverage uncertainty. (Sources: HadISDH [Willett et al. 2013, 2014, 2020]; ERA5 [Hersbach et al. 2020]; JRA-55 [Kobayashi et al. 2015]; JRA-3Q [Kosaka et al., 2024]; MERRA-2 [Gelaro et al. 2017].)

over land, despite the strong positive anomalies over the western United States, northwest India/Pakistan, and northern Australia. Dry anomalies were broadly similarly located compared to 2022. Over ocean, the Indian Ocean dipole is apparent with positive RH anomalies spatially matching positive q anomalies. The eastern tropical Pacific had a band of strong negative RH anomalies despite this being a region of strong positive q anomalies, indicating that the warming—and thus water-holding capacity—here (see Plate 2.1a) outpaced the actual water vapor increase.

The lack of in situ data, particularly over oceans, continues to limit our ability to robustly monitor near-surface humidity. The spatial coverage from HadISDH in the Southern Hemisphere is poor, especially over ocean. Figure 2.24 includes ERA5 masked to the lower coverage of HadISDH. This shows improved agreement and that the more positive q anomalies and less negative RH anomalies in HadISDH are partly artifacts of HadISDH undersampling regions where, according to ERA5, drying is stronger. The lower anomalies in ERA5 from 2020 onwards remain substantially lower than in HadISDH and other reanalyses in the masked version, suggesting that this feature is not related to coverage differences. ERA5 suffers from in situ data gaps similar to HadISDH but uses information from satellites and the background model to derive estimates for these regions. All datasets have their own strengths and weaknesses.

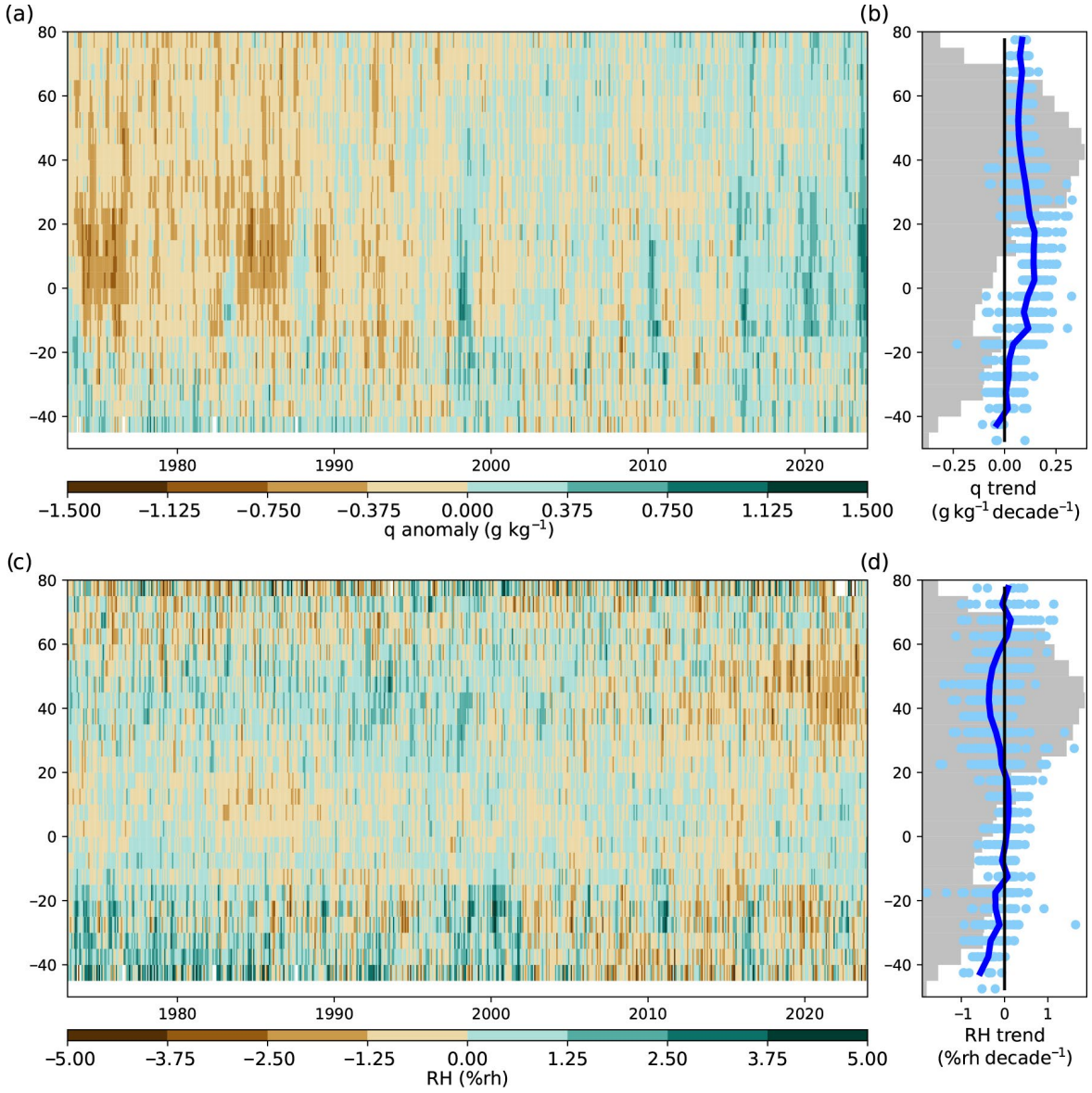

Fig. 2.25. Latitudinal monthly mean anomalies of (a) specific humidity (g kg^{-1}) and (c) relative humidity (%rh; from HadISDH.blend). (b),(d) Decadal trends for each gridbox (dots) and latitude band mean (line), fitted using an ordinary least-squares linear regression following Santer et al. (2008), with gray shading representing the percentage of globe covered by observations (in gridboxes) at each latitude band. Latitude band means are only calculated where there are at least five gridboxes (5° × 5°) at that latitude band.

2. HUMID-HEAT EXTREMES OVER LAND

—K. M. Willett, R. M. Horton, Y. T. E. Lo, C. Raymond, and C. D. W. Rogers

The year 2023 emerged as a record-breaking year by a considerable margin for humid heat over global land, based on daily maximum wet-bulb temperatures (T_wX), for all but one (T_wX31) of the six indices presented herein (see Table 2.6 for definitions of these indices). Humid-heat intensity, measured as the annual anomaly of T_wX, was 0.6°C above the 1991–2020 average (Fig. 2.26a), doubling the previous record of 0.3°C in 1998. Humid-heat frequency also increased by a large margin. The annual T_wX90p anomaly (Fig. 2.26b), a measure of local extremes, was 26.4 days year–1 above average, far exceeding the previous record of 16.2 days year–1 in 1998. Annual occurrence anomalies for T_wX25, T_wX27, and T_wX29 (Table 2.6) were 6.1, 9.3, and 1.3 days year–1 above average, respectively (Fig. 2.26c). These exceeded the previous records of 4.4, 6.7, and 0.9 days year–1 set in 2020 (equal with 2022 for T_wX25), respectively. For T_wX31, 2023 was equal with the previous record in 1998 at 0.2 days year–1.

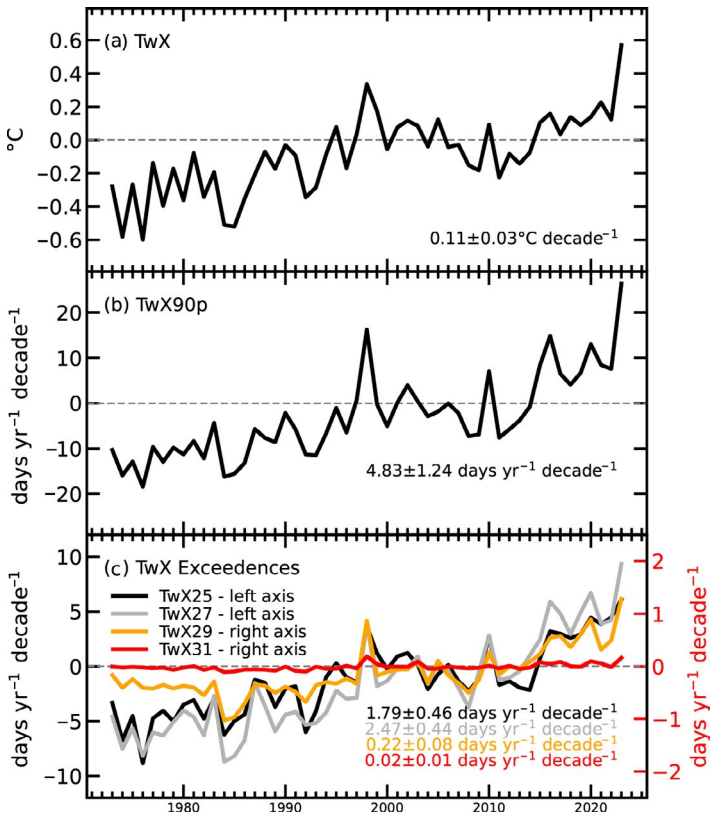

Fig. 2.26. Global land mean annual anomaly time series of various daily maximum wet-bulb temperature indices from HadISDH.extremes relative to a 1991–2020 base period. Decadal trends (significant at p<0.01) are also shown. Trends were fitted using an ordinary least-squares linear regression with an autoregressive (1) correction following Santer et al. (2008). (a) Anomaly of the annual median of the monthly maximum wet-bulb temperature (°C). (b) Anomaly of the annual sum of the daily maximum wet-bulb temperature exceedances of the locally defined daily 90th percentile (days yr⁻¹). (c) Anomaly of the annual sums of the daily maximum wet-bulb temperature ≥ 25°C, 27°C, 29°C, and 31°C thresholds (days yr⁻¹). Note that coverage is skewed towards the northern extratropical latitudes with large data gaps over Africa and considerable gaps over South America, Australia, and parts of Central Asia (see Plates 2.1a and 2.1b for spatial coverage).

Table 2.6. Definitions of six humid-heat indices and their respective 2023 global land annual anomalies (1991–2020 base period). The 2023 global annual anomaly for the exceedance indices (not T_wX) is the sum of the monthly spatial mean over the globe. For T_wX, the median is used as a more robust measure in the presence of outliers, averaging first over space for each month and then over time.

Index	Description	Meaning	2023 Global Anomaly
T_wX	Annual median of monthly maximum wet-bulb temperature	Intensity of humid-heat extremes	0.6°C
T_wX90p	Days per year exceeding the 90th percentile of the climatological daily maximum wet-bulb temperature (seasonally varying)	Frequency of humid-heat extremes relative to local climatology	26.4 days
T_wX25	Days per year where the daily maximum wet-bulb temperature ≥25°C	Frequency of moderately high humid-heat extremes	6.1 days
T_wX27	Days per year where the daily maximum wet-bulb temperature ≥27°C	Frequency of high humid-heat extremes	9.3 days
T_wX29	Days per year where the daily maximum wet-bulb temperature ≥29 °C	Frequency of very high humid-heat extremes	1.3 days
T_wX31	Days per year where the daily maximum wet-bulb temperature ≥31°C	Frequency of severe humid-heat extremes	0.2 days

The exceptionally large humid-heat index anomalies are in concert with record anomalies across many other variables in 2023. El Niño, present from May onwards and becoming strong by autumn (see section 4b for details), contributed to record humid-heat anomalies by influencing both atmospheric and sea-surface temperatures. In conjunction with significant positive trends in humid-heat intensity and frequency (Fig. 2.26), these record anomalies are clear indicators of a rapidly changing climate that is impacting society across the globe. Humid heat presents challenges to maintaining comfortable and safe temperatures for humans (Saeed et al. 2022; Wolf et al. 2022; Kjellstrom et al. 2017) and other large mammals (Buzan and Huber 2020) as evaporative cooling (including sweating) is less efficient in hot and humid conditions (Baldwin et al. 2023).

Thresholds of 25°C, 27°C, 29°C, and 31°C T_wX represent moderately high to severe humid-heat extremes. They may be exceeded during midlatitude warm seasons or year-round in the tropics but rarely or never at higher latitudes and elevations. Figure 2.27 shows 2023 anomalies for all indices in historical context, using deciles to identify "unusual" humid heat. Analysis excludes gridboxes with both no 2023 exceedances and <15 years with an exceedance within the 1991–2020 climatological period. "Very unusually high" (10th decile) occurrences for T_wX25 and

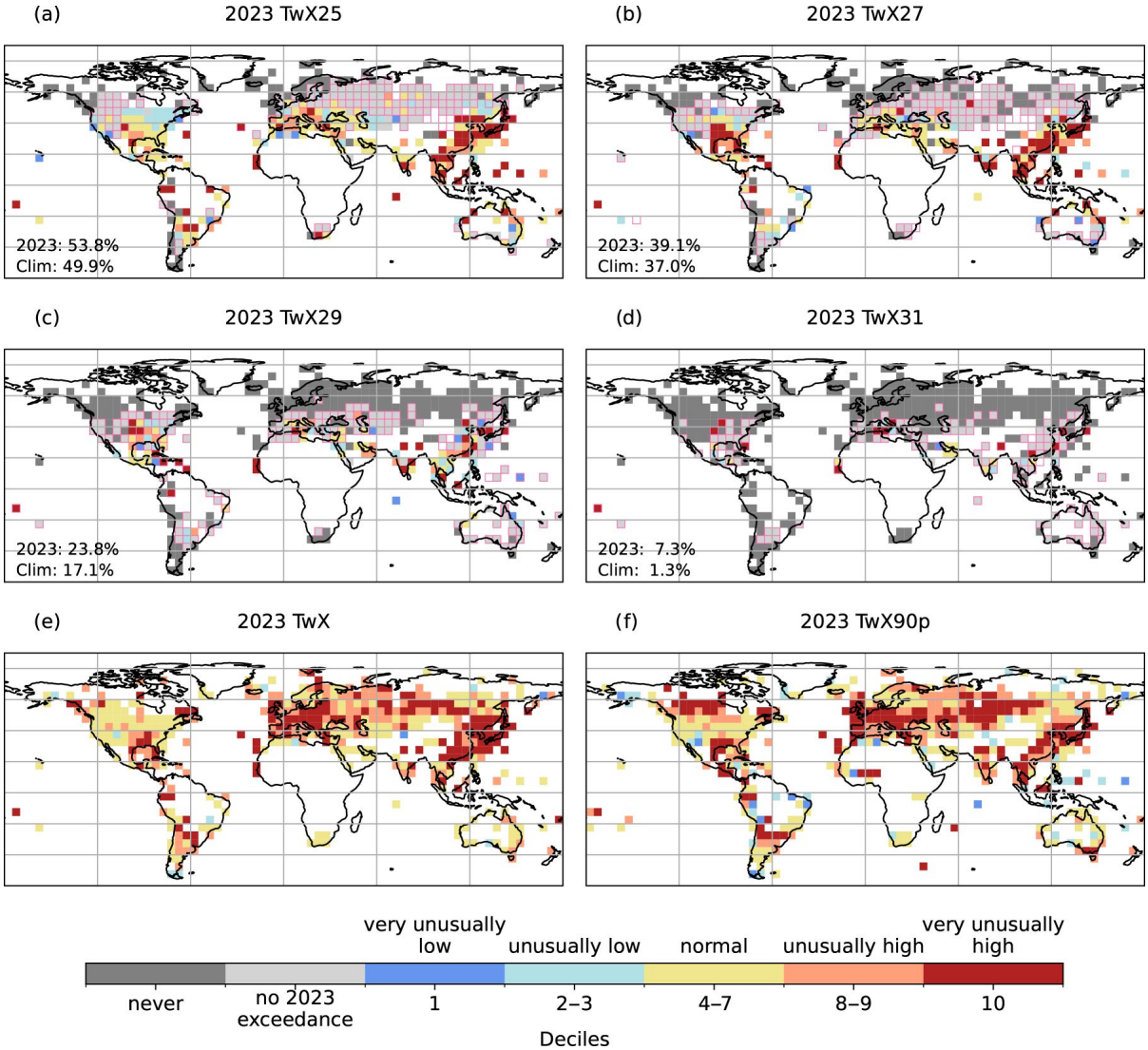

Fig. 2.27. Humid-heat extremes of 2023 as deciles over the period 1973–2023 for various indices. Number of days in 2023 with maximum wet-bulb temperature (T_w) ≥ (a) 25°C (T_wX25), (b) 27°C (T_wX27), (c) 29°C (T_wX29), and (d) 31°C (T_wX31). Gridboxes bounded in pink indicate that <15 years within the 1991–2020 period had an exceedance. These panels are annotated with the percentage of observed area where an exceedance occurred in 2023 and climatologically (≥15 years of at least one exceedance between 1991 and 2020). (e) Annual median anomaly of monthly maximum T_w (T_wX). (f) Number of days in 2023 with maximum T_w > local daily 90th percentile (T_wX90p) relative to a 1991–2020 base period. For (a)–(d) only, gridboxes bounded in pink indicate <15 years within the 1991–2020 period. For (e) and (f), the gray 'never' and 'no 2023 exceedance' categories are not relevant. Data have been screened to remove gridboxes where temporal completeness is less than 70% (<35 yrs in 51). All valid years have data present for all months.

T_wX27 in 2023 (Figs. 2.27a,b) covered 20.4% and 28.0% of analysis-relevant gridboxes, respectively. This is in contrast to 9.6% and 10.4 %, respectively, for those indices in the "no 2023 exceedance" and "very unusually low" (1st decile) categories combined. These "very unusually high" exceedances were mostly over the southeastern United States (T_wX27 only), eastern China, Japan, and Southeast Asia. In some higher latitudes (e.g., eastern North America, the Caspian Sea), exceedances were "unusually low" (2nd to 3rd deciles), pointing to the inherent interannual variability in rare events and potential differences between dry-bulb and wet-bulb measures of extremes. Sparse occurrences of T_wX29 and T_wX31 (Figs. 2.27c,d) with "very unusually high" frequencies covered 21.9% and 39.4% of analysis-relevant gridboxes, respectively. For T_wX29, these occurred over parts of the tropics, northern India, eastern China, and as far north as Japan and the central United States. "Very unusually high" T_wX31 occurrences were mostly outside the tropics, including over the Mediterranean, near Sicily, and the central United States. The Persian Gulf, a region with climatologically exceptionally high humid heat (Raymond et al. 2020), experienced "normal" (4th to 7th deciles) to "unusually high" (8th to 9th deciles) frequencies in 2023 for T_wX25 to T_wX31. For all absolute threshold indices (T_wX25 to T_wX31, Figs. 2.27a–d), 2023 saw a larger global land area experiencing ≥1 exceedance of +2.1 to +6.7 percent of gridboxes compared to the climatological mean.

The globally applicable measures of T_wX90p and T_wX (Plates 2.1i,j) had positive intensity and frequency anomalies over most of the observed land in 2023. "Unusually high" to "very unusually high" (8th to 10th deciles) local humid-heat intensity (T_wX) and frequency (T_wX90p) covered 57% and 53% of the observed land, respectively (Figs. 2.27e,f), with Europe and eastern Asia standing out. Few gridboxes had "unusually low" or "very unusually low" (1st to 3rd decile) intensities (2.5%) or frequencies (10%). Humid-heat events with notable impacts included those near Rio de Janeiro in November, in Florida and the United States Gulf Coast in June–July, South and Southeast Asia in April, and China in July. A lack of in situ data precludes confident statements about humid heat in many tropical, desert, high-elevation, and high-latitude areas. Absences are most prominent for Africa. The drying out of wet-bulb temperature (T_w) thermometers results in erroneously high readings. Although this is less common now due to the increasing prevalence of humidity probes, its influence in these high-value threshold exceedances cannot be ruled out.

Here, humid heat is explored using the in situ-based monitoring product HadISDH. extremes (Willett 2023a,b) for the period 1973–2023. This product calculates T_w using the Noniterative Evaluation of Wet-bulb Temperature method (Rogers and Warren 2024). Indices are calculated using daily maximum wet-bulb temperature following methods established for dry-bulb indices (section 2b4; https://climpact-sci.org).

3. TOTAL COLUMN WATER VAPOR

—O. Bock, C. A. Mears, S. P. Ho, and X. Shao

In 2023, global (60°S–60°N) mean total column water vapor (TCWV) was between 0.89 kg m^{-2} and 1.12 kg m^{-2} above the 1991–2020 average, according to five datasets (Fig. 2.28a; Table 2.7). Three of the datasets (MERRA2, JRA55, and GPS-RO) determined that 2023 was the wettest year on record. Over oceans (Fig. 2.28b), the moisture excess was even larger, with record-high anomalies between 1.01 kg m^{-2} and 1.23 kg m^{-2} in all five datasets (ERA5, MERRA2, JRA55, RSS TPW

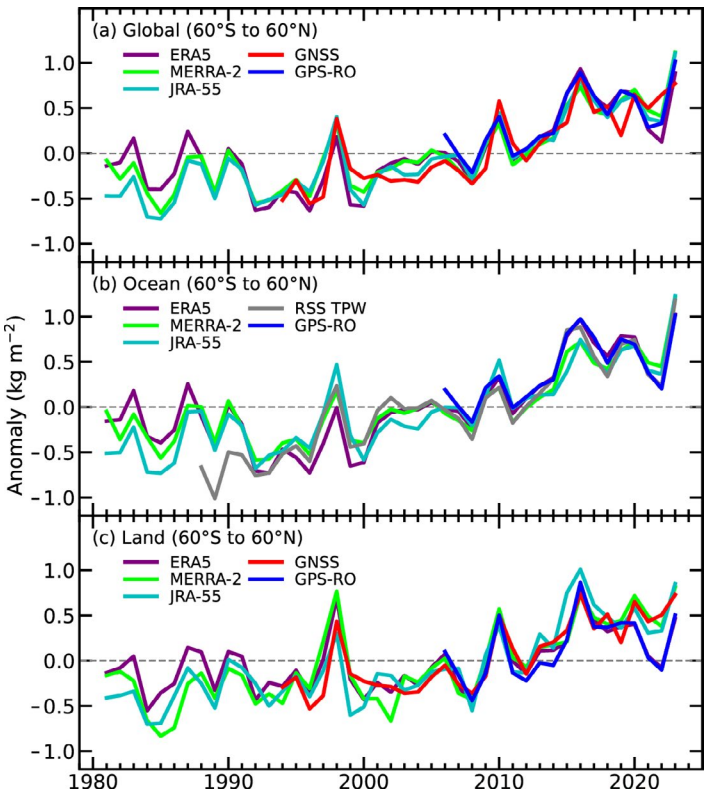

Fig. 2.28. Global mean total column water vapor (TCWV) annual anomalies (kg m^{-2}) over (a) land and ocean, (b) ocean-only, and (c) land-only from observations and reanalyses. The shorter time series from the observations have been adjusted so there is zero mean difference relative to the ERA5 results during their respective periods of record.

Table 2.7. Global mean (60°S–60°N) total column water vapor (TCWV) anomalies (kg m^{-2}; 1991–2020 base period) for 2023 and linear trends (kg m^{-2} $decade^{-1}$) over the period 1991–2023 (2006–23 for GPS-RO, 1995–2023 for GNSS). The GNSS data include 197 stations over land and ocean islands and 143 stations over land.

TCWV Anomalies (kg m^{-2})						
Dataset	ERA5	MERRA2	JRA-55	MWR	GPS-RO	GNSS
Global	0.89	1.12	1.10	--	1.01	0.77
Ocean	1.02	1.21	1.23	1.18	1.01	--
Land	0.46	0.81	0.85	--	0.50	0.73

TCWV Trends (kg m^{-2} $decade^{-1}$)						
Dataset	ERA5	MERRA2	JRA-55	MWR	GPS-RO	GNSS
Global	0.38±0.06	0.36±0.05	0.37±0.05	--	0.44±0.14	0.39±0.14
Ocean	0.45±0.06	0.39±0.05	0.38±0.05	0.43±0.06	0.44±0.16	--
Land	0.19±0.06	0.30±0.08	0.32±0.07	--	0.29±0.16	0.33±0.16

v7.0, and GPS-RO). Over land (Fig. 2.28c), TCWV was well above average, but ranked as the second- to fourth-wettest year in four datasets (ERA5, JRA55, GNSS, and GPS-RO) where 2016 holds the record. MERRA-2 ranked 2023 as the wettest. All global anomalies exceeded the linear trend estimate for 2023, coinciding with the El Niño–Southern Oscillation (ENSO) transition to a strong El Niño (see section 4b for details). This contrasts with 2021 and 2022 anomalies, when La Niña conditions prevailed, which were below the linear trend.

On average, moist anomalies were mainly located along the equatorial Pacific Ocean and in a C-shaped pattern extending from the east coast of equatorial Africa to China in the north and into the southern Indian Ocean to the south (Plate 2.1k; Fig. 2.29a). These patterns are typical of El Niño states (Fig. 2.29b; Timmermann et al. 2018), where 2023 resembled other strong October–December El Niños (e.g., 1997 [Fig. 2.29c] and 2015 [Fig. 2.29d]). Similar to 2015, several regions experienced wetter-than-average conditions in 2023 (central Africa, northern North America, Europe, and the Middle East), while other regions experienced drier-than-average conditions, leading to rainfall deficiencies and droughts (Australia and Indonesia, northwest and southwest Africa, and Brazil).

Global mean TCWV variations are strongly constrained by lower tropospheric temperature (LTT) variations following the Clausius-Clapeyron relation, with a typical rate of change in water vapor of ~7% per 1°C (O'Gorman and Muller 2010). This tight relation holds at interannual and longer time scales. The global TCWV trends lie between 0.36 kg m^{-2} $decade^{-1}$ and 0.44 kg m^{-2} $decade^{-1}$ (Table 2.7) or 1.30% $decade^{-1}$ and 1.67% $decade^{-1}$, considering a global mean TCWV of 26.3 kg m^{-2}. When related to the median LTT trend of ~0.18°C $decade^{-1}$ to 0.22°C $decade^{-1}$ reported in Table 2.3, the estimated rate of change of water vapor is in the range 7.6%–9.3% per °C, which is consistent with the Clausius-Clapeyron relation given the uncertainty in the trend estimates (Po Chedley et al. 2023). Superposed on the long-term trend are positive and negative excursions, which coincide with the warm (e.g., 1998 and 2016) and cold (e.g., 2021 and 2022) phases of ENSO.

This assessment used observations from satellite-borne microwave radiometers over the oceans (RSS TPW v7.0; Mears et al. 2018), GPS-RO observations from several satellite missions (Ho et al. 2020; Shao et al. 2023), both over land and oceans, and ground-based GNSS observations over land and islands (Bock 2022). Three global reanalysis products were used: ERA5 (Hersbach et al. 2020), MERRA-2 (Gelaro et al. 2017), and JRA-55 (Kobayashi et al. 2015). All three reanalyses assimilate satellite microwave radiometer data (in the form of radiances) and GPS-RO data (in the form of bending angles), but not ground-based GNSS measurements, which serve as an independent validation dataset.

There is reasonable agreement across datasets, both on interannual timescales and trends in the base period (1991–2020), but this deteriorates prior to 1991 (Figs. 2.28a–c) and in some extreme El Niño years (1997/98, 2010, 2015/16; Figs. 2.28b,c). The divergence from the linear trend and significant scatter between reanalyses prior to 1993 may be due to changes in the global observing system (Allan et al. 2014). Differences in the observations assimilated, in the assimilation systems, as well as in model physics, may all contribute to differences in the reanalysis products, especially in data-sparse regions and in the pre- and early-satellite era (before 1980). Few validation datasets are available prior to 1993. The microwave radiometers included here do not diverge from the linear trend (Fig. 2.28b), suggesting common structural inhomogeneities in the reanalyses. Furthermore, TCWV over land in ERA5 has been low since 2020 (Fig. 2.28c), almost halving the linear trend estimate compared to other datasets (Table 2.8). Comparison with ground-based GNSS data (Plate 2.1k) reveals that ERA5 has a widespread dry bias of 0.5 kg m^{-2}–1 kg m^{-2} in the tropical land areas and smaller wet anomalies (~0.5 kg m^{-2}) in the midlatitudes, consistent with a previous version of the reanalysis (Bock and Parracho 2019). MERRA2 also exhibits a dry bias of ~1 kg m^{-2}, mainly located over the Maritime Continent, which is compensated in the global mean by small wet biases in other regions (not shown).

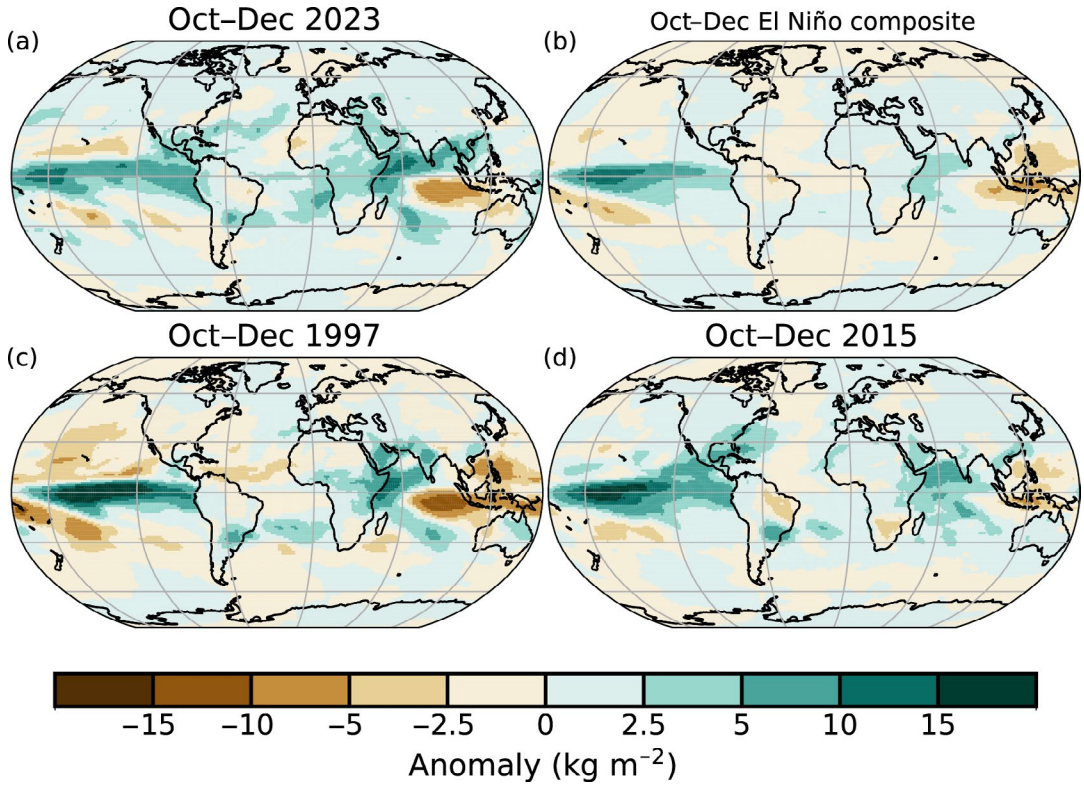

Fig. 2.29. (a) Oct–Dec 2023 mean total column water vapor (TCWV) anomaly from ERA5, compared to (b) Oct–Dec composite for six strong (1957, 1965, 1972, 1987, 1991, 2023) and three very-strong (1982, 1997, 2015) El Niño events (according to the Oceanic Niño Index from NOAA's Climate Prediction Center) and two individual recent very-strong events in (c) 1997 and (d) 2015. Units are given by kg m^{-2}.

4. UPPER-TROPOSPHERIC HUMIDITY

—V. O. John, L. Shi, E.-S. Chung, R. P. Allan, S. A. Buehler, and B. J. Soden

In 2023, the global mean upper-tropospheric humidity (UTH) anomaly, shown using relative humidity in Fig 2.30a, was slightly above normal in the first half of the year but below in the second half. The UTH exhibited expected behavior during El Niño, with regions of large drier-than-average relative humidity anomalies at subtropical latitudes over the Pacific Ocean. These were only partly balanced by more-than-humid anomalies near the equator (McCarthy and Toumi 2004), as depicted in Plate 2.1l. The mean and standard deviation of the global monthly anomalies in 2023 were −0.08±0.32%rh for the microwave-based data (Chung et al. 2013), 0.03±0.32%rh for the infrared-based data (Shi and Bates 2011), and −0.24±0.59%rh for ERA5 reanalysis data (Hersbach et al. 2020).

All datasets show near-zero and statistically insignificant global mean trends, which is in line with the theoretical consideration that the large-scale relative humidity in the upper troposphere remains approximately constant (Ingram 2010); however, this does not mean that the absolute humidity (amount of water vapor) in the upper troposphere remains unchanged in a warming upper troposphere. This is illustrated in Fig 2.30b, which shows the difference between mid-to-upper-tropospheric mean layer temperature (MSU T2; Zou et al. 2023) and the measured brightness temperature of the 6-μm water vapor channel (HIRS T12), which is sensitive to the upper-tropospheric relative humidity. The mid-to-upper-tropospheric mean layer temperature is derived from the brightness temperature of the 60-GHz oxygen channel. As the change of oxygen concentration is insignificant, the emission level in the troposphere of the oxygen channel remains constant and, therefore, the measurements correctly reflect tropospheric warming (Simmons 2022), and the time series of the measurements shows a positive trend (not shown, see tropospheric mean temperature in section 2b5). If there were no change in water vapor amount in the mid-to-upper troposphere, the time series of the upper-tropospheric water vapor channel would have a similar positive warming trend, and the time series of the difference between the two should have a nearly zero trend. On the contrary, the difference time series shows a positive trend. This is because as the amount of water vapor in the upper troposphere (UT) increases, the emission level of the water vapor channel shifts higher in the troposphere and measures water vapor emissions with a lower temperature, diverging from the oxygen emission levels. Therefore, the trend in the difference time series is from the moistening of the UT (Soden et al. 2005; Chung et al. 2014). The 2023 differences were larger than any other points within the record, pointing to record-high UT absolute humidity (water vapor).

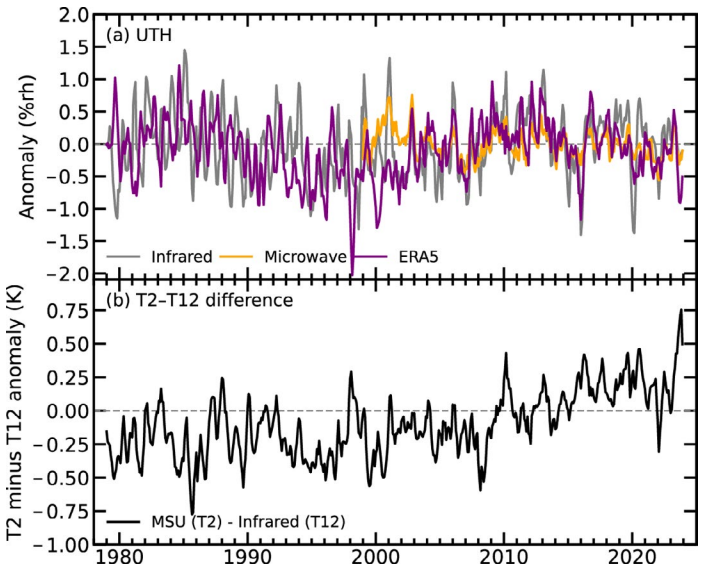

Fig. 2.30. Time series of (a) global monthly mean anomaly upper-tropospheric humidity (UTH) for the three datasets (%rh; see text for details) and (b) the difference between upper-tropospheric temperature (T2) and water vapor channel (T12) brightness temperatures (K). Anomalies are with respect to the 2001–20 base period.

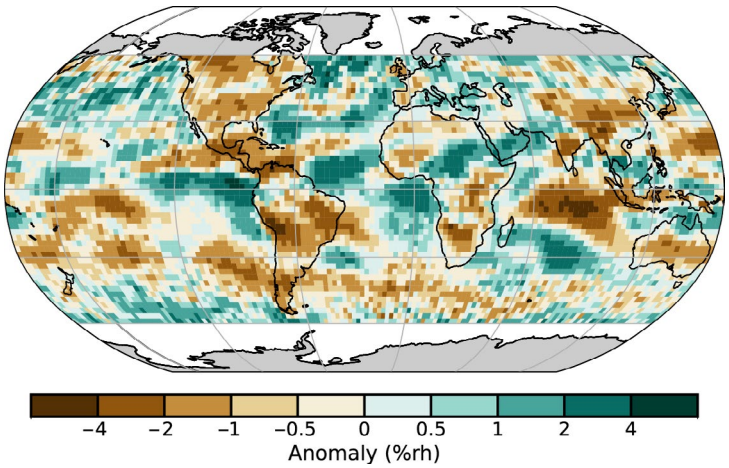

Fig. 2.31. Upper-tropospheric humidity anomaly map (%rh) for 2023 from the infrared data record (2001–20 base period).

Plate 2.1l shows the annual average anomaly map of relative UTH in 2023 derived from the microwave data, and the infrared equivalent is shown in Fig 2.31. The UTH anomalies reflect the large-scale circulation patterns. El Niño-like features were clearly represented, with a large positive anomaly in the eastern Pacific. The strong positive phase of the Indian Ocean dipole can also be seen. Here, the cooler-than-normal eastern Indian Ocean and warmer-than-normal western Indian Ocean led to reduced convection in the east and enhanced convection into the west. There were generally dry conditions over the North and South American continents, and moistening signatures in the UT over Africa.

5. PRECIPITATION

—R. S. Vose, R. Adler, G. Gu, X. Yin, and M. Ziese

Precipitation over global land areas in 2023, as estimated from two different monitoring products, was much below the 1991–2020 long-term average (Fig. 2.32a). In particular, the gauge-based product from the Global Precipitation Climatology Centre (GPCC; Becker et al. 2013) had an anomaly of –31.5 mm for 2023 (GPCC land mean is 780 mm), and the blended gauge–satellite product from the Global Precipitation Climatology Project (GPCP; Adler et al. 2018) had an anomaly of –28.1 mm. Both products indicate that mean global land precipitation in 2023 was much lower than in 2022 and that 2023 was one of the driest years on record (i.e., from 1979 to present). In contrast, precipitation over the global ocean (Fig. 2.32b) was 9.7 mm above the long-term average, according to the GPCP product, which resulted in near-average precipitation for the globe as a whole (Fig. 2.32c).

Over the global land surface, the highest positive precipitation anomalies in 2023 were concentrated in relatively small areas, including equatorial Africa and eastern Asia, though larger regions such as Europe and northern Asia were also wetter than the long-term average. The biggest negative precipitation anomalies over land were spread across a broad swath of the Americas (especially over the Amazon basin) as well as parts of southern Europe, southern Africa, southern Asia, and most of Australia (Plate 2.1m). Over the global oceans, high positive precipitation anomalies were apparent across the northern Indian Ocean, the western Pacific Ocean, and along the Pacific Intertropical Convergence Zone (ITCZ, the narrow band of heavy precipitation across the tropical Pacific just north of the equator). In contrast, large negative precipitation anomalies were evident over much of the southern Indian Ocean and the eastern Pacific Ocean (except along the ITCZ as noted above).

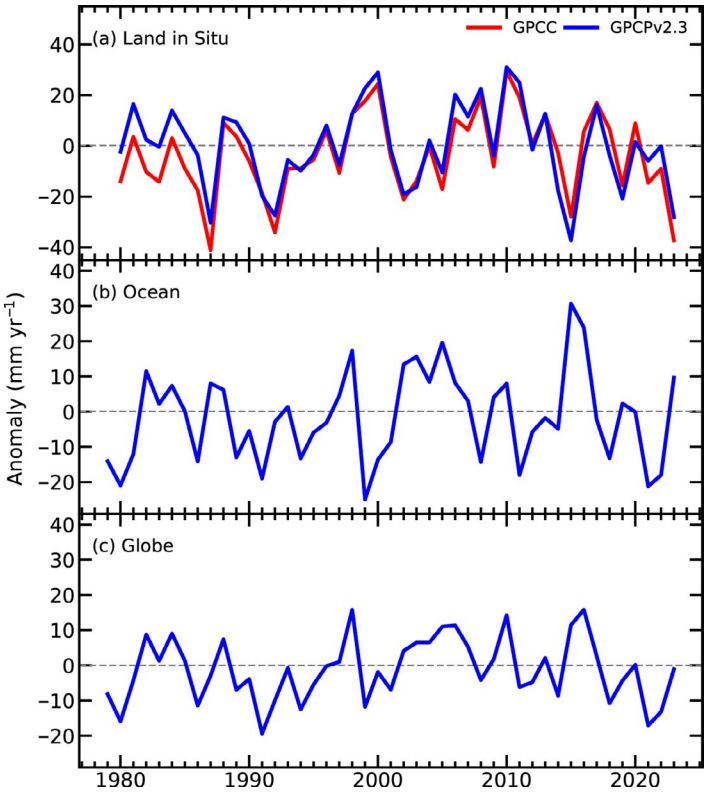

Fig. 2.32. Globally averaged precipitation anomalies (mm yr^{-1}) relative to the 1991–2020 base period over (a) land areas, (b) ocean areas, and (c) the globe. Land and ocean time series were created using a proportional land/sea mask at the 1° × 1° scale.

Consistent with the transition from La Niña to El Niño, anomaly patterns evolved substantially over the course of the year. The pattern for January–March contained a number of typical La Niña features (e.g., a large rainfall deficit over the central equatorial Pacific, a V-shaped positive anomaly over the Maritime Continent, a mostly dry Indian Ocean), but other typical features were absent (e.g., the Amazon was not wet), likely because La Niña was weakening. The pattern for April–June included positive anomalies along the Pacific ITCZ and in the western Pacific, a reflection of the emergence of El Niño. This trend continued to develop from July through December, with the strong El Niño pattern arising by the last three months of the year (e.g., negative anomalies in northern South America, southern Africa, and Australia). The establishment of the El Niño pattern was associated with occurrences of floods and landslides, for example, over Somalia and eastern Africa, and the continuation of the drought over the Amazon.

6. LAND SURFACE PRECIPITATION EXTREMES

—M. R. Tye, S. Blenkinsop, M. G. Bosilovich, M. G. Donat, I. Durre, C. Lennard, I. Pinto, A. J. Simmons, and M. Ziese

The year 2023 transitioned from La Niña to strong El Niño conditions (see section 4b), intensifying one-day/accumulated five-day maxima (Rx1day/Rx5day) in regions surrounding the Pacific and Indian Oceans. Meanwhile, severe drought coincided with a reduction in extreme precipitation over the Amazon basin. While global mean land precipitation was below the long-term (1991–2020) average (section 2d5), global mean Rx1day was close to average (Fig. 2.33). Positive one-day and/or five-day extremes covered large areas of Asia, Europe, northeastern Africa, and isolated locations in North and South America (Fig. 2.33; Plate 2.1n). Other heavy precipitation events were anomalous within regions surrounded by low precipitation (e.g., Brazil) or after long-lasting drought (e.g., Somalia). Some notable local meteorological extremes are listed below and in Appendix Table A2.1 but are not necessarily those with the greatest impact.

Here, Rx1day and Rx5day are derived from gauge-based (GHCNDEX; Donat et al. 2013; HadEX3, Dunn et al. 2020; GPCC, Ziese et al. 2022) and reanalysis (ERA5, Hersbach et al. 2020) data.

Late (January–March) and early (December) summers in Australasia brought notable precipitation extremes. Post-Cylone Gabrielle crossed New Zealand in February, bringing the wettest start to the year since records began (Murray 2023). In one location, 24-hour accumulations of 175.8 mm were recorded, more than three times the average February total. Northwestern Australia received record-breaking Rx5day in January and March. In December, ex-tropical Cyclone Jasper resulted in a concentration of record-breaking Rx1day and Rx5day over Queensland, with Rx5day exceeding 1000 mm at several locations, nearly triple previous records (Fig. 2.34), making Jasper the wettest tropical cyclone on record to affect Australia (Bureau of Meteorology 2024; Bowen et al. 2024; section 7h4).

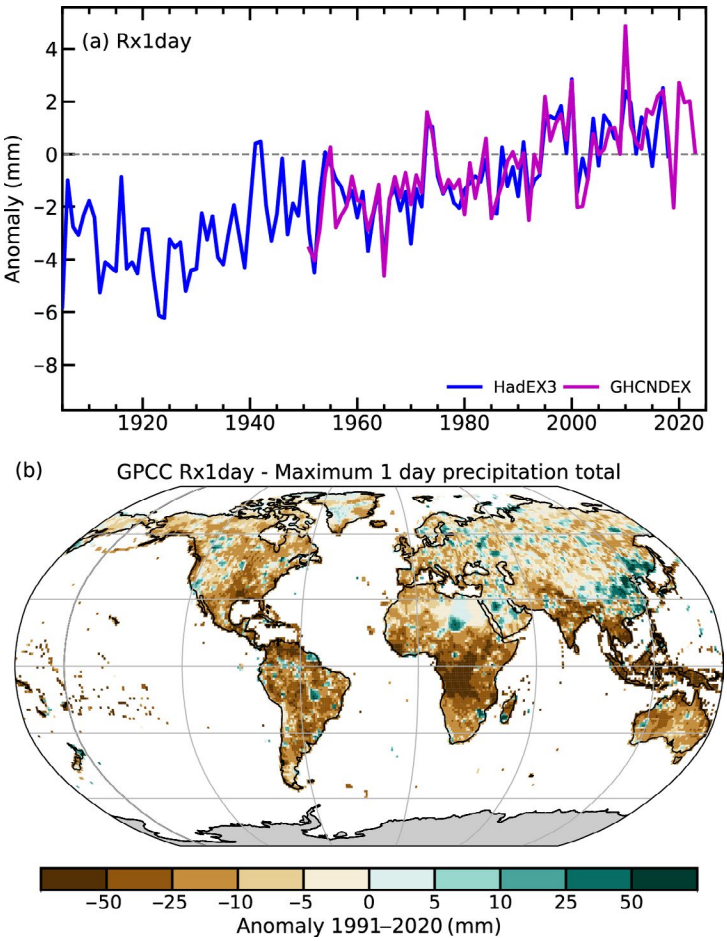

Fig. 2.33. (a) Global mean anomaly of Rx1day (mm) over land from HadEX3 (Dunn et al. 2020) and GHCNDEX gridded observations. (b) Global Rx1day anomalies (mm day^{-1}) in 2023 with respect to the 1991–2020 mean from the Global Precipitation Climatology Centre (GPCC).

Several notable events occurred over East Asia despite fewer-than-average western Pacific typhoons. Super Typhoon Betty (also named Mawar) brought flooding to the Philippines, Guam, and Japan in June, with record precipitation over Japan exceeded again in September. In July, Typhoon Doksuri generated intense precipitation over Beijing with many stations breaking records, while September's Typhoon Haikui generated record one-hour precipitation over Hong Kong.

The dominant modes of variability resulted in high storm and cyclone activity over the Indian Ocean (section 2e1). April–June monsoon rains included isolated exceptionally heavy events causing flash floods in Pakistan. Flood conditions were then exacerbated in India by Tropical Storm Biparjoy (see section 7g4). Cyclone Mocha brought flooding to Myanmar in May, while Tropical Cyclone Tej made landfall in Yemen in October. Long-term drought over East Africa was ended by exceptional flooding during October and November. Long-lived Tropical Cyclone Freddy compounded the effects from January's storm Cheneso over Madagascar, also bringing catastrophic flooding to Mozambique, Zimbabwe, and Malawi after causing damage and fatalities in Mauritius and

La Reunion (see Sidebar 4.2 for details). An extreme cut-off low-pressure system that was isolated from the main atmospheric flow over the Western Cape province of South Africa resulted in widespread flooding, with many stations reporting record daily rainfall amounts during the event, as well as record September totals.

In contrast, intense precipitation events around the Atlantic were isolated within exceptionally dry regions. In Africa, eastern Ghana experienced severe flooding during October. The area around São Paulo, Brazil, recorded its highest 24-hour precipitation totals in February, with high cyclone activity in September affecting Rio Grande do Sul. The percentage of the northeast United States with a much-greater-than-normal proportion of precipitation derived from extreme one-day precipitation was in the top 10th percentile of a 122-year record (NOAA NCEI 2024), although few events were record breakers. On the opposite coast, atmospheric rivers brought record precipitation to California in January–March (section 2d9), while Tropical Storm Hillary also brought persistent heavy rain to the southwest United States in August. In South America, Chile was affected by extreme precipitation in February, June, and, most significantly, August when a frontal system and atmospheric river coincided over the Ñuble region (section 2e1).

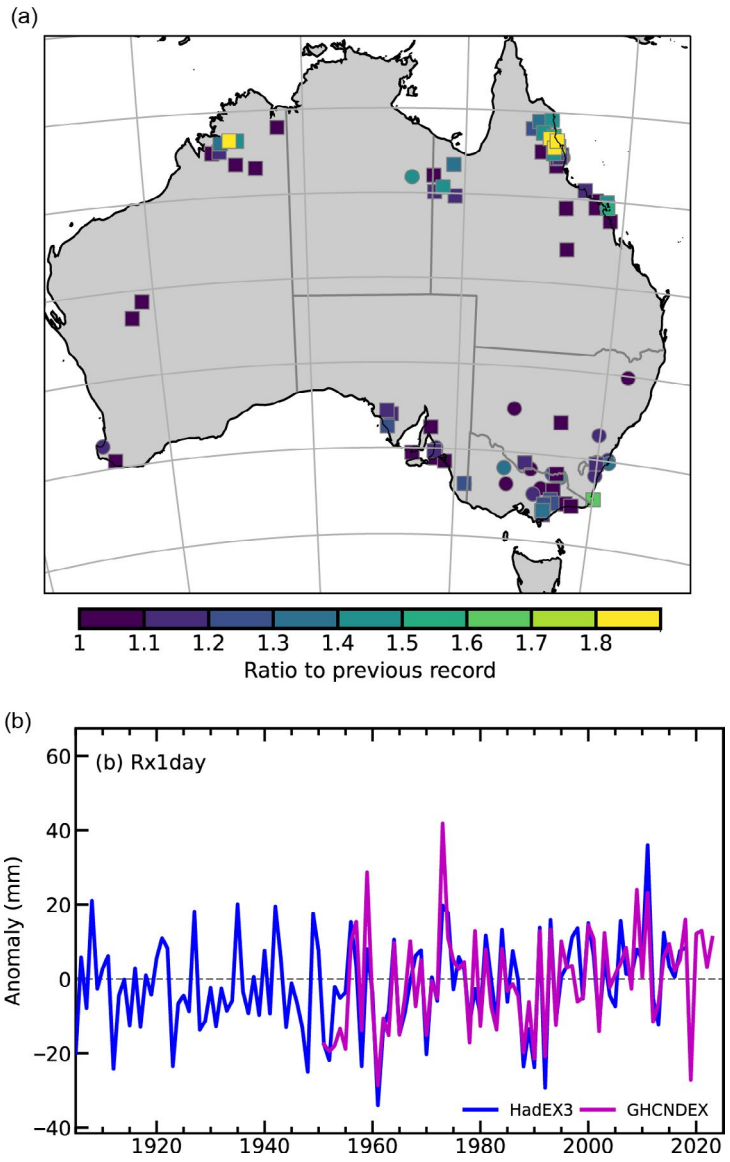

Fig. 2.34. (a) Ratio of new Rx1day (circles) and Rx5day (squares) records set over Australia in 2023 with respect to the previous record. (b) Regional mean anomaly of Rx1day (mm) over north Australia from HadEX3 and GHCNDEX gridded observations.

Storm Daniel formed in the eastern Mediterranean in September, causing flooding in Greece, Türkiye, and Bulgaria, resulting in the loss of at least 27 lives before making landfall in Libya. Here, 414.1 mm of rain was recorded over a 24-hour period in Bayda with an estimated 150 lives lost across the country. Other parts of Europe also experienced summer flooding and fatalities, including Italy in May, followed by a total of 60 new Rx1day and Rx5day records across Scandinavia, the Baltic States, Russia, and Slovenia in August.

7. CLOUDINESS

—C. Phillips and M. J. Foster

Global cloud area fraction in 2023 was 0.16% less than in 2022, the lowest fraction measured in the entire PATMOS-x record, which starts in 1980. A trend of −0.62% decade^{-1} has been observed since the start of the record, increasing the likelihood of record minimum years like 2023. This lower-than-average cloudiness (Plate 2.1o) was distributed globally, with the Indian Ocean, Arctic, and Northern Hemisphere land being especially low in cloudiness in 2023. In 2022, there was a notable increase over the equatorial western Pacific associated with La Niña (Phillips and Foster 2022) that did not appear in 2023 as La Niña ended and El Niño conditions emerged in Northern Hemisphere spring.

These PATMOS-x observations are consistent with independent measurements of cloud radiative effect (CRE) from CERES EBAF 4.2 (Loeb et al. 2018), which started in March 2000. Note

that CRE is the "all sky" value minus the "clear sky only" value in this analysis. This shows a record-high global shortwave CRE annual mean anomaly (SWCRE, 1.20 W m^{-2}) and record-low global longwave CRE annual mean anomaly (LWCRE, −0.62 W m^{-2}) in 2023, relative to a 2000–20 base period (Fig. 2.35).

In most cases, the shortwave effect of clouds is to reflect sunlight, which results in cooling, whereas the longwave effect of clouds is to insulate the lower atmosphere, resulting in heating. The sign convention here is that positive anomalies imply heating, so the decrease of clouds in 2023 caused both heating by reflecting less sunlight (+1.20 W m^{-2}) and cooling by insulating less (−0.62 W m^{-2}). In absolute terms, the SWCRE is negative and the LWCRE is positive. The annual mean SWCRE of −44.53 W m^{-2} was the least negative on record, and the annual mean LWCRE of 27.28 W m^{-2} was the least positive on record. Hence, the effect of clouds could be considered weaker than average as both shortwave (negative) and longwave (positive) were closer to zero. This represents the continuation of a decade-long trend (Phillips and Foster 2022), leading to five of the weakest SWCRE and LWCRE years occurring in the past six years.

Adding the shortwave and longwave CRE together, the annual mean total CRE in 2023 was record high at –17.25 W m^{-2} (0.58 W m^{-2} greater than the 2000–20 average). This means that, globally, clouds still had an overall cooling effect, but it was the weakest global cooling effect of any year measured. Unlike its components, total CRE does not exhibit a significant trend—the global long-term deviations SWCRE and LWCRE appear balanced. Related analysis of the radiative flux and energy budget can be found in section 2f1.

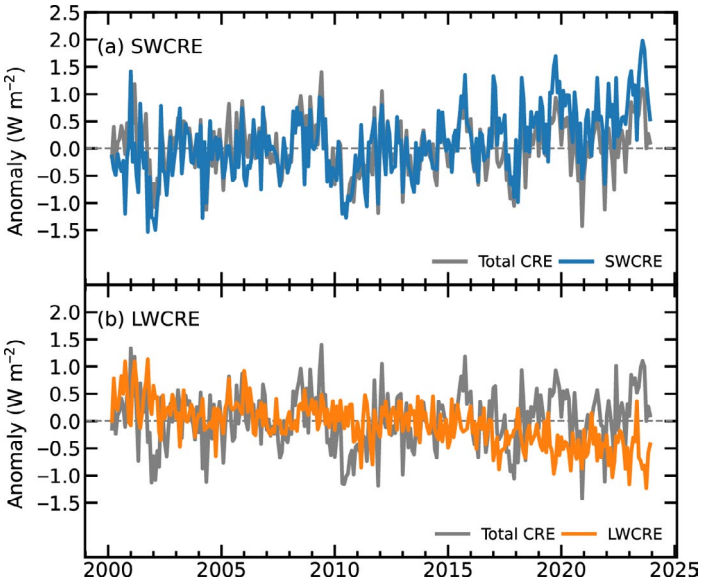

Fig. 2.35. Cloud radiative effect anomalies (W m^{-2}; 2000–20 base period) from CERES EBAF Ed4.2 (Loeb et al. 2018) representing the changes in top-of-atmosphere radiative forcing that are attributable to clouds (which could include both changes to clouds themselves and surface changes masked by clouds). Positive values indicate cloudiness-related warming through more radiation reaching the surface and less being reflected back out to space (shortwave cloud radiative effect [SWCRE]) or more being trapped close to the surface rather than escaping out to space (longwave cloud radiative effect [LWCRE]). Negative values indicate cloudiness-related cooling. Note that these are monthly anomalies whereas annual mean anomalies and absolute values are quoted in the main text.

The El Niño–Southern Oscillation transitioned from La Niña in January to El Niño in May. Hence, for analysis, 2023 is split into two periods: January–April and May–December. Figures 2.36a–d show the average anomalies (relative to 1991–2020; deseasonalized) for PATMOS-x cloud area fraction compared to a composite of all La Niñas and El Niños. Composites use the thresholds of Multivariate ENSO Index version 2 <–1 for La Niña and >1 for El Niño. The January–April and May–December averages show good agreement with the La Niña and El Niño composites, respectively. The La Niña cloud climate is characterized by about 5% more cloud cover over the Maritime Continent (MC) and about 5% less cloud cover directly to the east. During El Niño, anomalies are typically stronger, with up to 10% less MC cloud cover and 10% more cloud cover over the rest of the equatorial Pacific.

These anomalies in the PATMOS-x cloud area fraction are mirrored by CRE anomalies (from CERES EBAF Ed4.2, Figs. 2.36e–h). Regions with decreased cloud fraction are correlated with negative LWCRE anomalies and positive SWCRE anomalies, meaning that in absolute terms, these CRE quantities are closer to zero. For the most part, these large anomalies are balanced such that total CRE is unaffected. The strongest anomalies for the total CRE (not shown) are located off the coast of Ecuador, where both the SWCRE and LWCRE are positive (heating) during the El Niño period from May to December 2023.

PATMOS-x v6.0 provides twice-daily observed cloud products, including cloud area fraction, from each satellite from the set of NOAA Polar Orbiting Environmental Satellite series and

EUMETSAT Polar System (Foster et al. 2023). Producing a global cloud area fraction anomaly necessitates combining these individual observations into a single value representing the diurnal average. This is done by averaging the data for every observed local hour, month of the year, and gridbox to produce a joint diurnal-seasonal-regional climate average. This multidimensional average can be indexed for any individual observation to find the expected bias compared to the desired reference, which is then subtracted out. CERES EBAF Ed4.2 is an energy-balanced-and-filled dataset with top-of-atmosphere radiative flux derived from the CERES instruments onboard the Aqua, Terra, and NOAA-20 satellites (Loeb et al. 2018).

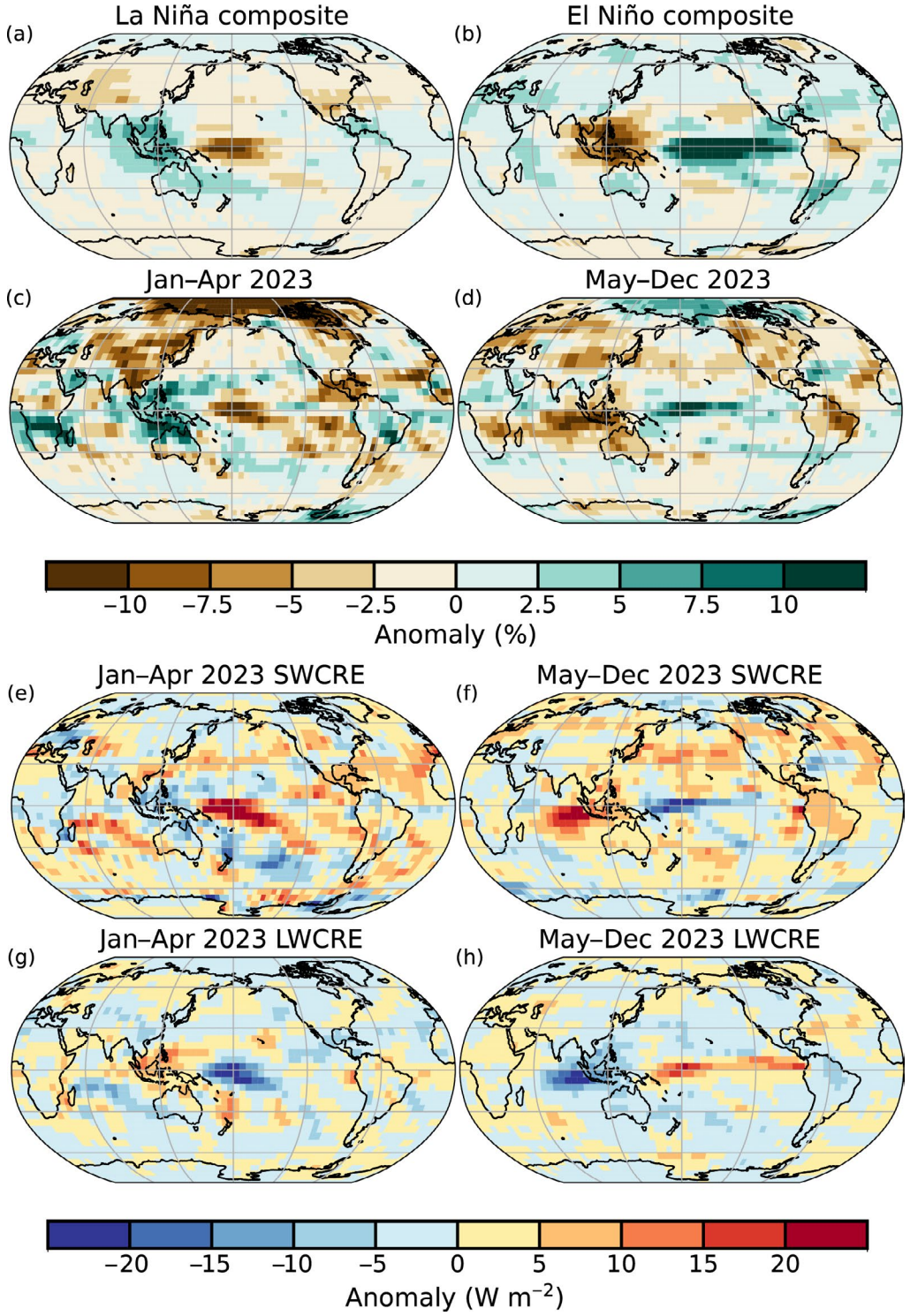

Fig. 2.36. (a) La Niña and (b) El Niño cloud area fraction anomaly composite compared to time averages for (c) Jan–Apr 2023 and (d) May–Dec 2023, respectively (%). PATMOS-x v6.0 composite cloud area fraction anomaly from 1991 to 2022. (e),(f) CERES EBAF-TOA Ed4.2 shortwave cloud radiative effect (SWCRE) anomalies and (g),(h) longwave cloud radiative effect (LWCRE) anomalies (W m^{-2}) for 2023 relative to 2000–20. All anomalies are implicitly deseasonalized.

8. LAKE WATER STORAGE

—M. E. Harlan, B. M. Kraemer, T. V. King, R. S. La Fuente, and M. F. Meyer

Water storage data for 5764 of the world's lakes, provided by a recently published dataset (GloLakes; Hou et al. 2024), reveals a complex picture of hydrological shifts in 2023 (Plate 2.1p). Cumulative lake water storage (LWS) was 1.2% higher in 2023 compared to the baseline period of 1991–2020, demonstrating a slight increase over average historical conditions. Collectively, the lakes with rising LWS increased by a total of 4828 million cubic meters (MCM) whereas those with declining LWS decreased by 2624 MCM. This led to a net increase of 2204 MCM in 2023 (Fig. 2.37). Notably, 64% of the lakes analyzed exhibited higher-than-average water levels relative to their 1991–2020 baseline, reflecting a partial reversal of the recently reported decline in global LWS (Yao et al. 2023; Fig. 2.38). These global, yet heterogenous anomalies underscore the influence of varying climatic and anthropogenic factors on LWS, including precipitation patterns, evaporation rates, and water management practices (Yao et al. 2023; Zhao et al. 2022).

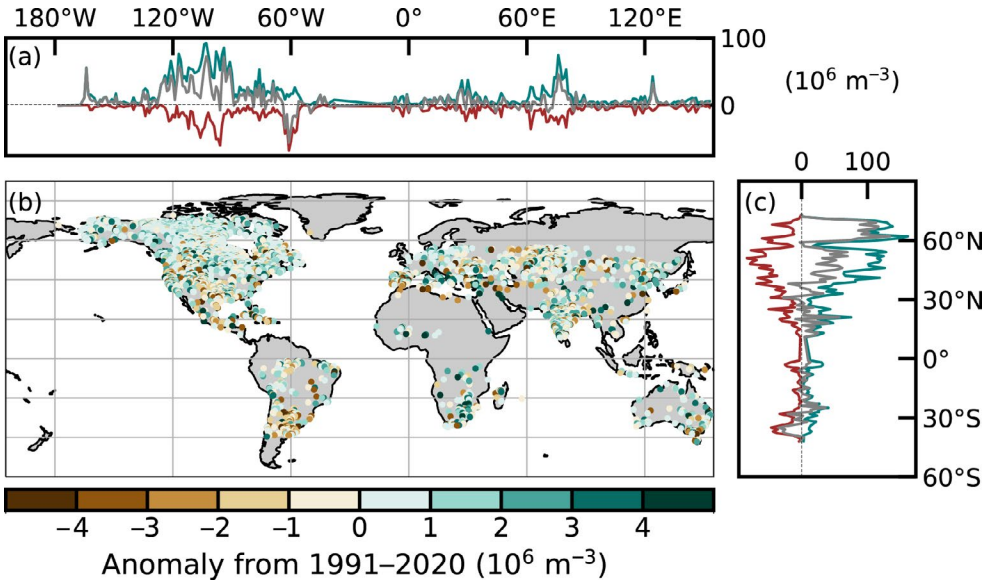

Fig. 2.37. Volumetric water level anomalies (× 10^6 m^3) relative to 1991–2020. The latitudinal and longitudinal insets show the cumulative increase (teal), cumulative decrease (brown), and the net change (gray) across one-degree latitudinal and longitudinal bins.

Excessive LWS fluctuations caused by droughts or floods can have major implications for the availability of essential resources like drinking water, irrigation, food, energy, and transportation, and they pose significant socio-economic challenges (Zohary and Ostrovsky 2011). Importantly, excessive fluctuations in lake volume can also cause considerable ecosystem disturbances, affecting key physical processes, community composition, and biodiversity (Jeppesen et al. 2015), underscoring the need for sustainable water management and conservation strategies in the face of changing global conditions.

While most LWS anomalies were positive, some countries, including Argentina, Algeria, Morocco, Spain, and Türkiye, experienced widespread decreases in lake water volume, with reductions ranging from 10% to 35%. Conversely, Mali, Cambodia, Australia,

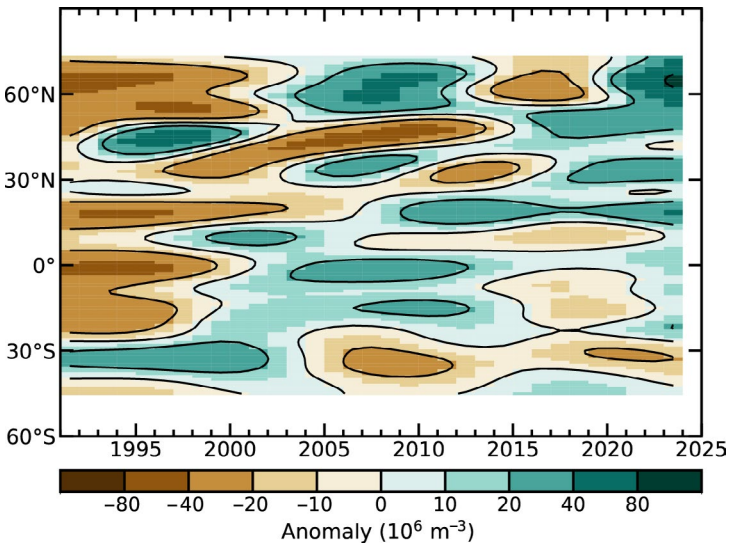

Fig. 2.38. Long-term change in volumetric water level anomalies (× 10^6 m^3) relative to the 1991–2020 mean for each one-degree latitudinal bin. Values are smoothed with a General Additive Model to aid in visualization where the cumulative lake storage anomaly was modeled as a function of an interactive smoothing function between both year and latitude.

South Africa, and India saw their lake volumes increase on average by 43%. The positive LWS anomalies at 60°N observed here contrast with reported water losses at these latitudes due to permafrost thaw (Webb et al. 2022), although previous analyses focused on 2000–20 trends rather than 2023 relative to a baseline of 1991–2020.

To identify changes in lake levels, we used the "GloLakes" lake and reservoir storage dataset (Hou et al. 2024), which combines altimetry and reflectance satellite data across Landsat (Pekel et al. 2016), ICESat2 (Jasinski et al. 2023), the Global Reservoirs and Lakes Monitor (Birkett et al. 2011), and Sentinel-2 (https://www.blue-dot-observatory.com/) to estimate LWS over recent decades. The data were generated using a geostatistical model (Messager et al. 2016) paired with innovative gap-filling methods (Hou et al. 2022). Here, we relied on a subset of the lakes from GloLakes (5764) with data from at least 20 years in the period of 1991 through 2023, with no more than a three-year gap of observations and at least three observations of lake storage in 2023. While the GloLakes dataset allowed us to expand our analysis from altimetry-based water levels in previous reports that focused solely on altimetry data (Kraemer et al. 2022) to include lake water storage, and to include many more lakes (5764 lakes compared to 264 in 2022), the dataset is still restricted in its spatiotemporal coverage. Additionally, the incorporation of optical remote sensing adds challenges such as those posed by clouds, atmospheric interferences, and vegetation, potentially reducing the accuracy of water detection. These challenges could be further mitigated in future years using technologies like passive microwave sensors, synthetic-aperture radars, and wide-swath altimetry (e.g., the Surface Water and Ocean Topography mission).

9. GROUNDWATER AND TERRESTRIAL WATER STORAGE

—M. Rodell and D. N. Wiese

Various regions of the world experienced large increases or decreases in terrestrial water storage (TWS) in 2023, with the global mean approaching a 21-year low. Changes in mean annual TWS between 2023 and 2022 are plotted in Plate 2.1q. Europe, which has been in a state of drought more often than not since 2019, experienced a partial respite in 2023, with TWS increasing slightly across much of the continent while remaining below the long-term average. TWS in parts of southeastern Asia declined from above normal to below normal, while wetness across the rest of Asia, excluding the ever-receding Caspian Sea, remained fairly stable.

Heavy rains in March caused flooding and contributed to TWS increases that exceeded 12 cm across a large area of northern Australia, with some parts experiencing record highs. Total water storage has been well above normal across most of sub-Saharan Africa since 2019, and 2023 was no different, with wet weather raising TWS, especially in the Congo River basin. This multi-year wet event is by far the most intense worldwide (in terms of extent, duration, and TWS anomaly) since satellite observations of TWS changes began in 2002 (Rodell and Li 2023). To the south, drought caused water-level declines across a region centered near the southeastern corner of Angola.

In North America at the start of the year, atmospheric rivers delivered heavy rains to California and parts of adjacent states, resulting in floods and reservoirs being filled to capacity. Despite this, TWS remained near or slightly below the long-term mean in southern California because the slowly recharging aquifers have not fully recovered after years of drought and an associated heavy reliance on groundwater for crop irrigation (Liu et al. 2022). Drought caused TWS to decrease to record lows in central and southern Canada and contributed to their worst year for wildfires on record. Drought also affected TWS in southern Mexico and the central Mississippi River basin, the former which continued into a second year. In South America, a major drought caused TWS to decline by more than 12 cm over a large area of the Amazon River basin, leading to record lows for both that basin and South America as a whole. Northern Argentina and Uruguay also saw water levels decline. On the other hand, a swath of southern Brazil gained a large amount of water.

Deseasonalized time series of monthly zonal-mean and global-mean TWS anomalies are plotted in Figs. 2.39 and 2.40. Data gaps occur when satellite observations are not available. Excluded from the calculation of these means are regions where TWS declines are dominated by

ice sheet and glacier ablation: Antarctica, Greenland, the Gulf Coast of Alaska, polar islands, High Mountain Asia, alpine western Canada, and the southern Andes. Land in the zone between about 25°N and 45°N has been drying gradually (roughly 0.5 cm yr^{-1} to 1.0 cm yr^{-1} on average) since the early 2000s, if not before, and that tendency seems to have gained momentum in recent years. This drying aligns with droughts in the central United States and Europe and the long-term declines of the Caspian Sea and groundwater levels in northern India. The latter two are ultimately attributable to agricultural irrigation (Rodell et al. 2018). A zone of elevated TWS between about 8°S and 15°N first appeared around 2019 and persisted in 2023. At its root is the ongoing wet event in sub-Saharan Africa, while contributions from excess TWS in eastern Brazil and southern India abated in 2023. Just south of that latitude band, TWS returned to normal levels within a ~10° latitude zone after having been low during the preceding four years. That zone includes wetting regions of Argentina and Uruguay, southern Africa, and northern Australia as seen in Plate 2.1q. Figure 2.40 shows that in 2023, global mean TWS, excluding ice sheet and glacier losses, reached its second lowest level since 2002, as declines in northern Brazil, Canada, Mexico, southeastern Asia, the Caspian Sea, and elsewhere outweighed gains in Africa, California, northern Australia, and southern Brazil. The three lowest levels of global mean, non-ice TWS—in 2016, 2023, and 2019—all occurred during El Niño events.

Since 2002, TWS anomalies have been derived from Gravity Recovery and Climate Experiment (GRACE) and GRACE Follow-On (GRACE-FO) satellite observations of Earth's time-varying gravity field (Tapley et al. 2004; Landerer et al. 2020). In situ networks do not observe the components of TWS (groundwater, soil moisture, surface waters, snow, and ice) with sufficient density to infer regional to global changes, hence the reliance on remote sensing. Uncertainty in the monthly TWS anomaly observations is about 1 cm–2 cm equivalent height of water over a 500,000 km^2 region at midlatitudes (Wiese et al. 2016). Groundwater is commonly the largest component of variations in TWS over periods longer than a year and outside of the humid tropics (surface water) and high-latitude and alpine regions (ice and snow; Getirana et al. 2017).

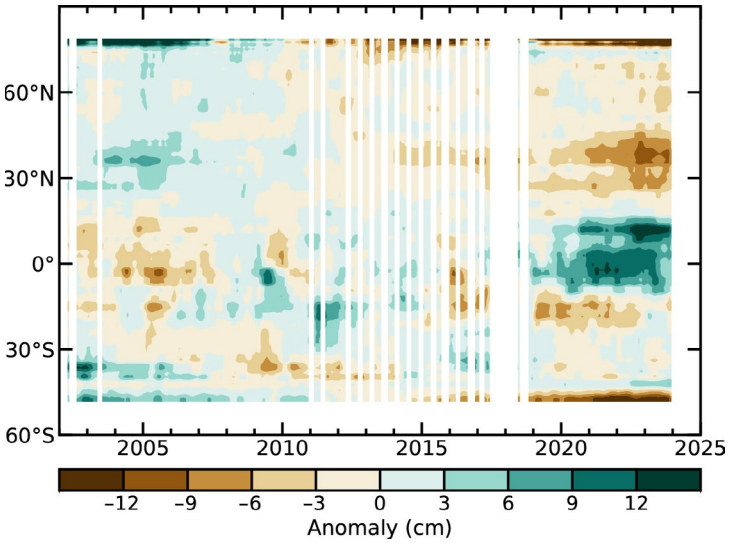

Fig. 2.39. Zonal means of monthly terrestrial water storage anomalies, excluding those in Antarctica, Greenland, the Gulf Coast of Alaska, polar islands, and major glacier systems (e.g., High Mountain Asia, alpine western Canada, and the southern Andes), in cm equivalent height of water, based on gravity observations from the Gravity Recovery and Climate Experiment (GRACE) and Gravity Recovery and Climate Experiment Follow-On (GRACE-FO). The anomalies are relative to a 2003–20 base period.

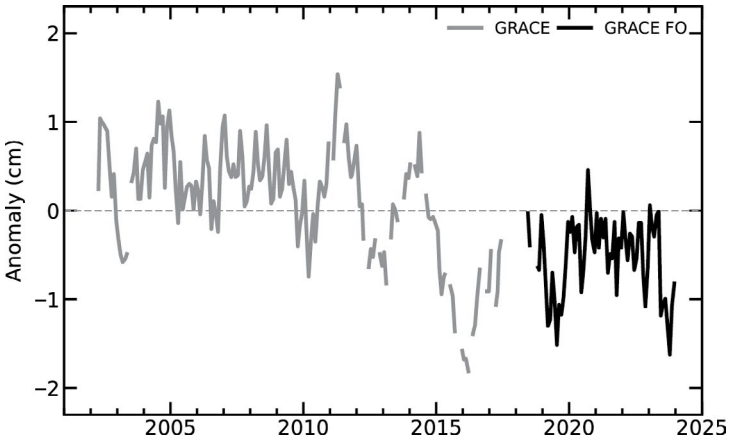

Fig. 2.40. Global average terrestrial water storage anomalies from the Gravity Recovery and Climate Experiment (GRACE; gray) and Gravity Recovery and Climate Experiment Follow-On (GRACE-FO; black), excluding those in Antarctica, Greenland, the gulf coast of Alaska, polar islands, and major glacier systems (e.g., High Mountain Asia, alpine western Canada, and the southern Andes), in cm equivalent height of water, relative to a 2003–20 base period.

10. SOIL MOISTURE

—M. Hirschi, P. Stradiotti, W. Preimesberger, R. van der Schalie, T. Frederikse, D. Duchemin, N. Rodriguez-Fernandez, A. Gruber, S. Hahn, W. A. Dorigo, R. A. M. de Jeu, S. I. Seneviratne, and R. Kidd

Due to its importance in the water, energy, and carbon cycles, soil moisture plays a crucial role in the land–atmosphere interaction (Seneviratne et al. 2010), with impacts on surface air temperature, precipitation generation, and extreme events such as heatwaves and forest fires. The increase in global soil moisture observed over the previous four years (van der Schalie et al. 2022; Stradiotti et al. 2023) reversed in 2023, and the soil moisture values declined back to 2020 levels (Fig. 2.41). While soil moisture in the Northern Hemisphere remained at a similar level to 2022, soil moisture in the Southern Hemisphere strongly decreased after the recent pronounced wetting tendency that began in 2020. This may be a sign of the transition of the ENSO from La Niña to El Niño conditions that occurred in 2023 (see section 4b). This transition is consistent with the occurrence of more widespread below-average soil moisture conditions in the Southern Hemisphere in 2023 (Fig. 2.42; e.g., Zhang et al. 2023). Accordingly, soil moisture in the Southern Hemisphere shifted from a wet to a dry anomaly in 2023, while soil moisture in the Northern Hemisphere remained slightly wetter than normal. Overall, the global soil moisture conditions were close to the 1991–2020 average.

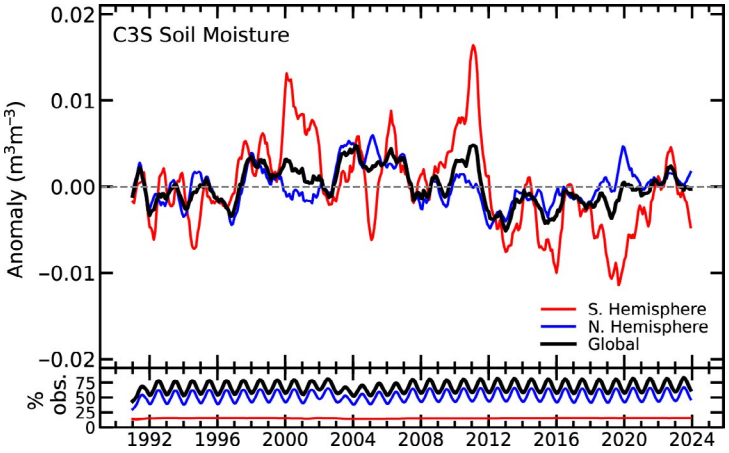

Fig. 2.41. (top) Time series of global (black), Northern Hemisphere (blue), and Southern Hemisphere (red) monthly surface soil moisture anomalies ($m^3\ m^{-3}$) for the period 1991–2023 (1991–2020 base period) and (bottom) the valid observations as a percentage (%) of total global land surface. Data are masked where no retrieval is possible or where the quality is not assured and flagged, for example due to dense vegetation, frozen soil, permanent ice cover, or radio frequency interference. (Source: Copernicus Climate Change Service [C3S] Soil Moisture.)

Wetter-than-normal conditions were present throughout most of the year in northern Australia, with wet anomalies that were particularly widespread in January, April, and July (up to 200% of normal in some places; Plate 2.1r, Appendix Fig. A2.6). Similarly strong wet anomalies were also observed in southern and northwestern India, particularly from January to July. Also, parts of East Asia experienced noticeable wetter-than-normal conditions in 2023, similar to 2022. In the Horn of Africa, the drought conditions of 2022 gave way to wet anomalies around March, which intensified again in November due to heavy rain (e.g., Kimutai et al. 2023; section 2d6). This change from a long-term drought in the region to flooding coincided with a switch of the Indian Ocean dipole (IOD) from a negative to positive mode in 2023 (see section 4f). This mode is associated with above-average rainfall in East Africa (Nicholson 2017; Marchant et al. 2007; see also section 2d5). Further areas of above-average soil moisture were also noticeable in parts of eastern Europe and Central Asia, in Türkiye, and in the western United States. Northeast Brazil

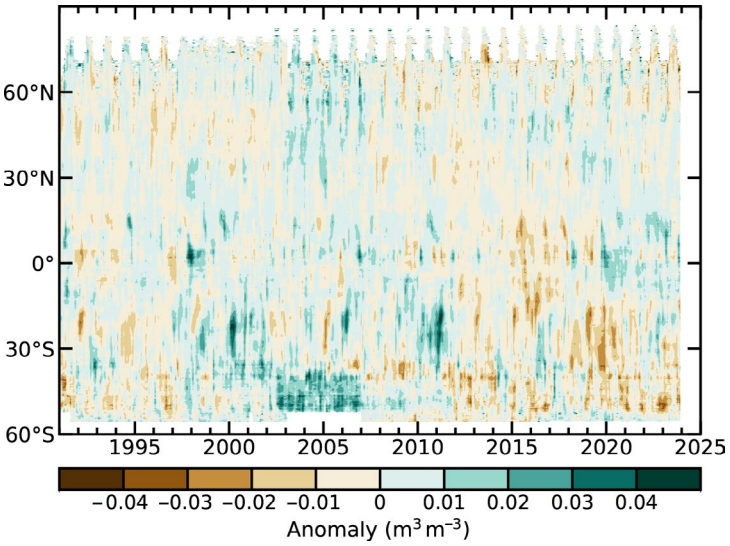

Fig. 2.42. Time–latitude diagram of monthly surface soil moisture anomalies ($m^3\ m^{-3}$; 1991–2020 base period). Data are masked where no retrieval is possible or where the quality is not assured and flagged, for example due to dense vegetation, frozen soil, permanent ice cover, or radio frequency interference. (Source: C3S Soil Moisture).

started the year with strong wet anomalies that persisted for most of the year, while in the central and southeast part of the country, severe below-normal conditions started to emerge at the end of 2023 (e.g., Clarke et al. 2024; see section 7d2).

In contrast to these regionally confined wet soil moisture anomalies of 2023, dry conditions were observed in numerous regions (Plate 2.1r). The most pronounced dry anomaly was observed in southern South America, especially in the River Plate basin and Patagonia (below 50% of normal soil moisture in some areas). This region has been suffering from a multi-year drought since 2019 (Naumann 2021). Pronounced dry conditions also persisted in the Canadian Prairies for the third consecutive year (see section 7b1; van der Schalie et al. 2022; Stradiotti et al. 2023). Although soil moisture remained below normal, drought conditions in the Great Plains of central North America weakened in 2023 compared to 2022. Mexico experienced drier-than-normal conditions during June–September (Appendix Fig. A2.6). Similarly, below-normal soil moisture was observed in southwestern Africa (including South Africa and Namibia), with the most pronounced dry anomalies recorded from February to May. Many of the regions around the Mediterranean Sea (including Spain, northern Morocco, Algeria, and Tunisia) also experienced moderately dry conditions in 2023. In addition, widespread mild-to-moderate negative soil moisture anomalies were observed over much of inland China, southern Central Asia, northern Asia, and in the higher latitudes in general. In southeast Australia, the strong positive soil moisture anomalies of 2022 (Stradiotti et al. 2023) turned into widespread dry anomalies covering most of the southern part of the continent (except for parts of Victoria), but with intermittent periods of wetter-than-normal conditions in January, April, June, and July.

Soil moisture was observed by microwave satellite remote sensing of the surface soil layer down to approximately 5-cm depth, as provided by the COMBINED product of the Copernicus Climate Change Service (C3S) version 202212 (Dorigo et al. 2023). C3S combines multi-sensor data in the 1978–2023 period through statistical merging (Dorigo et al. 2017; Gruber et al. 2017, 2019). Wet and dry anomalies here refer to the deviation from the 1991–2020 climatological average. Note that changes in spatiotemporal coverage (also between product versions, e.g., resulting from the inclusion of additional sensors) can introduce uncertainties in the domain-averaged soil moisture time series (e.g., Bessenbacher et al. 2023).

11. MONITORING GLOBAL DROUGHT USING THE SELF-CALIBRATING PALMER DROUGHT SEVERITY INDEX

—J. Barichivich, T. J. Osborn, I. Harris, G. van der Schrier, and P. D. Jones

The self-calibrating Palmer Drought Severity Index (scPDSI; Wells et al. 2004; van der Schrier et al. 2013) over the period 1950–2023 shows that the increasing trend in severity and extent of global drought, which has been ongoing since mid-2019 (Barichivich et al. 2020, 2021, 2022), reached a new historical peak during the second half of 2023 (Fig. 2.43). During June–September, extreme drought conditions (scPDSI ≤–4) surpassed 7% of the global land area for the first time in the record, peaking at a new historical maximum of 7.9% in July. Similarly, the extent of severe plus extreme drought conditions (scPDSI ≤–3) in 2023 exceeded 16% of the global land area for the first time during the same period, reaching a historical maximum of 16.8% in July. Moderate or worse drought conditions (scPDSI ≤–2) peaked in September at a historical maximum of 29.7% of the global land area.

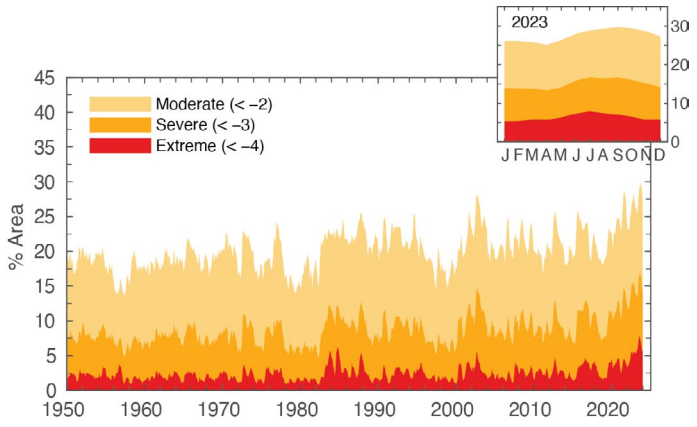

Fig. 2.43. Percentage of global land area (excluding ice sheets and deserts) with self-calibrating Palmer Drought Severity Index (scPDSI) indicating moderate (≤–2), severe (≤–3), and extreme (≤–4) drought for each month during the period 1950–2023. Inset: each month of 2023.

The global pattern of regional droughts seen in 2022 largely persisted through 2023, with the most extensive severe-to-extreme

drought conditions occurring over South America, parts of North America, the Mediterranean, and the midlatitudes of Asia (Plate 2.1s). Drought severity eased through western North America and parts of northern and eastern Europe but worsened in tropical South America and the midlatitudes of Asia (Fig. 2.44). In western North America, California experienced a shift from dry to wet conditions, but the overall west–east moisture contrast observed across the United States since 2017 continued as Arizona and New Mexico were under moderate drought (Plate 2.1s). Moderate drought conditions also affected Mexico and Central America. In South America, El Niño conditions during the latter half of 2023 led to extremely wet conditions in coastal areas of Peru and extreme drought through the Amazon basin to the La Plata basin and central Chile. By the end of October, the Rio Negro at Manaus, a major tributary of the Amazon River (Barichivich et al. 2018), fell to its lowest water level since records began in 1902. The megadrought of central Chile reached its 14th consecutive year in 2023, but an increase in winter rainfall broke the drought in the south-central part of the country (section 2d5).

Although precipitation was above normal in parts of northern, central, and eastern Europe in 2023 (section 2b5), most of the southern part of the continent, particularly countries around the Mediterranean, continued under severe-to-extreme drought (Plate 2.1s). In northern Africa, previous extreme drought conditions along the Mediterranean coast from Morocco to Tunisia continued through 2023 (Plate 2.1s). Most of the Middle East from eastern Türkiye to Pakistan also saw a continuation of severe-to-extreme drought conditions.

Although uncertain due to sparse in situ data, moisture patterns in Africa did not change much in 2023 (Plate 2.1s). Tropical Africa saw a continuation of moderate wet conditions that were observed since 2019. Southern Africa saw a continuation of drought conditions that began in 2018, and its severity remained mostly as moderate. In Australia, drought eased in many northern regions, was sustained in the southwest, and worsened in the easternmost parts during 2023; some parts of the country continued under moderate drought (Plate 2.1s). Wet conditions seen through most of India and southeast Asia in 2022 continued during 2023. In contrast, severe-to-extreme drought conditions extended farther through China, Mongolia, and Kazakhstan. Previous severe-to-extreme drought continued through part of northeastern Siberia (Plate 2.1s).

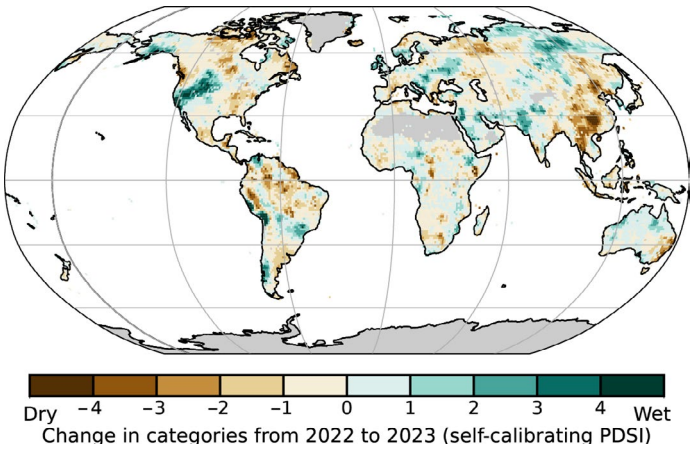

Fig. 2.44. Change in drought categories from 2022 to 2023 (mean self-calibrating Palmer Drought Severity Index [scPDSI] for 2023 minus mean scPDSI for 2022). Increases in drought severity are indicated by negative values (brown) and decreases by positive values (green). No calculation is made where a drought index is meaningless (gray areas: ice sheets or deserts with approximately zero mean precipitation).

Hydrological drought results from a period of abnormally low precipitation, sometimes exacerbated by a concurrent increase in evapotranspiration (ET). Its occurrence can be apparent in reduced river discharge, soil moisture, and/or groundwater storage, depending on the season and duration of the event. Here, the scPDSI is calculated, using gridded global precipitation and Penman-Monteith Potential ET from an early update of the CRU TS 4.08 dataset (Harris et al. 2020). A simple water balance at the core of the scPDSI estimates actual evapotranspiration, soil moisture content, and runoff based on the input precipitation and potential loss of moisture to the atmosphere. Estimated soil moisture categories are calibrated over the complete 1901–2023 period to ensure that "extreme" droughts and pluvials (wet periods) relate to events that do not occur more frequently than in approximately 2% of the months. This calibration affects direct comparison with other hydrological cycle variables in Plate 2.1s that use a different baseline period.

12. LAND EVAPORATION

—D. G. Miralles, O. M. Baez-Villanueva, A. Koppa, O. Bonte, E. Tronquo, F. Zhong, and H. E. Beck

Understanding the spatial and temporal dynamics of evaporation is crucial for agriculture and water management, as well as for diagnosing the influence of short-term climate variability and long-term climate trends on water resources. The year 2023 saw a mix of positive and negative evaporation anomalies across different regions, reflecting a complex interplay of meteorological variables and land surface processes (Plate 2.1t). Notably, semiarid regions of Australia, South America, and North America experienced negative anomalies, particularly towards the end of the year, consistent with the reversal of La Niña to El Niño conditions (Martens et al. 2018; Miralles et al. 2014). Meanwhile, positive anomalies were prevalent over the U.S. East Coast, most of Europe, boreal latitudes, tropical forests, and large parts of India and China. These anomalies mostly reflected regional climatic conditions, with high temperatures driving increased evaporation rates over the U.S. East Coast and Europe (section 2b1), while in tropical forests, positive anomalies were mostly attributed to enhanced precipitation (section 2d4), which increased interception loss, a primary component of evaporation in forested regions. Similarly, in northern India, positive anomalies correlated with higher-than-usual precipitation volumes. The high regional heterogeneity underscores the need for continued monitoring of evaporation for agriculture and water management applications. For example, in semiarid regions experiencing negative anomalies, such as parts of Australia and the Americas, decreased evaporation reflects reduced water availability (section 2d9), with potential implications for crop yields and freshwater security. Conversely, in regions with positive anomalies, like central Europe and parts of Asia, higher-than-usual evaporation rates may contribute to decreased water resources in following dry seasons.

Despite El Niño conditions usually being associated with lower-than-usual global mean evaporation due to the occurrence of persistent droughts in several global regions (Miralles et al. 2014), the average evaporation values in 2023 reached unprecedented high levels due to the high air temperatures (section 2b1), marking the highest on record for the Northern Hemisphere and the globe as a whole (Fig. 2.45). The global mean evaporation in 2023 was above the linear trend of +0.5 mm yr^{-1}, which can be attributed to positive anomalies in both hemispheres. The positive multidecadal trend has been attributed to the ongoing rise in global temperatures (Brutsaert 2017) and terrestrial greening (Yang et al. 2023; see also section 2h2). Arguably due to the positive temperature anomalies in 2023 in the Northern Hemisphere and tropics, particularly towards the end of the year (section 2b1), evaporation was consistently higher than usual in those latitudes (Fig. 2.46). Meanwhile, in the Southern Hemisphere, drought conditions led to negative anomalies in semiarid regions at latitudes between 25°S to 40°S during the second half of the year (Fig. 2.46).

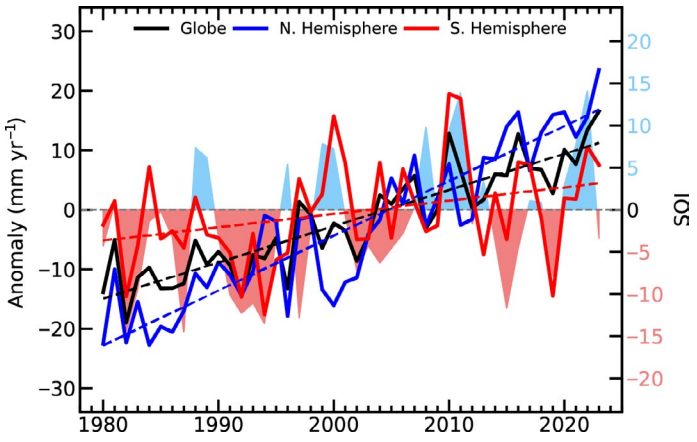

Fig. 2.45. Land evaporation anomaly (mm yr^{-1}; 1991–2020 base period) for the Northern Hemisphere, Southern Hemisphere, and the entire globe (blue, red, and black solid lines, respectively). Linear trends in evaporation (dashed lines) and the Southern Oscillation Index (SOI) from the Climatic Research Unit (right axis, shaded area) are also shown. (Source: Global Land Evaporation Amsterdam Model [GLEAM].)

In recent years, land evaporation has been gaining recognition as an essential climate variable by the World Meteorological Organization, and today multiple satellite-based approaches are advancing global evaporation monitoring. The results shown here correspond to the latest version of GLEAM, a set of algorithms dedicated to estimating evaporation based on satellite and reanalysis data (Miralles et al. 2011).

Despite improvements in global evaporation monitoring in recent years, challenges persist, particularly those related to the accurate depiction of ecosystem responses to drought stress and the representation of interception loss in forests (Fisher et al. 2017; McCabe et al. 2019). Efforts to further advance land evaporation monitoring are ongoing, with future advancements expected to leverage emerging technologies from thermal missions like ECOSTRESS (Fisher et al. 2020) and TRISHNA (Lagouarde et al. 2018), as well as hyper-resolution optical remote sensing facilitated by cubesat constellations (McCabe et al. 2017). These innovations hold promise for enhancing our understanding of evaporation dynamics and their implications for water resources, climate, and ecosystems.

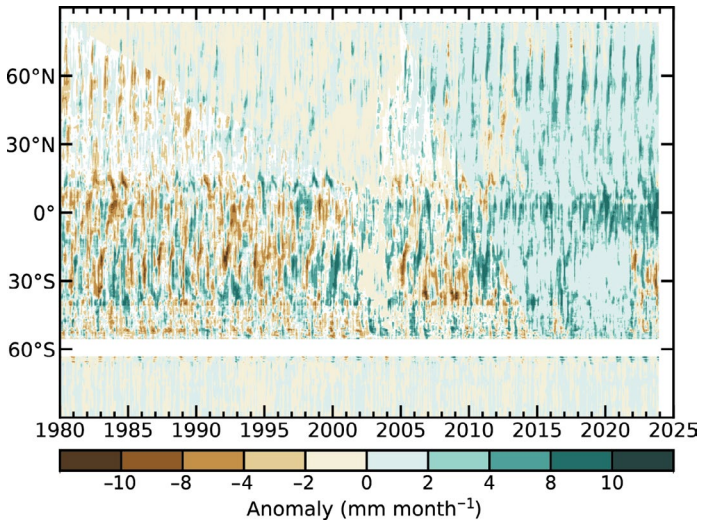

Fig. 2.46. Zonal-mean terrestrial evaporation anomalies (mm month^{-1}; 1991–2020 base period). (Source: Global Land Evaporation Amsterdam Model [GLEAM].)

e. Atmospheric circulation

1. MEAN SEA LEVEL PRESSURE AND RELATED MODES OF VARIABILITY

—B. Noll, D. Fereday, and D. Campos

Mean sea-level pressure (MSLP) variability is characterized by large-scale modes that drive weather and climate anomalies and extremes. These modes include the Arctic Oscillation, the North Atlantic Oscillation (NAO), and the Pacific/North American (PNA) in the Northern Hemisphere (NH) as well as the Southern Annular Mode (SAM)/Antarctic Oscillation in the Southern Hemisphere (SH; Kaplan 2011). Because of its direct impact in the tropics and important extratropical teleconnections to both hemispheres (Capotondi et al. 2015), the El Niño–Southern Oscillation (ENSO) is one of the most significant and well-tracked global climate drivers. ENSO can be described by the Southern Oscillation Index (SOI), the normalized MSLP difference between Tahiti and Darwin (Allan et al. 1996; Kaplan 2011).

The SOI was variable in early 2023, coinciding with a decaying La Niña, before turning consistently negative from July onward as El Niño became established (see section 4b). Early in the year, La Niña contributed to destructive floods and ex-tropical cyclones in New Zealand (see sections 4g8, 7h5), while the emerging El Niño contributed to seven consecutive months of record-breaking global warmth from June to December (section 2b1; C3S 2024), elevated wildfire activity in Canada (see section 7b1, Sidebar 7.1), and caused record-low annual maximum and minimum sea-ice extents in Antarctica (see section 6d). From June to August, the development of anomalous low pressure in the subtropical South Pacific, closely related to the strengthening El Niño, allowed an enhanced atmospheric river season across southern South America (e.g., Campos and Rondanelli 2023) and led to flooding in central Chile (DMC 2023a).

The Indian Ocean dipole (IOD) is an important mode of climatic variability in the Eastern Hemisphere (Saji et al. 1999). The positive IOD phase, which developed in September 2023 (see section 4f), comprises warm ocean temperatures in the tropical western Indian Ocean and cool ocean temperatures in the east. The IOD is often driven by ENSO via the Walker Circulation (Behera et al. 2006). The concurrent strongly positive IOD and El Niño contributed to Australia's driest three-month period of record from August to October 2023 (see section 7h4). It also strengthened the descending branch of the Walker Circulation over Indonesia and western Australia, which likely delayed the northern Australian monsoon (BoM 2024b; Lisonbee and Ribbe 2021).

In the NH, the NAO index was positive in January and February, consistent with mild winter conditions in Europe. Summer saw low pressure over the eastern United States, contributing to increased rainfall there (see section 7b2). A pressure dipole was seen over northwestern Europe, strongly projecting onto the summer NAO pattern (Fig 2.47c). This pattern is defined as the leading empirical orthogonal function (EOF) mode of variability in the North Atlantic/European region in July/August (Folland et al. 2009). The 2023 summer NAO index was the lowest in the time series back to 1959, in contrast to the second-highest value seen in 2022 (Fig 2.47e). Low pressure persisted across the North Atlantic, Europe, and east into Asia in autumn, and was associated with increased rainfall in these regions (see sections 2d5, 7f, 7g). Consistent with the positive ENSO phase in late 2023, the December PNA and NAO were both positive (Livezey et al. 1997; Ayarzagüena et al. 2018).

The SAM, which explains 22%–34% of the variability in extratropical SH atmospheric circulation (Fogt and Marshall 2020), was positive for 53% of days during 2023, fewer days than each year from 2020 to 2022. Annual MSLP was much above normal in the midlatitude South Pacific east of New Zealand and southwest of Australia, and below normal in the Bellingshausen Sea (Plate 2.1u; Fig. 2.48). Overall, this resembled the negative phase of the Pacific–South American (PSA) pattern (Irving and Simmonds 2016). The atmospheric circulation anomalies and blocking (e.g., Renwick and Revell 1999) associated with this pattern likely contributed to wetter conditions in northern New Zealand and the country's second-warmest year on record (see section 7h5) as well as to wetter conditions in late winter and spring over south-central Chile (see section 7d3). They also likely contributed to drier conditions in western and southern Western Australia (see section 7h4), as well as extremely low Antarctic sea-ice extent for most of the year (see

section 6d), which was linked to strengthened westerly winds around the continent. This pattern was also associated with a stronger-than-normal subtropical jet stream extending from eastern Australia to Chile and Argentina (e.g., Montecinos et al. 2011). The negative phase of the PSA showed a statistically significant increasing trend on an annual basis from 1979 to 2014 and is consistent with positive trends in the SAM, making it an important SH diagnostic (Irving and Simmonds 2016).

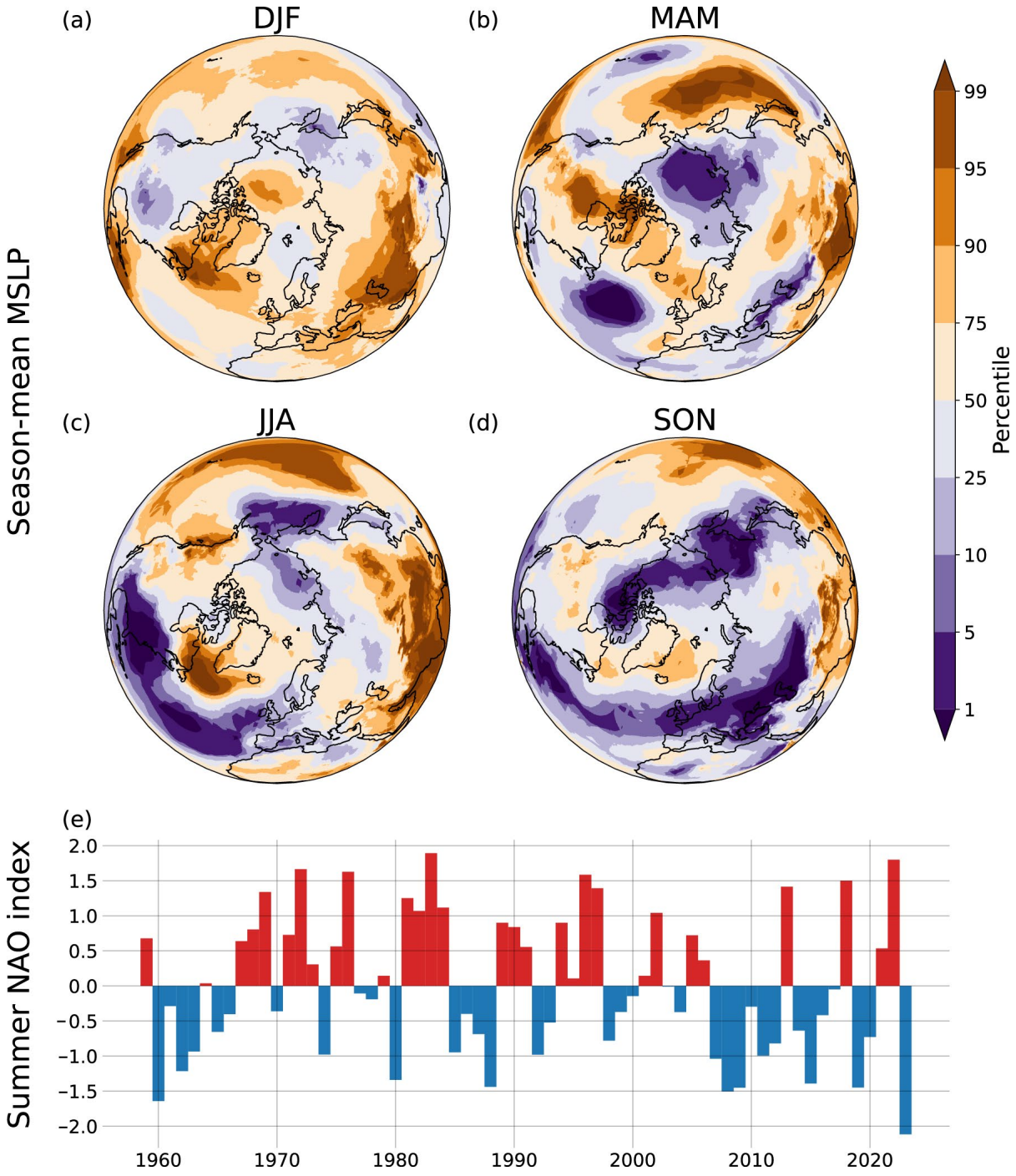

Fig. 2.47. Northern Hemisphere circulation in 2023. (a)–(d) seasonal mean sea level pressure (MSLP) anomalies with respect to the 1991–2020 base period, shown as percentiles based on the 1959–2023 period. (e) Jul/Aug summer North Atlantic Oscillation (NAO) index for the period 1959–2023 (Source: ERA5 [Hersbach et al. 2020].)

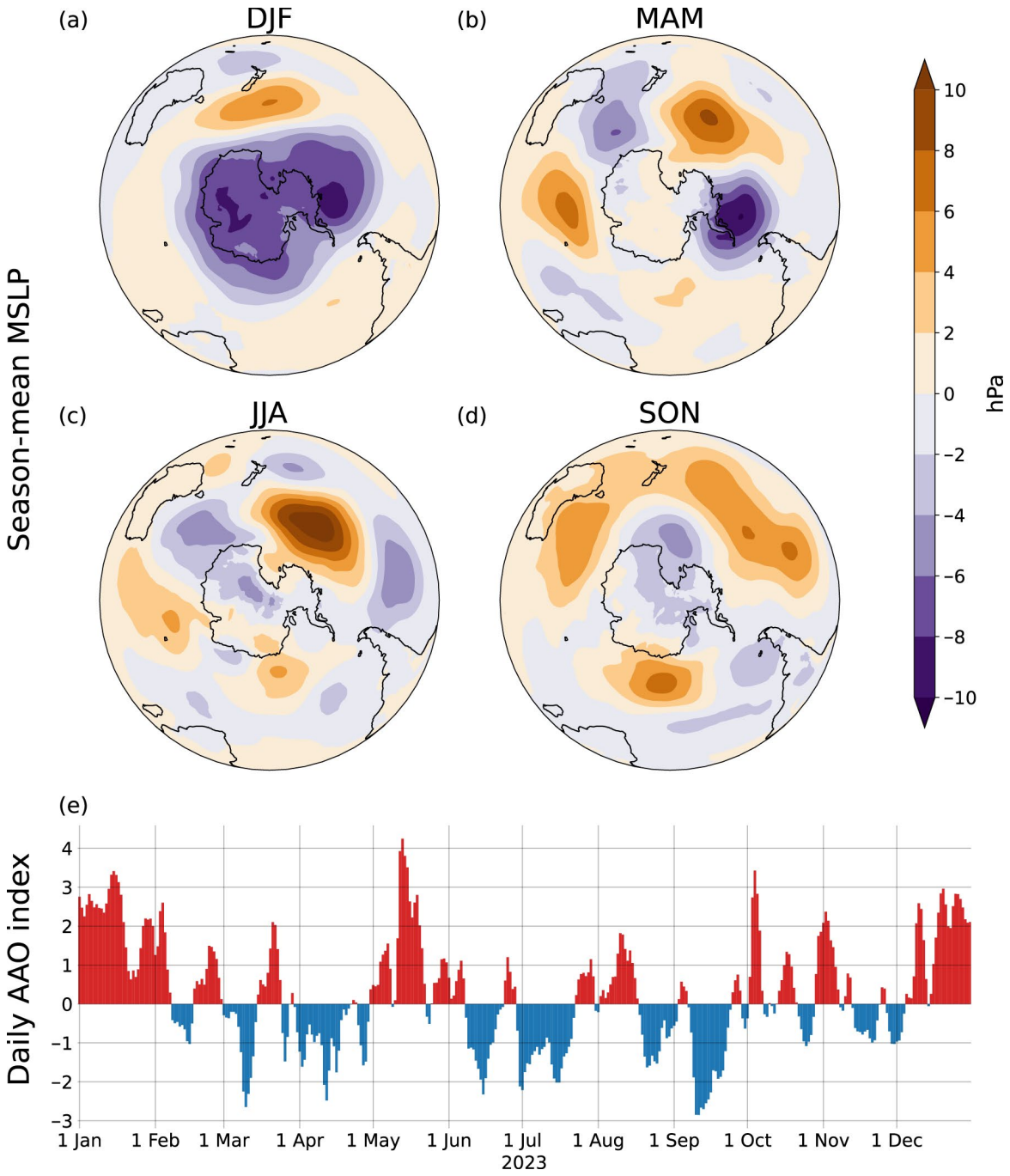

Fig. 2.48. Southern Hemisphere circulation in 2023. Seasonal mean sea-level pressure (MSLP) anomalies (hPa; 1991–2020 base period) for (a) DJF 2022/23, (b) MAM 2023, (c) JJA 2023, and (d) SON 2023. (Source: ERA5 reanalysis.) (e) Daily Antarctic Oscillation (AAO) index time series (Source: NOAA Climate Prediction Center.)

2. LAND AND OCEAN SURFACE WINDS

—C. Azorin-Molina, R. J. H. Dunn, L. Ricciardulli, C. A. Mears, J. P. Nicolas, T. R. McVicar, Z. Zeng, and M. G. Bosilovich

Annual mean wind speed at ~10 m above the ground was anomalously low over Northern Hemisphere lands in 2023 (−0.035 m s^{-1}) with respect to the 1991–2020 climatology (Table 2.8). This negative anomaly was primarily driven by the decline in winds observed in North America (−0.168 m s^{-1}) and, secondarily, in Europe (−0.011 m s^{-1}). This contrasts with the interhemispheric asymmetry of positive anomalies in South America (+0.145 m s^{-1}) and Central (+0.076 m s^{-1}) and East (+0.032 m s^{-1}) Asia (Plate 2.1v). After decades of "stilling" (McVicar et al. 2012), a weak "reversal" of winds occurred around the 2010s (Zeng et al. 2019) with almost neutral anomalies

dominating the last decade (Fig. 2.49a). Moreover, the observed changes are dominated by a declining frequency of winds at >3 m s^{-1} (Fig. 2.49c) and particularly at >10 m s^{-1} (Fig. 2.49d), which in 2023 reached the third lowest frequency value during the 1973–2023 record.

The assessment of terrestrial surface wind speed anomalies, trends, and multidecadal variability is based on: 1) the HadISD3 observational dataset (1973–2023; Dunn et al. 2012, 2016, 2019) with stations selected for completeness; 2) the ERA5 reanalysis (1979–2023; Hersbach et al. 2020; Bell et al. 2021); and 3) the MERRA-2 reanalysis (1980–2023; Gelaro et al. 2017). Reanalyses underestimated anomalies and failed in reproducing the decadal variability of both the observed "stilling" and "reversal"; however, their agreement with station observations improved since the mid-1990s (Fig. 2.49b; e.g. Torralba et al. 2017; Wohland et al. 2019).

The average land wind speed has declined across the Northern Hemisphere over the last 45 years (–0.053 m s^{-1} $decade^{-1}$ for the period 1979–2023), with a noticeable interhemispheric asymmetry of surface winds changes (Zha et al. 2021). Table 2.8 reports this opposite sign in trends between the northern continents, where the strongest negative trend is recorded in North America (–0.072 m s^{-1} $decade^{-1}$) and the strongest positive trend in South America (+0.052 m s^{-1} $decade^{-1}$). Due to the cessation of the "stilling" over the last decade, the global negative trend is of lesser magnitude compared to previous reports (Azorin-Molina et al. 2023a). The asymmetric trends between hemispheres are partly captured by the ERA5 reanalysis (Fig. 2.50a; Deng et al. 2021).

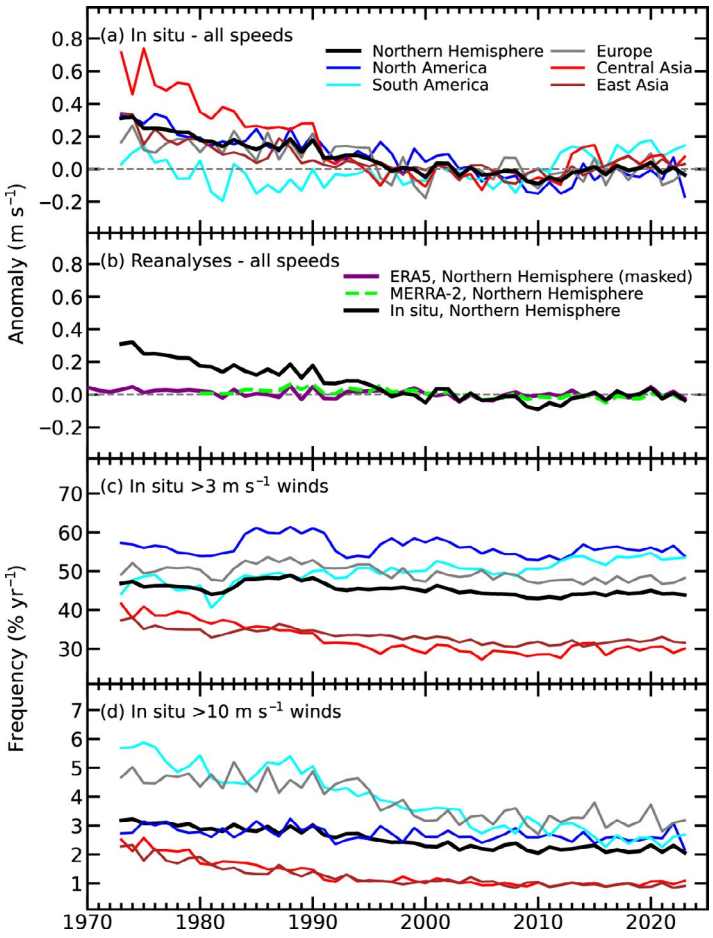

Fig. 2.49. Land surface Northern Hemisphere (20°N–70°N) and regional surface wind speed anomaly time series (m s^{-1}; 1991–2020 reference period): (a) HadISD3 observational dataset (1973–2023), (b) ERA5 (1970–2023 masked to only those grid boxes which contain one of the HadISD stations used in this section), and MERRA-2 (1980–2023 complete land surface) reanalyses. (c),(d) The HadISD3 occurrence frequencies (% yr^{-1}) for wind speeds (c) >3 m s^{-1} and (d) >10 m s^{-1}.

Table 2.8. Northern Hemisphere (20°N–70°N) and regional statistics for land surface wind speed (m s^{-1}) using the observational HadISD3 dataset for 1979–2023.

Region	Mean Wind Speed 1991–2020 (m s^{-1})	Wind Speed Anomaly 2023 (m s^{-1})	Wind Speed Trend 1979–2023 (m s^{-1} $decade^{-1}$), and 5th to 95th percentile confidence range	Number of stations
Northern Hemisphere	3.302	–0.035	–0.053 (–0.067 → –0.040)	2874
North America	3.642	–0.168	–0.072 (–0.086 → –0.053)	841
Europe	3.644	–0.011	–0.049 (–0.069 → –0.033)	931
Central Asia	2.738	+0.076	–0.069 (–0.105 → –0.041)	304
East Asia	2.711	+0.032	–0.027 (–0.042 → –0.013)	540
South America	3.452	+0.145	+0.052 (+0.036 → +0.071)	101

Changes in ocean surface winds for the period 1988–2023 were assessed using two products: 1) ERA5 and 2) satellite-based products as the merged radiometer winds (including Special Sensor Microwave/Imager [SSM/I], the Special Sensor Microwave Imager/Sounder [SSMIS], the Advanced Microwave Scanning Radiometer for the Earth Observation Satellite [AMSRE] and Advanced Microwave Scanning Radiometer 2 [AMSR2], Tropical Rainfall Measuring Mission's [TRMM] Microwave Imager [TMI], and WindSat), and the scatterometers Quick Scatterometer (QuikSCAT) and Advanced Scatterometer (ASCAT; Wentz 1997; Wentz et al. 2007, 2015; Ricciardulli and Wentz 2015; Ricciardulli and Manaster 2021), all processed at Remote Sensing Systems (RSS). Ocean wind speed anomalies were slightly negative in 2023: satellite radiometers (RSS, −0.055 m s^{-1}), satellite scatterometers (ASCAT, −0.038 m s^{-1}), and reanalyses (ERA5, −0.050 m s^{-1}, MERRA-2, −0.132 m s^{-1}; Fig. 2.51). Spatially (Plate 2.1v), there was a localized weak positive anomaly in the southern equatorial eastern Pacific, and a large negative anomaly in the tropical Atlantic, almost unprecedented over the past 30 years (2010 being the closest). The strong positive anomaly pattern seen in 2022 in the western and central equatorial Pacific Ocean (Azorin-Molina et al. 2023a) reversed to a weak negative pattern in 2023 (due to El Niño, albeit much weaker than in 1997 and 2015). Much smaller positive anomalies, or even negative ones, were observed in the Southern Ocean. Over the Indian Ocean, negative anomalies dominated except in a strip west of Sumatra. Due to the weak ocean surface winds in 2023, long-term trends (1988–2023) are of lesser magnitude with respect to previous reports (RSS Radiometers: <+0.1 m s^{-1} $decade^{-1}$; ERA5: +0.03 m s^{-1} $decade^{-1}$ over 60°S–60°N) but have similar spatial patterns (Fig. 2.50a). Positive trends dominate over the south Pacific trade winds, the Southern Ocean, the Bering Sea, and near coastlines, while negative trends persist across midlatitude ocean areas and the whole Indian Ocean.

Widespread warm sea-surface temperatures (coincident with El Niño, sections 2b1, 2b3, 3b) might have weakened pressure gradients and driven negative wind speed anomalies in 2023. Changes in both land and

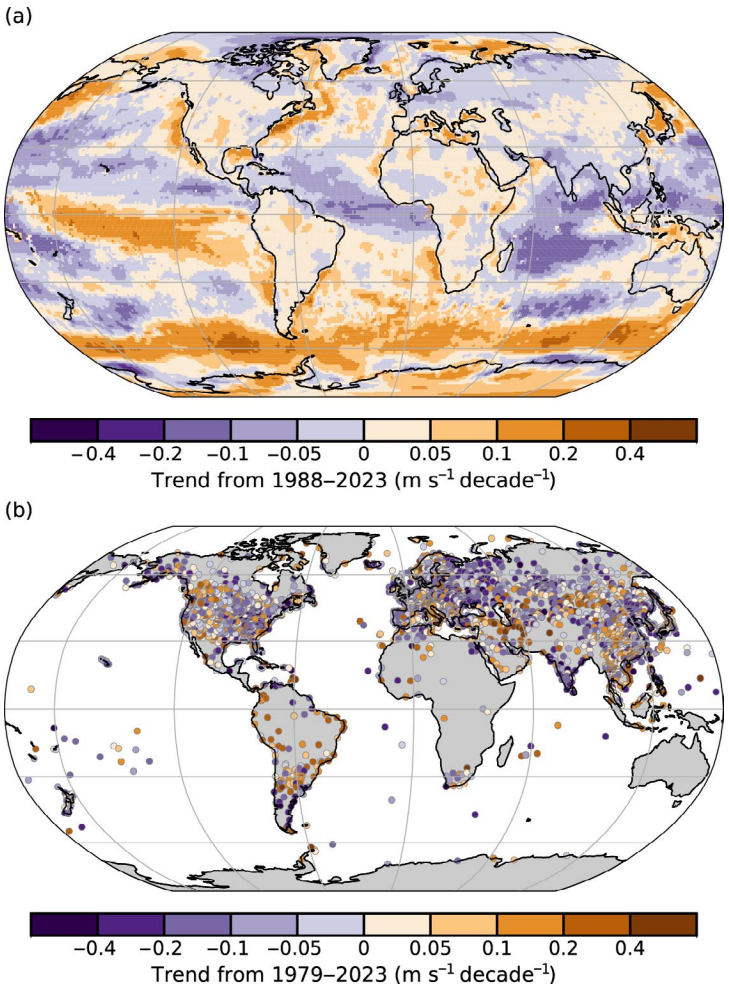

Fig. 2.50. Wind speed trends (m s^{-1} $decade^{-1}$) from the (a) ERA5 reanalysis output over land/ice and Remote Sensing Systems (RSS) satellite radiometers (Special Sensor Microwave/Imager [SSM/I], Special Sensor Microwave Imager / Sounder [SSMIS], Tropical Rainfall Measuring Mission's Microwave Imager [TMI], Advanced Microwave Scanning Radiometer 2 [AMSR2], Advanced Microwave Scanning Radiometer for the Earth Observing System [ASMR-E], and WindSat) over ocean for the period 1988–2023 (shaded areas) and (b) observational HadISD3 dataset over land (circles) for the period 1979–2023.

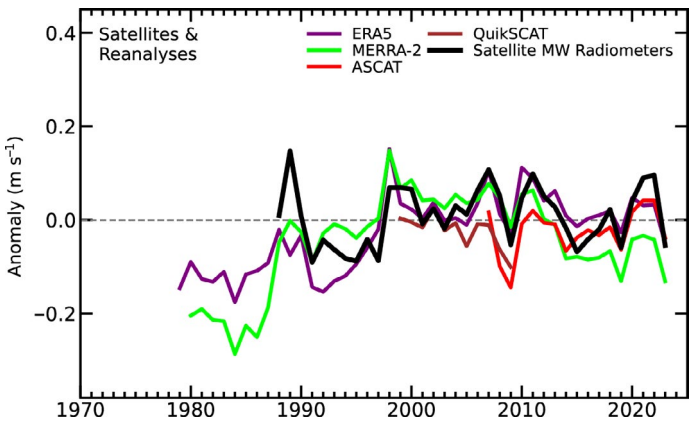

Fig. 2.51. Annual global mean wind speed anomalies (m s^{-1}; 1991–2020 baseline) over the ocean from satellite radiometers and scatterometers, ERA5, and MERRA-2 reanalyses.

ocean winds have been mainly attributed to decadal ocean–atmosphere oscillations characterized as the decadal variations of climate indices such as the tropical North Atlantic, North Atlantic Oscillation, and Pacific Decadal Oscillation (Zeng et al. 2019); however, changes in the pressure gradient (Zhang et al. 2021) forced by the anthropogenic warming partly explain the interhemispheric asymmetry with negative (positive) trends in the Northern (Southern) Hemisphere (Zha et al. 2021). Secondary drivers are linked to anemometer biases (Azorin-Molina et al. 2023b; Liu et al. 2024), encoding data issues (Dunn et al. 2022), and land cover changes (Minola et al. 2022).

3. UPPER AIR WINDS

—L. Haimberger, M. Mayer, P. Rohini, C. T. Sabeerali, V. Schenzinger, and O. P. Sreejith

Anomalies such as the El Niño–Southern Oscillation have profound impacts on upper-level circulation. Climate projections predict changes of upper-level wind patterns, such as the Hadley cell or jet stream intensity. Therefore, it is important to monitor the observed upper air winds. The 2023 global mean wind speed anomaly at 850 hPa (Fig. 2.52a) became negative (−0.1 m s^{-1}) in the second half of the year in a manner typical of El Niño conditions. Hence, linear trends decreased very slightly (0.02 m s^{-1} $decade^{-1}$ to 0.04 m s^{-1} $decade^{-1}$ for the period 1991–2023).

The Southern Annular Mode (SAM) Index (Marshal 2003) stayed high in 2023 (0.77) whereas the closely related Antarctic Oscillation index returned toward normal albeit still-positive values (0.24). This is consistent with the zonal 850-hPa wind speed anomalies between 70°S and 50°S (Fig. 2.52b), which were more than +1 m s^{-1} in the first and last months of the year (consistent with mostly positive values in this belt in Plate 2.1w), but were near zero or even slightly negative during austral winter. The positive wind speed trend in this latitude belt remained highly significant for the period 1991–2023, between 0.2 m s^{-1} $decade^{-1}$ and 0.26 m s^{-1} $decade^{-1}$, consistent with section 2e1.

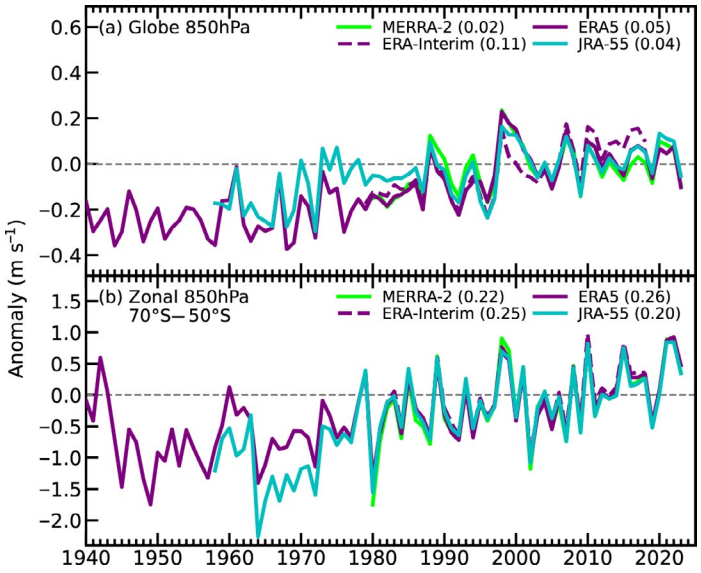

Fig. 2.52. Annual anomalies of (a) global mean, (b) 70°S–50°S belt mean wind speed (m s^{-1}; 1991–2020 base period) at 850 hPa from four reanalyses (ERA5 [Hersbach et al. 2020], ERA-Interim [Dee et al. 2011], MERRA-2 [Gelaro et al. 2017], and JRA-55 [Kobayashi et al. 2015]). The numbers in parentheses are linear trends in m s^{-1} $decade^{-1}$ for the period 1991–2023. The ERA-Interim time series ends in 2019.

The pattern of strong easterlies (negative anomalies in a region with negative wind climatology) wind at 850 hPa over September–December in 2023 (Plate 2.1w; fourth strongest in 50 years over the area 60°E–90°E, 10°S–10°N, stronger only in 2019, 2010, 1997) over the equatorial Indian Ocean is related to both strongly positive Indian Ocean dipole (IOD) (see section 4f) and El Niño (see section 4b) indices during that time. Due to El Niño, the easterlies were weaker (positive anomalies) in the tropical central and east Pacific. There was a relatively prominent westerly wind anomaly (positive anomaly) over western and central Europe during the whole year, but it was strongest in the summer and autumn months, which likely contributed to above-average precipitation over west-central Europe at the same time.

We investigate the impact of major tropical climate anomalies on the upper-air divergent circulation by assessing the anomalous 200-hPa velocity potential in October–December (OND) 2023 (Fig. 2.53a). A strong positive anomaly was present over the Indo-Pacific warm pool, indicative of upper-air convergence and sinking motion associated with the strongly positive IOD and Oceanic Niño Index (ONI). Combined with ascending motion over the tropical west Indian Ocean and connected by strong anomalous easterly (negative) flows over the central Indian Ocean (Plate 2.1w), this anomaly resulted in strong zonal-vertical circulation.

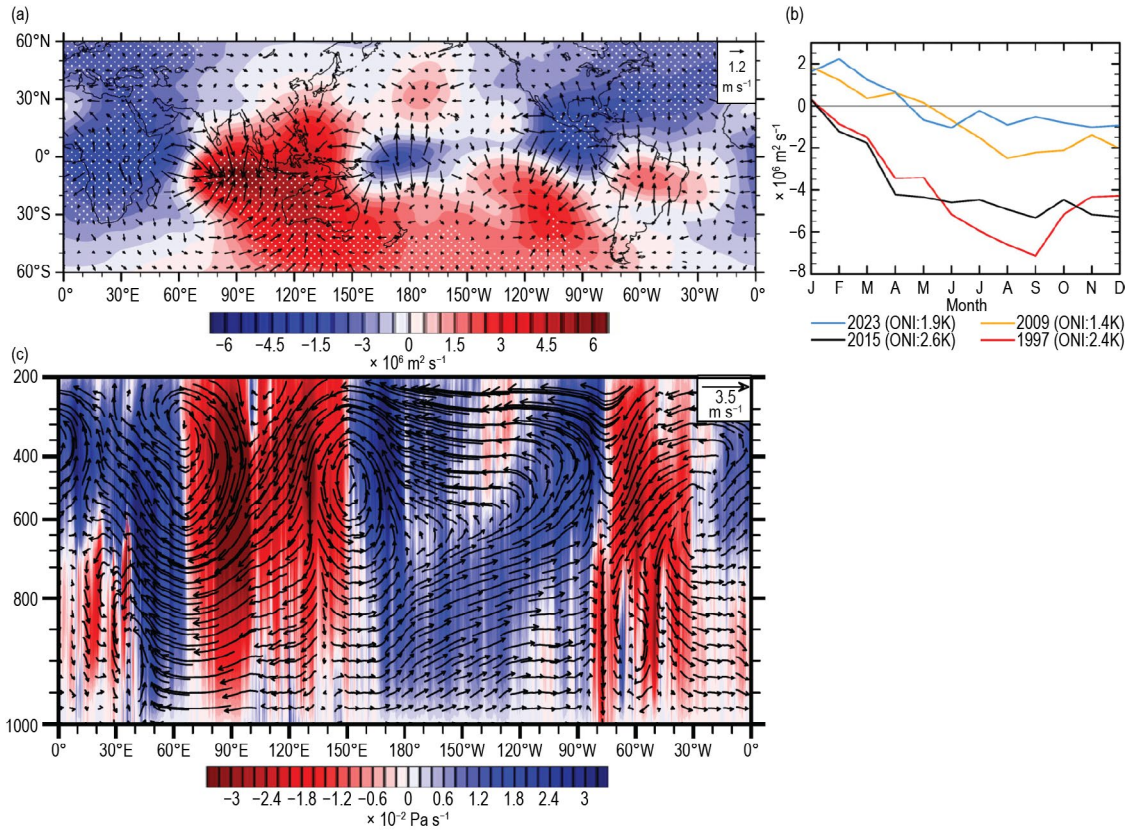

Fig. 2.53. (a) 200-hPa (colors) velocity potential (× 10^6 m^2 s^{-1}) and (arrows) divergent wind anomalies (m s^{-1}; 1991–2020 base period) for OND 2023; stippling indicates regions with anomalies exceeding 1.65 std. dev. of the seasonal anomalies; (b) evolution of anomalous velocity potential (× 10^6 m^2 s^{-1}) in the equatorial central Pacific (5°S–5°N, 170°E –130°W) for the four strongest El Niño years since 1991. The Nov Oceanic Niño Index (ONI) for the four years is provided in the legend. (Source: ERA5.) (c) Anomalies of pressure vertical velocity (shaded; units: × 10^{-2} Pa s^{-1}) and u/w anomalies (arrows) averaged over the region 10°S–10°N (zonal wind anomaly [u] unit: m s^{-1}, pressure vertical velocity anomaly [w] unit: × 10^{-2} Pa s^{-1}).

The IOD is also associated with the negative velocity potential anomaly over the western Indian Ocean and central Africa, and the ONI is associated with a negative anomaly over the central equatorial Pacific (both related to enhanced convection in their respective regions). Although the 2023 El Niño event was one of the strongest of the past decades, the velocity potential anomaly in the central Pacific was rather weak. The region was chosen based on the location of the typically strongest precipitation response to El Niño (see, e.g., Fig. 3b in Mayer et al. 2013). The relatively weak upper-air wind response to the 2023 El Niño conditions (also noted in section 2e2) is consistent with the surprisingly weak coupling of Pacific equatorial surface winds to central-to-eastern Pacific warm sea-surface temperature (SST) anomalies during the development phase of the event. Thus, the weakening of the Pacific Walker cell was modest during 2023 despite the strong warm Pacific SST anomalies.

There was a strong negative velocity potential anomaly over the far eastern tropical Pacific and Central America, which is consistent with the highly active eastern North Pacific hurricane season (see section 4g3). Together with high oceanic heat content, it likely contributed to the explosive development of Hurricane Otis that made landfall near Acapulco on 25 October (see section 4g3 and Sidebar 4.1 for details).

Figure 2.53c depicts anomalies in pressure vertical velocity and zonal/vertical velocities averaged over the region spanning from 10°S to 10°N in OND 2023. Consistent with Fig. 2.53a, positive anomalies in pressure vertical velocity were observed over the tropical central/east Pacific, indicating ascending motion associated with El Niño. Particularly noteworthy is the stronger ascending motion observed during OND compared to the June–August season, suggesting the intensification of El Niño as the season progressed.

In 2023, the quasi-biennial oscillation (QBO) of stratospheric zonal-mean zonal winds completed its regular westerly phase after 12.7 months. It reached its maximum value of 16.1 m s^{-1} at the 40-hPa level in April. The newly formed easterly descended from the 10-hPa pressure level to

60-hPa at a rate of 1.1±0.5 km month^{-1}, which is quite fast. Descent tends to stall between 40 hPa and 50 hPa in many years, but this did not happen in 2023. A new westerly had already formed at the 10-hPa level in late November, starting a new QBO cycle for 2024.

4. THUNDER HOURS

—M. Füllekrug, E. Williams, C. Price, S. Goodman, R. Holzworth, J. Lapierre, E. DiGangi, R. Said, M. McCarthy, K. Virts, A. M. Grimm, and Y. Liu

The lifetime of an ordinary thunderstorm is about one hour, and thunder can be heard over a ~15 km radius. Based on this, the definition of a thunder hour is that at least two lightning flashes occurred within one hour and 15 km from a given location. The mapping of thunder hours enables the characterization of thunderstorm frequencies around the world (DiGangi et al. 2021) that are indicative of high-impact weather including high wind speeds, intense rainfall, large hail, and lightning hazards. (Füllekrug et al. 2022 and references therein). Thunder hours can be derived from optical, radio, and sonic remote sensing and result in maps that offer a statistically robust measure of the frequency of deep convection—on time scales ranging from hours to decades—that is suitable for climate studies.

This contribution describes the first global climatic thunder hour anomaly map calculated from composite radio remote sensing using three different ground-based global lightning detection networks for comparison with optical remote sensing using the Geostationary Lightning Mapper (GLM) on board the NOAA GOES-16 (Rudlosky and Virts 2021). Vaisala's Global Lightning Detection Network (GLD360; Said et al. 2013), Earth Network's Total Lightning Network (ENTLN; Zhu et al, 2022), and the University of Washington's World-Wide Lightning Location Network (WWLLN; Holzworth et al. 2021) radio-locate lightning flashes around the world. The lightning occurrence times and locations are subsequently used to calculate the total number of thunder hours separately for each network and for each year from 2018 to 2023 with a geographic resolution of 0.05° × 0.05°, which corresponds to a spatial resolution of ~5.56 km × 5.56 km at the equator. Subsequently, the total number of thunder hours in 2023 is averaged across all three networks, revealing up to ~500 thunder hours in the Americas, Central Africa, and the Maritime Continent in Southeast Asia (Fig. 2.54a). The global thunder hour anomaly within the field of view of GLM in 2023 (Fig. 2.55) exhibits remarkable agreement with the anomaly calculated from the ground-based global lightning detection networks (Fig. 2.54b).

Thunder hour anomalies in 2023 were calculated against the preceding five-year average of annual thunder hours (2018–22). The anomaly of up to ~200 additional thunder hours over the eastern tropical Pacific (Fig. 2.54b) is attributed to increased convection associated with above-average SSTs (see sections 2b2, 3b) and El Niño (see sections 2d5, 4b).

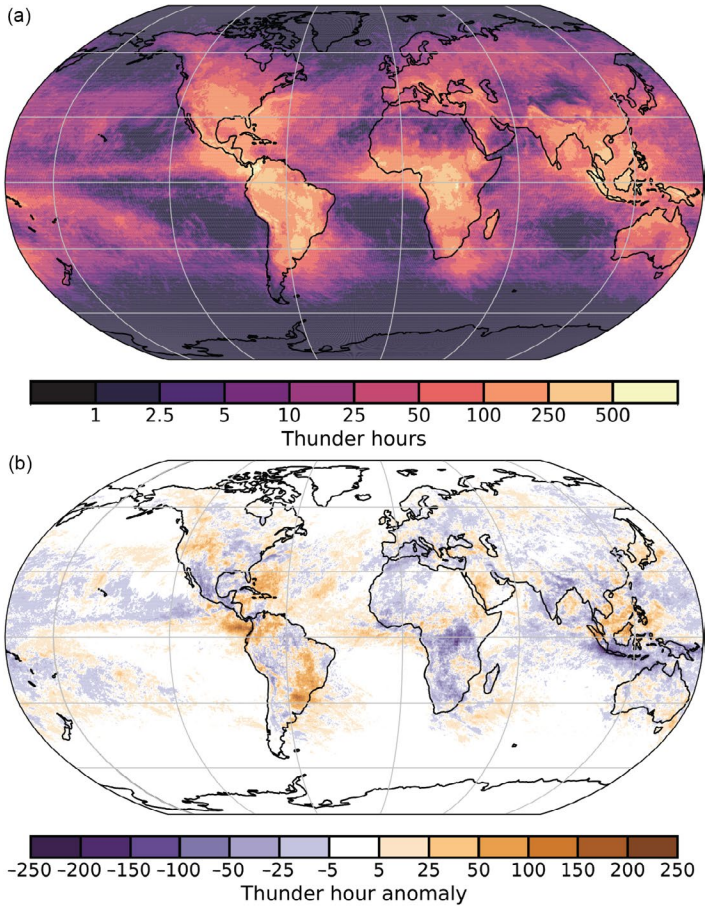

Fig. 2.54. (a) Total number of thunder hours for 2023 averaged from three ground-based global lightning detection networks (Vaisala Global Lightning Detection Network [GLD360], Advanced Environmental Monitoring Earth Networks Total Lightning Network [AEM ENTLN], and the University of Washington's World Wide Lightning Location Network [UW WWLLN]) and (b) thunder hour anomalies for 2023 (base period is 2018–22).

Above-average numbers of thunder hours and precipitation in southeastern South America has been attributed to a teleconnection between weather patterns in northwestern and southeastern South America in austral spring, albeit before the peak of El Niño's SST anomaly (Grimm 2003; Grimm and Natori 2006; Adler et al. 2017). The similarity of this feature with an increased number of days and hours with lightning during the 1997/98 El Niño along the northern Gulf of Mexico basin (Goodman et al. 2000) suggests a common physical mechanism. However, negative thunder hour anomalies prevailed along the northern Gulf of Mexico in 2023, possibly because the impact of El Niño on the location of the subtropical jet stream over North America is largest in Northern Hemisphere winter (Manney et al. 2021, Fig. 11 top row).

A third area of above-average numbers of thunder hours in 2023 is evident in the northern part of the Maritime Continent, where previous studies have shown maximum lightning responsiveness to "Super El Niño" events (Hansen et al. 2006; Williams et al. 2021), which are declared when the SST anomaly exceeds 2°C. The negative anomaly in the southern portion of the Maritime Continent is potentially attributed to a cold anomaly in SSTs (sections 2b3, 3b). A more detailed characterization of thunder hour anomalies over land and ocean is the subject of ongoing research.

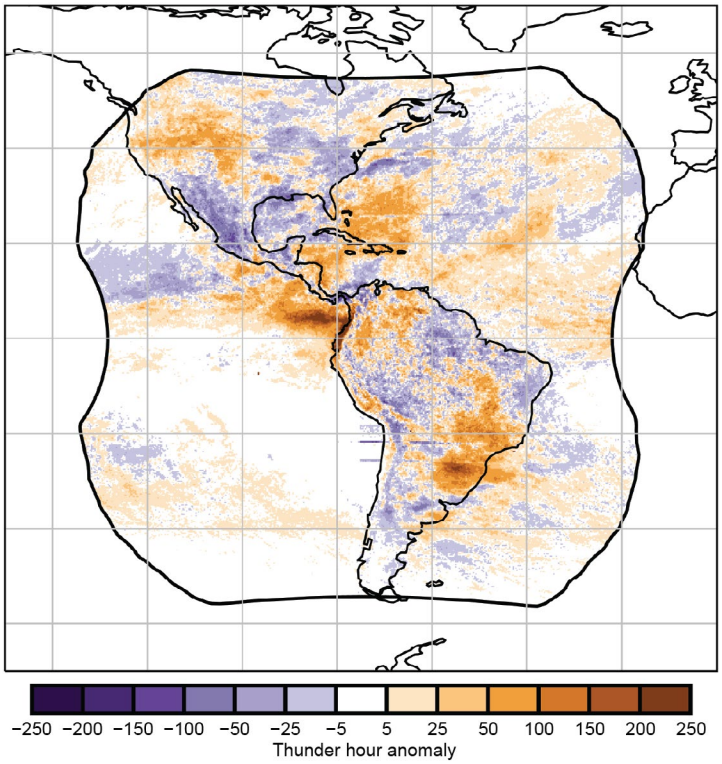

Fig. 2.55. Thunder hour anomaly for 2023 calculated from NOAA's Geostationary Lightning Mapper on GOES-16. This compares well to the 2023 anomalies calculated from ground-based lightning detection networks (Fig 2.54b).

Finally, our analysis shows a positive anomaly in thunder hours in the western United States and Canada during 2023. This was coincident with extreme wildfires in Canada over the summer (sections 2h3; Sidebar 7.1). Thunder hours are indicative of high-impact weather as part of weather and climate disasters documented for the United States (Bartow-Gillies et al. 2023).

f. Earth radiation budget

1. EARTH RADIATION BUDGET AT TOP-OF-ATMOSPHERE

—P. W. Stackhouse Jr., T. Wong, P. Sawaengphokhai, J. Garg, and N. G. Loeb

The Earth radiation budget (ERB) at top-of-atmosphere (TOA) involves the exchange of incoming total solar irradiance (TSI) and outgoing radiation from Earth given by the sum of reflected shortwave (RSW) and outgoing longwave radiation (OLR). This balance is crucial in understanding Earth's climate system and global temperature variations. Over the last 20 years, the observed climate system has been experiencing an increasing net positive imbalance, representing a surplus of energy to the Earth–atmosphere system (Loeb et al. 2022; von Schuckmann et al. 2023). This observed net positive imbalance continued in 2023, albeit with significant changes in all ERB components corresponding to the transition from La Niña to El Niño.

An analysis of CERES (Clouds and the Earth's Radiant Energy System) TOA ERB measurements (Table 2.9) shows that the global annual mean OLR, TSI, and net radiation increased by 0.60 W m^{-2}, 0.10 W m^{-2}, and 0.30 W m^{-2}, respectively, in 2023 relative to 2022 (rounded to the nearest 0.05 W m^{-2}). In contrast, the global annual mean RSW decreased by 0.80 W m^{-2} over the same period. Relative to the 2001–22 climatology, the 2023 global annual mean anomalies for all TOA radiative flux components (Table 2.9) are greater than their corresponding 2-sigma interannual variability; this is the first time this has occurred in the CERES record. These large TOA radiative flux anomalies are indicative of the extremely large climate anomalies that occurred in 2023. The TOA radiative impact of the La Niña to El Niño transition is shown in Fig. 2.56 as regional annual mean difference maps in OLR and RSW between 2023 and 2022.

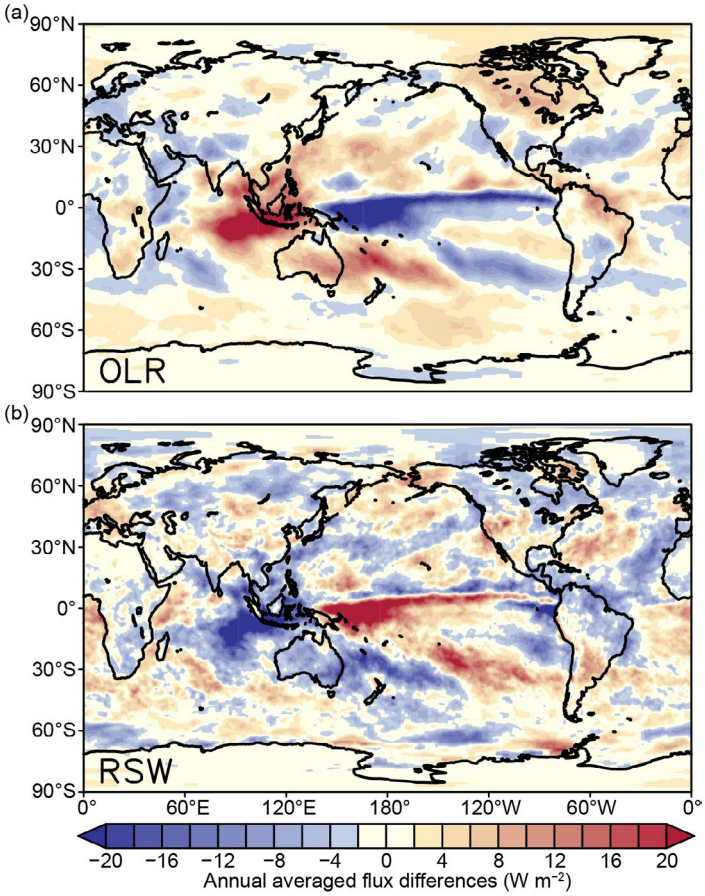

Fig. 2.56. Annual average top-of-atmosphere flux differences (W m^{-2}) between 2023 and 2022 for (a) outgoing longwave radiation (OLR) and (b) reflected shortwave radiation (RSW). The annual mean maps for 2023 were derived after adjusting Dec 2023 FLASHFlux version 4B data using the difference between CERES EBAF Ed4.2 and CERES FLASHFlux version 4B data in 2022.

Table 2.9. Global annual mean top-of-atmosphere (TOA) radiative flux changes between 2022 and 2023, the 2023 global annual mean radiative flux anomalies relative to their corresponding 2001–22 mean climatological values, the mean 2001–22 climatological values, and the 2-sigma interannual variabilities of the 2001–22 global annual mean fluxes (all units in W m^{-2}) for the outgoing longwave radiation (OLR), total solar irradiance (TSI), reflected shortwave (RSW), absorbed solar radiation (ASR, determined from TSI – RSW), and total net fluxes. All flux values have been rounded to the nearest 0.05 W m^{-2} and only balance to that level of significance.

Global	One Year Change (2023 minus 2022) (W m^{-2})	2023 Anomaly (Relative to 2001–22) (W m^{-2})	Climatological Mean (2001–22) (W m^{-2})	Interannual Variability (2001–22) (W m^{-2})
OLR	+0.60	+0.85	240.35	±0.65
TSI	+0.10	+0.25	340.20	±0.15
RSW	–0.80	–1.50	99.00	±1.05
ASR	+0.90	+1.75	241.20	±1.05
Net	+0.30	+0.90	0.85	±0.85

The largest reductions in OLR and increases in RSW, indicative of the increases in deep convection, are observed spanning from the tropical western Pacific (north of Australia) eastward in the equatorial region and southeastward into the South Pacific Ocean. The largest increases in OLR and decreases in RSW are observed over the Indian Ocean and the Maritime Continent, extending northeastward into the subtropical northern Pacific and southeastward over Australia in the subtropical southern Pacific Ocean.

The global monthly mean TOA OLR anomaly showed large variability in 2023 (Fig. 2.57), dropping to a minimum of −0.70 W m^{-2} for May, then peaking in October at +1.90 W m^{-2}. This is the largest range in monthly OLR anomaly for the CERES climatology for a given year. This variability is consistent with NOAA HIRS (Lee and NOAA CDR Program 2018) and NASA AIRS (Susskind et al. 2012) OLR datasets (not shown). The 2023 global annual mean TOA OLR anomaly was +0.85 W m^{-2}. The global monthly mean TOA absorbed solar radiation (ASR, determined from TSI minus RSW) anomaly increased throughout 2023, peaking at +2.35 W m^{-2} in August before slightly decreasing over the last few months. For the year as a whole, the 2023 global annual mean TOA ASR anomaly was +1.75 W m^{-2}. The global monthly mean TOA total net anomaly, which is calculated from ASR anomaly minus OLR anomaly, also stayed positive throughout 2023, peaking at +1.80 W m^{-2} in April, but decreasing strongly to about +0.15 W m^{-2} by October. The global annual mean TOA total net anomaly for 2023 was +0.90 W m^{-2}, representing a continuation of positive net imbalance in 2023 (known as the Earth energy imbalance) that has been observed through the 2020s (Loeb et al. 2021, 2022; von Schuckmann et al. 2023). That positive net imbalance continued to grow in early 2023 but appears to have been interrupted by the onset of the strong El Niño. Further analyses are needed to understand the significances and impacts of these observed global changes.

The TSI data are from a "Community-Consensus TSI Composite" using the methodology defined by Dudok de Wit et al. (2017). The TOA RSW and TOA OLR data come from two different CERES datasets. The data for March 2000–November 2023 are based on the CERES EBAF edition 4.2 product (Loeb et al. 2009, 2012, 2018), which are constructed with measurements from the CERES instruments (Wielicki et al. 1996, 1998) aboard *Terra*, *Aqua*, and NOAA-20 spacecraft. The data for December 2023 comes from the CERES FLASHFlux version 4B product (Kratz et al. 2014), which are created using CERES measurements from *Terra* and NOAA-20 spacecraft. The FLASHFlux to EBAF data normalization procedure (Stackhouse et al. 2016) results in 2-sigma monthly uncertainties of ±0.40 W m^{-2}, ±0.00 W m^{-2}, ±0.30 W m^{-2}, and ±0.45 W m^{-2} for the OLR, TSI, RSW, and total net radiation, respectively (rounded to nearest 0.05 W m^{-2}).

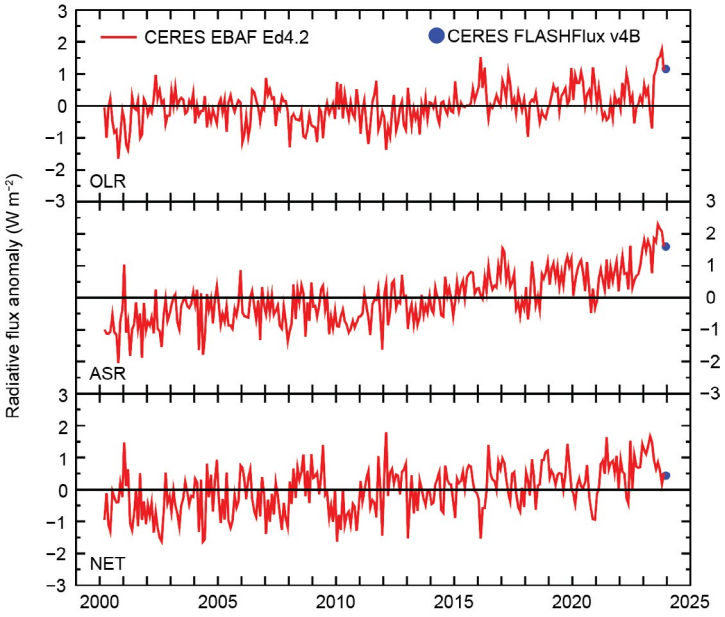

Fig. 2.57. Time series of global monthly mean deseasonalized anomalies (W m^{-2}) of top-of-atmosphere Earth radiation budget for outgoing longwave radiation (OLR; top), absorbed solar radiation (ASR, determined from total solar irradiance [TSI] minus reflected shortwave [RSW]; middle), and total net (TSI-RSW-OLR; lower) from Mar 2000 to Dec 2023. Anomalies are relative to their calendar month climatology (2001–22). Time series show the CERES EBAF Ed4.2 1-Deg data (Mar 2000–Nov 2023) in red and the CERES FLASHFlux version 4B data (Dec 2023) marked by the blue dot; see text for merging procedure. (Sources: https://ceres-tool.larc.nasa.gov/ord-tool/jsp/EBAFTOA42Selection.jsp and https://ceres-tool.larc.nasa.gov/ord-tool/jsp/FLASH_TISASelection.jsp.)

2. MAUNA LOA APPARENT TRANSMISSION RECORD

—J. A. Augustine, K. O. Lantz, J.-P. Vernier, and L. Soldo

The time series of monthly mean apparent atmospheric transmission from pyrheliometer measurements at NOAA's Mauna Loa Observatory (MLO) in Hawaii (19.536°N, 155.576°W, 3397 m a.s.l.) is one of the longest geophysical records, dating back to 1958. However, its extension to 2023 is abbreviated due to damage sustained from the eruption of Mauna Loa on 27 November 2022. Ten meters of lava buried approximately a mile of the road leading to the station and demolished the power lines. Power was restored in July 2023.

The apparent atmospheric transmission time series through 2023 is shown in Fig. 2.58. Lack of operations in the first half of the year precluded sampling of the perennial springtime passage of Asian dust that usually causes a reduction in transmission (Augustine et al. 2023; Bodhaine et al. 1981). Until November 2023, transmission levels are maintained at the relatively low levels (0.926±0.0026) that have been observed since 2018. A composite of Stratospheric Aerosol and Gas Experiment (SAGE) limb sounder imagery (Leckey et al. 2021; https://sage.nasa.gov/sageiii-iss/browse_images/expedited/) suggests that this long period of relatively low transmission may have been sustained by a series of volcanic eruptions, including Ambae-1 and -2 in 2018, Raikoke and Ulawun in 2019, Taal in 2020, Soufriere in 2021, and Hunga Tonga–Hunga Ha'apai (HTHH) in 2022. Although SAGE imagery covers only +10° to –10° latitude, Yu et al. (2023) attribute elevated stratospheric aerosols at 15.5 km and 18.5 km from balloon-borne Portable Optical Particle Spectrometer soundings at Boulder, Colorado (40°N), and the Tibetan Plateau (25°N–36°N) to those eruptions, indicating that the volcanic aerosols did spread northward over Mauna Loa.

High levels of stratospheric water vapor from HHTH may have also contributed to the low transmission after January 2022. However, successive upticks in November and December of 2023 (to 0.93) may hint at the onset of a recovery. That tendency continued into January 2024, when the MLO transmission remained >0.93 (not shown). A possible cause is the switching of the quasi-biennial oscillation to an easterly phase around October 2023, and the significant drying of the lower stratosphere thereafter, which has been confirmed by integrated water vapor measurements at Mauna Loa. Less absorption in the near-infrared from that drying likely contributed to the increase in transmission from November 2023 through January 2024.

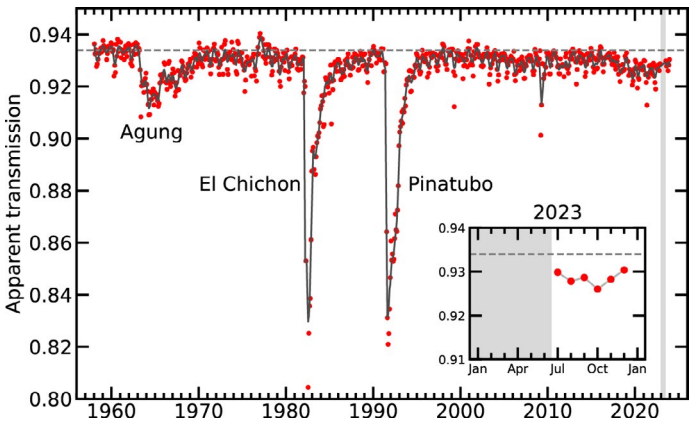

Fig. 2.58. Apparent transmission at Mauna Loa, Hawaii, from 1958 through 2023. Red dots are monthly averages of morning apparent transmission, and the gray curve is a lowess fit with a six-month smoother applied. Inset shows new data for 2023. The gray horizontal dashed line represents the average transmission of the clean period (Ammann et al. 2003; Solomon et al. 2011) before the eruption of Agung. Transmission is not available from Jan through Jun 2023 (gray areas in main figure and inset) because lava from the eruption of Mauna Loa in late Nov 2022 cut power to the station.

According to the Smithsonian/U.S. Geological Survey Weekly Volcanic Activity Report, 72 eruptions occurred in 2023. Of those, only one, specifically Lascar in Chile, attained a Volcanic Explosivity Index (VEI) of 3, with two others registering VEIs of 2 and 1. Other 2023 eruptions were, or have so far been too weak to be classified as explosive. Analyses of the CALIPSO data show that the plume from the January 2022 explosive eruption of HTHH remains in the lower stratosphere but is confined mainly to the Southern Hemisphere. However, CALIPSO and SAGE continue to show a weak but diminishing presence of that plume at the latitude of MLO at least through June and October 2023, respectively.

The primary aerosol event of 2023 was unprecedented wildfires across Canada from May through September that impacted air quality throughout the Northern Hemisphere (Wang et al. 2023; see Sidebar 7.1 for details). Pyrocumulus thunderstorms generated by some of those fires as well as solar heating of black carbon within initial plumes likely lofted smoke into the lower

stratosphere; however, a Copernicus Atmospheric Monitoring Service (CAMS) global analysis of daily mean organic matter aerosol optical depth at 550 nm (Garrigues et al. 2022) from May through September shows that smoke was confined mostly north of 40°N. A modeling study by Wang et al. (2023) shows very low concentrations of particulate matter (PM2.5) aerosol (<1 μg m^{-3}) over Hawaii from late June through September from wildfires in Canada and East Asia, but no presence of it there in the other months of the year. This evidence indicates that wildfire smoke may not have had a significant impact on MLO transmission in 2023.

To calculate apparent atmospheric transmission, three ratios of successive clear-morning pyrheliometer measurements made near the summit at solar air masses of 2, 3, 4, and 5 are averaged to get a representative daily transmission (Ellis and Pueschel 1971). The mean of daily transmissions for a particular month is considered to be a representative monthly transmission. It is referred to as "apparent" because atmospheric variability at longer pathlengths increases the uncertainty of the measurements.

g. Atmospheric composition

1. LONG-LIVED GREENHOUSE GASES

—X. Lan, B. D. Hall, G. Dutton, and I. Vimont

In 2023, the atmospheric burdens of the long-lived greenhouse gases (LLGHGs) carbon dioxide (CO_2), methane (CH_4), and nitrous oxide (N_2O), that are largely responsible for increasing global temperature (Forster et al. 2023; IPCC 2013), continued to rise to record-high levels. CO_2 is the most important and abundant anthropogenic GHG, and in 2023, globally averaged CO_2—as derived from remote marine boundary layer measurements made by NOAA's Global Monitoring Laboratory—reached 419.3±0.1 ppm (parts per million by moles in dry air; Fig. 2.59a; Table 2.10; uncertainties are reported as one sigma in this section). This is a 50% increase from the pre-industrial level of ~278 ppm (Etheridge et al. 1996). Annual growth in global mean CO_2 has risen from 0.6±0.1 ppm yr^{-1} in the early 1960s to an average of 2.5 ppm yr^{-1} during 2014–23 (Fig. 2.59a; Lan et al. 2024a). CO_2 growth in 2023 was 2.8 ppm, the fourth highest in the record since the 1960s.

The main driver of increasing atmospheric CO_2 is fossil fuel (FF) burning, with emissions increasing from 3.0±0.2 Pg C yr^{-1} in the 1960s to 9.6±0.5 Pg C yr^{-1} (including cement production) in the past decade (2013–22; Friedlingstein et al. 2023). Together with the measured atmospheric increase, we can conclude that about 45% of the FF-emitted CO_2 since 1958 has remained in the atmosphere, with the remaining portion entering the oceans and terrestrial biosphere (Friedlingstein et al. 2023). While increasing emissions of CO_2 from FF combustion are roughly monotonic, the CO_2 growth rate varies from year to year (standard deviation = 0.4 ppm in 2014–23) with variability mostly driven by terrestrial biosphere exchange of CO_2, as confirmed by measurements of the ^{13}C:^{12}C ratio in atmospheric CO_2 (e.g., Keeling et al. 1985; Alden et al. 2010). The El Niño–Southern Oscillation (ENSO) is the main driver of this interannual variability (Betts et al. 2016; Liu et al. 2017), which impacts photosynthetic CO_2 uptake, respiratory release, and fires.

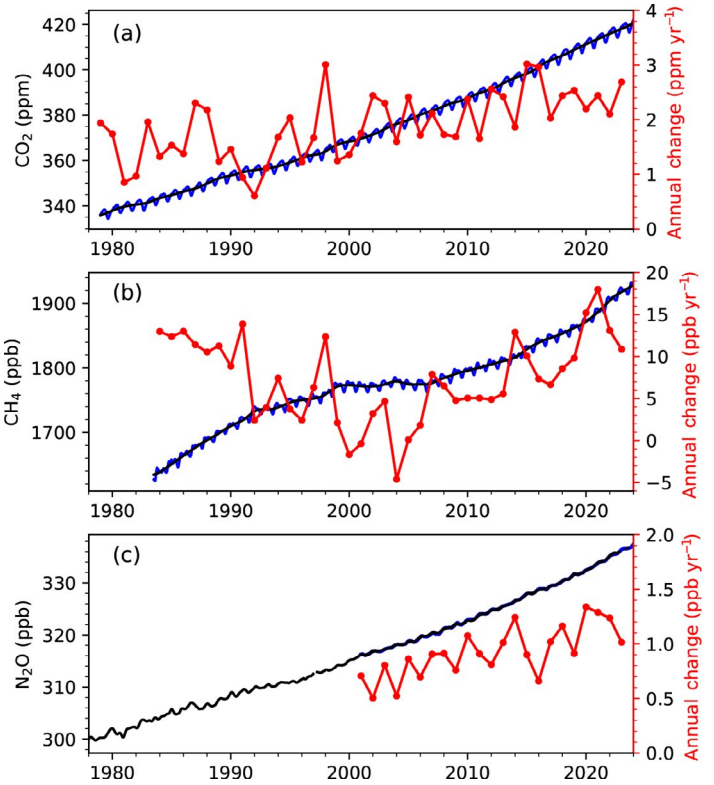

Fig. 2.59. Global mean dry air remote surface mole fractions (approximately weekly data in blue and the deseasonalized trend in black [see Dlugokencky et al. 1994 for methods]; left axis) and annual change (red, right axis) of (a) CO_2 (ppm), (b) CH_4 (ppb), and (c) N_2O (ppb) derived from the NOAA Global Greenhouse Gases Reference Network. N_2O data prior to 2000 are insufficient to accurately calculate its growth rate.

Atmospheric CH_4 is the second most important LLGHG, and in 2023 its atmospheric abundance reached 1922.6±0.6 ppb (parts per billion by moles in dry air; Lan et al. 2024b), about 2.6 times its pre-industrial level of 729±9 ppb (Mitchell et al. 2013). Global CH_4 increased by an average rate of 11.7±1.4 ppb yr^{-1} between 1984 and 1991, followed by a smaller increase of 4.4±1.8 ppb yr^{-1} between 1992 and 1998, and further reduced to near zero (0.5±3.0 ppb yr^{-1}) during 1999–2006. Atmospheric CH_4 growth restarted in 2007 and has accelerated since 2014 and further accelerated in 2020–22 with an average rate of increase of 15.4±2.0 ppb yr^{-1} (Fig. 2.59b). Its growth remained high in 2023 at about 11.1±0.4 ppb, which was the fifth-highest annual growth rate since the renewed growth started in 2007.

Atmospheric CH_4 is emitted by anthropogenic sources such as fossil fuel exploitation, livestock, waste and landfill, and rice cultivation, as well as natural sources such as wetlands and shallow lakes. The ongoing reduction in atmospheric $\delta^{13}C$-CH_4 since 2008 (Michel et al. 2022) indicates increased emissions from microbial sources (Basu et al. 2022), including emissions from livestock as well as natural wetland and lakes, which have more negative $\delta^{13}C$-CH_4 signatures. Small

increases in FF emissions may also play a role in the post-2006 global CH_4 increase (Oh et al. 2023; Lan et al. 2019, 2021; Basu et al. 2022). The contribution of hydroxyl radical, the main sink for CH_4, is still uncertain, but it is less likely to be a major contributor (Zhao et al. 2019; Lan et al. 2021). Recent studies suggest a dominant role of increased tropical wetland emissions in the post-2020 CH_4 surge (Feng et al. 2021; Peng et al. 2022), and sustained increases in wetland CH_4 emissions may be an indication of an emerging carbon climate feedback (Nisbet et al. 2023; Zhang et al. 2023). An increased contribution from wetland emissions is also consistent with the acceleration in the decline of atmospheric $\delta^{13}C$-CH_4 in 2020–22 (Michel et al. 2022).

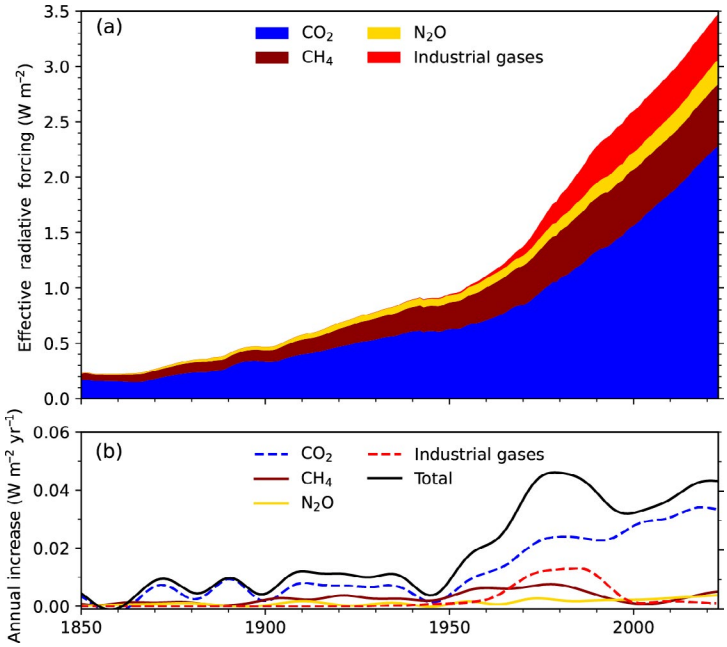

Fig. 2.60. (a) Effective radiative forcing (W m^{-2}) due to long-lived greenhouse gases (LLGHGs; see Table 2.10 for details on industrial gases). (b) Annual increase in direct radiative forcing (W m^{-2}).

Nitrous oxide (N_2O) is a potent greenhouse gas with an atmospheric lifetime of 120 years (Tian et al. 2023). It is produced by microbes that rely on nitrogen substrates from natural and agricultural soils, animal manure, and the oceans (Davidson 2009), and increased agricultural emissions related to fertilizer usage are the major source of its long-term increase (Tian et al. 2023). The mean global atmospheric abundance of N_2O in 2023 was 336.7±0.1 ppb, a 25% increase over its pre-industrial level of 270 ppb (Rubino et al. 2019). Recent growth reached an average rate of 1.3±0.1 ppb yr^{-1} from 2020 to 2022 (Fig. 2.59c), larger than the average rate between 2010 and 2019 (1.0±0.2 ppb yr^{-1}), strongly suggesting increased emissions. The N_2O growth rate in 2023 was 1.0±0.1 ppb.

The impacts of LLGHGs on global climate can be estimated using the effective radiative forcing (ERF) of LLGHGs, the change of radiative energy caused by added LLGHGs to the atmosphere, following the Intergovernmental Panel on Climate Change's Sixth Assessment Report (Forster et al. 2021). Increasing atmospheric CO_2 has accounted for 64% of the increase in ERF by LLGHGs, reaching 2.28 W m^{-2} in 2023 (Fig. 2.60) compared with preindustrial times (1750). The increase in CH_4 contributed a 0.56 W m^{-2} increase in ERF between 1750 and 2023 while the CH_4-related production of tropospheric ozone and stratospheric water vapor also contributes to ~0.30 W m^{-2} indirect radiative forcing (Myhre et al. 2014). The increase in atmospheric N_2O abundance contributed to a 0.22 W m^{-2} increase in ERF between 1750 and 2023.

Table 2.10. Summary table of long-lived greenhouse gases for 2023 (CO_2 mole fractions and changes from prior year, in brackets, are in ppm; N_2O and CH_4 in ppb; and all others in ppt).

Compound Class	Industrial Designation or Common Name	Chemical Formula	ERF[a]	Rad. Efficiency (W m^{-2} ppb^{-1})[b]	Rad. Forcing[a] (ERF/SARF) (W m^{-2})	Mean surface mole fraction, 2023 [change from prior year][c]	Lifetime (yrs)[b]
Acidic oxide	Carbon Dioxide	CO_2	Y	1.33×10^{-5}	2.28	419.3 [2.2]	
Alkane	Methane	CH_4	Y	3.88×10^{-4}	0.56	1922.6 [10.6]	9.1
Nitride	Nitrous Oxide	N_2O	Y	3.2×10^{-3}	0.22	336.7 [1.0]	123
Chlorofluorocarbon	CFC-11	CCl_3F	N(Y)[e]	0.26	0.057(0.064)	217.1 [–2.4][d]	52
Chlorofluorocarbon	CFC-12	CCl_2F_2	N(Y)[e]	0.32	0.156(0.174)	485.4 [–4.3][d]	102
Chlorofluorocarbon	CFC-113	CCl_2FCClF_2	N	0.30	0.020	67.1 [–0.6][d,f]	93

Compound Class	Industrial Designation or Common Name	Chemical Formula	ERF[a]	Rad. Efficiency (W m^{-2} ppb^{-1})[b]	Rad. Forcing[a] (ERF/SARF) (W m^{-2})	Mean surface mole fraction, 2023 [change from prior year][c]	Lifetime (yrs)[b]
Hydrochlorofluorocarbon	HCFC-22	$CHClF_2$	N	0.21	0.052	247.5 [–1.3]	11.9
Hydrochlorofluorocarbon	HCFC-141b	CH_3CCl_2F	N	0.16	0.004	24.5 [–0.1]	9.4
Hydrochlorofluorocarbon	HCFC-142b	CH_3CClF_2	N	0.19	0.004	21.0 [–0.2]	18
Hydrofluorocarbon	HFC-134a	CH_2FCF_3	N	0.17	0.021	129.5 [5.0]	14
Hydrofluorocarbon	HFC-152a	CH_3CHF_2	N	0.10	<0.001	7.4 [0.0]	1.6
Hydrofluorocarbon	HFC-143a	CH_3CF_3	N	0.17	0.005	28.4 [1.7]	51
Hydrofluorocarbon	HFC-125	CHF_2CF_3	N	0.23	0.009	38.8 [3.7]	30
Hydrofluorocarbon	HFC-32	CH_2F_2	N	0.11	0.002	28.3 [3.7]	5.4
Hydrofluorocarbon	HFC-23	CHF_3	N	0.18	0.007	36.8 [0.9]	228
Hydrofluorocarbon	HFC-365mfc	$CH_3CF_2CH_2CF_3$	N	0.22	<0.001	1.07 [0.00]	8.9
Hydrofluorocarbon	HFC-227ea	CF_3CHFCF_3	N	0.26	<0.001	2.20 [0.16]	36
Chlorocarbon	Methyl Chloroform	CH_3CCl_3	N	0.07	<0.001	0.98 [–0.12]	5.0
Chlorocarbon	Carbon Tetrachloride	CCl_4	N	0.17	0.013	73.8 [–0.9][d]	32
Chlorocarbon	Methyl Chloride	CH_3Cl	N	0.01	<0.001	549.9 [2.7]	0.9
Bromocarbon	Methyl Bromide	CH_3Br	N	0.004	<0.001	6.47 [–0.05]	0.8
Bromocarbon	Halon 1211	$CBrClF_2$	N	0.29	0.001	2.84 [–0.09]	16
Bromocarbon	Halon 1301	$CBrF_3$	N	0.30	0.001	3.32 [0.01]	72
Bromocarbon	Halon 2402	$CBrF_2CBrF_2$	N	0.31	<0.001	0.396 [–0.001]	28
Fully fluorinated species	Sulfur Hexafluoride	SF_6	N	0.57	0.006	11.40 [0.38]	>600
Fully fluorinated species	PFC-14	CF_4	N	0.09	0.005	89.4 [0.09]	~50,000
Fully fluorinated species	PFC-116	C_2F_6	N	0.25	0.001	5.24 [0.09]	~10,000
Fully fluorinated species	PFC-218	C_3F_8	N	0.28	<0.001	0.76 [0.02]	~2600
Fully fluorinated species	PFC-318	$c\text{-}C_4F_8$	N	0.32	<0.001	2.10 [0.11]	~3200

[a] Effective Radiative Forcing (ERF) calculated by multiplying the stratospheric-temperature adjusted radiative efficiency (SARF) by the global mole fraction (in ppb) and then applying a tropospheric adjustment factor for the species indicated based on recommended values from chapters 6 and 7 in the Intergovernmental Panel on Climate Change Sixth Assessment Report Working Group I (IPCC AR6 WGI) Report. The Radiative Forcing column is either ERF (where indicated) or SARF. The adjustments to the SARF are CO_2: 5% ± 5%, CH_4: –14% ± 15%, N_2O: 7% ±13%–16%.

[b] Radiative efficiencies and lifetimes were taken from Appendix A in WMO (2018) and Hodnebrog et al. (2020a), except for SF_6 lifetime from Ray et al. (2017), CH_4 lifetime from Prather et al. (2012). For CO_2, numerous removal processes complicate the derivation of a global lifetime. AGGI = Annual Greenhouse Gas Index. For radiative forcing, see https://www.esrl.noaa.gov/gmd/aggi/aggi.html.

[c] Mole fractions are global, annual, midyear surface means determined from the NOAA cooperative global air sampling network (Hofmann et al. 2006), except for PFC-14, PFC-116, PFC-218, PFC-318, and HFC-23, which were measured by the Advanced Global Atmospheric Gases Experiment (AGAGE; Mühle et al. 2010; Miller et al. 2010). Changes indicated in brackets are the differences between the 2023 and 2022 means, the relevant quantities for calculating radiative forcing. These changes are somewhat different from the 2023 annual increases reported in Section 2.g.1, which are determined as the difference between 1 Jan 2023 and 1 Jan 2024. All values are preliminary and subject to minor updates.

[d] Global mean estimates derived from multiple NOAA measurement programs ("Combined Dataset").

[e] ERF-calculated values for CFC-11 and CFC-12 are highly uncertain but recommended by the IPCC AR6 WGI Report. Thus, they are included in parentheses here as the lower confidence value. The adjustment to the SARF for these values is 12%±13% (Hodnebrog et al. (2020b).

[f] Measurements of CFC-113 are known to be a combination of CFC-113 and CFC-113a, with CFC-113a contributing approximately 0.4 ppt to CFC-113.

2. OZONE-DEPLETING SUBSTANCES

—I. J. Vimont, B. D. Hall, G. Dutton, S. A. Montzka, J. Mühle, M. Crotwell, K. Petersen, S. Clingan, and D. Nance

Since 1987, the Montreal Protocol and its Amendments (The Protocol; https://ozone.unep.org/treaties/montreal-protocol) have regulated the production and consumption of ozone-depleting substances (ODSs) and their replacement compounds. The broad categories of these compounds are the chlorofluorocarbons, hydrochlorofluorocarbons, hydrofluorocarbons, and perfluorocarbons (CFCs, HCFCs, HFCs, and PFCs, respectively), as well as halons and methyl bromide. While the primary goal of controlling ODSs through The Protocol was to limit damage to the ozone layer by limiting production for dispersive uses, these controls (and the subsequent amendments controlling the replacement compounds) have also reduced their radiative impact. Through the 2016 Kigali Amendment, The Protocol also addresses some HFCs that do not destroy stratospheric ozone, but are strong greenhouse gases. As of 2023, 155 nations have ratified the Kigali Amendment, which will aid the global effort to reduce the impacts of these gases on the climate.

Phase-out of the production for dispersive use is not the end of emissions of a chemical, nor are emissions the only factor controlling the atmospheric abundance of a trace gas species. Existing reservoirs of gases, such as those in insulating foams, are known as banks and continue to emit controlled chemicals for years after the final phase-out has occurred. The atmospheric lifetime, or rate of destruction, of a chemical in the atmosphere dictates how quickly a compound is removed, and these lifetimes vary over a large range between different species. As an example, CFC-11 and CFC-12 were reported to be globally phased out in 2010, but have long atmospheric lifetimes and large banks that continue to emit both compounds. These two gases have declined by only 18% and 10%, respectively, from their peak atmospheric abundances in 1994 and 2003 (Fig. 2.61). Conversely, methyl chloroform (CH_3CCl_3) has relatively few banks and a short lifetime and, despite having been phased out in 2015, has declined by 99% from its peak abundance in the atmosphere.

While the transition from CFCs to HCFCs resulted in an increase in the atmospheric abundance of several HCFCs during the 1990s and 2000s, the mole fractions of two of the three most abundant HCFCs (HCFC-22 and HCFC-141b) have not increased from 2021 to 2023, suggesting that their mole fractions may have peaked (Fig. 2.61; Table 2.10). The third most abundant HCFC, HCFC-142b, has been declining since about 2020 (Fig. 2.61; Table 2.10). Mole fractions of several HFCs, used as replacements for HCFCs, have increased substantially since their introduction in the mid-1990s, in particular HFC-134a, HFC-32, and HFC-23 (Fig. 2.61; Table 2.10).

Additionally, chemicals controlled under The Protocol are still allowed to be used as feedstocks for newer-generation products. Feedstock use may play a role in renewed release of ozone-depleting substances, such as CFC-112, CFC-113a, CFC-114a, and CFC-115 (e.g., Western et al. 2023). While these new releases do not yet pose a risk to the recovery

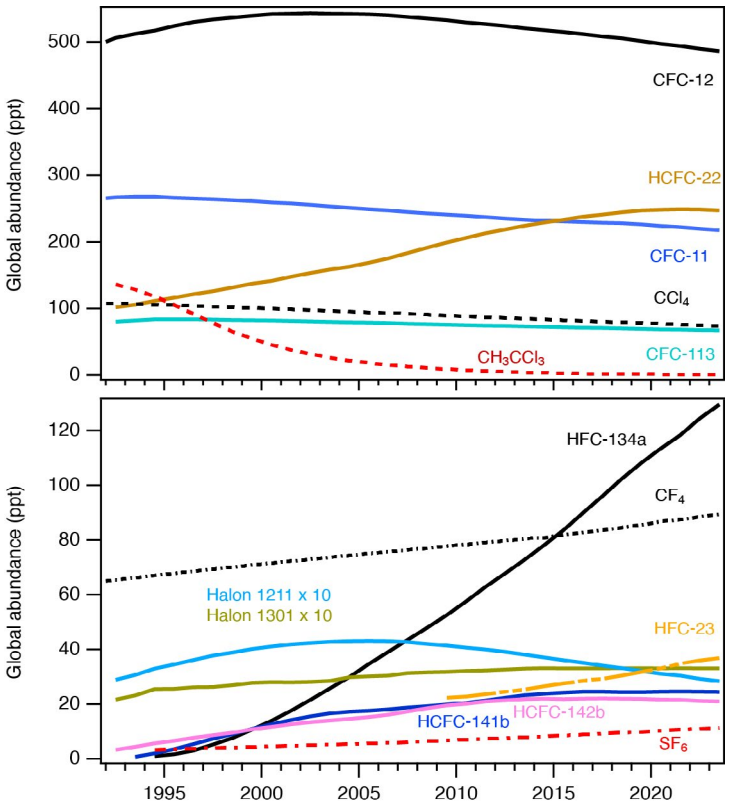

Fig. 2.61. Global mean abundances (mole fractions) at Earth's surface (ppt = nmol mol^{-1} in dry air) for several halogenated gases, many of which also deplete stratospheric ozone. See Table 2.10 for the 2023 global mean mole fractions of these and other gases.

of the ozone layer, continued emissions could begin to impact ozone layer recovery in the future (Western et al. 2023).

While global measurements of ODSs mainly represent the composition of the planetary boundary layer close to Earth's surface, destruction of the ozone layer is dependent on the amount of reactive halogen in the stratosphere. In order to track progress towards the ozone layer's recovery, equivalent effective stratospheric chlorine (EESC) is used as a measure of the reactive halogen loading in the stratosphere based on global tropospheric measurements, atmospheric transport (i.e., estimates of the mean age of the air in different parts of the stratosphere), and chemical reactivity (Daniel et al. 1995; Montzka et al. 1996; Newman et al. 2007). The destruction of the CFCs is the primary source of stratospheric reactive halogen and strongly contributes to the overall EESC. However, it is useful to scale the EESC relative to a benchmark by using the Ozone Depleting Gas Index (ODGI) to provide a more intuitive measure of the progress towards ozone layer recovery. The ODGI assesses the EESC relative to 1980, where an ODGI of 0 represents the EESC level in 1980, and an ODGI of 100 represents peak EESC (Hoffmann and Montzka 2009). The EESC, and therefore also the ODGI, are reported for the midlatitudes and the Antarctic, which spans the range of ozone layer recovery due to differences in transport processes in the stratosphere. The midlatitude EESC is expected to return to 1980 levels around 2045, while the Antarctic EESC is expected to recover by the 2070s (Fig. 2.62; https://gml.noaa.gov/odgi/).

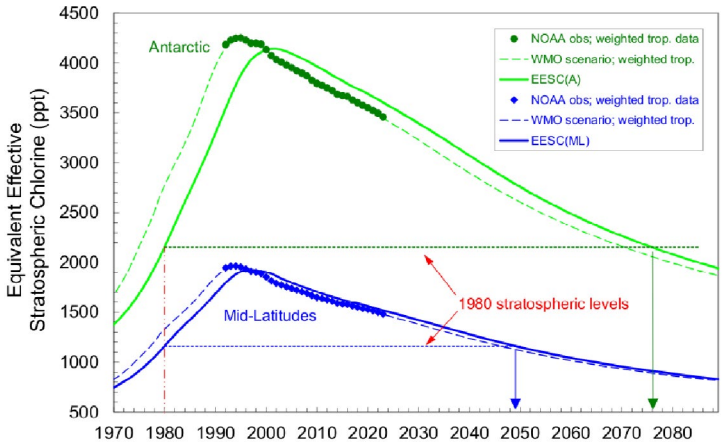

Fig. 2.62. The values of equivalent effective stratospheric chlorine in the Antarctic and midlatitudes (EESC[A] and EESC[ML], respectively) represent EESC on 1 Jan of each year since 1970. Dashed lines represent tropospheric measurement-derived scenarios, based on past measurements and, for the future, full adherence to all controls from The Protocol based on the World Meteorological Organization (WMO)/United Nations Environment Programme 2018 Ozone Assessment. Solid arrows indicate currently predicted dates for the return of EESC to 1980s levels. Solid lines depict inferred stratospheric changes based on the measured tropospheric curves. In 2023, midlatitude and Antarctic EESC were 1526 ppt and 3610 ppt, respectively, which represents a respective reduction of 21% and 13% in stratospheric reactive halogen loading from its peak. Translating this to the Ozone Depleting Gas Index (ODGI), the midlatitude ODGI is 47.1 and the Antarctic ODGI is 72.8, meaning the stratospheric reactive halogen loading has declined by 52.9% and 27.2%, respectively, relative to the 1980 benchmark reactive halogen abundance.

3. TROPOSPHERIC AEROSOLS

—S. Rémy, N. Bellouin, M. Parrington, M. Ades, M. Alexe, A. Benedetti, O. Boucher, and Z. Kipling

Aerosols represent a serious public health issue in many countries and are subject to monitoring and forecasting as part of air quality policies. They also impact weather and climate by scattering and absorbing radiation and by affecting the life cycle, optical properties, and precipitation activity of clouds (IPCC AR6, chapter 6; Szopa et al. 2021).

The Copernicus Atmosphere Monitoring Service (CAMS, https://atmosphere.copernicus.eu) produces a reanalysis of global aerosols and trace gases that covers the years 2003–23 (i.e., CAMSRA; Inness et al. 2019) by combining state-of-the-art numerical modeling and aerosol remote sensing retrievals from the Moderate-Resolution Imaging Spectroradiometer (MODIS; Levy et al. 2013) and the Advanced Along Track Scanning Radiometer (AATSR; Popp et al. 2016). This analysis uses data exclusively from the CAMS reanalysis, focusing on aerosol optical depth at 550 nm and surface particulate matter (PM2.5) concentrations.

Aerosol optical depth (AOD) at 550 nm and PM2.5 in 2023 show maxima over the polluted regions of India and China, as well as from dust over the Sahara and the Middle East (Figs. 2.63a,b). High values arose from seasonal vegetation fires in equatorial Africa and occasional extreme

fires, most notably across large parts of high-latitude North America, eastern Siberia, and parts of the Amazon basin (section 2h3; see Sidebar 7.1). Figure 2.63c shows the time series of monthly and yearly globally averaged total AOD during 2003–23. There is strong seasonality in AOD, driven mainly by dust episodes between March and July in the Sahara, Middle East, and the Taklamakan/Gobi deserts as well as seasonal biomass burning in Africa, South America, and Indonesia. Globally averaged AOD in 2023 was the lowest on record, on par with 2022. The summer maximum was slightly higher than in 2022 and significantly lower than in 2021, as the large fires in Canada in 2023 (see Sidebar 7.1) were compensated by lower-than-usual fire emissions elsewhere (section 2h3).

The AOD anomalies at 550 nm and PM2.5 anomalies (Plates 2.1x,y) are dominated by the exceptional fire events during summer 2023 over western and eastern Canada (section 2h3; see Sidebar 7.1) and the associated transported plumes over the North Atlantic. Positive anomalies due to fires are also seen over eastern Siberia, while the number of fires and associated emissions from equatorial Africa continued the downward trend of the last two decades. Dust storm activity was lower than usual over Northern Hemisphere (NH) deserts. The negative anomalies

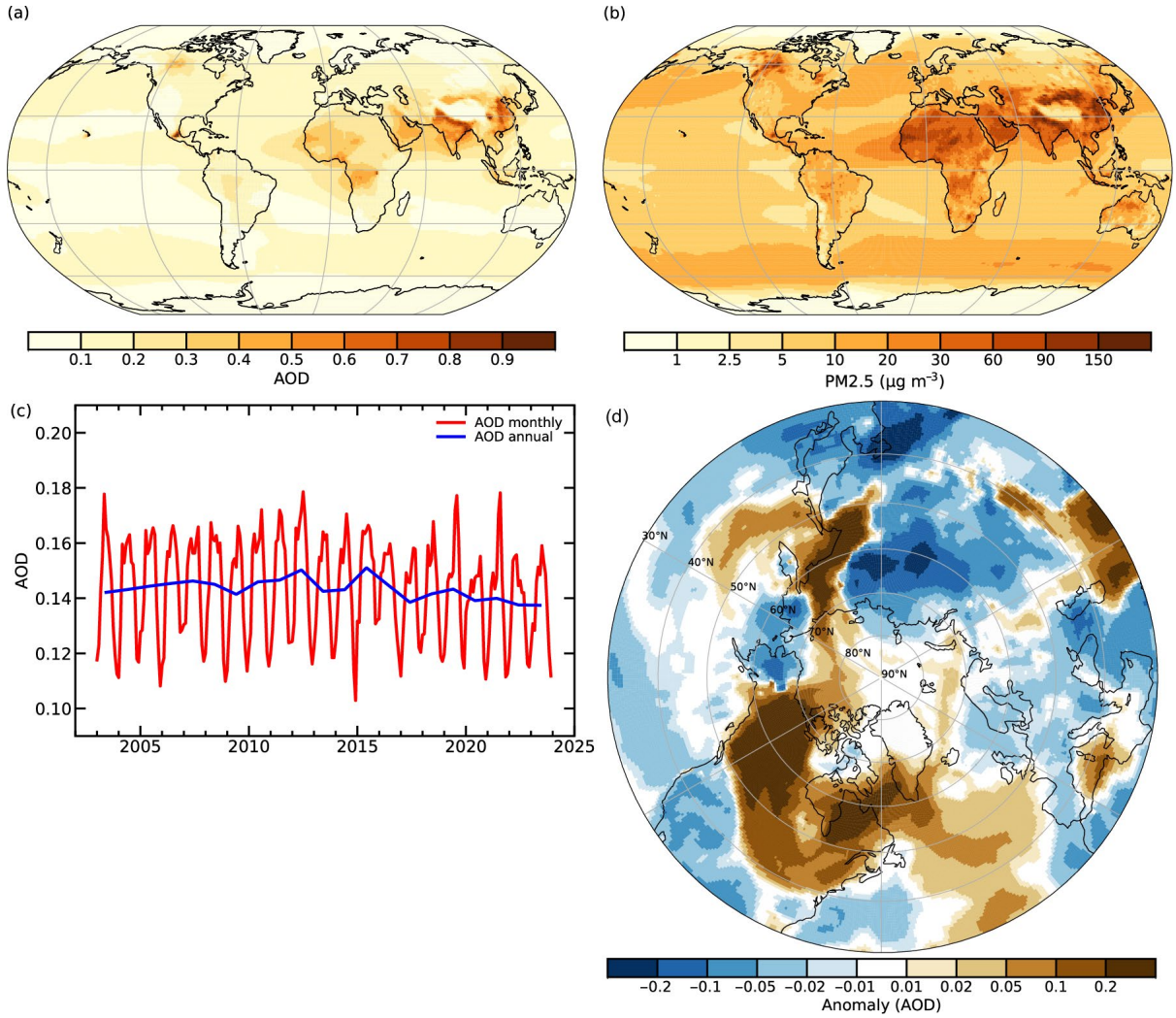

Fig. 2.63. (a) Global aerosol optical depth (AOD) at 550 nm in 2023; (b) global surface fine particulate matter (PM2.5) concentrations (µg m^{-3}) in 2023; (c) global average of total AOD at 550 nm averaged over monthly (red) and annual (blue) periods for 2003–23; and (d) monthly AOD anomalies at 550 nm for Jul 2023 compared to the Jul 2003–22 average, highlighting the extreme nature of the Canadian fires.

of AOD and PM2.5 over East Asia, Europe, and the Amazon basin (positive anomalies over India and Iran) can be explained by ongoing decreasing (increasing) trends in these regions. The exceptional nature of the summer 2023 Canada fires is highlighted by Plate 2.1z, which shows the number of extreme AOD days in 2023, and by Fig. 2.63d , which focuses on the AOD 550 nm anomaly in July 2023 over the North Hemisphere.

The AOD at 550 nm and PM2.5 trends for 2003–23 and 2012–23 are shown in Figs. 2.64a–d. The trends in AOD and PM2.5 are generally co-located. Between 2003 and 2023, there is a significant negative trend for both AOD and PM2.5 over most of the United States, Europe, East Asia, and parts of the Amazon basin, the latter from reduced deforestation activity. Positive trends are noted over parts of Siberia, which are driven by increased wildfire, as well as over India and Iran, which are driven by an increase in anthropogenic emissions (Satheesh et al. 2017). The trends between 2012 and 2023 show some contrast to those between 2003 and 2023: a stronger decrease over China reflecting a decrease in anthropogenic emissions (Quaas et al. 2022), smaller decreasing trends over Amazonia, Europe, and the United States, and new increases over Bolivia and Paraguay caused by a series of years with large fire events.

Anthropogenic AOD and radiative forcing resulting from aerosol–radiation (RFari) and aerosol–cloud interactions (RFaci) are shown in Fig. 2.65 for 2023 and the period 2003-23, as computed following Bellouin et al. (2020). There was a small increase in anthropogenic AOD in 2023 compared to 2022 (0.061 versus 0.059) and, consequently, aerosol radiative forcing has become slightly more negative by an estimated 0.05 W m^{-2}. These results are in contrast to the decreasing trend in anthropogenic AOD that started in 2018, but cannot yet signify a longer-term reversal.

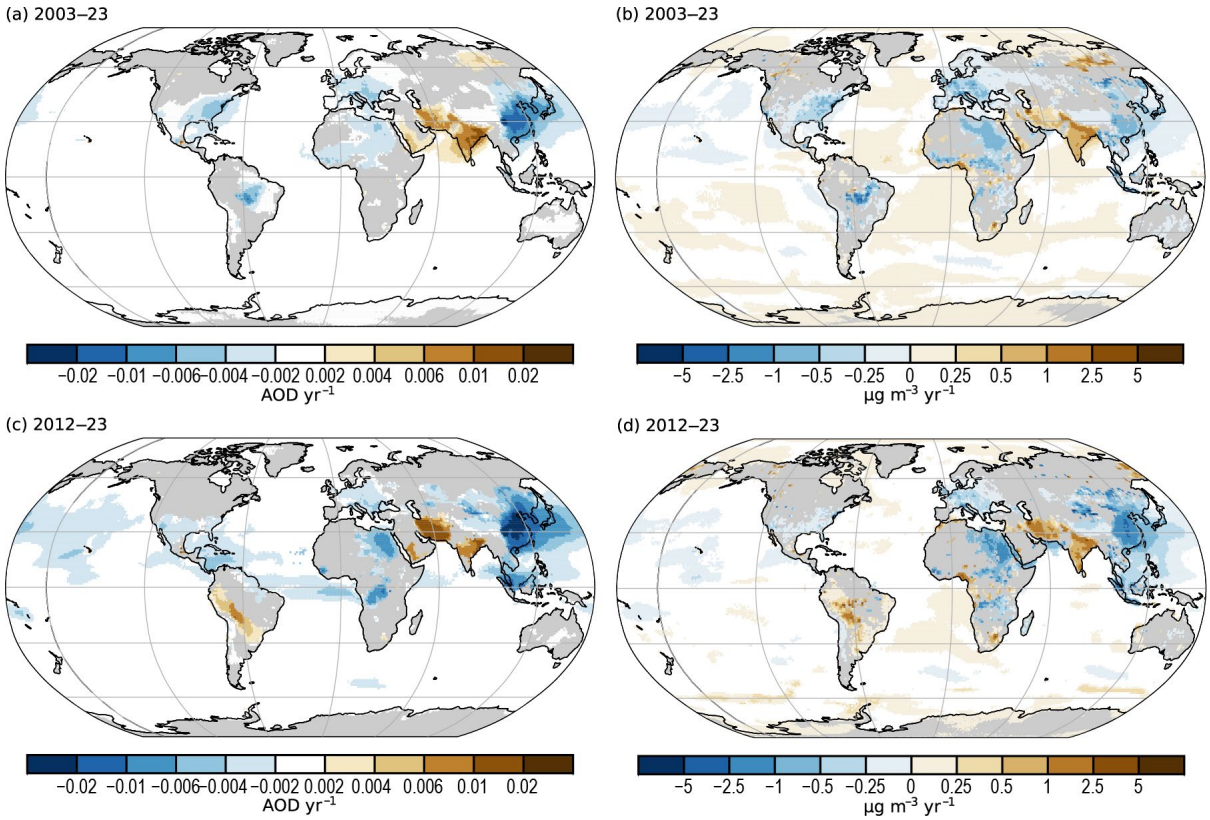

Fig. 2.64. (a),(b) Linear trends of total aerosol optical depth (AOD; AOD unit yr^{-1}) and fine particulate matter (PM2.5; µg m^{-3} yr^{-1}) for 2003–23; and (c),(d) linear trends of total AOD (AOD unit yr^{-1}) and PM2.5 (µg m^{-3} yr^{-1}) for 2012–23. Only trends that are statistically significant (95% confidence level) are shown.

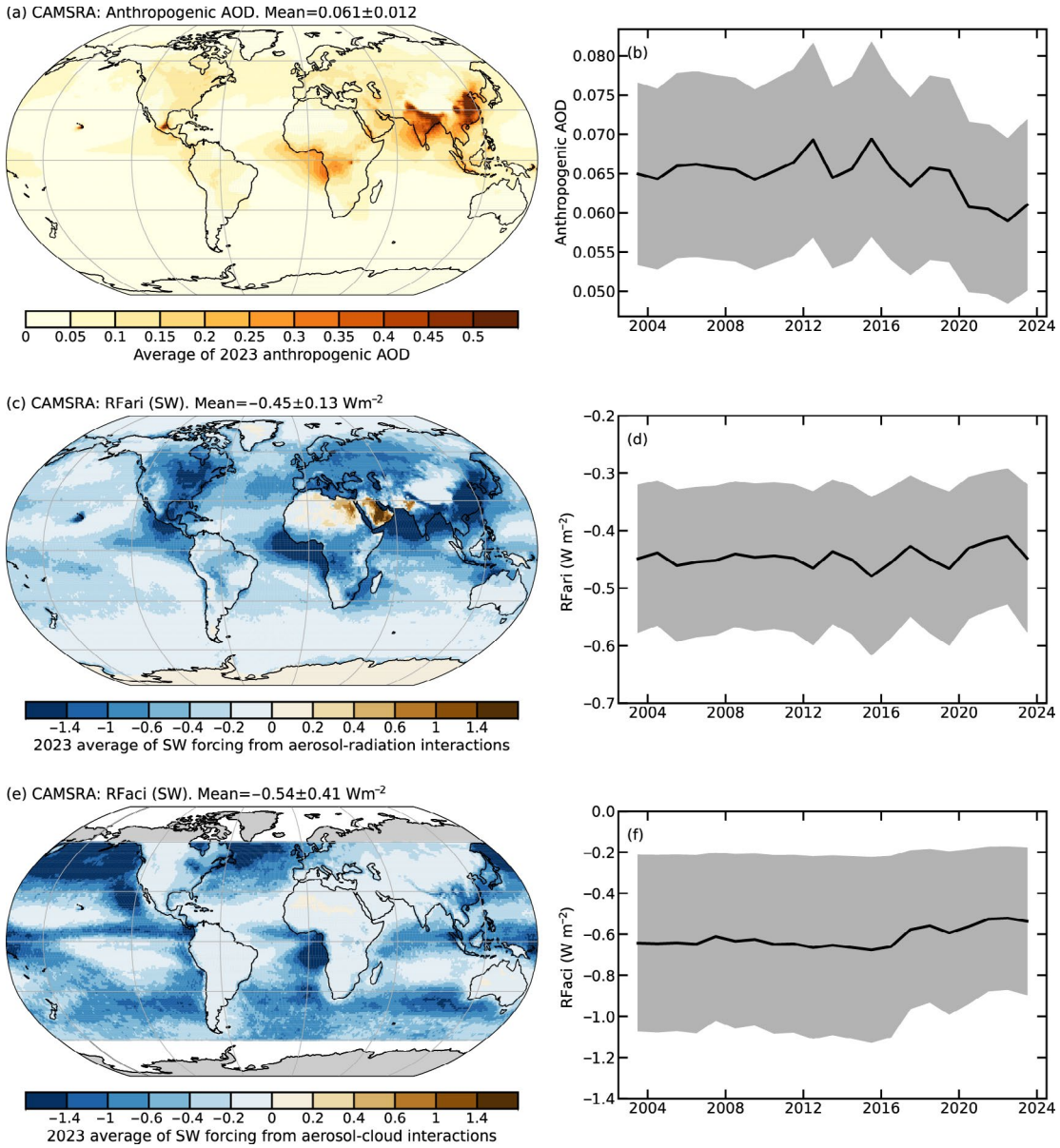

Fig. 2.65. CAMSRA (a) 2023 average of anthropogenic aerosol optical depth (AOD); (b) global annual average of anthropogenic AOD from 2003 to 2023. Radiative forcing in the shortwave (SW) spectrum due to (c),(d) aerosol-radiation (RFari) and (e),(f) aerosol-cloud interactions (RFaci). The left column shows the distributions for 2023. The right column shows time series of global averages for the period 2003–23, with the 1-σ uncertainties of these estimates shown in gray.

4. TROPOSPHERIC OZONE

—O. R. Cooper, J. R. Ziemke, and K.-L. Chang

Tropospheric ozone is a short-lived climate forcer with a global distribution that varies regionally, vertically, and on seasonal and interannual time scales (Forster et al. 2021; Szopa et al. 2021), posing a challenge for trend detection (Chang et al. 2021; Fiore et al. 2022). Atmospheric chemistry models indicate an approximately 40% increase of the tropospheric ozone burden (TOB) since the nineteenth century, and limited observations since the early and mid-twentieth century are consistent with the model estimates (Tarasick et al. 2019). Widespread in situ and satellite observations also record an increase of TOB since the mid-1990s (Gulev et al. 2021); however, new satellite-based observations suggest that the increase of TOB came to an end in 2020 in response to diminished ozone precursor emissions during the economic downturn that was triggered by the coronavirus (COVID-19) pandemic (Miyazaki et al. 2020; Ziemke et al. 2021). With three additional years (2021–23) of no growth in TOB as described below, the year 2020 may be a change point in the TOB record.

The unusual period (2020–23) of no growth in TOB (Fig. 2.66) coincides with observations of negative ozone anomalies (–5%) in the free troposphere above western North America and

Europe during 2020, which were recorded by ozonesondes, infrared spectrometers, and commercial aircraft (Steinbrecht et al. 2021; Clark et al. 2021; Chang et al. 2022, 2023). These anomalies were strongest in summer, when photochemical production is most active, and they are similar in magnitude to negative ozone anomalies detected at high-elevation rural sites in western North America and Europe (Putero et al. 2023). Model simulations of the COVID-19 period indicate that reduced emissions of ozone precursor gases across the Northern Hemisphere led to the ozone decreases (Miyazaki et al. 2020; Steinbrecht et al. 2021), reaching levels similar to those measured in the mid-1990s when ozone precursor emissions were less than 2019 levels (Chang et al. 2022). The models also indicate that the 2020 ozone anomalies were not caused by the unusual ozone depletion event that occurred above the Arctic during the spring of 2020 (Steinbrecht et al. 2021; Wang et al. 2023).

The combined Aura Ozone Monitoring Instrument and Microwave Limb Sounder satellite ozone measurements (OMI/MLS) provide a continuous record of the TOB from 60°S to 60°N for the period 2004–23 (Ziemke et al. 2019). The vertical resolution of OMI/MLS monthly tropospheric column ozone is ~3 km near the tropopause with a regional precision of ~2 Dobson units (DU; 7%); trend uncertainties are about 0.5 DU decade^{-1} (1.5% decade^{-1}). Positive tropospheric column ozone anomalies were widespread across the Northern Hemisphere in 2023 (relative to 2005–22), with peak values above South Asia, East Asia, and the North Pacific Ocean, while relatively weak negative anomalies occurred above southern Africa, Australia, and New Zealand (Plate 2.1aa). Global TOB (60°S–60°N) increased at the rate of 1.06±0.48 Tg yr^{-1} for the first 15 years of the record (2004–19), equal to a total increase of ~5% (Fig. 2.66). There was a slight drop in TOB in 2020, likely due to reduced ozone precursor emissions during the COVID-19 pandemic, as described above (Fig. 2.66). The tropospheric ozone burden remained at similar levels during 2021–23, mainly driven by decreases in northern midlatitudes (Figs. 2.66a–c). Regionally, the strongest positive trends (2004–23) have occurred above South and East Asia and across much of the North Pacific Ocean, along with Amazonia (Fig. 2.67). Weak but widespread ozone decreases are present above North America, Europe, Central Asia, Siberia, northern and southern Africa, Australia, and New Zealand, with the strongest decreases above North Africa and the western Mediterranean.

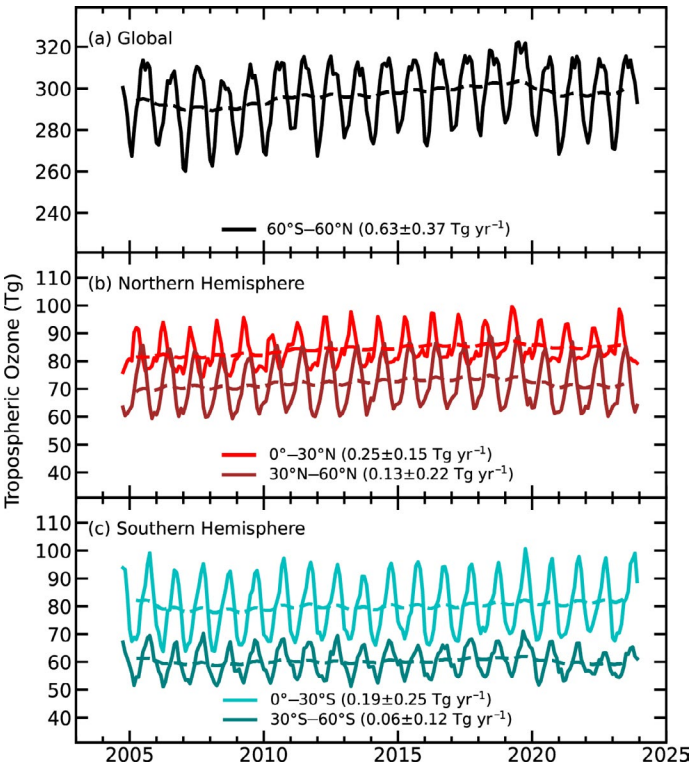

Fig. 2.66. Monthly averages (solid lines) and 12-month running means (dashed lines) of Ozone Monitoring Instrument (OMI)/Microwave Limb Sounder (MLS) tropospheric ozone burdens (Tg) from Oct 2004 through Dec 2023 for (a) 60°S–60°N (black), (b) the Northern Hemisphere tropics (red) and midlatitudes (dark red), and (c) the Southern Hemisphere tropics (blue) and midlatitudes (green). Slopes of linear fits to the data are presented with their 95% confidence-level uncertainties.

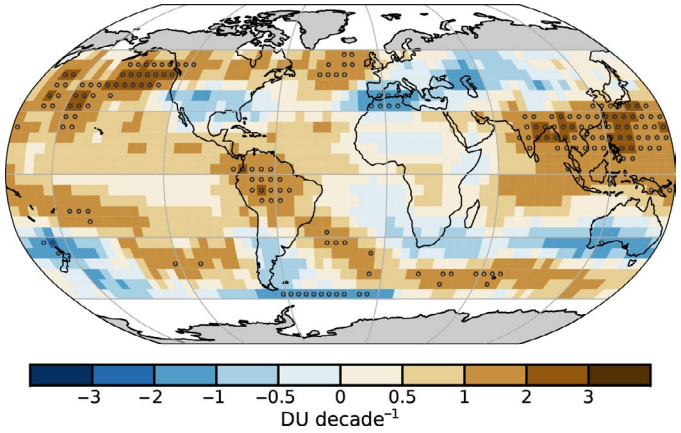

Fig. 2.67. Linear trends in Ozone Monitoring Instrument (OMI)/Microwave Limb Sounder (MLS) tropospheric column ozone (DU decade^{-1}) on a 5° × 5° grid from Oct 2004 through Dec 2023. Circles denote trends with p-values <0.05. Trends were calculated using a multivariate linear regression model (e.g., Randel and Cobb 1994 and references therein) that included a seasonal cycle fit and the Niño-3.4 index as an El Niño–Southern Oscillation proxy; trend uncertainties included autoregressive adjustment via Weatherhead et al. (1998).

Tropospheric ozone burden trends cannot be assessed from surface records because surface trends are often decoupled from the trends in the free troposphere above (Gulev et al. 2021), and the limited availability of long-term surface records precludes the construction of a data record that is globally representative; however, long-term surface records at remote locations are critical for evaluating the performance of global chemistry-climate models. Ozone trends from six such sites are reported here, based on records more than 20 years in length (Fig. 2.68; Table 2.11). Two records—those of the Mauna Loa Observatory in Hawaii, and the Barrow Atmospheric Observatory in Alaska—now span 50 years and report positive surface ozone trends of 0.93±0.39 ppbv decade^{-1} and 0.50±0.34 ppbv decade^{-1}, respectively. The 48-year record at South Pole also reports a positive albeit weaker trend of 0.32±0.34 ppbv decade^{-1}. The observations show no trend at Arrival Heights, Antarctica, since 1996. There is some evidence of a decrease at Tudor Hill, Bermuda, since 1988 (–0.81±1.10 ppbv decade^{-1}), as well as clear evidence of a decrease at Summit, Greenland, since 2000 (–2.00±0.93 ppbv decade^{-1}).

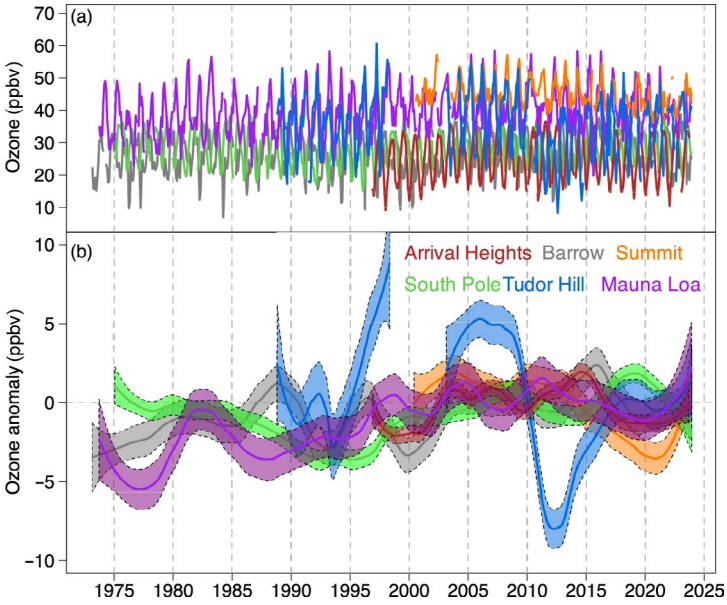

Fig. 2.68. (a) Monthly mean surface ozone (ppb) at Barrow Observatory, Alaska (gray), Summit, Greenland (orange), Tudor Hill, Bermuda (blue), Mauna Loa, Hawaii (purple), Arrival Heights, Antarctica (red), and South Pole (green). Monthly means are produced for months with at least 50% data availability using observations from all 24 hours of the day. The locations of each site are listed in Table 2.11. (b) As in panel (a), except the time series have been converted to monthly anomalies, referenced to the monthly climatological values over 2000–20, and smoothed using a locally weighted scatterplot smoothing regression.

Table 2.11. Surface ozone trends at the six baseline monitoring sites shown in Fig. 2.68 Trends are estimated by the generalized least squares method, based on monthly anomalies referenced to the monthly 2000–20 base period (Chang et al. 2021), and reported with 95% confidence intervals and *p*-values.

Site name — latitude, longitude, elevation (m)	Yrs with data	Trend, ppbv decade^{-1}	*p*-value
Summit, Greenland — 72.6°N, 38.5°W, 3238 m	2000–present	–2.00±0.93	p<0.01
Barrow Atmospheric Observatory, Alaska — 71.3°N, 156.6°W, 11 m	1973–present	0.50±0.34	p<0.01
Tudor Hill, Bermuda — 32.3°N, 64.9°W, 30 m	1988–1998, 2003–present	–0.81±1.10	p=0.14
Mauna Loa Observatory (MLO), Hawaii — 19.5°N, 155.6°W, 3397 m	1973–present	0.93±0.39	p<0.01
Arrival Heights, Antarctica — 77.8°S, 166.8°W, 50 m	1996–present	0.23±0.53	p=0.39
South Pole, Antarctica — 90.0°S, 59.0°E, 2840 m	1975–present	0.32±0.34	p=0.06

5. STRATOSPHERIC AEROSOLS

—S. Khaykin, G. Taha, T. Leblanc, T. Sakai, I. Morino, B. Liley, and S. Godin-Beekmann

Stratospheric aerosols play a large role in the chemical and radiative balance of the atmosphere (Kremser et al. 2016). Explosive volcanic eruptions may directly inject sulfur dioxide (SO_2) and ash into the stratosphere, leading to significant perturbations of stratospheric aerosol burden at hemispheric and global scales lasting from several months to several years. Another important source of particulate matter in the stratosphere is the increasingly intense wildfires (Peterson et al. 2021; Fromm et al. 2022).

Figure 2.69 shows 24 years of stratospheric aerosol optical depth (sAOD) observations by the ground-based Network for the Detection of Atmospheric Composition Change lidars at Observatoire de Haute Provence (OHP), France (43.9°N), and Lauder observatory, New Zealand (45.0°S), together with zonally averaged satellite data. These stations, antipodally located on the globe, respectively represent the northern and southern extratropics. The OHP time series (Fig. 2.69a) from 2000 to 2023 is largely modulated by several moderate volcanic eruptions as well as by the extreme British Columbia pyrocumulonimbus wildfire outbreak in August 2017 (Peterson et al. 2018), which led to a prolonged perturbation of stratospheric aerosol composition and burden. The largest impact on the NH sAOD in terms of magnitude and longevity of the perturbation was generated by the Raikoke volcanic eruption in 2019. The decay of the Raikoke sAOD perturbation appears to be longer than those of other midlatitude eruptions of similar magnitude. This is possibly due to the diabatic lofting of ash-rich Raikoke plumes that were shown to self-organize into persistent stratospheric anticyclones (Khaykin et al. 2022a). Such behavior has previously been reported for the wildfire smoke aerosols (Khaykin et al. 2020) that contain highly absorptive black carbon; however, it was unexpected for the volcanic aerosols, composed primarily of non-absorbing sulfates.

Significant sAOD perturbations in the Southern Hemisphere (SH; Fig. 2.69b) were nearly absent for more than two decades until the 2015 Calbuco volcanic eruption in Chile. The record-breaking 2019/20 "Australian New Year Super Outbreak" (ANYSO) wildfires boosted the SH sAOD to four times the background level according to Stratospheric Aerosol and Gas Experiment (SAGE) III and surpassed the Raikoke-induced NH perturbation (Khaykin et al. 2020), which was deemed

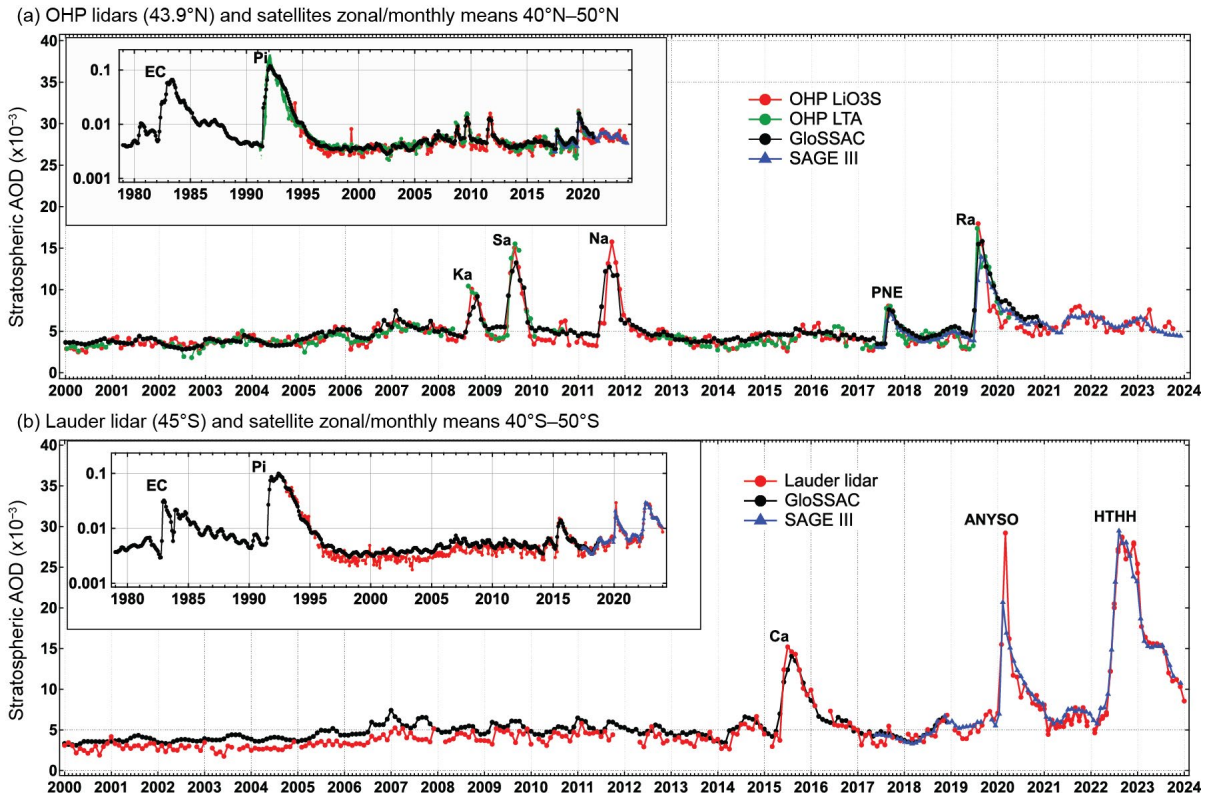

Fig. 2.69. Time series of monthly mean stratospheric aerosol optical depth (sAOD) at 532 nm of the stratospheric layer between 380 K and 1000 K potential temperature from ground-based lidars at (a) French Observatoire de Haute Provence (OHP, 43.9°N, 5.7°E, LiO_3S, and LTA lidars, red and green curves) and (b) New Zealand's Lauder station (45.0°S, 169.7°E, Lauder aerosol lidar, red curve) and the corresponding monthly/zonal-mean values from satellite observations within 40°N–50°N and 40°S–50°S latitude bands from the International Space Station's Stratospheric Aerosol and Gas Experiment (SAGE) III instrument (blue curves) and GloSSAC (Global Satellite-based Stratospheric Aerosol Climatology) merged satellite record (black curves). The embedded panels display the log-scaled time series from the beginning of the GloSSAC record. The literal notations indicate the most significant volcanic eruptions: El Chichon (EC), Pinatubo (Pi), Kasatochi (Ka), Sarychev (Sa), Nabro (Na), Raikoke (Ra), Calbuco (Ca), and Hunga Tonga–Hunga Haʻapai (HTHH); and wildfire events: Pacific Northwest Event (PNE; British Columbia, Canada), and Australian New Year Super Outbreak (ANYSO).

the 30-year high at that time (Leblanc et al. 2020). The ANYSO outbreak led to a prolonged perturbation in the entire SH with the decay exceeding one year.

More recently, the 30-year global sAOD record has been surpassed again, following the eruption of the Hunga Tonga–Hunga Ha'apai (HTHH) volcano on 15 January 2022, which was marked by extreme explosiveness with aerosols reaching an altitude above 50 km (Carn et al. 2022; Khaykin et al. 2022b). Aerosol layers were detected by the Ozone Mapping and Profiler Suite–Limb Profiler (OMPS-LP) instrument above 40 km, though the bulk of HHTH aerosols was bounded within the 20-km to 30-km layer (Taha et al. 2023).

The meridional evolution of the sAOD (Fig. 2.70a) shows that the HTHH-induced perturbation was mostly restricted to the tropical belt during the first four months after the eruption, although some transport into southern high latitudes occurred as early as February 2022 (Khaykin et al. 2022b). The transport of the bulk of volcanic material into the southern extratropics occurred in June 2022; however, its further penetration towards the pole was hindered by a strong transport barrier at the edge of the Antarctic stratospheric vortex that had been fully established by that time (Manney et al. 2023). By early 2023, the HTHH aerosols had spread across the entire SH and, unlike in 2022, were then entrained by the 2023 Antarctic vortex.

While the bulk of the HTHH sAOD perturbation has been restricted to the tropical belt and the SH, limited transport to the northern extratropics can be seen by tracking the anomalies in the aerosol extinction vertical profiles. Figure 2.70b displays the meridional transport of the HTHH sulfate aerosols expressed as the potential temperature of the peak extinction ratio (ER; aerosol-to-molecular extinction ratio) from OMPS-LP observations. The data suggest that the first intrusions into the northern extratropics occurred in April 2022, after which ground-based lidars in the NH extratropics started reporting weak yet distinct aerosol layers in the mid-stratosphere (Khaykin et al. 2022b). Further NH midlatitude intrusion episodes occurred during November 2022–January 2023. The vertical evolution of the peak ER (Fig. 2.70b) reveals that sedimentation of HTHH sulfate aerosols was slower in the tropics, where it is partly compensated by upwelling, and faster towards the poles.

Additional stratospheric aerosols detected in the NH mid- and high latitudes from April through November 2023 (Figs. 2.70a,b) can be traced to the eruption of Shiveluch volcano in the Kamchatka peninsula on 14 April 2023, as well as to a series of wildfire outbreaks in Canada and Siberia that led to a significant season-wide pollution of the lowermost stratosphere with smoke aerosols.

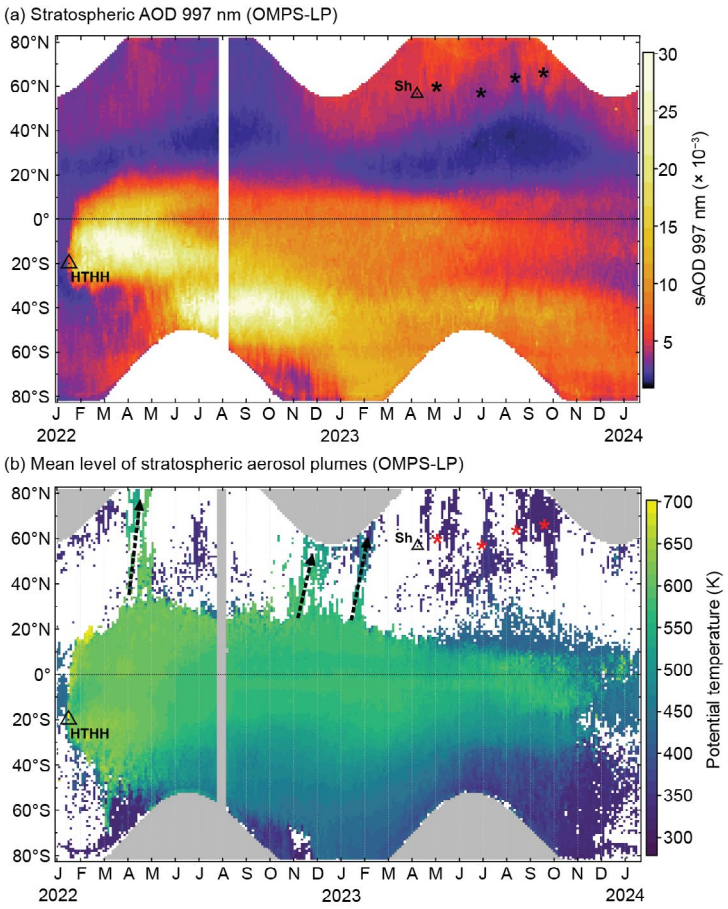

Fig. 2.70. Time–latitude evolution of the stratospheric aerosol from OMPS-LP observations at 997 nm in 2022/23. (a) Zonal-mean stratospheric aerosol optical depth (sAOD). (b) Mean potential temperature of the stratospheric peak of extinction ratio for the samples with ERmax>6, which corresponds to departures beyond ~7 sigma of the background variability in the given bin. This method allows for the detection of optically thin yet distinct aerosol layers, which are hard to spot using zonally averaged sAOD. The dashed arrows in (b) indicate the episodes of Hunga Tonga–Hunga Ha'apai (HTHH) aerosol intrusions into the Northern Hemisphere extratropics. The large and small triangles in (a) and (b) indicate the eruptions of HTHH and Shiveluch, respectively, whereas the black stars in (a) and red stars in (b) indicate wildfire events with measurable stratospheric impact in Canada and Russia during summer 2023.

6. STRATOSPHERIC OZONE

—M. Weber, W. Steinbrecht, C. Arosio, R. van der A, S. M. Frith, J. Anderson, L. M. Ciasto, M. Coldewey-Egbers, S. Davis, D. Degenstein, V. E. Fioletov, L. Froidevaux, D. Hubert, D. Loyola, A. Rozanov, V. Sofieva, K. Tourpali, R. Wang, T. Warnock, and J. D. Wild

Stratospheric ozone protects the ecosystem from harmful ultraviolet radiation. The total ozone column is an indicator of the level of protection from this radiation. About 90% of the total column amount resides in the stratosphere, and the number of ozone molecules is maximum at about 20-km to 25-km altitude (lower stratosphere), an altitude range that is called the ozone layer. Long-term changes in stratospheric ozone are governed by declining stratospheric halogens (chemistry) from man-made ozone-depleting substances (ODSs) and by the current and future greenhouse gas concentrations in the atmosphere (chemistry and circulation; WMO 2022).

In 2023, total column ozone was, on average, slightly lower compared to the 1998–2008 reference period in the NH, while in the SH from 35°S to 60°S, it was higher by up to 10 DU–15 DU (Plate 2.1ab). Antarctic total column ozone was close to the long-term mean except for in a small region south of Australia (Plate 2.1ab). The year 2023 ends a series of three years with below-average ozone values for the SH extratropics. The SH total column ozone was unusually low in 2022 (Figs. 2.71d,e), mainly due to circulation changes but also due to enhanced chemical destruction following the HTHH volcanic eruption in January 2022 (e.g., Santee et al. 2022; Evan et al. 2023; Fleming et al. 2024). In the tropics (Fig. 2.71c), total ozone was higher by a few DU compared to previous years but was within the year-to-year variability (two sigma) of the last two decades. Globally, total ozone levels

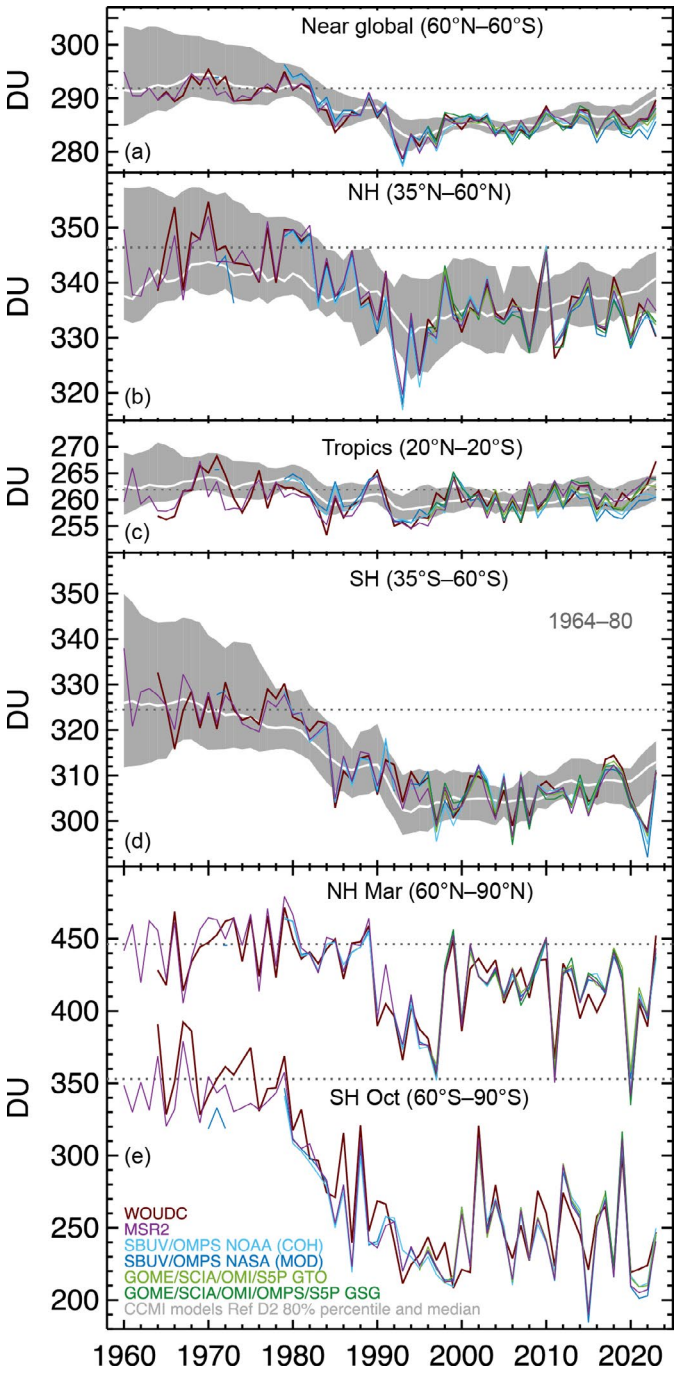

Fig. 2.71. Time series of annual mean total column ozone (DU) in (a)–(d) four zonal bands and (e) polar (60°–90°) total column ozone in Mar (Northern Hemisphere [NH]) and Oct (Southern Hemisphere [SH]), the months when polar ozone losses usually are largest. Data are from the World Ozone and Ultraviolet Radiation Data Centre (WOUDC) ground-based measurements combining Brewer, Dobson, SAOZ, and filter spectrometer data (red: Fioletov et al. 2002, 2008); the BUV/SBUV/SBUV2/OMPS merged products from NASA (V8.7; dark blue; Frith et al. 2014; 2017), and NOAA (SBUV V8.6, OMPS V4r1; light blue; Jeannette Wild, NOAA, 2024, personal communication); the GOME/SCIAMACHY/GOME-2/OMPS/TROPOMI products (GSG) from University of Bremen (dark green, Weber et al. 2022), and GTO from the EU's German Aerospace Center (DLR; light green; Coldewey-Egbers et al. 2022; Garane et al. 2018). MSR-2 (purple) assimilates nearly all ozone datasets after corrections based on the ground-based data (van der A et al. 2015). The dotted gray lines in each panel show the average total column ozone level for 1964–80 calculated from the WOUDC data. Most of the observational data for 2023 are preliminary. The thick white lines in (a)–(d) show the median from chemistry-climate CCMI-2022 ref D2 model runs (Plummer et al. 2021). The model data have been smoothed using a three-point triangle function. The gray-shaded areas provide the 80% percentile range for the model data. All datasets have been bias-corrected by subtracting individual data averages and adding the multi-instrument mean in the reference period (1998–2008).

in 2023 were close to the long-term average of the last 20 years and broadly agree with projections from chemistry-climate models (CCMs) using current scenarios of ODSs and greenhouse gases, as shown in Figs. 2.71a–d.

Figures 2.72d,e show that ozone at 50 hPa (~22-km altitude) in the tropics and northern midlatitudes behaved similarly to the total column (Figs. 2.71b,c). In 2023, the NH annual mean was nearly unchanged from previous years (Fig. 2.72d). Ozone at 50 hPa was slightly higher in the tropics in 2023 but still within the year-to-year variability of the last decade (Fig. 2.72e), and larger than in 2022 by about 5% in the SH (Fig. 2.72f), bringing it closer to the long-term average. In the upper stratosphere (2 hPa or 42-km altitude; Figs. 2.72a–c), ozone observations show a clear increase since the mid-1990s, averaging 0.2±0.15% yr^{-1}. The 2023 annual means follow the long-term trend, again in general agreement with the broad range predicted by CCMs.

In the SH midlatitude, elevated total column ozone (Plate 2.1ab; Fig. 2.71d) and ozone in lower stratosphere (Fig. 2.72f) in 2023 compared to 2022 is probably related to the strong El Niño that started to emerge in the middle of 2023. El Niños are linked to a strengthening of the Brewer-Dobson (BD) circulation and a weakening of the polar vortex, which both increase extratropical ozone by enhancing ozone transport from the tropical stratosphere to higher latitudes and by reducing the potential for the formation of widespread polar stratospheric clouds and subsequent large chemical ozone depletion in polar spring (e.g., Domeisen et al. 2022; Butchart 2014). The quasi-biennial oscillation (QBO) was in its westerly phase from September 2022 until the end of boreal summer 2023. This is associated with a weaker BD circulation and typically results in lower extratropical and higher tropical ozone columns. In the first half of 2023, this resulted in lower stratospheric ozone in the NH (e.g., Baldwin et al. 2001). The QBO turned easterly during the second half of 2023, coinciding with the strengthening of El Niño. The combined effect on SH ozone resulted in positive anomalies at southern midlatitudes (Plate 2.1ab; Figs. 2.71d,e, 2.72f).

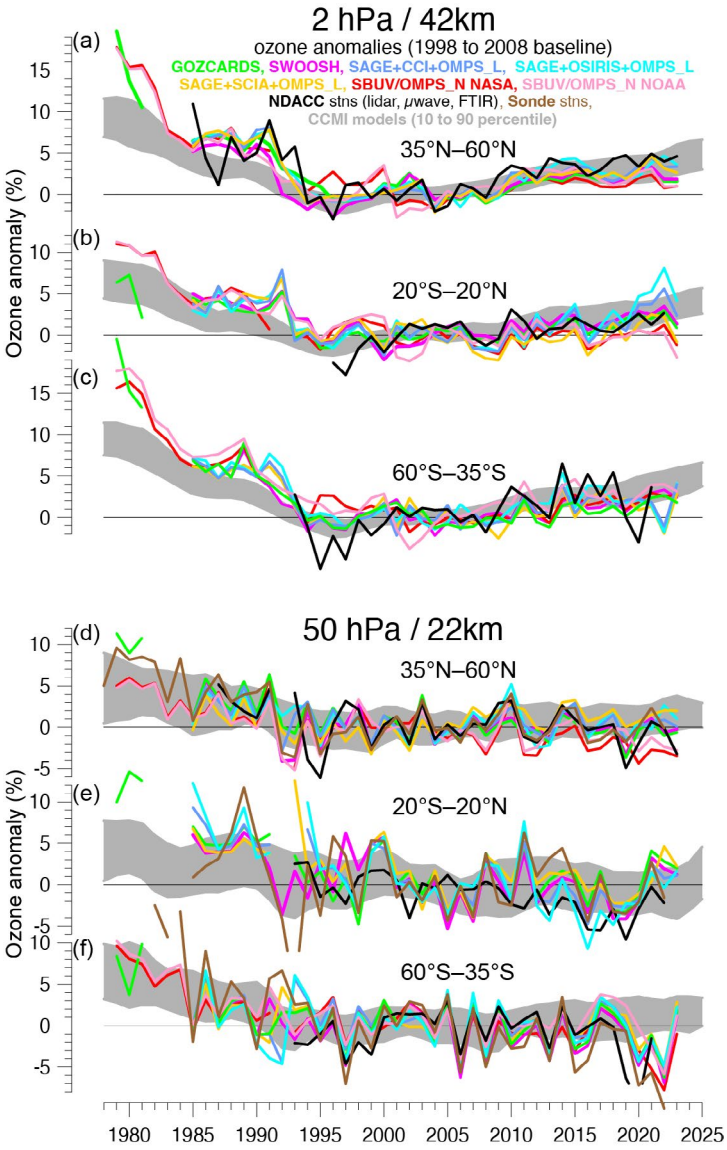

Fig. 2.72. Annual mean anomalies of ozone (%) in (a)–(c) the upper stratosphere near 42-km altitude or 2-hPa pressure, and (d)–(f) the lower stratosphere, near 22 km or 50 hPa for three zonal bands: 35°N–60°N, 20°S–20°N (tropics), and 35°S–60°S, respectively. Anomalies are with respect to the 1998–2008 baseline. Colored lines are long-term records obtained by merging different limb (GOZCARDS, SWOOSH, SAGE+CCI+OMPS_L, SAGE+OSIRIS+OMPS_L, SAGE+SCIAMACHY+OMPS_L) or nadir-viewing (SBUV, OMPS_N) satellite instruments. The nadir-viewing instruments have much coarser altitude resolution than the limb-viewing instruments. This can cause differences in some years, especially at 50 hPa. The black line is determined from merging ground-based ozone records at seven Network for the Detection of Atmospheric Composition Change (NDACC) stations employing differential absorption lidars and microwave radiometers. See Steinbrecht et al. (2017), Arosio et al. (2019), and Godin-Beekmann (2022) for details on the various datasets. Gray-shaded areas show the range of chemistry-climate model simulations from CCMI-1 refC2 (SPARC/IO3C/GAW 2019). Ozone data for 2023 are not yet complete for all instruments and are still preliminary.

7. STRATOSPHERIC WATER VAPOR

—S. M. Davis, K. H. Rosenlof, E. Asher, H. Vömel, R. M. Stauffer, and D. F. Hurst

In the aftermath of the January 2022 eruption of the Hunga Tonga–Hunga Ha'apai (HTHH) volcano (20.5°S, 175.4°W), which injected ~50 Tg–150 Tg water vapor (WV) into the stratosphere (3.5%–10% of the entire stratospheric burden; Millán et al. 2022; Vömel et al. 2022), WV concentrations remained at or near record-high levels through much of the stratosphere in 2023. By being injected into the tropical stratosphere between approximately 26 km (22 hPa) and 34 km (6 hPa), air from the eruption bypassed the tropical tropopause layer (TTL) "cold trap" that normally controls the amount of WV entering the stratosphere (Fig. 2.73a). This dramatic perturbation to WV and other stratospheric species (e.g., ozone; section 2g6) is expected to persist for years.

At the beginning of 2023, the HTHH stratospheric WV perturbation had already been transported upward within the rising branch of the Brewer-Dobson circulation in the tropics (Fig. 2.73a) and poleward into each hemisphere (Fig. 2.73b). The majority of the WV perturbation was still in the SH in January 2023. This hemispheric asymmetry was caused by the location and timing of the eruption, which was followed by strong poleward transport up to the SH polar vortex edge in the 2022 austral winter.

In 2023, the HTHH WV perturbation continued to spread poleward and downward in the NH (Figs. 2.74c,f,i). By the end of the year, elevated WV was evident in the lower stratosphere at high northern latitudes down to ~68 hPa/~19 km (Fig. 2.74i). Whereas the tropical (15°S–15°N) mean WV was at a record level in the mid-stratosphere (near ~30 hPa/24 km) for much of 2022 (relative to the 2004–21 mean), monthly WV anomalies in 2023 were at record levels in the upper stratosphere (Fig. 2.73a). For example, at and above 10 hPa/31 km, anomalies were 1.2 ppm to 1.8 ppm (parts per million, i.e., μmol mol^{-1}), corresponding to a deviation from the climatological mean of ~25%–30% (~10 std. dev.).

Even though the mid- and upper-stratospheric WV anomalies were most dramatic in 2023, lower-stratospheric WV anomalies (near 82 hPa/17 km) were also positive (wet) for all months (e.g., Figs. 2.73a,c), following a general trend towards more positive anomalies in the last five years, which is also evident in frost point measurements from the set of balloon-launching stations with long-term records (Fig. 2.75).

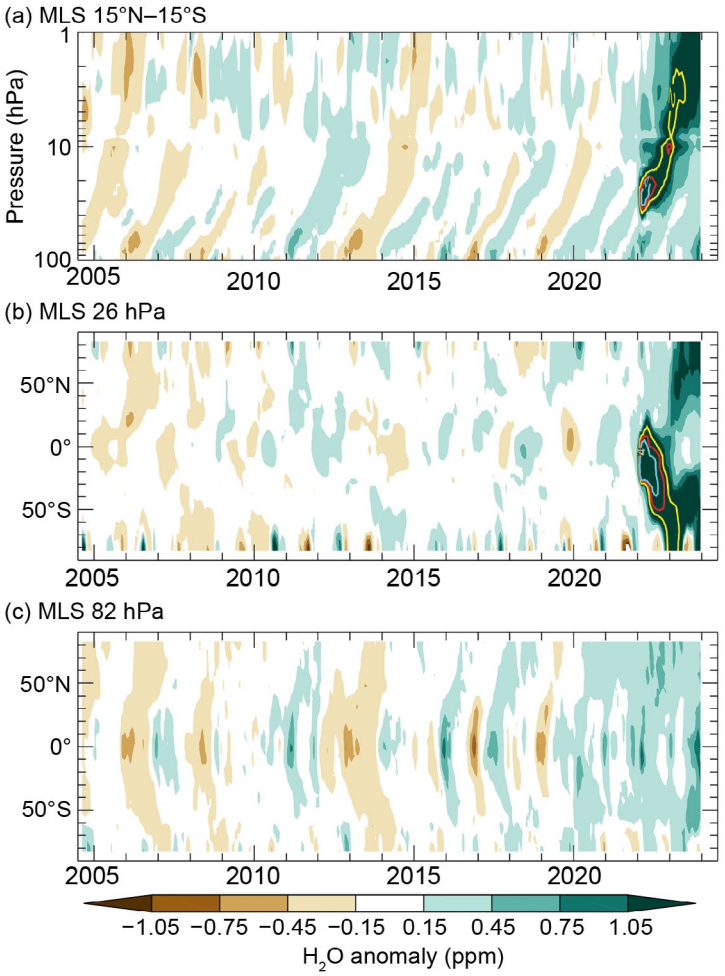

Fig. 2.73. (a) Vertical–time contour of tropical (15°S–15°N) lower-stratospheric water vapor (WV) anomalies, with the +2-, +3-, and +4-ppm values shown as yellow, red, and cyan contour lines, respectively. (b),(c) Latitude–time contour of WV anomalies at (b) 26 hPa and (c) 82 hPa, respectively. All panels are based on version 5.0 Aura Microwave Limb Sounder (MLS) data, which has collected near-global (82°S–82°N) measurements since Aug 2004. Anomalies are differences from the mean 2004–2021 water vapor mixing ratios (ppm) for each month. (a) shows the unprecedented injection of water vapor directly into the stratosphere by the Hunga Tonga–Hunga Ha'apai (HTHH) eruption, followed by its slow ascent through the tropical stratosphere. (b) shows the southward propagation of the plume at 26 hPa in 2022, followed by the downward transport of the HTHH-related anomalies in 2023, while (c) shows a more typical propagation of interannual-varying tropical lower-stratospheric WV anomalies to higher latitudes in both hemispheres following the second-warmest coldpoint and record wet tropical lower-stratospheric WV in 2023. (c) also shows the influences of dehydrated air masses from the Antarctic polar vortex as they are transported toward the Southern Hemisphere midlatitudes at the end of each year. Tick marks denote the beginning of each year.

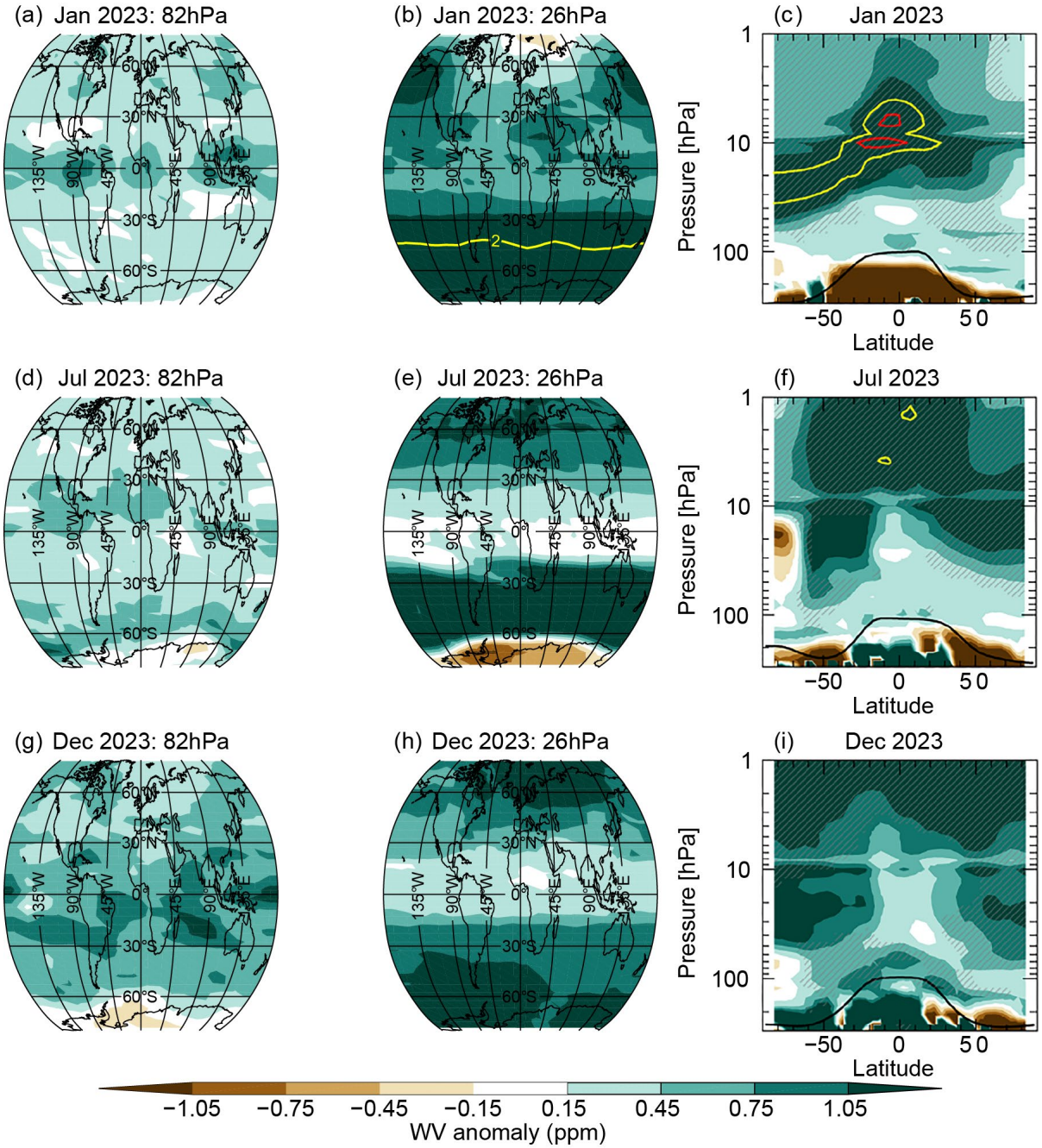

Fig. 2.74. Deseasonalized monthly lower stratospheric Aura Microwave Limb Sounder (MLS) anomalies (ppm; 2004–21 base period) at (a),(d),(g), 82 hPa and (b),(e),(h) 26 hPa. (c),(f),(i) show latitude–height cross-sections of the water vapor (WV) anomalies. Data are shown for Jan 2023 (top row), Jul 2023 (middle row), and Dec 2023 (bottom row). WV anomalies of +2 ppm and +3 ppm are shown with yellow and red contour lines, respectively. Hatching in the right column shows where the zonal-mean WV was at record values for the given month.

The 2023 WV anomalies in the lowermost tropical stratosphere are expected to be primarily caused by anomalies in tropical tropopause temperatures, although a contribution from WV-impacted air from higher latitudes via mixing is also plausible. Considering the whole time series, lower-stratospheric WV anomalies from the Aura Microwave Limb Sounder (MLS) and frost point hygrometers are highly correlated with tropical (15°S–15°N) cold-point tropopause (CPT) temperature anomalies (Figs. 2.75b,c). In 2023, tropical CPT temperatures were the second highest on record (annual mean anomaly was +0.73 K; second only to 2022, which was +0.76 K), and MLS tropical stratospheric WV entry values at 82 hPa were at their highest recorded levels in the 20-year MLS record (2023 annual mean anomaly was +0.39 ppm, compared to +0.27 ppm in 2022).

La Niña conditions were present at the beginning of 2023 (see section 4b), which during boreal winter are typified by weaker tropical lower-stratospheric upwelling and anomalously warmer CPTs (e.g., Garfinkel et al. 2021). The positive tropical lower-stratospheric WV anomalies at the beginning of 2023 are thus consistent with the expected La Niña response. Following a brief transition to neutral conditions, El Niño conditions emerged in May and strengthened through the rest of the year (see section 4b). The net effect of ENSO on water vapor is complex, but there is some evidence of moistening associated with strong El Niño events (Garfinkel et al. 2018).

The quasi-biennial oscillation (QBO) phase at 70 hPa was westerly throughout 2023 (section 2e3). The QBO westerly phase is associated with anomalously weak tropical upwelling and warm temperatures, which can impact the CPT. Thus, the QBO westerlies and La Niña likely enhanced lower-stratospheric WV at the beginning of 2023, while the effects of the strong El Niño may have contributed to the record-breaking stratospheric entry values of water vapor later in the year.

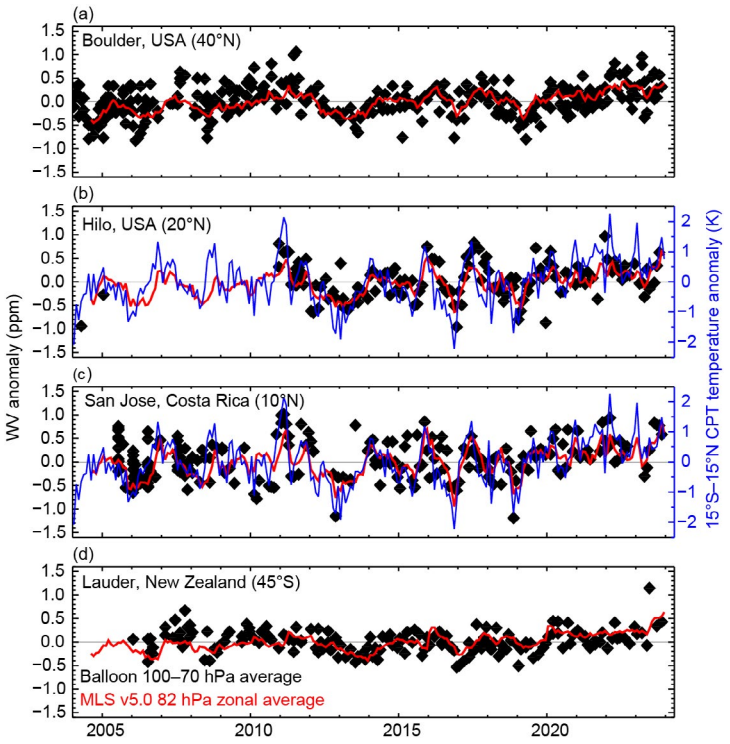

Fig. 2.75. Lower-stratospheric water vapor (WV) anomalies over four balloon-borne frost point (FP) hygrometer stations. Each panel shows the lower-stratospheric anomalies of individual FP soundings (black) and of monthly zonal averages from Microwave Limb Sounder (MLS) data at 82 hPa in the 5° latitude band containing the FP station (red). High-resolution FP vertical profile data were averaged between 70 hPa and 100 hPa to emulate the MLS averaging kernel for 82 hPa. Each MLS monthly zonal mean was determined from 2000–3000 profiles. Anomalies for MLS and FP data are calculated relative to the 2004–21 period for all sites except Hilo (2011–21). Tropical cold-point tropopause anomalies based on the MERRA-2 reanalysis ([b],[c], blue curve) are generally well correlated with the tropical lower-stratospheric WV anomalies.

8. CARBON MONOXIDE

—J. Flemming and A. Inness

The global burden of carbon monoxide (CO) increased in 2023 compared to previous years due to exceptionally high emissions from wildfires in Canada (Plate 2.1ac; Fig. 2.76; section 2h3; see Sidebar 7.1). Western Canada (i.e., Northwest Territories, Alberta) experienced increased fire frequency from May to September, and eastern Canada (i.e., Quebec) was the center of wildfires in May and June (see Sidebar 7.1). The resulting emissions led to increased total-column CO values of up to 25% in the affected areas and the outflow region over the Atlantic.

Carbon monoxide is emitted into the atmosphere by combustion processes originating from anthropogenic sources, such as road transport and energy generation, as well as from wildfires (Szopa et al. 2021). Of similar or larger size than these emissions is the chemical production of CO in the atmosphere from formaldehyde as part of the oxidation chains of methane, isoprene, and other volatile organic trace gases. Oxidation of CO by reaction with the hydroxyl radical is the main loss process for CO, resulting in an atmospheric lifetime of one to two months. The presence of CO is one of the factors that controls the abundance of tropospheric ozone, which is a short-lived pollutant and climate forcer (section 2g4).

According to the CAMS (https://atmosphere.copernicus.eu/) reanalysis of atmospheric composition (Inness et al. 2019), the global CO burden has decreased over the last 20 years (Fig. 2.76a). The decrease is likely caused by both decreased anthropogenic emissions in most parts of the world, as well as a strong decrease in fire frequency compared to the early 2000s, mainly in South America. In recent years, positive global and regional CO anomalies have occurred because of intense wildfires related to exceptional regional meteorological conditions such as the peat fires in Indonesia in 2015 that were associated with El Niño conditions, or boreal wildfires such

as those in Siberia during a heatwave in 2021. The positive CO anomalies in 2023 in North America (Fig. 2.76b) and western Australia were also caused by increased wildfire activity supported by exceptionally warm and dry conditions, some possibly related to the onset of El Niño in May 2023. The main areas of seasonal savanna wildfires, such as tropical Africa and tropical South America, showed negative anomalies in 2023 (Plate 2.1ac).

CAMS has produced a retrospective analysis of CO, aerosols, and ozone since 2003 by assimilating satellite retrievals of atmospheric composition with the European Centre for Medium-Range Weather Forecasts (ECMWF) model (Inness et al. 2019). This reanalysis assimilated global thermal infrared total-column CO retrievals (V6 from 2003 to 2016; NRT V7 from January 2017 to June 2019; NRT V8 from July 2019 to present) of the Measurement of Pollution in the Troposphere (MOPITT) instrument (Deeter et al. 2014, 2017, 2019), excluding observations poleward of 65°N and 65°S, using the ECWMF four-dimensional variational assimilation (4D-VAR) data assimilation system. Anthropogenic emissions were taken from the MACCity inventory (Granier et al. 2011) that accounts for projected emission trends according to the Representative Concentration Pathways (RCP) 8.5 scenario, but COVID-19-related emissions modifications were not applied. Biomass burning emissions were taken from the Global Fire Assimilation System (v1.4; Kaiser et al. 2012; section 2h3) that is based on MODIS fire radiative power retrievals (Giglio et al. 2016). Monthly mean biogenic emissions simulated by the Model of Emissions of Gases and Aerosols from Nature version 2.1 (MEGAN2.1) model following Sindelarova et al. (2014) were used for the period 2003–17, after which a monthly-mean climatology derived from the 2003–17 simulations was applied.

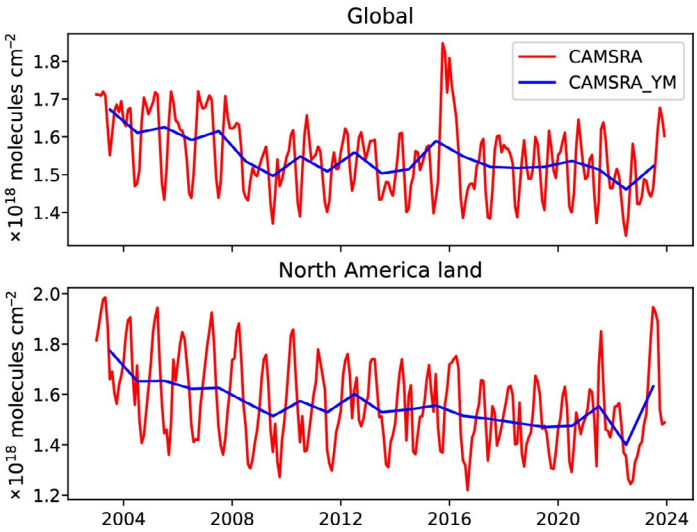

Fig. 2.76. Time series of the area-averaged monthly mean (red) and annual mean (blue, yearly mean [YM]) total column carbon monoxide (CO; × 10^{18} molecules cm^{-2}) over (a) the whole globe and (b) North America (30°N–70°N, 55°W–165°W, land points only for b) from the CAMS reanalysis for the period 2003–23.

h. Land surface properties

1. TERRESTRIAL SURFACE ALBEDO DYNAMICS

—F. Cappucci, N. Gobron, and G. Duveiller

The terrestrial surface albedo is the ratio between the solar radiation reflected by Earth's surface and the incident light. It is a key forcing parameter controlling the partitioning of radiative energy between the atmosphere and the surface. Increases in vegetation lead to a "darkening" effect, as more radiation is absorbed by plants in the visible spectrum. At the same time, the near-infrared albedo increases slightly, as healthy vegetation tends to reflect this part of the spectrum. Desertification and the related exposure of bare soil or increases in snowpack lead to a brighter surface and higher surface albedo.

In 2023, the normalized anomaly (2003–20 base period) of white-sky albedo in the visible broadband (Plate 2.1ad) indicated a notable surface darkening (values below –15%) of more than 17% of the land surface, compared to 6% recorded in 2022 (Duveiller and Gobron 2023). The darkening effect over Quebec and Nunavut and over large parts of Siberia was affected by the early melting of surface snow, starting in the second quarter of the year (section 2c5), together with the continuous decline in surface snow cover since the beginning of this century (Young 2023). The decreases in visible surface albedo recorded in central and eastern Europe, eastern China, western India, Japan, northern Australia, and sub-Saharan Africa were associated with a slight increase of the near-infrared albedo (Plate 2.1ae) as vegetation density increased over these areas (section 2h2).

In some regions, such as in eastern Australia, western Africa, and the Arabian Peninsula, 2023 displayed opposite signs of both albedo anomalies with respect to 2022. These fluctuations can be attributed to vegetation dynamics that are sensitive to water availability and temperature variations. Positive anomalies recorded over the central United States and Alaska resulted from above-average snow cover, which even extended during late spring after snowstorms in some of these regions.

The patterns of the zonally averaged albedo anomalies in the visible (Fig. 2.77a) and near-infrared (Fig. 2.77b) parts of the spectrum follow the darkening trend of previous years. Both figures show the large interannual variations related to seasonal snow in winter and spring at mid- and high-northern latitudes, but also the general trend in increased vegetation greening during summer periods. Persistent negative anomalies are noticeable for 2022 and 2023 between 15°N and 30°N in the visible albedo (with weak anomalies in the near-infrared domain), mainly due to the increase in vegetation density over China and India. Persistent negative anomalies in 2022/23 in both visible and near-infrared domains are detected between 10°S and 30°S, indicating a deviation from average conditions mainly over southern Africa and Australia.

The amplitude of the globally smoothed average anomaly (solid black line) is within

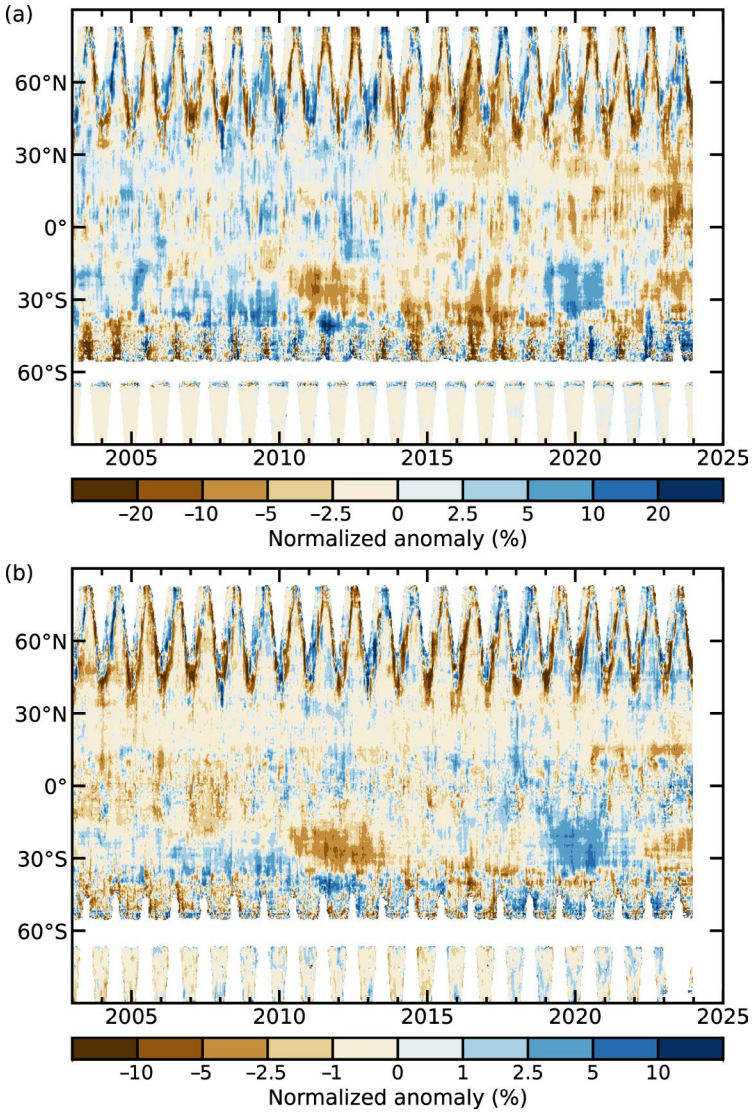

Fig. 2.77. Zonally averaged (a) white sky visible (%) and (b) near-infrared (%) broadband land surface albedo anomalies for the period 2003–23 (2003–20 base period).

±4% in the visible domain during 2003–23 (and within ±1% for the near-infrared; Fig. 2.78). The year 2023 is characterized by a trend to more negative anomalies in both the visible and near-infrared domains, driven by the dominant contribution from the Northern Hemisphere regions.

This analysis was based on satellite products derived from the Moderate Resolution Imaging Spectroradiometer (MODIS) instrument on board the *Aqua* and *Terra* satellite platforms to generate a long-term record from 2002 to 2022 (Schaaf et al. 2002). The 2023 data are from the Visible Infrared Imaging Radiometer Suite (VIIRS) on board the Suomi NPP. Although VIIRS has been assessed as a strong candidate for the continuation of the MODIS archive (Liu at al. 2017), a small difference between VIIRS and MODIS surface albedo was noted; VIIRS 2023 data were bias-corrected accordingly. The anomalies were calculated at a 10-day frequency, based on the 2003–20 reference period.

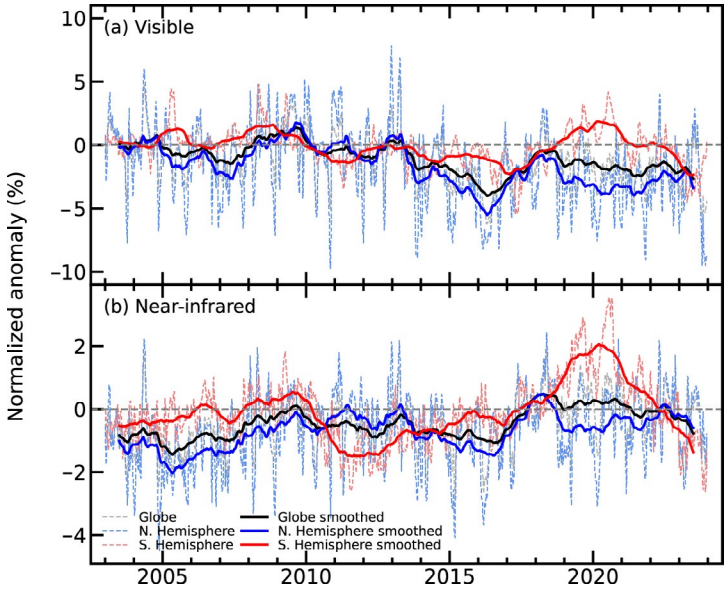

Fig. 2.78. Global (black lines), Northern Hemisphere (blue), and Southern Hemisphere (red) land surface (a) visible and (b) near-infrared broadband albedo normalized anomalies (%; 2003–20 base period) for the period 2003–23. Dotted lines denote each 10-day period; solid lines indicate the 12-month running averaged mean.

2. TERRESTRIAL VEGETATION DYNAMICS

—N. Gobron and F. Cappucci

The fraction of absorbed photosynthetically active radiation (FAPAR) reveals the amount of vegetation as well as its health and is important for assessing primary productivity and the associated fixing of atmospheric carbon dioxide by plants. FAPAR anomalies in 2023 compared to the 1998–20 average show a greater extent of positive values than negative values in the level of vegetation productivity across the world (Plate 2.1af).

Positive anomalies (increased plant photosynthesis) over the northern-central region of the United States and southern-central Canada (i.e., Great Plains) indicate that vegetation health recovered from last year due to above-average precipitation associated with higher temperatures. In contrast, fire events over the Quebec region (section 2h3) resulted in negative annual anomalies (decreased plant photosynthesis) as more than five million hectares of boreal forest burnt (see Sidebar 7.1 for details). The positive annual anomalies over Europe highlighted that Earth's surfaces continued the greening trend due to higher temperatures as well as plentiful rainfall.

Positive anomalies over southern Brazil and Paraguay were due to the transition to El Niño, which started in spring with extreme rainfall (section 2d4). In contrast, severe heatwaves, especially in Chile and southwestern Argentina (see section 7d3), impacted vegetation health, leading to negative FAPAR anomalies. The Central African Republic showed positive anomalies that were due to above-normal precipitation during the rainy seasons, whereas Namibia suffered from drought during the first half of the year (see section 7e). A major part of northern and southeastern Australia had positive FAPAR anomalies, as both precipitation and temperature were above normal (see section 7h4).

Figure 2.79 shows that all latitudes—though more markedly over the Southern Hemisphere (SH)—were affected by negative anomalies (i.e., less than −0.04) from 2002 to 2014, and that positive patterns were dominant in both hemispheres afterward. In 2023, the monthly anomalies were positive at nearly all latitudes, apart from a few places such as south of 20°S. Regions around 50°S had strong negative patterns at both the start and end of the year.

Figure 2.80 shows the global and hemispheric anomalies, with more seasonal variability in the less-landed SH than in the Northern Hemisphere (NH). FAPAR anomalies over the SH were positive before 2002, then negative until 2010. Thereafter, there were positive peaks in 2011,

2014, 2016/17, and 2022, with few negative months after 2013. The NH was positive in 1998, negative from 1999 to 2013, and positive thereafter. This trend towards positive values is linked to the trend for surface temperatures over land (see Fig. 2.1b). FAPAR annual anomalies were 0.013 (0.006) for NH (SH) in 2023 (with record values set in the NH [>0.02] at the end of the year).

Optical space sensors are used to infer FAPAR, an essential climate variable of the Global Climate Observation System (GCOS 2022). The 2023 analysis merges 26 years of global FAPAR products based on four optical sensors: Sea-Viewing Wide Field-of-View Sensor (SeaWiFS), Envisat/MERIS, Terra-Aqua/MODIS and Sentinel-3/Ocean and Land Colour Instrument (OLCI) from 1998 to 2023 (Gobron et al. 2010, 2022; Pinty et al. 2011; Gobron and Robustelli 2013). Uncertainties of each dataset were derived through error propagation techniques and comparisons against multiple proxies using ground-based measurements and radiative transfer simulations that all provide an estimate of the uncertainties and biases. This long-term FAPAR dataset has an estimated average uncertainty of ~5%–10%.

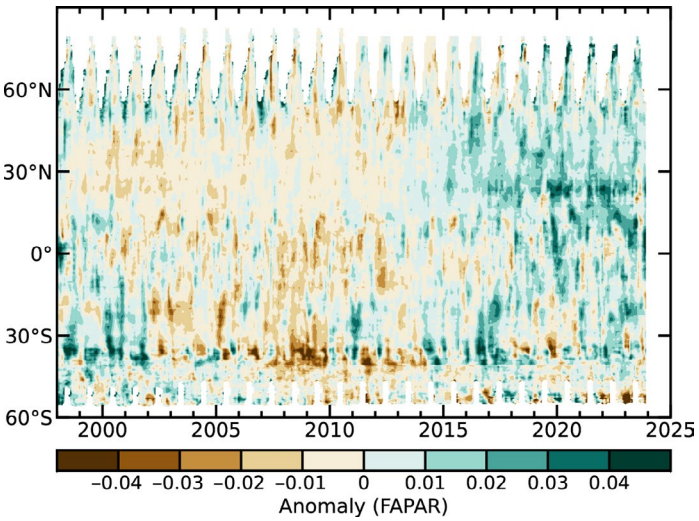

Fig. 2.79. Zonally averaged fraction of absorbed photosynthetically active radiation (FAPAR) anomalies for 1998–2023 (1998–2020 base period).

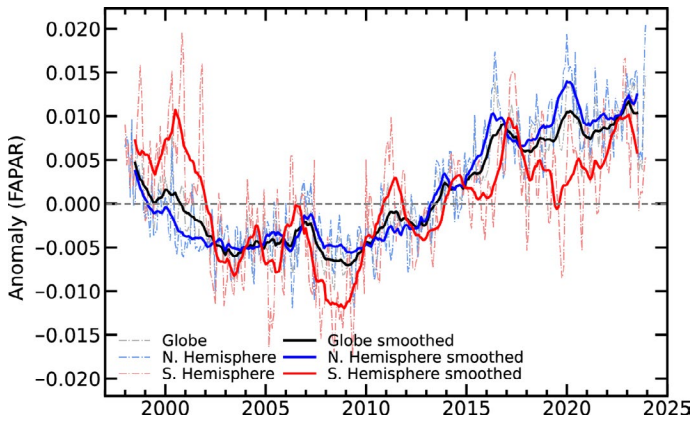

Fig. 2.80. Global (black lines), Northern Hemisphere (blue), and Southern Hemisphere (red) fraction of absorbed photosynthetically active radiation (FAPAR) anomalies for 1998–2023 (1998–2020 base period). Dotted lines denote each monthly period; solid lines indicate the six-month running averaged mean.

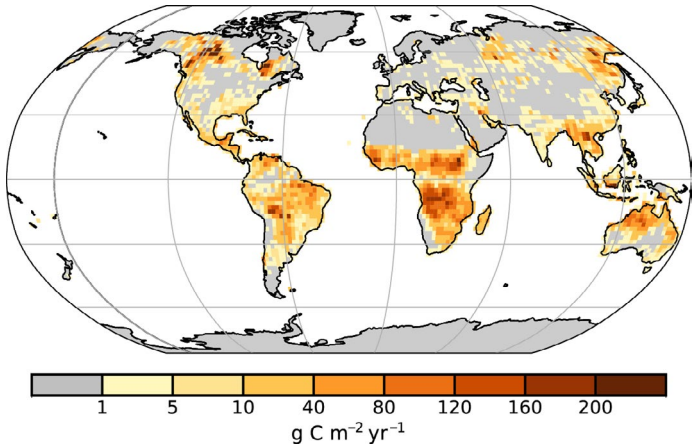

Fig. 2.81. Global map of fire activity (g C m^{-2} yr^{-1}) in 2023 in terms of carbon consumption. (Source: CAMS-GFASv1.4.)

3. BIOMASS BURNING

—J. W. Kaiser, M. Parrington, and D. Armenteras

Two distinct trends that have emerged in global biomass burning over the last decade continued in 2023. Many savanna regions, which dominate global fire emissions, saw a decline related to agricultural expansion, while many forested regions—where climate change with severe drought periods increases the flammability of the landscape (e.g., Xing and Wang 2023 for the Arctic)—experienced longer and more intense wildfire episodes (Plate 2.1ag). The amount of biomass burning, referred to here as "fire activity" and more commonly as wildfires, is characterized here as the amount of carbon that is consumed by fire and emitted into the atmosphere. Of this, 80%–95% is emitted as carbon dioxide (CO_2), and the rest is oxidized to CO_2 in the atmosphere or released as particulate matter. In a stable ecosystem, virtually all of this CO_2 is assimilated again by the regrowth of vegetation. Currently however, 20% is estimated to contribute to the long-term build-up of atmospheric CO_2 (Zheng et al. 2023).

Global annual total estimated fire emissions were close to the 2003–20 average in 2023 in the GFASv1.4 dataset (Table 2.12). However, 2022 had the lowest global emissions in GFAS, and the 2023 emissions represent an increase of 26% from 2022. The years 2019 and 2023 have similar

emission budgets, and both are higher than any other year after 2015. The increase in 2023 was driven by anomalously large-scale wildfires that burned persistently in forests across Canada from May to September (Fig. 2.81; Plate 2.1ag; see Sidebar 7.1). These wildfires consumed five times more biomass than the average for the 2003–20 reference period and three times more than the previously recorded maximum (2014; cf. Fig. 2.82a). In contrast, the United States experienced its lowest annual total fire emissions on record, and wildfire emissions from boreal Eurasia were 28% below the 2003–20 average.

African fire carbon emissions accounted for roughly half of the total global emissions during the 2000s but their contribution has since shrunk to ~40%. The decreasing trend in savanna regions continued in 2023 over Northern-Hemisphere Africa with emissions 20% below the 2003–20 average, the third successive year with lower fire activity than any years in the record prior to 2019 (Fig. 2.82b). Southern-Hemisphere Africa and South America also contributed to the

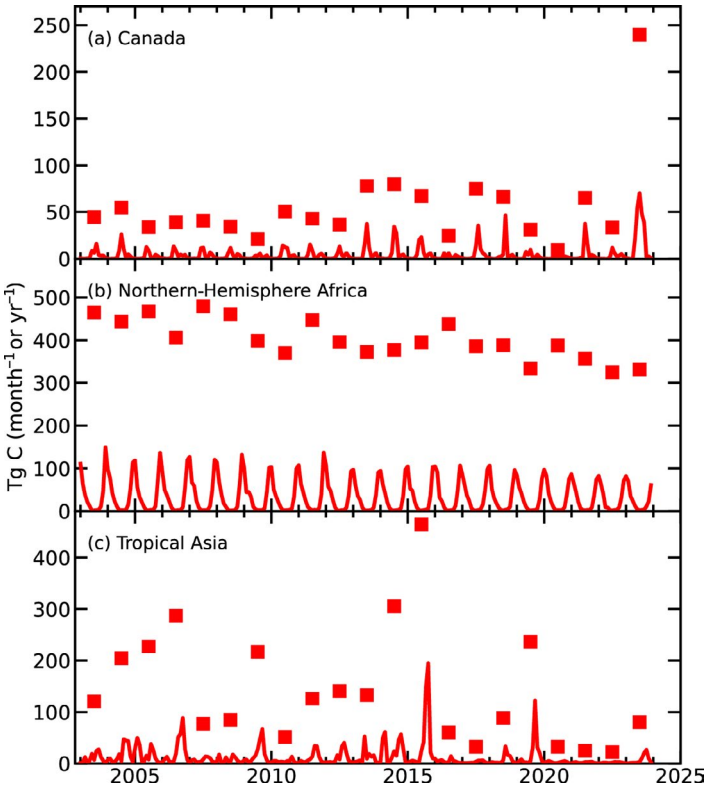

Fig. 2.82. Regional time series of monthly (lines in Tg C month^{-1}) and annual (symbols in Tg C yr^{-1}) biomass burning activity for (a) Canada, (b) Northern-Hemisphere Africa, and (c) tropical Asia.

Table 2.12. Annual continental-scale biomass burning budgets in terms of carbon emission (Tg C yr^{-1}). (Source: CAMS-GFASv1.4.)

Name of Region	Location	Biomass Burning 2003–20 Mean value (Range)	Biomass Burning 2023 Value	Biomass Burning 2023 Anomaly (%)
Global	–	2052 (1776– 2388)	1996	–53 (–3%)
North America	30°N–75°N, 190°E–330°E	88 (60–116)	265	+177 (–201%)
Central America	13°N–30°N, 190°E–330°E	49 (35–67)	53	+4 (+8%)
South America	13°N–60°S, 190°E–330°E	368 (243–540)	338	–30 (–8%)
Europe and Mediterranean	30°N–75°N, 330°E–60°E	41 (27–70)	29	–12 (–30%)
N. Hem. Africa	0°–30°N, 330°E–60°E	412 (333–479)	331	–81 (–20%)
S. Hem. Africa	0°–35°S, 330°E–60°E	486 (433–548)	459	–27 (–6%)
Northern Asia	30°N–75°N, 60°E–190°E	204 (118–446)	147	–57 (–28%)
Southeast Asia	10°N–30°N, 60°E–190°E	120 (85–157)	116	–4 (–3%)
Tropical Asia	10°N–10°S, 60°E–190°E	161 (33–464)	80	–80 (–50%)
Australia	10°S–50°S, 60°E–190°E	123 (54–226)	177	+54 (+44%)
Canada	47°N–75°N, 219°E–310°E	46 (10–80)	240	+194 (+421%)
Western United States (sub-region)	30°N–49°N, 230°E–260°E	19 (8–42)	16	–2 (–12%)

trend. Increased wildfire emissions related to warmer and drier conditions occurred in tropical regions of Australia between September and November (Plate 2.1ag). Fire activity in tropical Asia—including Indonesia—increased relative to the previous three years (Fig. 2.82c) but was significantly lower than the increased emissions of 2006, 2015, and 2019 despite the El Niño and positive Indian Ocean dipole-related conditions. In this region, extreme fires are driven by the combination of agricultural use of fires on plantations, in particular for palm oil and pulp production, and drought conditions during El Niño years, which lead to a high persistence of fires on peatlands that have become exposed by deforestation of tropical rainforest. The relatively low fire activity across the region in 2023 indicates that stricter policies by the Indonesian government that restrict the use of agricultural fires are largely effective.

While South America overall experienced moderately below-average fire activity (–8%; Plate 2.1ag), seasonal fires increased in several regions. Chile experienced its second-highest wildfire activity for any January–February period in 20 years, with almost 4 Tg C emissions (Fig. 2.81). In the same period, the Corrientes region in Argentina reached its second-highest emissions on record. The latter part of the year saw a spike in fires across Bolivia and some Brazilian states (including parts of the Amazon), which was largely driven by drought conditions in the Pantanal wetlands (section 2d11). Bolivia experienced its highest fire activity since 2010, with the peak shifting to October and November (peak monthly emissions of 30 Tg C in November) instead of the usual August and September. Fire emissions from the Brazilian Amazon continued the recent trend with below-average fire since 2003 emissions in Mato Grosso but increased fires in Amazonas (e.g., the highest for the month of June since 2007 [de Oliveira et al. 2023] and the highest for November [https://atmosphere.copernicus.eu/2023-year-intense-global-wildfire-activity]) despite decreased deforestation in the Brazilian Amazon relative to 2022 (http://www.obt.inpe.br/OBT/assuntos/programas/amazonia/prodes); this suggests that fire types other than those related to deforestation have become relatively more important in South America. The increasing wildfires indicate a possible effect of the 2023 El Niño, which favors hot and dry conditions and increases general vegetation flammability, but also a lag effect of a period of weakened enforcement of environmental laws that favored old pastures burning earlier in the dry season (de Oliveira et al. 2023).

The GFAS is operated by the Copernicus Atmosphere Monitoring Service (CAMS) and produces global fire emission estimates (Kaiser et al. 2012) in near-real-time based on the MODIS Fire Radiative Power products (Giglio et al. 2016). A combination of real-time and consistently reprocessed products by CAMS are used here, with input from MODIS Collection 6 for the entire period of 2003–23. The biases with respect to Collection 5 and between satellites have been corrected. The time series in Plate 1.1 also places GFAS in the context of GFED4s, which is primarily based on burnt area observation and dates to 1997 (van der Werf et al. 2017)

4. PHENOLOGY OF PRIMARY PRODUCERS

—D. L. Hemming, O. Anneville, Y. Aono, T. Crimmins, N. Estrella, S. -I. Matsuzaki, A. Menzel, I. Mrekaj, J. O'Keefe, A. D. Richardson, J. Rozkošný, T. Rutishauser, R. Shinohara, S. J. Thackeray, A. J. H. van Vliet, and J. Garforth.

Vegetation phenology, "the rhythm of the seasons", is strongly affected by climate variations and can influence the local and global climate via modifications in the land–atmosphere exchanges of energy, moisture, and carbon (Hassan et al. 2024). A range of satellite- and surface-based observations monitor phenological variability across space and time.

PhenoCam (http://phenocam.nau.edu/) is a network of over 800 automated digital cameras monitoring phenological changes in a wide range of ecosystems around the world (Richardson 2019; Seyednasrollah et al. 2019). The highest-density and longest-running PhenoCam sites (of which there are over 50 with more than 10 years of observations) are in the United States. Indicators of start of season (SOS_{PC}) and end of season (EOS_{PC}) were estimated from PhenoCam data and ground observation (GO) of red oak (*Quercus rubra*; SOS_{GO}, EOS_{GO}) in Harvard Forest, a deciduous forest in Massachusetts in the United States (Richardson and O'Keefe 2009; O'Keefe

2023), and from red oak observations across the northeastern United States contributed to *Nature's Notebook* (SOS_{NN}, EOS_{NN}), the USA-National Phenology Network's (USA-NPN) phenology monitoring platform (Rosemartin et al. 2014; Crimmins et al. 2022). Interannual variations in the start and end of season dates at Harvard Forest are broadly consistent with the broader-scale USA-NPN data (Figs. 2.83a,b; Table 2.13). In 2023, SOS_{PC}, SOS_{GO}, and SOS_{NN} were 6, 11, and 13 days earlier, respectively, than in 2022, while EOS_{PC}, EOS_{GO}, and EOS_{NN} were 11, 8, and 0 days later than in 2022. SOS_{PC} (EOS_{PC}) was 5 days earlier (5 days later) than the 2011–20 baseline mean, resulting in a growing season length of 177 days, 17 days longer than in 2022, and 10 days longer than the baseline (167±7 days).

The USA-NPN's extended Spring Index (SI-x), a model that reflects the onset of spring-season biological activity (Schwartz et al. 2013; Crimmins et al. 2017), estimated widespread earlier "first leaf" in 2023 across the eastern United States and later first leaf across the western United States compared with 2022 or the 2011–20 mean (Figs. 2.83a,b). These estimates were consistent with the SOS_{PC} and SOS_{GO} observations at Harvard Forest and SOS_{PC} observations from six other sites across the country (see Fig. 2.83 for details). They were more than 14 days earlier or later than recent years across many parts of the United States, largely due to warmer- (and cooler-) than-average late winter/spring 2023 temperatures across the eastern (and western) United States.

Start- and end-of-season indicators for native oak trees (*Quercus robur* and/or *Quercus petraea*) at European sites in Germany (D), Netherlands (NL), Slovakia (SK), and the United Kingdom (UK) are represented by observations of first leaf (SOS) and leaf fall or bare tree (EOS; Table 2.13; Figs. 2.84c,d). These events have been shown to be strongly influenced by spring and winter temperatures across Europe (Menzel et al. 2020). In 2023, SOS across all four European countries was later than usual. Compared to the 2000–20 mean, SOS dates in D, NL, SK, and UK were later by 3, 1, 5, and 2 days, respectively, and EOS dates were later by 8, 11, 6, and 4 days (Table 2.13). The later SOS and EOS dates across Europe were in part associated with relatively cool spring temperatures, delaying leaf out, followed by warm autumn temperatures, which

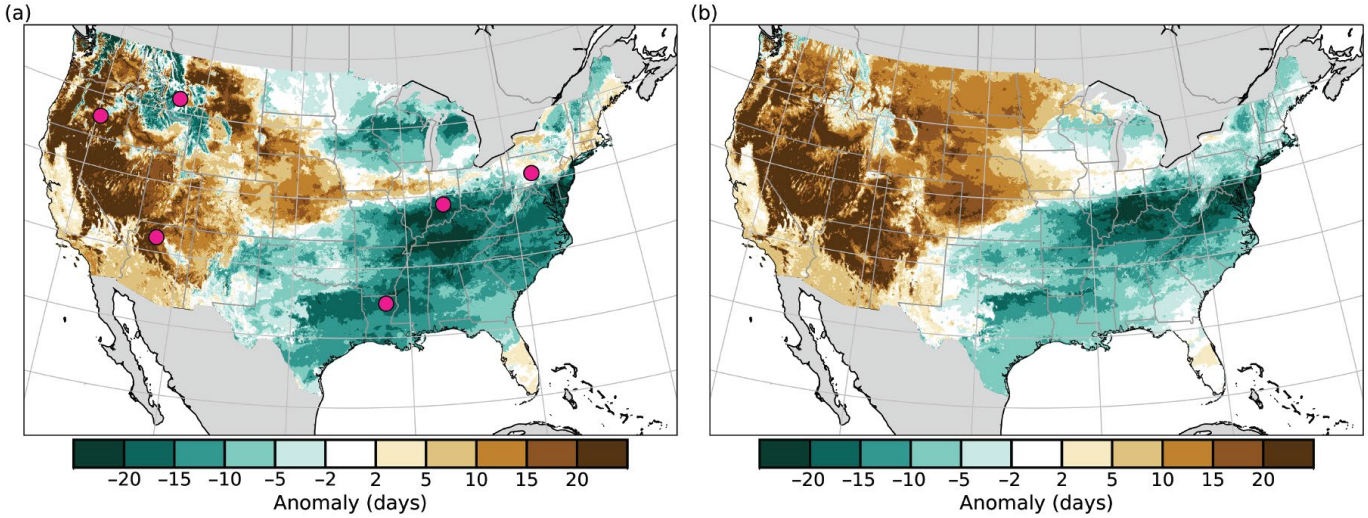

Fig. 2.83. 2023 'first leaf' date anomalies across the United States relative to (a) 2022 and (b) the 2011–20 baseline, estimated using the USA National Phenological Network's (USA-NPN) extended Spring Index (SI-x) model (Source: https://www.usanpn.org/data). Negative (green) values show earlier first leaf and positive (brown) values are later estimates for 2023. First leaf SI-x anomalies are generally consistent with start of season PhenoCam (SOS_{PC}) anomalies at the following six sites highlighted as points in (a): 1) a deciduous forest in Indiana (Morgan Monroe State Forest, SOS_{PC} = 15 days earlier than in 2022, and 6 days earlier than 2011–20); 2) a deciduous forest in Pennsylvania (Susquehanna Shale Hills Critical Zone Observatory, SOS_{PC} = 18 days earlier than in 2022); 3) a deciduous forest in Louisiana (Russell Sage State Wildlife Management Area, SOS_{PC} = 18 days earlier than in 2022); 4) a sagebrush site in Oregon (Eastern Oregon Agricultural Research Center, SOS_{PC} = 29 days later than in 2022); 5) a grassland site in Montana (Butte, SOS_{PC} = 6 days earlier than in 2022, but 1 day later than during 2011–20); and 6) a wooded shrubland site in Arizona (Grand Canyon National Park, SOS_{PC} = 12 days later than in 2022).

encouraged later leaf activity (for UK, see Kendon et al. 2023). The 2023 EOS in D was the latest since 2000, and this was associated with the warmest September temperatures on record (since 1881; Deutscher Wetterdienst [DWD] 2023; section 7f3). In SK, below-average temperatures during the end of March and April increased the prevalence of nocturnal frosts and delayed the first leaf onset, while extremely warm September and above-average October temperatures combined with ample precipitation resulted in the latest EOS dates across SK in 2023 since 2000. While the phenological timing of leaf out shifted later in the season in 2023, the length of the growing season for oak at the European locations was close to the baseline mean.

In Kyoto, Japan, full bloom dates (FBD) for a native cherry tree (*Prunus jamasakura*) have been recorded since 812 AD (Aono and Kazui 2008). For the Arashiyama district of Kyoto, these are updated with daily observations at train stations that are recorded in newspapers and on websites by railway passengers. In 2023, the FBD was the earliest on record for Arashiyama at 12 days earlier than the baseline (2000–20 mean; Table 2.13; Fig. 2.84e).

Monitoring data on lake water concentrations of the photosynthetic pigment chlorophyll-*a* were available to estimate spring phytoplankton phenology (nine Northern Hemisphere and one Southern Hemisphere lakes are reported; Fig. 2.85). The seasonal timing was estimated for start of season (SOS_L; Park et al. 2016), day of maximum concentration (DOM_L), and center of gravity (COG_L), which is an estimate of the mid-point of the plankton bloom (Edwards and Richardson 2004). The lake basins showed great interannual variation and mixed phenological behavior in 2023 relative to 2000–20. The SOS_L and COG_L occurred earlier than the baseline median for most of the lakes—7 and 8 of 10, respectively—whereas no consistent pattern was observed for DOM_L.

Table 2.13. Day of year (doy, equivalent to Julian day) and date of start of season (SOS), end of season (EOS), and full bloom date (FBD; cherry tree observations only) for land phenology records in USA (Harvard: PhenoCam, red oak, and USA National Phenology Network [USA-NPN] mean covering northeastern USA), Europe oak records (Germany, Netherlands, Slovakia, and United Kingdom), and Japan (native cherry tree observations in Japan). The baseline period is 2000–20 for all records except PhenoCam and USA-NPN which have baseline periods of 2008–22 and 2011–22, respectively, spanning the available observations. Growing season length for 2023 and the baseline mean are calculated as EOS minus SOS or FBD as appropriate for the record. Negative/positive values represent earlier/later dates for 2023 relative to the baseline mean.

Location/ Record	SOS/FBD 2023 (doy, date)	SOS/FBD Baseline (doy, date)	SOS/FBD Difference 2023 – Baseline (days)	EOS 2023 (doy, date)	EOS Baseline (doy, date)	EOS Difference 2023 – Baseline (days)	Growing season EOS–SOS 2023 (days)	Growing season EOS–SOS Baseline mean (days)
Harvard PhenoCam	123 3 May	128 8 May	–5	300 27 Oct	295 22 Oct	+5	177	167
Harvard red oak	122 2 May	128 8 May	–6	299 26 Oct	293 20 Oct	+6	177	165
Northeastern USA-NPN	113 23 Apr	125 5 May	–12	265 22 Sep	278 5 Oct	–13	152	153
Germany	121 1 May	118 28 Apr	+3	318 14 Nov	310 6 Nov	+8	197	192
Netherlands	111 21 Apr	110 20 Apr	+1	342 8 Dec	331 27 Nov	+11	231	221
Slovakia	121 1 May	116 26 Apr	+5	297 24 Oct	291 18 Oct	+6	176	175
UK	116 26 Apr	114 24 Apr	+2	339 5 Dec	335 1 Dec	+4	223	221
Japan	84 25 Mar	96 6 Apr	–12	--	--	--	--	--

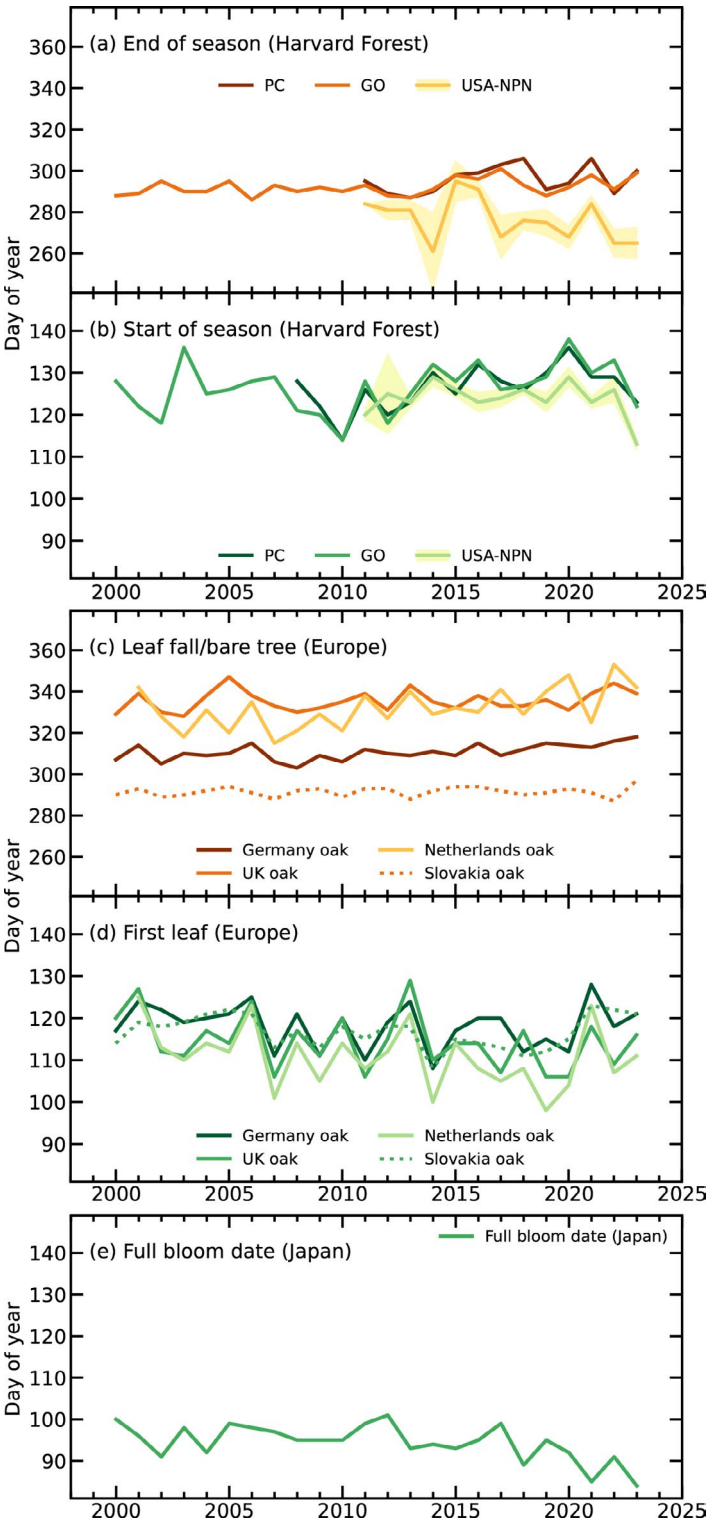

Fig. 2.84. Day of year of spring (greens) and autumn (oranges) vegetation phenology indicators for: (a),(b) Harvard Forest, Massachusetts, USA, derived from PhenoCam (PC), ground observations (GO) of red oak (Quercus rubra), and the USA-National Phenology Network (USA-NPN) regional-scale means of red oak observations (calculated across the northeastern states of Pennsylvania, New Jersey, New York, Connecticut, Rhode Island, Massachusetts, Vermont, New Hampshire, and Maine, ±1 std. error shaded); (c),(d) Germany, United Kingdom, Netherlands, and Slovakia mean of native oak observations (*Quercus robur* and/or *Quercus patrea*), and (e) Kyoto (Arashiyama district), Japan, full bloom date observations of native cherry trees (*Prunus jamasakura*).

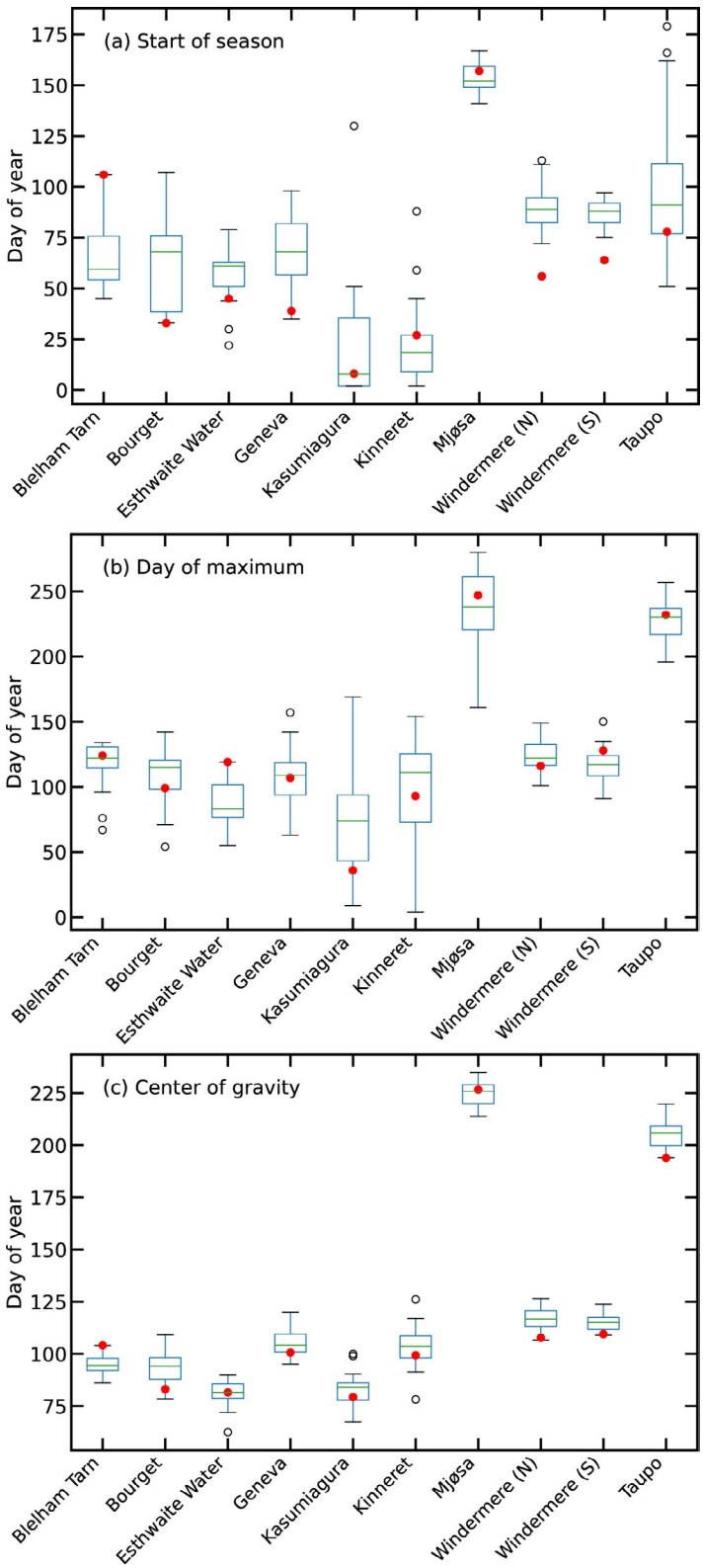

Fig. 2.85. Phenological metrics based on lake chlorophyll-*a* concentrations, as a proxy of phytoplankton biomass: (a) start of season, (b) day of maximum, and (c) center of gravity. Boxplots show variation during the 2000–20 baseline period, and red dots show 2023 values. Nine lakes are in the Northern Hemisphere (Blelham Tarn [United Kingdom], Bourget [France], Esthwaite Water [United Kingdom], Geneva [France/Switzerland], Kasumigaura [Japan], Kinneret [Israel], Mjøsa [Norway], north and south basins of Windermere [United Kingdom]), and one lake is in the Southern Hemisphere (Taupo [New Zealand]).

5. VEGETATION OPTICAL DEPTH

—R. M. Zotta, R. van der Schalie, T. Frederikse, W. Preimesberger, R. de Jeu, and W. Dorigo

Vegetation optical depth (VOD) derived from space-borne passive microwave radiometers is a non-dimensional parameter used in radiative transfer models to describe the interaction between radiance emitted from Earth's surface and vegetation and is an indicator of the water stored in plant structures. It has found utility in a wide range of studies, including drought- and vegetation-condition monitoring (Moesinger et al. 2022; Vreugdenhil et al. 2022). Positive VOD anomalies indicate above-average vegetation abundance, while negative VOD anomalies indicate underdeveloped or stressed vegetation.

Several trends resulting from land-use changes manifest prominently in VOD anomalies (Plate 2.1ah; Dorigo et al. 2021; Zotta et al. 2023), which are calculated as deviations from the 1991–2020 climatology. Notably, negative annual VOD anomalies in regions like Mongolia, Bolivia, Paraguay, and Brazil reflect the impacts of deforestation and land degradation, while positive anomalies in areas such as India and northeastern China signify agricultural intensification and reforestation efforts (Song et al. 2018). In order to exclude such long-term trends and isolate the year-to-year anomalies, we also look at the differences in VOD between 2023 and 2022 (Appendix Fig. A2.7).

In 2023, annual VOD anomaly patterns differed from those in recent years (e.g., Zotta et al. 2023; Dorigo et al. 2022, 2021). In the Southern Hemisphere, where there is a clear connection between vegetation activity and variations in the El Niño–Southern Oscillation (ENSO; Miralles et al. 2014; Martens et al. 2017), overall VOD was lower than in 2022 (Figs. 2.86, 2.87).

Compared to 2022, substantial increases in VOD can be observed across regions in North America, northern Australia, and the Horn of Africa (Appendix Fig. A2.7). In northern Australia, the patterns are likely due to above-average rainfall (sections 2d4, 7h4) driving vegetation growth. In the Horn of Africa, predominantly positive annual (Plate 2.1ah) and high monthly (Appendix Fig. A2.8) VOD anomalies in November and December coincided with heavy rains associated with El Niño (section 2d4) and with the switch of the Indian Ocean dipole from negative to positive in September 2023 (see section 4f). The remarkable increases in VOD across Ethiopia, Somalia, and Kenya (Appendix Fig. A2.7) were likely due to favorable growing conditions caused by large precipitation amounts and were also captured in other satellite-borne vegetation indicators (FEWS NET 2023). In North America, the increase in VOD can likely be attributed to vegetation recovery after persistent dry conditions, which ameliorated in many regions such as the northeastern United States, the western portion of the Great Plains, California, and in parts of the Great Lakes and the Southeast (NOAA 2024). Strong positive VOD anomalies in November

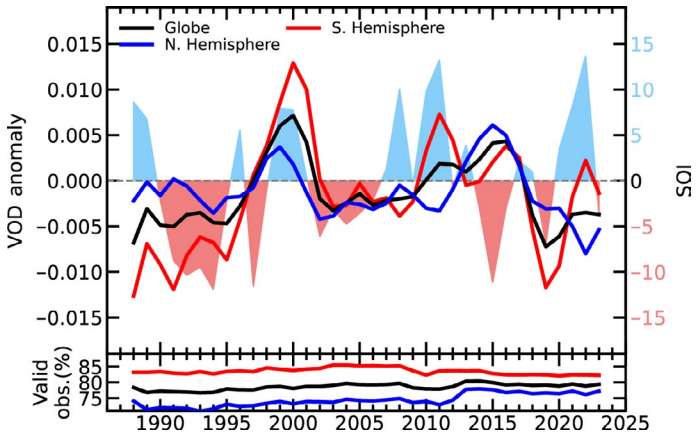

Fig. 2.86. Yearly vegetation optical depth (VOD) anomalies computed from the 1991–2020 climatology and their agreement with the Southern Oscillation Index (SOI). The SOI tracks the state of the El Nino–Southern Oscillation. (Source: VOD Climate Archive [VODCA]; http://www.bom.gov.au/climate/enso/soi/.)

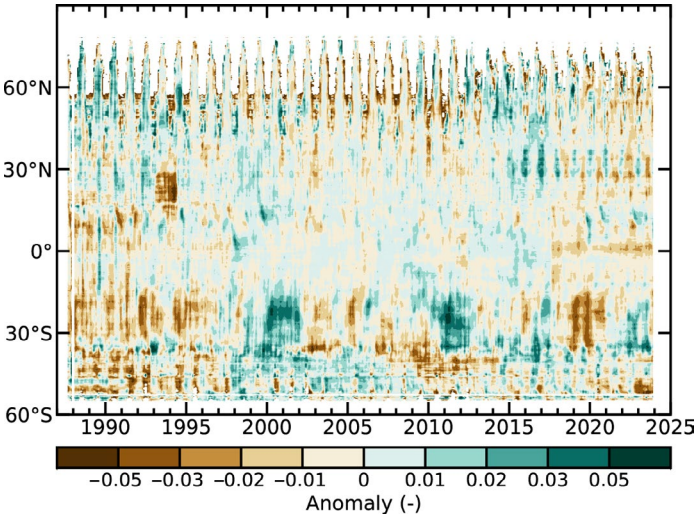

Fig. 2.87. Time–latitude diagram of vegetation optical depth (VOD) anomalies (1991–2020 base period). Data are masked where no retrieval is possible, or where the quality is not assured and flagged due to frozen soil, radio frequency interference, etc. (Source: VOD Climate Archive [VODCA].)

and December (Appendix Fig. A2.8) support the findings of crop reports that announced favorable conditions for winter wheat across the United States and Canada, especially in Ontario and Manitoba (GeoGlam 2023).

Similar to soil moisture (section 2d10), VOD decreased substantially across southern Africa in 2023, where ENSO is one of the strongest drivers impacting agricultural production (OCHA 2023). Here, optical satellite observations of vegetation health indicate stressed vegetation (section 2h2; NOAA 2023). In the Maghreb (west and central north Africa) and northern Africa, where satellite observations from the Gravity Recovery and Climate Experiment (GRACE) have indicated persistently low soil moisture and groundwater (section 2d9; NOAA 2023), patterns of decreased VOD and negative monthly VOD anomalies across most of the year have prevailed. VOD also decreased in Central America and Mexico. An extremely dry period led to crop damage and losses observed in FAPAR anomalies (section 2h2; Toreti et al. 2023). In the Amazon basin, the decrease in VOD and the negative monthly anomalies across most of the year were likely caused by severe heatwaves and below-average rainfall linked with ENSO. In Spain, the decrease in VOD coincided with sparse rainfall and heatwaves that dominated in spring and summer (sections 2b1, 2d4).

The VOD data are from the VOD Climate Archive v2 (VODCA v2; Moesinger et al. 2020; Zotta et al. 2024a,b). VODCA merges VOD observations from several space-borne radiometers (Special Sensor Microwave/Imager [SSM/I], Tropical Rainfall Measuring Mission [TRMM], WindSat, Advanced Microwave Scanning Radiometer-Earth Observing System [AMSR-E] and Advanced Microwave Scanning Radiometer 2 [AMSR2]) through the Land Parameter Retrieval Model (Meesters et al. 2005; van der Schalie et al. 2017) into a long-term, harmonized dataset. Here, we used VODCA CXKu, a multi-frequency product that blends C-, X-, and Ku band observations, has a spatial resolution of 0.25°, and provides daily observations.

Acknowledgments

a Introduction

Robert Dunn and Kate Willett were supported by the Met Office Hadley Centre Climate Programme funded by the U.K. Department for Science, Innovation and Technology (DSIT). The editors thank the five anonymous reviewers and also Lizzie Fuller, John Kennedy, David Parker, and Ruben Urraca Valle for their insight, thoughts, and suggestions when developing this chapter. We also thank Fumi Sezaki (Japanese Meteorological Association [JMA]), Julien Nicolas (European Centre for Medium-Range Weather Forecasts [ECMWF]), and Mike Bosilovich (NASA) for their help in providing the reanalysis data used in this chapter.

b2 Lake surface temperature

Lake surface water temperatures from satellite data have been generated within the Climate Change Initiative Lakes project funded by the European Space Agency (4000125030/18/I-NB) with adaptation funded by the E.U. Copernicus Climate Change Service (C3S) programme and extensions by the U.K. Earth Observation Climate Information Service (EOCIS) project (NE/X019071/1). Part of the in situ data used for the validation of the satellite data and for this report have kindly been made publicly available by Fisheries and Oceans Canada (FOC), the National Data Buoy Center (NDBC) from NOAA, the Hungarian Meteorological Office, the Upper Great Lakes Observing System (UGLOS), and the North Temperate Lakes Long-Term Ecological Research (NTL-LTER). The authors gratefully acknowledge the late Alon Rimmer for always supplying data for Lake Kinneret. Data from Lake Zurich were provided by the City of Zurich Water Supply and by the Amt für Abfall, Wasser, Energie und Luft of the Canton of Zurich.

b3 Night marine air temperature

R. C. Cornes was supported by the NERC NC CLASS programme (NE/R015953/1) and the NERC GloSAT project (NE/S015647/2). R. Junod was supported by funding from the U.S. Department of Energy (DE-SC0023332).

b4 Surface temperature extremes

Robert Dunn was supported by the Met Office Hadley Centre Climate Programme funded by the Department for Science, Innovation and Technology (DSIT).

b5 Tropospheric temperature

Work performed by Stephen Po-Chedley at Lawrence Livermore National Laboratory (LLNL) was supported by the Regional and Global Model Analysis Program of the Office of Science at the Department of Energy (DOE) and performed under the auspices of the DOE under Contract DE- AC52-07NA27344.

c1 Permafrost temperatures and active-layer thickness

Research on James Ross Island was supported by the Czech Antarctic Research Programme and Czech Science Foundation project (GM22-28659M). The Circumpolar Active Layer Monitoring (CALM) program is funded by the National Science Foundation (NSF) Project 1836377. The Svalbard permafrost data is part the Svalbard Integrated Earth Observing System (SIOS). The Swiss Permafrost Monitoring Network (PERMOS) is financially supported by MeteoSwiss (in the framework of GCOS Switzerland), the Federal Office for the Environment, and the Swiss Academy of Sciences, and acknowledges the contribution of its partner institutions. The French Network PermaFRANCE is financially supported by the Observatoire des Sciences de l'Univers Grenoble and the French Research Infrastructure OZCAR. The Chinese Permafrost Monitoring Network is financially supported by the Chinese National Science Foundation (41931180) and Cryosphere Research Station on Qinghai-Xizang Plateau, CAS.

c2 Rock glacier velocity

Rock glacier monitoring at Hinteres Langtalkar and Dösen rock glaciers (AT) is supported by the Hohe Tauern National Park Carinthia through its long-term permafrost monitoring program. Laurichard (FR)

survey is supported by Observation and Experimentation System for Environmental Research (SOERE/All'envi-OZCAR Research Infrastructure) and the PermaFrance observatory "monitoring the mountain permafrost in the French Alps" as well as the French National Research Agency in the framework of the Investissements d'Avenir programs: Risk@UGA (ANR-15-IDEX-02) and LabEx OSUG@2020 (ANR10 LABX56). The Ecrins National Park has helped field surveys since the early 2000s. The Swiss Permafrost Monitoring Network (PERMOS) is financially supported by MeteoSwiss in the framework of Global Climate Observing System (GCOS) Switzerland, the Federal Office for the Environment, and the Swiss Academy of Sciences. PERMOS acknowledges the important contribution of the partner institutions and principal investigators. The time series for Central Asian rock glaciers was compiled with the ESA Permafrost_CCI project (4000123681/18/I-NB). The time series for the Dry Andes was supported by the Centro de Estudios Avanzados en Zonas Áridas (CEAZA) and the Leading House for the Latin American Region (University of St. Gallen), grant number MOB1829.

c4 Lake ice cover

We thank Al and Sue Stangel, Alexander Mills, Ann LaLiberte, Beth Kohlman, BJ Bauer, Bob Katzenberger, Bonny Pederson, Brendan Wiltse, Brian D. Neill, Brian Vlach, John Barten, Rick Brascke, Calvin Maurer, Carl C. Nelson, Carol Wendorf, Cheryl and Dorothy Zingler, Clare and Dan Shirley, Craig Hillman, Dale Robertson, Dan Brumm, Daniel L. Anderson, Dave and Lynda J. Urshan, David Kahan, Don McClanathan, Donald and Mureil Fornasiere, Doug Fitzgerald, Douglas Pierzina, Dr. Neal D. Mundahl, Duane Williams and Edie Evarts, Duncan A. Brown, Earl Cook, Fred Buckley, Gary Teigen, Gay Alberts Ruby, Gene Cooper, George Grevich, Greg Sass, Holly Waterfield, Huaxia Yao, James and Sharon Fenner, James W. Danielson, Jan Henning L'Abée-Lund, Jeff Goelzer, Jeffrey G. Lowe, Jerry Evans, Jerry Sondreal, Jim and Judy Daugherty, Joe Jenkins, Joel Rasmussen, John and Catherine Bart, John Maier, Jonathan Ross, Dan Drumm, Dr. Lesly Knoll, Joy Krubsack, Kay and Rich Rezanka, Kay Olson, Kay Wepfer, Ken Blumenfeld, Larry and Marlene Lotto, Larry Peterson, Lars Rudstam, Lolita Olson, Lowell Dague, Marge Kellor, Mark Biller, Mark Holland, Mark J. and Rosie Peters, Mary Jane Dillingham, Mary Lou Fry, Randell Fry, Merja Pulkkanen, Michael Allen, Michael Bradley, Michael Kolecheck, Michael Traufler, Mickey and Dennis Chick, Mike, Jeff, and Thomm Backus, Molly Hibbard, Morris and Doris Whiting, Mr. and Mrs. Jay R. Mackie, Mr. and Mrs. William Bergersen, Mrs. Gale Wheeler, Mrs. Kathy Elhard, Mrs. Margery Armstrong, Myron Hagelstrom, Nancy Putnam, Nancy Steenport, Park Manager (L.C.), Patricia Bebak, Patrick Collins, Paulette Janssen, Pete Boulay, Peter Bearup, Rachel Dahlke, Raymond (Joe) Jenkins, Richard L. Tamke, Rock Anderson, Ron Pabich, Ronald Jones, Ross Swain, Sally Ketchen, Sandra Anderson, Scott Schoepp, Sharon Natzel, Shin-Ichiro Matsuzaki, Susan Reineking, Susan Verhaalen, Tana McNutt, Theodore (Ted) Peters, Thomas Sommerfeldt, Tom Stangl, Travis Campbell, Virgil Luehrs, Walt and Nancy Quillinan, Walter R. Brown, Water Dahlke III, William and Brenda Jones, and William Hanson, for their dedication and efforts to collecting and sharing in situ ice phenological records with us.

c5 Northern Hemisphere continental snow cover extent

This work is funded in part by NOAA's Climate Data Record (CDR) Program at the National Centers for Environmental Information (NCEI).

d1 Surface humidity

Kate Willett was supported by the Met Office Hadley Centre Climate Programme funded by the Department for Science, Innovation and Technology (DSIT). Adrian Simmons and David Lavers were supported by the Copernicus Climate Change Service (C3S) implemented by the European Centre for Medium-Range Weather Forecasts (ECMWF) on behalf of the European Commission.

d2 Humid-heat extremes over land

Kate Willett was supported by the U.K.-China Research and Innovation Partnership Fund through the Met Office Climate Science for Service Partnership (CSSP) China under the International Science Partnerships Fund (ISPF).

Cassandra Rogers is supported with funding from the Australian Government under the National Environmental Science Program.

Thank you to Tim Cowan from the University of Southern Queensland and Blair Trewin from the Bureau of Meteorology for providing initial reviews of the humid heat extremes over land section.

d7 Cloudiness

Clouds and Earth's Radiant Energy Systems Energy Balanced and Filled (CERES EBAF) data were obtained from the NASA Langley Research Center CERES ordering tool at https://ceres.larc.nasa.gov/data/.

d8 Lake water storage

B. M. Kraemer acknowledges support from the University of Freiburg Chair of Environmental Hydrosystems. M. F. Meyer and M. E. Harlan were supported by the United States Geological Survey (USGS) Mendenhall Fellowships from the Water Mission Area. The funders had no role in study design, data collection and analysis, decision to publish, or preparation of the manuscript. R. S. La Fuente was funded by the Irish HEA Landscape programme and Dundalk Institute of Technology (DkIT) Research Office. Any use of trade, firm, or product names is for descriptive purposes only and does not imply endorsement by the U.S. Government.

d9 Groundwater and terrestrial water storage

Work on the Groundwater and Terrestrial Water Storage section was funded by NASA's Gravity Recovery and Climate Experiment Follow-On (GRACE-FO) Science Team.

d10 Soil moisture

This study uses satellite soil moisture observations from the Copernicus Climate Change Service (C3S) Climate Data Store (CDS) (2018): Soil moisture gridded data from 1978 to present. C3S CDS. (Accessed on 16 01 2024), 10.24381/cds.d7782f18.

d11 Monitoring drought using the Self Calibrating Palmer Drought Severity Index

Jonathan Barichivich was supported by the European Research Council (ERC) under the Horizon Europe research and innovation programme (ERC-starting grant CATES, grant agreement No. 101043214). Tim Osborn received funding from the U.K. Natural Environment Research Council (NERC) (NE/S015582/1). Ian Harris received funding from U.K. National Centre for Atmospheric Science (NCAS). The research presented in the drought section was carried out on the High-Performance Computing Cluster supported by the Research and Specialist Computing Support service at the University of East Anglia.

d12 Land evaporation

D. G. Miralles acknowledges support from the European Research Council (ERC) under grant agreement no. 101088405 (HEAT). H. E. Beck is supported by the King Abdullah University of Science and Technology.

e2 Surface winds

C. Azorin-Molina was supported by CSIC-UV-GVA and funded by AICO/2021/023, LINCGLOBAL-CSIC ref. INCGLO0023, and PTI-CLIMA.

Robert Dunn was supported by the Met Office Hadley Centre Climate Programme funded by the Department for Business, Energy and Industrial Strategy (BEIS).

L. Ricciardulli was supported by NASA Ocean Vector Wind Science Team grant 80NSSC23K0984. Z. Zeng was supported by the National Natural Science Foundation of China grant 42071022.

e4 Lightning

The work of M. Füllekrug was sponsored by the Royal Society (U.K.) grant NMG/R1/180252 and the Natural Environment Research Council (U.K.) under grants NE/L012669/1 and NE/H024921/1.

E. Williams is supported for studies on global circuit response to climate change from the Physical and Dynamic Meteorology Program at the National Science Foundation (NSF) on grant no. 6942679.

C. Price was supported in his lightning research by the Israel Science Foundation (ISF) grant 2701/17, and the Ministry of Energy grant no. 220-17-002. S. Goodman was supported by NASA Grant 80NSSC21K0923 and NASA Contract 80GSFC20C044. The authors wish to thank Peter Thorne at Maynooth University in Ireland and at the European Centre for Medium Range Weather Forecast (ECMWF) for suggesting and initiating this work and for recommending that lightning be made an essential climate variable.

f1 Earth radiation budget at top-of-atmosphere

This research has been supported by the NASA Clouds and Earth's Radiant Energy Systems (CERES) project. The resources of the NASA Langley Atmospheric Sciences Data Center are utilized to process the instantaneous Single Scanner Footprint (SSF) data used as input to Energy Balance and Filled (EBAF) Ed4.2 and processes the FLASHFlux TISA version 4B. We further acknowledge the efforts of Walt Miller and Pam Mlynczak of the CERES team who monitor CERES data production and produce the FLASHFlux TISA 4B monthly averaged data products, respectively.

g3 Tropospheric aerosols

The data used for this section were provided by the European Union Copernicus Atmosphere Monitoring Service (CAMS).

g4 Tropospheric ozone

The NOAA Proving Ground and Risk Reduction (PGRR) Program supported the contributions by O. R. Cooper and K.-L. Chang. K.-L. Chang was also supported by NOAA cooperative agreement NA22OAR4320151. Funding for J. Ziemke for this research was provided in part by NASA NNH14ZDA001N-DSCOVR, NASA Suomi NPP and Joint Polar Satellite System (JPSS) Satellites Standard Products for Earth System Data Records, and Code 614 programmatic support for long-term ozone trends.

g5 Stratospheric aerosols

Lidar observations at Observatory de Haute-Provence (OHP) are funded by the French National Centre for Scientific Research (CNRS) National Institute of Sciences of the Universe (INSU) and CNES. S. Khaykin's work is supported by the ANR PyroStrat 21-CE01- 335 0007-01 project. We thank Christine David, Alain Hauchecorne, Julien Jumelet, Philippe Keckhut (LATMOS), and the lidar station operators for their contributions to long-term monitoring of stratospheric aerosol at OHP. Lidar observation at Lauder are funded in part by the Greenhouse gases Observing SATellite (GOSAT) project. We thank Richard Querel (National Institute of Water and Atmospheric Research [NIWA]), Osamu Uchino, Tomohiro Nagai (Meteorological Research Institute [MRI]) and Yushitaka Jin (MRI) for their contributions to long-term monitoring of stratospheric aerosol at Lauder.

g6 Stratospheric ozone

Carlo Arosio, Melanie Coldewey-Egbers, Diego Loyola, Viktoria Sofieva, Alexei Rozanov, and Mark Weber are grateful to the E.U. Copernicus Climate Change Service (C3S), C3S2_312a_Lot2 Ozone, and to European Space Agency's (ESA) Climate Change Initiative Ozone (CCI+) projects for supporting the generation and extension of the GTO-ECV total ozone and SAGE-CCI-OMPS data records. Carlo Arosio, Viktoria Sofieva, Kleareti Tourpali, Alexei Rozanov, and Mark Weber are grateful for the support of the ESA project Ozone Recovery from Merged Observational Data and Model Analysis (OREGANO). Stacey M. Frith is supported by the NASA Long Term Measurement of Ozone program WBS 479717. Lucien Froidevaux's contribution, with the assistance of Ryan Fuller, was performed at the Jet Propulsion Laboratory (JPL), California Institute of Technology, under contract with NASA. Jeannette Wild was supported by NOAA grant NA19NES4320002 (Cooperative Institute for Satellite Earth System Studies [CISESS]) at the University of Maryland's Earth System Science Interdisciplinary Center (ESSIC). Melanie Coldewey-Egbers and Diego Loyola acknowledge the partial support by the German Aerospace Center (DLR) projects MABAK and INPULS.

h2 Terrestrial vegetation dynamics

The authors thank the providers of the remote sensing dataset needed to perform this analysis and the Joint Research Centre's (JRC) Big Data Analytics Platform (BDAP).

h4 Phenology of primary producers

Debbie Hemming acknowledges support from the Met Office Hadley Centre Climate Programme funded by the Department for Science, Innovation and Technology (DSIT), and thanks all co-authors for their interesting and helpful contributions. Andrew Richardson acknowledges support from the National Science Foundation (NSF) Long Term Ecological Research (LTER) program (award 1832210). John O'Keefe also acknowledges support from the NSF through the LTER (award 1832210) program. Nature's Calendar (Woodland Trust) in the U.K. thanks all its volunteer recorders and support from players of People's Postcode Lottery. Theresa Crimmins and the USA National Phenology Network (USA-NPN) acknowledge support from the NSF through the Division of Biological Infrastructure (award 2031660), the US Fish and Wildlife Service (agreements F16AC01075 and F19AC00168) and the U.S. Geological Survey (G14AC00405 and G18AC00135). The USA-NPN thanks the many participants contributing phenology observations to *Nature's Notebook*. De Natuurkalender (Nature's Calendar) program in the Netherlands thanks all the volunteers and school children in the GLOBE program for their many observations. Annette Menzel and Nicole Estrella acknowledge support from the Bavarian State Ministry of Science and the Arts in the context of the Bavarian Climate Research Network (BayKlif) (Bavarian Citizen Science Portal for Climate Research and Science Communication [BAYSICS]). The Slovak Hydrometeorological Institute thanks all its volunteer observers for participating in the phenological observation program. Orlane Anneville acknowledges support from the National Institute of Agricultural Research (INRAE). Stephen Thackeray thanks Werner Eckert, Heidrun Feuchtmayr, Shin-Ichiro Matsuzaki, Ryuichiro Shinohara, Jan-Erik Thrane, Piet Verburg, Tamar Zohary and all field and lab workers associated with the provision of the lake chlorophyll-*a* data. We acknowledge funding from Vassdragsforbundet for Mjøsa med tilløpselver (https://www.vassdragsforbundet.no/om-oss/) and Natural Environment Research Council award number NE/R016429/1 as part of the U.K. Status, Change and Projections of the Environment (UK-SCAPE) programme delivering National Capability. Data for Lakes Geneva and Bourget were contributed by the Observatory of alpine LAkes (OLA), © SOERE OLA-IS, AnaEE-France, INRAE of Thonon-les-Bains, CIPEL, CISALB.

h5 Vegetation optical depth

R. M. Zotta and W. Dorigo acknowledge the TU Wien Wissenschaftspreis 2015, a personal grant awarded to W. Dorigo. We also acknowledge support from the European Space Agency (ESA) Climate Change Initiative and the Copernicus Climate Change Service (C3S).

Sidebar 2.1: Impacts of extreme temperatures in 2023

Robert Dunn and Kate Willett were supported by the Met Office Hadley Centre Climate Programme.

Appendix 1: Acronyms

4D-VAR	four-dimensional variational data assimilation
AAO	Antarctic Oscillation
AATSR	Advanced Along Track Scanning Radiometer
AEM ENTLN	Advanced Environmental Monitoring Earth Networks Total Lightning Network
ALT	active-layer thickness
AMSR2	Advanced Microwave Scanning Radiometer 2
AMSR-E	Advanced Microwave Scanning Radiometer-Earth Observing System
ANYSO	Australian New Year Super Outbreak
AOD	aerosol optical depth
ASCAT	Advanced Scatterometer
ASR	absorbed solar radiation
BD	Brewer-Dobson
C3S	Copernicus Climate Change Service
CALM	Circumpolar Active Layer Monitoring
CAMS	Copernicus Atmosphere Monitoring Service
CCI	Climate Change Initiative
CCM	chemistry climate model
CERES	Clouds and the Earth's Radiant Energy System
CFC	chlorofluorocarbon
CH_3CCl_3	methyl chloroform
CH_4	methane
CO	carbon monoxide
CO_2	carbon dioxide
COG	center of gravity
COVID-19	Coronavirus disease 2019
cp	specific heat capacity of air at constant pressure
CPT	cold-point tropopause
CRE	cloud radiative effect
DOM	day of maximum concentration
DWD	Deutscher Wetterdienst
DZAA	depth of zero annual amplitude
EBAF	Energy Balance and Filled
ECMWF	European Centre for Medium-Range Weather Forecasts
EESC	equivalent effective stratospheric chlorine
EESC(A)	equivalent effective stratospheric chlorine in the Antarctic
EESC(ML)	equivalent effective stratospheric chlorine in the midlatitudes
ENSO	El Niño–Southern Oscillation
EOCIS	Earth Observation Climate Information Service
EOF	empirical orthogonal function
EOS	end of season
ER	extinction ratio
ERB	Earth radiation budget
ERF	effective radiative forcing
ESA	European Space Agency
ET	evapotranspiration
EUR	Europe
FAPAR	fraction of absorbed photosynthetically active radiation
FBD	full bloom dates
FEWS NET	Famine Early Warning Systems Network

FF	fossil fuel
FP	frost point
GAM	General Additive Model
GCOS	Global Climate Observing System
GISS	Goddard Institute for Space Studies
GLAMOS	Glacier Monitoring Switzerland
GLD360	Global Lightning Detection Network
GLEAM	Global Land Evaporation Amsterdam Model
GLIMS	Global Land Ice Measurements from Space
GLM	Geostationary Lightning Mapper
GloSSAC	Global Satellite-based Stratospheric Aerosol Climatology
GO	ground observations
GPCC	Global Precipitation Climatology Centre
GPCP	Global Precipitation Climatology Project
GRACE	Gravity Recovery and Climate Experiment
GRACE-FO	Gravity Recovery and Climate Experiment Follow-On
GSL	Global Snow Lab
HCFC	hydrochlorofluorocarbon
HFC	hydrofluorocarbon
HTHH	Hunga Tonga–Hunga Ha‘apai
INRAE	Université Grenoble Alpes
IOD	Indian Ocean dipole
IPCC	Intergovernmental Panel on Climate Change
ITCZ	Intertropical Convergence Zone
LLGHG	long-lived greenhouse gas
LSWT	lake surface water temperature
LTT	lower-tropospheric temperature
Lv	latent heat of vaporization
LWCRE	longwave cloud radiative effect
LWS	lake water storage
MC	Maritime Continent
MCM	million cubic meters
MCS	mesoscale convective system
MCS	marine cold spell
MEGAN2.1	Model of Emissions of Gases and Aerosols from Nature version 2.1
MHW	marine heatwave
MLO	Mauna Loa Observatory
MLS	Microwave Limb Sounder
MODIS	Moderate Resolution Imaging Spectroradiometer
MOPITT	Measurement of Pollution in the Troposphere
MSLP	mean sea-level pressure
N_2O	nitrous oxide
NA	North America
NAO	North Atlantic Oscillation
NDACC	Network for the Detection of Atmospheric Composition Changes
NH	Northern Hemisphere
NMAT	night marine air temperature
NN	Nature’s Notebook
O_3	tropospheric ozone
OCHA	Office for the Coordination of Humanitarian Affairs
ODGI	Ozone Depleting Gas Index
ODS	ozone-depleting substance

OHP	Observatoire de Haute Provence
OLR	outgoing longwave radiation
OMI	Ozone Monitoring Instrument
OMPS	Ozone Mapping and Profiler Suite
OMPS-LP	Ozone Mapping and Profiler Suite–Limb Profiler
ONI	Oceanic Niño Index
PC	PhenoCam
PERMOS	Swiss Permafrost Monitoring Network
PM2.5	fine particulate matter
PNA	Pacific/North American
PSA	Pacific–South American
q	specific humidity
QBO	quasi-biennial oscillation
QTP	Qinghai-Tibet Plateau
QuikSCAT	Quick Scatterometer
RCP	representative concentration pathway
RFaci	aerosol-cloud interactions
RFari	aerosol-radiation
RGIK	rock glacier inventories and kinematics
RGV	rock glacier velocity
RH	relative humidity
RSS	Remote Sensing Systems
RSW	reflected shortwave
Rx1day	one-day maximum accumulation
SAGE	Stratospheric Aerosol and Gas Experiment
SAM	Southern Annular Mode
sAOD	stratospheric aerosol optical depth
SCE	snow cover extent
scPDSI	self-calibrating Palmer Drought Severity Index
SH	Southern Hemisphere
SNAO	summer North Atlantic Oscillation
SO_2	sulfur dioxide
SOI	Southern Oscillation Index
SOS	start of season
SSM/I	Special Sensor Microwave/Imager
SSMIS	Special Sensor Microwave Imager/Sounder
SST	sea surface temperature
SSU	Stratospheric Sounding Unit
SW	shortwave
SWCRE	shortwave cloud radiative effect
T	dry-bulb air temperature
Ta	air temperature
TCWV	total column water vapor
TEC	total energy content
Teq	equivalent temperature
TLS	lower stratosphere temperature
TLT	lower tropospheric temperature
TMI	Tropical Rainfall Measuring Mission's Microwave Imager
TOA	top-of-atmosphere
TOB	tropospheric ozone burden
Tq	latent temperature
TRMM	Tropical Rainfall Measuring Mission

TSI	total solar irradiance
TTL	tropical tropopause layer
T_w	wet-bulb temperature
TWS	terrestrial water storage
T_wX	daily maximum wet-bulb temperatures
Tx	zonal mean profiles
USA-NPN	USA National Phenology Network
UT	upper tropospheric
UTH	upper-tropospheric humidity
UW WWLLN	University of Washington's World Wide Lightning Location Network
VEI	Volcanic Explosivity Index
VIIRS	Visible Infrared Imaging Radiometer Suite
VOD	vegetation optical depth
VODCA	Vegetation Optical Depth Climate Archive
w.e.	water equivalent
WGMS	World Glacier Monitoring Service
WMO	World Meteorological Organization
WOUDC	World Ozone and Ultraviolet Radiation Data Centre
WV	water vapor

Appendix 2: Datasets and sources

Section 2b Temperature

Sub-section	General Variable or Phenomenon	Specific dataset or variable	Source
2b1	Temperature, [Near] Surface	Berkeley Earth	http://berkeleyearth.org/data/
2b1	Temperature, [Near] Surface	ERA5	https://www.ecmwf.int/en/forecasts/dataset/ecmwf-reanalysis-v5
2b1	Temperature, [Near] Surface	HadCRUT5 Global Temperature	https://www.metoffice.gov.uk/hadobs/hadcrut5/
2b1	Temperature, [Near] Surface	CRUTEM5	https://www.metoffice.gov.uk/hadobs/crutem5/
2b1, 2b3	Temperature, [Near] Surface	HadSST4	https://www.metoffice.gov.uk/hadobs/hadsst4/
2b1, 2b4	Temperature, [Near] Surface	JRA-55 Atmospheric Reanalysis	https://search.diasjp.net/en/dataset/JRA55
2b1	Temperature, [Near] Surface	JRA-3Q	https://search.diasjp.net/en/dataset/JRA3Q
2b1, 2b2	Temperature, [Near] Surface	NASA/GISS Global Temperature V4	https://data.giss.nasa.gov/gistemp/
2b1	Temperature, [Near] Surface	NOAA/NCEI NOAAGlobalTemp	https://www.ncei.noaa.gov/products/land-based-station/noaa-global-temp
2b2	Lake Temperature	Full Lake Surface Temperature Water dataset	https://cds.climate.copernicus.eu/cdsapp#!/dataset/satellite-lake-water-temperature
2b2	Lake Temperature	National Buoy Data Center Great Lakes Buoys	https://www.ndbc.noaa.gov/mobile/region.php?reg=great_lakes
2b2	Lake Temperature	Balaton Lakes	https://odp.met.hu/climate/observations_hungary/hourly/historical/
2b2	Lake Temperature	Canadian Lakes	https://www.meds-sdmm.dfo-mpo.gc.ca/isdm-gdsi/waves-vagues/data-donnees/index-eng.asp
2b2	Lake Temperature	Biel and Thun Lakes (Switzerland); Biwa and Mikata Lakes (Japan)	https://www.die3seen.ch/, https://portal.gemstat.org/applications/public.html?publicuser=PublicUser
2b2	Lake Temperature	Trout Lake	https://portal.edirepository.org/nis/mapbrowse?scope=knb-lter-ntl&identifier=116&revision=27
2b2	Lake Temperature	ESA CCI LAKES LSWT v2.0.2	https://catalogue.ceda.ac.uk/uuid/a07deacaffb8453e93d57ee214676304
2b2	Lake Temperature	Sentinel 3 Sea and Land Surface Temperature Radiometer (SLSTR)	https://sentinel.esa.int/web/sentinel/user-guides/sentinel-3-slstr/overview

Sub-section	General Variable or Phenomenon	Specific dataset or variable	Source
2b3	Nighttime marine Air Temperature	CLASSnmat	https://catalogue.ceda.ac.uk/uuid/5bbf48b128bd488dbb10a56111feb36a
2b3	Nighttime marine Air Temperature	UAHNMATv1	https://www.nsstc.uah.edu/climate/, https://doi.org/10.1002/joc.6354
2b4	Sea Surface Temperature	NOAA Optimum Interpolation Sea Surface Temperature (OISST) v2.1	https://www.ncei.noaa.gov/products/optimum-interpolation-sst
2b4	Temperature, [Near] Surface	GHCNDEX	https://www.climdex.org/
2b4	Temperature, [Near] Surface	MERRA-2	http://gmao.gsfc.nasa.gov/reanalysis/MERRA-2/
2b4, 2b5	Temperature, Upper Atmosphere	ERA5	https://www.ecmwf.int/en/forecasts/dataset/ecmwf-reanalysis-v5
2b4, 2b5	Temperature, Upper Atmosphere	JRA-55 Atmospheric Reanalysis	http://jra.kishou.go.jp/JRA-55/index_en.html
2b5	Temperature, Upper Atmosphere	MERRA-2	http://gmao.gsfc.nasa.gov/reanalysis/MERRA-2/
2b5	Temperature, Upper Atmosphere	NOAA/NESDIS/STAR MSU v5	https://www.star.nesdis.noaa.gov/data/mscat/MSU_AMSU_v5.0/Monthly_Atmospheric_Layer_Mean_Temperature/
2b5	Temperature, Upper Atmosphere	RAOBCORE, RICH	https://imgw.univie.ac.at/forschung/klimadiagnose/raobcore/
2b5	Temperature, Upper Atmosphere	RATPAC A2	https://www.ncei.noaa.gov/products/weather-balloon/radiosonde-atmospheric-temperature-products
2b5	Temperature, Upper Atmosphere	RSS v4.0	https://www.remss.com/measurements/upper-air-temperature/
2b5	Temperature, Upper Atmosphere	UAH MSU v6.0	https://www.nsstc.uah.edu/data/msu/v6.0/
2b5	Sea Surface Temperature	Niño 3.4 Index	https://psl.noaa.gov/gcos_wgsp/Timeseries/Nino34/
2b6	Temperature, Upper Atmosphere	Aura MLS	https://disc.gsfc.nasa.gov/datasets/ML2T_005/summary

Section 2c Cryosphere			
Sub-section	**General Variable or Phenomenon**	**Specific dataset or variable**	**Source**
2c1	Permafrost	Global Terrestrial Network for Permafrost (GTN-P)	http://gtnpdatabase.org/
2c1	Permafrost	GTN-P global mean annual ground temperature data for permafrost	https://doi.org/10.1594/PANGAEA.884711
2c1	Permafrost	Permafrost Temperature at Chinese (QTP) sites	https://nsidc.org/data/GGD700/versions/1
2c1	Permafrost	Permafrost Temperature at French sites	https://permafrance.osug.fr
2c1	Permafrost	Permafrost Temperature at Norwegian sites	https://cryo.met.no/
2c1, 2c2	Permafrost	Permafrost Temperature at Swiss sites (PERMOS)	https://www.permos.ch, https://www.permos.ch/doi/permos-dataset-2022-1
2c1	Active Layer Depth	Circumpolar Active Layer Monitoring (CALM)	https://www.gwu.edu/~calm/
2c2	Rock Glacier Velocity	Regional Rock Glacier Velocity	Available from authors upon request. Austria: V. Kaufmann and A. Kellerer-Pirklbauer, Central Asia: A. Kääb, Dry Andes: S. Vivero, France: X. Bodin, D. Cusicanqui and E. Thibert, Switzerland: R. Delaloye, J. Noetzli and C. Pellet
2c3	Glacier Mass, Area or Volume	World Glacier Monitoring Service	http://dx.doi.org/10.5904/wgms-fog-2022-09
2c3	Glacier Area	Copernicus Sentinel-2 MSI image	https://sentinels.copernicus.eu/web/sentinel/user-guides/sentinel-2-msi/overview
2c4	Lake Ice	ERA5	https://www.ecmwf.int/en/forecasts/dataset/ecmwf-reanalysis-v5
2c4	Lake Ice	Lake ice clearance and formation data for Green Lakes Valley, 1968 - ongoing. ver 5. Environmental Data Initiative	https://portal.edirepository.org/nis/mapbrowse?scope=knb-lter-nwt&identifier=106&revision=6
2c4	Lake Ice	Global Lake and River Ice Phenology Database, Version 1	https://doi.org/10.7265/N5W66HP8
2c4	Lake Ice	Mountain Lake Biology, Chemistry, Physics, and Climate Data since 1959 at Castle Lake ver 1. Environmental Data Initiative	https://doi.org/10.6073/pasta/a8e3b81cfe5864731b29ad42506c65d7
2c4	Lake Ice	Great Lakes Annual Maximum Ice Cover (%)	https://www.glerl.noaa.gov/data/ice/

Sub-section	General Variable or Phenomenon	Specific dataset or variable	Source
2c4	Lake Ice	Great Lakes Ice	www.glerl.noaa.gov/data/ice
2c4	Lake Ice	Geographic variation and temporal trends in ice phenology in Norwegian lakes during a century, Dryad	https://datadryad.org/stash/dataset/doi:10.5061/dryad.bk3j9kd9x
2c4	Lake Ice	lake surface water temperature and ice cover in subalpine Lake Lunz, Austria	https://doi.org/10.1080/20442041.2017.1294332
2c4	Temperature, [Near] Surface	NASA/GISS Global Temperature	https://data.giss.nasa.gov/gistemp/
2c5	Snow Properties	Northern Hemisphere (NH) Snow Cover Extent (SCE), Version 1	doi:10.7289/V5N014G9, https://www.snowcover.org

Section 2d Hydrological cycle

Sub-section	General Variable or Phenomenon	Specific dataset or variable	Source
2d1	Humidity, [Near] Surface	ERA5	https://www.ecmwf.int/en/forecasts/dataset/ecmwf-reanalysis-v5
2d1, 2d2	Humidity, [Near] Surface	HadISDH	www.metoffice.gov.uk/hadobs/hadisdh, https://catalogue.ceda.ac.uk/uuid/251474c7b09449d8b9e7aeaf1461858f
2d1	Humidity, [Near] Surface	JRA-55 Atmospheric Reanalysis	http://jra.kishou.go.jp/JRA-55/index_en.html
2d1	Humidity, [Near] Surface	MERRA-2	https://gmao.gsfc.nasa.gov/reanalysis/MERRA-2/
2d3	Water Vapor, Total Column	COSMIC	http://cosmic-io.cosmic.ucar.edu/cdaac/index.html
2d3	Water Vapor, Total Column	ERA5	https://www.ecmwf.int/en/forecasts/dataset/ecmwf-reanalysis-v5
2d3	Water Vapor, Total Column	GNSS Ground-Based Total Column Water Vapor	https://doi.org/10.25326/68
2d3	Water Vapor, Total Column	JRA-55 Atmospheric Reanalysis	http://jra.kishou.go.jp/JRA-55/index_en.html
2d3	Water Vapor, Total Column	MERRA-2	https://gmao.gsfc.nasa.gov/reanalysis/MERRA-2/
2d3	Water Vapor, Total Column	SSM/I -AMSR-E Ocean Total Column Water Vapor	http://www.remss.com
2d4	Humidity, Upper Atmosphere	Upper Troposphere Humidity (UTH)	Available on request to Brian Soden (bsoden@miami.edu)

Sub-section	General Variable or Phenomenon	Specific dataset or variable	Source
2d4	Humidity, Upper Atmosphere	ERA5	https://www.ecmwf.int/en/forecasts/dataset/ecmwf-reanalysis-v5
2d4	Humidity, Upper Atmosphere	High Resolution Infrared Sounder (HIRS)	https://www.ncei.noaa.gov/products/climate-data-records/hirs-ch12-brightness-temperature
2d4	Temperature, Upper Atmosphere	NOAA/NESDIS/STAR MSU v5	https://www.star.nesdis.noaa.gov/pub/smcd/emb/mscat/data/MSU_AMSU_v5.0/Monthly_Atmospheric_Layer_Mean_Temperature/
2d5, 2d6	Precipitation	GPCC	www.dwd.de/EN/ourservices/gpcc/gpcc.html
2d5	Precipitation	Global Precipitation Climatology Project (GPCP) v2.3	https://www.dwd.de/EN/ourservices/gpcc/gpcc.html, https://www.ncei.noaa.gov/products/global-precipitation-climatology-project
2d6	Precipitation	HadEX3	https://www.metoffice.gov.uk/hadobs/hadex3/
2d6	Precipitation	Climate Extremes Index Component 4	https://www.ncdc.noaa.gov/extremes/cei/
2d6	Precipitation	ERA5	https://www.ecmwf.int/en/forecasts/datasets/reanalysis-datasets/era5
2d6	Precipitation	GHCNDEX	https://www.climdex.org
2d6	Precipitation	MERRA-2	https://gmao.gsfc.nasa.gov/reanalysis/MERRA-2/
2d7	Cloud properties	PATMOS-x v6.0	https://www.ncei.noaa.gov/products/climate-data-records/avhrr-hirs-cloud-properties-patmos
2d7	Cloud Properties	Aqua MODIS C6.1 MYD08_M3	https://ladsweb.modaps.eosdis.nasa.gov/missions-and-measurements/products/MYD08_M3
2d7	Cloud Properties	Clouds and the Earth's Radiant Energy System Energy Balance and Filled (CERES EBAF) v4.2	https://ceres.larc.nasa.gov/data/
2d7	Modes of Variability	Multivariate ENSO Index (MEI) v2	https://psl.noaa.gov/enso/mei/
2d8	Lake Water Storage	'GloLakes' lake and reservoir storage	https://doi.org/10.5194/essd-16-201-2024
2d9	Groundwater and terrestrial water storage	GRACE / GRACE-FO	https://podaac.jpl.nasa.gov/dataset/TELLUS_GRAC-GRFO_MASCON_CRI_GRID_RL06.1_V3
2d10	Soil Moisture	Copernicus Climate Change Service (C3S) v202012 product based on the ESA Climate Change Initiative for Soil Moisture (ESA CCI SM) v05.2 merging algorithm	https://cds.climate.copernicus.eu/cdsapp#!/dataset/satellite-soil-moisture?tab=form

Sub-section	General Variable or Phenomenon	Specific dataset or variable	Source
2d11	Drought	Climatic Research Unit gridded Time Series (CRU TS) 4.07	https://crudata.uea.ac.uk/cru/data/hrg/cru_ts_4.07/
2d12	Land Evaporation	Climatic Research Unit gridded Time Series (CRU TS) 4.07	https://www.gleam.eu/
2d1	Modes of Variability	Southern Oscillation Index	https://crudata.uea.ac.uk/cru/data/soi/

Section 2e Atmospheric circulation

Sub-section	General Variable or Phenomenon	Specific dataset or variable	Source
2e1	Modes of Variability	Antarctic Oscillation (AAO)/Southern Annular Mode (SAM)	https://ftp.cpc.ncep.noaa.gov/cwlinks/norm.daily.aao.index.b790101.current.ascii
2e1	Pressure, Sea Level or Near-Surface	ERA5	https://www.ecmwf.int/en/forecasts/dataset/ecmwf-reanalysis-v5
2e2	Modes of Variability	Antarctic Oscillation (AAO)/Southern Annular Mode (SAM)	https://ftp.cpc.ncep.noaa.gov/cwlinks/norm.daily.aao.index.b790101.current.ascii
2e2	Wind, [Near] Surface	ERA5	https://www.ecmwf.int/en/forecasts/dataset/ecmwf-reanalysis-v5
2e2	Wind, [Near] Surface	HadISD v3.3.0.2022f	https://hadleyserver.metoffice.gov.uk/hadisd/v330_2022f/index.html
2e2	Wind, [Near] Surface	Modern-Era Retrospective Analysis for Research and Applications version 2 (MERRA-2)	http://gmao.gsfc.nasa.gov/reanalysis/MERRA-2/
2e2	Wind [Near Surface]	Remote Sensing System (RSS) Merged 1-deg monthly radiometer winds	https://www.remss.com/measurements/wind/
2e2	Wind [Near Surface]	Remote Sensing System (RSS) Advanced Scatterometer (ASCAT)	https://www.remss.com/missions/ascat/
2e2	Wind [Near Surface]	Remote Sensing System (RSS) QuickScat4	https://www.remss.com/missions/qscat/
2e3	Wind [Upper Atmosphere]	Quasi biennial Oscillation (QBO)	https://www.atmohub.kit.edu/data/singapore2023.dat
2e3	Modes of Variability	Antarctic Oscillation (AAO), Southern Annular Mode (SAM)	https://www.cpc.ncep.noaa.gov/products/precip/CWlink/daily_ao_index/aao/aao.shtml, http://www.nerc-bas.ac.uk/icd/gjma/sam.html

Sub-section	General Variable or Phenomenon	Specific dataset or variable	Source
2e3	Wind [Upper Atmosphere]	ERA5 hourly data on pressure levels from 1940 to present. Copernicus Climate Change Service (C3S) Climate Data Store (CDS)	https://cds.climate.copernicus.eu/cdsapp#!/dataset/reanalysis-era5-pressure-levels?tab=overview
2e3	Wind [Upper Atmosphere]	ERA-Interim	www.ecmwf.int/en/research/climate-reanalysis/era-interim
2e3	Wind [Upper Atmosphere]	MERRA-2	http://gmao.gsfc.nasa.gov/reanalysis/MERRA-2/
2e3	Wind [Upper Atmosphere]	JRA-55 Atmospheric Reanalysis	http://jra.kishou.go.jp/JRA-55/index_en.html
2e4	Lightning	GOES-R Geostationary Lightning Mapper (GLM) Gridded Data Products V1	http://doi.org/10.7289/V5KH0KK6

Section 2f Earth's radiation budget

Sub-section	General Variable or Phenomenon	Specific dataset or variable	Source
2f1	TOA Earth Radiation Budget	CERES Energy Balanced and Filled version 4.2	https://ceres-tool.larc.nasa.gov/ord-tool/jsp/EBAFTOA42Selection.jsp
2f1	TOA Earth Radiation Budget	CERES FLASHflux version 4A	https://ceres-tool.larc.nasa.gov/ord-tool/jsp/FLASH_TISASelection.jsp
2f1	TOA Earth Radiation Budget	Community-Consensus TSI Composit	https://spot.colorado.edu/~koppg/TSI/TSI_Composite-SIST.txt
2f2	Solar Transmission, Apparent	Mauna Loa Observatory	https://www.esrl.noaa.gov/gmd/webdata/grad/mloapt/mauna_loa_transmission.dat
2f2	Cloud Aerosol	Cloud-Aerosol LIDAR and Infrared Pathfinder Satellite Observations (CALIPSO)	http://www-calipso.larc.nasa.gov
2f2	Ozone, Stratospheric	Stratospheric Aerosol and Gas Experiment (SAGE) limb sounder	https://sage.nasa.gov/sageiii-iss/browse_images/expedited/

Section 2g Atmospheric composition

Sub-section	General Variable or Phenomenon	Specific dataset or variable	Source
2g1	Trace Gases	Atmospheric Gas trends	https://gml.noaa.gov/ccgg/trends/
2g1	Trace Gases	Global Greenhouse Gas Reference Network	https://gml.noaa.gov/ccgg/about.html

Sub-section	General Variable or Phenomenon	Specific dataset or variable	Source
2g1	Trace Gases	Atmospheric Greenhouse Gas Index (AGGI)	www.esrl.noaa.gov/gmd/aggi
2g2	Trace Gases	Halocarbons and other Atmospheric Trace Species	https://gml.noaa.gov/aftp/data/hats/
2g2	Trace Gases	Advanced Global Atmospheric Gases Experiment	https://agage2.eas.gatech.edu/data_archive/global_mean/global_mean_ms.txt
2g2	Trace Gases	Ozone-Depleting Gas Index (ODGI)	www.esrl.noaa.gov/gmd/odgi
2g3	Aerosols	Advanced Along Track Scanning Radiometer (AATSR)	https://earth.esa.int/eogateway/instruments/aatsr
2g3	Aerosols	Copernicus Atmosphere Monitoring Service Reanalysis (CAMSRA)	https://ads.atmosphere.copernicus.eu/cdsapp#!/dataset/cams-global-radiative-forcing-auxilliary-variables?tab=overview
2g4	Ozone, Tropospheric	NOAA Global Monitoring Laboratory	https://gml.noaa.gov/aftp/data/ozwv/SurfaceOzone/
2g5	Stratospheric Aerosols	OHP LTA lidar	https://www-air.larc.nasa.gov/missions/ndacc/data.html?station=haute.provence/ames/lidar/
2g5	Stratospheric Aerosols	OHP LiO3S lidar	https://www-air.larc.nasa.gov/missions/ndacc/data.html?station=haute.provence/ames/lidar/
2g5	Stratospheric Aerosols	Lauder aerosol lidar	https://www-air.larc.nasa.gov/missions/ndacc/data.html?station=lauder/ames/lidar/
2g5	Stratospheric Aerosols	SAGE III v5.3	https://asdc.larc.nasa.gov/project/SAGE%20III-ISS/g3bssp_53
2g5	Stratospheric Aerosols	GloSSAC v2.	https://asdc.larc.nasa.gov/project/GloSSAC
2g5	Stratospheric Aerosols	OMPS-LP v2.1	https://disc.gsfc.nasa.gov/datasets/OMPS_NPP_LP_L2_AER_DAILY_2/summary
2g6	Ozone, Total Column and Stratospheric	GOME/SCIAMACHY/GOME2 (GSG) Merged Total Ozone	http://www.iup.uni-bremen.de/UVSAT/datasets/merged-wfdoas-total-ozone
2g6	Ozone, Total Column and Stratospheric	GOME/SCIAMACHY/GOME2 (GTO) Merged Total Ozone	https://atmos.eoc.dlr.de/gto-ecv
2g6	Ozone, Total Column and Stratospheric	GOZCARDS ozone profiles	https://www.earthdata.nasa.gov/esds/competitive-programs/measures/gozcards
2g6	Ozone, Total Column and Stratospheric	Multi Sensor Reanalysis (MSR-2) of total ozone	http://www.temis.nl/protocols/O3global.html
2g6	Ozone, Total Column and Stratospheric	NASA BUV/SBUV/OMPS v8.7 (MOD) Merged Ozone	https://acd-ext.gsfc.nasa.gov/Data_services/merged/

Sub-section	General Variable or Phenomenon	Specific dataset or variable	Source
2g6	Ozone, Total Column and Stratospheric	NOAA SBUV V8.6 OMPS V4r1 cohesive data set (COH)	ftp://ftp.cpc.ncep.noaa.gov/SBUV_CDR/
2g6	Ozone, Total Column and Stratospheric	Network for the Detection of Atmospheric Composition Change (NDACC) lidar, microwave and FTIR	https://www-air.larc.nasa.gov/missions/ndacc
2g6	Ozone, Total Column and Stratospheric	CCMI-2022 model runs	https://blogs.reading.ac.uk/ccmi/ccmi-2022/
2g6	Ozone, Total Column and Stratospheric	SAGE-CCI-OMPS	https://climate.esa.int/en/projects/ozone/data
2g6	Ozone, Total Column and Stratospheric	SAGE/OSIRIS	Bourassa et al. (2018) doi:10.5194/amt-11-489-2018
2g6	Ozone, Total Column and Stratospheric	SAGE-SCIA-OMPS	Arosio et al., (2018) doi:10.5194/amt-2018-275
2g6	Ozone, Total Column and Stratospheric	SWOOSH	www.esrl.noaa.gov/csd/groups/csd8/swoosh/
2g6	Ozone, Total Column and Stratospheric	WOUDC Ground-based Ozone	ftp.tor.ec.gc.ca; cd /pub/woudc/Projects Campaigns/ZonalMeans
2g7	Stratospheric Water Vapor	the Aura Microwave Limb Sounder version 5.0 data, as merged into SWOOSH	www.esrl.noaa.gov/csd/groups/csd8/swoosh/
2g7	Tropopause Temperature	MERRA-2	http://gmao.gsfc.nasa.gov/reanalysis/MERRA-2/
2g7	Stratospheric Water Vapor	NOAA Frostpoint Hygrometer (FPH)	https://gml.noaa.gov/aftp/data/ozwv/WaterVapor/
2g7	Stratospheric Water Vapor	Cryogenic Frostpoint Hygrometer (CFH)	https://ndacc.org
2g8	Trace Gases	Copernicus Atmosphere Monitoring Service Reanalysis (CAMSRA) for Carbon Monoxide	https://ads.atmosphere.copernicus.eu/cdsapp#!/dataset/cams-global-radiative-forcing-auxilliary-variables?tab=overview

Section 2h Land surface properties

Sub-section	General Variable or Phenomenon	Specific dataset or variable	Source
2h1	Albedo	MODIS/Terra+Aqua BRDF/ Albedo Albedo Daily L3 Global 0.05Deg CMG V061	https://lpdaac.usgs.gov/products/mcd43c3v061/
2h1	Albedo	VIIRS VNP43C3 Collection 1.0	https://lpdaac.usgs.gov/products/vnp43c3v001 https://doi.org/10.5067/VIIRS/VNP43C3.001

Sub-section	General Variable or Phenomenon	Specific dataset or variable	Source
2h2	fraction of absorbed photosynthetically active radiation (FAPAR)	JRC TIP MODIS	https://fapar.jrc.ec.europa.eu
2h2	FAPAR	MERIS	https://fapar.jrc.ec.europa.eu
2h2	FAPAR	SeaWiFS FAPAR	http://fapar.jrc.ec.europa.eu/
2h2	FAPAR	OLCI	https://dataspace.copernicus.eu/
2h3	Biomass, Greenness or Burning	GFAS v1.4	https://ads.atmosphere.copernicus.eu/cdsapp#!/dataset/cams-global-fire-emissions-gfas
2h3	Biomass, Greenness or Burning	Global Fire Emissions Database	https://www.globalfiredata.org/data.html
2h3	Deforestation	PRODES Amazonia	http://www.obt.inpe.br/OBT/assuntos/programas/amazonia/prodes
2h4	Phenology	MODIS Normalized Difference Vegetative Inex	https://modis.gsfc.nasa.gov/data/dataprod/mod13.php
2h4	Temperature [Near] Surface	MERRIS-2 monthly temperature	https://goldsmr4.gesdisc.eosdis.nasa.gov/data/MERRA2_MONTHLY/M2TMNXLND.5.12.4/
2h4	Phenology	USA-National Phenology Network (NPN) phenology data	https://www.usanpn.org/data/observational
2h4	Phenology	USA-National Phenology Network (NPN) Spring Index raster data products	https://data.usanpn.org/geoserver-request-builder/
2h4	Phenology	German oak phenology data	https://opendata.dwd.de/
2h4	Phenology	Harvard Forest	https://harvardforest1.fas.harvard.edu/exist/apps/datasets/showData.html?id=hf003
2h4	Phenology	Natures Calendar	https://naturescalendar.woodlandtrust.org.uk/
2h4	Phenology	PhenoCam	http://phenocam.sr.unh.edu
2h4	Phenology	UK Cumbrian lakes data	https://catalogue.ceh.ac.uk/documents/bf30d6aa-345a-4771-8417-ffbcf8c08c28/
2h5	Vegetation Optical Depth	Global Long-term Microwave Vegetation Optical Depth Climate Archive (VODCA) v2	https://researchdata.tuwien.ac.at/records/t74ty-tcx62
2h5	Modes of Variability	Southern Oscillation Index	http://www.bom.gov.au/climate/enso/soi/

Sidebar 2.2 Near-surface equivalent temperature as a key climate change metric

Sub-section	General Variable or Phenomenon	Specific dataset or variable	Source
SB2.2	Temperature [Near] Surface	ERA5	https://www.ecmwf.int/en/forecasts/dataset/ecmwf-reanalysis-v5
SB2.2	Dewpoint	ERA5	https://www.ecmwf.int/en/forecasts/dataset/ecmwf-reanalysis-v5
SB2.2	Pressure [Near] Surface	ERA5	https://www.ecmwf.int/en/forecasts/dataset/ecmwf-reanalysis-v5
SB2.2	Humidity [Near] Surface	HadISDH	www.metoffice.gov.uk/hadobs/hadisdh, https://catalogue.ceda.ac.uk/uuid/251474c7b09449d8b9e7aeaf1461858f

Appendix 3: Supplemental materials

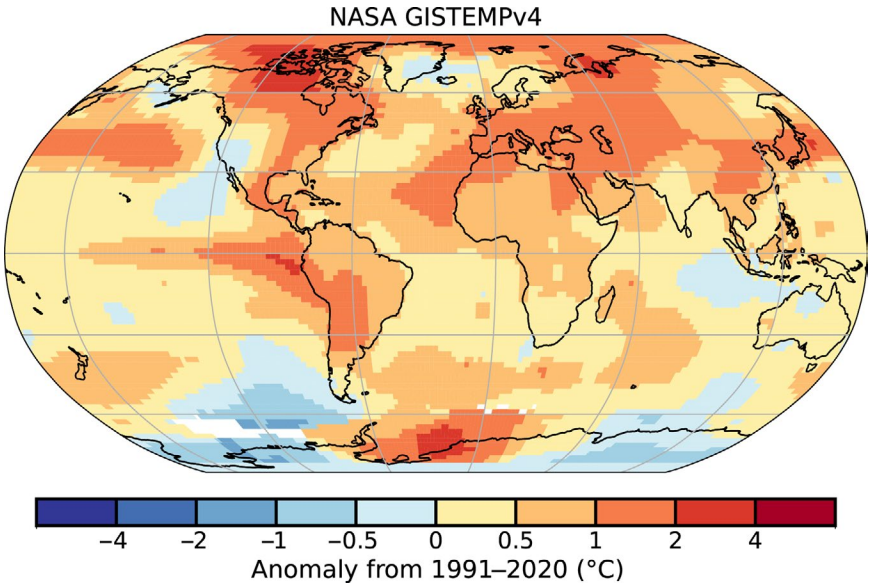

Fig. A2.1. Global surface temperature anomalies. (°C; Source: NASA-GISTEMPv4.)

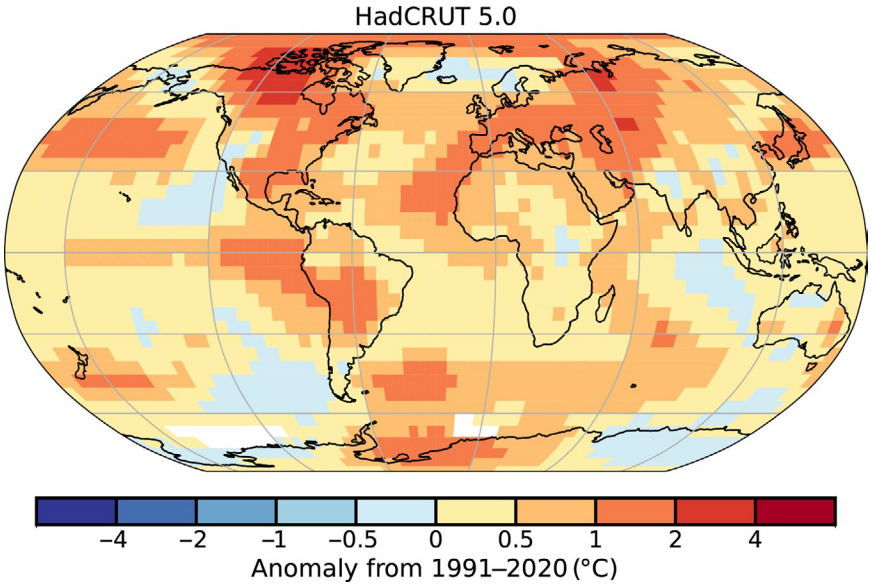

Fig. A2.2. Global surface temperature anomalies. (°C; Source: HadCRUT5.)

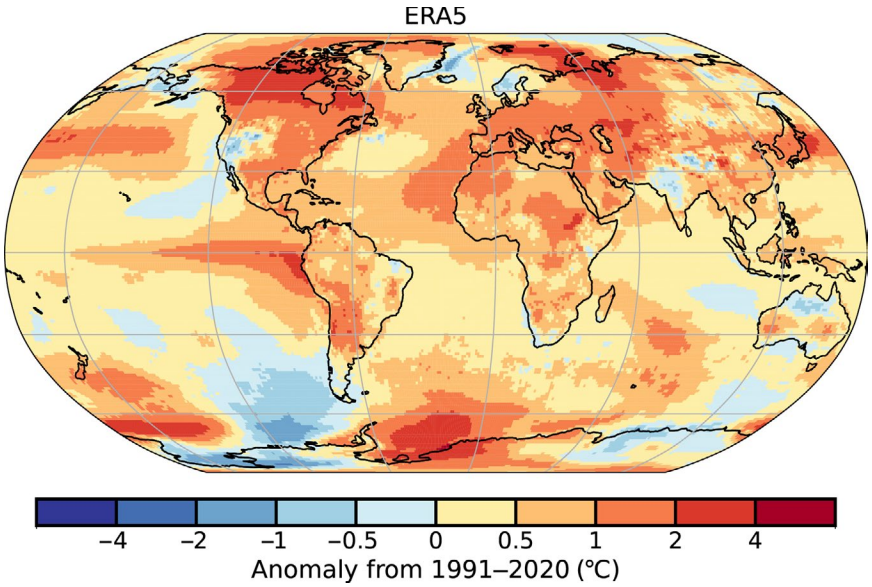

Fig. A2.3. Global surface temperature anomalies. (°C; Source: ERA5.).

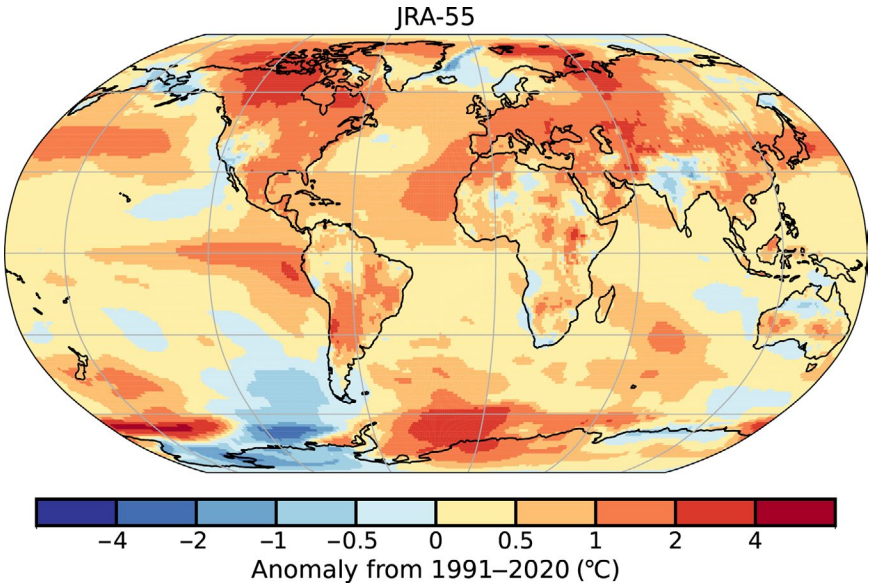

Fig. A2.4. Global surface temperature anomalies. (°C; Source: JRA-55.)

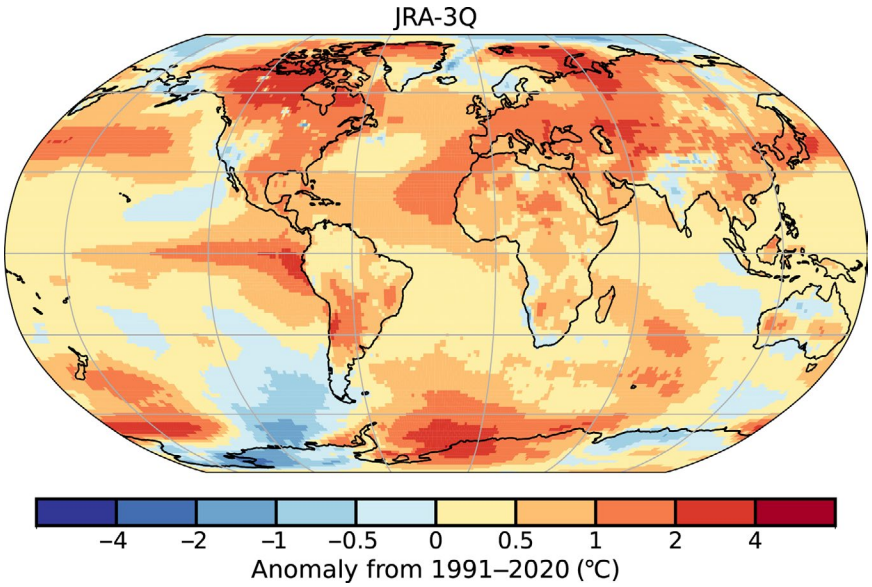

Fig. A2.5. Global surface temperature anomalies. (°C; Source: JRA-3Q.)

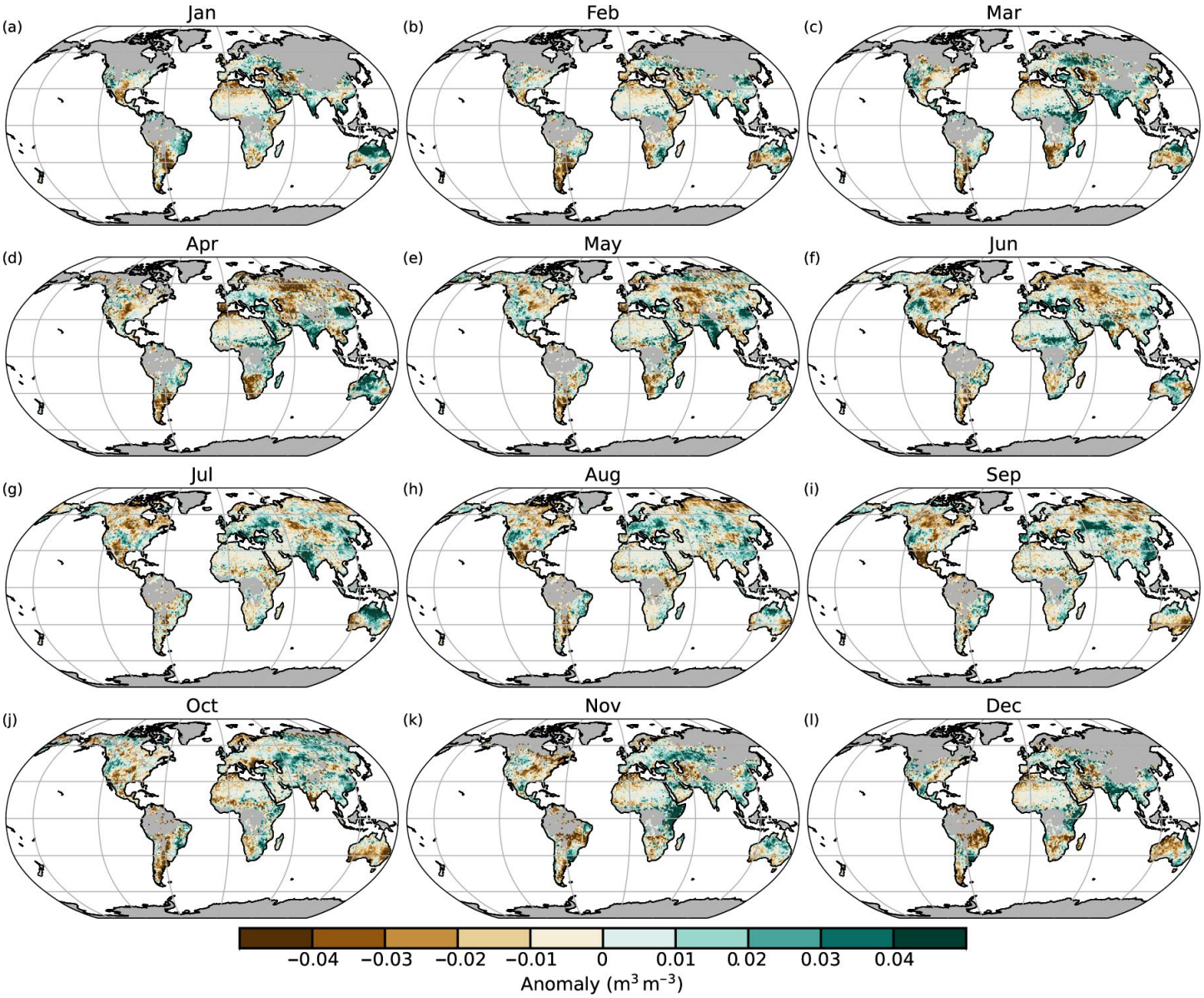

Fig. A2.6. Monthly average soil moisture anomalies for 2023 ($m^3\ m^{-3}$; 1991–2020 base period). Data are masked where no retrieval is possible or where the quality is not assured and flagged, for example due to dense vegetation, frozen soil, permanent ice cover, or radio frequency interference. (Source: C3S Soil Moisture.)

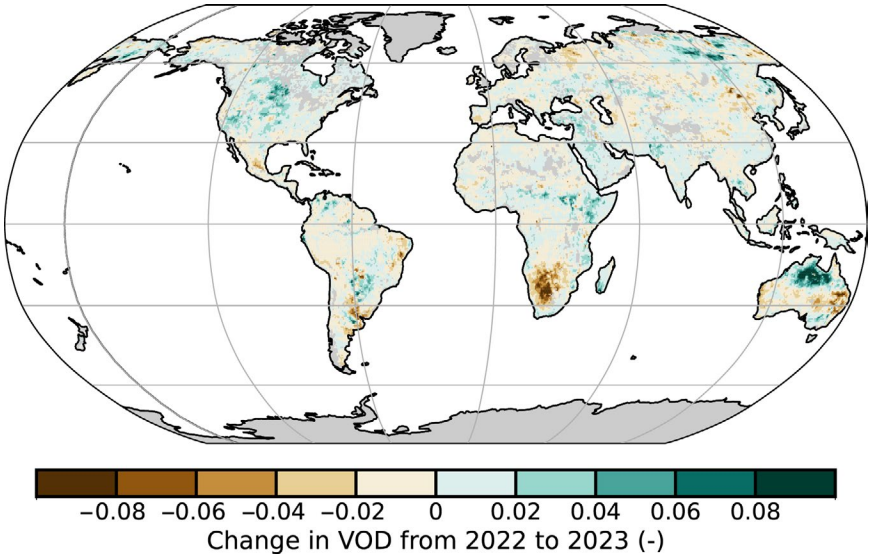

Fig. A2.7. The difference in average CXKu vegetation optical depth (VOD) between the years 2022 and 2023. Brown (green) colors indicate areas where VOD in 2023 were lower (higher) than in 2022. (Source: VODCA.)

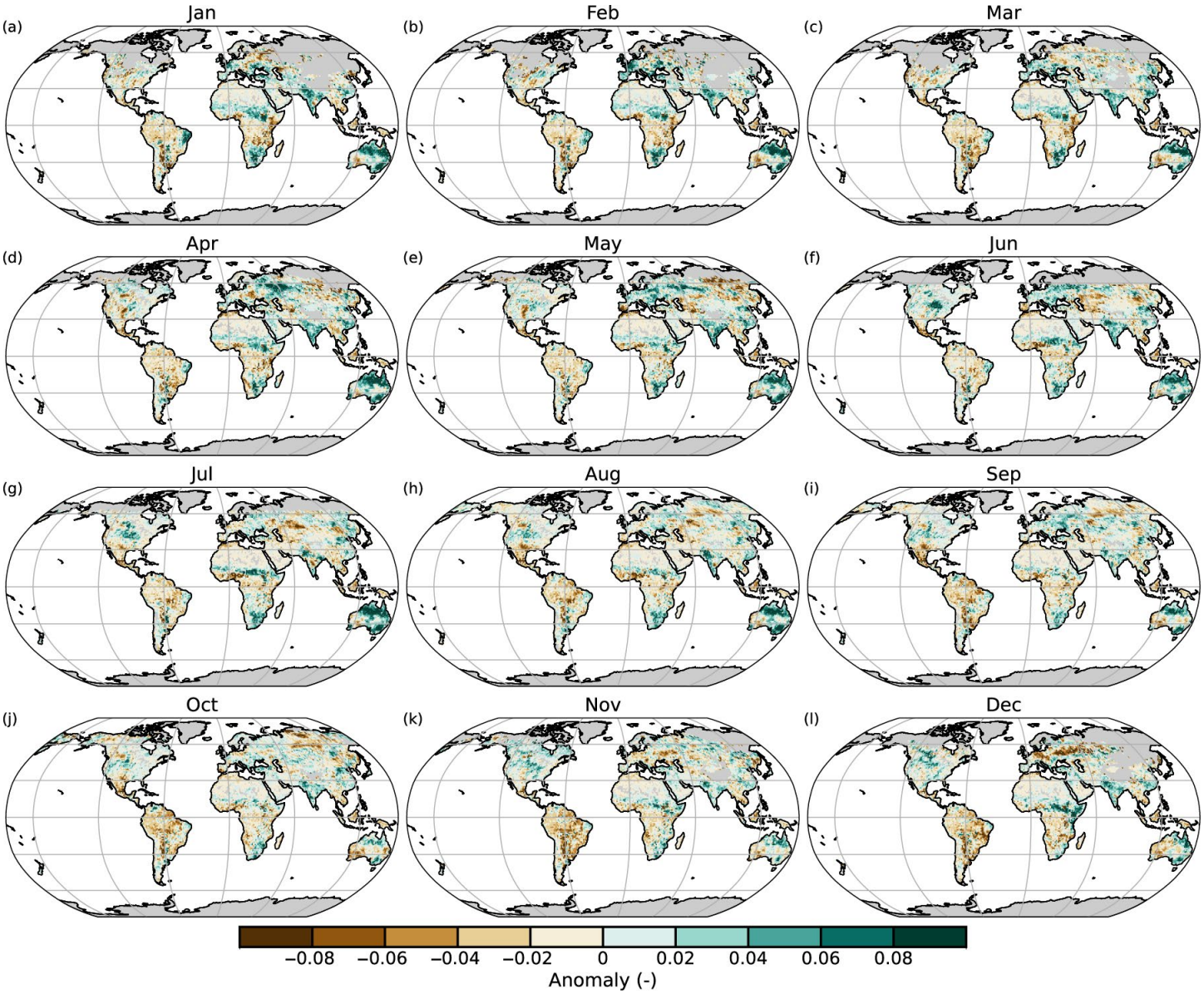

Fig. A2.8. VODCA monthly CXKu vegetation optical depth (VOD) anomalies in 2023 (1991–2020 base period). VOD cannot be retrieved over frozen or snow-covered areas, which is why they are masked out in winter.

Table A2.1. Notable precipitation events, with prior known record where long-term observations are available. (Source: GHCNDEX unless otherwise noted.)

Date	Index	Amount (mm)	Prior Record Year (Amount in mm)	Location	Reference
01/02/23	Rx5day	653.2	1987 (336.5)	Beverley Springs, Australia	
01/19/23	Rx1day	104		Antosyhihy, Madagascar	Davies (2023a)
02/14/23	Rx1day	183.8		Whangarei, New Zealand	Murray (2023)
02/14/23	Rx5day	408.7		Glenbervie Forest, Northland, New Zealand	Murray (2023)
02/14/23	Rx5day	447		The Pinnacles, New Zealand	Murray (2023)
02/19/23	Rx1day	682		Bertioga, Brazil	Davies (2023b)
02/24/23	Rx1day	672		Marromeu, Mozambique	United Nations Office for the Coordination of Humanitarian Affairs (2023)
08/03/23	Rx5day	488	1998 (264.4)	Almora Station, Australia	
09/03/23	Rx5day	421	2009 (294)	Undilla Station, Australia	Bureau of Meteorology (2024)
03/16/23	Rx1day	152.4	1962 (71.1)	Hat Creek, California, USA	
04/12/23	Rx1day	571.5	2003 (259.6)	Fort Lauderdale, Florida, USA	
05/02/23	Rx1day	182.6		Mushubati, Rwanda	World Meteorological Organization (WMO; 2023)
05/24/23	Rx1day	304.8	2018 (230.1)	Agat, Guam	
06/23/23	Rx1day	156.6		Retiro, Chile	Davies (2023c)
07/07/23	Rx5day	160.3	2001 (95.4)	Delsbo, Sweden	
07/20/23	Rx1day	198.6		Maharashtra, India	Davies (2023d)
07/28/23	Rx1day	649.8		Mulugu, India	The Watchers (2023)
08/19/23	Rx5day	371.9		Termas de Chillán, Chile	Davies (2023e)
08/22/23	Rx1day	73.7	2016 (38.1)	Rosette, Utah, USA	
08/24/23	Rx1day	123	2016 (73.6)	Harrow, Canada	
08/29/23	Rx5day	744.8		Wangjiayuan Reservoir, China	Du Yan (2023)

Date	Index	Amount (mm)	Prior Record Year (Amount in mm)	Location	Reference
09/04/23	Rx5day	1096.2		Zagora Pelion, Greece	WMO (2023)
09/05/23	Rx1day	759.6		Zagora Pelion, Greece	WMO (2023)
09/07/23	Rx1day	425	1926 (534.1)	Hong Kong Observatory	Hong Kong Observatory (2024)
09/07/23	Rx1h	158.1	2008 (145.5)	Hong Kong Observatory	Hong Kong Observatory (2024)
09/08/23	Rx1day	391.5	2013 (272)	Mobara City, Japan	Davies (2023f)
09/11/23	Rx1day	414.1		Al Badya, Libya	WMO (2023)
09/25/23	Rx1day	216		Dwarsberg, South Africa	Maswanganye (2023)
10/24/23	Rx1day	406		Al Ghadya Airport, Yemen	Davies (2023g)
10/29/23	Rx5day	1125.8	1995 (704.2)	Danang, Vietnam	
12/13/23	Rx5day	1933.8	1996 (1265.6)	Whyanbeel Valley, Australia	
12/13/23	Rx5day	1592.8	2018 (557.2)	White Cliff Point, Australia	
12/13/23	Rx5day	1295	2004 (745)	Copperlode Dam, Australia	
12/21/23	Rx5day	211.4	2022 (127)	Green Cape, Australia	

References

Adler, R., G. Gu, M. Sapiano, J. Wang, and G. Huffman, 2017: Global precipitation: Means, variations and trends during the satellite era (1979–2014). *Surv. Geophys.*, **38**, 679–699, https://doi.org/10.1007/s10712-017-9416-4.

—— , and Coauthors, 2018: The Global Precipitation Climatology Project (GPCP) monthly analysis (new version 2.3) and a review of 2017 global precipitation. *Atmosphere*, **9**, 138, https://doi.org/10.3390/atmos9040138.

Alden, C. B., J. B. Miller, and J. W. C. White, 2010: Can bottom-up ocean CO_2 fluxes be reconciled with atmospheric ^{13}C observations? *Tellus*, **62B**, 369–388, https://doi.org/10.1111/j.1600-0889.2010.00481.x.

Ali, H., H. J. Fowler, and V. Mishra, 2018: Global observational evidence of strong linkage between dew point temperature and precipitation extremes. *Geophys. Res. Lett.*, **45**, 12 320–12 330, https://doi.org/10.1029/2018GL080557.

Allan, R. J., J. A. Lindesay, and D. E. Parker, 1996: El Niño Southern Oscillation and Climatic Variability. CSIRO Publishing, 405 pp.

Allan, R. P., C. Liu, M. Zahn, D. A. Lavers, E. Koukouvagias, and A. Bodas-Salcedo, 2014: Physically consistent responses of the global atmospheric hydrological cycle in models and observations. *Surv. Geophys.*, **35**, 533–552, https://doi.org/10.1007/s10712-012-9213-z.

Ammann, C. M., G. A. Meehl, W. M. Washington, and C. S. Zender, 2003: A monthly and latitudinally varying volcanic forcing dataset in simulations of 20th century climate. *Geophys. Res. Lett.*, **30**, 1657, https://doi.org/10.1029/2003GL016875.

Aono, Y., and K. Kazui, 2008: Phenological data series of cherry tree flowering in Kyoto, Japan, and its application to reconstruction of springtime temperatures since the 9th century. *Int. J. Climatol.*, **28**, 905–914, https://doi.org/10.1002/joc.1594.

Arguez, A., S. Hurley, A. Inamdar, L. Mahoney, A. Sanchez-Lugo, and L. Yang, 2020: Should we expect each year in the next decade (2019–28) to be ranked among the top 10 warmest years globally? *Bull. Amer. Meteor. Soc.*, **101**, E655–E663, https://doi.org/10.1175/BAMS-D-19-0215.1.

Arosio, C., A. Rozanov, E. Malinina, M. Weber, and J. P. Burrows, 2019: Merging of ozone profiles from SCIAMACHY, OMPS and SAGE II observations to study stratospheric ozone changes. *Atmos. Meas. Tech.*, **12**, 2423–2444, https://doi.org/10.5194/amt-12-2423-2019.

Augustine, J. A., K. O. Lantz, J.-P. Vernier, and J. E. Barnes, 2023: Mauna Loa apparent transmission record update for 2022 [in "State of the Climate in 2022"]. *Bull. Amer. Meteor. Soc.*, **104** (9), S81–S84, https://doi.org/10.1175/BAMS-D-23-0090.1.

Ayarzagüena, B., S. Ineson, N. J. Dunstone, M. P. Baldwin, and A. A. Scaife, 2018: Intraseasonal effects of El Niño–Southern Oscillation on North Atlantic climate. *J. Climate*, **31**, 8861–8873, https://doi.org/10.1175/JCLI-D-18-0097.1.

Azisov, E., M. Hoelzle, S. Vorogushyn, T. Saks, R. Usubaliev, M. Esenaman uulu, and M. Barandun, 2022: Reconstructed centennial mass balance change for Golubin glacier, Northern Tien Shan. *Atmosphere*, **13**, 954, https://doi.org/10.3390/atmos13060954.

Azorin-Molina, C., R. J. H. Dunn, L. Ricciardulli, C. A. Mears, T. R. McVicar, J. P. Nicolas, Z. Zeng, and M. G. Bosilovich, 2023a: Land and ocean surface winds [in "State of the Climate in 2022"]. *Bull. Amer. Meteor. Soc.*, **104** (9), S72–S74, https://doi.org/10.1175/BAMS-D-23-0090.1.

—— , and Coauthors, 2023b: Biases in wind speed measurements due to anemometer changes. *Atmos. Res.*, **289**, 106771, https://doi.org/10.1016/j.atmosres.2023.106771.

Baldwin, J. W., T. Benmarhnia, K. L. Ebi, O. Jay, N. J. Lutsko, and J. K. Vanos, 2023: Humidity's role in heat-related health outcomes: A heated debate. *Environ. Health Perspect.*, **131**, 055001, https://doi.org/10.1289/EHP11807.

Baldwin, M. P., and Coauthors, 2001: The quasi-biennial oscillation. *Rev. Geophys.*, **39**, 179–229, https://doi.org/10.1029/1999RG000073.

Barichivich, J., E. Gloor, P. Peylin, R. J. Brienen, J. Schöngart, J. C. Espinoza, and K. C. Pattnayak, 2018: Recent intensification of Amazon flooding extremes driven by strengthened Walker circulation. *Sci. Adv.*, **4**, eaat8785, https://doi.org/10.1126/sciadv.aat8785.

—— , T. J. Osborn, I. Harris, G. van der Schrier, and P. D. Jones, 2020: Monitoring global drought using the self-calibrating Palmer Drought Severity Index [in "State of the Climate in 2019"]. *Bull. Amer. Meteor. Soc.*, **101** (8), S59–S60, https://doi.org/10.1175/BAMS-D-20-0104.1.

—— , —— , —— , —— , and —— , 2021: Monitoring global drought using the self-calibrating Palmer Drought Severity Index [in "State of the Climate in 2020"]. *Bull. Amer. Meteor. Soc.*, **102** (8), S68–S70, https://doi.org/10.1175/BAMS-D-21-0098.1.

—— , —— , —— , —— , and —— , 2022: Monitoring global drought using the self-calibrating Palmer Drought Severity Index [in "State of the Climate in 2021"]. *Bull. Amer. Meteor. Soc.*, **103** (8), S66–S67, https://doi.org/10.1175/BAMS-D-22-0092.1.

Bartow-Gillies, E., J. Blunden, and T. Boyer, 2023: A look at 2022: Takeaway points from the state of the climate. *Bull. Amer. Meteor. Soc.*, **104**, 810–820, https://doi.org/10.1175/BAMS-D-23-0192.1.

Basu, S., and Coauthors, 2022: Estimating emissions of methane consistent with atmospheric measurements of methane and $\delta^{13}C$ of methane. *Atmos. Chem. Phys.*, **22**, 15 351–15 377, https://doi.org/10.5194/acp-22-15351-2022.

Becker, A., P. Finger, A. Meyer-Christoffer, B. Rudolf, K. Schamm, U. Schneider, and M. Ziese, 2013: A description of the global land-surface precipitation data products of the Global Precipitation Climatology Centre with sample applications including centennial (trend) analysis from 1901–present. *Earth Syst. Sci. Data*, **5**, 71–99, https://doi.org/10.5194/essd-5-71-2013.

Behera, S. K., J. J. Luo, S. Masson, S. A. Rao, H. Sakuma, and T. Yamagata, 2006: A CGCM study on the interaction between IOD and ENSO. *J. Climate*, **19**, 1688–1705, https://doi.org/10.1175/JCLI3797.1.

Bell, B., and Coauthors, 2021: The ERA5 global reanalysis: Preliminary extension to 1950. *Quart. J. Roy. Meteor. Soc.*, **147**, 4186–4227, https://doi.org/10.1002/qj.4174.

Bell, G. D., and M. S. Halpert, 1998: Climate assessment for 1997. *Bull. Amer. Meteor. Soc.*, **79** (Suppl.), S1–S50, https://doi.org/10.1175/1520-0477-79.5s.S1.

Bellouin, N., and Coauthors, 2020: Radiative forcing of climate change from the Copernicus reanalysis of atmospheric composition. *Earth Syst. Sci. Data*, **12**, 1649–1677, https://doi.org/10.5194/essd-12-1649-2020.

Bessenbacher, V., D. L. Schumacher, M. Hirschi, S. I. Seneviratne, and L. Gudmundsson, 2023: Gap-filled multivariate observations of global land–climate interactions. *J. Geophys. Res. Atmos.*, **128**, e2023JD039099, https://doi.org/10.1029/2023JD039099.

Betts, R. A., C. D. Jones, J. R. Knight, R. F. Keeling, and J. J. Kennedy, 2016: El Niño and a record CO_2 rise. *Nat. Climate Change*, **6**, 806–810, https://doi.org/10.1038/nclimate3063.

Birkett, C., C. Reynolds, B. Beckley, and B. Doorn, 2011: From research to operations: The USDA Global Reservoir and Lake Monitor. *Coastal Altimetry*, S. Vignudelli et al., Eds., Springer, 19–50, https://doi.org/10.1007/978-3-642-12796-0_2.

Block, B. D., and Coauthors, 2019: The unique methodological challenges of winter limnology. *Limnol. Oceanogr. Methods*, **17**, 42–57, https://doi.org/10.1002/lom3.10295.

Bock, O., 2022: Global GNSS Integrated Water Vapour data, 1994–2022. AERIS, accessed 18 July 2024, https://doi.org/10.25326/68.

—— , and A. C. Parracho, 2019: Consistency and representativeness of integrated water vapour from ground-based GPS observations and ERA-Interim reanalysis. *Atmos. Chem. Phys.*, **19**, 9453–9468, https://doi.org/10.5194/acp-19-9453-2019.

Bodhaine, B. A., B. G. Mendonca, J. M. Harris, and J. M. Miller, 1981: Seasonal variations in aerosols and atmospheric transmission at Mauna Loa Observatory. *J. Geophys. Res.*, **86**, 7395–7398, https://doi.org/10.1029/JC086iC08p07395.

Bowen, S., B. Kerschner, and J. Z. Ng, 2024: Natural catastrophe and climate report 2023: Data, insights and perspective. Gallagher Re, 76 pp., https://www.ajg.com/gallagherre/-/media/files/gallagher/gallagherre/news-and-insights/2024/january/natural-catastrophe-and-climate-report-2023.pdf.

Brohan, P., J. J. Kennedy, I. Harris, S. F. Tett, and P. D. Jones, 2006: Uncertainty estimates in regional and global observed temperature changes: A new data set from 1850. *J. Geophys. Res.*, **111**, D12106, https://doi.org/10.1029/2005JD006548.

Brutsaert, W., 2017: Global land surface evaporation trend during the past half century: Corroboration by Clausius-Clapeyron scaling. *Adv. Water Resour.*, **106**, 3–5, https://doi.org/10.1016/j.advwatres.2016.08.014.

Bureau of Meteorology, 2024a: Annual climate statement 2023. Accessed 15 February 2024, http://www.bom.gov.au/climate/current/annual/aus/.

—— , 2024b: Tropical climate update. Accessed 15 January 2024, http://www.bom.gov.au/climate/tropical-note/.

Butchart, N., 2014: The Brewer-Dobson circulation. *Rev. Geophys.*, **52**, 157–184, https://doi.org/10.1002/2013RG000448.

Buzan, J. R., and M. Huber, 2020: Moist heat stress on a hotter Earth. *Annu. Rev. Earth Planet. Sci.*, **48**, 623–655, https://doi.org/10.1146/annurev-earth-053018-060100.

Byrne, M. P., and P. A. O'Gorman, 2013: Link between land–ocean warming contrast and surface relative humidities in simulations with coupled climate models. *Geophys. Res. Lett.*, **40**, 5223–5227, https://doi.org/10.1002/grl.50971.

—— , and —— , 2018: Trends in continental temperature and humidity directly linked to ocean warming. *Proc. Natl. Acad. Sci. USA*, **115**, 4863–4868, https://doi.org/10.1073/pnas.1722312115.

Caine, T., J. Morse, and Niwot Ridge LTER, 2023: Lake ice clearance and formation data for Green Lakes Valley, 1968 – ongoing, version 6. Environmental Data Initiative, accessed 17 January 2024, https://doi.org/10.6073/pasta/e89a9a6984ebbcdbbc85c16d65298dd2.

Campos, D., and R. Rondanelli, 2023: ENSO-related precipitation variability in Central Chile: The role of large scale moisture transport. *J. Geophys. Res. Atmos.*, **128**, e2023JD038671, https://doi.org/10.1029/2023JD038671.

Capotondi, A., and Coauthors, 2015: Understanding ENSO diversity. *Bull. Amer. Meteor. Soc.*, **96**, 921–938, https://doi.org/10.1175/BAMS-D-13-00117.1.

Carn, S., N. Krotkov, B. Fisher, and C. Li, 2022: Out of the blue: Volcanic SO2 emissions during the 2021–2022 eruptions of Hunga Tonga —— Hunga Ha'apai (Tonga). Front. *Earth Sci.*, **10**, 976962, https://doi.org/10.3389/feart.2022.976962.

Carrea, L., O. Embury, and C. J. Merchant, 2015: Datasets related to in-land water for limnology and remote sensing applications: Distance-to-land, distance-to-water, water-body identifier and lake-centre co-ordinates. *Geosci. Data J.*, **2**, 83–97, https://doi.org/10.1002/gdj3.32.

—— , and Coauthors, 2019: Lake surface temperature [in "State of the Climate in 2018"]. *Bull. Amer. Meteor. Soc.*, **100** (8), S13–S14, https://doi.org/10.1175/2019BAMSStateoftheClimate.1.

—— , and Coauthors, 2020: Lake surface temperature [in "State of the Climate in 2019"]. *Bull. Amer. Meteor. Soc.*, **101** (8), S26–S28, https://doi.org/10.1175/BAMS-D-20-0104.1.

—— , C. Merchant, B. Calmettes, and J.-F. Cretaux, 2021: Lake surface water temperature [in "State of the Climate in 2020"]. *Bull. Amer. Meteor. Soc.*, **102** (8), S28–S31, https://doi.org/10.1175/BAMS-D-21-0098.1.

—— , —— , and R. I. Woolway, 2022a: Lake surface water temperature [in "State of the Climate in 2021"]. *Bull. Amer. Meteor. Soc.*, **103** (8), S28–S30, https://doi.org/10.1175/BAMS-D-22-0092.1.

—— , and Coauthors, 2022b: ESA Lakes Climate Change Initiative (Lakes_cci): Lake products, version 2.0.2. NERC EDS Centre for Environmental Data Analysis[NR9][KW10], accessed March 2024, https://doi.org/10.5285/a07deacaffb8453e93d57ee214676304.

—— , and Coauthors, 2023: Satellite-derived multivariate worldwide lake physical variable timeseries for climate studies. *Sci. Data*, **10**, 30, https://doi.org/10.1038/s41597-022-01889-z.

Chandra, S., E. K. Suenaga, F. Scordo, and T. A. Daniel, 2022: Mountain lake biology, chemistry, physics, and climate data since 1959 at Castle Lake, version 1. Environmental Data Initiative, accessed 17 January 2024, https://doi.org/10.6073/pasta/a8e3b81cfe5864731b29ad42506c65d7.

Chang, K.-L., M. G. Schultz, X. Lan, A. McClure-Begley, I. Petropavlovskikh, X. Xu, and J. R. Ziemke, 2021: Trend detection of atmospheric time series: Incorporating appropriate uncertainty estimates and handling extreme events. *Elementa*, **9**, 00035, https://doi.org/10.1525/elementa.2021.00035.

—— , and Coauthors, 2022: Impact of the COVID-19 economic downturn on tropospheric ozone trends: An uncertainty weighted data synthesis for quantifying regional anomalies above western North America and Europe. *AGU Adv.*, **3**, e2021AV000542, https://doi.org/10.1029/2021AV000542.

—— , and Coauthors, 2023: Diverging ozone trends above western North America: Boundary layer decreases versus free tropospheric increases. *J. Geophys. Res. Atmos.*, **128**, e2022JD038090, https://doi.org/10.1029/2022JD038090.

Christianson, K. R., K. A. Loria, P. D. Blanken, N. Caine, and P. T. J. Johnson, 2021: On thin ice: Linking elevation and long-term losses of lake ice cover. *Limnol. Oceanogr. Lett.*, **6**, 77–84, https://doi.org/10.1002/lol2.10181.

Christy, J. R., R. W. Spencer, W. B. Norris, W. D. Braswell, and D. E. Parker, 2003: Error estimates of version 5.0 of MSU–AMSU bulk atmospheric temperatures. *J. Atmos. Oceanic Technol.*, **20**, 613–629, https://doi.org/10.1175/1520-0426(2003)20<613:EEOVOM>2.0.CO;2.

Chung, E.-S., B. Soden, and V. O. John, 2013: Intercalibrating microwave satellite observations for monitoring long-term variations in upper- and midtropospheric water vapor. *J. Atmos. Oceanic Technol.*, **30**, 2303–2319, https://doi.org/10.1175/JTECH-D-13-00001.1.

—— , —— , B. Sohn, and L. Shi, 2014: Upper-tropospheric moistening in response to anthropogenic warming. *Proc. Natl. Acad. Sci. USA*, **111**, 11636–11641, https://doi.org/10.1073/pnas.1409659111.

Cicoira, A., J. Beutel, J. Faillettaz, and A. Vieli, 2019: Water controls the seasonal rhythm of rock glacier flow. *Earth Planet. Sci. Lett.*, **528**, 115844, https://doi.org/10.1016/j.epsl.2019.115844.

Clark, H., and Coauthors, 2021: The effects of the COVID-19 lockdowns on the composition of the troposphere as seen by In-service Aircraft for a Global Observing System (IAGOS) at Frankfurt. *Atmos. Chem. Phys.*, **21**, 16237–16256, https://doi.org/10.5194/acp-21-16237-2021.

Clarke, B., and Coauthors, 2024: Climate change, not El Niño, main driver of extreme drought in highly vulnerable Amazon River Basin. World Weather Attribution, 43 pp., https://doi.org/10.25561/108761.

Coldewey-Egbers, M., D. G. Loyola, C. Lerot, and M. Van Roozendael, 2022: Global, regional and seasonal analysis of total ozone trends derived from the 1995–2020 GTO-ECV climate data record. *Atmos. Chem. Phys.*, **22**, 6861–6878, https://doi.org/10.5194/acp-22-6861-2022.

Cornes, R. C., E. C. Kent, D. I. Berry, and J. J. Kennedy, 2020: CLASSnmat: A global night marine air temperature data set, 1880–2019. *Geosci. Data J.*, **7**, 170–184, https://doi.org/10.1002/gdj3.100.

Crimmins, T. M., R. L. Marsh, J. Switzer, M. A. Crimmins, K. L. Gerst, A. H. Rosemartin, and J. F. Weltzin, 2017: USA National Phenology Network gridded products documentation. USGS Open-File Rep. 2017–1003, 34 pp., https://doi.org/10.3133/ofr20171003.

—— , E. G. Denny, E. E. Posthumus, A. H. Rosemartin, R. Croll, M. Montano, and H. Panci, 2022: Science and management advancements made possible by the USA National Phenology Network's Nature's Notebook platform. *BioScience*, **72**, 908–920, https://doi.org/10.1093/biosci/biac061.

Cropper, T. E., D. I. Berry, R. C. Cornes, and E. C. Kent, 2023: Quantifying daytime heating biases in marine air temperature observations from ships. *J. Atmos. Oceanic Technol.*, **40**, 427–438, https://doi.org/10.1175/JTECH-D-22-0080.1.

C3S, 2024: 2023 is the hottest year on record, with global temperatures close to the 1.5°C limit. Copernicus Climate Change Service, 9 January, https://climate.copernicus.eu/copernicus-2023-hottest-year-record.

Cusicanqui, D., A. Rabatel, C., Vincent, X., Bodin, E. Thibert, and B. Francou, 2021: Interpretation of volume and flux changes of the Laurichard rock glacier between 1952 and 2019, French Alps. *J. Geophys. Res. Earth Surface*, **126**, e2021JF006161, https://doi.org/10.1029/2021JF006161.

Daniel, J. S., S. Solomon, and D. L. Albritton, 1995: On the evaluation of halocarbon radiative forcing and global warming potentials. *J. Geophys. Res.*, **100**, 1271–1285, https://doi.org/10.1029/94JD02516.

Davidson, E. A., 2009: The contribution of manure and fertilizer nitrogen to atmospheric nitrous oxide since 1860. *Nat. Geosci.*, **2**, 659–662, https://doi.org/10.1038/ngeo608.

Davies, R., 2023a: Madagascar – 700 homes flooded as tropical storm Cheneso makes landfall. Floodlist, 20 January, accessed 13 February 2023, https://floodlist.com/africa/madagascar-tropical-storm-cheneso-january-2023.

—— , 2023b: Brazil – Death toll rises in Sao Paulo floods and landslide. Floodlist, 21 February, accessed 16 February 2024, https://floodlist.com/america/brazil-sao-paulo-floods-update-february-2023.

—— , 2023c: Chile – 2 Dead, 6 missing after floods in 7 regions. Floodlist, 25 June, accessed 15 February 2024, https://floodlist.com/america/chile-floods-june-2023.

—— , 2023d: India – 12 killed in landslide after heavy rain in Maharashtra. Floodlist, 20 July, accessed 16 February 2024, https://floodlist.com/asia/india-maharashtra-floods-landslide-july-2023.

—— , 2023e: Chile – Over 30,000 evacuate floods in 6 regions. Floodlist, 22 August, accessed 15 February 2024, https://floodlist.com/america/chile-floods-august-2023.

—— , 2023f: Japan – Floods impact Chiba, Fukushima and Ibaraki after record rain. Floodlist, 11 September, accessed 15 February 2024, https://floodlist.com/asia/japan-floods-september-2023.

—— , 2023g: Yemen – Thousands displaced by floods after cyclone Tej dumps 400 mm of rain. Floodlist, 25 October, accessed 16 February 2024, https://floodlist.com/asia/yemen-floods-cyclone-tej-october-2023.

Davis, S., and Coauthors, 2023: Hunga Tonga-Hunga Ha'apai eruption [in "State of the Climate 2022"]. *Bull. Amer. Meteor. Soc.*, **104** (9), S82–S84, https://doi.org/10.1175/BAMS-D-23-0090.1.

Dee, D. P., and Coauthors, 2011: The ERA-Interim reanalysis: Configuration and performance of the data assimilation system. *Quart. J. Roy. Meteor. Soc.*, **137**, 553–597, https://doi.org/10.1002/qj.828.

Deeter, M. N., and Coauthors, 2014: The MOPITT version 6 product: Algorithm enhancements and validation. *Atmos. Meas. Tech.*, **7**, 3623–3632, https://doi.org/10.5194/amt-7-3623-2014.

—— , D. P. Edwards, G. L. Francis, J. C. Gille, S. Martínez-Alonso, H. M. Worden, and C. Sweeney, 2017: A climate-scale satellite record for carbon monoxide: The MOPITT version 7 product. *Atmos. Meas. Tech.*, **10**, 2533–2555, https://doi.org/10.5194/amt-10-2533-2017.

—— , and Coauthors, 2019: Radiance-based retrieval bias mitigation for the MOPITT instrument: The version 8 product. *Atmos. Meas. Tech.*, **12**, 4561–4580, https://doi.org/10.5194/amt-12-4561-2019.

Deng, K., C. Azorin-Molina, L. Minola, G. Zhang, and D. Chen, 2020: Global near-surface wind speed changes over the last decades revealed by reanalyses and CMIP6 model simulations. *J. Climate*, **34**, 2219–2234, https://doi.org/10.1175/JCLI-D-20-0310.1.

de Oliveira, G., and Coauthors, 2023: Increasing wildfires threaten progress on halting deforestation in Brazilian Amazonia. *Nat. Ecol. Evol.*, **7**, 1945–1946, https://doi.org/10.1038/s41559-023-02233-3.

DiGangi, E. A., M. Stock, and J. Lapierre, 2021: Thunder hours: How old methods offer new insights into thunderstorm climatology. *Bull. Amer. Meteor. Soc.*, **103**, E548–E569, https://doi.org/10.1175/BAMS-D-20-0198.1.

Dlugokencky, E. J., L. P. Steele, P. M. Lang, and K. A. Masarie, 1994: The growth rate and distribution of atmospheric methane. *J. Geophys. Res.*, **99**, 17 021–17 043, https://doi.org/10.1029/94JD01245.

DMC, 2023a: Monthly Climate Bulletin, June Edition (in Spanish). Dirección Meteorológica de Chile, 28 pp., https://climatologia.meteochile.gob.cl/application/publicaciones/documentoPdf/boletinClimatologicoMensual/boletinClimatologicoMensual202306.pdf.

Domeisen, D. I. V., C. I. Garfinkel, and A. H. Butler, 2019: The teleconnection of El Niño Southern Oscillation to the stratosphere. *Rev. Geophys.*, **57**, 5–47, https://doi.org/10.1029/2018RG000596.

Donat, M. G., L. V. Alexander, H. Yang, I. Durre, R. Vose, and J. Caesar, 2013: Global land-based datasets for monitoring climatic extremes. *Bull. Amer. Meteor. Soc.*, **94**, 997–1006, https://doi.org/10.1175/BAMS-D-12-00109.1.

Dorigo, W., and Coauthors, 2017: ESA CCI soil moisture for improved Earth system understanding: State-of-the art and future directions. *Remote Sens. Environ.*, **203**, 185–215, https://doi.org/10.1016/j.rse.2017.07.001.

—— , L. Mösinger, R. van der Schalie, R.-M. Zotta, T. M. Scanlon, and R. De Jeu, 2021: Long-term monitoring of vegetation state through passive microwave satellites [in "State of the Climate in 2020"]. *Bull. Amer. Meteor. Soc.*, **102** (8), S110–S112, https://doi.org/10.1175/BAMS-D-21-0098.1.

—— , R. Zotta, R. van der Schalie, W. Preimesberger, L. Mösinger, and R. De Jeu, 2022: Vegetation optical depth [in "State of the Climate in 2021"]. *Bull. Amer. Meteor. Soc.*, **103** (8), S108–S109, https://doi.org/10.1175/BAMS-D-22-0092.1.

—— , W. Preimesberger, C. Reimer, R. van der Schalie, A. Pasik, R. De Jeu, and C. Paulik, 2023: Soil moisture gridded data from 1978 to present, v202212.0.0. Copernicus Climate Change Service (C3S) Climate Data Store (CDS), accessed 16 January 2024, https://cds.climate.copernicus.eu/cdsapp#!/dataset/satellite-soil-moisture?tab=overview.

Dudok de Wit, T., G. Kopp, C. Fröhlich, and M. Schöll, 2017: Methodology to create a new Total Solar Irradiance record: Making a composite out of multiple data records. *Geophys. Res. Lett.*, **44**, 1196–1203, https://doi.org/10.1002/2016GL071866.

Dunn, R. J. H., 2019: HadISD version 3: Monthly updates. Hadley Centre Tech. Note 103, 10 pp., www.metoffice.gov.uk/research/library-and-archive/publications/science/climate-science-technical-notes.

—— , and C. P. Morice, 2022: On the effect of reference periods on trends in percentile-based extreme temperature indices. *Environ. Res. Lett.*, **17**, 034026, https://doi.org/10.1088/1748-9326/ac52c8.

—— , K. M. Willett, P. W. Thorne, E. V. Woolley, I. Durre, A. Dai, D. E. Parker, and R. S. Vose, 2012: HadISD: A quality-controlled global synoptic report database for selected variables at long-term stations from 1973–2011. *Climate Past*, **8**, 1649–1679, https://doi.org/10.5194/cp-8-1649-2012.

—— , —— , D. E. Parker, and L. Mitchell, 2016: Expanding HadISD: Quality-controlled, sub-daily station data from 1931. *Geosci. Instrum. Methods Data Syst.*, **5**, 473–491, https://doi.org/10.5194/gi-5-473-2016.

—— , and Coauthors, 2020: Development of an updated global land in situ–based data set of temperature and precipitation extremes: HadEX3. *J. Geophys. Res. Atmos.*, **125**, e2019JD032263, https://doi.org/10.1029/2019JD032263.

—— , C. Azorin-Molina, M. J. Menne, Z. Zeng, N. W. Casey, and C. Shen, 2022a: Reduction in reversal of global stilling arising from correction to encoding of calm periods. *Environ. Res. Commun.*, **4**, 061003, https://doi.org/10.1088/2515-7620/ac770a.

—— , M. G. Donat, and L. V. Alexander, 2022b: Comparing extremes indices in recent observational and reanalysis products. *Front. Climate*, **4**, 989505, https://doi.org/10.3389/fclim.2022.989505.

Duveiller, G., and N. Gobron, 2023: Land surface properties: Terrestrial surface albedo dynamics [in "State of the Climate in 2022"]. *Bull. Amer. Meteor. Soc.*, **104** (9), S102–S103, https://doi.org/10.1175/BAMS-D-23-0090.1.

DWD, 2023: Deutschlandwetter im Jahr 2023. DWD, 29 December, https://www.dwd.de/DE/presse/pressemitteilungen/DE/2023/20231229_deutschlandwetter_jahr2023_news.html.

Edwards, M., and A. Richardson, 2004: Impact of climate change on marine pelagic phenology and trophic mismatch. *Nature*, **430**, 881–884, https://doi.org/10.1038/nature02808.

Ellis, H. T., and R. F. Pueschel, 1971: Solar radiation: Absence of air pollution trends at Mauna Loa. *Science*, **172**, 845–846, https://doi.org/10.1126/science.172.3985.845.

Estilow, T. W., A. H. Young, and D. A. Robinson, 2015: A long-term Northern Hemisphere snow cover extent data record for climate studies and monitoring. *Earth Syst. Sci. Data*, **7**, 137–142, https://doi.org/10.5194/essd-7-137-2015.

Etheridge, D. M., L. P. Steele, R. L. Langenfelds, R. J. Francey, J. M. Barnola, and V. I. Morgan, 1996: Natural and anthropogenic changes in atmospheric CO_2 over the last 1000 years from air in Antarctic ice and firn. *J. Geophys. Res.*, **101**, 4115–4128, https://doi.org/10.1029/95JD03410.

Etzelmüller, B., K. Isaksen, J. Czekirda, S. Westermann, C. Hilbich, and C. Hauck, 2023: Rapid warming and degradation of mountain permafrost in Norway and Iceland. *Cryosphere*, **17**, 5477–5497, https://doi.org/10.5194/tc-17-5477-2023.

Evan, S., and Coauthors, 2023: Rapid ozone depletion after humidification of the stratosphere by the Hunga Tonga Eruption. *Science*, **382**, eadg2551, https://doi.org/10.1126/science.adg2551.

Feng, L., P. I. Palmer, S. Zhu, R. J. Parker, and Y. Liu, 2022: Tropical methane emissions explain large fraction of recent changes in global atmospheric methane growth rate. *Nat. Commun.*, **13**, 1378, https://doi.org/10.1038/s41467-022-28989-z.

FEWS NET, 2023: Widespread extreme seasonal rains cause severe floods but improve agricultural productivity over eastern Horn. East Africa Seasonal Monitor, 30 November, 5 pp., https://fews.net/east-africa/seasonal-monitor/november-2023.

Fioletov, V. E., G. E. Bodeker, A. J. Miller, R. D. McPeters, and R. Stolarski, 2002: Global and zonal total ozone variations estimated from ground-based and satellite measurements: 1964–2000. *J. Geophys. Res.*, **107**, 4647, https://doi.org/10.1029/2001JD001350.

—— , and Coauthors, 2008: The performance of the ground-based total ozone network assessed using satellite data. *J. Geophys. Res.*, **113**, D14313, https://doi.org/10.1029/2008JD009809.

Fiore, A. M., and Coauthors, 2022: Understanding recent tropospheric ozone trends in the context of large internal variability: A new perspective from chemistry-climate model ensembles. *Environ. Res. Climate*, **1**, 025008, https://doi.org/10.1088/2752-5295/ac9cc2.

Fisher, J. B., and Coauthors, 2017: The future of evapotranspiration: Global requirements for ecosystem functioning, carbon and climate feedbacks, agricultural management, and water resources. *Water Resour. Res.*, **53**, 2618–2626, https://doi.org/10.1002/2016WR020175.

—— , and Coauthors, 2020: ECOSTRESS: NASA's next generation mission to measure evapotranspiration from the international space station. *Water Resour. Res.*, **56**, e2019WR026058, https://doi.org/10.1029/2019WR026058.

Fleming, E. L., P. A. Newman, Q. Liang, and L. D. Oman, 2024: Stratospheric temperature and ozone impacts of the Hunga Tonga-Hunga Ha'apai water vapor injection. *J. Geophys. Res. Atmos.*, **129**, e2023JD039298, https://doi.org/10.1029/2023JD039298.

Fogt, R. L., and G. J. Marshall, 2020: The Southern Annular Mode: Variability, trends, and climate impacts across the Southern Hemisphere. *Wiley Interdiscip. Rev.: Climate Change*, **11**, e652, https://doi.org/10.1002/wcc.652.

Folland, C. K., J. Knight, H. W. Linderholm, D. Fereday, S. Ineson, and J. W. Hurrell, 2009: The Summer North Atlantic Oscillation: Past, present and future. *J. Climate*, **22**, 1082–1103, https://doi.org/10.1175/2008JCLI2459.1.

Forster, P., and Coauthors, 2021: The Earth's energy budget, climate feedbacks, and climate sensitivity. Climate Change 2021: The Physical Science Basis, V. Masson-Delmotte et al., Eds., Cambridge University Press, 923–1054, https://doi.org/10.1017/9781009157896.009.

Forster, P. M., and Coauthors, 2023: Indicators of Global Climate Change 2022: Annual update of large-scale indicators of the state of the climate system and human influence. *Earth Syst. Sci. Data*, **15**, 2295–2327, https://doi.org/10.5194/essd-15-2295-2023.

Foster, M. J., C. Phillips, A. K. Heidinger, E. E. Borbas, Y. Li, W. P. Menzel, A. Walther, and E. Weisz, 2023: PATMOS-x version 6.0: 40 years of merged AVHRR and HIRS global cloud data. *J. Climate*, **36**, 1143–1160, https://doi.org/10.1175/JCLI-D-22-0147.1.

Fountain, A. G., B. Glenn, and C. McNeil, 2023: Inventory of glaciers and perennial snowfields of the conterminous USA. *Earth Syst. Sci. Data*, **15**, 4077–4104, https://doi.org/10.5194/essd-15-4077-2023.

Fowler, H. J., and Coauthors, 2021: Anthropogenic intensification of short-duration rainfall extremes. *Nat. Rev. Earth Environ.*, **2**, 107–122, https://doi.org/10.1038/s43017-020-00128-6.

Frauenfelder, R., W. Haeberli, and M. Hoelzle, 2003: Rock glacier occurrence and related terrain parameters in a study area of the Eastern Swiss Alps. Permafrost: Proceedings of the 8th International Conference on Permafrost, M. Phillips, S. M. Springman, and L. U. Arenson, Eds., A. A. Balkema, 253–258, https://www.arlis.org/docs/vol1/ICOP/55700698/Pdf/Chapter_046.pdf.

Free, M., D. J. Seidel, J. K. Angel, J. Lanzante, I. Durre, and T. C. Peterson, 2005: Radiosonde Atmospheric Temperature Products for Assessing Climate (RATPAC): A new dataset of large-area anomaly time series. *J. Geophys. Res.*, **110**, D22101, https://doi.org/10.1029/2005JD006169.

Friedlingstein, P., and Coauthors, 2023: Global carbon budget 2023. *Earth Syst. Sci. Data*, **15**, 5301–5369, https://doi.org/10.5194/essd-15-5301-2023.

Frith, S. M., N. A. Kramarova, R. S. Stolarski, R. D. McPeters, P. K. Bhartia, and G. J. Labow, 2014: Recent changes in total column ozone based on the SBUV Version 8.6 Merged Ozone Data Set. *J. Geophys. Res. Atmos.*, **119**, 9735–9751, https://doi.org/10.1002/2014JD021889.

—— , R. S. Stolarski, N. A. Kramarova, and R. D. McPeters, 2017: Estimating uncertainties in the SBUV Version 8.6 merged profile ozone data set. *Atmos. Chem. Phys.*, **17**, 14695–14707, https://doi.org/10.5194/acp-17-14695-2017.

Fritz, S., and Coauthors, 2019: Citizen science and the United Nations sustainable development goals. *Nat. Sustainability*, **2**, 922–930, https://doi.org/10.1038/s41893-019-0390-3.

Fromm, M., R. Servranckx, B. J. Stocks, and D. A. Peterson, 2022: Understanding the critical elements of the pyrocumulonimbus storm sparked by high-intensity wildland fire. *Commun. Earth Environ.*, **3**, 243, https://doi.org/10.1038/s43247-022-00566-8.

Füllekrug, M., E. Williams, C. Price, S. Goodman, R. Holzworth, K. Virts, and D. Buechler, 2022: Lightning ["State of the Climate in 2021"]. *Bull. Amer. Meteor. Soc.*, **103** (8), S79–S81, https://doi.org/10.1175/BAMS-D-22-0092.1.

Garane, K., and Coauthors, 2018: Quality assessment of the Ozone_cci Climate Research Data Package (release 2017): 1. Ground-based validation of total ozone column data products. *Atmos. Meas. Tech.*, **11**, 1385–1402, https://doi.org/10.5194/amt-11-1385-2018.

Garfinkel, C. I., A. Gordon, L. D. Oman, F. Li, S. Davis, and S. Pawson, 2018: Nonlinear response of tropical lower-stratospheric temperature and water vapor to ENSO. Atmos. *Chem. Phys.*, **18**, 4597–4615, https://doi.org/10.5194/acp-18-4597-2018.

—— , and Coauthors, 2021: Influence of the El Niño–Southern Oscillation on entry stratospheric water vapor in coupled chemistry–ocean CCMI and CMIP6 models. *Atmos. Chem. Phys.*, **21**, 3725–3740, https://doi.org/10.5194/acp-21-3725-2021.

Garrigues, S., and Coauthors, 2022: Monitoring multiple satellite aerosol optical depth (AOD) products within the Copernicus Atmosphere Monitoring Service (CAMS) data assimilation system. *Atmos. Chem. Phys.*, **22**, 14657–14692, https://doi.org/10.5194/acp-22-14657-2022.

GCOS, 2022: The 2022 Global Climate Observing System (GCOS) implementation plan. GCOS-244, WMO, 98 pp., https://gcos.wmo.int/en/publications/gcos-implementation-plan2022.

Gelaro, R., and Coauthors, 2017: The Modern-Era Retrospective Analysis for Research and Applications, version 2 (MERRA-2). *J. Climate*, **30**, 5419–5454, https://doi.org/10.1175/JCLI-D-16-0758.1.

GeoGlam, 2023: Global Crop Monitor December 2023. Accessed 30 January 2024, https://cropmonitor.org/index.php/cmreports/reports-archive/.

Getirana, A., S. Kumar, M. Girotto, and M. Rodell, 2017: Rivers and floodplains as key components of global terrestrial water storage variability. *Geophys. Res. Lett.*, **44**, 10359–10368, https://doi.org/10.1002/2017GL074684.

Giglio, L., W. Schroeder, and C. O. Justice, 2016: The collection 6 MODIS active fire detection algorithm and fire products. *Remote Sens. Environ.*, **178**, 31–41, https://doi.org/10.1016/j.rse.2016.02.054.

Gillooly, J. F., J. H. Brown, G. B. West, V. M. Savage, and E. L. Charnov, 2001: Effects of size and temperature on metabolic rate. *Science*, **293**, 2248–2251, https://doi.org/10.1126/science.1061967.

GISTEMP Team, 2024: GISS Surface Temperature Analysis (GISTEMP), v4. NASA Goddard Institute for Space Studies, accessed 14 February 2024, https://data.giss.nasa.gov/gistemp/.

GLAMOS, 2023: Swiss Glacier Volume Change, release 2023. Glacier Monitoring Switzerland, accessed 1 March 2024, https://doi.org/10.18750/volumechange.2023.r2023.

GLIMS, 2023: Glacier viewer. Accessed 2 January 2024, https://www.glims.org/maps/glims.

Gobron, N., and M. Robustelli, 2013: Monitoring the state of the global terrestrial surfaces. Proc. 2013 ESA Living Planet Symp., Edinburgh, United Kingdom, European Space Agency, JRC84937, https://publications.jrc.ec.europa.eu/repository/handle/JRC84937.

——, A. S. Belward, B. Pinty, and W. Knorr, 2010: Monitoring biosphere vegetation 1998–2009. *Geophys. Res. Lett.*, **37**, L15402, https://doi.org/10.1029/2010GL043870.

——, and Coauthors, 2022: Evaluation of Sentinel-3A and Sentinel-3B ocean land colour instrument green instantaneous fraction of absorbed photosynthetically active radiation. *Remote Sens. Environ.*, **270**, 112850, https://doi.org/10.1016/j.rse.2021.112850.

Godin-Beekmann, S., and Coauthors, 2022: Updated trends of the stratospheric ozone vertical distribution in the 60°S–60°N latitude range based on the LOTUS regression model. *Atmos. Chem. Phys.*, **22**, 11 657–11 673, https://doi.org/10.5194/acp-22-11657-2022.

Goodman, S. J., D. E. Buechler, K. Knupp, K. Driscoll, and E. W. McCaul Jr., 2000: The 1997-98 El Niño event and related wintertime lightning variations in the southeastern United States. *Geophys. Res. Lett.*, **27**, 541–544, https://doi.org/10.1029/1999GL010808.

Granier, C., and Coauthors, 2011: Evolution of anthropogenic and biomass burning emissions of air pollutants at global and regional scales during the 1980–2010 period. *Climatic Change*, **109**, 163–190, https://doi.org/10.1007/s10584-011-0154-1.

Grant, L., and Coauthors, 2021: Attribution of global lake systems change to anthropogenic forcing. *Nat. Geosci.*, **14**, 849–854, https://doi.org/10.1038/s41561-021-00833-x.

Grifoni, F., N. Cannone, P. Convey, and M. Guglielmin, 2024: A decade (2013–2022) of permafrost and active layer thickness monitoring in Antarctic Peninsula Area. Extended Abstracts, 12th Int. Conf. on Permafrost, Whitehorse, YT, Canada, 83–84, https://www.permafrost.org/proceedings-of-the-12th-international-conference-on-permafrost-icop/.

Grimm, A. M., 2003: The El Niño impact on the summer monsoon in Brazil: Regional processes versus remote influences. *J. Climate*, **16**, 263–280, https://doi.org/10.1175/1520-0442(2003)016<0263:TENIOT>2.0.CO;2.

——, and A. Natori, 2006: Climate change and interannual variability of precipitation in South America. *Geophys. Res. Lett.*, **33**, L19706, https://doi.org/10.1029/2006GL026821.

Gruber, A., W. A. Dorigo, W. Crow, and W. Wagner, 2017: Triple collocation-based merging of satellite soil moisture retrievals. *IEEE Trans. Geosci. Remote Sens.*, **55**, 6780–6792, https://doi.org/10.1109/TGRS.2017.2734070.

——, T. Scanlon, R. van der Schalie, W. Wagner, and W. Dorigo, 2019: Evolution of the ESA CCI Soil Moisture climate data records and their underlying merging methodology. *Earth Syst. Sci. Data*, **11**, 717–739, https://doi.org/10.5194/essd-11-717-2019.

Gulev, S. K., and Coauthors, 2021: Changing state of the climate system. Climate Change 2021: The Physical Science Basis, V. Masson-Delmotte et al., Eds., Cambridge University Press, 287–422, https://doi.org/10.1017/9781009157896.004.

Haimberger, L., C. Tavolato, and S. Sperka, 2012: Homogenization of the Global Radiosonde Temperature dataset through combined comparison with reanalysis background series and neighboring stations. *J. Climate*, **25**, 8108–8131, https://doi.org/10.1175/JCLI-D-11-00668.1.

Hansen, J., and S. Lebedeff, 1987: Global trends of measured surface air temperature. *J. Geophys. Res.*, **92**, 13 345–13 372, https://doi.org/10.1029/JD092iD11p13345.

——, S. Makiko, R. Ruedy, K. Lo, D. W. Lea, and M. Medina-Elizade, 2006: Global temperature change. *Proc. Natl. Acad. Sci. USA*, **103**, 14 288–14 293, https://doi.org/10.1073/pnas.0606291103.

——, R. Ruedy, M. Sato, and K. Lo, 2010: Global surface temperature change. *Rev. Geophys.*, **48**, RG4004, https://doi.org/10.1029/2010RG000345.

Harris, I., T. J. Osborn, P. D. Jones, and D. H. Lister, 2020: Version 4 of the CRU TS monthly high-resolution gridded multivariate climate dataset. *Sci. Data*, **7**, 109, https://doi.org/10.1038/s41597-020-0453-3.

Hassan, T., R. Gulzar, M. Hamid, R. Ahmad, S. A. Waza, and A. A. Khuroo, 2024: Plant phenology shifts under climate warming: A systematic review of recent scientific literature. *Environ. Monit. Assess.*, **196**, 36, https://doi.org/10.1007/s10661-023-12190-w.

Held, I. M., and B. J. Soden, 2006: Robust responses of the hydrological cycle to global warming. *J. Climate*, **19**, 5686–5699, https://doi.org/10.1175/JCLI3990.1.

Hersbach, H., and Coauthors, 2020: The ERA5 global reanalysis. *Quart. J. Roy. Meteor. Soc.*, **146**, 1999–2049, https://doi.org/10.1002/qj.3803.

Ho, S.-P., and Coauthors, 2020: The COSMIC/FORMOSAT-3 radio occultation mission after 12 years: Accomplishments, remaining challenges, and potential impacts of COSMIC-2. *Bull. Amer. Meteor. Sci.*, **101**, E1107–E1136, https://doi.org/10.1175/BAMS-D-18-0290.1.

Hobday, A. J., and Coauthors, 2016: A hierarchical approach to defining marine heatwaves. *Prog. Oceanogr.*, **141**, 227–238, https://doi.org/10.1016/j.pocean.2015.12.014.

——, and Coauthors, 2018: Categorizing and naming marine heatwaves. *Oceanography*, **31** (2), 162–173, https://doi.org/10.5670/oceanog.2018.205.

Hodnebrog, O., and Coauthors, 2020a: Updated global warming potentials and radiative efficiencies of halocarbons and other weak atmospheric absorbers. *Rev. Geophys.*, **58**, e2019RG000691, https://doi.org/10.1029/2019RG000691.

——, and Coauthors, 2020b: The effect of rapid adjustments to halocarbons and N_2O on radiative forcing. *npj Climate Atmos. Sci.*, **3**, 43, https://doi.org/10.1038/s41612-020-00150-x.

Hofmann, D. J., and S. A. Montzka, 2009: Recovery of the ozone layer: The ozone depleting gas index. *Eos, Trans. Amer. Geophys. Union*, **90** (1), 1–2, https://doi.org/10.1029/2009EO010001.

——, J. H. Butler, E. J. Dlugokencky, J. W. Elkins, K. Masarie, S. A. Montzka, and P. Tans, 2006: The role of carbon dioxide in climate forcing from 1979 to 2004: Introduction of the annual greenhouse gas index. *Tellus*, **58B**, 614–619, https://doi.org/10.1111/j.1600-0889.2006.00201.x.

Holzworth, R. H., J. B. Brundell, M. P. McCarthy, A. R. Jacobson, C. J. Rodger, and T. S. Anderson, 2021: Lightning in the Arctic. *Geophys. Res. Lett.*, **48**, e2020GL091366, https://doi.org/10.1029/2020GL091366.

Hong Kong Observatory, 2024: Ranking of air temperature and rainfall in annual in Hong Kong. Accessed 15 February 2024, https://www.hko.gov.hk/en/cis/statistic/erank.htm.

Hou, J., A. I. J. M. Van Dijk, and L. J. Renzullo, 2022: Merging Landsat and airborne LiDAR observations for continuous monitoring of floodplain water extent, depth and volume. *J. Hydrol.*, **609**, 127684, https://doi.org/10.1016/j.jhydrol.2022.127684.

—— , —— , —— , and P. R. Larraondo, 2024: GloLakes: Water storage dynamics for 27,000 lakes globally from 1984 to present derived from satellite altimetry and optical imaging. *Earth Syst. Sci. Data*, **16**, 201–218, https://doi.org/10.5194/essd-16-201-2024.

Hrbáček, F., and Coauthors, 2023: Active layer and permafrost thermal regimes in the ice-free areas of Antarctica. *Earth-Sci. Rev.*, **242**, 104458, https://doi.org/10.1016/j.earscirev.2023.104458.

Hu, G., and Coauthors, 2024: Spatiotemporal characteristics and variability in the thermal state of permafrost on the Qinghai–Tibet Plateau. *Permafrost Periglacial Processes*, **35**, 143–156, https://doi.org/10.1002/ppp.2219.

Huang, B., C. Liu, V. Banzon, E. Freeman, G. Graham, B. Hankins, T. Smith, and H.-M. Zhang, 2021: Improvements of the daily optimum interpolation sea surface temperature (DOISST) version 2.1. *J. Climate*, **34**, 2923–2939, https://doi.org/10.1175/JCLI-D-20-0166.1.

Huss, M., and M. Fischer, 2016: Sensitivity of very small glaciers in the Swiss Alps to future climate change. *Front. Earth Sci*, **4**, 34, https://doi.org/10.3389/feart.2016.00034.

Ingram, W., 2010: A very simple model for the water vapour feedback on climate change. *Quart. J. Roy. Meteor. Soc.*, **136**, 30–40, https://doi.org/10.1002/qj.546.

Inness, A., and Coauthors, 2019: The CAMS reanalysis of atmospheric composition. *Atmos. Chem. Phys.*, **19**, 3515–3556, https://doi.org/10.5194/acp-19-3515-2019.

IPCC, 2013: *Climate Change 2013: The Physical Science Basis*. T. F. Stocker et al., Eds., Cambridge University Press, 1535 pp.

—— , 2021: *Climate Change 2021: The Physical Science Basis*. V. Masson-Delmotte et al., Eds., Cambridge University Press, 2391 pp., https://doi.org/10.1017/9781009157896.

Irving, D., and I. Simmonds, 2016: A new method for identifying the Pacific-South American Pattern and its influence on regional climate variability. *J. Climate*, **29**, 6109–6125, https://doi.org/10.1175/JCLI-D-15-0843.1.

Jasinski, M. F., and Coauthors, 2023: ATLAS/ICESat-2 L3A Along Track Inland Surface Water Data, version 6. NASA National Snow and Ice Data Center Distributed Active Archive Center, accessed 11 January 2024, https://doi.org/10.5067/ATLAS/ATL13.006.

Jeppesen, E., and Coauthors, 2015: Ecological impacts of global warming and water abstraction on lakes and reservoirs due to changes in water level and related changes in salinity. *Hydrobiologia*, **750**, 201–227, https://doi.org/10.1007/s10750-014-2169-x.

Junod, R. A., and J. R. Christy, 2020: A new compilation of globally gridded night-time marine air temperatures: The UAHNMATv1 dataset. *Int. J. Climatol.*, **40**, 2609–2623, https://doi.org/10.1002/joc.6354.

Kääb, A., T. Strozzi, T. Bolch, R. Caduff, H. Trefall, M. Stoffel, and A. Kokarev, 2021: Inventory and changes of rock glacier creep speeds in Ile Alatau and Kungöy Ala-Too, northern Tien Shan, since the 1950s. *Cryosphere*, **15**, 927–949, https://doi.org/10.5194/tc-15-927-2021.

Kainz, M. J., R. Ptacnik, S. Rasconi, and H. H. Hager, 2017: Irregular changes in lake surface water temperature and ice cover in subalpine Lake Lunz, Austria. *Inland Waters*, **7**, 27–33, https://doi.org/10.1080/20442041.2017.1294332.

Kaiser, J. W., and Coauthors, 2012: Biomass burning emissions estimated with a global fire assimilation system based on observed fire radiative power. *Biogeosciences*, **9**, 527–554, https://doi.org/10.5194/bg-9-527-2012.

Kaplan, A., 2011: Patterns and indices of climate variability [in "State of the Climate in 2010"]. *Bull. Amer. Meteor. Soc.*, **92** (6), S20–S25, https://doi.org/10.1175/1520-0477-92.6.S1.

Keeling, C. D., and R. Revelle, 1985: Effects of El Nino/Southern Oscillation on the atmospheric content of carbon-dioxide. *Meteoritics*, **20**, 437–450.

Kellerer-Pirklbauer, A., and Coauthors, 2024: Acceleration and interannual variability of creep rates in mountain permafrost landforms (rock glacier velocities) in the European Alps in 1995–2022. *Environ. Res. Lett.*, **19**, 034022, https://doi.org/10.1088/1748-9326/ad25a4.

Kendon, M., M. McCarthy, S. Jevrejeva, A. Matthews, T. Sparks, and J. Garforth, 2023: State of the UK climate 2022. *Int. J. Climatol.*, **42** (S1), 1–80, https://doi.org/10.1002/joc.7787.

Kennedy, J. J., N. A. Rayner, C. P. Atkinson, and R. E. Killick, 2019: An ensemble data set of sea surface temperature change from 1850: The Met Office Hadley Centre HaadSST.4.0.0.0 data set. *J. Geophys. Res. Atmos.*, **124**, 7719–7763, https://doi.org/10.1029/2018JD029867.

Kenner, R., M. Phillips, J. Beutel, M. Hiller, P. Limpach, E. Pointner, and M. Volken, 2017: Factors controlling velocity variations at short-term, seasonal and multiyear time scales, Ritigraben rock glacier, western Swiss Alps. *Permafrost Periglacial Processes*, **28**, 675–684, https://doi.org/10.1002/ppp.1953.

Kent, E. C., N. A. Rayner, D. I. Berry, M. Saunby, B. I. Moat, J. J. Kennedy, and D. E. Parker, 2013: Global analysis of night marine air temperature and its uncertainty since 1880: The HadNMAT2 data set. *J. Geophys. Res. Atmos.*, **118**, 1281–1298, https://doi.org/10.1002/jgrd.50152.

Khaykin, S., and Coauthors, 2020: The 2019/20 Australian wildfires generated a persistent smoke-charged vortex rising up to 35-km altitude. *Commun. Earth Environ.*, **1**, 22, https://doi.org/10.1038/s43247-020-00022-5.

—— , A. T. J. de Laat, S. Godin-Beekmann, A. Hauchecorne, and M. Ratynski, 2022a: Unexpected self-lofting and dynamical confinement of volcanic plumes: The Raikoke 2019 case. *Sci. Rep.*, **12**, 22409, https://doi.org/10.1038/s41598-022-27021-0.

—— , and Coauthors, 2022b: Global perturbation of stratospheric water and aerosol burden by Hunga eruption. *Commun. Earth Environ*, **3**, 316, https://doi.org/10.1038/s43247-022-00652-x.

Kimutai, J., and Coauthors, 2023: Compounding natural hazards and high vulnerability led to severe impacts from Horn of Africa flooding exacerbated by climate change and Indian Ocean Dipole. World Weather Attribution, 30 pp., https://doi.org/10.25561/108015.

Kjellstrom, T., C. Freyberg, B. Lemke, M. Otto, and D. Briggs, 2017: Estimating population heat exposure and impacts on working people in conjunction with climate change. *Int. J. Biometeor.*, **62**, 291–306, https://doi.org/10.1007/s00484-017-1407-0.

Kobayashi, S., and Coauthors, 2015: The JRA-55 reanalysis: General specifications and basic characteristics. *J. Meteor. Soc. Japan*, **93**, 5–48, https://doi.org/10.2151/jmsj.2015-001.

Kosaka, Y., and Coauthors, 2024: The JRA-3Q reanalysis. *J. Meteor. Soc. Japan*, **102**, 49–109, https://doi.org/10.2151/jmsj.2024-004.

Kraemer, B. M., H. Dugan, S. La Fuente, and M. F. Meyer, 2023: Lake water levels [in "State of the Climate in 2022"]. *Bull. Amer. Meteor. Soc.*, **104** (9), S61–S63, https://doi.org/10.1175/BAMS-D-23-0090.1.

Kratz, D. P., P. W. Stackhouse Jr., S. K. Gupta, A. C. Wilber, P. Sawaengphokhai, and G. R. McGarragh, 2014: The Fast Longwave and Shortwave Flux (FLASHFlux) data product: Single-scanner footprint fluxes. *J. Appl. Meteor. Climatol.*, **53**, 1059–1079, https://doi.org/10.1175/JAMC-D-13-061.1.

Kremser, S., and Coauthors, 2016: Stratospheric aerosol —— Observations, processes, and impact on climate. *Rev. Geophys.*, **54**, 278–335, https://doi.org/10.1002/2015RG000511.

Lagouarde, J.-P., and Coauthors, 2018: The Indian-French Trishna Mission: Earth Observation in the thermal infrared with high spatio-temporal resolution. *IGARSS 2018 – 2018 IEEE Int. Geoscience and Remote Sensing Symp.*, Valencia, Spain, IEEE, 4078–4081, https://doi.org/10.1109/IGARSS.2018.8518720.

Lambiel, C., and R. Delaloye, 2004: Contribution of real-time kinematic GPS in the study of creeping mountain permafrost: Examples from the western Swiss Alps. *Permafrost Periglacial Processes*, **15**, 229–241, https://doi.org/10.1002/ppp.496.

Lan, X., and Coauthors, 2019: Long-term measurements show little evidence for large increases in total US methane emissions over the past decade. *Geophys. Res. Lett.*, **46**, 4991–4999, https://doi.org/10.1029/2018GL081731.

—— , and Coauthors, 2021: Improved constraints on global methane emissions and sinks using $\delta^{13}C\text{-}CH_4$. *Global Biogeochem. Cycles*, **35**, e2021GB007000, https://doi.org/10.1029/2021GB007000.

—— , K. W. Thoning, and E. J. Dlugokencky, 2024a: Trends in globally-averaged CH_4, N_2O, and SF_6 determined from NOAA Global Monitoring Laboratory measurements, version 2024-06. NOAA/GML, accessed 6 June 2024, https://doi.org/10.15138/P8XG-AA10.

—— , P. Tans, and K. W. Thoning, 2024b: Trends in globally-averaged CO_2 determined from NOAA Global Monitoring Laboratory measurements, version 2024-06. NOAA/GML, accessed 6 June 2024, https://doi.org/10.15138/9N0H-ZH07.

Landerer, F. W., and Coauthors, 2020: Extending the global mass change data record: GRACE Follow-On instrument and science data performance. *Geophys. Res. Lett.*, **47**, e2020GL088306, https://doi.org/10.1029/2020GL088306.

Leblanc, T., F. Chouza, G. Taha, S. Khaykin, J. Barnes, J.-P. Vernier, and L. Rieger, 2020: 2019: A 25-year high in global stratospheric aerosol loading [in "State of the Climate in 2019"]. *Bull. Amer. Meteor. Soc.*, **101** (8), S88–S89, https://doi.org/10.1175/2020BAMSStateoftheClimate.1.

Leckey, J. P., R. Damadeo, and C. A. Hill, 2021: Stratospheric Aerosol and Gas Experiment (SAGE) from SAGE III on the ISS to a free flying SAGE IV cubesat. *Remote Sens.*, **13**, 4664, https://doi.org/10.3390/rs13224664.

Lee, H.-T., and NOAA CDR Program, 2018: NOAA Climate Data Record (CDR) of monthly Outgoing Longwave Radiation (OLR), version 2.7. NOAA National Centers for Environmental Information, accessed 27 January 2024, https://doi.org/10.7289/V5W37TKD.

Legras, B., and Coauthors, 2022: The evolution and dynamics of the Hunga Tonga–Hunga Ha'apai sulfate aerosol plume in the stratosphere. *Atmos. Chem. Phys.*, **22**, 14 957–14 970, https://doi.org/10.5194/acp-22-14957-2022.

Lenssen, N. J. L., G. A. Schmidt, J. E. Hansen, M. J. Menne, A. Persin, R. Ruedy, and D. Zyss, 2019: Improvements in the GISTEMP uncertainty model. *J. Geophys. Res. Atmos.*, **124**, 6307–6326, https://doi.org/10.1029/2018JD029522.

Levy, R. C., S. Mattoo, L. A. Munchak, L. A. Remer, A. M. Sayer, F. Patadia, and N. C. Hsu, 2013: The Collection 6 MODIS aerosol products over land and ocean. *Atmos. Meas. Tech.*, **6**, 2989–3034, https://doi.org/10.5194/amt-6-2989-2013.

Lisonbee, J., and J. Ribbe, 2021: Seasonal climate influences on the timing of the Australian monsoon onset. *Wea. Climate Dyn.*, **2**, 489–506, https://doi.org/10.5194/wcd-2-489-2021.

Liu, J., and Coauthors, 2017: Contrasting carbon cycle responses of the tropical continents to the 2015–2016 El Niño. *Science*, **358**, eaam5690, https://doi.org/10.1126/science.aam5690.

Liu, P.-W., and Coauthors, 2022: Groundwater depletion in California's Central Valley accelerates during megadrought. *Nat. Commun.*, **13**, 7825, https://doi.org/10.1038/s41467-022-35582-x.

Liu, Y., and Coauthors, 2017: Evaluation of the VIIRS BRDF, Albedo and NBAR products suite and an assessment of continuity with the long term MODIS record. *Remote Sens. Environ.*, **201**, 256–274, https://doi.org/10.1016/j.rse.2017.09.020.

—— , L. Zhou, Y. Qin, C. Azorin-Molina, C. Shen, R. Xu, and Z. Zeng, 2024: Impacts of anemometer changes, site relocations and processing methods on wind speed trends in China. *Atmos. Meas. Tech.*, **17**, 1123–1131, https://doi.org/10.5194/amt-17-1123-2024.

Livezey, R. E., M. Masutani, A. Leetmaa, H. Rui, M. Ji, and A. Kumar, 1997: Teleconnective response of the Pacific–North American region atmosphere to large central equatorial Pacific SST anomalies. *J. Climate*, **10**, 1787–1820, https://doi.org/10.1175/1520-0442(1997)010<1787:TROTPN>2.0.CO;2.

Loeb, N. G., B. A. Wielicki, D. R. Doelling, G. L. Smith, D. F. Keyes, S. Kato, N. Manalo-Smith, and T. Wong, 2009: Toward optimal closure of the Earth's top-of-atmosphere radiation budget. *J. Climate*, **22**, 748–766, https://doi.org/10.1175/2008JCLI2637.1.

—— , S. Kato, W. Su, T. Wong, F. Rose, D. R. Doelling, and J. Norris, 2012: Advances in understanding top-of-atmosphere radiation variability from satellite observations. *Surv. Geophys.*, **33**, 359–385, https://doi.org/10.1007/s10712-012-9175-1.

—— , and Coauthors, 2018: Clouds and the Earth's Radiant Energy System (CERES) Energy Balanced and Filled (EBAF) Top-of-Atmosphere (TOA) edition-4.0 data product. *J. Climate*, **31**, 895–918, https://doi.org/10.1175/JCLI-D-17-0208.1.

—— , G. C. Johnson, T. J. Thorsen, J. M. Lyman, F. G. Rose, and S. Kato, 2021: Satellite and ocean data reveal marked increase in Earth's heating rate. *Geophys. Res. Lett.*, **48**, e2021GL093047, https://doi.org/10.1029/2021GL093047.

—— , and Coauthors, 2022: Evaluating twenty-year trends in Earth's energy flows from observations and reanalyses. *J. Geophys. Res. Atmos.*, **127**, e2022JD036686, https://doi.org/10.1029/2022JD036686.

Lopez, L. S., A. Basu, K. Blagrave, G. Bove, K. Stewart, D. Bazely, and S. Sharma, 2024: Establishing a long-term citizen science project? Lessons learned from the Community Lake Ice Collaboration spanning over 30 yr and 1000 lakes. *Limnol. Oceanogr. Lett.*, **9**, 99–111, https://doi.org/10.1002/lol2.10336.

MacCallum, S. N., and C. J. Merchant, 2012: Surface water temperature observations of large lakes by optimal estimation. *Can. J. Remote Sens.*, **38**, 25–45, https://doi.org/10.5589/m12-010.

Magnin, F., L. Ravanel, X. Bodin, P. Deline, E. Malet, J. Krysiecki, and P. Schoeneich, 2024: Main results of permafrost monitoring in the French Alps through the PermaFrance network over the period 2010–2022. *Permafrost Periglacial Processes*, **35**, 3–23, https://doi.org/10.1002/ppp.2209.

Manney, G. L., M. L. Santee, Z. D. Lawrence, K. Wargan, and M. J. Schwartz, 2021: A moments view of climatology and variability of the Asian summer monsoon anticyclone. *J. Climate*, **34**, 7821–7841, https://doi.org/10.1175/JCLI-D-20-0729.1.

—— , and Coauthors, 2023: Siege in the southern stratosphere: Hunga Tonga-Hunga Ha'apai water vapor excluded from the 2022 Antarctic polar vortex. *Geophys. Res. Lett.*, **50**, e2023GL103855, https://doi.org/10.1029/2023GL103855.

Marchant, R., C. Mumbi, S. Behera, and T. Yamagata, 2007: The Indian Ocean dipole – The unsung driver of climatic variability in East Africa. *Afr. J. Ecol.*, **45**, 4–16, https://doi.org/10.1111/j.1365-2028.2006.00707.x.

Marshall, G. J., 2003: Trends in the Southern Annular Mode from observations and reanalyses. *J. Climate*, **16**, 4134–4143, https://doi.org/10.1175/1520-0442(2003)016<4134:TITSAM>2.0.CO;2.

Martens, B., and Coauthors, 2017: GLEAM v3: Satellite-based land evaporation and root-zone soil moisture. *Geosci. Model Dev.*, **10**, 1903–1925, https://doi.org/10.5194/gmd-10-1903-2017.

—— , W. Waegeman, W. A. Dorigo, N. E. C. Verhoest, and D. G. Miralles, 2018: Terrestrial evaporation response to modes of climate variability. *npj Climate Atmos. Sci.*, **1**, 43, https://doi.org/10.1038/s41612-018-0053-5.

Maswanganye, S., 2023: Putting the Western Cape September rainfall event into perspective – SAEON eNews. South African Environmental Observation Network. SAEON eNews, https://enews.saeon.ac.za/issue-05-2023/putting-the-western-cape-september-rainfall-event-into-perspective/.

Matthews, T., 2018: Humid heat and climate change. *Prog. Phys. Geogr.*, **42**, 391–405, https://doi.org/10.1177/0309133318776490.

—— , M. Byrne, R. Horton, C. Murphy, R. Pielke Sr., C. Raymond, P. Thorne, and R. L. Wilby, 2022: Latent heat must be visible in climate communications. *Wiley Interdiscip. Rev.: Climate Change*, **13**, e779, https://doi.org/10.1002/wcc.779.

Mayer, M., K. E. Trenberth, L. Haimberger, and J. T. Fasullo, 2013: The response of tropical atmospheric energy budgets to ENSO. *J. Climate*, **26**, 4710–4724, https://doi.org/10.1175/JCLI-D-12-00681.1.

McCabe, M. F., B. Aragon, R. Houborg, and J. Mascaro, 2017: CubeSats in hydrology: Ultrahigh-resolution insights into vegetation dynamics and terrestrial evaporation. *Water Resour. Res.*, **53**, 10 017–10 024, https://doi.org/10.1002/2017WR022240.

—— , D. G. Miralles, T. R. H. Holmes, and J. B. Fisher, 2019: Advances in the remote sensing of terrestrial evaporation. *Remote Sens.*, **11**, 1138, https://doi.org/10.3390/rs11091138.

McCarthy, M. P., and R. Toumi, 2004: Observed interannual variability of tropical troposphere relative humidity. *J. Climate*, **17**, 3181–3191, https://doi.org/10.1175/1520-0442(2004)017<3181:OIVOTT>2.0.CO;2.

McVicar, T. R., and Coauthors, 2012: Global review and synthesis of trends in observed terrestrial near-surface wind speeds: Implications for evaporation. *J. Hydrol.*, **416–417**, 182–205, https://doi.org/10.1016/j.jhydrol.2011.10.024.

Mears, C. A., and F. J. Wentz, 2016: Sensitivity of satellite-derived tropospheric temperature trends to the diurnal cycle adjustment. *J. Climate*, **29**, 3629–3646, https://doi.org/10.1175/JCLI-D-15-0744.1.

—— , D. K. Smith, L. Ricciardulli, J. Wang, H. Huelsing, and F. J. Wentz, 2018: Construction and uncertainty estimation of a satellite-derived total precipitable water data record over the world's oceans. *Earth Space Sci.*, **5**, 197–210, https://doi.org/10.1002/2018EA000363.

Meesters, A. G., R. A. De Jeu, and M. Owe, 2005: Analytical derivation of the vegetation optical depth from the microwave polarization difference index. *IEEE Geosci. Remote Sens. Lett.*, **2**, 121–123, https://doi.org/10.1109/LGRS.2005.843983.

Menne, M. J., I. Durre, R. S. Vose, B. E. Gleason, and T. G. Houston, 2012: An overview of the global historical climatology network-daily database. *J. Atmos. Oceanic Technol.*, **29**, 897–910, https://doi.org/10.1175/JTECH-D-11-00103.1.

Menzel, A., Y. Yuan, M. Matiu, T. H. Sparks, H. Scheifinger, R. Gehrig, and N. Estrella, 2020: Climate change fingerprints in recent European plant phenology. *Global Change Biol.*, **26**, 2599–2612, https://doi.org/10.1111/gcb.15000.

Messager, M. L., B. Lehner, G. Grill, I. Nedeva, and O. Schmitt, 2016: Estimating the volume and age of water stored in global lakes using a geo-statistical approach. *Nat. Commun.*, **7**, 13603, https://doi.org/10.1038/ncomms13603.

Michel, S. E., J. R. Clark, B. H. Vaughn, M. Crotwell, M. Madronich, E. Moglia, D. Neff, and J. Mund, 2022: Stable isotopic composition of atmospheric methane (^{13}C) from the NOAA GML Carbon Cycle Cooperative Global Air Sampling Network, 1998–2021. University of Colorado, Institute of Arctic and Alpine Research (INSTAAR), accessed 15 December 2022, https://doi.org/10.15138/9p89-1x02.

Millán, L., and Coauthors, 2022: The Hunga Tonga-Hunga Ha'apai hydration of the stratosphere. *Geophys. Res. Lett.*, **49**, e2022GL099381, https://doi.org/10.1029/2022GL099381.

Miller, B. R., and Coauthors, 2010: HFC-23 (CHF_3) emission trend response to HCFC-22 ($CHClF_2$) production and recent HFC-23 emission abatement measures. *Atmos. Chem. Phys.*, **10**, 7875–7890, https://doi.org/10.5194/acp-10-7875-2010.

Minola, L., H. Reese, H. W. Lai, C. Azorin-Molina, J. A. Guijarro, S. W. Son, and D. Chen, 2022: Wind stilling-reversal across Sweden: The impact of land-use and large-scale atmospheric circulation changes. *Int. J. Climatol.*, **42**, 1049–1071, https://doi.org/10.1002/joc.7289.

Miralles, D. G., T. R. H. Holmes, R. A. M. De Jeu, J. H. Gash, A. G. C. A. Meesters, and A. J. Dolman, 2011: Global land-surface evaporation estimated from satellite-based observations. *Hydrol. Earth Syst. Sci.*, **15**, 453–469, https://doi.org/10.5194/hess-15-453-2011.

—— , and Coauthors, 2014: El Niño–La Niña cycle and recent trends in continental evaporation. *Nat. Climate Change*, **4**, 122–126, https://doi.org/10.1038/nclimate2068.

Mitchell, L., E. Brook, J. E. Lee, C. Buizert, and T. Sowers, 2013: Constraints on the late Holocene anthropogenic contribution to the atmospheric methane budget (2013b). *Science*, **342**, 964–966, https://doi.org/10.1126/science.1238920.

Miyazaki, K., K. Bowman, T. Sekiya, M. Takigawa, J. L. Neu, K. Sudo, G. Osterman, and H. Eskes, 2021: Global tropospheric ozone responses to reduced NO_x emissions linked to the COVID-19 worldwide lockdowns. *Sci. Adv.*, **7**, eabf7460, https://doi.org/10.1126/sciadv.abf7460.

Moesinger, L., W. Dorigo, R. de Jeu, R. van Der Schalie, T. Scanlon, I. Teubner, and M. Forkel, 2020: The global long-term microwave Vegetation Optical Depth Climate Archive (VODCA). *Earth Syst. Sci. Data*, **12**, 177–196, https://doi.org/10.5194/essd-12-177-2020.

—— , R.-M. Zotta, R. van Der Schalie, T. Scanlon, R. de Jeu, and W. Dorigo, 2022: Monitoring vegetation condition using microwave remote sensing: The Standardized Vegetation Optical Depth Index (SVODI). *Biogeosciences*, **19**, 5107–5123, https://doi.org/10.5194/bg-19-5107-2022.

Montecinos, A., M. V. Kurgansky, C. Muñoz, and K. Takahashi, 2011: Non-ENSO interannual rainfall variability in central Chile during austral winter. *Theor. Appl. Climatol.*, **106**, 557–568, https://doi.org/10.1007/s00704-011-0457-1.

Montzka, S. A., J. H. Butler, R. C. Myers, T. M. Thompson, T. H. Swanson, A. D. Clarke, L. T. Lock, and J. W. Elkins, 1996: Decline in the tropospheric abundance of halogen from halocarbons: Implications for stratospheric ozone depletion. *Science*, **272**, 1318–1322, https://doi.org/10.1126/science.272.5266.1318.

Morice, C. P., and Coauthors, 2021: An updated assessment of near-surface temperature change from 1850: The HadCRUT5 data set. *J. Geophys. Res. Atmos.*, **126**, e2019JD032361, https://doi.org/10.1029/2019JD032361.

Mühle, J., and Coauthors, 2010: Perfluorocarbons in the global atmosphere: Tetrafluoromethane, hexafluoroethane, and octafluoropropane. *Atmos. Chem. Phys.*, **10**, 5145–5164, https://doi.org/10.5194/acp-10-5145-2010.

Murray, L., 2023: Tropical Cyclone Gabrielle – Event summary February 2023. MetService Blog, accessed 14 February 2024, https://blog.metservice.com/TropicalCycloneGabrielleSummary.

Myhre, G., D. Shindell, and J. Pongratz, 2014: Anthropogenic and natural radiative forcing. *Climate Change 2013: The Physical Science Basis*, T. F. Stocker et al., Eds., Cambridge University Press, 659–740.

Naumann, G., and Coauthors, 2021: The 2019–2021 extreme drought episode in La Plata Basin. EUR 30833 EN, Publications Office of the European Union, 44 pp., https://doi.org/10.2760/773.

Newman, P. A., J. S. Daniel, D. W. Waugh, and E. R. Nash, 2007: A new formulation of equivalent effective stratospheric chlorine (EESC). *Atmos. Chem. Phys.*, **7**, 4537–4552, https://doi.org/10.5194/acp-7-4537-2007.

Nicholson, S. E., 2017: Climate and climatic variability of rainfall over eastern Africa. *Rev. Geophys.*, **55**, 590–635, https://doi.org/10.1002/2016RG000544.

Nisbet, E. G., and Coauthors, 2023: Atmospheric methane: Comparison between methane's record in 2006–2022 and during glacial terminations. *Global Biogeochem. Cycles*, **37**, e2023GB007875, https://doi.org/10.1029/2023GB007875.

NOAA/NCEI, 2023a: Global drought narrative for November 2023. Accessed 12 February 2024, https://www.ncei.noaa.gov/access/monitoring/monthly-report/global-drought/202311.

—— , 2023b: Monthly drought report for annual 2023. Accessed 30 January 2024, https://www.ncei.noaa.gov/access/monitoring/monthly-report/drought/202313.

—— , 2023c: Monthly national climate report for January 2023. Accessed 18 January 2024, https://www.ncei.noaa.gov/access/monitoring/monthly-report/national/202301.

—— , 2024: U.S. Climate Extremes Index (CEI). Accessed 16 February 2024, https://www.ncei.noaa.gov/access/monitoring/cei/graph.

Noetzli, J., and Coauthors, 2021: Best practice for measuring permafrost temperature in boreholes based on the experience in the Swiss Alps. *Front. Earth Sci.*, **9**, 607875, https://doi.org/10.3389/feart.2021.607875.

—— , H. H. Christiansen, M. Guglielmin, F. Hrbáček, K. Isaksen, S. L. Smith, L. Zhao, and D. A. Streletskiy, 2023: Permafrost temperature and active layer thickness [in "State of the Climate in 2022"]. *Bull. Amer. Meteor. Soc.*, **104** (9), S39–S41, https://doi.org/10.1175/BAMS-D-23-0090.1.

OCHA, 2023a: Mozambique: Severe Tropical Storm Freddy – Flash update No. 10 (as of 15 March 2023) – Mozambique. Reliefweb, accessed 14 February 2024, https://reliefweb.int/report/mozambique/mozambique-severe-tropical-storm-freddy-flash-update-no-10-15-march-2023.

—— , 2023b: Southern Africa: El Niño, positive Indian Ocean dipole forecast and humanitarian impact (October 2023). Accessed 30 January 2024, https://reliefweb.int/report/madagascar/southern-africa-el-nino-positive-indian-ocean-dipole-forecast-and-humanitarian-impact-october-2023.

O'Gorman, P. A., 2012: Sensitivity of tropical precipitation extremes to climate change. *Nat. Geosci.*, **5**, 697–700, https://doi.org/10.1038/ngeo1568.

—— , and C. J. Muller, 2010: How closely do changes in surface and column water vapor follow Clausius-Clapeyron scaling in climate change simulations? *Environ. Res. Lett.*, **5**, 025207, https://doi.org/10.1088/1748-9326/5/2/025207.

Oh, Y., and Coauthors, 2023: CarbonTracker-CH_4 2023. NOAA, accessed March 2024, https://doi.org/10.25925/40jt-qd67.

O'Keefe, J., 2023: Phenology of woody species at Harvard Forest since 1990. Harvard Forest Data Archive: HF003, accessed March 2024, https://harvardforest1.fas.harvard.edu/exist/apps/datasets/showData.html?id=HF003.

Osborn, T. J., P. D. Jones, D. H. Lister, C. P. Morice, I. R. Simpson, J. P. Winn, E. Hogan, and I. C. Harris, 2021: Land surface air temperature variations across the globe updated to 2019: The CRUTEM5 dataset. *J. Geophys. Res. Atmos.*, **126**, e2019JD032352, https://doi.org/10.1029/2019JD032352.

Park, T., and Coauthors, 2016: Changes in growing season duration and productivity of northern vegetation inferred from long-term remote sensing data. *Environ. Res. Lett.*, **11**, 084001, https://doi.org/10.1088/1748-9326/11/8/084001.

Parker, D. E., T. P. Legg, and C. K. Folland, 1992: A new daily central England temperature series, 1772–1991. *Int. J. Climatol.*, **12**, 317–342, https://doi.org/10.1002/joc.3370120402.

Peixoto, J. P., and A. H. Oort, 1992: *Physics of Climate*. American Institute of Physics, 520 pp.

Pekel, J.-F., A. Cottam, N. Gorelick, and A. S. Belward, 2016: High-resolution mapping of global surface water and its long-term changes. *Nature*, **540**, 418–422, https://doi.org/10.1038/nature20584.

Pellet, C., and Coauthors, 2023: Rock glacier velocity [in "State of the Climate in 2022"]. *Bull. Amer. Meteor. Soc.*, **104** (9), S41–S42, https://doi.org/10.1175/BAMS-D-23-0090.1.

Peng, S., and Coauthors, 2022: Wetland emission and atmospheric sink changes explain methane growth in 2020. *Nature*, **612**, 477–482, https://doi.org/10.1038/s41586-022-05447-w.

Perkins-Kirkpatrick, S., D. Barriopedro, R. Jha, L. Wang, A. Mondal, R. Libonati, and K. Kornhuber, 2024: Extreme terrestrial heat in 2023. *Nat. Rev. Earth Environ.*, **5**, 244–246, https://doi.org/10.1038/s43017-024-00536-y.

PERMOS, 2023: Swiss Permafrost Bulletin 2022. J. Noetzli and C. Pellet, Eds., Swiss Permafrost Monitoring Network, 23 pp., https://www.permos.ch/fileadmin/Files/publications/swiss_permafrost_bulletin/PERMOS_bulletin_2022.pdf.

—— , 2024: Swiss Permafrost Bulletin 2023. J. Noetzli and C. Pellet, Eds., Swiss Permafrost Monitoring Network, 25 pp., https://www.permos.ch/fileadmin/Files/publications/swiss_permafrost_bulletin/PERMOS_bulletin_2023.pdf.

Peterson, D. A., J. R. Campbell, E. J. Hyer, M. D. Fromm, G. P. Kablick III, J. H. Cossuth, and M. T. DeLand, 2018: Wildfire-driven thunderstorms cause a volcano-like stratospheric injection of smoke. *npj Climate Atmos. Sci.*, **1**, 30, https://doi.org/10.1038/s41612-018-0039-3.

—— , and Coauthors, 2021: Australia's Black Summer pyrocumulonimbus super outbreak reveals potential for increasingly extreme stratospheric smoke events. *npj Climate Atmos. Sci.*, **4**, 38, https://doi.org/10.1038/s41612-021-00192-9.

Phillips, C., and M. J. Foster, 2023: Cloudiness [in "State of the Climate in 2022"]. *Bull. Amer. Meteor. Soc.*, **104** (9), S60–S61, https://doi.org/10.1175/BAMS-D-23-0090.1.

Pielke, R. A., 2003: Heat storage within the Earth system. *Bull. Amer. Meteor. Soc.*, **84**, 331–336, https://doi.org/10.1175/BAMS-84-3-331.

Pinty, B., and Coauthors, 2011: Exploiting the MODIS albedos with the Two-stream Inversion Package (JRC-TIP): 2. Fractions of transmitted and absorbed fluxes in the vegetation and soil layers. *J. Geophys. Res.*, **116**, D09106, https://doi.org/10.1029/2010JD015373.

Plummer, D., and Coauthors, 2021: CCMI-2022: A new set of Chemistry-Climate Model Initiative (CCMI) Community simulations to update the assessment of models and support upcoming ozone assessment activities. *SPARC Newsletter*, No. 57, WCRP, Toronto, Ontario, Canada, 22–30, https://www.sparc-climate.org/wp-content/uploads/sites/5/2021/07/SPARCnewsletter_Jul2021_web.pdf.

Po-Chedley, S., J. R. Christy, C.-Z. Zou, C. A. Mears, and L. Haimberger, 2023: Tropospheric temperature [in "State of the Climate in 2022"]. *Bull. Amer. Meteor. Soc.*, **104** (9), S36–S38, https://doi.org/10.1175/BAMS-D-23-0090.1.

Pogliotti, P., E. Cremonese, and U. Morra di Cella, 2023: Warming permafrost in the western Alps: A further evidence of elevation dependent warming? *J. Alp. Res.*, **111** (2), https://doi.org/10.4000/rga.11784.

Popp, T., and Coauthors, 2016: Development, production and evaluation of aerosol climate data records from European satellite observations (Aerosol_cci). *Remote Sens.*, **8**, 421, https://doi.org/10.3390/rs8050421.

Prather, M. J., C. D. Holmes, and J. Hsu, 2012: Reactive greenhouse gas scenarios: Systematic exploration of uncertainties and the role of atmospheric chemistry. *Geophys. Res. Lett.*, **39**, L09803, https://doi.org/10.1029/2012GL051440.

Putero, D., and Coauthors, 2023: Fingerprints of the COVID-19 economic downturn and recovery on ozone anomalies at high-elevation sites in North America and western Europe. *Atmos. Chem. Phys.*, **23**, 15 693–15 709, https://doi.org/10.5194/acp-23-15693-2023.

Quaas, J., and Coauthors, 2022: Robust evidence for reversal of the trend in aerosol effective climate forcing. *Atmos. Chem. Phys.*, **22**, 12 221–12 239, https://doi.org/10.5194/acp-22-12221-2022.

Randel, W. J., and J. B. Cobb, 1994: Coherent variations of monthly mean total ozone and lower stratospheric temperature. *J. Geophys. Res.*, **99**, 5433–5447, https://doi.org/10.1029/93JD03454.

—— , and Coauthors, 2009: An update of observed stratospheric temperature trends. *J. Geophys. Res.*, **114**, D02107, https://doi.org/10.1029/2008JD010421.

Rantanen, M., and A. Laaksonen, 2024: The jump in global temperatures in September 2023 is extremely unlikely due to internal climate variability alone. *npj Climate Atmos. Sci.*, **7**, 34, https://doi.org/10.1038/s41612-024-00582-9.

Ray, E. A., F. L. Moore, J. W. Elkins, K. H. Rosenlof, J. C. Laube, T. Röckmann, D. R. Marsh, and A. E. Andrews, 2017: Quantification of the SF_6 lifetime based on mesospheric loss measured in the stratospheric polar vortex. *J. Geophys. Res. Atmos.*, **122**, 4626–4638, https://doi.org/10.1002/2016JD026198.

Raymond, C., T. K. Matthews, and R. M. Horton, 2020: The emergence of heat and humidity too severe for human tolerance. *Sci. Adv.*, **6**, eaaw1838, https://doi.org/10.1126/sciadv.aaw1838.

—— , —— , —— , E. M. Fischer, S. Fueglistaler, C. Ivanovich, L. Suarez-Gutierrez, and Y. Zhang, 2021: On the controlling factors for globally extreme humid heat. *Geophys. Res. Lett.*, **48**, e2021GL096082, https://doi.org/10.1029/2021GL096082.

Rayner, N. A., D. E. Parker, E. B. Horton, C. K. Folland, L. V. Alexander, D. P. Rowell, E. C. Kent, and A. Kaplan, 2003: Global analyses of sea surface temperature, sea ice, and night marine air temperature since the late nineteenth century. *J. Geophys. Res.*, **108**, 4407, https://doi.org/10.1029/2002JD002670.

Renwick, J. A., and M. J. Revell, 1999: Blocking over the South Pacific and Rossby wave propagation. *Mon. Wea. Rev.*, **127**, 2233–2247, https://doi.org/10.1175/1520-0493(1999)127<2233:BOTSPA>2.0.CO;2.

RGIK, 2023a: Guidelines for inventorying rock glaciers: Baseline and practical concepts (version 1.0). Tech. Rep., IPA Action Group Rock Glacier Inventories and Kinematics, 25 pp., https://doi.org/10.51363/unifr.srr.2023.002.

—— , 2023b: Rock Glacier Velocity as an associated parameter of ECV Permafrost: Baseline concepts (version 3.2). Tech. Rep., IPA Action Group Rock Glacier Inventories and Kinematics, 12 pp., https://bigweb.unifr.ch/Science/Geosciences/Geomorphology/Pub/Website/IPA/CurrentVersion/Current_RockGlacierVelocity.pdf.

Ricciardulli, L., and F. J. Wentz, 2015: A scatterometer geophysical model function for climate-quality winds: QuikSCAT Ku-2011. *J. Atmos. Oceanic Technol.*, **32**, 1829–1846, https://doi.org/10.1175/JTECH-D-15-0008.1.

—— , and A. Manaster, 2021: Intercalibration of ASCAT scatterometer winds from MetOp-A, -B, and -C, for a stable climate data record. *Remote Sens.*, **13**, 3678, https://doi.org/10.3390/rs13183678.

Richardson, A. D., 2019: Tracking seasonal rhythms of plants in diverse ecosystems with digital camera imagery. *New Phytol.*, **222**, 1742–1750, https://doi.org/10.1111/nph.15591.

—— , and J. O'Keefe, 2009: Phenological differences between understory and overstory. *Phenology of Ecosystem Processes*, A. Noormets, Ed., Springer, 87–117.

Rodell, M., and B. Li, 2023: Changing intensity of hydroclimatic extreme events revealed by GRACE and GRACE-FO. *Nat. Water*, **1**, 241–248, https://doi.org/10.1038/s44221-023-00040-5.

—— , J. S. Famiglietti, D. N. Wiese, J. T. Reager, H. K. Beaudoing, F. W. Landerer, and M.-H. Lo, 2018: Emerging trends in global freshwater availability. *Nature*, **557**, 651–659, https://doi.org/10.1038/s41586-018-0123-1.

Rogers, C. D. W., and R. A. Warren, 2024: Fast and accurate calculation of wet-bulb temperature for humid-heat extremes. ESS Open Archive, https://doi.org/10.22541/essoar.170560423.39769387/v1.

Rohde, R. A., and Z. Hausfather, 2020: The Berkeley Earth land/ocean temperature record. *Earth Syst. Sci. Data*, **12**, 3469–3479, https://doi.org/10.5194/essd-12-3469-2020.

Rosemartin, A. H., and Coauthors, 2014: Organizing phenological data resources to inform natural resource conservation. *Biol. Conserv.*, **173**, 90–97, https://doi.org/10.1016/j.biocon.2013.07.003.

Rubino, M., and Coauthors, 2019: Revised records of atmospheric trace gases CO_2, CH_4, N_2O, and $\delta^{13}C$-CO_2 over the last 2000 years from Law Dome, Antarctica. *Earth Syst. Sci. Data*, **11**, 473–492, https://doi.org/10.5194/essd-11-473-2019.

Rudlosky, S. D., and K. S. Virts, 2021: Dual geostationary lightning mapper observations. *Mon. Wea. Rev.*, **149**, 979–998, https://doi.org/10.1175/MWR-D-20-0242.1.

Saeed, W., I. Haqiqi, Q. Kong, M. Huber, J. R. Buzan, S. Chonabayashi, K. Motohashi, and T. W. Hertel, 2022: The poverty impacts of labor heat stress in West Africa under a warming climate. *Earth's Future*, **10**, e2022ef002777, https://doi.org/10.1029/2022EF002777.

Said, R., M. Cohen, and U. Inan, 2013: Highly intense lightning over the oceans: Estimated peak currents from global GLD360 observations. *J. Geophys. Res. Atmos.*, **118**, 6905–6915, https://doi.org/10.1002/jgrd.50508.

Saji, N. H., B. N. Goswami, P. N. Vinayachandran, and T. Yamagata, 1999: A dipole mode in the tropical Indian Ocean. *Nature*, **401**, 360–363, https://doi.org/10.1038/43854.

Santee, M. L., and Coauthors, 2023: Strong evidence of heterogeneous processing on stratospheric sulfate aerosol in the extrapolar Southern Hemisphere following the 2022 Hunga Tonga-Hunga Ha'apai eruption. *J. Geophys. Res. Atmos.*, **128**, e2023JD039169, https://doi.org/10.1029/2023JD039169.

Santer, B. D., and Coauthors, 2008: Consistency of modelled and observed temperature trends in the tropical troposphere. *Int. J. Climatol.*, **28**, 1703–1722, https://doi.org/10.1002/joc.1756.

Satheesh, S. K., S. Suresh Babu, B. Padmakumari, G. Pandithurai, and V. K. Soni, 2017: Variability of atmospheric aerosols over India. *Observed Climate Variability and Change over the Indian Region*, Springer, 221–248, https://doi.org/10.1007/978-981-10-2531-0_13.

Schaaf, C. B., and Coauthors, 2002: First operational BRDF, albedo nadir reflectance products from MODIS. Remote Sens. *Environ.*, **83**, 135–148, https://doi.org/10.1016/S0034-4257(02)00091-3.

Schmidt, G., 2024: Climate models can't explain 2023's huge heat anomaly —— We could be in uncharted territory. *Nature*, **627**, 467, https://doi.org/10.1038/d41586-024-00816-z.

Schwartz, M. D., T. R. Ault, and J. L. Betancourt, 2013: Spring onset variations and trends in the continental United States: Past and regional assessment using temperature-based indices. *Int. J. Climatol.*, **33**, 2917–2922, https://doi.org/10.1002/joc.3625.

Seneviratne, S. I., T. Corti, E. L. Davin, M. Hirschi, E. B. Jaeger, I. Lehner, B. Orlowsky, and A. J. Teuling, 2010: Investigating soil moisture–climate interactions in a changing climate: A review. *Earth-Sci. Rev.*, **99**, 125–161, https://doi.org/10.1016/j.earscirev.2010.02.004.

Seyednasrollah, B., A. M. Young, K. Hufkens, T. Milliman, M. A. Friedl, S. Frolking, and A. D. Richardson, 2019: Tracking vegetation phenology across diverse biomes using version 2.0 of the PhenoCam dataset. *Sci. Data*, **6**, 261, https://doi.org/10.1038/s41597-019-0270-8.

Shao, X., S.-P. Ho, X. Jing, X. Zhou, Y. Chen, T.-C. Liu, B. Zhang, and J. Dong, 2023: Characterizing the tropospheric water vapor spatial variation and trend using 2007–2018 COSMIC radio occultation and ECMWF reanalysis data. *Atmos. Chem. Phys.*, **23**, 14 187–14 218, https://doi.org/10.5194/acp-23-14187-2023.

Shi, L., and J. J. Bates, 2011: Three decades of intersatellite-calibrated high-resolution infrared radiation sounder upper tropospheric water vapor. *J. Geophys. Res.*, **116**, D04108, https://doi.org/10.1029/2010JD014847.

Simmons, A. J., 2022: Trends in the tropospheric general circulation from 1979 to 2022. *Wea. Climate Dyn.*, **3**, 777–809, https://doi.org/10.5194/wcd-3-777-2022.

Simpson, I. R., K. A. McKinnon, D. Kennedy, D. M. Lawrence, F. Lehner, and R. Seager, 2024: Observed humidity trends in dry regions contradict climate models. *Proc. Natl. Acad. Sci. USA*, **121**, e2302480120, https://doi.org/10.1073/pnas.2302480120.

Sindelarova, K., and Coauthors, 2014: Global data set of biogenic VOC emissions calculated by the MEGAN model over the last 30 years. *Atmos. Chem. Phys.*, **14**, 9317–9341, https://doi.org/10.5194/acp-14-9317-2014.

Smith, S., V. Romanovsky, K. Isaksen, K. Nyland, N. Shiklomanov, D. Streletskiy, and H. H. Christiansen, 2023: Permafrost [in "State of the Climate 2022"]. *Bull. Amer. Meteor. Soc.*, **104** (9), 302–305, https://doi.org/10.1175/BAMS-D-23-0090.1.

Smith, S. L., H. B. O'Neill, K. Isaksen, J. Noetzli, and V. E. Romanovsky, 2022: The changing thermal state of permafrost. *Nat. Rev. Earth Environ.*, **3**, 10–23, https://doi.org/10.1038/s43017-021-00240-1.

Soden, B. J., D. L. Jackson, V. Ramaswamy, M. D. Schwarzkopf, and X. Huang, 2005: The radiative signature of upper tropospheric moistening. *Science*, **310**, 841–844, https://doi.org/10.1126/science.1115602.

Solomon, S., J. S. Daniel, R. R. Neely III, J.-P. Vernier, E. G. Dutton, and L. W. Thomason, 2011: The persistently variable "background" stratospheric aerosol layer and global climate change. *Science*, **333**, 866–870, https://doi.org/10.1126/science.1206027.

Song, F., G. J. Zhang, V. Ramanathan, and L. R. Leung, 2022: Trends in surface equivalent potential temperature: A more comprehensive metric for global warming and weather extremes. *Proc. Natl. Acad. Sci. USA*, **119**, e2117832119, https://doi.org/10.1073/pnas.2117832119.

Song, X.-P., M. C. Hansen, S. V. Stehman, P. V. Potapov, A. Tyukavina, E. F. Vermote, and J. R. Townshend, 2018: Global land change from 1982 to 2016. *Nature*, **560**, 639–643, https://doi.org/10.1038/s41586-018-0411-9.

Sorg, A., A. Kääb, A. Roesch, C. Bigler, and M. Stoffel, 2015: Contrasting responses of central Asian rock glaciers to global warming. *Sci. Rep.*, **5**, 8228, https://doi.org/10.1038/srep08228.

SPARC/IO3C/GAW, 2019: SPARC/IO3C/GAW report on long-term ozone trends and uncertainties in the stratosphere. I. Petropavlovskikh et al., Eds., SPARC Rep. 9, WCRP-17/2018, GAW Rep. 241, 99 pp., https://doi.org/10.17874/f899e57a20b.

Spencer, R. W., J. R. Christy, and W. D. Braswell, 2017: UAH version 6 global satellite temperature products: Methodology and results. *Asia-Pac. J. Atmos. Sci.*, **53**, 121–130, https://doi.org/10.1007/s13143-017-0010-y.

Stackhouse, P. W., T. Wong, D. P. Kratz, P. Sawaengphokhai, A. C. Wiber, S. K. Gupta, and N. G. Loeb, 2016: Earth radiation budget at top-of-atmosphere [in "State of the Climate in 2015"]. *Bull. Amer. Meteor. Soc.*, **97** (8), S41–S43, https://doi.org/10.1175/2016BAMSStateoftheClimate.1.

Staub, B., C. Lambiel, and R. Delaloye, 2016: Rock glacier creep as a thermally-driven phenomenon: A decade of inter-annual observation from the Swiss Alps. XI Int. Conf. on Permafrost, Potsdam, Germany, Alfred Wegener Institute Helmholtz Center for Polar and Marine Research, 96–97, https://doi.org/10.2312/GFZ.LIS.2016.001.

Steinbrecht, W., and Coauthors, 2017: An update on ozone profile trends for the period 2000 to 2016. *Atmos. Chem. Phys.*, **17**, 10 675–10 690, https://doi.org/10.5194/acp-17-10675-2017.

—— , and Coauthors, 2021: COVID-19 crisis reduces free tropospheric ozone across the Northern Hemisphere. *Geophys. Res. Lett.*, **48**, e2020GL091987, https://doi.org/10.1029/2020GL091987.

Steiner, A. K., and Coauthors, 2020: Observed temperature changes in the troposphere and stratosphere from 1979 to 2018. *J. Climate*, **33**, 8165–8194, https://doi.org/10.1175/JCLI-D-19-0998.1.

Stocker, M., A. K. Steiner, F. Ladstädter, U. Foelsche, and W. J. Randel, 2024: Observed impacts of the Hunga Tonga eruption on stratospheric temperature. *EGU General Assembly 2024*, Vienna, Austria, EGU, EGU24-11683, https://doi.org/10.5194/egusphere-egu24-11683.

Stoy, P. C., J. Roh, and G. T. Bromley, 2022: It's the heat and the humidity: The complementary roles of temperature and specific humidity to recent changes in the energy content of the near-surface atmosphere. *Geophys. Res. Lett.*, **49**, e2021GL096628, https://doi.org/10.1029/2021GL096628.

Stradiotti, P., and Coauthors, 2023: Soil moisture [in "State of the Climate in 2022"]. *Bull. Amer. Meteor. Soc.*, **104** (9), S65–S66, https://doi.org/10.1175/BAMS-D-23-0090.1.

Streletskiy, D., J. Noetzli, S. L. Smith, G. Vieira, P. Schoeneich, F. Hrbacek, and A. M. Irrgang, 2021: Strategy and implementation plan for the Global Terrestrial Network for Permafrost (GTN-P) 2021-2024. Zenodo, https://doi.org/10.5281/ZENODO.6075468.

Susskind, J., G. Molnar, L. Iredell, and N. G. Loeb, 2012: Interannual variability of outgoing longwave radiation as observed by AIRS and CERES. *J. Geophys. Res.*, **117**, D23107, https://doi.org/10.1029/2012JD017997.

Szopa, S., and Coauthors, 2021: Short-lived climate forcers. *Climate Change 2021: The Physical Science Basis*, V. Masson-Delmotte et al., Eds., Cambridge University Press, 817–922, https://doi.org/10.1017/9781009157896.008.

Taha, G., R. Loughman, P. R. Colarco, T. Zhu, L. W. Thomason, and G. Jaross, 2022: Tracking the 2022 Hunga Tonga-Hunga Ha'apai aerosol cloud in the upper and middle stratosphere using space-based observations. *Geophys. Res. Lett.*, **49**, e2022GL100091, https://doi.org/10.1029/2022GL100091.

Tapley, B. D., S. Bettadpur, J. C. Ries, P. F. Thompson, and M. M. Watkins, 2004: GRACE measurements of mass variability in the Earth system. *Science*, **305**, 503–505, https://doi.org/10.1126/science.1099192.

Tarasick, D. W., and Coauthors, 2019: Tropospheric Ozone Assessment Report: Tropospheric ozone from 1877 to 2016, observed levels, trends and uncertainties. *Elementa*, **7**, 39, https://doi.org/10.1525/elementa.376.

The Watchers, 2023: Extreme rainfall in Telangana results in at least 23 fatalities, India. The Watchers, 30 July, accessed 16 February 2024, https://watchers.news/2023/07/30/extreme-rainfall-in-telangana-results-in-at-least-23-fatalities-india/.

Thibert, E., and X. Bodin, 2022: Changes in surface velocities over four decades on the Laurichard rock glacier (French Alps). *Permafrost Periglacial Processes*, **33**, 323–335, https://doi.org/10.1002/ppp.2159.

Tian, H., and Coauthors, 2024: Global nitrous oxide budget (1980–2020). *Earth Syst. Sci. Data*, **16**, 2543–2604, https://doi.org/10.5194/essd-16-2543-2024.

Timmermann, A., and Coauthors, 2018: El Niño–Southern Oscillation complexity. *Nature*, **559**, 535–545, https://doi.org/10.1038/s41586-018-0252-6.

Toreti, A., and Coauthors, 2023: Drought in Central America and Mexico August 2023. JRC Tech. Rep. 135033, 17 pp., https://doi.org/10.2760/00589.

Torralba, V., F. J. Doblas-Reyes, and N. Gonzalez-Reviriegol, 2017: Uncertainty in recent near-surface wind speed trends: A global reanalysis intercomparison. *Environ. Res. Lett.*, **12**, 114019, https://doi.org/10.1088/1748-9326/aa8a58.

Ultee, L., S. Coats, and J. Mackay, 2022: Glacial runoff buffers droughts through the 21st century. *Earth Syst. Dyn.*, **13**, 935–959, https://doi.org/10.5194/esd-13-935-2022.

van der A, R. J., M. A. F. Allaart, and H. J. Eskes, 2015: Extended and refined multi sensor reanalysis of total ozone for the period 1970–2012. *Atmos. Meas. Tech.*, **8**, 3021–3035, https://doi.org/10.5194/amt-8-3021-2015.

van der Schalie, R., and Coauthors, 2017: The merging of radiative transfer based surface soil moisture data from SMOS and AMSR-E. *Remote Sens. Environ.*, **189**, 180–193, https://doi.org/10.1016/j.rse.2016.11.026.

—— , and Coauthors, 2022: Soil moisture [in "State of the Climate in 2021"]. *Bull. Amer. Meteor. Soc.*, **103** (8), S64–S66, https://doi.org/10.1175/BAMS-D-22-0092.1.

van der Schrier, G., J. Barichivich, K. R. Briffa, and P. D. Jones, 2013: A scPDSI-based global dataset of dry and wet spells for 1901–2009. *J. Geophys. Res. Atmos.*, **118**, 4025–4048, https://doi.org/10.1002/jgrd.50355.

van der Werf, G. R., and Coauthors, 2017: Global fire emissions estimates during 1997–2016. *Earth Syst. Sci. Data*, **9**, 697–720, https://doi.org/10.5194/essd-9-697-2017.

Vivero, S., X. Bodin, D. Farías-Barahona, S. MacDonell, N. Schaffer, B. A. Robson, and C. Lambiel, 2021: Combination of aerial, satellite, and UAV photogrammetry for quantifying rock glacier kinematics in the Dry Andes of Chile (30°S) since the 1950s. *Front. Remote Sens.*, **2**, 784015, https://doi.org/10.3389/frsen.2021.784015.

Vömel, H., S. Evan, and M. Tully, 2022: Water vapor injection into the stratosphere by Hunga Tonga-Hunga Ha'apai. *Science*, **377**, 1444–1447, https://doi.org/10.1126/science.abq2299.

von Schuckmann, K., and Coauthors, 2023: Heat stored in the Earth system 1960–2020: Where does the energy go? *Earth Syst. Sci. Data*, **15**, 1675–1709, https://doi.org/10.5194/essd-15-1675-2023.

Vose, R. S., and Coauthors, 2021: Implementing full spatial coverage in NOAA's global temperature analysis. *Geophys. Res. Lett.*, **48**, e2020GL090873, https://doi.org/10.1029/2020GL090873.

Vreugdenhil, M., and Coauthors, 2022: Microwave remote sensing for agricultural drought monitoring: Recent developments and challenges. *Front. Water*, **4**, 1045451, https://doi.org/10.3389/frwa.2022.1045451.

Wang, M., Q. Fu, A. Hall, and A. Sweeney, 2023: Stratosphere-troposphere exchanges of air mass and ozone concentrations from ERA5 and MERRA2: Annual-mean climatology, seasonal cycle, and interannual variability. *J. Geophys. Res. Atmos.*, **128**, e2023JD039270, https://doi.org/10.1029/2023JD039270.

Wang, X., and Coauthors, 2023: Stratospheric climate anomalies and ozone loss caused by the Hunga Tonga-Hunga Ha'apai volcanic eruption. *J. Geophys. Res. Atmos.*, **128**, e2023JD039480, https://doi.org/10.1029/2023JD039480.

Wang, Z., and Coauthors, 2024: Severe global environmental issues caused by Canada's record-breaking wildfires in 2023. *Adv. Atmos. Sci.*, **41**, 565–571, https://doi.org/10.1007/s00376-023-3241-0.

Weatherhead, E. C., and Coauthors, 1998: Factors affecting the detection of trends: Statistical considerations and applications to environmental data. *J. Geophys. Res.*, **103**, 17 149–17 161, https://doi.org/10.1029/98JD00995.

Webb, E. E., A. K. Liljedahl, J. A. Cordeiro, M. M. Loranty, C. Witharana, and J. W. Lichstein, 2022: Permafrost thaw drives surface water decline across lake-rich regions of the Arctic. *Nat. Climate Change*, **12**, 841–846, https://doi.org/10.1038/s41558-022-01455-w.

Weber, M., and Coauthors, 2022: Global total ozone recovery trends attributed to ozone-depleting substance (ODS) changes derived from five merged ozone datasets. *Atmos. Chem. Phys.*, **22**, 6843–6859, https://doi.org/10.5194/acp-22-6843-2022.

Wells, N., S. Goddard, and M. J. Hayes, 2004: A self-calibrating Palmer drought severity index. *J. Climate*, **17**, 2335–2351, https://doi.org/10.1175/1520-0442(2004)017<2335:ASPDSI>2.0.CO;2.

Wentz, F. J., 1997: A well calibrated ocean algorithm for special sensor microwave/imager. *J. Geophys. Res.*, **102**, 8703–8718, https://doi.org/10.1029/96JC01751.

—— , 2015: A 17-year climate record of environmental parameters derived from the Tropical Rainfall Measuring Mission (TRMM) microwave imager. *J. Climate*, **28**, 6882–6902, https://doi.org/10.1175/JCLI-D-15-0155.1.

—— , L. Ricciardulli, K. Hilburn, and C. Mears, 2007: How much more rain will global warming bring? *Science*, **317**, 233–235, https://doi.org/10.1126/science.1140746.

Western, L. M., and Coauthors, 2023: Author correction: Global increase of ozone-depleting chlorofluorocarbons from 2010 to 2020. *Nat. Geosci.*, **16**, 546, https://doi.org/10.1038/s41561-023-01205-3.

WGMS, 2023: Global Glacier Change Bulletin No. 5 (2020–2021). ISC(WDS)/IUGG(IACS)/UNEP/UNESCO/WMO, World Glacier Monitoring Service, 134 pp., https://doi.org/10.5904/wgms-fog-2023-09.

Wielicki, B. A., B. R. Barkstrom, E. F. Harrison, R. B. Lee III, G. L. Smith, and J. E. Cooper, 1996: Clouds and the Earth's Radiant Energy System (CERES): An Earth observing system experiment. *Bull. Amer. Meteor. Soc.*, **77**, 853–868, https://doi.org/10.1175/1520-0477(1996)077<0853:CATERE>2.0.CO;2.

—— , and Coauthors, 1998: Clouds and the Earth's Radiant Energy System (CERES): Algorithm overview. *IEEE Trans. Geosci. Remote Sens.*, **36**, 1127–1141, https://doi.org/10.1109/36.701020.

Wiese, D. N., F. W. Landerer, and M. M. Watkins, 2016: Quantifying and reducing leakage errors in the JPL RL05M GRACE mascon solution. *Water Resour. Res.*, **52**, 7490–7502, https://doi.org/10.1002/2016WR019344.

Willett, K., 2023a: HadISDH.extremes Part I: A gridded wet bulb temperature extremes index product for climate monitoring. *Adv. Atmos. Sci.*, **40**, 1952–1967, https://doi.org/10.1007/s00376-023-2347-8.

—— , 2023b: HadISDH.extremes Part II: Exploring humid heat extremes using wet bulb temperature indices. *Adv. Atmos. Sci.*, **40**, 1968–1985, https://doi.org/10.1007/s00376-023-2348-7.

—— , C. N. Williams Jr., R. J. H. Dunn, P. W. Thorne, S. Bell, M. de Podesta, P. D. Jones, and D. E. Parker, 2013: HadISDH: An updated land surface specific humidity product for climate monitoring. *Climate Past*, **9**, 657–677, https://doi.org/10.5194/cp-9-657-2013.

—— , R. J. H. Dunn, P. W. Thorne, S. Bell, M. de Podesta, D. E. Parker, P. D. Jones, and C. N. Williams Jr., 2014: HadISDH land surface multi-variable humidity and temperature record for climate monitoring. *Climate Past*, **10**, 1983–2006, https://doi.org/10.5194/cp-10-1983-2014.

—— , —— , J. Kennedy, and D. Berry, 2020: Development of the HadISDH marine humidity climate monitoring dataset. *Earth Syst. Sci. Data*, **12**, 2853–2880, https://doi.org/10.5194/essd-12-2853-2020.

—— , A. J. Simmons, M. Bosilovich and D. A. Lavers, 2023: [Global climate] Surface humidity [in "State of the Climate in 2022"]. *Bull. Amer. Meteor. Soc.*, **104**, S49–S51, https://doi.org/10.1175/BAMS-D-23-0090.1.

Williams, E., and Coauthors, 2021: Evolution of global lightning in the transition from cold to warm phase preceding two super El Niño events. *J. Geophys. Res. Atmos.*, **126**, e2020JD033526, https://doi.org/10.1029/2020JD033526.

WMO, 2018: Scientific assessment of ozone depletion: 2018. Global Ozone Research and Monitoring Project Rep. 58, 588 pp., https://csl.noaa.gov/assessments/ozone/2018.

—— , 2022: Scientific assessment of ozone depletion: 2022. Global Ozone Research and Monitoring Project Rep. 278, 520 pp., https://ozone.unep.org/sites/default/files/2023-02/Scientific-Assessment-of-Ozone-Depletion-2022.pdf.

—— , 2023: Significant weather and climate events in 2023. Supplement to Provisional State of the Climate 2023 Rep., World Meteorological Organization, 7 pp., https://wmo.int/sites/default/files/2023-12/Supplement.pdf.

—— , 2024: State of the Global Climate 2023. WMO-1347, 53 pp., https://library.wmo.int/idurl/4/68835.

Wohland, J., N.-E. Omrani, D. Witthaut, and N.-S. Keenlyside, 2019: Inconsistent wind speed trends in current twentieth century reanalyses. *J. Geophys. Res. Atmos.*, **124**, 1931–1940, https://doi.org/10.1029/2018JD030083.

Wolf, S. T., D. J. Vecellio, and W. L. Kenney, 2022: Adverse heat-health outcomes and critical environmental limits (Pennsylvania State University Human Environmental Age Thresholds project). *Amer. J. Hum. Biol.*, **35**, e23801, https://doi.org/10.1002/ajhb.23801.

Woolway, R. I., and C. J. Merchant, 2018: Intralake heterogeneity of thermal responses to climate change: A study of large Northern Hemisphere lakes. *J. Geophys. Res. Atmos.*, **123**, 3087–3098, https://doi.org/10.1002/2017JD027661.

—— , and Coauthors, 2017: Lake surface temperature [in "State of the Climate in 2016"]. *Bull. Amer. Meteor. Soc.*, **98** (8), S13–S14, https://doi.org/10.1175/2017BAMSStateoftheClimate.1

—— , and Coauthors, 2018: Lake surface temperature [in "State of the Climate in 2017"]. *Bull. Amer. Meteor. Soc.*, **99** (8), S13–S15, https://doi.org/10.1175/2018BAMSStateoftheClimate.1.

Xing, J., and M. Wang, 2023: Trend and drivers of satellite-detected burned area changes across Arctic region since the 21st century. *J. Geophys. Res. Atmos.*, **128**, e2023JD038946, https://doi.org/10.1029/2023JD038946.

Yan, D., 2023: This extreme rainfall in Beijing is the largest rainfall in 140 years. Beijing China News, 2 August, accessed 16 February 2024, https://web.archive.org/web/20230805112504/http://www.bj.chinanews.com.cn/news/2023/0802/91478.html.

Yang, Y., and Coauthors, 2023: Evapotranspiration on a greening Earth. *Nat. Rev. Earth Environ.*, **4**, 626–641, https://doi.org/10.1038/s43017-023-00464-3.

Yao, F., B. Livneh, B. Rajagopalan, J. Wang, J.-F. Crétaux, Y. Wada, and M. Berge-Nguyen, 2023: Satellites reveal widespread decline in global lake water storage. *Science*, **380**, 743–749, https://doi.org/10.1126/science.abo2812.

Yosef, Y., E. Aguilar, and P. Alpert, 2021: Is it possible to fit extreme climate change indices together seamlessly in the era of accelerated warming? *Int. J. Climatol.*, **41**, E952–E963, https://doi.org/10.1002/joc.6740.

Young, S. S., 2023: Global and regional snow cover decline: 2000–2022. *Climate*, **11**, 162, https://doi.org/10.3390/cli11080162.

Yu, P., and Coauthors, 2023: Radiative forcing from the 2014–2022 volcanic and wildfire injections. *Geophys. Res. Lett.*, **50**, e2023GL103791, https://doi.org/10.1029/2023GL103791.

Zeng, Z., and Coauthors, 2019: A reversal in global terrestrial stilling and its implications for wind energy production. *Nat. Climate Change*, **9**, 979–985, https://doi.org/10.1038/s41558-019-0622-6.

Zha, J., and Coauthors, 2021: Projected changes in global terrestrial near-surface wind speed in 1.5°C–4.0°C global warming levels. *Environ. Res. Lett.*, **16**, 114016, https://doi.org/10.1088/1748-9326/ac2fdd.

Zhang, G. F., and Coauthors, 2021: Uneven warming likely contributed to declining near-surface wind speeds in northern China between 1961 and 2016. *J. Geophys. Res. Atmos.*, **126**, e2020JD033637, https://doi.org/10.1029/2020JD033637.

Zhang, X., L. Alexander, G. C. Hegerl, P. Jones, A. K. Tank, T. C. Peterson, B. Trewin, and F. W. Zwiers, 2011: Indices for monitoring changes in extremes based on daily temperature and precipitation data. *Wiley Interdiscip. Rev.: Climate Change*, **2**, 851–870, https://doi.org/10.1002/wcc.147.

Zhang, Y., and W. R. Boos, 2023: An upper bound for extreme temperatures over midlatitude land. *Proc. Natl. Acad. Sci. USA*, **120**, e2215278120, https://doi.org/10.1073/pnas.2215278120.

Zhang, Y., and Coauthors, 2023: Southern Hemisphere dominates recent decline in global water availability. *Science*, **382**, 579–584, https://doi.org/10.1126/science.adh0716.

Zhang, Z., B. Poulter, A. F. Feldman, Q. Ying, P. Ciais, S. Peng, and X. Li, 2023: Recent intensification of wetland methane feedback. *Nat. Climate Change*, **13**, 430–433, https://doi.org/10.1038/s41558-023-01629-0.

Zhao, G., Y. Li, L. Zhou, and H. Gao, 2022: Evaporative water loss of 1.42 million global lakes. *Nat. Commun.*, **13**, 3686, https://doi.org/10.1038/s41467-022-31125-6.

Zhao, L., and Coauthors, 2024: Investigation, monitoring, and simulation of permafrost on the Qinghai-Tibet Plateau: A review. *Permafrost Periglacial Processes*, https://doi.org/10.1002/ppp.2227, in press.

Zhao, Y., and Coauthors, 2019: Inter-model comparison of global hydroxyl radical (OH) distributions and their impact on atmospheric methane over the 2000–2016 period. *Atmos. Chem. Phys.*, **19**, 13 701–13 723, https://doi.org/10.5194/acp-19-13701-2019.

Zheng, B., and Coauthors, 2023: Record-high CO2 emissions from boreal fires in 2021. *Science*, **379**, 912–917, https://doi.org/10.1126/science.ade0805.

Zhu, Y., M. Stock, J. Lapierre, and E. DiGangi, 2022: Upgrades of the Earth networks total lightning network in 2021. *Remote Sens.*, **14**, 2209, https://doi.org/10.3390/rs14092209.

Ziemke, J. R., and Coauthors, 2019: Trends in global tropospheric ozone inferred from a composite record of TOMS/OMI/MLS/OMPS satellite measurements and the MERRA-2 GMI simulation. *Atmos. Chem. Phys.*, **19**, 3257–3269, https://doi.org/10.5194/acp-19-3257-2019.

——, and Coauthors, 2022: NASA satellite measurements show global-scale reductions in free tropospheric ozone in 2020 and again in 2021 during COVID-19. *Geophys. Res. Lett.*, **49**, e2022GL098712, https://doi.org/10.1029/2022GL098712.

Ziese, M., A. Rauthe-Schöch, S. Hänsel, P. Finger, E. Rustemeier, and U. Schneider, 2022: GPCC full data daily version 2022 at 1.0°: Daily land-surface precipitation from rain-gauges built on GTS-based and historic data. Global Precipitation Climatology Centre, accessed 12 February 2024, https://doi.org/10.5676/DWD_GPCC/FD_D_V2022_100.

Zohary, T., and I. Ostrovsky, 2011: Ecological impacts of excessive water level fluctuations in stratified freshwater lakes. *Inland Waters*, **1**, 47–59, https://doi.org/10.5268/IW-1.1.406.

Zotta, R. M., R. van der Schalie, W. Preimesberger, L. Mösinger, R. De Jeu, and W. Dorigo, 2023: Vegetation optical depth [in "State of the Climate in 2022"]. *Bull. Amer. Meteor. Soc.*, **104**, S110–S112, https://doi.org/10.1175/BAMS-D-23-0090.1.

——, L. Moesinger, R. van der Schalie, M. Vreugdenhil, W. Preimesberger, T. Frederikse, R. De Jeu, and W. Dorigo, 2024a: VODCA v2: Multi-sensor, multi-frequency vegetation optical depth data for long-term canopy dynamics and biomass monitoring (1.0.0). TU Wien, accessed 25 January 2024, https://doi.org/10.48436/t74ty-tcx62.

——, ——, ——, ——, ——, ——, ——, and ——, 2024b: VODCA v2: Multi-sensor, multi-frequency vegetation optical depth data for long-term canopy dynamics and biomass monitoring. *Earth Syst. Sci. Data Discuss.*, https://doi.org/10.5194/essd-2024-35.

Zou, C.-Z., H. Xu, X. Hao, Q. Liu, 2023: Mid-tropospheric layer temperature record derived from satellite microwave sounder observations with backward merging approach. *J. Geophys. Res. Atmos.*, **128**, e2022JD037472, https://doi.org/10.1029/2022JD037472.

STATE OF THE CLIMATE IN 2023

GLOBAL OCEANS

G. C. Johnson and R. Lumpkin, Eds.

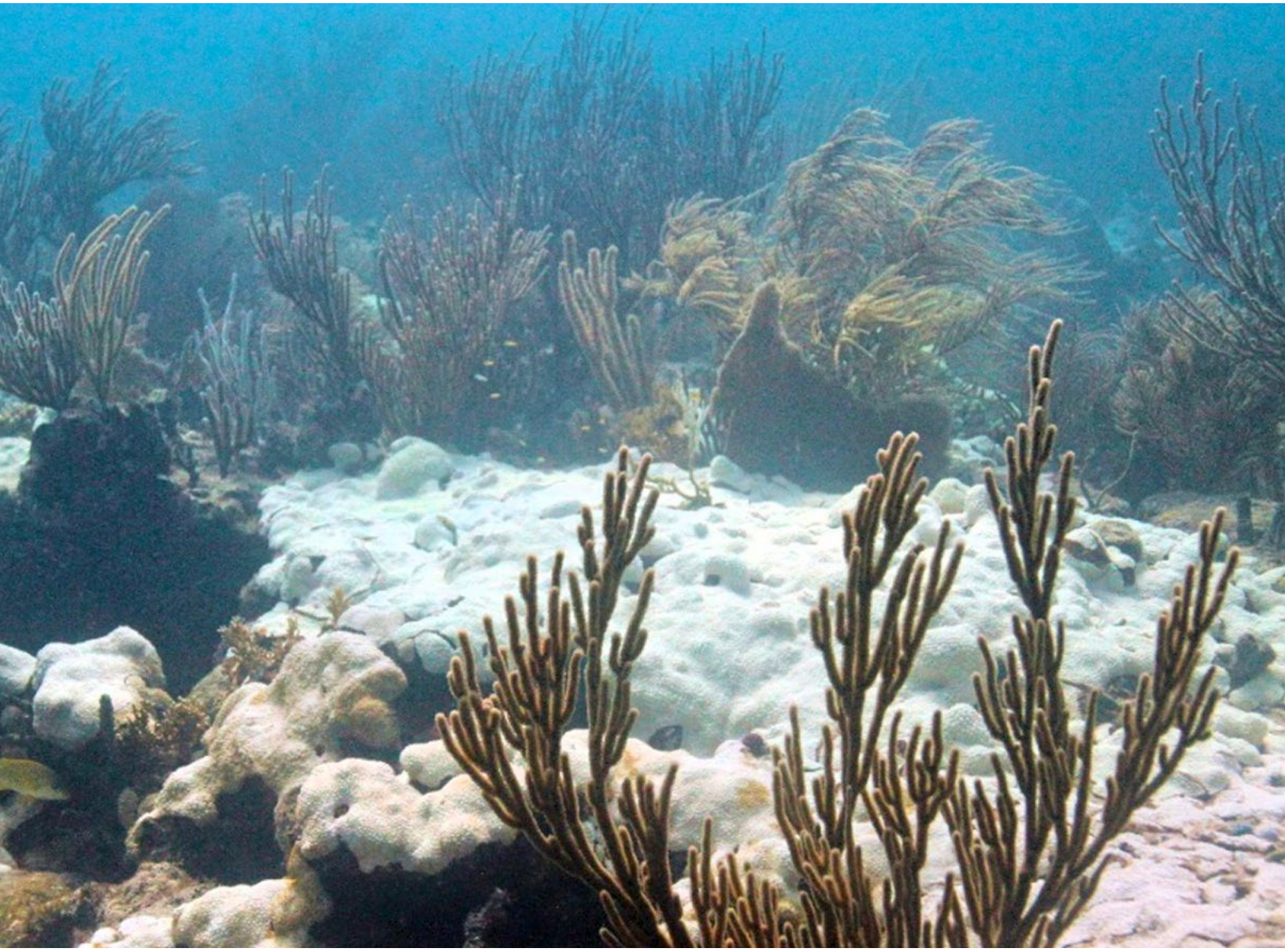

Special Online Supplement to the *Bulletin of the American Meteorological Society* Vol. 105, No. 8, August, 2024

https://doi.org/10.1175/BAMS-D-24-0100.2

Corresponding author: Gregory C. Johnson / Gregory.C.Johnson@noaa.gov

©2024 American Meteorological Society
For information regarding reuse of this content and general copyright information, consult the AMS Copyright Policy.

STATE OF THE CLIMATE IN 2023
Global Oceans

Editors

Jessica Blunden
Tim Boyer

Chapter Editors

Anthony Arguez
Josh Blannin
Peter Bissolli
Kyle R. Clem
Howard J. Diamond
Matthew L. Druckenmiller
Robert J. H. Dunn
Catherine Ganter
Nadine Gobron
Gregory C. Johnson
Rick Lumpkin
Rodney Martinez
Ademe Mekonnen
John B. Miller
Twila A. Moon
Marilyn N. Raphael
Carl J. Schreck III
Laura Stevens
Richard L. Thoman
Kate M. Willett
Zhiwei Zhu

Technical Editor

Lukas Noguchi

BAMS Special Editor for Climate

Timothy DelSole

American Meteorological Society

Cover Credit:
Extensive bleaching of the soft coral Palythoa caribaeorum on Emerald Reef, Key Biscayne, Florida. Image credit: NOAA

How to cite this document:
Global Oceans is one chapter from the *State of the Climate in 2023* annual report and is available from https://doi.org/10.1175/BAMS-D-24-0100.2. Compiled by NOAA's National Centers for Environmental Information, *State of the Climate in 2023* is based on contributions from scientists from around the world. It provides a detailed update on global climate indicators, notable weather events, and other data collected by environmental monitoring stations and instruments located on land, water, ice, and in space. The full report is available from https://doi.org/10.1175/2024BAMSStateoftheClimate.1.

Citing the complete report:
Blunden, J. and T. Boyer, Eds., 2024: "State of the Climate in 2023". Bull. Amer. Meteor. Soc., 105 (8), Si–S483 https://doi.org/10.1175/2024BAMSStateoftheClimate.1.

Citing this chapter:
Johnson, G. C. and R. L. Lumpkin, Eds., 2024: Global Oceans [in "State of the Climate in 2023"]. Bull. Amer. Meteor. Soc., 105 (8), S156–S213, https://doi.org/10.1175/BAMS-D-24-0100.2.

Citing a section (example):
Yu, L., C. Liu, P. W. Stackhouse, J. Garg, and R. A. Weller, 2024: Global ocean heat, freshwater, and momentum fluxes [in "State of the Climate in 2023"]. Bull. Amer. Meteor. Soc., 105 (8), S178–S182, https://doi.org/10.1175/BAMS-D-24-0100.2.

Editor and Author Affiliations (alphabetical by name)

Alexander, Michael A., NOAA/OAR Physical Sciences Laboratory, Boulder, Colorado

Amaya, Dillon J., NOAA/OAR Physical Sciences Laboratory, Boulder, Colorado

Beckley, Brian, KBR, Inc., Greenbelt, Maryland; NASA Goddard Space Flight Center, Greenbelt, Maryland

Boyer, Tim, NOAA/NESDIS National Centers for Environmental Information, Silver Spring, Maryland

Bringas, Francis, NOAA/OAR Atlantic Oceanographic and Meteorological Laboratory, Miami, Florida

Carter, Brendan R., Cooperative Institute for Climate, Ocean, and Ecosystem Studies, University of Washington, Seattle, Washington; NOAA/OAR Pacific Marine Environmental Laboratory, Seattle, Washington

Cetinić, Ivona, NASA Goddard Space Flight Center, Greenbelt, Maryland; Universities Space Research Association, Columbia, Maryland

Chambers, Don P., College of Marine Science, University of South Florida, St. Petersburg, Florida

Chan, Duo, School of Ocean and Earth Science, University of Southampton, Southampton, United Kingdom

Cheng, Lijing, International Center for Climate and Environment Sciences, Institute of Atmospheric Physics, Chinese Academy of Sciences, Beijing, China

Dong, Shenfu, NOAA/OAR Atlantic Oceanographic and Meteorological Laboratory, Miami, Florida

Elipot, Shane, Rosenstiel School of Marine, Atmospheric, and Earth Science, University of Miami, Miami, Florida

Feely, Richard A., NOAA/OAR Pacific Marine Environmental Laboratory, Seattle, Washington

Franz, Bryan A., NASA Goddard Space Flight Center, Greenbelt, Maryland

Fu, Yao, School of Earth and Atmospheric Sciences, Georgia Institute of Technology, Atlanta, Georgia

Gao, Meng, NASA Goddard Space Flight Center, Greenbelt, Maryland; Science Systems and Applications Inc., Lanham, Maryland

Garg, Jay, ADNET Systems, Inc., Hampton, Virginia

Giglio, Donata, Department of Atmospheric and Oceanic Sciences, University of Colorado Boulder, Boulder, Colorado

Gilson, John, Scripps Institution of Oceanography, University of California San Diego, La Jolla, California

Goes, Marlos, Cooperative Institute for Marine and Atmospheric Studies, University of Miami, Miami, Florida; NOAA/OAR Atlantic Oceanographic and Meteorological Laboratory, Miami, Florida

Graham, Garrett, Cooperative Institute for Satellite Earth System Studies, North Carolina State University, Asheville, North Carolina

Hamlington, Benjamin D., Center for Coastal Physical Oceanography, Old Dominion University, Norfolk, Virginia

Hobbs, Will, Australian Antarctic Program Partnership, Institute for Marine and Antarctic Studies; Australian Research Council Centre of Excellence for Climate Extremes, University of Tasmania, Hobart, Australia

Hu, Zeng-Zhen, NOAA/NWS National Centers for Environmental Prediction Climate Prediction Center, College Park, Maryland

Huang, Boyin, NOAA/NESDIS National Centers for Environmental Information, Asheville, North Carolina

Ishii, Masayoshi, Department of Atmosphere, Ocean, and Earth System Modeling Research, Meteorological Research Institute, Japan Meteorological Agency, Tsukuba, Japan

Jacox, Michael G., NOAA/NMFS Southwest Fisheries Science Center, Monterey, California; NOAA/OAR Physical Sciences Laboratory, Boulder, Colorado

Jersild, Annika, Earth System Science Interdisciplinary Center/Cooperative Institute for Satellite Earth System Studies, University of Maryland, College Park, Maryland

Jevrejeva, Svetlana, National Oceanography Centre, Liverpool, United Kingdom

Johns, William E., Rosenstiel School of Marine, Atmospheric, and Earth Science, University of Miami, Miami, Florida

Johnson, Gregory C., NOAA/OAR Pacific Marine Environmental Laboratory, Seattle, Washington

Killick, Rachel. E., Met Office Hadley Center, Exeter, United Kingdom

Kuusela, Mikael, Department of Statistics and Data Science, Carnegie Mellon University, Pittsburg, Pennsylvania

Landschützer, Peter, Flanders Marine Institute, InnovOcean Campus, Ostend, Belgium

Leuliette, Eric, NOAA/NWS NCWCP Laboratory for Satellite Altimetry, College Park, Maryland

Liu, Chao, Department of Physical Oceanography, Woods Hole Oceanographic Institution, Woods Hole, Massachusetts

Locarnini, Ricardo, NOAA/NESDIS National Centers for Environmental Information, Silver Spring, Maryland

Lozier, Susan M., School of Earth and Atmospheric Sciences, Georgia Institute of Technology, Atlanta, Georgia

Lumpkin, Rick, NOAA/OAR Atlantic Oceanographic and Meteorological Laboratory, Miami, Florida

Lyman, John M., Cooperative Institute for Marine and Atmospheric Research, University of Hawaii, Honolulu, Hawaii; NOAA/OAR Pacific Marine Environmental Laboratory, Seattle, Washington

Merrifield, Mark A., Scripps Institution of Oceanography, University of California San Diego, La Jolla, California

Mishonov, Alexey, Earth System Science Interdisciplinary Center/Cooperative Institute for Satellite Earth System Studies, University of Maryland, College Park, Maryland; NOAA/NESDIS National Centers for Environmental Information, Silver Spring, Maryland

Mitchum, Gary T., College of Marine Science, University of South Florida, St. Petersburg, Florida

Moat, Ben I., National Oceanography Centre, Southampton, United Kingdom

Nerem, R. Steven, Colorado Center for Astrodynamics Research, Cooperative Institute for Research in Environmental Sciences, University of Colorado Boulder, Boulder, Colorado

Oe, Mitsuho, Japan Meteorological Agency, Tokyo, Japan

Perez, Renellys C., NOAA/OAR Atlantic Oceanographic and Meteorological Laboratory, Miami, Florida

Pita, Ivenis, Cooperative Institute for Marine and Atmospheric Studies, University of Miami, Miami, Florida; NOAA/OAR Atlantic Oceanographic and Meteorological Laboratory, Miami, Florida

Purkey, Sarah G., Scripps Institution of Oceanography, University of California San Diego, La Jolla, California

Reagan, James, NOAA/NESDIS National Centers for Environmental Information, Silver Spring, Maryland

Sato, Kanako, Japan Agency for Marine-Earth Science and Technology, Yokosuka, Japan

Schmid, Claudia, NOAA/OAR Atlantic Oceanographic and Meteorological Laboratory, Miami, Florida

Smeed, David A., National Oceanography Centre, Southampton, United Kingdom

Smith, Ryan H., NOAA/OAR Atlantic Oceanographic and Meteorological Laboratory, Miami, Florida

Stackhouse, Jr., Paul W., NASA Langley Research Center, Hampton, Virginia

Sukianto, Thea, Department of Statistics and Data Science, Carnegie Mellon University, Pittsburg, Pennsylvania

Sweet, William, NOAA/NOS Center for Operational Oceanographic Products and Services, Silver Spring, Maryland

Thompson, Philip R., Cooperative Institute for Marine and Atmospheric Research, University of Hawaii, Honolulu, Hawaii

Editor and Author Affiliations (continued)

Triñanes, Joaquin A., Laboratory of Systems, Technological Research Institute, Universidad de Santiago de Compostela, Campus Universitario Sur, Santiago de Compostela, Spain; Cooperative Institute for Marine and Atmospheric Studies, University of Miami, Miami, Florida; NOAA/OAR Atlantic Oceanographic and Meteorological Laboratory, Miami, Florida

Volkov, Denis L., Cooperative Institute for Marine and Atmospheric Studies, University of Miami, Miami, Florida; NOAA/OAR Atlantic Oceanographic and Meteorological Laboratory, Miami, Florida

Wanninkhof, Rik, NOAA/OAR Atlantic Oceanographic and Meteorological Laboratory, Miami, Florida

Weller, Robert A., Department of Physical Oceanography, Woods Hole Oceanographic Institution, Woods Hole, Massachusetts

Westberry, Toby K., Oregon State University, Corvallis, Oregon

Widlansky, Matthew J., Cooperative Institute for Marine and Atmospheric Research, University of Hawaii, Honolulu, Hawaii

Willis, Josh K., Jet Propulsion Laboratory, California Institute of Technology, Pasadena, California

Yin, Xungang, NOAA/NESDIS National Centers for Environmental Information, Asheville, North Carolina

Yu, Lisan, Department of Physical Oceanography, Woods Hole Oceanographic Institution, Woods Hole, Massachusetts

Zhang, Huai-min, NOAA/NESDIS National Centers for Environmental Information, Asheville, North Carolina

Editorial and Production Team

Allen, Jessicca, Graphics Support, Cooperative Institute for Satellite Earth System Studies, North Carolina State University, Asheville, North Carolina

Camper, Amy V., Graphics Support, Innovative Consulting and Management Services, LLC, NOAA/NESDIS National Centers for Environmental Information, Asheville, North Carolina

Haley, Bridgette O., Graphics Support, NOAA/NESDIS National Centers for Environmental Information, Asheville, North Carolina

Hammer, Gregory, Content Team Lead, Communications and Outreach, NOAA/NESDIS National Centers for Environmental Information, Asheville, North Carolina

Love-Brotak, S. Elizabeth, Lead Graphics Production, NOAA/NESDIS National Centers for Environmental Information, Asheville, North Carolina

Ohlmann, Laura, Technical Editor, Innovative Consulting and Management Services, LLC, NOAA/NESDIS National Centers for Environmental Information, Asheville, North Carolina

Noguchi, Lukas, Technical Editor, Innovative Consulting and Management Services, LLC, NOAA/NESDIS National Centers for Environmental Information, Asheville, North Carolina

Riddle, Deborah B., Graphics Support, NOAA/NESDIS National Centers for Environmental Information, Asheville, North Carolina

Veasey, Sara W., Visual Communications Team Lead, Communications and Outreach, NOAA/NESDIS National Centers for Environmental Information, Asheville, North Carolina

3. Table of Contents

Authors and affiliations S159
a. Overview S162
b. Sea-surface temperature S163
Sidebar 3.1: Marine heatwaves in 2023 ..... S167
c. Ocean heat content S169
d. Salinity S173
1. Introduction S173
2. Sea-surface salinity S173
3. Subsurface salinity S175
e. Global ocean heat, freshwater, and momentum fluxes S178
1. Surface heat fluxes S179
2. Surface freshwater fluxes S181
3. Wind stress S181
4. Long-term perspective S182
f. Sea level variability and change S183
g. Surface currents S187
1. Pacific Ocean S187
2. Indian Ocean S189
3. Atlantic Ocean S189
h. Meridional overturning circulation and heat transport in the Atlantic Ocean S191
i. Global ocean phytoplankton S194
j. Global ocean carbon cycle S198
1. Introduction S198
2. Air–sea carbon dioxide fluxes S198
3. Ocean interior inventory estimates S200
Appendix 1: Acronyms S202
Appendix 2: Datasets and sources S204
References **S208**

3. GLOBAL OCEANS

G. C. Johnson and R. Lumpkin, Eds.

a. Overview

—G. C. Johnson and R. Lumpkin

A shift out of a triple-dip La Niña to a neutral state starting in February and then into an El Niño in May that strengthened through December was a defining event for the global oceans in 2023. Global sea-surface temperatures (SSTs) shattered record highs in 2023, as did global ocean heat content and global sea level. The global average annual SST anomaly was 0.13°C above the previous record set in 2016, also an El Niño year. Marine heatwaves were exceptionally widespread, long-lived, and record-breaking in many regions. From 2022 to 2023, ocean heat content from 0 dbar to 2000 dbar increased at a rate equivalent to ~0.7 W m^{-2} of energy applied over the surface area of Earth, and global sea level increased by ~8.1 mm. In addition, the oceans absorbed anthropogenic carbon at a rate of ~3.8 Pg C yr^{-1} in 2023, with concomitant acidification, slightly above the 2013–22 average of ~3.5 Pg C yr^{-1}. In haiku form:

El Niño roars in,
with record marine heatwaves,
as seas warm, rise, sour.

In the Pacific Ocean—with the shift from La Niña to El Niño—SSTs, sea-surface salinities, 0-m–2000-m ocean heat content, and sea level all increased in the eastern tropical Pacific and decreased in the western tropical Pacific from 2022 to 2023. Additionally, surface currents across the equatorial Pacific in 2023 were strongly anomalously eastward. Fluxes of carbon dioxide from ocean to atmosphere were lower than average during 2023 off Peru and out to about 120°W in the equatorial Pacific as a result of the strong coastal El Niño but higher than average in the central equatorial Pacific. Chlorophyll-*a* anomalies were low in a wedge in the central and eastern equatorial Pacific, but high just outside that wedge. The Pacific Decadal Oscillation continued in a negative phase in 2023 that has held since 2020, with SST, ocean heat content, and sea-surface height values in the center of the North Pacific basin all higher than average, and relatively lower values around the edges. A persistent 2020–23 poleward shift in the Kuroshio extension continued to be evident in both ocean heat content and zonal surface current anomalies.

The Indian Ocean dipole shifted from negative in 2022 to positive in 2023, with positive SST, ocean heat content, and sea-level anomalies in the west and negative anomalies in the east. Surface currents near the equator were anomalously westward. The most notable sea-surface salinity anomaly feature in the Indian Ocean in 2023 was a strong fresher-than-average patch north of the equator.

In the Atlantic, SST, ocean heat content, and sea level were all well above average across much of the basin in 2023, with below-average values of ocean heat content anomalies southeast of Greenland, and lower values of SST anomalies east of northern Greenland. In 2023, the anomaly patterns were similar to 2022, but values were generally higher. Sea-surface salinity was anomalously high in salty subtropical regions and anomalously low around the Intertropical Convergence Zone and in the Greenland Sea. Updates in time series of the Atlantic meridional overturning circulation at various latitudes revealed little direct evidence of a trend over the past few decades.

Arctic Ocean conditions for 2023 are discussed in detail in Chapter 5, and Southern Ocean conditions in Chapter 6.

b. Sea-surface temperature

—X. Yin, B. Huang, D. Chan, G. Graham, Z.-Z. Hu, and H.-M. Zhang

Here, sea-surface temperature (SST) changes over 2022–23 and their uncertainties are assessed over the global ocean and individual ocean basins based on the ERSSTv5 (Huang et al. 2017) and two supporting datasets, the HadSST.4.0.1.0 (Kennedy et al. 2019) and the DOISST v2.1 (Huang et al. 2021). SST anomalies (SSTAs) are calculated relative to 1991–2020 monthly climatologies. The magnitudes of SSTAs are compared against the SST standard deviations (SDs) during the baseline period.

With a transition from a triple-dip 2020–23 La Niña (Li et al. 2023; Jiang et al. 2023) to El Niño in early 2023, historic high SST records were continually set starting in March and throughout the remainder of the year. Based on the DOISST v2.1, daily global mean SST rapidly climbed, with a trend of 0.15°C per month during the first quarter of 2023 following the dissipation of La Niña. The daily mean global SST first surpassed the previous record-high SST of 18.78°C, which was set on 6 March 2016. Then, after a series of SST record-breaking events, it reached a new record high of 18.82°C on 4 April 2023. After a seasonal decrease during April–May, daily global mean SST began to rise again, setting new records numerous times until 22 August, when a historic high daily global mean SST of 18.99°C was recorded. Meanwhile, since 13 March 2023 and continuing through the end of the year, daily global mean SST had remained record high for the time of year in DOISST v2.1, which started in 1981. For the year as a whole, 2023 was the warmest year in the 170-year records, since the pre-industrial era, according to ERSSTv5, a monthly SST product with records since January 1854. The annual average global mean SSTA in 2023 was +0.41±0.01°C, exceeding that of 2016, now the second warmest year (+0.28±0.01°C) on record by a large margin. The warmest 10 years for the global ocean in terms of SST were all from the last decade, with SSTAs ranging from +0.13±0.1°C to +0.41±0.1°C. Here, the uncertainties, reported as 95% confidence intervals, were estimated by a Student's t-test using a 500-member ERSSTv5 ensemble with randomly drawn parameter values within reasonable ranges during SST reconstructions (Huang et al. 2015, 2020).

Annual mean SSTAs for 2023 (Fig. 3.1a) were above normal nearly globally, resulting in large-area, long-duration, high-magnitude marine heatwaves in many regions (see Sidebar 3.1 for details). With the emerging El Niño, SSTAs in the eastern tropical Pacific were more than +0.5°C near the dateline and increased eastward to more than +2°C off the coast of South America. In the North Pacific, except off the west coast of North America, SSTAs in the midlatitudes were above normal, reaching +1.5°C, consistent with a negative phase of the Pacific Decadal Oscillation (PDO; Mantua and Hare 2002). From the subtropical South Pacific to the Southern Ocean, SSTAs were positive (+0.5°C) in the west but negative (–0.5°C) in the east. The Indian Ocean in 2023 was characterized by warm anomalies in the west and weak cold anomalies in the east, congruent with an annual mean Indian Ocean dipole (IOD; Saji et al. 1999) index of +0.59, ranking as the third highest annual mean since 1854. Over nearly the entire Atlantic Ocean, SSTs were above normal, with SSTAs ranging between +0.2°C and +1.0°C. The North Atlantic Ocean was particularly warm, with SSTAs above +1.0°C in the east. SSTAs of +0.5°C and above were observed in parts of the Arctic and sub-Arctic Oceans, particularly in the Barents Sea.

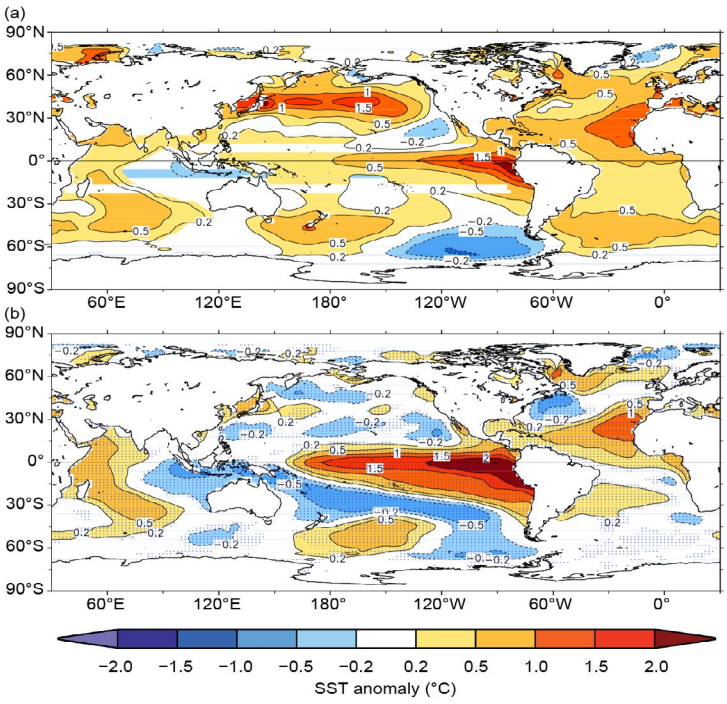

Fig. 3.1. (a) Annual mean sea-surface temperature anomalies (SSTAs) in 2023 (°C) and (b) difference of annual mean SSTAs from the previous year (2023 minus 2022; °C). SSTAs are based on the 1991–2020 climatologies. The stippled areas in panel (b) indicate that the 2023-minus-2022 SSTA difference is significant at 95% confidence.

The 2023-minus-2022 SST differences (Fig. 3.1b) show a substantial SST increase in the equatorial Pacific, owing to the transition from La Niña conditions in 2022 to the onset of El Niño in 2023. In this region, SSTs increased by over 1.5°C near the dateline and by more than 2.0°C east of approximately 120°W. In the Indian Ocean, the east–west SSTA contrast was reversed, consistent with negative monthly IOD indices in 2022 and positive values in 2023. In 2023, the North Atlantic became extremely warm with record-high monthly mean SSTs for the time of year observed from March through December in the 170-year records of the ERSSTv5. Over the subtropical North Atlantic and the seas south of Greenland, SSTs in 2023 were substantially higher than in 2022. The western North Atlantic Ocean in 2023 was substantially colder than in 2022 (Fig. 3.1b) but still warmer than the climatology (Fig. 3.1a).

Seasonal mean SSTAs (Fig. 3.2) provide detailed insights into the evolution of SSTs in 2023. The seasonal changes of the El Niño–Southern Oscillation (ENSO) status were reflected in the tropical Pacific Ocean seasonal SSTAs. In boreal winter (Fig. 3.2a), the La Niña conditions resulted in SSTAs between –1.0°C and –0.2°C. In boreal spring (Fig.3.2b), high positive SSTAs (+1.0°C to +2.0°C) in the seas off the coast of South America were associated with a strong coastal El Niño, a precursor of a basin-scale El Niño (Rasmusson and Carpenter 1982; Hu et al. 2019). El Niño conditions emerged in May and were evident in the June–August average (Fig. 3.2c) and strengthened in boreal autumn (Fig. 3.2d), as indicated by the progressive westward expansion of the positive SSTAs (>+1.0°C) and the areas encompassed by the 1-SD and 2-SD SSTA contours. Along with the ENSO phase transition, the zonal SSTA contrast in the tropical Indian Ocean also shifted from near-neutral IOD status in winter (+0.11 during January–March) to a strong positive IOD status in summer (+0.71 during July–September) and autumn (+1.34 during October–December). In the winter and spring, SSTAs in the North Pacific Ocean were mainly positive with negative values along the coastal and tropical regions (Figs. 3.2a,b). In the summer

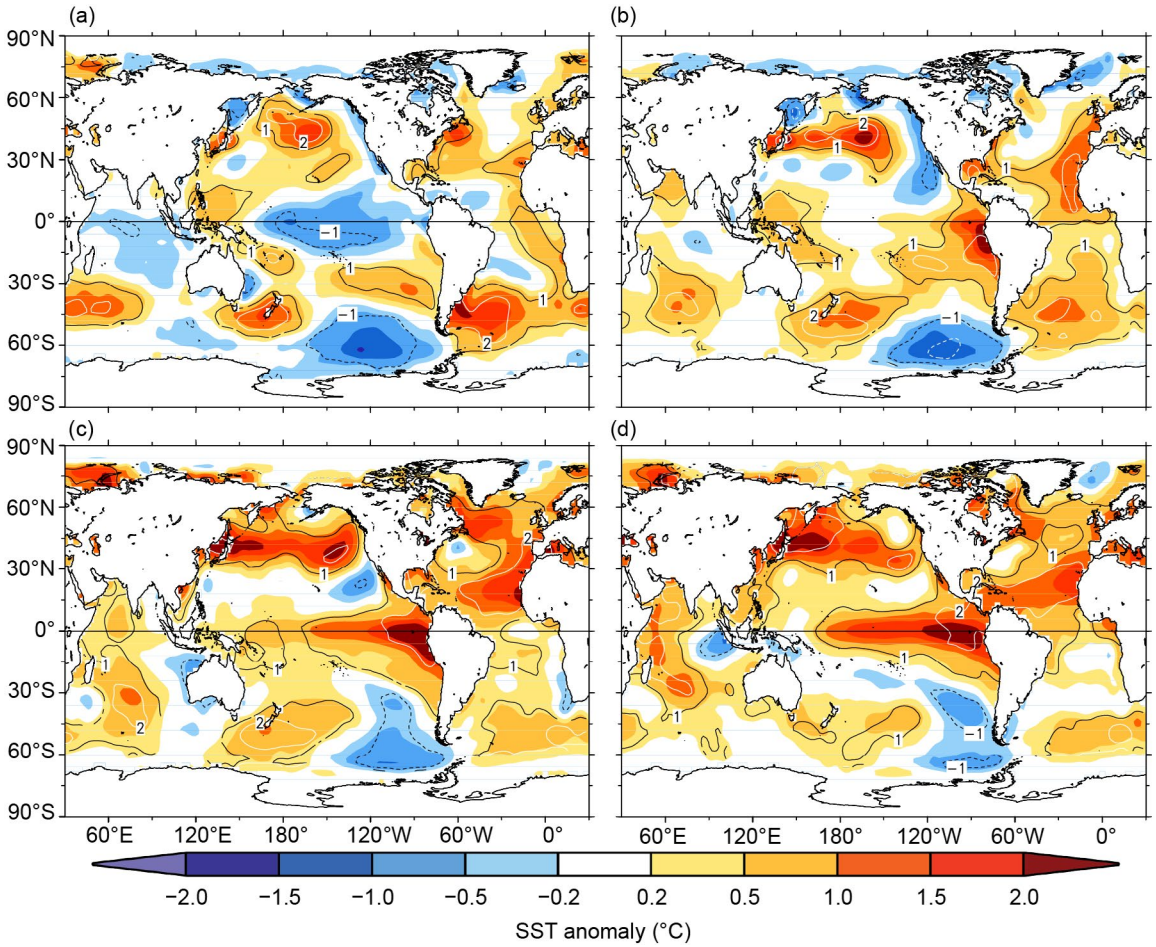

Fig. 3.2. Seasonal mean sea-surface temperature anomalies (SSTAs) of ERSSTv5 (°C; shading) for (a) Dec 2022–Feb 2023, (b) Mar–May 2023, (c) Jun–Aug 2023, and (d) Sep–Nov 2023. The normalized seasonal mean SSTAs based on the seasonal mean standard deviations (SDs) over 1991–2020 are indicated by contours of –2 (dashed white), –1 (dashed black), 1 (solid black), and 2 (solid white).

and autumn, SSTAs were almost all positive in the basin and exceeded +1.0°C in the midlatitudes (Figs. 3.2c,d). For the North Atlantic Ocean, positive SSTAs were dominant year round and were particularly strong in the summer and autumn with SSTAs greater than +0.5°C over almost the entire basin. Large warming areas with SSTAs greater than 2-SD were found in the southeastern part of the basin during the summer to autumn seasons, which significantly contributed to the record-breaking SSTs in the North Atlantic during that time. In the Southern Hemisphere, a sizable area of positive SSTA appeared in each ocean. Between the Pacific and Atlantic positive SSTA areas, there was a comparable area of negative SSTA in the South Pacific and Southern Ocean. This feature was present in all seasons, but it was most pronounced in boreal winter (Fig. 3.2a).

For the global ocean, southern oceans, and individual basins in the tropics and subtropics, annual mean SSTA time series based on ERSSTv5 (Fig. 3.3) are presented with time series from HadSST.4.0.1.0 and DOISST v2.1. The estimated linear trends (Table 3.1) for the period beginning at the start of the twenty-first century (2000–23) are larger than those for the longer period that dates to the mid-twentieth century (1950–2023) both globally and in all regions. The global ocean trends are 0.17±0.06°C decade^{-1} and 0.11±0.01°C decade^{-1} for the two periods, respectively. On a regional scale, for 1950–2023 vs. 2000–23 trends, the warming acceleration rate is the highest for the North Pacific (0.10±0.04°C decade^{-1} vs 0.42±0.13°C decade^{-1}) and the lowest for the tropical Indian Ocean (0.14±0.02°C decade^{-1} vs 0.16±0.08°C decade^{-1}). During the longer term since 1950, trends among different regions are comparable, ranging from 0.10°C decade^{-1} to 0.14°C decade^{-1} with the highest in the tropical Indian Ocean. During the shorter term since 2000, trends among different regions are widely spread, ranging from 0.14°C decade^{-1} to 0.42°C decade^{-1}, with the highest trend in the North Pacific.

Table 3.1. Linear trends (°C decade^{-1}) of global and regional mean annual sea-surface temperature anomalies (SSTAs) from ERSSTv5, HadSST4.0.1.0, and DOISST v2.1. The uncertainties at 95% confidence are estimated by accounting for the effective sampling number quantified by lag-1 autocorrelation on the degrees of freedom of annual mean SSTs.

Product	Region	1950–2023	2000–23
HadSST.4.0.1.0	Global	0.12±0.02	0.19±0.06
DOISST	Global	N/A	0.20±0.05
ERSSTv5	Global	0.11±0.01	0.17±0.06
ERSSTv5	Tropical Pacific (30°S–30°N)	0.10±0.03	0.14±0.14
ERSSTv5	North Pacific (30°N–60°N)	0.10±0.04	0.42±0.13
ERSSTv5	Tropical Indian (30°S–30°N)	0.14±0.02	0.16±0.08
ERSSTv5	North Atlantic (30°N–60°N)	0.13±0.05	0.21±0.10
ERSSTv5	Tropical Atlantic (30°S–30°N)	0.12±0.02	0.18±0.08
ERSSTv5	Southern oceans (30°S–60°S)	0.10±0.02	0.14±0.05

The global trends calculated from different SST products, ranging from 0.11°C decade^{-1} to 0.12°C decade^{-1} over 1950–2023 and from 0.17°C decade^{-1} to 0.20°C decade^{-1} over 2000–23, are statistically indistinguishable considering the uncertainties (Table 3.1). As shown in Fig. 3.3, the departures of both DOISST v2.1 and HadSST.4.0.1.0 from ERSSTv5 are largely within the 2-SD

envelope (gray shading), which was derived from a 500-member ensemble analysis based on ERSSTv5 and centered on the SSTAs of ERSSTv5 (Huang et al. 2020). Particularly, the long-term SST time series of the North Atlantic shows large interdecadal variations (Fig. 3.3f). These variations are mainly associated with the Atlantic Multidecadal Variability (AMV; Schlesinger and Ramankutty 1994; Yin et al. 2023).

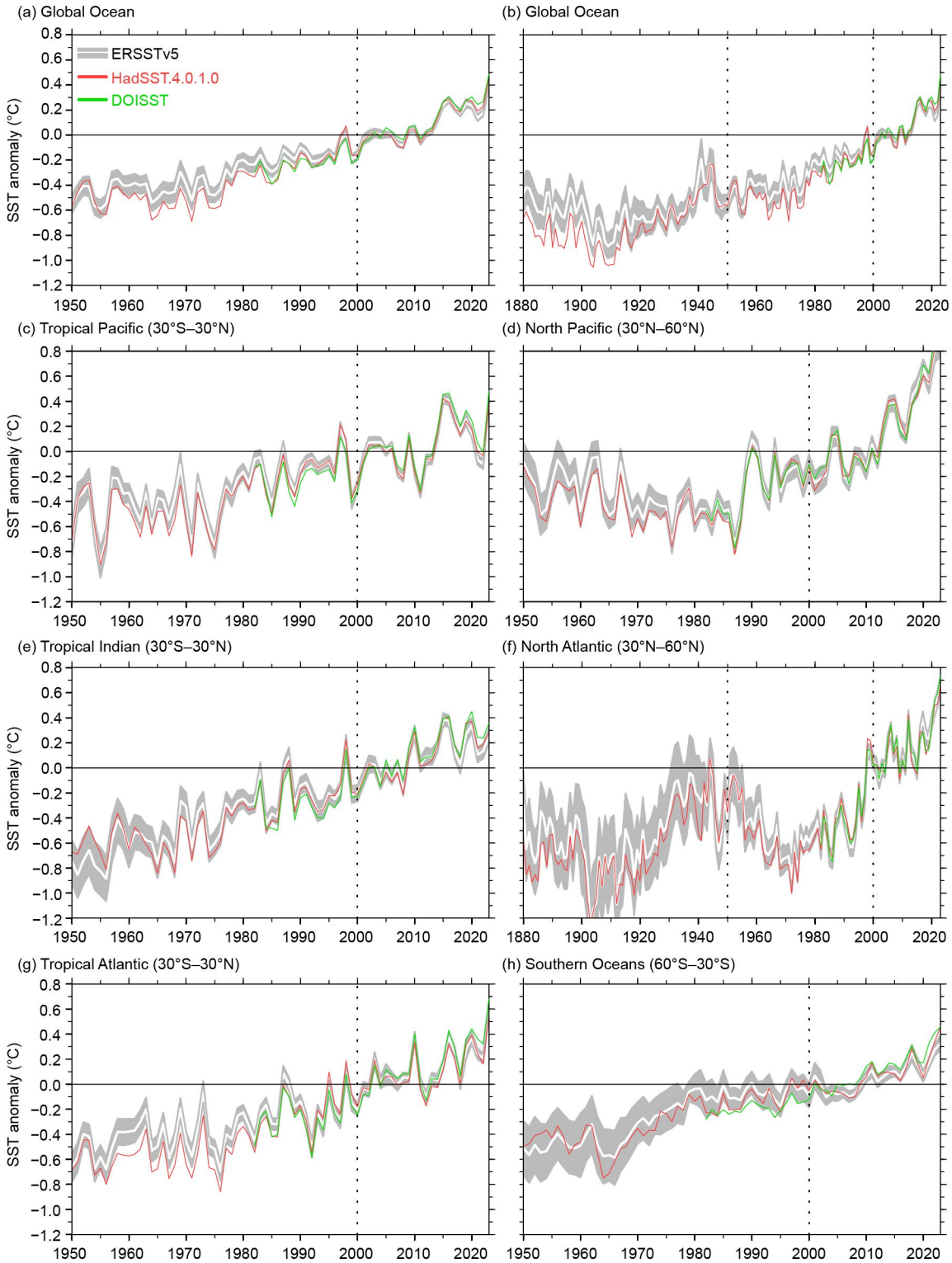

Fig. 3.3. Annual mean sea-surface temperature anomalies (SSTAs; °C) of ERSSTv5, (solid white) and 2 standard deviations (SDs, gray shading) of ERSSTv5, SSTAs of HadSST.4.0.1.0 (solid red), and SSTAs of DOISST (solid green) for the period 1950–2023 except for (b) and (f). (a) Global ocean, (b) global ocean in 1880–2023, (c) tropical Pacific, (d) North Pacific, (e) tropical Indian, (f) North Atlantic for 1880–2023, (g) tropical Atlantic, and (h) Southern oceans (30°S–60°S). The 2-SD envelope was derived from a 500-member ensemble analysis based on ERSSTv5 and centered on SSTAs of ERSSTv5. The years 2000 and 1950 are indicated by dotted vertical black lines.

Sidebar 3.1: **Marine heatwaves in 2023**

M. G. JACOX, D. J. AMAYA, AND M. A. ALEXANDER

Marine heatwaves (MHWs)—transient periods of exceptionally high ocean temperatures—have been linked to a myriad of impacts on ocean physics, chemistry, and biology, and consequently on human economies and communities (e.g., Holbrook et al. 2019; Smith et al. 2021, 2023). These events, which can last many months, are often defined as exceeding the 90th percentile of sea-surface temperature anomalies (SSTAs) for a given location and time of year (Hobday et al. 2016). As a result, MHWs are observed roughly 10% of the time at any given location by definition. However, MHW events in 2023 far exceeded what is considered "typical", with record-breaking extremes (in terms of area coverage and intensity) observed all over the world. Here, we use monthly SST data from NOAA's OISSTv2.1 dataset (Reynolds et al. 2007; Huang et al. 2021), using a 1991–2020 climatological period, to illustrate the exceptional global coverage and intensity of MHWs in 2023.

Marine heatwaves were widespread in 2023, with most of the ocean experiencing extreme temperatures at some point during the year (Fig. SB3.1). More than 85% of the global ocean experienced an MHW for at least one month in 2023, 50% experienced four months or more of MHWs, and 29% experienced six months or more. For reference, over 1982–2023, 44% of the ocean experienced at least one MHW month each year on average, with just 11% and 4% experiencing at least four and six months, respectively. Several regions, including the eastern tropical and North Atlantic, the Sea of Japan, the Arabian Sea, the Southern Ocean near New Zealand, and the eastern tropical Pacific, were in an MHW state for at least 10 months of 2023. These areas accounted for ~4% of the global ocean, or ~10 times the area that would typically experience such persistent MHWs in an average year (0.4%). In contrast, the regions with anomalously low MHW activity were concentrated in the northeast Pacific (subtropics, Gulf of Alaska, eastern Bering Sea), the eastern Indian Ocean, the Arctic Ocean, and several sectors of the Southern Ocean (Fig. SB3.1).

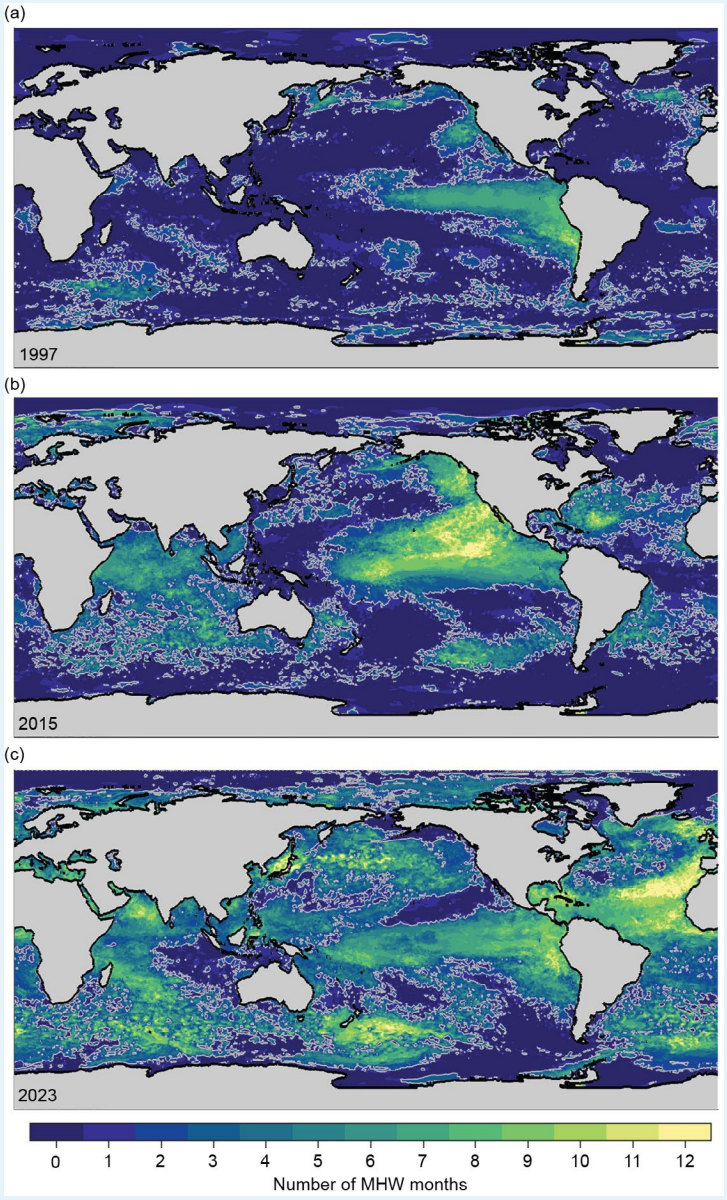

Fig. SB3.1. Global marine heatwave (MHW) coverage during three years characterized by the onset of major El Niño events: (a) 1997, (b) 2015, and (c) 2023. Colors indicate the number of months in each year for which an MHW was present at each OISSTv2.1 grid cell (0.25° resolution). The deepest blues, surrounded by a gray contour, indicate regions that experienced MHWs in only one month or not at all. MHWs were calculated using a 90% threshold of monthly sea-surface temperature anomalies relative to the 1991–2020 climatology from OISSTv2.1.

During 2023, global MHW coverage progressively increased through boreal winter, spring, and summer, reaching a peak coverage of ~40% of the global ocean area in August and remaining elevated through the end of the year (https://psl.noaa.gov/marine_heatwaves/#report). This increased prevalence of MHWs coincided with the development of a strong El Niño, a well-known driver of MHWs particularly in the eastern Pacific and Indian Oceans (Holbrook et al. 2019). However, relative to 1997 and 2015, two other years featuring the onset of strong El Niños, 2023 still stands out as exceptional for the widespread nature of MHWs (Fig. SB3.1). Throughout the year MHWs were persistent not only in hotspots typically associated with El Niño events, but also other areas including much of the Atlantic and western Pacific Oceans, which saw relatively little MHW activity in 1997 and 2015.

Marine heatwaves were not only widespread and persistent in 2023, but in many regions, they exhibited temperatures that were unprecedented in the observational record (section 3b). To contextualize MHW intensity in 2023 relative to 40+ years of observed ocean temperature anomalies, we compare the highest MHW intensity (i.e., warmest monthly SSTA) reached in 2023 to SSTAs from all prior months in the OISSTv2.1 observational period (1982–2023; 504 months total). Over portions of every major ocean basin as well as many inland seas—a total of 13% of the global ocean area—the highest monthly SSTA in at least the last 40 years (bright yellow areas in Fig. SB3.2) occurred in 2023. Similarly, 50% of the ocean areas experienced one of their top 10 monthly SSTAs on record. For reference, across all prior years (1982–2022), on average 2% of the ocean set an all-time high for monthly SSTA each year, and only 14% recorded a top-10 highest monthly SSTA. The exceptional coverage and intensity of MHWs in 2023 are closely related; comparison of MHW persistence (Fig. SB3.1) and maximum intensity (Fig. SB3.2) illustrates that regions exposed to MHW conditions for longer also tended to be regions with exceptionally high peak MHW intensities. In terms of cumulative intensity (i.e., the product of intensity and duration), those regions were especially heavily impacted.

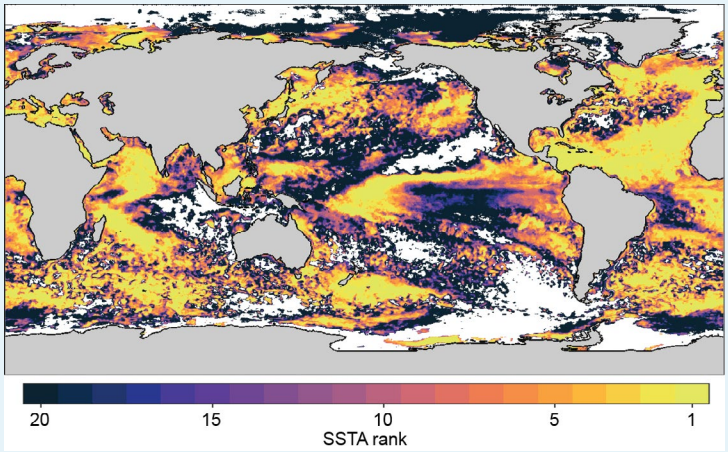

Fig. SB3.2. Intensity of 2023 marine heatwaves (MHWs) relative to historical conditions during the satellite record. Colors indicate the rank of 2023's highest monthly sea-surface temperature anomalies (SSTAs) relative to SSTAs for all months from 1982 to 2023 (N=504). SSTAs were calculated relative to the 1991–2020 climatology from OISSTv2.1. White areas did not experience any MHWs in 2023 based on monthly SSTAs.

c. Ocean heat content

—G. C. Johnson, J. M. Lyman, T. Boyer, L. Cheng, D. Giglio, J. Gilson, M. Ishii, R. E. Killick, M. Kuusela, R. Locarnini, A. Mishonov, M. Oe, S. G. Purkey, J. Reagan, K. Sato, and T. Sukianto

The oceans are central to the storage and transport of heat in Earth's climate system (IPCC 2021). They absorbed ~89% of the excess heat entering Earth's climate system from 1971 to 2020 (von Schuckmann et al. 2023). Since this warming is greatest at the surface, it has increased the strength and duration of marine heatwaves (e.g., Oliver et al. 2021; Sidebar 3.1) and the stratification of the upper ocean (e.g., Li et al. 2020), with impacts on biogeochemical cycles, ocean circulation, and ecosystems. This warming is linked to increased energy to fuel tropical cyclones (e.g., Walsh et al. 2016), sea-level rise (section 3f), melting of sea ice, ice shelves, and marine terminating glaciers and ice sheets (IPCC 2021), and coral bleaching (e.g., Hughes et al. 2017). Here, we discuss ocean temperature and heat content anomalies for 2023 relative to 2022 as well as a 1993–2022 climatology. We focus primarily on the upper 2 km, where temperature profiles collected by the Argo array, which first reached sparse near-global coverage around 2005, have greatly improved ocean sampling and the ability to map subsurface ocean temperature fields.

Weekly maps of ocean heat content anomaly (OHCA) relative to a 1993–2022 baseline mean (Fig. 3.4) as well as temperature for 58 pressure layers from 0 dbar to 2000 dbar were generated using Random Forest regression following Lyman and Johnson (2023) with V2.1 improvements as described at https://www.pmel.noaa.gov/rfrom/. In situ ocean temperature profiles, including Argo data downloaded from an Argo Global Data Assembly Centre in January 2024 (http://doi.org/10.17882/42182#98916), were used for training data for these maps, and prediction variables included satellite sea-surface height and temperature, location, and time. Since these maps are deeper than the 0 m–700 m maps shown in earlier reports, anomaly, year-to-year difference, and trend values are generally slightly larger. In situ global estimates of OHCA for three depth layers (0 m–700 m, 700 m–2000 m, and 2000 m–6000 m) from five different research groups (Fig. 3.6) are also discussed.

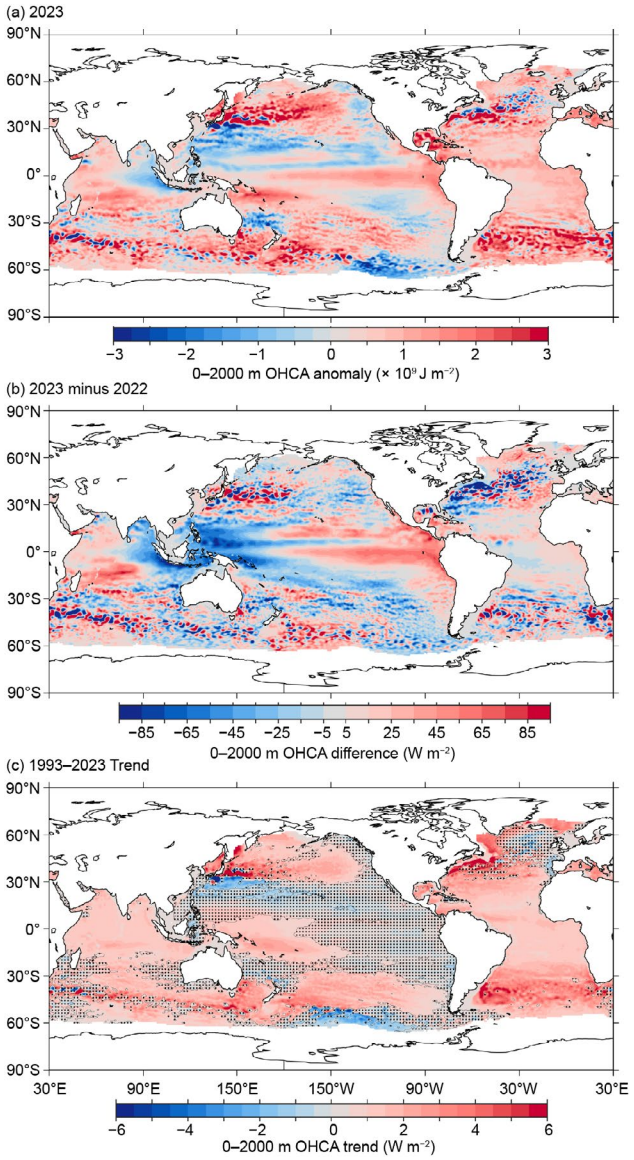

Fig. 3.4. (a) RFROM v2 estimate of 0-m–2000-m ocean heat content anomaly (OHCA; × 10^9 J m^{-2}) for 2023 analyzed following Lyman and Johnson (2023) with v2 improvements as in https://www.pmel.noaa.gov/rfrom/. In situ OHCA profiles are used as training data and satellite sea-surface height, satellite sea-surface temperatures, overlying layer properties, location, and time are predictors. Values are displayed relative to a 1993–2022 baseline. (b) 2023-minus-2022 combined estimates of OHCA expressed as a local surface heat flux equivalent (W m^{-2}). For (a) and (b) comparisons, note that 95 W m^{-2} applied over one year results in a 3 × 10^9 J m^{-2} change of OHCA. (c) Linear trend for 1993–2023 annual OHCA (W m^{-2}). Areas with statistically insignificant trends at 5%–95% confidence (taking into account the decorrelation time scale of the residuals when estimating effective degrees of freedom) are stippled.

After three consecutive years of La Niña conditions that persisted through January 2023, El Niño conditions were established by May 2023 and strengthened through the end of the year. Hence, the 2023-minus-2022 difference of 0-m–2000-m OHCA (Fig. 3.4b) shows a decrease in the west and an increase in the east in the tropical Pacific. Ocean heat content anomalies for 2023 (Fig. 3.4a) were positive all across the equatorial Pacific but stronger in the east, partly because anomalously near-surface eastward currents on the

equator (see Fig. 3.18a) driven by relaxation of the easterly trade winds (see Fig. 3.13a) carried warm water from the west to the east. Low values in 2023-minus-2022 differences are found close to the coast of the Americas at higher latitudes and farther west at lower latitudes, likely owing to a Rossby Wave signature of the La Niñas propagating from the eastern boundary westward. Differences around the western boundary current extensions exhibit energetic mesoscale features and are generally positive in 2023 relative to 2022. As in 2022, the centers of the North and South Pacific continued to be anomalously warm in 2023, with colder conditions around the edges, consistent with a continued negative Pacific Decadal Oscillation index in the Northern Hemisphere (section 3b). Again, the cold anomalies just south of the Kuroshio Extension and warm anomalies within that current that persisted in 2023 are associated with a northward shift of that current (see Figs. 3.18a, 3.20). Also again, Pacific marginal seas all remained warmer than climatological means in 2023.

In the tropical Indian Ocean, the 2023-minus-2022 difference of OHCA (Fig. 3.4b) decreased in the east and increased in the west, consistent with a transition from a negative to a positive phase of the Indian Ocean dipole index in 2023, with relatively cold SST anomalies in the east and warm anomalies in the west. The 2023 OHCA (Fig. 3.4a) were negative in the east between Australia and Indonesia and generally positive elsewhere.

The 2023-minus-2022 difference of OHCA (Fig. 3.4b) in the Atlantic Ocean was weakly positive in most of the tropics and the northern North Atlantic, with warming in the Caribbean Sea. Warming in the Labrador and Irminger Seas is consistent with a relatively warm vintage of Upper North Atlantic Deep Water formed in 2023. Among the substantial midlatitude variability was a cooling on the north side of the Gulf Stream extension from 2022 to 2023, suggesting a southward shift in the axis of that current. Again, the broad pattern of upper OHCA in 2023 (Fig. 3.4a) is similar to that in 2022 and 2021, with much of the Atlantic Ocean exhibiting upper OHCA above the 1993–2022 average (Fig. 3.4a). One exception, as in recent years, is the cooler-than-average conditions southeast of Greenland.

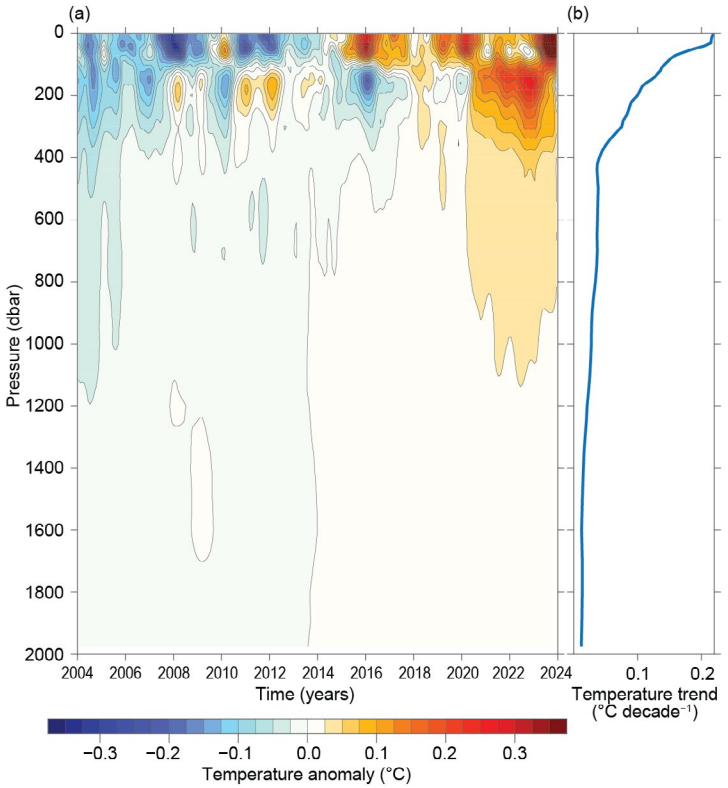

Fig. 3.5. (a) Near-global (66.5°S–81.5°N, but excluding seasonally ice-covered regions within that latitude range) average monthly ocean temperature anomalies (°C; from RFROM v2, Lyman and Johnson [2023]) relative to 2004–23 average monthly values, smoothed with a five-month Hanning filter and contoured at 0.025°C intervals (see color bar) vs. pressure and time. (b) Linear trend of temperature anomalies over time for 2004–23 in (a) plotted vs. pressure in °C decade^{-1} (blue line).

As expected, the large-scale statistically significant regional patterns in the 1993–2023 local linear trends of 0-m–2000-m OHCA (Fig. 3.4c) are similar to those for 0 m–700 m for 1993–2022 (Johnson et al. 2022) and earlier reports. However, since those earlier figures are for 0 m–700 m, and those of this year's report are for 0 m–2000 m, the amplitudes this year are higher, especially in the western boundary current extensions and Antarctic Circumpolar Current, where variability extends deep. A long-term warming trend in the Labrador Sea is also apparent in the deeper analysis, and the warming trend in the Greenland Sea is considerably stronger with the deeper maps. These are both locations of deep wintertime convection that has generally weakened and shoaled since 1993, resulting in warming of deep waters (e.g., Yashayaev and Loder 2017; Lauvset et al. 2018). Also, since the new machine learning algorithm used for the first time this year is less noisy, there are more areas with statistically significant trends, neither just because the time series is longer by one year, nor just because the analysis extends deeper.

Near-global average seasonal temperature anomalies (Fig. 3.5a) since 2004 show a marked contrast between 2023 and the previous three years, with warm anomalies surface-intensifying

as El Niño strengthened, in contrast to the subsurface warm anomalies from 100 m to 400 m evident during La Niña conditions from 2020 to 2022. This pattern arises as relaxation of the tropical Pacific trade winds allows warm waters in the western equatorial Pacific to spread eastward. The thermocline in the east deepens as a result. In the west, as the thermocline shoals, cold waters replace the warmer waters there as a consequence. Other El Niño years (e.g., 2009/10, 2015/16, and 2018/19) show a similar pattern, with La Niña years (e.g., 2007/08, 2010/11, and 2011/12, as well as 2020/21, 2021/22, and 2022/23) having the opposite signature. A warming trend (Fig. 3.5b) is strongest near the surface but extends all the way to the 2000-dbar sampling limit of Core Argo floats.

Globally integrated annually averaged OHCA estimates from 0 m–700 m and 700 m–2000 m from multiple research groups are presented in Fig. 3.6. Year-round, near-global sampling in both of those layers commenced around 2005 from Argo, making estimates relatively certain after that date. However, deep expendable bathythermographs sampling to 700 m were deployed extensively over much of the globe (with the notable exception of the high southern latitudes) starting in the early 1990s (Lyman and Johnson 2014), hence the upper layer results may be fairly robust back to 1993. Results for the 700-m–2000-m layer, which is quite sparsely sampled prior to about 2005, should be interpreted with caution in earlier years.

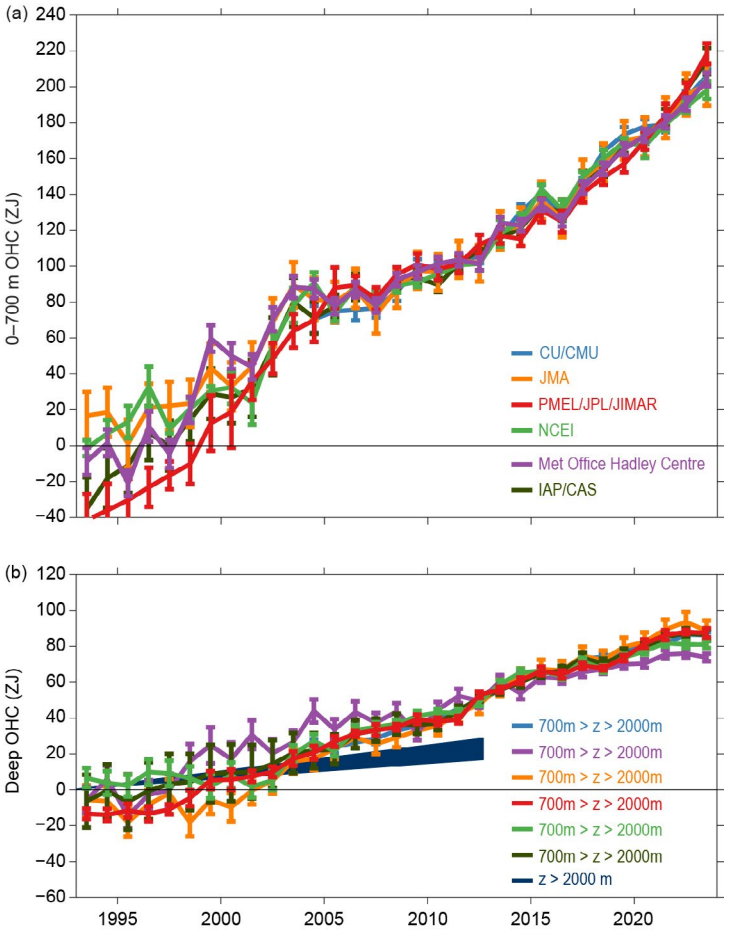

The various estimates of annual globally integrated 0-m–700-m OHCA (Fig. 3.6a) consistently show large increases since 1993, with all six analyses reporting 2023 as a record high. In contrast, 700-m–2000-m OHCA annual analyses (Fig. 3.6b) generally show negligible changes or small heat losses from 2022 to 2023, although a long-term warming trend is clear in this layer. The water column from 0 m to 700 m gained 13±5 ZJ and from 700 m to 2000 m lost 1.4±1.9 ZJ (means and standard deviations given) from 2022 to 2023. Causes of differences among estimates are discussed in Johnson et al. (2015), except for the new PMEL estimate, which differs considerably in methodology from the other estimates presented, as outlined in the second paragraph of this section.

The estimated linear rates of heat gain for each of the five global integral estimates of 0-m–700-m OHCA that extended from

Fig. 3.6. (a) Annual average global integrals of in situ estimates of upper (0-m–700-m) ocean heat content anomaly (OHCA; ZJ; 1 ZJ = 10^{21} J) for the period 1993–2022 with standard errors of the mean. The Meteorological Research Institute (MRI)/Japan Meteorological Agency (JMA) estimate is an update of Ishii et al. (2017). The Pacific Marine Environmental Laboratory (PMEL)/Jet Propulsion Laboratory (JPL)/Joint Institute for Marine and Atmospheric Research estimate is computed from RFROM v2 after Lyman and Johnson (2023). The Met Office Hadley Centre estimate is computed from gridded monthly temperature anomalies following Palmer et al. (2007) and Good et al. (2013). Both the PMEL and Met Office estimates use Cheng et al. (2014) eXpendable BathyThermograph (XBT) corrections and Gouretski and Cheng (2020) mechanical bathythermograph corrections. The NCEI estimate follows Levitus et al. (2012). The Institute of Atmospheric Physics (IAP)/Chinese Academy of Sciences (CAS) estimate was substantially revised from previous years as reported in Cheng et al. (2024). The CU/CMU estimate is detailed in Giglio et al. (2024). See Johnson et al. (2014) for details on uncertainties, methods, and datasets. For comparison, all estimates have been individually offset (vertically on the plot), first to their individual 2005–22 means (the best sampled time period) and then to their collective 1993 mean. (b) Annual average global integrals of in situ estimates of intermediate (700-m–2000-m) OHCA for 1993–2022 (ZJ) with standard errors of the mean and a long-term trend with one standard error uncertainty shown from September 1992 to July 2013 for deep and abyssal (z>2000 m) OHCA following Purkey and Johnson (2010) but updated using all repeat hydrographic section data available from https://cchdo.ucsd.edu/ as of Jan 2024.

1993 through 2023 (Fig. 3.6a) range from 0.39±0.05 W m^{-2} to 0.49±0.13 W m^{-2} applied over the surface area of Earth (Table 3.2) rather than the surface area of the ocean, to better compare to the top-of-the-atmosphere energy imbalance (e.g., Loeb et al. 2021; section 2f1). Linear trends from the 700-m–2000-m layer over the same time period range from 0.17±0.03 W m^{-2} to 0.24±0.04 W m^{-2}. Using repeat hydrographic section data collected from 1981 through 2023 to update the estimate of Purkey and Johnson (2010) for 2000 m–6000 m, the linear trend is 0.07±0.03 W m^{-2} from September 1992 to July 2013 (these dates are global average times of first and last sampling of the sections), consistent with previously reported decadal warming of Antarctic Bottom Water. Summing the three layers (despite their slightly different time periods as given above), the full-depth ocean heat gain rate applied to Earth's entire surface ranges from 0.65 W m^{-2} to 0.79 W m^{-2}.

Table 3.2. Trends of ocean heat content increase (in W m^{-2} applied over the 5.1 × 10^{14} m^2 surface area of Earth) from six different research groups over three depth ranges (see Fig. 3.6 for details). For the upper (0-m–700-m) and intermediate (700-m–2000-m) depth ranges, estimates cover 1993–2022, with 5%–95% uncertainties based on the residuals taking their temporal correlation into account when estimating degrees of freedom (Von Storch and Zwiers 1999). The 2000-m–6000-m depth range estimate, an update of Purkey and Johnson (2010), uses data from 1981 to 2022, having a global average start and end date of September 1992 to July 2013, again with 5%–95% uncertainty.

Research Group	0 m–700 m Global ocean heat content trends (W m^{-2})	700 m–2000 m Global ocean heat content trends (W m^{-2})	2000 m–6000 m Global ocean heat content trends (W m^{-2})
MRI/JMA	0.39±0.05	0.24±0.04	—
PMEL/JPL/JIMAR	0.49±0.13	0.23±0.01	—
NCEI	0.40±0.05	0.19±0.04	—
Met Office Hadley Centre	0.41±0.07	0.17±0.03	—
IAP/CAS	0.45±0.07	0.21±0.03	—
Purkey and Johnson	—	—	0.07±0.03

d. Salinity

—G. C. Johnson, J. Reagan, J. M. Lyman, T. Boyer, C. Schmid, and R. Locarnini

1. INTRODUCTION

The density of the ocean, crucial for its vertical stratification and interaction with the atmosphere, is determined by variations in ocean salinity and temperature. The thermal wind relation connects lateral density variations and vertical shear of ocean currents. In cold high latitudes, where temperature fluctuations are minimal, salinity variation mostly determines the vertical density structure. Various factors, including advection, precipitation and evaporation, river run-off, ice melt, and ice freezing (Ren et al. 2011; Yu 2011) contribute to salinity variations that impact crucial ocean–atmosphere exchanges of heat and dissolved gases, influencing phenomena like marine heatwaves, ocean carbon dioxide uptake, tropical cyclones, and deep or bottom water formation, as well as nutrient and oxygen exchange between the surface mixed layer and denser waters below.

The global average practical salinity stands at approximately 34.7, with surface values falling below 28.0 or exceeding 37.4 for only 1% of the ocean surface area each. Note that all salinity values used in this section are reported as observed, on the dimensionless Practical Salinity Scale-78 (PSS-78; Fofonoff and Lewis 1979). Generally, regions dominated by evaporation, such as the subtropics, exhibit higher salinity values, while areas where precipitation prevails, like the Intertropical Convergence Zone (ITCZ) and high latitudes, have fresher water (e.g., Wüst 1936; Schmitt 1995). Multi-decadal trends in ocean salinity have provided evidence for increases in the hydrological cycle over the ocean with global warming (Durack et al. 2012; Skliris et al. 2014, 2016). Springtime sea-surface salinity (SSS) values in the subtropical North Atlantic Ocean have exhibited skill in forecasting summer monsoon rainfall in the African Sahel (Li et al. 2016).

To investigate interannual changes of subsurface salinity, all available salinity profile data are quality controlled following Boyer et al. (2018) and then used to derive 1° monthly mean gridded salinity anomalies relative to a long-term monthly mean for the years 1955–2017 (Zweng et al. 2018) at standard depths from the surface to 2000 m. In recent years, the largest source of salinity profiles are the profiling floats of the Argo program (Riser et al. 2016). These data are a mix of real-time (preliminary) and delayed-mode (scientific quality-controlled) observations. Hence, the estimates presented here may be subject to instrument biases, such as a positive salinity drift identified in a subset of Argo Conductivity-Temperature-Depth, and will change after all data are subjected to scientific quality control. The SSS analysis relies on Argo data downloaded in January 2024, with annual anomaly maps relative to a seasonal climatology generated following Johnson and Lyman (2012) as well as monthly maps of bulk (as opposed to skin) SSS data from the Blended Analysis of Surface Salinity (BASS; Xie et al. 2014). BASS blends in situ SSS data with data from the *Aquarius* (Le Vine et al. 2014; mission ended in June 2015), Soil Moisture and Ocean Salinity (SMOS; Font et al. 2013), and the Soil Moisture Active Passive (SMAP; Fore et al. 2016) satellite missions. Despite the larger uncertainties of satellite data relative to Argo data, their higher spatial and temporal sampling allows higher spatial and temporal resolution maps than are possible using in situ data alone at present.

2. SEA-SURFACE SALINITY

—G. C. Johnson and J. M. Lyman

As noted in previous reports (e.g., Johnson et al. 2020), since salinity has no direct feedback to the atmosphere, unlike sea-surface temperature (SST) anomalies, which are often damped by heat exchange with the atmosphere, large-scale SSS anomalies can be quite persistent. In the tropical Pacific, both the ITCZ and the South Pacific Convergence Zone became saltier from 2022 to 2023 (Fig. 3.7b), with a slight freshening band just south of the ITCZ. The western equatorial Pacific became much fresher over that time period, although anomalies in the freshening region were of both signs in 2023 (Fig. 3.7a). There was also a large freshening in the climatologically fresh area west of Central America. As in 2022, in the North Pacific, the center of the basin was mostly anomalously salty in 2023, and the periphery was generally anomalously fresh. South of 30°S, the Pacific remained primarily salty in 2023, as it was in 2022, with a relatively fresh band to the north and northeast of New Zealand.

In the Atlantic, SSS freshened from 2022 to 2023 in the region of the ITCZ and the eastern equatorial area, as well off the coast of North America. The center of the subtropics in both hemispheres tended a bit saltier. The largest change was in the Caribbean Sea, which got much saltier from 2022 to 2023 (Fig. 3.7b), although its eastern portion remained anomalously fresh in 2023 compared to the long-term mean (Fig. 3.7a), as it was very anomalously fresh in 2022. The regions around the subtropical salinity maximum were anomalously salty in both the North and South Atlantic, as for many other recent years, including 2022, and the ITCZ was anomalously fresh.

The equatorial Indian Ocean freshened all the way across from 2022 to 2023, whereas south of about 8°S the basin mostly got saltier (Fig. 3.7b). These changes resulted in an anomalously fresh band across much of the Indian Ocean just north of the equator in 2023 (Fig. 3.7a), while south of the equator the ocean was mostly anomalously fresh about halfway across the basin west of Australia and mostly anomalously salty elsewhere.

Sea-surface salinity trends from 2005 to 2023 are mostly statistically insignificant, but there is statistically significant freshening around Hawaii and in the eastern third of the Pacific ITCZ, as well as in the Gulf of Alaska, the northeastern portion of the North Atlantic Ocean, and the Greenland, Iceland, and Norwegian Seas. With the exception of the area around Hawaii, these are all climatologically fresh areas. Salty trends are evident in portions of the subtropics in all the ocean basins, which are climatologically salty, as well as in the western Pacific sector of the Southern Ocean, which is not. This "salty gets saltier and fresh gets fresher" trend, which has been evident to varying degrees and discussed in *State of the Climate* reports since 2006, is expected on a warming Earth: As the atmosphere warms, it can hold more moisture, enabling an increased hydrological cycle over the ocean (Held and Soden 2006; Durack and Wijffels 2010).

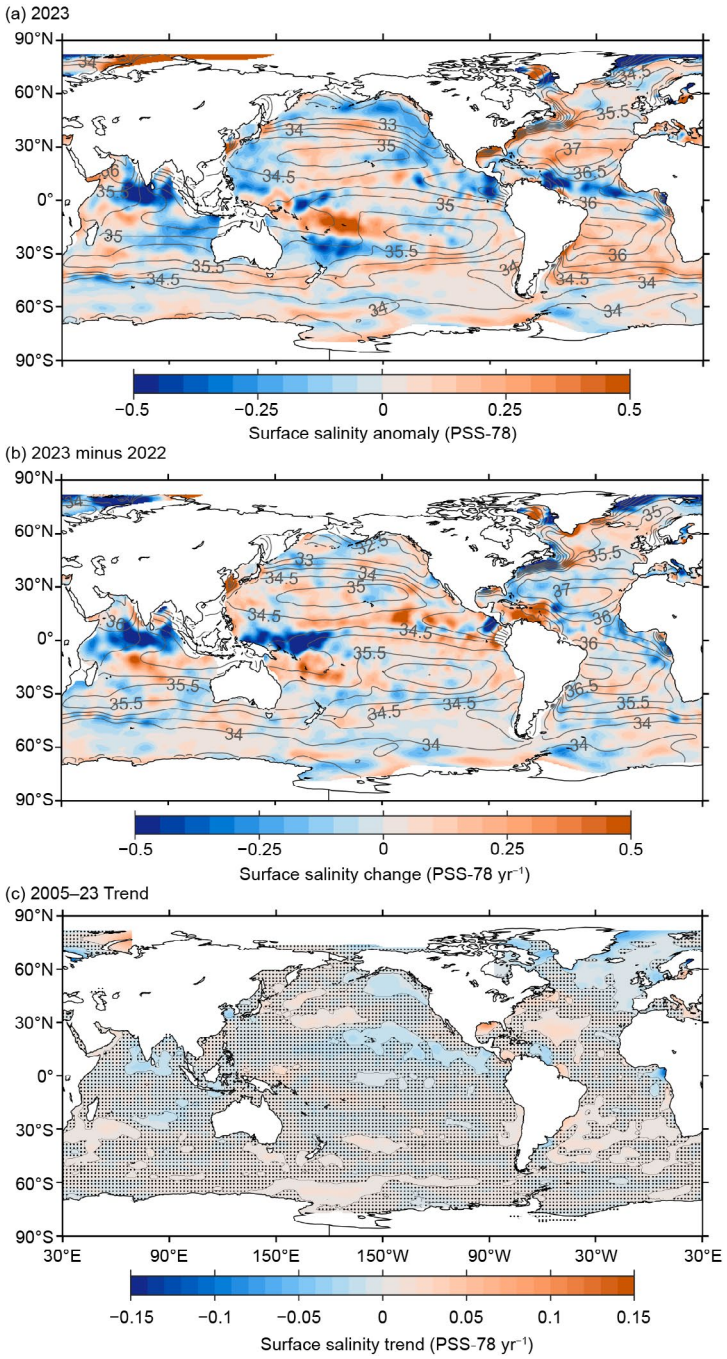

Fig. 3.7. (a) Map of the 2023 annual surface salinity anomaly (colors, PSS-78) with respect to monthly climatological 1955–2012 salinity fields from WOA13v2 (yearly average; gray contours at 0.5 intervals, PSS-78). (b) Difference of 2023 and 2022 surface salinity maps (colors, PSS-78 yr^{-1}). White ocean areas are too data-poor (retaining <80% of a large-scale signal) to map. (c) Map of local linear trends estimated from annual surface salinity anomalies for 2005–23 (colors, PSS-78 yr^{-1}). Areas with statistically insignificant trends at 5%–95% confidence (taking into account the decorrelation time scale of the residuals when estimating effective degrees of freedom) are stippled. All maps are made using Argo data.

In 2023, the seasonal BASS (Xie et al. 2014) SSS anomalies (Fig. 3.8) show the progressions of many of the features in the annual anomaly map using Argo data alone (Fig. 3.7a) and with higher spatial resolution, albeit with less accuracy. Fresh anomalies build in the far western equatorial Pacific while salty anomalies build in the Pacific ITCZ. The South Pacific Convergence Zone stays anomalously salty all year long, with the fresh band to the south of it diminishing slightly in amplitude over the course of the year. In the Atlantic, the build-up of a fresh anomaly in the ITCZ is apparent as the year

progresses. In September–November 2023, the fresh anomaly across much of the equatorial Indian Ocean becomes apparent, while over the course of the year in that basin the eastern fresh anomalies seen west of Australia diminish in amplitude.

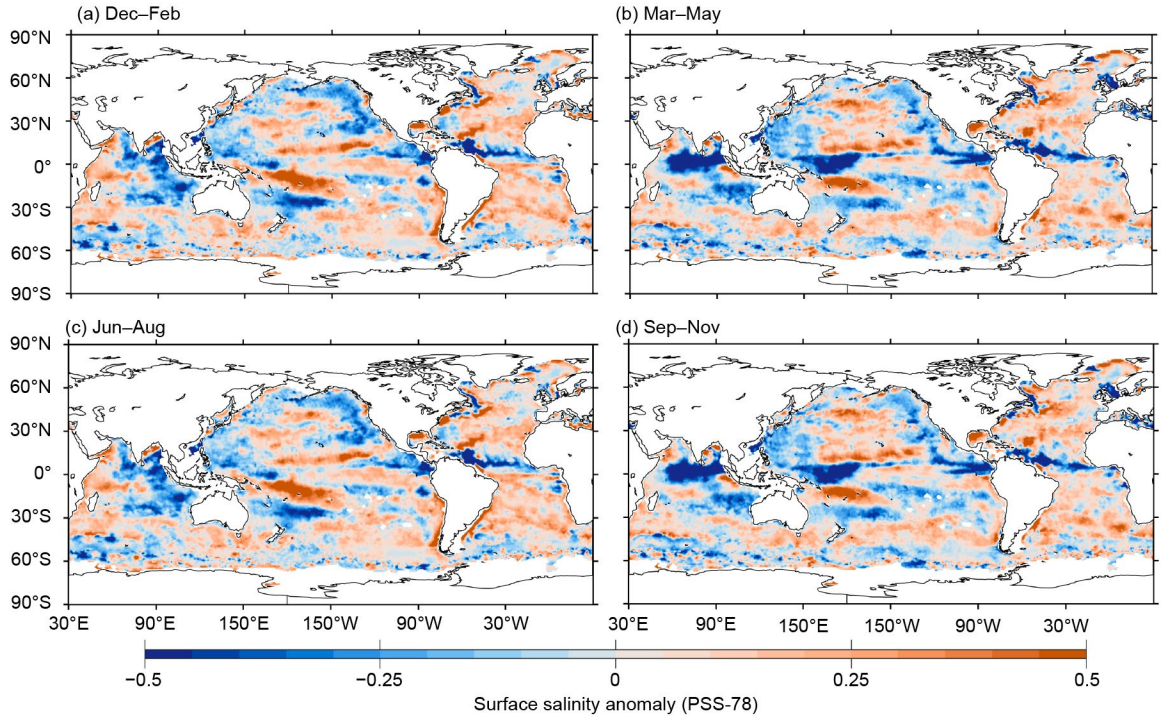

Fig. 3.8. Seasonal maps of sea-surface salinity (SSS) anomalies (colors) from monthly blended maps of satellite and in situ salinity data (BASS; Xie et al. 2014) relative to monthly climatological 1955–2012 salinity fields from WOA13v2 for (a) Dec 2022–Feb 2023, (b) Mar–May 2023, (c) Jun–Aug 2023, and (d) Sep–Nov 2023.

3. SUBSURFACE SALINITY

—J. Reagan, T. Boyer, C. Schmid, and R. Locarnini

Surface salinity enters the ocean interior primarily through two pathways (Talley 2002): subduction (downward movement along isopycnal [constant density] surfaces) and convection (deep vertical mixing). Salinity is a nearly conservative tracer, which allows the SSS footprint to be tracked through the interior ocean. Thus, SSS anomalies can propagate through the deep ocean, which can impact subsurface ocean dynamics through changes in density and is therefore an important seawater component to monitor.

The basin-average Atlantic salinity anomalies (Fig. 3.9a) for 2023 continue a pattern that has been evident since 2020 of persistent positive anomalies throughout the entire 0-m–1000-m water column, with the largest anomalies (>0.07) in the upper 100 m. From 2022 to 2023, the Atlantic became saltier from the surface down to 600 m (Fig. 3.9b), with the largest change occurring at ~30 m (change of ~+0.012 from 2022 to 2023). This contrasts with the freshening of ~−0.015 that occurred between 2021 and 2022 in the upper 50 m of the Atlantic (Reagan et al. 2023). Based on the zonal average salinity changes from 2022 to 2023 in the Atlantic (Fig. 3.9c), the salinity increase in Fig. 3.9b is primarily associated with basin-wide salinification at depth (>200 m) and localized increases in the upper 200 m centered at 40°S, 20°S, 15°N, and >60°N. The large (>0.09) near-surface increase near 15°N is due to the 2022 to 2023 salinity increase in the Caribbean Sea (Fig 3.7b) dominating the Atlantic zonal average in this area.

The 2023 basin-average Pacific salinity anomalies (Fig. 3.9d) are quite different than what was observed from 2018 through 2022 in the upper 300 m. In 2023, there is a transition of positive (~0.01) salinity anomalies to weak (<|−0.01|) fresh salinity anomalies in the 100-m–300-m layer and a transition of weak fresh anomalies (<|−0.01|) to salty anomalies (>0.01) in the upper 100 m throughout the year. This transition is apparent when looking at the 2022-to-2023 difference in basin-average Pacific salinity anomalies (Fig. 3.9e), where there is salinification in the upper 125 m (max of ~0.015 in the upper 50 m) and freshening between 150 m and 300 m (max of ~−0.015 at 200 m). The primary reason for the upper 125-m salinification can be seen in the

2022 to 2023 changes in zonal-average salinity (Fig. 3.9f), where there are zonal increases in near-surface salinity (>0.03) between 10°S and 25°S, and 10°N and 30°N that are subducted equatorward to ~150-m depth. The 2022 to 2023 freshening between 150 m and 300 m can be attributed to weak large-scale freshening (Fig. 3.9f).

The Indian basin-average salinity anomaly pattern that has prevailed since 2020 continued into 2023, but with some noticeable changes (Fig. 3.9g). The weak (<0.01) positive salinity anomalies that were prevalent in 2022 dissipated in 2023 over much of 0 m–1000 m, with a clear freshening trend throughout 2023 in the upper 50 m (>|−0.06| by the end of 2023). These changes manifest as an overall freshening between 2022 and 2023 (Fig. 3.9h) for nearly the entire 0-m–1000-m water column of the Indian basin, with the strongest freshening (~−0.025) in the upper 30 m. This overall freshening from 2022 to 2023 contrasts with what was seen between 2021 and 2022, where there was salinification (Reagan et al. 2023). The strong freshening near the surface is primarily associated with the freshening between 5°S and 10°N (Fig 3.7b) and is evident in the 2022-to-2023 zonally-averaged salinity changes for the Indian basin (Fig. 3.9i). In the upper 50 m just north of the equator, the zonally-averaged salinity change from 2022 to 2023 approaches ~−0.30. There are also large (> |−0.06|) zonally-averaged freshening changes between 2022 and 2023 of between 75 m–175 m and 10°S and 20°S.

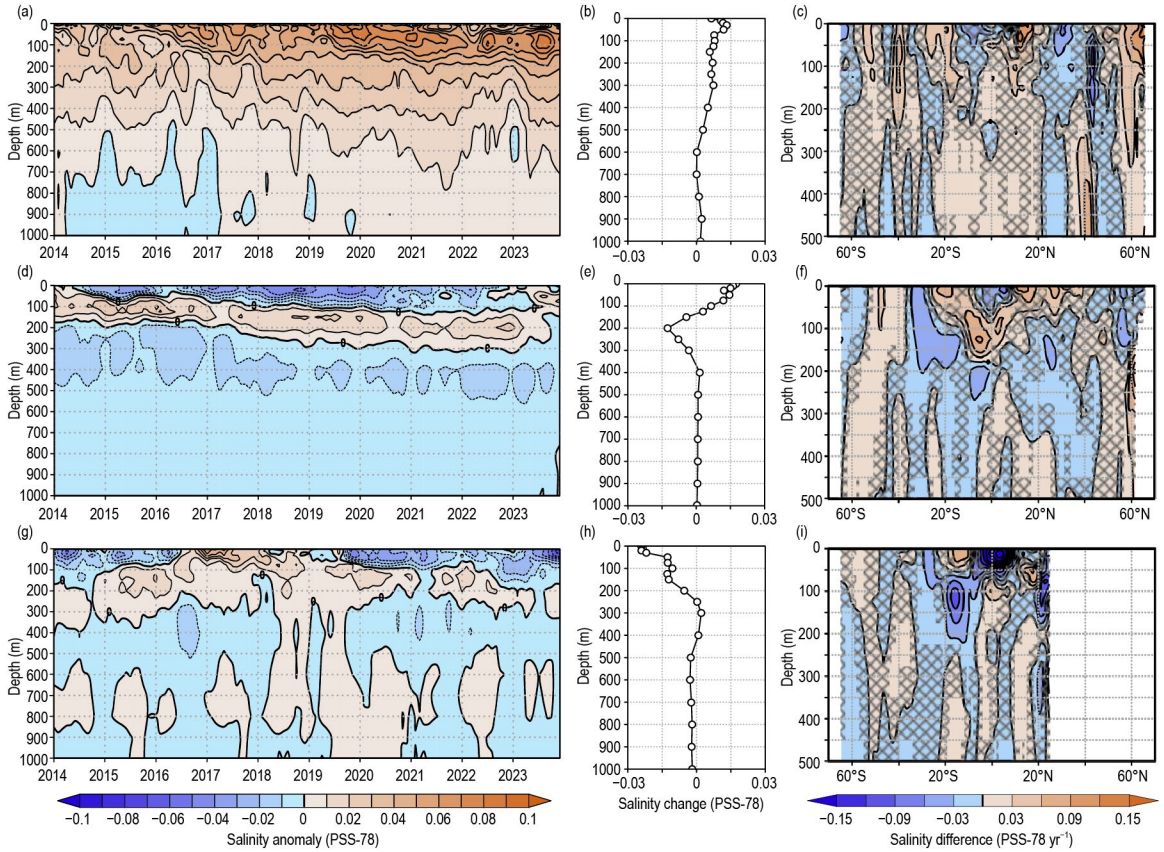

Fig. 3.9. Average monthly salinity anomalies from 0 m to 1000 m for the period 2014–23 for the (a) Atlantic, (d) Pacific, and (g) Indian basins. Change in salinity from 2022 to 2023 for the (b) Atlantic, (e) Pacific, and (h) Indian basins. Change in the 0-m–500-m zonal-average salinity from 2022 to 2023 in the (c) Atlantic, (f) Pacific, and (i) Indian basins with areas of statistically insignificant change, defined as <±1 std. dev. and calculated from all year-to-year changes between 2005 and 2023, stippled in dark gray. Data were smoothed using a three-month running mean. Anomalies are relative to the long-term (1955–2017) WOA18 monthly salinity climatology (Zweng et al. 2018).

The zonally-averaged salinity trends for 2005–23 for all three major ocean basins (Fig. 3.10) are similar in time and space to what was shown for the 2005–21 (Reagan et al. 2022) and 2005–22 (Reagan et al. 2023) time periods; thus, this discussion will focus on regions where the 2022-to-2023 salinity change (Fig. 3.9) has acted to strengthen or weaken these trends. The Atlantic 2022-to-2023 salinification north of 50°N (Fig. 3.9c) and between 0 m and 100 m acts to weaken the predominant freshening trend that has been observed since 2005 (Fig. 3.10a), whereas the 2022-to-2023 freshening between 25°N and 35°N in the upper 150 m has acted to weaken the

predominant salinification trend in this region. The Pacific freshening from 2022 to 2023 (Fig. 3.9f) between 20°S and 35°S in the upper 200 m has acted to weaken the longer-term salinification trend in this region (Fig. 3.10b). Finally, despite salinity decreasing from 2022 to 2023 by ~0.24 in the upper 50 m near the equator of the Indian basin (Fig. 3.9i), this region remains an area of insignificant salinity trends over the longer term (Fig. 3.10c) due to its large interannual variability. Overall, the significant salinity trends in all three major basins are reflective of the footprint of an amplifying hydrological cycle (Durack and Wijffels 2010; Durack et al. 2012; Skliris et al. 2014) where fresh regions are becoming fresher due to enhanced precipitation and salty regions are becoming saltier due to enhanced evaporation. These changes are then subducted into the interior ocean where they are evident in the trends shown in Fig. 3.10.

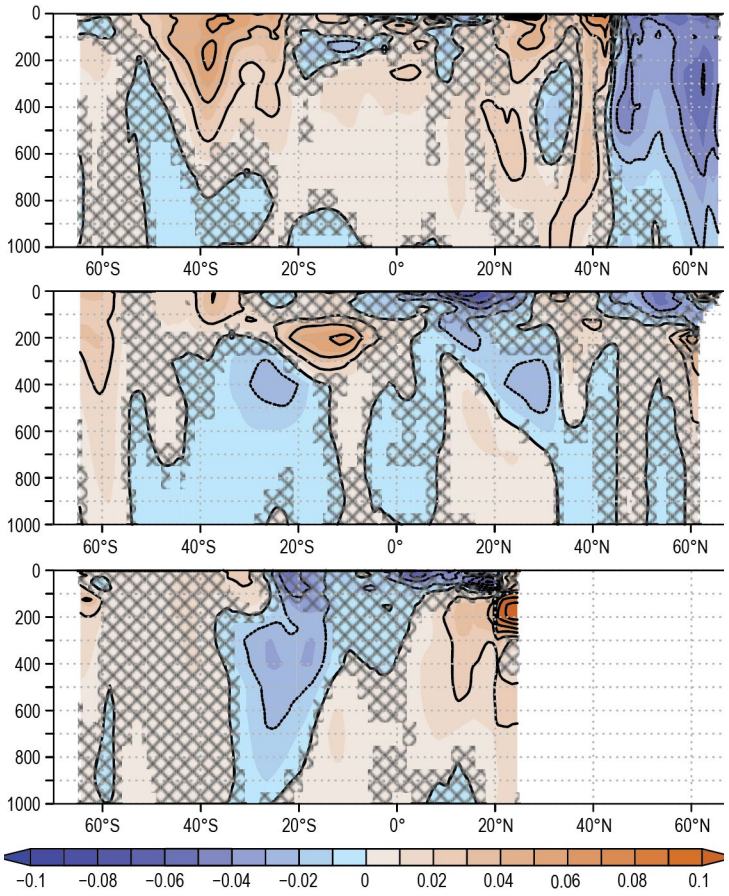

Fig. 3.10. Linear trend of zonally-averaged salinity from 2005 to 2023 over the upper 1000 m for the (a) Atlantic, (b) Pacific, and (c) Indian basins. The salinity trend is per decade and computed using least squares regression. Areas that are stippled in dark gray are not significant at the 95% confidence interval.

e. Global ocean heat, freshwater, and momentum fluxes

—L. Yu, C. Liu, P. W. Stackhouse, J. Garg, and R. A. Weller

The ocean and the atmosphere interact through the exchange of heat, freshwater, and momentum across their interface. These air–sea fluxes are key to maintaining the global climate system's equilibrium in response to incoming solar radiation. The ocean absorbs the majority of shortwave radiation reaching Earth's surface and redistributes this energy to the atmosphere through longwave radiation, evaporation (latent heat flux), and conduction (sensible heat flux). Any remaining heat is stored in the ocean and transported by the ocean's surface currents, predominantly driven by wind stress. Evaporation not only mediates heat but also moisture transfer, the latter of which, together with precipitation, determines the surface freshwater flux across the open ocean. Changes in these air–sea fluxes act as pivotal drivers for changes in ocean circulation, thereby affecting the global distribution of heat and salt from the tropics to the poles.

Here we examine the surface heat flux, freshwater flux, and wind stress in 2023 and their changes from 2022. The net surface heat flux (Q_{net}) comprises four components: net shortwave (SW), net longwave (LW), latent heat (LH), and sensible heat (SH). We calculate the net surface freshwater flux into the ocean, excluding inputs from rivers and glaciers, as the difference between precipitation (P) and evaporation (E), referred to as the $P–E$ flux. Data from multiple research groups are synthesized to produce global maps of Q_{net}, $P–E$, and wind stress (Figs. 3.11, 3.12, 3.13) and provide a long-term time series (Fig. 3.14).

The net SW and LW fluxes in 2022 and 2023 were sourced from the Fast Longwave and Shortwave Radiative Fluxes (FLASHFlux) version 4B product (Stackhouse et al. 2006), which have been radiometrically scaled to the surface SW and LW products from the Clouds and the Earth's Radiant Energy Systems (CERES) Surface Energy Balanced and Filled (EBAF) Edition 4.2

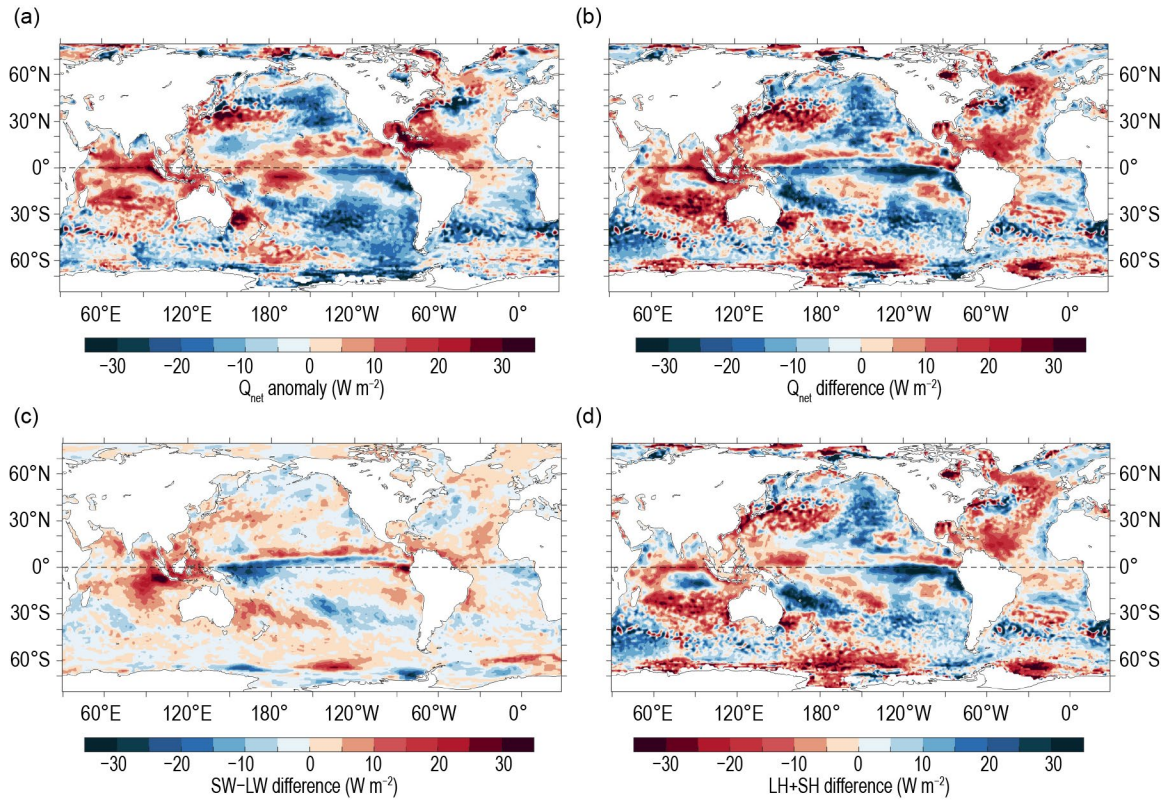

Fig. 3.11. (a) Surface heat flux (Q_{net}) anomalies (W m^{-2}) for 2023 relative to the 2001–15 climatology. Positive values denote ocean heat gain. (b) 2023-minus-2022 difference for (b) Q_{net}, (c) net surface radiation shortwave (SW) + longwave (LW), and (d) turbulent heat fluxes latent heat (LH) + sensitive heat (SH), respectively. Positive tendencies denote more ocean heat gain in 2023 than in 2022. LH+SH are from WHOI OAFlux2, and SW+LW is from the NASA FLASHFlux version 4B adjusted to CERES Surface EBAF Ed4.2. Net radiative fluxes defined as the difference between the incoming and outgoing radiation (positive indicates radiative flux into the ocean).

(Loeb et al. 2018; Kato et al. 2018). *P* was derived from the Global Precipitation Climatology Project (GPCP) version 2.3 products (Adler et al. 2018). Estimates for LH, SH, *E*, and wind stress were produced by the second generation of the Objectively Analyzed Air–Sea Heat Fluxes (OAFlux2; Yu and Weller 2007; Yu 2019), computed from satellite retrievals and the bulk parameterization Coupled Ocean Atmosphere Response Experiment (COARE) version 3.6 (Fairall et al. 2003). The Q_{net} time series begins in 2001, aligning with the availability of CERES EBAF 4.2 products, while the *P*–*E* and wind-stress time series extend back 36 years, starting in 1988.

1. SURFACE HEAT FLUXES

The 2023 Q_{net} anomaly pattern (Fig. 3.11a) highlights positive anomalies (indicating downward heat input and a warming effect on the ocean surface) in the western equatorial Pacific warm pool, the northwestern tropical Atlantic warm pool (including the Gulf of Mexico), and the tropical Indian Ocean. In contrast, negative Q_{net} anomalies (indicating upward heat release and a cooling effect on the ocean surface) are observed in the eastern equatorial Pacific cold tongue, as well as the northeastern and southeastern Pacific and the South Atlantic. This distinct east–west contrast in Q_{net} anomalies across the equatorial Pacific Ocean reflects the sea-surface temperature anomaly (SSTA) pattern (see Fig. 3.1a) associated with the shifting El Niño–Southern Oscillation (ENSO) conditions in 2023. The shift from a triple-dip La Niña early in the year to El Niño conditions by May resulted in substantial surface warming of over 1.5°C in the eastern equatorial Pacific. Concurrently, the Indian Ocean transitioned from a near-neutral condition to a positive Indian Ocean dipole (IOD) in boreal summer, leading to extensive warming in its western basin and moderate cooling in the eastern basin. Interestingly, the surface warming in the tropical Indian Ocean is positively correlated with Q_{net} anomalies, whereas the warming in the eastern equatorial Pacific shows a negative correlation with Q_{net} anomalies. The positive Q_{net} anomalies in the Indian Ocean suggest that the heat absorbed at the surface contributed to regional warming during the positive IOD phase. Conversely, the negative Q_{net} anomalies in the eastern equatorial Pacific cold tongue indicate that heat was released from the ocean to the atmosphere, tempering the surface warming induced by El Niño.

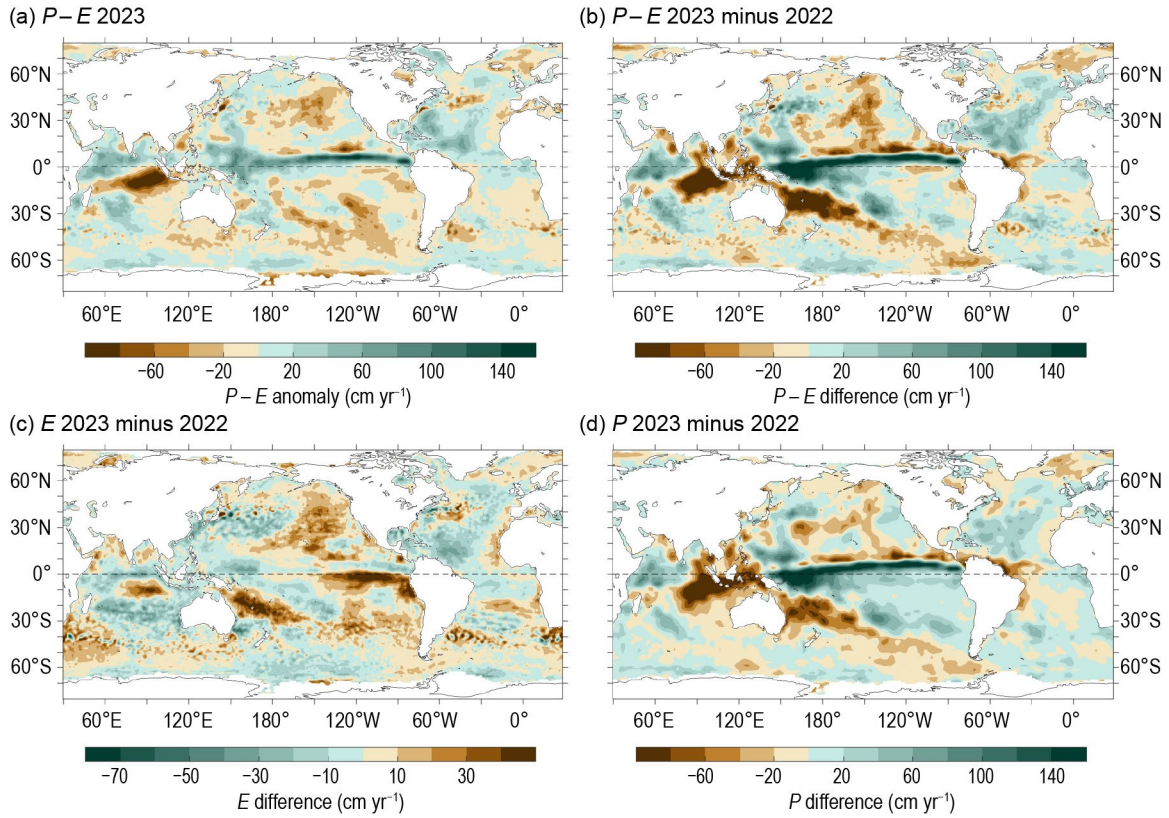

Fig. 3.12. (a) Surface freshwater precipitation (*P*) – evaporation (*E*) flux anomalies (cm yr^{-1}) for 2023 relative to the 1988–2015 climatology. Positive values denote ocean freshwater gain. 2023-minus-2022 differences for (b) *P*–*E*, (c) *E*, and (d) *P*. Positive (negative) values denote ocean freshwater gain (loss). *P* is the GPCP version 2.3 product, and *E* is from WHOI OAFlux2.

The 2023-minus-2022 Q_{net} difference pattern (Fig. 3.11b) deviates from the 2023 anomaly pattern in the tropical Pacific, largely due to the intricate impacts of ENSO on the four Q_{net} components. Net downward surface radiation (SW+LW; Fig. 3.11c) reduced along the Intertropical Convergence Zone (ITCZ) north of the equator and in the South Pacific Convergence Zone (SPCZ) in the western equatorial Pacific (indicated by blue shading). Meanwhile, upward surface turbulent heat flux (LH+SH; Fig. 3.11d) increased in the central and eastern equatorial Pacific (also highlighted by blue shading), driven by surface warming from El Niño. This combination led to predominantly net heat loss in the equatorial Pacific during 2023. In contrast, in the tropical Indian Ocean, the positive 2023-minus-2022 Q_{net} differences were attributed to increased downward surface radiation in the eastern basin, associated with reduced convection due to a positive IOD. Turbulent heat loss increased by about 15 W m^{-2} at the center of SW+LW positive anomalies but decreased by over 15 W m^{-2} across a broader area around the periphery, leading to a marked net heat gain in the Indian Ocean from 2022 to 2023. Comparatively, the Q_{net} changes in the tropical Pacific were moderate, with predominantly weak positive tendencies.

The extratropical North Pacific in 2023 was characterized by negative Q_{net} anomalies in the east, which encircled the positive anomalies extending along the Kuroshio Extension and its recirculation gyre between 20°N and 40°N. Interestingly, the North Atlantic displayed a reversed pattern: large positive Q_{net} anomalies across the basin surrounded negative anomalies near the Gulf Stream extension between 30°N and 50°N. These patterns of Q_{net} anomalies were primarily driven by surface turbulent heat fluxes in response to contrasting changes in surface winds across these two basins (Fig. 3.13b). Weaker winds in the broad North Atlantic reduced turbulent heat loss, resulting in increased Q_{net} (positive anomalies), while stronger winds in the eastern North Pacific intensified turbulent heat loss, leading to reduced Q_{net} (negative anomalies).

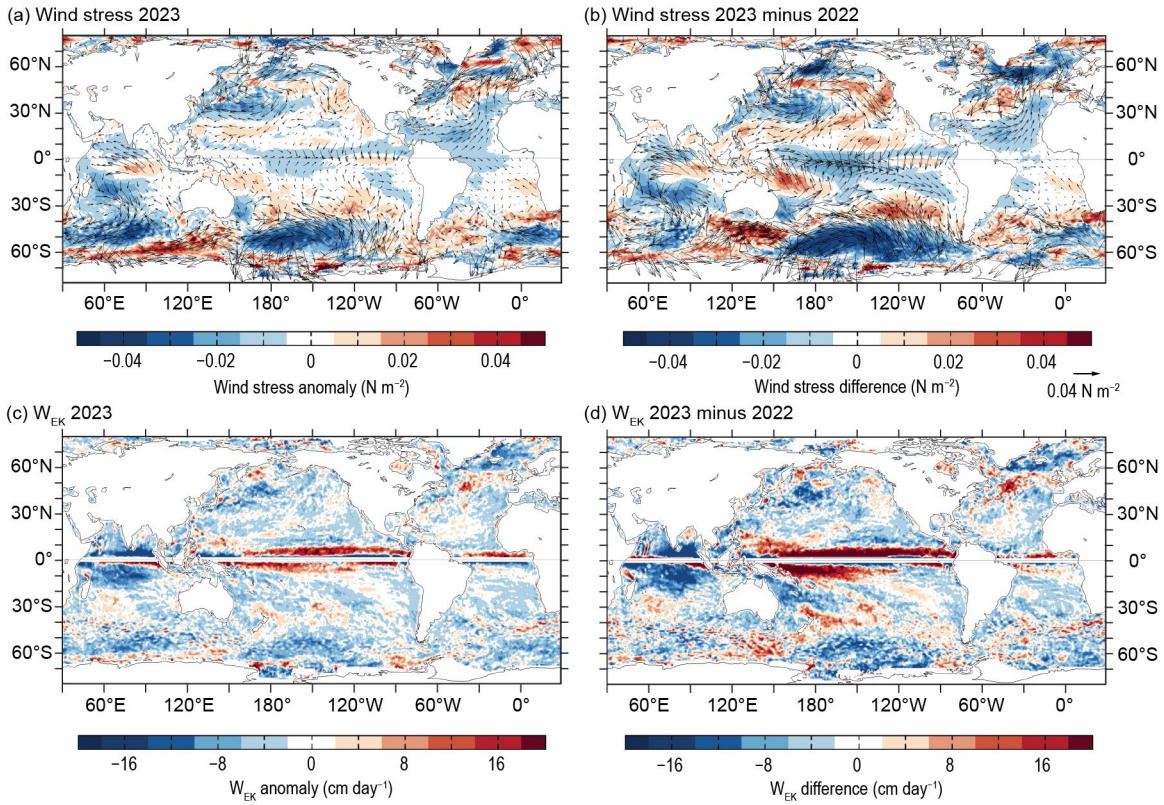

Fig. 3.13. (a) Wind stress magnitude (shaded) and vector anomalies (N m^{-2}) for 2023 relative to a 2001–22 climatology. (b) 2023-minus-2022 differences in wind stress. (c) Ekman vertical velocity (W_{EK}; cm day^{-1}) anomalies for 2023 relative to a 1988–2015 climatology. Positive (negative) values denote upwelling (downwelling). (d) 2023-minus-2022 differences of W_{EK}. Wind stress and W_{EK} fields are from WHOI OAFlux2.

In the North Atlantic, positive Q_{net} anomalies occurred at two locations: the Gulf of Mexico and the Sargasso Sea to its east (10°N–30°N) and the subpolar gyre including the Labrador and the Irminger Seas (40°N–65°N). Negative Q_{net} anomalies (net upward heat release; a cooling effect on the ocean surface) dominated the tropical Atlantic between 30°S and 30°N and also the subtropical North Pacific (5°N–20°N) and the eastern North Pacific (30°N–60°N). The magnitude of maximum positive and negative anomalies exceeded 20 W m^{-2} in some localized bands.

2. SURFACE FRESHWATER FLUXES

The 2023 *P*–*E* anomalies (Fig. 3.12a) show increased rainfall across the ITCZ and SPCZ of the tropical Pacific. This contrasts sharply with the substantial decrease in *P*–*E*, exceeding 30 cm yr^{-1}, in the southeastern equatorial Indian Ocean. These anomalies corresponded with SST changes, marking the transition weakly negative IOD index in the tropical Indian Ocean to a strongly positive one (IOD index of 0.596). This coincided with the ENSO phase transition, as shown in Figs. 3.2c,d. In the eastern Indian Ocean, cooler SSTAs suppressed rainfall, whereas warmer SSTAs in the western basin enhanced rainfall. The *P*–*E* modifications associated with the ENSO and IOD transitions are more readily seen in the 2023-minus-2022 difference pattern (Fig. 3.12b), which displays the anomalies with larger magnitudes because the change in phase between years is more marked than the 2023 difference from the long-term mean.

The 2023-minus-2022 differences in *E* reveal a marked increase (>20 cm yr^{-1}) in ocean evaporation across the Pacific Ocean, most notably in the eastern equatorial Pacific, along the southern periphery of the SPCZ in the southern Pacific and in the eastern regions of both the northern and southern Pacific. The 2023-minus-2022 differences in *P* (Fig. 3.12d) show that the drying condition was most acute in the southeastern tropical Indian Ocean, where rainfall reduced by over 80 cm within a year. Similar drying trends were observed in the southwestern Pacific along the southern periphery of the SPCZ. In the Atlantic Ocean, the most substantial change occurred in the North Atlantic, where a reduction in *E* and an increase in *P* amplified the net *P*–*E* by over 40 cm yr^{-1}. In other parts of the Atlantic, changes in *P*–*E* were comparatively mild.

3. WIND STRESS

In 2023, the equatorial Pacific was marked by predominantly negative wind stress anomalies, indicating a decrease in the strength of equatorial easterly winds associated with the transition to El Niño (Fig. 3.13a). The northeast trade winds slightly increased in the tropical North Pacific but weakened in the tropical North Atlantic. In mid- to high latitudes, wind anomalies exceeding 0.02 N m^{-2} occurred in the eastern Pacific and Atlantic. Over the Antarctic Circumpolar Current (ACC) region between 50°S and 60°S, the Southern Hemisphere westerlies exhibited a substantial weakening, especially in the Indo-Pacific sector where the largest anomalies fell below −0.04 N m^{-2}. Meanwhile, the midlatitude westerlies in both the North Pacific and North Atlantic also weakened, despite a marginal strengthening of their core near 50°N. The 2023-minus-2022 differences (Fig. 3.13b) emphasize the year's distinct anomaly pattern: a strengthening of trade winds in the tropical North Pacific and a weakening in the tropical South Pacific, coupled with a general decrease in westerlies across both hemispheres.

Wind patterns exhibit substantial spatial variability. These spatial variations in winds lead to divergence and convergence in Ekman transport, resulting in a vertical velocity known as Ekman pumping, characterized by downwelling (directed downward) and upwelling (directed upward) velocities, represented by W_{EK}, at the base of the Ekman layer. The computation of W_{EK} follows the equation: $W_{EK} = 1/\rho\nabla\times(\tau/f)$, where ρ is the density and *f* the Coriolis force. The 2023 W_{EK} anomalies showed distinct positive values in narrow equatorial bands of the Pacific and Atlantic Oceans and marked negative values in the equatorial Indian Ocean, each with magnitudes exceeding 16 cm day^{-1} (Fig. 3.13c). These patterns indicate a weakening of the regional climatological conditions, attributable to the resurgence of El Niño in the second half of the year. The 2023-minus-2022 W_{EK} differences (Fig.3.13d) display a similar spatial pattern but with greater intensities, highlighting the transition from La Niña in 2022 to El Niño in 2023. Outside of the equatorial zones, W_{EK} anomalies with substantial magnitudes were observed at higher latitudes, notably negative anomalies in the Pacific sector of the ACC regions. These anomalies correlate with a decrease in the strength of the Southern Hemisphere westerlies (Fig. 3.13b).

4. LONG-TERM PERSPECTIVE

A long-term perspective on the change in ocean-surface forcing functions in 2023 is presented within the framework of three-decade annual-mean time series of Q_{net}, *P*–*E*, and wind stress averaged across the global ice-free oceans (Figs. 3.14a–c). Anomalies in Q_{net} are referenced to the 2001–15 mean, where positive anomalies indicate increased net downward heat flux into the ocean, thereby contributing to ocean surface warming. The *P*–*E* and wind stress time series span 36 years, starting in 1988, and are referenced to the 1988–2015 mean. Positive anomalies in *P*–*E* denote increased freshwater flux into the ocean, leading to sea-surface freshening. Similarly, positive anomalies in wind stress denote increased magnitude of wind stress. The error bars in the time series represent one standard deviation of year-to-year variability.

Annual means of Q_{net}, *P*–*E*, and wind stress serve as indicators of the heat, freshwater, and momentum balance at the ocean surface. Q_{net} remained relatively stable from 2001 to 2010 but showed an upward trend between 2011 and 2016. During the later period, Q_{net} increased by approximately 3±1 W m^{-2}, from ~–1±1 W m^{-2} during the 2011 La Niña to a peak at ~2±1 W m^{-2} during the strong 2016 El Niño event. This increase in Q_{net} coincided with a 0.35°C increase in global-mean SST (see Fig. 3.3). Subsequently, Q_{net} decreased during the 2017/18 La Niña and continued its decline throughout the 2020–23 triple-dip La Niña. In 2023, Q_{net} was approximately 0.6±1 W m^{-2} lower than in 2022 but still higher than the 2001–10 average.

The *P*–*E* time series shows distinct decadal variability across the three decades. There was a notable downward trend in the 1990s, followed by a relatively stable period in the 2000s, and marked interannual fluctuations in the 2010s. Following its peak during 2015/16, *P*–*E* decreased by approximately 4±2 cm yr^{-1} to a low in 2019, remaining near this low throughout the 2020–23 La Niña. This reduction in *P*–*E* can be primarily attributed to increased evaporation in recent years, driven by higher SSTs (see Fig. 3.3). The 2023 *P*–*E* was slightly up by 0.8±2 cm yr^{-1} compared to 2022.

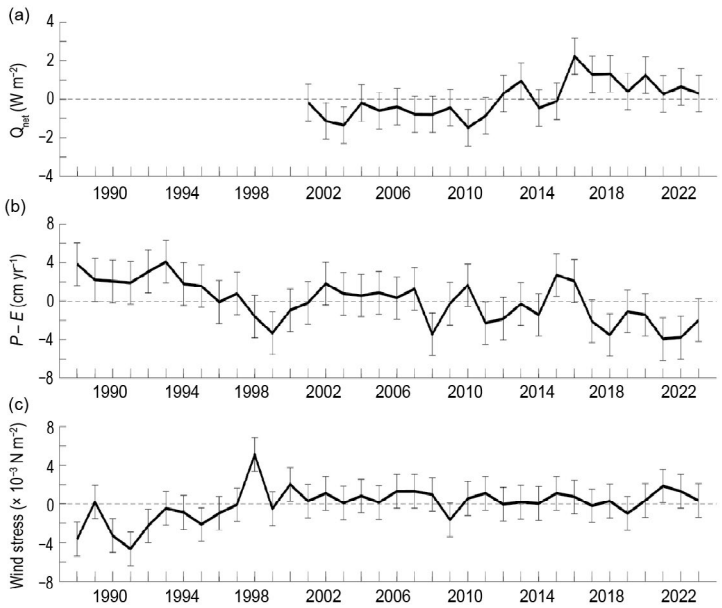

Fig. 3.14. Annual mean time series of global ocean-surface (a) net surface heat flux (Q_{net}; W m^{-2}) from a combination of CERES EBAF4.2 shortwave (SW) + longwave (LW) and WHOI OAFlux2 latent heat (LH) + sensitive heat (SH). The 2023 Q_{net} is based on FLASHFlux SW+LW as adjusted to EBAF and OAFlux2 LH+SH. (b) Net freshwater flux anomaly (*P*–*E*; cm yr^{-1}) from a combination of GPCP *P* and OAFlux2 *E*. (c) Wind stress magnitude anomalies (N m^{-2}) from WHOI OAFlux2. Error bars denote one standard deviation of annual-mean variability.

The wind stress time series features a generally stable value over the past two decades, following a substantial regime shift around 1999. The 1990s were characterized by a marked intensification of wind stress. From 2000 onward, the values have been relatively consistent, despite minor interannual fluctuations. There was a slight reduction in wind stress in 2009 and a minor increase in 2021. In 2023, wind stress levels showed a marginal decrease compared to the prior year.

f. Sea level variability and change

—P. R. Thompson, M. J. Widlansky, E. Leuliette, D. P. Chambers, B. Beckley, W. Sweet, B. D. Hamlington, S. Jevrejeva, M. A. Merrifield, G. T. Mitchum, and R. S. Nerem

Annual average global mean sea level (GMSL) from satellite altimetry (1993–present; Beckley et al. 2021) reached a new high in 2023, rising to 101.4 mm above 1993 (Fig. 3.15a). This marks the 12th consecutive year (and 28th out of the last 30) that GMSL increased relative to the previous year, continuing a multi-decadal trend of 3.2±0.4 mm yr^{-1} and acceleration of 0.075±0.025 mm yr^{-2} in GMSL during the satellite altimetry era (Fig. 3.15a). A quadratic fit with corrections for the eruption of Mount Pinatubo (Fasullo et al. 2016) yields a climate-driven trend of 3.1±0.4 mm yr^{-1} and acceleration of 0.092±0.025 mm yr^{-2} (updated from Nerem et al. 2018).

In addition to long-term change, record-high GMSL during 2023 reflects the onset of a strong El Niño event during May 2023 (see section 4b for details), which caused GMSL to increase sharply due to the impact of the El Niño–Southern Oscillation on precipitation patterns and ocean heat content (Nerem et al. 1999; Hamlington et al. 2020). Annually averaged GMSL from satellite altimetry increased 8.1±1.5 mm from 2022 to 2023, which is the third largest year-over-year increase in the satellite record. During previous strong El Niño events in 1997/98 and 2015/16, GMSL anomalies about the trend peaked in September and October, respectively. The ongoing 2023/24 event will peak later, as GMSL during 2023 reached its maximum during December and could continue to increase into 2024.

Data from Argo profiling floats analyzed by Scripps Institution of Oceanography (SIO; Roemmich and Gilson 2009) show the 0-dbar–2000-dbar steric (i.e., density-related) contribution to GMSL change was 1.4±0.3 mm yr^{-1} during 2005–23 (Fig. 3.15a). Mass concentration anomalies from the Gravity Recovery and Climate Experiment (GRACE) and GRACE Follow-On (GRACE-FO) missions produced by the NASA Jet Propulsion Laboratory (JPL; Wiese et al. 2022) show the mass contribution to GMSL change was 2.1±0.3 mm yr^{-1} during 2005–23 (Fig. 3.15a). The trend in the sum of steric and mass contributions, 3.4±0.5 mm yr^{-1}, agrees within uncertainties with the GMSL trend of

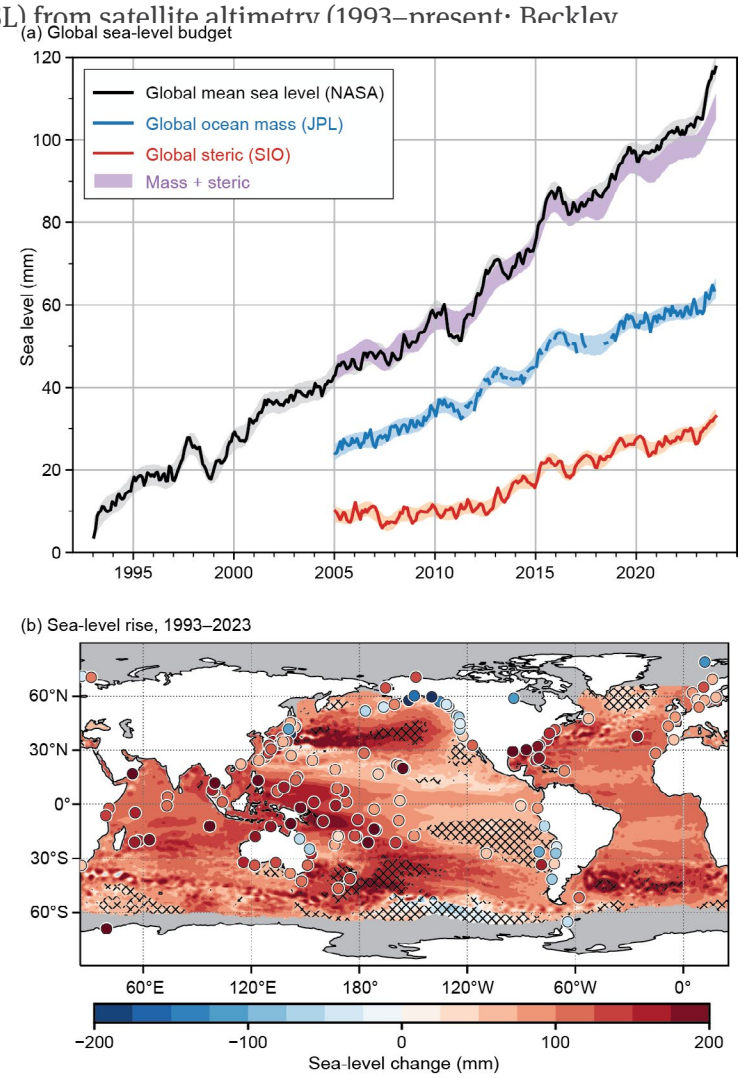

Fig. 3.15. (a) Global mean sea level (GMSL; mm) observed by satellite altimeters (1993–2023) produced with support from the NASA Sea Level Change and Ocean Surface Topography Science Teams (black). Monthly global ocean mass (2005–23) from GRACE and GRACE-FO calculated from mass concentrations produced by the NASA Jet Propulsion Laboratory (blue). GRACE and GRACE-FO data within 300 km of land were excluded in both ocean mass time series. Monthly global mean steric sea level (2005–23) from Scripps Institute of Oceanography (SIO) Argo data (red). Shading around the mass and steric series represents a 95% confidence range based on Gaussian process regressions, which are used to produce a 95% confidence range for the sum of global ocean mass plus steric (purple). (b) Total local sea-level change (mm) during 1993–2023 as measured by satellite altimetry (contours) and tide gauges (circles). Hatching indicates local changes that differ from the change in GMSL by more than one standard deviation. The trend map was generated using gridded delayed-mode and near-real-time altimetry data produced by the Copernicus Climate Change Service and obtained from the Copernicus Marine Service. Tide-gauge observations were obtained from the University of Hawaii Sea Level Center Fast Delivery database.

3.8±0.4 mm yr^{-1} measured by satellite altimetry since 2005 (Leuliette and Willis 2011; Chambers et al. 2017).

Consistency between the GMSL time series and the sum of independent estimates of steric and mass contributions (i.e., the "sea-level budget") is a significant achievement that increases confidence in estimates of Earth's global energy imbalance (e.g., Hakuba et al. 2021; Marti et al. 2022). However, misclosure in the budget emerged around 2016, which motivated several investigations into the origin of the discrepancy (e.g., Chen et al. 2020; Barnoud et al. 2021). Recent reprocessing and retracking of satellite altimetry data (including Topography Experiment [TOPEX]), radiometer recalibrations during the Jason-3 mission (Brown et al. 2023), and revision of the altimeter orbit standard have reduced misclosure in the budget relative to previous analyses (Fig. 3.15a). These updates to the altimeter record lowered the observed linear trend during the budget period, 2005–23, by approximately 0.2 mm yr^{-1} (Beckley et al. 2023). Over the complete altimeter record, 1993–2023, the adjustments reduced the linear trend by approximately 0.2 mm yr^{-1} and decreased the acceleration by nearly 0.016 mm yr^{-2} (Beckley et al. 2023). Remaining misclosure in the budget since 2016 may be related to uncertainties in the global ocean mass budget (Chen et al. 2020), additional error sources in the altimeter measurements (Barnoud et al. 2021), and/or steric changes below 2000 m not sampled by Argo.

Spatial structure in sea-level change (Fig. 3.15b) has become increasingly uniform as the altimetry record has grown in length, because the impact of natural fluctuations on regional sea-level trends decreases as the record length increases. Presently, only a small fraction of the global ocean has experienced sea-level trends that differ from the global mean trend by more than one standard deviation (hatched areas, Fig. 3.15b). However, sea-level changes relative to land (i.e., the quantity measured by tide gauges; circles, Fig. 3.15b), which is most relevant for societal impacts, can differ substantially from satellite-derived changes in tectonically active regions (e.g., Japan) and areas strongly affected by glacial isostatic adjustment (e.g., Alaska; Fig. 3.15b).

Relative to the 1993–2022 altimetry baseline, annual sea-level anomalies during 2023 were positive nearly everywhere (Fig. 3.16a), which primarily reflects the increasingly uniform long-term trends in rising sea levels (Fig. 3.15b). The abrupt yearly change of sea levels in the tropical Indo-Pacific basin (Fig. 3.16b) reflects the onset of El Niño conditions, which ended three years of La Niña conditions, as well as a concurrent reversal of the Indian Ocean dipole

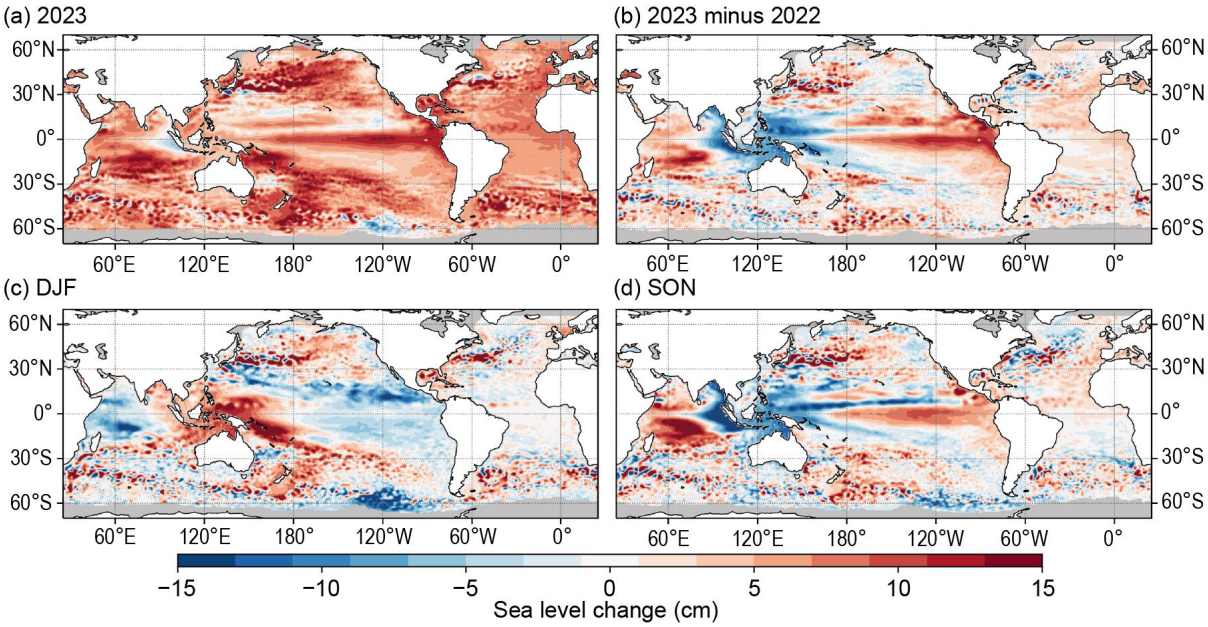

Fig. 3.16. (a) Annual average sea-level anomaly during 2023 relative to average sea level at each location during 1993–2022. (b) Average 2023-minus-2022 sea-level anomaly. (c) Average sea-level anomaly during DJF 2023 relative to the 1993–2022 DJF average. (d) Same as (c), but for SON. Units are given in cm. Global mean sea level was subtracted from panels (c),(d) to emphasize regional, non-secular change. These maps were generated using gridded delayed-mode and near-real-time altimetry data produced by the Copernicus Climate Change Service and obtained from the Copernicus Marine Service.

(IOD) from a weakly negative to positive phase. Compared to 2022, the two most noticeable sea-level changes were in the equatorial Pacific (falling and rising by up to 15 cm in the far western and eastern regions, respectively). Decreasing sea levels during 2023 compared to 2022 were also observed in the eastern Indian Ocean, both north and south of the equator, as well as throughout the Indonesian Throughflow region. Areas in the tropical south-central Indian Ocean and the tropical north-central Pacific also experienced notable year-over-year sea-level changes. The latter region, which includes Hawaii, is interesting because while the 2023 sea level compared to 2022 increased by 10 cm or more, the 2023 annual mean sea level was much closer to the long-term mean (i.e., locally, the year-to-year change only partly canceled the much lower sea levels of the preceding La Niña years). In the Atlantic, the 2023-minus-2022 differences were mostly either positive or nearly unchanged along all the continental coasts and throughout the basin interior (changes of generally 5 cm or less). In the midlatitudes as well as the Gulf of Mexico, year-to-year sea-level changes were larger in localized areas (positive and negative differences), which is common in such regions that are strongly affected by mesoscale oceanic eddies.

Development of El Niño combined with reversal of the IOD, both of which occurred during mid-2023, explains most of the inter-seasonal sea-level changes evident in the comparison of December–February (DJF) and September–November (SON) anomalies (Figs. 3.16c,d). In the Indian Ocean, the sea-level pattern clearly showed evidence of the Dipole Mode Index changing

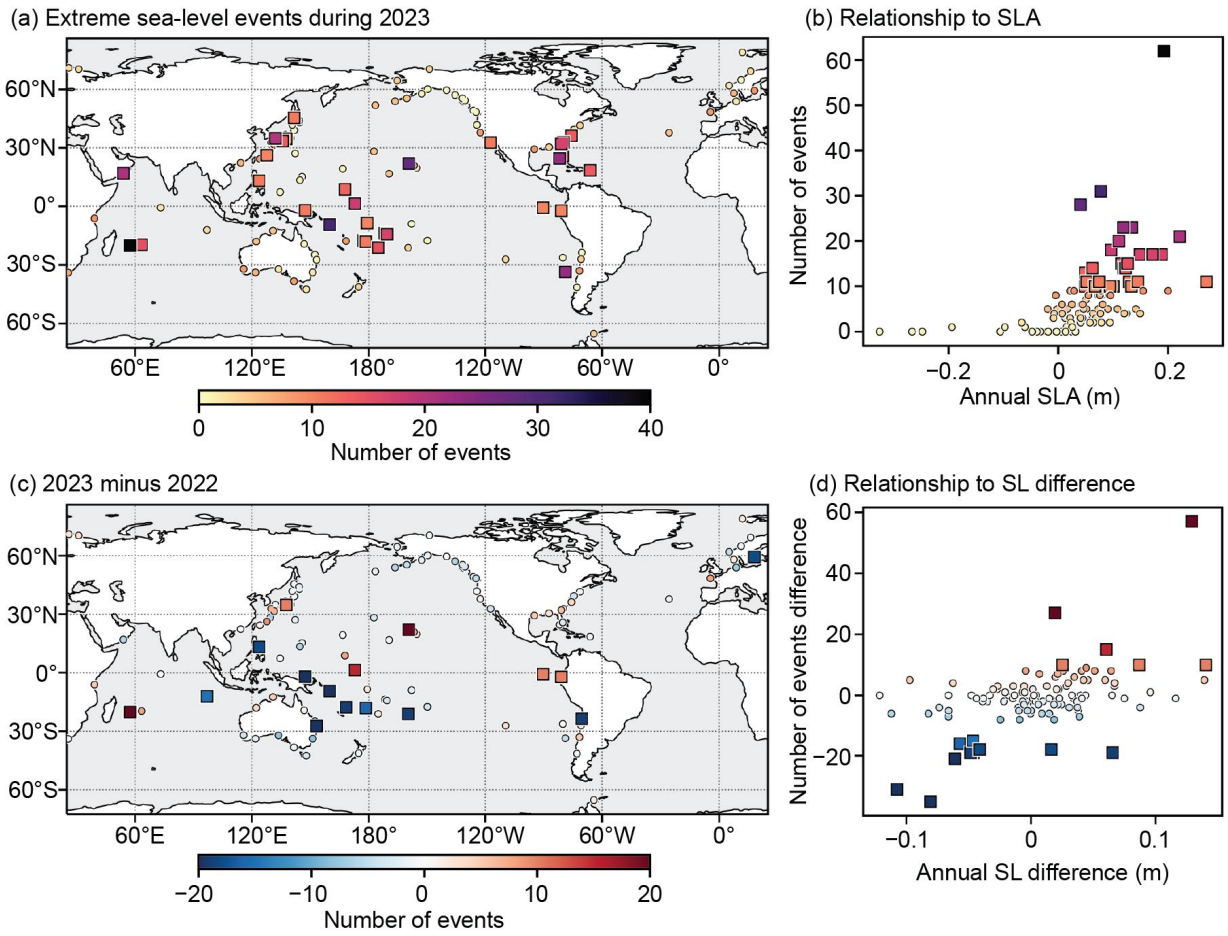

Fig. 3.17. (a) Number of extreme sea-level events from tide gauges during 2023. (b) Counts in (a) as a function of annual sea-level anomaly during 2023. Square markers in (a) and (b) highlight locations with more than 10 extreme events. (c) Change in the number of extreme sea-level events from 2022 to 2023. (d) Counts in (c) as a function of the change in annual sea level from 2022 to 2023. Square markers in (c) and (d) highlight locations where the magnitudes of changes in counts of extreme events were greater than 10. Counts of extreme sea-level events were calculated from hourly tide-gauge observations obtained from the University of Hawaii Sea Level Center Fast Delivery database. Only records with at least 80% completeness during 1993–2023 and 80% completeness during both 2022 and 2023, individually, were analyzed.

from weakly negative to positive during 2023 (i.e., sea-level anomalies increasing in the west and decreasing in the east; e.g., Fig. 8 in Kumar et al. 2020). Some of the highest regional sea-level anomalies during 2023 affected archipelagos in the Indian Ocean, such as Mauritius, Chagos, and the Seychelles, especially toward the end of the year. In the eastern Pacific, comparing DJF and SON, seasonal sea-level anomalies were also drastically different, especially around the Galapagos Islands and near the coasts of South and North America where 2023 ended with sea levels more than 15 cm above normal.

Ongoing trends, year-to-year variability, and seasonal changes in sea level impact coastal communities by increasing the magnitude and frequency of positive sea-level extremes that contribute to flooding and erosion. Minor impacts tend to emerge when local water levels exceed the 99th percentile of daily sea-level maxima (Sweet et al. 2014). Using 1993–2022 as the analysis epoch (consistent with the altimetry baseline), daily sea-level maxima that exceed the 99th percentile—hereafter referred to as extreme sea-level events—occurred more frequently in recent years compared to previous decades. Across 114 tide-gauge locations with sufficient data for analysis, the median number of extreme sea-level events per year and location increased from one during the 1993–97 pentad to four during the 2019–23 pentad. The 90th percentile of events per year and location increased from six during 1993–97 to 17 during 2019–23.

Thirty of the 114 locations experienced more than 10 extreme sea-level events during 2023, concentrated in the southwestern and equatorial Pacific Ocean, western boundary current regions in the Northern Hemisphere, and southern Indian Ocean (Fig. 3.17a) where annual sea-level anomalies were largest (Figs. 3.16a, 3.17b). The greatest number of events occurred in Mauritius (62), which experienced record-high monthly sea-level anomalies related to the strong positive IOD conditions during late 2023 (Fig. 3.16a). Large numbers of events also occurred in Kaua‘i, Hawai‘i (28), which were primarily related to local mesoscale variability rather than a basin-scale pattern of variability. Interestingly, the elevated numbers of extreme events in the southwestern Pacific during 2023 (Fig. 3.17a) also represent substantial year-over-year decreases from 2022 (Fig. 3.17b). Most of these events occurred early in 2023 prior to the development of El Niño and concurrent reduction of mean sea level in the region. The elevated numbers of events along the North Atlantic western boundary current system reflect a continuation of increased extreme sea levels from the previous year (Fig. 3.17c), which reflects warm ocean heat content anomalies (Fig. 3.4a) consistent with heat convergence in the subtropical gyre associated with the North Atlantic meridional overturning circulation (Volkov et al. 2023a) and weaker-than-average geostrophic currents (Fig. 3.22c).

g. Surface currents

—R. Lumpkin, F. Bringas, and R. C. Perez

This section describes variations of ocean surface currents, transports, and associated features, such as rings. Surface currents are obtained from in situ and satellite observations. Transports are derived from a combination of sea-surface height anomaly (from altimetry) and climatological hydrography. See Lumpkin et al. (2012) for details of these calculations. Zonal surface current anomalies are calculated with respect to a 1993–2022 climatology and are discussed below for individual ocean basins.

1. PACIFIC OCEAN

In 2023, zonal currents in the equatorial Pacific (Fig. 3.18a) exhibited annual mean eastward current anomalies exceeding 10 cm s^{-1} from 2°S to 4°N and between 160°E and 100°W, with the strongest anomalies of 23 cm s^{-1} at 160°E–170°W, associated with the May–December El Niño and weakened trade winds (Fig. 3.13a).

In 2020–23, the annual-average latitude of the Kuroshio Extension in the region 32°N–38°N, 141°E–153°E was shifted north of its long-term (1993–2023) location of 35.4°N, to a maximum of 36.8°N in 2021 and to 36.2°N in 2023 (Fig. 3.20b). This can be seen as alternating eastward/westward anomalies in

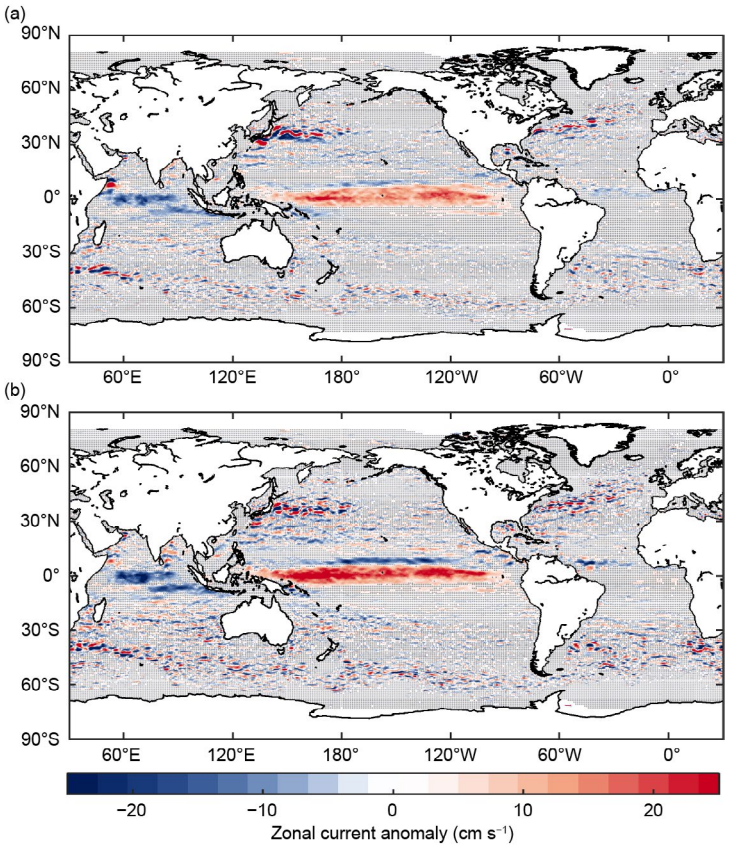

Fig. 3.18. Annually-averaged geostrophic zonal current anomalies with respect to the seasonal climatology (cm s^{-1}) for (a) 2023 and (b) 2023-minus-2022 anomalies, derived from a synthesis of drifters, altimetry, and winds. Values are only shown where they are significantly different from zero.

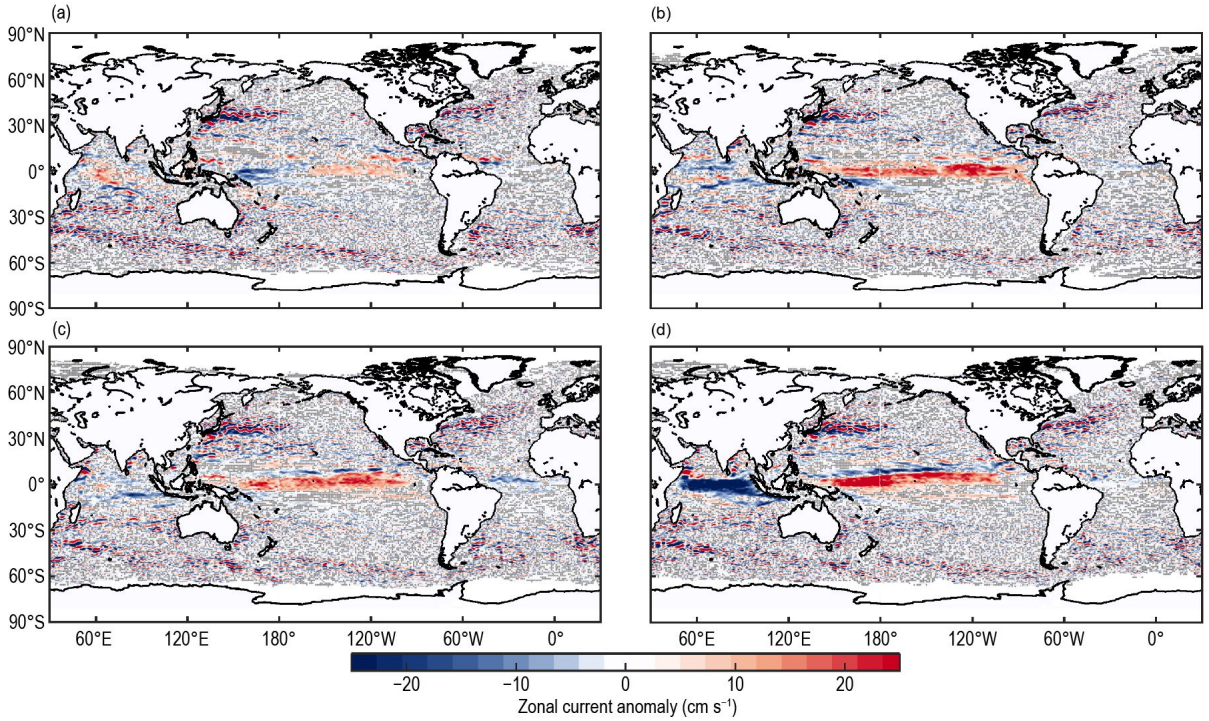

Fig. 3.19. Seasonally averaged zonal geostrophic anomalies with respect to seasonal climatology for (a) Dec 2022–Feb 2023, (b) Mar–May 2023, (c) Jun–Aug 2023, and (d) Sep–Nov 2023. Values are only shown where they are significantly different from zero.

Fig. 3.18a that persisted through the year (Fig. 3.19) and also in a band of increased ocean heat content anomalies (Fig. 3.4a). This large 2020–23 northward shift of the Kuroshio Extension (Fig. 3.20c) corresponded with an increase in averaged eddy kinetic energy (EKE; Fig 3.20d); this pattern is inconsistent with decadal shifts between increased/decreased EKE and a southward/northward shift of the Kuroshio Extension and arises due to a meander of the Kuroshio off the southern coast of Japan that has been present since 2017 (Qiu et al. 2020; Qiu and Chen 2021) and was still present in 2023 (Fig. 3.20b).

Because the equatorial eastward anomalies are a reversal of the La Niña-associated westward anomalies of 2022, the 2023-minus-2022 difference map (Fig. 3.18b) reaches eastward values exceeding 30 cm s^{-1} in the western equatorial Pacific. The lack of an intensified North Equatorial Countercurrent (NECC) in 2023, present in 2022, led to negative (westward) anomalies of 10 cm s^{-1}–15 cm s^{-1} in the difference map at 7°N–9°N across the central Pacific.

Equatorial zonal current anomalies were close to zero in December 2022–February 2023 (Fig. 3.19a), with weak (5 cm s^{-1}–10 cm s^{-1}) eastward anomalies at 3°S–3°N in the central and eastern basin consistent with a weakening of the westward South Equatorial Current (SEC) but residual westward anomalies in the western basin creating a dipole pattern. By March–May 2023 (Fig. 3.19b) the situation had changed dramatically, with equatorial eastward anomalies reaching 20 cm s^{-1} across the basin. These anomalies persisted through June–August (Fig. 3.19c), exceeding 10 cm s^{-1} from 2°S to 4°N. By September–November (Fig. 3.19d), the strongest anomalies were observed in the western basin, peaking at 40 cm s^{-1} between 0° and 1°N averaged in the longitude band 150°E–165°W and weakening anomalies in the central and eastern basin.

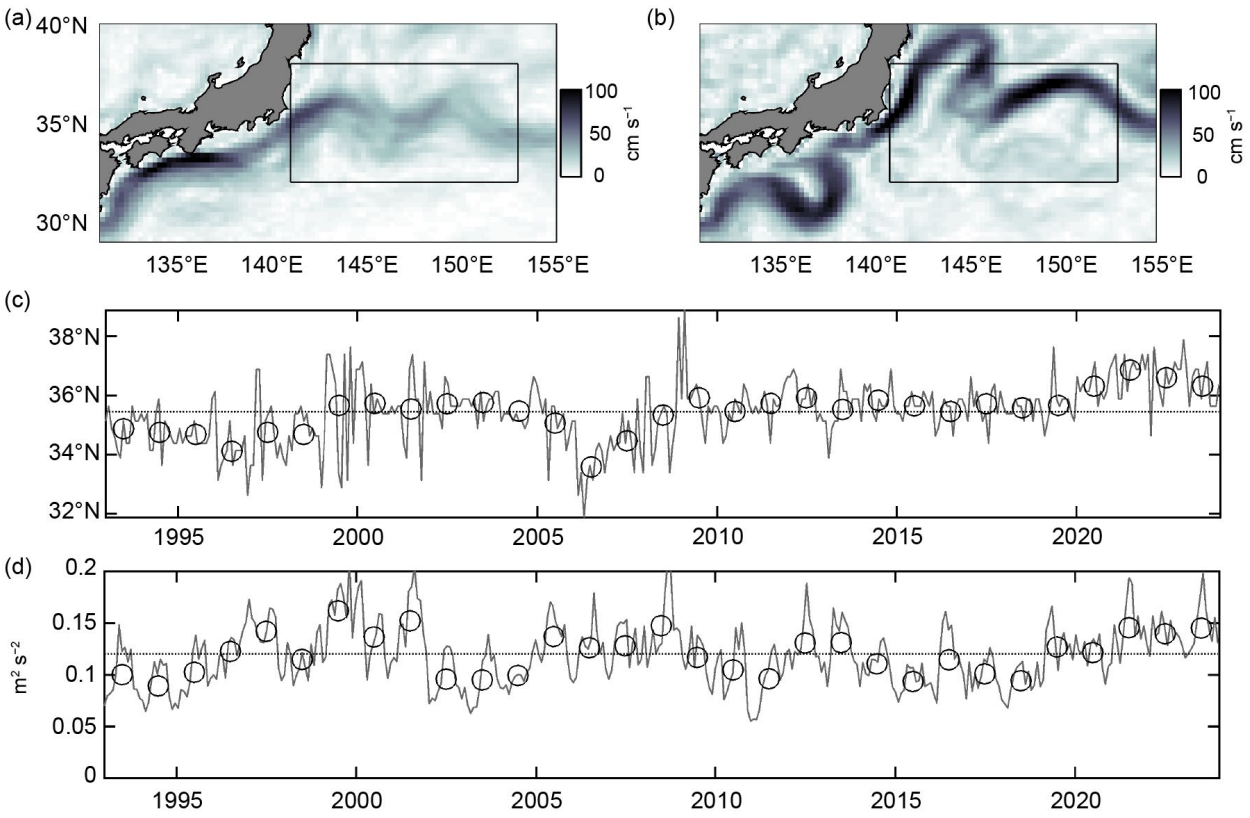

Fig. 3.20. (a) Climatological geostrophic surface current speed (cm s^{-1}) from Mulet et al. (2021) in the Kuroshio Current region (box) and surrounding regions. (b) 2023 mean geostrophic currents from MDT13 and Copernicus near-real-time altimetry. (c) Latitude of maximum zonal currents averaged in the Kuroshio Current region. (d) Mean eddy kinetic energy (m^2 s^{-2}) in the Kuroshio Current region.

2. INDIAN OCEAN

Annually-averaged zonal currents in the Indian Ocean (Fig. 3.18a) exhibited 5 cm s^{-1}–10 cm s^{-1} westward anomalies across the basin between 2°S and 3°N, with the strongest anomalies around 0°–1°N, driven by anomalously strong easterly wind anomalies (Fig. 3.13a). Because these current anomalies were much stronger than observed anomalies in 2022, the 2023-minus-2022 difference map (Fig. 3.18b) is similar to the 2023 anomaly map except near the western boundary offshore of Somalia. These anomalies were not present throughout much of the year (Fig. 3.19); they developed rapidly in September–November (Fig. 3.19d), when they exceeded 40 cm s^{-1} between the equator and 1°S.

As seen in 2022, relatively strong (15 cm s^{-1}–20 cm s^{-1}) negative/positive anomalies in the 2023 anomaly map (Fig. 3.18a) immediately offshore Somalia indicate a southward shift of the Somali Current extension (after leaving the coast and flowing eastward) and southern edge of the Great Whirl (Beal et al. 2013) compared to climatology. As in 2022, these alternating-sign anomalies developed in June–August 2023 (Fig. 3.19c) and strengthened to ±40 cm s^{-1} in September–November (Fig. 3.19d).

3. ATLANTIC OCEAN

Annual mean zonal current anomalies in the tropical Atlantic Ocean in 2023 did not exceed 4 cm s^{-1} (Fig. 3.18a). The 2023-minus-2022 difference map (Fig. 3.18b) is therefore dominated by the 2022 eastward anomalies of 10 cm s^{-1} at 7°N–8°N (Lumpkin et al. 2023). The year began (Fig. 3.19a) with ~10 cm s^{-1} eastward/westward anomalies north/south of 6°N in the western tropical Atlantic, indicating an acceleration and northward shift of the NECC. This pattern disappeared by March–May (Fig. 3.19b). In June–August (Fig. 3.19c), 5 cm s^{-1}–10 cm s^{-1} westward anomalies were present across the basin at 1°N–3.5°N, indicating a slight strengthening of the westward northern core of the SEC (see Lumpkin and Garzoli 2005). No significant zonal current anomalies were present in September–November (Fig. 3.19d).

The variability of key Atlantic Ocean currents is continuously monitored in near-real-time using a combination of in situ data and satellite altimetry (https://www.aoml.noaa.gov/phod/altimetry/cvar). In the southeastern Atlantic, the Agulhas Current shed six rings during 2023, a level of activity that, similar to the previous year, lies within the 1993–2022 average of four to six rings per year. At the same time, the annual transport was 50.9 Sv (1 Sv=10^6 m^3 s^{-1}) along a cross section at ~28°E and between 34°S and 40°S, only 0.1 Sv higher than the previous year, continuing the pattern of annual transports that have remained within 1 standard deviation of the long-term mean of 50.9±2.8 Sv since 2018. In the southwestern Atlantic, the Brazil Current transports waters of subtropical origin into subpolar regions. During 2023, the Brazil-Malvinas Confluence was located at 37.9°S, a southward shift of 0.5°S compared to 2022 and compatible with the long term mean of 37.8±0.6°S (see https://www.aoml.noaa.gov/phod/altimetry/cvar/mal/BM_ts.php), continuing the southward trend of the Confluence observed since 1993 at decadal time scales (Lumpkin and Garzoli 2011; Goni et al. 2011). In the tropical North Atlantic, the North Brazil Current (NBC) and associated rings serve as interhemispheric conduits for water masses and heat from the South Atlantic to reach the North Atlantic (Goni and Johns 2003). A portion of these waters enter the Caribbean Sea carrying low salinity Amazon River waters (Ffield 2007), known for creating barrier layer conditions that are often associated with hurricane intensification (e.g., Balaguru et al. 2012; Domingues et al. 2015). The average northwestward flow of the NBC in 2023 was 5.9 Sv, a decrease of 1.8 Sv with respect to the previous year and 1.1 Sv lower than its long term (1993–2022) mean value of 7.1±0.8 Sv. Similarly, during 2023 the retroflected flow experienced a sharp decrease of 7.6 Sv with respect to the previous year, for an average of 12.7 Sv, an anomaly of –2.2 Sv from the long-term mean transport of 14.9±1.8 Sv. This average transport during 2023 was within the lowest 15th percentile in terms of its annual mean transport and consistent with the decreased 2023 NECC strength compared to 2022, as the NECC is fed by this retroflection. While this retroflected flow exhibited positive anomalies during the first three months of 2023, negative anomalies prevailed during the rest of the year reaching values as large as 6 Sv during September and October. To the north, the Yucatan Current (YC) and Florida

Current (FC) also exhibited negative anomalies of –0.3 Sv and –1.1 Sv, respectively, compared to their 1993–2022 mean values of 27.8±0.9 Sv and 30.9±1.2 Sv. The YC transport was 0.6 Sv below its 2022 annual mean while the FC transport increased 0.5 Sv from the previous year. The negative anomalies observed in the NBC, especially during the first few months of 2023, are consistent with the negative anomalies by similar magnitude also observed during the last quarter of 2023 in the FC. These three currents constitute an important part of the Atlantic meridional overturning circulation surface pathways and, therefore, negative transport anomalies in the NBC may have first propagated through the Caribbean Sea, then into the Gulf of Mexico by the YC, and finally into the Florida Strait by the FC where anomalies of –5 Sv were observed at the end of 2023. With negative anomalies in the FC transport tied to higher coastal sea level and "sunny day" flooding events along the southeast coast of the United States (Ezer and Atkinson 2014; Domingues et al. 2016; Volkov et al. 2020), further studies addressing the delayed NBC to FC connection may help develop early warnings for such flooding events.

h. Meridional overturning circulation and heat transport in the Atlantic Ocean

—D. L. Volkov, J. K. Willis, W. Hobbs, Y. Fu, S. M. Lozier, W. E. Johns, D. A. Smeed, B. I. Moat, I. Pita, M. Goes, S. Dong, R. H. Smith, and S. Elipot

The meridional overturning circulation (MOC) and meridional heat transport (MHT) are essential indicators of the state of the large-scale ocean circulation and Earth's climate system. Most climate models and proxy-based reconstructions indicate that the Atlantic MOC may already be slowing down towards the end of this century in response to anthropogenic forcing (Weijer et al. 2020; Rahmstorf et al. 2015; Caesar et al. 2018, 2021). In this report, we provide updates on the MOC/MHT estimates across the Atlantic Ocean from the following observing platforms: 1) the Overturning in the Subpolar North Atlantic Program (OSNAP) array (Lozier et al. 2017), which consists of a West section from Canada to Greenland across the Labrador Sea and an East section from Greenland to Scotland, 2) the RAPID-Meridional Overturning Circulation and Heat-flux Array - Western Boundary Time Series (henceforth RAPID) array at ~26.5°N (Moat et al. 2023), and 3) from the combination of satellite and in situ data (synthetic MOC/MHT) at 41°N and at several latitudes in the South Atlantic (Fig. 3.21). As a highlight of this report, initial estimates indicate a record-high MOC/MHT at 41°N, albeit over a short (20-year) observational record.

The most recently published OSNAP time series covers August 2014 to June 2020 (Fu et al. 2023; Fig. 3.22a). The time-mean MOC across the full OSNAP array, consisting of West and East sections, is 16.7±0.6 Sv (the uncertainty is the standard error of the mean). The monthly MOC time series exhibits strong variability ranging from 10 Sv to 25 Sv. The overturning at OSNAP East (16.3±0.6 Sv) dominates the mean and variability of the total subpolar overturning in comparison to that at OSNAP West (3.0±0.5 Sv), consistent with the previously published results (Lozier et al. 2019; Li et al. 2021). Focusing on the seasonal variability, Fu et al. (2023) identified that the MOC peaks in spring (21.1±1.2 Sv) and reaches a minimum in winter (12.3±1.2 Sv) with an amplitude of ~9.0 Sv. Dense water formation in winter and its export are responsible for the peak of the MOC, while the southward Ekman transport, reaching its maximum strength in winter, corresponds to the minimum of the MOC and explains the timing of the MOC trough. The time-mean MHT across the full OSNAP array is 0.50±0.01 PW. The OSNAP East and West sections contribute 0.42±0.01 PW and 0.08±0.01 PW, respectively. The overturning circulation explains 73% of the total MHT variability. The time-mean freshwater transport across the full OSNAP array is −0.36±0.01 Sv (minus denotes southward transport), with nearly equal contributions from West and East sections (−0.18±0.01 Sv and −0.17±0.01 Sv, respectively). This highlights the important role of the Labrador Sea in exporting freshwater to the North Atlantic.

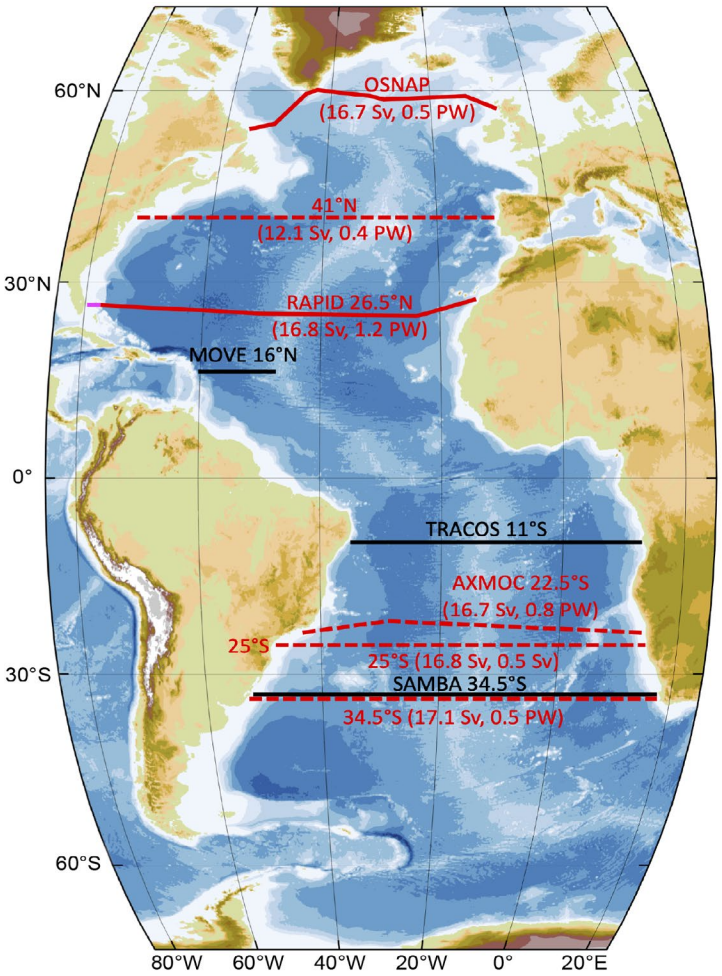

Fig. 3.21. The Atlantic meridional overturning circulation (MOC) observing system: moored arrays (solid red and black lines) and sections across which the MOC and meridional heat transport (MHT) are estimated by synthesizing in situ measurements (Argo, eXpendable BathyThermograph [XBT]) with satellite altimetry data (dashed red lines). The red lines show the sections that have updates covered in this report, while the black lines show the sections for which updates are pending. The record mean MOC and MHT values are shown in parentheses.

The RAPID array, operational since April 2004, is the oldest trans-basin MOC observing array in existence. Since the previous *State of the Climate* report (Volkov et al. 2023b), the RAPID MOC time series has been extended by 14 months to 15 February 2022 (Moat et al. 2023; Fig. 3.22c). The RAPID MHT time series is available through December 2020 (an update will become available upon the processing of cruise data in the Florida Straits). The record mean MOC at ~26.5°N is 16.8 Sv and the standard deviation is 4.6 Sv. The annual mean MOC in 2021 was 15.3 Sv, which is significantly smaller than both the record mean and the annual mean in 2020 (16.9 Sv), given the 0.9 Sv uncertainty of annual transport estimates (McCarthy et al. 2015). The interannual variability of the MOC at ~26.5°N was largely due to the variations in the upper mid-ocean transport (between the Bahamas and Africa) prior to 2018, and it has mainly been driven by the variations in the Florida Current transport after 2018. While an extension of the RAPID MHT time series through February 2022 is pending, the 2004–20 MHT time series has been updated by accounting for the flow-weighted temperature of the Florida Current (Johns et al. 2023). The time-mean MHT at ~26.5°N is 1.20 PW and its standard deviation is 0.38 PW. The MHT variability is dominated by the overturning circulation (and not by the horizontal gyre circulation), as suggested by high correlation between the MHT and MOC (r = 0.96 for 10-day averages). During the decade of 2011–20, the MHT was about 11% smaller than during the first five years of observations. This change was concurrent with a broadening of the Gulf Stream and with altered patterns of ocean heat and freshwater contents (Smeed et al. 2018; Bryden et al. 2020). In 2010–18, both the MOC and MHT were gradually recovering from the 2009/10 dip (Moat et al. 2020), which contributed to oceanic heat convergence in the subtropical gyre, leading to an accelerated sea-level rise along the U.S. southeastern coast and increased flood risk (Domingues et al. 2018; Volkov et al. 2019, 2023a). Johns et al. (2023) explored the ratio MHT/MOC, which is 0.07 PW/Sv on average. Interestingly, the long-term variations of the MHT/MOC ratio are mainly related to the changes in the flow-weighted temperature of the Florida Current that are now included in the overall MHT estimate. There was an overall decrease of the MHT/MOC ratio in 2004–09 and an increase in 2010–20, associated with the cooling and warming of the Florida Current, respectively.

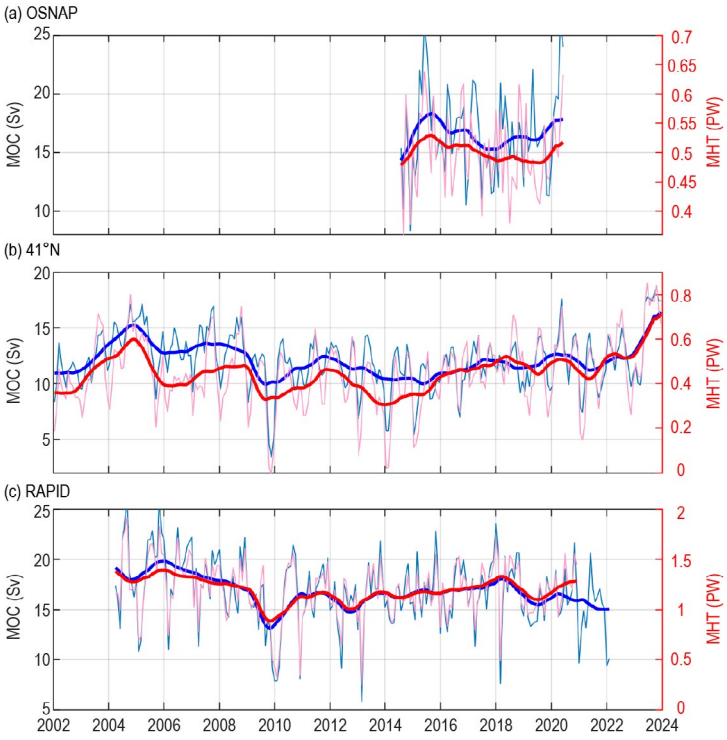

Fig. 3.22. The meridional overturning circulation (MOC) and meridional heat transport (MHT) estimates at the (a) Subpolar North Atlantic Program (OSNAP), (b) 41°N, and (c) RAPID (26.5°N) sections in the North Atlantic. The light blue (pink) lines show the monthly MOC (MHT) time series and the bold blue (red) lines show their yearly moving averages.

The synthetic estimates at 41°N (Fig. 3.22b), based on satellite altimetry and Argo measurements, were reproduced from Willis (2010) and Hobbs and Willis (2012) and extended up to December 2023 (Willis and Hobbs 2024). Each individual estimate represents a three-month average with an uncertainty of 2.3 Sv for the MOC and 0.23 PW for the MHT. The record-high MOC and MHT in 2002–23 were 12.1 Sv and 0.45 PW, respectively. The MOC transport at 41°N was 15.4 Sv in 2023, 12.7 Sv in 2022, and 10.6 Sv in 2021, with only the 2023 mean being statistically different from the time mean given the uncertainty. The MHT in 2022 was 0.67 PW, which is significantly greater than the time mean and the MHT of 0.53 PW in 2022. As the quality control of Argo and altimeter data is always ongoing, improvements in the estimate over the past few years are common. The improvements implemented since the *State of the Climate in 2022* report (Volkov et al. 2023b) resulted in a small decrease in the MOC transport equivalent to about 0.7 Sv in the 2022 values, relative to last year's report. While this change is smaller than the year-to-year

uncertainty in the estimate at 41°N, the recent high values of the MOC in 2023 could be revised after another year of data processing is complete. Nevertheless, last year's increase makes 2023 the highest year on record for MOC volume and heat transports at this latitude in 22 years.

As an assessment of South Atlantic transports, we present novel synthetic MOC/MHT estimates at 22.5°S covering the period from 2007 to 2023 (the AXMOC transect; Fig. 3.23a). The AXMOC time series is obtained by an objective analysis of eXpendable BathyThermograph (XBT) and Argo profiles, optimized by minimizing the difference between the surface in situ dynamic height and sea-surface height from satellite altimetry (Pita et al. 2024). The method adequately represents the energetic Brazil Current, westward propagating signals, and coastal sea-level variability. The time-mean MOC and MHT at 22.5°S are 16.70±0.87 Sv and 0.75±0.06 PW, respectively. In 2023, the MOC and MHT were not significantly different from the record-mean values (by 0.3 Sv and 0.03 PW, respectively). The 2007–23 trends are not statistically significant: 0.50±0.89 Sv decade^{-1} for the MOC and 0.04±0.05 PW decade^{-1} for the MHT. The time-mean and trend estimates agree with those from the synthetic estimates obtained at 25°S using the methodology of Dong et al. (2021); however, the variability in the two estimates is quite different (Fig. 3.23b). This means that the methodology-specific uncertainties are still an important constraint in the overall accuracy of synthetic estimates. At 34.5°S, the MOC and MHT anomalies in 2023 were small and not statistically different from the time mean (Fig. 3.23c).

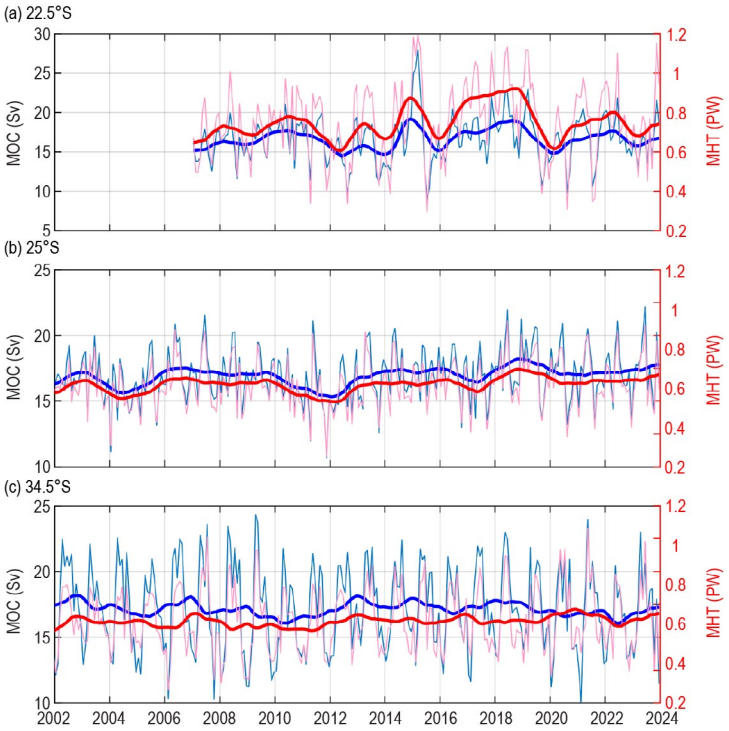

Fig. 3.23. The synthetic meridional overturning circulation (MOC) and meridional heat transport (MHT) estimates at the AXMOC section at (a) 22.5°S and at the (b) 25°S and (c) 34.5°S sections in the South Atlantic. The light blue (pink) lines show the monthly MOC (MHT) time series and the bold blue (red) lines show their yearly moving averages.

The existing observations of the MOC and MHT in the Atlantic Ocean allow an assessment of the climate-relevant state of the large-scale ocean circulation. Because the observational records are still very short compared to climate time scales, it is still not clear whether the MOC has started weakening in response to anthropogenic forcing as suggested by climate models and proxy-based reconstructions. This possible weakening has neither yet been reflected in direct measurements of the MOC at cross-basin moored arrays, nor in synthetic MOC estimates, nor in reconstructions based on sparse hydrographic section data (Caínzos et al. 2022; Worthington et al. 2021; Fu et al. 2020). Continued observations of the MOC and MHT are thus necessary for timely detection of anthropogenic signals and for validating and improving ocean and climate models.

i. Global ocean phytoplankton

—B. A. Franz, I. Cetinić, M. Gao, and T. K. Westberry

Marine phytoplankton contribute roughly 50% of global net primary production, serving the energy needs of oceanic ecosystems and providing a critical pathway for carbon sequestration to the deep oceans (Field et al. 1998; Siegel et al. 2023). The diversity, abundance, and spatio-temporal distribution of phytoplankton are controlled by biotic factors such as zooplankton grazing and viruses, as well as abiotic factors such as nutrient and light availability that are highly dependent on physical properties and processes, including ocean temperature, stratification, and circulation (e.g., Behrenfeld et al. 2006). Spaceborne ocean color radiometers such as Sea-viewing Wide Field-of-view Sensor (SeaWiFS), Moderate Resolution Imaging (MODIS), and the Visible Infrared Imaging Radiometer Suite (VIIRS) provide a synoptic view of spatial and temporal changes in phytoplankton through measurements of near-surface concentrations of phytoplankton pigment chlorophyll-*a* (Chl*a*; mg m^{-3}) and phytoplankton carbon (C_{phy}; mg m^{-3}). Measurements of Chl*a* contain the combined signal of both phytoplankton biomass and physiology, while C_{phy} measures phytoplankton carbon biomass. C_{phy} and Chl*a* often covary, but discrepancies in their distributions are indicative of changes in the physiological or compositional characteristics of phytoplankton communities (Dierssen 2010; Geider et al. 1997; Siegel et al. 2013; Westberry et al. 2016).

In this report, we evaluate the global distribution of phytoplankton over the one-year period from October 2022 through September 2023 (the analysis year) using remotely sensed Chl*a* and C_{phy} measurements from a continuous 26-year record (1997–2023) that combines observations of SeaWiFS (1997–2010), MODIS on Aqua (MODIS-A, 2002–present), and VIIRS on NOAA20 (VIIRS-N_{20}, 2017–present). The MODIS-A daytime sea-surface temperature (SST; °C) is also assessed over a consistent time period to provide context on the physical state of the oceans. The ocean color data from VIIRS-N_{20}, MODIS-A, and SeaWiFS correspond to NASA processing version R2022.0. The Chl*a* product was derived using the Ocean Color Index algorithm of Hu et al. (2012), but with updated algorithm coefficients applied in R2022.0 (Hu et al. 2019; O'Reilly and Werdell 2019). C_{phy} was derived from the particle backscattering coefficient, b_{bp}, at 443 nm (Generalized Inherent Optical Properties algorithm; Werdell et al. 2013; McKinna et al. 2016) and a linear relationship between b_{bp} and C_{phy} (Graff et al. 2015). In merging the time series of SeaWiFS and MODIS-A, differences between the sensors were assessed over the overlapping period from 2003 through 2008, and a mean bias correction (−0.0021 mg m^{-3} in Chl*a* and −6.7e-5 m^{-1} in b_{bp} or −0.78 mg m^{-3} of C_{phy}) was derived and applied to the SeaWiFS time series. Similarly, the overlap period of 2018 to 2020 was used to assess the differences between MODIS-A and VIIRS-N_{20}, and a bias correction (−0.0017 mg m^{-3} in Chl*a* and −3.1e-4 m^{-1} in b_{bp} or −3.6 mg m^{-3} of C_{phy}) was applied to the VIIRS-N_{20} time series. MODIS-A data for 2023 were specifically excluded from this analysis due to as yet uncorrected radiometric calibration instability (G. Meister, NASA/GSFC, personal communication 2024). In contrast, the newer VIIRS-N_{20} instrument has been shown to be very stable (Twedt et al. 2022), and thus it provides the primary reference for the current analysis year. The derived bias corrections between the VIIRS-N_{20} and MODIS-A b_{bp} time series are largely due to the impact of sensor radiometric calibration errors and sensitivity of the b_{bp} retrievals to spectral sampling differences between the sensors (i.e., Werdell and McKinna 2019). While efforts are underway at NASA to reduce this retrieval bias, some additional caution is warranted here in the interpretation of C_{phy} anomalies from VIIRS-N_{20} relative to the climatological record that is dominated by MODIS-A.

Changes in the global distribution of phytoplankton were assessed by subtracting monthly climatological means for MODIS-A Chl*a* and C_{phy} (October 2002–September 2022) from the VIIRS-N_{20} bias-adjusted monthly mean values for the 2023 analysis year. These monthly anomalies were then averaged to produce the global Chl*a* and C_{phy} annual mean anomaly maps (Figs. 3.24a,b). Similar calculations were performed on MODIS-A SST data to produce an equivalent SST annual mean anomaly for the same time period and climatological reference period (Fig. 3.24c). The permanently stratified ocean (PSO), which is used for the analyses depicted in Figs. 3.25 and 3.26, is defined as the region spanning the tropical and subtropical oceans, where

annual average SST is greater than 15°C and surface mixed layers are typically low in nutrients and shallower than the nutricline (black lines near 40°N and 40°S in Fig. 3.24; Behrenfeld et al. 2006).

For the 2023 analysis year, the distribution of SST anomalies (Fig. 3.24c), similar to that of Fig. 3.1a despite the shorter climatological reference period, is consistent with the transition to El Niño conditions in 2023, including a pronounced tongue of anomalously warm waters extending across the equatorial Pacific with anomalously cool waters to the north and south of the tongue. A similar but inverse feature is evident in the Chl*a* anomalies, with concentrations depressed (<10%) within the warm tongue and strongly elevated (>40%) in the adjacent cooler waters (Fig. 3.24a). Similarly, elevated Chl*a* concentrations are observed in the anomalously cool waters of the tropical Indian Ocean. Negative SST anomalies within the PSO generally coincide with deeper surface mixed layers (Deser et al. 2010), resulting in reduced phytoplankton light exposure rates and thus increased cellular Chl*a* and a decoupling between Chl*a* and C_{phy} variability (Behrenfeld et al. 2015). While C_{phy} and Chl*a* anomalies appear to covary in the equatorial Pacific and Indian Oceans, C_{phy} is depressed where Chl*a* is elevated in the North and South Atlantic and in the subtropical North and South Pacific. Patches of elevated and depressed Chl*a* are visible throughout the subpolar and polar regions above and below the PSO (Fig. 3.24a), and the C_{phy} anomalies are generally elevated (Fig. 3.24b). Observed heterogeneity in biomass indicators outside of the PSO is a result of the ephemeral nature of phytoplankton blooms in these waters, as well as poor spatial and temporal sampling due to clouds and low-light conditions that limit our ability to interpret interannual variability in higher-latitude regions.

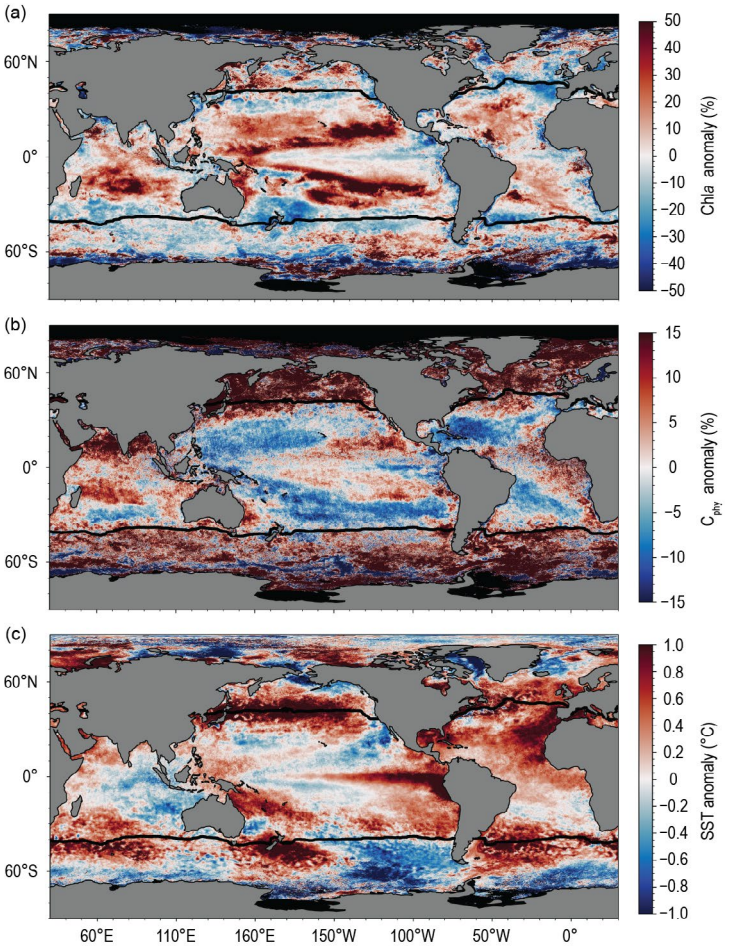

Fig. 3.24. Spatial distribution of average monthly (a) VIIRS-N_{20} chlorophyll-*a* (Chl*a*) anomalies (%), (b) VIIRS-N_{20} phytoplankton carbon (C_{phy}) anomalies (%), and (c) MODIS-A sea-surface temperature (SST) anomalies (°C) for Oct 2022–Sep 2023, where monthly differences were derived relative to the MODIS-A climatological record (Oct 2002–Sep 2022). Chl*a* and C_{phy} are stated as % difference from climatology, while SST is shown as an absolute difference. Also shown in each panel is the location of the mean 15°C SST isotherm (black lines) delineating the permanently stratified ocean (PSO). Differences in the SST anomalies here versus in Fig. 3.1 are owing to differences in climatological periods, smoothing, and data sources.

Annual variability of Chl*a* and C_{phy} within the PSO typically displays two distinct peaks (Figs. 3.25a,b), reflecting the springtime increases of biomass in the Northern Hemisphere (Figs. 3.25c,d) and Southern Hemisphere (SH; Fig. 3.25g,h). The timing of peaks in C_{phy} lag two to three months behind those of Chl*a*, reflecting a reduction in phytoplankton chlorophyll-to-carbon ratios as the seasonal bloom progresses (e.g., Westberry et al. 2016), and the tight coupling between phytoplankton biomass and its losses (e.g., grazing). While the timing of seasonal peaks and troughs observed in the 2023 analysis year is similar to previous years, the SH PSO values for C_{phy} (Fig. 3.25h) and to a lesser degree Chl*a* (Fig. 3.25g) are anomalously low in the first half of the year. This is consistent with the state of the time series at the end of 2022 as reported in Franz et al. (2023) and reflects, at least in part, an erroneous bias in the SH phytoplankton metrics due to the influence of stratospheric aerosols from the 2022 Hunga Tonga–Hunga Ha'apai volcanic eruptions on the atmospheric correction process used for ocean color retrieval

(Zhu et al. 2022; Franz et al. 2024). Another notable feature observed in 2023 is the pronounced outlier of elevated Chl*a* within the tropical PSO in February (Figs. 3.25a,e). This outlier can be traced to an intense bloom of *Noctiluca scintilans* covering the Gulf of Oman and much of the Arabian Sea, where climate-driven seasonal outbreaks of this harmful plankton have been increasing in intensity and range (do Rosário Gomes et al. 2014; Goes et al. 2020).

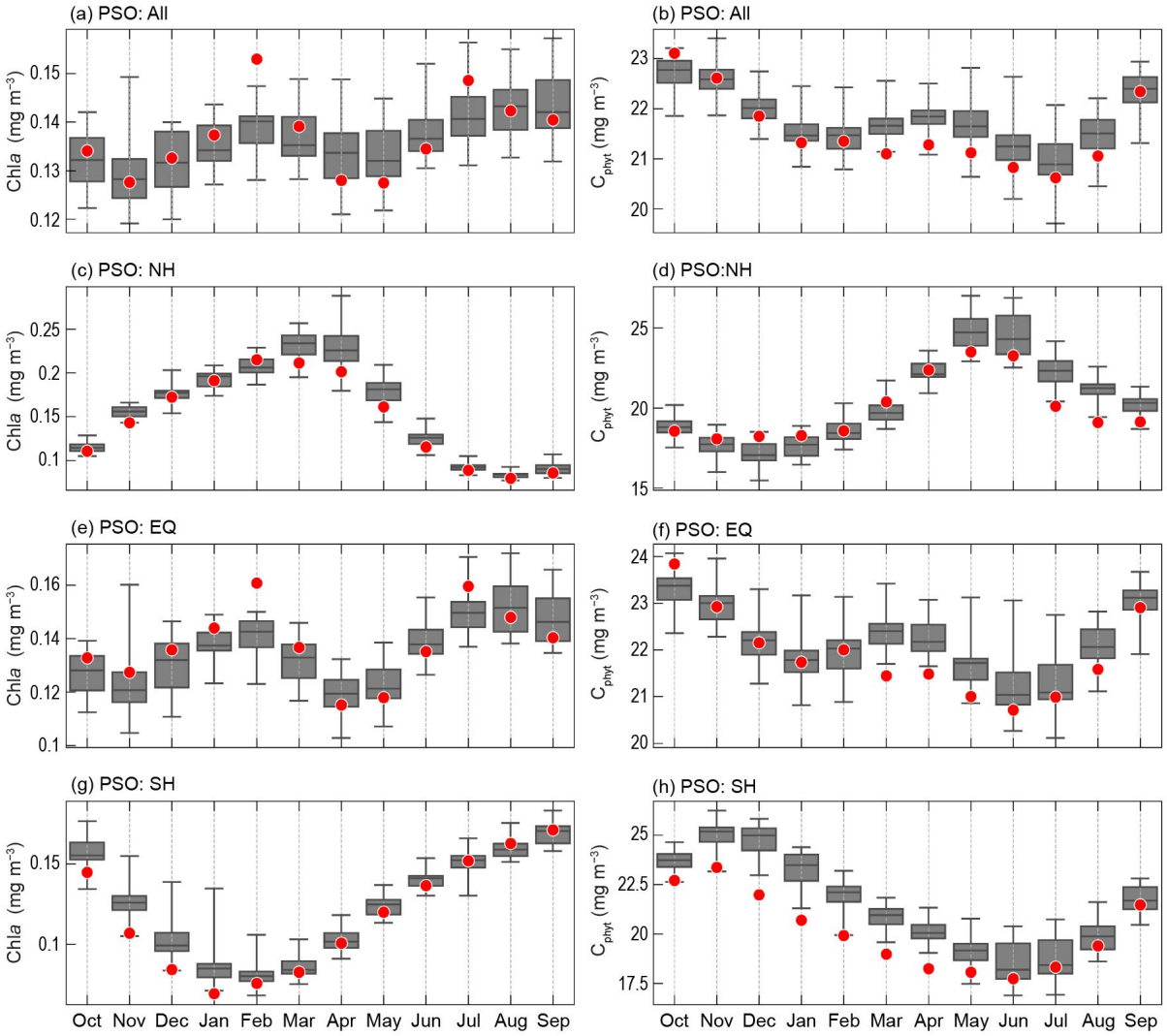

Fig. 3.25. Distribution of Oct 2022–Sep 2023 monthly means (red circles) for (a) VIIRS-N_{20} chlorophyll-*a* (Chl*a*) and (b) VIIRS-N_{20} phytoplankton carbon (C_{phy}) for the permanently stratified ocean (PSO) region (see Fig. 3.26), superimposed on the climatological values as derived from the combined time series of SeaWiFS, MODIS-A, and VIIRS-N_{20} over the period of Oct 1998–Sep 2022. Gray boxes show the interquartile range of the climatology, with a black line for the median value and whiskers extending to minimum and maximum values. Subsequent panels show latitudinally segregated subsets of the PSO for the (c),(d) Northern Hemisphere (NH; above tropics), (e),(f) tropical ±23.5° latitude subregion (EQ), and (g),(h) Southern Hemisphere (SH; below tropics). Units for (a), (c), (e), and (g) are Chl*a* (mg m^{-3}) and those for (b), (d), (f), and (h) are C_{phy} (mg m^{-3}).

Over the 26-year time series of spatially averaged monthly mean Chl*a* within the PSO, concentrations vary by 5.8% (0.008 mg m^{-3}, standard deviation) around a long-term average of 0.136 mg m^{-3} (Fig. 3.26a). C_{phy} over the same 26-year period varies by 3.2% (0.69 mg m^{-3}) around an average of 21.8 mg m^{-3} (Fig. 3.26c). Chl*a* monthly anomalies within the PSO (Fig. 3.26b) vary by 4.5% (0.006 mg m^{-3}) over the multi-mission time series, with the largest deviations generally associated with El Niño–Southern Oscillation (ENSO) events (r=−0.38), as demonstrated by the correspondence of Chl*a* anomaly variations with the Multivariate ENSO Index (MEI; Wolter and Timlin 1998; presented in the inverse to illustrate the covariation). C_{phy} anomalies (Fig. 3.26d), which vary by 2.0% (0.45 mg m^{-3}), are less correlated with the MEI (r=−0.27) due to the inherent lag between environmental change, phytoplankton growth, and biomass accumulation. The

anomalies in 2023 for Chl*a* and C_{phy} within the PSO indicate modestly depressed concentrations overall, consistent with the transition to El Niño conditions that limit phytoplankton production.

Through the continuous observation of ocean color, we are able to track variability in the global distribution of phytoplankton that drive biogeochemical processes, govern the role of the oceans in the global carbon cycle, and through their productivity exert a controlling influence on marine ecosystems, food webs, and fisheries. Subtle changes in Chl*a* and C_{phy} allow us to distinguish climate-driven variability in phytoplankton biomass from changes in physiology and community response. The recently launched Plankton, Aerosol, Cloud, ocean Ecosystem (PACE) mission, which carries the first global hyperspectral instrument designed for the measurement of ocean color, should enable a more precise identification of phytoplankton absorption features (Werdell et al. 2019) and separation of those features from non-algal optical contributions (e.g., Pahlevan et al. 2021; Siegel et al. 2005) and thereby facilitate the assessment of changes in phytoplankton species or community composition (e.g., Kramer et al. 2022; Lange et al. 2020) that will further advance our ability to disentangle the impacts of climate forcing on global phytoplankton communities.

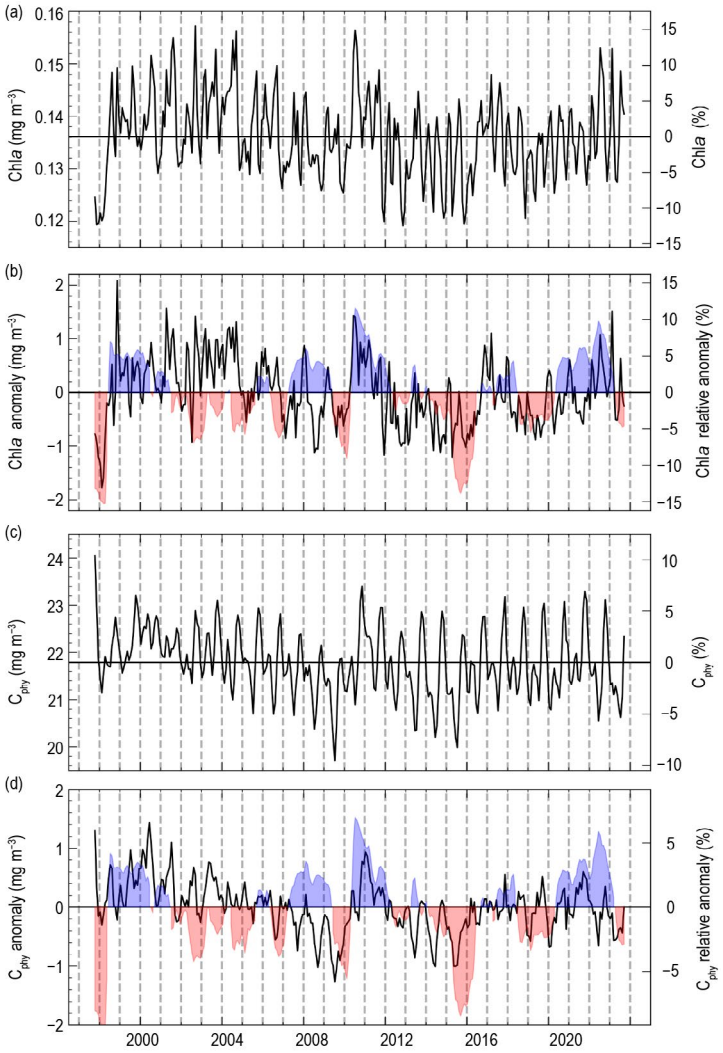

Fig. 3.26. Twenty-six-year, multi-mission record of chlorophyll-*a* (Chl*a*; mg m^{-3}) and phytoplankton carbon (C_{phy}; mg m^{-3}) averaged over the permanently stratified ocean (PSO; Oct 1997–Sep 2023). (a) Monthly Chl*a*, with the horizontal line indicating the multi-mission mean Chl*a* concentration for the entire PSO region. (b) Monthly Chl*a* anomalies after subtraction of the multi-mission climatological mean (Fig. 3.25a). (c) Monthly C_{phy}, with the horizontal line indicating the multi-mission mean C_{phy} concentration for the entire PSO region. (d) Monthly C_{phy} anomalies after subtraction of the multi-mission climatological mean (Fig. 3.25b). Shaded blue and red colors show the Multivariate El Niño–Southern Oscillation (ENSO) Index (MEI), inverted and scaled to match the range of the Chl*a* and C_{phy} anomalies, where blue indicates La Niña and red indicates El Niño conditions.

j. Global ocean carbon cycle

—R. Wanninkhof, J. A. Triñanes, P. Landschützer, A. Jersild, R. A. Feely, and B. R. Carter

1. INTRODUCTION

The oceans play a major role in the global carbon cycle by taking up a substantial fraction of the excess carbon dioxide that humans release into the atmosphere. As a consequence of humankind's collective carbon dioxide (CO_2) release into the atmosphere, referred to as anthropogenic CO_2 (C_{ant}) emissions, the atmospheric CO_2 concentration has risen from pre-industrial levels of about 278 ppm (parts per million) to 419.3±0.1 ppm in 2023 (see section 2g1 for details). Marine C_{ant} is the major cause of anthropogenic ocean acidification. Over the last decade the global ocean has continued to take up C_{ant} and therefore is a major mediator of global climate change. Of the 10.9±0.8 Pg C yr^{-1} C_{ant} released during the period 2013–22, 2.8±0.4 Pg C yr^{-1} (26%) accumulated in the ocean, 3.3±0.8 Pg C yr^{-1} (28%) accumulated on land, and 5.2±0.02 Pg C yr^{-1} (46%) remained in the atmosphere, with an imbalance of −0.4 Pg C yr^{-1} (–3%; see Table 7 in Friedlingstein et al. 2023). This decadal C_{ant} uptake estimate is a consensus view from a combination of measured ocean decadal CO_2 inventory changes, global ocean biogeochemical models, and global air–sea CO_2 flux estimates based on surface ocean fugacity of CO_2 (fCO_{2w})[1] measurements.

This year saw the release of several significant syntheses of ocean C_{ant}, including global and regional chapters of the second REgional Carbon Cycle Assessment and Processes (RECCAP2) assessment (see e.g., DeVries et al. 2023). The C_{ant} accumulation rate estimates from these studies agree with the overall rates given by Friedlingstein et al. (2023), but show differing patterns of variability in the ocean C_{ant} accumulation rate with time.

2. AIR–SEA CARBON DIOXIDE FLUXES

Ocean uptake of CO_2 is estimated from the net air–sea CO_2 flux derived from a bulk flux formula determined from the product of air and surface-seawater fCO_2 difference (ΔfCO_2) and gas transfer coefficients. Gas transfer is parameterized with wind as described in Wanninkhof (2014). This provides a net flux estimate. Here, 0.65 Pg C yr^{-1} is applied as the river adjustment (Regnier et al. 2022) as recommended in the Global Carbon Budget 2023 and RECCAP2 to convert the net flux to the C_{ant} flux. The data sources for fCO_{2w} are annual updates of observations from the Surface Ocean CO_2 Atlas (SOCAT) composed of moorings, autonomous surface vehicles, and ship-based observations (Bakker et al. 2016), with SOCAT v2023 containing 35.6 million data points from 1957 through 2022 (Bakker et al. 2023). The increased observations and improved mapping techniques, including machine learning methods summarized in Rödenbeck et al. (2015), now provide annual global fCO_{2w} fields on a 1° latitude × 1° longitude grid at monthly time scales. For this report, we use a self-organizing maps feed-forward neural network (SOM-FNN) approach of Landschützer et al. (2013, 2014) using SOCATv2023 for training. The monthly 2023 fCO_{2w} maps use as predictor variables: sea-surface temperature (SST; Rayner et al. 2003); chlorophyll-*a* (Globcolour; Maritorena et al. 2010); mixed-layer depth (de Boyer Montégut et al. 2004; Schmidtko et al. 2013), and salinity (Good et al. 2013). For atmospheric CO_2, the zonally-resolved NOAA marine boundary layer atmospheric CO_2 product is used (Dlugokencky et al. 2021). The gas transfer coefficients are determined using European Centre for Medium-Range Weather Forecasts Reanalysis version 5 (ERA5) winds (Hersbach et al. 2018). The air–sea CO_2 flux maps for 2023 do not include fCO_{2w} observations for 2023 but rather are created by extrapolation using the predictor variables. The uptake of the fCO_2-based models such as the Flanders Marine Institute (VLIZ) SOM-FNN used here is substantially larger than the model-based estimates, with differences in uptake of ≈1 Pg C in 2022.

The VLIZ SOM FNN results (Fig. 3.27) show a steady ocean CO_2 sink from 1982 to 1998, followed by a period of decreasing uptake from 1998 to 2002. There is a strong increase in the ocean sink from 2002 onward that continues through 2016, after which the global uptake shows a small increase up to 2023. The C_{ant} flux of 3.8 Pg C yr^{-1} for 2023 (green line in Fig. 3.27) shows a substantial 0.34 Pg C increase in uptake above the 2013–22 average of 3.46±0.11 Pg C yr^{-1}. The amplitude of seasonal variability is ≈1.2 Pg C with a minimum uptake in June–September.

[1] The fugacity is the partial pressure of CO_2 (pCO_2) corrected for non-ideality. They are numerically similar for surface waters with $fCO_2 \approx 0.994\ pCO_2$.

Sea-surface temperature anomalies can manifest themselves in differing ways on fCO_{2w}. Positive SST anomalies will decrease solubility and thereby increase fCO_{2w}. However, in regions with high fCO_{2w} due to upwelling, warmer SSTs as a result of decreased upwelling of cold CO_2-rich water will lower fCO_{2w}.

The annual average flux map for 2023 (Fig. 3.28a) shows the characteristic pattern of high effluxes (ocean-to-air CO_2 fluxes) in tropical, coastal upwelling, and open-ocean upwelling regions. Coastal upwelling regions include those in the Arabian Sea and off the west coasts of North and South America. The western Bering Sea was a strong CO_2 source in 2023, a clear juxtaposition to the strong sink in the surrounding regions. This regional source is hypothesized to result from a local outcropping of shallow isopycnals with high CO_2 values, but this has not been independently verified. Cumulatively, the regions of effluxes are substantial CO_2 sources to the atmosphere (≈1 Pg C). The primary CO_2 uptake regions are in the subtropical and subpolar regions. The largest sinks are poleward of the sub-tropical fronts. In the Southern Ocean, the area near the polar front (~60°S) was a weak to moderate sink in 2023.

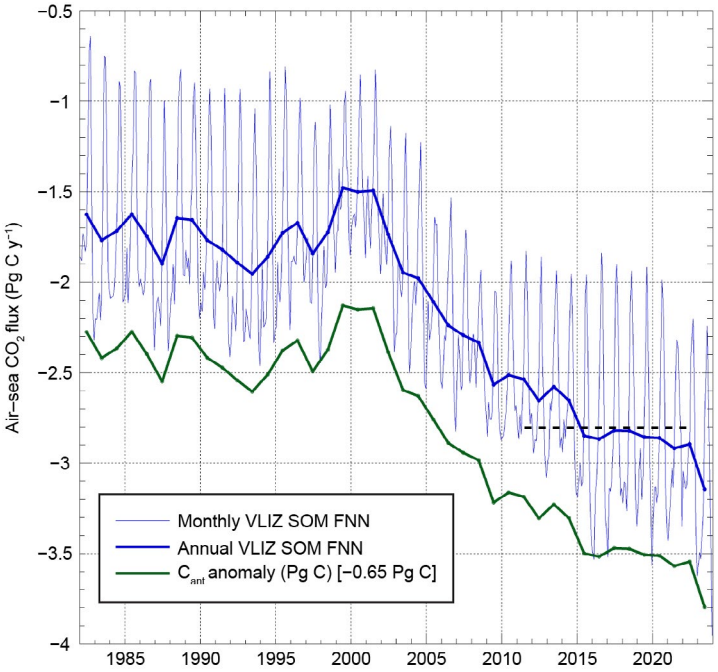

Fig. 3.27. Global annual (thick blue line) and monthly (thin blue line) net air-sea carbon dioxide (CO_2) fluxes (Pg C yr^{-1}) for 1982–2023 using the Flanders Marine Institute (VLIZ) self-organizing maps feed-forward neural network (SOM-FNN) output. The annual anthropogenic CO_2 (C_{ant}) air–sea flux (thick green line) includes a riverine adjustment of –0.65 Pg C. The black dashed line is the 2013–22 mean C_{ant} flux based on models and fCO_2 products (Friedlingstein et al. 2023). Negative values indicate CO_2 uptake by the ocean.

In the Northern Hemisphere, the entire North Atlantic is a large sink while in the North Pacific the sink region is punctuated by a substantial source of CO_2 in the western to central Bering Sea. The Northern Hemisphere sinks are, in part, due to the position of the western boundary currents whose cooling waters when transported poleward cause an increase in solubility and contribute to CO_2 uptake at high latitudes. The Gulf Stream/North Atlantic Drift in the Atlantic extends farther north than the Kuroshio in the Pacific, extending the region of a strong sink in the North Atlantic.

The ocean carbon uptake anomalies (Fig. 3.28c) in 2023 relative to the 1990–2020 average, adjusted for the 20-year trend, show the substantial effect of the El Niño condition in the second half of 2023, with reduced upwelling and lower effluxes in the eastern equatorial Pacific (EEP). The Southern Ocean shows a band of increased uptake (≈45°S–60°S), associated with a weak positive SST anomaly. The larger sink is attributed to weaker exchange with deep water in these regions of mode water outcropping (Hauck et al. 2023). Large regions in the subtropical gyres show positive anomalies due to the marine heat waves prevalent during 2023 (Sidebar 3.1) and the associated lower solubility enhancing outgassing or decreased uptake. Of note is the wedge of anomalously high outgassing in the central equatorial Pacific adjacent to the region of decreased outgassing due to repressed upwelling showing that in the Central Pacific, the thermal effects are larger than the impact of decreased upwelling. Globally, the impact of reduced outgassing in the EEP due to the El Niño, and increasing uptake in the Southern Ocean due to decreased exposure of the surface-to-mode waters, is much greater than the increase in fCO_{2w} due to the marine heatwaves in mid- and high latitudes (Sidebar 3.1).

The spatial differences in CO_2 fluxes between 2023 and 2022 (Fig. 3.28b) resemble that of the longer-term anomaly (Fig. 3.28c). The negative flux anomalies in the EEP are due to the transition from the triple dip La Niña to a strong El Niño in the summer of 2023. The regions of increased effluxes/decreased influxes in the Northern Hemisphere correspond with the positive SST anomalies in the boreal summer. The increased uptake in the Southern Ocean (45°S–60°S) latitude

band resembles that of the longer-term anomaly with the same attribution. The strong source in the western Bering Sea (Fig 3.28a) shows up as a positive anomaly compared to the long-term average but has decreased in the last year.

3. OCEAN INTERIOR INVENTORY ESTIMATES

An important insight from the RECCAP2 synthesis study is that the global air-to-sea CO_2 flux, which was found to have increased by 0.61±0.12 PgC yr^{-1} from 2001 to 2018, is dominated by the flux of C_{ant}. C_{ant} accumulation rate estimates averaged across years therefore provide a constraint on the decadal air–sea CO_2 flux. The C_{ant} in Fig. 3.27 is derived from the net air–sea CO_2 flux by assuming a constant source of CO_2 to the ocean from land and sediment fluxes and assuming that there are no natural variations in the ocean carbon inventory; however, the RECCAP2 synthesis also finds that climate-driven variability in the natural ocean carbon inventory is potentially a significant component of the overall CO_2 flux variations and is inconsistently represented across CO_2 flux estimation methods. It is therefore important to obtain independent estimates of C_{ant} and to separately quantify both the C_{ant} changes and the overall ocean carbon inventory changes.

Ocean carbon inventory changes provide means of estimating ocean C_{ant} accumulation quantity directly. The global RECCAP2 synthesis (DeVries et al. 2023) estimated an overall C_{ant} accumulation rate of 2.7±0.3 Pg C yr^{-1} from 2001 to 2018 based on a collection of reanalysis-forced global ocean biogeochemical model experiments and simulations with an ocean circulation inverse model fit to measurements of ocean physics and transient tracers for air–sea gas exchange. This result is indistinguishable from the consensus estimate of 2.8±0.4 Pg C yr^{-1} for 2013–22 of Friedlingstein et al. (2023) and the 2.8±0.3 Pg C yr^{-1} estimate for 1994–2014 given by Müller et al. (2023) from an analysis of multiple decades of seawater ocean carbon content measurements; however, the RECCAP2 synthesis finds that the global ocean C_{ant} accumulation rate increased by 0.34±0.06 PgC yr^{-1} $decade^{-1}$ and 0.41±0.03 PgC yr^{-1} $decade^{-1}$ from 2001 to 2018 from reanalysis-forced and steady-state ocean circulation inverse models, respectively, whereas the observational study by Müller et al. (2023) showed that the accumulation rate instead slowed by ~0.2 PgC yr^{-1} $decade^{-1}$ between 1994–2004 and 2004–14. Müller et al. (2023) argue that C_{ant} accumulation would be expected to intensify by ~0.2 PgC yr^{-1} $decade^{-1}$ given steady state ocean circulation, constant seawater chemistry, and the observed accelerating atmospheric C_{ant} accumulation between these time periods, so the observed accumulation rate in fact slowed down by 15±11% relative to expectations; however, this claim of a slowing ocean C_{ant} sink, which they attribute to changing ocean chemistry and circulation, can

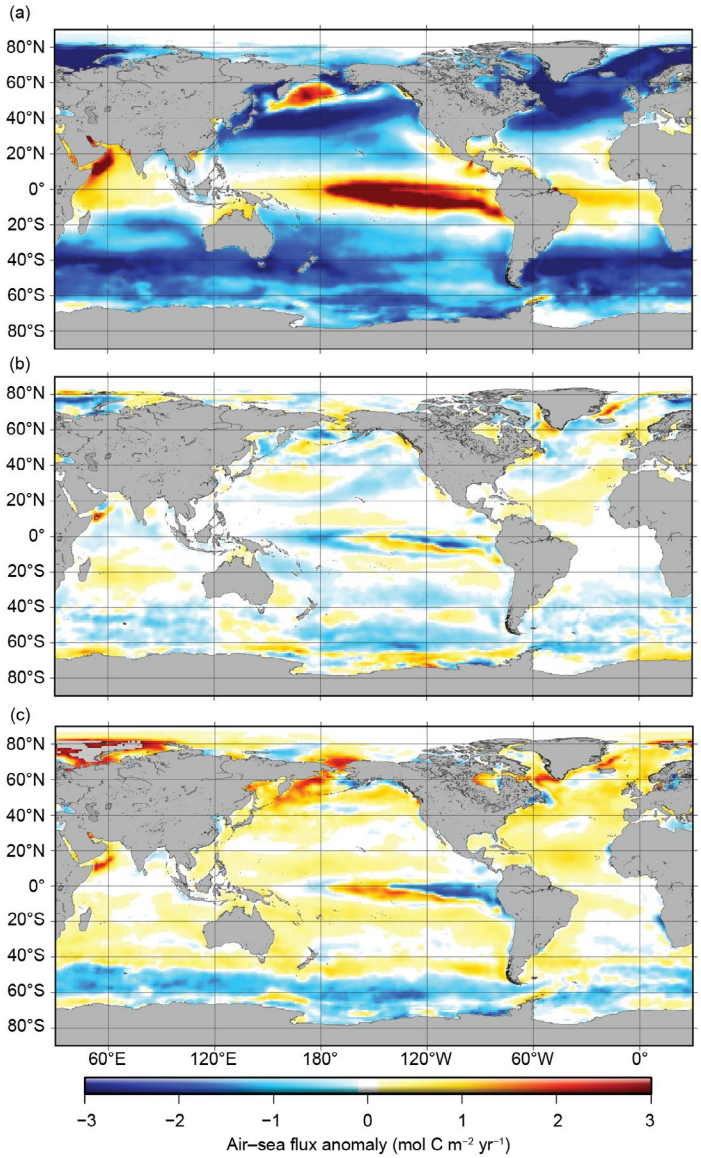

Fig. 3.28. Global map of (a) net air–sea carbon dioxide (CO_2) fluxes for 2023, (b) net air–sea CO_2 flux anomalies for 2023 minus 2022, and (c) net air–sea CO_2 flux anomalies for 2023 relative to 1990–2020 average values adjusted for the 20-year trend using the Flanders Marine Institute (VLIZ) self-organizing maps feed-forward neural network (SOM-FNN) approach. Units are all mol C m^{-2} yr^{-1}. Ocean CO_2 uptake regions are shown in blue. For reference, a global ocean CO_2 uptake of 2.8 Pg C yr^{-1} equals a flux density of –0.65 mol C m^2 yr^{-1}.

only be made with modest statistical confidence. Müller et al. (2023) find meaningful differences from earlier regional estimates: In the South Pacific and the North Atlantic, Müller et al. (2023) find statistically insignificant decreases in accumulation rates where earlier studies (Carter et al. 2019; Woosley et al. 2016) found statistically significant increasing rates; in the South Atlantic, they find a rapidly increasing accumulation rate where an earlier study (Woosley et al. 2016) found a consistent accumulation rate. Methodological decisions that differed among these studies can lead to meaningful variations in the findings.

Comparisons of C_{ant} accumulation rate variations from Müller et al. (2023), the RECCAP2 synthesis, and earlier analyses reveal consistency between the multi-decadal C_{ant} accumulation rates but also show different patterns of regional and temporal accumulation rate variability (Fig. 3.29; Sabine et al. 2004; Gruber et al. 2019; Mueller et al. 2023; Lauvset et al. 2016; DeVries 2014; Davila et al. 2022; Khatiwala et al. 2009; Waugh et al. 2006). The disagreements in the findings from these various C_{ant} accumulation rate estimates therefore parallel an increasing disagreement noted in CO_2 flux estimates derived from global ocean biogeochemistry models and fCO_2 products (Friedlingstein et al. 2023). In both cases the broad patterns of natural and anthropogenic ocean carbon accumulation are clear, but the decadal variations in ocean carbon accumulation are less well constrained and in need of robust uncertainty quantification.

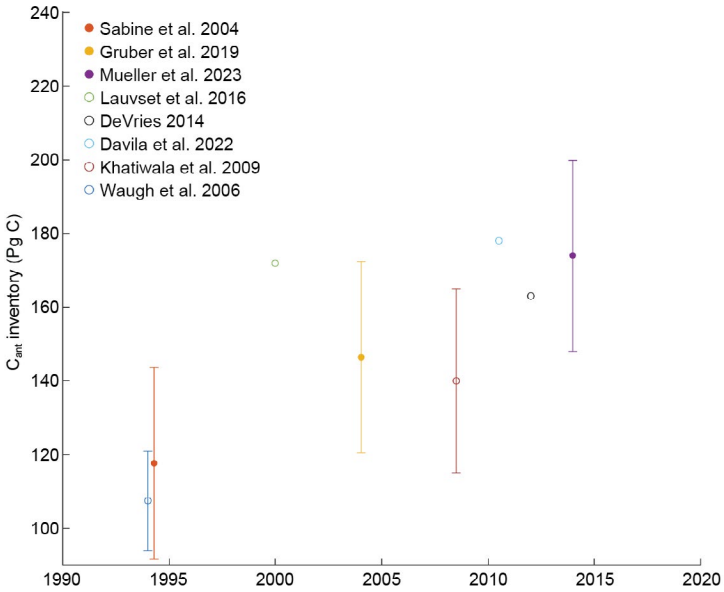

Fig. 3.29. A compilation of data-based global ocean anthropogenic carbon inventory estimates vs. the year for which the estimate is made. While these estimates vary considerably with respect to methodology and the underlying measurements, a general increasing trend can be seen consistent with ongoing ocean anthropogenic CO_2 (C_{ant}) accumulation.

Appendix 1: Acronyms

ACC	Antarctic Circumpolar Current
BASS	Blended Analysis of Surface Salinity
b_{bp}	particle backscattering coefficient
C_{ant}	anthropogenic CO_2
CERES	Clouds and the Earth's Radiant Energy Systems
Chl*a*	chlorophyll-*a*
CO_2	carbon dioxide
COARE	Coupled Ocean Atmosphere Response Experiment
C_{phy}	phytoplankton carbon
E	Evaporation
EBAF	Energy Balanced and Filled
EEP	eastern equatorial Pacific
EKE	eddy kinetic energy
ENSO	El Niño–Southern Oscillation
ERA5	European Centre for Medium-Range Weather Forecasts Reanalysis version 5
FC	Florida Current
fCO_{2w}	surface ocean fugacity of CO_2
FlashFlux	Fast Longwave And Shortwave Radiative Fluxes
GMSL	global mean sea level
GPCP	Global Precipitation Climatology Project
IOD	Indian Ocean dipole
ITCZ	Intertropical Convergence Zone
LH	latent heat
LW	longwave radiation
MEI	Multivariate ENSO Index
MHT	meridional heat transport
MHW	marine heatwave
MOC	meridional overturning circulation
MODIS	Moderate Resolution Imaging Spectroradiometer
MODIS-A	Moderate Resolution Imaging Spectroradiometer on Aqua
NBC	North Brazil Current
NECC	North Equatorial Countercurrent
OAFlux	Objectively Analyzed Air–Sea Heat Fluxes
OHCA	ocean heat content anomaly
OSNAP	Overturning in the Subpolar North Atlantic Program
P	Precipitation
PACE	Plankton, Aerosol, Cloud, ocean Ecosystem
pCO_2	partial pressure of CO_2
PDO	Pacific Decadal Oscillation
PSO	permanently stratified ocean
Q_{net}	net surface heat flux
RAPID	Rapid Climate Change
RECCAP2	REgional Carbon Cycle Assessment and Processes
SD	standard deviation
SeaWiFS	Sea-viewing Wide Field-of-view Sensor
SEC	South Equatorial Current
SH	Southern Hemisphere
SIO	Scripps Institution of Oceanography
SMAP	Soil Moisture Active Passive

SMOS	Soil Moisture and Ocean Salinity
SOCAT	Surface Ocean CO_2 Atlas
SOM-FNN	self-organizing maps feed-forward neural network
SPCZ	South Pacific Convergence Zone
SSS	sea-surface salinity
SST	sea-surface temperature
SSTA	sea-surface temperature anomaly
SW	shortwave radiation
VIIRS	Visible Infrared Imaging Radiometer Suite
VIIRS-N_{20}	Visible Infrared Imaging Radiometer Suite on NOAA20
VLIZ	Flanders Marine Institute
XBT	Expendable Bathythermograph
YC	Yucatan Current
$\Delta\, fCO_2$	fCO_2 difference

Appendix 2: Datasets and sources

Section 3b Sea Surface Temperature

Sub-section	General Variable or Phenomenon	Specific dataset or variable	Source
3b	Sea Surface Temperature	ERSSTv5	https://doi.org/10.7289/V5T72FNM
3b	Sea Surface Temperature	HadSST4	https://www.metoffice.gov.uk/hadobs/hadsst4/
3b	Sea Surface Temperature	NOAA Daily Optimum Interpolated Temperature (DOISST)	https://doi.org/10.25921/RE9P-PT57

Section 3c Ocean Heat Content

Sub-section	General Variable or Phenomenon	Specific dataset or variable	Source
3c	Ocean Heat Content	Argo	http://doi.org/10.17882/42182#98916
3c	Ocean Heat Content	RFROM	https://www.pmel.noaa.gov/rfrom/
3c	Ocean Heat Content	CLIVAR and Carbon Hydrographic Data Office	https://cchdo.ucsd.edu/
3c	Ocean Heat Content	IAP/CAS	http://www.ocean.iap.ac.cn/pages/dataService/dataService.html
3c	Ocean Heat Content	MRI/JMA	www.data.jma.go.jp/gmd/kaiyou/english/ohc/ohc_global_en.html
3c	Ocean Heat Content	NCEI	https://www.ncei.noaa.gov/access/global-ocean-heat-content/
3c	Ocean Heat Content	PMEL/JPL/JIMAR	http://oceans.pmel.noaa.gov
3c	Ocean Heat Content	UK Met Office EN4.2.2	https://www.metoffice.gov.uk/hadobs/en4/download-en4-2-2.html

Section 3d Salinity

Sub-section	General Variable or Phenomenon	Specific dataset or variable	Source
3d2	Ocean Salinity	Argo	https://usgodae.org/argo/argo.html
3d2	Ocean Salinity	Blended Analysis for Surface Salinity	ftp://ftp.cpc.ncep.noaa.gov/precip/BASS
3d2	Ocean Salinity	World Ocean Atlas 2013	www.nodc.noaa.gov/OC5/woa13/
3d3	Ocean Salinity	NCEI salinity anomaly	https://www.ncei.noaa.gov/access/global-ocean-heat-content/
3d3	Ocean Salinity	World Ocean Atlas 2018	www.nodc.noaa.gov/OC5/woa18/

Section 3e Global ocean heat, freshwater, and momentum flux

Sub-section	General Variable or Phenomenon	Specific dataset or variable	Source
3e1	Air-sea fluxes (shortwave/longwave radiation)	CERES Energy Balanced and Filled version 4.2	https://asdc.larc.nasa.gov/project/CERES/CERES_EBAF_Edition4.2
3e1	Air-sea fluxes (shortwave/longwave radiation)	CERES FLASHflux 4A product	https://cmr.earthdata.nasa.gov/search/concepts/C1719147151-LARC_ASDC.html
3e1	Air-sea fluxes (latent heat/sensible heat)	OAFlux2	https://oaflux.whoi.edu/
3e2	Precipitation	Global Precipitation Climatology Project (GPCP) v2.3	https://psl.noaa.gov/data/gridded/data.gpcp.html
3e2	Evaporation	OAFlux2	https://oaflux.whoi.edu/
3e3	Wind stress	OAFlux2	https://oaflux.whoi.edu/

Section 3f Sea Level variability and change

Sub-section	General Variable or Phenomenon	Specific dataset or variable	Source
3f	Ocean Heat Content	Argo monthly climatology	https://sio-argo.ucsd.edu/RG_Climatology.html
3f	Ocean Mass	GRACE/GRACE FO	https://grace.jpl.nasa.gov/data/get-data
3f	Sea Level / Sea Surface Height	Argo	https://usgodae.org/argo/argo.html
3f	Sea Level / Sea Surface Height	NASA MEaSURES	https://podaac.jpl.nasa.gov/dataset/SEA_SURFACE_HEIGHT_ALT_GRIDS_L4_2SATS_5DAY_6THDEG_V_JPL2205
3f	Sea Level/Sea Surface Height	NASA Sea Level Change Program	https://podaac.jpl.nasa.gov/dataset/MERGED_TP_J1_OSTM_OST_ALL_V51
3f	Sea Level / Sea Surface Height	NCEI steric sea level	https://www.ncei.noaa.gov/access/global-ocean-heat-content/
3f	Sea Level / Sea Surface Height	NOAA Laboratory for Sea Level Altimetry	www.star.nesdis.noaa.gov/sod/lsa/SeaLevelRise/LSA_SLR_timeseries.php
3f	Sea Level / Sea Surface Height	Tide Gauge	http://uhslc.soest.hawaii.edu/
3f	Sea Level / Sea Surface Height	University of Texas Center for Space Research Gravity field	https://podaac.jpl.nasa.gov/dataset/TELLUS_GRAC_L3_CSR_RL06_OCN_v04

Section 3g Surface Currents

Sub-section	General Variable or Phenomenon	Specific dataset or variable	Source
3g	ocean currents	Global Drifter Program	https://www.aoml.noaa.gov/phod/gdp/interpolated/data/all.php
3g3	ocean currents	Atlantic ocean monitoring	https://www.aoml.noaa.gov/phod/altimetry/cvar/

Section 3h Meridional Overturning Circulation and Heat Transport in the Atlantic Ocean

Sub-section	General Variable or Phenomenon	Specific dataset or variable	Source
3h	ocean currents	Atlantic Ship of Opportunity XBT	https://www.aoml.noaa.gov/phod/goos/xbt_network/
3h	ocean currents	Argo	https://usgodae.org/argo/argo.html
3h	ocean currents	Florida Current transport	https://www.aoml.noaa.gov/phod/floridacurrent/data_access.php
3h	ocean currents	Global Temperature and Salinity Profile Program (GTSPP)	https://www.ncei.noaa.gov/products/global-temperature-and-salinity-profile-programme
3h	ocean currents	MOVE array	http://www.oceansites.org/tma/move.html
3h	ocean currents	OSNAP	https://www.o-snap.org/
3h	ocean currents	RAPID array	https://rapid.ac.uk/rapidmoc/
3h	ocean currents	SAMBA	http://www.oceansites.org/tma/samba.html

Section 3i Global Ocean Phytoplankton

Sub-section	General Variable or Phenomenon	Specific dataset or variable	Source
3i	Phytoplankton, Ocean Color	MODIS-Aqua	https://oceancolor.gsfc.nasa.gov/reprocessing/

Section 3j Global Ocean Carbon Cycle

Sub-section	General Variable or Phenomenon	Specific dataset or variable	Source
3j2	Ocean Carbon	SOCAT version 2022	https://doi.org/10.25921/r7xa-bt92
3j2	Sea Surface Temperature	NOAA Optimum Interpolation SST (OISST) v2.1	https://www.ncei.noaa.gov/products/optimum-interpolation-sst
3j2	Chlorophyll	GlobColour	https://www.globcolour.info/
3j2	Atmospheric Carbon Dioxide	NOAA Greenhouse Gas Marine Boundary Layer Reference	https://gml.noaa.gov/ccgg/mbl/mbl.html
3j2	Winds [Near] Surface	ERA5	https://www.ecmwf.int/en/forecasts/datasets/reanalysis-datasets/era5
3j2	Ocean Salinity	Hadley Center EN4	https://www.metoffice.gov.uk/hadobs/en4/
3j3	Ocean Temperature	Argo monthly climatology	https://sio-argo.ucsd.edu/RG_Climatology.html
3j3	Ocean Salinity	Argo monthly climatology	https://sio-argo.ucsd.edu/RG_Climatology.html

Sidebar 3.1 Marine Heatwaves in 2023

Sub-section	General Variable or Phenomenon	Specific dataset or variable	Source
SB3.1	Sea Surface Temperature	OISSTv2.1.	https://www.ncei.noaa.gov/products/optimum-interpolation-sst

References

Adler, R. F., and Coauthors, 2018: The Global Precipitation Climatology Project (GPCP) monthly analysis (new version 2.3) and a review of 2017 global precipitation. *Atmosphere*, **9**, 138, https://doi.org/10.3390/atmos9040138.

Bakker, D. C. E., and Coauthors, 2016: A multi-decade record of high-quality fCO_2 data in version 3 of the Surface Ocean CO_2 Atlas (SOCAT). Earth Syst. *Sci. Data*, **8**, 383–413, https://doi.org/10.5194/essd-8-383-2016.

—— , and Coauthors, 2023: Surface Ocean CO2 Atlas Database version 2023 (SOCATv2023) (NCEI Accession 0278913). NOAA/NCEI, accessed 4 January 2024, https://doi.org/10.25921/r7xa-bt92.

Balaguru, K., P. Chang, R. Saravanan, L. R. Leung, Z. Xu, M. Li, and J. S. Hsieh, 2012: Ocean barrier layers' effect on tropical cyclone intensification. *Proc. Natl. Acad. Sci. USA*, **109**, 14343–14347, https://doi.org/10.1073/pnas.1201364109.

Barnoud, A., and Coauthors, 2021: Contributions of altimetry and Argo to non-closure of the global mean sea level budget since 2016. *Geophys. Res. Lett.*, **48**, e2021GL092824, https://doi.org/10.1029/2021GL092824.

Beal, L., V. Hormann, R. Lumpkin, and G. Foltz, 2013: The response of the surface circulation of the Arabian Sea to monsoonal forcing. *J. Phys. Oceanogr.*, **43**, 2008–2022, https://doi.org/10.1175/JPO-D-13-033.1.

Beckley, B., and Coauthors, 2021: Global mean sea level trend from integrated multi-mission ocean altimeters TOPEX/Poseidon, Jason-1, OSTM/Jason-2, and Jason-3 version 5.1. PODAAC, accessed 29 January 2024, https://doi.org/10.5067/GMSLM-TJ151.

—— , and Coauthors, 2023: Assessment of reprocessed TOPEX/Jason/Sentinel-6 altimetry: Impact on global mean sea level estimates. 2023 Ocean Surface Topography Science Team Meeting, San Juan, PR, AVISO, https://doi.org/10.24400/527896/a03-2023.3813.

Behrenfeld, M. J., and Coauthors, 2006: Climate-driven trends in contemporary ocean productivity. *Nature*, **444**, 752–755, https://doi.org/10.1038/nature05317.

—— , and Coauthors, 2015: Reevaluating ocean warming impacts on global phytoplankton. *Nat. Climate Change*, **6**, 323–330, https://doi.org/10.1038/nclimate2838.

Boyer, T. P., and Coauthors, 2018: World Ocean Database 2018. NOAA Atlas NESDIS 87, 207 pp., https://www.nodc.noaa.gov/OC5/WOD/pr_wod.html.

Brown, S., S. Desai, and C. S. Chae, 2023: Progress on the wet path delay correction: Historical, current and future. 2023 Ocean Surface Topography Science Team Meeting, San Juan, PR, AVISO, https://doi.org/10.24400/527896/a03-2023.3701.

Bryden, H. L., W. E. Johns, B. A. King, G. McCarthy, E. L. McDonagh, B. I. Moat, and D. A. Smeed, 2020: Reduction in ocean heat transport at 26°N since 2008 cools the eastern subpolar gyre of the North Atlantic Ocean. *J. Climate*, **33**, 1677–1689, https://doi.org/10.1175/JCLI-D-19-0323.1.

Caesar, L., S. Rahmstorf, A. Robinson, G. Fuelner, and V. Saba, 2018: Observed fingerprint of a weakening Atlantic Ocean overturning circulation. *Nature*, **556**, 191–196, https://doi.org/10.1038/s41586-018-0006-5.

—— , G. D. McCarthy, D. J. R. Thornalley, N. Cahill, and S. Rahmstorf, 2021: Current Atlantic meridional overturning circulation weakest in last millennium. *Nat. Geosci.*, **14**, 118–120, https://doi.org/10.1038/s41561-021-00699-z.

Caínzos, V., A. Hernández-Guerra, G. D. McCarthy, E. L. McDonagh, M. Cubas Armas, and M. D. Pérez-Hernández, 2022: Thirty years of GOSHIP and WOCE data: Atlantic overturning of mass, heat, and freshwater transport. *Geophys. Res. Lett.*, **49**, e2021GL096527, https://doi.org/10.1029/2021GL096527.

Carter, B. R., and Coauthors, 2019: Pacific anthropogenic carbon between 1991 and 2017. *Global Biogeochem. Cycles*, **33**, 597–617, https://doi.org/10.1029/2018GB006154.

Chambers, D. P., A. Cazenave, N. Champollion, H. Dieng, W. Llovel, R. Forsberg, K. von Schuckmann, and Y. Wada, 2017: Evaluation of the global mean sea level budget between 1993 and 2014. *Surv. Geophys.*, **38**, 309–327, https://doi.org/10.1007/s10712-016-9381-3.

Chen, J., B. Tapley, C. Wilson, A. Cazenave, K. W. Seo, and J. S. Kim, 2020: Global ocean mass change from GRACE and GRACE Follow-On and altimeter and Argo measurements. *Geophys. Res. Lett.*, **47**, e2020GL090656, https://doi.org/10.1029/2020GL090656.

Cheng, L., J. Zhu, R. Cowley, T. Boyer, and S. Wijffels, 2014: Time, probe type, and temperature variable bias corrections to historical expendable bathythermograph observations. *J. Atmos. Oceanic Technol.*, **31**, 1793–1825, https://doi.org/10.1175/JTECH-D-13-00197.1.

—— , and Coauthors, 2024: New record ocean temperatures and other related climate indicators in 2023. *Adv. Atmos. Sci.*, **41**, 1068–1082, https://doi.org/10.1007/s00376-024-3378-5.

Davila, X., G. Gebbie, A. Brakstad, S. K. Lauvset, E. L. McDonagh, J. Schwinger, and A. Olsen, 2022: How is the ocean anthropogenic carbon reservoir filled? *Global Biogeochem. Cycles*, **36**, e2021GB007055, https://doi.org/10.1029/2021GB007055.

de Boyer Montégut, C., G. Madec, A. S. Fischer, A. Lazar, and D. Ludicone, 2004: Mixed layer depth over the global ocean: An examination of profile data and a profile-based climatology. *J. Geophys. Res.*, **109**, C12003, https://doi.org/10.1029/2004JC002378.

Deser, C., M. A. Alexander, S.-P. Xie, and A. S. Phillips, 2010: Sea surface temperature variability: Patterns and mechanisms. *Annu. Rev. Mar. Sci.*, **2**, 115–143, https://doi.org/10.1146/annurev-marine-120408-151453.

DeVries, T., and Coauthors, 2023: Magnitude, trends, and variability of the global ocean carbon sink from 1985 to 2018. *Global Biogeochem. Cycles*, **37**, e2023GB007780, https://doi.org/10.1029/2023GB007780.

Dierssen, H. M., 2010: Perspectives on empirical approaches for ocean color remote sensing of chlorophyll in a changing climate. *Proc. Natl. Acad. Sci. USA*, **107**, 17073–17078, https://doi.org/10.1073/pnas.0913800107.

Dlugokencky, E. J., K. W. Thoning, X. Lan, and P. P. Tans, 2021: NOAA greenhouse gas reference from atmospheric carbon dioxide dry air mole fractions from the NOAA GML Carbon Cycle Cooperative Global Air Sampling Network. Accessed 19 January 2024, ftp://aftp.cmdl.noaa.gov/data/trace_gases/co2/flask/surface/.

Domingues, R., and Coauthors, 2015: Upper ocean response to Hurricane Gonzalo (2014): Salinity effects revealed by sustained and targeted observations from underwater gliders. *Geophys. Res. Lett.*, **42**, 7131–7138, https://doi.org/10.1002/2015GL065378.

—— , M. Baringer, and G. Goni, 2016: Remote sources for year-to-year changes in the seasonality of the Florida Current transport. *J. Geophys. Res. Oceans*, **121**, 7547–7559, https://doi.org/10.1002/2016JC012070.

—— , G. Goni, M. Baringer, and D. L. Volkov, 2018: What caused the accelerated sea level changes along the United States East Coast during 2010–2015? *Geophys. Res. Lett.*, **45**, 13 367–13 376, https://doi.org/10.1029/2018GL081183.

Dong, S., G. Goni, R. Domingues, F. Bringas, M. Goes, J. Christophersen, and M. Baringer, 2021: Synergy of in situ and satellite ocean observations in determining meridional heat transport in the Atlantic Ocean. *J. Geophys. Res. Oceans*, **126**, e2020JC017073, https://doi.org/10.1029/2020JC017073.

do Rosário Gomes, H., J. Goes, S. Matondkar, E. Buskey, S. Basu, S. Parab, and P. Thoppil, 2014: Massive outbreaks of *Noctiluca scintillans* blooms in the Arabian Sea due to spread of hypoxia. *Nat. Commun.*, **5**, 4862, https://doi.org/10.1038/ncomms5862.

Durack, P. J., and S. E. Wijffels, 2010: Fifty-year trends in global ocean salinities and their relationship to broad-scale warming. *J. Climate*, **23**, 4342–4362, https://doi.org/10.1175/2010JCLI3377.1.

—— , —— , and R. J. Matear, 2012: Ocean salinities reveal strong global water cycle intensification during 1950 to 2000. *Science*, **336**, 455–458, https://doi.org/10.1126/science.1212222.

Ezer, T., and L. P. Atkinson, 2014: Accelerated flooding along the U.S. East Coast: On the impact of sea-level rise, tides, storms, the Gulf Stream, and the North Atlantic Oscillations. *Earth's Future*, **2**, 362–382, https://doi.org/10.1002/2014EF000252.

Fairall, C. W., E. F. Bradley, J. E. Hare, A. A. Grachev, and J. B. Edson, 2003: Bulk parameterization of air–sea fluxes: Updates and verification for the COARE algorithm. *J. Climate*, **16**, 571–591, https://doi.org/10.1175/1520-0442(2003)016<0571:BPOASF>2.0.CO;2.

Fasullo, J. T., R. S. Nerem, and B. Hamlington, 2016: Is the detection of accelerated sea level rise imminent? *Sci. Rep.*, **6**, 31245, https://doi.org/10.1038/srep31245.

Ffield, A., 2007: Amazon and Orinoco River plumes and NBC rings: Bystanders or participants in hurricane events? *J. Climate*, **20**, 316–333, https://doi.org/10.1175/JCLI3985.1.

Field, C. B., M. J. Behrenfeld, J. T. Randerson, and P. Falkowski, 1998: Primary production of the biosphere: Integrating terrestrial and oceanic components. *Science*, **281**, 237–240, https://doi.org/10.1126/science.281.5374.237.

Fofonoff, N. P., and E. L. Lewis, 1979: A practical salinity scale. *J. Oceanogr. Soc. Japan*, **35**, 63–64, https://doi.org/10.1007/BF02108283.

Font, J., and Coauthors, 2013: SMOS first data analysis for sea surface salinity determination. *Int. J. Remote Sens.*, **34**, 3654–3670, https://doi.org/10.1080/01431161.2012.716541.

Fore, A. G., S. H. Yueh, W. Q. Tang, B. W. Stiles, and A. K. Hayashi, 2016: Combined active/passive retrievals of ocean vector wind and sea surface salinity with SMAP. IEEE Trans. *Geosci. Remote Sens.*, **54**, 7396–7404, https://doi.org/10.1109/TGRS.2016.2601486.

Franz, B. A., I. Cetinić, M. Gao, A. Siegel, and T. K. Westberry, 2023: Global ocean phytoplankton [in "State of the Climate in 2022"]. *Bull. Amer. Meteor. Soc.*, **104** (9), S184–S188, https://doi.org/10.1175/BAMS-D-23-0076.2.

—— , —— , A. Ibrahim, and A. Sayer, 2024: Anomalous trends in global ocean carbon concentrations following the 2022 eruptions of Hunga Tonga-Hunga Ha'apai. *Commun. Earth Environ.*, **5**, 247, https://doi.org/10.1038/s43247-024-01421-8.

Friedlingstein, P., and Coauthors, 2023: Global Carbon Budget 2023. *Earth Syst. Sci. Data*, **15**, 5301–5369, https://doi.org/10.5194/essd-15-5301-2023.

Fu, Y., F. Li, J. Karstensen, and C. Wang, 2020: A stable Atlantic meridional overturning circulation in a changing North Atlantic Ocean since the 1990s. *Sci. Adv.*, **6**, eabc7836, https://doi.org/10.1126/sciadv.abc7836.

—— , and Coauthors, 2023: Seasonality of the meridional overturning circulation in the subpolar North Atlantic. *Commun. Earth Environ.*, **4**, 181, https://doi.org/10.1038/s43247-023-00848-9.

Geider, R. J., H. L. MacIntyre, and T. M. Kana, 1997: Dynamic model of phytoplankton growth and acclimation: Responses of the balanced growth rate and the chlorophyll *a*: Carbon ratio to light, nutrient limitation and temperature. *Mar. Ecol. Prog. Ser.*, **148**, 187–200, https://doi.org/10.3354/meps148187.

Giglio, D., T. Sukianto, and M. Kuusela, 2024: Global ocean heat content anomalies and ocean heat uptake based on mapping Argo data using local Gaussian processes (3.0.0). Accessed 10 February 2024, https://doi.org/10.5281/zenodo.10645137.

Goes, J. I., and Coauthors, 2020: Ecosystem state change in the Arabian Sea fuelled by the recent loss of snow over the Himalayan-Tibetan Plateau region. *Sci. Rep.*, **10**, 7422, https://doi.org/10.1038/s41598-020-64360-2.

Goni, G. J., and W. E. Johns, 2003: Synoptic study of warm rings in the North Brazil Current retroflection region using satellite altimetry. *Interhemispheric Water Exchange in the Atlantic Ocean, G. J. Goni and P. Malanotte-Rizzoli, Eds., Elsevier Oceanography Series*, Vol. 68, Elsevier, 335–356, https://doi.org/10.1016/S0422-9894(03)80153-8.

—— , F. Bringas, and P. N. Di Nezio, 2011: Observed low frequency variability of the Brazil Current front. *J. Geophys. Res.*, **116**, C10037, https://doi.org/10.1029/2011JC007198.

Good, S. A., M. J. Martin, and N. A. Rayner, 2013: EN4: Quality controlled ocean temperature and salinity profiles and monthly objective analyses with uncertainty estimates. *J. Geophys. Res. Oceans*, **118**, 6704–6716, https://doi.org/10.1002/2013JC009067.

Gouretski, V., and L. Cheng, 2020: Correction for systematic errors in the global dataset of temperature profiles from mechanical bathythermographs. *J. Atmos. Oceanic Technol.*, **37**, 841–855, https://doi.org/10.1175/JTECH-D-19-0205.1.

Graff, J. R., T. K. Westberry, A. J. Milligan, M. B. Brown, G. Dall'Olmo, V. van Dongen-Vogels, K. M. Reifel, and M. J. Behrenfeld, 2015: Analytical phytoplankton carbon measurements spanning diverse ecosystems. *Deep-Sea Res. I*, **102**, 16–25, https://doi.org/10.1016/j.dsr.2015.04.006.

Gruber, N., and Coauthors, 2019: The oceanic sink for anthropogenic CO_2 from 1994 to 2007. *Science*, **363**, 1193–1199, https://doi.org/10.1126/science.aau5153.

Hakuba, M. Z., T. Frederikse, and F. W. Landerer, 2021: Earth's energy imbalance from the ocean perspective (2005–2019). Geophys. *Res. Lett.*, **48**, e2021GL093624, https://doi.org/10.1029/2021GL093624.

Hamlington, B. D., C. G. Piecuch, J. T. Reager, H. Chandanpurkar, T. Frederikse, R. S. Nerem, J. T. Fasullo, and S.-H. Cheon, 2020: Origin of interannual variability in global mean sea level. *Proc. Natl. Acad. Sci. USA*, **117**, 13 983–13 990, https://doi.org/10.1073/pnas.1922190117.

Hauck, J., and Coauthors, 2023: The Southern Ocean Carbon Cycle 1985–2018: Mean, seasonal cycle, trends, and storage. *Global Biogeochem. Cycles*, **37**, e2023GB007848, https://doi.org/10.1029/2023GB007848.

Held, I. M., and B. J. Soden, 2006: Robust responses of the hydrological cycle to global warming. *J. Climate*, **19**, 5686–5699, https://doi.org/10.1175/JCLI3990.1.

Hersbach, H., and Coauthors, 2018: ERA5 hourly data on single levels from 1959 to present. Copernicus Climate Change Service (C3S) Climate Data Store (CDS), accessed 2 January 2024, https://doi.org/10.24381/cds.adbb2d47.

Hobbs, W. R., and J. K. Willis, 2012: Midlatitude North Atlantic heat transport: A time series based on satellite and drifter data. *J. Geophys. Res.*, **117**, C01008, https://doi.org/10.1029/2011JC007039.

Hobday, A. J., and Coauthors, 2016: A hierarchical approach to defining marine heatwaves. *Prog. Oceanogr.*, **141**, 227–238, https://doi.org/10.1016/j.pocean.2015.12.014.

Holbrook, N. J., and Coauthors, 2019: A global assessment of marine heatwaves and their drivers. *Nat. Commun.*, **10**, 2624, https://doi.org/10.1038/s41467-019-10206-z.

Hu, C., Z. Lee, and B. Franz, 2012: Chlorophyll algorithms for oligotrophic oceans: A novel approach based on three-band reflectance difference. *J. Geophys. Res.*, **117**, C01011, https://doi.org/10.1029/2011JC007395.

—— , L. Feng, Z. Lee, B. A. Franz, S. W. Bailey, P. J. Werdell, and C. W. Proctor, 2019: Improving satellite global chlorophyll *a* data products through algorithm refinement and data recovery. *J. Geophys. Res. Oceans*, **124**, 1524–1543, https://doi.org/10.1029/2019JC014941.

Hu, Z.-Z., B. Huang, J. Zhu, A. Kumar, and M. J. McPhaden, 2019: On the variety of coastal El Niño events. *Climate Dyn.*, **52**, 7537–7552, https://doi.org/10.1007/s00382-018-4290-4.

Huang, B., and Coauthors, 2015: Extended Reconstructed Sea Surface Temperature version 4 (ERSST.v4), Part I. Upgrades and intercomparisons. *J. Climate*, **28**, 911–930, https://doi.org/10.1175/JCLI-D-14-00006.1.

—— , and Coauthors, 2017: Extended Reconstructed Sea Surface Temperature version 5 (ERSSTv5), Upgrades, validations, and intercomparisons. *J. Climate*, **30**, 8179–8205, https://doi.org/10.1175/JCLI-D-16-0836.1.

—— , and Coauthors, 2020: Uncertainty estimates for sea surface temperature and land surface air temperature in NOAAGlobalTemp version 5. *J. Climate*, **33**, 1351–1379, https://doi.org/10.1175/JCLI-D-19-0395.1.

—— , C. Liu, V. Banzon, E. Freeman, G. Graham, B. Hankins, T. Smith, and H.-M. Zhang, 2021: Improvements of the Daily Optimum Interpolation Sea Surface Temperature (DOISST) version 2.1. *J. Climate*, **34**, 2923–2939, https://doi.org/10.1175/JCLI-D-20-0166.1.

Hughes, T., and Coauthors, 2017: Global warming and recurrent mass bleaching of corals. *Nature*, **543**, 373–377, https://doi.org/10.1038/nature21707.

IPCC, 2021: Climate Change 2021: The Physical Science Basis. V. Masson-Delmotte et al., Eds., Cambridge University Press, 2391 pp., https://doi.org/10.1017/9781009157896.

Ishii, M., Y. Fukuda, S. Hirahara, S. Yasui, T. Suzuki, and K. Sato, 2017: Accuracy of global upper ocean heat content estimation expected from present observational datasets. *SOLA*, **13**, 163–167, https://doi.org/10.2151/sola.2017-030.

Jiang, S., C. Zhu, Z.-Z. Hu, N. Jiang, and F. Zheng, 2023: Triple-dip La Niñas in 2020-2022: Understanding the role of the annual cycle in the tropical Pacific SST. Environ. *Res. Lett.*, **18**, 084002, https://doi.org/10.1088/1748-9326/ace274.

Johns, W. E., S. Elipot, D. A. Smeed, B. Moat, B. King, D. L. Volkov, and R. H. Smith, 2023: Towards two decades of Atlantic Ocean mass and heat transports at 26.5°N. Philos. *Trans. Roy. Soc.*, **A381**, 20220188, https://doi.org/10.1098/rsta.2022.0188.

Johnson, G. C., and J. M. Lyman, 2012: Sea surface salinity [in "State of the Climate in 2011"]. *Bull. Amer. Meteor. Soc.*, **93** (7), S68–S69, https://doi.org/10.1175/2012BAMSStateoftheClimate.1.

—— , —— , J. K. Willis, T. Boyer, J. Antonov, S. A. Good, C. M. Domingues, and N. Bindoff, 2014: Ocean heat content [in "State of the Climate in 2013"]. *Bull. Amer. Meteor. Soc.*, **95** (7), S54–S57, https://doi.org/10.1175/2014BAMSStateoftheClimate.1.

—— , and Coauthors, 2015: Ocean heat content [in "State of the Climate in 2014"]. *Bull. Amer. Meteor. Soc.*, **96** (7), S64–S66, https://doi.org/10.1175/2015BAMSStateoftheClimate.1.

—— , J. Reagan, J. M. Lyman, T. Boyer, C. Schmid, and R. Locarnini, 2020: Salinity [in "State of the Climate in 2019"]. *Bull. Amer. Meteor. Soc.*, **101** (8), S129–S183, https://doi.org/10.1175/BAMS-D-20-0105.1.

—— , and Coauthors, 2022: Ocean heat content [in "State of the Climate in 2021"]. *Bull. Amer. Meteor. Soc.*, **103** (8), S153–S157, https://doi.org/10.1175/2022BAMSStateoftheClimate.1.

Kato, S., and Coauthors, 2018: Surface Irradiances of Edition 4.0 Clouds and the Earth's Radiant Energy System (CERES) Energy Balanced and Filled (EBAF) data product. *J. Climate*, **31**, 4501–4527, https://doi.org/10.1175/JCLI-D-17-0523.1.

Kennedy, J. J., N. A. Rayner, C. P. Atkinson, and R. E. Killick, 2019: An ensemble data set of sea surface temperature change from 1850: The Met Office Hadley Centre HadSST.4.0.0.0 data set. *J. Geophys. Res. Atmos.*, **124**, 7719–7763, https://doi.org/10.1029/2018JD029867.

Khatiwala, S., F. Primeau, and T. Hall, 2009: Reconstruction of the history of anthropogenic CO_2 concentrations in the ocean. *Nature*, **462**, 346–349, https://doi.org/10.1038/nature08526.

Kramer, S. J., D. A. Siegel, S. Maritorena, and D. Catlett, 2022: Modeling surface ocean phytoplankton pigments from hyperspectral remote sensing reflectance on global scales. *Remote Sens. Environ.*, **270**, 112879, https://doi.org/10.1016/j.rse.2021.112879.

Kumar, P., B. Hamlington, S. Cheon, W. Han, and P. Thompson, 2020: 20th century multivariate Indian Ocean regional sea level reconstruction. *J. Geophys. Res. Oceans*, **125**, e2020JC016270, https://doi.org/10.1029/2020JC016270.

Landschützer, P., N. Gruber, D. C. E. Bakker, U. Schuster, S. Nakaoka, M. R. Payne, T. P. Sasse, and J. Zeng, 2013: A neural network-based estimate of the seasonal to inter-annual variability of the Atlantic Ocean carbon sink. *Biogeosciences*, **10**, 7793–7815, https://doi.org/10.5194/bg-10-7793-2013.

—— , —— , —— , and —— , 2014: Recent variability of the global ocean carbon sink. *Global Biogeochem. Cycles*, **28**, 927–949, https://doi.org/10.1002/2014GB004853.

Lange, P. K., and Coauthors, 2020: Radiometric approach for the detection of picophytoplankton assemblages across oceanic fronts. *Opt. Express*, **28**, 25 682–25 705, https://doi.org/10.1364/OE.398127.

Lauvset, S. K., and Coauthors, 2016: A new global interior ocean mapped climatology: The 1° x 1° GLODAP version 2. *Earth Syst. Sci. Data*, **8**, 325–340, https://doi.org/10.5194/essd-8-325-2016.

—— , A. Brakstad, K. Våge, A. Olsen, E. Jeansson, and K. A. Mork, 2018: Continued warming, salinification and oxygenation of the Greenland Sea gyre. *Tellus*, **70A** (1), 1–9, https://doi.org/10.1080/16000870.2018.1476434.

Leuliette, E. W., and J. K. Willis, 2011: Balancing the sea level budget. *Oceanography*, **24** (2), 122–129, https://doi.org/10.5670/oceanog.2011.32.

Le Vine, D. M., E. P. Dinnat, G. S. E. Lagerloef, P. de Matthaeis, S. Abraham, C. Utku, and H. Kao, 2014: Aquarius: Status and recent results. *Radio Sci.*, **49**, 709–720, https://doi.org/10.1002/2014RS005505.

Levitus, S., and Coauthors, 2012: World ocean heat content and thermosteric sea level change (0–2000 m), 1955–2010. *Geophys. Res. Lett.*, **39**, L10603, https://doi.org/10.1029/2012GL051106.

Li, F., and Coauthors, 2021: Subpolar North Atlantic western boundary density anomalies and the Meridional Overturning Circulation. *Nat. Commun.*, **12**, 3002, https://doi.org/10.1038/s41467-021-23350-2.

Li, G., L. Cheng, J. Zhu, K. E. Trenberth, M. E. Mann, and J. P. Abraham, 2020: Increasing ocean stratification over the past half-century. *Nat. Climate Change*, **10**, 1116–1123, https://doi.org/10.1038/s41558-020-00918-2.

Li, L., R. W. Schmitt, C. C. Ummenhofer, and K. B. Karnauskas, 2016: North Atlantic salinity as a predictor of Sahel rainfall. *Sci. Adv.*, **2**, e1501588, https://doi.org/10.1126/sciadv.1501588.

Li, X., Z.-Z. Hu, M. J. McPhaden, C. Zhu, and Y. Liu, 2023: Triple-dip La Niñas in 1998–2001 and 2020–2023: Impact of mean state changes. *J. Geophys. Res. Atmos.*, **128**, e2023JD038843, https://doi.org/10.1029/2023JD038843.

Loeb, N. G., and Coauthors, 2018: Clouds and the Earth's Radiant Energy System (CERES) Energy Balanced and Filled (EBAF) top-of-atmosphere (TOA) edition-4.0 data product. *J. Climate*, **31**, 895–918, https://doi.org/10.1175/JCLI-D-17-0208.1.

—— , G. C. Johnson, T. J. Thorsen, J. M. Lyman, F. G. Rose, and S. Kato, 2021: Satellite and ocean data reveal marked increase in Earth's heating rate. *Geophys. Res. Lett.*, **48**, e2021GL093047, https://doi.org/10.1029/2021GL093047.

Lozier, M. S., and Coauthors, 2017: Overturning in the Subpolar North Atlantic Program: A new international ocean observing system. *Bull. Amer. Meteor. Soc.*, **98**, 737–752, https://doi.org/10.1175/BAMS-D-16-0057.1.

—— , and Coauthors, 2019: A sea change in our view of overturning in the subpolar North Atlantic. *Science*, **363**, 516–521, https://doi.org/10.1126/science.aau6592.

Lumpkin, R., and S. L. Garzoli, 2005: Near-surface circulation in the tropical Atlantic Ocean. *Deep-Sea Res. I*, **52**, 495–518, https://doi.org/10.1016/j.dsr.2004.09.001.

—— , and —— , 2011: Interannual to decadal changes in the western South Atlantic's surface circulation. *J. Geophys. Res.*, **116**, C01014, https://doi.org/10.1029/2010JC006285.

—— , G. Goni, and K. Dohan, 2012: Surface currents [in "State of the Climate in 2011"]. *Bull. Amer. Meteor. Soc.*, **93** (7), S75–S78, https://doi.org/10.1175/2012BAMSStateoftheClimate.1.

—— , F. Bringas, G. Goni, and B. Qiu, 2023: Surface currents [in "State of the Climate in 2022"]. *Bull. Amer. Meteor. Soc.*, **104** (9), S177–S180, https://doi.org/10.1175/BAMS-D-23-0076.2.

Lyman, J. M., and G. C. Johnson, 2014: Estimating global ocean heat content changes in the upper 1800 m since 1950 and the influence of climatology choice. *J. Climate*, **27**, 1945–1957, https://doi.org/10.1175/JCLI-D-12-00752.1.

—— , and —— , 2023: Global high-resolution random forest regression maps of ocean heat content anomalies using in situ and satellite data. *J. Atmos. Oceanic Technol.*, **40**, 575–586, https://doi.org/10.1175/JTECH-D-22-0058.1.

Mantua, N. J., and S. R. Hare, 2002: The Pacific decadal oscillation. *J. Oceanogr.*, **58**, 35–44, https://doi.org/10.1023/A:1015820616384.

Maritorena, S., O. Hembise Fanton d'Andon, A. Mangin, and D. A. Siegel, 2010: Merged satellite ocean color data products using a bio-optical model: Characteristics, benefits and issues. *Remote Sens. Environ.*, **114**, 1791–1804, https://doi.org/10.1016/j.rse.2010.04.002.

Marti, F., and Coauthors, 2022: Monitoring the ocean heat content change and the Earth energy imbalance from space altimetry and space gravimetry. *Earth Syst. Sci. Data*, **14**, 229–249, https://doi.org/10.5194/essd-14-229-2022.

McCarthy, G., and Coauthors, 2015: Measuring the Atlantic meridional overturning circulation at 26°N. Prog. *Oceanogr.*, **130**, 91–111, https://doi.org/10.1016/j.pocean.2014.10.006.

McKinna, L. I. W., P. J. Werdell, and C. W. Proctor, 2016: Implementation of an analytical Raman scattering correction for satellite ocean-color processing. *Opt. Express*, **24**, A1123–A1137, https://doi.org/10.1364/OE.24.0A1123.

Moat, B. I., and Coauthors, 2020: Pending recovery in the strength of the meridional overturning circulation at 26°N. Ocean Sci., **16**, 863–874, https://doi.org/10.5194/os-16-863-2020.

—— , D. Smeed, D. Rayner, W. E. Johns, R. H. Smith, D. L. Volkov, M. O. Baringer, and J. Collins, 2023: Atlantic meridional overturning circulation observed by the RAPID-MOCHA-WBTS (RAPID-Meridional Overturning Circulation and Heatflux Array-Western Boundary Time Series) array at 26N from 2004 to 2022 (v2022.1). Accessed 18 January 2024, https://doi.org/10.5285/04c79ece-3186-349a-e063-6c86abc0158c.

Mulet, S., and Coauthors, 2021: The new CNES-CLS18 global mean dynamic topography. *Ocean Sci.*, **17**, 789–808, https://doi.org/10.5194/os-17-789-2021.

Müller, J. D., and Coauthors, 2023: Decadal trends in the oceanic storage of anthropogenic carbon from 1994 to 2014. *AGU Adv.*, **4**, e2023AV000875, https://doi.org/10.1029/2023AV000875.

Nerem, R. S., D. P. Chambers, E. W. Leuliette, G. T. Mitchum, and B. S. Giese, 1999: Variations in global mean sea level associated with the 1997–1998 ENSO event: Implications for measuring long term sea level change. *Geophys. Res. Lett.*, **26**, 3005–3008, https://doi.org/10.1029/1999GL002311.

—— , B. D. Beckley, J. T. Fasullo, B. D. Hamlington, D. Masters, and G. T. Mitchum, 2018: Climate-change–driven accelerated sea-level rise detected in the altimeter era. *Proc. Natl. Acad. Sci. USA*, **115**, 2022–2025, https://doi.org/10.1073/pnas.1717312115.

Oliver, E. C. J., J. A. Benthuysen, S. Darmaraki, M. G. Donat, A. J. Hobday, N. J. Holbrook, R. W. Schlegel, and A. Sen Gupta, 2021: Marine heatwaves. *Annu. Rev. Mar. Sci.*, **13**, 313–342, https://doi.org/10.1146/annurev-marine-032720-095144.

O'Reilly, J. E., and P. J. Werdell, 2019: Chlorophyll algorithms for ocean color sensors – OC4, OC5 & OC6. *Remote Sens. Environ.*, **229**, 32–47, https://doi.org/10.1016/j.rse.2019.04.021.

Pahlevan, N., B. Smith, C. Binding, D. Gurlin, L. Li, M. Bresciani, and C. Giardino, 2021: Hyperspectral retrievals of phytoplankton absorption and chlorophyll-*a* in inland and nearshore coastal waters. *Remote Sens. Environ.*, **253**, 112200, https://doi.org/10.1016/j.rse.2020.112200.

Palmer, M. D., K. Haines, S. F. B. Tett, and T. J. Ansell, 2007: Isolating the signal of ocean global warming. *Geophys. Res. Lett.*, **34**, L23610, https://doi.org/10.1029/2007GL031712.

Pita, I., M. Goes, D. L. Volkov, S. Dong, G. Goni, and M. Cirano, 2024: An ARGO and XBT observing system for the Atlantic Meridional Overturning Circulation and Meridional Heat Transport (AXMOC) at 22.5°S. J. Geophys. *Res. Oceans*, **129**, e2023JC020010, https://doi.org/10.1029/2023JC020010.

Purkey, S. G., and G. C. Johnson, 2010: Warming of global abyssal and deep Southern Ocean waters between the 1990s and 2000s: Contributions to global heat and sea-level rise budgets. *J. Climate*, **23**, 6336–6351, https://doi.org/10.1175/2010JCLI3682.1.

Qiu, B., and S. Chen, 2021: Revisit of the occurrence of the Kuroshio Large Meander south of Japan. *J. Phys. Oceanogr.*, **51**, 3679–3694, https://doi.org/10.1175/JPO-D-21-0167.1.

——, ——, N. Schneider, E. Oka, and S. Sugimoto, 2020: On the reset of the wind-forced decadal Kuroshio extension variability in late 2017. *J. Climate*, **33**, 10813–10828, https://doi.org/10.1175/JCLI-D-20-0237.1.

Rahmstorf, S., J. Box, G. Feulner, M. E. Mann, A. Robinson, S. Rutherford, and E. J. Schaffernicht, 2015: Exceptional twentieth-century slowdown in Atlantic Ocean overturning circulation. *Nat. Climate Change*, **5**, 475–480, https://doi.org/10.1038/nclimate2554.

Rasmusson, E. M., and T. H. Carpenter, 1982: Variation in tropical sea surface temperature and surface wind fields associated with Southern Oscillation/El Niño. *Mon. Wea. Rev.*, **110**, 354–384, https://doi.org/10.1175/1520-0493(1982)110<0354:VITSST>2.0.CO;2.

Rayner, N. A., D. E. Parker, E. B. Horton, C. K. Folland, L. V. Alexander, D. P. Rowell, E. C. Kent, and A. Kaplan, 2003: Global analyses of sea surface temperature, sea ice, and night marine air temperature since the late nineteenth century. *J. Geophys. Res.*, **108**, 4407, https://doi.org/10.1029/2002JD002670.

Reagan, J., T. Boyer, C. Schmid, and R. Locarnini, 2022: Subsurface salinity [in "State of the Climate in 2021"]. *Bull. Amer. Meteor. Soc.*, **103** (8), S160–S162, https://doi.org/10.1175/BAMS-D-22-0072.1.

——, ——, ——, and ——, 2023: Subsurface salinity [in "State of the Climate in 2022"]. *Bull. Amer. Meteor. Soc.*, **104** (9), S165–S167, https://doi.org/10.1175/BAMS-D-23-0076.2.

Regnier, P., L. Resplandy, R. G. Najjar, and P. Ciais, 2022: The land-to-ocean loops of the global carbon cycle. *Nature*, **603**, 401–410, https://doi.org/10.1038/s41586-021-04339-9.

Ren, L., K. Speer, and E. P. Chassignet, 2011: The mixed layer salinity budget and sea ice in the Southern Ocean. *J. Geophys. Res.*, **116**, C08031, https://doi.org/10.1029/2010JC006634.

Reynolds, R. W., T. M. Smith, C. Liu, D. B. Chelton, K. S. Casey, and M. G. Schlax, 2007: Daily high-resolution-blended analyses for sea surface temperature. *J. Climate*, **20**, 5473–5496, https://doi.org/10.1175/2007JCLI1824.1.

Riser, S. C., and Coauthors, 2016: Fifteen years of ocean observations with the global Argo array. *Nat. Climate Change*, **6**, 145–153, https://doi.org/10.1038/nclimate2872.

Rödenbeck, C., and Coauthors, 2015: Data-based estimates of the ocean carbon sink variability – First results of the Surface Ocean pCO_2 Mapping intercomparison (SOCOM). *Biogeosciences*, **12**, 7251–7278, https://doi.org/10.5194/bg-12-7251-2015.

Roemmich, D., and J. Gilson, 2009: The 2004–2008 mean and annual cycle of temperature, salinity, and steric height in the global ocean from the Argo Program. *Prog. Oceanogr.*, **82**, 81–100, https://doi.org/10.1016/j.pocean.2009.03.004.

Sabine, C. L., and Coauthors, 2004: The oceanic sink for anthropogenic CO_2. *Science*, **305**, 367–371, https://doi.org/10.1126/science.1097403.

Saji, N. H., B. N. Goswami, P. N. Vinayachandran, and T. Yamagata, 1999: A dipole mode in the tropical Indian Ocean. *Nature*, **401**, 360–363, https://doi.org/10.1038/43854.

Schlesinger, M. E., and N. Ramankutty, 1994: An oscillation in the global climate system of period 65–70 years. *Nature*, **367**, 723–726, https://doi.org/10.1038/367723a0.

Schmidtko, S., G. C. Johnson, and J. M. Lyman, 2013: MIMOC: A global monthly isopycnal upper-ocean climatology with mixed layers. *J. Geophys. Res. Oceans*, **118**, 1658–1672, https://doi.org/10.1002/jgrc.20122.

Schmitt, R. W., 1995: The ocean component of the global water cycle. *Rev. Geophys.*, **33**, 1395–1409, https://doi.org/10.1029/95RG00184.

Siegel, D. A., S. Maritorena, N. B. Nelson, M. J. Behrenfeld, and C. R. McClain, 2005: Colored dissolved organic matter and its influence on the satellite-based characterization of the ocean biosphere. *Geophys. Res. Lett.*, **32**, L20605, https://doi.org/10.1029/2005GL024310.

——, and Coauthors, 2013: Regional to global assessments of phytoplankton dynamics from the SeaWiFS mission. *Remote Sens. Environ.*, **135**, 77–91, https://doi.org/10.1016/j.rse.2013.03.025.

——, T. DeVries, I. Cetinić, and K. M. Bisson, 2023: Quantifying the ocean's biological pump and its carbon cycle impacts on global scales. *Annu. Rev. Mar. Sci.*, **15**, 329–356, https://doi.org/10.1146/annurev-marine-040722-115226.

Skliris, N., R. Marsh, S. A. Josey, S. A. Good, C. Liu, and R. P. Allan, 2014: Salinity changes in the World Ocean since 1950 in relation to changing surface freshwater flux. *Climate Dyn.*, **43**, 709–736, https://doi.org/10.1007/s00382-014-2131-7.

——, J. D. Zika, G. Nurser, S. A. Josey, and R. Marsh, 2016: Global water cycle amplifying at less than the Clausius-Clapeyron rate. *Sci. Rep.*, **6**, 38752, https://doi.org/10.1038/srep38752.

Smeed, D. A., and Coauthors, 2018: The North Atlantic Ocean is in a state of reduced overturning. *Geophys. Res. Lett.*, **45**, 1527–1533, https://doi.org/10.1002/2017GL076350.

Smith, K. E., M. T. Burrows, A. J. Hobday, A. Sen Gupta, P. J. Moore, M. Thomsen, T. Wernberg, and D. A. Smale, 2021: Socioeconomic impacts of marine heatwaves: Global issues and opportunities. *Science*, **374**, eabj3593, https://doi.org/10.1126/science.abj3593.

——, and Coauthors, 2023: Biological impacts of marine heatwaves. *Annu. Rev. Mar. Sci.*, **15**, 119–145, https://doi.org/10.1146/annurev-marine-032122-121437.

Stackhouse, P. W., D. P. Kratz, G. R. McGarragh, S. K. Gupta, and E. B. Geier, 2006: Fast Longwave and Shortwave Radiative Flux (FLASHFlux) products from CERES and MODIS measurements. 12th Conf. on Atmospheric Radiation, Madison, WI, Amer. Meteor. Soc., P1.10, https://ams.confex.com/ams/Madison2006/techprogram/paper_113479.htm.

Sweet, W. V., J. Park, J. J. Marra, C. Zervas, and S. Gill, 2014: Sea level rise and nuisance flood frequency changes around the United States. NOAA Tech. Rep. NOS CO-OPS 073, 66 pp., https://tidesandcurrents.noaa.gov/publications/NOAA_Technical_Report_NOS_COOPS_073.pdf.

Talley, L. D., 2002: Salinity patterns in the ocean. *The Earth System: Physical and Chemical Dimensions of Global Environmental Change*, Vol. 1, Encyclopedia of Global Environmental Change, M. C. MacCracken and J. S. Perry, Eds., John Wiley and Sons, 629–640.

Twedt, K., N. Lei, X. Xiong, A. Angal, S. Li, T. Chang, and J. Sun, 2022: On-orbit calibration and performance of NOAA-20 VIIRS reflective solar bands. *IEEE Trans. Geosci. Remote Sens.*, **60**, 1–13, https://doi.org/10.1109/TGRS.2021.3108970.

Volkov, D. L., S.-K. Lee, R. Domingues, H. Zhang, and M. Goes, 2019: Interannual sea level variability along the southeastern seaboard of the United States in relation to the gyre-scale heat divergence in the North Atlantic. *Geophys. Res. Lett.*, **46**, 7481–7490, https://doi.org/10.1029/2019GL083596.

—— , R. Domingues, C. S. Meinen, R. Garcia, M. Baringer, G. Goni, and R. H. Smith, 2020: Inferring Florida Current volume transport from satellite altimetry. *J. Geophys. Res. Oceans*, **125**, e2020JC016763, https://doi.org/10.1029/2020JC016763.

—— , K. Zhang, W. E. Johns, J. K. Willis, W. Hobbs, M. Goes, H. Zhang, and D. Menemenlis, 2023a: Atlantic meridional overturning circulation increases flood risk along the United States southeast coast. *Nat. Commun.*, **14**, 5095, https://doi.org/10.1038/s41467-023-40848-z.

—— , and Coauthors, 2023b: Meridional overturning circulation and heat transport in the Atlantic Ocean [in "State of the Climate in 2022"]. *Bull. Amer. Meteor. Soc.*, **104** (9), S181–S184, https://doi.org/10.1175/BAMS-D-23-0076.2.

von Schuckmann, K., and Coauthors, 2023: Heat stored in the Earth system 1960–2020: Where does the energy go? *Earth Syst. Sci. Data*, **15**, 1675–1709, https://doi.org/10.5194/essd-15-1675-2023.

Von Storch, H., and F. W. Zwiers, 1999: Statistical Analysis in Climate Research. Cambridge University Press, 484 pp.

Walsh, K. J. E., and Coauthors, 2016: Tropical cyclones and climate change. *Wiley Interdiscip. Rev.: Climate Change*, **7**, 65–89, https://doi.org/10.1002/wcc.371.

Wanninkhof, R., 2014: Relationship between wind speed and gas exchange over the ocean revisited. *Limnol. Oceanogr. Methods*, **12**, 351–362, https://doi.org/10.4319/lom.2014.12.351.

Waugh, D. W., T. M. Hall, B. I. McNeil, R. Key, and R. J. Matear, 2006: Anthropogenic CO_2 in the oceans estimated using transit time distributions. *Tellus*, **58B**, 376–389, https://doi.org/10.1111/j.1600-0889.2006.00222.x.

Weijer, W., W. Cheng, O. A. Garuba, A. Hu, and B. T. Nadiga, 2020: CMIP6 models predict significant 21st century decline of the Atlantic meridional overturning circulation. *Geophys. Res. Lett.*, **47**, e2019GL086075, https://doi.org/10.1029/2019GL086075.

Werdell, P. J., and L. I. McKinna, 2019: Sensitivity of inherent optical properties from ocean reflectance inversion models to satellite instrument wavelength suites. *Front. Earth Sci.*, **7**, 54, https://doi.org/10.3389/feart.2019.00054.

—— , and Coauthors, 2013: Generalized ocean color inversion model for retrieving marine inherent optical properties. *Appl. Opt.*, **52**, 2019–2037, https://doi.org/10.1364/AO.52.002019.

—— , and Coauthors, 2019: The Plankton, Aerosol, Cloud, Ocean Ecosystem mission: Status, science, advances. *Bull. Amer. Meteor. Soc.*, **100**, 1775–1794, https://doi.org/10.1175/BAMS-D-18-0056.1.

Westberry, T. K., and Coauthors, 2016: Annual cycles of phytoplankton biomass in the subarctic Atlantic and Pacific Ocean. *Global Biogeochem. Cycles*, **30**, 175–190, https://doi.org/10.1002/2015GB005276.

Wiese, D. N., D.-N. Yuan, C. Boening, F. W. Landerer, and M. M. Watkins, 2022: JPL GRACE and GRACE-FO Mascon Ocean, Ice, and Hydrology Equivalent HDR Water Height RL06.1M CRI Filtered version 3.0. PODAAC, accessed 13 February 2024, https://doi.org/10.5067/TEMSC-3MJ62.

Willis, J. K., 2010: Can in situ floats and satellite altimeters detect long-term changes in Atlantic Ocean overturning? *Geophys. Res. Lett.*, **37**, L06602, https://doi.org/10.1029/2010GL042372.

—— , and W. R. Hobbs, 2024: Atlantic meridional overturning circulation near 41N from altimetry and Argo observations. Zenodo, accessed 10 January 2024, https://doi.org/10.5281/zenodo.8170366.

Wolter, K., and M. S. Timlin, 1998: Measuring the strength of ENSO events: How does 1997/98 rank? *Weather*, **53**, 315–324, https://doi.org/10.1002/j.1477-8696.1998.tb06408.x.

Woosley, R. J., F. J. Millero, and R. Wanninkhof, 2016: Rapid anthropogenic changes in CO_2 and pH in the Atlantic Ocean: 2003–2014. *Global Biogeochem. Cycles*, **30**, 70–90, https://doi.org/10.1002/2015GB005248.

Worthington, E. L., B. I. Moat, D. A. Smeed, J. V. Mecking, R. Marsh, and G. D. McCarthy, 2021: A 30-year reconstruction of the Atlantic meridional overturning circulation shows no decline. *Ocean Sci.*, **17**, 285–299, https://doi.org/10.5194/os-17-285-2021.

Wüst, G., 1936: Oberflächensalzgehalt, Verdunstung und Niederschlag auf dem Weltmeere. Länderkundliche Forschung: Festschrift zur Vollendung des sechzigsten Lebensjahres Norbert Krebs, J. Engelhorns Nachfahren, 347–359.

Xie, P., and Coauthors, 2014: An in situ-satellite blended analysis of global sea surface salinity. *J. Geophys. Res. Oceans*, **119**, 6140–6160, https://doi.org/10.1002/2014JC010046.

Yashayaev, I., and J. W. Loder, 2017: Further intensification of deep convection in the Labrador Sea in 2016. *Geophys. Res. Lett.*, **44**, 1429–1438, https://doi.org/10.1002/2016GL071668.

Yin, X., B. Huang, Z.-Z. Hu, D. Chan, and H.-M. Zhang, 2023: Sea-surface temperatures [in "State of the Climate in 2022"]. *Bull. Amer. Meteor. Soc.*, **104** (9), S153–S156, https://doi.org/10.1175/BAMS-D-23-0076.2.

Yu, L., 2011: A global relationship between the ocean water cycle and near-surface salinity. *J. Geophys. Res.*, **116**, C10025, https://doi.org/10.1029/2010JC006937.

—— , 2019: Global air–sea fluxes of heat, fresh water, and momentum: Energy budget closure and unanswered questions. *Annu. Rev. Mar. Sci.*, **11**, 227–248, https://doi.org/10.1146/annurev-marine-010816-060704.

—— , and R. A. Weller, 2007: Objectively analyzed air–sea heat fluxes for the global ice-free oceans (1981–2005). Bull. *Amer. Meteor. Soc.*, **88**, 527–540, https://doi.org/10.1175/BAMS-88-4-527.

Zhu, Y., and Coauthors, 2022: Perturbations in stratospheric aerosol evolution due to the water-rich plume of the 2022 Hunga-Tonga eruption. *Commun. Earth Environ.*, **3**, 248, https://doi.org/10.1038/s43247-022-00580-w.

Zweng, M. M., and Coauthors, 2018: Salinity. Vol. 2, World Ocean Atlas 2018, NOAA Atlas NESDIS 82, 50 pp., https://www.ncei.noaa.gov/sites/default/files/2020-04/woa18_vol2.pdf.

STATE OF THE CLIMATE IN 2023

THE TROPICS

H. J. Diamond and C. J. Schreck, Eds.

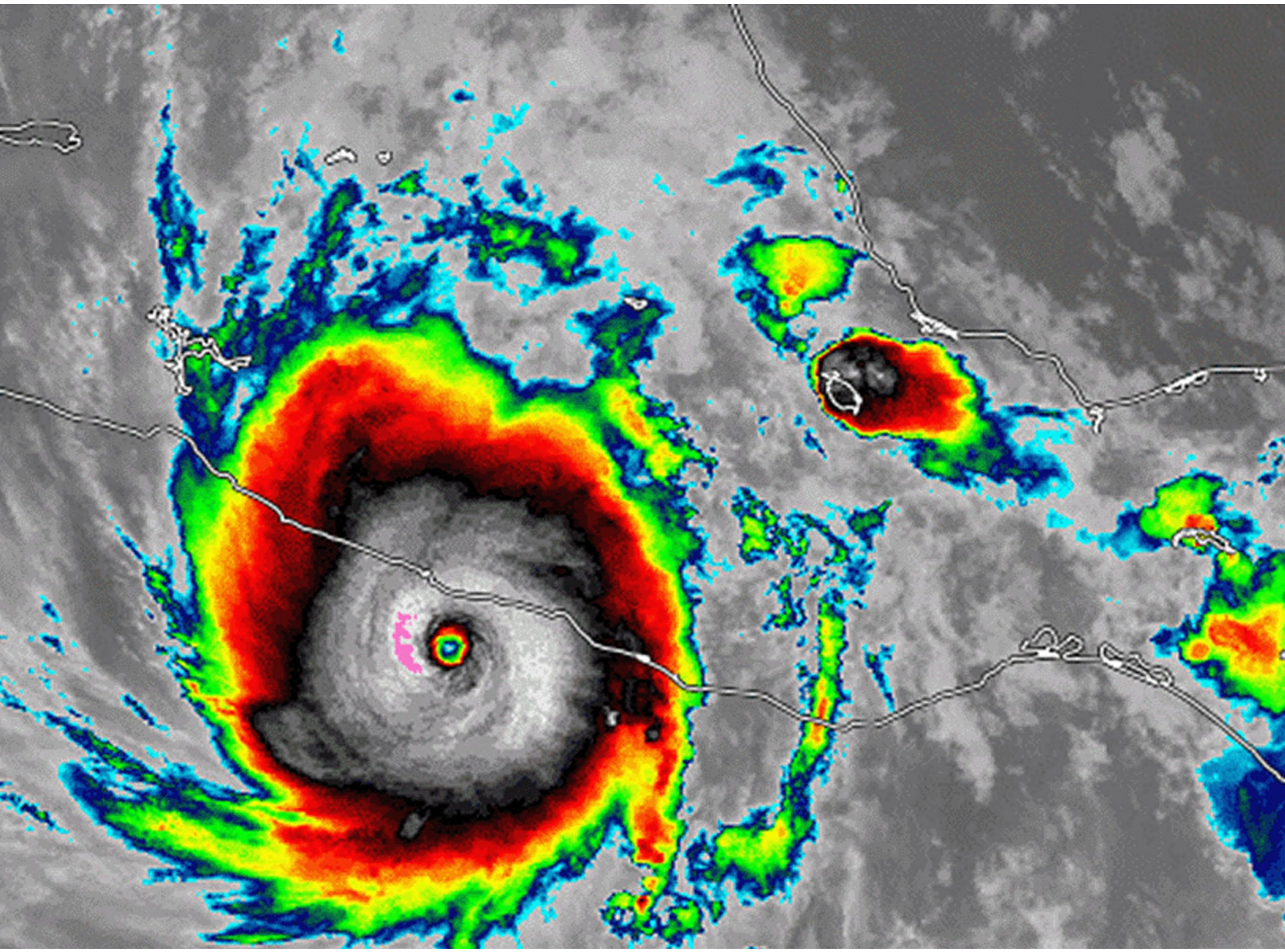

Special Online Supplement to the *Bulletin of the American Meteorological Society* Vol. 105, No. 8, August, 2024

https://doi.org/10.1175/BAMS-D-24-0098.1

Corresponding author: Howard J. Diamond / howard.diamond@noaa.gov

©2024 American Meteorological Society
For information regarding reuse of this content and general copyright information, consult the AMS Copyright Policy.

STATE OF THE CLIMATE IN 2023
The Tropics

Editors

Jessica Blunden
Tim Boyer

Chapter Editors

Anthony Arguez
Josh Blannin
Peter Bissolli
Kyle R. Clem
Howard J. Diamond
Matthew L. Druckenmiller
Robert J. H. Dunn
Catherine Ganter
Nadine Gobron
Gregory C. Johnson
Rick Lumpkin
Rodney Martinez
Ademe Mekonnen
John B. Miller
Twila A. Moon
Marilyn N. Raphael
Carl J. Schreck III
Laura Stevens
Richard L. Thoman
Kate M. Willett
Zhiwei Zhu

Technical Editor

Lukas Noguchi

BAMS Special Editor for Climate

Timothy DelSole

American Meteorological Society

Cover Credit:
Hurricane Otis 25 October 2023

Hurricane Otis experienced extremely rapid intensification in the 12 hours before it made landfall near Acapulco, Mexico, as a Category 5 storm on 25 October 2023.

Imagery courtesy of CIMSS - Cooperative Institute for Meteorological Satellite Studies, University of Wisconsin-Madison

How to cite this document:
The Tropics is one chapter from the *State of the Climate in 2023* annual report and is available from https://doi.org/10.1175/BAMS-D-24-0098.1. Compiled by NOAA's National Centers for Environmental Information, *State of the Climate in 2023* is based on contributions from scientists from around the world. It provides a detailed update on global climate indicators, notable weather events, and other data collected by environmental monitoring stations and instruments located on land, water, ice, and in space. The full report is available from https://doi.org/10.1175/2024BAMSStateoftheClimate.1.

Citing the complete report:
Blunden, J. and T. Boyer, Eds., 2024: "State of the Climate in 2023". Bull. Amer. Meteor. Soc., 105 (8), Si–S483 https://doi.org/10.1175/2024BAMSStateoftheClimate.1.

Citing this chapter:
Diamond, H.J. and C. J. Schreck, Eds., 2024: The Tropics [in "State of the Climate in 2023"]. Bull. Amer. Meteor. Soc., 105 (8), S214–S276, https://doi.org/10.1175/BAMS-D-24-0098.1.

Citing a section (example):
Klotzbach, P., C. Fogarty, and R. Truchelut, 2024: Hurricane Otis: The strongest landfalling hurricane on record for the west coast of Mexico [in "State of the Climate in 2023"]. Bull. Amer. Meteor. Soc., 105 (8), S264–S265, https://doi.org/10.1175/BAMS-D-24-0098.1.

Editor and Author Affiliations (alphabetical by name)

Allgood, Adam, NOAA/NWS National Centers for Environmental Prediction Climate Prediction Center, College Park, Maryland

Becker, Emily J., Rosenstiel School of Marine and Atmospheric Science, University of Miami, Miami, Florida

Blake, Eric S., NOAA/NWS National Hurricane Center, Miami, Florida

Bringas, Francis G., NOAA/OAR Atlantic Oceanographic and Meteorological Laboratory, Miami, Florida

Camargo, Suzana J., Lamont-Doherty Earth Observatory, Columbia University, Palisades, New York

Cerveny, Randall, Department of Geography, Arizona State University, Tempe, Arizona

Chen, Lin, Institute for Climate and Application Research (ICAR)/KLME/ILCEC/CIC-FEMD, Nanjing University of Information Science and Technology, Nanjing, China

Coelho, Caio A.S., Centro de Previsão do Tempo e Estudos Climáticos/National Institute for Space Research, Center for Weather Forecasts and Climate Studies, Cachoeira Paulista, Brazil

Diamond, Howard J., NOAA/OAR Air Resources Laboratory, College Park, Maryland

Earl-Spurr, Craig, Bureau of Meteorology, Perth, Australia

Fauchereau, Nicolas, National Institute of Water and Atmospheric Research, Ltd., Auckland, New Zealand

Fogarty, Chris, Canadian Hurricane Centre, Dartmouth, Canada

Goldenberg, Stanley B., NOAA/OAR Atlantic Oceanographic and Meteorological Laboratory, Miami, Florida

Harnos, Daniel S., NOAA/NWS National Centers for Environmental Prediction Climate Prediction Center, College Park, Maryland

He, Qiong, Earth System Modeling Center, Nanjing University of Information Science and Technology, Nanjing, China

Hu, Zeng-Zhen, NOAA/NWS National Centers for Environmental Prediction Climate Prediction Center, College Park, Maryland

Klotzbach, Philip J., Department of Atmospheric Science, Colorado State University, Fort Collins, Colorado

Knaff, John A., NOAA/NESDIS Center for Satellite Applications and Research, Fort Collins, Colorado

Kumar, Arun, NOAA/NWS National Centers for Environmental Prediction Climate Prediction Center, College Park, Maryland

L'Heureux, Michelle, NOAA/NWS National Centers for Environmental Prediction Climate Prediction Center, College Park, Maryland

Landsea, Chris W., NOAA/NWS National Hurricane Center, Miami, Florida

Lin, I-I, National Taiwan University, Taipei, Taiwan

Lopez, Hosmay, NOAA/OAR Atlantic Oceanographic and Meteorological Laboratory, Miami, Florida

Lorrey, Andrew M., National Institute of Water and Atmospheric Research, Ltd., Auckland, New Zealand

Luo, Jing-Jia, Institute for Climate and Application Research, Nanjing University of Information Science and Technology, Nanjing, China

Magee, Andrew D., Centre for Water, Climate and Land, School of Environmental and Life Sciences, University of Newcastle, Callaghan, Australia

Pasch, Richard J., NOAA/NWS National Hurricane Center, Miami, Florida

Paterson, Linda, Bureau of Meteorology, Perth, Australia

Pezza, Alexandre B., Greater Wellington Regional Council, Wellington, New Zealand

Rosencrans, Matthew, NOAA/NWS National Centers for Environmental Prediction Climate Prediction Center, College Park, Maryland

Schreck, Carl J., Cooperative Institute for Satellite Earth System Studies, North Carolina State University, Asheville, North Carolina

Trewin, Blair C., Bureau of Meteorology, Melbourne, Australia

Truchelut, Ryan E., WeatherTiger, Tallahassee, Florida

Uehling, John, Cooperative Institute for Satellite Earth System Studies, North Carolina State University, Asheville, North Carolina

Wang, Bin, School of Ocean and Earth Science and Technology, Department of Meteorology, University of Hawaii at Manoa, Honolulu, Hawaii; International Pacific Research Center, Honolulu, Hawaii

Wang, Hui, NOAA/NWS National Centers for Environmental Prediction Climate Prediction Center, College Park, Maryland

Wood, Kimberly M., Department of Hydrology and Atmospheric Sciences, University of Arizona, Tucson, Arizona

Editorial and Production Team

Allen, Jessicca, Graphics Support, Cooperative Institute for Satellite Earth System Studies, North Carolina State University, Asheville, North Carolina

Camper, Amy V., Graphics Support, Innovative Consulting and Management Services, LLC, NOAA/NESDIS National Centers for Environmental Information, Asheville, North Carolina

Haley, Bridgette O., Graphics Support, NOAA/NESDIS National Centers for Environmental Information, Asheville, North Carolina

Hammer, Gregory, Content Team Lead, Communications and Outreach, NOAA/NESDIS National Centers for Environmental Information, Asheville, North Carolina

Love-Brotak, S. Elizabeth, Lead Graphics Production, NOAA/NESDIS National Centers for Environmental Information, Asheville, North Carolina

Ohlmann, Laura, Technical Editor, Innovative Consulting and Management Services, LLC, NOAA/NESDIS National Centers for Environmental Information, Asheville, North Carolina

Noguchi, Lukas, Technical Editor, Innovative Consulting and Management Services, LLC, NOAA/NESDIS National Centers for Environmental Information, Asheville, North Carolina

Riddle, Deborah B., Graphics Support, NOAA/NESDIS National Centers for Environmental Information, Asheville, North Carolina

Veasey, Sara W., Visual Communications Team Lead, Communications and Outreach, NOAA/NESDIS National Centers for Environmental Information, Asheville, North Carolina

3. Table of Contents

Authors and affiliations S217
a. Overview S219
b. ENSO and the tropical Pacific S221
1. Oceanic conditions S221
2. Atmospheric circulation S223
3. Global precipitation S224
c. Tropical intraseasonal activity S225
d. Intertropical convergence zones S228
1. Pacific S228
2. Atlantic S230
e. Global monsoon summary S232
1. NH and SH land monsoon precipitation S232
2. Regional monsoon precipitation and circulation S233
f. Indian Ocean dipole S236
g. Tropical cyclones S238
1. Overview S238
2. Atlantic basin S239
3. Eastern North Pacific and central North Pacific basins S245
4. Western North Pacific basin S248
5. North Indian Ocean basin S253
6. South Indian Ocean basin S255
7. Australian basin S257
8. Southwest Pacific basin S258
h. Tropical cyclone heat potential S261
Sidebar 4.1: Hurricane Otis: The strongest landfalling hurricane on record for the west coast of Mexico S264
Sidebar 4.2: Tropical Cyclone Freddy: The world's longest-lived tropical cyclone S266
Appendix 1: Acronyms S267
Appendix 2: Datasets and sources S269
Appendix 3: Supplemental materials S272
References S273

4. THE TROPICS

H. J. Diamond and C. J. Schreck, Eds.

a. Overview

—H. J. Diamond and C. J. Schreck

In 2023, the El Niño–Southern Oscillation (ENSO) transitioned to El Niño after three years of La Niña conditions. ENSO-neutral conditions were briefly present in the tropical Pacific between January–March and March–May, before El Niño conditions emerged in April–June. El Niño strengthened steadily through the second half of 2023, with the Oceanic Niño Index reaching a value of +1.9°C in October–December.

For the global tropics (defined here as 20°S–20°N), the NOAA Merged Land Ocean Global Surface Temperature Analysis (NOAA GlobalTemp; Vose et al. 2021) indicates that the combined average land and ocean surface temperature was 0.5°C above the 1991–2020 average, the warmest year for the tropics in the 174-year data record. The six warmest years in the tropics since 1850 have all occurred since 2015. Data from the Global Precipitation Climatology Project indicate a mean annual total precipitation value of 1318 mm across the tropics (20°S–20°N latitude band) over land. This is 86 mm below the 1991–2020 average and was the third lowest for the 1979–2023 period of record.

Globally, 82 named tropical cyclones (TCs; ≥34 kt; or ≥17 m s^{-1}) were observed during the 2023 Northern Hemisphere season (January–December 2023) and the 2022/23 Southern Hemisphere season (July–June 2022/23; see Table 4.2), as documented by the National Hurricane Center and the Joint Typhoon Warning Center in International Best Track Archive for Climate Stewardship Version 4 (Knapp et al. 2010). Overall, this number was below the 1991–2020 global average of 87 TCs and also below the 85 TCs reported during the 2022 season (Diamond and Schreck 2023). The record for most named storms in a single TC season is 104 in 1992.

Of the 82 named storms, 45 reached hurricane strength (one-minute maximum sustained winds ≥64 kt) and 30 reached major hurricane strength (one-minute maximum winds ≥96 kt). Both of these counts were below their 1991–2020 averages. The accumulated cyclone energy (ACE; an integrated metric of the strength, frequency, and duration of tropical storms and hurricanes; Bell et al. 2000) rebounded from the lowest on record in 2022 (since reliable data began in 1981) to an above-normal level in 2023. Four of the seven TC basins were above normal in 2023 in contrast to zero in 2022. The North Indian Ocean had its second highest ACE on record behind 2019, and the North Atlantic had its seventh above-normal season in the last eight years. The western North Pacific had its fourth consecutive season with below-normal activity. A total of seven storms reached Category 5 intensity on the Saffir-Simpson Hurricane Wind Scale (one-minute maximum sustained winds ≥137 kt) during 2023, compared with only three in 2022. All of the basins, except for the Australian and southwest Pacific, had at least one Category 5 storm.

The 20 named storms in the North Atlantic during 2023 was equal with 1933 for the fourth-highest total in the HURDAT2 database (Landsea and Franklin 2013). In contrast, the number of hurricanes and major hurricanes were at their long-term (1991–2020) average of seven and three, respectively. The 2023 hurricane season was classified by NOAA as an above-normal season.

NOAA uses 1951–2020 terciles of ACE to delineate below-normal, normal, and above-normal seasons, and 2023's ACE of 146 × 10^4 kt^2 places it in the upper tercile. Two storms of particular note this season were Hurricane Otis, which was the strongest landfalling hurricane on record for the west coast of Mexico (see Sidebar 4.1), and Cyclone Freddy in the Southern Hemisphere (see Sidebar 4.2). Freddy is now recognized as the world's longest-lived TC (Earl-Spur et. al. 2024), crossing the full width of the Indian Ocean. Freddy is the first TC since 2000 to form in the Australian region and make landfall on the mainland African coast. Freddy made a total of three landfalls: one in Madagascar and two in Mozambique.

b. ENSO and the tropical Pacific

—E. Becker, M. L'Heureux, Z.-Z. Hu, and A. Kumar

The El Niño–Southern Oscillation (ENSO) is an ocean and atmosphere-coupled climate phenomenon across the tropical Pacific Ocean, with its warm (cold) phases called El Niño (La Niña). NOAA's Climate Prediction Center classifies and assesses the strength and duration of El Niño and La Niña events using the Oceanic Niño Index (ONI, shown for mid-2022 through 2023 in Fig. 4.1). The ONI is the three-month (seasonal) running average of sea-surface temperature (SST) anomalies in the Niño-3.4 region (5°S–5°N, 170°W–120°W), currently calculated as the departure from the 1991–2020 base period mean[1]. El Niño is classified when the ONI is at or greater than +0.5°C for at least five consecutive, overlapping seasons, while La Niña is classified when the ONI is at or less than –0.5°C for at least five consecutive, overlapping seasons.

The time series of the ONI (Fig. 4.1) shows a transition from 2022's La Niña conditions—the third La Niña year in a row—to strong El Niño in 2023, where strong El Niño is defined in this chapter as ONI ≥1.5°C. La Niña developed in July–September 2020 and lasted nearly continuously through December–February (DJF) 2022/23, with a brief period of ENSO-neutral conditions in the summer of 2021. ENSO-neutral conditions were briefly present in the tropical Pacific in 2023, between January–March and March–May (MAM), before El Niño emerged in April–June. El Niño strengthened steadily through the second half of 2023, with the ONI reaching a value of +1.9°C in October–December.

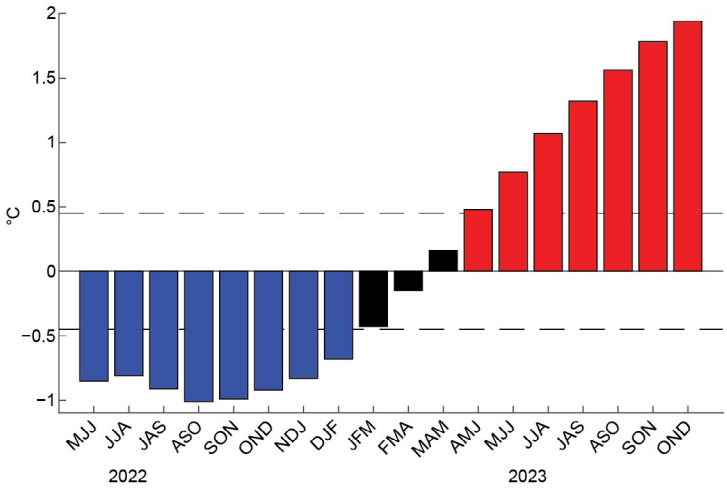

Fig. 4.1. Time series of the Oceanic Niño Index (ONI, °C) from mid-2022 through 2023. Overlapping three-month seasons are labeled on the x-axis, with initials indicating the first letter of each month in the season. Blue bars indicate negative values that are less than –0.5°C. Black bars indicate values between –0.5°C and 0.5°C, while red bars indicate positive values greater than 0.5°C. ONI values are derived from the ERSSTv5 dataset and are based on departures from the 1991–2020 period monthly means (Huang et al. 2017).

1. OCEANIC CONDITIONS

Figure 4.2 displays the mean SST (left column) and SST anomalies (right column) during DJF 2022/23 through September–November (SON) 2023. During DJF, below-average SST anomalies were on the order of –0.5°C to –1.0°C across the central equatorial Pacific (approximately 170°E–260°E), reflecting a weak and waning La Niña (Fig. 4.2b). During MAM, a small region of SST anomalies exceeding +2.5°C developed off the coast of Peru and Ecuador, while most of the tropical Pacific was near average, with a slight positive anomaly (+0.5°C to +1.0°C) in the western Pacific (Fig. 4.2d). By June–August (JJA), positive anomalies spread westward along the equator, with western Pacific SSTs closer to average (Fig. 4.2f). The SST pattern in SON reflects a strong El Niño, with equatorial Pacific anomalies in excess of +1.0°C extending from the dateline to the coast of South America (Fig. 4.2h). Some weak off-equatorial negative SST anomalies in the eastern half of the tropical basin were present from MAM through SON (Figs. 4.2d,f,h). Also of note in SON 2023 was the positive phase of the Indian Ocean dipole (IOD), with negative SST anomalies in the east and positive SST anomalies in the west (Fig. 4.2h).

[1] The ONI is an index measuring ENSO, and to highlight its seasonal-to-interannual component, the base period is updated every five years with a rolling 30-year climatology. SSTs in the Niño3.4 region have multi-decadal and longer trends going back to 1950 or earlier. The rolling climatology reduces the influence of trend on the state of ENSO.

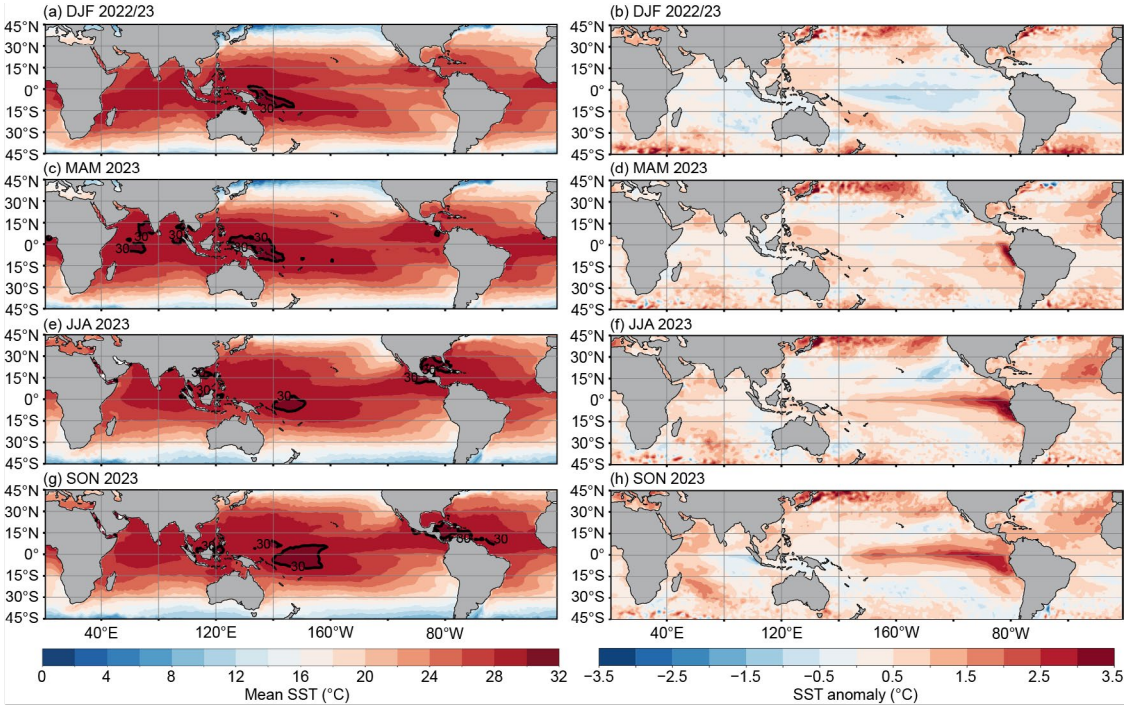

Fig. 4.2. Mean sea-surface temperatures (SSTs; left) and SST anomalies (right) for (a),(b) Dec–Feb (DJF) 2022/23, (c),(d) Mar–May (MAM) 2023, (e),(f) Jun–Aug (JJA) 2023, and (g),(h) Sep–Nov (SON) 2023. The bold contour for SST is for 30°C. Anomalies are departures from the 1991–2020 seasonal adjusted OIv2.1 climatology (Huang et al. 2021).

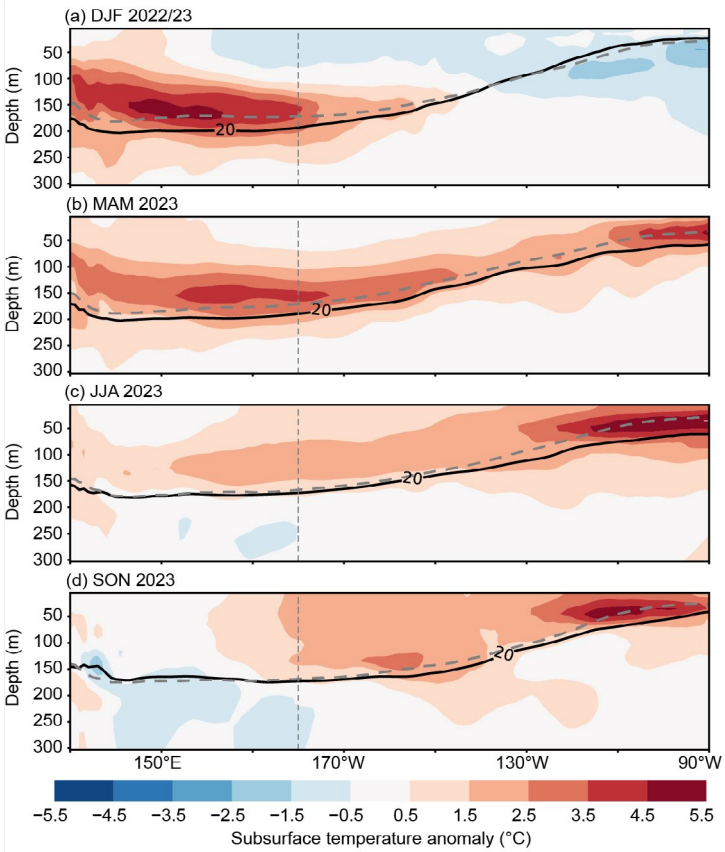

The weakening La Niña of DJF 2022/23 is also reflected in the subsurface temperature anomalies (Fig. 4.3a). The subsurface temperatures in the eastern Pacific were slightly below average, with a slightly shoaled thermocline. Warm anomalies in the west contributed to a deeper-than-average thermocline, leading to a slightly deeper-than-average west–east thermocline slope (Fig. 4.3a). During the transition from La Niña to El Niño in MAM, the thermocline across the entire basin was deeper than average (Fig, 4.3b). As El Niño strengthened into JJA and SON 2023, the depth of the thermocline in the western Pacific returned to near-average. In the central and eastern equatorial Pacific, the thermocline deepened as warm subsurface anomalies expanded in the central and eastern equatorial Pacific. The slope of the thermocline across the equatorial Pacific was shallower than average during the last half of the year (Figs. 4.3c,d). Overall, the subsurface SST in the western Pacific was warmer than would be expected during strong El Niño events (e.g., Kumar and Hu 2014).

Fig 4.3. Equatorial depth–longitude section of Pacific Ocean temperature anomalies (°C) averaged between 5°S and 5°N during (a) Dec–Feb (DJF) 2022/23, (b) Mar–May (MAM) 2023, (c) Jun–Aug (JJA) 2023, and (d) Sep–Nov (SON) 2023. The 20°C isotherm (thick solid line) approximates the center of the oceanic thermocline. The gray dashed line shows the climatology of the 20°C isotherm based on the 1991–2020 mean. The data are derived from a reanalysis system that assimilates oceanic observations into an oceanic general circulation model (Behringer 2007). Anomalies are departures from the 1991–2020 period monthly means.

2. ATMOSPHERIC CIRCULATION

December–February 2022/23 featured large-scale tropical atmospheric circulation anomalies consistent with La Niña. During La Niña, convection is typically suppressed (positive outgoing longwave radiation [OLR] anomalies, brown shading) over the western and central tropical Pacific and enhanced (negative OLR anomalies, green shading) over the Maritime Continent (Fig. 4.4a). This pattern mostly dissipated by MAM 2023, as ENSO-neutral conditions returned to the tropical Pacific (Fig. 4.4b). Near coastal South America, where strongly above-average SSTs were present, rainfall was enhanced during MAM. By JJA, El Niño's expected atmospheric circulation pattern, with enhanced convection (green) over the warmer waters of the central/eastern Pacific and suppressed convection (brown) over the Maritime Continent, indicated a reduced Walker circulation (Fig. 4.4c). Just north of the equator, enhanced convection stretched from the dateline to the coast of South America. The anomalous dipole of suppressed convection in the western Pacific and enhanced convection in the central and eastern Pacific strengthened in SON (Fig. 4.4d). The positive IOD was also evident in a region of strongly suppressed convection in the central and eastern Indian Ocean (Fig. 4.4d).

Similar to convection, the lower- and upper-level wind anomalies showed the transition from La Niña in DJF to neutral in MAM to El Niño in JJA and SON. The tropical low-level 850-hPa easterly trade winds were enhanced across most of the equatorial Pacific Ocean in DJF 2022/23 (Fig. 4.5a). In MAM, the lack of a coherent low-level wind anomaly pattern reflected ENSO-neutral (Fig. 4.5b). This lack of coherence continued into JJA, despite a developing El Niño and weak convection pattern (Fig. 4.4c). By SON, the low-level trade winds slowed, exhibiting seasonally

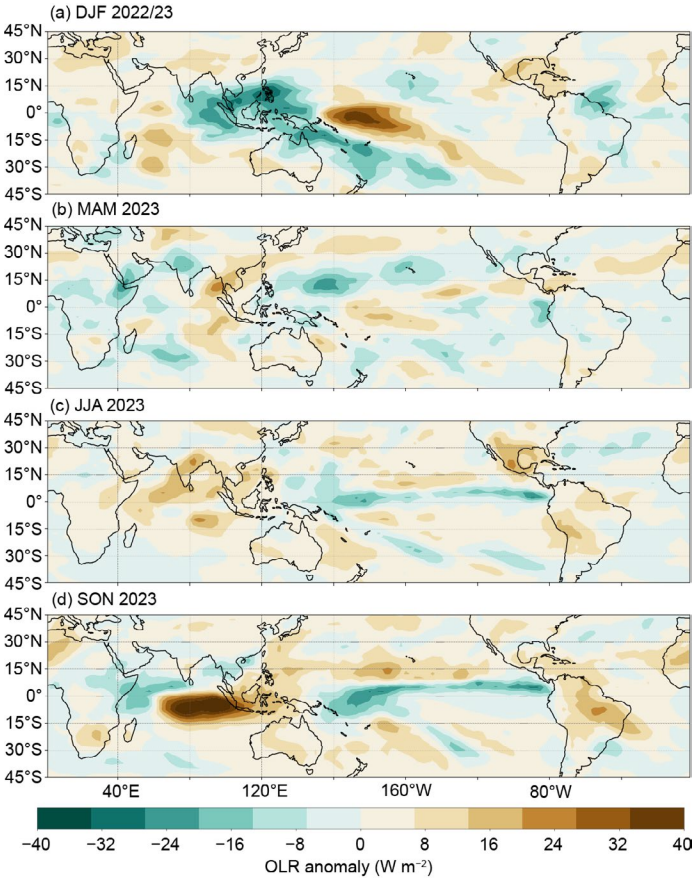

Fig. 4.4. Outgoing longwave radiation (OLR) anomalies (W m^{-2}) during (a) Dec–Feb (DJF) 2022/23, (b) Mar–May (MAM) 2023, (c) Jun–Aug (JJA) 2023, and (d) Sep–Nov (SON) 2023. Anomalies are departures from the 1991–2020 period monthly means. Data are from Liebmann and Smith (1996).

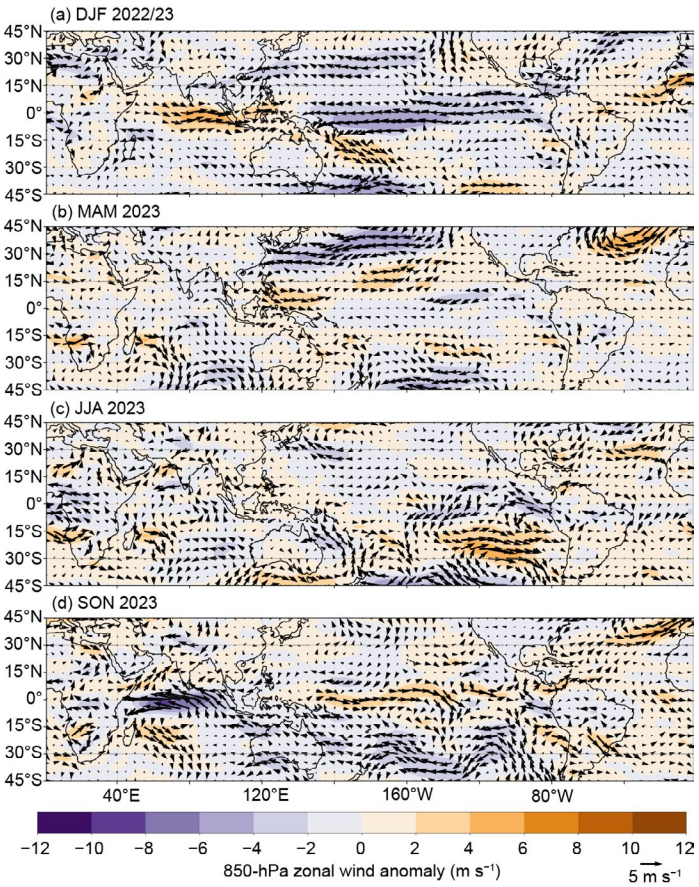

Fig. 4.5. Anomalous 850-hPa wind vectors (m s^{-1}, arrows) and zonal wind speed (m s^{-1}, shading) during (a) Dec–Feb (DJF) 2022/23, (b) Mar–May (MAM) 2023, (c) Jun–Aug (JJA) 2023, and (d) Sep–Nov (SON) 2023. The reference wind vector is located on the bottom left. Anomalies are departures from the 1991–2020 period monthly means. Data are from the National Centers for Environmental Prediction (NCEP) National Center for Atmospheric Research (NCAR) reanalysis (Kalnay et al. 1996).

averaged westerly anomalies along the equatorial Pacific (Fig. 4.5d).

Reflecting La Niña, upper-level (200-hPa) westerly wind anomalies also prevailed over most of the equatorial Pacific Ocean during DJF 2022/23 (Fig. 4.6a). Upper-level westerly anomalies persisted over much of the central and eastern Pacific through MAM (Fig. 4.6b), but diminished by JJA when weak easterly anomalies developed over the central Pacific (Fig. 4.6c). Easterly upper-level wind anomalies, expected during El Niño and its associated weaker Walker circulation, were more widespread and noticeable in SON 2023 (Fig. 4.6d).

Collectively, these oceanic and atmospheric anomalies reflected the well-known, basin-wide atmospheric and oceanic coupling of ENSO (Bjerknes 1969). Overall, the atmospheric circulation reflected the transition from La Niña early in the year to a strong El Niño by the end of 2023.

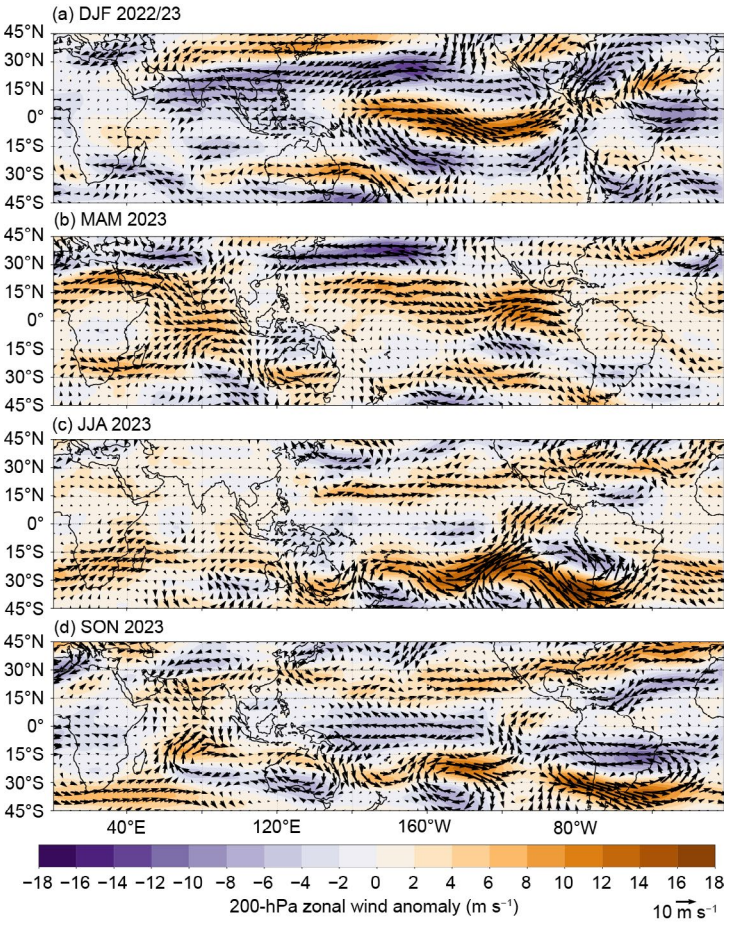

Fig. 4.6. Anomalous 200-hPa wind vectors (m s^{-1}, arrows) and zonal wind speed (m s^{-1}, shading) during (a) Dec–Feb (DJF) 2022/23, (b) Mar–May (MAM) 2023, (c) Jun–Aug (JJA) 2023, and (d) Sep–Nov (SON) 2023. The reference wind vector is located on the bottom left. Anomalies are departures from the 1991–2020 period monthly means. Data are from the National Centers for Environmental Prediction (NCEP) National Center for Atmospheric Research (NCAR) reanalysis (Kalnay et al. 1996).

3. GLOBAL PRECIPITATION

ENSO-driven teleconnections can affect precipitation anomalies globally (Bjerknes 1969; Ropelewski and Halpert 1989). While a rigorous attribution is beyond the scope of this chapter, some precipitation anomalies during JJA and SON 2023 that resemble the expected ENSO teleconnection impacts can be identified. In JJA, drier-than-average conditions were evident across eastern Australia (with some stations recording less than 25% of their average precipitation) and through central America and northern South America (Fig. A4.1a). Many stations in India recorded below-average precipitation, although some were above average. Drier-than-average conditions continued in eastern Australia and central America in SON 2023 (Fig. A4.1b). Also in SON 2023, stations in southern Brazil and Uruguay observed positive precipitation anomalies.

c. Tropical intraseasonal activity

—A. Allgood and C. J. Schreck

Organized tropical intraseasonal activity is modulated by several different modes of coherent atmospheric variability, most notably the Madden-Julian Oscillation (MJO; Madden and Julian 1971, 1972, 1994; Zhang 2005). The MJO is characterized by eastward-propagating envelopes of large-scale anomalous enhanced and suppressed convection that typically circumnavigate the globe in a 30-to-60-day period. MJO-related convective anomalies are similar in spatial extent to those generated by the atmospheric response to the El Niño–Southern Oscillation (ENSO), but the latter signal remains largely stationary and lasts for several months. Other impactful modes of variability include convectively-coupled atmospheric waves, such as Kelvin waves (which exhibit a faster phase speed than the MJO), and westward propagating equatorial Rossby waves (Wheeler and Kiladis 1999; Kiladis et al. 2009). These waves are typically narrower (zonally) than the MJO and may not couple as well to the broader convective regime. The MJO can be identified through time–longitude analyses of various atmospheric fields, including anomalous 200-hPa velocity potential (Fig. 4.7b), anomalous zonal winds at 200 hPa and 850 hPa (Fig. 4.8a), and anomalous outgoing longwave radiation (OLR; Fig. 4.7a). Another diagnostic tool frequently used to identify MJO activity is the Wheeler-Hendon (2004) Real-time Multivariate MJO (RMM) index. In RMM plots, robust atmospheric anomalies on a spatial scale resembling the MJO appear as a signal outside of the unit circle (Fig. 4.9). Eastward propagation is represented by counter-clockwise looping of the index about the origin.

The rapid transition from La Niña to emerging El Niño conditions that commenced during the first half of 2023 was partly facilitated by periods of strong MJO activity. The MJO was active at the beginning of 2023, with the enhanced convective phase crossing the Pacific (Figs. 4.7, 4.9a). While destructive interference between this intraseasonal signal and the ongoing La Niña

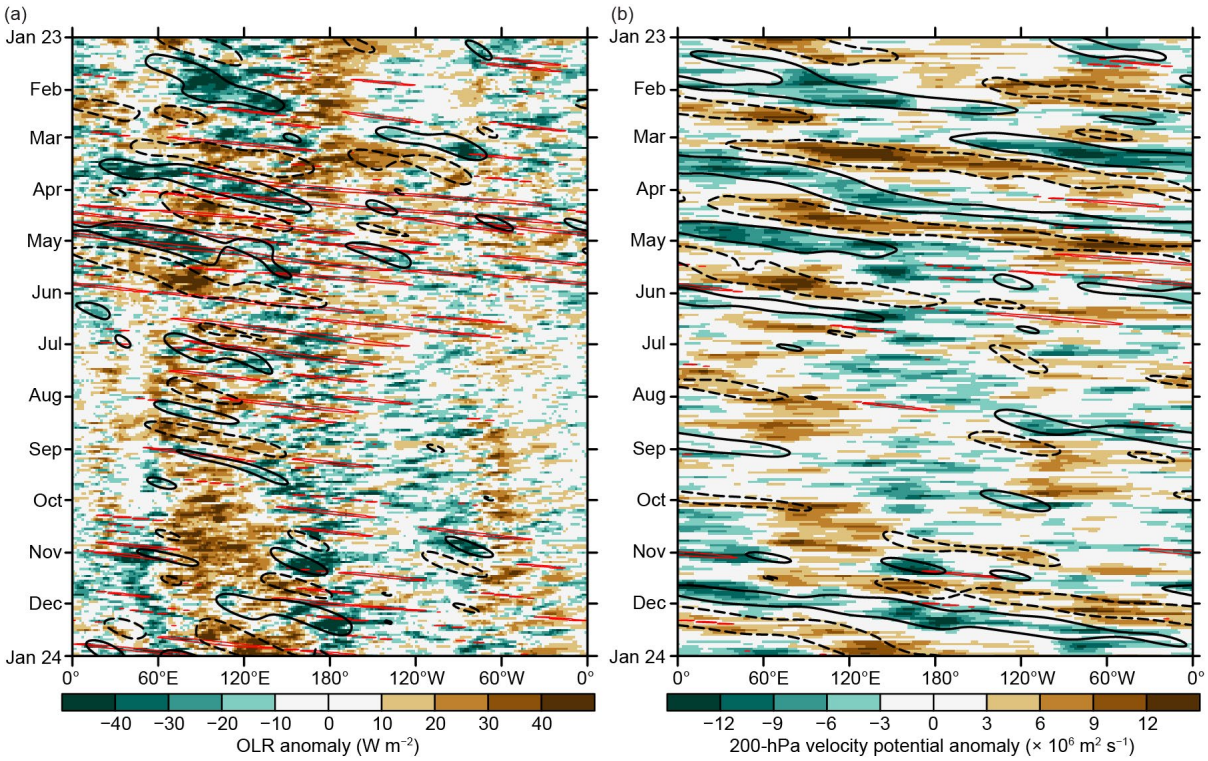

Fig. 4.7. Time–longitude section with (a) outgoing longwave radiation (OLR) anomalies (W m^{-2}; Schreck et al. 2018) and (b) 200-hPa velocity potential anomalies (× 10^6 m^2 s^{-1}) from the Climate Forecast System Reanalysis (Saha et al. 2014). Both variables are averaged over 10°S–10°N. Time increases downward on this graph, beginning with Jan 2023 at the top and ending with Jan 2024 at the bottom. Negative anomalies indicate enhanced convection, and positive anomalies indicate suppressed convection. Contours identify anomalies filtered for the Madden-Julian Oscillation (black) and atmospheric Kelvin waves (red). Contours are drawn at ±12 W m^{-2} and ±4 × 10^6 m^2 s^{-1} with the enhanced (suppressed) convective phase of these phenomena indicated by solid (dashed) contours. Anomalies are departures from the 1991–2020 base period daily means.

prevented the development of widespread equatorially focused convection, a low-level westerly wind burst was observed (Fig. 4.8a). This westerly wind burst helped generate a downwelling oceanic Kelvin wave that reduced the extent of below-average upper-oceanic heat content across the central and eastern Pacific (Fig. 4.8b). MJO activity persisted during February, with the signal generally constructively interfering with the cold ENSO base state as the enhanced convective phase crossed the Maritime Continent and the suppressed phase crossed the Pacific and Western Hemisphere. During late February and March, the MJO achieved a major disruption of the La Niña base state as it re-entered the Pacific, evidenced by an almost off-the-chart amplitude of the RMM-based MJO index in phases 7 and 8 (Fig. 4.9a). A strong, equatorially centered westerly wind burst generated a much stronger downwelling oceanic Kelvin wave in March than was generated during the January event. This rapid transport of warm ocean water from the anomalously warm West Pacific Warm Pool to the eastern Pacific brought an end to La Niña conditions. An active MJO signal persisted from April through early June (Fig. 4.9b), helping to reinforce the rapid transition away from La Niña conditions across the equatorial Pacific and setting the stage for the emerging El Niño.

El Niño conditions emerged during June, and MJO activity weakened during the boreal summer and autumn months as the low-frequency base state became the dominant driver of global tropical convective anomalies (Figs. 4.7a, 4.9c). Intraseasonal activity during this period was primarily associated with other modes, including Kelvin waves and Rossby waves. By boreal spring, a strong positive Indian Ocean dipole (IOD) event emerged, providing a secondary stationary signal that largely disrupted coherent MJO activity. The IOD activity was apparent in the MJO diagnostic figures primarily as strong low-level easterlies across the eastern Indian Ocean (Fig. 4.8a) and the RMM-based MJO index showing persistence in phases 8 and 1 during October (Fig. 4.9d).

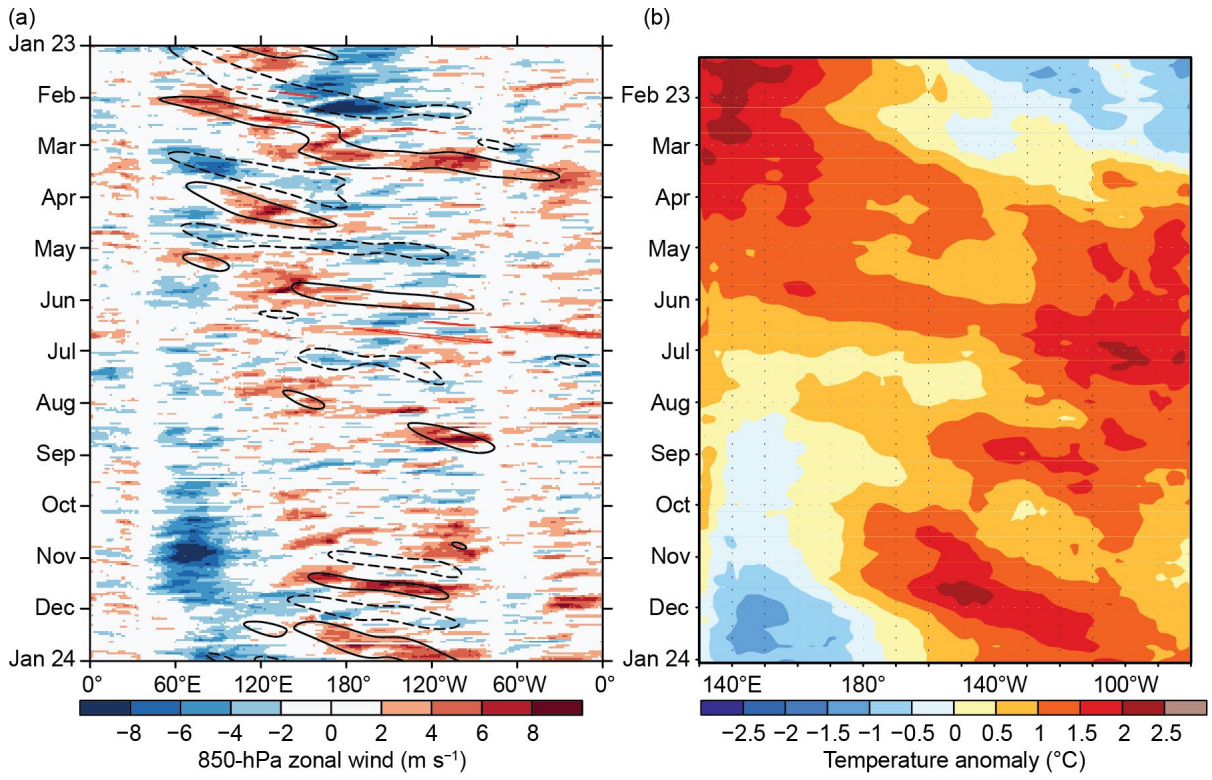

Fig. 4.8. (a) Time–longitude section for 2023 of anomalous 850-hPa zonal wind (m s^{-1}) averaged over 10°S–10°N. Contours identify anomalies filtered for the Madden-Julian Oscillation (black). (b) Time–longitude section for 2023 of the anomalous equatorial Pacific Ocean heat content, calculated as the mean temperature anomaly (°C) between 0-m and 300-m depth. Yellow/red (blue) shading indicates above- (below-) average heat content. Anomalies are departures from the 1991–2020 base period pentad means. Data in (b) are derived from an analysis system that assimilates oceanic observations into an oceanic general circulation model (Behringer et al. 1998).

Despite the increasing maturity of the El Niño event and the ongoing strong IOD in November and December, both of which typically degrade MJO propagation, robust MJO activity initiated in November, triggering an unusually strong low-level westerly wind burst over the equatorial West Pacific. The signal strengthened over the Western Hemisphere, circumnavigating the globe in approximately 40 days and triggering additional strong westerly wind bursts across the Pacific during the latter half of December. While El Niño-related SST anomalies were strongest across the central and eastern Pacific, positive SST anomalies remained in place across the West Pacific Warm Pool region despite the repeated downwelling oceanic Kelvin wave events. This unusual structure may have aided in continued MJO propagation, allowing strong convection to develop over the far western Pacific region.

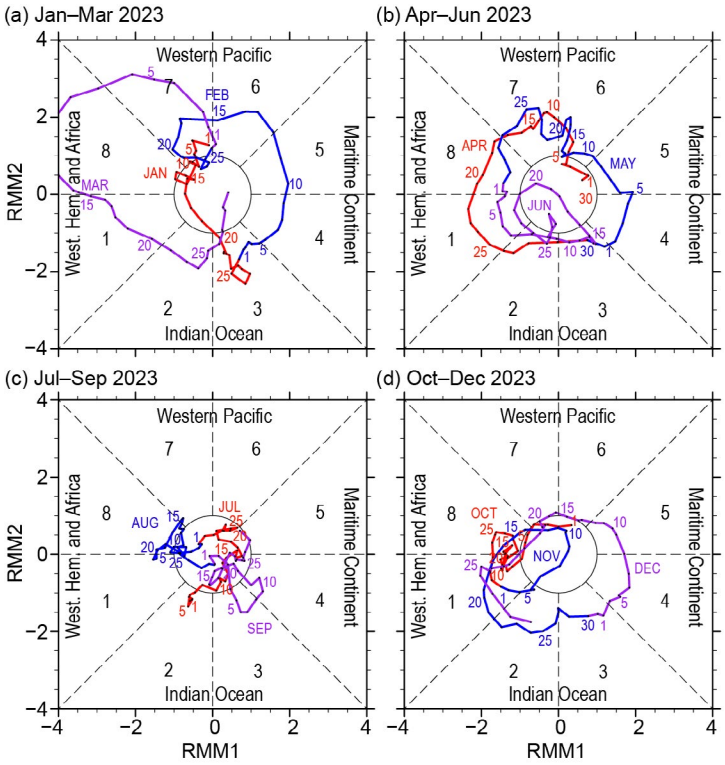

Fig. 4.9. Wheeler and Hendon (2004) Real-time Multivariate (RMM) index for (a) Jan–Mar, (b) Apr–Jun, (c) Jul–Sep, and (d) Oct–Dec 2023. Each point represents the Madden-Julian Oscillation (MJO) amplitude and location on a given day, and the connecting lines illustrate its propagation. The MJO amplitude as diagnosed by the RMM was so strong that it went off the plot in March. Amplitude is indicated by distance from the origin, with points inside the unit circle representing weak or no MJO. The eight phases around the origin identify the region experiencing enhanced convection, and counter-clockwise movement is consistent with eastward propagation.

d. Intertropical convergence zones

1. PACIFIC

N. Fauchereau

Tropical Pacific rainfall patterns are dominated by two convergence zones: the Intertropical Convergence Zone (ITCZ; Schneider et al. 2014) north of the equator and the South Pacific Convergence Zone (SPCZ; Vincent 1994) in the southwest Pacific. The position and intensity of these convergence zones throughout the year are highly sensitive to sea-surface temperature anomalies (SSTAs) and, therefore, the state of the El Niño–Southern Oscillation (ENSO; Trenberth 1984). During the course of 2023, the Pacific region underwent a transition from weak La Niña conditions to a strong El Niño. These dramatic changes in SSTAs were reflected in rainfall patterns, driven by significant changes in the position and intensity of the ITCZ and SPCZ.

Figure 4.10 summarizes the behavior for both convergence zones during 2023 using rainfall from the Multi-Source Weighted-Ensemble Precipitation (MSWEP) 2.8.0 dataset (Beck et al. 2019). Rainfall transects over 30°S to 20°N are presented for each quarter of the year, averaged across successive 30-degree longitude bands, starting in the western Pacific at 150°E–180°E. The 2023 seasonal variations are compared against the longer-term 1991–2020 climatology.

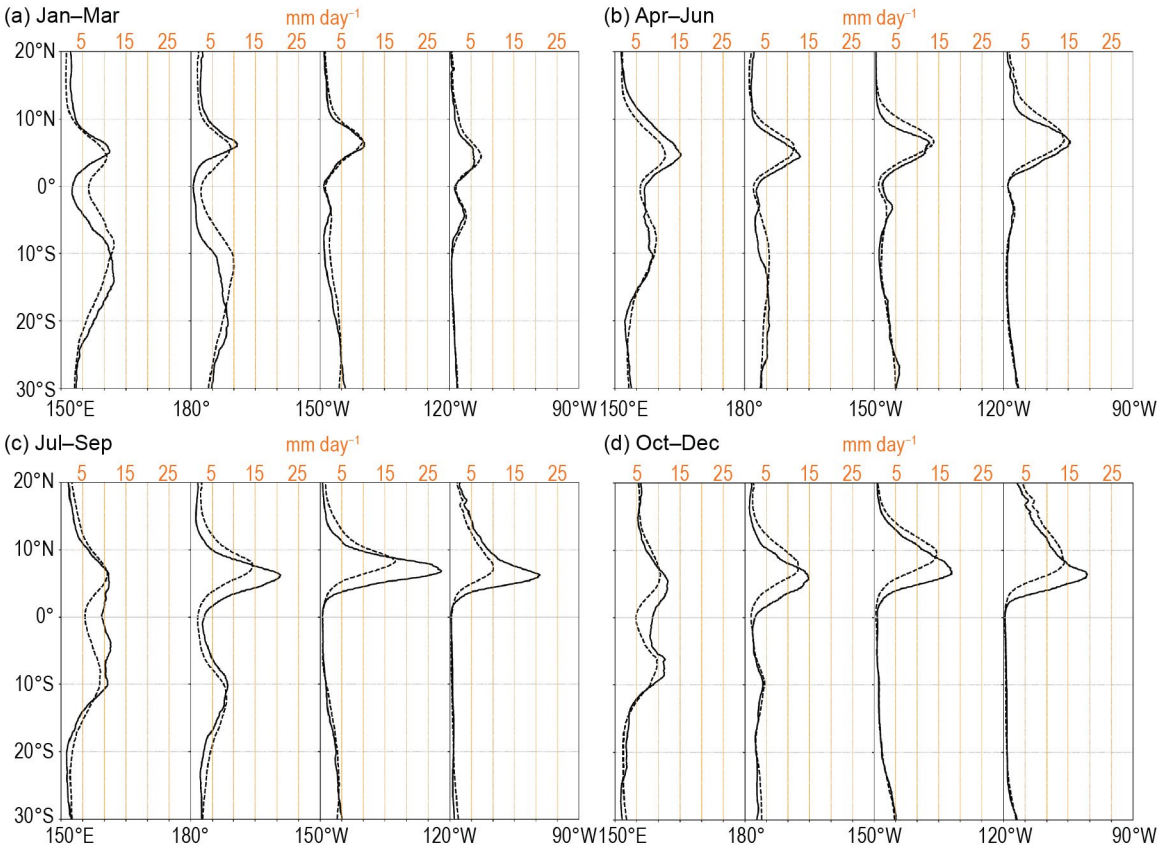

Fig. 4.10. Rainfall rate (mm day^{-1}) for (a) Jan–Mar, (b) Apr–Jun, (c) Jul–Sep, and (d) Oct–Dec 2023. The separate panels for each quarter show the 2023 rainfall latitudinal cross-section between 30°S and 20°N (solid line) and the 1991–2020 climatology (dotted line), separately for four 30° sectors from 150°E–180 to 120°W–90°W. (Source: MSWEP v2.8.0.)

The transects for January–March (Fig. 4.10a) for the western and central Pacific (150°E–150°W, especially from 150°E to the dateline) show that at the beginning of 2023, the SPCZ was shifted south and west of its climatological position. Rainfall rates within the ITCZ were reduced compared to climatology, a signature consistent with typical anomalies recorded in the Southern Hemisphere summer during La Niña. By contrast, in October–December, when the SSTAs were fully consistent with strong El Niño conditions, this pattern was broadly reversed: Fig. 4.10d shows that the ITCZ, especially in the central Pacific (180°–150°W and 150°W–120°W sectors)

was positioned south of its climatological position, with strong positive anomalies (enhanced rainfall rates compared to climatology) south of ~8°N and negative anomalies (decreased rainfall rates compared to climatology) to the north. Accordingly, the SPCZ appeared to be shifted north and east of its climatological position, although the amplitude of the anomalies was smaller than those observed during the opposite situation (i.e., the La Niña-like pattern) observed at the beginning of the year.

The shift in precipitation anomaly patterns in the tropical Pacific is exemplified in Fig. 4.11, which presents the rainfall anomalies for January–March 2023 (Fig. 4.11a) and October–December 2023 (Fig. 4.11b), respectively, compared to the 1991–2020 climatological period. During the first quarter of 2023 in the tropics zone, the defining pattern was a band of strong negative rainfall anomalies (decreased rainfall compared to normal) stretching along and just north of the equator, from the Maritime Continent to the central and eastern Pacific, capped by positive anomalies to the north. This anomaly pattern corresponded to a northward-shifted ITCZ, a typical La Niña response. In the western part of the Pacific, south of the equator, the main signal was enhanced rainfall south of a line extending approximately diagonally from Papua New Guinea in the western Pacific to the islands of French Polynesia in the eastern Pacific and suppressed rainfall to the north. This can be interpreted as an SPCZ shifted southwest of its climatological position, which is another typical La Niña signal. In contrast, the pattern of rainfall anomalies in October–December was broadly reversed. Of note during the last quarter of 2023 was the large amplitude of the anomalies recorded, especially along the equator eastward from about the dateline to about 120°W, with positive anomalies exceeding 10 mm day^{-1} just north of the equator.

The exceptional nature of the rainfall anomalies observed during the last quarter of 2023, when El Niño conditions were fully established, are well illustrated in Fig. 4.12, which shows a more detailed comparison of the central Pacific (180°–150°W) rainfall transect during October–December, relative to all other years in this dataset. During this three-month period, the recorded rainfall north of ~5°N, averaged over all longitudes

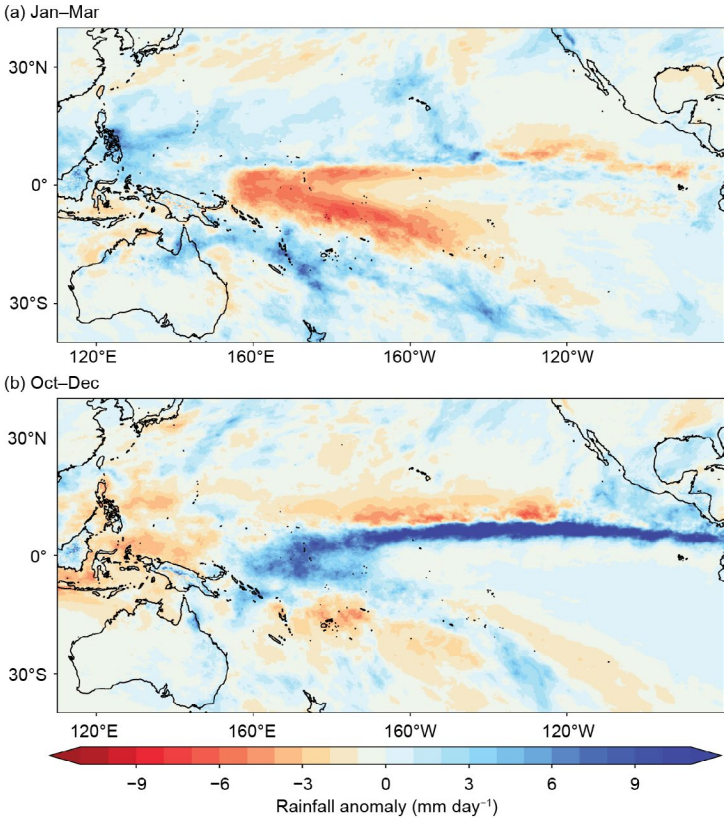

Fig. 4.11. Rainfall anomalies (mm day^{-1}) from for (a) Jan–Mar 2023 and (b) Oct–Dec 2023. The anomalies are calculated with respect to the 1991–2020 climatology. (Source: MSWEP v2.8.0.)

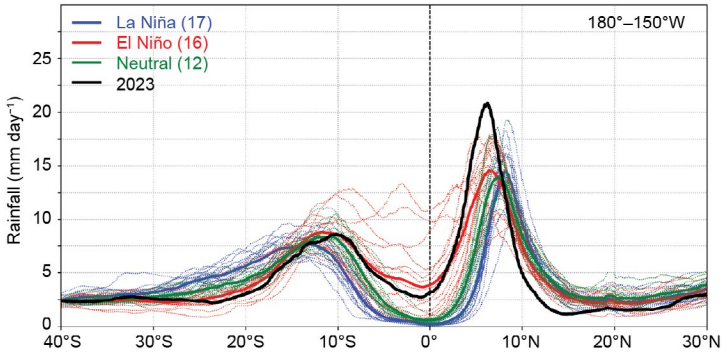

Fig. 4.12. Rainfall rate (mm day^{-1}) for Oct–Dec for each year from 1979 to 2023, averaged over the longitude sector 180°–150°W. The cross-sections are color-coded according to NOAA's Oceanic Niño Index (with a threshold of ±0.5°C), except 2023, which is shown in black. Dotted lines are individual years, and solid lines are the average overall years in each El Niño–Southern Oscillation phase. The inset legend indicates how many years went into each composite sample. (Source: MSWEP v2.8.0.)

(black line), exceeded by a large margin the rainfall rates recorded on average for all El Niño years (thick red line in Fig. 4.12).

In summary, precipitation anomaly patterns throughout 2023 underwent a dramatic shift from La Niña to El Niño-like and reached exceptional amplitude, especially just north of the equator in the eastern Pacific, corresponding to rainfall rates greatly enhanced within an ITCZ shifted south of its climatological position and, according to the MSWEP 2.8.0, the strongest anomalies on record going back to 1979.

2. ATLANTIC

A. B. Pezza and C. A. S. Coelho

The Atlantic ITCZ is a well-organized convective band that oscillates between approximately 5°N–12°N during July–November and 5°S–5°N during January–May (Waliser and Gautier 1993; Nobre and Shukla 1996). Equatorial atmospheric Kelvin waves can modulate ITCZ intraseasonal variability (Guo et al. 2014). ENSO and the Southern Annular Mode (SAM) can also influence the ITCZ on interannual time scales (Münnich and Neelin 2005). The SAM, also known as the Antarctic Oscillation, describes the north–south movement of the westerly wind belt that circles Antarctica. A positive SAM event reflects a contraction of the westerly wind belt away from the equator, with stronger subtropical ridges and less precipitation in the midlatitudes (Ding et al. 2012; Liu et al. 2021; Moreno et al. 2018).

The South Atlantic responded to the demise of the last three years of La Niña from January to May with a slightly stronger-than-normal subtropical anticyclone accompanied by anomalously warm water north of the equator and increased pressure gradients towards Antarctica, where anomalous cyclonic activity prevailed. As a result, well-below-average precipitation was widespread over much of the area in and around northern Brazil (Figs. 4.13a,b). The precipitation deficit was much stronger than observed in 2022 when La Niña was at its peak. This pattern was accompanied by a largely positive SAM, as seen by the negative pressure anomalies over the Antarctic Peninsula (Fig. 4.13a). The movement of the ITCZ was markedly north of climatology during its lifecycle (Fig. 4.14a). The Atlantic Index (see Fig. 4.14b for definition) was strongly negative, as expected for a northerly-displaced ITCZ. This pattern was associated with low-level wind convergence well north of the equator toward the areas of anomalously warm waters, with subsidence and drought conditions resulting for much of the area in and around tropical Brazil.

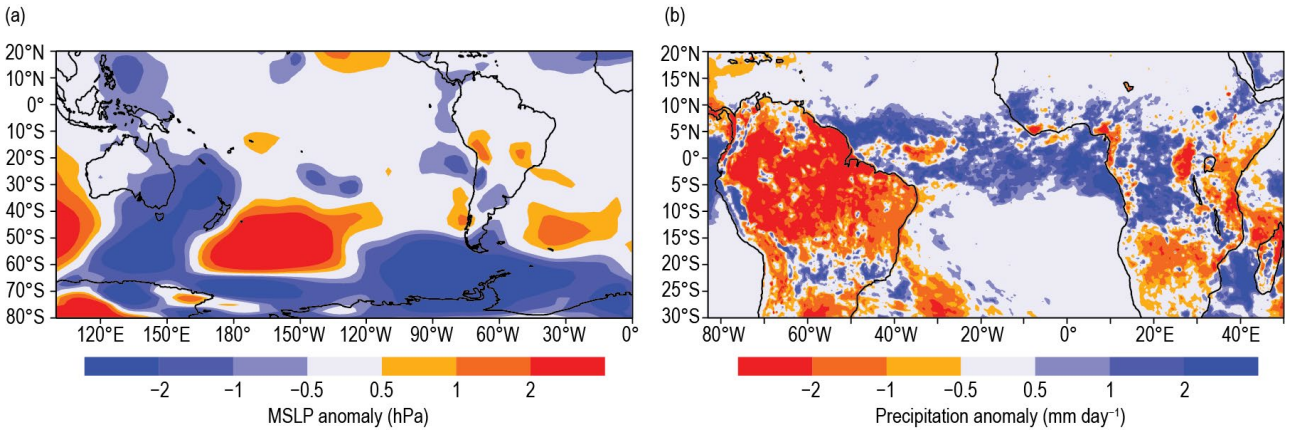

Fig. 4.13. Jan–May 2023 (a) tropical and Southern-Hemisphere mean sea-level pressure (MSLP; hPa) anomalies and (b) precipitation anomalies (mm day^{-1}) over the Atlantic sector. MSLP anomalies are calculated with respect to the 1991–2020 climatology and are derived from National Centers for Environmental Prediction (NCEP) National Center for Atmospheric Research (NCAR) reanalysis (Kalnay et al. 1996). Precipitation anomalies are calculated with respect to the 1998–2022 climatology and are derived from Climate Prediction Center Morphing technique (CMORPH; Joyce et al. 2004).

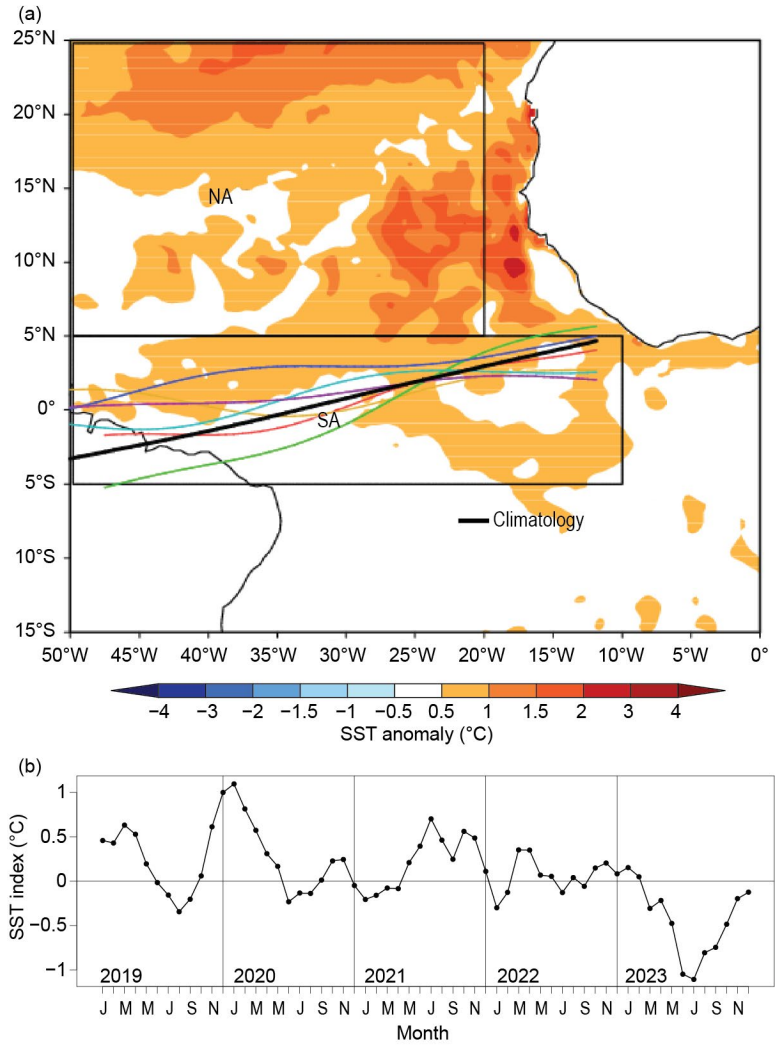

Fig. 4.14. (a) Atlantic Intertropical Convergence Zone (ITCZ) position inferred from outgoing longwave radiation (Liebmann and Smith 1996) during Mar 2023. The colored thin lines indicate the approximate position for the six pentads of the month. The thick black line indicates the Atlantic ITCZ climatological position for Mar. The sea-surface temperature (SST) anomalies (°C) for Mar 2023 calculated with respect to the 1982–2020 climatology are shaded. The two boxes indicate the areas used for the calculation of the Atlantic index in panel (b), which shows the monthly OISST (Reynolds et al. 2002) anomaly time series averaged over the South Atlantic (SA) sector (SA region: 5°S–5°N, 10°W–50°W) minus the SST anomaly time series averaged over the North Atlantic (NA) sector (NA region: 5°N–25°N, 20°W–50°W) for the period of 2019–23, forming the Atlantic index. A positive phase of the index indicates favorable conditions for enhanced Atlantic ITCZ activity south of the equator.

e. Global monsoon summary

—B. Wang and Q. He

The global monsoon is the dominant mode of annual precipitation and circulation variability and is one of the defining features of Earth's climate system (Wang and Ding 2008). Figure 4.15 depicts the monsoon domain (red lines) defined by rainfall characteristics (rainy summer versus dry winter; Wang 1994) rather than the traditional definition by winds (Ramage 1971). The Northern Hemisphere (NH) monsoon includes five regional monsoons: northern Africa, India, East Asia, the western North Pacific, and North America. The Southern Hemisphere (SH) monsoon consists of three monsoons: southern Africa, Australia, and South America. Here, we summarize both global and regional monsoon anomalies in the 2023 "monsoon year", focusing on the SH summer (November 2022–April 2023) and NH summer (May–October 2023) monsoons.

1. NH AND SH LAND MONSOON PRECIPITATION

Since monsoon rainfall over land has more important socioeconomic impacts than oceanic-monsoon rainfall, we first examine land-monsoon rainfall (LMR) in the NH (May–October) and the SH (November–April) summer monsoon. The NH and SH LMR are measured by the mean precipitation rate averaged over the land areas only in the NH and SH monsoon domains, respectively.

Historically, the year-to-year variations of the NH and SH LMR are dominated by the El Niño–Southern Oscillation (ENSO; Wang et al. 2012). Figure 4.16 highlights

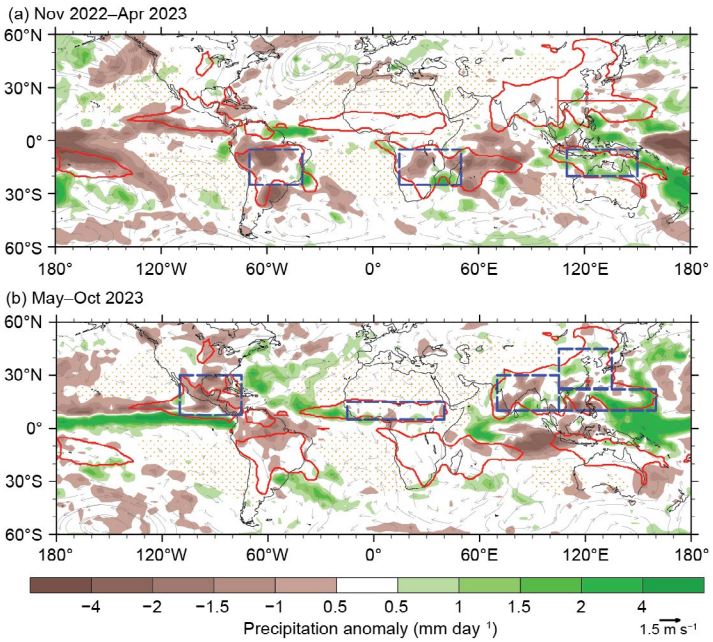

Fig. 4.15. Mean precipitation anomalies (mm day^{-1}) and 850-hPa wind anomalies (m s^{-1}) for (a) the Southern Hemisphere summer monsoon season: Nov 2022–Apr 2023 and (b) the Northern Hemisphere summer monsoon season: May–Oct 2023. The anomalies are departures from the 1991–2020 climatology. Red lines outline the global monsoon precipitation domain. Two criteria define the monsoon domain: 1) the annual precipitation range (summer-minus-winter mean) exceeds 300 mm, and 2) the summer precipitation is greater than 55% of the total annual precipitation amount, where summer here means Nov–Mar for the Southern Hemisphere and May–Oct for the Northern Hemisphere (Wang and Ding 2008). The blue rectangular boxes denote the regions where the regional monsoon precipitation indices are measured. The dotted area represents the dry region with a local summer precipitation rate below 1 mm day^{-1}. (Source: GPCP; Huffman et al. 2009.)

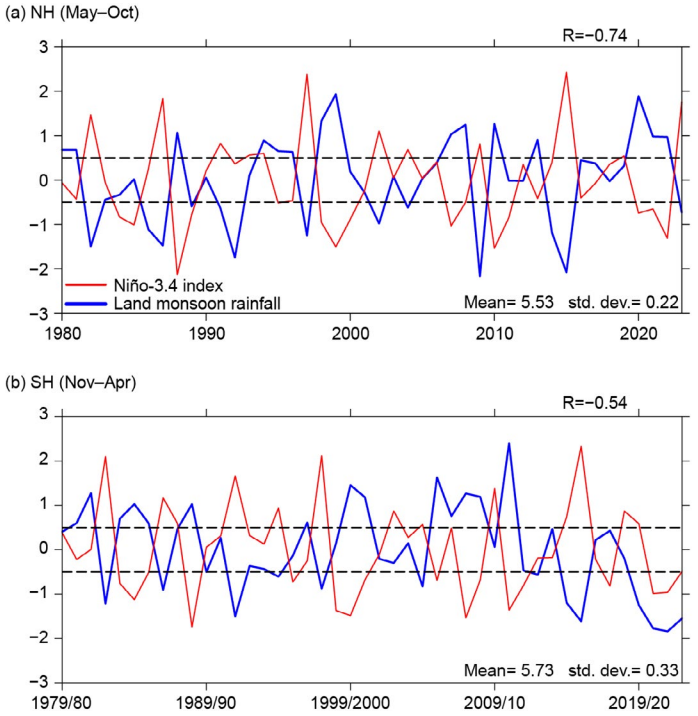

Fig. 4.16. Correlation between the El Niño–Southern Oscillation and the Northern Hemisphere (NH) and Southern Hemisphere (SH) land monsoon rainfall. (a) NH summer (May–Oct) land monsoon precipitation anomaly (blue) normalized by its standard deviation. The climatological mean NH summer land monsoon precipitation (mean) and std. dev. are shown in the lower right panel (mm day^{-1}). Numbers in the top right of each panel denote the correlation coefficient (R) between the seasonal mean precipitation anomaly and the simultaneous Niño-3.4 index (red). Dashed lines indicate ±0.5. (b) As in (a) except for the SH summer (Nov–Apr). The land monsoon precipitation excludes the monsoon rainfall over the oceanic monsoon domain. (Source: GPCP for precipitation; HadISST and ERSSTv5 for SST.)

this relationship. Both the NH and SH summer LMR are significantly anti-correlated with the corresponding Niño-3.4 index. The NH LMR has a correlation of −0.74 from 1980 to 2023 (Fig. 4.16a). The SH LMR was also negatively correlated with the Niño-3.4 index (r = −0.75) during 1979/80–2019/20. However, in the past three years the SH LMR and Niño-3.4 indices have both been negative (Fig. 4.16) such that the correlation coefficient for 1979/80–2022/23 is only −0.54 (Fig. 4.16b).

During November 2022–April 2023, the tropical Pacific experienced La Niña conditions (the third year of the 2020–22 triple La Niña). The SH LMR was well below average (–1.5 std. dev.) as noted in Fig. 4.16b. This positive relationship between ENSO and SH LMR is at odds with the historical negative correlation. As noted in the previous paragraph, this is the third consecutive year during which the SH LMR is positively related to the Niño-3.4 index. The breakdown of the negative correlation between the ENSO and SH LMR deserves further exploration.

El Niño conditions developed during May–October 2023, which were likely the predominant driver of the reduced NH LMR (−0.7 std. dev., i.e., about 0.15 mm day^{-1} or 23 mm per six months in the NH land monsoon regions; Fig. 4.16a). The decreased NH LMR in response to the 2023 El Niño is consistent with the historically observed negative El Niño–NH LMR relationship.

2. REGIONAL MONSOON PRECIPITATION AND CIRCULATION

We use regional monsoon precipitation and circulation indices to measure the integrated regional monsoon intensity. The regional summer monsoon precipitation indices signify the anomalous precipitation rate averaged over each of the blue rectangular box regions shown in Fig. 4.15. The precipitation averaged in each blue box can represent well the precipitation averaged over the corresponding, actual regional monsoon domain (Yim et al. 2014). The definitions of the circulation indices for each monsoon region are provided in Table 4.1. The circulation indices are generally defined by the meridional shear of the zonal winds at 850 hPa, which measures the intensity (shear relative vorticity) of the monsoon troughs, except for the northern African and East Asian monsoons. The northern African monsoon circulation index is defined by the westerly monsoon strength, reflecting the south–north thermal contrast between the South and North Atlantic. The East Asian summer monsoon circulation index is determined by

Table 4.1. Definition of the regional summer monsoon circulation indices and their correlation coefficients with the corresponding regional summer monsoon precipitation indices for 1979/80–2022/23. The precipitation indices are defined by the areal mean precipitation anomalies over the blue box regions shown in Fig. 4.15. R (r) represents the correlation coefficient between the total (land) monsoon precipitation and the corresponding circulation index. The correlation coefficients were computed using monthly time series (176 summer months; Jun–Sep in the Northern Hemisphere [1980–2023] and Dec–Mar in the Southern Hemisphere [1979/80–2022/23]). Bolded numbers represent significance at the 99% confidence level.

Regional monsoon	Definition of the circulation index	R (r)
Indian (ISM)	U850 (5°N–15°N, 40°E–80°E) minus U850 (25°N–30°N, 60°E–90°E)	**0.71 (0.58)**
Western North Pacific (WNPSM)	U850 (5°N–15°N, 100°E–130°E) minus U850 (20°N–35°N, 110°E–140°E)	**0.87 (0.71)**
East Asian (EASM)	V850 (20°N–35°N, 120°E–140°E) plus V850 (10°N–25°N, 105°E–115°E)	**0.72 (0.72)**
North American (NASM)	U850 (5°N–15°N, 130°W–100°W) minus U850 (20°N–30°N, 110°W–80°W)	**0.86 (0.79)**
Northern African (NAFSM)	U850 (0°–10°N, 40°W–10°E)	**0.71 (0.71)**
South American (SASM)	U850 (20°S–5°S, 70°W–40°W) minus U850 (35°S–20°S, 70°W–40°W)	**0.80 (0.80)**
Southern African (SAFSM)	U850 (12°S–2°S, 10°W–30°E) minus U850 (30°S–10°S, 40°E–60°E)	**0.58 (0.45)**
Australian (AUSSM)	U850 (15°S–0°, 90°E–130°E) minus U850 (30°S–20°S, 100°E–140°E)	**0.88 (0.79)**

the meridional wind strength, reflecting the east–west thermal contrast between the Asian continent and the western North Pacific. The precipitation and circulation indices are well correlated for most regional monsoons, with monthly mean correlation coefficients ranging from 0.71 to 0.88, except for the southern African monsoon (Table 4.1). Thus, the regional precipitation and circulation indices generally provide consistent measurements of the strength of each regional monsoon system. Notably, in the Indian and southern African monsoon regions, the circulation indices represent land monsoon rainfall less faithfully due to the fact that the leading modes of the precipitation anomalies in these two regions show a dipolar pattern (Yim et al. 2014).

During SH summer from November 2022 to April 2023, the La Niña-enhanced Walker Circulation contributed to suppressed rainfall over the central-eastern Pacific and increased rainfall over the Maritime Continent and northern Australia (Fig. 4.15a). However, precipitation was significantly reduced over the South American and southern African monsoon regions, which is abnormal for La Niña. Figure 4.17 shows areal-averaged monsoon precipitation and circulation intensities for each regional monsoon. Both the Australian summer monsoon precip-

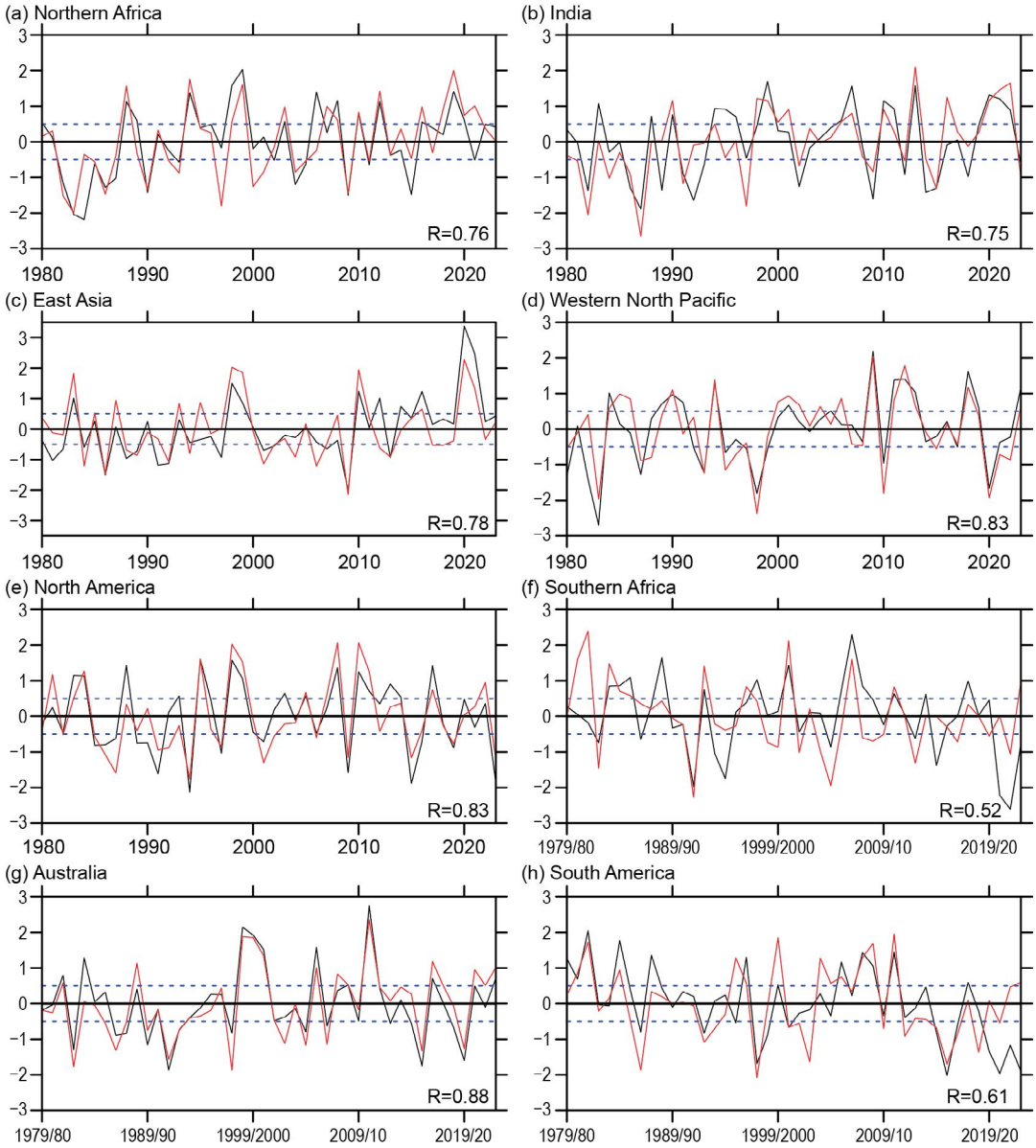

Fig. 4.17. (a)–(h). Temporal variations of summer monsoon precipitation (black lines) and low-level circulation (red lines) indices for eight regional monsoons. The precipitation indices represent the anomalous precipitation rate averaged over the blue rectangular box regions shown in Fig. 4.15. The corresponding circulation indices are defined in Table 4.1. All indices were normalized by their corresponding standard deviations (ordinate) derived for the period 1979/80–2022/23. Numbers in the bottom right of each panel denote the correlation coefficient (R) between the seasonal mean precipitation and circulation indices (sample size: 44). Dashed lines indicate ±0.5 std. dev. The summer monsoon seasons are May–Oct for the Northern Hemisphere and Nov–Apr for the Southern Hemisphere. (Data source: GPCP for precipitation; ERA5 [Hersbach et al. 2020] for circulation).

itation and circulation index showed above-normal intensity (Fig. 4.17g). The South American monsoon precipitation was 2 std. dev. below average, but the related circulation strength was 0.5 std. dev. above average (Fig. 4.17h). The southern African summer monsoon precipitation was 1 std. dev. below average, while the circulation intensity was 0.7 std. dev. above average (Fig. 4.17f). Over the South American and southern African regions, the precipitation and circulation anomalies showed opposite tendencies, which is abnormal. Overall, the circulation indices of the three SH regional monsoon systems indicate enhanced monsoons, consistent with the historically observed negative correlations between the SH regional monsoons and ENSO. However, inconsistencies in the precipitation with the expected La Niña response remain to be explored.

During the 2023 NH summer monsoon season, an El Niño developed, which severely suppressed the North American monsoon by drawing convection southward (Fig. 4.15b). The Pacific warming pattern increased precipitation in the far western Pacific (north of New Guinea) and the Philippine Sea and reduced precipitation over the western Maritime Continent and the southeast tropical Indian Ocean (Fig. 4.15b). Compared to the canonical response for eastern Pacific El Niño development, the dry anomalies over the Maritime Continent were shifted westward, possibly due to the relatively warm central Pacific. The suppressed rainfall anomaly over the western Maritime Continent and the eastern Indian Ocean could excite atmospheric descending Rossby waves residing on both sides of the equator. This pattern then reduces Indian summer monsoon rainfall and triggers the development of a positive phase of the Indian Ocean (IO) dipole sea-surface temperature anomalies (e.g., anomalous east IO cooling and west IO warming). Regionally, the Indian and North American monsoon precipitation and circulation indices all showed significant negative anomalies (Figs. 4.17b,e), which contributed to the decreased NH LMR (Fig. 4.16a). Over the northern African and East Asian summer monsoon regions, both the precipitation and circulation patterns were near normal (Figs. 4.17a,c). The western North Pacific monsoon circulation and rainfall were both positive. In summary, regardless of the westward shift of the convective anomalies over the Maritime Continent during the development of the 2023 El Niño, the NH regional monsoon responses basically followed the typical El Niño–monsoon relationships.

f. Indian Ocean dipole

—L. Chen and J.-J. Luo

The Indian Ocean dipole (IOD) is the dominant interannual mode in the tropical Indian Ocean (IO), characterized by a zonal dipole of sea-surface temperature (SST) anomalies in the equatorial IO (Saji et al. 1999; Luo et al. 2010, 2012). The dipole originates from local air–sea interaction processes in the tropical IO and/or ENSO forcing (Luo et al. 2007, 2010). The IOD typically develops in boreal spring and summer, matures in autumn, and rapidly terminates in early winter. A positive IOD (pIOD) event usually features negative SST anomalies in the eastern IO and positive SST anomalies in the west during boreal summer and autumn, and vice versa for a negative IOD (nIOD). The IOD phenomenon has a strong nonlinear feature, that is, the pIOD is usually stronger than the nIOD due to the asymmetric strength of the air–sea feedback between the two phases of the IOD (Luo et al. 2007; Hong et al. 2008).

In 2023, the tropical IO witnessed a strong pIOD event with significant negative SST anomalies in the eastern IO and positive SST anomalies in the western IO (Fig. 4.18a). The IOD index reached ~1.2°C in boreal autumn 2023 based on the OISST dataset (Fig. 4.18b). There have been 12 pIOD events from 1982 to the present (1982, 1991, 1994, 1997, 2006, 2007, 2011, 2012, 2015, 2018, 2019, 2023), and they tend to be associated with El Niño events as in 2023. The pIOD event in 2023 was the fourth-strongest pIOD event in the past 42 years (the three stronger events occurred in 2019, 1997, and 1994).

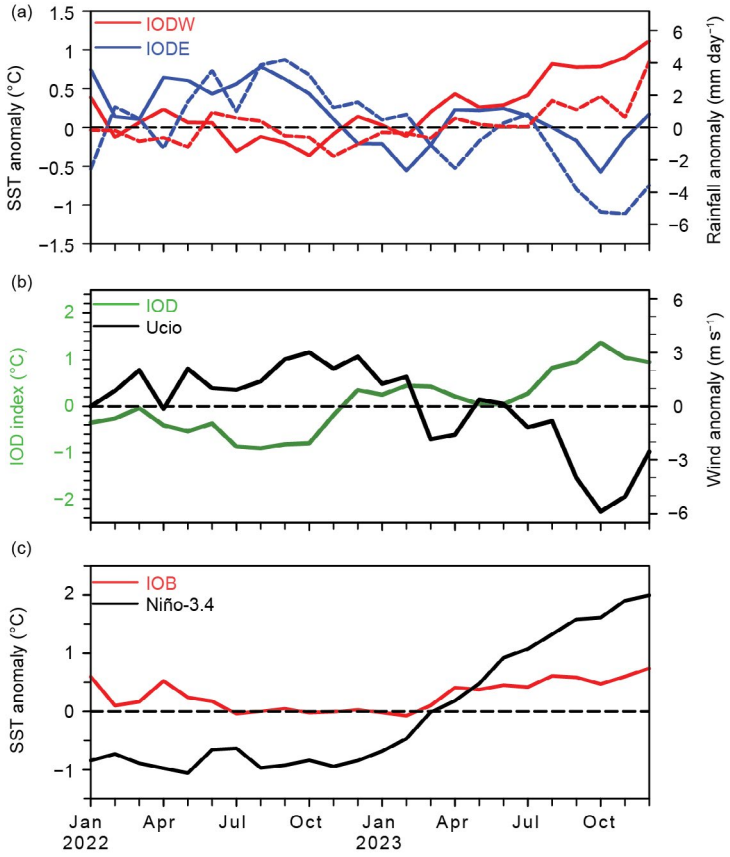

Fig. 4.18. (a) Monthly anomalies of sea-surface temperature (SST; °C; solid lines) and precipitation (mm day^{-1}; dashed lines) of the Indian Ocean dipole (IOD) in the eastern pole (IODE; 10°S–0°, 90°E–110°E; blue lines) and the western pole (IODW; 10°S–10°N, 50E°–70°E; red lines) of the IOD. (b) As in (a), but for the IOD index (measured by the SST difference between IODW and IODE, green line) and surface zonal wind anomaly (m s^{-1}) in the central equatorial IO (Ucio; 5°S–5°N, 70°E–90°E; black line). (c) As in (a), but for the SST anomalies in the Niño-3.4 region (5°S–5°N, 170°W–120°W; black line) and the tropical IO (IOB; 20°S–10°N, 40°E–120°E; red line). Anomalies are relative to the 1982–2023 base period. (Sources: NOAA OISST [Reynolds et al. 2002]; monthly CMAP precipitation analysis] available at http://ftpprd.ncep.noaa.gov/pub/precip/cmap/]; and JRA-55 atmospheric reanalysis [Ebita et al. 2011].)

Following a negative IOD event in 2022, the tropical IO was characterized by a weak Indian Ocean basin (IOB) mode from late boreal winter to early spring 2023 (Figs. 4.18a–c). The IOB mode is believed to favor the decay of El Niño via modulating the zonal wind anomalies in the western equatorial Pacific as noted by Wu et al. (2024). Easterly wind anomalies then developed over the central IO during boreal spring and summer 2023 (Figs. 4.18b, 4.19). As a result, a pIOD event began to develop in boreal spring and summer 2023 and strengthened in boreal autumn 2023 (Fig. 4.18b). From the perspective of the tropical Indo-Pacific Ocean, these easterly wind anomalies over the central IO region are closely associated with the rapidly developing El Niño conditions in the tropical Pacific (Fig. 4.18c). In response to El Niño, an anomalous Walker Circulation occurs over the equatorial sector of the Indo-Pacific Ocean. As indicated by the anomalous precipitation and surface winds (Fig. 4.19) and the anomalous 200-hPa velocity potential field (contours in Fig. 4.20), anomalous ascending motion and increased rainfall occur over the central equatorial Pacific, while anomalous descending motion and below-normal rainfall occurred over the western equatorial Pacific, the Maritime Continent, and the eastern equatorial IO region. Consequently, anomalous easterly winds over the equatorial IO began to develop in the boreal spring of 2023.

Due to the positive feedback between the easterly wind anomalies and the dipole of SST anomalies over the equatorial sector of the IO, the pIOD event rapidly grew from late spring to boreal summer 2023, as shown in Figs. 4.18b, 4.19b,c, 4.20b,c. As a result of the positive air–sea feedback processes among the anomalous SST, low-level winds, and precipitation fields, an obvious dipole structure of SST and precipitation anomalies occurred in the tropical IO during boreal autumn 2023, with anomalous cool and dry conditions in the eastern IO and warm and wet conditions in the western IO (Figs. 4.19, 4.20).

In summary, a strong pIOD event occurred in 2023, with the IOD index reaching 1.2°C during boreal autumn. The development of this pIOD event appears to have been driven by El Niño conditions, following two consecutive negative IOD events in 2021 and 2022 that coincided with La Niña conditions in the Pacific (Chen and Luo 2022). In response to the development of El Niño in 2023, an anomalous Walker circulation occurred over the tropical Indo-Pacific sector, with a stronger descending branch over the western equatorial Pacific, the Maritime Continent, and the eastern equatorial IO. Consequently, anomalous easterly winds developed in boreal summer 2023, causing a dipole of SST anomalies to develop. There was a clear zonal dipole of SST and precipitation anomalies in the equatorial IO during boreal autumn 2023. In early winter (November–December) 2023, the pIOD started to decay due to IOD dynamics.

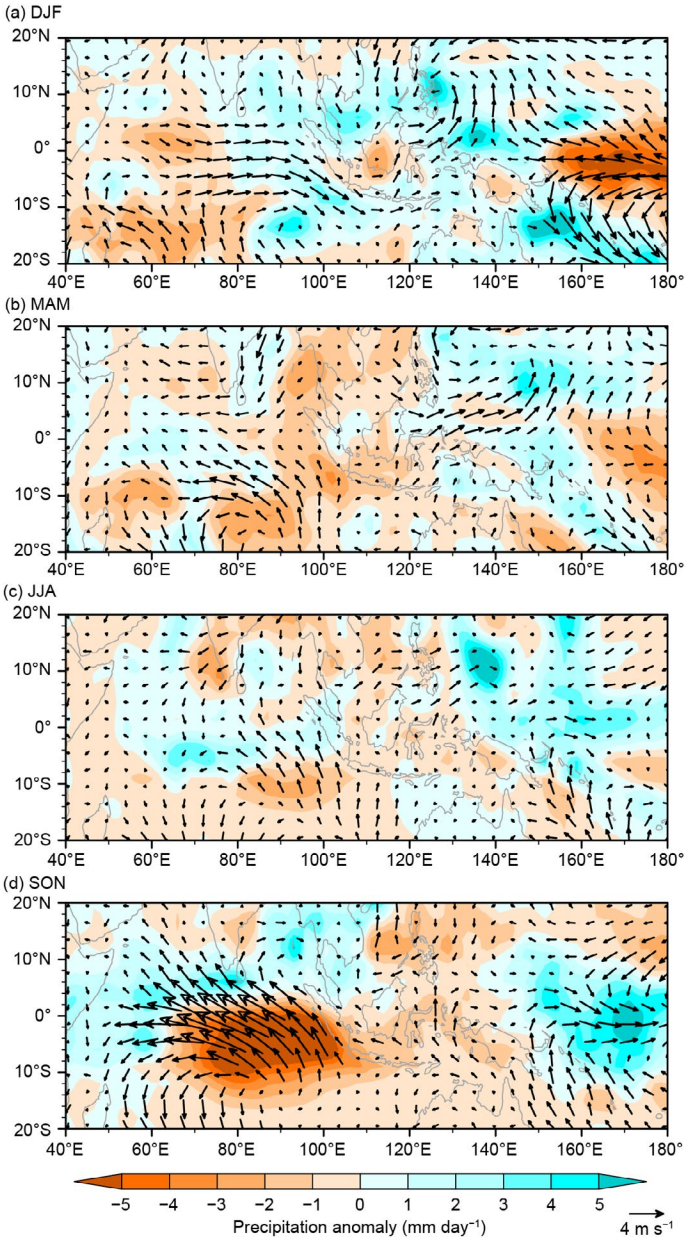

Fig. 4.19. Precipitation (mm day^{-1}) and surface wind (m s^{-1}) anomalies during (a) Dec 2022–Feb 2023, (b) Mar–May 2023, (c) Jun–Aug 2023, and (d) Sep–Nov 2023. (Sources: monthly CMAP precipitation analysis [available at ftp://ftp.cpc.ncep.noaa.gov/precip/cmap] and JRA-55 atmospheric reanalysis [Ebita et al. 2011].)

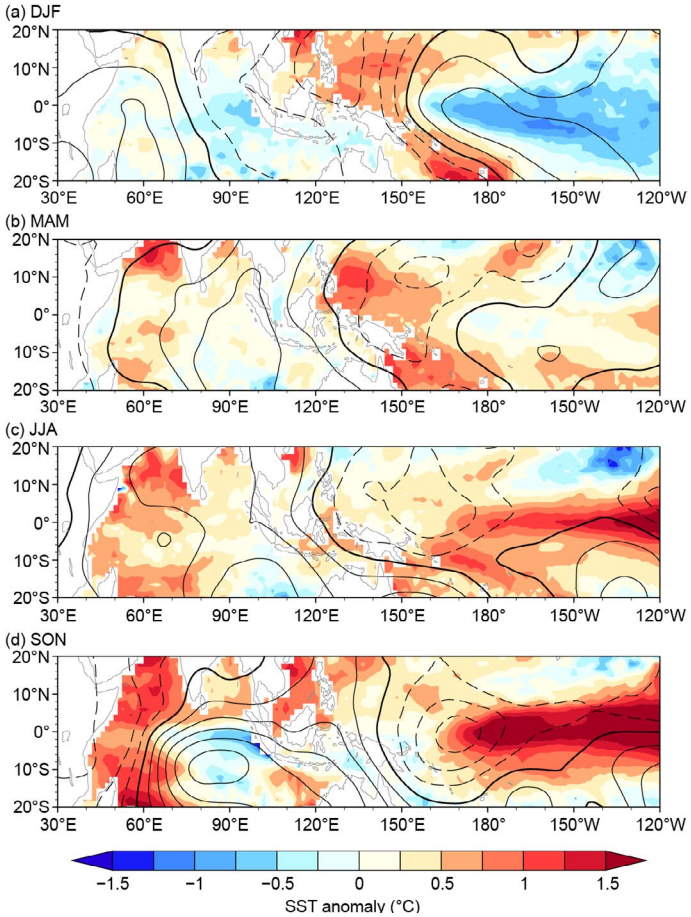

Fig. 4.20. Sea-surface temperature anomalies (°C, colored scale) superimposed by 200-hPa velocity potential (× 10^6 m^2 s^{-1}, contours with an interval of 1, and solid/dashed/bold curves denote positive/negative/zero values) during (a) Dec 2022–Feb 2023, (b) Mar–May 2023, (c) Jun–Aug 2023 and (d) Sep–Nov 2023. Anomalies were calculated relative to the climatology over the period 1982–2023. (Sources: NOAA OISST [Reynolds et al. 2002] and JRA-55 atmospheric reanalysis [Ebita et al. 2011].)

g. Tropical cyclones

1. OVERVIEW

H. J. Diamond and C. J. Schreck

The International Best Track Archive for Climate Stewardship (IBTrACS) dataset comprises historical tropical cyclone (TC) best-track data from numerous sources around the globe, including all of the World Meteorological Organization (WMO) Regional Specialized Meteorological Centers (RSMCs; Knapp et al. 2010). This dataset represents the most complete compilation of global TC data. From these data, 1991–2020 climatological values of TC activity for each basin using statistics from both the WMO RSMCs and the Joint Typhoon Warning Center (JTWC) are calculated following Schreck et al. (2014). These values are referenced in each subsection. Tallying the global TC numbers is challenging and involves more than simply adding up basin totals, as some storms cross TC basin boundaries, some TC basins overlap, and multiple agencies track and categorize them. The Northern Hemisphere (NH) basins are typically measured from January to December while Southern Hemisphere (SH) basins are typically measured from July to June. Global values here are the sum of NH for 2023 and SH for 2022/23. Unless otherwise noted, the statistics are based on preliminary data from NOAA's National Hurricane Center (NHC) and the JTWC. However, differences between the JTWC and the WMO RSMCs or other local agencies will be noted as appropriate.

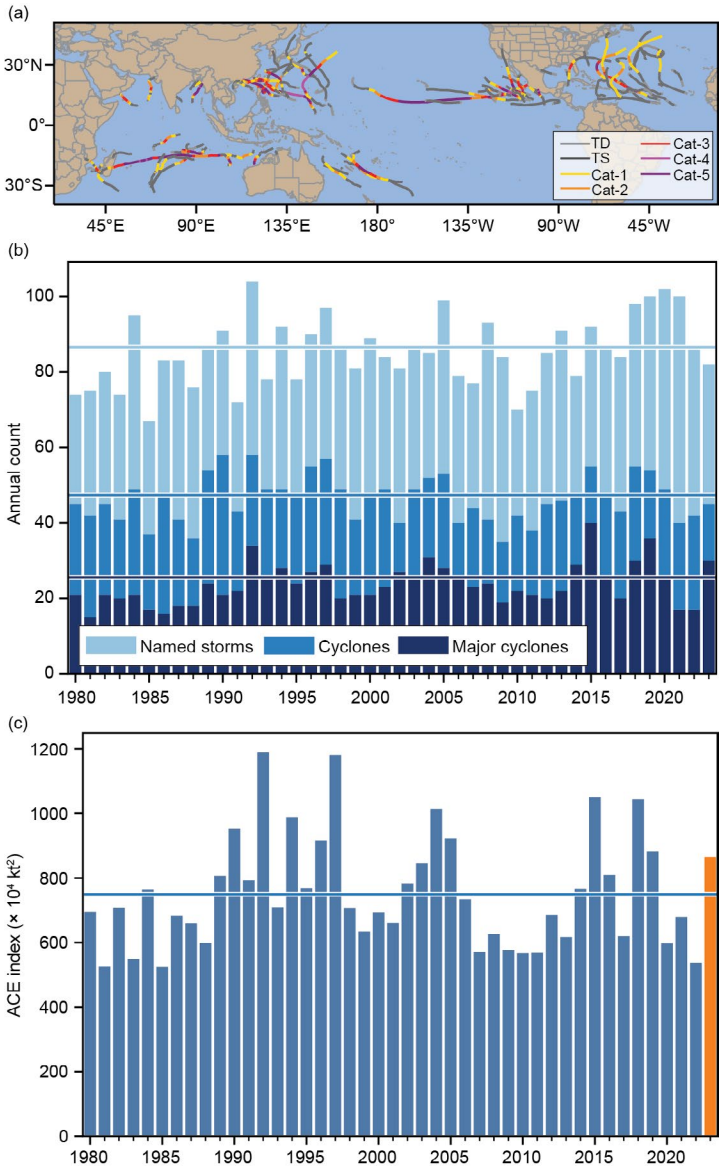

Fig. 4.21. (a) Global summary of tropical cyclone (TC) tracks overlaid on associated OISST anomalies (°C; Reynolds et al. 2002) for the 2023 season relative to 1991–2020; (b) global TC counts; and (c) global accumulated cyclone energy (ACE) values (× 10^4 kt²). Horizontal lines in (b) and (c) are the 1991–2020 normal values.

Based on preliminary data from the NHC and the JTWC as archived in IBTrACS (Fig. 4.21), the combined 2023 season had 82 named storms (sustained wind speeds ≥34 kt or 17 m s^{-1}), which is 15 fewer than the previous season (2022; Diamond and Schreck 2022) and also below the 1991–2020 average of 87. There were 45 hurricanes/typhoons/cyclones (HTCs; sustained wind speeds ≥64 kt or 33 m s^{-1}), 30 of which reached major HTC status (sustained wind speeds ≥96 kt or 49 m s^{-1}), which was nearly double the amount from 2022. The accumulated cyclone energy (ACE) for the season was 866 × 10^4 kt², which was 67.5% greater than that of last year (Diamond and Schreck 2022).

In sections 4g2–4g8, 2022/23 SH and 2023 NH seasonal TC activity are described and compared to the historical record for each of the seven WMO-defined TC basins. For simplicity, all counts are broken down by the U.S. Saffir-Simpson Hurricane Wind Scale (SSHWS)[2]. The overall picture of global TCs during 2023 is shown in Fig. 4.21, and counts by category and intensity are documented in Table 4.2.

[2] SSHWS is based on 1-minute averaged winds, and the categories are defined at: https://www.weather.gov/mfl/saffirsimpson; the Australian category scale is based on 10-minute averaged winds, and those categories are defined at https://australiasevereweather.com/cyclones/tropical_cyclone_intensity_scale.htm.

The eastern North Pacific, North Indian Ocean, and South Indian Ocean basins each had above-normal ACE relative to 1991–2020. Table 4.2 uses this climatological period for classifying seasons for consistency amongst basins. However, NOAA uses the terciles from 1951–2020 to classify North Atlantic ACE owing to the longer record of data there. The North Atlantic ACE was above normal relative to 1951–2020 but near normal relative to 1991–2020. By NOAA's definition, 2023 was the seventh above-normal season in the last eight years. Activity in the North Indian Ocean was particularly pronounced. Depending on the metric, it was either the second- or third-most-active season since 1981.

While the western North Pacific was near normal in terms of ACE, it was the fourth consecutive year with below-normal numbers of typhoons. The count of 17 named storms in the western North Pacific was the second lowest since 1951. The South Indian Ocean was the only SH basin with above-normal ACE, which was largely due to the exceptionally long-lived Cyclone Freddy (Sidebar 4.2).

Freddy was one of seven storms globally that achieved Category 5 on the Saffir-Simpson Hurricane Wind Scale (1-minute maximum sustained winds ≥137 kt) during 2023. Sidebar 4.1 discusses another of these Category 5 storms, Hurricane Otis, which was the strongest landfalling hurricane on record for the west coast of Mexico.

Table 4.2. Global counts of tropical cyclone (TC), hurricane/typhoon/cyclone (HTC), major HTC, Saffir-Simpson Category 5 (SS Cat 5) storm activity by basin, and accumulated cyclone energy (ACE) for 2023. "+" denotes top tercile; "++" is top 10%; "–" is bottom tercile; "––" is bottom 10% (all relative to 1991–2020). Note that some inconsistencies between Table 4.2 and the text of the various basin write-ups in section 4g exist and are unavoidable, as tallying global TC numbers is challenging and involves more than simply adding up basin totals. This is because some storms cross TC basin boundaries, some TC basins overlap, and multiple agencies are involved in tracking and categorizing TCs.

Basin	TCs	HTCs	Major HTCs	SS Cat 5	ACE
North Atlantic	20 ++	7	3	1 +	144
Eastern Pacific	17	10 +	8 +	2 +	166 +
Western Pacific	17 – –	12 –	8	2	268
North Indian	8 ++	4 ++	3 ++	1 ++	56 ++
South Indian	9 –	7 +	4 +	1 ++	134 +
Australia	9 –	5	4 +	0	67
Southwest Pacific	6	3	2	0	31
Global	82 –	45	30 +	7 +	866 +

2. ATLANTIC BASIN

M. Rosencrans, E. S. Blake, C. W. Landsea, H. Wang, S. B. Goldenberg, R. J. Pasch, D. S. Harnos, and H. Lopez

(i) 2023 Seasonal activity

The 2023 Atlantic hurricane season produced 20 named storms (plus one tropical depression), of which 7 became hurricanes and 3 of those became major hurricanes (Fig. 4.22a). The HURDAT2 1991–2020 seasonal averages (included in IBTrACS) are 14.4 named storms, 7.2 hurricanes, and 3.2 major hurricanes (Landsea and Franklin 2013). The 20 named storms during 2023 equaled 1933 for the fourth-highest total in the HURDAT2 database, with the top three seasons for most named storms being 2020 (30), 2005 (27), and 2021 (21). In contrast, the number of hurricanes and major hurricanes were at the long-term average. The 2023 hurricane season was classified by NOAA as an above-normal season, as ACE exceeded the threshold necessary

for an above-normal season (discussed in detail later in this section). This was the seventh above-normal season since 2016, with only 2022 being classified as a near-normal season and no years in that period classified as below normal.

Seven of the 20 named storms during 2023 were short-lived (≤2 days), including the subtropical storm that developed in January. There has been a large artificial increase (approximately five per year) in these "shorties" since 2000 (Landsea et al. 2010). These increased counts primarily reflect new observational capabilities such as scatterometers, Advanced Microwave Sounding Units, and the Advanced Dvorak Technique, and have no association with any known climate variability (Villarini et al. 2011).

The 2023 seasonal accumulated cyclone energy ACE value was 144% of the 1951–2020 median of 96.7 × 10^4 kt^2 as noted in Fig. 4.22b. This value is above NOAA's threshold for an above-normal season (126.1 × 10^4 kt^2, or 130% of the 1951–2020 median). Since the current Atlantic high-activity era began in 1995 (Goldenberg et al. 2001; Bell et al. 2019, 2020), there have been 20 above-normal seasons, with 10 classified as extremely (aka hyper-) active (ACE >165% of median). By comparison, the preceding 24-year low-activity era of 1971–94 had only two above-normal seasons, with none classified as extremely active.

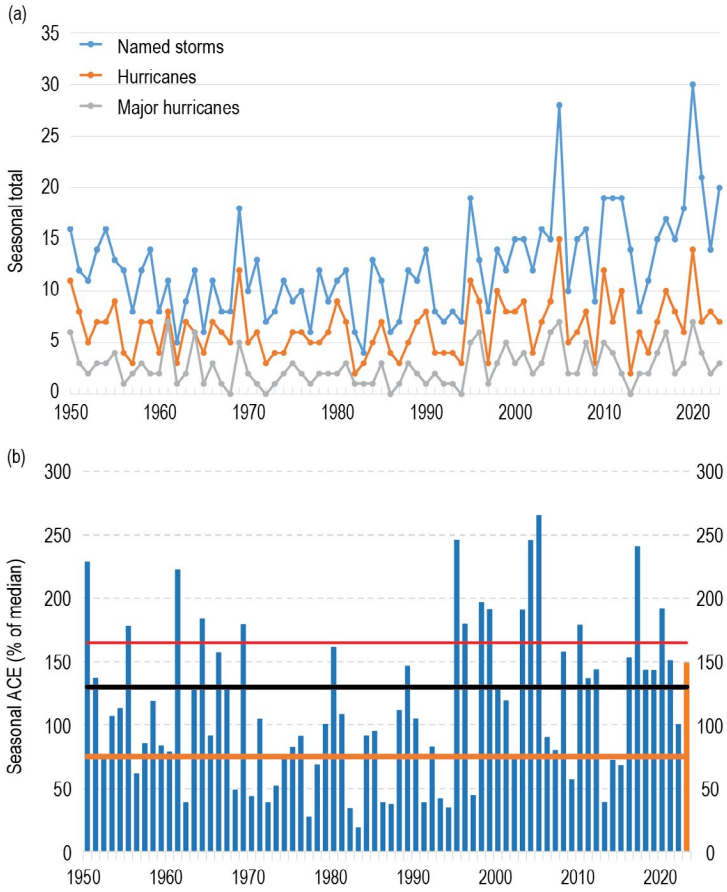

Fig. 4.22. Seasonal Atlantic hurricane activity during the period 1950–2023. (a) Numbers of named storms (blue), hurricanes (orange), and major hurricanes (gray). (b) The accumulated cyclone energy (ACE) index expressed as percent of the 1950–2020 median value. ACE is calculated by summing the squares of the six-hourly maximum sustained surface wind speed (kt) for all periods while the storm is at least of tropical storm strength. The black (orange) line represents NOAA's threshold for an above-normal (below-normal) season (https://www.cpc.ncep.noaa.gov/products/outlooks/Background.html). Note that there is a low bias in activity during the 1950s to the early 1970s due to the lack of satellite imagery and a technique (Dvorak) to interpret tropical cyclone intensity for systems over the open ocean. (c) 2023 Atlantic basin storm tracks. (Source: HURDAT2 [Landsea and Franklin 2013].)

(ii) Storm formation times, regions, and landfalls

Tropical cyclone activity was abundant during August–October (Fig. 4.23a), the core months of the season, with one early formation in January and no activity in November. Activity for the calendar year started on 16 January with the development of an unnamed subtropical storm. During the Atlantic hurricane season, at least one named storm developed in every month except November, including three named storm formations during June. Named storm formations during August and September were about twice the average for each of those months. October had near-average activity with two named storms. This was the first year on record that the tropical Atlantic (east of 60°W, south of 23.5°N) had two named storm formations—Bret and Cindy—in June. Notably, 13 named storms formed between 20 August and 28 September, the most on record and breaking the old record of 12 set in 2020.

Of the 20 named storms that occurred during 2023, 60% (12 of 20) formed in the Main Development Region (MDR; Fig. 4.23b). The MDR spans the tropical Atlantic Ocean and Caribbean Sea between 9.5°N and 21.5°N (Goldenberg and Shapiro 1996; Goldenberg et al. 2001). Since 1950, approximately 42% of named storms form in the MDR in any given year, with about 18% in the Gulf of Mexico. In 2023, only two tropical storms and no hurricanes formed in the Gulf of Mexico (Fig. 4.23c), which is a smaller-than-average fraction of the overall tropical activity,

contributing just 0.6% of the total annual ACE. The associated MDR-related ACE value was 180% of the median annual MDR ACE. The storm tracks during 2023 highlight the lack of activity in the Gulf of Mexico and the relatively higher activity originating in the MDR (Fig. 4.23c).

Even though the season had above-normal activity overall, there were only two landfalling hurricanes and several non-hurricane-strength landfalls. Despite the low overall activity in the Gulf of Mexico, it did include the season's only major hurricane landfall—Category 3 Hurricane Idalia, which came ashore in the Big Bend area of Florida. Other notable landfalling systems include Hurricane Lee, which made landfall as a post-tropical cyclone in Nova Scotia with winds of ~60 kt (30 m s^{-1}), and Hurricane Tammy, which made landfall on Barbuda with winds of 75 kt (39 m s^{-1}).

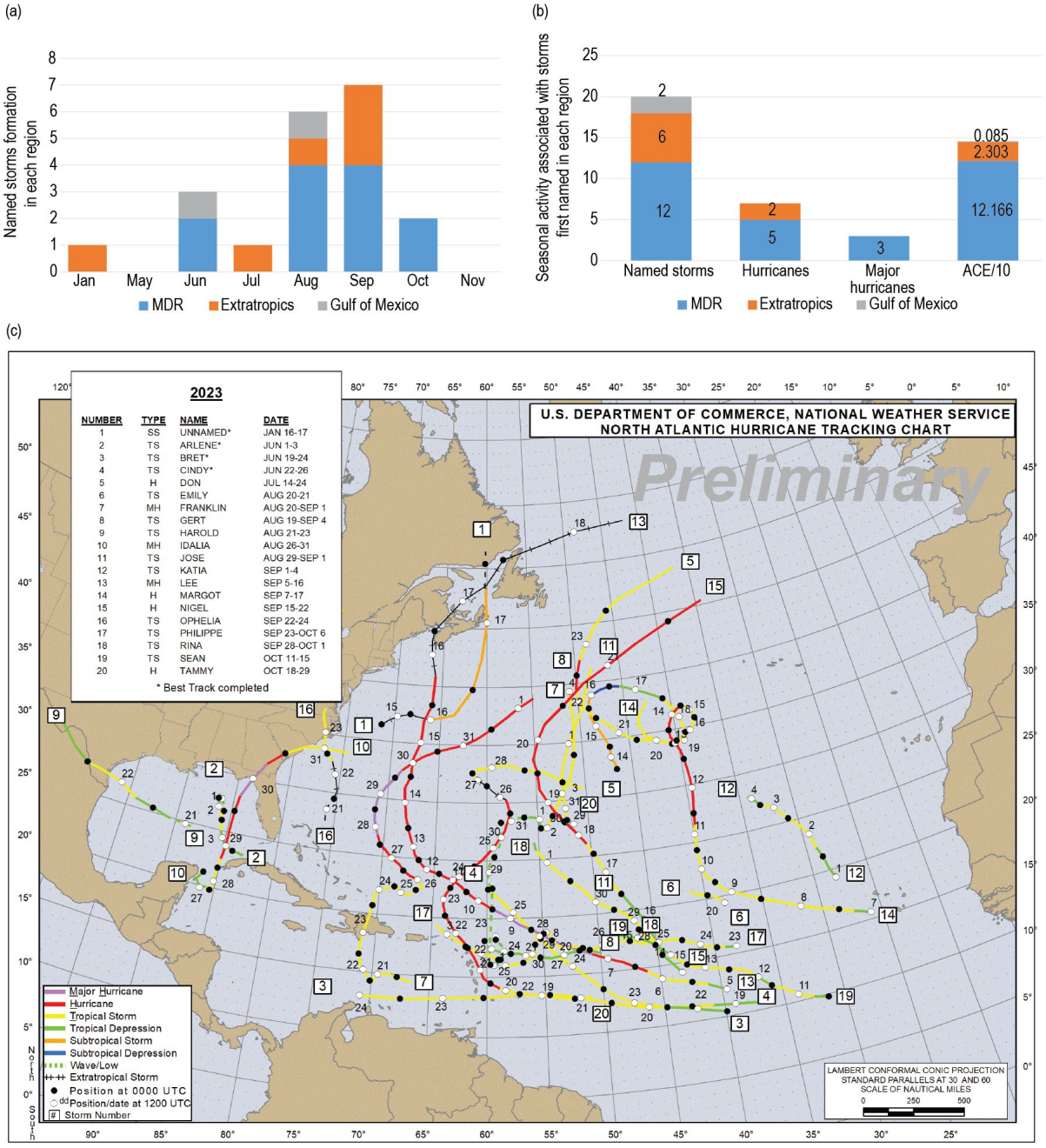

Fig. 4.23. Atlantic tropical cyclone (TC) activity in 2023. (a) Named storm counts for the month and region where the storm was first named and (b) total seasonal counts for the three storm classifications and accumulated cyclone energy (ACE) for each region where the storm was first named. ACE reflects the entire storm ACE and is attributed to the region in which the storm was first named. Regions in (a) and (b) are indicated by the color bar below panel (b). In (c), the tracks of named storms are plotted and show the relative dearth of storms in the Gulf of Mexico. The "extratropics" includes all regions except for the Main Development Region and the Gulf of Mexico. (Source: HURDAT2; Landsea and Franklin 2013].)

(iii) Sea-surface temperatures

Sea-surface temperatures (SSTs) were exceptionally warm throughout the MDR (Fig. 4.24a), with an August–October (ASO)-area-averaged SST anomaly of +1.16°C (Fig. 4.24b), setting a record since at least 1950 by more than 0.5°C. Within the MDR, SST anomalies ranged from just above +0.5°C to greater than +1.5°C. The area-averaged SST anomaly in the MDR was 0.55°C higher than that of the remainder of the global tropics (Fig. 4.24c), with the global tropics reflecting an El Niño state for the entire ASO period. This signal typifies the warm phase of the Atlantic Multidecadal Oscillation (Enfield and Mestas-Nuñez 1999; Bell and Chelliah 2006) and is a ubiquitous characteristic of Atlantic high-activity eras such as 1950–69 and 1995–present (Goldenberg et al. 2001; Vecchi and Soden 2007; Bell et al. 2018).

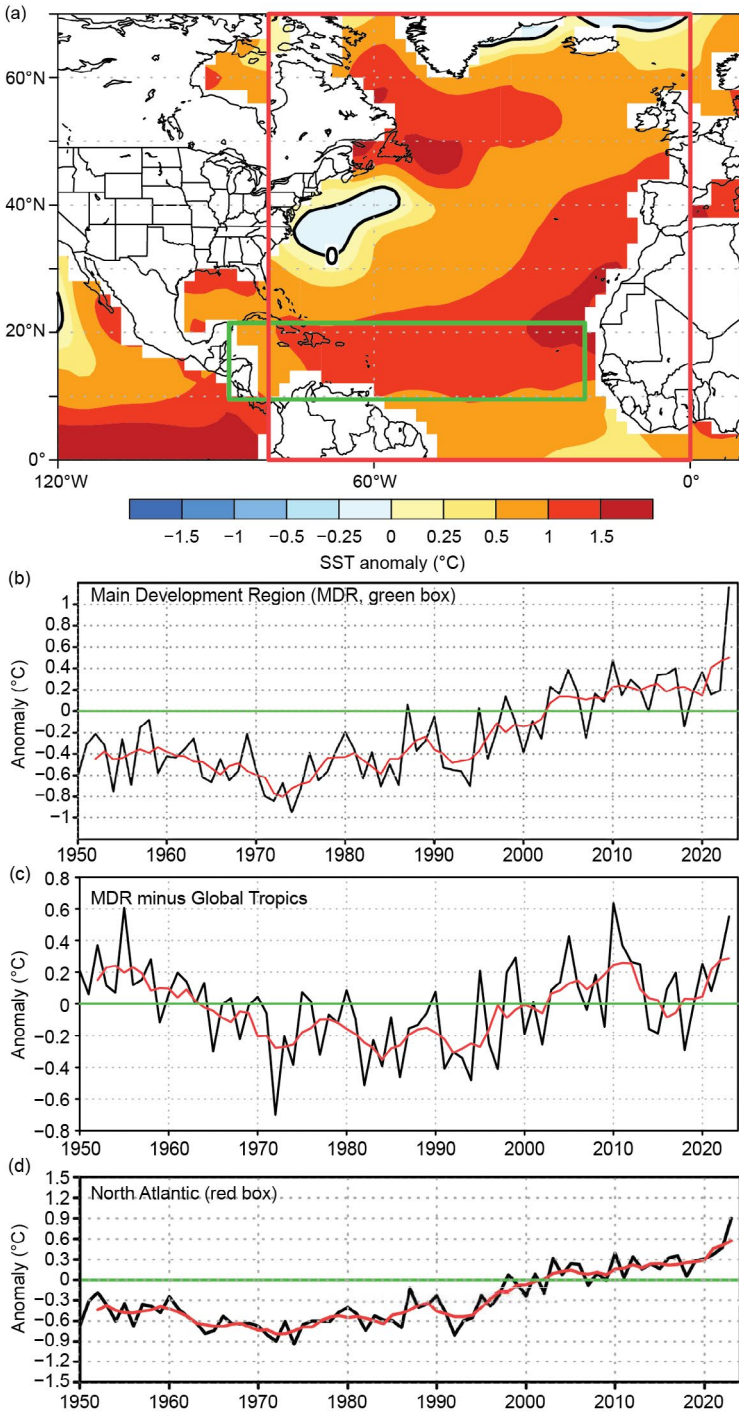

Fig. 4.24. (a) Aug–Oct 2023 sea-surface temperature (SST) anomalies (°C). (b)–(d) Time series of Aug–Oct area-averaged SST anomalies (black) and five-point running mean of the time series (red): (b) in the Main Development Region (MDR, green box in [a] spanning 20°W–87.5°W and 9.5°N–21.5°N), (c) difference between the MDR and the global tropics (20°S–20°N), and (d) in the North Atlantic (red box in [a] spanning 0°–80°W and 0°–70°N). Anomalies are departures from the 1991–2020 period means. (Source: ERSST-v5 [Huang et al. 2017].)

During ASO 2023, above-average temperatures were also reflected across most of the North Atlantic Ocean. Outside of the MDR, the largest anomalies (exceeding +1.5°C) occupied portions of the central North Atlantic (Fig. 4.24a). The area-averaged SST anomaly in the western North Atlantic (red box, Fig. 4.24a) was +0.90°C, reflecting a continuation of exceptional warmth that began in 2012 (Fig. 4.24d). Another major SST forcing during the North Atlantic hurricane season was the ongoing El Niño (see section 4b).

(iv) Atmospheric conditions

Climatologically, the ASO peak in Atlantic hurricane activity largely reflects the June–September peak in the West African monsoon. The inter-related circulation features of an enhanced monsoon act to further increase hurricane activity, while those of an anomalously weak monsoon act to suppress it (Gray 1990; Hastenrath 1990; Landsea et al. 1992; Bell and Chelliah 2006; Bell et al. 2018, 2020). The association on multi-decadal time scales between the AMO and Atlantic hurricane activity in part exists because of their common relationship to the West African monsoon (Bell and Chelliah 2006).

The West African monsoon was near-average, as indicated by a mix of negative outgoing longwave radiation (OLR) anomalies and near-average values across the African Sahel (red box, Fig. 4.25a). Total OLR values in this region averaged 241 W m^{-2} (Fig. 4.25b), while values farther south (blue box, Fig. 4.25a) averaged 228 W m^{-2}, with values less than 240 W m^{-2} indicating deep tropical convection. The OLR time series shows that an enhanced monsoon has largely prevailed throughout the current Atlantic high-activity era and warm AMO of 1995–present (Fig. 4.25b). By contrast, a much weaker monsoon with OLR values well above 240 W m^{-2} in the Sahel region was typical of the low-activity era and cool AMO period of the 1980s and early 1990s. June precipitation across the Sahel region was well above normal, July and August precipitation were below normal, and September precipitation was near normal (NOAA 2023), further indicating a varied signal from the West African monsoon.

Consistent with a near-normal monsoon, the large-scale divergent circulation at 200 hPa featured a weak signal over western Africa (Fig. 4.25c). The strongest negative velocity potential anomalies were over the Atlantic, with strong positive anomalies over the Gulf of Mexico and Central America, consistent with reduced activity in the western portion of the Atlantic basin. Analysis of the streamfunction at 200 hPa (Fig. 4.26a) shows anomalous anticyclones over the Caribbean

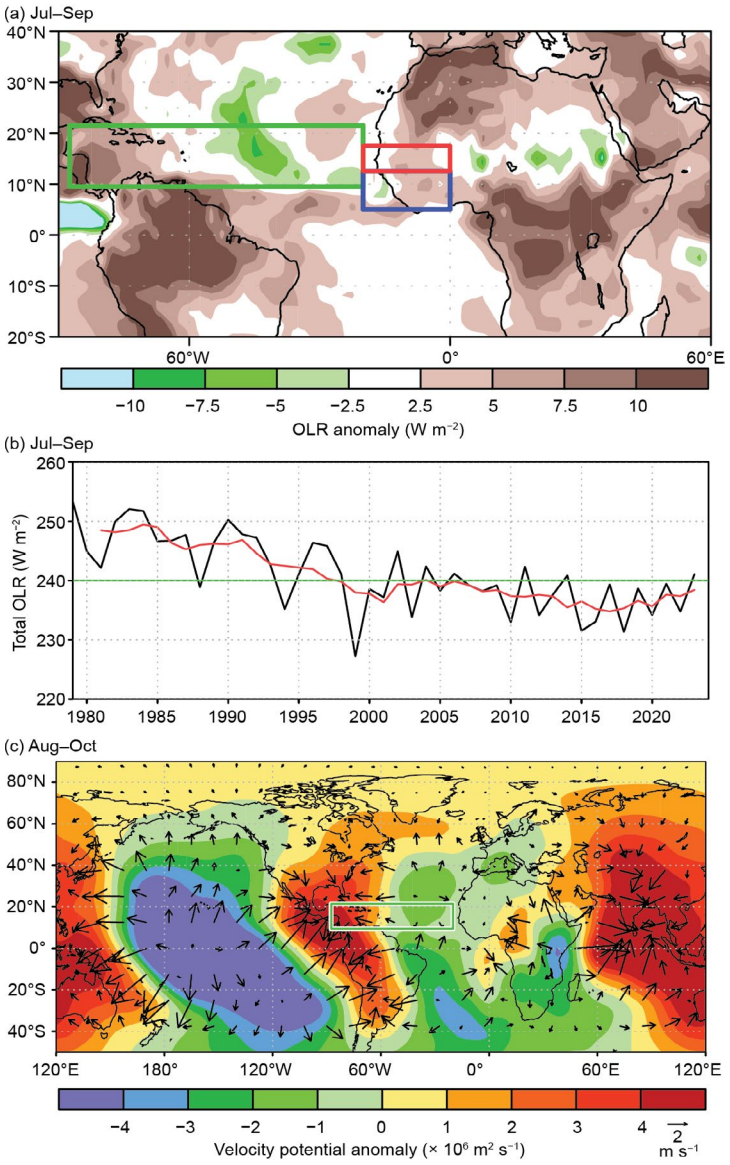

Fig. 4.25. (a) Jul–Sep 2023 anomalous outgoing longwave radiation (OLR; W m^{-2}), with negative (positive) values indicating enhanced (suppressed) convection. (b) Time series of Jul–Sep total OLR (black), five-point running mean of the time series (red) averaged over the African Sahel region (red box in (a) spanning 20°W–0° and 12.5°N–17.5°N). (c) Aug–Oct 2023 anomalous 200-hPa velocity potential (× 10^6 m^2 s^{-1}) and divergent wind vectors (m s^{-1}). In (a), the green box denotes the Atlantic Main Development Region. In (b), the green line represents the threshold for deep convection (240 W m^{-2}). Anomalies are departures from the 1991–2020 means. (Source: [Kalnay et al. 1996] for velocity potential and wind; [Liebmann and Smith 1996] for OLR.)

and much of the MDR, though anomalous cyclonic flow is evident over the eastern Atlantic and western Africa. In 2023, there were no indications of significant midlatitude wave-train breaking into the tropical Atlantic. In contrast, significant wave breaking into the Atlantic was evident during 2022, as was a lack of moisture in the upper levels during August. During 2023, mid-level and upper-level moisture were abundant across the tropical Atlantic during ASO (Fig. 4.26b). The 1000-hPa anomalous height and wind field (Fig. 4.26c) shows that heights were below normal across the MDR, a signal typically associated with busy Atlantic hurricane seasons (Knaff 1997). Indications are that the West African monsoon was a minor contributor to the heightened named-storm total.

August–October 2023 200-hPa-to-850-hPa vertical wind shear was below average for much of the MDR and slightly higher than average for the Gulf of Mexico (Fig. 4.27a). The area-averaged magnitude of the vertical wind shear for the entire MDR was 6.5 m s^{-1} (Fig. 4.27b) and for the Gulf of Mexico was 10.3 m s^{-1} (Fig. 4.27c). The 200-hPa-to-850-hPa vertical wind shear over the MDR was in the lowest decile since 1950, while over the Gulf of Mexico, the value was above the upper threshold of 10 m s^{-1} considered conducive to hurricane formation on monthly time scales (Bell et al. 2017). Note that the MDR shows a strong multidecadal variability of vertical wind shear, which is correlated with multidecadal fluctuations in TC activity, whereas there is no such variability in the Gulf of Mexico (Figs. 4.27b,c; Goldenberg et al. 2001). The low wind shear over the MDR is particularly notable since strong El Niño events typically enhance the shear over much of the Caribbean and MDR. During 2023, the MDR SSTAs minus global tropical SSTAs were still positive (Fig. 4.24c), dampening potential El Niño teleconnections. The record-warm SSTs in the Atlantic and low surface pressure reduced the trade winds (Fig. 4.26c), combined with some persistent anticyclonic flow and northeasterly anomalies at 200 hPa over the MDR (Fig. 4.6) contributed to a reduction of the vertical wind shear over the MDR.

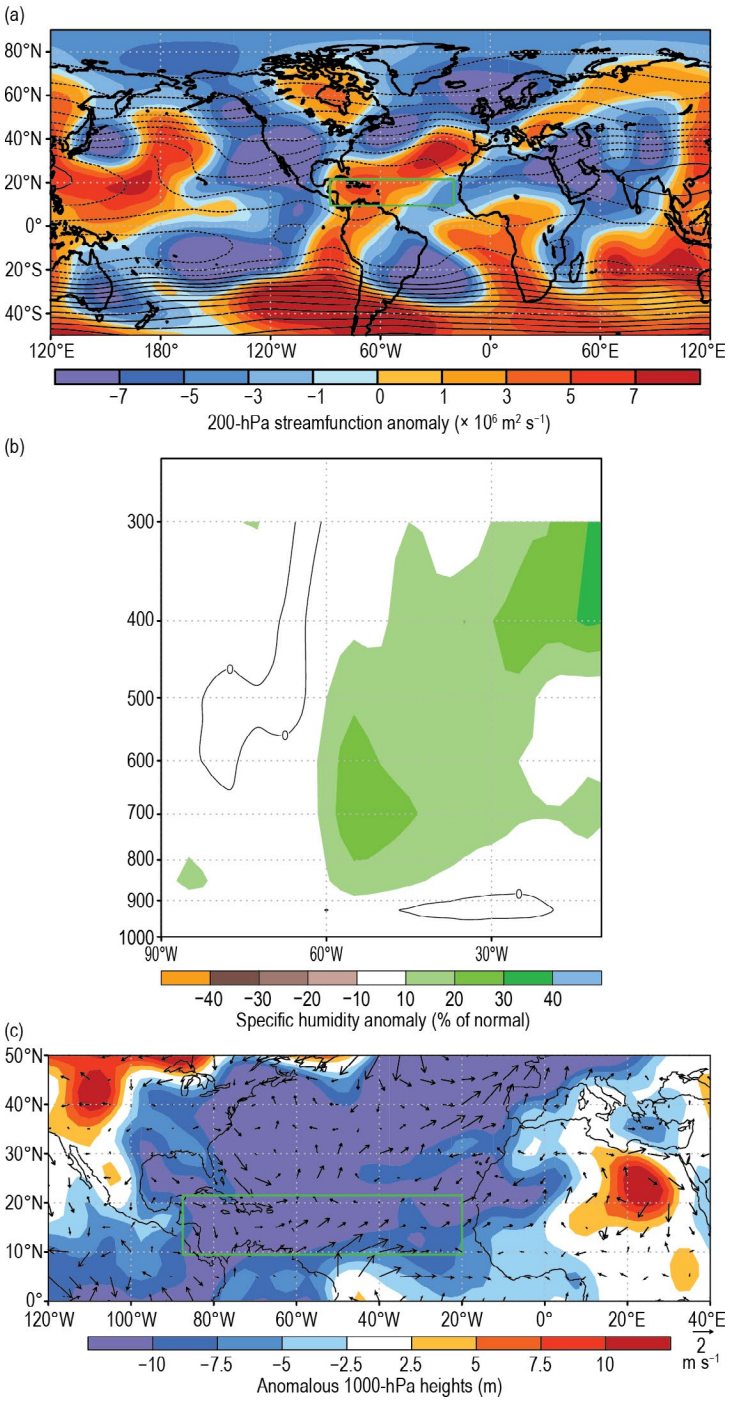

Fig. 4.26. (a) Aug–Oct 200-hPa streamfunction (contours, interval is 5 × 10⁶ m² s⁻¹) and anomalies (shaded); (b) Aug–Oct 2023 Main Development Region (MDR)-specific humidity deviations from normal (%). Brown (green) shading represents below- (above-) normal values, with the thin black line representing no deviation; (c) Aug–Oct anomalous 1000-hPa heights (shaded, m) and vector winds (m s⁻¹). The green box denotes the Atlantic MDR. Anomalies are departures from the 1991–2020 means. (Source: National Centers for Environmental Prediction [NCEP]/National Center for Atmospheric Research [NCAR] reanalysis [Kalnay et al. 1996].)

(v) Unique aspects of the 2023 Atlantic hurricane season

The below-normal TC activity over the Gulf of Mexico and subtropical Atlantic were probably related to high vertical wind shear, since the shear over the Gulf of Mexico was at its highest value since 2017 and is likely related to El Niño (Goldenberg and Shapiro 1996). El Niño conditions are typically related to lower levels of tropical cyclone activity in the Atlantic (Gray 1984), though the ACE in 2023 was above normal and the total count for named storms was well above normal. The count of named storms was the highest on record during a year with a strong El Niño. The El Niño-linked impacts in 2023 are less coherent in the initial analyses than in other El Niño years. Vertical wind shear was below normal (Fig. 4.27a) in the MDR, and mid-level moisture was above normal for most of the MDR (Fig. 4.26b), but anomalous subsidence was evident over the western portions. Additionally, although the named storm activity was relatively high, the fraction of named storms that developed into hurricanes was low (35%) compared to the average (53%). The fraction of hurricanes that became major hurricanes (43%) was close to the average (40%). The proximal cause of the lower relative fraction could be due to El Niño-related subsidence impacting intensification. The supportive influence of record-high SSTs and above-normal mid-level moisture (not present during 2022) could have been enough to promote more tropical cyclone formations, while the detrimental impacts from El Niño (higher vertical wind shear over the Gulf of Mexico and anomalous subsidence over the western MDR) might have limited intensification for several of these tropical cyclones, keeping the number of major hurricanes to near-average and the ACE to just slightly above average.

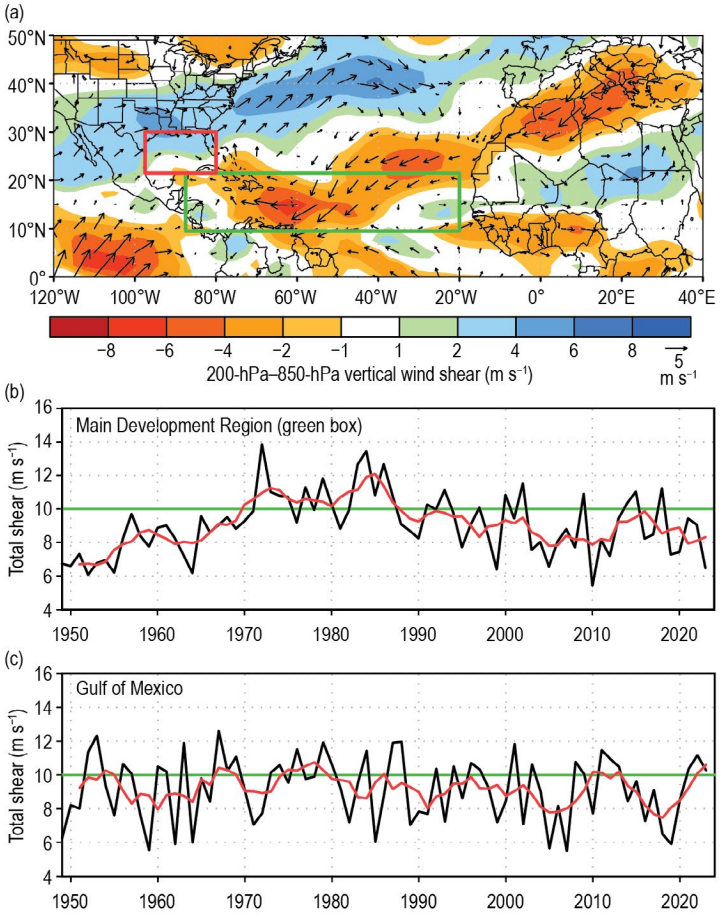

Fig. 4.27. Aug–Oct (ASO) magnitude of the 200-hPa–850-hPa vertical wind shear (m s^{-1}): (a) 2023 anomalous magnitude and vector, and (b),(c) time series of ASO vertical shear magnitude (black) and five-point running mean of the time series (red) averaged over (b) the Main Development Region (MDR; spanning 85°W–20°W and 10°N–21.5°N) and (c) the western Gulf of Mexico (spanning 80°W–97.5°W and 21.5°N–30°N). Anomalies are departures from the 1991–2020 means. (Source: National Centers for Environmental Prediction [NCEP] National Center for Atmospheric Research [NCAR] reanalysis [Kalnay et al. 1996].)

The unnamed subtropical storm that developed in January was the first system to develop before May since Tropical Storm Arlene in April 2017 and the first January Atlantic storm formation since Hurricane Alex in 2016.

3. EASTERN NORTH PACIFIC AND CENTRAL NORTH PACIFIC BASINS

K. M. Wood and C. J. Schreck

(i) Seasonal activity

Tropical cyclone activity in this section is combined from the two agencies responsible for issuing advisories and warnings in the eastern North Pacific (ENP) basin: NOAA's National Hurricane Center in Miami, Florida (for the region from the Pacific Coast of North America to 140°W), and NOAA's Central Pacific Hurricane Center in Honolulu, Hawaii (for the region between 140°W and the dateline, known as the Central North Pacific [CNP]).

A total of 17 named storms formed within the combined ENP/CNP basin in 2023, 10 of which became hurricanes and 8 became major hurricanes (Fig. 4.28a). This activity was near normal for named storms and above normal for hurricanes and major hurricanes compared with the

1991–2020 averages of 16.9 named storms, 8.8 hurricanes, and 4.6 major hurricanes. All storms in 2023 occurred between the official ENP hurricane season start date of 15 May and end date of 30 November. The first named storm of the season, Hurricane Adrian, marked the second-latest first formation on record (27 June) after Tropical Storm Agatha in 2016 (2 July). The final named storm, Tropical Storm Ramon, weakened to a tropical depression on 26 November. No named storms formed within the CNP, but three ENP TCs crossed 140°W (Calvin, Dora, and Greg), which is near the 1991–2020 average of 3.4 named storms for the CNP.

The 2023 seasonal ACE index was 165 × 10^4 kt^2, which was 124% of the 1991–2020 mean of 133 × 10^4 kt^2 (Fig. 4.28b; Bell et al. 2000), breaking a four-year streak of below-normal activity (Wood and Schreck 2020, 2021, 2022, 2023). Almost half of the season's activity occurred during August (49%) from three tropical storms (Eugene, Greg, and Irwin) and three major hurricanes (Dora, Fernanda, and Hilary). In contrast, July contributed 10% of the season's ACE compared with an average of 22%, and September ACE was 11% compared with an average of 24%. October 2023 marked an increase in TC activity, producing 22% of the season's ACE (October average ACE is 13%). The eight 2023 ENP TCs that reached major hurricane intensity (≥96 kt; 49 m s^{-1}) on the Saffir-Simpson Hurricane Wind Scale contributed about 84% of the season's total ACE: Calvin, Dora, Fernanda, Hilary, Jova, Lidia, Norma, and Otis.

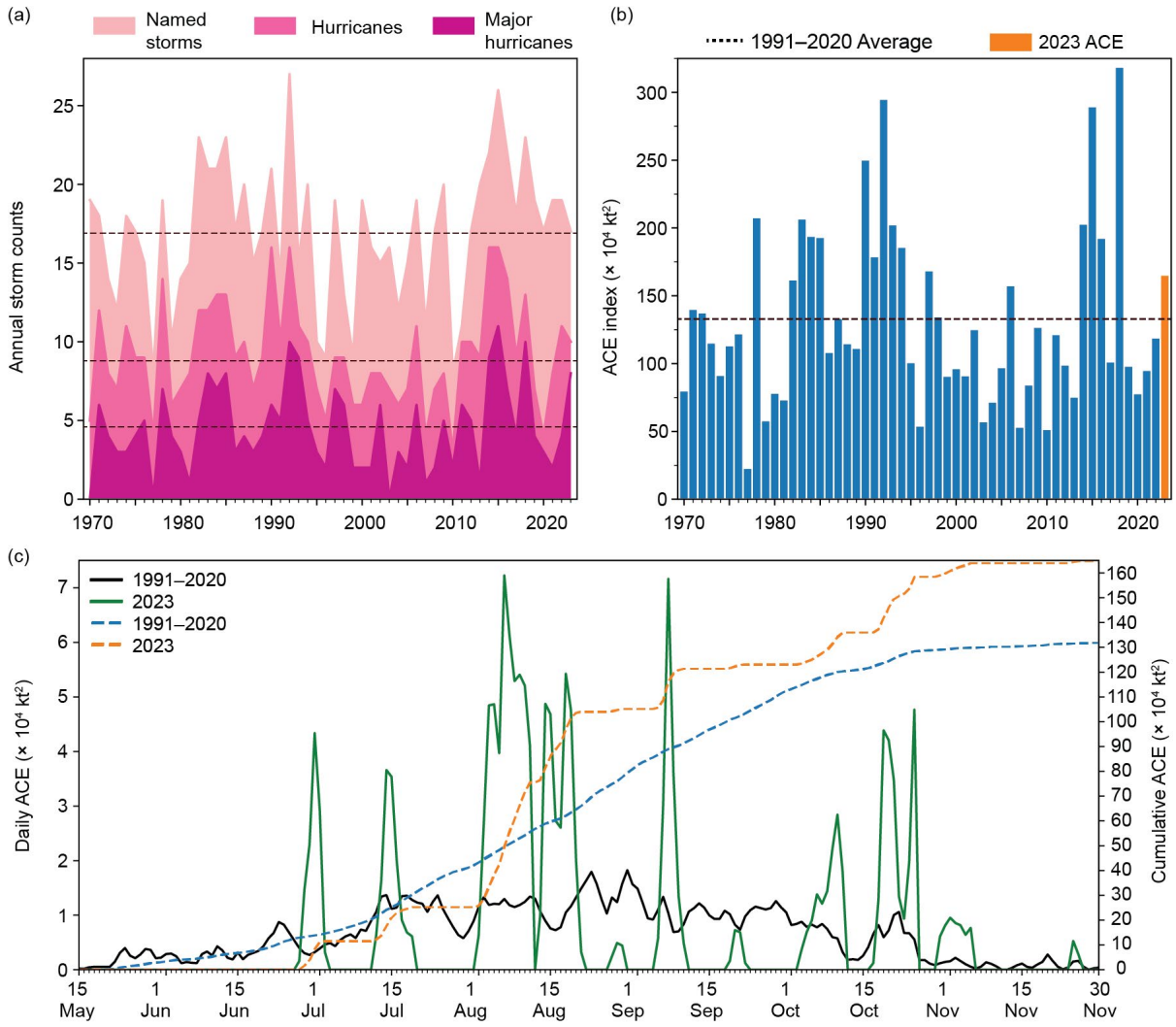

Fig. 4.28. (a) Annual eastern North Pacific and central North Pacific storm counts by category during the period 1970–2023, with the 1991–2020 average by category denoted by dashed lines. (b) Annual accumulated cyclone energy (ACE) during 1970–2023, with 2023 highlighted in orange, and the 1991–2020 average denoted by the dashed line. (c) Daily ACE for the 1991–2020 average (solid black line) and during 2023 (solid green line); accumulated daily ACE for the 1991–2020 average (dashed blue line) and during 2023 (dashed orange line).

(ii) Environmental influences on the 2023 season

Positive SST anomalies related to a strengthening El Niño event characterized the equatorial eastern Pacific during the 2023 ENP hurricane season. Accompanying these positive SST anomalies were 850-hPa westerly wind anomalies, which predominated over the region east of 140°W (Fig. 4.29). Though TCs generally formed north of the largest SST anomalies, they largely occurred in regions of relatively warm water, below-normal vertical wind shear, and below- or near-normal OLR anomalies. Most TCs tracked within the region of below-normal wind shear and above-normal SSTs, generally dissipating once they reached both anomalously and climatologically cooler SSTs, along with positive wind shear anomalies west of 120°W. The below-normal SSTs in the subtropical central Pacific were unusual for a strong El Niño and may have limited the TC activity there. Only Calvin approached Hawaii as a weakening tropical storm, and Dora's longevity was likely supported by its relatively low-latitude track maintaining proximity to warmer water and away from higher wind shear.

The formation and life cycle of ENP TCs can be influenced by the Madden-Julian Oscillation (MJO) as well as convectively coupled equatorial Kelvin waves (e.g., Maloney and Hartmann 2001; Aiyyer and Molinari 2008; Schreck and Molinari 2011; Ventrice et al. 2012a,b; Schreck 2015, 2016). A strong MJO crossed the Pacific in late July and early August, which likely contributed to unusually high August activity, including the formations of Fernanda, Greg, and Hilary. The subsequent suppressed MJO phase probably played a role in the relatively quiet conditions in September. Another active MJO may have contributed to the October formation of Lidia, Max, Norma, Otis, and Pilar, with passing equatorial Kelvin waves also enhancing these October TC formations (Fig. 4.30). A Kelvin wave may have also favored Adrian's development since cyclogenesis is generally favored within three days

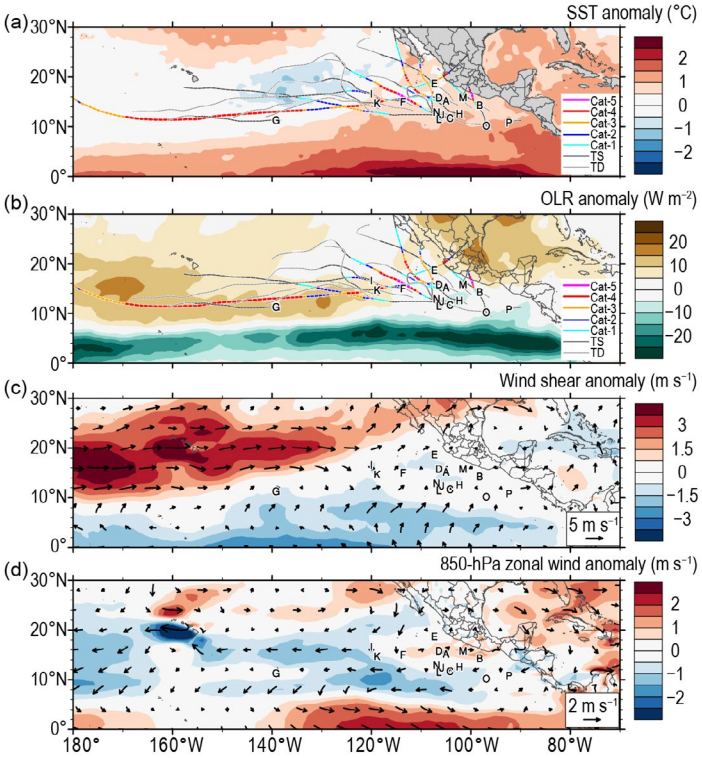

Fig. 4.29. 15 Jun–30 Nov 2023 anomaly maps of (a) sea-surface temperature (SST; °C, Banzon and Reynolds 2013), (b) outgoing longwave radiation (OLR; W m^{-2}; Schreck et al. 2018), (c) 200-hPa–850-hPa vertical wind shear (m s^{-1}) vector (arrows) and scalar (shading) anomalies, and (d) 850-hPa wind (m s^{-1}, arrows) and zonal wind (shading) anomalies. Anomalies are relative to the annual cycle from 1991–2020. Letters denote where each tropical cyclone attained tropical storm intensity. Wind data are obtained from CFSR (Saha et al. 2014).

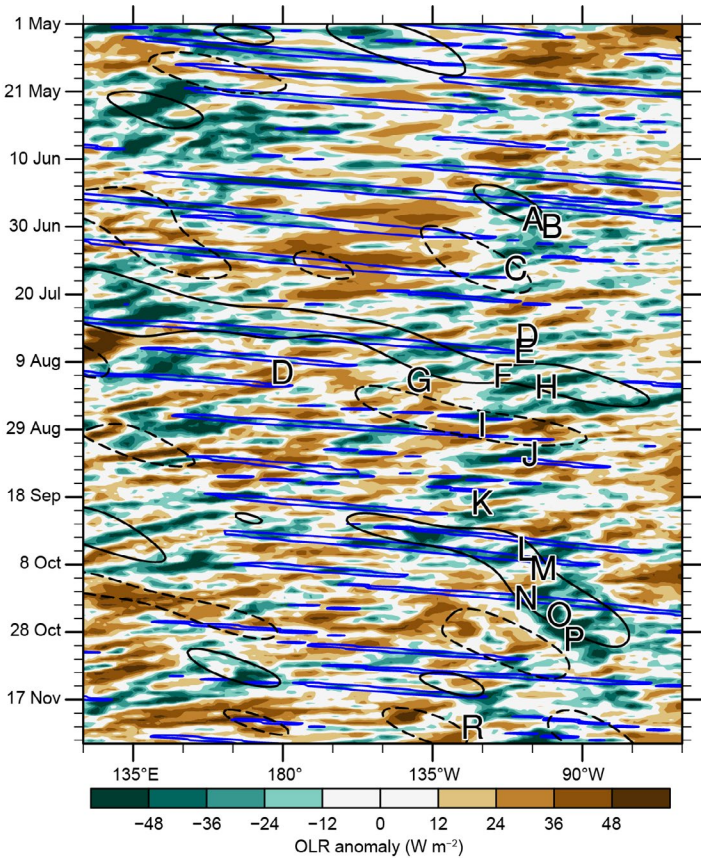

Fig. 4.30. Longitude–time Hovmöller diagram of 5°N–15°N average outgoing longwave radiation (W m^{-2}; Schreck et al. 2018). Unfiltered anomalies from a daily climatology are shaded. Negative anomalies (green) indicate enhanced convection. Anomalies filtered for Kelvin waves are contoured in blue at –10 W m^{-2} and Madden-Julian Oscillation-filtered anomalies are contoured in black at ±10 W m^{-2} (dashed for positive, solid for negative). Letters denote the longitude and time when each tropical cyclone attained tropical storm intensity.

after a Kelvin wave passage. In addition, easterly wave activity as denoted by westward-moving (negative) OLR anomalies in Fig. 4.30 likely contributed to the genesis of many ENP TCs, including Calvin, Dora, Hilary, Jova, and Lidia.

(iii) Notable ENP tropical cyclones and impacts in 2023

Eight TCs exceeded the major hurricane threshold in 2023, nearly double the 1991–2020 average of 4.6. Two hurricanes achieved Category 5 intensity: Jova and Otis.

Of the eight major hurricanes, four made landfall: Norma and Hilary made landfall after weakening, and Lidia and Otis made landfall near peak intensity. Three additional TCs made landfall or directly impacted land: Hurricane Beatriz and Tropical Storms Max and Pilar. Of these seven storms, all but Pilar hit Mexico, making 2023 the third consecutive season during which landfalling ENP TC activity well exceeded the average for Mexico (1.8; Raga et al. 2013; Wood and Schreck 2022, 2023). Likely related in part to below-average wind shear and above-average SSTs, all eight major hurricanes exhibited periods of rapid intensification (≥30 kt; 15.4 m s^{-1} in 24 hours). In fact, the two hurricanes that did not reach major hurricane strength, Adrian and Beatriz, also reached this intensification threshold. Of the 10 TCs that peaked as either hurricanes or major hurricanes, 7 underwent at least one rapid weakening period while over the open ocean (≤–30 kt or –15.4 m s^{-1} in 24 hours; Wood and Ritchie 2015): Adrian, Calvin, Dora, Fernanda, Hilary, Jova, and Norma.

The 2023 ENP hurricane season exemplified the range of intensities at which TCs affecting land can produce significant impacts. Heavy rain from Beatriz caused isolated flooding in Mexico while the system was making landfall as a tropical storm (Blake 2024). Hurricane Dora spent an estimated 132 hours at Category 4 intensity and may have affected strong winds in Hawaii that impacted devastating wildfires in August, though Dora's exact role has yet to be quantified. Hurricane Hilary peaked as a Category 4 storm and weakened prior to landfall in Baja California but prompted the first-ever tropical storm warning for the U.S. state of California, with damage largely due to heavy rain estimated at $675 million (U.S. dollars; Aon 2024). Hurricane Lidia made landfall with estimated winds of 120 kt (62 m s^{-1}), tying Hurricane Kenna from 2002 as the fourth-strongest storm to make landfall in Mexico. Damage was estimated in the tens of millions of U.S. dollars (Aon 2024). Two deaths were attributed to Tropical Storm Max, and rain from this TC affected communities in Guerrero, Mexico, that were impacted by Hurricane Otis two weeks later (Berg 2024). Though Hurricane Norma rapidly weakened prior to landfall, the storm caused estimated economic losses of $50 million (U.S. dollars; Aon 2024), largely attributed to flooding and mudslides due to heavy rainfall. Hurricane Otis caused $12–$16 billion (U.S. dollars) in economic losses (Reinhart and Reinhart 2024) when it devastated Acapulco as a Category 5 hurricane (see Fig. SB4.1). Its estimated landfall intensity of 140 kt (70 m s^{-1}) broke the record for the strongest ENP TC landfall previously held by Hurricane Patricia (2015). Finally, Tropical Storm Pilar dumped heavy rain in Central America when it stalled offshore of El Salvador, with damage estimated at $40 million (U.S. dollars; Aon 2024).

4. WESTERN NORTH PACIFIC BASIN

S. J. Camargo

(i) Overview

This was the fourth consecutive season with below-normal activity in the western North Pacific (WNP) for most measures of tropical cyclone (TC: tropical storms and typhoons) activity. Figure 4.31 compares the activity for 2023 as identified by both the JTWC and the Japan Meteorological Agency (JMA) with their climatologies for 1991–2020. Only 17 storms reached tropical-storm intensity in 2023 (bottom quartile <23; Fig. 4.31a) based on the JTWC (best-track dataset for 1945–2022, preliminary operational data for 2023), matching the number in 1951 and close to the historical lows of 2010 (14) and 1946 (15), the only two years with fewer storms in the historical record. From these, 12 reached typhoon intensity (bottom quartile <13), with 3 reaching super-typhoon status (≥130 kt, bottom quartile <3), matching exactly the number of typhoons and super typhoons in 2022. This corresponds to 71% of the tropical storms intensifying into typhoons (top quartile >69%), with 25% of the typhoons reaching super-typhoon intensity (median: 29%). These statistics include Typhoon Dora, which formed in the eastern North

Pacific, where it was named Hurricane Dora. Dora then tracked across the dateline into the WNP. There were also two tropical depressions (bottom quartile <2) in 2023. The JMA also recorded 17 TCs (bottom quartile <23; Fig. 4.31b), including 5 tropical storms (bottom quartile <5), 2 severe tropical storms (bottom quartile <4), and 10 typhoons (bottom quartile <11). 58.8% of the storms reached typhoon intensity (top quartile >59%). Similar to other years, there were some differ-

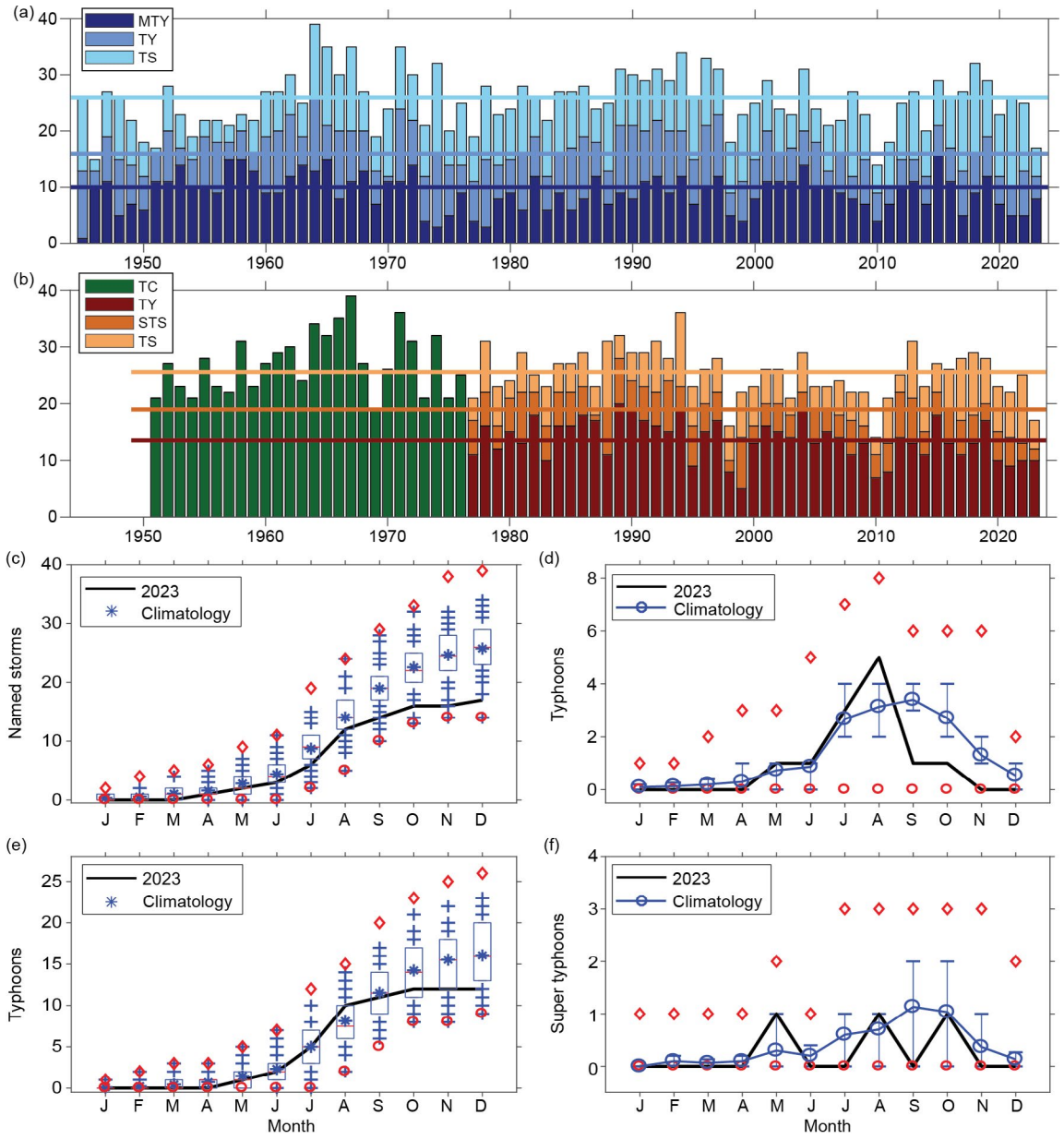

Fig. 4.31. (a) Number of tropical storms (TS), typhoons (TY), and major typhoons (MTY ≥96 kt) per year in the western North Pacific (WNP) for the period 1945–2023 based on the Joint Typhoon Warning Center. (b) Number of tropical cyclones (TCs, all storms that reach TS intensity or higher) from 1951 to 1976; number of TS, severe tropical storms (STS) and TY from 1977 to 2023 based on the Japan Meteorological Agency (JMA). (c) Cumulative number of tropical cyclones with TS intensity or higher (named storms) per month in the WNP in 2023 (black line), and climatology (1991–2020) as box plots (interquartile range: box, median: red line, mean: blue asterisk, values in the top or bottom quartile: blue crosses, high [low] records in the 1945–2022 period: red diamonds [circles]). (e) As in (c) but for the number of typhoons. (d),(f) Number of typhoons and super typhoons (≥130kt), respectively, per month in 2023 (black line) and the climatological mean (blue line). The red diamonds and circles denote the maximum and minimum monthly historical records, and the blue error bars show the climatological interquartile range for each month (in the case of no error bars, the upper and/or lower percentiles coincide with the median). (Sources: 1945–2022 Joint Typhoon Warning Center [JTWC] best-track dataset, 2023 JTWC preliminary operational track data for panels [a], [c], [d], [e], and [f]. 1951–2023 Regional Specialized Meteorological Centre-Tokyo, JMA best-track dataset for panel [b].)

ences between the JTWC and JMA storm counts, intensities, and categories[3]. Talim and Damrey were considered typhoons by the JTWC and severe tropical storms by JMA. Seventeen TCs correspond to the third-lowest value in the JMA record. The only years with less TC activity were 2010 (14) and 1998 (16). The Philippine Atmospheric, Geophysical and Astronomical Services Administration (PAGASA) named 10 TCs that entered its area of responsibility, including Tropical Depression Amang (10–13 April), which was not numbered or named by either the JMA or the JTWC.

(ii) Seasonal activity

The 2023 typhoon season had a late start, with the first storm (Tropical Storm Sanvu) forming on 19 April. The next formation, Super Typhoon Mawar, was in late May, followed by Typhoon Guchol in June. The early season (January–June) had a total of 3 TCs (bottom quartile <3), with 2 typhoons (median: 2) and 1 super typhoon (top quartile >1). The cumulative monthly number of TCs and typhoons for 2023 are depicted in Figs. 4.31c,e, respectively, with the number of typhoons and super typhoons per month displayed in Figs. 4.31d,f. In Figs. 4.31c–f, the 2023 values are compared against the climatological values, as well as the historical maxima and minima.

Three typhoons were present in the WNP basin in July (median: 3): Typhoons Talim, Doksuri, and Khanun. August was the most active month of the season, with a total of 6 TCs (top quartile >6), including Tropical Storm Kirogi (30 August–4 September) and Hurricane/Typhoon Dora (31 July–22 August). Hurricane Dora formed in the eastern North Pacific and crossed the central Pacific basin before reaching the dateline and being renamed Typhoon Dora, remaining at hurricane/typhoon intensity across the three basins. Dora was the second storm in the historical record to achieve this feat, following Hurricane John in 1994. Besides Typhoon Dora, 4 other typhoons were active in August, for a total of 5 (top quartile >4). Only 2 TCs formed in September (bottom quartile <3), including just one typhoon. The formation of a single typhoon in September (bottom quartile <3) has occurred only six times previously (1950, 1983, 1984, 2002, 2004, and 2020); no typhoons occurred in September 1960. Tropical Depression #13 was also active in September. October also had only 2 TCs (bottom quartile <2) and 1 typhoon (bottom quartile <2). In total, the peak season (July–October) had 13 TCs (bottom quartile <16), including 10 typhoons (bottom quartile <9) and 2 super typhoons (bottom quartile <2).

The season ended quietly as well. Tropical Depression #17 was the only storm active in November, and Tropical Storm Jelawat was the only storm in December. The late typhoon season (November and December) had therefore 1 tropical storm (bottom quartile <2) and no typhoons (bottom quartile <1).

In contrast with the diagnostics for TC counts, the total ACE in 2023 (Fig. 4.32a) was

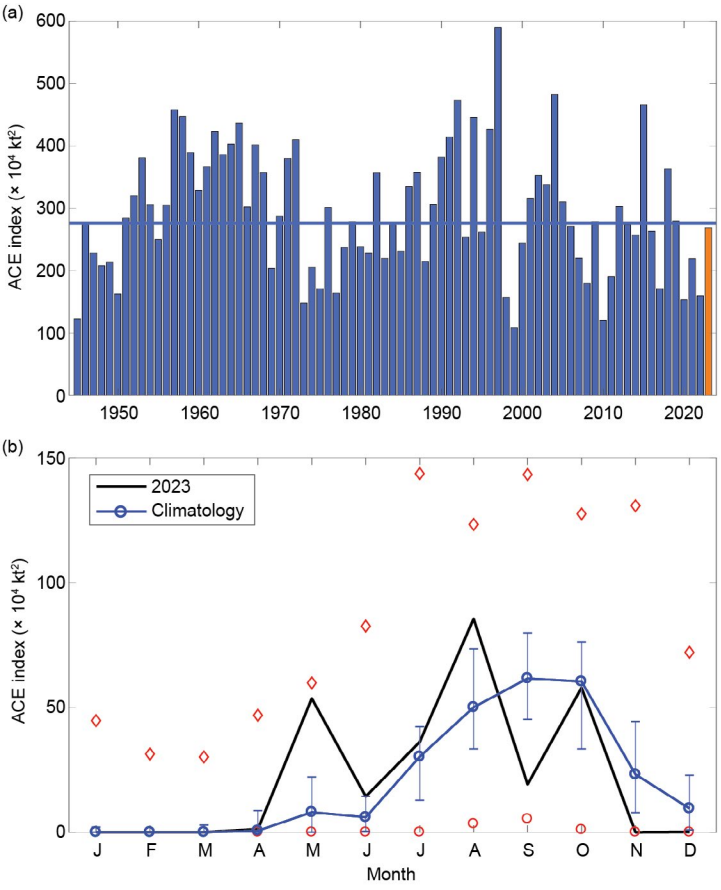

Fig. 4.32. (a) Accumulated cyclone energy (ACE; × 10^4 kt^2) per year in the western North Pacific for the period 1945–2023. The solid blue line indicates the median for the climatology (1991–2020). (b) ACE per month in 2023 (black line) and the median during 1991–2020 (blue line), the blue error bars indicate the climatological interquartile range. In the case of no error bars, the upper and/or lower percentiles coincide with the median. The red diamonds and circles denote the maximum and minimum values per month during the 1945–2022 period. (Source: 1945–2022 Joint Typhoon Warning Center [JTWC] best-track dataset; 2023 JTWC preliminary operational track data.)

[3] It is well known that there are systematic differences between the JMA and JTWC datasets, which have been extensively documented in the literature (e.g. Knapp et al. 2013; Schreck et al. 2014).

close to the median of the climatological distribution due to the occurrence of eight typhoons that reached Category 3 (major) intensity on the Saffir–Simpson Hurricane Wind Scale, with three of these reaching super-typhoon status (maximum intensity >130 kt). As noted earlier, of the 17 TCs that formed in 2023, 12 reached typhoon intensity. Therefore, since ACE is dominated by the storms' intensity (e.g., the square of the maximum wind speed), this led to a near-normal value of ACE, despite the low number of TCs. ACE was zero in January, February, March, and November and in the bottom quartile in September and December. October ACE was close to the climatological median, while ACE was above the climatological median in April and July. In May, June, and August, ACE was in the top quartile. A super typhoon was active during each of these months: Mawar in May, Saola in August, and Bolaven in October. ACE was in the top quartile in the early season, below the median in the peak season, and in the bottom quartile in the late season. The ACE value in the late season was the second lowest in the historical record, above only 2010, which had zero ACE in that period. Typically, high seasonal ACE values are typical of El Niño events in the WNP basin (Camargo and Sobel 2005), in contrast to 2023. Strong and long-lived typhoons are typical of El Niño events, leading to high ACE values. While there were several strong typhoons in 2023, the low number of total storms contributed to a near-normal ACE value.

Seven typhoons in 2023 had ACE values in the top quartile of the ACE for individual storms' climatological distribution: Mawar, Doksuri, Khanun, Lan, Saola, Koinu, and Bolaven. The ACE values of Super Typhoons Saola and Mawar were in the 95th and the 99th percentile of the climatological distribution, respectively. The ACE value of Super Typhoon Mawar was the 13th highest in the historical record (since 1945). These two super typhoons combined to produce 37.3% of the total ACE of the 2023 season.

Typically, during El Niño events, the typhoon genesis location is shifted to the southeast part of the WNP basin (Chia and Ropelewski 2002; Camargo and Sobel 2005; Camargo et al. 2007a). This shift in genesis location contributes to long tracks, strong storms, and high ACE values. The mean genesis position in 2023 was 14.2°N and 136.8°E, northwest of the climatological mean of 13.3°N and 140.5°E, with standard deviations of 1.9 and 7.7, respectively. These values exclude storms that formed in the eastern and central North Pacific, such as Dora in 2023. Therefore, the mean genesis position in 2023 (see July–October [JASO] 2023 storms' genesis and track locations in Figs. 4.33a,b) did not display the typical mean southeast shift of other El Niño events in the 1950–2022 period (mean genesis position of 12.6°N and 144.0°E). Similarly, the mean track position in 2023 (18.3°N, 129.0°E) was northwest of the mean climatological track position (17.8°N, 135.9°E, with standard deviations of 1.6 and 5.2, respectively).

In 2023 there were 83 days with active TCs (bottom quartile <86 days). Of these, 52 days had active typhoons (median: 52.4 days) and 27.75 days had active major typhoons (SSHWS categories 3–5; median: 23 days). The percentage of active days with typhoons and major typhoons was 53.1% (top quartile >41.3%) and 28.3% (top quartile >18.5%), respectively. In other words, while the total number of days with TCs in 2023 was low, a high percentage of these had active typhoons or major typhoons. The median TC lifetime in 2023 was 7 days (bottom quartile <7 days) and that of typhoons was 8.9 days, matching the climatological median. Hurricane/Typhoon Dora had the longest lifespan in 2023 (18.5 days), but only 4 of those days were in the western North Pacific basin. Of the storms that spent their whole lifetime in the basin, Super Typhoon Mawar had the longest lifetime (14.5 days), followed by Typhoon Khanun (14 days). Super Typhoon Saola (11 days) and Typhoon Koinu (10.75 days) also reached the top quartile of the lifetime climatological distribution (>10 days). From 30 August to 2 September, there were three storms active simultaneously in the basin: Super Typhoon Saola, Typhoon Haikui, and Tropical Storm Kirogi. The historical record for most active TCs in the WNP simultaneously is six, set in August 1996.

(iii) Environmental conditions

Figure 4.33 shows the environmental conditions and tracks during the peak typhoon season (JASO). In early 2023, a third successive year of La Niña conditions was still present, which then

transitioned to El Niño in April–June. The event was classified as a strong El Niño by August–October (section 4b). Therefore, during the peak typhoon season, there were El Niño conditions influencing the overall characteristics of the TC season. The SST anomalies (Fig. 4.33a) show a typical El Niño pattern, with above-normal SST anomalies in the equatorial region, east of 152°E, surrounded by cooler, albeit still above-normal, SST. There was also a region of high SST anomalies north of 30°N with a maximum around 40°N near the coast of Asia and north of Japan. The typhoon tracks in JASO 2023 (Fig. 4.33a) are located in the western part of the basin north of 10°N, except Hurricane/Typhoon Dora, which originated in the ENP basin.

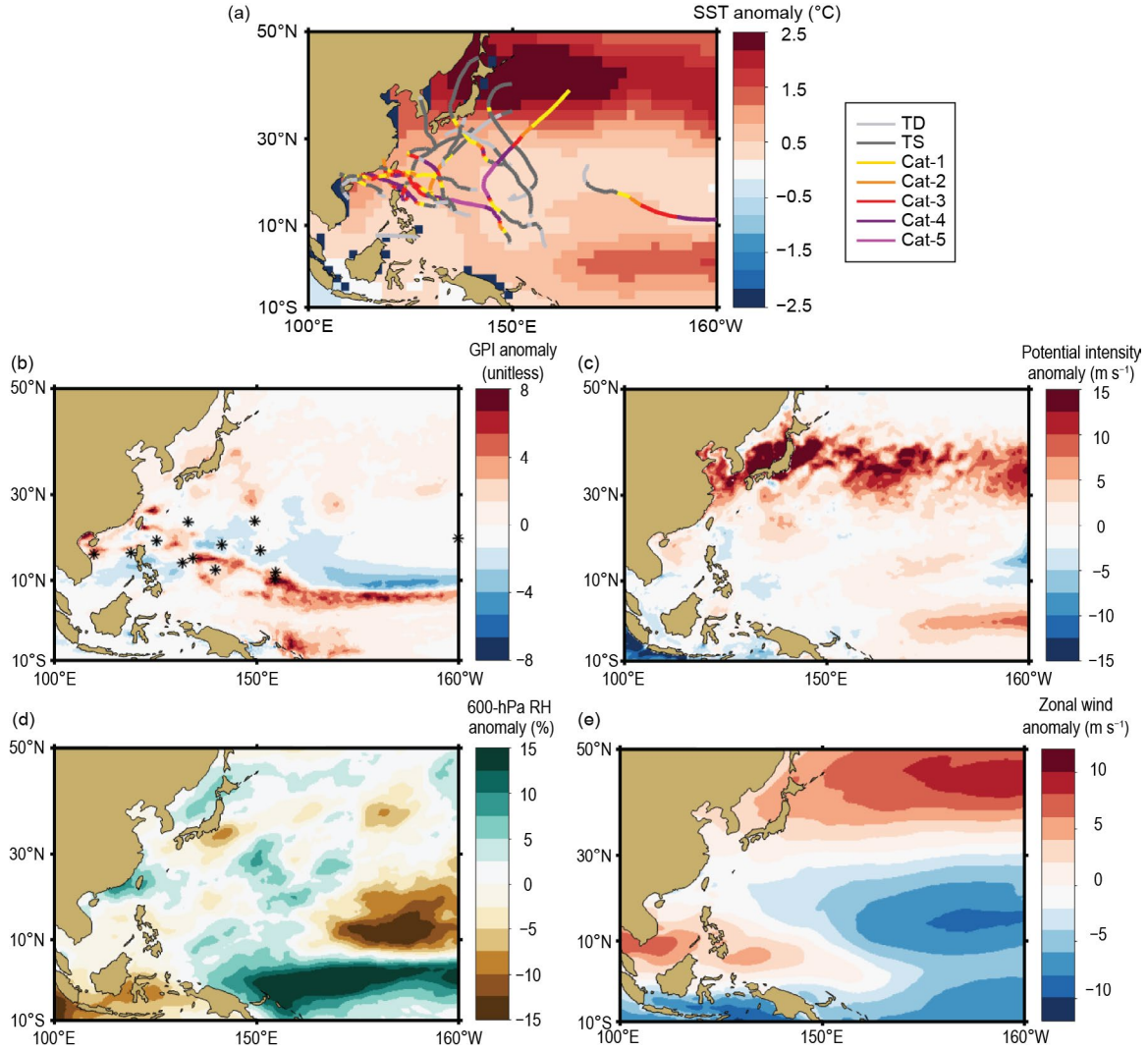

Fig. 4.33. Jul–Oct (JASO) 2023: (a) Sea-surface temperature (SST) anomalies (°C) and the tracks of all 2023 storms (including tropical depressions [TDs], tropical storms [TSs], and typhoon-strength storms [Cat]), with colors denoting their intensity, (b) genesis potential index anomalies and first position of JASO 2023 storms marked with an asterisk, (c) potential intensity anomalies (m s^{-1}), (d) 600-hPa relative humidity anomalies (%), and (e) zonal winds at 850-hPa (m s^{-1}). (Data sources: SST: ERSSTv5 [Huang et al. 2017]; other environmental fields: ERA5 reanalysis [Hersbach et al. 2020]; tracks and first position: Joint Typhoon Warning Center preliminary operational track data.)

The genesis potential index (Fig. 4.33b; Emanuel and Nolan 2004; Camargo et al. 2007) expresses the enhanced or reduced probability of TC formation through a nonlinear empirical combination of environmental factors known to affect TC genesis. The genesis potential index anomalies have a bimodal pattern, with a narrow zonal region of positive anomalies south of 10°N and negative anomalies north of that. The region of positive genesis anomalies shifted northward in the western part of the basin, where the TCs formed in those months. The potential

intensity anomalies (Fig. 4.33c; Emanuel 1988) reflect the SST pattern, with positive anomalies in the equatorial region in the eastern part of the basin and a large zonal region of positive anomalies centered on 40°N.

Similar to the genesis potential index, the relative humidity anomalies present a zonal dipole pattern (Fig. 4.33d) in the eastern portion of the basin, with dry anomalies north of 10°N and wet anomalies to the south and east of the Maritime Continent. The monsoon trough, which is defined by the 850-hPa zonal winds anomalies, tends to expand eastward in El Niño events. In 2023, the positive zonal wind anomalies (Fig. 4.33e) encompassed the region from the South China Sea to east of the Philippines. Tropical cyclones tend to form in the edge of the monsoon trough. This was again the case in 2023, with some TCs forming on the northern edge of the monsoon trough.

These environmental conditions help explain the low levels of activity in 2023, as only a small area in the WNP basin had environmental conditions conducive to genesis formation (i.e., high SST, potential intensity, and mid-level relative humidity) during the peak typhoon season. Furthermore, a strong subtropical high and suppressed MJO activity contributed to the low level of typhoon activity in 2023, and the tropical cyclone heat potential values discussed in section 4h may shed some light on this low number of TCs. Several recent papers have related the decrease in TC activity in the WNP in the last few years to decadal variability (e.g., Zhao et al. 2018, 2020; Chan and Liu 2022).

(iv) Impacts

In 2023, 11 storms (including TCs) made landfall in the WNP basin (bottom quartile <15, climatology 1961–90). From these, 2 made landfall as tropical depressions (median: 5), 3 made landfall as tropical storms (bottom quartile <8), 4 made landfall as Saffir-Simpson Category 1–2 typhoons (Talim, Doksuri, Lan, and Saola; median: 4), and 2 made landfall as major typhoons (Haiku and Koinu; median: 2). Here, landfalls are defined as instances when the center of a storm that is over the ocean moves over land. The observed TC tracks were interpolated into 15-minute intervals, and we then used a high-resolution land mask in order to determine the occurrence of landfall. In our analysis, we only considered the highest-intensity landfall event for each storm in cases of multiple landfalls.

The largest impacts from the 2023 typhoon season were caused by Typhoon Doksuri (named Egay in the Philippines), which affected the northern Philippines and China, leading to $18.4 billion (U.S. dollars) in economic losses (Gallagher Re 2024). The remnants of Typhoon Doksuri led to high rainfall rates, causing floods and landslides in northern China, in particular in the Beijing area. The total rainfall from the storm in Beijing was 744.8 mm in a 40-hour period, which was the heaviest in the 140-year record, according to the China Meteorological Administration. The resulting floods caused 137 deaths and displaced 92,000 people in China and 313,000 in the Philippines, in addition to causing numerous power outages and a lack of running water across the region, according to Relief Web.

5. NORTH INDIAN OCEAN BASIN

J. Uehling and C. J. Schreck

(i) Seasonal activity

The North Indian Ocean (NIO) TC season typically occurs between April and December, with two peaks of activity: May–June and October–December, due to the presence of the monsoon trough over tropical waters of the NIO during these periods. Tropical cyclone genesis typically occurs in the Arabian Sea and the Bay of Bengal between 8°N and 15°N. The Bay of Bengal, on average, experiences four times more TCs than the Arabian Sea (Dube et al. 1997).

The 2023 NIO TC season had 8 named storms according to the JTWC, which was above the IBTrACS JTWC 1991–2020 climatology of 5.5. Two of those reached tropical storm strength according to the JTWC but were considered depressions by the India Meteorological Department. Four storms reached cyclone strength, and three of those reached major cyclone strength. These values were above the climatological average of 2.2 cyclones and well above the average of

1.1 major cyclones (Fig. 4.34). The 2022 seasonal ACE index (January–December) of 57.5 × 10^4 kt^2 was more than double the 1991–2020 mean of 24.7 × 10^4 kt^2.

Conditions were particularly favorable during the pre-monsoon period (May–June) when two of the major cyclones occurred. Sea-surface temperatures were unusually warm across the basin, with large anomalies in the Arabian Sea (Fig. 4.35a). Convection was also enhanced in the Arabian Sea, where Very Severe Cyclone Biparjoy formed (Fig. 4.35b). The Indian monsoon was delayed; thus, convection was generally suppressed over India and the Bay of Bengal where Super Cyclone Mocha formed. The delayed monsoon was associated with below-normal vertical wind shear southward from around 16°N–18°N to the equator (Fig. 4.35c). Low-level easterlies dominated the basin throughout the season (Fig. 4.35d). The conditions for tropical cyclones overall were favorable with low shear and high SSTs, which helped to explain the enhanced activity this year. These favorable factors were enough to overcome the drier and less convectively favorable conditions in the Bay of Bengal. During the post-monsoon period, the Indian Ocean dipole became strongly positive. The associated high SSTs in the Arabian Sea provided conditions conducive to the development of Very Severe Cyclone Tej's intensity.

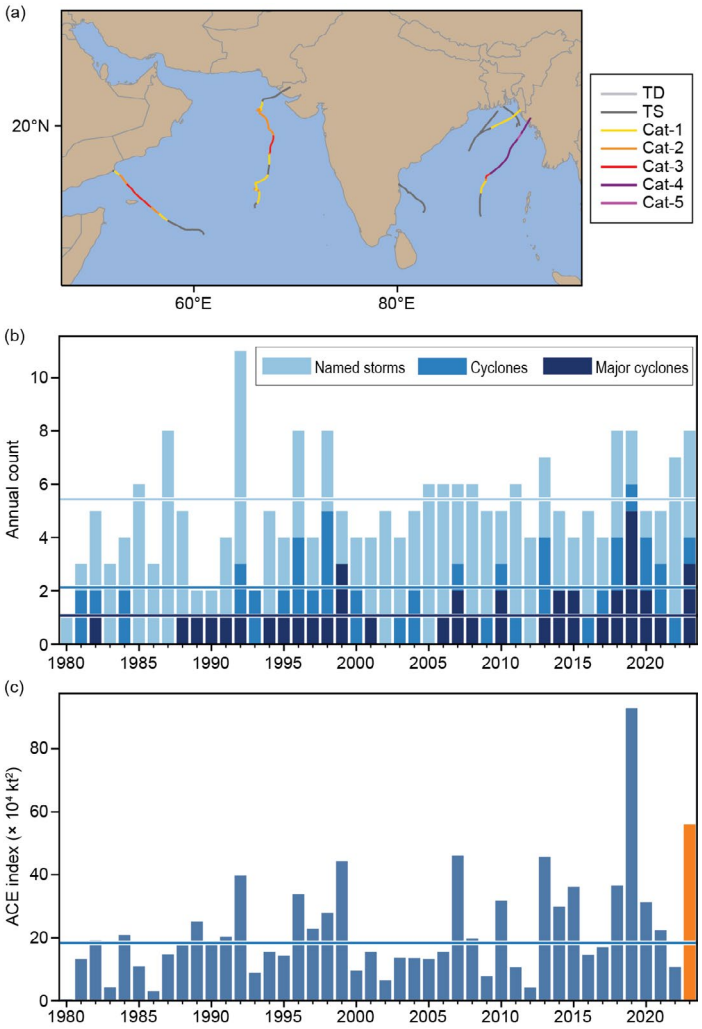

Fig. 4.34. (a) North Indian Ocean (NIO) tropical cyclone tracks in 2023. (b),(c) Annual tropical cyclone statistics for the NIO basin for the period 1990–2023: (b) number of named storms, cyclones, and major cyclones, and (c) accumulated cyclone energy (ACE; × 10^4 kt^2). Horizontal lines, representing the 1991–2020 climatology, are included in both (b) and (c).

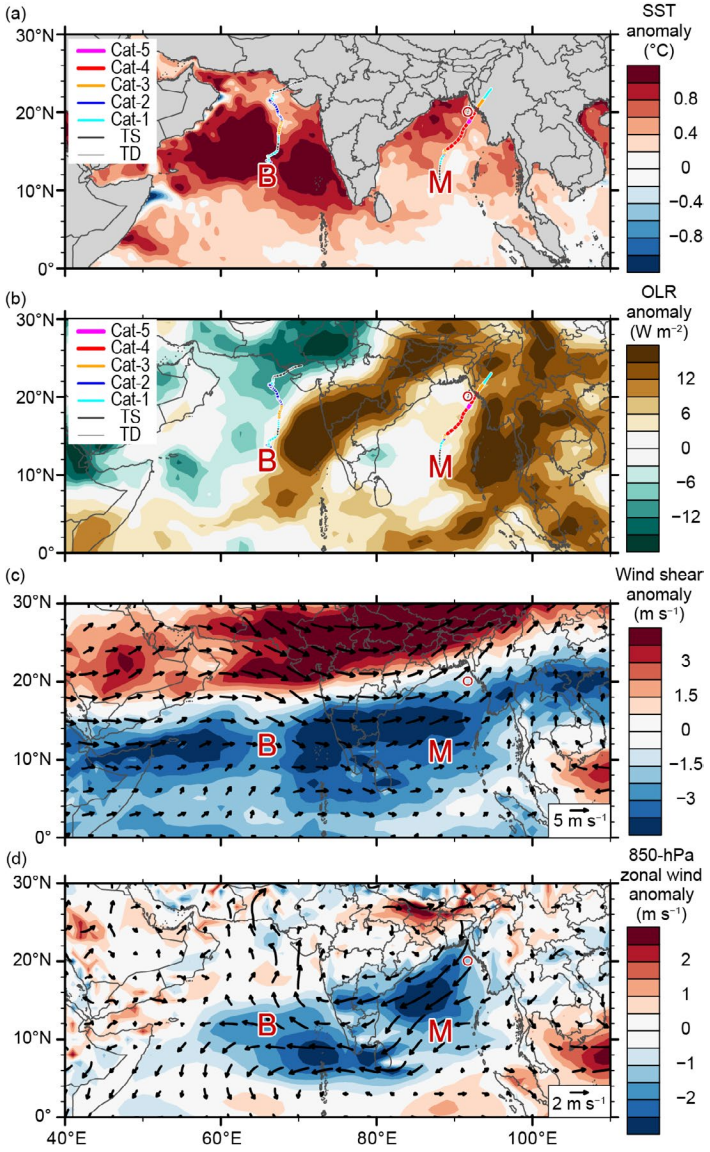

Fig. 4.35. May–Jun 2023 North Indian Ocean (NIO) anomaly maps of: (a) sea-surface temperature (SST; °C; Banzon and Reynolds 2013), (b) outgoing longwave radiation (OLR; W m^{-2}; Schreck et al. 2018); (c) 200-hPa–850-hPa vertical wind shear (m s^{-1}) vector (arrows) and scalar anomalies (shading), and (d) 850-hPa winds (m s^{-1}, arrows) and zonal wind anomalies (shading). Anomalies are relative to the annual cycle for 1991–2020. Letter symbols denote where each NIO tropical cyclone attained its initial tropical storm intensity, and the red circle represents an unnamed tropical storm. (Source: wind data from CFSR [Saha et al. 2014].)

(ii) Individual tropical cyclones and impacts

The North Indian Ocean cyclone season began on 11 May with the formation of Super Cyclonic Storm Mocha. This was also the strongest storm of the year in the basin, with winds peaking at 140 kt (72 m s^{-1}) and a minimum central pressure of 918 hPa, equivalent to a Category 5 hurricane on the SSHWS. Super Cyclone Mocha made a catastrophic landfall in Myanmar, causing over $1 billion (U.S. dollars) in damage and hundreds of fatalities between Myanmar and Bangladesh (Aon 2024). In June, the second major cyclone of the year, Very Severe Cyclone Biparjoy formed in the Arabian Sea and peaked with sustained winds of 105 kt (54 m s^{-1}). The storm made landfall in India after weakening to a tropical storm and comparatively minor impacts were felt. Very Severe Cyclone Tej, the final major cyclone of the year, occurred from 20 to 23 October. The storm peaked as a Category 3 equivalent over the Arabian Sea with maximum sustained winds of 110 kt (57 m s^{-1}) and a minimum pressure of 956 hPa. The cyclone brought flooding rains as it passed near the island of Socotra and caused minor impacts after landfall as a weakening tropical storm in Yemen.

The final cyclone-strength storm of the year was Severe Cyclone Hamoon, which peaked with winds of 80 kt (41 m s^{-1}) and a central pressure of 978 hPa. Hamoon occurred during late October over the Bay of Bengal and made landfall as a cyclone in Bangladesh. Hamoon brought heavy rainfall, strong winds, and storm surge to the country, resulting in numerous fatalities and extensive damage (Aon 2024). Late in the year, Cyclone Midhili and Cyclone Michaung caused flooding and damages after landfalls in Bangladesh and India, respectively.

6. SOUTH INDIAN OCEAN BASIN

A. D. Magee and C. J. Schreck

(i) Seasonal activity

The South Indian Ocean (SIO) TC basin extends south of the equator from the east African coastline to 90°E. While tropical cyclone activity can occur year-round, the peak season is typically between November and April when the Intertropical Convergence Zone is situated in the Southern Hemisphere. The 2022/23 season includes TCs that occurred from July 2022 to June 2023. Landfalling TCs typically impact Madagascar, Mozambique, and the Mascarene Islands, including Mauritius and La Réunion; however, impacts can be felt in other locations within the region.

A below-average storm count during the 2022/23 season was observed in the SIO basin, with 9 named storms according to the JTWC, compared to the IBTrACS-JTWC 1991–2020 mean of 10.4 (Fig. 4.36). There were 7 cyclones, of which 4 became major cyclones, above-normal compared to a 1991–2020 mean of 6.0 and 3.5, respectively. The season had an earlier-than-normal start, with Tropical Storms Ashley and Balita developing in September and October, respectively.

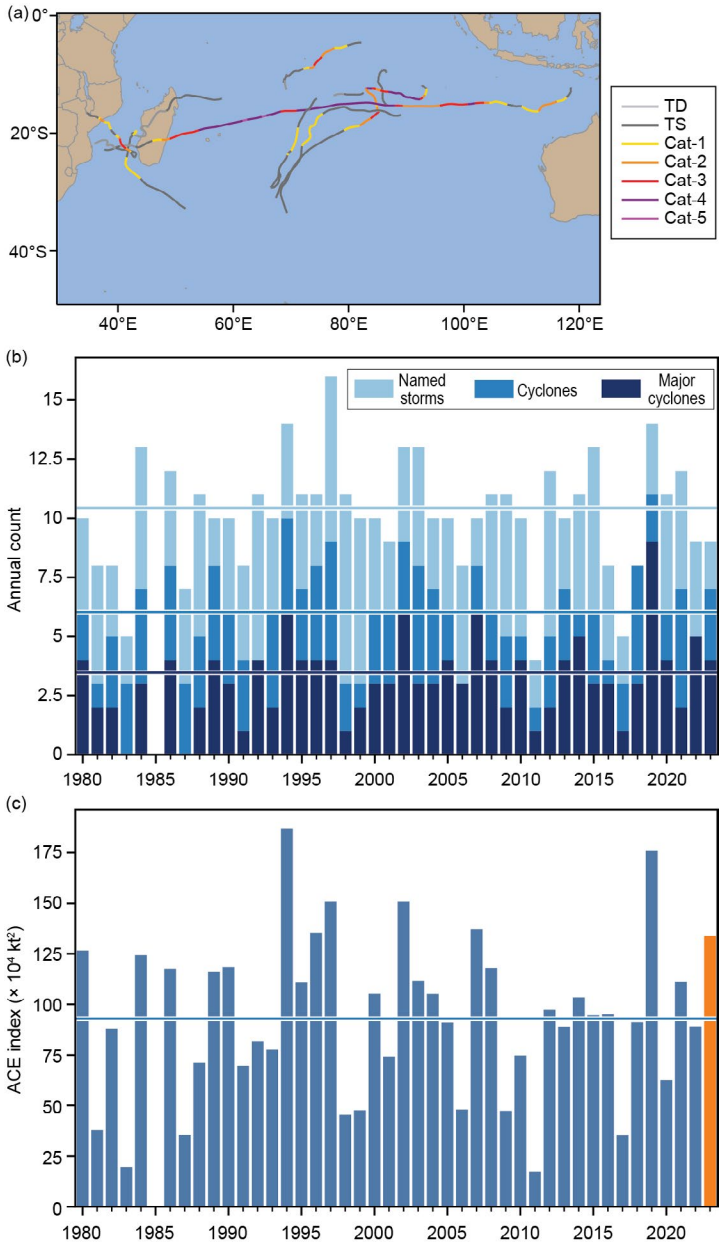

Fig. 4.36. (a) South Indian Ocean (SIO) tropical cyclone tracks in 2023. (b),(c) Annual tropical cyclone statistics for the SIO basin for the period 1980–2023: (b) number of named storms, cyclones, and major cyclones, and (c) accumulated cyclone energy (ACE; × 10^4 kt^2). Horizontal lines, representing the 1991–2020 climatology, are included in both (b) and (c).

The 2022/23 seasonal ACE index was 133.7 × 10^4 kt^2, which is 142% of the 1991–2020 climatology of 94.3 × 10^4 kt^2. Cyclone-favorable conditions, including anomalously high SSTs, were present to the northeast of Madagascar and south of 20°S (Fig. 4.37a), and favorable wind shear anomalies persisted across much of the basin between December and March (Fig. 4.37c).

(ii) Noteworthy tropical cyclones and impacts

The first tropical cyclone of the 2022/23 SIO TC season, Severe Tropical Cyclone Darian, initially began to the north of Cocos (Keeling) Islands in the Australian western region. On 21 December, the system passed into the SIO basin as a highly compact Category 4 tropical cyclone on the SSHWS. The system tracked southwest and then west, where it temporarily weakened. Darian then began intensifying again, reaching its peak intensity on 23 December, with maximum sustained winds of 135 kt (69 m s^{-1}) and a minimum central pressure of 922 hPa, a Category 4 system on the SSHWS. Darian continued to move on a southwesterly track, and on 28 December the system was downgraded to a tropical storm.

Tropical Cyclone Cheneso, the second tropical cyclone of the 2022/23 SIO TC season, formed on 16 January to the south of Diego Garcia. The system tracked southwest as it intensified to a severe tropical storm before making landfall across northern Madagascar, where it weakened. When Cheneso emerged into the Mozambique Channel, it briefly intensified into a Category 1 tropical cyclone on the SSHWS, reaching a peak intensity with sustained winds of 80 kt (41 m s^{-1}) and a minimum central pressure of 967 hPa on 28 January. Tropical Cyclone Cheneso resulted in 33 fatalities and widespread damage to over 10,000 homes as well as several healthcare and school facilities. Damage was estimated to total around $20 million (U.S. dollars).

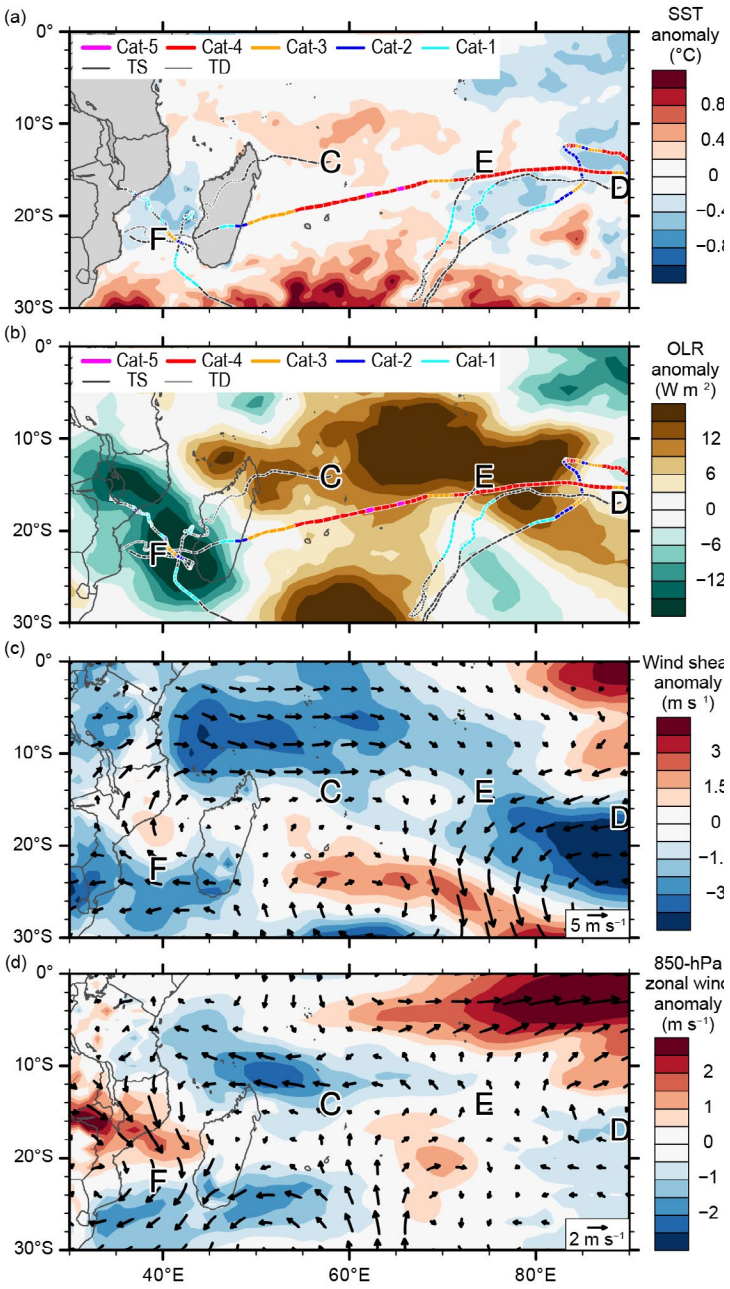

Fig. 4.37. 15 Dec 2022–15 Mar 2023 Southern Indian Ocean (SIO) anomaly maps of: (a) sea-surface temperature (SST; °C; Banzon and Reynolds 2013), (b) outgoing longwave radiation (OLR; W m^{-2}; Schreck et al. 2018); (c) 200-hPa–850-hPa vertical wind shear (m s^{-1}) vector (arrows) and scalar anomalies (shading), and (d) 850-hPa winds (m s^{-1}, arrows) and zonal wind anomalies (shading). Anomalies are relative to the annual cycle for 1991–2020. Letter symbols denote where each SIO tropical cyclone attained its initial tropical storm intensity (Source: wind data from CFSR [Saha et al. 2014]).

Severe Tropical Cyclone Freddy was a remarkable and record-breaking tropical cyclone that traversed the southern Indian Ocean for over five weeks in February and March 2023, establishing itself as one of the longest-lasting tropical cyclones on record (see Sidebar 4.2). Freddy alone accounted for about half of the ACE in the South Indian Ocean in 2022/23.

The final TC of the season, Severe Tropical Cyclone Fabien, formed from an active pulse of the Madden-Julian Oscillation, which initiated conditions conducive for cyclone development. Emerging from a low-pressure system on 8 May, the system began to intensify, organizing into a tropical disturbance by 13 May. Fabien tracked southwest from the central Southern Indian

Ocean and reached its peak intensity with sustained winds of 100 kt (51 m s^{-1}) and a minimum central pressure of 962 hPa on 16 May—a Category 3 system on the SSHWS. Although the system did not make landfall, high waves caused a fishing boat to capsize, resulting in 16 fatalities.

7. AUSTRALIAN BASIN

B. C. Trewin and L. Paterson

(i) Seasonal activity

The 2022/23 TC season was below average in the broader Australian basin (areas south of the equator and between 90°E and 160°E[4], which includes Australian, Papua New Guinea, and Indonesian areas of responsibility). The season produced 7 TCs, well below the 1991–2020 average[5] of 9.5. This reduction in activity was atypical for a season with weak to moderate La Niña conditions and equaling 2011/12 as having the lowest number of cyclones in a La Niña season on record. The 1991–2020 IBTrACS seasonal averages for the basin are 10.2 named storms, 5.0 TCs, and 2.5 major TCs, which compares with the 2022/23 IBTrACS-based counts of 9, 7, and 4, respectively (Fig. 4.38). Two of those storms reached tropical storm strength according to the JTWC but were considered tropical lows by the Australia's Bureau of Meteorology.

There were five TCs in the western sector[6] of the broader Australian region, one in the northern sector, and one in the eastern sector during 2022/23. Three of the seven cyclones reached Australian Category 5 intensity within the Australian basin, and a fourth did so after leaving the basin.

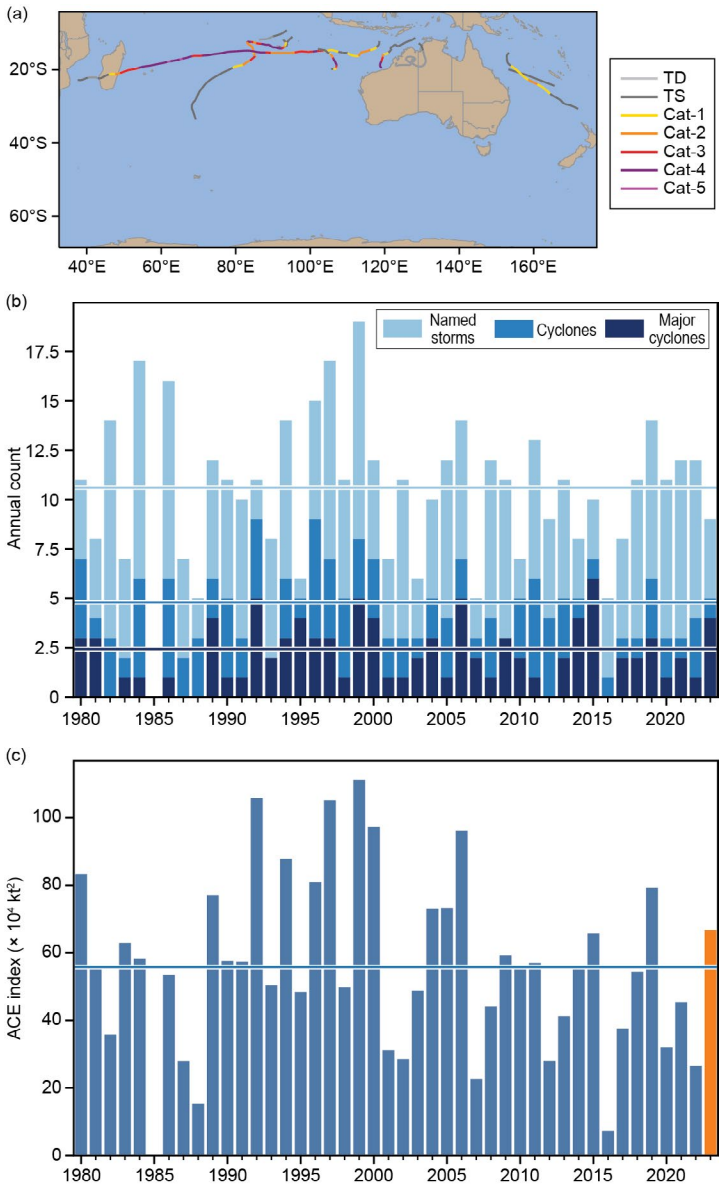

Fig. 4.38. (a) Australian tropical cyclone tracks in 2023. (b),(c) Annual tropical cyclone statistics for the Australian basin for the period 1980–2023: (b) number of named storms, cyclones, and major cyclones, and (c) accumulated cyclone energy (ACE; × 10^4 kt^2). Horizontal lines, representing the 1991–2020 climatology, are included in both (b) and (c).

(ii) Landfalling and other significant tropical cyclones

There were two landfalls in mainland Australia during the season at tropical cyclone intensity: Ellie in the Northern Territory in December and Ilsa in Western Australia in April. Ellie reached tropical cyclone intensity on 22 December while off the west coast of the Northern Territory Top End and made landfall as a Category 1 system near the Daly River mouth later the same day. While Ellie only spent a short period as a tropical cyclone, the post-landfall tropical low persisted for more than two weeks, initially over areas of the Northern Territory south of the landfall point and then moving west into the Kimberley region of Western Australia, finally dissipating after returning to the central Northern Territory on 8 January.

[4] The Australian Bureau of Meteorology's warning area overlaps both the southern Indian Ocean and southwest Pacific.

[5] References to cyclone category in this section are to the Australian scale (http://www.bom.gov.au/cyclone/tropical-cyclone-knowledge-centre/understanding/categories/), which differs from the Saffir-Simpson scale.

[6] The western sector covers areas between 90°E and 125°E. The eastern sector covers areas east of the eastern Australian coast to 160°E, as well as the eastern half of the Gulf of Carpentaria. The northern sector covers areas from 125°E east to the western half of the Gulf of Carpentaria. The western sector incorporates the Indonesian area of responsibility, while the Papua New Guinea area of responsibility is incorporated in the eastern sector.

The tropical low brought heavy rainfall along its path, with especially high accumulations in the Kimberley region due to the slow movement of the system. Totals exceeding 400 mm for the week ending 3 January were widespread, with Dimond Gorge, 70 km northeast of Fitzroy Crossing, reporting the highest total of 830.2 mm, including 355.6 mm on 2 January. Major flooding occurred over large parts of Western Australia and the Northern Territory. The Fitzroy River at Fitzroy Crossing reached a new high peak of 14.23 m, 0.27 m above the previous record. The main road bridge at Fitzroy Crossing collapsed, severing the only wet-season link through the region until a temporary crossing could be built in late March. Many other transport links were also severely disrupted. Numerous Aboriginal communities were evacuated to larger towns.

Ilsa reached named TC intensity north of Broome on 11 April and intensified steadily over the following 48 hours as it moved southwest, reaching Category 5 intensity at 0600 UTC on 13 April about 180 km north of Port Hedland. The storm then turned southeast and made landfall around 1600 UTC that day near Pardoo Station, east of Port Hedland. The landfall was near peak intensity with maximum sustained 10-minute winds estimated at 124 kt (64 m s^{-1}), the first Australian scale Category 5 landfall in Australia since Marcia in 2015 (and in Western Australia since Laurence in 2009). Bedout Island recorded 10-minute sustained winds of 119 kt (61 m s^{-1}) and a maximum gust of 156 kt (80 m s^{-1}), both of which were the highest values observed at a Bureau of Meteorology site in Australia, although higher values have been observed at non-Bureau sites (Courtney et al. 2012). Ilsa weakened rapidly as it moved inland, with the remnant low dissipating near the Northern Territory border early on 15 April. The landfall was in a sparsely populated area, with the main impact being the destruction of the Pardoo Roadhouse, along with significant damage to nearby pastoral stations. Nine fishermen were reported missing at sea after their vessel sank near Rowley Shoals and were presumed drowned.

In addition to Ilsa, two other cyclones off the Western Australian coast reached Category 5 intensity: Darian, which was within the region from 18 to 21 December with a peak 10-minute wind speed of 124 kt (64 m s^{-1}), and Herman, which peaked at 115 kt (59 m s^{-1}) during its lifetime from 29 March to 2 April. Neither system approached land areas or had any known impacts. Freddy, which formed northwest of Broome on 6 February and reached Category 4 intensity on 12 February with 10-minute winds of 115 kt (49 m s^{-1}), left the Australian region on 14 February and subsequently reached Saffir-Simpson Category 5 intensity in the South Indian Ocean basin, becoming the world's longest-lived tropical cyclones (see Sidebar 4.2). While it had no known impacts in the Australian region, Freddy had major impacts in Africa (section 4g6). Gabrielle, the season's only TC in the eastern region, peaked at Australian Category 3 intensity on 10 February before leaving the region, subsequently crossing the Australian territory of Norfolk Island (with minor damage) and having major impacts in New Zealand as a post-tropical cyclone (section 4g8).

8. SOUTHWEST PACIFIC BASIN

A. D. Magee and A. M. Lorrey

(i) Seasonal activity

The 2022/23 southwest Pacific tropical cyclone season officially began in November 2022 and ended in April 2023. The data for the season were gathered from the Fiji Meteorological Service, Australia's Bureau of Meteorology, and New Zealand MetService, Ltd. The Southwest Pacific basin, as defined by Diamond et al. (2012) as 135°E–120°W, experienced a total of four TCs, including three severe storms. One storm was considered to be a tropical storm by the JTWC, but a tropical depression by the WMO RSMC in Fiji. In comparison to the 1991–2020 seasonal average of 9.8 named tropical cyclones, including 4.3 severe storms, as reported by SPEArTC, the 2022/23 southwest Pacific TC season was considered to be below normal. Despite this, the 2022/23 southwest Pacific TC season was the costliest on record in the Southern Hemisphere, primarily due to Severe Tropical Cyclone Gabrielle.

Figure 4.39 illustrates the TC activity in the basin, which spans the area 160°E–120°W to avoid overlap with the Australian basin and double counting of storms. It is important to note that the climatological definition of the southwest Pacific basin (Diamond et al. 2012) is used for this seasonal description and does not align with WMO-designated boundaries for the

Regional Specialized Meteorological Center's nor the Tropical Cyclone Warning Center's areas of responsibility.

(ii) Storm tracks, landfalls, and impacts

Tropical Cyclone Irene, the first tropical cyclone of the 2022/23 southwest Pacific tropical cyclone season, initially formed as a tropical low to the west of Vanuatu on 13 January. The system was named on 18 January to the north of New Caledonia as it continued to track towards the east. Cyclone Irene reached peak intensity as an Australian scale Category 2 tropical cyclone, with sustained winds of 55 kt (28 m s^{-1}) and a minimum central pressure of 980 hPa on 18 January. Irene passed over Tanna Island in Vanuatu and continued to track toward the east-southeast.

The first severe tropical cyclone of the season and the costliest on record in the Southern Hemisphere, Severe Tropical Cyclone Gabrielle, formed on 5 February as a tropical low southeast of the Solomon Islands. Initially moving westward before tracking toward the south, Gabrielle intensified swiftly, becoming an Australian-scale Category 3 severe tropical cyclone on 9 February, reaching its peak intensity with sustained winds of 89 kt (46 m s^{-1}) and a minimum central pressure of 958 hPa the following day. Norfolk Island issued a red alert as Gabrielle neared, and New Zealand extended existing states of emergency in Auckland and the Coromandel due to the cyclone's imminent threat. Although not included in the IBTrACS preliminary track (Fig. 4.39a), the storm impacted New Zealand from 11 to 17 February, prompting a national state of emergency on 14 February for only the third time in the history of the country. Gabrielle tracked in a southeasterly direction in the Bay of Plenty, east of Northland and Auckland, and then followed an east-southeasterly track (not shown). As it passed by Great Barrier Island, a pressure reading of 967 hPa was recorded. Gabrielle brought heavy rain, with 250 mm–400 mm totals recorded across much of the northern part of North Island. Gabrielle was responsible for widespread power outages, and national transport networks were disrupted. There were also mandatory evacuations in some locations due to expected storm impacts. In New Zealand, severe flooding and property damage ensued, with gale-force winds ripping roofs off buildings and causing landslides. In some locations on the eastern seaboard, there was also significant coastal inundation. Fluvial flooding was extensive, and dozens of communities were temporarily cut off due to road closures or from bridges being destroyed. Multiple dams in Hawke Bay burst due to flash flooding, and significant volumes of silt blanketed vineyards and orchards. At some locations, buildings were lifted off their foundations and moved hundreds of meters due to the force of floodwaters. Over 140,000 landslides were recorded post-cyclone. The cyclone's passage through New Zealand left over 225,000 homes without power, thousands of displaced people, and significant infrastructure damage, including to water supplies, roads,

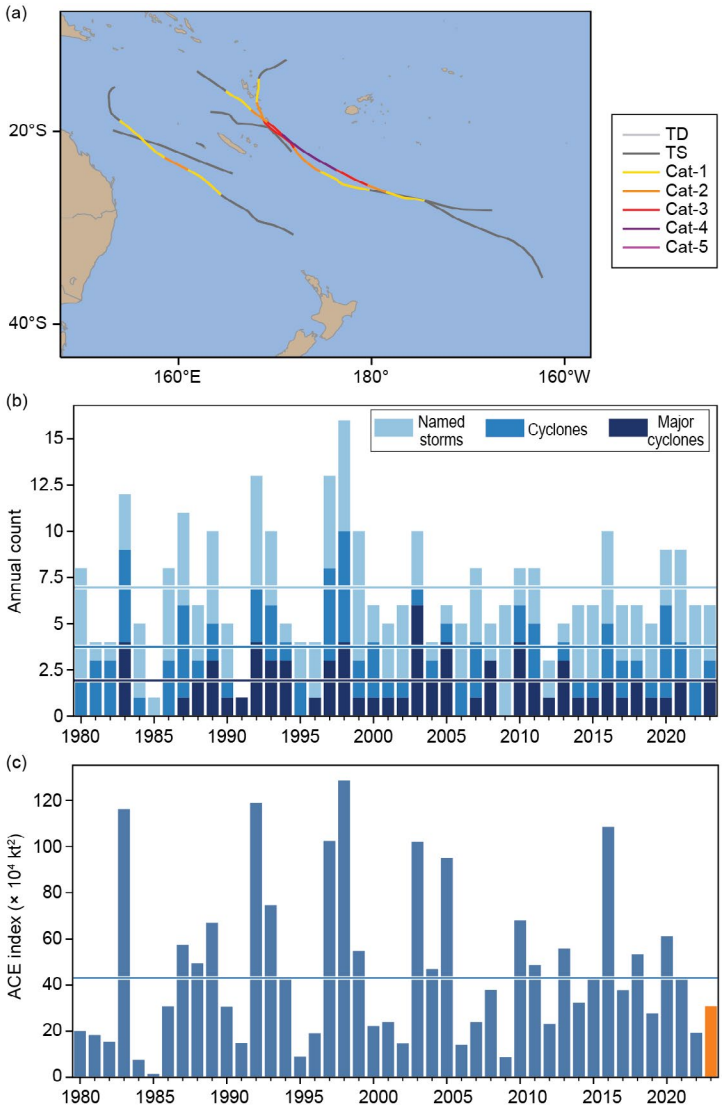

Fig. 4.39. (a) Southwest Pacific tropical cyclone tracks in 2023. (b),(c) Annual tropical cyclone statistics for the southwest Pacific basin for the period 1980–2023: (b) number of named storms, cyclones, and major cyclones, and (c) accumulated cyclone energy (ACE; × 10^4 kt^2). Horizontal lines, representing the 1991–2020 climatology, are included in both (b) and (c).

railways, and bridges. With 11 direct fatalities, Gabrielle became the deadliest New Zealand weather event since 1968 (NIWA 2023). Total damage associated with Gabrielle exceeded $13.5 billion New Zealand dollars ($9.5 billion U.S. dollars), the costliest on record in the Southern Hemisphere to date.

Severe Tropical Cyclone Judy began as a low-pressure system located south of Samoa. Favorable conditions, including moderate wind shear and high sea-surface temperatures, helped the system to organize quickly. The system developed into a tropical cyclone on 27 February near the Solomon Islands and continued to track in a southwesterly direction. As it approached central Vanuatu, Severe Tropical Cyclone Judy reached its peak intensity with sustained winds of 100 kt (51m s^{-1}) and a minimum central pressure of 940 hPa, becoming an Australian-scale Category 4 tropical cyclone on 1 March. The system passed over Shefa Province, close to Port Vila, and made landfall across Tanna Island. Residents in Port Vila were evacuated, and more than 50% of households reported damage. Strong winds brought down communication lines and damaged Vanuatu Central Hospital. The system continued to track towards the southeast, where increasing wind shear weakened the system.

Severe Tropical Cyclone Kevin formed initially within a monsoonal trough near Queensland, Australia. While Cyclone Judy was moving in a south-southeast direction away from the Vanuatu group, Kevin quickly strengthened while tracking toward Vanuatu and underwent rapid intensification promoted by favorable sea-surface temperatures and atmospheric conditions. The system passed over Erromango and Tanna Island in Vanuatu as an Australian scale Category 4 storm on 3 March before reaching its peak intensity the next day, with sustained winds of 125 kt (64 m s^{-1}) and a minimum central pressure of 913 hPa, an Australian-scale Category 5 intensity. The event coincided with a 6.5 magnitude earthquake that struck just west of Espiritu Santo, exacerbating the cyclone's impacts.

Severe Tropical Cyclones Judy and Kevin passed Vanuatu within 48 hours of each other, exacerbating impacts and complicating the humanitarian and emergency response. In total, around two-thirds of the country's population was directly affected. Over 19,000 houses were destroyed or damaged across Malampa, Shefa, and Tafea. Temporary and seasonal crops were also severely impacted, and many home gardens were destroyed. The coffee and commercial fruit and vegetable sectors were also significantly affected. No fatalities were reported; however, property damage of over $400 million New Zealand dollars ($248 million U.S. dollars) was reported, which amounts to about 25% of the gross domestic product for Vanuatu.

h. Tropical cyclone heat potential

—F. Bringas, I-I. Lin, and J. A. Knaff

Tropical cyclone heat potential (TCHP) is an indicator of the amount of heat stored in the upper ocean that can potentially promote tropical cyclone (TC) intensification and regulate ocean–atmosphere enthalpy fluxes and TC-induced sea-surface temperature (SST) cooling (e.g., Lin et al. 2013). TCHP is calculated by integrating the ocean temperature between the sea surface and the 26°C isotherm (D26), which has been reported as the minimum temperature required for TC genesis and intensification (Leipper and Volgenau 1972; Dare and McBride 2011). TCs traveling over regions of high TCHP conditions experience higher heat fluxes from the ocean into the atmosphere, favoring intensification and leading to reduced SST cooling (e.g., Lin et al. 2013). Areas in the ocean with TCHP values above 50 kJ cm^{-2} have been statistically linked with TC intensification, including rapid intensification when the maximum sustained wind speed increases by at least 30 kt in 24 hours in situations in which atmospheric conditions are favorable (e.g., Shay et al. 2000; Mainelli et al. 2008; Lin et al. 2021; Knaff et al. 2018, 2020). In addition to upper-ocean heat content, upper-ocean salinity conditions may also modulate TC intensification as storms traveling over areas of fresh water-induced barrier layers may receive increased air–sea heat fluxes caused by reduced upper-ocean mixing and cooling (e.g., Balaguru, 2012; Domingues et al. 2015).

We present an assessment and analysis of the upper-ocean heat content conditions during 2023, based on estimates of two parameters: 1) TCHP (e.g., Goni et al. 2009, 2017) global anomalies with respect to their long-term mean (1993–2022) and 2) TCHP in 2023 compared to conditions observed in 2022. TCHP anomalies during 2023 (Fig. 4.40) are computed for June–November in the Northern Hemisphere and November 2022–April 2023 in the Southern Hemisphere. The seven regions where TCs typically form, travel, and weaken/intensify are highlighted in Fig. 4.40. In all these regions, TCHP values exhibit large temporal and spatial variability due to mesoscale features (e.g., surface currents and associated eddies and rings) and short- to long-term modes of climate variability (e.g., North Atlantic Oscillation, El Niño–Southern Oscillation, and the Pacific Decadal Oscillation). The differences in TCHP anomalies between 2023 and 2022, as depicted in Fig. 4.41, were computed for the primary months of TC activity in each hemisphere as described above.

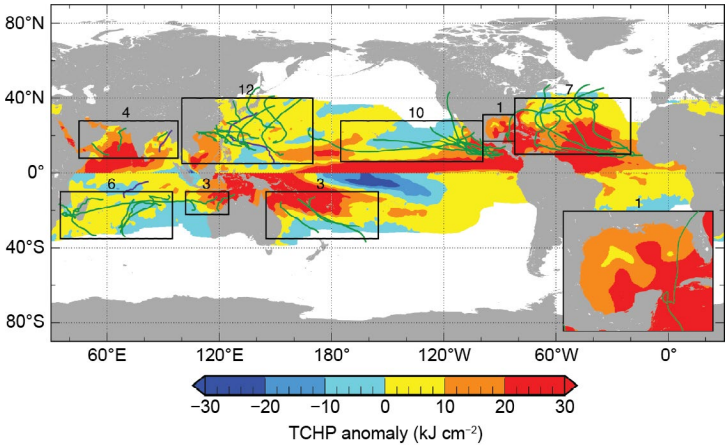

Fig. 4.40. Global anomalies of tropical cyclone heat potential (TCHP; kJ cm^{-2}) during 2023 computed as described in the text. The boxes indicate the seven regions where TCs typically occur; from left to right: southwest Indian, North Indian, northwest Pacific, southeast Indian, South Pacific, northeast Pacific, and North Atlantic (shown as Gulf of Mexico and tropical Atlantic separately). The green lines indicate the trajectories of all tropical cyclones reaching at least Category 1 (1-minute average wind ≥64 kt) and above during Nov 2022–Apr 2023 in the Southern Hemisphere and Jun–Nov 2023 in the Northern Hemisphere, and purple lines indicate Category 1 TCs that occurred outside these periods. The number above each box corresponds to the number of Category 1 and above cyclones that traveled within that box. Gulf of Mexico is shown in the inset in the lower right corner.

TCHP anomalies during 2023 exhibited above-average values in all TC regions and basins, including the eastern North Pacific and western North Pacific and the southwest Indian Ocean where, despite smaller areas of negative anomalies, average values in the regions were positive albeit closer to the long-term mean (Fig. 4.40). These positive TCHP anomalies were particularly large in most areas of the North Indian, the southwest Pacific, the North Atlantic, the Gulf of Mexico, and the equatorial regions of the eastern North Pacific where most TCs travel and intensify. TCHP anomalies reached values up to 30 kJ cm^{-2}, which are indicative of favorable oceanic conditions for the development and intensification of TCs. These same regions had TCHP anomalies during 2023 that were more than 20 kJ cm^{-2} larger than in 2023. Meanwhile, the South Indian Ocean, the western North Pacific, and the Bay of Bengal had near- or below-average

TCHP anomalies during 2023, and their TCHP was lower in 2023 compared to the previous year (Fig. 4.41).

The positive anomalies in the eastern North Pacific and central Pacific equatorial areas, with values during 2023 larger than 50 kJ cm^{-2} compared to 2022 (Fig. 4.41), were associated with the El Niño. In contrast, over the western North Pacific, negative anomalies of –10 kJ cm^{-2} to –20 kJ cm^{-2} as compared to 2022 were observed, consistent with a strong El Niño, which is known to reduce TCHP in the northwest Pacific (Zheng et al. 2015; Lin et al. 2020).

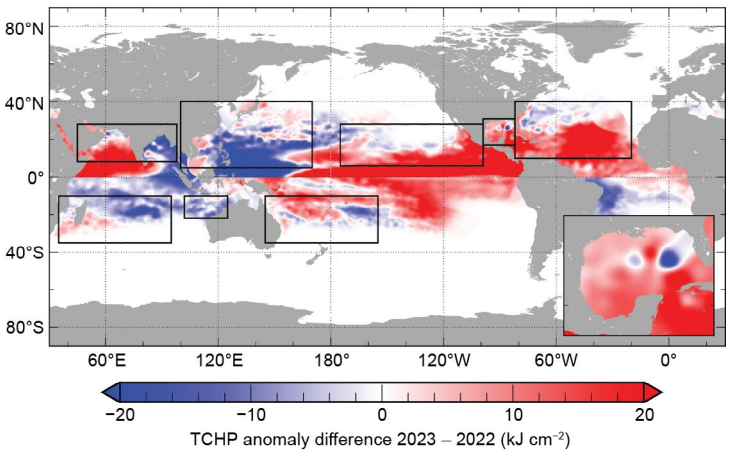

Fig. 4.41. Tropical cyclone heat potential (TCHP) anomaly difference between the 2023 and 2022 tropical cyclone seasons (kJ cm^{-2}; Jun–Nov in the Northern Hemisphere and Nov–Apr in the Southern Hemisphere). The Gulf of Mexico is shown in the inset in the lower right corner.

Consistent with the observed slightly above-average TCHP anomalies during 2023 in the region, the 2022/23 southwest Indian Ocean cyclone season was below average in terms of named storms but above average in terms of accumulated cyclone energy (ACE; Fig. 4.40). The most intense storm of the season was Cyclone Freddy. During its westward track until making landfall in Madagascar and Mozambique, Freddy weakened and re-intensified repeatedly, completing seven independent cycles of rapid intensification while traveling over areas with SSTs greater than 28°C and a TCHP greater than 40 kJ cm^{-2} (see Sidebar 4.2 for details).

Large positive areas of high TCHP anomaly values, in excess of 30 kJ cm^{-2} from the long-term average, were observed in regions of the southwest Indian and southwest Pacific, where TCs typically form and develop. However, 2022/23 generated near-average TC activity in these regions with a total of six TCs, of which four reached Category 1 intensity or above.

In the North Indian Ocean, above-average TCHP anomalies in excess of 30 kJ cm^{-2} and 10 kJ cm^{-2} were observed during 2023 in the northern Arabian Sea and the southern Bay of Bengal, respectively (Fig. 4.40). The most intense storm was Category 5 TC Mocha, which occurred in May (Fig. 4.40, in purple). After being named in the Bay of Bengal on 9 May, Mocha experienced two cycles of rapid intensification on 12 May and then 13 May, reaching its estimated peak intensity of 1-minute sustained wind speed of 140 kt (72 m s^{-1}) and a minimum central barometric pressure of 918 hPa, according to the Joint Typhoon Warning Center (JTWC), while traveling over extremely favorable oceanic conditions characterized by SSTs greater than 30°C and a TCHP greater than 120 kJ cm^{-2}.

Upper-ocean thermal conditions are largely modulated by the state of the El Niño–Southern Oscillation (ENSO) in the North Pacific Ocean (e.g., Zheng et al. 2015; Lin et al. 2020). While La Niña was predominant in the region during 2022, a shift to El Niño started early in 2023 with the transition occurring by June. El Niño became strong by late 2023 (section 4b). Consistent with this change in the ENSO state, TCHP anomalies were positive in the equatorial region of the eastern North Pacific with values well above 30 kJ cm^{-2}, while in the western North Pacific TCHP anomalies were positive although closer to the long-term mean (Fig. 4.40). Compared to 2022, TCHP anomalies in the eastern North Pacific during 2023 were larger by more than 20 kJ cm^{-2} in the equatorial regions while they were mostly negative by a similar magnitude in the western North Pacific (Fig. 4.41).

Tropical cyclone activity in the western North Pacific in 2023 was relatively low, although seven TCs reached Category 4 or 5 status. Among them, Super Typhoon Mawar was the most intense TC of the northwest Pacific in 2023, with a maximum intensity of 160 kt (82 m s^{-1}), according to the JTWC. Mawar originated and intensified at relatively low latitudes (~15°N) in May. At this low latitude, even in May, TCHP values were still high (~140 kJ cm^{-2}) and could favor Mawar's intensification.

The favorable oceanic conditions for TC intensification noted in the eastern North Pacific likely contributed to the above-average hurricane season observed during 2023. The two most

intense TCs of the season were Category 5 Hurricanes Jova and Otis, which underwent short periods of rapid intensification while traveling over regions of similar upper ocean thermal conditions characterized by SSTs greater than 29°C and a TCHP greater than 80 kJ cm^{-2}.

In the North Atlantic basin, upper-ocean thermal conditions during the 2023 hurricane season were characterized by TCHP anomalies larger than the long-term average, except in a reduced area near the northeast coast of the United States, where TCHP anomalies were slightly negative with respect to the long-term mean (Fig. 4.40). In particular, large TCHP anomalies were observed in the southeast portion of the basin west of Africa, the Caribbean Sea and the tropical North Atlantic around Cuba, and the Gulf of Mexico, where TCHP anomalies reached average values of up to 35 kJ cm^{-2} during the season. The same spatial distribution was observed for areas of TCHP anomalies that were larger in 2023 compared to the previous year throughout most of the region (Fig. 4.41), with anomalies in excess of 25 kJ cm^{-2} in the areas with the largest TCHP anomalies during 2023. It is likely that these favorable upper ocean thermal conditions contributed to 2023 being the fourth most active on record for named storm formations, with a total of 20 named storms (Fig. 4.40). The 2023 season was also the most active season on record for a year with a strong El Niño; Category 5 Hurricane Lee was the strongest storm of the season in this region. The system traveled over areas of favorable oceanic conditions with SSTs greater than 30°C and a TCHP greater than 90 kJ cm^{-2}, reaching its estimated peak intensity of 145 kt (75 m s^{-1}) and a minimum central barometric pressure of 926 hPa. Lee rapidly intensified from Category 1 to Category 5 during a 24-hour period with an increase in wind speed of 75 kt (39 m s^{-1}). Despite these favorable oceanic conditions, Lee subsequently weakened due to TC-unfavorable atmospheric conditions, including an increase in vertical wind shear.

In summary, favorable upper-ocean thermal conditions were observed in all TCHP basins during the 2023 season, except for the western North Pacific and southeast Indian Ocean, where conditions were slightly above average compared to the long-term mean. TCHP anomalies during 2023 were higher in most basins compared to the previous year, with the exception of the same two regions (western North Pacific and southeast Indian Ocean basins) where anomalies during 2023 were lower than those of the previous year. TC activity based on the number of named storms was consistent with these thermal conditions for every region. Several storms, including Intense Cyclone Freddy in the southwest Indian, Super Typhoon Mawar in the western North Pacific, Major Hurricanes Jova and Otis in the eastern North Pacific, and Major Hurricane Lee in the North Atlantic underwent rapid intensification, including several independent rapid intensification cycles in some cases, while traveling over areas with favorable oceanic conditions with high SST and TCHP values.

Sidebar 4.1: Hurricane Otis: The strongest landfalling hurricane on record for the west coast of Mexico

P. KLOTZBACH, C. FOGARTY, AND R. TRUCHELUT

Hurricane Otis was the strongest hurricane on record to strike the west coast of Mexico, making landfall with maximum winds of 140 kt (75 m s^{-1}) on 25 October (Reinhart and Reinhart 2024). The storm came ashore just west of Acapulco, causing devastation across the city and resulting in $12–16 billion (U.S. dollars) in property damage and at least 52 fatalities. The storm's extremely rapid intensification was poorly predicted by dynamical and statistical models. The official forecast from the National Hurricane Center (NHC) around 24 hours prior to landfall called for Otis to peak at Category 1 strength on the Saffir-Simpson Hurricane Wind Scale (64 kt–82 kt; 34 m s^{-1}–42 m s^{-1}). The explosive strengthening and lack of forecast warning led to a "nightmare scenario" for the Acapulco metropolitan area per the NHC forecast discussion[7] issued at 0300 UTC on 25 October.

This sidebar discusses the meteorological history of Otis, including some of the records that the storm achieved during its lifetime and the damage that the storm caused. Eastern North Pacific hurricane records from 1971 to 2022 are taken from the NHC's hurricane database (e.g., HURDAT2; Landsea and Franklin 2013)[8]. Otis' observed values are taken from the NHC's Tropical Cyclone Report on the storm (Reinhart and Reinhart 2024).

Otis formed from an area of low pressure off the west coast of Mexico, becoming a tropical depression at 1200 UTC on 22 October and intensifying to a tropical storm six hours later. Over the next 24 hours, the system strengthened slowly from 35 kt (18 m s^{-1}) to 45 kt (23 m s^{-1}) as it meandered northward. While Otis was tracking over ~29°C–30°C sea-surface temperatures during this time, it also was battling moderate levels of easterly vertical wind shear which left the center of the circulation somewhat exposed. Continued easterly shear checked Otis' intensification rate through 0600 UTC on 24 October, at which time sustained winds had reached 55 kt (28 m s^{-1}). In the next 24 hours, vertical wind shear relaxed, and the system responded by undergoing one of the strongest 24-hour rapid intensification episodes on record in the eastern North Pacific, intensifying from a 55-kt (28-m s^{-1}) tropical storm to a 145-kt (75-m s^{-1}) Category 5 hurricane. Otis weakened slightly before landfall, making landfall at 0645 UTC with maximum sustained winds of 140 kt (72 m s^{-1}; Fig. SB4.1). The storm dissipated quickly after landfall, weakening to a tropical storm by 1800 UTC on 25 October and degenerating into a remnant low over the mountainous terrain of western Mexico three hours later.

Hurricane Otis' 24-hour increase in intensity of 90 kt (46 m s^{-1}) tied with Hurricane Linda (1997) for the second-most intensification in a 24-hr period for an eastern North Pacific tropical cyclone on record (since 1971), lagging only Hurricane Patricia's (2015) 24-hour increase of 105 kt (54 m s^{-1}). Otis also intensified by 65 kt (31 m s^{-1}) in 12 hours, from a Category 1 hurricane (65 kt; 33 m s^{-1}) at 1200 UTC on 24 October to a Category 4 hurricane (130 kt; 67 m s^{-1}) at 0000 UTC on 25 October. This tied Hurricane Patricia for the strongest 12-hour intensification rate in the eastern North Pacific on record (65 kt; 33 m s^{-1}). Otis' maximum intensity of 145 kt (75 m s^{-1}) reached on 25 October tied with Hurricane Kenna (2002) for the strongest eastern North Pacific hurricane that late in the calendar year on record. As noted earlier, Otis was the strongest hurricane on record to make landfall on the west coast of Mexico (140 kt; 72 m s^{-1}). It was also the fifth Category 5 hurricane since 1950 to make landfall in mainland Mexico, joining Atlantic Hurricanes Janet (1955), Anita (1977), Gilbert (1988), and Dean (2007).

In Acapulco and the surrounding region of Guerrero, Otis inflicted catastrophic damage to most structures, including many hotels and high-rise buildings as well as downing and defoliating trees and causing severe rainfall-related flooding and mudslides. Windows and interior walls were blown out of most high-rise buildings and luxury hotels (e.g., Fig. SB4.2), resulting in catastrophic impacts to the city's tourism-based economy. Damage was also reported at many hospitals and medical clinics. Several electrical substations and a power plant were also heavily damaged, and thousands of utility poles were destroyed, resulting in widespread power and internet communication outages across the region. Storm

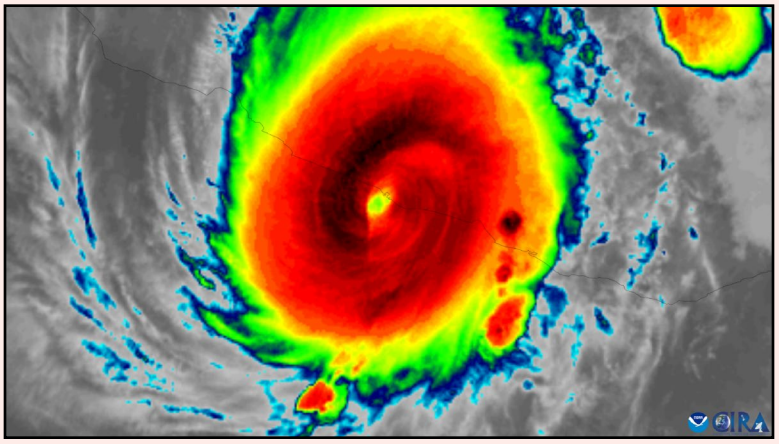

Fig. SB4.1. GOES-18 infrared satellite image of Hurricane Otis near the time of its landfall at 0610 UTC on 25 October 2023. (Image credit: NOAA/CIRA.)

[7] https://www.nhc.noaa.gov/archive/2023/ep18/ep182023.discus.012.shtml?
[8] https://www.nhc.noaa.gov/data/hurdat/hurdat2-nepac-1949-2022-050423.txt

surge and waves resulted in extensive damage to vessels and marina infrastructure exacerbated by the very short preparation time to secure property.

Mudslides on the outskirts of the city in mountainous terrain combined with severe winds caused more loss of life and the complete destruction of many private dwellings. The flooding and mudslides also blocked major highways, including the Mexico City-to-Acapulco "Highway of the Sun," preventing crews from traveling to the city to provide aid. Acapulco's commercial and military airports were also badly damaged, further hampering relief efforts. As noted earlier, Otis caused $12–16 billion (U.S. dollars) in damage. To put this damage in perspective, Mexico's Gross Domestic Product (GDP) is $1.3 trillion (U.S. dollars), and Otis' damage was approximately 1% of the Mexican GDP. For comparison, the costliest storm in U.S. history was Hurricane Katrina in (2005), which caused damage totaling $195 billion (U.S. dollars), equivalent to about 0.6% of the U.S.' GDP.

Hurricane Otis merits further study in multiple scientific and social dimensions. Operational intensity forecast errors were near recent upper bounds, with 48- and 24-hour projections underestimating Otis' 145 kt (75 m s^{-1}) peak maximum sustained winds by 95 kt (49 m s^{-1}) and 70 kt (36 m s^{-1}), respectively. This explosive intensification was coupled with an accelerated track towards a densely populated urban area, limiting the effective preparation window in Acapulco for hurricane-force winds to a day or less. Otis is also the first instance of the most intense portion of a Category 5 hurricane making landfall at near-peak intensity with a coastal area that has large-scale multistory structures, resulting in widespread, catastrophic structural damage. The wind profile power law and the observational height adjustments from Franklin et al. (2003) both suggest one-minute sustained winds atop the 100 m–125 m residential towers in eastern Acapulco likely reached at least 165 kt (85 m s^{-1}), with possible three-second gusts of 190 kt–200 kt (98 m s^{-1}–103 m s^{-1}). The extraordinary wind stresses and resulting destruction observed during Otis may hold valuable lessons for improving the resilience of coastal structures. Additionally, this earthquake-prone area of Mexico may also have unique building codes that, while well-suited to minimizing earthquake damage, might provide some challenges for those same structures in withstanding high winds from hurricanes, as documented in Crosti et al. (2011), which notes that while seismic design explicitly allows for inelastic behavior, it is in opposition to the requirements for high-wind design. This is certainly an issue for structural engineers to consider in compound-risk areas that are undoubtedly not limited to the Mexican coast.

Fig. SB4.2. (a) Before and (b) after view of high-rise buildings and surrounding vegetation highlighting the severe wind impacts from Hurricane Otis in Acapulco, Mexico. (Photo credit: Parvez 2023.)

Sidebar 4.2: Tropical Cyclone Freddy: The world's longest-lived tropical cyclone

B. TREWIN, C. EARL-SPURR, AND R. CERVENY

Tropical Cyclone Freddy in February and March 2023 was the world's longest-lived tropical cyclones (TCs) on record. It crossed the full width of the Indian Ocean, the first time since 2000 that a cyclone that formed in the Australian region made landfall on the mainland African coast. Freddy made three landfalls in total: one in Madagascar and two in Mozambique.

Freddy was first identified south of Bali (Indonesia) on 5 February. It reached TC intensity at 0600 UTC on 6 February at 12.3°S, 118.8°E, to the north of Broome in Western Australia. The storm then took a generally westward track, reaching an initial intensity peak on 11 February with maximum sustained one-minute winds of 115 kt (59 m s^{-1}), according to the Joint Typhoon Warning Center (making it a Category 4 system on the Australian scale), near 15°S, 102°E.

On 14 February, Freddy crossed the 90°E meridian into the southwest Indian Ocean basin. It intensified over the next few days, reaching its peak intensity on 19 February near 18°S, 62°E with maximum one-minute sustained winds of 140 kt (72 m s^{-1}), a Category 5 system on the Saffir-Simpson scale. It passed north of Mauritius and La Réunion on 20 February, still close to maximum intensity.

Freddy's first landfall was at about 1800 UTC on 21 February, near Mananjary on the east coast of Madagascar. The storm weakened somewhat before landfall but was still a significant cyclone at this point, with maximum one-minute sustained winds of 90 kt (46 m s^{-1}). The cyclone rapidly weakened over land while crossing Madagascar, but quickly re-intensified as it crossed the Mozambique Channel, making a second landfall near Vilankulos, Mozambique, on 24 February with maximum one-minute sustained winds of 60 kt (31 m s^{-1}).

Although it dropped below cyclone intensity, the system remained organized over land and re-emerged over the Mozambique Channel on 1 March, re-intensifying to become a cyclone again. It remained slow-moving over the Mozambique Channel, intensifying to reach maximum one-minute sustained winds of at least 95 kt (49 m s^{-1}) on two separate days, 7 and 11 March. The second of these maximum gusts occurred as it was moving northwest to make its final landfall near Quelimane, Mozambique, on 11 March. The storm weakened only slightly before landfall, which occurred with maximum one-minute sustained winds of 95 kt (49 m s^{-1}). The system then moved northwest as a remnant low, falling below cyclone intensity on 12 March and dissipating altogether by 14 March.

The major impacts of Freddy occurred as a result of flooding during and after the final landfall, both in Mozambique and Malawi, as extremely heavy rain fell (up to 672 mm in Mozambique) over the period of its landfalls. In some cases, one month's worth of rainfall fell in a single day, and six months of rain fell within six days. Malawi was especially hard hit with at least 679 deaths reported, according to the International Disaster Database EM-DAT. A further 165 deaths were reported in Mozambique, which had also experienced substantial flooding and wind damage during Freddy's first landfall. Casualties were also reported in Madagascar and Zimbabwe and at sea near Mauritius. In total, Severe Tropical Cyclone Freddy resulted in over 1400 fatalities and caused damage exceeding $655 million (U.S. dollars), making it the second-costliest tropical cyclone on record in the south Indian Ocean basin (Aon 2024).

A World Meteorological Organization expert committee recently confirmed that Freddy should be classified as the world's longest-lived tropical cyclone, and had the second longest track after Hurricane John in 1994 (Earl-Spurr et al. 2024). The system's total lifetime was clearly longer than that of the existing record holder, Hurricane John (which lasted for about 30 days in the northeast Pacific in August and September 1994), and even after periods over land when Freddy dropped below tropical cyclone intensity were discounted, it was at tropical cyclone strength for substantially longer than John's total lifetime.

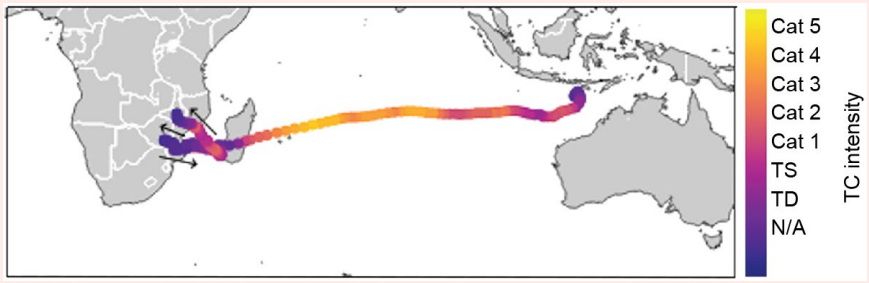

Fig. SB4.3. Cyclone Freddy storm track from 2 to 24 February 2023. Saffir-Simpson storm intensities along the track are indicated by the color scale.

Appendix 1: Acronyms

ACE	accumulated cyclone energy
AMO	Atlantic Multi-decadal Oscillation
ASO	August–October
AUSSM	Australian summer monsoon
CMORPH	Climate Prediction Center Morphing technique
CNP	Central North Pacific
DJF	December–February
EASM	East Asian summer monsoon
ENP	Eastern North Pacific
ENSO	El Niño–Southern Oscillation
GDP	gross domestic product
HTC	hurricane/typhoon/cyclone
IBTrACS	International Best Track Archive for Climate Stewardship
IO	Indian Ocean
IOB	Indian Ocean basin
IOD	Indian Ocean Dipole
IODE	Eastern Indian Ocean Dipole
IODW	Western Indian Ocean Dipole
ISM	Indian summer monsoon
ISM	Indian summer monsoon
ITCZ	Intertropical Convergence Zone
JASO	July–October
JJA	June–August
JMA	Japan Meteorological Agency
JTWC	Joint Typhoon Warning Center
LMR	Land Monsoon rainfall
MAM	March–May
MDR	Main Development Region
MJO	Madden-Julian Oscillation
MSLP	mean sea-level pressure
MSWEP	Multi-Source Weighted-Ensemble Precipitation
NA	North Atlantic
NAFSM	northern African summer monsoon
NASM	North American summer monsoon
NCAR	National Center for Atmospheric Research
NCEP	National Centers for Environmental Prediction
NH	Northern Hemisphere
NHC	National Hurricane Center
NIO	North Indian Ocean
nIOD	negative Indian Ocean Dipole
NOAA GlobalTemp	NOAA Merged Land Ocean Global Surface Temperature Analysis
OISST	Optimum Interpolation Sea Surface Temperature
OLR	outgoing longwave radiation
ONI	Oceanic Niño Index
PAGASA	Philippine Atmospheric, Geophysical and Astronomical Services Administration
pIOD	positive Indian Ocean Dipole
RMM	Real-time Multivariate Madden-Julian Oscillation

RSMC	Regional Specialized Meteorological Center
SA	South Atlantic
SAFSM	southern African summer monsoon
SAM	Southern Annular Mode
SASM	South American summer monsoon
SH	Southern Hemisphere
SIO	South Indian Ocean
SON	September–November
SPCZ	South Pacific Convergence Zone
SSHWS	Saffir-Simpson Hurricane Wind Scale
SST	sea-surface temperature
SSTA	sea-surface temperature anomaly
TC	tropical cyclone
TCHP	tropical cyclone heat potential
WMO	World Meteorological Organization
WNP	Western North Pacific
WNPSM	western North Pacific summer monsoon

Appendix 2: Datasets and sources

Section 4b ENSO and the tropical Pacific

Sub-section	General Variable or Phenomenon	Specific dataset or variable	Source
4b	Sea Surface Temperature	ERSSTv5	https://doi.org/10.7289/V5T72FNM
4b1	Sea Surface Temperature	NOAA Optimum Interpolation SST (OISST) v2.1	https://www.ncei.noaa.gov/products/optimum-interpolation-sst
4b1	Subsurface ocean temperature	Global Ocean Data Assimilation System (GODAS, Behringer 2007)	https://www.cpc.ncep.noaa.gov/products/GODAS/
4b2	Outgoing longwave radiation	NCEP CPC OLR (Liebmann and Smith, 1996)	https://www.cpc.ncep.noaa.gov/products/global_precip/html/wpage.olr.html
4b2	wind vectors/wind speed	NCEP NCAR reanalysis 1	https://psl.noaa.gov/data/gridded/data.ncep.reanalysis.html

Section 4c Tropical Intraseasonal Activity

Sub-section	General Variable or Phenomenon	Specific dataset or variable	Source
4c	Outgoing longwave radiation	HIRS OLR (Schreck et al. 2018)	https://www.ncei.noaa.gov/access/metadata/landing-page/bin/iso?id=gov.noaa.ncdc:C00875
4c	wind velocity potential anomalies	Climate Forecast System Reanalysis (CFSR)	https://climatedataguide.ucar.edu/climate-data/climate-forecast-system-reanalysis-cfsr
4c	Subsurface ocean heat content	Global Ocean Data Assimilation System (GODAS, Behringer et al. 1998)	https://www.cpc.ncep.noaa.gov/products/GODAS/

Section 4d Intertropical Convergence Zone

Sub-section	General Variable or Phenomenon	Specific dataset or variable	Source
4d1	Precipitation	Multisource weighted ensemble precipitation (MSWEP v2.8.0)	https://www.gloh2o.org/mswep/
4d2	Sea level pressure	NCEP NCAR reanalysis 1	https://psl.noaa.gov/data/gridded/data.ncep.reanalysis.html
4d2	Precipitation	CPC Morphing technique (CMORPH)	https://www.ncei.noaa.gov/products/climate-data-records/precipitation-cmorph
4d2	Outgoing Longwave Radiation	NCEP CPC OLR (Liebmann and Smith, 1996)	https://www.cpc.ncep.noaa.gov/products/global_precip/html/wpage.olr.html
4d2	Sea Surface Temperature	NOAA Optimum Interpolation SST (OISST) v2.1	https://www.ncei.noaa.gov/products/optimum-interpolation-sst

Section 4e Global Monsoon Summary

Sub-section	General Variable or Phenomenon	Specific dataset or variable	Source
4e	Precipitation	Global Precipitation Climatology Project (GPCP)	https://www.ncei.noaa.gov/products/climate-data-records/precipitation-gpcp-monthly
4e	Sea Surface Temperature	ERSSTv5	https://doi.org/10.7289/V5T72FNM
4e	Sea Surface Temperature	HadISST	https://www.metoffice.gov.uk/hadobs/hadisst/
4e	Wind, [Near] Surface	ERA5	https://www.ecmwf.int/en/forecasts/dataset/ecmwf-reanalysis-v5
4e	Wind, Upper Atmosphere	ERA5	https://www.ecmwf.int/en/forecasts/dataset/ecmwf-reanalysis-v5

Section 4f Indian Ocean Dipole

Sub-section	General Variable or Phenomenon	Specific dataset or variable	Source
4f	Precipitation	Climate Prediction Center (CPC) Merged Analysis of Precipitation (CMAP)	https://www.cpc.ncep.noaa.gov/products/global_precip/html/wpage.cmap.html
4f	Sea Surface Temperature	NOAA Optimum Interpolation SST (OISST) v2	https://www.ncei.noaa.gov/products/optimum-interpolation-sst
4f	Wind, [Near] Surface	JRA-55 Atmospheric Reanalysis	http://jra.kishou.go.jp/JRA-55/index_en.html

Section 4g Tropical Cyclones

Sub-section	General Variable or Phenomenon	Specific dataset or variable	Source
4g1, 4g2, 4g3, 4g5, 4g6, 4g7	Tropical Cyclone Data	International Best Track Archive for Climate Stewardship (IBTrACS)	https://www.ncei.noaa.gov/products/international-best-track-archive
4g2	Tropical Cyclone Data	Hurdat2	www.aoml.noaa.gov/hrd/hurdat/Data_Storm.html
4g2, 4g4	Sea Surface Temperature	ERSSTv5	https://doi.org/10.7289/V5T72FNM
4g2	Outgoing Longwave Radiation	NCEP CPC OLR (Liebmann and Smith, 1996)	https://www.cpc.ncep.noaa.gov/products/global_precip/html/wpage.olr.html
4g2, 4g4	Wind, [Near] Surface	ERA5	https://www.ecmwf.int/en/forecasts/dataset/ecmwf-reanalysis-v5

Sub-section	General Variable or Phenomenon	Specific dataset or variable	Source
4g3, 4g5, 4g6	Sea Surface Temperature	NOAA Optimum Interpolation SST (OISST) v2	https://www.ncei.noaa.gov/products/optimum-interpolation-sst
4g3, 4g5, 4g6	Wind, [Near] Surface	Climate Forecast System Reanalysis (CFSR)	https://climatedataguide.ucar.edu/climate-data/climate-forecast-system-reanalysis-cfsr
4g3, 4g5	Outgoing longwave radiation	HIRS OLR (Schreck et al. 2018)	https://www.ncei.noaa.gov/access/metadata/landing-page/bin/iso?id=gov.noaa.ncdc:C00875
4g4	Tropical Cyclone Data	RSMC-Tokyo, JMA best-track data	www.jma.go.jp/jma/jma-eng/jma-center/rsmc-hp-pub-eg/besttrack.html
4g4	Tropical Cyclone Data	Joint Typhoon Warning Center (JTWC) best-track database	https://www.metoc.navy.mil/jtwc/jtwc.html?best-tracks
4g6	Temperature, [Near] Surface	GHCNDEX	www.climdex.org/
4g8	Tropical Cyclone Data	Southwest Pacific Enhanced Archive of Tropical Cyclones (SPEArTC)	https://apdrc.soest.hawaii.edu/projects/speartc/

Sidebar 4.1 Hurricane Otis: The strongest landfalling hurricane on record for the west coast of Mexico

Sub-section	General Variable or Phenomenon	Specific dataset or variable	Source
SB4.1	Tropical Cyclone Data	Hurdat2	www.aoml.noaa.gov/hrd/hurdat/Data_Storm.html
SB4.1	Tropical Cyclone Data	National Hurricane Center (NHC) operational b-decks	https://ftp.nhc.noaa.gov/atcf/btk/

Sidebar 4.2 Tropical Cyclone Freddy—the world's longest-lived tropical cyclones

Sub-section	General Variable or Phenomenon	Specific dataset or variable	Source
SB4.2	Tropical Cyclone Data	Joint Typhoon Warning Center (JTWC) best-track database	https://www.metoc.navy.mil/jtwc/jtwc.html?best-tracks

Appendix 3: Supplemental materials

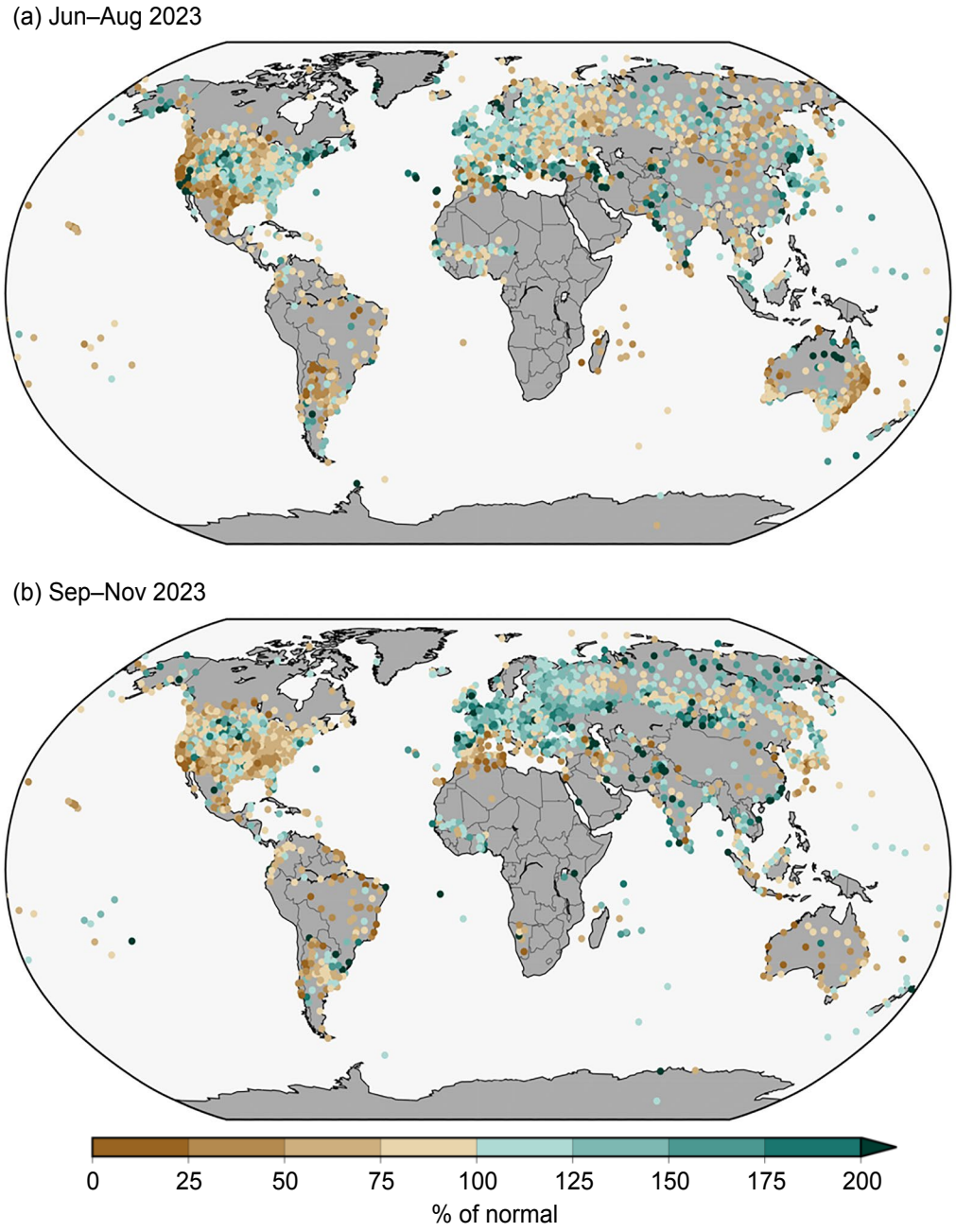

Appendix Fig. A4.1. Land-only precipitation (% of normal) during (a) Jun–Aug 2023 and (b) Sep–Nov 2023 (relative to a 1961–90 base period). (Sources: figure provided by NOAA NCEI, with data from GHCN-M version 4beta [Menne et al. 2017].)

References

Aiyyer, A., and J. Molinari, 2008: MJO and tropical cyclogenesis in the Gulf of Mexico and eastern Pacific: Case study and idealized numerical modeling. *J. Atmos. Sci.*, **65**, 2691–2704, https://doi.org/10.1175/2007JAS2348.1.

Aon, 2024: Climate and catastrophe insight report. Aon, 118 pp., https://assets.aon.com/-/media/files/aon/reports/2024/climate-and-catastrophe-insights-report.pdf.

Balaguru, K., P. Chang, R. Saravanan, L. R. Leung, Z. Xu, M. Li, and J. S. Hsieh, 2012: Ocean barrier layers' effect on tropical cyclone intensification. *Proc. Natl. Acad. Sci. USA*, **109**, 14343–14347, https://doi.org/10.1073/pnas.1201364109.

Banzon, V. F., and R. W. Reynolds, 2013: Use of WindSat to extend a microwave-based daily optimum interpolation sea surface temperature time series. *J. Climate*, **26**, 2557–2562, https://doi.org/10.1175/JCLI-D-12-00628.1.

Beck, H. E., E. F. Wood, M. Pan, C. K. Fisher, D. G. Miralles, A. I. J. M. van Dijk, T. R. McVicar, and R. F. Adler, 2019: MSWEP V2 Global 3-hourly 0.1° precipitation: Methodology and quantitative assessment. *Bull. Amer. Meteor. Soc.*, **100**, 473–500, https://doi.org/10.1175/BAMS-D-17-0138.1.

Behringer, D. W., 2007: The Global Ocean Data Assimilation System (GODAS) at NCEP. 11th Symp. on Integrated Observing and Assimilation Systems for Atmosphere, Oceans, and Land Surface, San Antonio, TX, Amer. Meteor. Soc., 3.3, http://ams.confex.com/ams/87ANNUAL/techprogram/paper_119541.htm.

——, M. Ji, and A. Leetmaa, 1998: An improved coupled model for ENSO prediction and implications for ocean initialization. Part I: The ocean data assimilation system. *Mon. Wea. Rev.*, **126**, 1013–1021, https://doi.org/10.1175/1520-0493(1998)126<1013:AICMFE>2.0.CO;2.

Bell, G. D., and M. Chelliah, 2006: Leading tropical modes associated with interannual and multi-decadal fluctuations in North Atlantic hurricane activity. *J. Climate*, **19**, 590–612, https://doi.org/10.1175/JCLI3659.1.

——, and Coauthors, 2000: The 1999 North Atlantic Hurricane season [in "Climate Assessment for 1999"]. *Bull. Amer. Meteor. Soc.*, **81** (6), S19–S22, https://doi.org/10.1175/1520-0477(2000)81[s1:CAF]2.0.CO;2.

——, E. Blake, C. Landsea, K. Mo, R. Pasch, M. Chelliah, and S. Goldenberg, 2006: Atlantic basin [in "State of the Climate in 2005"]. *Bull. Amer. Meteor. Soc.*, **87** (6), S33–S37, https://doi.org/10.1175/1520-0477-87.6.S1.

——, ——, C. W. Landsea, C. Wang, J. Schemm, T. Kimberlain, R. J. Pasch, and S. B. Goldenberg, 2017: Atlantic basin [in "State of the Climate in 2016"]. *Bull. Amer. Meteor. Soc.*, **98** (8), S108–S112, https://doi.org/10.1175/2017BAMSStateoftheClimate.1.

——, ——, ——, S. B. Goldenberg, and R. J. Pasch, 2018: Atlantic basin [in "State of the Climate in 2017"]. *Bull. Amer. Meteor. Soc.*, **99** (8), S114–S118, https://doi.org/10.1175/2018BAMSStateoftheClimate.1.

——, ——, ——, H. Wang, S. B. Goldenberg, and R. J. Pasch 2019: Atlantic basin [in "State of the Climate in 2018"]. *Bull. Amer. Meteor. Soc.*, **100** (9), S113–S119, https://doi.org/10.1175/2019BAMSStateoftheClimate.1.

——, E. S. Blake, C. W. Landsea, M. Rosencrans, H. Wang, S. B. Goldenberg, and R. J. Pasch, 2020: Atlantic basin [in "State of the Climate in 2019"]. *Bull. Amer. Meteor. Soc.*, **101** (7), S204–S212, https://doi.org/10.1175/BAMS-D-20-0077.1.

Berg, R., 2024: Tropical cyclone report: Tropical Storm Max (EP162023). NHC NHC Tropical Cyclone Rep., 20 pp., https://www.nhc.noaa.gov/data/tcr/EP162023_Max.pdf.

Bjerknes, J., 1969: Atmospheric teleconnections from the equatorial Pacific. *Mon. Wea. Rev.*, **97**, 163–172, https://doi.org/10.1175/1520-0493(1969)097<0163:ATFTEP>2.3.CO;2.

Blake, E. S., 2024: Tropical cyclone report: Hurricane Beatriz (EP022023). NHC Tropical Cyclone Rep., 17 pp., https://www.nhc.noaa.gov/data/tcr/EP022023_Beatriz.pdf.

Camargo, S. J., and A. H. Sobel, 2005: Western North Pacific tropical cyclone intensity and ENSO. *J. Climate*, **18**, 2996–3006, https://doi.org/10.1175/JCLI3457.1.

——, A. W. Robertson, S. J. Gaffney, P. Smyth, and M. Ghil, 2007a: Cluster analysis of typhoon tracks: Part II: Large-scale circulation and ENSO. J. Climate, **20**, 3654–3676, https://doi.org/10.1175/JCLI4203.1.

——, K. A. Emanuel, and A. H. Sobel, 2007b: Use of a genesis potential index to diagnose ENSO effects on tropical cyclone genesis. *J. Climate*, **20**, 4819–4834, https://doi.org/10.1175/JCLI4282.1.

Chan, J. C. L., and K. S. Liu, 2002: Recent decrease in the difference in tropical cyclone occurrence between the Atlantic and the western North Pacific. *Adv. Atmos. Sci.*, **39**, 1387–1397.

Chen, L., and J.-J. Luo, 2021: Indian Ocean dipole and unique Indian Ocean basin warming in 2020 [in "State of the climate in 2020"]. *Bull. Amer. Meteor. Soc.*, **102** (8), S220–S222, https://doi.org/10.1175/BAMS-D-21-0080.1.

——, and ——, 2022: Indian Ocean dipole [in "State of the Climate in 2021"]. *Bull. Amer. Meteor. Soc.*, **103** (8), S213–S217, https://doi.org/10.1175/BAMS-D-22-0069.1.

Chia, H. H., and C. F. Ropelewski, 2002: The interannual variability in the genesis location of tropical cyclones in the northwest Pacific. *J. Climate*, **15**, 2934–2944, https://doi.org/10.1175/1520-0442(2002)015<2934:TIVITG>2.0.CO;2.

Courtney, J., and Coauthors, 2012: Documentation and verification of the world extreme wind gust record: 113.3 m s^{-1} on Barrow Island, Australia, during passage of tropical cyclone Olivia. *Aust. Meteor. Oceanogr. J.*, **62**, 1–9, https://doi.org/10.22499/2.6201.001.

Crosti, C., D. Duthinh, and E. Simiu, 2011: Risk consistency and synergy in multihazard design. *J. Struct. Eng.*, **137**, 844–849, https://doi.org/10.1061/(ASCE)ST.1943-541X.0000335.

Dare, R. A., and J. L. McBride, 2011: Sea surface temperature response to tropical cyclones. *Mon. Wea. Rev.*, **139**, 3798–3808, https://doi.org/10.1175/MWR-D-10-05019.1.

Diamond, H. J.,, and C. J. Schreck III, Eds., 2022: The tropics [in "State of the Climate in 2021"]. *Bull. Amer. Meteor. Soc.*, **103** (8), S193–S256, https://doi.org/10.1175/BAMS-D-22-0069.1.

——, and ——, Eds., 2023: The tropics [in "State of the Climate in 2022"]. *Bull. Amer. Meteor. Soc.*, **104** (8), S207–S270, https://doi.org/10.1175/BAMS-D-23-0078.1.

——, A. M. Lorrey, K. R. Knapp, and D. H. Levinson, 2012: Development of an enhanced tropical cyclone tracks database for the Southwest Pacific from 1840 to 2011. *Int. J. Climatol.*, **32**, 2240–2250, https://doi.org/10.1002/joc.2412.

Ding, Q., E. J. Steig, D. S. Battisti, and J. M. Wallace, 2012: Influence of the tropics on the southern annular mode. *J. Climate*, **25**, 6330–6348, https://doi.org/10.1175/JCLI-D-11-00523.1.

Domingues, R., and Coauthors, 2015: Upper ocean response to Hurricane Gonzalo (2014): Salinity effects revealed by targeted and sustained underwater glider observations. *Geophys. Res. Lett.*, **42**, 7131–7138, https://doi.org/10.1002/2015GL065378.

Dube, S. K., D. Rao, P. C. Sinha, T. S. Murty, and N. Bahuluyan, 1997: Storm surge in the Bay of Bengal and Arabian Sea: The problem and its prediction. *Mausam*, **48**, 283–304, https://doi.org/10.54302/mausam.v48i2.4012.

Earl-Spurr, C., and Coauthors, 2024: New WMO certified tropical cyclone duration extreme: TC Freddy (04 February to 14 March 2023) lasting for 36 days. *Bull. Amer. Meteor. Soc.*, in press, https://doi.org/10.1175/BAMS-D-24-0071.1.

Ebita, A., and Coauthors, 2011: The Japanese 55-Year Reanalysis "JRA-55": An interim report. *SOLA*, **7**, 149–152, https://doi.org/10.2151/sola.2011-038.

Emanuel, K. A., 1988: The maximum intensity of hurricanes. *J. Atmos. Sci.*, **45**, 1143–1155, https://doi.org/10.1175/1520-0469(1988)045<1143:TMIOH>2.0.CO;2.

—— , and D. S. Nolan, 2004: Tropical cyclone activity and the global climate system. 26th Conf. on Hurricanes and Tropical Meteorology, Miami, FL, Amer. Meteor. Soc., 10A.2, https://ams.confex.com/ams/26HURR/techprogram/paper_75463.htm.

Enfield, D. B., and A. M. Mestas-Nuñez, 1999: Multiscale variabilities in global sea surface temperatures and their relationships with tropospheric climate patterns. *J. Climate*, **12**, 2719–2733, https://doi.org/10.1175/1520-0442(1999)012<2719:MVIGSS>2.0.CO;2.

Franklin, J. L., M. L. Black, and K. Valde, 2003: GPS dropwindsonde wind profiles in hurricanes and their operational implications. *Wea. Forecasting*, **18**, 32–44, https://doi.org/10.1175/1520-0434(2003)018<0032:GDWPIH>2.0.CO;2.

Gallagher Re, 2024: Natural Catastrophe and Climate Report: 2023. 76 pp., https://www.ajg.com/gallagherre/news-and-insights/2024/january/2023-natural-catastrophe-and-climate-report/.

Goldenberg, S. B., and L. J. Shapiro, 1996: Physical mechanisms for the association of El Niño and West African rainfall with Atlantic major hurricane activity. *J. Climate*, **9**, 1169–1187, https://doi.org/10.1175/1520-0442(1996)009<1169:PMFTAO>2.0.CO;2.

—— , C. W. Landsea, A. M. Mestas-Nuñez, and W. M. Gray, 2001: The recent increase in Atlantic hurricane activity: Causes and implications. *Science*, **293**, 474–479, https://doi.org/10.1126/science.1060040.

Goni, G. J., and Coauthors, 2009: Applications of satellite-derived ocean measurements to tropical cyclone intensity forecasting. *Oceanography*, **22** (3), 190–197, https://doi.org/10.5670/oceanog.2009.78.

—— , and Coauthors, 2017: Autonomous and Lagrangian ocean observations for Atlantic tropical cyclone studies and forecasts. *Oceanography*, **30** (2), 92–103, https://doi.org/10.5670/oceanog.2017.227.

Gray, W. M., 1984: Atlantic seasonal hurricane frequency. Part I: El Niño and 30 mb quasi-biennial oscillation influences. *Mon. Wea. Rev.*, **112**, 1649–1668, https://doi.org/10.1175/1520-0493(1984)112<1649:ASHFPI>2.0.CO;2.

—— , 1990: Strong association between West African rainfall and U.S. landfall of intense hurricanes. *Science*, **249**, 1251–1256, https://doi.org/10.1126/science.249.4974.1251.

Guo, Y., X. Jiang, and D. E. Waliser, 2014: Modulation of the convectively coupled Kelvin waves over South America and the tropical Atlantic Ocean in association with the Madden–Julian oscillation. *J. Atmos. Sci.*, **71**, 1371–1388, https://doi.org/10.1175/JAS-D-13-0215.1.

Hastenrath, S., 1990: Decadal-scale changes of the circulation in the tropical Atlantic sector associated with Sahel drought. *Int. J. Climatol.*, **10**, 459–472, https://doi.org/10.1002/joc.3370100504.

Hersbach, H., and Coauthors, 2020: The ERA5 global reanalysis. *Quart. J. Roy. Meteor. Soc.*, **146**, 1999–2049, https://doi.org/10.1002/qj.3803.

Hong, C.-C., T. Li, and J.-J. Luo, 2008: Asymmetry of the Indian Ocean dipole. Part II: Model diagnosis. *J. Climate*, **21**, 4849–4858, https://doi.org/10.1175/2008JCLI2223.1.

Huang, B., and Coauthors, 2017: Extended Reconstructed Sea Surface Temperature, version 5 (ERSSTv5): Upgrades, validations, and intercomparisons. *J. Climate*, **30**, 8179–8205, https://doi.org/10.1175/JCLI-D-16-0836.1.

—— , C. Liu, V. Banzon, E. Freeman, G. Graham, B. Hankins, T. Smith, and H.-M. Zhang, 2021: Improvements of the Daily Optimum Interpolation Sea Surface Temperature (DOISST) version 2.1. *J. Climate*, **34**, 2923–2939, https://doi.org/10.1175/JCLI-D-20-0166.1.

Huffman, G., R. F. Adler, D. T. Bolvin, and G. Gu, 2009: Improving the global precipitation record: GPCP version 2.1. *Geophys. Res. Lett.*, **36**, L17808, https://doi.org/10.1029/2009GL040000.

Joyce, R. J., J. E. Janowiak, P. A. Arkin, and P. Xie, 2004: CMORPH: A method that produces global precipitation estimates from passive microwave and infrared data at high spatial and temporal resolution. *J. Hydrometeor.*, **5**, 487–503, https://doi.org/10.1175/1525-7541(2004)005<0487:CAMTPG>2.0.CO;2.

Kalnay, E., and Coauthors, 1996: The NCEP/NCAR 40-Year Reanalysis Project. *Bull. Amer. Meteor. Soc.*, **77**, 437–471, https://doi.org/10.1175/1520-0477(1996)077<0437:TNYRP>2.0.CO;2.

Kiladis, G. N., M. C. Wheeler, P. T. Haertel, K. H. Straub, and P. E. Roundy, 2009: Convectively coupled equatorial waves. *Rev. Geophys.*, **47**, RG2003, https://doi.org/10.1029/2008RG000266.

Knaff, J. A., 1997: Implications of summertime sea level pressure anomalies in the tropical Atlantic region. *J. Climate*, **10**, 789–804, https://doi.org/10.1175/1520-0442(1997)010<0789:IOSSLP>2.0.CO;2.

—— , C. R. Sampson, and K. D. Musgrave, 2018: An operational rapid intensification prediction aid for the western North Pacific. *Wea. Forecasting*, **33**, 799–811, https://doi.org/10.1175/WAF-D-18-0012.1.

—— , —— , and B. R. Strahl, 2020: A tropical cyclone rapid intensification prediction aid for the Joint Typhoon Warning Center's areas of responsibility. *Wea. Forecasting*, **35**, 1173–1185, https://doi.org/10.1175/WAF-D-19-0228.1.

Knapp, K. R., M. C. Kruk, D. H. Levinson, H. J. Diamond, and C. J. Neumann, 2010: The International Best Track Archive for Climate Stewardship (IBTrACS): Unifying tropical cyclone data. *Bull. Amer. Meteor. Soc.*, **91**, 363–376, https://doi.org/10.1175/2009BAMS2755.1.

—— , J. A. Knaff, C. R. Sampson, G. M. Riggio, and A. D. Schnapp, 2013: A pressure-based analysis of the historical western North Pacific tropical cyclone intensity record. *Mon. Wea. Rev.*, **141**, 2611–2631, https://doi.org/10.1175/MWR-D-12-00323.1.

Kumar, A., and Z.-Z. Hu, 2014: Interannual and interdecadal variability of ocean temperature along the equatorial Pacific in conjunction with ENSO. *Climate Dyn.*, **42**, 1243–1258, https://doi.org/10.1007/s00382-013-1721-0.

Landsea, C. W., and J. L. Franklin, 2013: Atlantic hurricane database uncertainty and presentation of a new database format. *Mon. Wea. Rev.*, **141**, 3576–3592, https://doi.org/10.1175/MWR-D-12-00254.1.

—— , W. M. Gray, P. W. Mielke, and K. J. Berry, 1992: Long-term variations of western Sahelian monsoon rainfall and intense U.S. landfalling hurricanes. *J. Climate*, **5**, 1528–1534, https://doi.org/10.1175/1520-0442(1992)005<1528:LTVOWS>2.0.CO;2.

—— , G. A. Vecchi, L. Bengtsson, and T. R. Knutson, 2010: Impact of duration thresholds on Atlantic tropical cyclone counts. *J. Climate*, **23**, 2508–2519, https://doi.org/10.1175/2009JCLI3034.1.

Leipper, D. F., and D. Volgenau, 1972: Hurricane heat potential of the Gulf of Mexico. *J. Phys. Oceanogr.*, **2**, 218–224, https://doi.org/10.1175/1520-0485(1972)002<0218:HHPOTG>2.0.CO;2.

Liebmann, B., and C. A. Smith, 1996: Description of a complete (interpolated) outgoing longwave radiation dataset. *Bull. Amer. Meteor. Soc.*, **77**, 1275–1277, https://doi.org/10.1175/1520-0477-77.6.1274.

Lin, I. I., and Coauthors, 2013: An ocean coupling potential intensity index for tropical cyclones. *Geophys. Res. Lett.*, **40**, 1878–1882, https://doi.org/10.1002/grl.50091.

—— , and Coauthors, 2020: ENSO and tropical cyclones. *El Niño Southern Oscillation in a Changing Climate, Geophys. Monogr.*, Vol. 253, Amer. Geophys. Union, 377–408, https://doi.org/10.1002/9781119548164.ch17.

—— , and Coauthors, 2021: A tale of two rapidly-intensifying supertyphoons: Hagibis (2019) and Haiyan (2013). Bull. *Amer. Meteor. Soc.*, **102**, E1645–E1664, https://doi.org/10.1175/BAMS-D-20-0223.1.

Liu, T., J. Li, C. Sun, T. Lian, and Y. Zhang, 2021: Impact of the April–May SAM on central Pacific Ocean sea temperature over the following three seasons. *Climate Dyn.*, **57**, 775–786, https://doi.org/10.1007/s00382-021-05738-4.

—— , S. Masson, S. Behera, and T. Yamagata, 2007: Experimental forecasts of the Indian Ocean dipole using a coupled OAGCM. *J. Climate*, **20**, 2178–2190, https://doi.org/10.1175/JCLI4132.1.

—— , R. Zhang, S. K. Behera, Y. Masumoto, F.-F. Jin, R. Lukas, and T. Yamagata, 2010: Interaction between El Niño and extreme Indian Ocean dipole. *J. Climate*, **23**, 726–742, https://doi.org/10.1175/2009JCLI3104.1.

—— , W. Sasaki, and Y. Masumoto, 2012: Indian Ocean warming modulates Pacific climate change. *Proc. Natl. Acad. Sci. USA*, **109**, 18 701–18 706, https://doi.org/10.1073/pnas.1210239109.

Madden, R., and P. Julian, 1971: Detection of a 40–50 day oscillation in the zonal wind in the tropical Pacific. *J. Atmos. Sci.*, **28**, 702–708, https://doi.org/10.1175/1520-0469(1971)028<0702:DOADOI>2.0.CO;2.

—— , and —— , 1972: Description of global-scale circulation cells in the tropics with a 40–50 day period. *J. Atmos. Sci.*, **29**, 1109–1123, https://doi.org/10.1175/1520-0469(1972)029<1109:DOGSCC>2.0.CO;2.

—— , and —— , 1994: Observations of the 40–50-day tropical oscillation: A review. *Mon. Wea. Rev.*, **122**, 814–837, https://doi.org/10.1175/1520-0493(1994)122<0814:OOTDTO>2.0.CO;2.

Mainelli, M., M. DeMaria, L. Shay, and G. Goni, 2008: Application of oceanic heat content estimation to operational forecasting of recent Atlantic category 5 hurricanes. *Wea. Forecasting*, **23**, 3–16, https://doi.org/10.1175/2007WAF2006111.1.

Maloney, E. D., and D. L. Hartmann, 2001: The Madden–Julian oscillation, barotropic dynamics, and North Pacific tropical cyclone formation. *Part I: Observations. J. Atmos. Sci.*, **58**, 2545–2558, https://doi.org/10.1175/1520-0469(2001)058<2545:TMJOBD>2.0.CO;2.

Menne, M. J., B. E. Gleason, J. Lawrimore, J. Rennie, and C. N. Williams, 2017: Global Historical Climatology Network – Monthly temperature, version 4 (BETA). NOAA National Centers for Environmental Information, accessed 31 January 2024, https://doi.org/10.7289/V5XW4GTH.

Moreno, P. I., and Coauthors, 2018: Onset and evolution of southern annular mode-like changes at centennial timescale. *Sci. Rep.*, **8**, 3458, https://doi.org/10.1038/s41598-018-21836-6.

Münnich, M., and J. D. Neelin, 2005: Seasonal influence of ENSO on the Atlantic ITCZ and equatorial South America. *Geophys. Res. Lett.*, **32**, L21709, https://doi.org/10.1029/2005GL023900.

NIWA, 2023: Aotearoa New Zealand climate summary: February 2023 (issued 3 March 2023). Accessed 2 February 2024, https://niwa.co.nz/monthly/climate-summary-february-2023.

NOAA, 2023: Climate diagnostics bulletin, September 2023. NOAA, 87 pp., https://www.cpc.ncep.noaa.gov/products/CDB/CDB_Archive_pdf/PDF/CDB.sep2023_color.pdf.

Nobre, P., and J. Shukla, 1996: Variations of sea surface temperature, wind stress and rainfall over the tropical Atlantic and South America. *J. Climate*, **9**, 2464–2479, https://doi.org/10.1175/1520-0442(1996)009<2464:VOSSTW>2.0.CO;2.

Parvez, C. (@ChaudharyParvez), 2023: Residential building in Acapulco, Mexico that was shredded by Category 5 Hurricane Otis's extreme winds. Twitter/X, 28 October 2023, 10:40 p.m., https://twitter.com/ChaudharyParvez/status/1718457833468125236.

Raga, G. B., B. Bracamontes-Ceballos, L. Farfán, and R. Romero-Centeno, 2013: Landfalling tropical cyclones on the Pacific coast of Mexico: 1850–2010. *Atmósfera*, **26**, 209–220, https://doi.org/10.1016/S0187-6236(13)71072-5.

Ramage, C. S., 1971: *Monsoon Meteorology*. Academic Press, 296 pp.

Reinhart, B. J., and A. Reinhart, 2024: Hurricane Otis (EP182023). NHC Tropical Cyclone Rep., 39 pp., https://www.nhc.noaa.gov/data/tcr/EP182023_Otis.pdf.

Reynolds, R. W., N. A. Rayner, T. M. Smith, D. C. Stokes, and W. Wang, 2002: An improved in situ and satellite SST analysis for climate. *J. Climate*, **15**, 1609–1625, https://doi.org/10.1175/1520-0442(2002)015<1609:AIISAS>2.0.CO;2.

Ropelewski, C. F., and M. S. Halpert, 1989: Precipitation patterns associated with the high index phase of the Southern Oscillation. *J. Climate*, **2**, 268–284, https://doi.org/10.1175/1520-0442(1989)002<0268:PPAWTH>2.0.CO;2.

Saha, S., and Coauthors, 2014: The NCEP Climate Forecast System version 2. *J. Climate*, **27**, 2185–2208, https://doi.org/10.1175/JCLI-D-12-00823.1.

Saji, N. H., B. N. Goswami, P. N. Vinayachandran, and T. Yamagata, 1999: A dipole mode in the tropical Indian Ocean. *Nature*, **401**, 360–363, https://doi.org/10.1038/43854.

Schneider, T., T. Bischoff, and G. H. Haug, 2014: Migrations and dynamics of the intertropical convergence zone. *Nature*, **513**, 45–53, https://doi.org/10.1038/nature13636.

Schreck, C. J., 2015: Kelvin waves and tropical cyclogenesis: A global survey. *Mon. Wea. Rev.*, **143**, 3996–4011, https://doi.org/10.1175/MWR-D-15-0111.1.

—— , 2016: Convectively coupled Kelvin waves and tropical cyclogenesis in a semi-Lagrangian framework. *Mon. Wea. Rev.*, **144**, 4131–4139, https://doi.org/10.1175/MWR-D-16-0237.1.

—— , and J. Molinari, 2011: Tropical cyclogenesis associated with Kelvin waves and the Madden–Julian oscillation. *Mon. Wea. Rev.*, **139**, 2723–2734, https://doi.org/10.1175/MWR-D-10-05060.1.

—— , K. R. Knapp, and J. P. Kossin, 2014: The impact of best track discrepancies on global tropical cyclone climatologies using IBTrACS. Mon. *Wea. Rev.*, **142**, 3881–3899, https://doi.org/10.1175/MWR-D-14-00021.1.

—— , H.-T. Lee, and K. R. Knapp, 2018: HIRS outgoing longwave radiation —— Daily climate data record: Application toward identifying tropical subseasonal variability. *Remote Sens.*, **10**, 1325, https://doi.org/10.3390/rs10091325.

Shay, L. K., G. J. Goni, and P. G. Black, 2000: Effects of a warm oceanic feature on Hurricane Opal. *Mon. Wea. Rev.*, **128**, 1366–1383, https://doi.org/10.1175/1520-0493(2000)128<1366:EOAWOF>2.0.CO;2.

Trenberth, K. E., 1984: Signal versus noise in the Southern Oscillation. *Mon. Wea. Rev.*, **112**, 326–332, https://doi.org/10.1175/1520-0493(1984)1122.0.CO;2.

Vecchi, G. A., and B. J. Soden, 2007: Effect of remote sea surface temperature change on tropical cyclone potential intensity. *Nature*, **450**, 1066–1070, https://doi.org/10.1038/nature06423.

Ventrice, M. J., C. D. Thorncroft, and M. A. Janiga, 2012a: Atlantic tropical cyclogenesis: A three-way interaction between an African easterly wave, diurnally varying convection, and a convectively coupled atmospheric Kelvin wave. *Mon. Wea. Rev.*, **140**, 1108–1124, https://doi.org/10.1175/MWR-D-11-00122.1.

—— , —— , and C. J. Schreck, 2012b: Impacts of convectively coupled Kelvin waves on environmental conditions for Atlantic tropical cyclogenesis. *Mon. Wea. Rev.*, **140**, 2198–2214, https://doi.org/10.1175/MWR-D-11-00305.1.

Villarini, G., G. A. Vecchi, T. R. Knutson, and J. A. Smith, 2011: Is the recorded increase in short duration North Atlantic tropical storms spurious? *J. Geophys. Res.*, **116**, D10114, https://doi.org/10.1029/2010JD015493.

Vincent, D. G., 1994: The South Pacific Convergence Zone (SPCZ): A review. *Mon. Wea. Rev.*, **122**, 1949–1970, https://doi.org/10.1175/1520-0493(1994)122<1949:TSPCZA>2.0.CO;2.

Vose, R. S., and Coauthors, 2021: Implementing full spatial coverage in NOAA's Global Temperature Analysis. *Geophys. Res. Lett.*, **48**, e2020GL090873, https://doi.org/10.1029/2020GL090873.

Waliser, D. E., and C. Gautier, 1993: A satellite-derived climatology of the ITCZ. *J. Climate*, **6**, 2162–2174, https://doi.org/10.1175/1520-0442(1993)006<2162:ASDCOT>2.0.CO;2.

Wang, B., 1994: Climatic regimes of tropical convection and rainfall. *J. Climate*, **7**, 1109–1118, https://doi.org/10.1175/1520-0442(1994)007<1109:CROTCA>2.0.CO;2.

—— , and Q. Ding, 2008: Global monsoon: Dominant mode of annual variation in the tropics. *Dyn. Atmos. Ocean*, **44**, 165–183, https://doi.org/10.1016/j.dynatmoce.2007.05.002.

—— , J. Liu, H. J. Kim, P. J. Webster, and S. Y. Yim, 2012: Recent change of the global monsoon precipitation (1979–2008). *Climate Dyn.*, **39**, 1123–1135, https://doi.org/10.1007/s00382-011-1266-z.

Wheeler, M., and G. N. Kiladis, 1999: Convectively coupled equatorial waves: Analysis of clouds and temperature in the wavenumber-frequency domain. *J. Atmos. Sci.*, **56**, 374–399, https://doi.org/10.1175/1520-0469(1999)056<0374:CCEWAO>2.0.CO;2.

Wheeler, M. C., and H. H. Hendon, 2004: An all-season real-time multivariate MJO index: Development of an index for monitoring and prediction. *Mon. Wea. Rev.*, **132**, 1917–1932, https://doi.org/10.1175/1520-0493(2004)132<1917:AARMMI>2.0.CO;2.

Wood, K. M., and E. A. Ritchie, 2015: A definition for rapid weakening in the North Atlantic and eastern North Pacific. *Geophys. Res. Lett.*, **42**, 10 091–10 097, https://doi.org/10.1002/2015GL066697.

—— , and C. J. Schreck, 2020: Eastern North Pacific and central North Pacific basins [in "State of the Climate in 2019"]. *Bull. Amer. Meteor. Soc.*, **101** (8), S212–S214, https://doi.org/10.1175/BAMS-D-20-0077.1.

—— , and —— , 2021: Eastern North Pacific and central North Pacific basins [in "State of the Climate in 2020"]. *Bull. Amer. Meteor. Soc.*, **102** (8), S233–S235, https://doi.org/10.1175/BAMS-D-21-0080.1.

—— , and —— , 2022: Eastern North Pacific and central North Pacific basins [in "State of the Climate in 2021"]. *Bull. Amer. Meteor. Soc.*, **103** (8), S229–S231, https://doi.org/10.1175/BAMS-D-22-0069.1.

—— , and —— , 2023: Eastern North Pacific and central North Pacific basins [in "State of the Climate in 2022"]. *Bull. Amer. Meteor. Soc.*, **104** (8), S239–S243, https://doi.org/10.1175/BAMS-D-23-0078.1.

Wu, J., F. Hanjie, L. Shuheng, Z. Wenxiu, S. Yang, S. He, and N. Keenlyside, 2024: Boosting effect of strong western pole of the Indian Ocean dipole on the decay of El Niño events. *npj Climate Atmos. Sci.*, **7**, 6, https://doi.org/10.1038/s41612-023-00554-5.

Yim, S. Y., B. Wang, J. Liu, and Z. W. Wu, 2014: A comparison of regional monsoon variability using monsoon indices. *Climate Dyn.*, **43**, 1423–1437, https://doi.org/10.1007/s00382-013-1956-9.

Zhang, C., 2005: Madden–Julian oscillation. *Rev. Geophys.*, **43**, RG2003, https://doi.org/10.1029/2004RG000158.

Zhao, J. W., R. F. Zhan, Y. Q. Wang, and H. M. Xu, 2018: Contribution of the Interdecadal Pacific oscillation to the recent abrupt decrease in tropical cyclone genesis frequency over the western North Pacific since 1998. *J. Climate*, **31**, 8211–8224, https://doi.org/10.1175/JCLI-D-18-0202.1.

—— , —— , —— , S.-P. Xie, and Q. Wu, 2020: Untangling impacts of global warming and interdecadal Pacific Oscillation on long-term variability of North Pacific tropical cyclone track density. *Sci. Adv.*, **6**, eaba6813, https://doi.org/10.1126/sciadv.aba6813.

Zheng, Z.-W., I.-I. Lin, B. Wang, H.-C. Huang, and C.-H. Chen, 2015: A long neglected Rdamper in the El Nino–typhoon relationship: A 'Gaia-like' process. *Sci. Rep.*, **5**, 11103, https://doi.org/10.1038/srep11103.

STATE OF THE CLIMATE IN 2023

THE ARCTIC

M. L. Druckenmiller, R. L. Thoman, and T. A. Moon, Eds.

Special Online Supplement to the *Bulletin of the American Meteorological Society* Vol. 105, No. 8, August, 2024

https://doi.org/10.1175/BAMS-D-24-0101.1

Corresponding author: Matthew L. Druckenmiller / druckenmiller@colorado.edu

©2024 American Meteorological Society
For information regarding reuse of this content and general copyright information, consult the AMS Copyright Policy.

STATE OF THE CLIMATE IN 2023
The Arctic

Editors

Jessica Blunden
Tim Boyer

Chapter Editors

Anthony Arguez
Josh Blannin
Peter Bissolli
Kyle R. Clem
Howard J. Diamond
Matthew L. Druckenmiller
Robert J. H. Dunn
Catherine Ganter
Nadine Gobron
Gregory C. Johnson
Rick Lumpkin
Rodney Martinez
Ademe Mekonnen
John B. Miller
Twila A. Moon
Marilyn N. Raphael
Carl J. Schreck III
Laura Stevens
Richard L. Thoman
Kate M. Willett
Zhiwei Zhu

Technical Editor

Lukas Noguchi

BAMS Special Editor for Climate

Timothy DelSole

American Meteorological Society

Cover Credit:
Windblown icebergs in Kong Oscars Harbor at Tasiilaq, Greenland, most likely sourced from the peripheral glaciers and ice caps feeding Angmagssalik Fjord. (Photo credit: Kristin Poinar, 10 June 2023.)

How to cite this document:
The Arctic is one chapter from the *State of the Climate in 2023* annual report and is available from https://doi.org/10.1175/BAMS-D-24-0101.1. Compiled by NOAA's National Centers for Environmental Information, *State of the Climate in 2023* is based on contributions from scientists from around the world. It provides a detailed update on global climate indicators, notable weather events, and other data collected by environmental monitoring stations and instruments located on land, water, ice, and in space. The full report is available from https://doi.org/10.1175/2024BAMSStateoftheClimate.1.

Citing the complete report:
Blunden, J. and T. Boyer, Eds., 2024: "State of the Climate in 2023". Bull. Amer. Meteor. Soc., 105 (8), Si–S483 https://doi.org/10.1175/2024BAMSStateoftheClimate.1.

Citing this chapter:
M. L. Druckenmiller, R. L. Thoman, and T. A. Moon, Eds., 2024: The Arctic [in "State of the Climate in 2023"]. Bull. Amer. Meteor. Soc., 105 (8), S277–S330, https://doi.org/10.1175/BAMS-D-24-0101.1.

Citing a section (example):
Burgess, D., G. Wolken, B. Wouters, L. M. Andreassen, C. Florentine, J. Kohler, B. Luks, F. Pálsson, L. Sass, L. Thomson, and T. Thorsteinsson, 2024: Glaciers and ice caps outside Greenland [in "State of the Climate in 2023"]. Bull. Amer. Meteor. Soc., 105 (8), S307–S310, https://doi.org/10.1175/BAMS-D-24-0101.1.

Editor and Author Affiliations (alphabetical by name)

Andreassen, Liss Marie, Section for Glaciers, Ice and Snow, Norwegian Water Resources and Energy Directorate, Oslo, Norway

Ballinger, Thomas J., International Arctic Research Center, University of Alaska Fairbanks, Fairbanks, Alaska

Berner, Logan T., School of Informatics, Computing, and Cyber Systems, Northern Arizona University, Flagstaff, Arizona

Bernhard, Germar H., Biospherical Instruments Inc., San Diego, California

Bhatt, Uma S., Geophysical Institute, University of Alaska Fairbanks, Fairbanks, Alaska

Bigalke, Siiri, Plant, Soils and Climate Department, Utah State University, Logan, Utah

Bjerke, Jarle W., Norwegian Institute for Nature Research, Trondheim, Norway; FRAM – High North Research Centre for Climate and the Environment, Tromsø, Norway

Box, Jason E., Geological Survey of Denmark and Greenland (GEUS), Copenhagen, Denmark

Brettschneider, Brian, NOAA/NWS Alaska Region, Anchorage, Alaska

Brubaker, Mike, Alaska Native Tribal Health Consortium, Anchorage, Alaska

Burgess, David, Geological Survey of Canada, Natural Resources Canada, Ottawa, Canada

Butler, Amy H., NOAA Chemical Sciences Laboratory, Boulder, Colorado

Christiansen, Hanne H., Arctic Geophysics Department, University Centre in Svalbard, Longyearbyen, Norway; Geology Department, University Centre in Svalbard, Longyearben, Norway

Decharme, Bertrand, Centre National de Recherches Météorologiques, Météo-France/CNRS, Toulouse, France

Derksen, Chris, Climate Research Division, Environment and Climate Change Canada, Toronto, Canada

Divine, Dmitry, Norwegian Polar Institute, Fram Centre, Tromsø, Norway

Drost Jensen, Caroline, Danish Meteorological Institute, Copenhagen, Denmark

Druckenmiller, Matthew L., National Snow and Ice Data Center, Cooperative Institute for Research in Environmental Sciences, University of Colorado, Boulder, Boulder, Colorado

Elias Chereque, Alesksandra, Department of Physics, University of Toronto, Toronto, Canada

Epstein, Howard E., Department of Environmental Sciences, University of Virginia, Charlottesville, Virginia

Farrell, Sinead, Department of Geographical Sciences, University of Maryland, College Park, Maryland

Fausto, Robert S., Geological Survey of Denmark and Greenland (GEUS), Copenhagen, Denmark

Fettweis, Xavier, University of Liège, Liège, Belgium

Fioletov, Vitali E., Environment and Climate Change Canada, Toronto, Canada

Florentine, Caitlyn, Northern Rocky Mountain Science Center, U.S. Geological Survey, Bozeman, Montana

Forbes, Bruce C., Arctic Centre, University of Lapland, Rovaniemi, Finland

Frost, Gerald V. (JJ), Alaska Biological Research, Inc., Fairbanks, Alaska

Gerland, Sebastian, Norwegian Polar Institute, Fram Centre, Tromsø, Norway

Grooß, Jens-Uwe, Forschungszentrum Jülich (IEK-7), Jülich, Germany

Hanna, Edward, Department of Geography and Lincoln Climate Research Group, Lincoln, United Kingdom

Hanssen-Bauer, Inger, Norwegian Meteorological Institute, Oslo, Norway

Heatta, Máret J., Saami Council, Kárášjohka, Norway

Hendricks, Stefan, Alfred Wegener Institute, Helmholtz Centre for Polar and Marine Research, Bremerhaven, Germany

Ialongo, Iolanda, Finnish Meteorological Institute, Helsinki, Finland

Isaksen, Ketil, Norwegian Meteorological Institute, Oslo, Norway

Jeuring, Jelmer, Norwegian Meteorological Institute, Bergen, Norway

Jia, Gensuo, Institute of Atmospheric Physics, Chinese Academy of Sciences, Beijing, China

Johnsen, Bjørn, Norwegian Radiation and Nuclear Safety Authority, Østerås, Norway

Kaleschke, Lars, Alfred Wegener Institute, Helmholtz Centre for Polar and Marine Research, Bremerhaven, Germany

Kim, Seong-Joong, Korea Polar Research Institute, Incheon, South Korea

Kohler, Jack, Norwegian Polar Institute, Fram Centre, Tromsø, Norway

Labe, Zachary, M., Atmospheric and Oceanic Sciences Program, Princeton University, Princeton, New Jersey

Lader, Rick, International Arctic Research Center, University of Alaska Fairbanks, Fairbanks, Alaska

Lakkala, Kaisa, Finnish Meteorological Institute, Sodankylä, Finland

Lara, Mark J., Department of Plant Biology, University of Illinois, Urbana, Illinois; Department of Geography, University of Illinois, Urbana, Illinois

Lee, Simon H., Department of Applied Physics and Applied Mathematics, Columbia University, New York, New York

Loomis, Bryant D., NASA Goddard Space Flight Center, Greenbelt, Maryland

Luks, Bartłomiej, Institute of Geophysics, Polish Academy of Sciences, Warsaw, Poland

Luojus, Kari, Arctic Research Centre, Finnish Meteorological Institute, Helsinki, Finland

Macander, Matthew J., Alaska Biological Research, Inc., Fairbanks, Alaska

Magnússon, Rúna Í., Plant Ecology and Nature Conservation Group, Wageningen University & Research, Wageningen, Netherlands

Mankoff, Ken D., Business Integra, New York, New York; NASA Goddard Institute for Space Studies, New York, New York

Manney, Gloria, NorthWest Research Associates, Inc, Socorro, New Mexico; Department of Physics, New Mexico Institute of Mining and Technology, Socorro, New Mexico

Medley, Brooke, Cryospheric Sciences Laboratory, NASA Goddard Space Flight Center, Greenbelt, Maryland

Meier, Walter N., National Snow and Ice Data Center, Cooperative Institute for Research in Environmental Sciences, University of Colorado, Boulder, Colorado

Montesano, Paul M., NASA Goddard Space Flight Center, Greenbelt, Maryland

Moon, Twila A., National Snow and Ice Data Center, Cooperative Institute for Research in Environmental Sciences, University of Colorado, Boulder, Colorado

Mote, Thomas L., Department of Geography, University of Georgia, Athens, Georgia

Mudryk, Lawrence, Climate Research Division, Environment and Climate Change Canada, Toronto, Canada

Müller, Rolf, Forschungszentrum Jülich (IEK-7), Jülich, Germany

Neigh, Christopher S. R., NASA Goddard Space Flight Center, Greenbelt, Maryland

Nyland, Kelsey E., Department of Geography, George Washington University, Washington, DC

Overland, James E., NOAA Pacific Marine Environmental Laboratory, Seattle, Washington

Pálsson, Finnur, Institute of Earth Sciences, University of Iceland, Reykjavík, Iceland

Poinar, Kristin, University at Buffalo, Buffalo, New York

Perovich, Donald K., University of Dartmouth, Hanover, New Hampshire

Petty, Alek, NASA Goddard Space Flight Center, Greenbelt, Maryland

Phoenix, Gareth K., School of Biosciences, University of Sheffield, Sheffield, United Kingdom

Ricker, Robert, NORCE Norwegian Research Centre, Tromsø, Norway

Romanovsky, Vladimir E., Geophysical Institute, University of Alaska Fairbanks, Fairbanks, Alaska; Earth Cryosphere Institute, Tyumen Science Center, Tyumen, Russia

Sass, Louis, Alaska Science Center, U.S. Geological Survey, Anchorage, Alaska

Scheller, Johan H., Department of Ecoscience, Arctic Research Centre Aarhus University, Roskilde, Denmark

Serreze, Mark C., National Snow and Ice Data Center, Cooperative Institute for Research in Environmental Sciences, University of Colorado, Boulder, Colorado

Shiklomanov, Nikolay I., Department of Geography, George Washington University, Washington, DC

Editor and Author Affiliations (continued)

Smith, Benjamin E., Polar Science Center, Applied Physics Laboratory, University of Washington, Seattle, Washington

Smith, Sharon L., Geological Survey of Canada, Natural Resources Canada, Ottawa, Canada

Streletskiy, Dmitry A., Department of Geography, George Washington University, Washington, DC

Svendby, Tove, Norwegian Institute for Air Research (NILU), Kjeller, Norway

Tedesco, Marco, Lamont-Doherty Earth Observatory, Columbia University, Palisades, New York; NASA Goddard Institute of Space Studies, New York, New York

Thoman, Richard L., International Arctic Research Center, University of Alaska Fairbanks, Fairbanks, Alaska

Thomson, Laura, Queen's University, Kingston, Canada

Thorsteinsson, Thorsteinn, Icelandic Meteorological Office, Reykjavík, Iceland

Tian-Kunze, Xiangshan, Alfred Wegener Institute, Helmholtz Centre for Polar and Marine Research, Bremerhaven, Germany

Timmermans, Mary-Louise, Yale University, New Haven, Connecticut

Tømmervik, Hans, Norwegian Institute for Nature Research, Trondheim, Norway; FRAM – High North Research Centre for Climate and the Environment, Tromsø, Norway

Waigl, Christine F., Geophysical Institute, University of Alaska Fairbanks, Fairbanks, Alaska

Walker, Donald (Skip) A., Institute of Arctic Biology, University of Alaska Fairbanks, Fairbanks, Alaska

Walsh, John E., International Arctic Research Center, University of Alaska Fairbanks, Fairbanks, Alaska

Wang, Muyin, NOAA Pacific Marine Environmental Laboratory, Seattle, Washington, Cooperative Institute for Climate, Ocean, and Ecosystem Studies, University of Washington, Seattle, Washington

Webster, Melinda, Polar Science Center, Applied Physics Laboratory, University of Washington, Seattle, Washington

Wehrlé, Adrian, University of Zürich, Zürich, Switzerland

Wolken, Gabriel J., Alaska Division of Geological & Geophysical Surveys, Fairbanks, Alaska; University of Alaska Fairbanks, Fairbanks, Alaska

Wouters, Bert, Department of Geoscience & Remote Sensing, Delft University of Technology, Delft, The Netherlands

Yang, Dedi, Environmental Sciences Division, Oak Ridge National Laboratory, Oak Ridge, Tennessee

Editorial and Production Team

Allen, Jessicca, Graphics Support, Cooperative Institute for Satellite Earth System Studies, North Carolina State University, Asheville, North Carolina

Camper, Amy V., Graphics Support, Innovative Consulting and Management Services, LLC, NOAA/NESDIS National Centers for Environmental Information, Asheville, North Carolina

Haley, Bridgette O., Graphics Support, NOAA/NESDIS National Centers for Environmental Information, Asheville, North Carolina

Hammer, Gregory, Content Team Lead, Communications and Outreach, NOAA/NESDIS National Centers for Environmental Information, Asheville, North Carolina

Love-Brotak, S. Elizabeth, Lead Graphics Production, NOAA/NESDIS National Centers for Environmental Information, Asheville, North Carolina

Ohlmann, Laura, Technical Editor, Innovative Consulting and Management Services, LLC, NOAA/NESDIS National Centers for Environmental Information, Asheville, North Carolina

Noguchi, Lukas, Technical Editor, Innovative Consulting and Management Services, LLC, NOAA/NESDIS National Centers for Environmental Information, Asheville, North Carolina

Riddle, Deborah B., Graphics Support, NOAA/NESDIS National Centers for Environmental Information, Asheville, North Carolina

Veasey, Sara W., Visual Communications Team Lead, Communications and Outreach, NOAA/NESDIS National Centers for Environmental Information, Asheville, North Carolina

5. Table of Contents

Authors and affiliations S280
a. Overview S283
b. Atmosphere S285
1. The arctic troposphere in 2023 ..... S286
2. The arctic stratosphere in 2023 ..... S286
Sidebar 5.1: The February 2023 major sudden stratospheric warming S288
c. Surface air temperature S291
1. Brief summary of impacts and overview S291
2. Annual perspectives S291
3. Seasonal patterns S291
Sidebar 5.2: Summer 2023 weather and climate impacts S293
d. Precipitation S295
1. Introduction S295
2. 2023 Summary S295
3. Regional anomalies S295
4. Historical perspective S296
5. Heavy precipitation events S296
e. Sea-surface temperature S298
f. Sea ice S301
1. Sea-ice extent S301
2. Sea-ice age, thickness, and volume S302
g. Greenland Ice Sheet S304
h. Glaciers and ice caps outside Greenland S307
i. Terrestrial snow cover S311
j. Permafrost S314
1. Permafrost temperatures S314
2. Active layer thickness S316
k. Tundra greenness S318
Appendix 1: Acronyms S321
Appendix 2: Datasets and sources S322
References S326

5. THE ARCTIC

M. L. Druckenmiller, R. L. Thoman, and T. A. Moon, Eds.

a. Overview

—M. L. Druckenmiller, R. L. Thoman, and T. A. Moon

Arctic observations in 2023 provided clear evidence of rapid and pronounced climate and environmental change, shaped by past and ongoing human activities that release greenhouse gases into the atmosphere and push the broader Earth system into uncharted territory. This chapter provides a snapshot of 2023 and summarizes decades-long trends observed across the Arctic, including warming surface air and sea-surface temperatures, decreasing snow cover, diminishing sea ice, thawing permafrost, and continued mass loss from the Greenland Ice Sheet and Arctic glaciers. These changes are driving a transition to a wetter, greener, and less frozen Arctic, with serious implications for Arctic peoples and ecosystems, as well as for low- and midlatitudes.

Average surface air temperatures for 2023 (January–December) for the Arctic as a whole were the fourth highest since 1900, with the Arctic summer (July–September) being the warmest on record. These unprecedented surface temperatures aligned with record-positive geopotential height anomalies in the polar troposphere, which have been increasing alongside warming air temperatures since 1958, indicating the strong connection between long-term atmospheric circulation and regional temperature patterns.

Large-scale atmospheric circulation also strongly influences year-to-year variability and regional differences. For example, in 2023, a colder-than-normal spring across Alaska slowed snowpack and sea-ice melt, while parts of north-central Canada experienced their highest spring average temperatures on record. Short-term atmospheric events can also influence Arctic and midlatitude connections. A major Arctic sudden stratospheric warming (SSW) event in February 2023 is described in Sidebar 5.1—an event that can increase the likelihood of midlatitude cold-air outbreaks for several weeks to months, influencing subseasonal-to-seasonal predictability for midlatitude surface weather.

Warming seasonal air temperatures together with the timing and extent of summer sea-ice loss significantly influence multi-decadal trends and the substantial regional and year-to-year variability seen across both marine and terrestrial systems. Driven by accelerated sea-ice retreat and melt that started in July, the September 2023 sea-ice monthly extent, which is the lowest monthly extent of the year, was 4.37 million square kilometers—about 10% lower than the past two years and overall the fifth lowest in the 45-year satellite record. Additionally, the 17 lowest September sea-ice monthly extents have all occurred in the last 17 years. Spring and early-summer sea-ice loss exposes the dark ocean surface and allows time for solar heating of the ocean. Linked to early sea-ice loss, average sea-surface temperatures for August 2023 were much higher than the 30-year average in the Barents, Kara, Laptev, and Beaufort Seas. Anomalously low August 2023 sea-surface temperatures were observed in Baffin Bay and parts of the Greenland, Bering, and Chukchi Seas. Despite considerable year-to-year variability, almost all Arctic Ocean and marginal seas studied show a statistically significant 1982–2023 warming trend.

On land, the Arctic tundra is greening due to its sensitivity to rapidly increasing summer temperatures, as well as to rapidly evolving sea-ice, snow, and permafrost conditions. In 2023, circumpolar average peak tundra greenness was the third highest in the 24-year Moderate Resolution Imaging Spectroradiometer (MODIS) satellite record, a slight decline from the previous year. Closely aligned with air temperatures and nearshore sea-ice anomalies, peak vegetation greenness in 2023 was much higher than usual in the North American tundra, particularly in

the Beaufort Sea region. In contrast, tundra greenness was relatively low in the Eurasian Arctic, particularly in northeastern Siberia.

Long-term changes in permafrost conditions are also largely controlled by changes in air temperature. Across all Arctic regions, permafrost temperatures and active layer thickness (i.e., thickness of the soil layer above the permafrost that seasonally thaws and freezes) continue to increase on decadal time scales. In 2023, permafrost temperatures were the highest on record at over half of the reporting sites across the Arctic. Permafrost thaw disrupts Arctic communities and infrastructure and can also affect the rate of greenhouse gas release to the atmosphere, potentially accelerating global warming.

Analyses of Arctic precipitation reveal additional connections between a changing atmosphere and land. Precipitation in 2023 was above normal in all seasons for the Arctic as a whole, with short-duration heavy precipitation events breaking existing records at various locations. Arctic precipitation in the past year was also marked by important seasonal and regional variations. Unusually low precipitation and high temperatures produced severe drought and contributed to the record-breaking wildfire season in Canada's Northwest Territory. Snowpack in early spring 2023 was above normal for North America and Eurasia, but then rapid snow loss in much of the Arctic resulted in record-low average snow-water equivalent for the North American Arctic in May and near-record-low snow cover for the Eurasian Arctic in June.

Precipitation patterns also influence the Greenland Ice Sheet. Above-average snowfall over parts of the Greenland Ice Sheet between autumn 2022 and spring 2023 contributed to a relatively low (for the twenty-first century) total mass loss from the Greenland Ice Sheet despite extensive late-June-to-September ice melt. So, while the Greenland Ice Sheet lost mass in the past year, as it has every year since 1998, the loss for September 2022 to August 2023 was much lower than the 22-year average and similar to that of 2020/21. However, the cumulative melt-day area during summer 2023 was the second-highest in the 45-year satellite observational record.

Beyond the Greenland Ice Sheet, the Arctic's other glaciers and ice caps show a continuing trend of significant ice loss, especially in Alaska and Arctic Canada. All of the 25 monitored Arctic glaciers reported in this chapter for the 2022/23 mass balance year show an annual loss of ice, and for many glaciers these data indicate continued rapid wastage with substantial total contributions to global sea level.

The exceptionally warm Arctic summer alongside persistent long-term climate changes contributed to a range of societal and environmental impacts in 2023 (see Sidebars 5.2 and 7.1), providing stark reminders of the varied climate disruptions that Arctic peoples and broader societies increasingly face. For example, Canada experienced its worst national wildfire season on record. Multiple communities in the Northwest Territories were evacuated during August, including more than 20,000 people from the capital city of Yellowknife. In August 2023 near Juneau, Alaska, a glacial lake on a tributary of the Mendenhall Glacier burst through its ice dam and caused unprecedented flooding and severe property damage on Mendenhall River, a direct result of dramatic glacial thinning over the past 20 years. With increasing seasonal shifts and widespread disturbances influencing the flora, fauna, ecosystems, and peoples of the Arctic, the need for ongoing observation and collaborative research and adaptation has never been higher.

Special Note: This chapter includes a focus on glaciers and ice caps outside of Greenland (section 5h), which alternates yearly with a section on Arctic river discharge, as the scales of regular observation for both of these climate components are better suited for reporting every two years.

b. Atmosphere

—A. H. Butler, S. H. Lee, G. H. Bernhard, V. E. Fioletov, J.-U. Grooß, I. Ialongo, B. Johnsen, K. Lakkala, R. Müller, T. Svendby, and T. J. Ballinger

The Arctic is warming rapidly, not only at the surface but vertically throughout the troposphere (Cohen et al. 2020). Against the background of long-term warming, the atmospheric circulation contributes to the large year-to-year variability in regional temperature and precipitation patterns across the Arctic. The chemical composition in the Arctic stratosphere, which overlies the troposphere, may also have important climate effects (Polvani et al. 2020; Friedel et al. 2022). The Arctic atmosphere in 2023 was marked by a major sudden stratospheric warming (SSW) in February (Sidebar 5.1) and a persistent anticyclonic high-pressure system during summer that corresponded to record surface temperatures over the Arctic (section 5c), higher-than-normal melt days in Greenland (section 5g), and enhanced wildfire activity in the Northwest Territories (see Sidebar 7.1 for details).

One measure of large-scale atmospheric circulation is geopotential height, which is the altitude of a given atmospheric pressure (Fig. 5.1). The geopotential height tends to be higher where the atmosphere is warmer and lower where it is colder. In general, when the polar cap (60°N–90°N) averaged geopotential heights (PCHs) are anomalously positive, the stratospheric polar winds are weaker than normal, and the tropospheric jet stream is shifted equatorward (and vice versa when the PCHs are anomalously negative). Therefore, the PCHs encapsulate both the thermodynamic and dynamic variability of the high-latitude atmosphere and indicate when the polar atmosphere is vertically coupled (i.e., have the same-signed anomalies from the surface to the upper stratosphere). In 2023 (Fig. 5.1), a major SSW is evident as positive anomalies that first appeared in the stratosphere in February and descended to the troposphere (Sidebar 5.1). The other notable feature is a period of

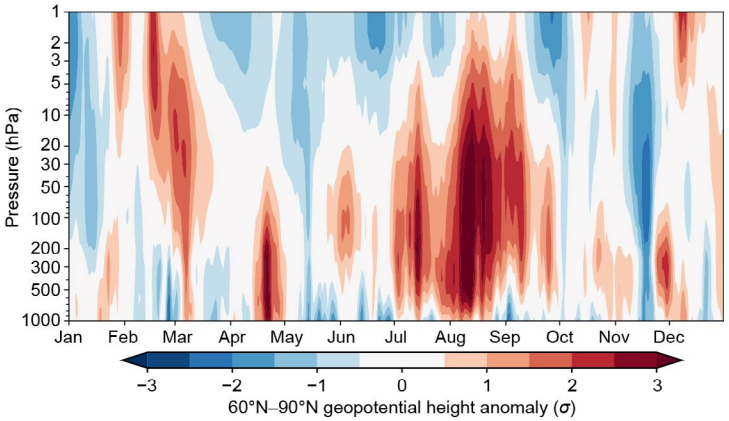

Fig. 5.1. Vertical profile of daily Arctic polar cap (60°N–90°N) standardized geopotential height anomalies (hPa) during 2023. Anomalies are shown with respect to a 30-day centered running-mean 1991–2020 climatology and standardized at each pressure level by the standard deviation of each calendar day during 1991–2020 (smoothed with a 30-day running mean). Data are from once-daily 0000 UTC ERA5 reanalysis (Hersbach et al. 2020).

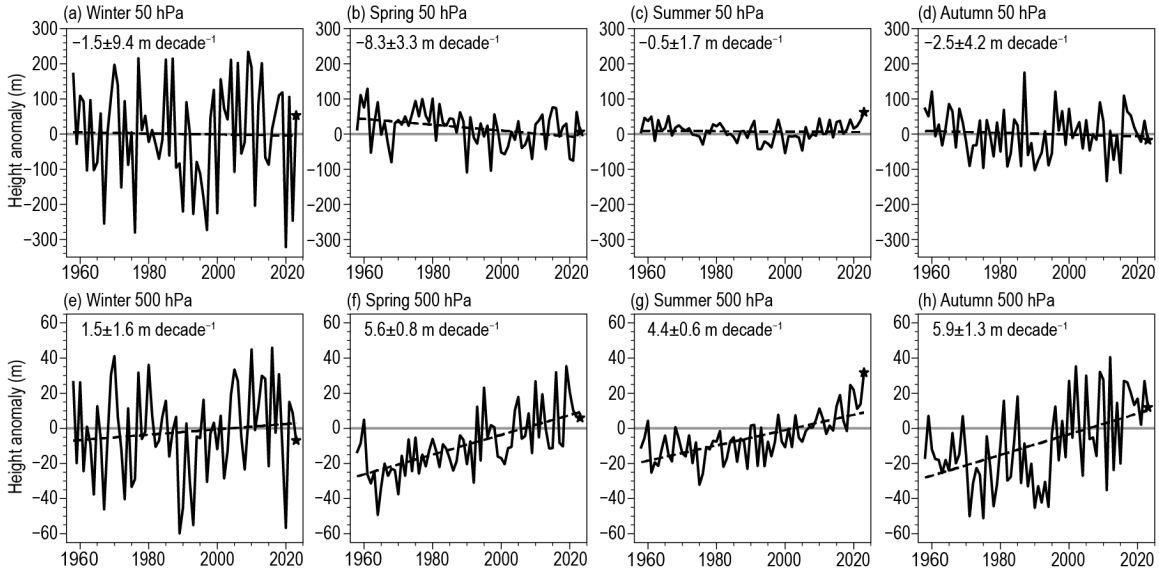

Fig. 5.2. Time series over the 1958–2023 period of polar-cap averaged height anomalies (m) at (a)–(d) 50 hPa and (e)–(h) 500 hPa for the four seasons: (a),(e) winter (JFM), (b),(f) spring (AMJ), (c),(g) summer (JAS), and (d),(h) autumn (OND). The dashed line is the linear least-squares fit, where the trend value ± the standard error of the trend (m decade^{-1}) is shown in the upper left. Geopotential height anomaly data are from monthly-mean ERA5 reanalysis; anomalies are calculated relative to the 1991–2020 climatology. The 2023 values are marked by a star.

persistent, record-high PCH from July to September that extended vertically from the surface to the mid-stratosphere.

Figure 5.2 illustrates the large year-to-year variability of the Arctic atmospheric circulation, particularly in winter, and places 2023 in the context of the historical record. The 2023 PCH anomalies in the troposphere (500 hPa) and stratosphere (50 hPa) were generally close to 1991–2020 climatological values in winter (January–March), spring (April–June), and autumn (October–December); however, record positive PCH anomalies in both the troposphere and stratosphere were observed in summer (July–September). In the troposphere, the record-high summer value is consistent with a significant linear trend in summer towards increasing tropospheric heights and thus warming air temperatures since 1958 (also evident in spring and autumn). In the stratosphere, linear trends since 1958 are negative in all seasons but generally not significant, except in spring (indicative of cooling stratospheric temperatures).

1. THE ARCTIC TROPOSPHERE IN 2023

Figure 5.3 shows the seasonally averaged 500-hPa geopotential height and wind anomalies across the Arctic in 2023. Winter (Fig. 5.3a) was marked by anomalously positive heights near the North Pacific and central Arctic and anomalously negative heights across northeastern Eurasia and North America. This pattern was associated both with La Niña teleconnections and the downward coupling of the stratospheric anomalies following the SSW (Fig. 5.1).

Spring (Fig. 5.3b) was characterized by negative height anomalies over the central Arctic and Alaska, associated with anomalous cold, and positive height anomalies over Canada and Scandinavia, associated with anomalous warmth. However, the seasonal average does not reflect strong monthly variations that occurred. In particular, PCH anomalies at 500 hPa were at their second most positive value since 1958 for April but were moderately negative in May (Fig. 5.1).

Summer (Fig. 5.3c) exhibited strongly anomalous positive heights (anticyclonic wind flow) across a broad region of the Arctic. This is consistent with the observed record-high surface temperatures (section 5c). The persistence and vertical extent (Fig. 5.1) of positive height anomalies likely contributed to higher-than-normal melt days in Greenland (section 5g) and enhanced wildfire activity in the Northwest Territories (see Sidebar 7.1).

A notable feature of autumn (Fig. 5.3d) was the presence of strongly negative height anomalies over the Scandinavian region, linked to cold anomalies there. Height anomalies were otherwise broadly positive, particularly over Canada, where the associated strong anticyclonic wind anomalies likely contributed (via advection) to above-normal temperatures over the Canadian Arctic Archipelago (section 5c).

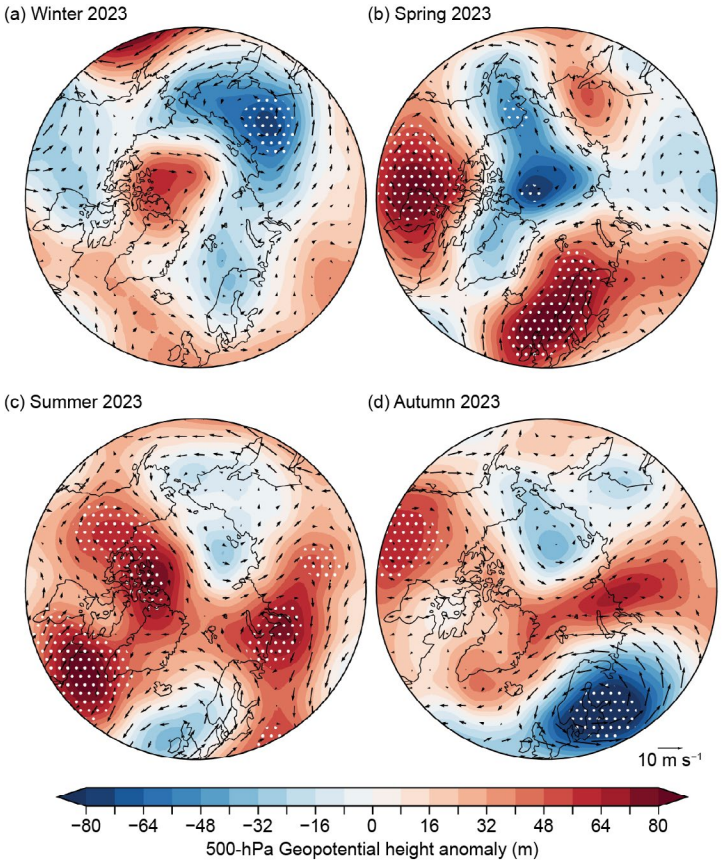

Fig. 5.3. 500-hPa geopotential height (m; shading) and 200-hPa wind (m s^{-1}; vectors) anomalies for (a) winter, (b) spring, (c) summer, and (d) autumn. Anomalies are calculated relative to the 1991–2020 climatology. Stippling indicates that the anomaly exceeds ±2 std. dev. of the 1991–2020 mean. The dashed circle indicates the 60°N latitude, and the area within denotes the polar-cap region. (Source: ERA5 reanalysis.)

2. THE ARCTIC STRATOSPHERE IN 2023

In January 2023, the Arctic stratospheric polar vortex was anomalously strong and cold, leading to strong chlorine activation and initiating chemical ozone loss. This was interrupted, however,

by a major SSW on 16 February (Sidebar 5.1), which resulted in higher-than-average polar total ozone column (TOC) in March. The stratospheric winds at 10 hPa and 60°N weakly returned to westerlies after the SSW and had a slightly later-than-average spring transition to easterly summer conditions. After the westerly winds returned in autumn, their strength stayed near climatological values until November when they strengthened for a couple of weeks (Fig. 5.1), setting near-records for daily zonal-mean wind speeds at 10 hPa and 60°N.

March has historically been the month with the largest potential for chemical ozone depletion in the Arctic (WMO 2022). In March 2023, the minimum Arctic daily TOC was 3.5% (13 Dobson units; DU) above the average since the start of satellite observations in 1979 (Fig. 5.4a). While the recovery of Arctic TOC to pre-1979 levels is expected due to the phase-out of ozone-depleting substances by the Montreal Protocol, it is difficult to detect due to large year-to-year variability (WMO 2022). Spatially, Arctic TOC anomalies varied between −8% and +24% but stayed within 2 std. dev. of past observations from the Ozone Monitoring Instrument (OMI; 2005–22), with the exception of a small area in northern Scandinavia and the adjacent Barents Sea (Fig. 5.4b). This enhancement of TOC was related to the February 2023 SSW, which transported ozone into the polar stratosphere and raised stratospheric temperatures enough to halt chemical processing and ozone loss.

Anomalies in monthly averages of the noontime ultraviolet (UV) Index (a measure of the intensity of solar ultraviolet radiation in terms of causing erythema [sunburn] in human skin) for March 2023 varied spatially between −55% and +67% and generally did not exceed 2 std. dev. of past OMI (2005–22) observations (Fig. 5.4c). Areas with high UV index values roughly match areas with low TOCs and vice versa, but UV index anomalies have larger spatial variability because of their added dependence on clouds (Bernhard et al. 2023). Anomalies calculated from satellite data (OMI instrument) and ground-based measurements generally agree well (Fig. 5.4c). Differences in excess of 5% can be explained by coastal (Andøya: OMI anomaly −6%; ground-based anomaly 0%) or urban (Trondheim: OMI anomaly −6%; ground-based anomaly +2%) effects.

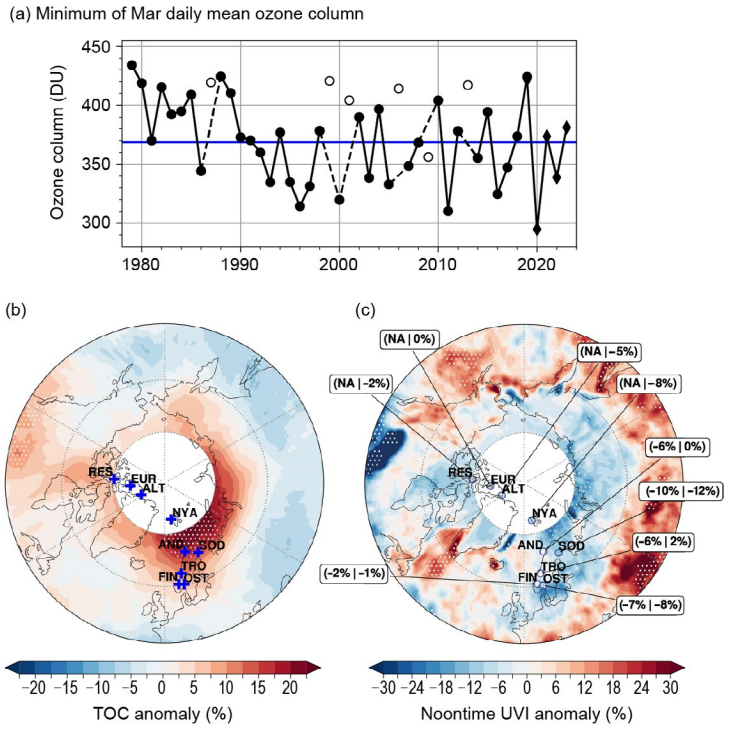

Fig. 5.4. (a) Time series of the minimum daily-mean total ozone column (TOC; Dobson units, DU) for March poleward of 63°N equivalent latitude, which represents the area enclosed by the stratospheric polar vortex (Butchart and Remsberg 1986) and is determined using ERA5 reanalysis data (adapted from Müller et al. [2008] and WMO [2022]). The blue line indicates the average TOC for 1979–2023. Open circles represent years in which the polar vortex was not well-defined in March. Ozone data for 1979–2019 are based on the combined NIWA-BS total column ozone database version 3.5.1 (Bodeker and Kremser 2021). Ozone data for 2020–23 are from the Ozone Monitoring Instrument (OMI). Monthly mean anomaly maps of (b) total ozone column (%) and (c) noontime ultraviolet index (UVI; %) for Mar 2023 relative to 2005–22 means, based on the OMTO$_3$ Version 3 total ozone product (Bhartia and Wellemeyer 2002), which is derived from OMI measurements. (c) compares UVI anomalies from OMI (first value in parenthesis) with ground-based measurements at nine locations (second value presented). Site acronyms of ground stations are ALT: Alert; EUR: Eureka; NYA: Ny-Ålesund; RES: Resolute; AND: Andøya; SOD: Sodankylä; TRO: Trondheim; FIN: Finse; and OST: Østerås. White areas centered at the North Pole indicate latitudes where OMI data are not available because of polar darkness. Stippling in (b) and (c) indicates pixels where anomalies exceed ±2 std. dev. of the 2005–22 OMI measurement climatology.

Sidebar 5.1: The February 2023 major sudden stratospheric warming

S. H. LEE, G. MANNEY, AND A. H. BUTLER

A major sudden stratospheric warming (SSW) occurred in the Arctic on 16 February 2023. Major SSWs, which occur in the Arctic on average six times per decade, are characterized by a rapid warming of the Arctic stratosphere by as much as 50°C in less than a week and a breakdown and reversal of the mean westerly circulation of the stratospheric polar vortex. Sudden stratospheric warming events induce long-lasting impacts on stratospheric chemical composition (notably ozone; section 5b) and can increase the likelihood of midlatitude cold-air outbreaks for several weeks to two months afterward, acting as a source of subseasonal-to-seasonal predictability for midlatitude surface weather (Domeisen et al. 2020).

CAUSE AND EVOLUTION OF THE EVENT

The SSW in February 2023 was the fourth major SSW in six consecutive winters, part of a recent clustering of events following no major SSWs during the preceding four winters from 2013/14 to 2016/17. The major 2023 SSW was preceded by a minor warming during the last few days of January that was driven by a pulse of enhanced upward-propagating planetary wave activity (Fig. SB5.1a, shading) that weakened the zonal-mean zonal winds in the mid-stratosphere to ~10 m s^{-1} (Fig. SB5.1a, contours). Around 14 February, another pulse of anomalous wave activity confined mostly within the stratosphere fully disrupted the vortex, and the winds at 10 hPa and 60°N reversed from westerly to easterly on 16 February, marking the date of the major SSW. During an SSW, the polar vortex either splits into two or more smaller vortices or is displaced away from the Arctic. The February 2023 SSW fell into the latter category, with the vortex in the stratosphere displaced toward Eurasia.

Because the SSW was not preceded by sustained anomalous tropospheric wave activity, the circulation anomalies prior to the event (Fig. SB5.1b) do not strongly resemble precursors of many SSWs. Nonetheless, pressure near the Aleutian Islands was slightly lower than normal during this time, while an anomalous anticyclone extended across parts of northwest Europe. Both of these features have been shown to contribute to SSWs by constructively interfering with the mean stationary wave pattern in the troposphere (Martius et al. 2009; Garfinkel et al. 2010).

At 10 hPa, the winds then returned to westerly during 22–23 February, reversed back to easterly on 24 February, became westerly again on 26 February, and then easterly once again through 10 March. Although several zonal wind reversals occurred, these all formed part of a single SSW event. Such fluctuations occasionally occur during SSWs, but are not typical. The multiple zonal wind reversals resulted from continued wave activity (Fig. SB5.1a) that eventually destroyed the vortex in the lower to mid-stratosphere sufficiently (Karpechko et al. 2017) for likely downward impacts on the troposphere in early March.

INFLUENCE ON WEATHER PATTERNS AND THEIR PREDICTABILITY

Following the February 2023 SSW, there was no immediate coupling between the stratosphere and the troposphere; in fact, for the first two weeks after the SSW, geopotential heights over the Arctic in the troposphere (below ~6 km) were anomalously low, in direct contrast to those in the stratosphere. However, during the first half of March, a brief period of stratosphere–troposphere coupling occurred, characterized by a negative North Atlantic Oscillation pattern at the surface (Fig. SB5.1c) as is typical following SSWs. The coupling occurred around 28 February together with the downward propagation of the weakened vortex into the lower stratosphere. This is consistent with the role of lower-stratospheric circulation anomalies in modulating the surface response to SSWs (e.g., Afargan-Gerstman et al. 2022). During this period of stratosphere–troposphere coupling, anomalously high surface temperatures were present around the Labrador Sea and Baffin Bay, with marginally below-normal temperatures across northwest Europe and northern Eurasia. This pattern of temperature anomalies is consistent with the average surface response to SSWs, albeit weaker and more transient. Unusually low temperatures also occurred after the SSW in western North America; however, this is more likely related to North Pacific ridging arising from the then-ongoing La Niña conditions, rather than the SSW itself. The lack of prolonged downward coupling, combined with onset of spring, meant that surface impacts from the February 2023 SSW were relatively minimal.

TRANSPORT OF WATER VAPOR FROM 2022 HUNGA-TONGA HA'APAI ERUPTION

The January 2022 eruption of the underwater Hunga Tonga–Hunga Ha'apai (HTHH) volcano increased the mass of water vapor in the stratosphere by about 10% (e.g., Millán et al. 2022). Water vapor injected in the southern tropics spread across the globe, with high anomalies extending above 60-km altitude in the tropics and midlatitudes and concentrated in the middle stratosphere (around 25 km–35 km) in the polar regions (see section 2g7 for details). The influence on radiative forcing of surface climate from the HTHH stratospheric water vapor increase is uncertain (including whether it produced net heating or cooling), but the impact is minor compared to that of climate change (e.g., Schoeberl et al. 2023).

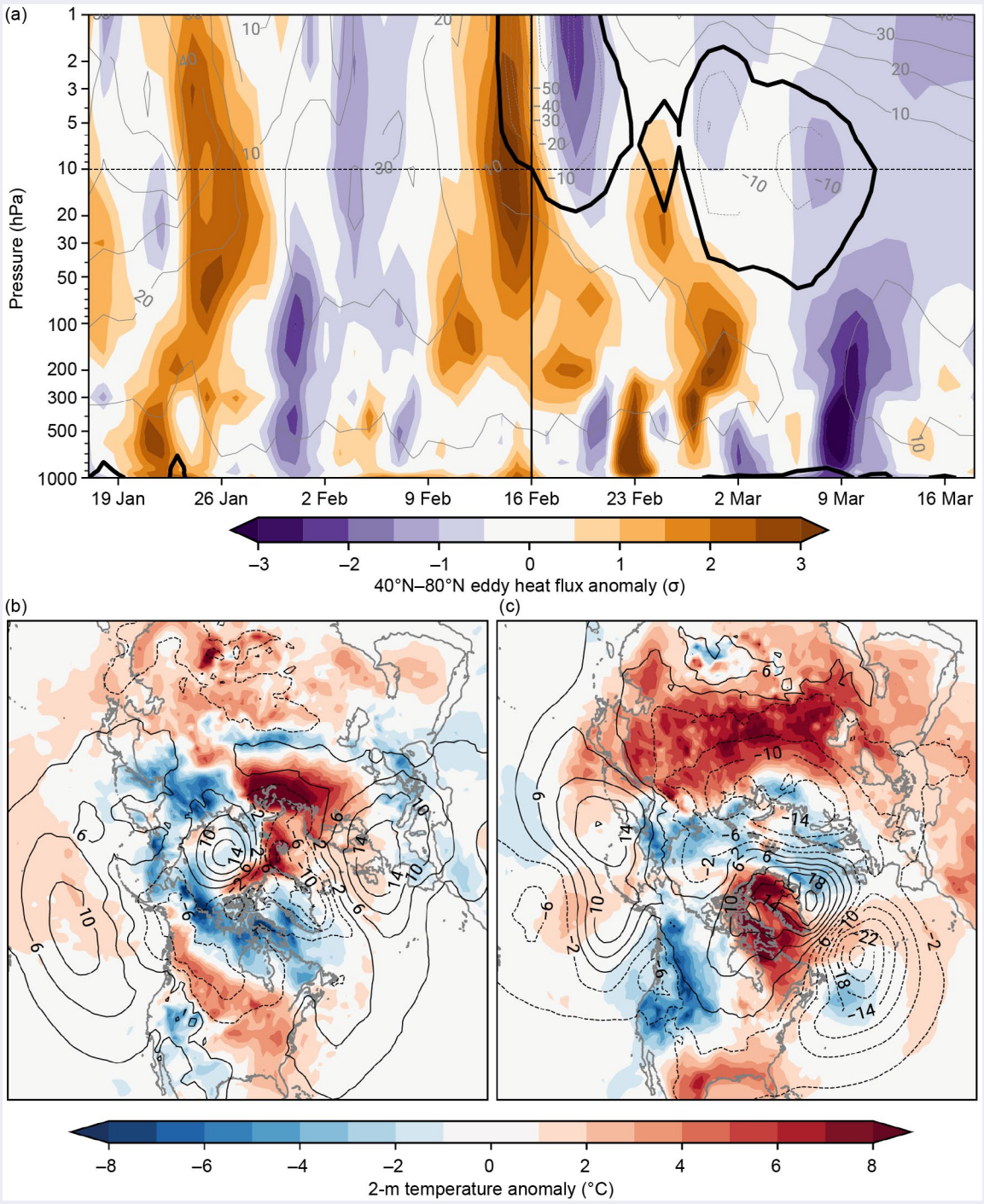

Fig. SB5.1. (a) Vertical profile of daily 40°N–80°N eddy heat flux anomalies (std. dev.; shading) and 60°N zonal-mean zonal winds (m s^{-1}; gray contours, with the zero-wind line in black) for 30 days before to 30 days after the 16 February 2023 sudden stratospheric warming (SSW). (b) Average 2-m temperature anomalies (°C, shading) and mean sea-level pressure anomalies (hPa, contours) for the 15 days prior to the SSW (1–15 February) and (c) during a period of stratosphere–troposphere coupling following the SSW (1–15 March). Data are from the ERA5 reanalysis (Hersbach et al. 2023a,b) and all anomalies are shown with respect to a 30-day centered smoothed 1991–2020 climatology.

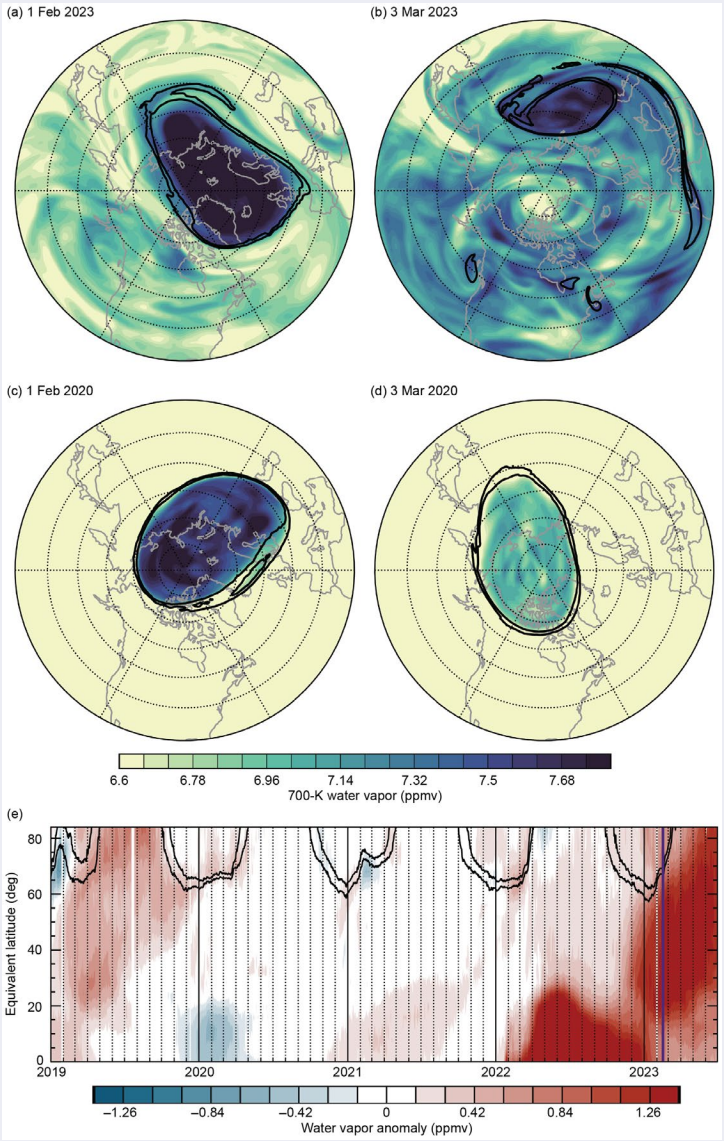

High water vapor concentrations from the HTHH eruption reached the Arctic stratospheric polar vortex edge in early January 2023. By that time, the vortex was well-developed, and the excess water vapor was largely blocked from crossing its edge (Fig. SB5.2e). Water vapor concentrations are typically high inside the vortex and low outside the vortex (Figs. SB5.2c,d show 2020, a year with a strong vortex). Prior to the SSW (Fig. SB5.2a), exceptionally high water vapor concentrations outside the vortex were well separated across the vortex edge from even higher water vapor concentrations inside (but the high water vapor concentrations inside the vortex were not as anomalous; Fig. SB5.2e).

The vortex rapidly broke down in the mid-stratosphere after the SSW, allowing mixing of the record-high midlatitude water vapor concentrations with the high concentrations inside the vortex by early March (Fig. SB5.2b). Compared to other winters with SSWs, the water vapor anomalies following the HTHH eruption resulted in increased water vapor near the polar vortex, whereas SSWs typically result in water vapor reductions near the vortex (e.g., low anomalies in Fig. SB5.2e in January/February 2019 and February 2021). Changes in radiative heating from these different water vapor distributions can affect polar vortex dynamics as well as heating or cooling at lower altitudes.

Fig. SB5.2. (a)–(d) Maps of water vapor concentration (mixing ratio in parts per million by volume [ppmv]) in the Northern Hemisphere mid-stratosphere near 27-km altitude (approx. 18 hPa) on the same two days of year in (a),(b) 2023 and (c),(d) 2020, from a gridded product based on Aura Microwave Limb Sounder (MLS) data (Global Modeling and Assimilation Office 2022; Wargan et al. 2023). (e) Time series of anomalies (departure from the daily mean for 2005–21) of MLS water vapor at the same altitude as the maps (Lambert et al. 2021). The purple vertical line is the initial date of the sudden stratospheric warming. In all panels, the black overlaid lines demarcate the stratospheric polar vortex edge, based on MERRA2 reanalysis (Global Modeling and Assimilation Office 2015).

c. Surface air temperature

—T. J. Ballinger, S. Bigalke, B. Brettschneider, R. L. Thoman, M. C. Serreze, A. H. Butler, U. S. Bhatt, E. Hanna, I. Hanssen-Bauer, S.-J. Kim, J. E. Overland, J. E. Walsh, and M. Wang

1. BRIEF SUMMARY OF IMPACTS AND OVERVIEW

Near-surface (i.e., two-meter) air and upper-ocean temperatures (section 5e) are increasing in today's Arctic. The air temperature warming rate in the Arctic continues to exceed the global mean rate, a phenomenon known as Arctic Amplification (e.g., Serreze and Barry 2011). Warming is leading to changes in the northern high-latitude hydrologic cycle, including increased seasonal precipitation (section 5d), as well as declines in terrestrial snow cover, Greenland Ice Sheet and glacier mass, permafrost stability, and sea-ice extent and thickness (Box et al. 2021; sections 5f, 5g, 5h, 5i). Rising Arctic air temperatures are aligned with more frequent temperature extremes that impact life and property within and beyond the Arctic (Moon et al. 2019; Walsh et al. 2020). Record Arctic warmth in summer 2023 was punctuated by widespread, high temperatures in the Northwest Territories, Canada. These high temperatures contributed to the region's amplified wildfire activity that devastated local communities and ecosystems and contributed to poor down-wind air quality that engulfed much of eastern North America (see Sidebar 7.1 for details). In this section, we provide historical context to 2023 Arctic (60°N–90°N) air temperatures followed by a seasonal overview of notable 2023 air temperature patterns.

2. ANNUAL PERSPECTIVES

Figure 5.5 shows the annual (January–December mean), long-term Arctic and global (90°S–90°N) surface air temperature anomalies from NASA's GISTEMP version 4 data product. The 2023 Arctic annual anomaly just exceeded +1°C and ranked as the fourth-warmest year since 1900. Moreover, all seasons in the Arctic during 2023 experienced >90th percentile warmth, highlighted by the warmest summer and second-warmest autumn since the onset of the twentieth century. While 2023 has emerged as the warmest year on record globally, Arctic temperature anomalies were comparatively higher. This Arctic Amplification signal remains persistent as 2023 marks the 14th consecutive year, and 18th out of the last 20, where the Arctic-averaged temperature exceeded the 1991–2020 mean. The six warmest years in the Arctic have all occurred since 2016, while the 16 warmest years have taken place from 2005 onward.

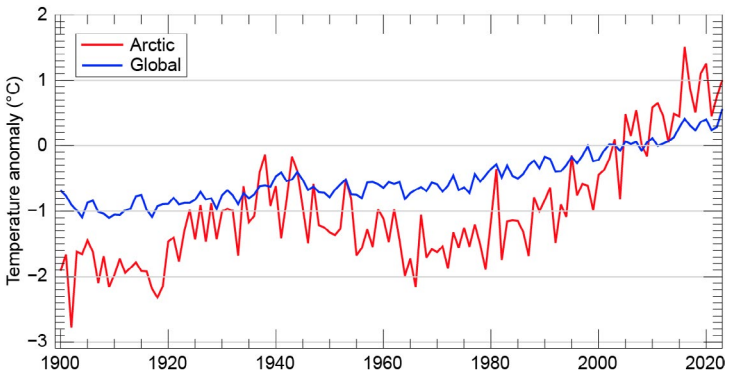

Fig. 5.5. Arctic (60°N–90°N, red) and global (90°S–90°N, blue) surface air temperature anomalies (°C) averaged across land and ocean areas. Temperature anomalies are shown relative to their 1991–2020 means. (Source: NASA GISTEMP v4 data are obtained from the NASA Goddard Institute for Space Studies.)

Complex and often interrelated processes and feedbacks underlie amplified Arctic warming. Less extensive and thinner sea ice (section 5f) tends to melt out earlier in the year. Longer open-water duration results in prolonged transfer of atmospheric energy into the Arctic Ocean. As a result, upper-ocean cooling and sea-ice production are delayed while accumulated upper-ocean heat is released back to the overlying atmosphere, warming the surface air temperatures in autumn and early winter. This process is a key contributor to Arctic Amplification (Serreze and Barry 2011). Marginal sea environments are rapidly changing, most notably in the Chukchi and Beaufort Seas (Ballinger et al. 2023) and Barents Sea (Isaksen et al. 2022) and are also influencing overlying air temperatures. These and other examples are further touched upon in a seasonal context within the following section.

3. SEASONAL PATTERNS

Figure 5.6 shows seasonal surface air temperature anomalies for 2023, with seasons defined as: winter (January–March), spring (April–June), summer (July–September), and autumn (October–December).

The highest positive temperature anomalies in winter 2023 were observed over parts of the Barents Sea and northwestern Eurasia (~+5°C; Fig. 5.6a). Other notable positive anomalies were found over the Lincoln Sea and just north of the Canadian Arctic Archipelago and Greenland. This contrasts with much of central and eastern Siberia, Hudson Bay, the southern Canadian Arctic Archipelago, and the Greenland Sea, where negative anomalies prevailed. Negative sea-level pressure (SLP) anomalies across much of the Arctic landscape and over the Barents Sea (Fig. 5.7a) suggest that an active high-latitude winter storm track supported the observed mild temperatures, broadly consistent with above-average winter precipitation over the Arctic as a whole (section 5d).

Spring 2023 exhibited notable warmth over the Northwest Territories and Nunavut (~+5°C anomalies; Fig. 5.6b) associated with reduced snow cover and a shorter snow-cover duration (section 5i). The area stretching from the Labrador Sea southeast of Greenland to the Barents Sea was also characterized by above-average temperatures. In contrast, below-average air temperatures (~–2°C to –3°C) were found across Alaska, the northern Bering Sea, the southern Chukchi Sea, and Chukotka. Arctic Ocean air temperatures appeared near or slightly below average, associated with a negative SLP anomaly across the central Arctic Ocean (Fig. 5.7b).

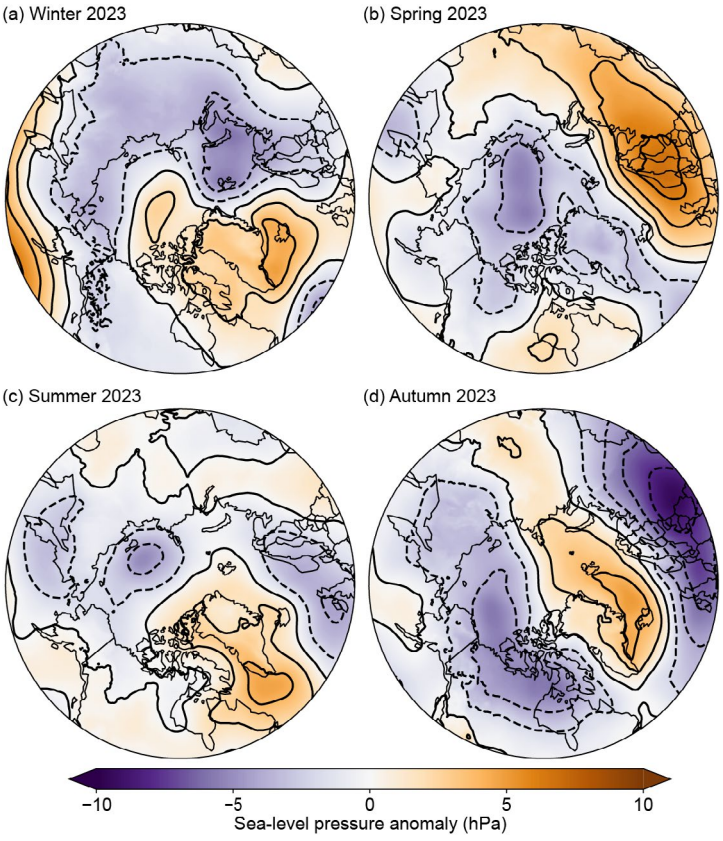

Fig. 5.7. Seasonal sea-level pressure (SLP) anomalies (hPa) during 2023 for (a) winter, (b) spring, (c) summer, and (d) autumn. SLP anomalies are shown relative to their 1991–2020 means. (Source: ERA5 reanalysis SLP data are obtained from the Copernicus Climate Change Service.)

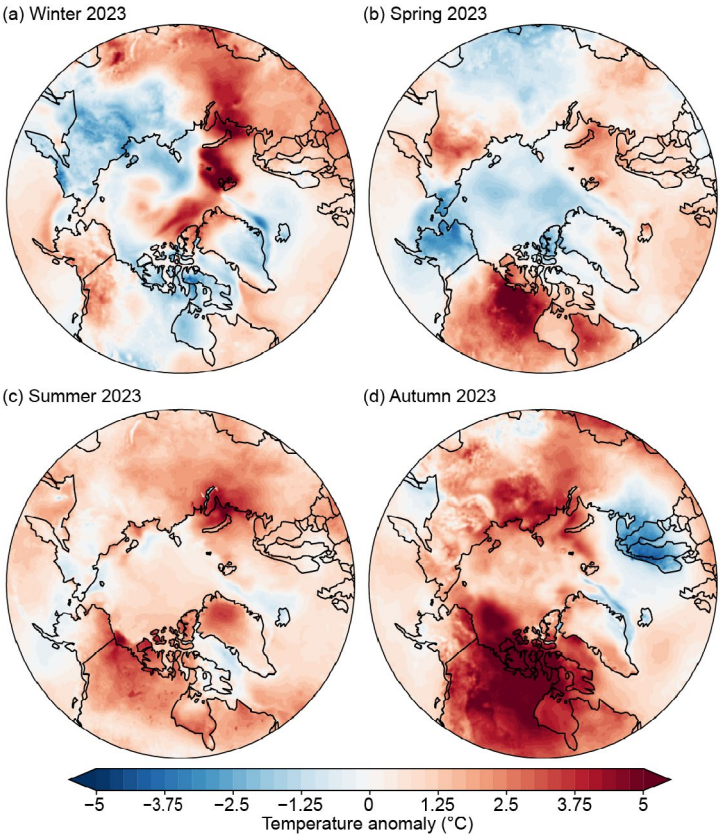

Fig. 5.6. Seasonal surface air temperature anomalies (°C) during 2023 for (a) winter, (b) spring, (c) summer, and (d) autumn. Temperature anomalies are shown relative to their 1991–2020 means. (Source: ERA5 reanalysis air temperature data are obtained from the Copernicus Climate Change Service.)

Summer 2023 was the warmest on record since at least 1900. This record-warm summer was characterized by anomalously high air temperatures over most of northern Canada and the southern reaches of the Barents and Kara Seas (Fig. 5.6c). The anomalous warmth in the Northwest Territories, Nunavut, and the Canadian Arctic Archipelago coincided with dry conditions over these areas (section 5d), supporting extreme wildfire activity (see Sidebar 5.2 for summer 2023 weather and climate impacts and Sidebar 7.1). Positive anomalies over Greenland were associated with an anomalously high number of surface melt days and extent (section 5g).

Above-normal air temperatures were also associated with negative SLP anomaly patterns over much of northern Europe, the Laptev Sea, the western Bering Sea, Kamchatka, and the Sea of Okhotsk (Fig. 5.7c).

Autumn 2023 exhibited a large magnitude and extensive pattern of unusual warmth (Fig. 5.6d), reflecting the second-warmest autumn in the available record. Surface air temperatures approaching 5°C above the 1991–2020 mean characterized most of Arctic Canada to the west and north of Hudson Bay. The Beaufort Sea and adjacent North Slope of Alaska and northwest Siberian lands extending south of the Kara Sea and Laptev Sea coastlines were also much warmer than normal. Meanwhile, isolated cold anomalies appeared confined to Scandinavia. The Canadian Arctic, northern Alaska, and Beaufort Sea warm anomalies were associated with lower-than-normal SLP (Fig. 5.7d). Such below-normal air pressure extended through the troposphere (section 5b), suggesting that a more active storm track may be responsible for sustaining the warm pattern.

Sidebar 5.2: Summer 2023 weather and climate impacts

R. L. THOMAN, M. BRUBAKER, M. HEATTA, AND J. JEURING

Summer 2023 (July–September) in the Arctic (land and sea poleward of 60°N) was the warmest on record, with nearly 90% of the Arctic having an average temperature above the 1991–2020 mean (based on ERA5 reanalysis data; section 5c). This sidebar summarizes some representative examples of societal and environmental impacts during the record warm 2023 Arctic summer (see Fig. SB5.3) that are consistent with expectations of environmental extremes in a rapidly warming Arctic. Some of these impacts were directly related to the record-high temperatures.

Wildfires in Arctic Canada burned the most area since comprehensive records began in 1980 (Thoman et. al. 2023; see Sidebar 7.1 for details). At some time during the summer, more than two-thirds of the Northwest Territories' 46,000 residents were displaced from their homes, in many cases for weeks at a time, with significant economic impacts from lost income, disrupted traditional activities, and infrastructure lost to the fires (Thompson 2023). The community of Enterprise, Northwest Territory, was largely destroyed by a fast-moving fire during 13–14 August 2023 (CBC News 2023). Smoke from these wildfires, and wildfires farther south, contributed to haze and reduced air quality from Alaska to Iceland. Poor air quality was also reported during August in portions of Siberia from wildfires in the region (Reuters 2023).

Drought conditions in August and September were observed over much of the Canadian Northwest Territories, including extreme drought in the area near and south of Great Slave Lake. Moderate to severe drought also covered parts of the Yukon Territory but did not extend westward into Alaska (North American Drought Monitor 2024). This dryness was a contributor to both the record coverage of wildfires in the region and the longevity of the fire season, with some fires

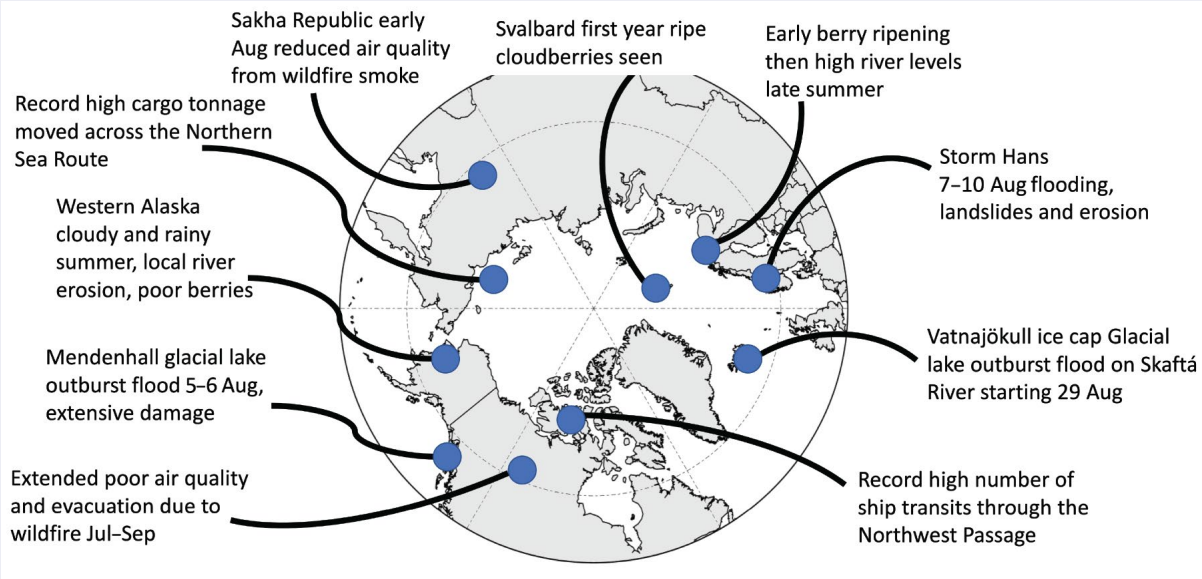

Fig. SB5.3. Impact headlines from around the Arctic during the record-warm 2023 Arctic summer.

actively burning into September, long past the typical end of the Arctic wildfire season (see Sidebar 7.1).

Two significant glacier outburst floods occurred in summer 2023. In Iceland, the Skaftá River (east of Reykjavik) flooded in late August. Flooding on this river occurs every year or two due to geothermal heating under the Vatnajökull ice cap. The 2023 flood was typical for most recent years and did not impact major roadways (Icelandic Met Office 2023). In dramatic contrast, flooding from a catastrophic glacial lake outburst flood occurred on the Mendenhall River near Juneau, Alaska, during 5–6 August. Glacial dam outbursts did not occur here prior to 2011, but thinning of side branches of the Mendenhall Glacier has resulted in annual releases of lake water since then. The 2023 outburst flood event was by far the most destructive on record for the Mendenhall Glacier due to unprecedented high-water levels and extreme erosion rates, which in some places exceeded 50 meters of riverbank lost within 36 hours. At least one home was swept into the river due to this erosion, and many homes and businesses suffered severe flooding, including structures that had no previous history of flooding (Juneau Empire 2023).

In the Nordic Arctic, Sámi observers reported a mild and dry early summer with low river levels and early berry ripening, followed by wet conditions later in the summer, which in some cases caused problems for reindeer herds due to high river levels. An early arrival of spring led to increased snow melt in the mountains and deprived reindeer of their refuge amongst the snow patches in higher elevations, where they typically seek relief from heat and insects (Skarin et al. 2004). The early summer's dryness and heat delayed the green-up process at a time when nutritious vegetation is crucial to provide for the high energy demand of small reindeer calves and lactating females. Overall, a poorer physical condition of reindeer due to insufficient access to food diminishes their preparedness for the coming winter season (Arctic Climate Forum 2023). Much farther north, at the Svalbard Airport (78.2°N), the mean July temperature exceeded 10°C for the first time on record (Sciencenorway 2024). Also for the first time, ripe cloudberries (sp. *Rubus chamaemorus*), usually a lower-latitude fruit, were seen in the Svalbard archipelago (Barents Observer 2023).

Portions of southern Norway and Sweden had extreme rainfall as Storm Hans passed through the region during 7–10 August (section 5d), producing severe flooding, erosion, and landslides. An estimated 4000 people were evacuated across parts of southern Norway as a result of the flooding, including 2000 residents from Hønefoss when the Storelva River flooded the town center. A railway bridge in Ringebu collapsed into the Lagen River on 14 August, and the Braskereidfoss hydro-electric power plant on the Glama River partially collapsed on 9 August. Many major roads were closed and rail services were disrupted during the days following the storm. In Hudiksvall, Sweden, on 7 August, a train partially derailed after heavy rains eroded an embankment, requiring clean-up and repairs into September (Guardian 2023; DW 2023).

With a record-warm summer, both the Northern Sea Route and Northwest Passage became accessible to non-ice-hardened marine traffic. The Northern Sea Route, connecting the European Arctic to the Pacific Ocean via the north coast of Russia and Bering Strait, saw 75 ship transits in the 2023 open season. This is the second-highest number of ships, but the 2.1 million tons of transported cargo (including crude oil) was the highest on record (High North News 2023). The Northwest Passage, connecting the Atlantic to the Pacific via northern Canada and Alaska waters, saw a record number of ship passages. A total of 42 ships made the complete Northwest Passage transit, including 13 cargo ships. The previous high was 33 ships in 2017 (McCague 2023).

Portions of western Alaska were among the few Arctic areas that were not warmer than normal in summer 2023, due in part to unusually persistent cloudy and rainy weather. At Nome, Alaska, measurable rain (≥0.3mm) fell on 62 days during summer, the highest number of days in more than 110 years of observation. This rain exacerbated Noatak River bank erosion near Noatak, Alaska, which has now accelerated for several years due to permafrost thaw and high-water events (LEO Network 2023).

d. Precipitation

—M. C. Serreze, S. Bigalke, R. Lader, T. J. Ballinger, and J. E. Walsh

1. INTRODUCTION

Climate models project increased Arctic precipitation and more frequent heavy precipitation events as the climate warms (see Walsh et al. [2023] and references therein). The latter includes more rain-on-snow events, which will in turn lead to icy crusts that inhibit foraging by semi-domesticated reindeer, caribou, and musk oxen, sometimes leading to mass starvation events (Serreze et al. 2021). However, obtaining accurate measurements of Arctic precipitation is challenging. The precipitation gauge network is sparse (Serreze et al. 2003) and limited to land areas (Barrett et al. 2020). Gauges also suffer from undercatch of solid precipitation (Ye et al. 2021), and correction techniques have large uncertainties (Behrangi et al. 2019). Studies of Arctic precipitation have hence increasingly relied on output from atmospheric reanalyses based on the European Center for Medium Range Weather Forecasts' ERA-Interim and ERA5 products. ERA5 performs slightly better than other atmospheric reanalyses at matching observed precipitation (Barrett et al. 2020; Loeb et al. 2022) and is used here to provide an overview of 2023 Arctic precipitation anomalies. In this section, the Arctic is taken as the region poleward of 60°N and winter, spring, summer, and autumn are defined as January–March, April–June, July–September, and October–December, respectively.

Studies report that Arctic precipitation trends over the past several decades vary regionally (Walsh et al. 2020; White et al. 2021; Yu and Zhong 2021). However, as discussed in the *State of the Climate in 2022* report (Walsh et al. 2023), pan-Arctic precipitation now has a detectable upward trend based on ERA5 (land and ocean measurements; Hersbach et al. 2020) and the gauged-based GPCC V.2022 dataset (land-only measurements; Becher et al. 2013; Schneider et al. 2022) back to 1950.

2. 2023 SUMMARY

Pan-Arctic precipitation for 2023 was about 102% of the 1991–2020 average based on ERA5. Corresponding percentages for winter, spring, summer, and autumn are 107%, 95%, 100%, and 105%. Computed trends remain essentially unchanged since the *State of the Climate in 2022* report (Walsh et al. 2023), which showed that the pan-Arctic trends are positive and statistically significant in all seasons. Short-duration (several days) heavy precipitation broke existing records at various locations within the Arctic.

3. REGIONAL ANOMALIES

Regional anomalies with respect to 1991–2020 means are compared in Fig. 5.8. Winter anomalies were generally small. Modest positive departures characterized the Bering Sea, the panhandle of Alaska, the Barents Sea, and part of northern Europe. Spring was characterized by dry conditions over northern Canada, extending across much of the northern North Atlantic and across western Eurasia. The dry conditions over western Eurasia are consistent with above-average sea-level pressure (as much as +10 hPa) over the region (section 5c,

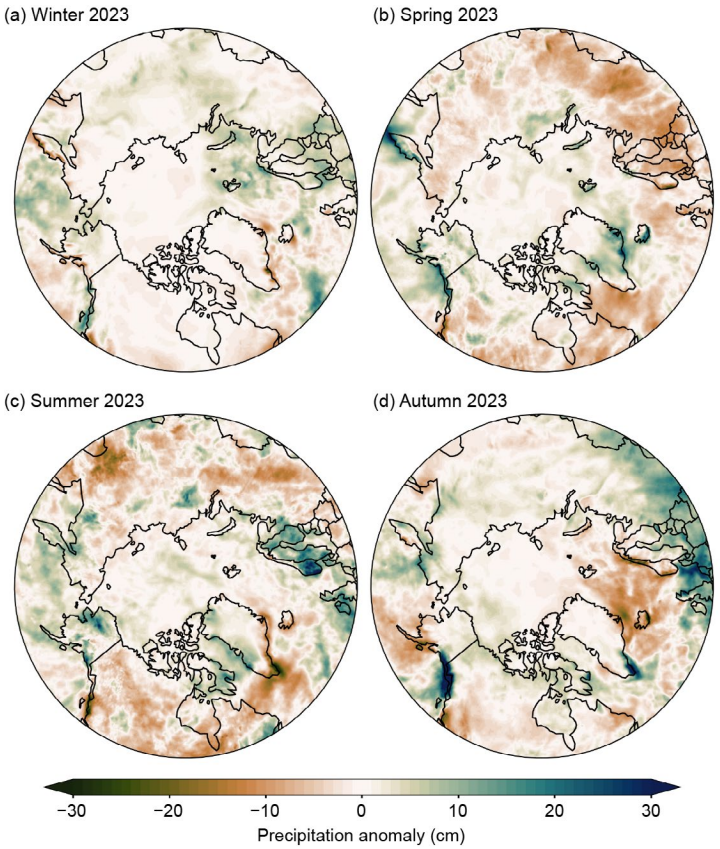

Fig. 5.8. Seasonal departures of Arctic precipitation in 2023 from the 1991–2020 climatological means for (a) winter, (b) spring, (c) summer, and (d) autumn. Green shades denote above-normal precipitation, brown shades denote below-normal precipitation. (Source: ERA5.)

see Fig. 5.7b). Above-average temperatures contributed to the dryness in regions of Canada (section 5c, see Fig. 5.6b). While spring had below-average precipitation for the Arctic as a whole, the season was modestly wet along the Pacific coast of Alaska, part of Greenland, and Kamchatka.

Summer remained notably dry over northern Canada, as well as over parts of Eurasia, contrasting with wet conditions and flood-producing rains over Scandinavia in August. Summer precipitation was also above average over much of Alaska. Portions of the Northwest Territories, Canada, experienced extreme drought during August and September (NOAA North American Drought Monitor), contributing to wildfires that continued through late summer in the Northwest Territories (see Sidebar 7.1 for details). Parts of the Greenland Ice Sheet saw high precipitation (snow) in June (section 5g), but this is not readily seen in the ERA5 data.

Autumn was extremely wet in southeastern Alaska. The airport at Anchorage, Alaska, had the wettest October–December in its 71-year history, breaking the record set just a year earlier in autumn 2022. Autumn also featured positive precipitation anomalies from the United Kingdom to southern Norway, consistent with the belt of negative sea-level pressure anomalies from the United Kingdom to northern Europe (Fig. 5.10d).

4. HISTORICAL PERSPECTIVE

Time series of Arctic precipitation anomalies using ERA5 and the GPCC follow in Fig. 5.9. There are some substantial differences in anomalies between ERA5 and GPCC for individual years, including the considerably lower 2023 precipitation from GPCC for winter, spring and, to a lesser extent, the annual mean. This is not surprising given that the GPCC product covers land only, while ERA5 covers both ocean and land. However, trends computed from the GPCC and ERA5 are similar. ERA5 depicts increases of about 10% in annual precipitation over 1950–2023, with more substantial increases in winter than in summer. For the more recent period 1979–2023, when ERA5 satellite data assimilation increased, trends in ERA5 (and also GPCC) precipitation are larger and remain statistically significant ($p < 0.05$) for the full year and for all seasons except spring. Spring trends for 1979–2023 are weaker than for 1950–2023 and insignificant in both datasets. Increased precipitation is especially pronounced in the subpolar Pacific south of Alaska during autumn, winter, and summer and in the subpolar North Atlantic during winter. The southwestern coast of Norway is dominated by increases in all seasons. Negative trends are most prominent in the subarctic during spring and summer.

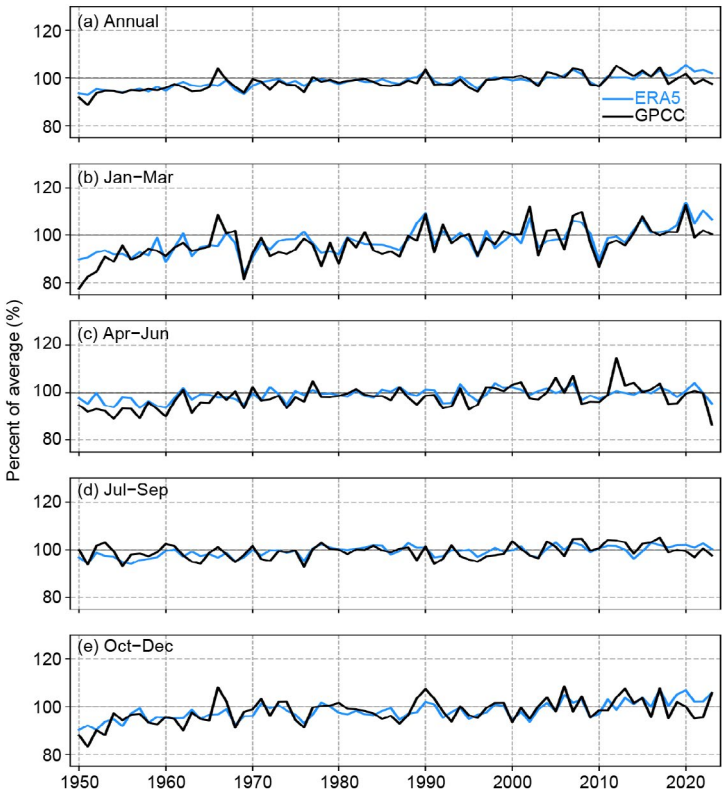

Fig. 5.9. Time series of Arctic precipitation (poleward of 60°N) from 1950 through 2023 expressed as a percentage of the 1991–2020 average (the average, which is 100%, is shown by the horizontal black lines). The 1950–2020 data are from the GPCC Full Data Monthly Version 2022, January 2021–November 2023 data are from the GPCC Monitoring Product Version 2022, and the December 2023 data are from the GPCC First Guess Monthly dataset.

5. HEAVY PRECIPITATION EVENTS

Figure 5.10 shows ranks (relative to the 1950–2023 historical period) of the maximum five-day precipitation events in each season of 2023. During all seasons, heavy precipitation events were scattered across the Arctic, with no clear spatial pattern. Several spatially elongated features are apparent, such as the ones extending poleward along the dateline in

winter and north of the Svalbard Archipelago in summer. Southeastern Greenland also experienced heavy precipitation in spring. There were very few heavy precipitation events in Canada in summer, consistent with drought conditions that contributed to the record wildfire year.

Locally, based on ground station data, northern Europe experienced heavy rains in early August, though this is not readily apparent in Fig. 5.10, likely due to the challenge of comparing station (point) measurements to ERA5 grid cell values (31-km grid resolution). The heaviest rains in 25 years occurred in southern Norway, causing a dam to break (see Sidebar 5.2). In the North American subarctic, more than 100 mm of rain that fell over a two-day period in late November, which was attributable to an atmospheric river, led to landslides and multiple fatalities in Wrangell, Alaska.

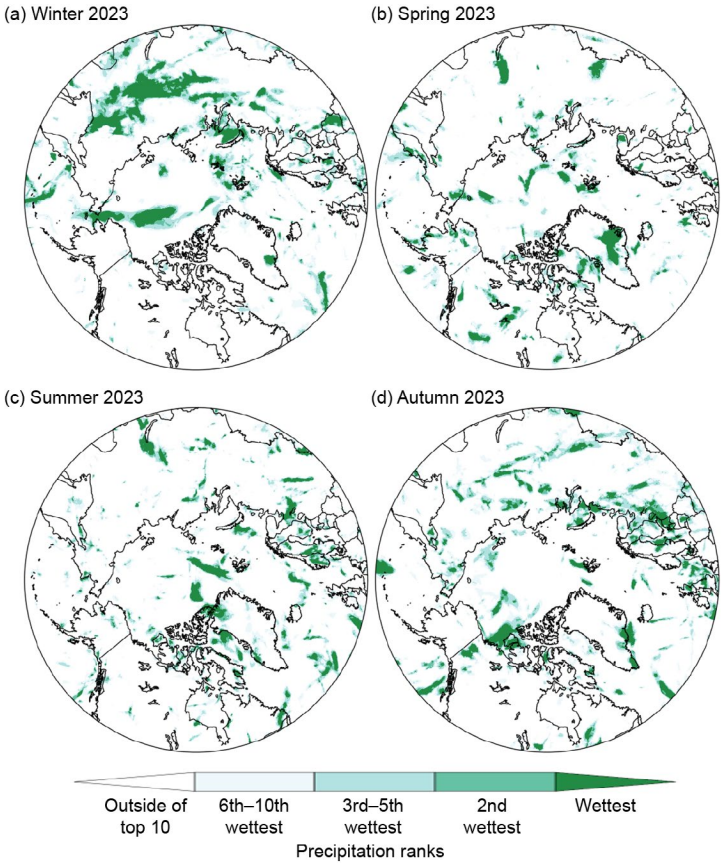

Fig. 5.10. Ranks of maximum five-day precipitation amounts in 2023 for (a) winter, (b) spring, (c) summer, and (d) autumn (based on events from 1950–2023). (Source: ERA5.)

e. Sea-surface temperature

—M.-L. Timmermans and Z. Labe

Arctic Ocean sea-surface temperatures (SSTs) in the summer are driven by the amount of incoming solar radiation absorbed by the sea surface and by the flow of warm waters into the Arctic from the North Atlantic and North Pacific Oceans. Solar warming of the Arctic Ocean surface is influenced by sea-ice distribution (with greater warming occurring in ice-free regions), cloud cover, and upper-ocean stratification. Inflows of relatively warm Arctic river waters can provide an additional heat source in the coastal regions.

Arctic SST is an essential indicator of the strength of the ice–albedo feedback cycle in any given summer sea-ice melt season. As the sea-ice cover decreases, more incoming solar radiation is absorbed by the darker ocean surface and, in turn, the warmer ocean melts more sea ice. Marine ecosystems are also influenced by SSTs, which affect the timing and development of primary production cycles, as well as available habitat. In addition, higher SSTs are associated with delayed autumn freeze-up and increased ocean heat storage throughout the year. An essential point for consideration, however, is that the total heat content contained in the ocean surface layer (i.e., the mixed layer) depends on mixed-layer depth; a shallower mixed layer with higher SSTs could contain the same amount of heat as a deeper mixed layer with lower SSTs. We discuss only SSTs here and do not quantify ocean heat content due to a lack of in situ observations.

The monthly mean SST data presented here are from the 0.25° × 0.25° NOAA OISST Version 2.1 product, a blend of in situ and satellite measurements (Reynolds et al. 2002, 2007; Huang et al. 2021; NOAA 2024). In January 2023, OISST Version 2.1 replaced the 1° × 1° NOAA OISST Version 2, which was analyzed in previous annual *State of the Climate* reports; reported trends are statistically indistinguishable between the two versions (for further details, see Timmermans and Labe 2023). The period of analysis is June 1982 to September 2023, with 1991–2020 used as the climatological reference period.

Here, we focus most closely on August 2023 mean SSTs in context with the climatological record. August mean SSTs provide the most appropriate representation of Arctic Ocean summer SSTs because sea-ice extent is near a seasonal low at this time of year, and there is not yet the influence of surface cooling and subsequent sea-ice growth that typically takes place in the latter half of September.

August 2023 mean SSTs were as high as ~11°C in the Barents, Kara, and Beaufort Seas

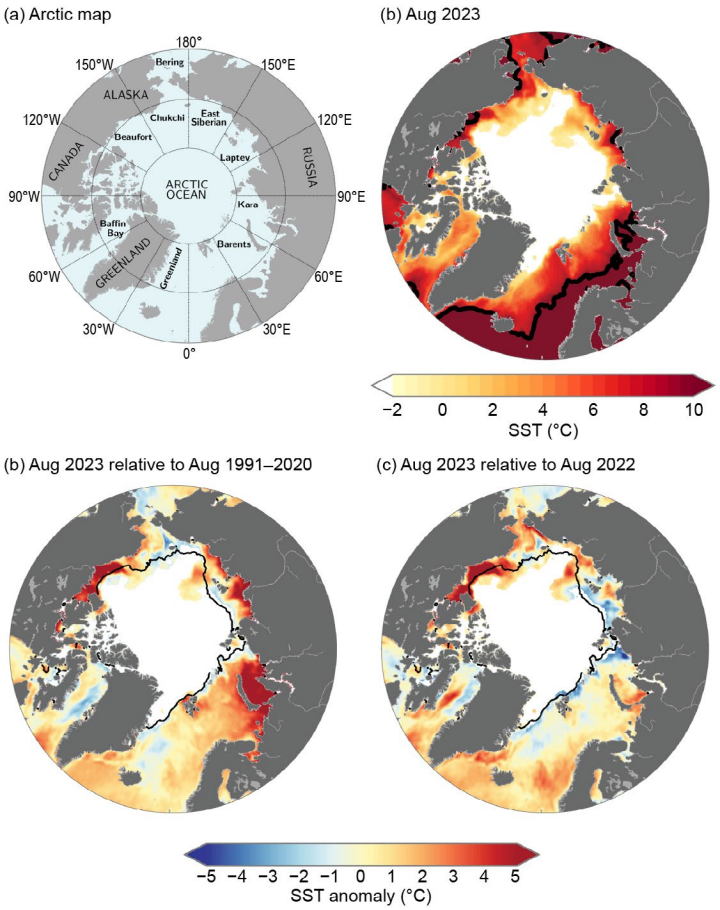

Fig. 5.11. (a) Arctic Ocean map showing marginal sea locations. (b) Mean sea-surface temperature (SST; °C) in Aug 2023. Black contours indicate the 10°C-SST isotherm. (c) SST anomalies (°C) in Aug 2023 relative to the Aug 1991–2020 mean. (d) Difference between Aug 2023 SSTs and Aug 2022 SSTs (negative values indicate where 2023 was cooler). White shading in all panels is the Aug 2023 mean sea-ice extent. Black lines in (c) and (d) indicate the Aug 1991–2020 median ice edge. Sea-ice concentration data are the NOAA National Snow and Ice Data Center's (NSIDC) Climate Data Record of Passive Microwave Sea Ice Concentration, Version 4 (https://nsidc.org/data/g02202) for the 1982–2022 period of record, and Near-Real-Time NOAA/NSIDC Climate Data Record of Passive Microwave Sea Ice Concentration, Version 2 (https://nsidc.org/data/g10016) (Peng et al. 2013; Meier et al. 2021a,b) for Jun–Sep 2023; a threshold of 15% concentration is used to calculate sea-ice extent.

and reached values as high as ~8°C in other Arctic basin marginal regions (e.g., eastern Chukchi Sea and Laptev Sea; Figs. 5.11a,b). August 2023 mean SSTs were anomalously high compared to the 1991–2020 August mean (around 5°C–7°C higher) in the Barents, Kara, Laptev, and Beaufort Seas, and anomalously low in Baffin Bay and parts of the Greenland, Bering, and Chukchi Seas (around 1°C–3°C lower than the 1991–2020 mean; Fig. 5.11c). These regional variations differ significantly from year to year. For example, there were considerably higher SSTs in the Beaufort Sea in August 2023 compared to August 2022, with differences of up to 7°C, and mostly lower 2023 SSTs in the Laptev Sea (Fig. 5.11d).

Warm river inflows may have influenced marginal sea SSTs with anomalously high August 2023 SSTs in the Beaufort Sea where the Mackenzie River enters, in the Kara Sea in the vicinity of the Ob and Yenisei River inflows, and in the Laptev Sea where the Lena River enters (Fig. 5.11c). This corresponds with anomalously high surface air temperatures in June–August 2023 over northern North America and Siberia that warmed the rivers (section 5c).

The above-normal SSTs in the Beaufort Sea in August 2023, which were also observed in July (Fig. 5.12b), relate to relatively low August 2023 sea-ice concentrations in the region extending from the Beaufort to East Siberian Seas (second only to the record-low August 2012 sea-ice conditions for the area; section 5f). The timing of seasonal sea-ice retreat from the Beaufort Sea, where sea ice was almost entirely absent by July 2023 (Fig. 5.12), also links to high SSTs via the ice–albedo feedback (section 5f). A similar spatial pattern of SST anomalies persisted through the melt season end in September (Fig. 5.12d) although with generally reduced warm anomalies in the marginal seas, signifying cooling in the latter half of the month.

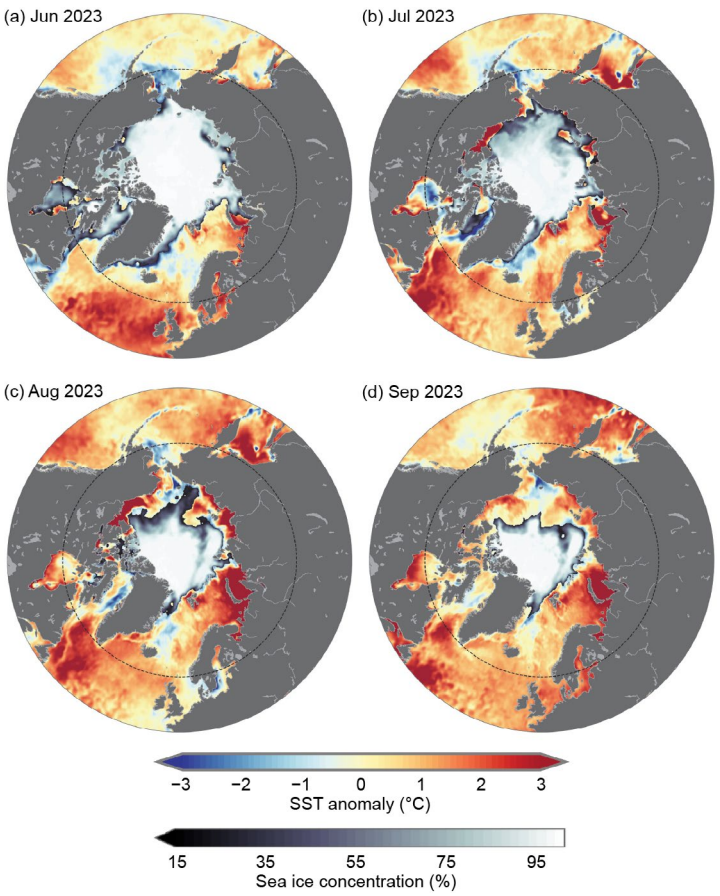

Fig. 5.12. Sea-surface temperature (SST) anomalies (°C) for (a) Jun 2023, (b) Jul 2023, (c) Aug 2023, and (d) Sep 2023 relative to the 1991–2020 mean for the respective months. The mean sea-ice concentration for the corresponding month is also shown. The evolution of sea-ice concentration over the months of Jun to Aug illustrates why it is not appropriate to evaluate long-term SST trends in Jun and Jul over most of the Arctic marginal seas, which still have significant sea-ice cover in those months. While sea-ice extent is lowest in Sep, SSTs cool in the latter part of the month. The dashed circle indicates the latitudinal bound of the Fig. 5.11 and Fig. 5.13 map images. See Fig. 5.11 caption for sea-ice dataset information.

The below-normal August 2023 SSTs in Baffin Bay are consistent with below-normal surface air temperatures in the region in June–August 2023 (section 5c). Early summer sea-ice extent in Baffin Bay was close to the climatological average, with almost full ice cover in June 2023 (Fig. 5.12a), which is further consistent with the anomalously low SSTs (section 5f).

The Arctic Ocean has experienced mean August SST warming trends from 1982 to 2023, with statistically significant (at the 95% confidence interval) linear warming trends in almost all regions (Fig. 5.13a). Mean August SSTs for the Arctic Ocean and marginal seas between 65°N and 80°N exhibit a linear warming trend of 0.05±0.01°C yr^{-1} (Fig. 5.13b; SSTs for 80°N–90°N are omitted since this region is largely perennially ice covered). Even while anomalously low SSTs in

Baffin Bay were prominent in August 2023 (Fig. 5.11c), SSTs show a linear warming trend over 1982–2023 of 0.07±0.02°C yr^{-1} for this region (Fig. 5.13c) although with considerable interannual variability in mean August values.

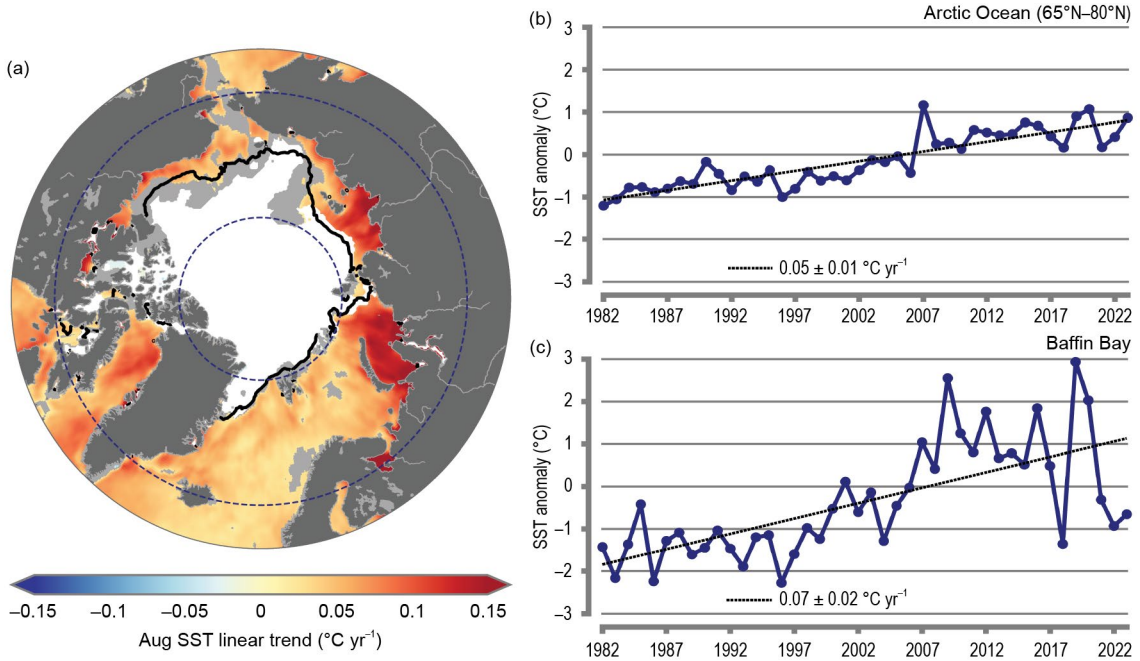

Fig. 5.13. (a) Linear sea-surface temperature (SST) trend (°C yr^{-1}) for Aug of each year from 1982 to 2023. The trend is only shown for values that are statistically significant at the 95% confidence interval; the region is shaded light gray otherwise. White shading is the August 2023 mean sea-ice extent, and the black line indicates the August 1991–2020 median ice edge. (b),(c) Area-averaged SST anomalies (°C) for Aug of each year (1982–2023) relative to the 1991–2020 Aug mean for (b) the Arctic Ocean between 65°N and 80°N (indicated by the dashed blue circles in [a]), and (c) Baffin Bay (see Fig. 5.11a). The dotted lines show the linear regression of the SST anomaly over the period shown with trends in °C yr^{-1} (with 95% confidence intervals) indicated on the plots. See Fig. 5.11 caption for sea-ice dataset information.

f. Sea ice

—W. N. Meier, A. Petty, S. Hendricks, D. Perovich, S. Farrell, M. Webster, D. Divine, S. Gerland, L. Kaleschke, R. Ricker, and X. Tian-Kunze

Sea ice is the frozen interface between the ocean and atmosphere in the Arctic. It limits ocean–atmosphere exchanges of energy and moisture and plays a critical role in Arctic ecosystems and Earth's climate. The presence of sea ice modulates human activities in the Arctic, including Indigenous hunting and transportation, marine navigation, and national security responsibilities. Arctic sea-ice conditions during 2023 continued to illustrate the profound changes underway in the Arctic due to climate change.

1. SEA-ICE EXTENT

Arctic sea-ice extent in winter (January–March) 2023 was lower than in 2022 and overall was the third-lowest winter average in the record that began in 1979. Extent values are from the National Snow and Ice Data Center's Sea Ice Index (Fetterer et al. 2017), one of several extent products (Ivanova et al. 2014; Lavergne et al. 2019) derived from satellite-borne passive microwave sensors operating since 1979. Winter extent was particularly low in the Barents Sea region and slightly lower than the 1991–2020 average in the Sea of Okhotsk and Gulf of St. Lawrence.

By March, the month with the most extensive coverage, the total sea-ice extent of 14.44×10^6 km^2 was 0.59×10^6 km^2 (3.9%) lower than the 1991–2020 average and the sixth-lowest March extent in the 45-year record. The March 2023 extent continued the statistically significant downward trend of –2.6% per decade over the 1979–2023 record (Fig. 5.14a). On a regional basis, March 2023 was characterized by below-average extent across most of the Arctic, with slightly higher-than-average extent in the Greenland Sea (Fig. 5.14b).

After March, the seasonal retreat of sea ice began. The Northern Sea Route along the northern Russian coast was relatively slow to open; sea ice extended southward to the coast in the eastern Kara Sea and the East Siberian Sea through July, but by late August, open water was present throughout the entire route. The Northwest Passage through the Canadian Arctic Archipelago became relatively clear of ice by September. And though ice largely blocked the western end of the northern route through M'Clure Strait throughout the melt season, ice extent in the Passage reached near-record lows (Sidebar 5.2).

September, the month of the annual minimum extent, was characterized by below-average coverage in the Pacific sector with open water extending far northward from the coast in the Beaufort, Chukchi, and Siberian Seas (Fig. 5.14c). The September 2023 sea-ice extent of 4.37×10^6 km^2 was 1.21×10^6 km^2 (21.6%) lower than the 1991–2020 average and the fifth-lowest September extent on record. The September trend from 1979 through 2023 is

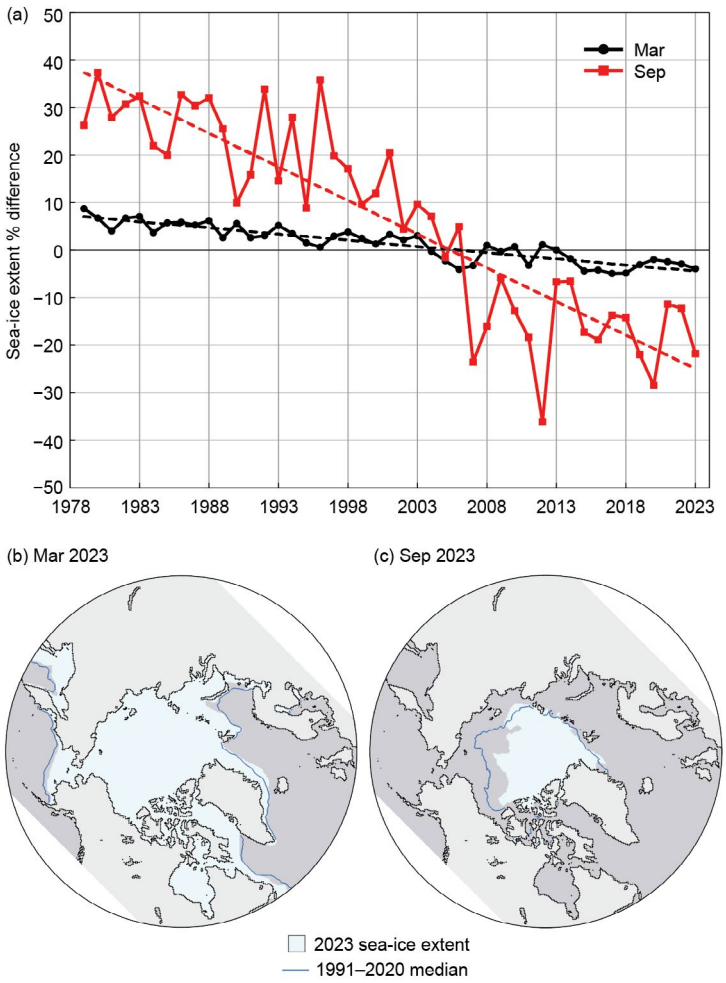

Fig. 5.14. (a) Monthly sea-ice extent anomalies (%, solid lines) and linear trend lines (%, dashed lines) for Mar (black) and Sep (red) from 1979 to 2023. The anomalies are relative to the 1991–2020 average for each month. (b) Mar 2023 and (c) Sep 2023 monthly average sea-ice extent; the 1991–2020 median extent is shown by the blue contour.

–13.9% per decade and like all other monthly trends is statistically significant. The 17 lowest September extents in the satellite record have all occurred in the last 17 years (2007–23).

2. SEA-ICE AGE, THICKNESS, AND VOLUME

Sea-ice age is a rough proxy for thickness as multiyear ice (ice that survives at least one summer melt season) grows thicker over successive winters. Sea-ice age is presented here (Fig. 5.15) for the period 1985–2023 based on Tschudi et al. (2019a,b). One week before the 2023 annual minimum extent, when the age values of the remaining sea ice are incremented by one year, the amount of multiyear ice remaining in the Arctic continued to be far lower than that in the 1990s (Fig. 5.15). Since 2012, the Arctic has been nearly devoid of the oldest ice (>4 years old); this continued in 2023, with an end-of-summer old ice extent of 93,000 km^2. In the 39 years since ice-age records began in 1985, the Arctic has changed from a region dominated by multiyear sea ice to one where seasonal sea ice prevails. A younger ice cover implies a thinner, less voluminous sea-ice pack and one that is more sensitive to atmospheric and oceanic changes.

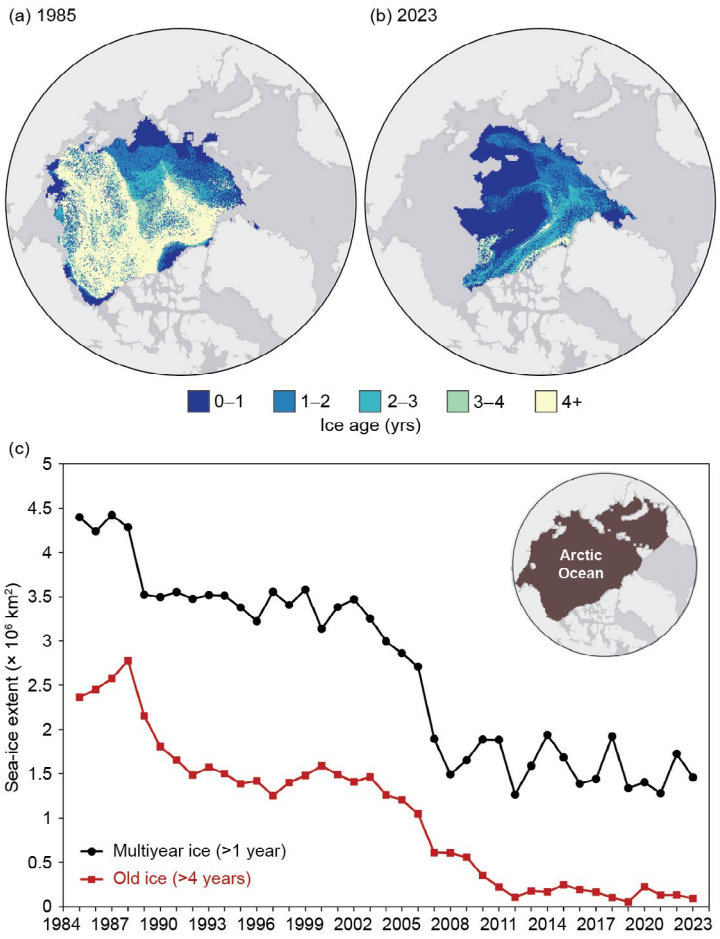

Fig. 5.15. Sea-ice age coverage map for the week before minimum total extent (when age values are incremented to one year older) in (a) 1985 and (b) 2023; (c) extent of multiyear ice (black) and ice >4 years old (red) within the Arctic Ocean (inset) for the week of the minimum total extent (× 10^6 km^2).

Sea ice drifts with winds and ocean currents, while growing and melting thermodynamically. Ice divergence creates open water leads and, in freezing conditions, new ice forms, while ice convergence leads to dynamic thickening. Sea-ice thickness provides a record of the cumulative effect of dynamic and thermodynamic processes and thus is an important indicator of overall ice conditions. The ESA CryoSat-2/SMOS satellites have provided a record of seasonal (October–April) ice thickness and volume (Ricker et al. 2017; ESA 2023) since the 2010/11 winter. Since 2018, the NASA ICESat-2 satellite has also provided thickness estimates (Petty et al. 2020; 2023a,b). Some differences between these two products are seen in the monthly average winter Arctic thickness, but both products show monthly thicknesses from autumn 2022 through early spring 2023 (October through April) similar to the mean of this short period of observational overlap (2018 onwards, Fig. 5.16a). April 2023 thickness (Fig. 5.16b) from CryoSat-2/SMOS relative to the 2011–2023 April mean (Fig. 5.16c) shows that the eastern Beaufort Sea and the East Siberian Sea had relatively thinner sea ice than the 2011–22 mean, particularly near the Canadian Archipelago. Thickness was higher than average in much of the Laptev and Kara Seas and along the western and northwestern coasts of Alaska, extending northward toward the pole. The East Greenland Sea had a mixture of thicker- and thinner-than-average ice.

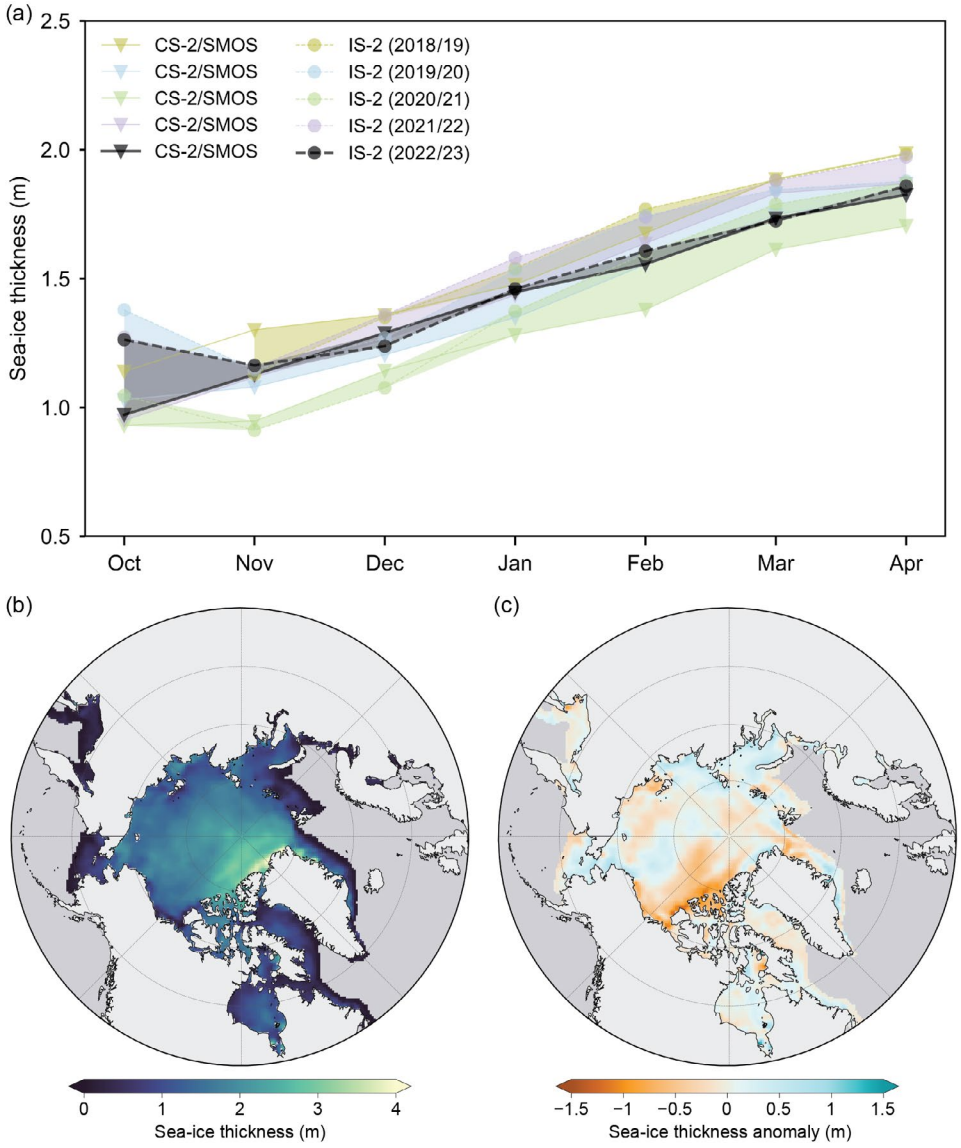

Fig. 5.16. (a) Oct–Apr monthly average sea-ice thickness (m), calculated over an Inner Arctic Ocean Domain, from ICESat-2 (circles) and CryoSat-2/SMOS (triangles) for 2018/19 through 2022/23; (b) average Apr 2023 sea-ice thickness (m) map from CryoSat-2/SMOS; (c) CryoSat-2/SMOS thickness anomaly (m) map for Apr 2023 relative to the 2010–22 average.

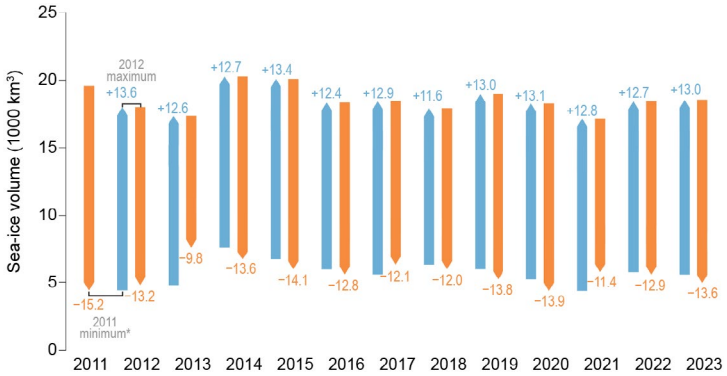

Fig. 5.17. Annual sea-ice volume loss (orange) and gain (blue) between the annual maximum and minimum values from CryoSat-2/SMOS. Units are in 1000 km³. Note: CryoSat-2/SMOS overestimates annual minimum sea-ice volume because Sep data are not available.

Sea-ice thickness from CryoSat-2/SMOS is integrated with ice concentration to provide winter volume estimates for 2010–23. The change from winter maximum volume to summer minimum and back to winter over the years illustrates the strong seasonal cycle and interannual variability (Fig. 5.17). There is little indication of a trend in the relatively short 12-year time series. Volume gain throughout the October 2022 to April 2023 growth season of 12,900 km³ was within the range of earlier years in the record and balanced the volume loss during the summer 2022 melt season, though the subsequent 2023 summer loss was greater.

g. Greenland Ice Sheet

—K. Poinar, K. D. Mankoff, X. Fettweis, B. D. Loomis, R. S. Fausto, B. E. Smith, B. Medley, A. Wehrlé, C. D. Jensen, M. Tedesco, J. E. Box, T. L. Mote, and J. H. Scheller

Mass loss from the Greenland Ice Sheet raises global mean sea level, affects coastal infrastructure, and increases coastal erosion, flooding, saltwater intrusion, and habitat loss. Its mass balance is the difference between accumulated snowfall and melt, sublimation, evaporation, and discharge of solid ice directly into the ocean (iceberg calving). We present three independent estimates of the total mass balance of the Greenland Ice Sheet over the 2023 mass balance year, 1 September 2022 to 31 August 2023: input-output-derived (–170±69 Gt), gravity-derived (–205±76 Gt), and elevation-derived (–183±43 Gt), values that agree within measurement uncertainties and that are close to or slightly more negative than the 1991–2020 mean. Although winter snow accumulation was above average, net mass loss occurred because ice discharge and meltwater runoff exceeded accumulation.

Surface mass balance (SMB), one component of total mass balance, comprises mass input from net snow accumulation and mass loss from meltwater runoff. Surface mass balance is driven by air temperature, snow cover, albedo, and bare-ice area. We summarize in situ and satellite observations of these quantities over the 2023 mass balance year.

Meteorological data collected by land-based weather stations (operated by the Danish Meteorological Institute) and on-ice weather station transects (operated by the Programme for Monitoring of the Greenland Ice Sheet, PROMICE) across Greenland (Fausto et al. 2021) indicate that monthly air temperatures during autumn (September–November 2022) were predominantly higher than the 1991–2020 mean, winter (December–February 2022/23) temperatures were close to or below average, and spring (March–May 2023) temperatures were close to or above average. At Summit Station in the ice sheet interior (3216 m a.s.l.), the autumn mean was record high (–23.0°C, +7.6°C anomaly). Summer (June–August [JJA] 2023) temperatures were below average in west Greenland and predominantly slightly above average in south and east Greenland. At Summit Station, the mean summer temperature was –10.3°C (+3.5°C anomaly). Summer snow accumulation was also the highest since 1940, at 34% above the mean.

Cooler-than-average conditions characterized the beginning of the 2023 melt season. In late June through mid-July, however, a persistent high-pressure system promoted multiple melt events. During a single week in July, record-setting ice ablation (loss) of 40 cm was recorded high on the ice sheet at South Dome (2893 m a.s.l.). Over 21–26 August, another high-pressure system caused warm, dry conditions in the north. On 21 August, the temperature at Summit Station reached –0.6°C, and PROMICE (Programme for Monitoring of the Greenland Ice Sheet) stations

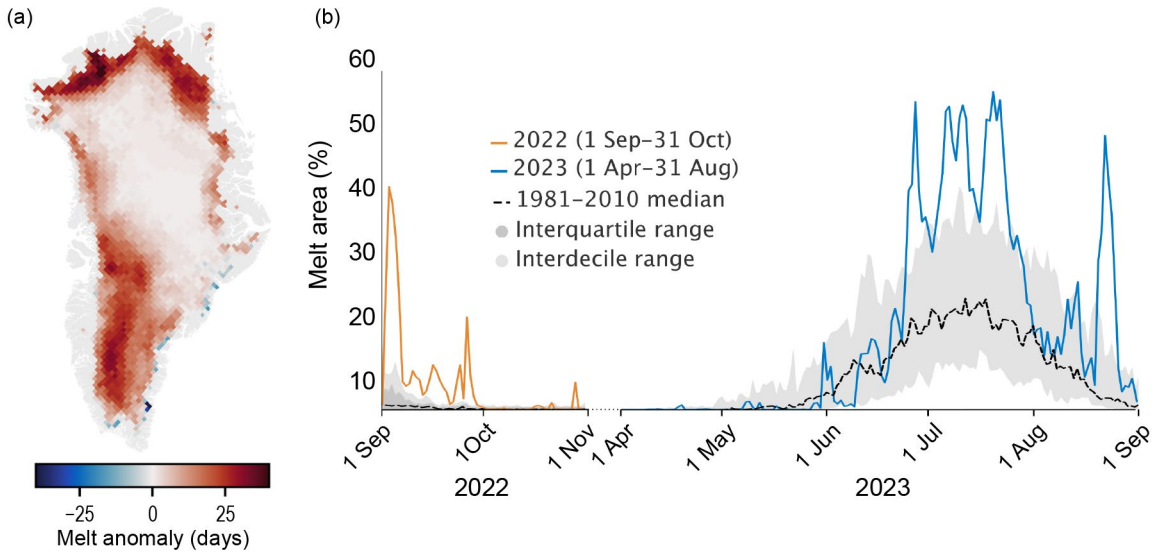

Fig. 5.18. (a) Number of surface melt days from 1 Apr to 31 Aug 2023, expressed as an anomaly with respect to the 1991–2020 period, from the daily Special Sensor Microwave Imager / Sounder (SSMIS) 37-GHz horizontally polarized passive microwave radiometer satellite data (Mote 2007). (b) Surface melt extent as a percentage of ice-sheet area across the 2023 mass balance year, also derived from SSMIS and including autumn 2022 (orange) and spring/summer 2023 (blue) and omitting winter 2022/23.

on the north and east coasts recorded temperatures up to 16°C above seasonal averages. Southern Greenland experienced high rainfall rates during this period. The total number of melt days measured across the ice sheet exceeded the 1991–2020 mean virtually everywhere (Fig. 5.18a). The cumulative melt-day area in 2023 (Fig. 5.18b) was the third-largest on record, 40% greater than the 1991–2020 mean.

The average albedo across Greenland, measured by the Moderate Resolution Imaging Spectroradiometer (MODIS) following Box et al. (2017), was the fifth lowest over the period 2000–23 (Fig. 5.19a), in part because melt onset did not occur until late June. This yielded low bare-ice area measured by Sentinel-3 SICE (Kokhanovsky et al. 2020; Wehrlé et al. 2021) in the early melt season, but by the end of the summer, the bare-ice area was above average (Fig. 5.19b). The late-summer warmth caused a lower- (darker-) than-average melt-season albedo, especially across southwestern and northern Greenland (Fig. 5.19c), although the climatic baseline for this dataset is quite short (2017–22).

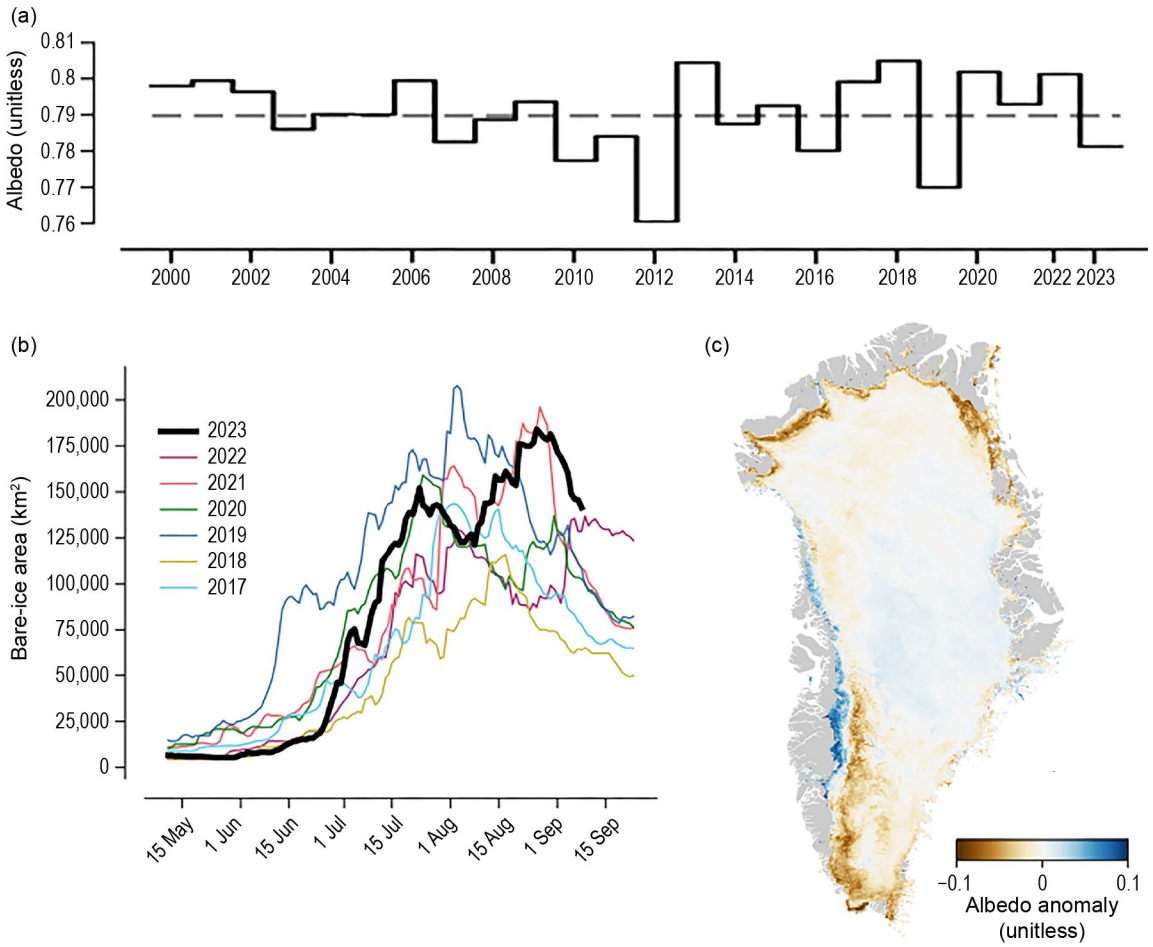

Fig. 5.19. (a) Time series of average summer albedo since 2000, from the Moderate Resolution Imaging Spectroradiometer (MODIS), with dashed line showing mean. (b) Bare-ice area (km²) measured from Sentinel-3 observations (Wehrlé et al. 2021). (c) Albedo anomaly for summer (June–August) 2023 measured from Sentinel-3 data, relative to summers 2017–22 (Wehrlé et al. 2021).

The MARv3.14 model (MAR; Fettweis et al. 2020) forced by ERA5 (Hersbach et al. 2020) provides SMB values at 5-km horizontal resolution. The ice-sheet-wide total SMB over the 2023 mass balance year was 337±51 Gt, 12% below the 1991–2020 mean. Snowfall accumulation in autumn 2022 and summer 2023 were each 34% higher than the 1991–2020 mean and were the highest on record since MAR-based reconstructions began in 1940. Winter and spring snow accumulation were each close to the mean. Total snowfall accumulation was 831 Gt, 14% above the mean and the sixth highest in the 84-year record dating back to 1940. Exceptional rainfall in September 2022 and above-average JJA 2023 rainfall pushed the rainfall total to 94 Gt, the highest on record and more than 4 std. dev. above the mean. Total precipitation (snowfall plus

rainfall) was also the highest on record, but this was compensated by high runoff, 542±81 Gt, 60% above the 1991–2020 mean, and 43 Gt of sublimation and evaporation.

Hundreds of marine-terminating glaciers discharge Greenland ice into the ocean as icebergs; this discharge is the other main way, alongside meltwater runoff, that the ice sheet loses mass. PROMICE combines satellite-derived ice velocity and ice thickness data to produce an ice-sheet-wide glacier discharge time series (Mankoff et al. 2020). For the 2023 mass balance year, this showed that Greenland Ice Sheet glaciers discharged 508±47 Gt. This is 10% above the 1991–2020 mean discharge of 465±43 Gt yr^{-1} but falls below the 1991–2020 increasing discharge trend of +2.4 Gt yr^{-1}.

We difference the SMB ice input from MAR (337±51 Gt) and the discharge ice output from PROMICE (508±47 Gt) to obtain an input-output total mass balance of –170±69 Gt over the 2023 mass balance year (Fig. 5.20). This is within 5% of the 1991–2020 input-output-derived mean of –162±88 Gt yr^{-1}.

The GRACE (2002–17) and GRACE-FO (2018–present) satellite missions measure gravity anomalies to deduce changes in total ice mass (Tapley et al. 2019). These data include ice-sheet ice and surrounding glaciers and ice masses; we therefore scale the results by 0.84 to include the ice sheet only (Colgan et al. 2015; see section 5h for glaciers and ice caps outside of Greenland). This yields –205±76 Gt over the 2023 mass balance year (Fig. 5.20), which is 20% less loss than the 2002–23 yearly mean of –257±9 Gt from GRACE/GRACE-FO.

The ICESat-2 mission measures ice-sheet surface height. Changes in this value reflect ice mass loss as well as changes in firn air content and short-term SMB anomalies. We thus subtract model-based estimates of these quantities from ICESat-2 data produced following the processing strategy outlined in Smith (2023), then recover the total mass change by adding back the modeled SMB anomalies (Fig. 5.20). The mass change over the 2023 mass balance year was –183±43 Gt.

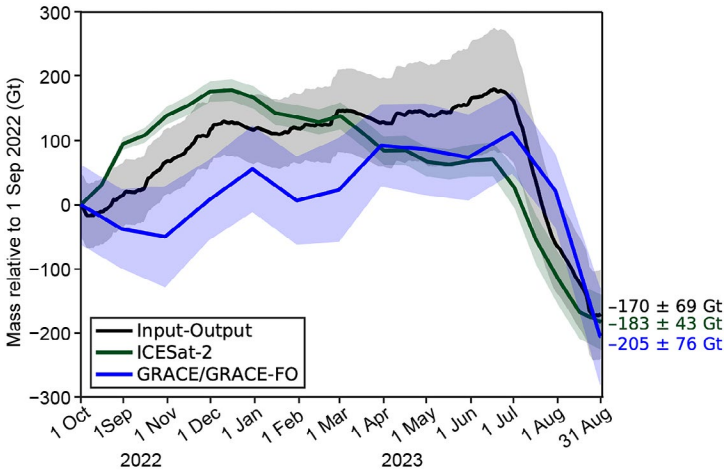

Fig. 5.20. Time series of three independent measurements of ice-sheet mass balance from 1 Sep 2022 through 31 Aug 2023. Results from ICESat-2 (green), the Gravity Recovery and Climate Experiment (GRACE)/GRACE Follow-On (GRACE-FO) (blue), input-output (black), and their associated uncertainties (shaded), each shown at appropriate time resolution (15, 30, and 1 days, respectively) with mass balance year totals to the right. For GRACE/GRACE-FO, 2-st. dev. uncertainties that include noise, processing differences, and non-trend leakages are shown.

Overall, in the 2023 mass balance year, the Greenland Ice Sheet lost a near-average to above-average amount of ice due to above-average accumulation that was nearly balanced by above-average meltwater runoff and slightly above-average solid ice discharge.

h. Glaciers and ice caps outside Greenland

—D. Burgess, G. Wolken, B. Wouters, L. M. Andreassen, C. Florentine, J. Kohler, B. Luks, F. Pálsson, L. Sass, L. Thomson, and T. Thorsteinsson

The Arctic hosts 60% of the world's mountain glaciers and ice caps by area outside of the ice sheets of Greenland and Antarctica (RGI Consortium 2023; Fig. 5.21). While their potential longer-term contribution to sea-level rise is small compared to the ice sheets, they are highly sensitive to changes in climate (Box et al. 2019) and have been a large contributor to recent sea-level rise in response to continued atmospheric warming (Hugonnet et al. 2021; Ciracì et al. 2020; Wouters et al. 2019). Recent increases in global temperature, amplified at high northern latitudes (section 5c; Fig. 5.21), have accelerated melting of Arctic glaciers and ice caps three-fold since the mid-1990s (Zemp et al. 2019). Observations of monitored Arctic glaciers and ice caps from 2022 and 2023 show regional and inter-annual variations in mass change, with a continuing trend of significant ice loss throughout the Arctic, especially in Alaska and Arctic Canada.

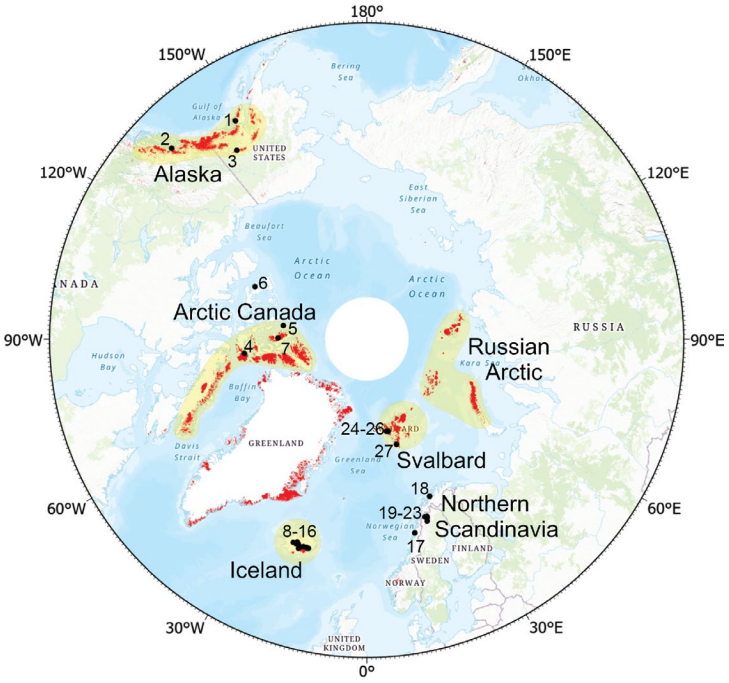

Fig. 5.21. Arctic glaciers and ice caps (red), including ice caps in Greenland that are separate from the ice sheet. Dashed lines delineate the Gravity Recovery and Climate Experiment (GRACE) and GRACE Follow-On (GRACE-FO)-derived mass anomaly domains used to estimate changes in annual glacier mass balance for heavily glacierized Arctic regions. Black dots indicate long-term Arctic glacier monitoring sites, with numbers linked to glacier/ice cap names in Table 5.1.

Glaciers and ice caps gain mass by snow accumulation and lose mass by surface melt and runoff as well as by iceberg calving, where they terminate in oceans or lakes. The total mass balance is defined as the difference between annual snow accumulation and annual mass losses (iceberg calving plus runoff). Of the 27 Arctic glaciers monitored, only Kongsvegen, Hansbreen, and Devon Ice Cap lose mass by iceberg calving, which is not accounted for in this study. We report the climatic mass balance (annual snow accumulation minus annual runoff), which is a measure of annual thickness change (in mm w.e., water equivalent) averaged across the entire ice cap or glacier.

Climatic mass balance (Bclim) is reported for the 2022/23 mass balance year (September 2022 to August 2023) for the 25 monitored Arctic glaciers for which data were available (Table 5.1). As some of these data are provisional, we add context to recent changes in pan-Arctic glacier mass balance by also reporting on 26 glaciers measured in the previous mass balance year of 2021/22 (WGMS 2024; Kjøllmoen et al. 2023). Of the 25 glaciers for which Bclim was measured in both years, five glaciers (four in Iceland, one in Norway) registered positive Bclim in 2021/22, while all glaciers monitored in 2022/23 experienced negative Bclim. Negative Bclim for all regions combined indicates net thinning for pan-Arctic monitored glaciers, with 2021/22 and 2022/23 being the 16th- and 2nd-most-negative years on record. Cumulative measurements of Bclim indicate regional thinning of ~–15 m w.e. across glaciers in Arctic Canada (1959–2023) to ~–37 m w.e. for glaciers in Alaska (1953–2023), with an overall average of ~–26 m w.e. for all regions combined (Fig. 5.22).

Regionally, the most thinning in the 2021/22 balance year occurred over Svalbard, where negative values of Bclim were recorded for Midtre Lovénbreen (–1416 mm w.e.), Austre Brøggerbreen (–1516 mm w.e.), Kongsvegen (–954 mm w.e.), and Hansbreen (–1457 mm w.e.) glaciers (Table 5.1). In Arctic Canada, the fourth-most-negative Bclim on record for the Melville Ice Cap (–1077 mm w.e.) coincided with a persistent warm surface air mass; 3°C–4°C above the 1991–2020 mean (Ballinger et al. 2022) situated over the western Queen Elizabeth Islands and

Beaufort Sea in 2022. Moderate summer melting and slightly higher-than-normal (~10%) winter snow accumulation (WGMS 2024) resulted in an average Bclim anomaly (relative to the 1991–2020 mean) of –290 mm w.e. for Alaskan monitored glaciers in 2022. Cool summer temperatures (Ballinger et al. 2022) and high winter accumulation (~20% above the 1991–2020 mean; WGMS 2024) resulted in a slightly negative mass balance of –111 mm w.e. (+637 mm w.e. relative to the 1991–2020 mean) for the monitored ice caps and glaciers in Iceland. Of the nine glaciers monitored, four on the Hofsjökull (Hofsjökull N) and Vatnajökull Ice Caps (Köldukvislarjökull, Dyngjujökull, and Bruarjökull) averaged a positive Bclim of +296 mm w.e. (st. dev. = 180 mm w.e.) for the 2021/22 balance year. Since the start of mass balance measurements in Iceland, positive Bclim has only been observed five times on Hofsjökull (since 1988), four times on Vatnajökull (since 1991), and two times on Langjökull (since 1997).

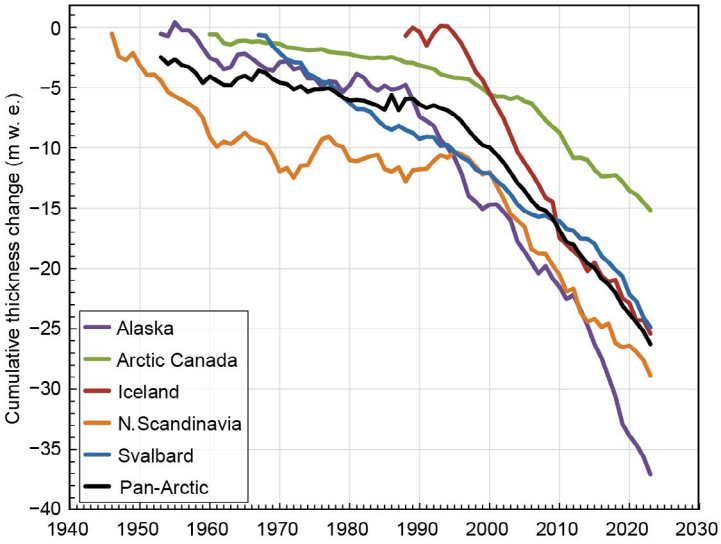

Fig. 5.22. Cumulative climatic mass balance (Bclim) in meters of water equivalent (m w.e.) for monitored glaciers in five Arctic regions and for the Arctic as a whole (pan-Arctic). Regional Bclim are derived as arithmetic means for all monitored glaciers within each region for each year, and these means are summed over the period of record and interpreted as cumulative thickness changes. Note the variable time periods over which cumulative changes are measured. Data are from the World Glacier Monitoring Service (WGMS 2024: https://wgms.ch/).

Table 5.1. Measured climatic mass balance (Bclim) for 26 glaciers in Alaska (3), Arctic Canada (4), Iceland (9), Svalbard (4), and northern Scandinavia (6) in 2021/22 and 25 measured glaciers in 2022/23, together with the 1991–2020 mean and standard deviation (* indicates one or more years of data missing from the record) for each glacier. Negative (positive) values for Bclim indicate mass loss (gain). Data were obtained from the World Glacier Monitoring Service (WGMS 2024: https://wgms.ch/) with results for 2022/23 as tentative and subject to revision. Bias corrections were applied to Bclim for Hofsjökull glaciers (N, E, and SW), Iceland, using methods outlined in Jóhannesson et al. (2013). Numbers in the left-hand column correspond to glacier locations in Fig. 5.21.

Alaska				
Glacier (record length, years)	**Bclim Mean** (mm w.e. yr^{-1}) 1991–2020	**Bclim Std. dev.** (mm w.e. yr^{-1}) 1991–2020	**Bclim** (mm w.e. yr^{-1}) 2021/22	**Bclim** (mm w.e. yr^{-1}) 2022/23
1) Wolverine (58)	–770	984	–1110	–1080
2) Lemon Creek (71)	–1200	839	–1440	–2250
3) Gulkana (58)	–759	830	–1050	–180
Arctic Canada				
Glacier (record length, years)	**Bclim Mean** (mm w.e. yr^{-1}) 1991–2020	**Bclim Std. dev.** (mm w.e. yr^{-1}) 1991–2020	**Bclim** (mm w.e. yr^{-1}) 2021/22	**Bclim** (mm w.e. yr^{-1}) 2022/23
4) Devon Ice Cap (63)	–257	215	–508	–388
5) Meighen Ice Cap (64)	–326	422	–451	–549
6) Melville S. Ice Cap (61)	–458	487	–1077	–1032
7) White (64)	–341	323	–545	–660

Iceland				
Glacier (record length, years)	**Bclim Mean** (mm w.e. yr^{-1}) 1991–2020	**Bclim Std. dev.** (mm w.e. yr^{-1}) 1991–2020	**Bclim** (mm w.e. yr^{-1}) 2021/22	**Bclim** (mm w.e. yr^{-1}) 2022/23
8) Langjökull S. Dome (27)	–1247	841*	–50	–1430
9) Hofsjökull E (35)	–980	840	–490	–1510
10) Hofsjökull N (36)	–820	706	+30	–1320
11) Hofsjökull SW (35)	–960	951	–50	–1200
12) Köldukvislarjökull (32)	–466	707*	+386	–740
13) Tungnaarjökull (32)	–1141	780*	–1355	–1529
14) Dyngjujökull (31)	–44	792	+422	–308
15) Brúarjökull (30)	–237	621*	+344	–713
16) Eyjabakkajökull (32)	–700	766	–359	–1417

Scandinavia				
Glacier (record length, years)	**Bclim Mean** (mm w.e. yr^{-1}) 1991–2020	**Bclim Std. dev.** (mm w.e. yr^{-1}) 1991–2020	**Bclim** (mm w.e. yr^{-1}) 2021/22	**Bclim** (mm w.e. yr^{-1}) 2022/23
17) Engabreen (54)	–62	972	+145	–1101
18) Langfjordjokulen (33)	–953	771*	–1909	–1652
19) Marmaglaciaren (32)	–494	568*	–427	–1256
20) Rabots (42)	–533	648*	–943	–1565
21) Riukojietna (37)	–701	734*	–795	–1347
22) Storglaciaren (78)	–235	747	–212	–812
23) Tarfalaglaciaren (30)	–331	1170	—	—

Svalbard				
Glacier (record length, years)	**Bclim Mean** (mm w.e. yr^{-1}) 1991–2020	**Bclim Std. dev.** (mm w.e. yr^{-1}) 1991–2020	**Bclim** (mm w.e. yr^{-1}) 2021/22	**Bclim** (mm w.e. yr^{-1}) 2022/23
24) Midre Lovenbreen (56)	–498	407	–1416	–976
25) Austre Broggerbreen (57)	–619	451	–1516	–948
26) Kongsvegen (37)	–146	404	–954	–622
27) Hansbreen (34)	–419	469*	–1457	—

Arctic-wide glacier thinning in 2022/23 was strongest in Scandinavia, where the Bclim average was ~801 mm w.e. more negative than the 1991–2020 mean. Notably, extreme melt across Langfjordjokulen (Bclim = –1652 mm w.e.) coincided with the second consecutive year that summer ablation has extended across the entire glacier surface (Kjøllmoen et al. 2023). Icelandic glacier mass balance in 2022/23 was opposite of the previous year, with enhanced summer melting (section 5c) and reduced winter accumulation resulting in the seventh-most-negative Bclim on record (–1238 mm w.e.; WGMS 2024) for this region. Reduced winter accumulation along the Gulf of Alaska coastline (section 5i) contributed to a low negative Bclim anomaly of –260 mm w.e. for Alaskan glaciers in the 2022/23 balance year.

Glaciers and ice caps at high northern latitudes have been increasingly important contributors to global sea-level rise since the early 1990s (Box et al. 2018). Gravity anomalies measured from the combined GRACE (2002–16) and GRACE-FO (2018–23) satellite missions indicate that pan-Arctic glaciers and ice caps have lost mass at a rate of –177±21 Gt yr^{-1} since 2002 (Fig. 5.23; methods as per Wouters et al. 2019). This rate of annual mass loss was sustained primarily by shrinkage of ice caps and glaciers in Arctic Canada (44%), Svalbard (25%), and the Russian Arctic (21%), which resulted in pan-Arctic losses of –191±20 Gt for the 2021/22 balance year. Decreased mass loss from pan-Arctic glaciers to –157±29 Gt in 2022/23 was associated mainly with reduced mass loss from Arctic Canada, which accounted for only 11% of the 2022/23 total. Conversely, mass loss of –86±40 Gt from Alaskan glaciers accounted for 55% of the total ablated mass in the 2022/23 balance year. Mass loss from pan-Arctic glaciers and ice caps totaling –348±49 Gt between September 2021 and August 2023 contributed 0.96±0.14 mm to global sea-level rise for this two-year period.

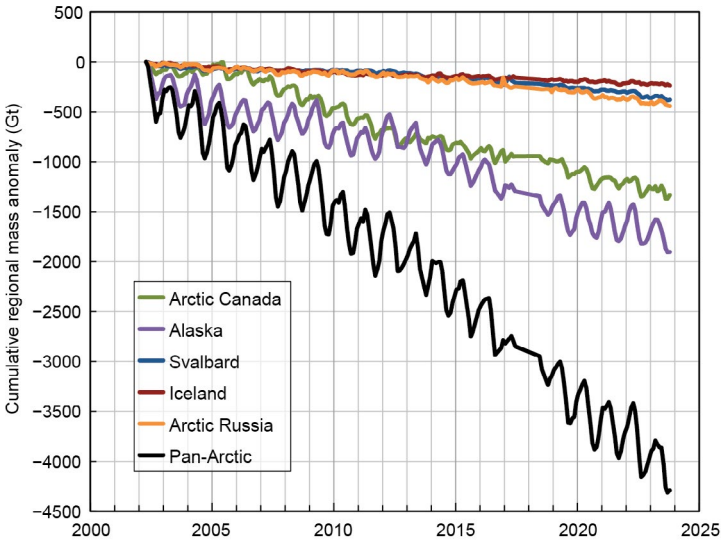

Fig. 5.23. Cumulative changes in regional total stored water (Gt) for the period 2002–23 derived from the Gravity Recovery and Climate Experiment (GRACE) and GRACE Follow-On (GRACE-FO) satellite gravimetry for the five regions shown in Fig. 5.21 and for the total of these five regions (i.e., pan-Arctic). Linear interpolation is applied through a measurement gap between the GRACE and GRACE-FO missions from Jul 2017 to May 2018.

i. Terrestrial snow cover

—L. Mudryk, A. Elias Chereque, C. Derksen, K. Luojus, and B. Decharme

Many components of the Arctic land surface are directly influenced by snow cover, including the surface energy budget, permafrost, terrestrial and freshwater ecosystems, and the ground thermal regime, with implications on the carbon cycle (Brown et al. 2017; Meredith et al. 2019; and references therein). Even following the snow-cover season, the influence of spring snow-melt timing persists through impacts on river-discharge timing and magnitude, surface water, soil moisture, vegetation phenology, and fire risk (Meredith et al. 2019).

Historical snow-cover extent (SCE) anomalies (relative to the 1991–2020 baseline) for May and June are shown separately for the North American and Eurasian sectors of the Arctic in Fig. 5.24 (data from the NOAA snow chart climate data record; Robinson et al. 2012; see also section 2c5). In 2023, North American May SCE was at a record low (lowest extent in the 57-year record) associated with spring temperatures up to 5°C above normal across the region (section 5c, see Fig. 5.6b), but rebounded slightly by June (fourth lowest). In the Eurasian sector, May anomalies were close to the 1991–2020 average but were well below normal by June (ninth lowest in the 57-year record).

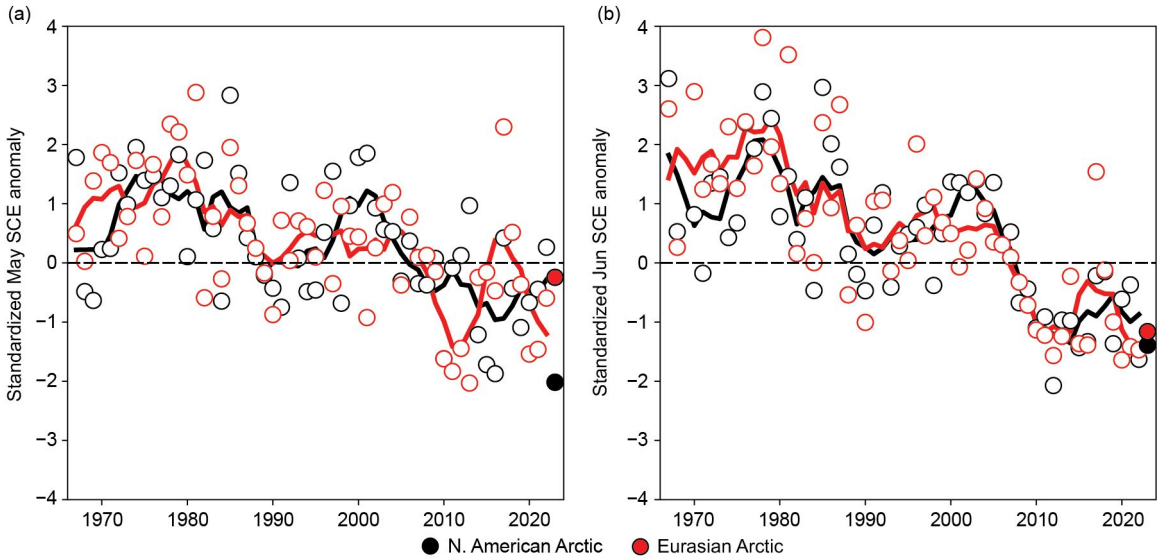

Fig. 5.24. Monthly snow cover extent (SCE) anomalies for Arctic terrestrial land areas (>60°N) for (a) May and (b) Jun from 1967 to 2023. Anomalies are relative to the average for 1991–2020 and standardized (each observation differenced from the mean and divided by the standard deviation, and thus unitless). Solid black and red lines depict five-year running means for North America and Eurasia, respectively. Filled circles highlight 2023 anomalies. (Source: Robinson et al. 2012.)

Snow-cover duration (SCD) anomalies for the 2022/23 snow season (relative to a 1998/99 to 2017/18 climatology) are shown across the Arctic in Figs. 5.25a,b (data from the NOAA daily Interactive Multisensor Snow and Ice Mapping System snow cover product; U.S. National Ice Center 2008). Anomalies in the total number of days with snow cover were computed separately for each half of the snow season: August 2022 to January 2023, referred to as "onset period" (Fig. 5.25a), and February 2023 to July 2023, referred to as "melt period" (Fig. 5.25b). Snow-cover duration anomalies indicate a combination of early and late snow onset with an especially variable pattern across the North American Arctic. Across central and eastern Eurasia, Arctic snow onset occurred earlier than normal while across western Eurasia there was a modest delay. While spring snow melt across Eurasia was not as extensive as in the previous two years (Thoman et al. 2022; Moon et al. 2023), far northern coastal regions across the continent still had above-normal numbers of snow-free days, indicative of earlier snow melt. Across North America, the extensive snow melt signaled by record-low May SCE is also apparent in spring SCD anomalies, where a broad swath of mainland Nunavut and Northwest Territories in Canada saw an increase of more than 50% in the number of snow-free days during the melt period. The early spring snow melt seen there was compounded by summer precipitation deficits (section 5d, see

Fig. 5.8c) and together likely contributed to the extensive summer 2023 wildfire season (see Sidebar 7.1), which forced the complete evacuation of numerous communities in the western Canadian Arctic.

Finally, snow-water equivalent (SWE), a measure of snow amount, is used to characterize Arctic snow accumulation over the 2022/23 season. The SWE fields during April–June were obtained from four daily-frequency gridded products over the 1981–2023 period: 1) the European Space Agency Snow Climate Change Initiative (CCI) SWE version 1 product derived through a combination of satellite passive microwave brightness temperatures and climate station snow depth observations (Luojus et al. 2022); 2) MERRA-2; (GMAO 2015) daily SWE fields; 3) SWE output from the ERA5-Land analysis (Muñoz Sabater 2019); and 4) the physical snowpack model

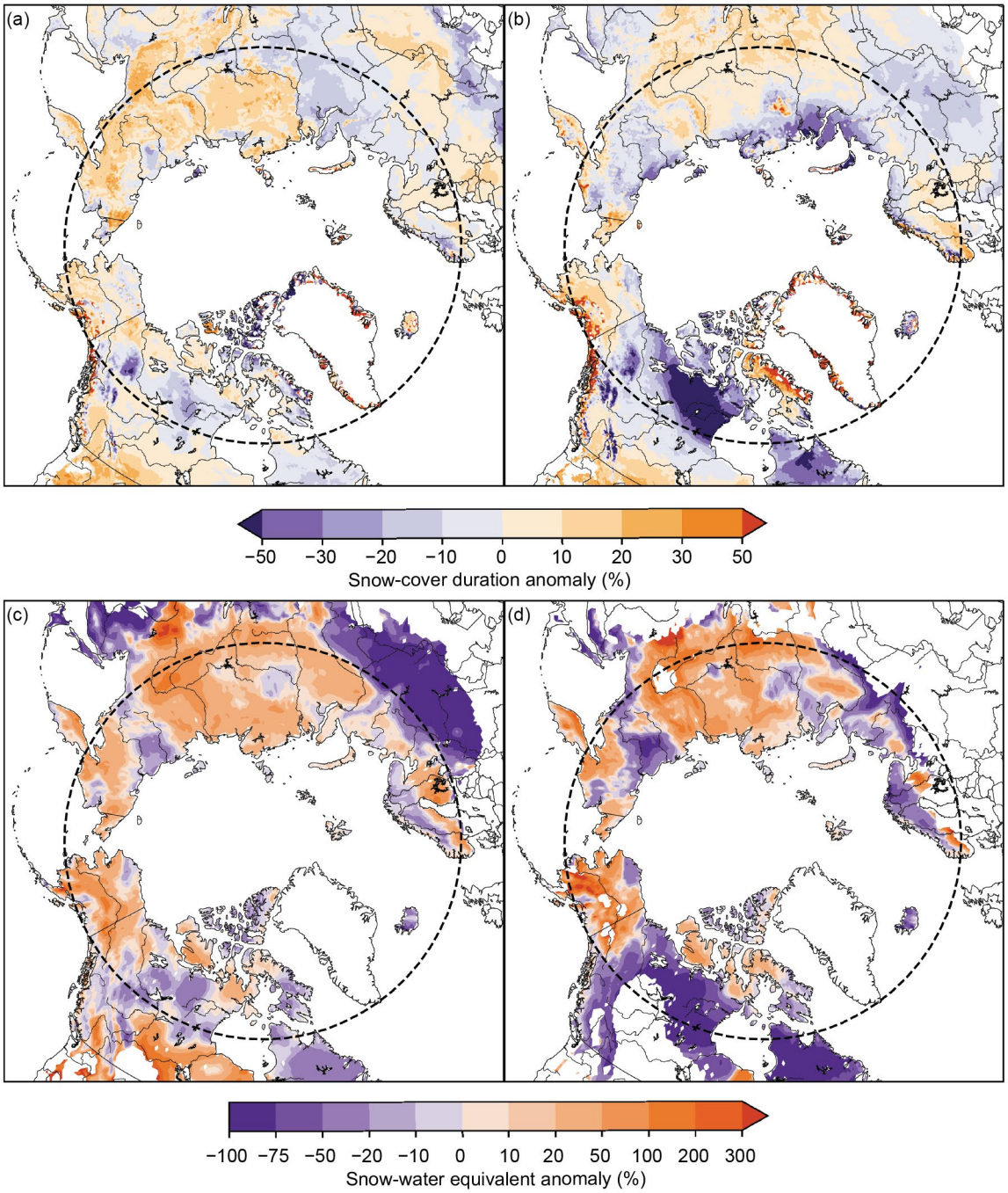

Fig. 5.25. Snow-cover duration anomalies (% difference relative to the climatological number of snow-free days for the 1998/99–2017/18 baseline) for the 2022/23 snow year: (a) snow onset period (Aug 2022–Jan 2023) and (b) snow melt period (Feb 2023–Jul 2023). Purple (orange) indicates more (fewer) snow-free days than average. Snow water equivalent (SWE) anomalies (% difference from the 1991–2020 baseline) in 2023 for (c) Apr and (d) May. Purple (orange) indicates lower (higher) snow amounts than average. Latitude 60°N is marked by the gray dashed circle; land north of this defines the Arctic terrestrial area considered in this study. (Source: [a],[b] U.S. National Ice Center [2008]; [c],[d] four SWE products from Snow CCI [Luojus et al. 2022]; MERRA2 [GMAO 2015]; ERA5-Land [Muñoz Sabater 2019]; and Crocus [Brun et al. 2013].)

Crocus (Brun et al. 2013) driven by near-surface meteorological variables from ERA5. Reduced availability of climate-station snow depth measurements limits the accuracy of the Snow CCI SWE product during May and June, hence it is omitted for those months. An approach using gridded products is required because in situ observations alone are too sparse to be representative of hemispheric snow conditions, especially in the Arctic.

For April, the SWE fields from each product were aggregated across the Arctic land surface (>60°N) for both North American and Eurasian sectors and standardized relative to the 1991–2020 baseline to produce standardized April snow-mass anomalies. The ensemble mean anomalies and the range of product estimates are presented in Fig. 5.26. April is chosen because it is the approximate month that total snow mass across the terrestrial pan-Arctic region peaks, reflecting total snowfall accumulations since the preceding autumn and before increasing May and June temperatures lead to melt. Snow-mass anomalies for April 2023 indicate snow accumulation above the 1991–2020 baseline across both continents (consistent with the wet winter reported in section 5d), but especially in Eurasia where it was the fifth-highest accumulation in the record. The spatial patterns of monthly mean SWE (Figs. 5.25c,d) illustrate how this accumulation varied regionally during April and May. Regions with positive SWE anomalies in April intensified through May (most of Alaska, large parts of central and eastern Siberia), which suggests that snow in these regions took longer to melt compared to the historical baseline (also supported by the longer-than-normal snow-cover duration during the melt season in Fig. 5.25b). However, mainland Arctic Canada experienced extensive reductions in SWE during May that extended northward into the southern Canadian Arctic Archipelago during June (not shown). By this time, snow had mostly melted across both continents except for Baffin and the Queen Elizabeth Islands in the Canadian Arctic Archipelago.

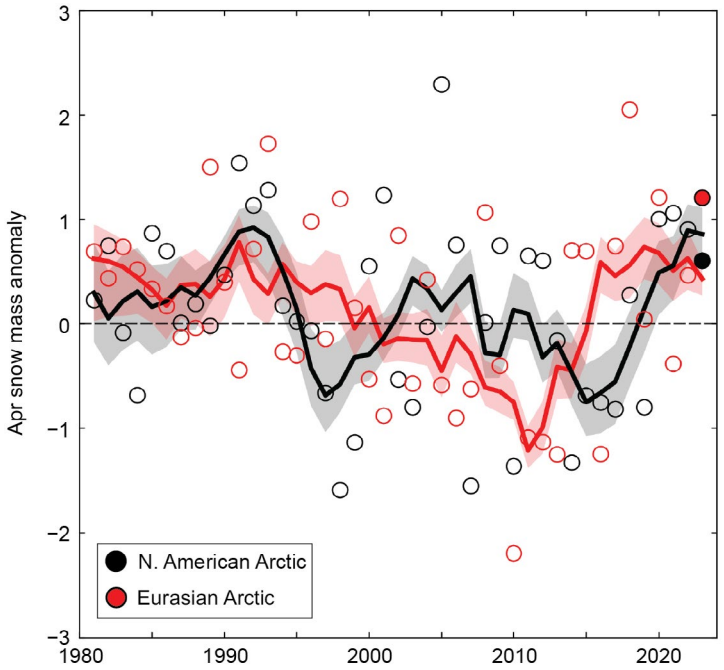

Fig. 5.26. Mean Apr snow-mass anomalies for Arctic terrestrial areas calculated for North American (black) and Eurasian (red) sectors of the Arctic over the period 1981–2023. Anomalies are relative to the 1991–2020 average and standardized (each observation differenced from the mean and divided by the standard deviation, and thus unitless). Filled circles highlight 2023 anomalies. Solid black and red lines depict five-year running means for North America and Eurasia, respectively, and the spread among the running means for individual datasets is shown in shading. (Source: Four snow water equivalent products from Snow CCI [Luojus et al. 2022], MERRA2 [GMAO 2015], ERA5-Land [Muñoz Sabater 2019], and Crocus [Brun et al. 2013].)

Overall, the 2022/23 snow season shares similarities with those from several recent years. Despite above-average seasonal snow accumulation, large springtime temperature anomalies still resulted in earlier-than-normal melt. During the 2022/23 season, this earlier-than-normal melt occurred across portions of North America, whereas in previous years, it occurred on the Eurasian continent. Looking historically across Eurasia, the June snow-extent values for 11 of the past 14 years represent near-complete absence of snow cover across the continent except for residual amounts in higher-elevation locations. Compared to historical conditions, early Eurasian spring melt has resulted in approximately two additional weeks of snow-free conditions.

j. Permafrost

—S. L. Smith, V. E. Romanovsky, K. Isaksen, K. E. Nyland, N. I. Shiklomanov, D. A. Streletskiy, and H. H. Christiansen

Permafrost refers to earth materials (e.g., bedrock, mineral soil, organic matter) that remain at or below 0°C for at least two consecutive years, although most permafrost has existed for centuries to many millennia. Extensive regions of high-latitude landscapes are underlain by permafrost. The active layer, which thaws and refreezes annually, overlies the permafrost. Warming of permafrost (especially if ice-rich), active layer thickening, and ground-ice melt cause changes in surface topography, hydrology, and landscape stability, with implications for Arctic infrastructure, ecosystem integrity, and human livelihoods (Romanovsky et al. 2017; Hjort et al. 2022; Wolken et al. 2021). Changes in permafrost conditions can also affect the rate of greenhouse gas release to the atmosphere, potentially accelerating global warming (Miner et al. 2022; Schuur et al. 2022).

Permafrost conditions respond to shifts in the surface energy balance through a combination of interrelated changes in ground temperature and active layer thickness (ALT). Ground temperatures fluctuate seasonally near the surface, while below the depth of seasonal temperature variation they reflect longer-term climate. Long-term changes in permafrost temperatures are driven by changes in air temperature (Romanovsky et al. 2017); however, permafrost temperature trends also show local variability due to other influences such as snow cover, vegetation characteristics, and soil moisture (Smith et al. 2022). Monitoring sites across the Arctic (Fig. 5.27) have been recording ground temperature in the upper 30 m for up to five decades, providing critical data on changes in permafrost condition. Observed changes in ALT are more reflective of shorter-term (year-to-year) fluctuations in climate and are especially sensitive to changes in summer air temperature and precipitation.

Permafrost temperatures continue to increase on a decadal time scale across the Arctic. Greater increases are generally observed in colder permafrost (temperature <–2°C) at higher latitudes (Smith et al. 2022, 2023), partly due to greater increases in air temperature (Figs. 5.27, 5.28). Over the last 29 years, positive ALT trends (Fig. 5.29) are evident from all permafrost regions examined, but trends are less apparent for the Alaskan North Slope, northwest Canada, and East Siberia (Smith et al. 2023).

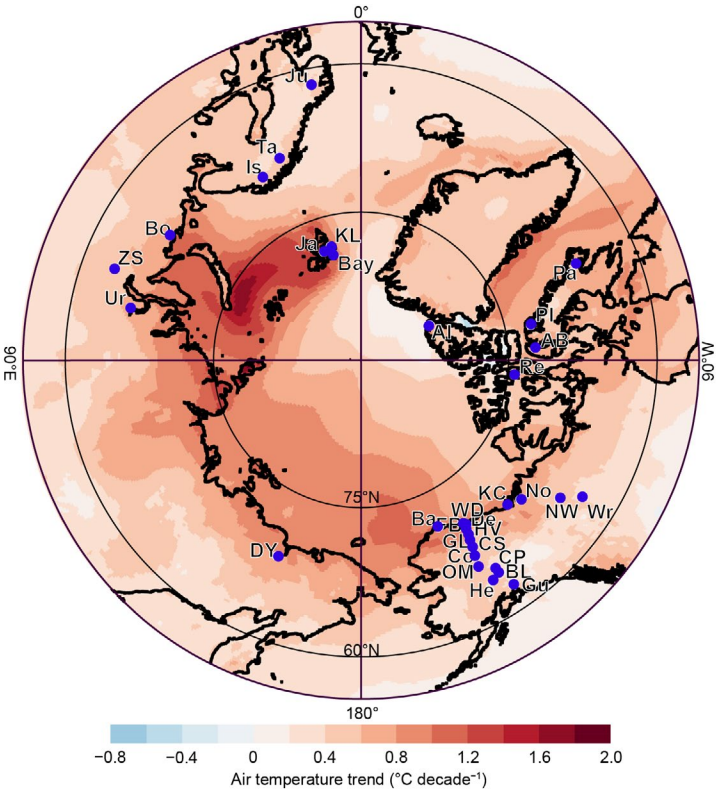

Fig. 5.27. Locations of the permafrost temperature monitoring sites (for which data are shown in Fig. 5.28), superimposed on average surface air temperature trends (°C decade^{-1}) during 1981–2023 from ERA5 reanalysis (Hersbach et al. 2020; data available at https://cds.climate.copernicus.eu), which largely covers the period of record for permafrost monitoring. See Table 5.2 for site names. Information about these sites is available at http://gtnpdatabase.org/ and https://permafrost.gi.alaska.edu/sites_map.

1. PERMAFROST TEMPERATURES

Permafrost temperatures in 2023 were the highest on record at 9 of 17 sites reporting (Table 5.2). However, cooling that began in 2020 has continued at some sites, and temperatures were lower in 2023 compared to 2022 at six North American sites (Figs. 5.28a,b). In the Beaufort-Chukchi region, permafrost temperatures in 2023 were <0.1°C lower than in 2022 at three sites (Fig. 5.28a). The observed permafrost cooling in this region resulted from lower mean annual air temperatures after 2019. At Deadhorse (Prudhoe Bay, Alaska), for example, the average air temperature was almost 4°C lower in 2022 compared to 2018 and 2019. However, the air temperature in 2023 was similar to 2018 and 2019, being 3°C higher than 2022,

but the full effect is not yet observed at depths of 15 m–20 m. For discontinuous permafrost in Alaska and northwestern Canada, the 2023 permafrost temperatures were the highest on record at two of six sites reporting with slightly lower or similar temperatures compared to 2022 at the other sites (Fig. 5.28b). In the high Arctic cold permafrost of Svalbard, where there was a short period of cooling after 2020 (Isaksen et al. 2022), permafrost was warmer in 2023 compared to 2022 (Fig. 5.28d). In warmer permafrost at other Nordic sites, temperatures in 2023 were the highest on record (Fig. 5.28d; Table 5.2).

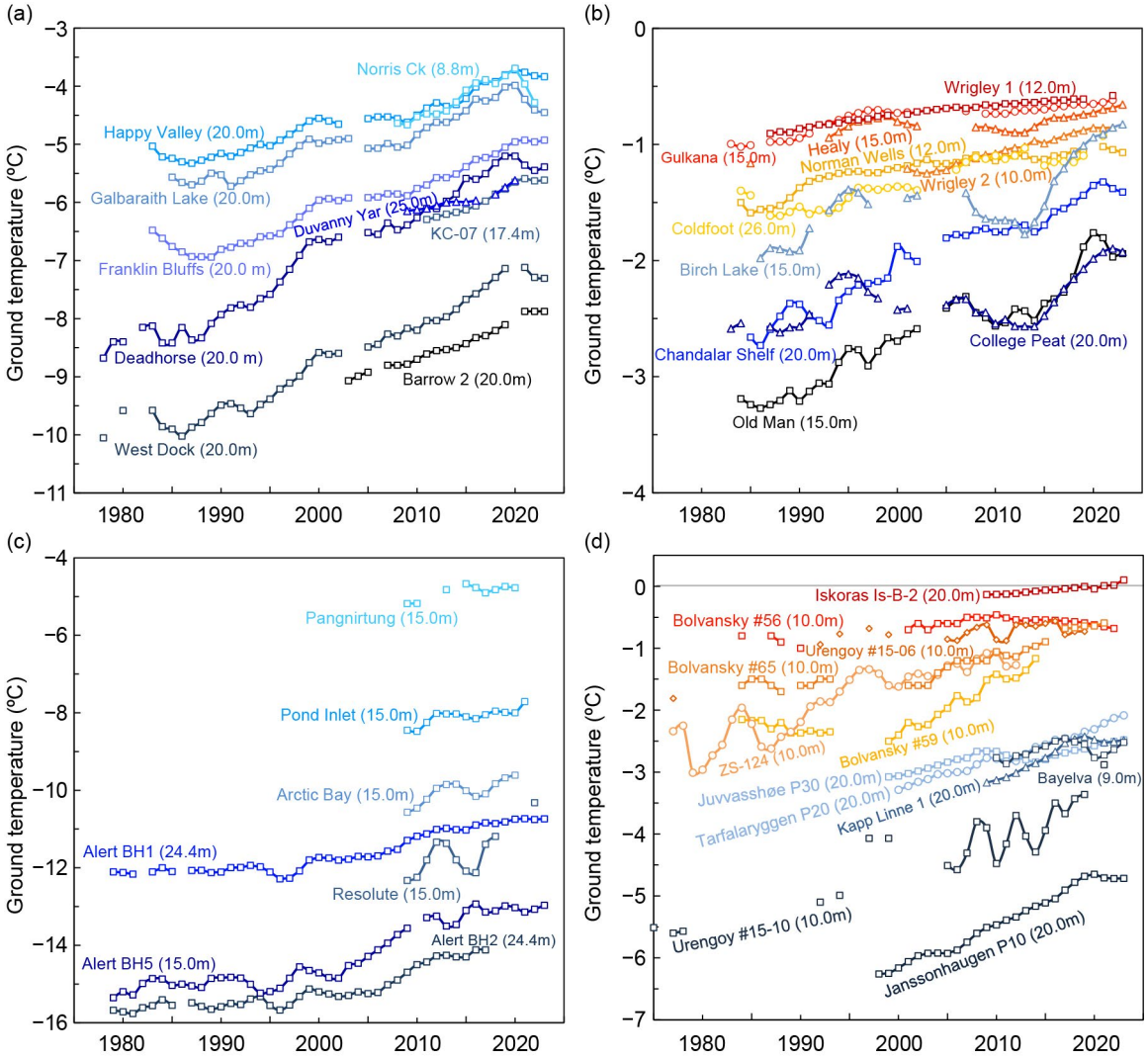

Fig. 5.28. Time series of mean annual ground temperature (°C) at depths of 9 m–26 m below the surface at selected measurement sites that fall roughly into Adaptation Actions for a Changing Arctic Project priority regions (see Romanovsky et al. 2017): (a) cold continuous permafrost of northwestern North America and northeastern East Siberia (Beaufort-Chukchi region); (b) discontinuous permafrost in Alaska and northwestern Canada; (c) cold continuous permafrost of eastern and High Arctic Canada (Baffin Davis Strait); and (d) continuous to discontinuous permafrost in Scandinavia, Svalbard, and Russia/Siberia (Barents region). Temperatures are measured at or near the depth of zero annual amplitude where the seasonal variations of ground temperature are less than 0.1°C. Note differences in y-axis value ranges. Red and orange lines are used for warmer permafrost, and blue and black lines are used for colder permafrost. Borehole locations are shown in Fig. 5.27 (data are updated from Smith et al. 2023).

Throughout the Arctic, warming of permafrost with temperatures ~0°C to –2°C is slower (generally <0.3°C decade^{-1}) than colder permafrost sites due to latent heat effects related to melting ground ice. At cold continuous permafrost sites in the Beaufort-Chukchi region, permafrost temperatures have increased by 0.4°C decade^{-1} to 0.8°C decade^{-1} with similar increases (0.4°C decade^{-1} to 1.1°C decade^{-1}) for the eastern and high Canadian Arctic (Figs. 5.28a,c; Table 5.2). Permafrost in Svalbard (Janssonhaugen and Kapp Linne) has warmed by up to 0.7°C decade^{-1} (Fig. 5.28d; Table 5.2), and significant permafrost warming has been detected to 100-m depth at Janssonhaugen (Isaksen et al. 2022).

Table 5.2. Rate of change in mean annual ground temperature (°C decade^{-1}) for permafrost monitoring sites shown in Fig. 5.27. The periods of record are shown in parenthesis below the rates of change. For sites where measurements began prior to 2000, the rate of change for the entire available record and the period after 2000 are provided. Stations with record-high 2023 temperatures are underlined in red. Asterisks denote sites not reporting in 2023.

Region	Site	Entire Record	Since 2000
Northeast Siberia *(Beaufort-Chukchi Region)*	Duvany Yar (DY)*	NA	+0.4 (2009–20)
Alaskan Arctic plain *(Beaufort-Chukchi Region)*	West Dock (WD), Deadhorse (De), Franklin Bluffs (FB), Barrow (Ba)	+0.5 to +0.8 (1978–2023)	+0.5 to +0.7 (2000–23)
Northern foothills of the Brooks Range, Alaska *(Beaufort-Chukchi Region)*	Happy Valley (HV), Galbraith Lake (GL)	+0.4 (1983–2023)	+0.4 (2000–23)
Northern Mackenzie Valley *(Beaufort-Chukchi Region)*	Norris Ck (No)*, KC-07 (KC)	NA	+0.6 to +0.7 (2008–23)
Southern foothills of the Brooks Range, Alaska *(Discontinuous Permafrost: Alaska and NW Canada)*	Coldfoot (Co)*, Chandalar Shelf (CS), Old Man (OM)	+0.1 to +0.3 (1983–2023)	+0.2 to +0.3 (2000–23)
Interior Alaska *(Discontinuous Permafrost: Alaska and NW Canada)*	College Peat (CP), Birch Lake (BL), Gulkana (Gu)*, Healy (He)	+0.1 to +0.3 (1983–2023)	<+0.1 to +0.4 (2000–23)
Central Mackenzie Valley *(Discontinuous Permafrost: Alaska and NW Canada)*	Norman Wells (NW), Wrigley (Wr)*	+0.1 (1984–2023)	+0.1 to +0.2 (2000–23)
Baffin Island *(Baffin Davis Strait Region)*	Pangnirtung (Pa)*, Pond Inlet (PI)*	NA	+0.4 (2009–21)
High Canadian Arctic *(Baffin Davis Strait Region)*	Resolute (Re)*	NA	+1.1 (2009–22)
High Canadian Arctic *(Baffin Davis Strait Region)*	Alert (Al) @ 15 m, Alert (Al) @ 24 m	+0.6, +0.4 (1979–2023)	+0.9, +0.6 (2000–23)
Northwest Siberia *(Barents Region)*	Urengoy 15-06* and 15-08* (Ur)	+0.2 to +0.5 (1974–2021)	+0.1 to +0.8 (2005–21)
Russian European North *(Barents Region)*	Bolvansky 56* and 65* (Bo)	+0.1 to +0.3 (1984–2022)	0 to +0.5 (2001–22)
Svalbard *(Barents Region)*	Janssonhaugen (Ja), Bayelva (Bay)*, Kapp Linne 1 (KL)	+0.7 (1998–2023)	+0.1 to +0.7 (2000–23)
Northern Scandinavia *(Barents Region)*	Tarfalarggen (Ta), Iskoras Is-B-2 (Is)	NA	+0.1 to +0.5 (2000–23)
Southern Norway *(Barents Region)*	Juvvasshøe (Ju)	+0.2 (1999–2023)	+0.2 (2000–23)

In the discontinuous permafrost regions of Scandinavia (Juvvasshøe and Iskoras), warming is continuing at rates of about 0.1°C decade^{-1} to 0.2°C decade^{-1}, with thawing occurring at Iskoras (Fig. 5.28d; Isaksen et al. 2022). Similar rates (Figs. 5.28b,d) are observed in the warm permafrost of northwestern North America (e.g., Smith et al. 2024) and Russia (Malkova et al. 2022).

2. ACTIVE LAYER THICKNESS

Active layer thickness is measured directly using mechanical probing and thaw tubes and indirectly by interpolating the maximum seasonal depth of the 0°C isotherm from borehole

temperature records. The ALT trends shown in Fig. 5.29 are primarily generated from spatially distributed mechanical probing across representative landscapes to determine the depth to the top of permafrost.

The Alaskan Interior and West Siberia experienced 2023 ALT well above the 2009–18 mean, continuing a several-year extreme trend in these regions (e.g., Kaverin et al. 2021). Increases in ALT are greatest for the Alaskan Interior, the Russian European North, and West Siberia at 0.03 m yr^{-1}, 0.01 m yr^{-1}, and 0.02 m yr^{-1}, respectively.

The ALT regional anomalies for 2023 were within 0.1 m of the 2009–18 mean for the North Slope of Alaska, Greenland, northwest Canada (2022), and East Siberia. Negligible trends in ALT from ice-rich sites on the North Slope of Alaska have been attributed to subsidence (Nyland et al. 2021). Widespread thaw and subsidence across northwest Canada have been documented (O'Neill et al. 2023). Consolidation within the ice-rich shallow permafrost layer resulting from decadal and longer-term thaw may not be detected with manual probing alone, and correcting ALT for ground surface displacement can improve the correspondence between increasing air temperatures and thaw depth (Nyland et al. 2021; Smith et al. 2022). Reduced ALT in 2023 for some regions, including Greenland, the Russian European North, and East Siberia, could also be due to short-term cooling superimposed on the overall positive trend (Smith et al. 2023). In Svalbard, record-high ALT anomalies occurred after western Spitsbergen experienced its warmest summer on record.

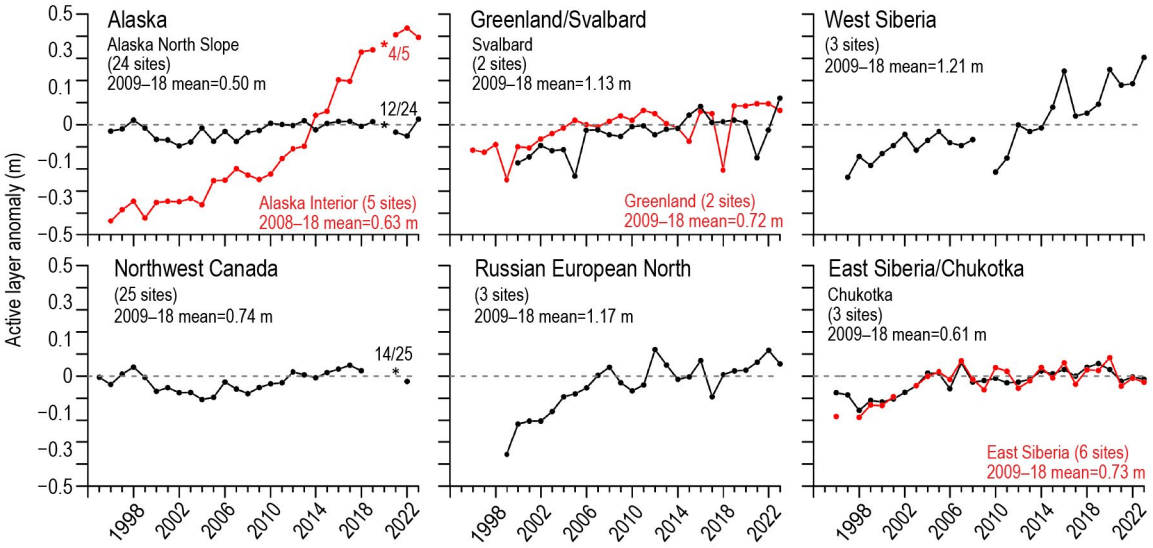

Fig. 5.29. Average annual active layer thickness (ALT) anomalies, relative to the 2009–18 mean, for six Arctic regions observed by the Circumpolar Active Layer Monitoring program. Positive and negative anomalies indicate thicker or thinner ALT than the 10-yr reference, respectively. Numbers of sites vary by region because only sites with >20 years of continuous thaw depth observations from the end of the thaw season are included. Asterisks represent atypical observations, for example, due to pandemic-related restrictions (fraction of sites for these years are provided on graph). Canadian ALT is derived from thaw tubes that record the maximum thaw depth over the previous year. Since Canadian sites were not visited in 2020 and 2021, the maximum thaw depth recorded during the 2022 visit could have occurred any summer from 2019 through 2021, although the data point is plotted in 2021. Site-specific data and metadata are available at www2.gwu.edu/~calm/.

k. Tundra greenness

—G. V. Frost, M. J. Macander, U. S. Bhatt, L. T. Berner, J. W. Bjerke, H. E. Epstein, B. C. Forbes, G. Jia, M. J. Lara, P. M. Montesano, R. Í. Magnússon, C. S. R. Neigh, G. K. Phoenix, H. Tømmervik, C. Waigl, D. A. Walker, and D. Yang

The Arctic tundra biome occupies Earth's northernmost lands, collectively encompassing a 5.1 million km^2 region that resembles a wreath bound by the Arctic Ocean to the north and the boreal forest biome to the south (Raynolds et al. 2019). While Arctic tundra ecosystems are treeless and lack the vertical structure of forest ecosystems, they are heterogeneous across multiple spatial scales, ranging from large-scale latitudinal climate gradients to local-scale gradients of soil, hydrological, and permafrost conditions (Fig. 5.30). The Arctic tundra biome is a global hotspot of contemporary environmental change due to the sensitivity of these ecosystems to rapidly changing temperature, sea-ice, snow, and permafrost conditions (Bhatt et al. 2021; sections 5c, 5e, 5i, 5j, respectively). In the late 1990s, Earth-observing satellites began to detect a sharp increase in the productivity of tundra vegetation, a phenomenon known today as "the greening of the Arctic."

Global vegetation has been continuously monitored from space since late 1981 by the Advanced Very High Resolution Radiometer (AVHRR), a series of sensors that is well into its fifth decade of operation onboard a succession of polar-orbiting satellites. In 2000, the Moderate Resolution Imaging Spectroradiometer (MODIS) entered service and provides an independent, complementary data record with higher spatial resolution and improved calibration, with future continuity ensured by the Visible Infrared Imaging Radiometer Suite (VIIRS) sensors, first launched in 2011 (Román et al. 2024). All of these spaceborne sensors monitor global vegetation greenness using

Fig. 5.30. The Arctic tundra biome spans wide climatic and environmental gradients that produce strong contrasts in vegetation biomass and height. High Arctic ecosystems support discontinuous cover of low-growing plants (upper left; Svalbard Archipelago, Norway), while warmer parts of the Low Arctic support mosaics of open tundra and tall shrubs (upper right; Ural Mountains foothills, northwestern Siberia). Tundra shrub expansion is a key driver of Arctic greening; tree expansion has also been documented but has generally been much slower (lower left; Brooks Range, Alaska). Permafrost processes, ecological disturbances, extreme weather events, and Arctic herbivores such as muskox (lower right; Yukon-Kuskokwim Delta, Alaska) introduce important sources of local variability that operate against the backdrop of long-term trends. Photos by G. Phoenix (upper left), G. V. Frost (upper right), and L. Berner (bottom row).

the Normalized Difference Vegetation Index (NDVI), a spectral metric that exploits the unique way in which green vegetation absorbs and reflects visible and infrared light.

The long-term AVHRR NDVI dataset reported here is GIMMS-3g+ with a spatial resolution of about 8 km (Pinzon et al. 2023). For MODIS, we computed trends at a much higher spatial resolution of 500 m, combining 16-day NDVI products from the *Terra* (MOD13A1, version 6.1) and *Aqua* (MYD13A1, version 6.1) satellites (Didan 2021a,b), referred to as MODIS MCD13A1. All data were masked to the extent of the Circumpolar Arctic Vegetation Map (Raynolds et al. 2019) and exclude permanent ice and water. We summarize the GIMMS-3g+ and MODIS records for the annual maximum NDVI (MaxNDVI), the peak greenness value observed in midsummer.

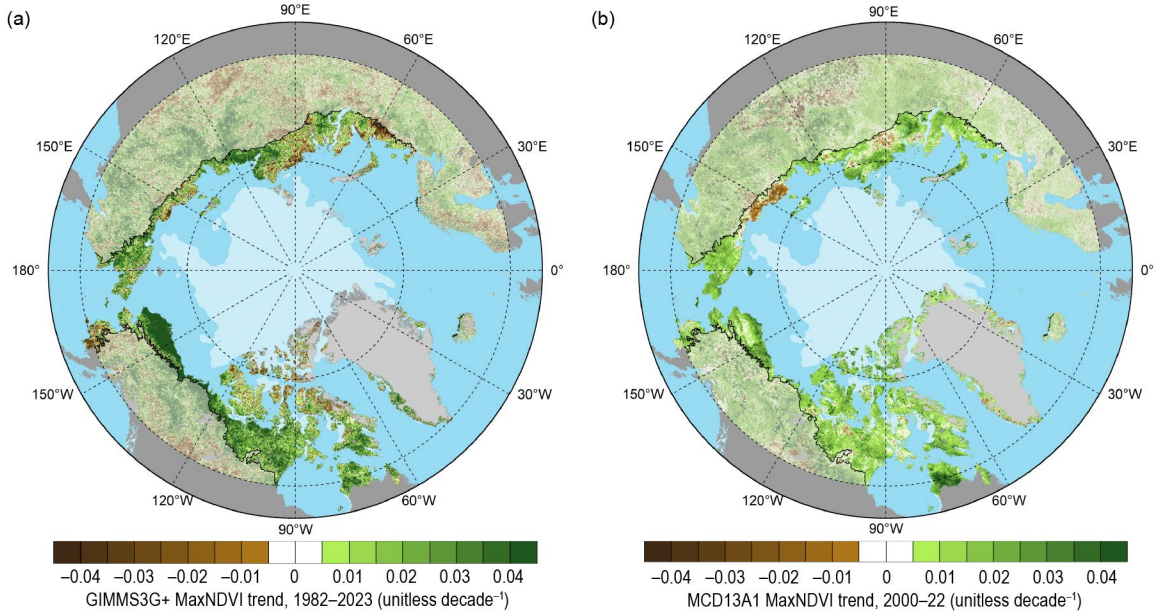

Fig. 5.31. Magnitude of the maximum Normalized Difference Vegetation Index (MaxNDVI) trend calculated as the change decade^{-1} via ordinary least-squares regression for Arctic tundra (solid colors), and boreal forest (muted colors) north of 60° latitude during (a) 1982–2022 based on the AVHRR GIMMS 3-g+ dataset, and (b) 2000–23 based on the MODIS MCD13A1 dataset. The circumpolar treeline is indicated by a black line, and the 2023 minimum sea-ice extent is indicated by light shading in each panel.

Both AVHRR and MODIS have recorded increasing MaxNDVI across most of the Arctic since 1982 and 2000, respectively (Figs. 5.31a,b), with the strongest greening trends in northern Alaska, continental Canada, and north-central Siberia. Both sensors show virtually identical trends in circumpolar mean MaxNDVI for the period of overlap (2000–23; Fig. 5.32), but the AVHRR record displays higher interannual variability and there are some differences in the trend spatial pattern. The AVHRR record generally shows strong greening in warmer, continental areas near treeline, but declining NDVI ("browning") in the High Arctic, particularly the Canadian Arctic Archipelago. MODIS has recorded greening virtually throughout the circumpolar Arctic except in portions of north-central and northeastern Siberia. Some of the AVHRR versus MODIS differences may reflect the different observational periods of the two records. The neighboring boreal forest biome

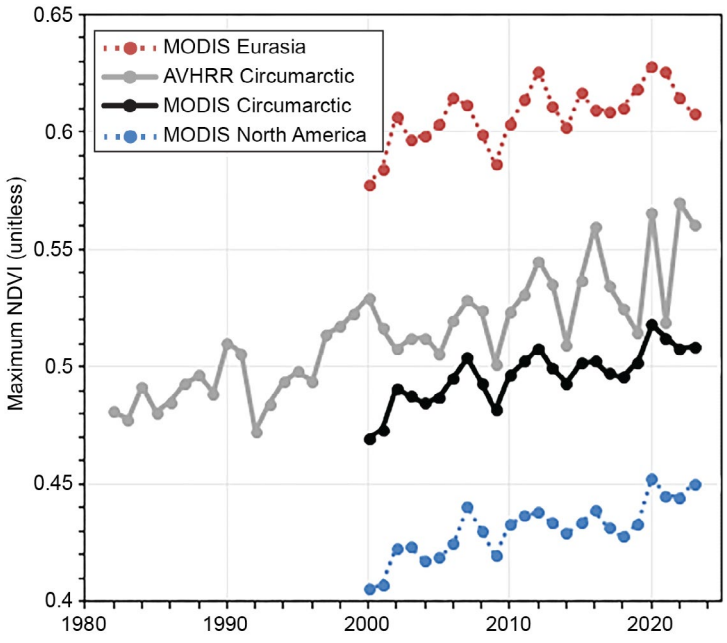

Fig. 5.32. Time series of the maximum Normalized Difference Vegetation Index (MaxNDVI) from the long-term AVHRR GIMMS-3g+ dataset (1982–2023) for the circumpolar Arctic (gray) and from the MODIS MCD13A1 (2000–23) dataset for the Eurasian Arctic (red), North American Arctic (blue), and the circumpolar Arctic (black).

(see Figs. 5.30a,b, 5.31), distributed across the North American and Eurasian continents, has also experienced rapid environmental change in recent decades and exhibits mixed trends that are linked to interactions among climate change, wildfire, human land use, and other factors (Berner and Goetz 2022).

In 2023, the circumpolar mean MaxNDVI for tundra regions was the third-highest value ever observed in both satellite records (Fig. 5.32). The AVHRR-observed MaxNDVI declined 1.9% from the record-high value set the previous year, while the MODIS-observed value increased slightly (0.3%) from the previous year. Notably, the three highest values in both the 42-year AVHRR and 24-year MODIS records have all been recorded within the last four years. Tundra greenness was much higher than normal across most of the North American Arctic and especially in the eastern Beaufort Sea region, which experienced exceptionally warm summer temperatures (Fig. 5.33; section 5c). The Eurasian Arctic, however, displayed comparatively low tundra greenness values, particularly in the East Siberian Sea region where sea ice remained extensive for much of the summer (Fig. 5.33), and newly burned areas have accumulated after multiple wildfires during 2019–23 (Zhu et al. 2023). Nonetheless, the overall trend in MODIS-observed circumpolar MaxNDVI remains strongly positive (greening).

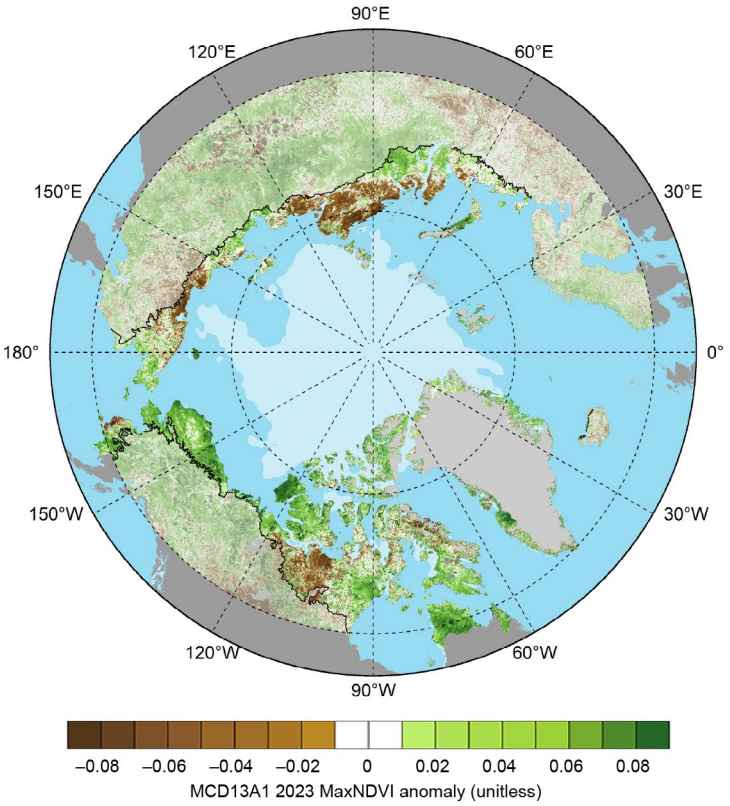

Fig. 5.33. Circumpolar maximum Normalized Difference Vegetation Index (MaxNDVI) anomalies for the 2023 growing season relative to mean values (2000–23) for Arctic tundra (solid colors) and boreal forest (muted colors) north of 60° latitude from the MODIS MCD13A1 dataset.

Earth-observing satellites provide foundational datasets for monitoring Arctic environmental change and help to overcome the long-standing barriers to access this region posed by its remoteness, along with new ones arising from the Russian invasion of Ukraine (López-Blanco et al. 2024). Nonetheless, field studies provide crucial information needed to connect spaceborne observations with patterns of change (or stability) on the ground. Increases in the abundance, distribution, and height of Arctic shrubs are a major driver of Arctic greening, and have important impacts on biodiversity, surface energy balance, permafrost temperatures, and biogeochemical cycling, particularly in the Low Arctic (Mekonnen et al. 2021). However, detailed vegetation datasets from colder tundra ecosystems of Victoria Island in the Canadian Arctic Archipelago reveal general increases in the cover of sedges and other herbaceous plants, but decreases in dwarf shrub cover from the early 1990s to circa 2020 (Schaefer 2023). While the driving of Artic greening by warming is likely to continue, ecological disturbances, extreme events, and other causes of browning are also increasing in frequency (Christensen et al. 2021; Magnússon et al. 2023). Understanding the regional variability of complex Arctic greening trends and attributing its drivers continues to be a subject of multi-disciplinary scientific research.

Appendix 1: Acronyms

ALT	active layer thickness
AVHRR	Advanced Very High Resolution Radiometer
Bclim	climatic mass balance
CCI	Climate Change Initiative
DU	Dobson unit
GRACE	Gravity Recovery and Climate Experiment
GRACE-FO	Gravity Recovery and Climate Experiment Follow-on
MaxNDVI	Maximum Normalized Difference Vegetation Index
MLS	microwave limb sounder
MODIS	Moderate Resolution Imaging Spectroradiometer
NDVI	Normalized Difference Vegetation Index
NSIDC	National Snow and Ice Data Center
OMI	Ozone Monitoring Instrument
PCH	polar cap averaged geopotential heights
PROMICE	Programme for Monitoring of the Greenland Ice Sheet
SCD	snow-cover duration
SCE	snow-cover extent
SLP	sea-level pressure
SMB	surface mass balance
SSMIS	Special Sensor Microwave Imager/Sounder
SST	sea-surface temperature
SSW	sudden stratospheric warming
SWE	snow water equivalent
TOC	total ozone column
UV	ultraviolet
UVI	ultraviolet index
VIIRS	Visible Infrared Imaging Radiometer Suite
WMO	World Meteorological Organization

Appendix 2: Datasets and sources

Section 5b Atmosphere

Sub-section	General Variable or Phenomenon	Specific dataset or variable	Source
5b, 5b1, 5b2	Geopotential Height	ERA5	https://www.ecmwf.int/en/forecasts/dataset/ecmwf-reanalysis-v5
5b2	Ozone, Total Column and Stratospheric	Aura OMI/MLS	https://disc.gsfc.nasa.gov/datasets/ML2O3_004/summary
5b2	Ozone, Total Column and Stratospheric	Bodeker Scientific	http://www.bodekerscientific.com/data/total-column-ozone
5b2	Ozone, Total Column and Stratospheric	OMTO3	https://disc.gsfc.nasa.gov/datasets/OMTO3_003/summary

Section 5c Surface air temperature

Sub-section	General Variable or Phenomenon	Specific dataset or variable	Source
5c2	Temperature, [Near] Surface	NASA GISTEMP v4	https://data.giss.nasa.gov/gistemp/
5c3	Temperature, [Near] Surface	ERA5	https://www.ecmwf.int/en/forecasts/dataset/ecmwf-reanalysis-v5
5c3	Pressure, Sea Level or Near-Surface	ERA5	https://www.ecmwf.int/en/forecasts/dataset/ecmwf-reanalysis-v5

Section 5d Precipitation

Sub-section	General Variable or Phenomenon	Specific dataset or variable	Source
5d2, 5d3, 5d4, 5d5	Precipitation	ERA5	https://www.ecmwf.int/en/forecasts/dataset/ecmwf-reanalysis-v5
5d4	Precipitation	GPCC	https://opendata.dwd.de/climate_environment/GPCC/html/download_gate.html

Section 5e Sea-surface temperature

Sub-section	General Variable or Phenomenon	Specific dataset or variable	Source
5e	Sea Surface Temperature	NOAA Optimum Interpolation SST (OISST) v2	https://www.ncei.noaa.gov/products/optimum-interpolation-sst
5e	Sea Ice Concentration	NOAA NSIDC Climate Data Record of Passive Microwave Sea Ice Concentration, Version 4	https://nsidc.org/data/g02202
5e	Sea Ice Concentration	NOAA/NSIDC Climate Data Record of Passive Microwave Sea Ice Concentration, Version 2	https://nsidc.org/data/g10016

Section 5f Sea ice

Sub-section	General Variable or Phenomenon	Specific dataset or variable	Source
5f1	Sea Ice Extent	NSIDC Sea Ice Extent	https://nsidc.org/data/g02135
5f2	Sea Ice Thickness	Cryosat-2/SMOS	https://earth.esa.int/eogateway/catalog/smos-cryosat-l4-sea-ice-thickness
5f2	Sea Ice Thickness	ICESat-2	https://icesat-2.gsfc.nasa.gov/icesat-2-data

Section 5g Greenland Ice Sheet

Sub-section	General Variable or Phenomenon	Specific dataset or variable	Source
5g	Albedo	MODIS (Greenland)	https://nsidc.org/data/MODGRNLD/versions/1
5g	Glacier Ablation	PROMICE Glacier Front Line (Greenland)	https://doi.org/10.22008/promice/data/calving_front_lines
5g	Glacier Mass, Area or Volume	Gravity Recovery and Climate Experiment Follow-on (GRACE/GRACE-FO)	https://grace.jpl.nasa.gov/data/get-data/
5g	Air temperature	DMI/PROMICE Weather Stations	https://eng.geus.dk/products-services-facilities/data-and-maps/glaciological-data-from-greenland-promice
5g	Ice Sheet Melt	Special Sensor Microwave Imager/Sounder (SSMIS)	https://nsidc.org/data/nsidc-0001

Sub-section	General Variable or Phenomenon	Specific dataset or variable	Source
5g	Ice Sheet Albedo	Moderate Resolution Imaging Spectroradiometer (MODIS)	https://nsidc.org/data/MODGRNLD/versions/1
5g	Ice Sheet Albedo	Sentinel-3 Snow and Ice Products (SICE)	https://eo4society.esa.int/projects/pre-operational-sentinel-3-snow-and-ice-products-sice/
5g	Ice Sheet Surface-Height	ICESat-2	https://icesat-2.gsfc.nasa.gov/icesat-2-data
5g	Ice Sheet Discharge	Ice Discharge (Greenland)	https://doi.org/10.22008/promice/data/ice_discharge/d/v02
5g	Ice Sheet Surface Mass Balance	Modèle Atmosphérique Régionale surface mass	https://mar.cnrs.fr/

Section 5h Glaciers and ice caps outside Greenland

Sub-section	General Variable or Phenomenon	Specific dataset or variable	Source
5h	Glacier Mass, Area or Volume	World Glacier Monitoring Service	http://dx.doi.org/10.5904/wgms-fog-2022-09
5h	Glacier Mass, Area or Volume	Gravity Recovery and Climate Experiment Follow-on (GRACE/GRACE-FO)	https://grace.jpl.nasa.gov/data/get-data/

Section 5i Terrestrial snow cover

Sub-section	General Variable or Phenomenon	Specific dataset or variable	Source
5i	Snow Properties	Crocus Snowpack Model	http://www.umr-cnrm.fr/spip.php?article265
5i	Snow Properties	ERA5	https://www.ecmwf.int/en/forecasts/dataset/ecmwf-reanalysis-v5
5i	Snow Properties	MERRA-2	http://gmao.gsfc.nasa.gov/reanalysis/MERRA-2/
5i	Snow Properties	European Space Agency Snow CCI SWE	https://snow-cci.enveo.at/
5i	Snow Properties	NOAA Interactive Multi-sensor Snow and Ice Mapping System (Snow Cover Duration)	https://usicecenter.gov/Products/ImsHome
5i	Snow Properties	Northern Hemisphere (NH) Snow Cover Extent (SCE), Version 1	http://doi.org/10.7289/V5N014G9

Section 5j Permafrost

Sub-section	General Variable or Phenomenon	Specific dataset or variable	Source
5i1	Permafrost	Global Terrestrial Network for Permafrost (GTN-P)	http://gtnpdatabase.org/
5i1	Permafrost	Permafrost Temperature	http://permafrost.gi.alaska.edu/sites_map
5i1	Temperature, [Near] Surface	ERA5	https://www.ecmwf.int/en/forecasts/dataset/ecmwf-reanalysis-v5
5i2	Permafrost	CALM Active Layer Thickness	www2.gwu.edu/~calm/

Section 5k Tundra greenness

Sub-section	General Variable or Phenomenon	Specific dataset or variable	Source
5k	Vegetative Index	Global Inventory Modeling and Mapping Studies (GIMMS) 3gv1	https://iridl.ldeo.columbia.edu/SOURCES/.NASA/.ARC/.ECOCAST/.GIMMS/.NDVI3g/.v1p0/index.htm
5k	Vegetative Index	MODIS Normalized Difference Vegetative Index (NDVI)	https://modis.gsfc.nasa.gov/data/dataprod/mod13.php

Sidebar 5.1: The February 2023 major sudden stratospheric warming

Sub-section	General Variable or Phenomenon	Specific dataset or variable	Source
SB5.1	Temperature, [Near] Surface	ERA5	https://www.ecmwf.int/en/forecasts/dataset/ecmwf-reanalysis-v5
SB5.1	Pressure	ERA5	https://www.ecmwf.int/en/forecasts/dataset/ecmwf-reanalysis-v5
SB5.1	Heat Flux	ERA5	https://www.ecmwf.int/en/forecasts/dataset/ecmwf-reanalysis-v5
SB5.1	Stratospheric Water vapor	Aura Microwave Limb Sounder (MLS)	https://gmao.gsfc.nasa.gov/reanalysis/MERRA-2/
SB5.1	Water Vapor, Total Column	MERRA-2	https://gmao.gsfc.nasa.gov/reanalysis/MERRA-2/

References

Afargan-Gerstman, H., B. Jiménez-Esteve, and D. I. V. Domeisen, 2022: On the relative importance of stratospheric and tropospheric drivers for the North Atlantic jet response to sudden stratospheric warming events. *J. Climate*, **35**, 6453–6467, https://doi.org/10.1175/JCLI-D-21-0680.1.

Arctic Climate Forum, 2023: 12th Arctic Climate Forum. Virtual, NOAA, https://www.arctic-rcc.org/acf-fall-2023.

Ballinger, T. J., and Coauthors, 2022: Surface air temperature. Arctic Report Card 2022, M. L. Druckenmiller, R. L. Thoman, and T. A. Moon, Eds., NOAA Tech. Rep. OAR ARC 22-02, 8–14, https://doi.org/10.25923/13qm-2576.

—— , and Coauthors, 2023: Alaska terrestrial and marine climate trends, 1957–2021. *J. Climate*, **36**, 4375–4391, https://doi.org/10.1175/JCLI-D-22-0434.1.

Barents Observer, 2023: Climate change brings cloudberry to Svalbard. Barents Observer, 3 October, https://thebarentsobserver.com/en/arctic/2023/10/climate-change-brings-cloudberry-svalbard.

Barrett, A. P., J. C. Stroeve, and M. C. Serreze, 2020: Arctic Ocean precipitation from atmospheric reanalyses and comparisons with North Pole drifting stations. *J. Geophys. Res. Oceans*, **125**, e2019JC015415, https://doi.org/10.1029/2019JC015415.

Becker, A., P. Finger, A. Meyer-Christoffer, B. Rudolf, K. Schamm, U. Schneider, and M. Ziese, 2013: A description of the global land-surface precipitation data products of the Global Precipitation Climatology Centre with sample applications including centennial (trend) analysis from 1901–present. *Earth Syst. Sci. Data*, **5**, 71–99, https://doi.org/10.5194/essd-5-71-2013.

Behrangi, A., A. Singh, Y. Song, and M. Panahi, 2019: Assessing gauge undercatch corrections in Arctic basins in light of GRACE observations. *Geophyis. Res. Lett.*, **46**, 11358–11366, https://doi.org/10.1029/2019GL084221.

Berner, L. T., and S. J. Goetz, 2022: Satellite observations document trends consistent with a boreal forest biome shift. *Global Change Biol.*, **28**, 3275–3292, https://doi.org/10.1111/gcb.16121.

Bernhard, G. H., A. F. Bais, P. J. Aucamp, A. R. Klekociuk, J. B. Liley, and R. L. McKenzie, 2023: Stratospheric ozone, UV radiation, and climate interactions. *Photochem. Photobiol. Sci.*, **22**, 937–989, https://doi.org/10.1007/s43630-023-00371-y.

Bhartia, P. K., and C. W. Wellemeyer, 2002: TOMS-V8 total O3 algorithm. OMI Algorithm Theoretical Basis Document Vol. II, NASA Goddard Space Flight Center Tech. Doc. ATBD-OMI-02, 15–31, https://eospso.gsfc.nasa.gov/sites/default/files/atbd/ATBD-OMI-02.pdf.

Bhatt, U. S., and Coauthors, 2021: Climate drivers of Arctic tundra variability and change using an indicators framework. *Environ. Res. Lett.*, **16**, 055019, https://doi.org/10.1088/1748-9326/abe676.

Bodeker, G. E., and S. Kremser, 2021: Indicators of Antarctic ozone depletion: 1979 to 2019. *Atmos. Chem. Phys.*, **21**, 5289–5300, https://doi.org/10.5194/acp-21-5289-2021.

Box, J. E., D. van As, and K. Steffen, 2017: Greenland, Canadian and Icelandic land-ice albedo grids (2000–2016). GEUS Bull., **38**, 53–56, https://doi.org/10.34194/geusb.v38.4414.

—— , W. Colgan, B. Wouters, D. Burgess, S. O'Neel, L. Thomson, and S. Mernild, 2018: Global sea-level contribution from Arctic land ice: 1971–2017. *Environ. Res. Lett.*, **13**, 125012, https://doi.org/10.1088/1748-9326/aaf2ed.

—— , and Coauthors, 2019: Key indicators of Arctic climate change: 1971–2017. *Environ. Res. Lett.*, **14**, 045010, https://doi.org/10.1088/1748-9326/aafc1b.

—— , and Coauthors, 2021: Recent developments in Arctic climate observational indicators. AMAP Arctic Climate Change Update 2021: Key Trends and Impacts, Arctic Monitoring and Assessment Programme, 7–29, https://www.amap.no/documents/doc/arctic-climate-change-update-2021-key-trends-and-impacts.-summary-for-policy-makers/3508.

Brown, R., D. V. Schuler, O. Bulygina, C. Derksen, K. L. Wang, and D. Yang, 2017: Arctic terrestrial snow cover. Snow, Water, Ice and Permafrost in the Arctic (SWIPA) 2017, Arctic, Monitoring and Assessment Programme, 25–64, https://www.amap.no/documents/doc/snow-water-ice-and-permafrost-in-the-arctic-swipa-2017/1610.

Brun, E., V. Vionnet, A. Boone, B. Decharme, Y. Peings, R. Valette, F. Karbou, and S. Morin, 2013: Simulation of northern Eurasian local snow depth, mass, and density using a detailed snowpack model and meteorological reanalyses. *J. Hydrometeor.*, **14**, 203–219, https://doi.org/10.1175/JHM-D-12-012.1.

Butchart, N., and E. E. Remsberg, 1986: The area of the stratospheric polar vortex as a diagnostic for tracer transport on an isentropic surface. *J. Atmos. Sci.*, **43**, 1319–1339, https://doi.org/10.1175/1520-0469(1986)043<1319:TAOTSP>2.0.CO;2.

CBC News, 2023: Enterprise, N.W.T., '90 per cent gone' after wildfire ravages community. Accessed 10 February 2024, https://www.cbc.ca/news/canada/north/enterprise-damage-wildfire-1.6936652.

Christensen, T. R., and Coauthors, 2021: Multiple ecosystem effects of extreme weather events in the Arctic. *Ecosystems*, **24**, 122–136, https://doi.org/10.1007/s10021-020-00507-6.

Ciracì, E., I. Velicogna, and S. Swenson, 2020: Continuity of the mass loss of the world's glaciers and ice caps from the GRACE and GRACE Follow-On missions. *Geophys. Res. Lett.*, **47**, e2019GL086926, https://doi.org/10.1029/2019GL086926.

Cohen, J., and Coauthors, 2020: Divergent consensuses on Arctic amplification influence on midlatitude severe winter weather. Nat. Climate Change, 10, 20–29, https://doi.org/10.1038/s41558-019-0662-y.

Colgan, W., and Coauthors, 2015: Hybrid glacier Inventory, Gravimetry and Altimetry (HIGA) mass balance product for Greenland and the Canadian Arctic. *Remote Sens. Environ.*, **168**, 24–39, https://doi.org/10.1016/j.rse.2015.06.016.

Didan, K., 2021a: MODIS/terra vegetation indices 16-day L3 global 500m SIN grid V061 [Data set]. NASA EOSDIS Land Processes DAAC, accessed 27 February 2023, https://doi.org/10.5067/MODIS/MOD13A1.061.

—— , 2021b: MODIS/aqua vegetation indices 16-day L3 global 500m SIN Grid V061 [Data set]. NASA EOSDIS Land Processes DAAC, accessed 27 February 2023, https://doi.org/10.5067/MODIS/MYD13A1.061.

Domeisen, D. I. V, and Coauthors, 2020: The role of the stratosphere in subseasonal to seasonal prediction: 2. *Predictability arising from stratosphere?troposphere coupling. J. Geophys. Res. Atmos.*, **125**, e2019JD030923, https://doi.org/10.1029/2019JD030923.

DW, 2023: Storm 'Hans' batters Scandinavia. DW, accessed 20 February 2024, https://www.dw.com/en/storm-hans-batters-scandinavia/a-66477645.

ESA, 2023: European Space Agency SMOS-CryoSat L4 sea ice thickness, version 206 accessed 3 October 2023, https://doi.org/10.57780/sm1-4f787c3.[463151][MLD2]

Fausto, R. S., and Coauthors, 2021: Programme for Monitoring of the Greenland Ice Sheet (PROMICE) automatic weather station data. *Earth Syst. Sci. Data*, **13**, 3819–3845, https://doi.org/10.5194/essd-13-3819-2021.

Fetterer, F., K. Knowles, W. N. Meier, M. Savoie, and A. K. Windnagel, 2017: Sea Ice Index, version 3 (updated daily). National Snow and Ice Data Center, accessed 27 August 2021, https://doi.org/10.7265/N5K072F8.

Fettweis, X., and Coauthors, 2020: GrSMBMIP: Intercomparison of the modelled 1980–012 surface mass balance over the Greenland Ice Sheet. *Cryosphere*, **14**, 3935–3958, https://doi.org/10.5194/tc-14-3935-2020.

Friedel, M., G. Chiodo, A. Stenke, D. I. V. Domeisen, and T. Peter, 2022: Effects of Arctic ozone on the stratospheric spring onset and its surface impact. *Atmos. Chem. Phys.*, **22**, 13 997–14 017, https://doi.org/10.5194/acp-22-13997-2022.

Garfinkel, C. I., D. L. Hartmann, and F. Sassi, 2010: Tropospheric precursors of anomalous Northern Hemisphere stratospheric polar vortices. *J. Climate*, **23**, 3282–3299, https://doi.org/10.1175/2010JCLI3010.1.

GMAO, 2015a: MERRA-2 inst3_3d_asm_nv: 3d, 3-hourly, instantaneous, model-level, assimilation, assimilated meteorological fields v5.12.4. Goddard Earth Sciences Data and Information Services Center (GES DISC), accessed 3 August 2023, https://doi.org/10.5067/WWQSXQ8IVFW8.

——, 2015b: MERRA-2tavg1_2d_lnd_Nx:2d, 1-hourly, time-averaged, single-level, assimilation, land surface diagnostics V5.12.4. Goddard Earth Sciences Data and Information Services Center (GESDISC), accessed 3 August 2023, https://doi.org/10.5067/RKPHT8KC1Y1T.

——, 2022: M2-SCREAM: 3d, 3-hourly, instantaneous, model-level, assimilation, assimilated constituent fields, replayed MERRA-2 meteorological fields. Goddard Earth Sciences Data and Information Services Center (GES DISC), accessed 3 August 2023, https://doi.org/10.5067/7PR3XRD6Q3NQ.

Hersbach, H., and Coauthors, 2020: The ERA5 global reanalysis. *Quart. J. Roy. Meteor. Soc.*, **146**, 1999–2049, https://doi.org/10.1002/qj.3803.

——, and Coauthors, 2023a: ERA5 hourly data on pressure levels from 1940 to present. Copernicus Climate Change Service (C3S) Climate Data Store (CDS[NR3][MLD4]), accessed 7 February 2024, https://doi.org/10.24381/cds.bd0915c6.

——, and Coauthors, 2023b: ERA5 hourly data on single levels from 1940 to present. Copernicus Climate Change Service (C3S) Climate Data Store (CDS[NR5][MLD6]), accessed 7 February 2024, https://doi.org/10.24381/cds.adbb2d47.

High North News, 2023: China pushes northern sea route transit cargo to new record. Accessed 10 February 2024, https://www.highnorthnews.com/en/china-pushes-northern-sea-route-transit-cargo-new-record.

Hjort, J., D. Streletskiy, G. Doré, Q. Wu, K. Bjella, and M. Luoto, 2022: Impacts of permafrost degradation on infrastructure. *Nat. Rev. Earth Environ.*, **3**, 24–38, https://doi.org/10.1038/s43017-021-00247-8.

Huang, B., C. Liu, V. Banzon, E. Freeman, G. Graham, B. Hankins, T. Smith, and H. Zhang, 2021: Improvements of the Daily Optimum Interpolation Sea Surface Temperature (DOISST) version 2.1. *J. Climate*, **34**, 2923–2939, https://doi.org/10.1175/JCLI-D-20-0166.1.

Hugonnet, R., and Coauthors, 2021: Accelerated global glacier mass loss in the early twenty-first century. *Nature*, **592**, 726–731, https://doi.org/10.1038/s41586-021-03436-z.

Icelandic Met Office, 2023: Flood in Skaftá. Accessed 8 February 2024, https://en.vedur.is/about-imo/news/flood-in-skafta.

Isaksen, K., and Coauthors, 2022a: Exceptional warming over the Barents area. *Sci. Rep.*, **12**, 9371, https://doi.org/10.1038/s41598-022-13568-5.

——, J. Lutz, A. M. Sorensen, O. Godoy, L. Ferrighi, S. Eastwood, and S. Aaboe, 2022b: Advances in operational permafrost monitoring on Svalbard and in Norway. *Environ. Res. Lett.*, **17**, 095012, https://doi.org/10.1088/1748-9326/ac8e1c.

Ivanova, N., O. M. Johannessen, L. T. Pedersen, and R. T. Tonboe, 2014: Retrieval of Arctic sea ice parameters by satellite passive microwave sensors: A comparison of eleven sea ice concentration algorithms. *IEEE Trans. Geosci. Remote Sens.*, **52**, 7233–7246, https://doi.org/10.1109/TGRS.2014.2310136.

Jóhannesson, T., H. Björnsson, E. Magnússon, S. Gu?mundsson, F. Pálsson, O. Sigur?sson, T. Thorsteinsson, and E. Berthierand, 2013: Ice-volume changes, bias estimation of mass-balance measurements and changes in subglacial lakes derived by lidar mapping of the surface of Icelandic glaciers. *Ann. Glaciol.*, **54**, 63–74, https://doi.org/10.3189/2013AoG63A422.

Karpechko, A. Y., P. Hitchcock, D. H. Peters, and A. Schneidereit, 2017: Predictability of downward propagation of major sudden stratospheric warmings. *Quart. J. Roy. Meteor. Soc.*, **143**, 1459–1470, https://doi.org/10.1002/qj.3017.

Kaverin, D., and Coauthors, 2021: Long-term active layer monitoring at CALM sites in the Russian European North. *Polar Geogr.*, **44**, 203–216, https://doi.org/10.1080/1088937X.2021.1981476.

Kjøllmoen, B., Ed., L. M. Andreassen, and H. Elvehøy, 2023: Glaciological investigations in Norway 2022. NVE Rapport 23-2023, 100 pp., https://publikasjoner.nve.no/rapport/2023/rapport2023_23.pdf.

Kokhanovsky, A., J. E. Box, B. Vandecrux, K. D. Mankoff, M. Lamare, A. Smirnov, and M. Kern, 2020: The determination of snow albedo from satellite measurements using fast atmospheric correction technique. Remote Sens., 12, 234, https://doi.org/10.3390/rs12020234.

Lambert, A., N. Livesey, W. Read, and R. Fuller, 2021: MLS/Aura level 3 daily binned water vapor (H2O) mixing ratio on zonal and similar grids V005. Goddard Earth Sciences Data and Information Services Center (GES DISC[NR7][MLD8]), accessed 26 February 2024, https://doi.org/10.5067/Aura/MLS/DATA3568.

Larson, C., and M. Sabbatini, 2023: Record flooding from Suicide Basin destroys one home, swamps others and cuts off access. Juneau Empire, 6 August, accessed 21 February 2024, https://www.juneauempire.com/news/record-flooding-from-suicide-basin-swamps-homes-cuts-off-access/.

Lavergne, T., and Coauthors, 2019: Version 2 of the EUMETSAT OSI SAF and ESA CCI sea-ice concentration climate data records. *Cryosphere*, **13**, 49–78, https://doi.org/10.5194/tc-13-49-2019.

LEO Network, 2023: Rain continues to impact the Noatak River. Accessed 10 February 2024, https://www.leonetwork.org/en/posts/show/F7361480-8E14-44C2-B42A-FED1F3D9AED4.

Loeb, N. G., M. Mayer, S. Kato, J. T. Fasullo, H. Zuo, R. Senan, J. M. Lyman, G. C. Johnson, and M. Balmaseda, 2022: Evaluating twenty-year trends in Earth's energy flows from observations and reanalyses. *J. Geophys. Res. Atmospheres*, **127**, e2022JD036686, https://doi.org/10.1029/2022JD036686.

López-Blanco, E., and Coauthors, 2024: Towards an increasingly biased view on Arctic change. *Nat. Climate Change*, **14**, 152–155, https://doi.org/10.1038/s41558-023-01903-1.

Luojus, K., and Coauthors, 2022: ESA Snow Climate Change Initiative (Snow_cci): Snow Water Equivalent (SWE) level 3C daily global climate research data package (CRDP) (1979–2020), version 2.0. NERC EDS Centre for Environmental Data Analysis, accessed 27 August 2023, https://doi.org/10.5285/4647cc9ad3c044439d6c643208d3c494.

Magnússon, R. Í., F. Groten, H. Bartholomeus, K. Van Huissteden, and M. M. P. D. Heijmans, 2023: Tundra browning in the Indigirka Lowlands (north?eastern Siberia) explained by drought, floods and small?scale vegetation shifts. *J. Geophys. Res. Biogeosci.*, **128**, e2022JG007330, https://doi.org/10.1029/2022JG007330.

Malkova, G., and Coauthors, 2022: Spatial and temporal variability of permafrost in the western part of the Russian Arctic. *Energies*, **15**, 2311, https://doi.org/10.3390/en15072311.

Mankoff, K. D., A. Solgaard, W. Colgan, A. P. Ahlstrøm, S. A. Khan, and R. S. Fausto, 2020: Greenland Ice Sheet solid ice discharge from 1986 through March 2020. *Earth Syst. Sci. Data*, **12**, 1367–1383, https://doi.org/10.5194/essd-12-1367-2020.

Martius, O., L. M. Polvani, and H. C. Davies, 2009: Blocking precursors to stratospheric sudden warming events. *Geophys. Res. Lett.*, **36**, L14806, https://doi.org/10.1029/2009GL038776.

McCague, F., 2023: Record year in the Northwest Passage as part of busy Arctic season. Chartered Institute of Logistics and Transport, 30 October, accessed 10 February 2024, https://ciltna.com/2023/10/30/record-year-in-the-northwest-passage-as-part-of-busy-arctic-season-by-fred-mccague-cmilt/.

Meier, W. N., F. Fetterer, A. K. Windnagel, and J. S. Stewart, 2021a: NOAA/NSIDC Climate Data Record of passive microwave sea ice concentration, version 4. National Snow and Ice Data Center, accessed 10 September 2022, https://doi.org/10.7265/efmz-2t65.

—— , —— , —— , and —— , 2021b: Near-real-time NOAA/NSIDC Climate Data Record of passive microwave sea ice concentration, version 2. National Snow and Ice Data Center, accessed 5 February 2024, https://doi.org/10.7265/tgam-yv28.

Mekonnen, Z. A., and Coauthors, 2021: Arctic tundra shrubification: A review of mechanisms and impacts on ecosystem carbon balance. *Environ. Res. Lett.*, **16**, 053001, https://doi.org/10.1088/1748-9326/abf28b.

Meredith, M., and Coauthors, 2019: Polar regions. The Ocean and Cryosphere in a Changing Climate, H.-O. Pörtner et al., Eds., Cambridge University Press, 203–320, https://doi.org/10.1017/9781009157964.005.

Millán, L., and Coauthors, 2022: The Hunga Tonga?Hunga Ha'apai hydration of the stratosphere. *Geophys. Res. Lett.*, **49**, e2022GL099381, https://doi.org/10.1029/2022GL099381.

Miner, K. R., and Coauthors, 2022: Permafrost carbon emissions in a changing Arctic. *Nat. Rev. Earth Environ.*, **3**, 55–67, https://doi.org/10.1038/s43017-021-00230-3.

Moon, T. A., and Coauthors, 2019: The expanding footprint of rapid Arctic change. *Earth's Future*, **7**, 212–218, https://doi.org/10.1029/2018EF001088.

—— , R. Thoman, and M. L. Druckenmiller, Eds., 2023: The Arctic [in "State of the Climate in 2022"]. *Bull. Amer. Meteor. Soc.*, **104** (9), S271–S321, https://doi.org/10.1175/BAMS-D-23-0079.1.

Mote, T., 2007: Greenland surface melt trends 1973–2007: Evidence of a large increase in 2007. *Geophys. Res. Lett.*, **34**, L22507, https://doi.org/10.1029/2007GL031976.

Müller, R., J.-U. Grooß, C. Lemmen, D. Heinze, M. Dameris, and G. Bodeker, 2008: Simple measures of ozone depletion in the polar stratosphere. *Atmos. Chem. Phys.*, **8**, 251–264, https://doi.org/10.5194/acp-8-251-2008.

Muñoz Sabater, J., 2019: ERA5-Land hourly data from 1981 to present. Copernicus Climate Change Service (C3S) Climate Data Store (CDS), accessed 3 October 2023, https://doi.org/10.24381/cds.e2161bac.

NOAA, 2024a: Optimum Interpolation Sea Surface Temperature (OISST) high resolution dataset, version 2.1. NOAA/PSL[NR9][MD10], accessed 5 February 2024, https://psl.noaa.gov/data/gridded/data.noaa.oisst.v2.highres.html.

—— , 2024b: North American Drought Monitor (MADM) map. NOAA/NCEI, accessed 8 February 2024, https://www.ncei.noaa.gov/access/monitoring/nadm/maps.

Nyland, K. E., N. I. Shiklomanov, D. A. Streletskiy, F. E. Nelson, A. E. Klene, and A. L. Kholodov, 2021: Long-term Circumpolar Active Layer Monitoring (CALM) program observations in Northern Alaskan tundra. *Polar Geogr.*, **44**, 167–185, https://doi.org/10.1080/1088937X.2021.1988000.

O'Neill, H. B., S. L. Smith, C. R. Burn, C. Duchesne, and Y. Zhang, 2023: Widespread permafrost degradation and thaw subsidence in northwest Canada. *J. Geophys. Res.: Earth Surf.*, **128**, e2023JF007262, https://doi.org/10.1029/2023JF007262.

Peng, G., W. N. Meier, D. J. Scott, and M. H. Savoie, 2013: A long-term and reproducible passive microwave sea ice concentration data record for climate studies and monitoring. *Earth Syst. Sci. Data*, **5**, 311–318, https://doi.org/10.5194/essd-5-311-2013.

Petty, A. A., N. T. Kurtz, R. Kwok, T. Markus, and T. A. Neumann, 2020: Winter Arctic sea ice thickness from ICESat?2 freeboards. *J. Geophys. Res. Oceans*, **125**, e2019JC015764, https://doi.org/10.1029/2019JC015764.

—— , N. Keeney, A. Cabaj, P. Kushner, and M. Bagnardi, 2023a: Winter Arctic sea ice thickness from ICESat-2: Upgrades to freeboard and snow loading estimates and an assessment of the first three winters of data collection. *Cryosphere*, **17**, 127–156, https://doi.org/10.5194/tc-17-127-2023.

—— , N. Kurtz, R. Kwok, T. Markus, and T. A. Neumann, and N. Keeney, 2023b: ICESat-2 L4 monthly gridded sea ice thickness, version 3. NASA National Snow and Ice Data Center Distributed Active Archive Center, accessed December 2023, https://doi.org/10.5067/ZCSU8Y5U1BQW.

Pinzon, J. E., C. J. Tucker, U. S. Bhatt, G. V. Frost, and M. J. Macander, 2023: Global Vegetation Greenness (NDVI) from AVHRR GIMMS-3G+, 1981-2022. ORNL DAAC[NR11][MLD12], accessed 20 May 2024, https://doi.org/10.3334/ORNLDAAC/2187.

Polvani, L. M., M. Previdi, M. R. England, G. Chiodo, and K. L. Smith, 2020: Substantial twentieth-century Arctic warming caused by ozone-depleting substances. *Nat. Climate Change*, **10**, 167, https://doi.org/10.1038/s41558-020-0711-6.

Raynolds, M. K., and Coauthors, 2019: A raster version of the Circumpolar Arctic Vegetation Map (CAVM). Remote Sens. *Environ.*, **232**, 111297, https://doi.org/10.1016/j.rse.2019.111297.

Reuters, 2023: Smoke from forest fires engulfs city in Russia's far east. 9 August, accessed 20 March 2024, https://www.reuters.com/world/europe/smoke-forest-fires-engulfs-city-russias-far-east-2023-08-09/.

Reynolds, R. W., N. A. Rayner, T. M. Smith, D. C. Stokes, and W. Wang, 2002: An improved in situ and satellite SST analysis for climate. *J. Climate*, **15**, 1609–1625, https://doi.org/10.1175/1520-0442(2002)015<1609:AIISAS>2.0.CO;2.

—— , T. M. Smith, C. Liu, D. B. Chelton, K. S. Casey, and M. G. Schlax, 2007: Daily high-resolution-blended analyses for sea surface temperature. *J. Climate*, **20**, 5473–5496, https://doi.org/10.1175/2007JCLI1824.1.

RGI Consortium, 2023: Randolph Glacier Inventory – A dataset of global glacier outlines, version 7.0. National Snow and Ice Data Center[NR13][MLD14], accessed 16 October 2024, https://doi.org/10.5067/f6jmovy5navz.

Ricker, R., S. Hendricks, L. Kaleschke, X. Tian-Kunze, J. King, and C. Haas, 2017: A weekly Arctic sea-ice thickness data record from merged CryoSat-2 and SMOS satellite data. *Cryosphere*, **11**, 1607–1623, https://doi.org/10.5194/tc-11-1607-2017.

Robinson, D. A., T. W. Estilow, and NOAA CDR Program, 2012: NOAA Climate Data Record (CDR) of Northern Hemisphere (NH) Snow Cover Extent (SCE), version 1. NOAA National Centers for Environmental Information, accessed 3 August 2023, https://doi.org/10.7289/V5N014G9.

Román, M. O., and Coauthors, 2024: Continuity between NASA MODIS Collection 6.1 and VIIRS Collection 2 land products. *Remote Sens. Environ.*, **302**, 113963, https://doi.org/10.1016/j.rse.2023.113963.

Romanovsky, V., and Coauthors, 2017: Changing permafrost and its impacts. Snow, Water, Ice and Permafrost in the Arctic (SWIPA) 2017, Arctic Monitoring and Assessment Programme, 65–102, https://www.amap.no/documents/doc/snow-water-ice-and-permafrost-in-the-arctic-swipa-2017/1610.

Schaefer, J. A., 2023: Increases in graminoids after three decades of change in the High Arctic. Polar Res., 42, https://doi.org/10.33265/polar.v42.9560.

Schneider, U., P. Finger, E. Rustemeier, M. Ziese, and S. Hänsel, 2022: Global precipitation analysis products of the GPCC. DWD, 17 pp., https://opendata.dwd.de/climate_environment/GPCC/PDF/GPCC_intro_products_v2022.pdf.

Schoeberl, M. R., Y. Wang, R. Ueyama, A. Dessler, G. Taha, and W. Yu, 2023: The estimated climate impact of the Hunga Tonga-Hunga Ha'apai eruption plume. *Geophy. Res. Lett.*, **50**, e2023GL104634, https://doi.org/10.1029/2023GL104634.

Schuur, E. A. G., and Coauthors, 2022: Permafrost and climate change: Carbon cycle feedbacks from the warming Arctic. *Annu. Rev. Environ. Resour.*, **47**, 343–371, https://doi.org/10.1146/annurev-environ-012220-011847.

Sciencenorway.no, 2024: Svalbard in 2023: Record hot, record cold, record wet, and record dry. 8 January, accessed 22 February 2024, https://www.sciencenorway.no/climate-ntb-english-svalbard/svalbard-in-2023-record-hot-record-cold-record-wet-and-record-dry/2304908.

Serreze, M. C., and R. G. Barry, 2011: Processes and impacts of Arctic amplification: A research synthesis. *Global Planet. Change*, **77**, 85–96, https://doi.org/10.1016/j.gloplacha.2011.03.004.

—— , M. P. Clark, and D. H. Bromwich, 2003: Monitoring precipitation over the Arctic terrestrial drainage system: Data requirements, shortcomings, and applications of atmospheric reanalysis. *J. Hydrometeor.*, **4**, 387–407, https://doi.org/10.1175/1525-7541(2003)4<387:MPOTAT>2.0.CO;2.

—— , J. Gustafson, A. P. Barrett, M. L. Druckenmiller, S. Fox, J. Voveris, J. Stroeve, B. Sheffield, B. C. Forbes, and S. Rasmus, 2021: Arctic rain on snow events: bridging observations to understand environmental and livelihood impacts. *Environ. Res. Lett.*, **16**, 105009, https://doi.org/10.1088/1748-9326/ac269b.

Skarin, A., Ö. Danell, R. Bergström, and J. Moen, 2004: Insect avoidance may override human disturbances in reindeer habitat selection. *Rangifer*, **24**, 95–103, https://doi.org/10.7557/2.24.2.306.

Smith, B., 2023: Algorithm Theoretical Basis Document (ATBD) for Land-ice DEM (ATL14) and Land-ice height change (ATL15). https://nsidc.org/sites/default/files/documents/technical-reference/icesat2_atl14_atl15_atbd_v003.pdf.

Smith, S. L., H. B. O'Neill, K. Isaksen, J. Noetzli, and V. E. Romanovsky, 2022: The changing thermal state of permafrost. *Nat. Rev. Earth Environ.*, **3**, 10–23, https://doi.org/10.1038/s43017-021-00240-1.

—— , V. E. Romanovsky, K. Isaken, K. Nyland, N. I. Shiklomanov, D. A. Streletskiy, and H. H. Christiansen, 2023: Permafrost [in "State of the Climate in 2022"]. *Bull. Amer. Meteor. Soc.*, **104** (9), S301–S305, https://doi.org/10.1175/10.1175/BAMS-D-23-0079.1.

<conf> —— , C. Duchesne, and H. B. O'Neill, 2024: Long-term permafrost monitoring in northern Canada – What have we learned? 12th Int. Conf. on Permafrost, Whitehorse, Yukon, Canada, Yukon University, 398–404, https://doi.org/10.52381/ICOP2024.84.1.</conf>

Tapley, B. D., and Coauthors, 2019: Contributions of GRACE to understanding climate change. *Nat. Climate Change*, **9**, 358–369, https://doi.org/10.1038/s41558-019-0456-2.

The Guardian, 2023: Storm Hans causes havoc in Norway with heaviest rain in 25 years forecast. Guardian, 9 August, https://www.theguardian.com/world/2023/aug/08/storm-hans-causes-havoc-in-norway-with-heaviest-rain-in-25-years-forecast.

Thoman, R. L., M. L. Druckenmiller, and T. Moon, Eds, 2022: The Arctic [in "State of the Climate in 2021"]. *Bull. Amer. Meteor. Soc.*, **103** (8), S257–S306, https://doi.org/10.1175/BAMS-D-22-0082.1.

—— , —— , and —— , Eds., 2023: Arctic Report Card 2023: Executive Summary. NOAA Tech. Rep. OAR ARC, 23-01, 5 pp., https://doi.org/10.25923/5vfa-k694.

Thompson, S., 2023: Remarks on September 28, 2023. Government of Northwest Territories, accessed 10 February 2024, https://www.gov.nt.ca/en/newsroom/shane-thompson-historic-2023-wildfire-season.

Timmermans, M.-L., and Z. M. Labe, 2023: Sea surface temperature. NOAA Arctic Report Card 2023, NOAA Tech. Rep. OAR ARC, 23-07, 7 pp., https://doi.org/10.25923/e8jc-f342.

Tschudi, M., W. N. Meier, and J. S. Stewart, 2019a: Quicklook Arctic weekly EASE-Grid Sea Ice Age, version 1. NASA National Snow and Ice Data Center Distributed Active Archive Center, accessed 1 September 2021, https://doi.org/10.5067/2XXGZY3DUGNQ.

—— , —— , —— , C. Fowler, and J. Maslanik, 2019b: EASE-Grid Sea Ice Age, version 4. NASA National Snow and Ice Data Center Distributed Active Archive Center, accessed 1 September 2021, https://doi.org/10.5067/UTAV7490FEPB.

U.S. National Ice Center, 2008: IMS daily Northern Hemisphere snow and ice analysis at 1 km, 4 km, and 24 km resolutions, version 1. National Snow and Ice Data Center, accessed 18 August 2023, https://doi.org/10.7265/N52R3PMC.

Walsh, J. E., T. J. Ballinger, E. S. Euskirchen, E. Hanna, J. Mård, J. E. Overland, H. Tangen, and T. Vihma, 2020: Extreme weather and climate events in northern areas: A review. *Earth-Sci. Rev.*, **209**, 103324, https://doi.org/10.1016/j.earscirev.2020.103324.

—— , S. Bigalke, S. A. McAfee, R. Lader, M. C. Serreze, and T. J. Ballinger, 2023: Precipitation [in "State of the Climate in 2022"]. *Bull. Amer. Meteor. Soc.*, **104** (9), S281–S284, https://doi.org/10.1175/BAMS-D-23-0079.1.

Wargan, K., B. Weir, G. L. Manney, S. E. Cohn, K. E. Knowland, P. A. Wales, and N. J. Livesey, 2023: M2-SCREAM: A stratospheric composition reanalysis of Aura MLS data with MERRA-2 transport. *Earth Space Sci.*, **10**, e2022EA002632, https://doi.org/10.1029/2022EA002632.

Wehrlé, A., J. E. Box, A. M. Anesio, and R. S. Fausto, 2021: Greenland bare-ice albedo from PROMICE automatic weather station measurements and Sentinel-3 satellite observations. *GEUS Bull.*, **47**, 5284, https://doi.org/10.34194/geusb.v47.5284.

WGMS, 2024: Fluctuations of glaciers database. World Glacier Monitoring Service[NR15][MLD16], accessed 6 February 2024, https://doi.org/10.5904/wgms-fog-2024-01.

White, J., J. E. Walsh, and R. L. Thoman Jr., 2021: Using Bayesian statistics to detect trends in Alaskan precipitation. *Int. J. Climatol.*, **41**, 2045–2059, https://doi.org/10.1002/joc.6946.

Wolken, G. J., and Coauthors, 2021: Glacier and permafrost hazards. Arctic Report Card 2021, NOAA Tech. Rep. OAR ARC; 21-13, 9 pp., https://doi.org/10.25923/v40r-0956.<<?CE: Please check and confirm the edits to the reference is correct>>

World Meteorological Organization, 2022: Scientific assessment of ozone depletion: 2022. WMO GAW Rep. 278, 509 pp.

Wouters, B., A. Gardner, and G. Moholdt, 2019: Global glacier mass loss during the GRACE Satellite Mission (2002-2016). Front. *Earth Sci.*, **7**, 96, https://doi.org/10.3389/feart.2019.00096.

Ye, H., D. Yang, A. Behrangi, S. L. Stuefer, X. Pan, E. Mekis, Y. Dibike, and J. E. Walsh, 2021: Precipitation characteristics and changes. Arctic Hydrology, Permafrost and Ecosystems, D. Yang and D. L. Kane, Eds., Springer, 25–59, https://doi.org/10.1007/978-3-030-50930-9_2.

Yu, L., and S. Zhong, 2021: Trends in Arctic seasonal and extreme precipitation in recent decades. *Theor. Appl. Climatol.*, **145**, 1541–1559, https://doi.org/10.1007/s00704-021-03717-7.

Zemp, M., and Coauthors, 2019: Global glacier mass changes and their contributions to sea-level rise from 1961 to 2016. *Nature*, **568**, 382–386, https://doi.org/10.1038/s41586-019-1071-0.

Zhu, X., X. Xu, and G. Jia, 2023: Recent massive expansion of wildfire and its impact on active layer over pan-Arctic permafrost. *Environ. Res. Lett.*, **18**, 084010, https://doi.org/10.1088/1748-9326/ace205.

STATE OF THE CLIMATE IN 2023

ANTARCTICA AND THE SOUTHERN OCEAN

K. R. Clem and M. N. Raphael, Eds.

Special Online Supplement to the *Bulletin of the American Meteorological Society* Vol. 105, No. 8, August, 2024

https://doi.org/10.1175/BAMS-D-24-0099.1

Corresponding author: Kyle R. Clem / kyle.clem@vuw.ac.nz

©2024 American Meteorological Society
For information regarding reuse of this content and general copyright information, consult the AMS Copyright Policy.

STATE OF THE CLIMATE IN 2023
Antarctica and the Southern Ocean

Editors

Jessica Blunden
Tim Boyer

Chapter Editors

Anthony Arguez
Josh Blannin
Peter Bissolli
Kyle R. Clem
Howard J. Diamond
Matthew L. Druckenmiller
Robert J. H. Dunn
Catherine Ganter
Nadine Gobron
Gregory C. Johnson
Rick Lumpkin
Rodney Martinez
Ademe Mekonnen
John B. Miller
Twila A. Moon
Marilyn N. Raphael
Carl J. Schreck III
Laura Stevens
Richard L. Thoman
Kate M. Willett
Zhiwei Zhu

Technical Editor

Lukas Noguchi

BAMS Special Editor for Climate

Timothy DelSole

American Meteorological Society

Cover Credit:
Summer ice floes in December 2015. Photo taken by Dr Sandy Thomalla on board the SA Agulhas II during the third Southern Ocean Seasonal Cycle Expedition (SOSCEx III).

How to cite this document:
Antarctica and the Southern Ocean is one chapter from the *State of the Climate in 2023* annual report and is available from https://doi.org/10.1175/BAMS-D-24-0099.1. Compiled by NOAA's National Centers for Environmental Information, *State of the Climate in 2023* is based on contributions from scientists from around the world. It provides a detailed update on global climate indicators, notable weather events, and other data collected by environmental monitoring stations and instruments located on land, water, ice, and in space. The full report is available from https://doi.org/10.1175/2024BAMSStateoftheClimate.1.

Citing the complete report:
Blunden, J. and T. Boyer, Eds., 2024: "State of the Climate in 2023". Bull. Amer. Meteor. Soc., 105 (8), Si–S483 https://doi.org/10.1175/2024BAMSStateoftheClimate.1.

Citing this chapter:
Clem, K. R. and M. N. Raphael, Eds., 2024: Antarctica and the Southern Ocean [in "State of the Climate in 2023"]. Bull. Amer. Meteor. Soc., 105 (8), S331–S370, https://doi.org/10.1175/BAMS-D-24-0099.1.

Citing a section (example):
Trusel, L. D., R. Baiman, C. Amory, D. Bozkurt, R. T. Datta, P. Deb, J. Kromer, and M. L. Maclennan, 2024: Ice-sheet surface mass balance [in "State of the Climate in 2023"]. Bull. Amer. Meteor. Soc., 105 (8), S343–S345, https://doi.org/10.1175/BAMS-D-24-0099.1.

Editor and Author Affiliations (alphabetical by name)

Adusumilli, Susheel, Scripps Institution of Oceanography, University of California, San Diego, La Jolla, California

Amory, Charles, Université Grenoble Alpes, Institut des Géosciences de l'Environnement, IRD, CNRS, Grenoble INP, Grenoble, France

Baiman, Rebecca, Department of Atmospheric and Oceanic Sciences, University of Colorado Boulder, Boulder, Colorado

Banwell, Alison F., Earth Science and Observation Center, Cooperative Institute for Research in Environmental Sciences (ESOC/CIRES), University of Colorado Boulder, Boulder, Colorado

Barreira, Sandra, Argentine Naval Hydrographic Service, Buenos Aires, Argentina

Beadling, Rebecca L., Department of Earth and Environmental Science, Temple University, Philadelphia, Pennsylvania

Bozkurt, Deniz, Department of Meteorology, University of Valparaíso, Valparaíso, Chile; Center for Climate and Resilience Research (CR)2, Santiago, Chile

Clem, Kyle R., School of Geography, Environment and Earth Sciences, Victoria University of Wellington, Wellington, New Zealand

Colwell, Steve, British Antarctic Survey, Cambridge, United Kingdom

Coy, Lawrence, Science Systems and Applications, Inc., Lanham, Maryland; NASA Goddard Space Flight Center, Greenbelt, Maryland

Datta, Rajashree T., Department of Atmospheric and Oceanic Sciences, University of Colorado Boulder, Boulder, Colorado

Deb, Pranab, Centre for Ocean, River, Atmosphere and Land Sciences (CORAL), Indian Institute of Technology Kharagpur, Kharagpur, India

De Laat, Jos, Royal Netherlands Meteorological Institute (KNMI), DeBilt, The Netherlands

du Plessis, Marcel, Department of Marine Sciences, University of Gothenburg, Gothenburg, Sweden

Fernandez, Denise, National Institute of Water and Atmospheric Research, Ltd. (NIWA) Auckland, New Zealand

Fogt, Ryan L., Department of Geography, Ohio University, Athens, Ohio

Fricker, Helen A., Scripps Institution of Oceanography, University of California, San Diego, La Jolla, California

Gille, Sarah T., Scripps Institution of Oceanography, University of California, San Diego, La Jolla, California

Johnson, Bryan, NOAA/OAR Earth System Research Laboratory, Global Monitoring Laboratory, Boulder, Colorado; University of Colorado Boulder, Boulder, Colorado

Josey, Simon A., Marine Systems Modelling, National Oceanography Center, Southampton, United Kingdom

Keller, Linda M., Department of Atmospheric and Oceanic Sciences, University of Wisconsin-Madison, Madison, Wisconsin; Antarctic Meteorological Research and Data Center, Space Science and Engineering Center, University of Wisconsin-Madison, Madison, Wisconsin

Kramarova, Natalya A., NASA Goddard Space Flight Center, Greenbelt, Maryland

Kromer, Jessica, Department of Geography, Pennsylvania State University, State College, Pennsylvania

Lait, Leslie, R., Science Systems and Applications, Inc., Lanham, Maryland; NASA Goddard Space Flight Center, Greenbelt, Maryland

Lazzara, Matthew A., Department of Physical Sciences, School of Science, Technology, Engineering, and Mathematics, Madison Area Technical College, Madison, Wisconsin; Antarctic Meteorological Research and Data Center, Space Science and Engineering Center, University of Wisconsin-Madison, Madison, Wisconsin

Lieser, Jan L., Bureau of Meteorology, Melbourne, Australia; Institute for Marine and Antarctic Studies (IMAS), University of Tasmania, Hobart, Australia

MacFerrin, Michael, Earth Science and Observation Center, CIRES, University of Colorado, Boulder, Colorado

MacGilchrist, Graeme M., University of St. Andrews, St Andrews, United Kingdom

MacLennan, Michelle L., Department of Atmospheric and Oceanic Science, University of Colorado Boulder, Boulder, Colorado

Marouchos, Andreas, CSIRO Environment, Canberra, Australia

Massom, Robert A., Australian Antarctic Division, Australian Antarctic Program Partnership (AAPP) and Australian Centre for Excellence in Antarctic Science (ACEAS), Hobart, Australia

McMahon, Clive R., Sydney Institute of Marine Science, IMOS Animal Tagging, Mosman, Australia

Mikolajczyk, David E., Antarctic Meteorological Research and Data Center, Space Science and Engineering Center, University of Wisconsin-Madison, Madison, Wisconsin

Mote, Thomas L., Department of Geography, University of Georgia, Athens, Georgia

Newman, Paul A., NASA Goddard Space Flight Center, Greenbelt, Maryland

Norton, Taylor, Antarctic Meteorological Research and Data Center, Space Science and Engineering Center, University of Wisconsin-Madison, Madison, Wisconsin

Petropavlovskikh, Irina, NOAA/OAR Earth System Research Laboratory, Global Monitoring Laboratory, Boulder, Colorado; University of Colorado Boulder, Boulder, Colorado

Pezzi, Luciano P., National Institute for Space Research (INPE), São José dos Campos, São Paulo, Brazil

Pitts, Michael, NASA Langley Research Center, Hampton, Virginia

Raphael, Marilyn N., Department of Geography, University of California, Los Angeles, Los Angeles, California

Reid, Phillip, Bureau of Meteorology, Melbourne, Australia; Australian Antarctic Program Partnership (AAPP), Hobart, Australia

Santee, Michelle L., NASA Jet Propulsion Laboratory, Pasadena, California

Scambos, Theodore A., Cooperative Institute for Research in Environmental Sciences, University of Colorado Boulder, Boulder, Colorado

Schulz, Cristina, Department of Marine and Environmental Sciences, Northeastern University, Massachusetts

Shi, Jia-Rui, Woods Hole Oceanographic Institution, Woods Hole, Massachusetts

Souza, Everaldo, Federal University of Pará (UFPA), Belém, Brazil

Stammerjohn, Sharon, Institute of Arctic and Alpine Research, University of Colorado Boulder, Boulder, Colorado

Thomalla, Sandy, Southern Ocean Carbon-Climate Observatory, Council for Scientific and Industrial Research (CSIR), Pretoria, South Africa; Marine and Antarctic Research Centre for Innovation and Sustainability, Department of Oceanography, University of Cape Town, Cape Town, South Africa

Tripathy, Sarat Chandra, National Centre for Polar and Ocean Research, Vasco da Gama, India

Trusel, Luke D., Department of Geography, Pennsylvania State University, State College, Pennsylvania

Turner, Katherine, Department of Geosciences, University of Arizona, Tucson, Arizona; Geophysical Fluid Dynamics Laboratory, Princeton, New Jersey; Department of Atmospheric and Oceanic Sciences, Princeton University, Princeton, New Jersey

Yin, Ziqi, Department of Atmospheric and Oceanic Sciences, University of Colorado Boulder, Boulder, Colorado

Editorial and Production Team

Allen, Jessicca, Graphics Support, Cooperative Institute for Satellite Earth System Studies, North Carolina State University, Asheville, North Carolina

Camper, Amy V., Graphics Support, Innovative Consulting and Management Services, LLC, NOAA/NESDIS National Centers for Environmental Information, Asheville, North Carolina

Haley, Bridgette O., Graphics Support, NOAA/NESDIS National Centers for Environmental Information, Asheville, North Carolina

Hammer, Gregory, Content Team Lead, Communications and Outreach, NOAA/NESDIS National Centers for Environmental Information, Asheville, North Carolina

Love-Brotak, S. Elizabeth, Lead Graphics Production, NOAA/NESDIS National Centers for Environmental Information, Asheville, North Carolina

Ohlmann, Laura, Technical Editor, Innovative Consulting and Management Services, LLC, NOAA/NESDIS National Centers for Environmental Information, Asheville, North Carolina

Noguchi, Lukas, Technical Editor, Innovative Consulting and Management Services, LLC, NOAA/NESDIS National Centers for Environmental Information, Asheville, North Carolina

Riddle, Deborah B., Graphics Support, NOAA/NESDIS National Centers for Environmental Information, Asheville, North Carolina

Veasey, Sara W., Visual Communications Team Lead, Communications and Outreach, NOAA/NESDIS National Centers for Environmental Information, Asheville, North Carolina

6. Table of Contents

Authors and affiliations S334
a. Overview S337
b. Atmospheric circulation and surface observations S339
c. Ice-sheet surface mass balance S343
d. Ice-sheet seasonal melt extent and duration S346
e. Ice-sheet mass balance S349
f. Sea-ice extent, concentration, and seasonality S351
g. Southern Ocean S355
1. Sea-surface temperature, salinity, and mixed-layer depth S355
2. Air–sea heat flux S355
3. Upper ocean heat content S356
4. Ocean biogeochemistry S356
h. 2023 Antarctic ozone hole S358
Acknowledgments S362
Appendix 1: Acronyms S363
Appendix 2: Datasets and sources S364
References S367

6. ANTARCTICA AND THE SOUTHERN OCEAN

K. R. Clem and M. N. Raphael, Eds.

a. Overview

—K. R. Clem

Antarctica experienced strong to record below-average pressure and stronger-than-average circumpolar westerlies to start (January) and close (December) 2023, marking the third and fourth consecutive summers with such conditions (2020/21, 2021/22, 2022/23, 2023/24). During austral autumn, winter, and spring, the atmospheric circulation over the South Pacific underwent a marked transition from the previous three years as the "triple dip" La Niña officially transitioned to El Niño during autumn 2023. Consistent with El Niño, positive pressure anomalies developed in the Ross and Amundsen Seas, and anomalous low pressure developed over the Antarctic Peninsula and western Weddell Sea. These two circulation anomalies produced two regions of persistent warm northerly flow and above-average atmospheric river activity: across the Weddell Sea and Dronning Maud Land (on the eastern side of the low) and in the Wilkes Land region (on the western side of the high). These two regions saw Antarctica's most pronounced climate anomalies in 2023, including well-above average temperatures and surface mass balance. These anomalies were most pronounced in the Weddell Sea region where western Dronning Maud Land, Coates Land, and the Ronne-Filchner Ice Shelf saw Antarctica's highest surface mass balance anomalies for the year, and temperatures for much of the year ranged from 2°C to 6°C above average over the Weddell Sea and along coastal Dronning Maud Land. The Antarctic Peninsula also experienced well-above-average temperatures and surface melting during the 2022/23 summer melt season, marking the fourth consecutive summer of anomalous high surface melt on the Peninsula.

Overall, net surface mass balance over the ice sheet was above average in 2023; however, surface mass balance was significantly less than the record-high values seen in 2022. With closer-to-average surface mass balance, ice discharge—mainly from the West Antarctic Ice Sheet—overwhelmed surface mass gains, and the Antarctic Ice Sheet had a net ice-sheet mass loss of 170 Gt between January and November 2023. This marks a return of Antarctica contributing to sea-level rise after the short-lived record-high mass gains seen in 2022 due to record-high snowfall.

The most significant feature of the southern polar region in 2023 was the record-low sea-ice coverage over the Southern Ocean. On 21 February, Antarctic sea-ice extent and sea-ice area both reached all-time record lows of 1.85×10^6 km^2 and 1.10×10^6 km^2, respectively, surpassing the previous record lows that were set just a year earlier in February 2022. Eight months saw new monthly-mean record lows in sea-ice extent and sea-ice area, and 76% of the days in 2023 set new daily record-low sea-ice extents. Also unprecedented were the number of daily record lows that occurred during sea-ice growth months, in contrast to previous years where the record lows predominantly occurred during the summer retreat season. For example, 6 July had a record-low daily sea-ice extent that was a remarkable 1.8×10^6 km^2 lower than the previous record low for that day. Additionally, the absence of pack ice resulted in an unprecedented 154 days of record-high coastal exposure during which there was a complete lack of a protective sea-ice "buffer".

Consistent with the low sea-ice coverage, Southern Ocean sea-surface temperatures and heat content in the upper 2000 m were both well above average in 2023, marking a continuation of the Southern Ocean warming trend observed since 2005 (Cai et al. 2023). The most pronounced positive sea-surface temperature and ocean heat content anomalies were in the South Atlantic and southwest Pacific, coinciding with the two regions of warm northerly atmospheric flow

discussed above. These regions also spatially align with some of the largest deficits in sea-ice extent observed throughout most of 2023.

Lastly, the ozone hole emerged once again in the Antarctic stratosphere during late August and September 2023. The 2023 ozone hole appeared earlier than normal and persisted longer than normal, not breaking up until 20 December, while its overall size was near average and was the 16th largest in 44 years of satellite observations. The long duration of the ozone hole can be attributed to weaker planetary-scale wave activity in late spring, which resulted in stronger-than-average circumpolar westerlies and colder-than-average temperatures in the stratosphere. Additionally, anomalously high stratospheric water vapor from the January 2022 Hunga volcano eruption entered the southern polar stratosphere in early 2023 ahead of the annual formation of the polar vortex during autumn, leading to a 25% to 50% increase in water vapor observed in the stratosphere in May and June. The anomalously high water vapor increased the temperature threshold for polar stratospheric cloud formation, and thus resulted in earlier-than-normal chlorine activation, but overall, this did not appear to significantly contribute to the 2023 Antarctic ozone hole size or duration.

The remainder of this chapter provides a detailed overview of the state of Antarctica's climate and cryosphere, the Southern Ocean, and the ozone hole in 2023. The details are split into seven sections, beginning with the atmospheric circulation and temperature and ending with the 2023 ozone hole. In most cases, 2023 anomalies and standard deviations are based on the 1991–2020 climatological average unless otherwise stated due to data availability. The period of record over which "records" are determined is also provided in each respective section. The geographical locations and place names mentioned throughout the chapter are provided in Fig. 6.1.

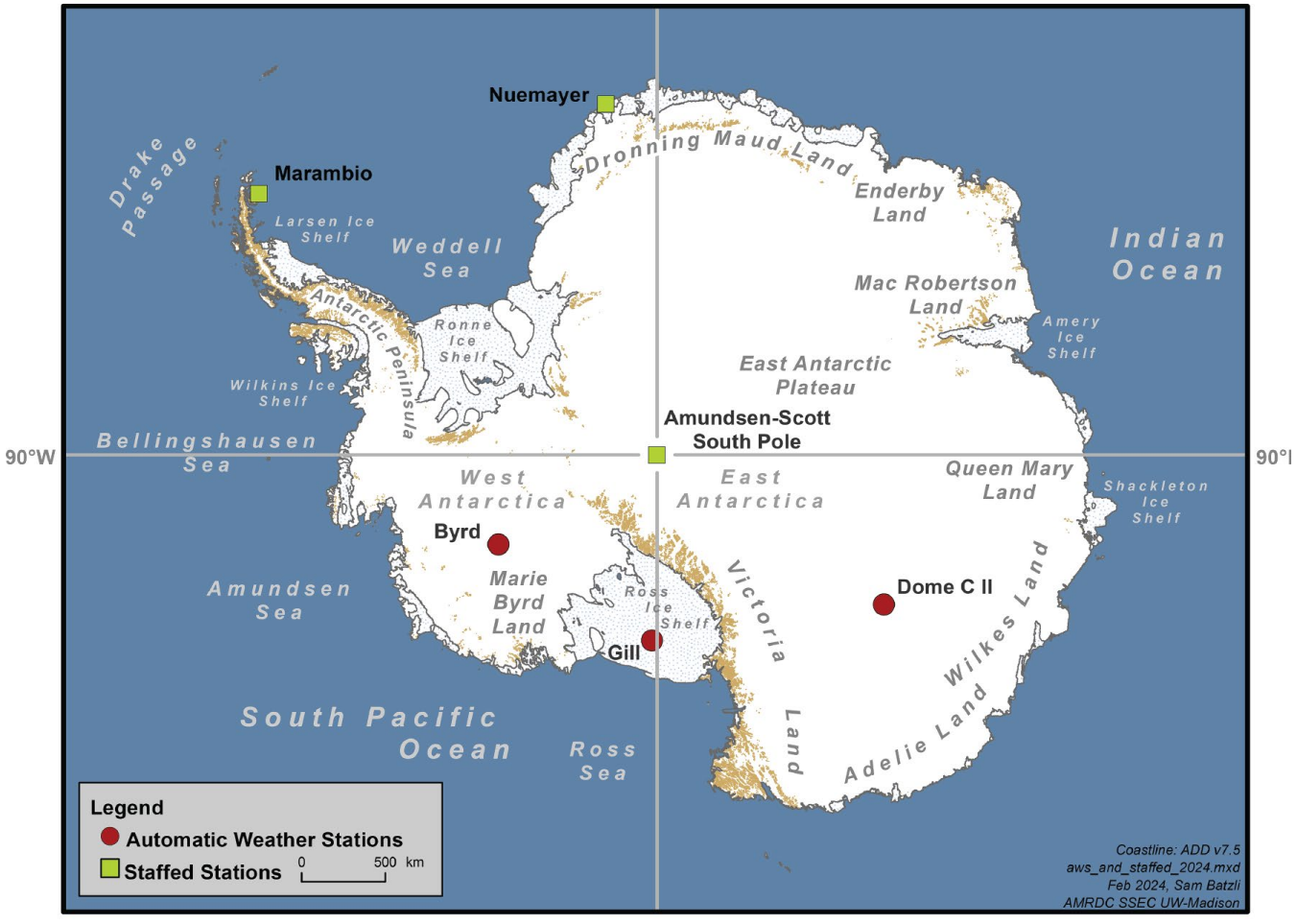

Fig. 6.1. Map of stations and geographic regions discussed in this chapter.

b. Atmospheric circulation and surface observations

—K. R. Clem, S. Barreira, S. Colwell, R. L. Fogt, L. M. Keller, M. A. Lazzara, D. E. Mikolajczyk, and T. Norton

Here we examine the major climate and atmospheric circulation anomalies across Antarctica in 2023. Monthly-mean atmospheric circulation and temperature data are from ERA5 (Hersbach et al. 2020). Figure 6.2 shows the vertical structure of the monthly geopotential height (Fig. 6.2a) and temperature (Fig. 6.2b) anomalies averaged over the polar cap (60°S–90°S) and the monthly circumpolar zonal wind anomalies (Fig. 6.2c) averaged over 50°S–70°S; the monthly Marshall (2003) Southern Annular Mode (SAM) index is provided at the bottom of Fig. 6.2. Despite masking individual months, the surface climate anomalies were grouped into and averaged across four periods of relatively persistent patterns seen in 2023: January–March, April–June, July–September, and October–December (Fig. 6.3). Observed monthly temperature and pressure anomalies for select Antarctic staffed and automatic weather stations (AWS) are also examined in Fig. 6.4; see Fig. 6.1 for station locations. The period of record for the stations is provided in the caption of Fig. 6.4.

January 2023 was marked by strong negative geopotential height (Fig. 6.2a) and surface pressure (Fig. 6.3a) anomalies across Antarctica (>2 std. dev. below average), and the circumpolar westerlies (Fig. 6.2c) were much stronger than average (+2 m s^{-1} to +5 m s^{-1}, 2–2.5 std. dev. above average). This pattern initially developed the month prior in December 2022 and thus continued into January 2023. The below-average pressure and strong circumpolar westerlies extended vertically through the depth of the troposphere and stratosphere, while at the surface almost all stations in East Antarctica set record-low monthly pressure values in January: Amundsen-Scott and Dome C II AWS (shown in Figs. 6.4c,d), as well as Relay AWS, Vostok and all coastal East Antarctic stations (not shown) had record-low pressure in January. The Marshall (2003) SAM index in January was also record high for January (+4.6) and the second highest on record for any month (both since 1957); the NOAA Climate Prediction Center's Antarctic Oscillation index (defined as the leading mode of monthly 700-hPa geopotential height anomalies) in January was also the highest January value on record (since 1979; not shown). During February and March, the polar-cap geopotential height and the

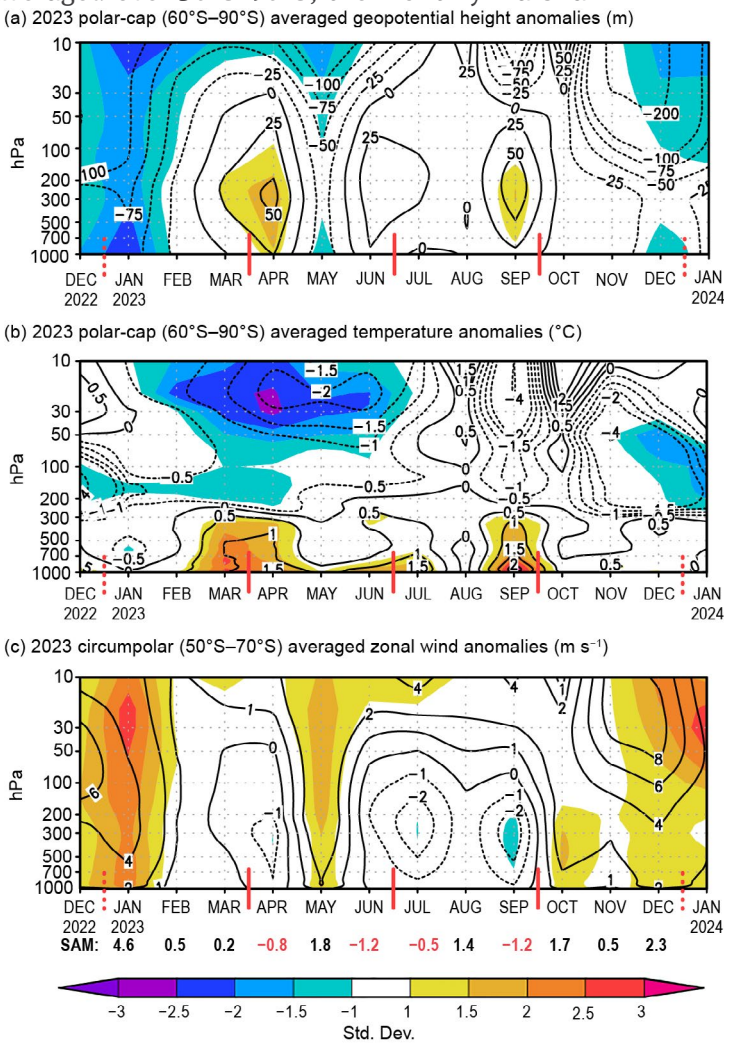

Fig. 6.2. Area-averaged (weighted by cosine of latitude) monthly anomalies over the southern polar region in 2023 relative to 1991–2020: (a) polar-cap (60°S–90°S) averaged geopotential height anomalies (m; contour interval is 25 m up to ±100 m and 100 m after ±100 m); (b) polar-cap averaged temperature anomalies (°C; contour interval is 0.5°C up to ±2°C and 2°C after ±2°C); (c) circumpolar (50°S–70°S) averaged zonal wind anomalies (m s^{-1}; contour interval is 2 m s^{-1} with an additional contour at ±1 m s^{-1}). Shading depicts standardized monthly anomalies as indicated by the color bar at the bottom. Red vertical bars indicate the four climate periods used for compositing in Fig. 6.3; the dashed lines near Dec 2022 and Dec 2023 indicate circulation anomalies wrapping around the calendar year. Values from the Marshall (2003) Southern Annular Mode (SAM) index are shown below (c) in black (positive values) and red (negative values). (Source: ERA5 reanalysis.)

circumpolar westerly wind anomalies dissipated and returned to their long-term average (Fig. 6.2).

Regionally, the January–March average surface pressure anomalies (Fig. 6.3a) reveal the strongest and most persistent negative pressure/cyclonic anomaly was located over the Bellingshausen Sea (reflecting a deep Amundsen Sea Low) where pressure was 8 hPa–10 hPa below average (>3 std. dev.). To the east of the cyclone, where warm northerly flow prevailed, Antarctic Peninsula temperatures were 1°C–3°C above average during January–March (Figs. 6.3b, 6.4ba), Antarctic Peninsula surface melt was 56% above the baseline median average in January–February (see section 6d, Fig. 6.8b), and there was an above-average number of atmospheric rivers and snowfall/surface mass balance across the Ronne-Filchner Ice Shelf in March (see section 6c, Fig. 6.6b). To the west of the cyclone, cold offshore flow resulted in substantially less-than-average surface melt across coastal West Antarctica, Wilkes Land, and Adélie Land during January–February. These regional impacts associated with the deep Amundsen Sea Low are consistent with previous studies (e.g., Raphael et al. 2016) as well as the impact of large-scale modes of variability on the depth of the Amundsen Sea Low, namely the La Niña conditions (see section 4b) and the strongly positive SAM conditions that were observed during this period (Clem and Fogt 2013; Ding and Steig 2013). Lastly, the vertical temperature profile reveals a strong positive temperature anomaly that developed over the polar cap in March (>1.0°C, 2 std. dev. averaged) despite near-average circulation (SAM index of 0.2), while this was contrasted by strong negative temperature anomalies in the stratosphere during February and March (1°C–2°C below average, >2 std. dev.).

From April to June, the monthly polar-cap averaged pressure anomalies flipped from strongly positive in April (Figs. 6.2a, 6.4)—during which Amundsen-Scott recorded its highest monthly-mean April pressure on record (Fig. 6.4c)—to negative in May, including a brief but intense strengthening of the circumpolar westerlies (Fig. 6.2c), then back to positive in June. The most

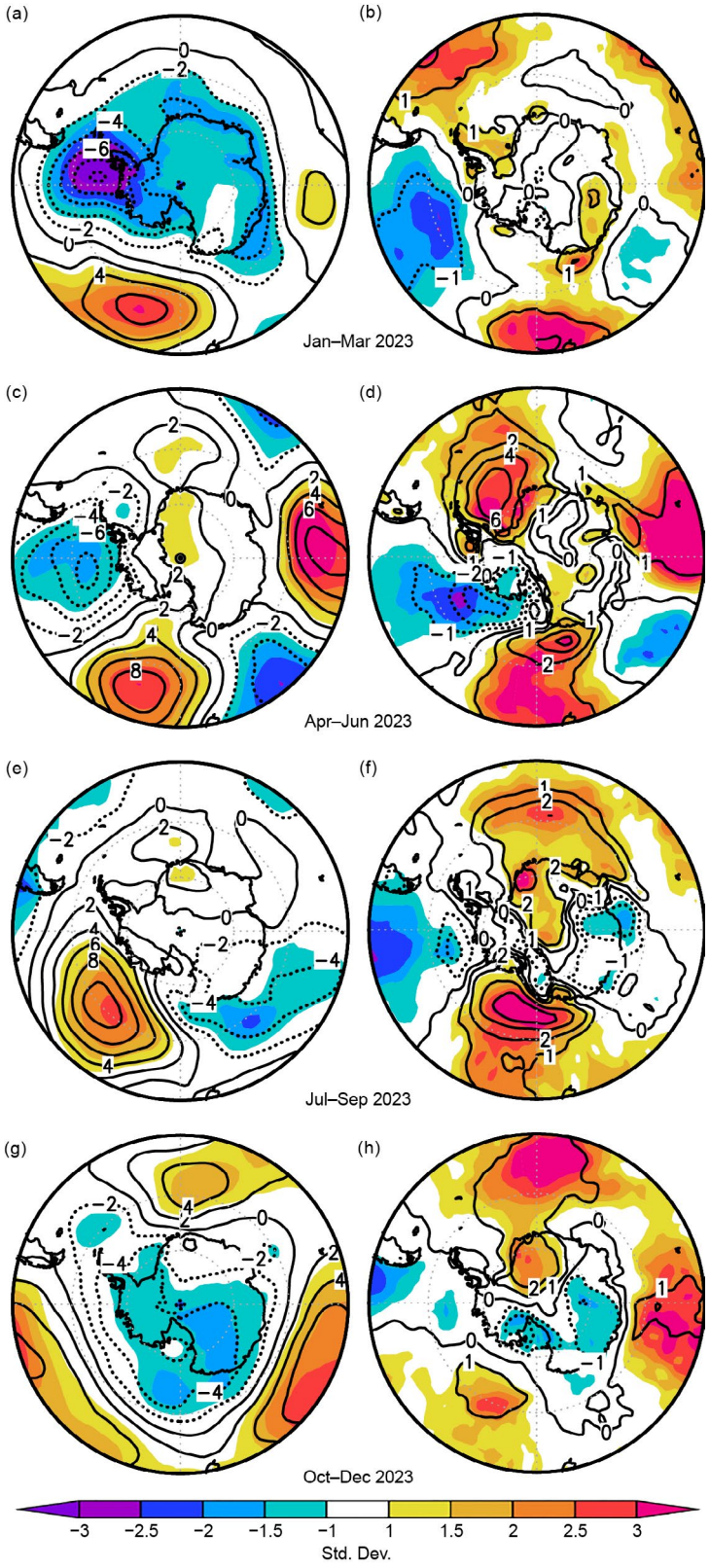

Fig. 6.3. (left) Surface pressure (hPa) and (right) 2-m temperature (°C) anomalies relative to 1991–2020 for (a),(b) Jan–Mar 2023; (c),(d) Apr–Jun 2023; (e),(f) Jul–Sep 2023, and (g),(h) Oct–Dec 2023. Contour interval is 2 hPa for surface pressure anomalies and 1°C for 2-m temperature anomalies. Shading shows the standardized anomalies. (Source: ERA5 reanalysis.)

pronounced surface pressure anomalies averaged over April–June continued to be a strong negative pressure/cyclonic anomaly in the Bellingshausen Sea, but a strong ridge of high pressure also developed over Dronning Maud Land and the adjacent South Atlantic from April onward (Fig. 6.3c; the three-month average dampens the most intense positive pressure anomaly in April). Together, this cyclone-anticyclone pair produced intense warm northerly flow across the South Atlantic sector, resulting in positive temperature anomalies of +4°C to +6°C (2–3 std. dev.) across the Weddell Sea averaged over April–June as well as a substantial delay (by up to 60 days) in sea-ice advance across the South Atlantic/Weddell Sea (see section 6f, Fig. 6.12a). In coastal Dronning Maud Land, Neumayer recorded its warmest April on record (–11.2°C, 7.0°C above average) when the ridge of high pressure over the South Atlantic and Dronning Maud Land was strongest (Fig. 6.4b).

The anomalously deep Amundsen Sea Low that dominated late summer and autumn was consistent with the (weakening) La Niña conditions in the tropical Pacific (Ding and Steig 2013). During the winter months (July–September), La Niña transitioned to El Niño (see section 4b) and the deep Amundsen Sea Low dissipated while a pronounced positive pressure anomaly developed off the coast of West Antarctica (Fig. 6.3e). With the anomalous anticyclonic/counterclockwise circulation centered north of the Ross and Amundsen Seas, cold offshore flow developed over Marie Byrd Land (Fig. 6.3f), which was most marked in August when Byrd AWS recorded its coldest August on record (–45.6°C, 10.7°C below average; Fig. 6.4e). The anticyclone shifted eastward to the Bellingshausen Sea in September (not shown, but seen in the pressure anomalies at Marambio in Fig. 6.4a). This resulted in warm northerly flow to the Ross Ice Shelf in September where Gill AWS had its warmest September on record (–26.3°C, 11.4°C above average; Fig. 6.4f). Meanwhile, the strong positive pressure anomalies across coastal Dronning Maud Land and the South Atlantic continued, producing locally intense anomalous warm conditions in eastern Dronning Maud Land during July–September. This region also experienced anomalous high surface mass balance through the winter (section 6c), indicating the northerly flow was both warm and moisture-rich.

During October–December, for the fourth spring/summer in a row (2020, 2021, 2022, and 2023), strong negative geopotential height and temperature anomalies and stronger-than-average circumpolar westerlies developed in the stratosphere (Fig. 6.2) in conjunction with the development of the 2023 ozone hole (see section 6h). The stronger-than-average polar vortex was associated with weaker wave activity in the stratosphere, and this helped maintain a longer-than-average ozone hole duration also like that seen in the previous three years (see section 6h). In December, the negative geopotential height and strong circumpolar westerly anomalies developed downward from the stratosphere through

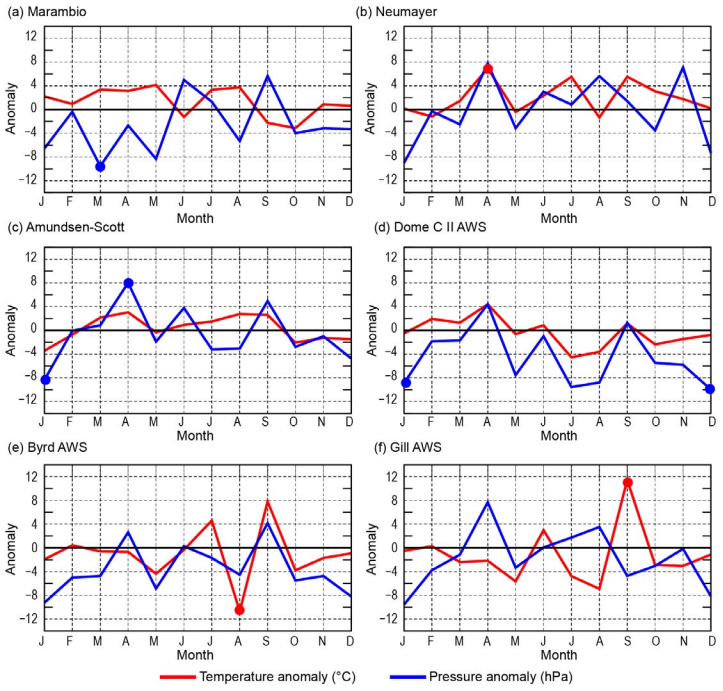

Fig. 6.4. Observed monthly Antarctic surface air temperature and station pressure anomalies during 2023 from six representative stations (three staffed [a]–[c], and three automatic [d]–[f]). Anomalies for temperature (°C) are shown in red and for mean sea-level pressure /surface pressure (hPa) are shown in blue, with filled circles denoting monthly records set for each station in 2023. All anomalies are based on the monthly 1991–2020 averages where possible. The station observation records start in 1970 for Marambio, 1981 for Neumayer, 1957 for Amundsen-Scott, 1980 for Dome C II automatic weather station (AWS), 1980 for Byrd AWS, and 1985 for Gill AWS. See Fig. 6.1 for station locations.

the troposphere, suggesting dynamical coupling between the stratosphere and troposphere circulations (Thompson et al. 2006). Strong negative pressure anomalies developed at the surface during October–December (Fig. 6.3g), also similar to the previous three years, becoming most pronounced in December when all six stations analyzed here reported below-average pressure (Fig. 6.4), and Dome C II AWS recorded its lowest monthly-mean December pressure on record.

In Dronning Maud Land, the ridge of high pressure continued and even strengthened offshore over the South Atlantic during September–December (Fig. 6.3g). This resulted in continued warm northerly flow in the South Atlantic sector and strong positive temperature anomalies of +1°C to +2°C (>2 std. dev.) in eastern Dronning Maud Land. The blocking high in the South Atlantic was strongest in November and was further coupled with a cyclonic anomaly to the west over the southeast Pacific (not shown). This coincided with an above-average number of atmospheric rivers and above-average to record-high surface mass balance across Dronning Maud Land, Coates Land, and the Ronne-Filchner ice shelf in November. Furthermore, the persistent ridge of high pressure and warm northerly flow throughout the year resulted in Neumayer recording a record-high annual average temperature of –14.0°C (2.0°C above average) in 2023.

c. Ice-sheet surface mass balance

—L. D. Trusel, R. Baiman, C. Amory, D. Bozkurt, R. T. Datta, P. Deb, J. Kromer, and M. L. Maclennan

Surface mass balance (SMB) represents the net effect of all processes that add or remove mass from the surface of an ice sheet. For the Antarctic Ice Sheet (AIS), snowfall is the dominant SMB term, with approximately 2300 Gt accumulating each year (van Wessem et al. 2018; Agosta et al. 2019; Mottram et al. 2021). Strong coast-to-plateau SMB gradients exist across the AIS (Fig. 6.5a), with typical mass gains along the coasts exceeding 500 mm water equivalent (w.e.) yr^{-1}, particularly in higher relief areas abutting the prevailing winds. In contrast, low-magnitude mass gains of <50 mm w.e. yr^{-1} are typically spread across the high-elevation plateau of the East Antarctic Ice Sheet. Much of the annual SMB gains occur during high-magnitude, extreme precipitation events, often delivered by atmospheric rivers (ARs; Turner et al. 2019; Wille et al. 2021; Maclennan et al. 2022). Sea ice can also play an influential role in SMB and precipitation patterns by modulating the amount and extent of moisture transport over the ice sheet (Kromer and Trusel 2023; Hanna et al. 2024). Snowfall-driven mass gains are countered by losses from sublimation, the leading negative SMB term for the AIS (Mottram et al. 2021). Surface melting primarily occurs across AIS ice shelves (Arthur et al. 2022; Banwell et al. 2023), with runoff and lake drainages occurring in some areas (Bell et al. 2018; Trusel et al. 2022). However, most AIS surface melt is thought to refreeze within the firn (Mottram et al. 2021), the layer of partially compacted snow from previous years located beneath the new surface snow accumulation (The Firn Symposium team 2024).

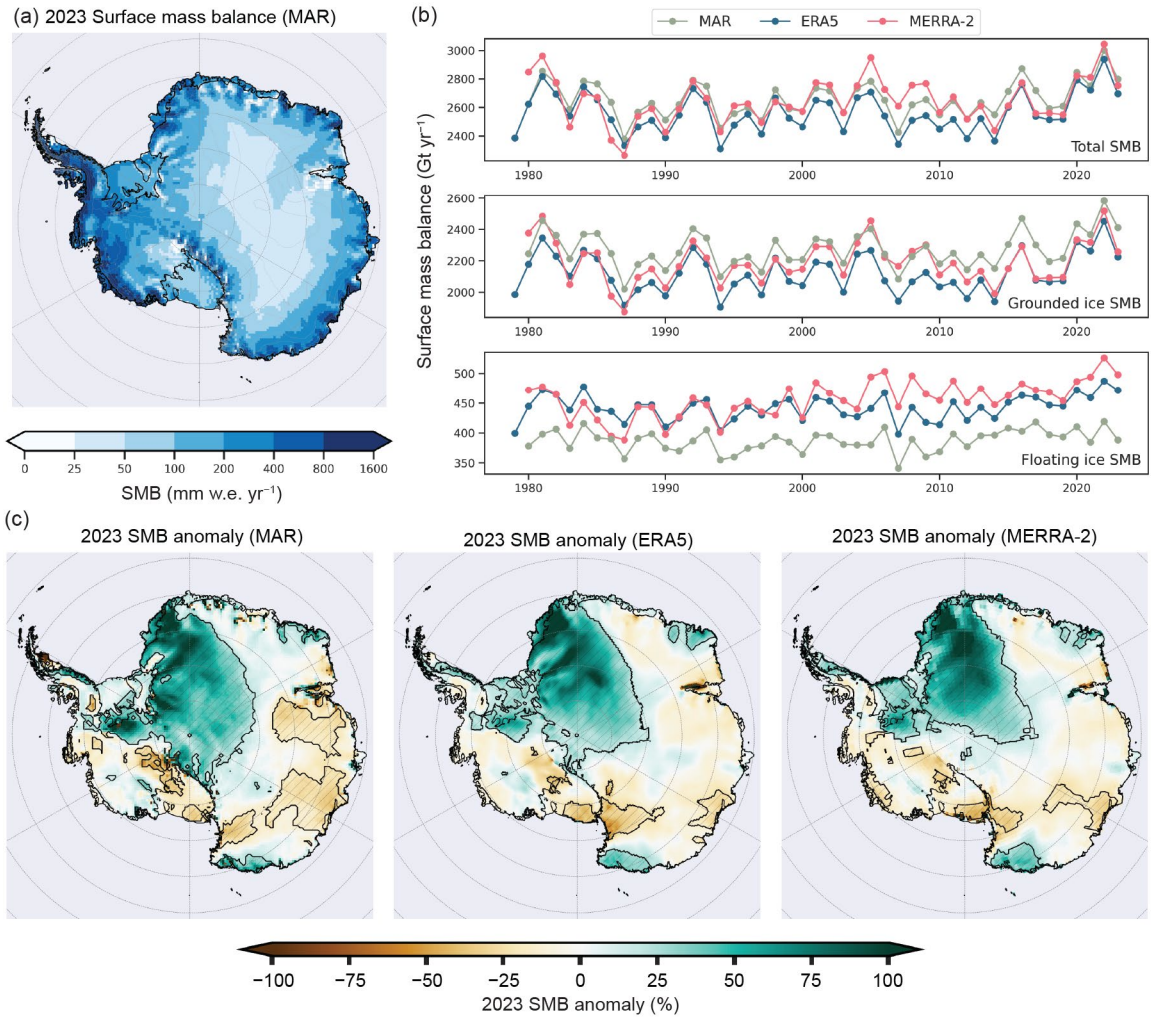

Fig. 6.5. (a) MAR 2023 surface mass balance (SMB; mm water equivalent yr^{-1}). (b) Time series of annual surface mass balance in Gt (10^{12} kg) yr^{-1} over the full ice sheet and its grounded and floating portions. (c) Annual MAR, ERA5, and MERRA-2 SMB anomalies for 2023 relative to their 1991–2020 mean (%). The 2023 SMB anomalies are higher than the 1991–2020 standard deviation of the respective datasets in the stippled areas.

Here, we use the ERA5 (Hersbach et al. 2020) and MERRA-2 (Gelaro et al. 2017) reanalyses to estimate the 2023 SMB as total precipitation minus evaporation and sublimation ($P-E$), following recent studies (e.g., Medley and Thomas 2019; Lenaerts et al. 2019). Although important biases remain associated with, for example, ice-sheet–cloud–radiation feedbacks and precipitation, evaluations of various reanalysis products over Antarctica indicate that MERRA-2 and ERA5 represent recent Antarctic climate well (Gossart et al. 2019; Medley and Thomas 2019; Wang et al. 2016). We also assess SMB as simulated by the polar-oriented regional climate model, Modèle Atmosphérique Régional (MAR), forced by ERA5 (Kittel et al. 2021). Relative to the reanalyses, MAR provides a more explicit treatment of ice-sheet surface climate and SMB, including firn evolution and meltwater runoff. Of these datasets, ERA5 is the highest resolution at 0.25°, followed by MAR at 35 km and MERRA-2 at 0.625° × 0.5°. To calculate SMB across a consistent spatial extent, we first bilinearly regridded each dataset to the ERA5 grid, following a recent SMB intercomparison (Mottram et al. 2021), before masking each using grounded and floating ice extents as defined in the Antarctic Digital Database (version 7.8; Gerrish et al. 2023). For the SMB datasets, annual and monthly anomalies are compared to 1991–2020 climatologies. We also use monthly sea-ice concentration observational data (DiGirolamo et al. 2022) and an atmospheric river (AR) detection algorithm adopted from Wille et al. (2021) applied to MERRA-2 reanalysis with a meridional moisture transport climatology of 1991–2020.

We assess SMB across both grounded and floating ice (Figs. 6.5b,c). While only the grounded SMB is relevant to sea level, SMB across floating ice shelves is important to the health of the firn layer and ice shelf stability (The Firn Symposium team 2024). The total grounded AIS SMB in 2023 equaled 2225 Gt, 2257 Gt, or 2411 Gt, according to ERA5, MERRA-2, and MAR, respectively, representing anomalies of roughly 1 std. dev. above the 1991–2020 climatological SMBs (ERA5: 2104±109 Gt yr^{-1}; MERRA-2: 2186±106 Gt yr^{-1}; MAR: 2258±97 Gt yr^{-1}). The 2023 grounded AIS SMB ranked as 11th highest since 1979 according to ERA5 (5th in MAR and 15th in MERRA-2 since 1980). Notably, 2023's grounded SMB equates to ~170 Gt, 225 Gt lower than occurred in 2022, when the AIS set a record-high SMB for the observational era in response to high snow accumulation (Datta et al. 2023), resulting in the AIS having a net positive ice-sheet mass balance in 2022 (Adusumilli et al. 2023). Thus, 2023 marked the return of a negative ice-sheet mass balance and the AIS contributing to sea-level rise driven by solid ice discharge (see section 6e for more details). Considering SMB across Antarctica's floating ice shelves only, 2023 ranked as the third and fifth highest on record in MERRA-2 and ERA5, respectively. Comparatively, ice shelf SMB is lower in MAR, both in 2023 and overall, at least partially resulting from MAR simulating surface meltwater runoff on some ice shelves. This discrepancy points to the need for improved observations and understanding of the drivers of surface melt and its magnitude. Despite elevated SMB in recent years, no method shows a significant trend for total or grounded SMB, and only MERRA-2 indicates a significant positive SMB trend for floating ice shelves (1.4 Gt yr^{-1}; $p<0.01$).

The 2023 AIS total SMB (grounded + floating) varies seasonally (Fig. 6.6a), with a minimum in austral summer (December–February; 160 Gt $month^{-1}$ to 210 Gt $month^{-1}$ in MERRA-2) and a maximum in austral autumn (March–May; 235 Gt $month^{-1}$ to 322 Gt $month^{-1}$ in MERRA-2; Fig 6.6a). Spatially, the highest SMB anomaly in 2023 was concentrated in the South Atlantic sector between 75°W and 45°E, including western Dronning Maud Land, Coates Land, and the Ronne-Filchner ice shelf (Fig. 6.5c). April, May, June, August, September, October, and November all featured anomalously high AR frequency over this region tied to the anticyclonic circulation anomalies east of AR landfall (see Figs. 6.3c,e,g). In November, this pattern resulted in a SMB anomaly of 1.5 std. dev. above the MERRA-2 climatology (Fig. 6.6a), coincident with record-high monthly-mean mean sea-level pressure values over the eastern Weddell Sea in November (since 1979, based on ERA5 reanalysis; not shown). In addition to the blocking high located off the coast of eastern Dronning Maud Land in November, a deep and elongated trough and associated surface cyclonic anomaly together produced a particularly conducive environment for AR landfall (Pohl et al. 2021; Baiman et al. 2023). The attendant cyclone had asymmetries with

shortwave troughs and ridges favorable for AR family events (Maclennan et al. 2023). Starting on 5 November, consecutive ARs made landfall just east of the Ronne-Filchner Ice Shelf over Dronning Maud Land (Fig. 6.6e) with 70% of the timesteps from 14 to 18 November featuring ARs over the AIS between 35°W and 10°W (not shown).

March was also particularly notable with total SMB anomalies exceeding 2 std. dev. in each dataset (Fig. 6.6a) and ranking as the first-, second-, or third-highest March SMB on record in MAR, MERRA-2, and ERA5, respectively. Significant and anomalous SMB in March occurred over four main regions: the Ronne-Filchner Ice Shelf, Enderby Land, Wilkes Land, and just east and west of Ross Ice Shelf (Fig. 6.6b). While AR activity near the Ronne-Filchner Ice Shelf was not anomalous in March, negative pressure anomalies (e.g., Fig. 6.3a), relatively high sea-surface temperatures (see Figs. 6.13a,b), and negative sea-ice concentration anomalies (Fig. 6.6b) likely contributed to local moisture transport and resulting snowfall. Enderby Land and Wilkes Land both saw above-average AR activity (Fig. 6.6d), consistent with high SMB anomalies. The dominant atmospheric pattern in March of higher-than-average values of surface pressure over the Ross-Amundsen Sea sector (see Fig. 6.3a), which, in combination with below-average sea ice east and west of the Ross Ice Shelf (Fig. 6.6b), is consistent with higher SMBs in these areas, particularly along the steep slopes of the Executive Committee Range.

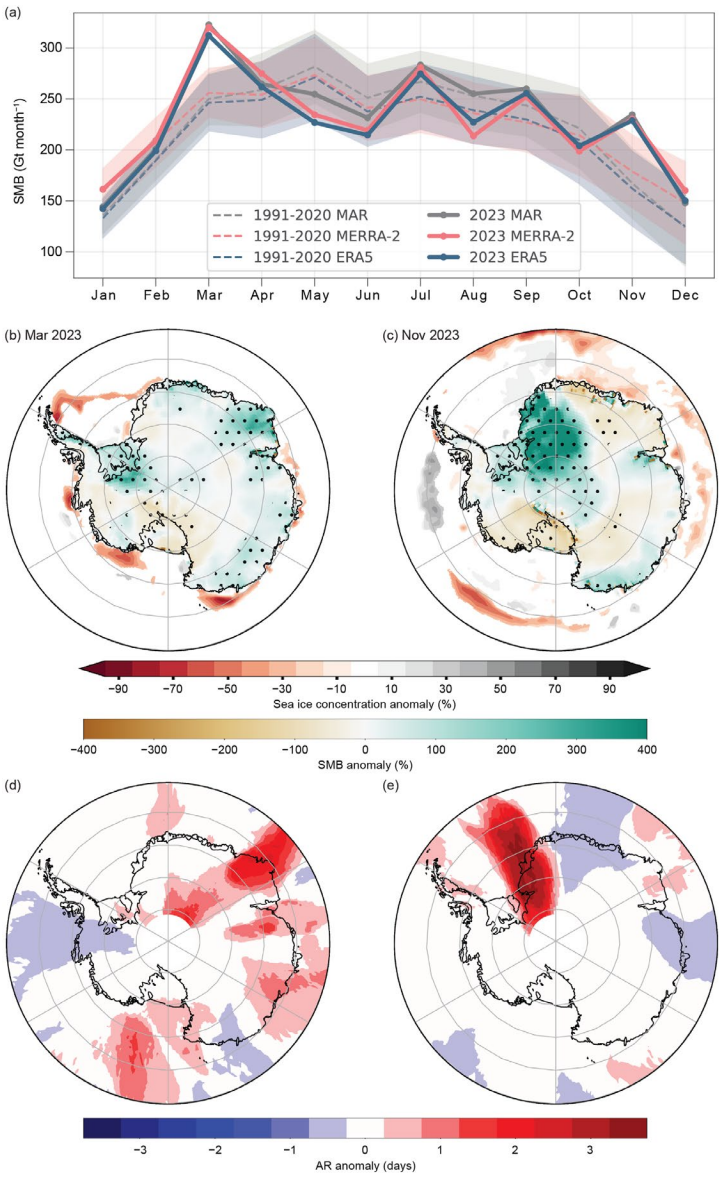

Fig. 6.6. (a) Monthly cycle of (grounded and floating) Antarctic Ice Sheet surface mass balance (SMB) in Gt month^{-1} for MERRA-2 (pink), ERA5 (blue), and MAR (gray). 2023 values are shown with a solid line, 1991–2020 average in a dotted line, 1 std. dev. is shaded. Green and brown shading over the continent shows 2023 SMB anomaly (%) for (b) Mar and (c) Nov. The 2023 SMB anomalies are higher than the 1991–2020 std. dev. of the respective datasets in the stippled areas. Stippling shows where the 2023 SMB anomalies are above or below the 1991–2020 std. dev. of the respective datasets. Gray and red shading in the Southern Ocean shows significant (>1 std. dev.) anomalous observational sea-ice concentration (%) for (b) Mar and (c) Nov. Anomalies of atmospheric river (AR) frequency (days) in (d) Mar and (e) Nov 2023 compared to 1991–2020 climatology are shown in red and blue shading.

d. Ice-sheet seasonal melt extent and duration

—M. MacFerrin, T. Mote, A. F. Banwell, Z. Yin, and T. A. Scambos

Surface melt on the Antarctic Ice Sheet (AIS) occurs primarily on the low-elevation coastal margins, especially on the Antarctic Peninsula and on the ice shelves surrounding the continent. It plays a small role in the total mass balance of the AIS relative to far larger contributions from snow accumulation, glacier calving, and basal melting. However, surface melting is a key measure of ice-sheet stability. As meltwater percolates and re-freezes, it increases the density of the underlying firn, and if melt volume is sufficient, the accumulated meltwater can induce ice-shelf break up (Banwell et al. 2013) and glacier acceleration through hydrofracture (Scambos et al. 2014).

Here, daily surface melt is mapped using satellite-derived passive-microwave brightness temperatures. The source data are distributed as daily composited polar stereographic brightness-temperatures by the National Snow and Ice Data Center (products NSIDC-0001; Meier et al. 2019 and NSIDC-0007; Gloerson 2006) spanning 1979 through the present day. Daily passive microwave brightness temperatures using the 37-GHz horizontal polarization as well as the 37- and 19-GHz vertical polarization channels are acquired by the Scanning Multichannel Microwave Radiometer (SMMR), Special Sensor Microwave/Imager (SSM/I), and Special Sensor Microwave Imager/Sounder (SSMIS) sensors aboard the NOAA Nimbus-7 and Defense Meteorological Satellite Program (DMSP) F8, F11, F13, F17, and F18 satellites. The austral melt season is defined here as 1 October through 30 April. Although small brief melt events can be measured along Antarctica's northern coastal margins during the austral winter, the vast majority of melt happens during these seven months, with the most typically occurring in December and January. An ice-extent mask of 25-km grid cells for the AIS was developed from the Quantarctica v3.0 Detailed Basemap dataset (Norwegian Polar Institute 2018). All 25-km cells that contain ≥50% land ice or ice shelf are included. We divide the AIS into seven melt extent and climate regions (Fig. 6.8a) by clustering glaciological drainage basins from Shepherd et al. (2012). Melt is determined by 37-GHz horizontally polarized brightness temperatures that exceed a dynamically established threshold each season from a simple microwave emission model that would be expected in the presence of liquid water in near-surface layers of ice and snowpack. The method used here was first developed to track the Greenland Ice Sheet's surface melt daily (Mote and Anderson 1995, 2007, 2014). Large seasonal fluctuations in passive microwave emissions from some areas of dry polar firn in Antarctica can create false positive melt indications in an unmodified version of the Greenland algorithm. This was mitigated by filtering areas that only marginally exceed the melt threshold (<10K) in the 37-GHz horizontal polarization in regions with a negative 18/19-GHz minus 37-GHz frequency gradient in the vertical polarization and has been used in previous season reports of Antarctic melt (MacFerrin et al. 2021, 2022, 2023). We focus here on the melt season spanning 1 October 2022 through 30 April 2023. The 2023/24 Antarctic melt season will be discussed in next year's report.

According to passive-microwave satellite observations (Fig. 6.7), the 2022/23 melt season recorded an overall slightly-above-average cumulative melt index (days · area) of 7.66 million km^2 days, about 1.3% greater than the median melt index of 7.55 million km^2 days during the 1990–2020 baseline period. However, the 2022/23 melt season was punctuated by substantial spatial and temporal anomalies in individual regions. The Antarctic Peninsula (Fig. 6.8a) saw an annual melt index nearly 56% above the baseline median value (Fig. 6.8b). Antarctic Peninsula melt was affected by extensive melt events in December 2022, extended melt through the majority of January 2023, and strong melt again in early February 2023. A majority of the Larsen C, George VI, and Wilkins Ice Shelves on the Peninsula observed between 20 and 30 more melt days compared to the 1990–2020 reference period. The persistent melting was likely tied to the stronger-than-average westerly winds, a pattern reflected in the exceptionally high Marshall (2003) Southern Annular Mode (SAM) index values for November and December 2022 and January 2023 (+3.7, +2.9, and +4.6, respectively; see Fig. 6.2; Clem et al. 2023). Notably, the 2022/23 melt season marks the fourth consecutive year in which the Antarctica Peninsula had a melt index that was more than 30% higher than that of the median extent from the reference period. These four summer seasons comprise the February 2020 and February 2022 extreme

warm events on the Antarctic Peninsula tied to tropical variability (Clem et al. 2022 and Gorodetskaya et al. 2023, respectively) along with the three consecutive summers (2020/21, 2021/2022, 2022/23) of stronger-than-average circumpolar westerlies (see section 6b).

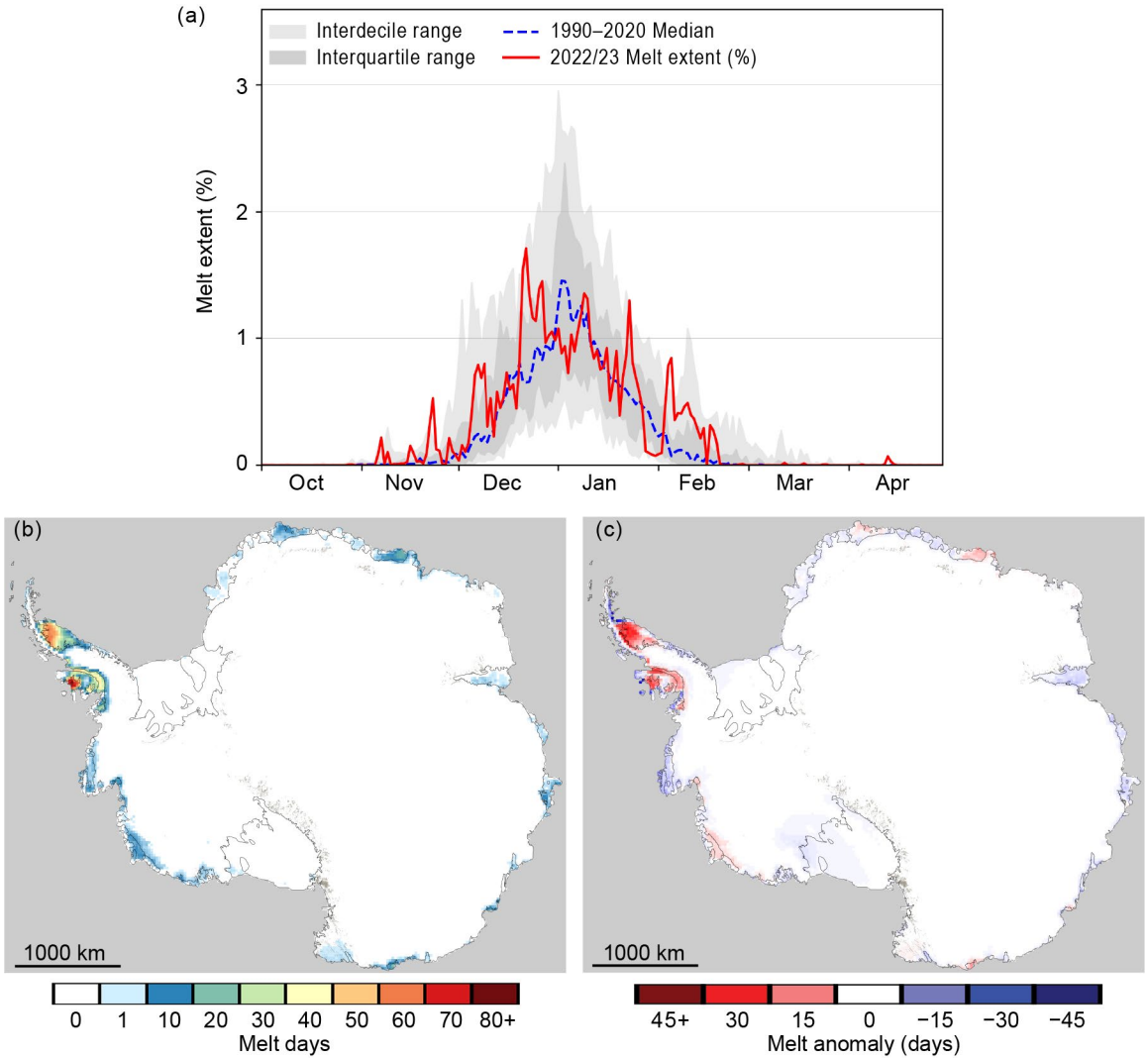

Fig. 6.7. (a) Daily surface melt extent (%) across the Antarctic Ice Sheet for the 2022/23 melt season, with 1990–2020 median values in blue and interdecile and interquartile ranges shaded in gray. (b) Map of the sum of melt days across the Antarctic Ice Sheet. (c) Map of the anomaly of the sum of melt days compared to mean values from the 1990–2020 reference period.

The Dronning Maud Land and Enderby Land (near 50°E) regions also displayed a higher-than-average-extent melt season, recording a total melt index of 41% more than the baseline period, with five extensive melt events hitting the region from late December 2022 through most of January 2023 (Fig. 6.8c). The former coincides with a region of warm northerly flow on the eastern side of a strong cyclonic anomaly over the Bellingshausen Sea and Antarctic Peninsula during January and February, while the latter coincides with warm northerly flow on the western side of an anticyclonic anomaly over the Indian Ocean (see Fig. 6.3a). Following the warmer months that are conducive for surface melt (January and February), these regions then experienced above-average surface mass balance in March (see Fig. 6.6b), suggesting regions of high surface melt transitioned to high snowfall accumulation with the onset of colder conditions. However, the Dronning Maud and Enderby Land's 2022/23 melt seasons were overall considerably less extensive than the 2021/22 melt season in which the total extent was more than triple the baseline median, as discussed in last year's report (MacFerrin et al. 2023). All other regions of the AIS observed below-average melt indices for the 2022/23 season, with the Ronne

Embayment receiving almost no observed surface melt and the Wilkes and Adélie lands region totaling only 39% melt index compared to the baseline median. Notably, the Amundsen-Bellingshausen region had a lower melt extent than average for the majority of the 2022/23 season where cold offshore flow occurred on the western side of the cyclone in the Bellingshausen Sea (see Fig. 6.3a), with the exception of an extensive event that resulted in surface melting across a majority of the Getz Ice Shelf for nearly two weeks in mid-December 2022 (Fig. 6.8d).

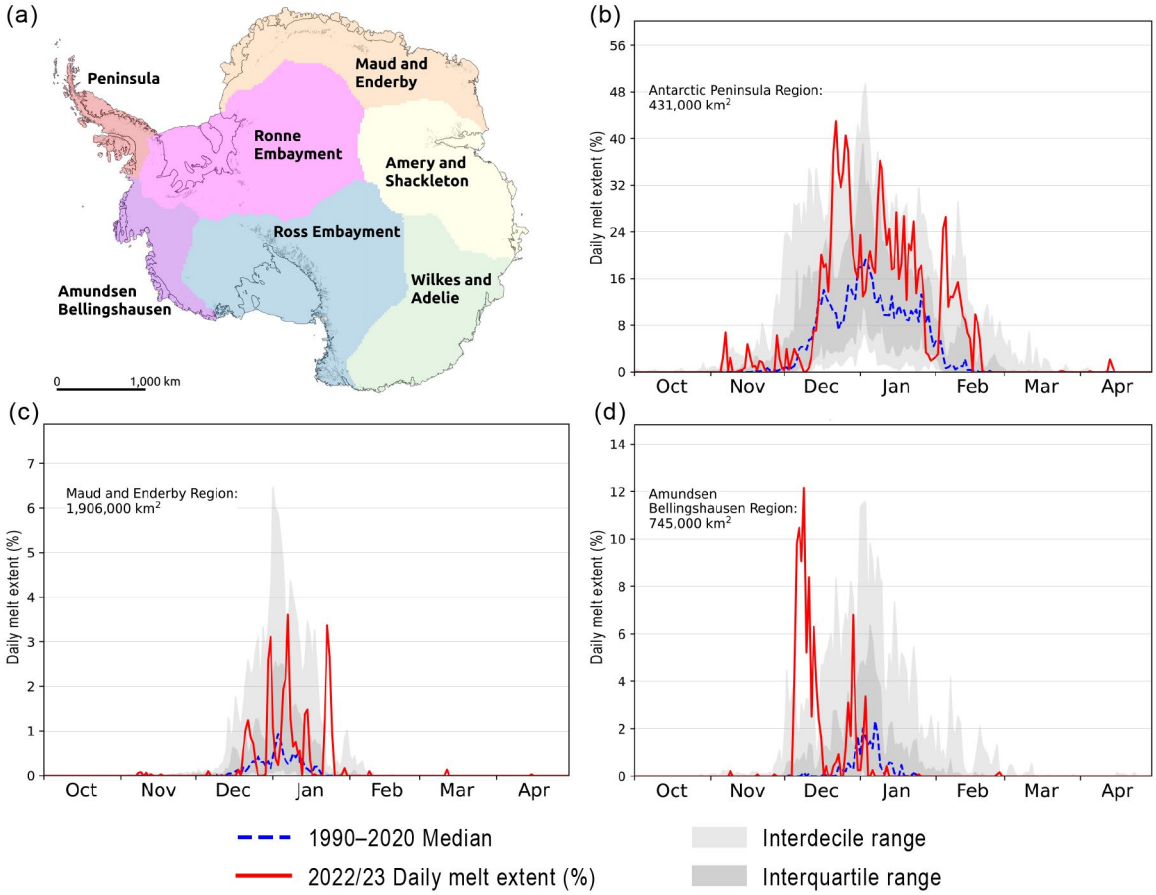

Fig. 6.8. (a) Map of Antarctic regions used in this analysis. (b)–(d) Daily 2022/23 melt extent (%) over the (b) Antarctic Peninsula region, (c) Maud and Enderby region, and (d) Amundsen Bellingshausen region.

e. Ice-sheet mass balance

—S. Adusumilli and H. A. Fricker

The mass balance of the Antarctic Ice Sheet (AIS) is the difference between mass gained through accumulation (snowfall minus sublimation) at the surface and mass lost around margins where ice is fed to the ocean through its floating ice-shelf extensions. Net ice-shelf mass loss does not add to sea level, but ice shelves play an important role in regulating the flow of grounded ice to the ocean across the grounding line through a process called "buttressing" (e.g., Gudmundsson et al. 2019). Buttressing can be reduced by an ice shelf losing mass (Paolo et al. 2015; Smith et al. 2020) or retreating from pinning points (Miles and Bingham 2024). Buttressing is lost completely if the ice shelf collapses, usually through hydrofracture (Scambos et al. 2004). Reduced buttressing leads to increased flow of ice across the grounding line, which adds to sea level (360 Gt of ice is around 1 mm global sea-level equivalent). For any given time period, the net mass balance for the grounded AIS is the difference between competing processes (mass gain from accumulation and mass loss from dynamic thinning), which depends on the integrated effects of interactions between the ice, ocean, and atmosphere (e.g., Smith et al. 2020).

Mass loss from ice shelves occurs through two main processes: calving of icebergs at ice-shelf fronts, which occurs episodically on multi-annual to multi-decadal time scales, and ocean-driven basal melting (Rignot et al. 2013; Depoorter et al. 2013; Adusumilli et al. 2020), which occurs continuously. Since 1992, the AIS has experienced overall net mass loss of grounded ice (Otosaka et al. 2022), dominated by trends in the West Antarctic Ice Sheet (WAIS). Most of this loss is attributed to net ice-shelf mass loss (Paolo et al. 2015) and a corresponding reduction in buttressing (Gudmundsson et al. 2019). Mass gains occur mainly in the interior grounded ice through changes in precipitation; as discussed in last year's report (Clem and Raphael 2023), in 2022, AIS showed record mass gains, primarily due to an increase in precipitation events over East Antarctica associated with an above-average number of landfalling atmospheric rivers.

At the time of writing, there were no published estimates of total AIS mass or height change for 2023. Here, we derived estimates of height changes over the grounded ice sheet from NASA's Ice, Cloud, and land Elevation Satellite (ICESat)-2 laser altimeter using data for 2023 until the latest available date (26 October 2023). We used the Advanced Topographic Laser Altimeter System (ATLAS)/ICESat-2 L3B Slope-Corrected Land Ice Height Time Series version 5 (Smith et al. 2022), which provides precise estimates of height along repeated ground tracks at 60-m along-track resolution. We derived along-track height changes between the available data in Cycle 21 (September/October 2023) and the corresponding data from Cycle 17 (September/October 2022; Fig. 6.9). To analyze seasonal variability, we also derived height changes over three-month intervals between successive ICESat-2 data acquisition cycles during the October 2022 to October 2023 period (Fig. 6.10). We smoothed the final height change map using a Gaussian filter with a 30-km diameter.

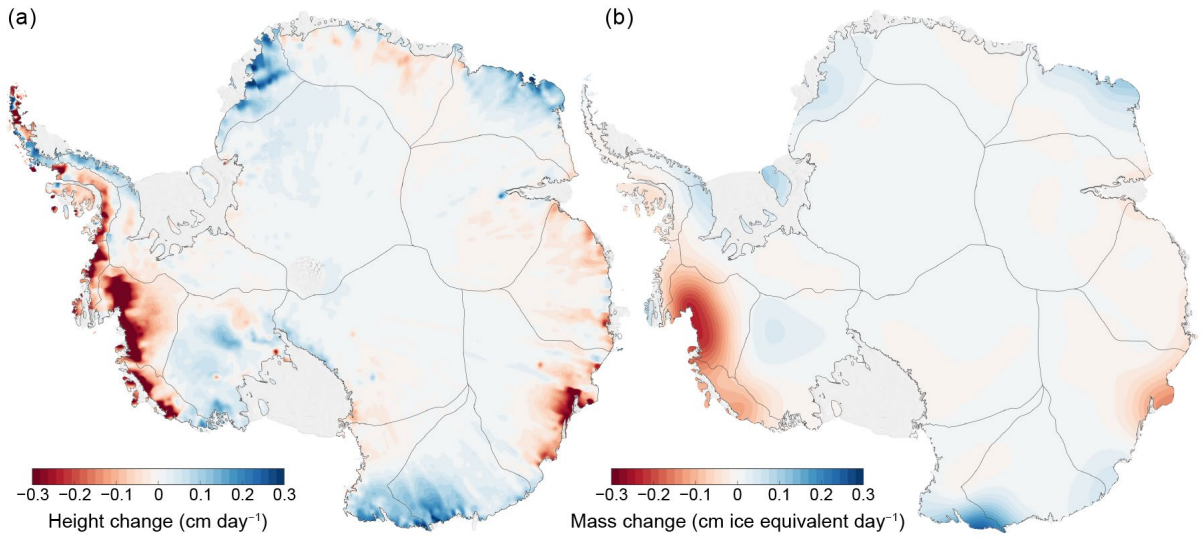

Fig. 6.9. Maps of (a) height change (cm day^{-1}) from ICESat-2 for the Oct 2022 to Oct 2023 period and (b) ice-equivalent mass change (cm ice equivalent day^{-1}) from GRACE-FO for the Oct 2022 to Oct 2023 period.

For further context, we provide annual mass anomalies derived from NASA's satellite gravimeter Gravity Recovery and Climate Experiment Follow-On (GRACE-FO; Fig. 6.9b) for 2023. We used data from the Jet Propulsion Laboratory GRACE and GRACE-FO Ocean, Ice, and Hydrology Equivalent Water Height Coastal Resolution Improvement (CRI) Filtered Release 06 version 02 "mascon data". Mascons (or mass concentration blocks) are 3° × 3° spherical caps placed on an elliptical approximation of Earth's surface over which these data are provided (Wiese et al. 2023a). We calculated gravity-derived mass anomalies for approximately the same period as used for ICESat-2 (November 2022 to November 2023), with the same three-month averaging. To determine ice-sheet mass anomalies, we identified all mascons containing more than 10,000 km^2 of land, according to the provided CRI land mask. We interpolated the area-averaged rates of change using bilinear interpolation according to the location of the geometric center of the land area contained within the mascon. We then masked all non-land areas using the Bedmachine ice mask (Morlighem et al. 2020). We also retrieved time series of mass changes integrated over the ice sheet (Fig. 6.10a) from the Level 4 Antarctica Mass Anomaly Time Series data product (Wiese et al. 2023b).

The maps of annual changes in ice-sheet height from ICESat-2 (Fig. 6.9a) and mass from GRACE-FO (Fig. 6.9b) for 2023 show ongoing losses of ice in the Amundsen Sea sector of WAIS, the same region where losses have been observed over the previous decade (e.g., Smith et al. 2020a; Adusumilli et al. 2023). GRACE-FO data show a net mass loss over AIS between January 2023 and November 2023 of 170 Gt (red line in Fig. 6.10a), which was higher than the average annual mass loss of 100 Gt yr^{-1} between 2003 and 2023, and significantly different from the record-breaking 294 Gt mass gain that occurred in the previous year (2022). Monthly mass gains in 2023 were in part due to surface mass gains across Wilkes Land and Dronning Maud Land (see section 6c for surface mass balance details), which offset some of the large mass losses in coastal WAIS.

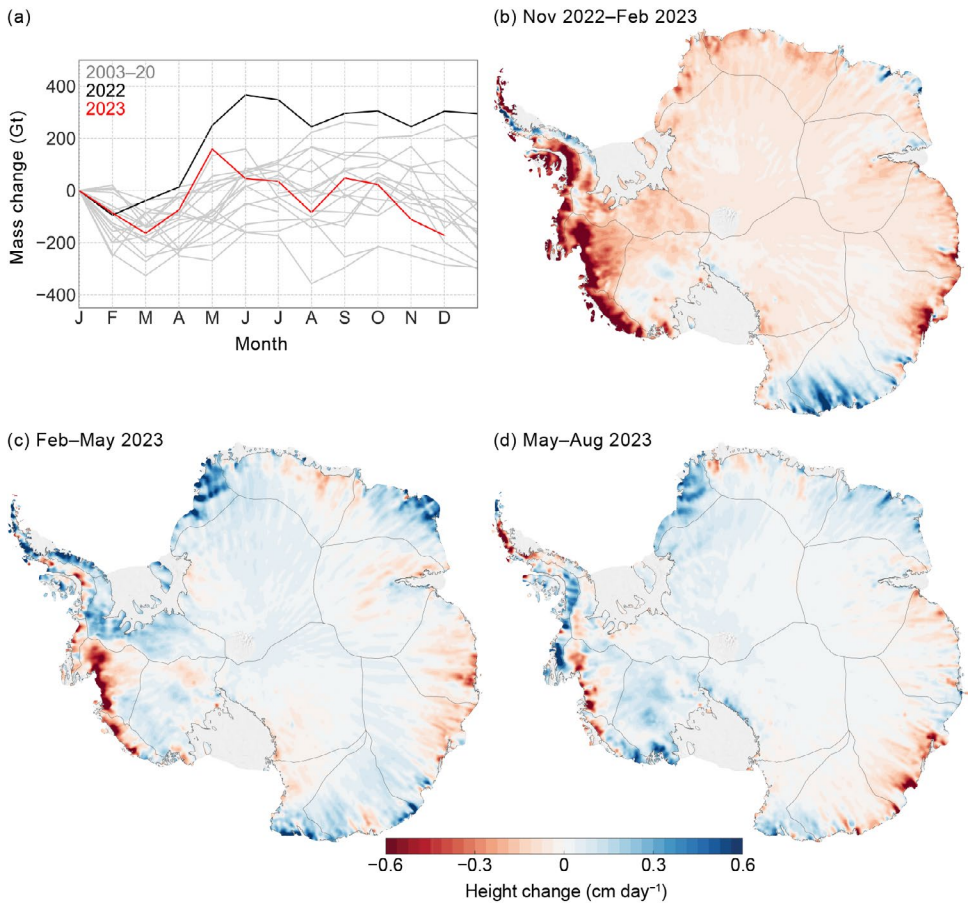

Fig. 6.10. (a) Time series of monthly mass changes (Gt) from GRACE and GRACE-FO, with 2022 and 2023 highlighted in black and red, respectively. Maps of height change (cm day^{-1}) from ICESat-2 shown at three-month intervals for (b) Oct–Dec 2022 to Jan–Mar 2023, (c) Jan–Mar 2023 to Apr–Jun 2023, and (d) Apr–Jun to Jul–Sep 2023. Dates inset on Fig. 6.10 represent the central month of each three-month ICESat-2 data acquisition cycle.

f. Sea-ice extent, concentration, and seasonality

—P. Reid, S. Stammerjohn, R. A. Massom, S. Barreira, T. A. Scambos, and J. L. Lieser

Net sea-ice extent (SIE; the area enclosed by greater than 15% sea-ice concentration) and sea-ice area (SIA; the product of sea-ice extent and concentration) were well below average or at record-low levels throughout 2023 (Fig. 6.11a). Monthly-mean low SIE and SIA records were significantly shattered for eight months in 2023 i.e., January, February, and May through October, and this is mirrored in the extreme curtailment of sea-ice growth around much of Antarctica during the autumn-winter advance season (Fig. 6.12a). The sea-ice deficit at a time of the year

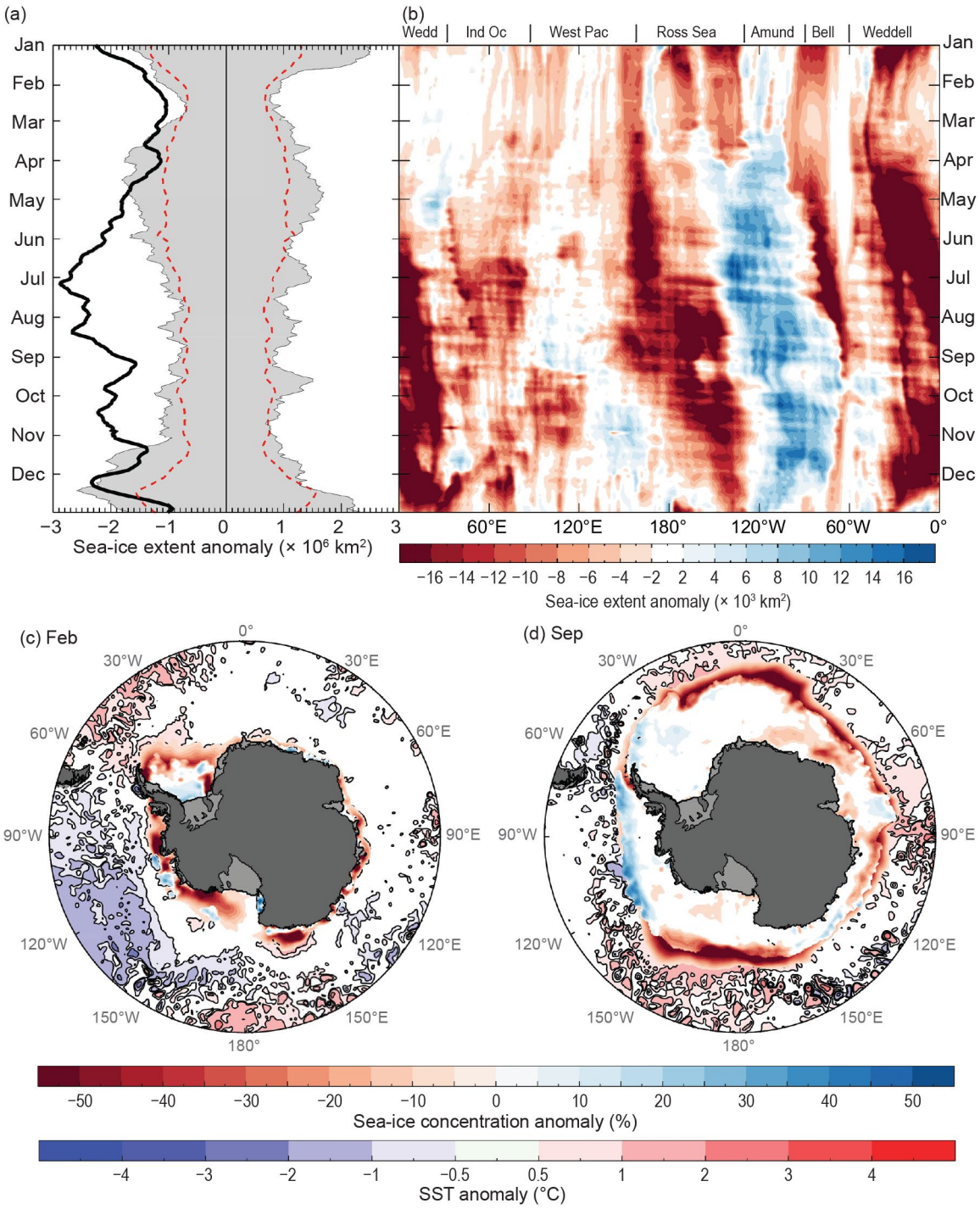

Fig. 6.11. (a) Time series of net daily sea-ice extent (SIE) anomaly (× 10^6 km²) for 2023 (solid black line; based on a 1991–2020 climatology). Gray shading represents historical (1979–2020) daily SIE anomaly, red dashed line represents ±2 std. dev., and (b) Hovmöller (time–longitude) representation of daily SIE anomaly (× 10^3 km² per degree of longitude) for 2023. (c),(d) Maps of sea-ice concentration anomaly (%) and sea-surface temperature (SST) anomaly (°C; Huang et al. 2020) for (c) Feb 2023 and (d) Sep 2023. Sea-ice concentration is based on satellite passive-microwave ice concentration data (Cavalieri et al. 1996, updated yearly for climatology; Maslanik and Stroeve 1999, for the 2023 sea-ice concentration). See Fig. 6.1 for relevant place names.

when the sea-ice zone should be growing is unprecedented in the satellite time series in both timing and magnitude. For example, net SIE was as much as ~2.9 × 10^6 km^2 below the long-term (1991–2020; used throughout) mean on 6 July, ~1.8 × 10^6 km^2 less than the previous record low for that date (in 2022; Reid et al. 2023). This situation is in contrast with the last seven years, starting with the first major downturn in Antarctic sea-ice coverage in 2016, when most record lows largely occurred during the late-spring through summer retreat/melt phase of the annual sea-ice cycle (Parkinson and DiGirolamo 2021). Regionally, SIE remained well below average almost everywhere apart from in the eastern Ross and Amundsen Seas for much of the year and in the Bellingshausen Sea for the second half of the year (Fig. 6.11b).

The unprecedented nature of Antarctic sea-ice coverage in 2023 is further highlighted by the 278 days (i.e., 76% of the entire year) and 245 days (67%) of record-low net daily SIE and SIA, respectively (Fig. 6.11a). The net daily SIE anomaly exceeded 2 std. dev. below the long-term mean throughout the entire year, apart from in late December. Moreover, the annual daily minimum SIE of 1.85 × 10^6 km^2 and SIA of 1.10 × 10^6 km^2 (both recorded on 21 February) were new all-time record lows, surpassing previous record-low annual minima set in 2022 (by 60,000 km^2 for SIE and 160,000 km^2 for SIA). Similarly, annual daily maximum SIE (of 17.00 × 10^6 km^2 on 7 September) and SIA (13.43 × 10^6 km^2 on 6 September) set new record lows and occurred two weeks earlier than normal.

Over the last eight years, 352 and 310 (out of 365) record-low daily values of SIE and SIA, respectively, have been broken. Despite the numerous record lows broken since 2016, but especially in 2023, it is worth noting that 1980 still retains a number of daily and monthly record lows (e.g., April for SIE and April–May for SIA).

Changes in upper-ocean conditions may be largely responsible for the increasing persistence in negative Antarctic SIE anomalies and reduced duration observed since 2016 (Cheng et al. 2022; Purich and Doddridge 2023; Hobbs et al., 2024). Although regional sea-ice anomalies can often be linked to regional atmospheric circulation anomalies (Massom et al. 2008), the persistence and wide distribution of negative SIE anomalies, as observed during 2022 and 2023 especially, point to circumpolar shifts in ocean–ice interactions. Within this context, the regional and temporal patterns and variations through 2023 are discussed below and closely reflect patterns and phenomena in the high-latitude atmospheric circulation and Southern Ocean (see sections 6b and 6g, respectively).

From January through March, Antarctic SIE was very much below average around most of the continent, except within small pockets of the Amundsen Sea and off Victoria Land within the western Ross Sea where SIE was slightly above average (Fig. 6.11b). Prior to this, in late 2022, a deep Amundsen Sea Low in the Pacific, contraction of circumpolar lows (associated with a strong polar vortex), and an associated strongly positive Southern Annular Mode (SAM) pattern enhanced advection of sea ice to more northerly latitudes and higher SSTs. This likely led to an early sea-ice retreat for 2022/23, setting the stage for the second consecutive record-low annual minimum. Negative SIE anomalies across parts of East Antarctica and most of the Ross and Bellingshausen Seas ranged between 1 std. dev. and 3 std. dev. below average, with the Bellingshausen Sea having persistently low SIE since August 2022 (see last year's report, Reid et al. 2023). During this time, above-average SSTs were present off Oates Land (~150°E–170°E) and within the Weddell Sea, with below-normal SSTs in the Ross, Amundsen, and Bellingshausen Seas (Fig. 6.11c; section 6g), while north of the Antarctic Circumpolar Current (ACC) there were extensive pools of anomalously high SSTs in the three major Southern Hemisphere basins (Indian, Atlantic, and western Pacific Oceans).

From April through August, sea ice advanced earlier than normal in only the Amundsen and eastern Ross Seas (Fig. 6.12a), consistent with the below-normal SSTs to the north of the ice edge in this region (see Fig. 6.13e). Regionally, sea ice within the eastern Ross Sea, at a deficit until the end of March, suddenly advanced quickly from April onwards (Fig. 6.11b), possibly as a result of the fresher-than-normal surface waters in that region (see Fig. 6.13f). Over these mid-autumn through winter months, net SIE was substantially below average (Fig. 6.11a), with substantial parts of the Ross and Weddell Seas being over 6 std. dev. below daily average during July and August. Notably, the largest SIE anomalies were region-specific and centered on the Indian Ocean sector of East Antarctica (~30°E–90°E), the western Pacific to Ross Sea (~150°E–130°W),

and the Bellingshausen and Weddell Seas (~80°W–10°E). In these regions, lack of typical annual sea-ice advance (Fig. 6.12a) and the subsequent major deficit in sea-ice coverage through winter coincided with above-normal SSTs (by ~2°C; Fig. 6.11c) in each of the three ocean basins, stretching poleward across the ACC, with the anomalously high SSTs and upper-ocean temperatures delaying sea-ice growth and intensifying the negative SIE anomalies in the Indian, Atlantic, and western Pacific sectors in late June through early July (Fig. 6.11b). During August, as a positive pressure/anticyclonic circulation anomaly developed over the Ross-Amundsen Seas region, consistent with the onset of El Niño (see section 6b), there was a sudden growth of sea ice within the Bellingshausen Sea such that SIE changed from well below to slightly above average by the end of August, with this pattern continuing through November.

By the start of September, SSTs that were above normal by as much as 2°C, largely encircled the sea-ice edge (Fig. 6.11d). A marked change occurred in the atmospheric synoptic pattern, whereby anomalous high pressure that had been observed in the Ross Sea during July and August migrated east into the Bellingshausen Sea in September to be replaced by a deep low-pressure system in the Ross Sea (not shown but see Fig. 6.3e). This change brought about a burst of sea-ice growth in the western Ross Sea, reducing the magnitude of the anomalously low SIE in that region while simultaneously reducing the SIE across East Antarctica (~90°E–120°E). Anomalous low pressure also developed briefly in the Weddell Sea during October and enhanced sea-ice growth in the Bellingshausen and western Weddell Seas. Thus, SIE within the western Pacific retreated slowly from September to November (Fig 6.12b), albeit from a very low extent, so that by the end of November the SIE within this region was close to its long-term average. Elsewhere, the SIE anomaly pattern remained reasonably static from September through November, with very low SIE across much of East Antarctica and the eastern Ross and Weddell Seas.

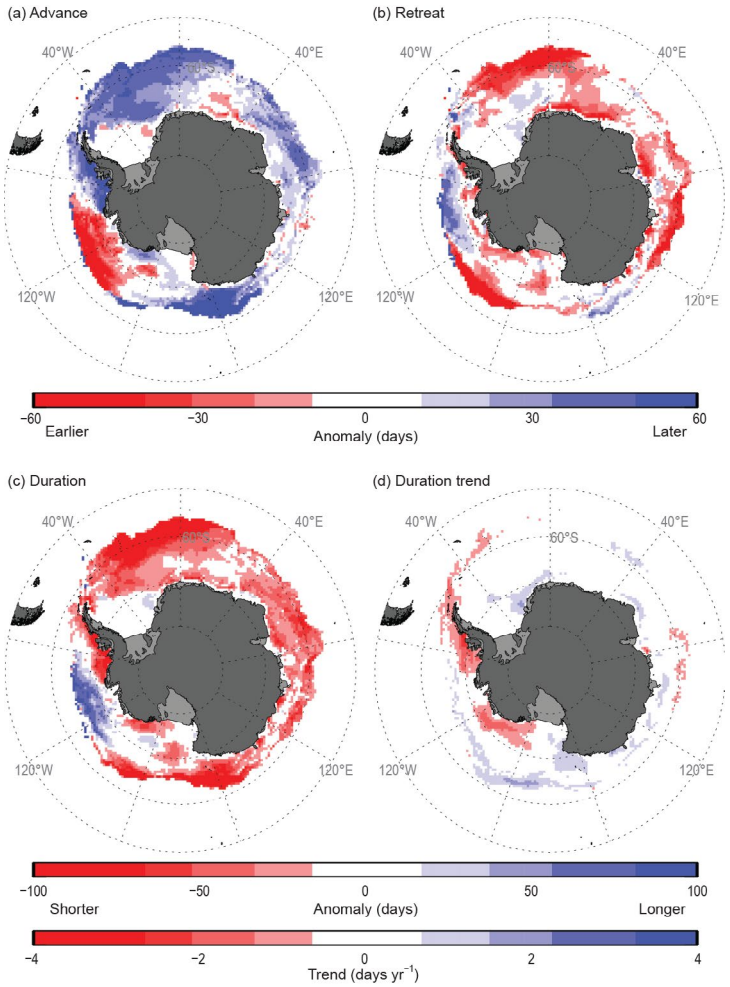

Fig. 6.12. Maps of seasonal sea-ice anomalies (days) in 2023 during (a) autumn ice-edge advance, (b) spring ice-edge retreat, and (c) winter ice-season duration; together with (d) winter ice-season duration trend (days yr^{-1}; Stammerjohn et al. 2008). The seasonal anomalies (a)–(c) are computed against the 1991/92 to 2020/21 climatology; the trend (d) is computed over 1979/80–2023/24. The climatology (for computing the anomalies) is based on data from Comiso (2017; updated yearly), while the 2023/24 ice-edge retreat duration-year data are from the NASA Team NRTSI dataset (Maslanik and Stroeve 1999); the trend is based on the merged dataset containing 1979–2022 data from Comiso (2017) and 2023/24 data from the NASA Team NRTSI dataset (Maslanik and Stroeve 1999).

December saw an intensification of the circumpolar westerlies (section 6b) leading to a distinct change in the regional SIE anomaly. Notable during this month was the formation of two deep low-pressure anomalies (see Fig. 6.3g). One, to the north of the sea-ice edge in the Weddell Sea (~20°W), appears to have initially caused a reduction in regional SIE and a coincident compaction of the sea-ice zone by northerly winds (cf. Massom et al. 2008) within the central Weddell Sea. This led to persistence of a broad band of high-concentration ice in the eastern Weddell Sea (from ~0° to 30°W) and slower-than-normal sea-ice retreat there during December (Fig. 6.12b). The other negative pressure anomaly was centered to the south of the ice edge in the Ross Sea, slowing seasonal sea-ice retreat off Oates Land and parts of the Ross Sea (~150°E–150°W).

In terms of seasonality, records were broken across most Antarctic sectors, with greater than two-month delays in the ice edge advance and greater than two-month earlier ice edge retreat (Figs. 6.12a,b). Regional exceptions during the autumn advance were the western Bellingshausen, Amundsen, and eastern Ross Seas (~90°W–150°W) and the Bellingshausen-Amundsen Seas (~60°W–120°W) during the retreat. Taken together, 2023 was marked by the largest and most widespread decreases in ice-season duration (Fig. 6.12c) yet observed since 1979, with most regions experiencing a three-to-four-month shorter ice season, the only exception being the western Bellingshausen and eastern Amundsen offshore areas (~80°W–120°W). Anomalously low coverage of sea ice in 2023 also resulted in 154 days of record-high coastal exposure (i.e., total lack of a protective sea-ice "buffer" offshore; Reid and Massom 2022), with implications for ice-shelf stability (Massom et al. 2018; Teder et al. 2022). This occurred mostly during the late 2022/23 retreat and early advance periods, with many days having more than twice the usual coastal exposure.

The recent abrupt switch from record and near-record high SIE in 2012–14 and the first half of 2015 to record lows after 2016 indicates a potential transition in the Southern Ocean–ice–atmosphere system. After nearly four decades of gradual increase in net SIE, unreconciled with climate models that predict general Antarctic sea-ice decline with an increasingly warmer global climate, it is now plausible that oceanic and atmospheric warmth have begun to transform the Southern Ocean system and that non-linear feedbacks may have been activated.

g. Southern Ocean

—S. Thomalla, R. L. Beadling, M. du Plessis, E. Souza, D. Fernandez, S. T. Gille, S. A. Josey, G. A. MacGilchrist, A. Marouchos, C. R. McMahon, L. Pezzi, C. Schultz, J.-R. Shi, S. C. Tripathy, and K. Turner

The Southern Ocean (SO) plays a critical role in buffering the impacts of climate change by accounting for 50% of the oceanic uptake of anthropogenic carbon dioxide (CO_2) and 75% of the oceanic uptake of anthropogenic heat (Frölicher et al. 2015). Physical processes influence air–sea exchanges of heat, while carbon fluxes are additionally strongly affected by biological processes. Both physical and biological processes exhibit seasonal, inter-annual, and decadal variability, reflecting large-scale responses to atmospheric drivers, all of which affect the transfer of carbon and heat with complex feedbacks on ocean biogeochemistry and climate (Henley et al. 2020). Here, we assess the 2023 anomalies in key physical and biological SO metrics. Results for 2023 are intriguing in the context of the record-low sea-ice coverages discussed in section 6f that may reflect alterations in the underlying processes that determine the state of sea-ice (Purich and Doddridge 2023). Key outcomes highlight substantial ocean warming with a dominance of SO positive anomalies in sea-surface temperature (SST), ocean heat content (OHC), and air–sea heat flux. Such changes may be exacerbated by the warm conditions of the 2023 El Niño, with evidence of cascading impacts on ocean biogeochemistry. These results highlight the impact of changing atmosphere–ocean dynamics that are of particular concern given the central role that the SO exerts on the climate system.

1. SEA-SURFACE TEMPERATURE, SALINITY, AND MIXED-LAYER DEPTH

Sea-surface temperature anomalies for 2023 (relative to 2004–20) were determined from NOAA OI SST V2 (Reynolds et al. 2002). Positive SST anomalies across much of the SO (Fig. 6.13a) revealed warming (up to 1.5°C). Overall, the SO remained warmer than normal throughout the year (Fig. 6.13e), following the warming tendency in previous years (Beadling et al. 2022; Pezzi et al. 2023). A notable exception is the eastern Pacific sector, which revealed negative anomalies (up to −0.8°C; Fig. 6.13a) particularly in late summer (February–April; Fig. 6.13e). The Pacific temperature anomaly dipole in 2023 reflects the emergence of a positive pressure/anticyclonic anomaly over the high-latitude South Pacific associated with the transition to El Niño (section 6b). Anomalies of sea-surface salinity (SSS) derived from the Argo dataset (Roemmich and Gilson 2009) relative to the 2004–18 climatology were similar to 2022 values discussed in last year's report (Pezzi et al. 2023), with positive anomalies (up to 0.12 PSU) dominating large parts of the SO (Fig. 6.13b), especially in winter and spring with the most extreme positive anomalies occurring in the Atlantic sector (Fig. 6.13f). The SO overall expressed a slight negative SSS anomaly in late summer (January–April) due predominantly to anomalies in the Indian basin (Fig. 6.13f). The annual anomaly in mixed-layer depth (MLD, defined according to de Boyer Montégut [2004] applied to Argo) relative to 2004–22 is dominated by wintertime anomalies and characterized by negative (shallower) MLDs in the western Pacific and central Indian Ocean sectors interspersed with positive (deeper) MLDs in the eastern Pacific and Indian up to ±~80 m (Figs. 6.13c,g). In contrast, 2022 was characterized by deeper MLD anomalies over the majority of the SO (including both western and eastern Pacific and the central Indian) with only a small negative anomaly within the eastern Indian sector. The zonal dipole in Pacific MLD anomalies (Fig. 6.13c) reflects that of SST, with warmer anomalies in the western Pacific aligned with shallower winter MLDs, while cooler SST anomalies in the eastern Pacific are associated with deeper winter MLDs (Figs. 6.13a,c).

2. AIR–SEA HEAT FLUX

Net heat-flux anomalies for 2023 (relative to 1998–22) were derived from the ERA5 reanalysis (Hersbach et al. 2020). The effects of positive pressure anomaly in the South Pacific associated with El Niño are similarly present in the net heat-flux pattern (Fig. 6.13d), with positive anomalies (less heat loss from the ocean) dominating in the western Pacific (synchronous with high SST and shallow winter MLD) and negative anomalies (more heat loss from the ocean) in the eastern Pacific. The seasonal cycle of anomalies (Fig. 6.13h) suggests that these effects are most prominent in winter when the positive pressure anomalies are strongest (see Fig. 6.3e). The SO heat-flux asymmetry index (Josey et al. 2023), which measures the difference in Atlantic–Indian and

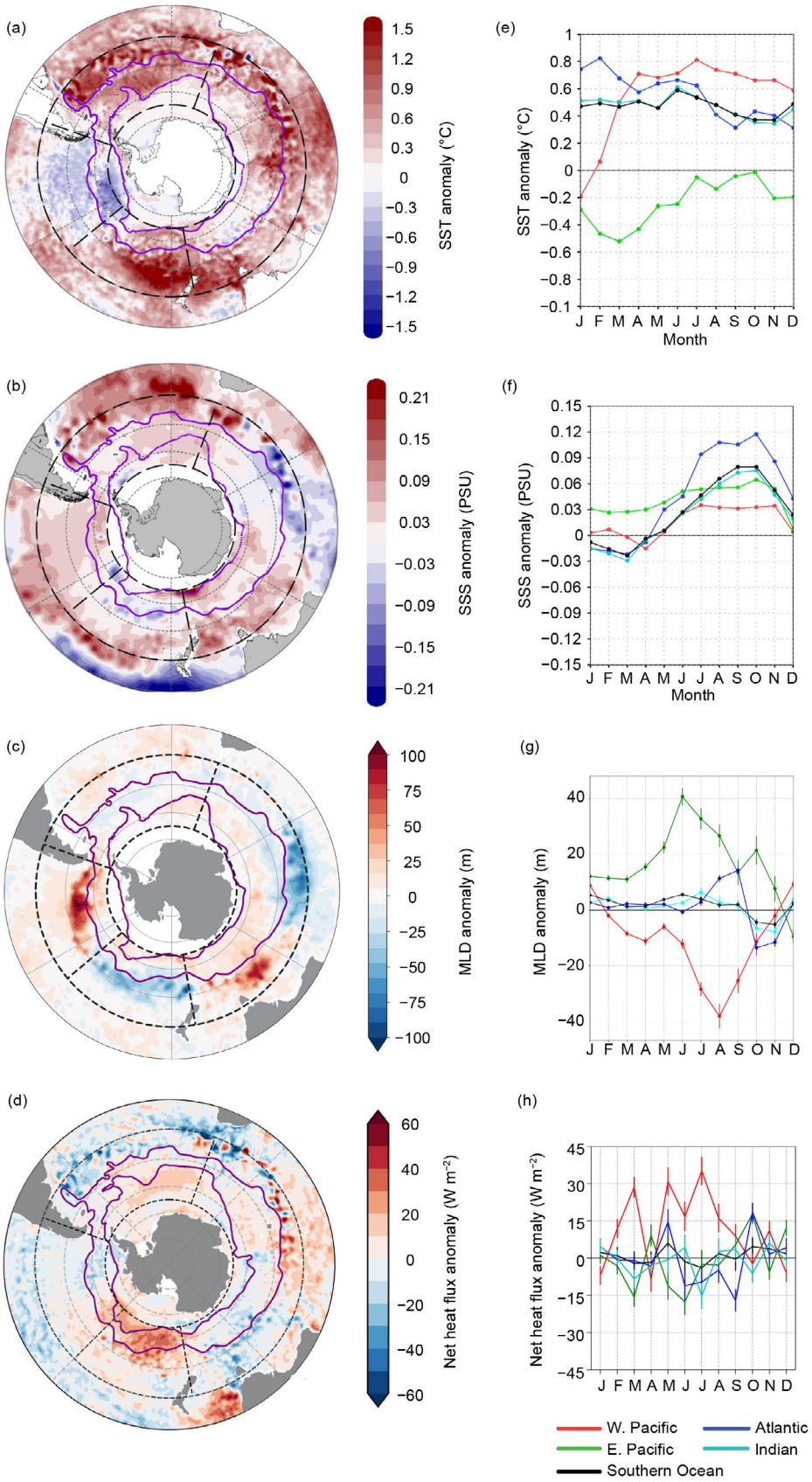

Fig. 6.13. Annual-average anomalies (Jan–Dec 2023) of (a) sea-surface temperature (SST; °C), (b) sea-surface salinity (SSS; PSU), (c) mixed-layer depth (MLD; m), and (d) net heat flux (W m^{-2}). Overlaid are the positions of the Subantarctic and Southern Boundary Antarctic Circumpolar Fronts (purple lines) as defined by Orsi et al. (1995). Four distinct regions between 40°S and 65°S are delineated by black dashed contours corresponding to the Atlantic (70°W–20°E), Indian (20°E–170°E), western Pacific (170°W–120°W), and eastern Pacific (120°W–70°W) sectors. The 2023 seasonal cycle of anomalies in (e) SST (°C), (f) SSS (PSU), (g) MLD (m), and (h) net heat flux (W m^{-2}) separated according to the four sectors defined above. Error bars in (g),(h) represent the standard error of the climatological mean (i.e., std. dev. divided by √N, where N is the number of years, the number of years in the climatology).

Pacific sector surface heat exchange, was –1.48 in 2023, which reflects a weakening of the asymmetry that is commonly seen during El Niño.

3. UPPER OCEAN HEAT CONTENT

The 0-m–2000-m OHC was retrieved from monthly gridded Argo temperature data (Roemmich and Gilson 2009), with 2023 anomalies determined relative to 2005–20 climatology. The annual OHC anomaly (Fig. 6.14a) gained heat with positive anomalies to the north of the Antarctic Circumpolar Current (ACC). The OHC cooling anomalies east of Australia and within the ACC of the eastern Pacific, in addition to the patchy cooling evident in the Indian sector east of South Africa, typically align with negative SST anomalies (Fig. 6.13a). The OHC anomaly time series shows a long-term warming since 2005 (Fig. 6.14b). Although globally the 0-m–2000-m OHC in 2023 exceeded that of 2022 by around 10 ZJ (Cheng et al. 2024), the SO shows a decrease in OHC (–1.0 ZJ) in 2023 relative to 2022 (Fig. 6.14b).

4. OCEAN BIOGEOCHEMISTRY

Chlorophyll data from the eight-day European Space Agency Ocean Colour Climate Change Initiative (OC-CCI) product (v6.0; Sathyendranath et al. 2019) were processed as per Thomalla et al. (2023), with 2023 anomalies computed relative to 1999–2023 climatology (Fig. 6.14c). For the SO as a whole, chlorophyll shows a typical alignment with the long-term average during winter, spring, and autumn, but a strong positive anomaly during the summer bloom. The positive anomaly in summer chlorophyll was dominated by the eastern Pacific, which coincided with cooler SSTs, negative heat-flux anomalies, and deeper MLDs (Figs. 6.13a,c,d). Conversely, the

western Pacific expressed negative chlorophyll anomalies in both spring and late summer aligned with higher SSTs, positive heat flux, and shallower MLDs (Figs. 6.13a,c,d). Anomalies in dissolved oxygen (DO) for 2023 relative to 2003–22 climatology were derived per ocean basin from Biogeochemical Argo (BGC-Argo; Wong et al. 2020; Fig. 6.14d). The Pacific dipole is similarly reflected in DO with negative 0-m–250-m anomalies in the western Pacific, consistent with warmer waters, shallower mixed layers, and below-average chlorophyll concentrations, while in the eastern Pacific the opposite occurred (with the positive DO anomaly particularly evident at 150-m–300-m depth). The most distinctive feature in DO was a strong negative anomaly in the top ~250 m in the Atlantic, which aligned with pronounced positive anomalies in SST, SSS, and OHC (Figs. 6.13a,b; Fig. 6.14a), despite positive anomalies in chlorophyll (Fig. 6.14c).

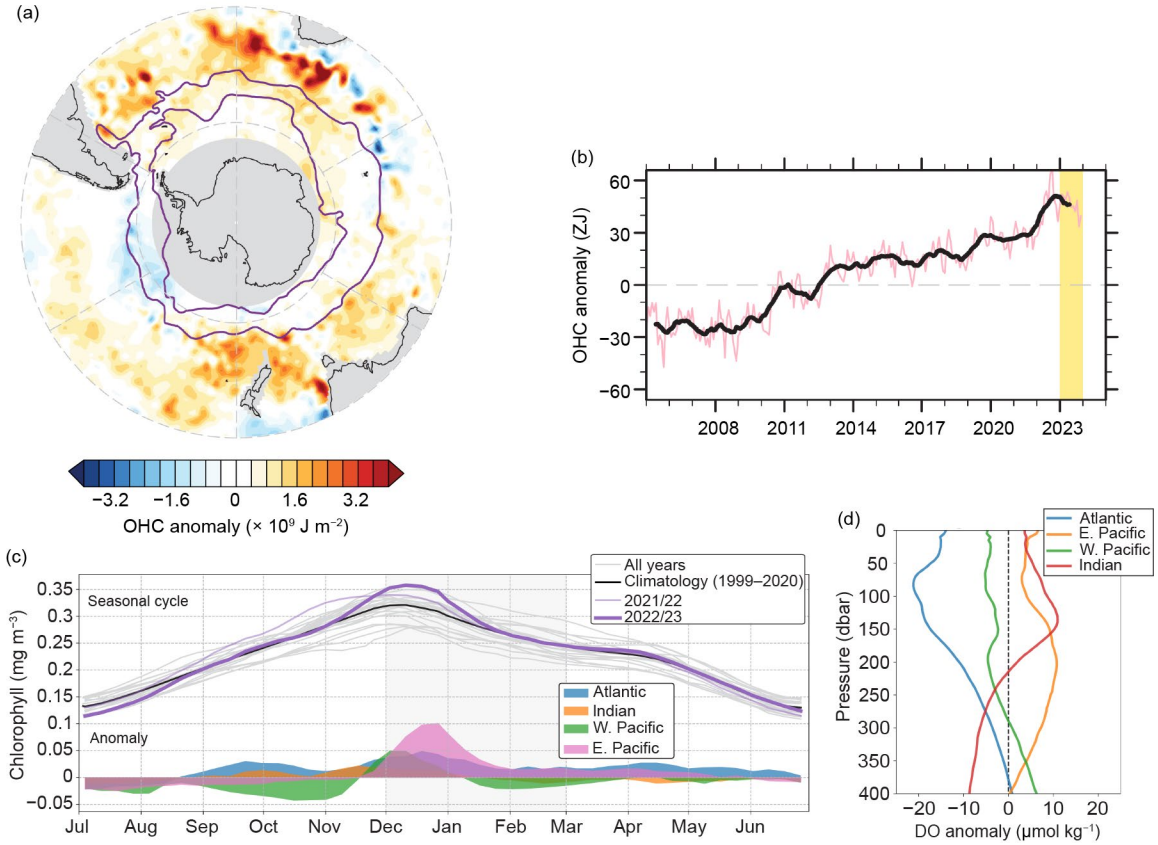

Fig. 6.14. (a) 2023 annual average ocean heat content (OHC; × 10^9 J m^{-2}) anomalies. Overlaid are the Subantarctic and Southern Boundary Antarctic Circumpolar Fronts (purple lines) as defined by Orsi et al. (1995). (b) Time series of monthly average 0-m–2000-m OHC anomaly (ZJ or 10^{21} J) relative to 2005–20 Argo climatology south of 30°S (red line) with 12-month running mean on top (black line) and 2023 highlighted (yellow shading). (c) Seasonal cycle of area-weighted (40°S–65°S) daily-mean chlorophyll concentration (mg m^{-3}) depicting all historical years (gray lines), the climatological 1999–2023 mean (black line), and the most recent two growing seasons (purple lines); anomalies for Jul 2022–Jun 2023 relative to the 1999–2023 climatological mean are depicted for each ocean sector (colored shading). (d) Dissolved oxygen (DO) anomalies (kg m^{-3}) with pressure (dbar) for Jul 2022–Jun 2023 relative to the 2005–20 Argo climatology.

h. 2023 Antarctic ozone hole

—N. A. Kramarova, P. A. Newman, L. R. Lait, B. Johnson, M. Pitts, M. L. Santee, I. Petropavlovskikh, L. Coy, and J. De Laat

The 2023 Antarctic ozone hole was the 16th largest in 44 years of satellite observations since 1979, with an average area of 23.08 × 10^6 km^2 (averaged for 7 September–13 October) and a minimum daily total ozone column of 99 Dobson Units (DU; 1 DU is equivalent to a layer of pure ozone 0.01 mm thick at standard temperature and pressure) on 3 October. The 2023 Antarctic ozone hole appeared earlier than in recent years and exceeded 20 × 10^6 km^2 by 2 September. In early September—a critical period for ozone depletion—lower stratospheric temperatures were below average. A strong wave event warmed the lower stratosphere by 6.1 K and reduced the ozone hole area by 4.9 × 10^6 km^2 between 17 and 28 September. Meteorological conditions in the lower Antarctic stratosphere and the area of the ozone hole were close to average from late September to mid-November. Weak wave activity in late austral spring slowed the seasonal transition to summer, similar to the situation in the three previous years (2020, 2021, and 2022). As a result, lower stratospheric temperatures were below average and the ozone hole persisted longer than normal in 2023, breaking up on 20 December (the 1990–2019 average breakup date is 9 December).

In January 2022, the Hunga volcano (previously referred to as Hunga Tonga–Hunga Ha'apai) injected volcanic material (e.g., Carr et al. 2022; Taha et al. 2022) and a record amount of water vapor (~146 ±5 Tg) directly into the stratosphere (e.g., Millán et al. 2022; Blunden et al. 2023), increasing global stratospheric water vapor by ~10%. In 2022, Hunga volcanic aerosols and excess water vapor did not penetrate into the southern stratospheric vortex (Manney et al. 2023) and therefore did not directly affect the 2022 ozone hole development and the chemical composition inside the Antarctic vortex (Kramarova et al. 2023).

Following the 2022 Southern Hemisphere (SH) vortex breakup, the Hunga plume was advected to Antarctic polar latitudes (Manney et al. 2023; Santee et al. 2024). Water vapor observations in May and the first half of June 2023 (Fig. 6.15b) showed a 25%–50% increase above average on the 440-K isentropic surface (~60 hPa or ~19 km). Excess moisture shifted the threshold temperatures for polar stratospheric cloud formation upward by ~1 K–2 K (Santee et al. 2024). Antarctic lower stratospheric temperatures were near average in May and dropped to below average in June (Fig. 6.15a). The combination of colder temperatures and excess water vapor in the stratosphere facilitated earlier-than-usual polar stratospheric cloud formation (Fig. 6.15d) over an extended vertical range. Polar stratospheric clouds provide surface area for heterogeneous reactions that convert reservoir chlorine species into active forms (e.g., chlorine monoxide [ClO]; Fig. 6.15c) that can catalytically destroy ozone. The record-high polar stratospheric cloud volume in May and June (Fig. 6.15d) resulted in unusually early chlorine activation in the Antarctic stratosphere (Santee et al. 2024), particularly at higher altitudes near 600 K–800 K (not shown). However, while unprecedented, this early winter chlorine activation was much weaker than that occurring later in the season and did not induce substantial ozone depletion.

Seasonal dehydration—the process whereby water vapor concentrations decline in the polar lower stratosphere every year due to sedimentation of ice polar stratospheric particles—occurred at higher altitudes, and the amount of water vapor removed was also higher than average (Santee et al. 2024). The sharp peak in water vapor mixing ratios (above the already-elevated values) evident in late May on the 440-K surface (Fig. 6.15b) is likely a signature of rehydration from evaporation of ice polar stratospheric cloud particles sedimenting from above. Water vapor dropped to below-average levels on this surface by the end of June (Fig. 6.15b) and then stayed near the average until December.

In 2023, chlorine activation, represented by ClO (Fig. 6.15c), lasted longer than usual, reaching its maximum in the second half of September (a critical period for ozone depletion). Because of the Montreal Protocol (World Meteorological Organization 2022), chlorine and bromine concentrations in the Antarctic stratosphere are slowly declining. Effective equivalent stratospheric chlorine (EESC, a metric for the abundance of chlorine and bromine species; Newman et al.

2007) levels in 2023 were around 3.23 ppbv, ~15% lower than the maximum values observed in the early 2000s. The EESC decline resulted in lower ClO concentrations in 2023 compared to those in 2006. The 2023 ozone depletion between early July and early October was about 2.18 ppmv, smaller than the 2.24 ppmv ozone depletion in 2006 when the stratospheric ClO concentration in September was a record high.

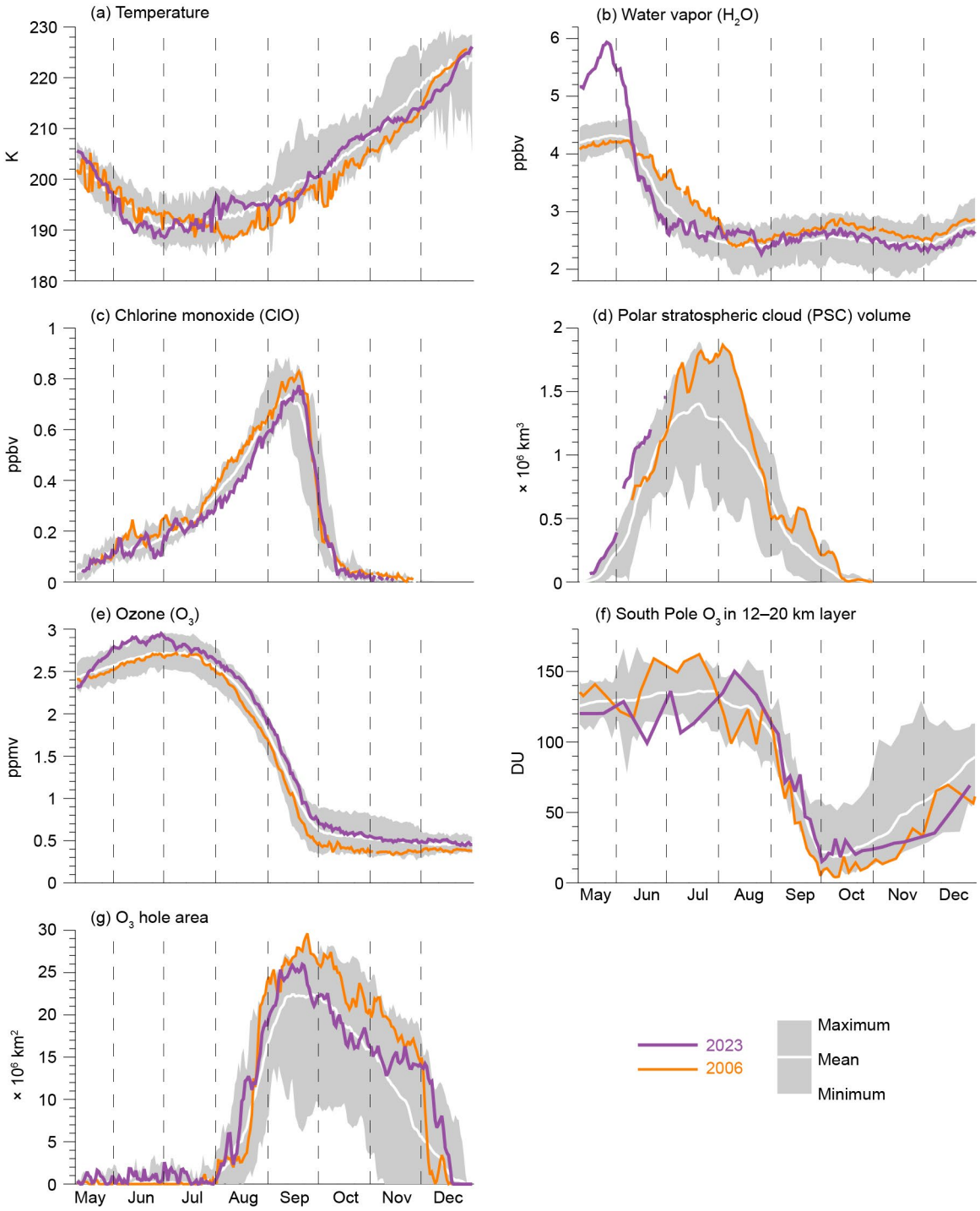

Fig. 6.15. Antarctic values of (a) vortex-averaged MERRA-2 temperature (K) on the 440-K potential temperature surface (~19 km or 60 hPa, vortex-averaged), (b) H_2O (ppmv), (c) ClO (ppbv), and (e) O_3 (ppmv) on the 440-K potential temperature surface from Aura MLS (updated from Manney et al. 2011), (d) CALIPSO polar stratospheric cloud (PSC) volume (× 10^6 km^3) updated from Pitts et al. 2018), (f) lower stratospheric ozone columns (12 km–20 km; DU) based on sonde measurements at South Pole, (g) Ozone Monitoring Instrument (OMI)/Ozone Mapping and Profiler Suite (OMPS) Antarctic ozone hole area (× 10^6 km^2; area with ozone total column less than 220 DU). Gray shading shows the range of daily Antarctic values for 2005 (for all but [d], which starts in 2006) through 2022. The white curve indicates the 2005–22 long-term mean. CALIPSO measurements ceased at the end of June 2023.

Lower stratospheric ozone column between 12 km and 20 km derived from sonde measurements at South Pole (SP) station was near or below average during May–July 2023 (Fig. 6.15f) and then above average in August. SP columns quickly declined in September, reaching the minimum value of 15.3 DU on 1 October. The Antarctic ozone hole area—the area with total ozone columns below 220 DU—appeared earlier than in recent years (Fig. 6.15g) and reached its peak on 21 September at 25.96 × 10^6 km^2. The area of the ozone hole was then sharply reduced by 4.9 × 10^6 km^2 following the mid-September warming event (Fig. 6.15a). Another strong wave event in early October kept temperatures, ozone hole area, and SP columns near average in October and early November. From mid-October, the planetary-scale wave activity was very low, coinciding with the strong polar vortex (section 6b), resulting in a delayed vortex breakup (winter-to-spring transition) as in the previous three years (2020–22). Weaker wave activity kept the ozone hole area larger and the SP column and stratospheric temperatures lower than usual from mid-November through December (Figs. 6.15a,f,g).

Reduced ozone depletion due to declining EESC is observable on decadal timescales (Fig. 6.16), with year-to-year hole variations modulated by Antarctic lower stratospheric temperatures. The relationship between September lower stratospheric temperatures and area deviations in September, obtained by fitting a quadratic function of EESC with a 5.2-year mean age (shown as a gray line in Fig. 6.16a) to the observed ozone hole areas, reveals that ozone holes are larger in colder-than-average years (Fig. 6.16b). Model simulations (e.g., Fleming et al. 2024) suggest that excess water vapor should lead to an additional 10 DU–20 DU ozone depletion, thereby increasing ozone hole area by ~1 × 10^6 km^2 to 3 × 10^6 km^2, but such an increase is difficult to detect because of the natural year-to-year variability of ~4 × 10^6 km^2 (Newman et al. 2004). The 2023 ozone hole lasted longer than usual (Fig. 6.16c). The 2023 November hole severity can be explained by

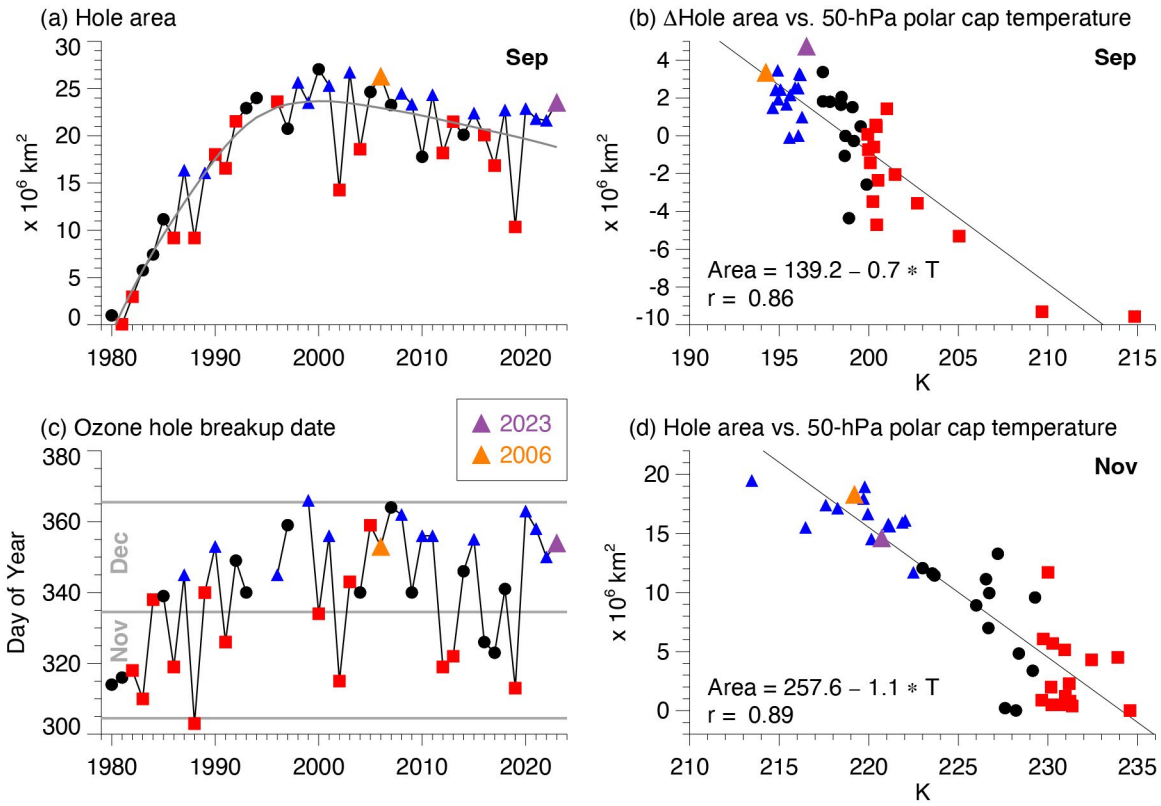

Fig. 6.16. (a) Sep average Antarctic ozone hole area. (b) Sep anomalies of the ozone hole area (see text) vs. MERRA-2 Sep 50-hPa temperatures averaged over the polar cap (60°S–90°S). (c) Ozone hole disappearance dates. (d) Nov ozone hole areas vs. MERRA-2 Nov 50-hPa temperatures. In (a), the gray curve shows a quadratic fit of effective equivalent stratospheric chlorine with a 5.2-year mean age of air (Newman et al. 2007) to the Sep hole areas. Years with temperatures in the lowest (highest) third are shown as blue triangles (red squares), and the years 2006 and 2023 are highlighted in orange and purple, respectively. Ozone data for 1979–92 are from Total Ozone Mapping Spectrometer (TOMS) Nimbus-7, 1993–94 are from TOMS Meteor-3, 1996–2004 are from TOMS-Earth Probe, 2005–15 are from Aura Ozone Monitoring Instrument (OMI), and 2015–23 are from Suomi National Polar-orbiting Partnership (SNPP) Ozone Mapping and Profiler Suite (OMPS). There were no satellite total ozone observations for 1995.

below-average stratospheric temperatures (Fig. 6.16d) due to weak wave activity in late austral spring. This weaker-than-average wave activity slowed the winter-to-summer transition, resulting once again in a longer-lasting ozone hole, similar to the behavior in 2020, 2021, and 2022.

Despite exceptional water vapor from the Hunga eruption and earlier onset of chlorine activation at the beginning of austral winter, the 2023 Antarctic ozone hole was quite ordinary. The levels of active chlorine in 2023 and seasonal ozone losses were smaller than in 2006 due to the Montreal Protocol and consistent with our understanding of polar ozone depletion. The excess water vapor may have caused some small additional ozone depletion particularly early in the season, but the losses are too small to decisively isolate and estimate the Hunga contribution to the 2023 Antarctic ozone hole.

Acknowledgments

- L. P. Pezzi acknowledges support from PROANTAR's Antarctic Modeling and Observation System (ATMOS) Project under the CNPq/PROANTAR award 443013/2018-7.
- S. A. Josey acknowledges funding from the European Union Horizon 2020 research and innovation programme under grant agreement no. 821001 SO-CHIC.
- S. T. Gille received support from NSF Award OPP-1936222.
- S. J. Thomalla acknowledges institutional support from the CSIR Parliamentary Grant (0000005278) and the Department of Science and Innovation.
- K. R. Clem acknowledges support from the Royal Society of New Zealand Marsden Fund grant MFP-VUW2010.
- D. E. Mikolajczyk, L. M. Keller, T. P. Norton, and M. A. Lazzara thank the support of the US National Science Foundation, Office of Polar Programs, grants #2301362, 1924730, and 1951603.
- Work at the Jet Propulsion Laboratory, California Institute of Technology, was done under contract with the National Aeronautics and Space Administration (NASA). Support was also provided by the NASA Modeling and Analysis Program. We are indebted to the many NOAA Corps Officers and GML technical personnel who spend the winters at South Pole Station to obtain the ongoing balloon and ground-based data sets. We also acknowledge the logistics support in Antarctica provided by the National Science Foundation Office of Polar Programs. © 2024. All rights reserved.
- P. Reid and J. Lieser were supported through the Australian Bureau of Meteorology, and R. Massom by the Australian Antarctic Division. The work of P. Reid and R. Massom also contributes to the Australian Government's Australian Antarctic Partnership Program (AAPP). For R. Massom, this work was also supported by the Australian Research Council Special Research Initiative the Australian Centre for Excellence in Antarctic Science (Project Number SR200100008).
- S. Stammerjohn was supported under NSF PLR–1552226; she also thanks the Institute of Arctic and Alpine Research and the National Snow and Ice Data Center, both at the University of Colorado Boulder, for institutional and data support.
- L. D. Trusel and J. D. Kromer acknowledge support from the NASA Cryospheric Sciences Program award 80NSSC$_{20}$K0888.

Appendix 1: Acronyms

ACC	Antarctic Circumpolar Current
AIS	Antarctic ice sheet
AR	atmospheric river
ATLAS	Advanced Topographic Laser Altimeter System
AWS	automatic weather station
BGC	biogeochemical
ClO	chlorine monoxide
CRI	coastal resolution improvement
DMSP	Defense Meteorological Satellite Program
DO	dissolved oxygen
DU	Dobson Units
EESC	effective equivalent stratospheric chlorine
ERA5	European Centre for Medium-Range Weather Forecasts Reanalysis version 5
GRACE	Gravity Recovery and Climate Experiment
GRACE-FO	Gravity Recovery and Climate Experiment Follow-on
H_2O	water
IceSat-2	Ice, Cloud and Land Elevation Satellite
MAR	Modèle Atmosphérique Régional
MERRA-2	Modern-Era Retrospective Analysis for Research and Applications version 2
MLD	mixed layer depth
MLS	Microwave Limb Sounder
NSIDC	National Snow and Ice Data Center
O_3	ozone
OC-CCI	Ocean Colour Climate Change Initiative
OHC	ocean heat content
OMI	Ozone Monitoring Instrument
OMPS	Ozone Mapping and Profiler Suite
PSC	polar stratospheric cloud
SAM	Southern Annular Mode
SH	Southern Hemisphere
SIA	sea-ice area
SIE	sea-ice extent
SMB	surface mass balance
SMMR	Scanning Multi-Channel Microwave Radiometer
SO	Southern Ocean
SP	South Pole
SSM/I	Special Sensor Microwave Imager
SSMIS	Special Sensor Microwave Imager/Sounder
SSS	sea-surface salinity
SST	sea-surface temperature
TOMS	Total Ozone Mapping Spectrometer
WAIS	West Antarctic Ice Sheet

Appendix 2: Datasets and sources

Section 6b Atmospheric circulation and surface observations

Sub-section	General Variable or Phenomenon	Specific dataset or variable	Source
6b	Modes of Variability	Marshall Southern Annular Mode Index	http://www.nerc-bas.ac.uk/icd/gjma/sam.html
6b	Temperature, [Near] Surface	ERA5	https://www.ecmwf.int/en/forecasts/dataset/ecmwf-reanalysis-v5
6b	Geopotential Height	ERA5	https://www.ecmwf.int/en/forecasts/dataset/ecmwf-reanalysis-v5
6b	Pressure, Sea Level or Near-Surface	ERA5	https://www.ecmwf.int/en/forecasts/dataset/ecmwf-reanalysis-v5
6b	Pressure, Sea Level or Near-Surface	University of Wisconsin Madison automatic weather stations - Antarctic Meteorological Research and Data Center	https://amrdcdata.ssec.wisc.edu
6b	Pressure, Sea Level or Near-Surface	Staffed weather station data	https://legacy.bas.ac.uk/met/READER/
6b	Temperature, [Near] Surface	University of Wisconsin Madison automatic weather stations - Antarctic Meteorological Research and Data Center	https://amrdcdata.ssec.wisc.edu
6b	Temperature, [Near] Surface	Staffed weather station data	https://legacy.bas.ac.uk/met/READER/
6b	Temperature, Upper Atmosphere	ERA5	https://www.ecmwf.int/en/forecasts/dataset/ecmwf-reanalysis-v5
6b	Wind, Upper Atmosphere	ERA5	https://www.ecmwf.int/en/forecasts/dataset/ecmwf-reanalysis-v5

Section 6c Ice-sheet surface mass balance

Sub-section	General Variable or Phenomenon	Specific dataset or variable	Source
6c	Ice-sheet surface mass balance	polar-oriented regional climate model (MAR)	https://arcticdata.io/catalog/view/doi%3A10.18739%2FA28G8FJ7F
6c	Ice-sheet surface mass balance	ERA5	https://www.ecmwf.int/en/forecasts/dataset/ecmwf-reanalysis-v5
6c	Ice-sheet surface mass balance	MERRA-2	http://gmao.gsfc.nasa.gov/reanalysis/MERRA-2/

Section 6d Ice-sheet melt extent and duration			
Sub-section	**General Variable or Phenomenon**	**Specific dataset or variable**	**Source**
6d	Ice-Sheet Surface Melt	DMSP-SSMIS	https://nsidc.org/data/nsidc-0001/versions/6
6d	Sea Ice Extent / Area / Concentration	Nimbus-7 SMMR Sea Ice Concentration	https://nsidc.org/data/nsidc-0007

Section 6e Ice-sheet mass balance			
Sub-section	**General Variable or Phenomenon**	**Specific dataset or variable**	**Source**
6e	Ice-Sheet Surface Height	ATLAS/ICESat-2 Land Height	https://nsidc.org/data/atl06/versions/5
6e	Ice-Sheet Surface Height	ICESat-2	https://icesat-2.gsfc.nasa.gov/
6e	Ice-Sheet Mass	GRACE - GRACE FO CRI	https://podaac.jpl.nasa.gov/dataset/TELLUS_GRAC-GRFO_MASCON_CRI_GRID_RL06_V2

Section 6f Sea-ice extent, concentration, and seasonality			
Sub-section	**General Variable or Phenomenon**	**Specific dataset or variable**	**Source**
6f	Sea Ice Duration	Near-Real-Time DMSP SSM/I-SSMIS Daily Polar Gridded	https://nsidc.org/data/nsidc-0081/versions/2
6f	Sea Ice Duration	Nimbus-7 SMMR and DMSP SSM/I (Bootstrap)	https://nsidc.org/data/nsidc-0079/versions/3
6f	Sea Surface Temperature	NOAA Optimum Interpolation SST (OISST) v2.1	https://www.ncei.noaa.gov/products/optimum-interpolation-sst

Section 6g Southern Ocean

Sub-section	General Variable or Phenomenon	Specific dataset or variable	Source
6g1	Sea Surface Temperature	NOAA Optimum Interpolation SST (OISST) v2.1	https://www.ncei.noaa.gov/products/optimum-interpolation-sst
6g1	Sea Surface Salinity	Argo monthly climatology	https://sio-argo.ucsd.edu/RG_Climatology.html
6g1	Mixed Layer Depth	Argo monthly climatology	https://sio-argo.ucsd.edu/RG_Climatology.html
6g2	Surface Heat flux	ERA5	https://www.ecmwf.int/en/forecasts/dataset/ecmwf-reanalysis-v5
6g3	Ocean Heat Content	Argo monthly climatology	https://sio-argo.ucsd.edu/RG_Climatology.html
6g4	Dissolved Oxygen	Argo profiling floats	https://argo.ucsd.edu/data/
6g4	Ocean Chlorophyll	ocean colour climate change initiative (OC-CCI) product v6.0	https://www.oceancolour.org/

Section 6h 2023 Antarctic ozone hole

Sub-section	General Variable or Phenomenon	Specific dataset or variable	Source
6h	Cloud Volume	CALIPSO	http://www-calipso.larc.nasa.gov
6h	Temperature, [Near] Surface	MERRA-2	http://gmao.gsfc.nasa.gov/reanalysis/MERRA-2/
6h	Temperature, upper atmosphere	MERRA-2	https://gmao.gsfc.nasa.gov/reanalysis/MERRA-2/
6h	Ozone, Total Column and Stratospheric	Aura MLS	http://disc.sci.gsfc.nasa.gov/Aura/data-holdings/MLS/index.shtml
6h	Ozone, Total Column and Stratospheric	Ozone Mapping Istrument (OMI) Ozone Mapping & Profiler Suite (OMPS), Total Ozone Mapping Spectrum (TOMS), Earth Probe TOMS (EPTOMS)	https://ozoneaq.gsfc.nasa.gov/data/ozone/
6h	Ozone, Lower Stratosphere	Ozonesonde	https://gml.noaa.gov/dv/spo_oz/

References

Adusumilli, S., H. A. Fricker, B. Medley, L. Padman, and M. R. Siegfried, 2020: Interannual variations in meltwater input to the Southern Ocean from Antarctic ice shelves. *Nat. Geosci.*, **13**, 616–620, https://doi.org/10.1038/s41561-020-0616-z.

—— , —— , and A. S. Gardner, 2023: Ice-sheet mass balance [in "State of the Climate in 2022"]. *Bull. Amer. Meteor. Soc.*, **104** (9), S341–S343, https://doi.org/10.1175/BAMS-D-23-0077.1.

Agosta, C., and Coauthors, 2019: Estimation of the Antarctic surface mass balance using the regional climate model MAR (1979–2015) and identification of dominant processes. *Cryosphere*, **13**, 281–296, https://doi.org/10.5194/tc-13-281-2019.

Arthur, J. F., C. R. Stokes, S. S. R. Jamieson, J. Rachel Carr, A. A. Leeson, and V. Verjans, 2022: Large interannual variability in supraglacial lakes around East Antarctica. *Nat. Commun.*, **13**, 1711, https://doi.org/10.1038/s41467-022-29385-3.

Baiman, R., A. C. Winters, J. Lenaerts, and C. A. Shields, 2023: Synoptic drivers of atmospheric river induced precipitation near Dronning Maud Land, Antarctica. *J. Geophys. Res. Atmos.*, **128**, e2022JD037859, https://doi.org/10.1029/2022JD037859.

Banwell, A. F., D. R. MacAyeal, and O. V. Sergienko, 2013: Breakup of the Larsen B Ice Shelf triggered by chain reaction drainage of supraglacial lakes. *Geophys. Res. Lett.*, **40**, 5872–5876, https://doi.org/10.1002/2013GL057694.

—— , N. Wever, D. Dunmire, and G. Picard, 2023: Quantifying Antarctic-wide ice-shelf surface melt volume using microwave and firn model data: 1980 to 2021. *Geophys. Res. Lett.*, **50**, e2023GL102744, https://doi.org/10.1029/2023GL102744.

Beadling, R. L., N. M. Freeman, G. A. MacGilchrist, M. Mazloff, J.-R. Shi, A. F. Thompson, and E. Wilson, 2022: Southern Ocean [in "State of the Climate in 2021"]. *Bull. Amer. Meteor. Soc.*, **103** (8), S329–S332, https://doi.org/10.1175/BAMS-D-22-0078.1.

Bell, R. E., A. F. Banwell, L. D. Trusel, and J. Kingslake, 2018: Antarctic surface hydrology and impacts on ice-sheet mass balance. *Nat. Climate Change*, **8**, 1044–1052, https://doi.org/10.1038/s41558-018-0326-3.

Blunden, J., T. Boyer, and E. Bartow-Gillies, Eds., 2023: "State of the Climate in 2022." Bull. *Amer. Meteor. Soc.*, **104** (9), S1–S501, https://doi.org/10.1175/2023BAMSStateoftheClimate.1.

Cai, W., and Coauthors, 2023: Southern Ocean warming and its climatic impacts. *Sci. Bull.*, **68**, 946–960, https://doi.org/10.1016/j.scib.2023.03.049.

Carr, J. L., Á. Horváth, D. L. Wu, and M. D. Friberg, 2022: Stereo plume height and motion retrievals for the record-setting Hunga Tonga-Hunga Ha'apai eruption of 15 January 2022. *Geophys. Res. Lett.*, **49**, e2022GL098131, https://doi.org/10.1029/2022GL098131.

Cavalieri, D. J., C. L. Parkinson, P. Gloersen, and H. J. Zwally, 1996: Sea ice concentrations from Nimbus-7 SMMR and DMSP SSM/I-SSMIS passive microwave data, version 1. NASA National Snow and Ice Data Center Distributed Active Archive Center, accessed 12 March 2024, https://doi.org/10.5067/8GQ8LZQVL0VL.

Cheng, L., and Coauthors, 2022: Past and future ocean warming. *Nat. Rev. Earth Environ.*, **3**, 776–794, https://doi.org/10.1038/s43017-022-00345-1.

—— , and Coauthors, 2024: New record ocean temperatures and related climate indicators in 2023. *Adv. Atmos. Sci.*, **41**, 1068–1082, https://doi.org/10.1007/s00376-024-3378-5.

Clem, K. R., and R. L. Fogt, 2013: Varying roles of ENSO and SAM on the Antarctic Peninsula climate in austral spring. *J. Geophys. Res. Atmos.*, **118**, 11 481–11 492, https://doi.org/10.1002/jgrd.50860.

—— , and M. N. Raphael, Eds., 2023: Antarctica and the Southern Ocean [in "State of the Climate in 2022"]. *Bull. Amer. Meteor. Soc.*, **104** (9), S322–S365, https://doi.org/10.1175/BAMS-D-23-0077.1.

—— , D. Bozkurt, D. Kennett, J. C. King, and J. Turner, 2022: Central tropical Pacific convection drives extreme high temperatures and surface melt on the Larsen C Ice Shelf, Antarctic Peninsula. *Nat. Commun.*, **13**, 3906, https://doi.org/10.1038/s41467-022-31119-4.

—— , S. Barreira, S. Colwell, R. L. Fogt, L. M. Keller, M. A. Lazzara, D. E. Mikolajczyk, and T. Norton, 2023: Atmospheric circulation and surface observations [in "State of the Climate in 2022"]. *Bull. Amer. Meteor. Soc.*, **104** (9), S329–S332, https://doi.org/10.1175/BAMS-D-23-0077.1.

Comiso, J. C., 2017: Bootstrap sea ice concentrations from Nimbus-7 SMMR and DMSP SSM/I-SSMIS, version 3. NASA National Snow and Ice Data Center Distributed Active Archive Center, accessed 12 March 2024, https://doi.org/10.5067/7Q8HCCWS4I0R.

Datta, R. T., R. Baiman, Z. Yin, J. D. Wille, D. Dunmire, M. L. Maclennan, L. D. Trusel, and D. Bozkurt, 2023: Ice-sheet surface mass balance [in "State of the Climate in 2022"]. *Bull. Amer. Meteor. Soc.*, **104** (9), S336–S339, https://doi.org/10.1175/BAMS-D-23-0077.1.

de Boyer Montégut, C., G. Madec, A. S. Fischer, A. Lazar, and D. Iudicone, 2004: Mixed layer depth over the global ocean: An examination of profile data and a profile-based climatology. *J. Geophys. Res.*, **109**, C12003, https://doi.org/10.1029/2004JC002378.

Depoorter, M. A., J. L. Bamber, J. A. Griggs, J. T. M. Lenaerts, S. R. M. Ligtenberg, M. R. van den Broeke, and G. Moholdt, 2013: Calving fluxes and basal melt rates of Antarctic ice shelves. *Nature*, **502**, 89–92, https://doi.org/10.1038/nature12567.

DiGirolamo, N. E., C. L. Parkinson, D. J. Cavalieri, P. Gloersen, and H. J. Zwally, 2022: Sea ice concentrations from Nimbus-7 SMMR and DMSP SSM/I-SSMIS passive microwave data. NASA National Snow and Ice Data Center Distributed Active Archive Center, accessed 5 February 2024, https://doi.org/10.5067/MPYG15WAA4WX.

Ding, Q., and E. J. Steig, 2013: Temperature change on the Antarctic Peninsula linked to the tropical Pacific. *J. Climate*, **26**, 7570–7585, https://doi.org/10.1175/JCLI-D-12-00729.1.

Fleming, E. L., P. A. Newman, Q. Liang, and L. D. Oman, 2024: Stratospheric temperature and ozone impacts of the Hunga Tonga-Hunga Ha'apai water vapor injection. *J. Geophys. Res. Atmos.*, **129**, e2023JD039298, https://doi.org/10.1029/2023JD039298.

Frölicher, T. L., J. L. Sarmiento, D. J. Paynter, J. P. Dunne, J. P. Krasting, and M. Winton, 2015: Dominance of the Southern Ocean in anthropogenic carbon and heat uptake in CMIP5 models. *J. Climate*, **28**, 862–886, https://doi.org/10.1175/JCLI-D-14-00117.1.

Gelaro, R., and Coauthors, 2017: The Modern-Era Retrospective Analysis for Research and Applications, version 2 (MERRA-2). *J. Climate*, **30**, 5419–5454, https://doi.org/10.1175/JCLI-D-16-0758.1.

Gerrish, L., L. Ireland, P. Fretwell, and P. Cooper, 2023: High resolution vector polygons of the Antarctic coastline, version 7.8. BAS Data Catalogue, accessed 5 February 2024, https://doi.org/10.5285/C7FE759D-E042-479A-9ECF-274255B4F0A1.

Gloersen, P., 2006: Nimbus-7 SMMR polar gridded radiances and sea ice concentrations, version 1. NASA National Snow and Ice Data Center Distributed Active Archive Center, accessed 1 December 2019, https://doi.org/10.5067/QOZIVYV3V9JP.

Gorodetskaya, I. V., and Coauthors, 2023: Record-high Antarctic Peninsula temperatures and surface melt in February 2022: A compound event with an intense atmospheric river. *npj Climate Atmos. Sci.*, **6**, 202, https://doi.org/10.1038/s41612-023-00529-6.

Gossart, A., S. Helsen, J. T. M. Lenaerts, S. V. Broucke, N. P. M. van Lipzig, and N. Souverijns, 2019: An evaluation of surface climatology in state-of-the-art reanalyses over the Antarctic Ice Sheet. *J. Climate*, **32**, 6899–6915, https://doi.org/10.1175/JCLI-D-19-0030.1.

Gudmundsson, G. H., F. S. Paolo, S. Adusumilli, and H. A. Fricker, 2019: Instantaneous Antarctic Ice Sheet mass loss driven by thinning ice shelves. *Geophys. Res. Lett.*, **46**, 13 903–13 909, https://doi.org/10.1029/2019GL085027.

Hanna, E., and Coauthors, 2024: Short- and long-term variability of the Antarctic and Greenland ice sheets. *Nat. Rev. Earth Environ.*, **5**, 193–210, https://doi.org/10.1038/s43017-023-00509-7.

Henley, S. F., and Coauthors, 2020: Changing biogeochemistry of the Southern Ocean and its ecosystem implications. *Front. Mar. Sci.*, **7**, 581, https://doi.org/10.3389/fmars.2020.00581.

Hersbach, H., and Coauthors, 2020: The ERA5 global reanalysis. *Quart. J. Roy. Meteor. Soc.*, **146**, 1999–2049, https://doi.org/10.1002/qj.3803.

Hobbs, W., and Coauthors, 2024: Observational evidence for a regime shift in summer Antarctic sea ice. *J. Climate*, **37**, 2263–2275, https://doi.org/10.1175/JCLI-D-23-0479.1.

Huang, B., C. Liu, V. Banzon, E. Freeman, G. Graham, B. Hankins, T. Smith, and H.-M. Zhang, 2021: Improvements of the Daily Optimum Interpolation Sea Surface Temperature (DOISST) version 2.1. *J. Climate*, **34**, 2923–2939, https://doi.org/10.1175/JCLI-D-20-0166.1.

Josey, S. A., J. P. Grist, J. V. Mecking, B. I. Moat, and E. Schulz, 2023: A clearer view of Southern Ocean air–sea interaction using surface heat flux asymmetry. *Philos. Trans. Roy. Soc.*, **A381**, 20220067, https://doi.org/10.1098/rsta.2022.0067.

Kittel, C., and Coauthors, 2021: Diverging future surface mass balance between the Antarctic ice shelves and grounded ice sheet. *Cryosphere*, **15**, 1215–1236, https://doi.org/10.5194/tc-15-1215-2021.

Kramarova, N. A., and Coauthors, 2023: 2022 Antarctic ozone hole [in "State of the Climate in 2022"]. *Bull. Amer. Meteor. Soc.*, **104** (9), S355–S359, https://doi.org/10.1175/BAMS-D-23-0077.1.

Kromer, J. D., and L. D. Trusel, 2023: Identifying the impacts of sea ice variability on the climate and surface mass balance of West Antarctica. *Geophys. Res. Lett.*, **50**, e2023GL104436, https://doi.org/10.1029/2023GL104436.

Lenaerts, J. T. M., B. Medley, M. R. Van Den Broeke, and B. Wouters, 2019: Observing and modeling ice sheet surface mass balance. *Rev. Geophys.*, **57**, 376–420, https://doi.org/10.1029/2018RG000622.

MacFerrin, M., T. Mote, H. Wang, L. Liu, L. Montgomery, and T. Scambos, 2021: Ice sheet seasonal melt extent and duration [in "State of the Climate in 2020"]. *Bull. Amer. Meteor. Soc.*, **102** (8), S331–S334, , https://doi.org/10.1175/BAMS-D-21-0081.1.

—— , —— , A. Banwell, and T. Scambos, 2022: Ice sheet seasonal melt extent and duration [in "State of the Climate in 2021"]. *Bull. Amer. Meteor. Soc.*, **103** (8), S321–S323, https://doi.org/10.1175/BAMS-D-22-0078.1

—— , —— , —— , and —— , 2023: Ice-sheet seasonal melt extent and duration [in "State of the Climate in 2022"]. *Bull. Amer. Meteor. Soc.*, **104** (9), S339–S341, https://doi.org/10.1175/BAMS-D-23-0077.1.

Maclennan, M. L., J. T. M. Lenaerts, C. Shields, and J. D. Wille, 2022: Contribution of atmospheric rivers to Antarctic precipitation. *Geophys. Res. Lett.*, **49**, e2022GL100585, https://doi.org/10.1029/2022GL100585.

—— , and Coauthors, 2023: Climatology and surface impacts of atmospheric rivers on West Antarctica. *Cryosphere*, **17**, 865–881, https://doi.org/10.5194/tc-17-865-2023.

Manney, G. L., and Coauthors, 2011: Unprecedented Arctic ozone loss in 2011. *Nature*, **478**, 469–475, https://doi.org/10.1038/nature10556.

—— , and Coauthors, 2023: Siege in the southern stratosphere: Hunga Tonga-Hunga Ha'apai water vapor excluded from the 2022 Antarctic polar vortex. *Geophys. Res. Lett.*, **50**, e2023GL103855, https://doi.org/10.1029/2023GL103855.

Marshall, G. J., 2003: Trends in the southern annular mode from observations and reanalyses. *J. Climate*, **16**, 4134–4143, https://doi.org/10.1175/1520-0442(2003)016<4134:TITSAM>2.0.CO;2.

Maslanik, J., and J. Stroeve, 1999: Near-real-time DMSP SSM/I-SSMIS daily polar gridded sea ice concentrations (updated daily). National Snow and Ice Data Center, accessed 12 March 2024, https://doi.org/10.5067/U8C09DWVX9LM.

Massom, R. A., S. E. Stammerjohn, W. Lefebvre, S. A. Harangozo, N. Adams, T. A. Scambos, M. J. Pook, and C. Fowler, 2008: West Antarctic Peninsula sea ice in 2005: Extreme ice compaction and ice edge retreat due to strong anomaly with respect to climate. *J. Geophys. Res.*, **113**, C02S20, https://doi.org/10.1029/2007JC004239.

—— , T. A. Scambos, L. G. Bennetts, P. Reid, V. A. Squire, and S. E. Stammerjohn, 2018: Antarctic ice shelf disintegration triggered by sea ice loss and ocean swell. *Nature*, **558**, 383–389, https://doi.org/10.1038/s41586-018-0212-1.

Matsuoka, K., and Coauthors, 2018: Quantarctica. https://doi.org/10.21334/NPOLAR.2018.8516E961.

Medley, B., and E. R. Thomas, 2019: Increased snowfall over the Antarctic Ice Sheet mitigated twentieth-century sea-level rise. *Nat. Climate Change*, **9**, 34–39, https://doi.org/10.1038/s41558-018-0356-x.

Meier, W. N., H. Wilcox, M. A. Hardman, and J. S. Stewart, 2019: DMSP SSM/I-SSMIS daily polar gridded brightness temperatures, version 5. Subset: 37 & 19 GHz, h-polarization, 25 km grid, October 1987–April 2020. NASA National Snow and Ice Data Center Distributed Active Archive Center, accessed 11 February 2021, https://doi.org/10.5067/QU2UYQ6T0B3P.

Miles, B. W. J., and R. G. Bingham, 2024: Progressive unanchoring of Antarctic ice shelves since 1973. *Nature*, **626**, 785–791, https://doi.org/10.1038/s41586-024-07049-0.

Millán, L., and Coauthors, 2022: The Hunga Tonga-Hunga Ha'apai hydration of the stratosphere. *Geophys. Res. Lett.*, **49**, e2022GL099381, https://doi.org/10.1029/2022GL099381.

Morlighem, M., and Coauthors, 2020: Deep glacial troughs and stabilizing ridges unveiled beneath the margins of the Antarctic Ice Sheet. *Nat. Geosci.*, **13**, 132–137, https://doi.org/10.1038/s41561-019-0510-8.

Mote, T. L., 2007: Greenland surface melt trends 1973–2007: Evidence of a large increase in 2007. *Geophys. Res. Lett.*, **34**, L22507, https://doi.org/10.1029/2007GL031976.

—— , 2014: MEaSUREs Greenland Surface Melt Daily 25km EASE-Grid 2.0, version 1. NASA National Snow and Ice Data Center Distributed Active Archive Center, https://doi.org/10.5067/MEASURES/CRYOSPHERE/nsidc-0533.001.

—— , and M. R. Anderson, 1995: Variations in snowpack melt on the Greenland ice sheet based on passive-microwave measurements. *J. Glaciol.*, **41**, 51–60, https://doi.org/10.3189/S0022143000017755.

Mottram, R., and Coauthors, 2021: What is the surface mass balance of Antarctica? An intercomparison of regional climate model estimates. *Cryosphere*, **15**, 3751–3784, https://doi.org/10.5194/tc-15-3751-2021.

Newman, P. A., S. R. Kawa, and E. R. Nash, 2004: On the size of the Antarctic ozone hole. *Geophys. Res. Lett.*, **31**, L21104, https://doi.org/10.1029/2004GL020596.

—— , J. S. Daniel, D. W. Waugh, and E. R. Nash, 2007: A new formulation of equivalent effective stratospheric chlorine (EESC). Atmos. *Chem. Phys.*, **7**, 4537–4552, https://doi.org/10.5194/acp-7-4537-2007.

Orsi, A. H., T. Whitworth, and W. D. Nowlin, 1995: On the meridional extent and fronts of the Antarctic Circumpolar Current. *Deep-Sea Res. I*, **42**, 641–673, https://doi.org/10.1016/0967-0637(95)00021-W.

Otosaka, I. N., and Coauthors, 2023: Mass balance of the Greenland and Antarctic ice sheets from 1992 to 2020. *Earth Syst. Sci. Data*, **15**, 1597–1616, https://doi.org/10.5194/essd-15-1597-2023.

Paolo, F. S., H. A. Fricker, and L. Padman, 2015: Volume loss from Antarctic ice shelves is accelerating. *Science*, **348**, 327–331, https://doi.org/10.1126/science.aaa0940.

Parkinson, C. L., and N. E. DiGirolamo, 2021: Sea ice extents continue to set new records: Arctic, Antarctic, and global results. *Remote Sens. Environ.*, **267**, 112753, https://doi.org/10.1016/j.rse.2021.112753.

Pezzi, L., and Coauthors, 2023: Southern Ocean [in "State of the Climate in 2022"]. *Bull. Amer. Meteor. Soc.*, **104** (9), S351–S355, https://doi.org/10.1175/BAMS-D-23-0077.1.

Pitts, M. C., L. R. Poole, and R. Gonzalez, 2018: Polar stratospheric cloud climatology based on CALIPSO spaceborne lidar measurements from 2006 to 2017. *Atmos. Chem. Phys.*, **18**, 10 881–10 913, https://doi.org/10.5194/acp-18-10881-2018.

Pohl, B., and Coauthors, 2021: Relationship between weather regimes and atmospheric rivers in East Antarctica. *J. Geophys. Res. Atmos.*, **126**, e2021JD035294, https://doi.org/10.1029/2021JD035294.

Purich, A., and E. W. Doddridge, 2023: Record low Antarctic sea ice coverage indicates a new sea ice state. *Commun. Earth Environ.*, **4**, 314, https://doi.org/10.1038/s43247-023-00961-9.

Raphael, M. N., and Coauthors, 2016: The Amundsen Sea low: Variability, change, and impact on Antarctic climate. *Bull. Amer. Meteor. Soc.*, **97**, 111–121, https://doi.org/10.1175/BAMS-D-14-00018.1.

Reid, P. A., and R. A. Massom, 2022: Change and variability in Antarctic coastal exposure, 1979–2020. *Nat. Commun.*, **13**, 1164, https://doi.org/10.1038/s41467-022-28676-z.

Reid, P., S. Stammerjohn, R. A. Massom, S. Barreira, T. Scambos, and J. L. Lieser, 2023: Sea-ice extent, concentration, and seasonality [in "State of the Climate in 2022"]. *Bull. Amer. Meteor. Soc.*, **104** (9), S344–S348, https://doi.org/10.1175/BAMS-D-23-0077.1.

Reynolds, R. W., N. A. Rayner, T. M. Smith, D. C. Stokes, and W. Wang, 2002: An improved in situ and satellite SST analysis for climate. *J. Climate*, **15**, 1609–1625, https://doi.org/10.1175/1520-0442(2002)015<1609:AIISAS>2.0.CO;2.

Rignot, E., S. Jacobs, J. Mouginot, and B. Scheuchl, 2013: Ice-shelf melting around Antarctica. *Science*, **341**, 266–270, https://doi.org/10.1126/science.1235798.

Roemmich, D., and J. Gilson, 2009: The 2004–2008 mean and annual cycle of temperature, salinity, and steric height in the global ocean from the Argo Program. *Prog. Oceanogr.*, **82**, 81–100, https://doi.org/10.1016/j.pocean.2009.03.004.

Santee, M. L., and Coauthors, 2024: The influence of stratospheric hydration from the Hunga eruption on chemical processing in the 2023 Antarctic vortex. ESS Open Archive, https://doi.org/10.22541/essoar.170542085.55151307/v1.

Sathyendranath, S., and Coauthors, 2019: An ocean-colour time series for use in climate studies: The experience of the Ocean-Colour Climate Change Initiative (OC-CCI). *Sensors*, **19**, 4285, https://doi.org/10.3390/s19194285.

Scambos, T. A., J. A. Bohlander, C. A. Shuman, and P. Skvarca, 2004: Glacier acceleration and thinning after ice shelf collapse in the Larsen B embayment, Antarctica. *Geophys. Res. Lett.*, **31**, L18402, https://doi.org/10.1029/2004GL020670.

—— , E. Berthier, T. Haran, C. A. Shuman, A. J. Cook, S. R. M. Ligtenberg, and J. Bohlander, 2014: Detailed ice loss pattern in the northern Antarctic Peninsula: Widespread decline driven by ice front retreats. *Cryosphere*, **8**, 2135–2145, https://doi.org/10.5194/tc-8-2135-2014.

Shepherd, A., and Coauthors, 2012: A reconciled estimate of ice-sheet mass balance. *Science*, **338**, 1183–1189, https://doi.org/10.1126/science.1228102.

Smith, B., and Coauthors, 2020: Pervasive ice sheet mass loss reflects competing ocean and atmosphere processes. *Science*, **368**, 1239–1242, https://doi.org/10.1126/science.aaz5845.

—— , S. Dickinson, B. J. Jelley, T. A. Neumann, D. Hancock, and K. Harbeck, 2022: ATLAS/ICESat-2 L3B slope-corrected land ice height time series, version 5. NASA National Snow and Ice Data Center Distributed Active Archive Center, accessed 12 February 2024, https://doi.org/10.5067/ATLAS/ATL11.005.

Stammerjohn, S. E., D. G. Martinson, R. C. Smith, X. Yuan, and D. Rind, 2008: Trends in Antarctic annual sea ice retreat and advance and their relation to El Niño–Southern Oscillation and Southern Annular Mode variability. *J. Geophys. Res.*, **113**, C03S90, https://doi.org/10.1029/2007JC004269.

Taha, G., R. Loughman, P. R. Colarco, T. Zhu, L. W. Thomason, and G. Jaross, 2022: Tracking the 2022 Hunga Tonga-Hunga Ha'apai aerosol cloud in the upper and middle stratosphere using space-based observations. *Geophys. Res. Lett.*, **49**, e2022GL100091, https://doi.org/10.1029/2022GL100091.

Teder, N. J., L. G. Bennetts, P. A. Reid, and R. A. Massom, 2022: Sea ice-free corridors for large swell to reach Antarctic ice shelves. *Environ. Res. Lett.*, **17**, 045026, https://doi.org/10.1088/1748-9326/ac5edd.

The Firn Symposium Team, 2024: Firn on ice sheets. *Nat. Rev. Earth Environ.*, **5**, 79–99, https://doi.org/10.1038/s43017-023-00507-9.

Thomalla, S. J., S.-A. Nicholson, T. J. Ryan-Keogh, and M. E. Smith, 2023: Widespread changes in Southern Ocean phytoplankton blooms linked to climate drivers. *Nat. Climate Change*, **13**, 975–984, https://doi.org/10.1038/s41558-023-01768-4.

Thompson, D. W. J., J. C. Furtado, and T. G. Shepherd, 2006: On the tropospheric response to anomalous stratospheric wave drag and radiative heating. *J. Atmos. Sci.*, **63**, 2616–2629, https://doi.org/10.1175/JAS3771.1.

Trusel, L. D., Z. Pan, and M. Moussavi, 2022: Repeated tidally induced hydrofracture of a supraglacial lake at the Amery Ice Shelf grounding zone. *Geophys. Res. Lett.*, **49**, e2021GL095661, https://doi.org/10.1029/2021GL095661.

Turner, J., and Coauthors, 2019: The dominant role of extreme precipitation events in Antarctic snowfall variability. *Geophys. Res. Lett.*, **46**, 3502–3511, https://doi.org/10.1029/2018GL081517.

Van Wessem, J. M., and Coauthors, 2018: Modelling the climate and surface mass balance of polar ice sheets using RACMO2 – Part 2: Antarctica (1979–2016). *Cryosphere*, **12**, 1479–1498, https://doi.org/10.5194/tc-12-1479-2018.

Wang, Y., D. Zhou, A. Bunde, and S. Havlin, 2016: Testing reanalysis data sets in Antarctica: Trends, persistence properties, and trend significance. *J. Geophys. Res. Atmos.*, **121**, 12 839–12 855, https://doi.org/10.1002/2016JD024864.

Wiese, D. N., D.-N. Yuan, C. Boening, F. W. Landerer, and M. M. Watkins, 2023a: JPL GRACE Mascon Ocean, ice, and hydrology equivalent water height RL06.1 CRI filtered version 03. Ver. RL06.1Mv03. PO.DAAC, accessed 10 February 2023, https://doi.org/10.5067/TEMSC-3JC63.

——, ——, ——, ——, and ——, 2023b: Tellus level-4 ocean mass anomaly time series from JPL GRACE/GRACE-FO Mascon CRI filtered release 06.1 version 03. Ver. RL06.1Mv03. PO.DAAC, accessed 10 February 2023, https://doi.org/10.5067/TEMSC-AT613.

Wille, J. D., and Coauthors, 2021: Antarctic atmospheric river climatology and precipitation impacts. *J. Geophys. Res. Atmos.*, **126**, e2020JD033788, https://doi.org/10.1029/2020JD033788.

Wong, A. P. S., and Coauthors, 2020: Argo Data 1999–2019: Two million temperature-salinity profiles and subsurface velocity observations from a global array of profiling floats. *Front. Mar. Sci.*, **7**, 700, https://doi.org/10.3389/fmars.2020.00700.

WMO, 2022: Scientific Assessment of Ozone Depletion: 2022. GAW Rep. 278, 509 pp., https://csl.noaa.gov/assessments/ozone/2022/

STATE OF THE CLIMATE IN 2023

REGIONAL CLIMATES

A. Arguez, P. Bissolli, C. Ganter, R. Martinez, A. Mekonnen, L. Stevens, and Z. Zhu, Eds.

Special Online Supplement to the *Bulletin of the American Meteorological Society* Vol. 105, No. 8, August, 2024

https://doi.org/10.1175/2024BAMSStateoftheClimate_Chapter7.1

Corresponding authors:
North America: Laura Stevens / Laura.Stevens@noaa.gov
Central America and the Caribbean: Anthony Arguez / Anthony.Arguez@noaa.gov
South America: Rodney Martinez / rmartinez@wmo.int
Africa: Ademe Mekonnen / amekonne@ncat.edu
Europe: Peter Bissolli / Peter.Bissolli@dwd.de
Asia: Zhiwei Zhu / zwz@nuist.edu.cn
Oceania: Catherine Ganter / Catherine.Ganter@bom.gov.au

©2024 American Meteorological Society
For information regarding reuse of this content and general copyright information, consult the AMS Copyright Policy.

STATE OF THE CLIMATE IN 2023
Regional Climates

Editors

Jessica Blunden
Tim Boyer

Chapter Editors

Anthony Arguez
Josh Blannin
Peter Bissolli
Kyle R. Clem
Howard J. Diamond
Matthew L. Druckenmiller
Robert J. H. Dunn
Catherine Ganter
Nadine Gobron
Gregory C. Johnson
Rick Lumpkin
Rodney Martinez
Ademe Mekonnen
John B. Miller
Twila A. Moon
Marilyn N. Raphael
Carl J. Schreck III
Laura Stevens
Richard L. Thoman
Kate M. Willett
Zhiwei Zhu

Technical Editor

Lukas Noguchi

BAMS Special Editor for Climate

Timothy DelSole

American Meteorological Society

Cover Credit:
Wildfire EWF-031 located southeast of Edson in Alberta, Canada, on 5 May 2023. (Photo credit: Alberta Forestry and Parks)

How to cite this document:
Regional Climates is one chapter from the *State of the Climate in 2023* annual report and is available from https://doi.org/10.1175/2024BAMSStateoftheClimate_Chapter7.1. Compiled by NOAA's National Centers for Environmental Information, *State of the Climate in 2023* is based on contributions from scientists from around the world. It provides a detailed update on global climate indicators, notable weather events, and other data collected by environmental monitoring stations and instruments located on land, water, ice, and in space. The full report is available from https://doi.org/10.1175/2024BAMSStateoftheClimate.1.

Citing the complete report:
Blunden, J. and T. Boyer, Eds., 2024: "State of the Climate in 2023". Bull. Amer. Meteor. Soc., 105 (8), Si–S484 https://doi.org/10.1175/2024BAMSStateoftheClimate.1.

Citing this chapter:
Arguez, A., Bissolli, P., C. Ganter, R. Martinez, A. Mekonnen, L. Stevens, and Z. Zhu, Eds., 2024: Regional Climates [in "State of the Climate in 2023"]. Bull. Amer. Meteor. Soc., 105 (8), S371–S484, https://doi.org/10.1175/2024BAMSStateoftheClimate_Chapter7.1.

Citing a section (example):
Kabidi, K., A. Sayouri, M. ElKharrim, S. Hakmi, and A. E. Mostafa, 2024: North Africa [in "State of the Climate in 2023"]. Bull. Amer. Meteor. Soc., 105 (8), S406–S408, https://doi.org/10.1175/2024BAMSStateoftheClimate_Chapter7.1.

Editor and Author Affiliations (alphabetical by name)

Agyakwah, W., NOAA/NWS National Centers for Environmental Prediction Climate Prediction Center, College Park, Maryland

Ahmadpour, Somayeh, Brandenburg University of Technology (BTU), Cottbus-Senftenberg, Germany

Aldeco, Laura S., Servicio Meteorológico Nacional, Buenos Aires, Argentina

Alfaro, Eric J., Center for Geophysical Research and School of Physics, University of Costa Rica, San José, Costa Rica

Alves, Lincoln M., Centro Nacional de Monitoramento e Alertas de Desastres Naturais CEMADEN, São Paulo, Brazil

Amador, Jorge A., Center for Geophysical Research and School of Physics, University of Costa Rica, San José, Costa Rica

Andrade, B., Seychelles Meteorological Authority, Mahe, Seychelles

Arguez, Anthony, NOAA/NESDIS National Centers for Environmental Information, Asheville, North Carolina

Avalos, Grinia, Servicio Nacional de Meteorología e Hidrología del Perú, Lima, Perú

Bardin, M. Yu., Yu. A. Izrael Institute of Global Climate and Ecology, Institute of Geography, Russian Academy of Sciences, Moscow, Russia

Beauchemin, Marc, Environment and Climate Change Canada, Montreal, Canada

Bekele, E., NOAA/NWS National Centers for Environmental Prediction Climate Prediction Center, College Park, Maryland

Berne, Christine, Météo France, Toulouse, France

Bissolli, Peter, Deutscher Wetterdienst, WMO RA VI Regional Climate Centre Network, Offenbach, Germany

Bochníček, Oliver, Slovak Hydrometeorological Institute, Bratislava, Slovakia

Bukunt, Brandon, NOAA/NWS Weather Forecast Office, Tiyan, Guam

Calderón, Blanca, Center for Geophysical Research, University of Costa Rica, San José, Costa Rica

Campbell, Jayaka, Department of Physics, The University of the West Indies, Kingston, Jamaica

Chandler, Elise, Bureau of Meteorology, Melbourne, Australia

Charlton, Candice S., Department of Physics, The University of the West Indies, Kingston, Jamaica

Chen, Jack, Environment and Climate Change Canada, Ottawa, Canada

Cheng, Vincent Y. S., Environment and Climate Change Canada, Toronto, Canada

Chisholm, Lucy, Environment and Climate Change Canada, Halifax, Canada

Clarke, Leonardo, Department of Physics, The University of the West Indies, Kingston, Jamaica

Correa, Kris, Servicio Nacional de Meteorología e Hidrología del Perú, Lima, Perú

Costa, Felipe, Centro Internacional para la Investigación del Fenómeno de El Niño (CIIFEN), Guayaquil, Ecuador

Cunha, Ana P., Centro Nacional de Monitoramento e Alertas de Desastres Naturais CEMADEN, São Paulo, Brazil

De Bock, Veerle, Royal Meteorological Institute, Ukkel, Belgium

Dindyal, S., Mauritius Meteorological Service, Vacoas, Mauritius

Dulamsuren, Dashkhuu, Institute of Meteorology, Hydrology and Environment, National Agency for Meteorology, Ulaanbaatar, Mongolia

Echeverría Garcés, Paola, Instituto Nacional de Meteorología e Hidrología de Ecuador (INAMHI), Quito, Ecuador

Ekici, Mithat, Turkish State Meteorological Service, Ankara, Türkiye

ElKharrim, M., General Directorate of Meteorology, Rabat, Morocco

Espinoza, Jhan-Carlo, Université Grenoble Alpes, Institut des Géosciences de l'Environnement, IRD, CNRS, Grenoble INP, Grenoble, France

Fenimore, Chris, NOAA/NESDIS National Centers for Environmental Information, Asheville, North Carolina

Fu, Shanshan, Nanjing University of Information Science and Technology, Nanjing, China

Ganter, Catherine, Bureau of Meteorology, Melbourne, Australia

Gevorgyan, Artur, Hydrometeorology and Monitoring Center, Yerevan, Armenia

Gleason, Karin, NOAA/NESDIS National Centers for Environmental Information, Asheville, North Carolina

Gómez Camacho, Julio, National Meteorological Service of Mexico, Mexico City, Mexico

González Hernández, Yolanda, Centro Internacional para la Investigación del Fenómeno de El Niño (CIIFEN), Guayaquil, Ecuador

Hakmi, S., General Directorate of Meteorology, Rabat, Morocco

Heim, Richard R. Jr., NOAA/NESDIS National Centers for Environmental Information, Asheville, North Carolina

Hicks, J., NOAA/NWS National Centers for Environmental Prediction Climate Prediction Center, College Park, Maryland

Hidalgo, Hugo G., Center for Geophysical Research and School of Physics, University of Costa Rica, San José, Costa Rica

Huang, Hongjie, Nanjing University of Information Science and Technology, Nanjing, China

Jadra, Gerardo, Instituto Uruguayo de Meteorología, Montevideo, Uruguay

Jain, Piyush, Natural Resources Canada, Edmonton, Canada

Jumaux, G., Meteo France, Direction Interregionale Pour L'Ocean Indien, Reunion

Kabidi, K., General Directorate of Meteorology, Rabat, Morocco

Kazemi, Amin Fazl, Iran National Meteorology Organization, Tehran, Iran

Kendon, Michael, Met Office Hadley Centre, Exeter, United Kingdom

Kennedy, John, Independent Researcher, Verdun, France

Khalatyan, Yelena, Hydrometeorology and Monitoring Center, Yerevan, Armenia

Khan, Valentina, Hydrometeorological Centre of Russia, World Meteorological Organization (WMO) North EurAsia Climate Center, Moscow, Russia

Khiem, Mai Van, National Center for Hydro-Meteorological Forecasting, Vietnam Meteorological and Hydrological Administration, Hanoi, Vietnam

Kirchmeier-Young, Megan, Environment and Climate Change Canada, Toronto, Canada

Korshunova, Natalia N., All-Russia Research Institute of Hydrometeorological Information, World Data Center, Obninsk, Russia

Kruger, A. C., Climate Service, South African Weather Service, Pretoria, South Africa

Lakatos, Mónika, Climatology Unit, Hungarian Meteorological Service, Budapest, Hungary

Lam, Hoang Phuc, National Center for Hydro-Meteorological Forecasting, Vietnam Meteorological and Hydrological Administration, Hanoi, Vietnam

Lavado-Casimiro, Waldo, Servicio Nacional de Meteorología e Hidrología del Perú, Lima, Perú

Lee, Tsz-Cheung, Hong Kong Observatory, Hong Kong, China

Lu, Rui, Nanjing University of Information Science and Technology, Nanjing, China

Mamen, Jostein, Climate Division, Norwegian Meteorological Institute, Oslo, Norway

Marengo, Jose A., Centro Nacional de Monitoramento e Alertas de Desastres Naturais CEMADEN, São Paulo, Brazil

Marjan, Mohammadi, Iran National Meteorology Organization, Tehran, Iran

Martinez, Rodney, World Meteorological Organization, San Jose, Costa Rica

McBride, C., Climate Service, South African Weather Service, Pretoria, South Africa

Mekonnen, Ademe, North Carolina A&T University, Greensboro, North Carolina

Meyers, Tristan, National Institute of Water and Atmospheric Research (NIWA), Auckland, New Zealand

Minney, Caitlin, Bureau of Meteorology, Melbourne, Australia

Moise, Aurel, Centre for Climate Research Singapore, Meteorological Service Singapore, Singapore

Molina-Carpio, Jorge, Universidad Mayor de San Andrés, La Paz, Bolivia

Moody, Ronald, Meteorological Service Jamaica, Kingston, Jamaica

Mora, Natali, Center for Geophysical Research, University of Costa Rica, San José, Costa Rica

Mostafa, A. E., Department of Seasonal Forecast and Climate Research, Cairo Numerical Weather Prediction, Egyptian Meteorological Authority, Cairo, Egypt

Muharsyah, Robi, Division of Climate Variability Analysis, Meteorological, Climatological, and Geophysical Agency, Jakarta, Indonesia

Editor and Author Affiliations (continued)

Okunaka, Yuka, Tokyo Climate Center, Japan Meteorological Agency, Tokyo, Japan

Orlik, Alexander, GeoSphere, Vienna, Austria

Pascual Ramírez, Reynaldo, National Meteorological Service of Mexico, Mexico City, Mexico

Porat, Amos, Israel Meteorological Service, Bet Dagan, Israel

Quispe, Willy R., Servicio Nacional de Meteorología e Hidrología de Bolivia, La Paz, Bolivia

Ramos, Andrea M., Instituto Nacional de Meteorología, Brasilia, Brazil

Ressl, Hans, GeoSphere, Vienna, Austria

Rivera, Patricia P., Servicio Nacional de Meteorología e Hidrología del Perú, Lima, Perú

Robjhon, M., NOAA/NWS National Centers for Environmental Prediction Climate Prediction Center, College Park, Maryland

Rodriguez Guisado, Esteban, Agencia Estatal de Meteorología, Madrid, Spain

Roebeling, Maarit, Deutscher Wetterdienst, WMO RA VI Regional Climate Centre Network, Offenbach, Germany

Ronchail, Josyane, Laboratoire LOCEAN-IPSL, Paris, France

Rösner, Benjamin, Remote Sensing Section, Deutscher Wetterdienst, Offenbach, Germany

Sabeerali, C. T., India Meteorological Department, Ministry of Earth Sciences, Pune, India

Salinas, Roberto, Dirección de Meteorología e Hidrología / Dirección Nacional de Aeronáutica Civil, Asunción, Paraguay

Sayouri, A., General Directorate of Meteorology, Rabat, Morocco

Segele, Z. T., NOAA/NWS National Centers for Environmental Prediction Climate Prediction Center, College Park, Maryland

Sensoy, Serhat, Turkish State Meteorological Service, Ankara, Türkiye

Seong, Ji-In, Climate Change Monitoring Division, Korea Meteorological Administration, Seoul, South Korea

Serna Cuenca, Julieta, Instituto de Hidrología, Meteorología y Estudios Ambientales de Colombia (IDEAM), Bogotá, Colombia

Shukla, R., ERT, Laurel, Maryland

Smith, Adam, NOAA/NESDIS National Centers for Environmental Information, Asheville, North Carolina

Spence-Hemmings, Jacqueline, Meteorological Service Jamaica, Kingston, Jamaica

Spillane, Sandra, Met Éireann, Dublin, Ireland

Sreejith, O. P., India Meteorological Department, Ministry of Earth Sciences, Pune, India

Srivastava, A. K., India Meteorological Department, Ministry of Earth Sciences, Pune, India

Stella, Jose L., Servicio Meteorológico Nacional, Buenos Aires, Argentina

Stephenson, Tannecia S., Department of Physics, The University of the West Indies, Kingston, Jamaica

Stevens, Laura, Cooperative Institute for Satellite Earth System Studies, North Carolina State University, Asheville, North Carolina

Takahashi, Kiyotoshi, Tokyo Climate Center, Japan Meteorological Agency, Tokyo, Japan

Takemura, Kazuto, Tokyo Climate Center, Japan Meteorological Agency, Tokyo, Japan

Taylor, Michael A., Department of Physics, The University of the West Indies, Kingston, Jamaica

Thiaw, W. M., NOAA/NWS National Centers for Environmental Prediction Climate Prediction Center, College Park, Maryland

Trachte, Katja, Brandenburg University of Technology (BTU), Cottbus-Senftenberg, Germany

Trotman, Adrian, Caribbean Institute for Meteorology and Hydrology, Bridgetown, Barbados

van der Linden, Roderick, Deutscher Wetterdienst, Offenbach, Germany

van der Schrier, Gerard, Royal Netherlands Meteorological Institute (KNMI), De Bilt, The Netherlands

Van Meerbeeck, Cédric J., Caribbean Institute for Meteorology and Hydrology, Bridgetown, Barbados

Vazife, Ahad, Iran National Meteorology Organization, Tehran, Iran

Virasami, R., Mauritius Meteorological Service, Vacoas, Mauritius

Willems, An, Royal Meteorological Institute, Ukkel, Belgium

Wu, Francis, Environment and Climate Change Canada, Vancouver, Canada

Zhang, Peiqun, Beijing Climate Center, Beijing, China

Zhu, Zhiwei, Nanjing University of Information Science and Technology, Nanjing, China

Editorial and Production Team

Allen, Jessicca, Graphics Support, Cooperative Institute for Satellite Earth System Studies, North Carolina State University, Asheville, North Carolina

Camper, Amy V., Graphics Support, Innovative Consulting and Management Services, LLC, NOAA/NESDIS National Centers for Environmental Information, Asheville, North Carolina

Haley, Bridgette O., Graphics Support, NOAA/NESDIS National Centers for Environmental Information, Asheville, North Carolina

Hammer, Gregory, Content Team Lead, Communications and Outreach, NOAA/NESDIS National Centers for Environmental Information, Asheville, North Carolina

Love-Brotak, S. Elizabeth, Lead Graphics Production, NOAA/NESDIS National Centers for Environmental Information, Asheville, North Carolina

Ohlmann, Laura, Technical Editor, Innovative Consulting and Management Services, LLC, NOAA/NESDIS National Centers for Environmental Information, Asheville, North Carolina

Noguchi, Lukas, Technical Editor, Innovative Consulting and Management Services, LLC, NOAA/NESDIS National Centers for Environmental Information, Asheville, North Carolina

Riddle, Deborah B., Graphics Support, NOAA/NESDIS National Centers for Environmental Information, Asheville, North Carolina

Veasey, Sara W., Visual Communications Team Lead, Communications and Outreach, NOAA/NESDIS National Centers for Environmental Information, Asheville, North Carolina

7. Table of Contents

Authors and affiliations S374
a. Overview S379
b. North America S380
1. Canada S380
2. United States S382
3. Mexico S385
Sidebar 7.1: Record-breaking wildfire season in Canada S387
c. Central America and the Caribbean S390
1. Central America S390
2. Caribbean S392
d. South America S395
1. Northern South America S395
2. Central South America S397
3. Southern South America S401
Sidebar 7.2: Drought in South America in 2023: Amazonia and Altiplano S403
e. Africa S405
1. North Africa S406
2. West Africa S409
3. Central Africa S411
4. Eastern Africa S413
5. Southern Africa S416
6. Western Indian Ocean island countries S419
f. Europe and the Middle East S423
1. Overview S423
2. Western Europe S427
3. Central Europe S428
4. Iberian Peninsula S430
5. The Nordic and Baltic countries S432
6. Central Mediterranean region S433
7. Eastern Europe S435
8. Middle East S437
9. Türkiye and South Caucasus S438
Sidebar 7.3: European drought conditions in 2023 ..... S440
g. Asia S442
1. Overview S442
2. Russia S445
3. East and Southeast Asia S448
4. South Asia S449
5. Southwest Asia S452
6. Central Asia S454

7. Table of Contents

Sidebar 7.4: Record-breaking high temperatures over North China in October 2023 S456
h. Oceania S459
1. Overview S459
2. Northwest Pacific and Micronesia S459
3. Southwest Pacific S463
4. Australia S466
5. Aotearoa New Zealand S469
Acknowledgments S472
Appendix 1: Acronyms S473
Appendix 2: Supplemental materials S475
References S482

7. REGIONAL CLIMATES

A. Arguez, P. Bissolli, C. Ganter, R. Martinez, A. Mekonnen, L. Stevens, and Z. Zhu, Eds.

a. Overview

This chapter provides summaries of the 2023 temperature and precipitation conditions across seven broad regions: North America, Central America and the Caribbean, South America, Africa, Europe and the Middle East, Asia, and Oceania. In most cases, summaries of notable weather events are also included. Local scientists provided the annual summary for their respective regions and, unless otherwise noted, the source of the data used is typically the agency affiliated with the authors. The base period used for these analyses is 1991–2020, unless otherwise stated. Please note that on occasion different nations, even within the same section, may use unique periods to define their normal. Section introductions typically define the prevailing practices for that section, and exceptions will be noted within the text. In a similar way, many contributing authors use languages other than English as their primary professional language. To minimize additional loss of fidelity through re-interpretation after translation, editors have been conservative and careful to preserve the voice of the author. In some cases, this may result in abrupt transitions in style from section to section.

b. North America

—L. Stevens, Ed.

Above-average temperatures were observed across Canada, large portions of the contiguous United States, and the majority of Mexico in 2023, with record-high annual temperatures in many locations. All other regions were near or slightly below average. Averaged as a whole, North America's annual temperature was 1.13°C above the 1991–2020 base period and was the warmest year in the 114-year continental record (extends back to 1910).

Precipitation varied across North America in 2023. All three countries experienced widespread drought events, with Mexico reporting its driest year on record (since 1950).

Several extreme events occurred during the year, including a record-breaking Canadian wildfire season (Sidebar 7.1). Other notable events included heavy rainfall and flooding in Nova Scotia (NS), heatwaves in both the United States and Mexico, and Hurricane Otis.

Information in this section relates to the geographic continent of North America. Regions of the United States outside the contiguous United States are described in other sections of the report: Alaska (Chapter 5), Puerto Rico (section 7c1), and Guam and the U.S.-Affiliated Pacific Islands (section 7h2). Limited temperature and precipitation data are available for Hawaii but will be included in future reports. Tropical cyclone events affecting all regions are described in Chapter 4.

Anomalies in this section are all with respect to the 1991–2020 base period, unless otherwise noted.

1. CANADA

—V. Y. S. Cheng, F. Wu, M. Beauchemin, and L. Chisholm

Overall, Canada had its second-warmest year on record. National average temperatures for summer and autumn of 2023 were the highest recorded in the nation's 76-year record (1948–2023). National winter and spring temperatures were also above the 1991–2020 average. The temperature records presented in this section are based on adjusted and homogenized Canadian climate data.

(i) Temperature

The annual 2023 average temperature for Canada was 1.8°C above the 1991–2020 average and ranked as the second-warmest year on record, behind only 2010 (Fig. 7.1). Over the past 76 years (1948–2023), the national annual average temperature exhibited a warming of 2.0°C, with 3 of the 10 warmest years occurring since 2015. Spatially, annual anomalies of more than +1.0°C were recorded across most of Canada in 2023, with annual anomalies of more than +2.5°C recorded in most of the Northwest Territories and the western part of Nunavut (Fig. 7.2). Four of the 13 provinces and territories (British Columbia, Alberta, the Yukon, and the Northwest Territories) experienced their highest annual temperatures on record.

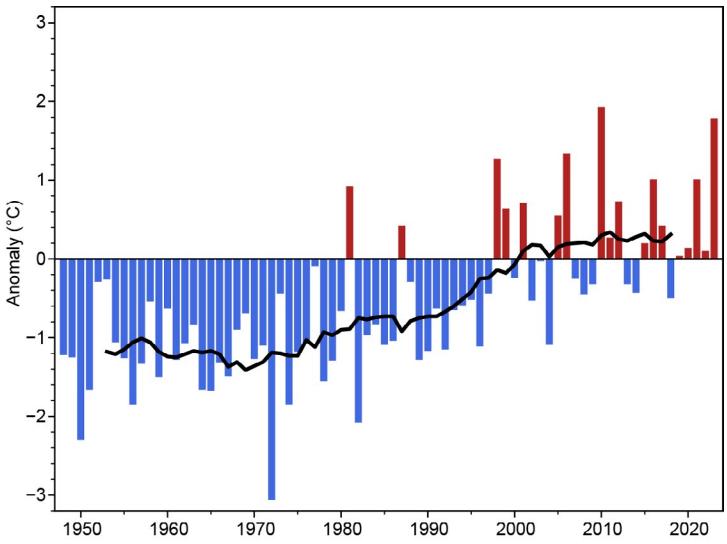

Fig. 7.1. Annual average temperature anomalies (°C; 1991–2020 base period) in Canada for the period 1948–2023. The black line represents an 11-year running mean. (Source: Environment and Climate Change Canada.)

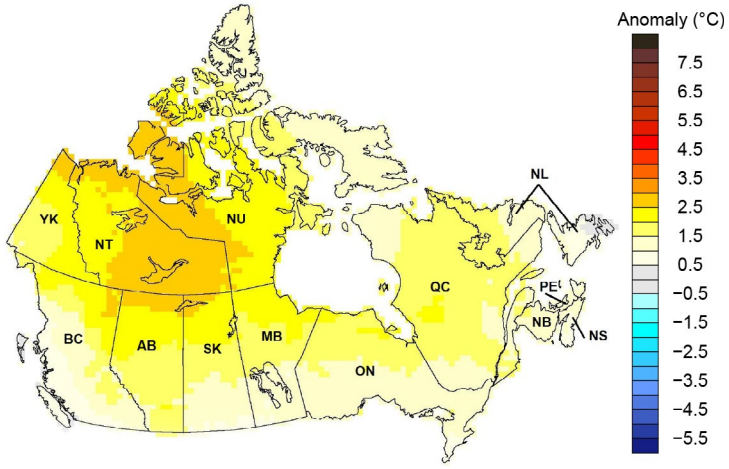

Fig. 7.2. Annual average temperature anomalies (°C; 1991–2020 base period) in Canada for 2023. (Source: Environment and Climate Change Canada.)

Seasonally, the national average temperature for winter (December 2022–February 2023) was 0.3°C above the 1991–2020 average, making it the 19th warmest on record. The highest winter anomalies of +2.5°C were recorded in eastern Ontario and western Quebec.

During spring (March–May), temperature anomalies of at least +0.5°C were observed in most of northern and eastern Canada, while temperature anomalies of at least −0.5°C were observed in the western Yukon, southern Saskatchewan, and Manitoba and western Ontario. The national average temperature for spring 2023 was 1.1°C above average, making it the seventh-warmest spring on record.

The national average temperature for summer (June–August) was 1.2°C above average, the highest on record. Summer anomalies of more than +2.5°C were recorded in the northern region of the Yukon and the Northwest Territories. British Columbia, the Yukon, and the Northwest Territories each had their highest summer temperatures on record.

The national average temperature for autumn (September–November) was 2.4°C above average, making it the warmest autumn on record. Most of the Northwest Territories and Nunavut experienced temperatures 3.0°C or more above average. The Northwest Territories observed their highest autumn temperatures on record, with Nunavut, Quebec, and Alberta each having their second-highest temperatures on record. All provinces and territories had average temperatures among their 10 highest on record for autumn 2023.

(ii) Precipitation

With the evolution of precipitation monitoring technology, Environment and Climate Change Canada (ECCC) and its partners implemented a transition from manual observations to the use of automatic precipitation gauges. Extensive data integration is required to link the current precipitation observations to the long-term historical manual observations. The update and reporting of historical adjusted precipitation trends and variations has been on temporary hiatus pending an extensive data reconciliation, and will be resumed thereafter. ECCC remains committed to providing credible climate data to inform adaptation decision making, while ensuring that the necessary data reconciliation occurs as monitoring technology evolves.

(iii) Notable events and impacts

Canada experienced yet more extremes in 2023. Several heatwaves occurred, and nationwide wildfires set records. A subtropical storm affected the Atlantic Northeast in January, and Hurricane Lee made landfall as a post-tropical cyclone in NS in September. Meanwhile, drought conditions lingered across the country (see the North American Drought Monitor for monthly maps of drought conditions [National Drought Mitigation Center 2024]).

Most notable was the unprecedented wildfire activity across the country (see Sidebar 7.1 for more information). The second most notable was the heavy rainfall in NS that took place on 21–22 July, where a slow-moving trough of low pressure interacted with moist flow from the tropics. Widespread rainfall with totals ranging from 50 mm to 150 mm was observed across NS and eastern Prince Edward Island (Fig. 7.3); locally heavier precipitation of 200 mm to 260 mm fell in parts of Halifax, NS. This event resulted in more than twice the monthly average total rainfall for July (75 mm to 110 mm) in just over two days in the hardest hit areas—the most rain to affect the region in 50 years. Bedford Range, NS, just northwest of Halifax, broke the national rainfall

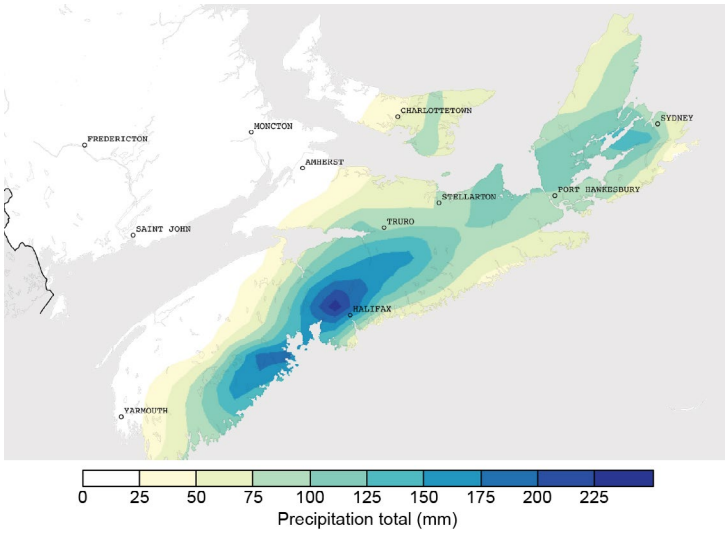

Fig. 7.3. Total precipitation accumulation (mm) during 21–22 July 2023 over Nova Scotia and eastern Prince Edward Island. Darkest blue indicates over 225 mm of rain. (Source: National Laboratory, Meteorological Service of Canada, Environment and Climate Change Canada [ECCC].)

rates record (based on ECCC stations) with 173.4 mm falling over six hours, well exceeding a 1-in-100-year event.

The compounding effect (Singh et al. 2023) of abnormally wet antecedent conditions made this torrential rainfall event even more impactful. Rain had been falling over the region for much of the previous six weeks leading up to the July storm. The already saturated ground led to catastrophic flooding, which damaged infrastructure and led to the loss of four lives when their vehicles were caught in flood waters.

A province-wide state of emergency was declared in NS, with some areas receiving evacuation orders that displaced about 1000 residents (ECCC 2024). Numerous roads and highways were impassable. More than 80,000 homes and businesses lost power. Agricultural losses were also extensive owing to flooded fields, where crops were left submerged for several days (ECCC 2024). In total, this event caused over $236 million Canadian dollars ($179 million U.S. dollars) in insured damage according to the CatIQ database (CatIQ 2024).

2. UNITED STATES

—K. Gleason, C. Fenimore, R. R. Heim Jr., and A. Smith

The annual average temperature for the contiguous United States (CONUS) in 2023 was 12.5°C, which was 0.6°C above the 1991–2020 average, making 2023 the fifth-warmest year in the 129-year record (Fig. 7.4a). Above-average to record-high temperatures were concentrated from the Plains to the East Coast and across portions of the Northwest, while near-average temperatures were observed from California to the central Rockies (Fig. 7.5a). Based on a linear regression of data from 1895 to 2023, the annual CONUS temperature is increasing at an average rate of 0.09°C decade^{-1} (0.27°C decade^{-1} since 1970). Average annual precipitation for the nation totaled 749 mm, which is 94% of the 1991–2020 average (Fig. 7.4b). Overall, the annual precipitation total has been increasing at an average rate of 4 mm decade^{-1} since 1895 (1 mm decade^{-1} since 1970). The average annual temperature across Alaska in 2023 was 0.2°C above average and 17th highest in the 99-year record. Precipitation was 116 mm above average and fifth wettest on record. The annual temperature for Alaska has been increasing at an average rate of 0.17°C decade^{-1} since 1925 (0.44°C decade^{-1} since 1970). Precipitation is increasing at an average rate of 2 mm decade^{-1} since 1925 (21 mm decade^{-1} since 1970).

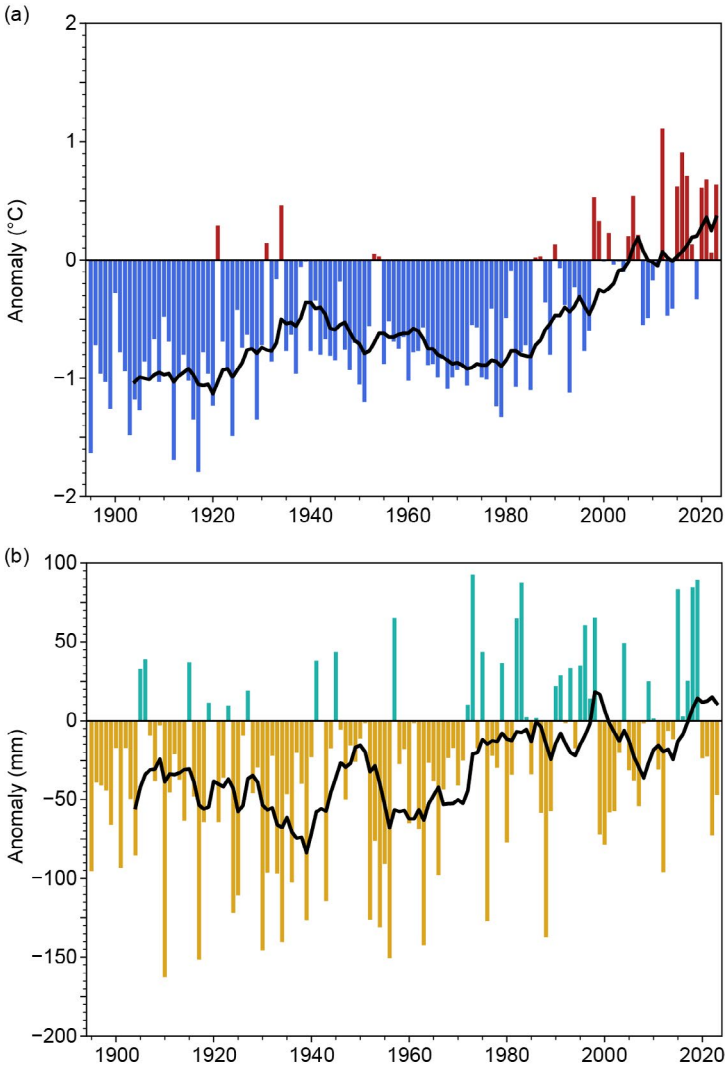

Fig. 7.4. Annual (a) mean temperature anomalies (°C) and (b) precipitation anomalies (mm; 1991–2020 base period) for the contiguous United States during the period 1895–2023. The black lines represent a 10-year running mean. (Source: NOAA/NCEI.)

(i) Temperature

The winter (December 2022–February 2023) CONUS temperature was 0.5°C above average, with anomalous warmth stretching from the southern Plains to the Great Lakes and East Coast. Conversely, the CONUS spring (March–May) temperature was 0.4°C below average with below-average temperatures extending from the West Coast to the northern Plains and above-average temperatures east of a line from southern New Mexico

to the Great Lakes. The summer (June–August) CONUS temperature was 0.4°C above average with record warmth along parts of the Gulf Coast. Louisiana had its warmest summer on record while Texas was second warmest. The autumn (September–November) CONUS temperature was 0.9°C above average, the sixth highest on record. Most of the CONUS experienced above-average temperatures with record heat observed across portions of New Mexico and Texas.

(ii) Precipitation

The climate of the CONUS in 2023 was driven by a broad ridge of high pressure over the central United States, particularly during the second half of the year, which was coincident with a rapid shift from La Niña conditions that lasted for three winters to a strong El Niño by October of 2023 (see section 4b). Louisiana had its ninth-driest year on record while Maine observed its fifth wettest (Fig. 7.5b).

Winter precipitation across the CONUS was 110% of average and ranked in the wettest third of the historical record. Precipitation was above average from California to the Great Lakes and across portions of the Mississippi River Valley and the Northeast. Precipitation totals for Minnesota and Iowa were both third highest on record, and for Wisconsin were the second highest for this winter season. Spring precipitation was near-average (95% of average) for the CONUS, but was below average across portions of the central Plains, Midwest, and Mid-Atlantic. Both Pennsylvania and Maryland had their ninth-driest spring on record. Summer precipitation across the CONUS was 97% of average. Conditions were dry from the Southwest to the central Gulf Coast and in portions of the Northwest and Upper Midwest. Above-average rainfall impacted parts of the West, Plains, and much of the Northeast. Wyoming, Maine, New Hampshire, and Vermont each had their wettest summer on record, while New Mexico and Louisiana both observed their third driest. The autumn CONUS precipitation total was 15th lowest on record at 77% of average. Precipitation was below average across portions of the West, central Plains, and a large portion of the Midwest, Tennessee, and Lower Mississippi River valleys. Tennessee had its third-driest autumn on record.

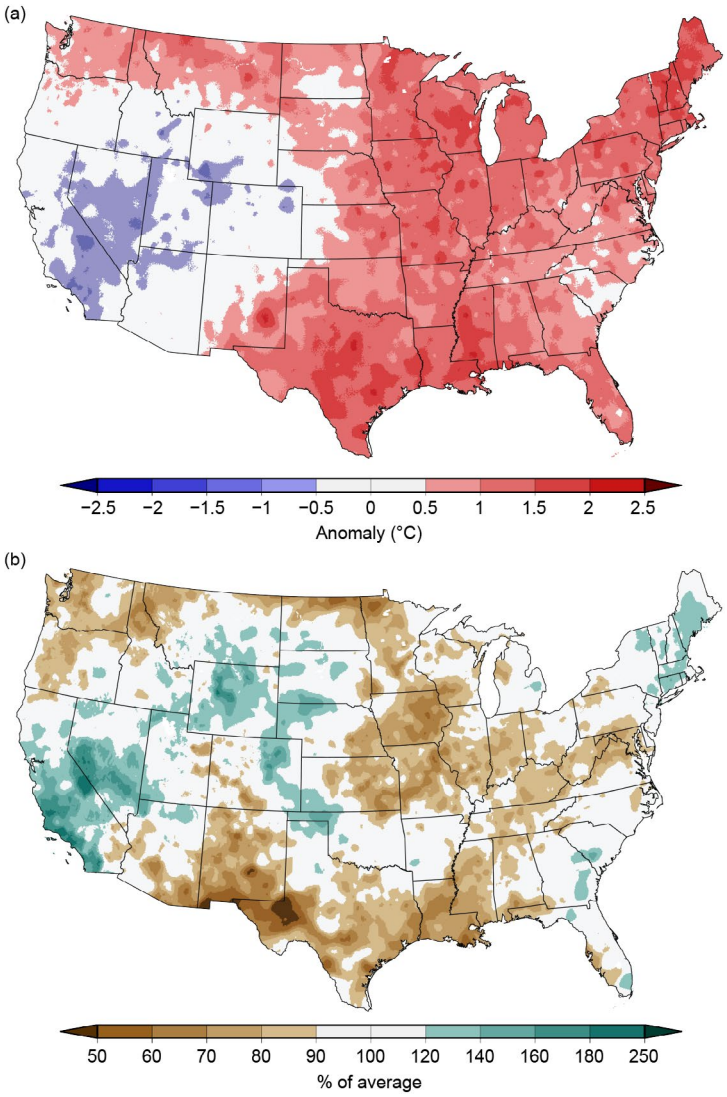

Fig. 7.5. Annual (a) average temperature anomalies (°C) and (b) total precipitation (% of average) in the contiguous United States for 2023 (1991–2020 base period). (Source: NOAA/NCEI.)

Drought coverage across the CONUS remained significant for the fourth consecutive year, beginning with maximum coverage for the year of 46% on 3 January when the most intense areas of drought spanned parts of the West as well as the central and southern Plains. The drought area contracted over the first half of the year, reaching a minimum extent of 19% on 30 May, as drought waned across the West, Midwest, Plains, and Southeast. It expanded throughout the summer and early autumn, reaching a secondary peak of 40% on 3 October, with the epicenter expanding from the central Plains to the Upper Midwest, Deep South, and Pacific Northwest. Warm temperatures and dry conditions led to a flash drought that emerged across portions of the Gulf Coast states and Southeast, with parts of the Mississippi River reaching record-low levels in

October. By the end of 2023, the drought area contracted to 33% of the CONUS, impacting portions of the Southeast, Plains, and Lower Mississippi River Valley. In Hawaii, the lower elevations of Maui saw an expansion of severe drought in early August. These dry conditions, combined with strong, dry winds instigated by Hurricane Dora, contributed to the deadliest wildfire in the United States in more than a century.

(iii) Notable events and impacts

There were a record 28 weather and climate events across the United States during 2023 with losses each exceeding $1 billion: 19 severe storms, 4 flooding, 2 tropical cyclones, and 1 each of drought, wildfire, and winter storm events (Fig. 7.6; Smith 2024). Total disaster costs for these events reached $92.9 billion (note that costs are in U.S. dollars and have been adjusted for inflation; NOAA NCEI 2024). The Southern/Midwestern drought and heatwave that occurred from spring to autumn was the costliest event of the year ($14.5 billion; Smith 2024). Over the last seven years (2017–2023), 137 separate billion-dollar disasters have killed at least 5500 people and incurred costs greater than $1.1 trillion in damage (Smith 2024).

The tornado count for 2023 was 8% above average with 1321 tornadoes reported across the CONUS (SPC 2024). January was an unusually active month with 130 confirmed tornadoes, more than three times the 1991–2020 January average of 39. This was the first time since 2017 and only the third time since 1950 that more than 100 tornadoes occurred during the month of January. Two EF-4 tornadoes were confirmed during the year: the long-lived Rolling Fork, Mississippi, tornado on 24 March that was responsible for 17 fatalities, and the 31 March Keota, Iowa, tornado that destroyed multiple homes. This was the fifth consecutive March with at least one violent tornado (≥EF-4), tying the record streak of five from 1963 to 1967.

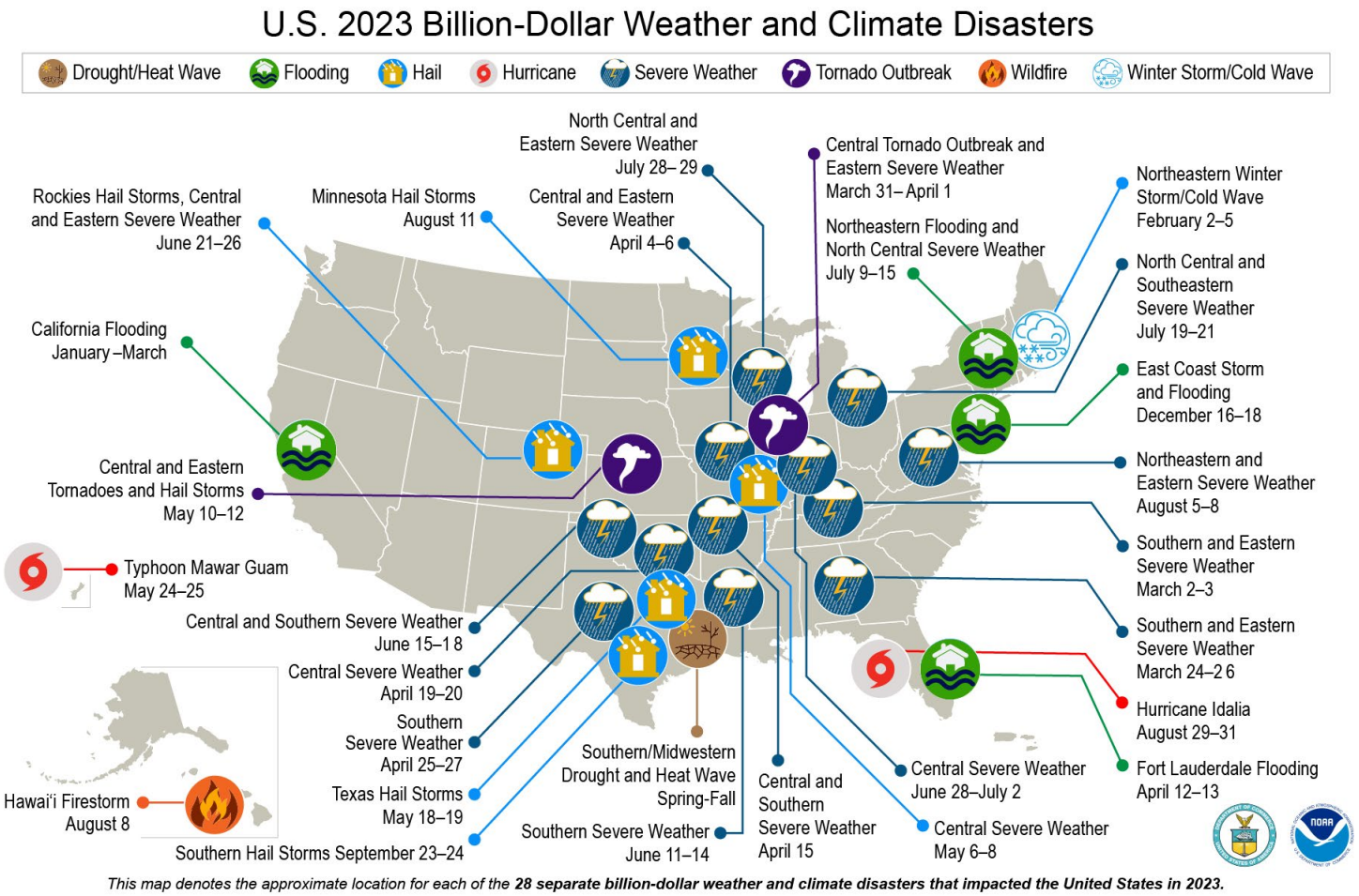

Fig. 7.6. Map depicting date, approximate location, and type of the 28 weather and climate disasters in the United States in 2023 for which losses each exceeded $1 billion (U.S. dollars). (Source: NOAA/NCEI.)

3. MEXICO

—R. Pascual Ramírez and J. Gómez-Camacho

Mexico's annual average temperature for 2023 was the highest since national records began in 1950 (Fig. 7.7a), and the total annual precipitation was the lowest on record (Fig. 7.7b). Only the Baja California Peninsula, the northeast, and southeast recorded above-average annual rainfall throughout the year (Fig. 7.8b); the rest of the country was below average.

(i) Temperature

The 2023 national annual average temperature was 22.7°C, 1.3°C above the 1991–2020 average (Fig. 7.7a) and the highest in the 74-year record. Mexico continues to experience a warming trend, and 2023 marked the 14th consecutive year with an above-average national temperature. Above-average temperatures and persistent heatwaves were prevalent across most of the country, especially during summer; however, regions in the northwest and west experienced near- to below-average annual temperatures (Fig. 7.8a). With the exceptions of February and December, national monthly temperatures were above average, with all months from June to October having been warmest on record for their respective months. From January to March, the northwest and west coast experienced below-average temperatures, while the rest of the country had temperatures much above average. From April through June, below-average temperatures were recorded on the northeast, northwest, and western coasts as the rainy season slowly began; in the central, northern, and southern regions, temperatures were above average.

From July through September, several strong high-pressure systems developed, resulting in very-high temperatures throughout the country. From October to December, above-average temperatures covered the north, central, and south of the country, while slightly below- to near-normal temperatures prevailed along the Gulf of Mexico region.

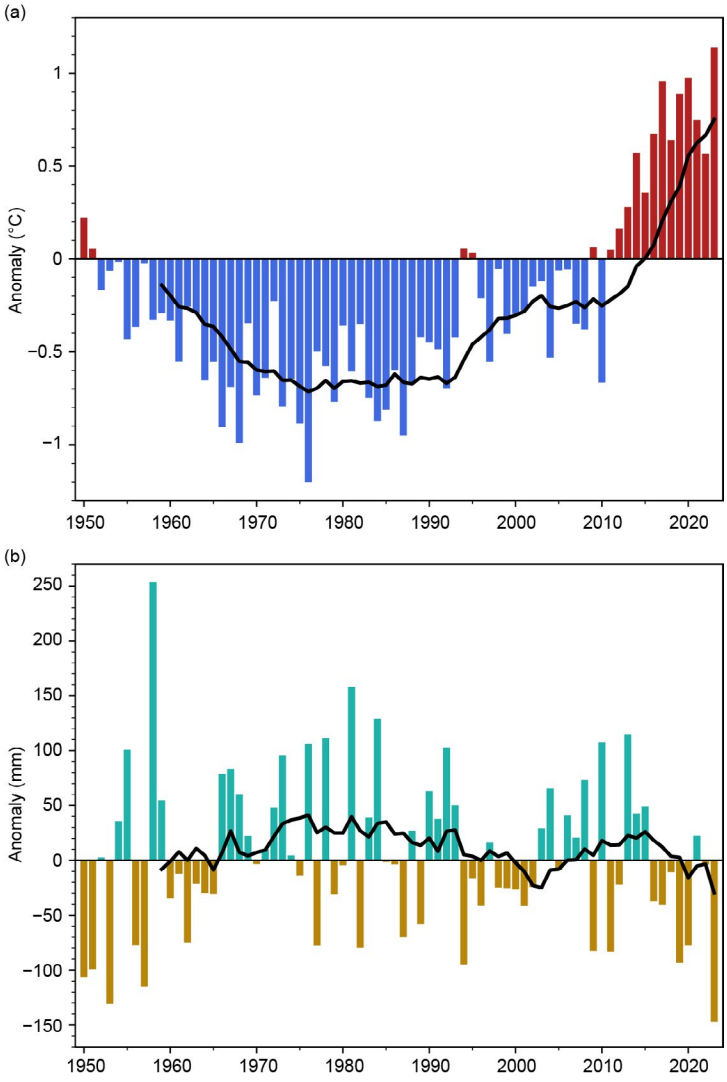

Fig. 7.7. Nationally averaged annual anomalies of (a) temperature (°C) and (b) precipitation (mm) for Mexico from 1950 to 2023 (1991–2020 base period). The black lines represent a 10-year running mean. (Source: National Meteorological Service of Mexico.)

(ii) Precipitation

The national precipitation total for 2023 was 589.9 mm (78.9% of the 1991–2020 average), the lowest annual precipitation total on record for Mexico. Both the dry and wet 2023 seasons recorded below-normal precipitation nationally. Accumulated precipitation for the dry season (November 2022–April 2023) was 115.9 mm, compared to the 1991–2020 average of 133.9 mm. Accumulated precipitation for the wet season (May–October) was 452.0 mm, compared to the 1991–2020 average of 614.0 mm.

Climatologically, September tends to be the country's rainiest month, contributing 18.8% of the annual precipitation; however, for the third year in a row, August contributed more than any other month, with 18.9% of the 2023 annual precipitation. This is a signal of low tropical cyclone activity in September in Mexico over the last two years; September 2023 only provided 11.2% of

the annual rainfall and was the driest September on record. Likewise, June 2023 was the driest June on record. Statistically, March is the driest month of the year, contributing an average of 2.1% of the annual precipitation. In 2023, however, February contributed the least amount of precipitation, with only 2.0% of the annual total. Below-average precipitation fell across most of the country from January to March, with above-average rainfall recorded in the Yucatan Peninsula and the Isthmus of Tehuantepec, as well as in southern and northwest Mexico. The onset of the rainy season in spring was delayed across most of the country, resulting in April–May precipitation deficits, with only the Baja California Peninsula experiencing slightly-above-average precipitation.

Hurricane Beatriz in the Pacific was the only precursor of rainfall in early July, with much less rain occurring during the monsoon season (typically June–September) than in previous years. The 2023 monsoon rainfall was weaker than normal, with 201.9 mm of accumulated precipitation within the region, compared to the 1991–2020 average of 364.9 mm. This was much lower than the 2022 monsoon rainfall, which totaled 453.0 mm.

From July through September, there was less rain than is typically associated with tropical cyclones on both Mexican coasts; in the Atlantic basin, the only two impactful events were Tropical Storm Harold and Hurricane Idalia, both in August. On the Pacific side, Hurricane Hilary, also in August, brought considerable precipitation to the Baja California Peninsula. However, because of minimal moisture transport during these months, widespread drought conditions still occurred, covering up to 75% of the country by the end of September. The last quarter of the year marks the transition between the end of the rainy season and the beginning of the dry season. During this period, it is common to see a combination of tropical and winter systems. From October to December, Tropical Storm Max, three Pacific hurricanes (Lidia, Norma, and Otis), and several cold fronts were the main sources of precipitation in Mexico, thus making it the wettest quarter of the year.

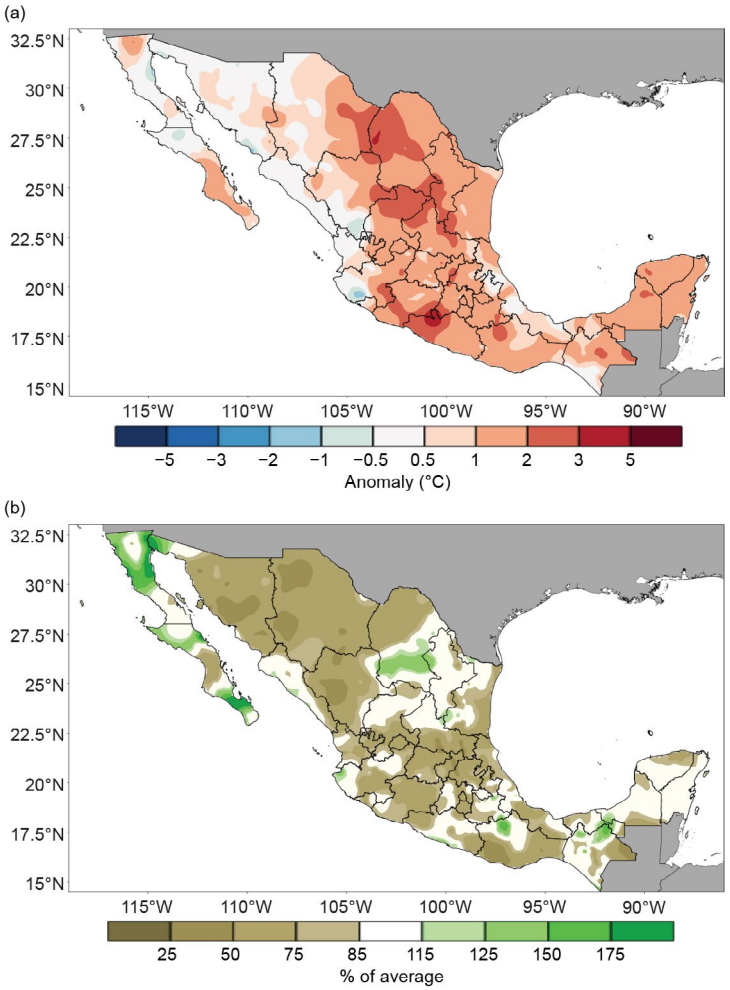

Fig. 7.8. Annual anomalies of (a) mean temperature (°C) and (b) precipitation (% of average) across Mexico in 2023 (1991–2020 base period). (Source: National Meteorological Service of Mexico.)

(iii) Notable events and impacts

From April through June, three heatwaves generated very hot conditions throughout the country, with maximum temperatures surpassing 45°C in places. The heat lasted until September. The heatwave recorded in June was both the most extensive and most intense, with 35 weather observatories or airports across the country reporting record-high temperatures. The highest recorded temperature was 48.0°C at the Ciudad Obregón Observatory in Sonora, which was 9.0°C above the average June high temperature at that location. July 2023 was both the warmest July and the overall warmest month on record for Mexico. According to the Mexican Ministry of Health, 286 deaths associated with heat stroke and dehydration were reported through the end of July, with 35% of these deaths occurring in the state of Nuevo Léon (DGE 2023).

Only two tropical cyclones from the Atlantic basin (Tropical Storm Harold and Hurricane Idalia) affected the eastern coasts of Mexico during 2023. In comparison, the 1991–2020 average number of tropical cyclone impacts is 2.4, with the years 2010 and 2020 each experiencing

impacts from six Atlantic basin tropical cyclones. On the Pacific coast, Tropical Storm Max and Hurricanes Beatriz, Hilary, Lidia, Norma, and Otis all made landfall or tracked near the country and brought significant rainfall to western Mexico. Hurricane Otis had an unprecedented rapid strengthening, intensifying from Category 1 to Category 5 in a record nine hours. Based on records since 1950, Hurricane Otis became the first Category 5 hurricane to make landfall in the state of Guerrero, Mexico, and is one of only two Category 5 hurricanes to make landfall from the Eastern Pacific basin (along with Hurricane Patricia in 2015). The impacts on the city of Acapulco were devastating, with winds of up to 270 km h^{-1} and up to 266 mm of accumulated precipitation in just 24 hours, causing floods and severe damage to infrastructure (see section 4g3 and Sidebar 4.1 for more details on Otis).

Sidebar 7.1: **Record-breaking wildfire season in Canada**

—M. KIRCHMEIER-YOUNG, P. JAIN, J. CHEN, AND F. WU

The 2023 wildfire season in Canada was exceptional. Approximately 15 million hectares (150,000 km^2) burned across the country (Jain et al. 2024), an area more than twice the size of Ireland. The total area burned set a new record for Canada, considering data from the modern satellite era, more than doubling the previous record from 1989 (Fig. SB7.1a). A notable characteristic of this fire season was the extent of the country that experienced record wildfires. The area burned in 2023 was the highest fire-season total for Quebec, Northwest Territories, Alberta, and British Columbia and second highest for Yukon and the Maritimes, based on the satellite record beginning in 1986. The long-range transport of emissions from these fires resulted in high pollutant levels far downwind, including cross-border transport of these pollutants into the United States and overseas. Across the country, approximately 232,000 people were evacuated due to the threat of wildfires, including the entire city of Yellowknife (Northwest Territories) and large populations of Kelowna/West Kelowna (British Columbia) and Halifax (Nova Scotia). Extensive property losses from six large fires led to 17,000 insurance claims for a total of over $1.1 billion Canadian dollars ($815 million U.S. dollars) in damage. The 2023 wildfire season was long, intense, and widespread, and several firefighters died responding to the fires.

Wildfire seasons in Canada typically begin with the loss of snow cover in the spring, and in 2023 the snowmelt was earlier than normal across much of the country. Following snowmelt, the fire season got off to a quick start, with fires of concern occurring in British Columbia, Alberta, and Nova Scotia. In anticipation of nationwide constraints on firefighting capacity, the Interagency Forest Fire Centre set the national preparedness level at its most extreme category on 11 May, the earliest date on record, and kept it at that level for an unprecedented continuous 120 days (CIFFC 2023). Western Canada began the fire season with pre-existing drought conditions that lasted throughout the year. On the other hand, eastern Canada began the fire season with more normal conditions but underwent a

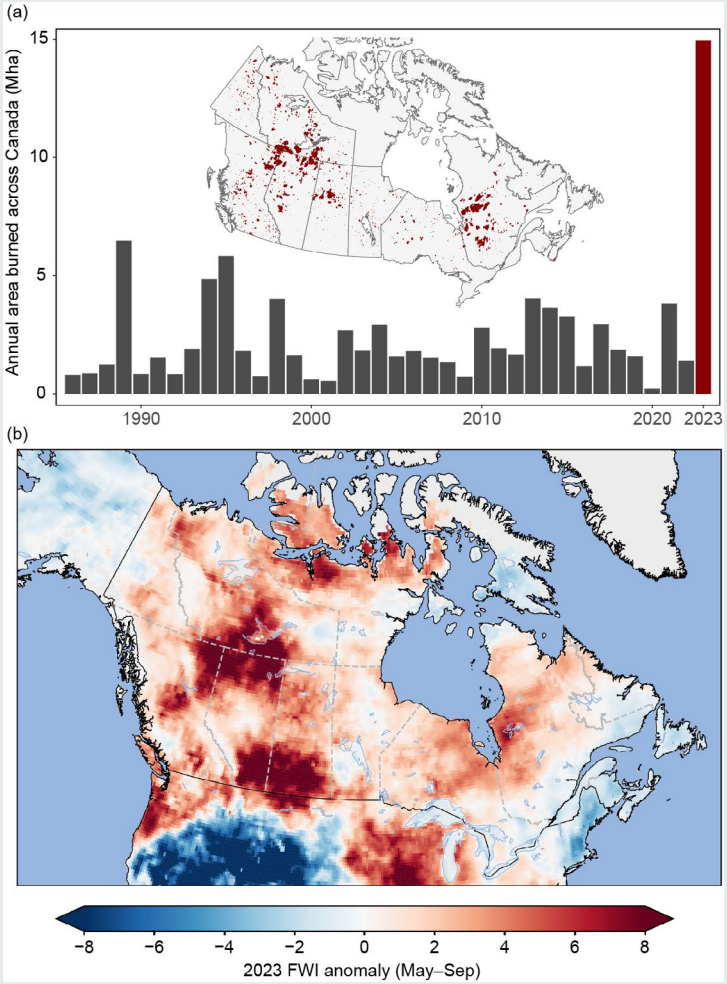

Fig. SB7.1. (a) Annual area burned by wildfires (million ha) in Canada based on data from the National Burned Area Composite (NBAC; Skakun et al. 2022). Inset map: fire perimeters for the 2023 fire season. The data for 2023 were generated from NBAC mapped perimeters and satellite thermal anomalies (Jain et al. 2024). (b) Anomalies of the mean 2023 fire season (May–Sep) value of the Canadian Fire Weather Index relative to 1991–2020. Calculated from the Canadian Forest Fire Danger Rating System and using ERA5 surface weather as inputs.

rapid intensification of drought into June. Southern Quebec, in particular, experienced strong decreases in soil moisture during this time (Jain et al. 2024).

Canada was hot and dry throughout the 2023 fire season. Both summer and autumn were the warmest on record for the country (section 7b1). Much of the area burned in western Canada (Fig. SB7.1a) aligns with the regions that experienced their hottest year on record (see Fig. 7.2), as well as those that experienced prolonged drought conditions (see National Drought Mitigation Center 2024). The Canadian Forest Fire Weather Index System consists of a set of indices that use temperature, precipitation, relative humidity, and wind speed to describe the potential of wildfires to ignite and spread. The system's Fire Weather Index (FWI) largely followed the drought patterns, with local extreme values in western Canada beginning in May and emerging in eastern Canada in June. Considerable portions of the country experienced sustained high FWI values during the fire season, which were driven by well-above-normal temperatures that dried out vegetation through evaporation and a lack of rainfall needed to replenish the moisture. This is confirmed in the 2023 May–September FWI anomaly shown in Fig. SB7.1b, with higher-than-normal FWI conditions occurring throughout the country.

Sustained fire weather conditions primed the landscape, allowing for fire growth following ignition, which was caused by lightning for most of the large fires. Across the country, several days with large increases in area burned occurred with high winds, when already-large fires experienced rapid spread. Another key factor for the extreme fire season was that the established fires tended to burn longer and grow larger than is usually the case. The 20 largest fires in the country contributed to about half of the total area burned (Jain et al. 2024). Many of the fires that ignited during the extreme fire weather conditions in May and June continued to burn through September. This longevity of fires and unusually persistent extreme fire weather helped drive the record fire season.

Smoke from wildfires can impact communities both near and far. In 2023, Environment and Climate Change Canada issued almost 5000 air quality alerts, which is considerably higher than in recent years (compared to about 1800 in 2021, which accompanied the next largest area burned in the last decade). This drastic increase is attributed directly to the extreme poor air quality conditions from wildfires throughout the summer across Canada. The number of smoke hours from May to early September, as defined when visibility is less than 9.7 km, revealed record-breaking smoke conditions across much of western, central, and northern Canada. The city with the highest number of smoke hours was Fort Nelson (British Columbia) with 1054 hours, and several major cities, including Kamloops (British Columbia), Calgary, Edmonton (Alberta), Regina, Saskatoon (Saskatchewan), and Yellowknife (Northwest Territories) experienced more than 200 hours of smoke. Fine particulate matter (PM2.5) measurements are a common indicator of air quality, and high values have been shown to have significant negative impacts on human health. During the fire season in 2023, the most extreme levels of PM2.5 were found in the regions with the most area burned (Fig. SB7.2). Smoke can also be transported hundreds

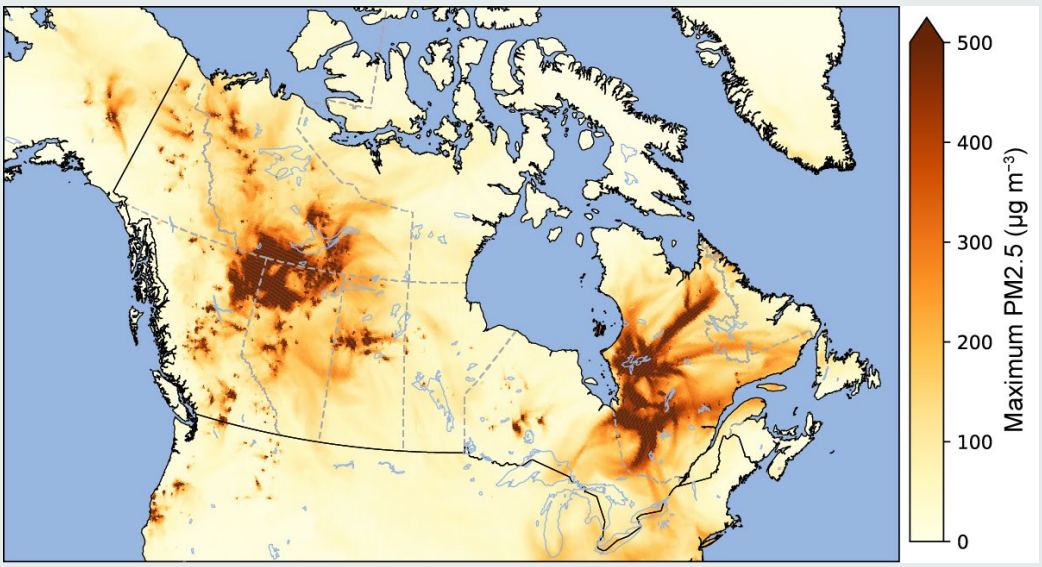

Fig. SB7.2. Maximum daily fine particulate matter (PM2.5) values (µg m^{-3}) across northern North America for May–Sep 2023, calculated from Environment and Climate Change Canada's FireWork model (Chen et al. 2019). The highest values correspond to the locations of the fires in northeastern British Columbia/northern Alberta/southern Northwest Territories and in northwestern Quebec. High-concentration surface plumes extending outward from the fire regions can also be seen.

of kilometers downwind, where it exposes populations to elevated levels of PM2.5 at regional to continental scales. Residents across the country, including those in most of Canada's major cities, experienced numerous days with high smoke and PM2.5 levels, resulting in canceled outdoor events and adverse impacts on physical and mental health from pollutant exposures (Mao et al. 2024; Lowe et al. 2023; Matz et al. 2020). This prompted the immediate release of public health warnings by the Government of Canada in response to the 2023 wildfire season (Public Health Agency of Canada 2023).

Impacts of the wildfires also extended beyond Canada. In early June, cyclonic flow around an area of low pressure over eastern Canada carried smoke from wildfires burning in northern Quebec into the northeastern United States, prompting severe air quality alerts in New York City and other major metropolitan areas (US EPA 2023), and again in late June, impacting Chicago and much of the Great Lakes region. Smoke from the wildfires in Quebec was also transported across the Atlantic to countries in western Europe, further increasing the widespread impacts of Canada's record wildfire season.

c. Central America and the Caribbean

1. CENTRAL AMERICA

—H. G. Hidalgo, J. A. Amador, E. J. Alfaro, B. Calderón, and N. Mora

For this region, nine stations from five countries were analyzed (see Fig. 7.9 for data, station list, and specific data sources). The station distribution is representative of the relevant seasonal and intraseasonal regimes of precipitation (Amador 1998; Magaña et al. 1999; Amador et al. 2016a,b), wind (Amador 2008), and temperature (Hidalgo et al. 2019) on the Caribbean and Pacific slopes of Central America (CA). Precipitation, temperature, and regional wind data for the stations analyzed were provided either by CA National Weather Services (CA-NWS), NOAA, or the University of Costa Rica; in some cases, missing daily precipitation data were filled with the nearest grid point data from the Climate Hazards and Infrared Precipitation with Stations dataset (CHIRPS; Funk et al. 2015). Anomalies are reported using a 1991–2020 base period and were calculated from data provided by CA-NWS. The precise methodologies used for all variables are described by Amador et al. (2011). The Puerto San José station in Guatemala, used in past reports, was substituted with the nearby Montufar station due to lack of data in 2023.

(i) Temperature

The mean temperature (Tm, °C) frequency distributions in 2023 as well as the climatology for all stations analyzed are shown in Fig. 7.9. Most stations across Central America had well-above-normal annual temperatures. Only the station of Liberia, Costa Rica (Tm7), had near-normal temperatures. The two northernmost stations in the Caribbean coast, Philip Goldson International Airport, Belize (Tm1), and Puerto Barrios, Guatemala (Tm2), exhibited a bimodal temperature distribution over the course of the seasonal cycle during the 1991–2020 reference period. This was also reported in the last two yearly climate reports. This feature is also hinted at in the two-peak distribution of Tm in both stations in 2023 (more so in Belize).

(ii) Precipitation

The accumulated pentad precipitation (mm) time series for the nine stations in Central America are presented in Fig. 7.9. Most stations had below-average rainfall totals, with the exceptions of Puerto Barrios (P2) and Montufar (P9) in Guatemala, which presented near-normal conditions, and Tocumen (P5) and David (P6) in Panama, which presented wetter-than-normal conditions. Notably, 2023 showed an atypical precipitation response to the prevailing El Niño–Southern Oscillation event, most likely related to the prevailing above-average sea surface temperature anomalies in the Atlantic/Caribbean basin. Most of the stations on the Pacific and Caribbean side ended the year with below-average annual accumulations (except for the Panama stations) with no contrast between the usual opposite responses in the Pacific and Caribbean slopes. Despite reported problems in the operation of the Panama Canal due to low water levels in Gatun Lake, the Panama stations generally tracked near- to above-normal precipitation throughout 2023, suggesting that rainfall accumulations were not a likely cause of the operational issues in the canal zone. The prevailing wind anomaly pattern (Fig. 7.9) in July implies a light flow from the Caribbean to the Pacific coast from the Nicaragua–Costa Rica border to the north; negative wind anomalies and drier-than-normal Pacific conditions are typical during an El Niño event.

(iii) Notable events and impacts

During 2023, Central America was impacted by various stages of low-pressure systems, including tropical depressions and tropical storms. However, tropical cyclone activity in the Caribbean and eastern tropical Pacific affecting Central America was below normal in 2023. A low-pressure system formed near the southwest coast of Costa Rica in the eastern tropical Pacific on 25 June, becoming Tropical Depression Two-E on 29 June, and eventually developing into Tropical Storm Beatriz. Later, a tropical wave crossed Central America into the eastern tropical Pacific on 29 July off the coast of El Salvador, producing a large area of rain and thunderstorms before becoming Tropical Depression Five-E on 31 July and, later, Tropical Storm Dora. On 12 August, another tropical wave crossed Central America to the eastern tropical Pacific, affecting Guatemala and El Salvador on 14 August. Then, a low-pressure system crossed the isthmus from the eastern tropical Pacific on 24–25 August and persisted offshore of the Caribbean Central America coast, becoming Tropical Depression 10 on 26 August and later becoming Hurricane

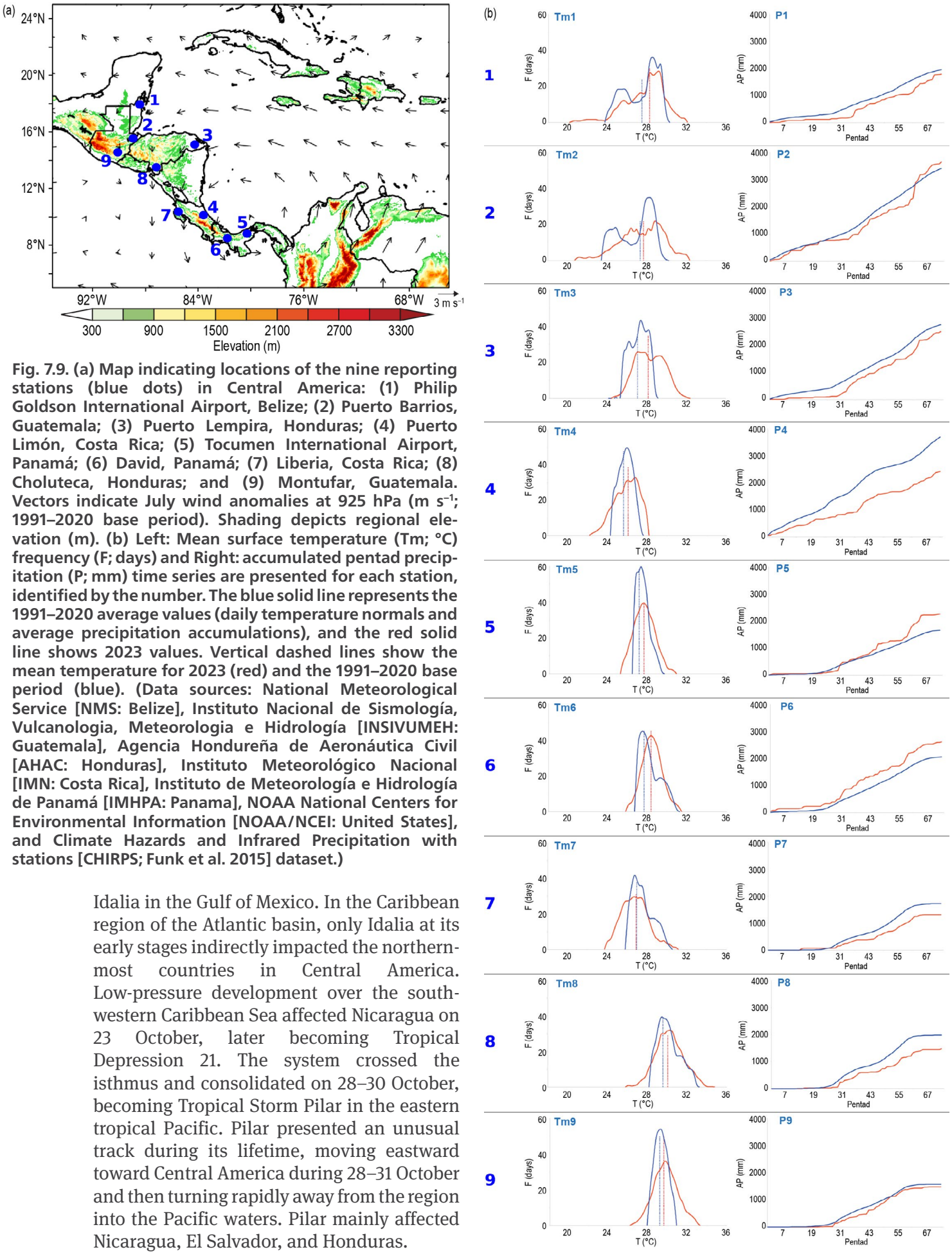

Fig. 7.9. (a) Map indicating locations of the nine reporting stations (blue dots) in Central America: (1) Philip Goldson International Airport, Belize; (2) Puerto Barrios, Guatemala; (3) Puerto Lempira, Honduras; (4) Puerto Limón, Costa Rica; (5) Tocumen International Airport, Panamá; (6) David, Panamá; (7) Liberia, Costa Rica; (8) Choluteca, Honduras; and (9) Montufar, Guatemala. Vectors indicate July wind anomalies at 925 hPa (m s^{-1}; 1991–2020 base period). Shading depicts regional elevation (m). (b) Left: Mean surface temperature (Tm; °C) frequency (F; days) and Right: accumulated pentad precipitation (P; mm) time series are presented for each station, identified by the number. The blue solid line represents the 1991–2020 average values (daily temperature normals and average precipitation accumulations), and the red solid line shows 2023 values. Vertical dashed lines show the mean temperature for 2023 (red) and the 1991–2020 base period (blue). (Data sources: National Meteorological Service [NMS: Belize], Instituto Nacional de Sismología, Vulcanologia, Meteorologia e Hidrología [INSIVUMEH: Guatemala], Agencia Hondureña de Aeronáutica Civil [AHAC: Honduras], Instituto Meteorológico Nacional [IMN: Costa Rica], Instituto de Meteorología e Hidrología de Panamá [IMHPA: Panama], NOAA National Centers for Environmental Information [NOAA/NCEI: United States], and Climate Hazards and Infrared Precipitation with stations [CHIRPS; Funk et al. 2015] dataset.)

Idalia in the Gulf of Mexico. In the Caribbean region of the Atlantic basin, only Idalia at its early stages indirectly impacted the northernmost countries in Central America. Low-pressure development over the southwestern Caribbean Sea affected Nicaragua on 23 October, later becoming Tropical Depression 21. The system crossed the isthmus and consolidated on 28–30 October, becoming Tropical Storm Pilar in the eastern tropical Pacific. Pilar presented an unusual track during its lifetime, moving eastward toward Central America during 28–31 October and then turning rapidly away from the region into the Pacific waters. Pilar mainly affected Nicaragua, El Salvador, and Honduras.

Other rain-producing systems caused landslides and flooding that killed 94 people: 1 each in Panama and Costa Rica, 2 in Nicaragua, 17 in El Salvador, 7 in Honduras, and 66 in Guatemala. Reported lightning strikes caused 24 fatalities in the region during the season (one each in Panama and Costa Rica, six in Nicaragua, seven in El Salvador, five in Guatemala, and four in Honduras). Mortality statistics provided above were obtained from newspaper publications and/or national emergency management agencies such as the following: Guatemala: https://conred.gob.gt/; El Salvador: https://www.proteccioncivil.gob.sv, https://www.gobernacion.gob.sv, https://diario.elmundo.sv; Honduras: https://copeco.gob.hn; Panama: https://www.sinaproc.gob.pa, https://www.panamaamerica.com.pa; Costa Rica: https://www.nacion.com; Nicaragua: https://nicaraguainvestiga.com; https://www.elmundo.es/; https://www.laprensani.com/. Please see sections 4g2 and 4g3 for more details on the 2023 Atlantic basin and eastern Pacific basin tropical cyclones.

2. CARIBBEAN

—T. S. Stephenson, M. A. Taylor, A. Trotman, C. J. Van Meerbeeck, L. Clarke, J. Spence-Hemmings, R. Moody, C. Charlton, and J. Campbell

(i) Temperature

In 2023, the annually averaged 2-m temperature over the Caribbean was 26.68°C, which was 0.73°C above the 1991–2020 average, making it the warmest year since the start of the record in 1950 (Fig. 7.10a). Seasonally, the Caribbean observed its sixth-warmest December–February (0.39°C above normal); fourth-warmest March–May (0.44°C); and record-warmest June–August (0.96°C) and September–November (1.03°C). Overall, the region has been warming at a rate of 0.12°C decade^{-1} since 1950 (0.18°C decade^{-1} since 1970). At the island scale (Fig. 7.11a), the year was characterized by record and near-record mean annual temperatures for 14 of 36 stations archived in the Caribbean Institute for Meteorology and Hydrology CAROGEN database (Table 7.1). The Caribbean heat season, defined here as May–October, was record warm at 18 of 36 stations, with 30 stations measuring values exceeding their 90th percentile.

(ii) Precipitation

Annually averaged rainfall for 2023 over the Caribbean was ~0.16 mm day^{-1} drier than normal, which is ~95% of the 1991–2020 average (3.22 mm day^{-1}; Fig. 7.10b). Normal to below-normal precipitation was observed over the eastern Caribbean, and above-normal precipitation was observed in the north (Fig. 7.11b). December–February rainfall was generally normal to below normal. More intense drying was observed over northern islands, including Jamaica, Haiti, and southeastern Cuba and the Dominican Republic. For March–May, above-normal anomalies were recorded over

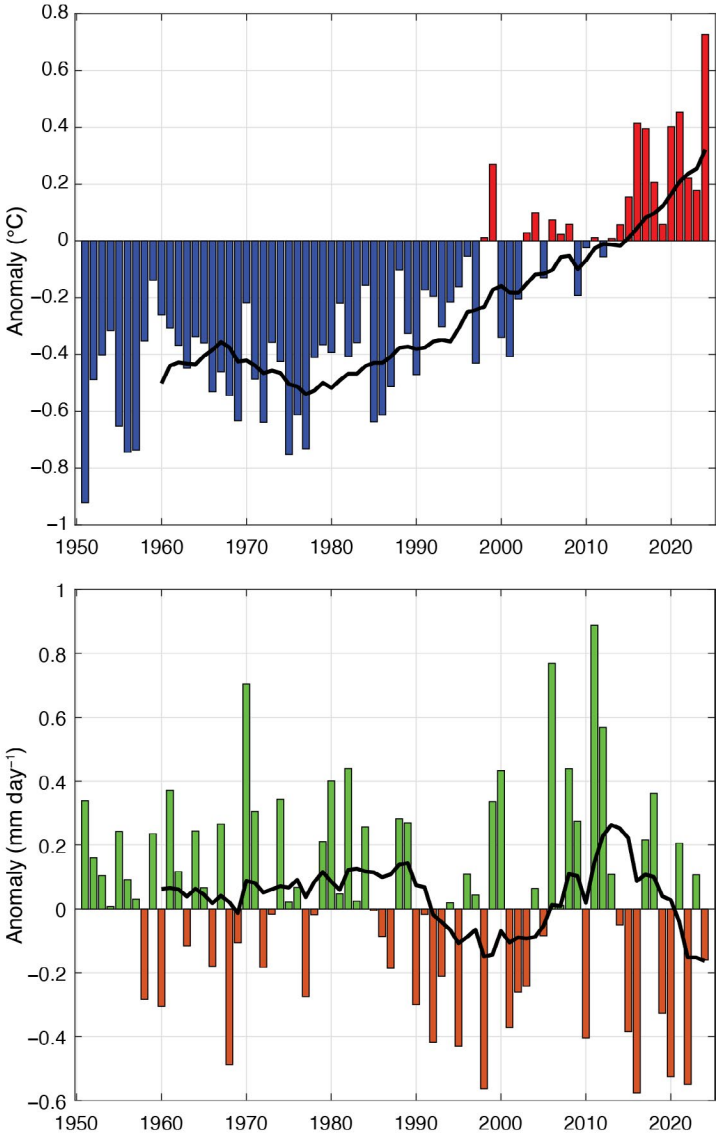

Fig. 7.10. Annually averaged (a) 2-m temperature anomaly (°C) and (b) rainfall anomaly (mm day^{-1}) time series for the Caribbean (9°N–27°N, 58°W–90°W) for the period 1950–2023 relative to the 1991–2020 average. The black line represents the 10-year running mean. (Source: ERA5 from the Copernicus Climate Data Store.)

most of the northern islands, while near-normal to dry conditions continued over the east. During June–August, the region continued to transition to wetter-than-normal conditions in the north and to normal conditions over the rest of the region; however, very-dry conditions were observed over Tobago in the south. An expansion of the drying in the southeast was observed for September–November. Similarly, southeast Cuba and southern Puerto Rico reported drier-than-normal conditions; in contrast, the Bahamas recorded wetter-than-normal conditions during this period.

Since the start of the record in 1971, Jimani, Dominican Republic, recorded its wettest year in 2023 (1105.8 mm, 159% of average); Padre Las Casas, Azua, Dominican Republic, its second wettest (1251.4 mm; 170.9%); Barrah, Dominican Republic, its seventh wettest (1510 mm; 154.0%); and Lynden Pindling International Airport, Bahamas, its fourth-wettest year (1911.0 mm, 133.3%). El Valle, Hato Mayor, Dominican Republic, observed its second-driest year since 1971 (662.4 mm, 47.6%); La Desirade, Guadeloupe, its fifth driest since 1971 (745.9 mm, 65.0%); Lajas, Puerto Rico, its second driest since 1973 (619.8 mm; 56.0%); E.T. Joshua Airport, St. Vincent, its third driest since 1979 (1606.9 mm; 76.0%); and Piarco, Trinidad, its sixth-driest year since 1971 (1498.9 mm; 81.6%).

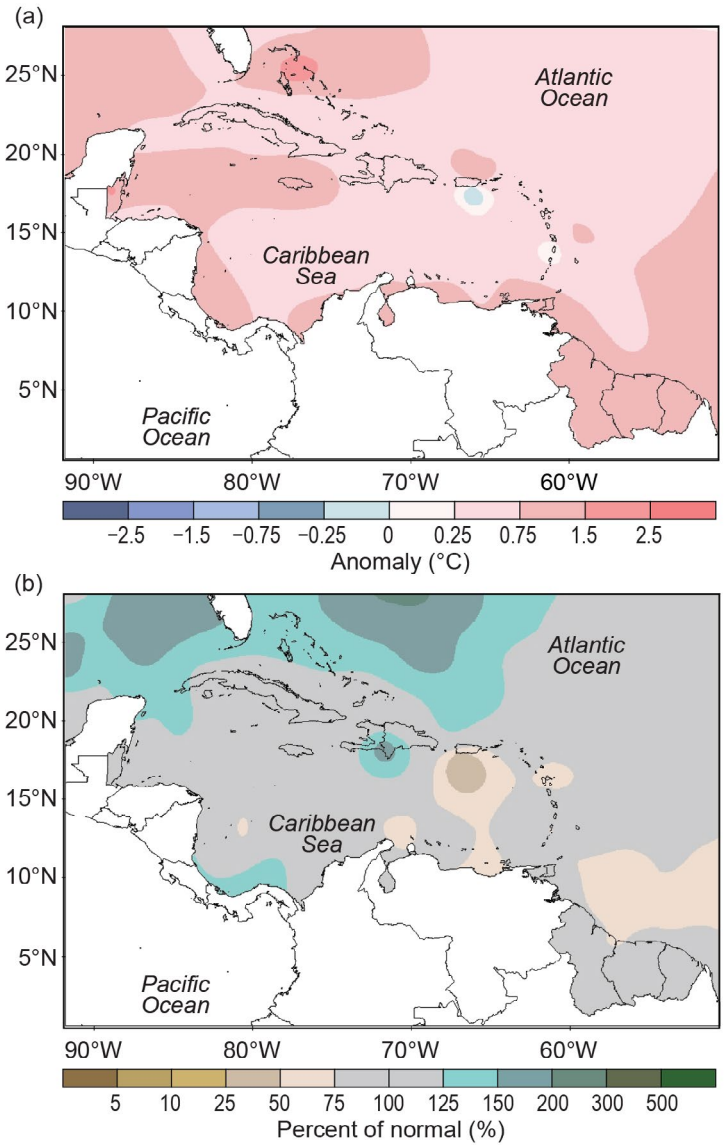

Fig. 7.11. Annual (a) mean temperature anomalies (°C) and (b) total precipitation anomalies (% of normal) relative to 1991–2020. (Source: Caribbean Climate Outlook Forum [CariCOF] and the Caribbean Institute for Meteorology and Hydrology.)

(iii) Notable events and impacts

During 2–6 June, Tropical Storm Arlene caused flooding and landslides in Haiti. Seventy-eight deaths and damage in excess of $420 million (U.S. dollars) were reported (Delforge et al. 2023). During 8–13 June, excessive rainfall due to Tropical Depression Two impacted the central Bahamas, resulting in flooded homes, businesses, and vehicles in the district of Exuma (CCRIF SPC 2023a). Cuba was impacted by heavy rains from the same system on 8–10 June, affecting 18,500 residents (Delforge et al. 2023). On 22–23 June, the center of Tropical Storm Bret passed north of Barbados and over northern St. Vincent and the Grenadines, impacting over 300 people on these islands (Delforge et al. 2023). Bret also impacted St. Lucia, where heavy rains and strong winds downed power lines, flattened banana crops, damaged roofs, and caused flooding and mudslides in some communities (CCRIF SPC 2023b). Tropical Storm Franklin traversed the Dominican Republic during 20–23 August and caused flooding that impacted more than 289,000 residents (Delforge et al. 2023). During 26–29 August, Hurricane Idalia traveled close to the western tip of Cuba, causing flooding in that region. Tropical Storm Philippe impacted Dominica and Antigua and Barbuda on 2–3 October. Excess rainfall from the storm caused flooding and severe landslides in Dominica (CCRIF SPC 2023c). In Antigua and Barbuda, heavy rains and severe flooding impacted low-lying areas, damaged businesses, and caused power

outages (CCRIF SPC 2023d). Many residents were forced to evacuate their homes. On 16–17 November, Jamaica was impacted by a broad area of low pressure over the central Caribbean Sea to the southwest of the island. Sixteen roadways were impacted by the excessive rain, flood waters, and fallen rocks and trees; 22 people marooned in the parish of St. Thomas had to be rescued by the Jamaica Defence Force (CCRIF SPC 2023e).

Table 7.1. Annual temperature extremes for 2023 at Caribbean weather stations contained in CAROGEN (https://carogen.cimh.edu.bb). Included are summary statistics for stations where the annual mean 2-m temperature exceeded the 90th percentile for the reference period 1991–2020. Among the requirements for inclusion are 1) a complete record for 2023, 2) at least 80% of years between 1991 and 2020 being complete, and 3) a period of record spanning at least 30 years since 1971 or the start of station operations, whichever the more recent date may be. Shaded rows with a thermometer icon (🌡) indicate stations registering their warmest years on record in 2023.

Country	Station	Temperature (°C)	Anomaly (°C)	Number of years in data	Rank
Antigua and Barbuda	VC Bird Airport, Antigua	30.1	0.4	53	5
The Bahamas	Freeport, Grand Bahama	29.5	0.9	51	3
The Bahamas	Lynden Pindling International Airport, New Providence	30.3	0.8	53	3
Barbados	Caribbean Institute for Meteorology and Hydrology	30.4	0.4	43	2
Cayman Islands 🌡	Owen Roberts International Airport, Grand Cayman	31.7	1.2	48	1
Cuba	Casa Blanca, Havana	30.9	1.4	53	2
Cuba	National Airport of Camagüey	31.5	1.0	53	2
Cuba	Punta de Maisi	30.9	0.8	53	3
Dominica 🌡	Canefield Airport	32.4	1.2	39	1
Grenada	Maurice Bishop International Airport	30.9	0.4	39	3
Jamaica 🌡	Norman Manley International Airport	32.4	0.5	31	1
Jamaica 🌡	Sangster International Airport	32.9	1.3	50	1
Martinique	Aimé Césaire International Airport	31.2	0.7	53	2
Puerto Rico	Aibonito	26.5	1.0	38	5
Puerto Rico	San Juan	31.0	0.6	53	6
St. Croix	Henry E. Rohlsen Airport	31.5	1.0	52	4
Sint Maarten	Princess Juliana International Airport	31.0	0.7	43	5

d. South America

—R. Martinez, Ed.

1. NORTHERN SOUTH AMERICA

—F. Costa, P. Echeverría, Y. González, and J. Serna

The northern South America region includes Colombia, Ecuador, French Guiana, Guyana, Suriname, and Venezuela. Throughout this section, 1991–2020 is the base period used for both temperature and precipitation unless otherwise specified.

Temperature and precipitation patterns in northern South America during the early months of 2023 showed the influence of the end of the triple La Niña period, which concluded near the start of the year. For the remainder of 2023, the influence of El Niño conditions emerged and strengthened, particularly notable with the excessive rainfall in Ecuador, due to the intense warming of sea surface temperatures in the Niño 1+2 region, known as the Coastal El Niño. By June, when international agencies declared a global El Niño (recorded in the Niño 3.4 region; see section 4b for details), the influence of the positive El Niño–Southern Oscillation (ENSO) phase on air temperatures throughout the region was observed, along with a decrease in precipitation in Venezuela and Colombia.

(i) Temperature

Overall, annual maximum temperatures across northern South America were higher than usual in 2023. In Suriname, recorded values were 1.0°C–1.5°C above the 1991–2020 climatological average. In Venezuela, all records showed anomalies of more than +1.0°C. In Colombia, maximum temperatures had positive anomalies in the range of +1.0°C to +1.5°C. Notably, since El Niño conditions began around mid-2023, most of the country, both continental and insular, recorded above-normal temperatures. The months with warmest temperatures were August, October, and December. In Ecuador, maximum temperatures were also above normal in 2023. The highest anomaly observed in the coastal region was in January with an average maximum temperature of 36.5°C, 4.1°C above normal. In the inter-Andean and Amazon regions, the maximum temperature was recorded in September, at 29°C and 36.9°C, which was 3.4°C and 3.2°C above normal, respectively (Fig. 7.12a).

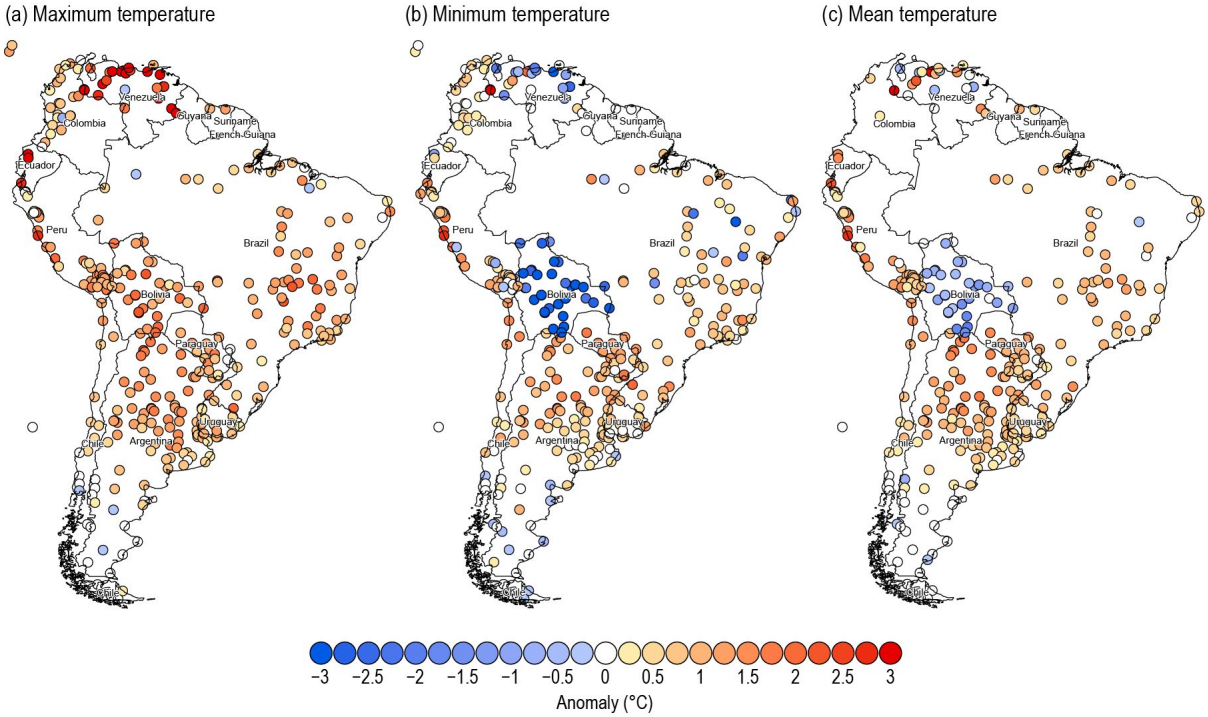

Fig. 7.12. Annual (a) maximum, (b) minimum, and (c) mean temperature anomalies (°C; 1991–2020 base period) for 2023. (Source: data from National Meteorological and Hydrological Services of Argentina, Bolivia, Brazil, Chile, Colombia, Ecuador, Paraguay, Peru, Suriname, Uruguay, and Venezuela. Processed by Centro Internacional para la Investigación del Fenómeno de El Niño [CIIFEN].)

Regarding minimum and mean temperatures, northern South America experienced variable conditions in 2023 (Figs. 7.12b,c). In Suriname, annual minimum temperatures were close to normal, while in Venezuela temperatures ranged from near normal to 3.5°C below normal. The average minimum temperature anomaly from weather stations distributed throughout the country was −0.8°C. In Colombia, minimum temperature anomalies ranged from near normal to +1.0°C. In Ecuador, annual average minimum anomalies were between −1.0°C and +0.5°C. January was the coldest month in the country's coastal region, with a monthly minimum temperature of 20.2°C, which was 1.6°C below normal. In the inter-Andean region, the monthly minimum temperature was −2.1°C in September, which was 3.0°C below normal. In the Amazon, the January minimum temperature was 14.5°C, 4.1°C below normal. The average mean temperature reached its minimum in January in the coastal and Andes region at 25.2°C (normal) and 10°C (0.6°C below normal), respectively. In the Amazon, the average March temperature was 20.9°C, 0.6°C below normal. The highest mean temperature was recorded in May in the coastal region, 28.5°C, which was 1.4°C above normal. In the Andes, the highest mean temperature was 24.1°C in July, 0.3°C above normal, and in the Amazon the July temperature was 29.2°C, 2.3°C above normal.

(ii) Precipitation

Precipitation was variable across northern South America in 2023. Annual totals in Suriname ranged from 30% below normal to 20% above. Venezuela's average precipitation was 30% below normal, with some stations in the north as much as 70% below normal. In Colombia, according to records from Instituto de Hidrología, Meteorología y Estudios Ambientales' meteorological station network, excess rainfall was observed in January, March, and December across much of the country, while deficits were recorded in February, June, and September. Notably, the dry conditions in September were typical of El Niño events. Overall, annual precipitation totals across the country ranged from about 20% below to 20% above normal. In Ecuador, precipitation was generally above normal in 2023. The wettest months were March, April, and May. The coastal region recorded maximum precipitation of 910.4 mm in April and 733.5 mm in May, exceeding normal precipitation levels by 42% and 114%, respectively. In the inter-Andean region, maximum precipitation values of 234.0 mm and 245.3 mm were recorded in March and April, respectively, exceeding normal levels by 29% and 55%, respectively. In the Ecuadorian Amazon, maximum precipitation occurred in April and May, with 588.0 mm and 746.5 mm, exceeding normal levels by 55% and 59%, respectively. The least rainy months in the Ecuadorian Amazon were August and September, with 33.7 mm and 63 mm, corresponding to +14% and +34% of the expected normal precipitation value, respectively (Fig. 7.13).

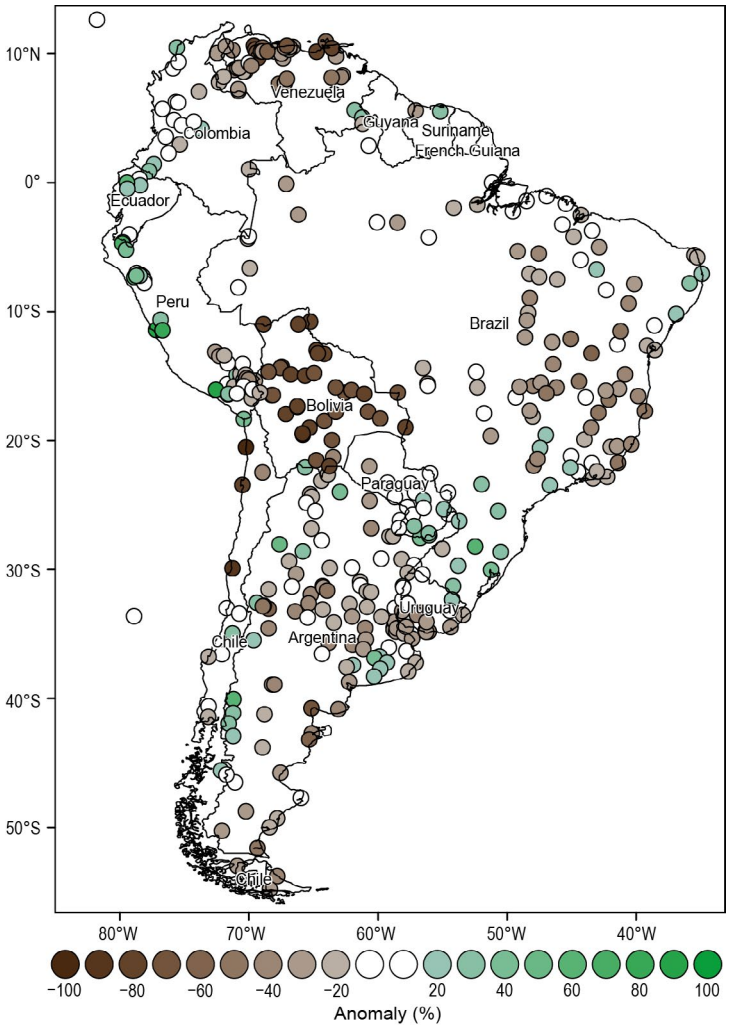

Fig. 7.13. Annual precipitation anomalies (%; 1991–2020 base period) for 2023. (Source: Data from National Meteorological and Hydrological Services of Argentina, Bolivia, Brazil, Chile, Colombia, Ecuador, Paraguay, Peru, Suriname, Uruguay, and Venezuela. Processed by Centro Internacional para la Investigación del Fenómeno de El Niño [CIIFEN].)

(iii) Notable events and impacts

The El Niño phenomenon intensified drought conditions during the second half of 2023 in Colombia. High temperatures and reduced rainfall primarily affected the Caribbean, Andean, and La Guajira regions. Reported impacts included scarcity of drinking water for human consumption and agriculture, crop losses and impacts on livestock, multiple forest fires, deterioration of air quality, water rationing, and decreased energy production.

Ecuador experienced several extreme rainfall events in 2023 with significant impacts, particularly notable in the coastal and Andean regions. On 22–23 March, intense rainfall of 249.5 mm was recorded. This led to flooding in the coastal city of Guayaquil and the overflow of the Guayas River, exacerbated by the high external tide of 5.1 m. The areas most affected by the flooding in the city were Urdesa, Suburbio, Vía Daule, Alborada, Samanes, Guayacanes, and Avenida Tanca Marengo. Structural collapses, disruptions to vehicular traffic, fallen trees, and landslides were reported.

On the night of 26 March, a landslide occurred in Alausí, located in the Andean province of Chimborazo, Ecuador. The landslide was triggered by five days of persistent heavy rains and resulted in seven fatalities, with 16 people injured, 46 missing, and more than 500 affected. The landslide caused significant damage to homes and infrastructure in the area.

On 15 April, 111.2 mm of rain was recorded in 24 hours in Guayaquil, Ecuador, causing flooding in several sectors of the city, including El Fortín, Vía Daule, Mapasingue, La Alborada, and Sauces. The flooding affected roads, homes, and businesses and caused a landslide that killed one person who was trapped inside a vehicle. Several people were also injured, and power outages and disruptions to transportation were reported. The government declared a state of emergency.

2. CENTRAL SOUTH AMERICA

—J. A. Marengo, J. C. Espinoza, J. Ronchail, A. P. Cunha, A. M. Ramos, J. Molina-Carpio, K. Correa, G. Avalos, W. Lavado-Casimiro, R. Salinas, P. P. Rivera, and W. R. Quispe

The central South America region includes Brazil, Peru, Paraguay, and Bolivia. Throughout this section, 1991–2020 is the base period used for both temperature and precipitation unless otherwise specified.

(i) Temperature

The 2023 mean temperature for central South America was 1.62°C above the 1991–2020 average, the highest in the last 50 years and far surpassing the previous record set in 2015 (Fig. 7.14). From January to May, the northern coast of Peru was about 1°C–2°C warmer than normal. As the year progressed, consistent with the intensification of El Niño, the region experienced anomalies of +3°C across western Brazil, northern Paraguay, and Bolivia; these high temperatures were related to six heatwaves that affected the region (See Notable events and impacts).

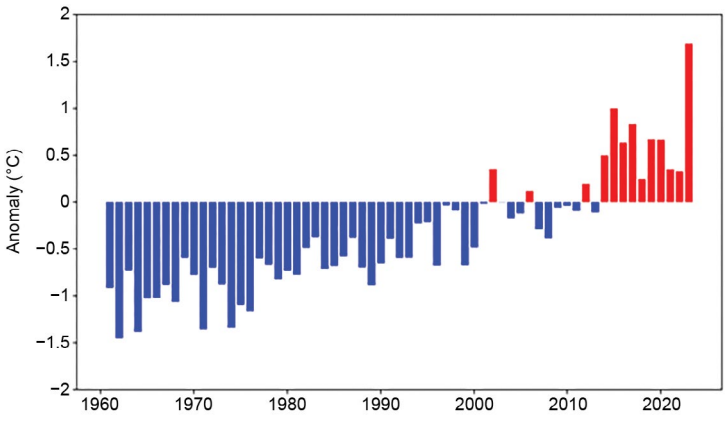

Fig. 7.14. Time series of mean annual regional air temperature anomalies (°C; 1991–2020 base period) for the period 1961–2023 for central South America (Brazil, Bolivia, Paraguay, and Peru). (Source: NOAA National Centers for Environmental Prediction GHCN CAMS data.)

(ii) Precipitation

During January–July, above-average precipitation was observed across northern Peru. During February–May, above-normal rainfall was recorded in western Bolivia and northern Paraguay, while rainfall was below normal in Peru and north-central and southern Brazil. From August to December, rainfall in southern Brazil was 200 mm month^{-1}–300 mm month^{-1} above normal, while dry conditions prevailed over tropical Brazil, Bolivia, and Paraguay. The abundant rainfall in southern Brazil and drought in Amazonia (see Notable events and impacts) were associated with El Niño.

(iii) Notable events and impacts

Several significant extreme events occurred across central South America in 2023 (Fig. 7.15). The Integrated Drought Index (Fig. 7.16) shows drought conditions in the La Plata basin (LPB), in the southern Andes, and the Altiplano during austral summer. During winter and spring, the drought situation was alleviated in the LPB, but drought developed in the Amazon, Pantanal, Bolivian Chiquitania, and parts of northeast Brazil.

With respect to the El Niño–Southern Oscillation, 2023 can be divided in two parts, the first part corresponding with the end of the 2020–23 La Niña and the second to the intensification of El Niño conditions beginning in May.

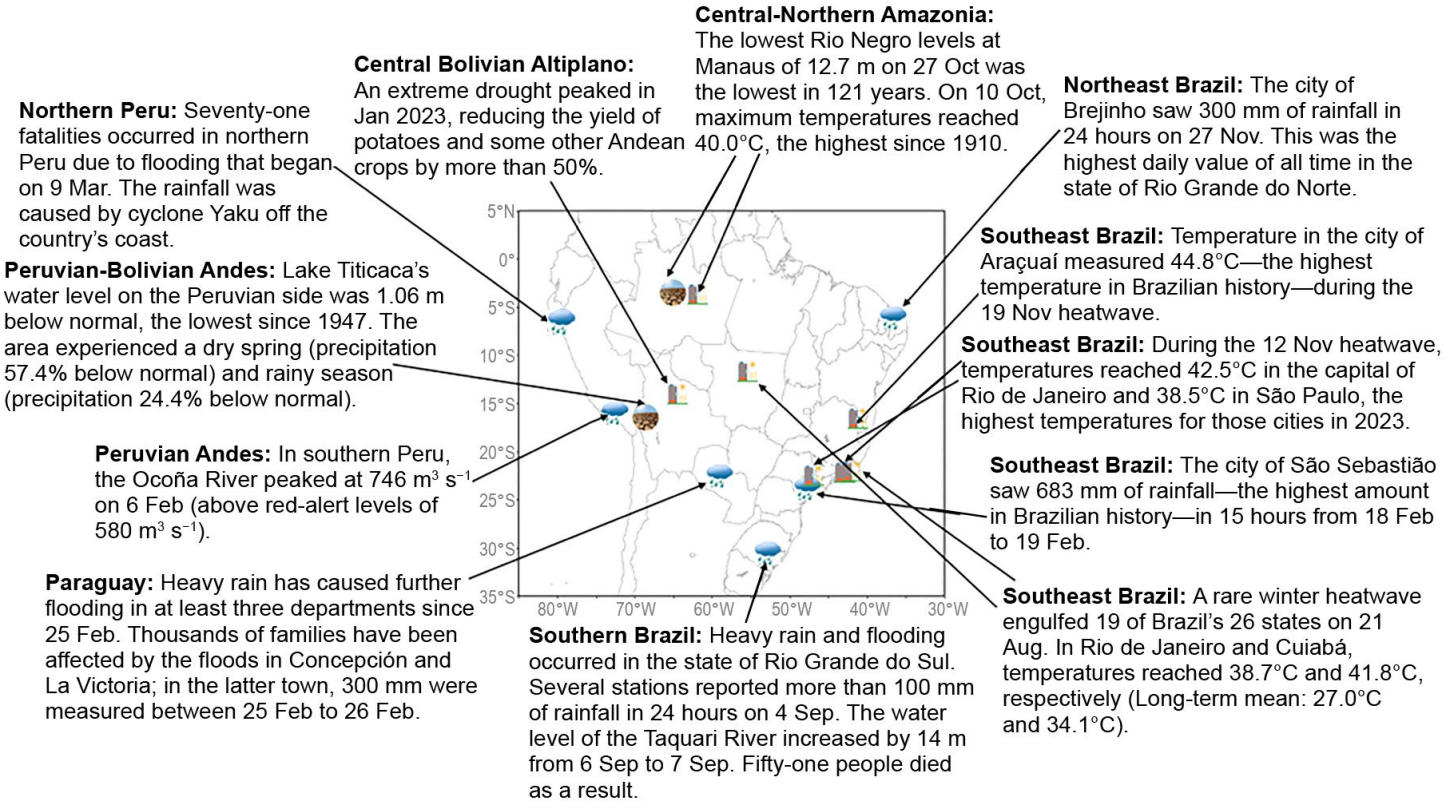

Fig. 7.15. Extreme and notable events across central South America in 2023. (Sources: Peru, Bolivia: Servicio Nacional de Meteorología e Hidrología [SENAMHI]; Paraguay: Dirección de Meteorología e Hidrología [DMH]; Brazil: Instituto Nacional de Meteorologia [INMET], National Center for Monitoring and Early Warning of Natural Disasters [CEMADEN], Instituto Nacional de Pesquisas Espaciais [INPE]; International: UN Office for the Coordination of Humanitarian Affairs [OCHA], Flood list.)

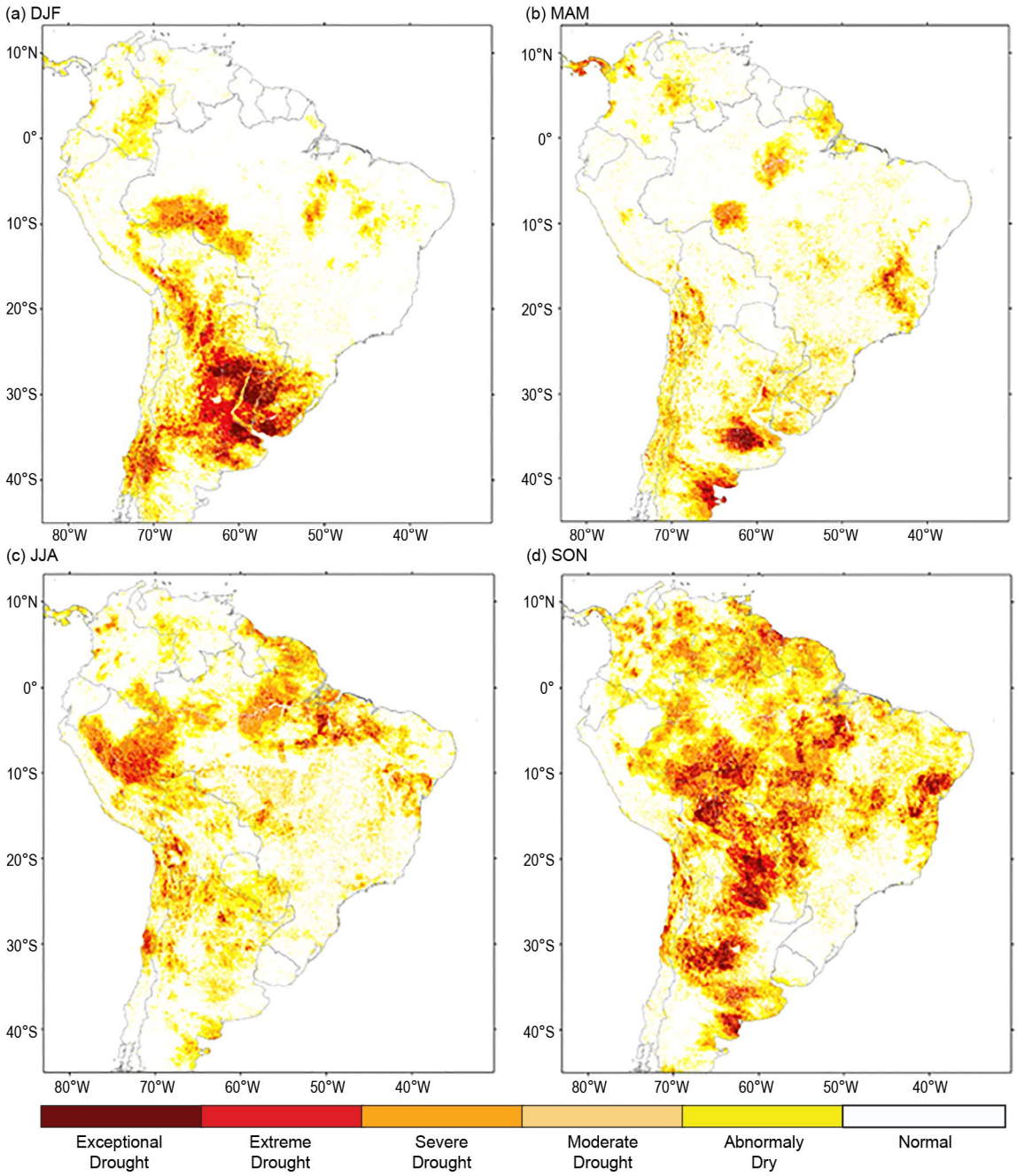

Fig. 7.16. Integrated Drought Index (IDI) maps for central South America during austral (a) summer (DJF) 2022/23, (b) autumn (MAM) 2023, (c) winter (JJA) 2023, and (d) spring (SON) 2023. (Source: Centro Nacional de Monitoramento e Alertas de Desastres Naturais [CEMADEN].)

First half of 2023

During 18–19 February, a cold front over the anomalously warm South Atlantic Ocean that interacted with the Serra de Mar Mountains in southeastern Brazil produced 683 mm rainfall in 15 hours along the coast of the state of São Paulo, and at least 61 people died after floods and landslides impacted the area (Marengo et al. 2024). In southwestern Amazonia on 23 March, heavy rainfall produced flooding in the city of Santa Cruz de la Sierra (Bolivia) and in Rio Branco (Acre-Brazil) where 124.4 mm fell in a 24-hour period; the Acre River rose from 8 m to 15.80 m (critical flood level is 14 m [INMET]). In Southern Peru, a landslide triggered by heavy rains on 5 February destroyed approximately 200 homes and killed 36 people in the Arequipa region. In Paraguay, heavy rain caused flooding in at least three departments at the end of February. Thousands of families were affected by floods in Concepción and La Victoria, with La Victoria receiving 300 mm during 25–26 February (Dirección de Meteorologia e Hidrologia [DMH]; https://www.meteorologia.gov.py/). On the Peruvian coast in early March, Cyclone Yaku caused

flooding, river overflows, and landslides in northern Peru. Seventy-one people died and nearly 113,000 residents were affected, according to the United Nations Office for the Coordination of Humanitarian Affairs (OCHA).

From November 2022 to February 2023, extreme dry conditions were reported over southwestern Amazonia, where rainfall anomalies reached −41 mm month^{-1} (a historical record that was exceeded only during the 1998 El Niño year with −42 mm month^{-1}).

Three cold waves were observed in Brazil in 2023 between May and July. In June, a friagem (cold air outbreak from the south) impacted the Brazilian Amazon. On 13 June, some cities in the Amazon experienced notably below-average temperatures: Cuiabá, 13.1°C (long-term mean [LTM]: 18.0°C), Campo Grande (Mato Grosso do Sul), 8.5°C (LTM: 15.8°C), Vilhena (Rondônia), 9.4°C (LTM: 19.0°C). In Bolivia, Cobija (8.8°C, LTM: 16.8°C) and Santa Ana de Yacuma (7.0°C, LTM: 17°C) recorded their lowest temperatures on record for June.

Second half of 2023

The State of Rio Grande do Sul in southern Brazil was affected by intense precipitation in 2023. On 16 June, torrential rain from an extra-tropical cyclone caused flooding and landslides. As much as 300 mm fell in 24 hours in Maquiné. On 4 September, several stations reported more than 100 mm rainfall totals, leading to a 12-m increase of the Taquari River level on 6–7 September (Alvala et al. 2024). Heavy rain continued to affect the state throughout September and early October, affecting at least 341,000 people across 93 municipalities, with 46 fatalities reported. In certain areas, river levels surged to 17 m above average, obstructing access from the capital city of Porto Alegre and the state's northern regions, according to OCHA. Flash floods on 7–8 October in the Bolivian Andes-Amazon caused severe infrastructure damage, and six people were killed in the Chapare region. On 10 October, 136 municipalities (of 295) in Santa Catarina were affected by rain and floods; 89 of those declared a state of emergency. On 29 October, 300 mm of rain was recorded in Foz do Iguaçu. The Iguaçu Falls recorded a flow of 24,200 m^3 s^{-1} on October 30, its highest flow in recent years (mean flow is 500 m^3 s^{-1} to 10^{00} m^3 s^{-1}).

Drought began in central and northern Amazonia in austral winter (dry season) and spring (pre-rainy season), respectively (see Sidebar 7.2 for details). Coincidentally, a warmer-than-normal winter and spring were observed in southwestern Amazonia due in part to the presence of hot, dry air that developed a heat dome, which occurs when high pressure accumulates over an area and remains for a prolonged period. During August–December, six intense heatwaves impacted central tropical South America on the following dates: 22–29 August, 18–30 September, 3–8 October, 16–25 October, 8–21 November, and 1–19 December (see Appendix Table 7.1 for selected statistics).

At least 27 Bolivian cities recorded their highest (monthly or absolute) temperatures from July to November. Every Andean (Altiplano, valleys, and Yungas) and lowland (Chaco, Chiquitania, Beni savanna, and Amazon rainforest) region was affected. At several locations, maximum temperature records were broken two or more times, even within the same month or heatwave event. El Niño was associated with the extreme temperatures in the Andes but not necessarily with the heatwaves in the lowlands. In August, a rare winter heatwave engulfed 19 of Brazil's 26 states and Bolivia. On 23 September, temperatures reached 31.8°C in Curitiba (LTM: 21.4°C) and 34.8°C in São Paulo (LTM: 24.4°C), and on 24 September reached 41.3°C in the western Amazon in Tingo de Ponaza, Peru (LTM: 33.5°C). The heatwave during 16–25 October led to some all-time records set in the Bolivian Amazon and in the Chaco (Bolivia-Paraguay). At least 10 deaths were attributed to heat in the lowlands of Bolivia as well as 10 in the Paraguayan Chaco. By 12 November, 1120 Brazilian cities recorded their highest temperatures, including 40.4°C in Rio de Janeiro (LTM: 29.4°C). The temperature reached 44.8°C in Araçuaí in Minas Gerais on 20 November (LTM: 32.0°C), potentially the record-highest value observed in Brazil, according to Instituto Nacional de Meteorologia.

Large wildfires raged across the heat-affected regions in Paraguay and Brazil, including in Bahia, Pantanal, and the Amazon where at least 22,050 fires were recorded since October, resulting in heavy smoke that impacted the entire city of Manaus, Brazil (over two million people). More than 3.5 million hectares were burned in Bolivia, including 1 million hectares of forests, causing severe air pollution that affected many Bolivian cities from September to November.

3. SOUTHERN SOUTH AMERICA

—L. S. Aldeco and J. L. Stella

This region includes Argentina, Chile, and Uruguay. Throughout this section, 1991–2020 is the base period used for both temperature and precipitation unless otherwise specified.

(i) Temperature

Above-normal annual temperatures were observed in most parts of the region and during almost every month of the year. Argentina recorded its warmest year on record with an estimated anomaly of +0.83°C. Uruguay had its second-warmest year on record (+0.7°C), and Chile had its third warmest (+0.5°C). Many stations (45 in Argentina and 4 in Uruguay) recorded their highest annual temperatures on record. Temperature anomalies ranged between +1°C and +2°C north of 35°S, where most of these records were set.

Austral summer 2022/23 was extremely hot across most of the region. An unprecedented number of heatwaves occurred between November 2022 and March 2023. It was the warmest summer on record at several locations with seasonal anomalies between +2°C and +3°C, including Paso de Los Libres, Reconquista, Rosario, Junín, Buenos Aires, Santa Rosa, and Neuquén in Argentina; Artigas, Durazno, and Mercedes in Uruguay; and General Bernardo O'Higgins and General Freire in Chile. Following a February heatwave, an unusual polar air irruption produced a significant drop in temperature, and several minimum temperature records were broken across Argentina and Uruguay. Early frosts were recorded with values close to 0°C, severely impacting agricultural areas already affected by drought and extreme heat. On 17–18 February, typical winter conditions occurred in the middle of what would become the warmest summer on record for Argentina.

Austral autumn over southern South America had temperature anomalies similar to summer, with the highest anomalies recorded over central Argentina and Chile. March was extremely warm in Argentina and Uruguay, due in part to a late, prolonged, and intense heatwave. During this heatwave, dozens of daily maximum temperature records were broken. Durazno (+1.8°C), Colonia (+1.8°C), and Prado (+1.7°C) in Uruguay each reported their warmest autumn on record, along with several locations in Argentina.

In accordance with the developing El Niño, austral winter was particularly mild in the central and northern regions of southern South America (SSA), while in southern Argentina and Chile, normal to below-normal temperatures were predominant. During 21–28 July, a cold wave affected extreme southern Argentina and Chile.

During austral spring, below-normal temperatures were observed in central and southern Argentina and Chile and in Uruguay, with anomalies between −0.5°C and −2°C. Above-normal temperatures continued over northern Argentina and Chile. An unusual heatwave affected Misiones province in Argentina during 21–26 September. Extreme high temperatures also severely affected the provinces of Salta, Formosa, and Chaco during spring.

(ii) Precipitation

Most of southern SSA had below-average annual rainfall during 2023, especially during summer and autumn, which were the two seasons that were under the influence of the ending of La Niña (Fig. 7.17). During winter, some cold fronts brought rainfall to different parts of the region, and during spring, precipitation events in Uruguay, northeastern Argentina, and central Chile were consistent with the development of El Niño. Despite high rain totals, the precipitation was not enough to counteract the deficits of the first part of the year in central, northern, and southern Argentina, central Chile, and southern Uruguay, where, overall, annual precipitation was below normal. Northeastern Argentina and Uruguay had above-average annual rainfall, along with some local stations in Patagonia.

During austral summer 2022/23, drier-than-normal conditions were observed in most of southern South America due to the influence of La Niña. The highest deficits were up to 79% below normal in most of Uruguay, northeastern Argentina, and central Patagonia of Chile and Argentina. Some stations recorded their lowest precipitation on record for the season: Florida (Uruguay) was 79% below normal, the lowest since 1980, and Paso de Los Libres (Argentina) was 75% below normal, the lowest since 1961. Agraciada in Uruguay recorded its lowest monthly

precipitation for February since 1980. However, some localized precipitation events led to above-normal rainfall at some stations in central-western Argentina, with totals 64% to 100% above normal.

During autumn, drier-than-average conditions were present across most of the region, with totals 40% to 80% below normal; however, some regions of Argentina and Chile recorded above-average rainfall during this period due to synoptic activity. Santiago del Estero in Argentina recorded its highest rainfall for the season since 1961 (91% above normal) and Teniente Vidal in southern Chile recorded its highest monthly rainfall for March since 1967.

During winter, below-average precipitation was recorded in Uruguay, central Chile, and eastern and southern Argentina, with June having been the driest month of the season (60% to 99% below normal). Nevertheless, in central Argentina, some stations set daily rainfall records for August: 117 mm in San Fernando and 112 mm in Aeroparque on 17 August, the highest daily rainfall totals since 1961. The heavy rain was due to the interaction of an unusual mass of warm and humid air in the region and the advance of cold air, which produced convective development with strong storms that affected extreme northeastern Buenos Aires and southern Uruguay. Central and west Patagonia of Chile and Argentina also recorded above-normal precipitation, setting some monthly and daily records. General Freire in Chile recorded 150.2 mm on 21 August, its highest daily rainfall for August since 1963, which also led to floods. Bariloche in Argentina recorded its highest precipitation total for winter since 1961.

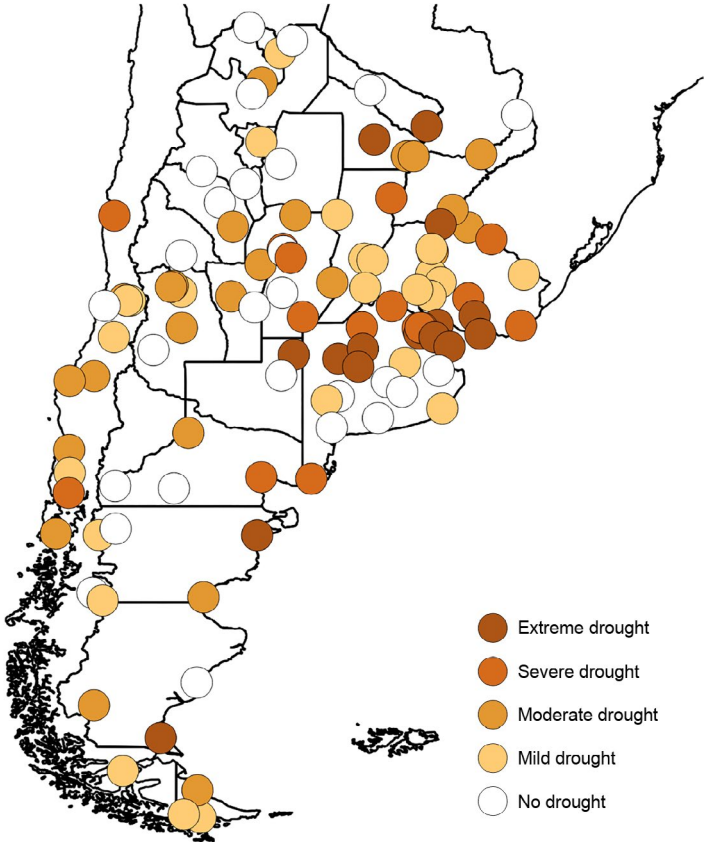

Fig. 7.17. Standardized precipitation index (SPI) for the six-month period 1 Jan–30 Jun 2023. SPI values can be referenced at: https://droughtmonitor.unl.edu/About/AbouttheData/DroughtClassification.aspx.

During austral spring, some regions in central Argentina had below-normal rainfall, but El Niño favored above-normal precipitation in central and northern Uruguay, central Chile, northwestern Patagonia, and northeastern Argentina. On 1 September, heavy rainfall due to a stationary front was observed over northeastern Argentina and Uruguay, and some stations reported new record-high daily totals, including Ituzaingó, Argentina (267 mm), and Bañado Medina, Uruguay (138 mm). Monthly records were set also in Uruguay: Cuchilla Caraguatá Sur, Bañado Medina, and Melo (since 1980), and Posadas and Oberá in Argentina (since 1961). Above-normal rainfall was also observed in Uruguay and eastern Argentina in November.

(iii) Notable events and impacts

Figure 7.18 shows numerous notable events that occurred across the region during 2023. Some of these are discussed in more detail below.

A persistent drought affected several areas in Uruguay, central and northeastern Argentina, and central Chile due to the effects of La Niña. Some of these regions experienced severe or extreme drought, according to the standard precipitation index (Fig. 7.17). In Montevideo, Uruguay's most populous city, there was a lack of water supply between May and June. This situation improved at the beginning of spring as El Niño developed, and precipitation events were favored.

Dry conditions and a blocking pattern with a persistent high-pressure system in the region led to several heatwaves in Uruguay and central-east Argentina. The longest and most intense heatwave occurred during early March in both countries and set new daily records of highest

minimum and maximum temperatures at several stations: Santa Rosa (Argentina) recorded 40.7°C on 3 March, and Nueve de Julio (Argentina) recorded 40°C on 2 March, both the highest on record since 1961; Mercedes (Uruguay) recorded 40.5°C and Durazno (Uruguay) recorded 40.2°C on 11 March, both the highest on record since 1981. In Argentina, the electric energy consumption set a record on 13 March with 29,105 megawatts.

During spring, El Niño favored several precipitation events, mostly convective with different impacts. In northeastern Argentina, heavy precipitation led to river overflows, floods, and the closure of Iguazú Falls National Park; in Paso de Los Libres, a new daily record of 130 mm was set on 22 October, the highest since the start of records in 1961.

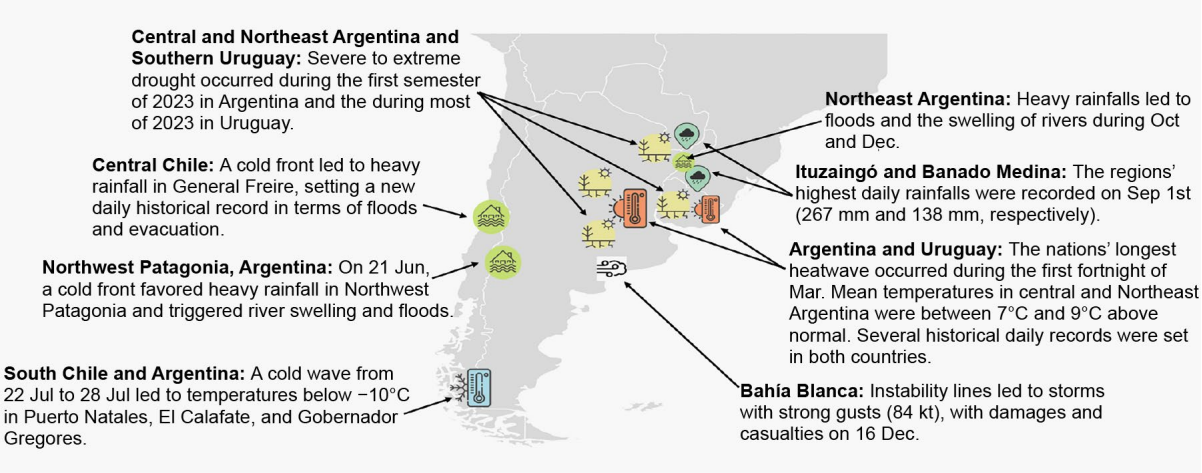

Fig. 7.18. Extreme and notable events in southern South America during 2023.

Sidebar 7.2: Drought in South America in 2023: Amazonia and Altiplano

—J. MARENGO AND J. C. ESPINOZA

Amazonia

A severe drought affected the western Amazon River basin countries and most of northern South America due to a dry period from July 2023 through the end of the year. The spatial-temporal evolution of the drought shows an increase in extent and severity in the Brazilian, Peruvian, and Bolivian Amazon. A series of six heatwaves during winter and spring exacerbated the impact of the precipitation deficits. The average temperature was abnormally high, up to 5°C above normal during austral spring, which is the pre-rainy season in Amazonia (section 7d2). The El Niño event that developed in mid-2023 intensified the drought in Amazonia during austral winter and spring during the low rainfall and pre-rainy seasons, respectively (Espinoza et al. 2024). In September and October, the basin recorded below-average rainfall in the Peruvian and Bolivian Amazonia and northwest and southwest Brazilian Amazonia in the Solimões, Purus, Juruá, and Madeira River basin headwaters. Eight Brazilian states recorded their lowest rainfall totals from July to September in over 40 years, with deficits of 100 mm month^{-1}–300 mm month^{-1} (Toreti et al. 2023).

Due to the warm and dry conditions in spring 2023, most of the main rivers in the Amazon, including the Solimões, Purus, Acre, and Branco, either suffered extreme drops in their levels in some regions, or dried up completely. According to the National Water Agency of Brazil (ANA) and the Brazilian Geological Survey, the level of the Madeira River in Porto Velho reached its lowest level in the 56-year record (15 m on 15 October). According to the Port of Manaus, the Rio Negro recorded a tide of 12.70 m at Manaus on 26 October, its lowest since 1902 (Fig. SB7.3). In the Peruvian Amazon, the flows and levels of the Amazonas, Marañón, Huallaga, and Ucayalí Rivers were

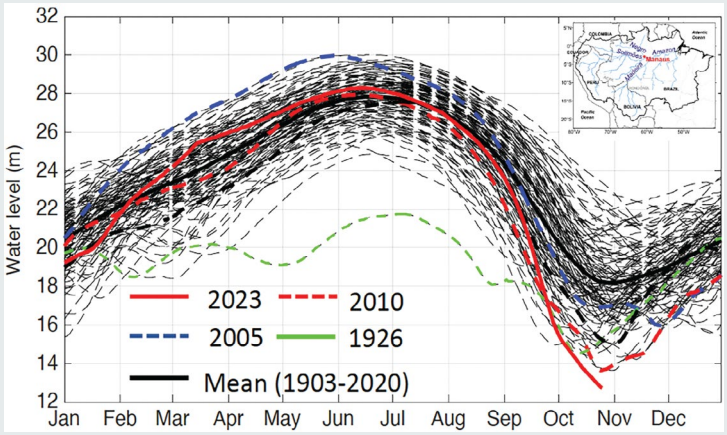

Fig. SB7.3. Rio Negro water levels measured at the Port of Manaus. Solid red line shows the levels in 2023 (Espinoza et al. 2024).

average to much lower than usual. Discharge for the Huallaga River at Tingo María was 45% below normal in October (Servicio Nacional de Meteorología e Hidrología [SENAMHI] 2023b). In Bolivia, the Mamoré-Guaporé and Madeira Rivers were low due to deficient rainfall from July 2022 to June 2023. In Tefé Lake, over 180 botos cor de rosa—an Amazon River dolphin—were found dead after the water reached 40°C, a record-high temperature unprecedented in the region (Costa and Marengo 2023).

Forest vegetation showed signs of wilting during the heatwaves, and high tree mortality increased the risk of wildfire hazard. The drought affected navigation, commerce, and basic food and water supply. The most affected were indigenous communities and the Ribeirinhos (people who live along the shores of the rivers), who are highly vulnerable to changes in the hydrology of the rivers.

Peruvian and Bolivian Altiplano

An extreme drought that started in August–September 2022 peaked in January 2023 in the Peruvian-Bolivian Altiplano, involving most of the Titicaca, Desaguadero, Poopó, and Salar de Coipasa hydrological system (Fig. SB7.4a). The level of Lake Titicaca reported an unusually low rise (0.09 m) between December 2022 and April 2023, representing the fourth-lowest seasonal lake rise since 1940 (Fig. SB7.4b).

Intense El Niño events in this region are related to drought situations during austral summer. However, November–February 2022/23 was characterized by La Niña. Basin wide-averaged precipitation anomalies during austral spring 2022 was 57% below the 1981–2020 September–November normal. From November to the end of austral summer, a historical deficit of atmospheric moisture flux from the southern and western Amazon toward the Altiplano was detected, which favored dry conditions over this region. While this climatic feature was related to La Niña conditions during 2022/23, studies also suggest the potential role of Amazon deforestation in the substantial lack of atmospheric moisture flux reported in this event (Arias et al. 2024; Gutierrez et al. 2024).

Agriculture is the main economic activity in the Peruvian-Bolivian Altiplano and depends directly on precipitation and its variability. The 2022/23 drought in this region reduced the yield of potatoes and some other Andean crops by more than 50%, causing large economic losses to thousands of farmers. According to government figures, the lack of water in Bolivia affected more than 487,000 families. Residents in the La Paz, Cochabamba, Santa Cruz, Oruro, Chuquisaca, Potosí, and Tarija departments in Bolivia all faced drought conditions. In Peru, drought prevailed over the Andean region's northern and southern sections. The city of Puno and surrounding areas experienced its worst drought of the last 60 years, which affected crops, harvest, and the regional economy. It is estimated that the water deficit generated economic losses in Puno, including 80% loss in potatoes and sweet potatoes and 90% loss in Andean grains (Servicio Nacional de Meteorología e Hidrología [SENAMHI] 2023).

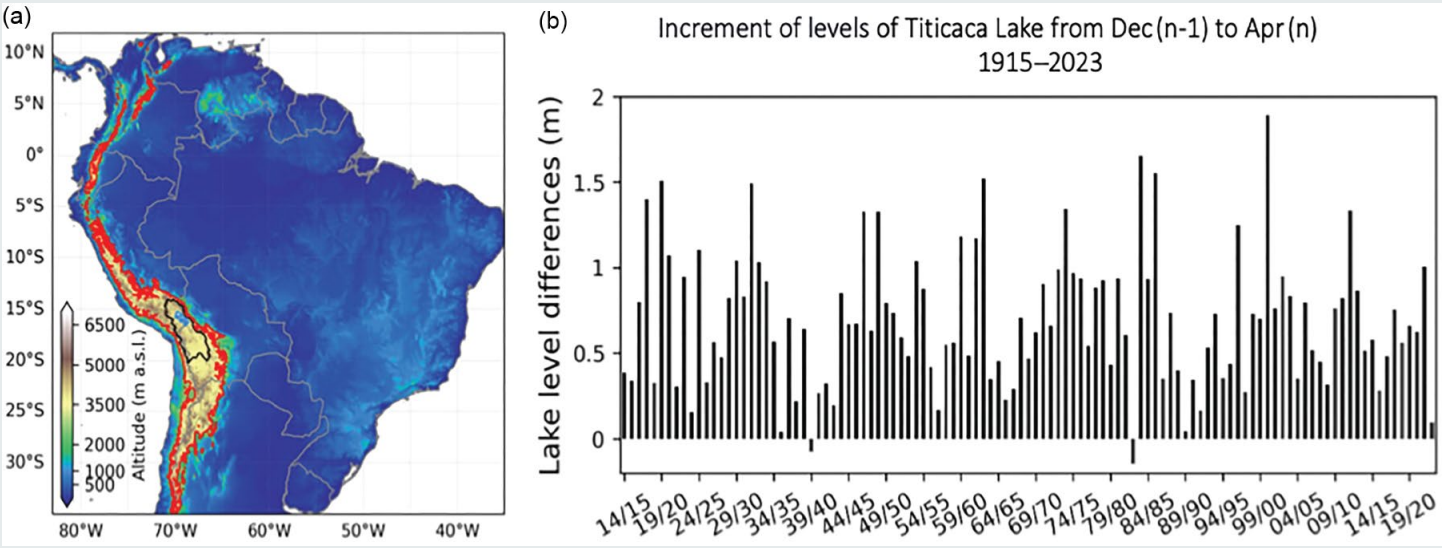

Fig. SB7.4. (a) Location of the Titicaca, Desaguadero, Poopó, and Salar de Coipasa hydrological system (black line) over tropical South America. Red lines in the Andean cordillera denote altitudes of 3000 m a.s.l. (b) Interannual increment of levels of Titicaca Lake from Dec to Apr for the period 1915–2023.

e. Africa

—A. Mekonnen, Ed.

The 2023 analysis for Africa is based on observational records from meteorological and hydrological services including rainfall from the Global Precipitation Climatology Project and reanalysis products from the National Centers for Environmental Prediction/ National Center for Atmospheric Research. Notable events in this year were compiled based on reports from government agencies, regional and international organizations, and research/Early Warning organizations. The climatological base period is 1991–2020, and the terms "normal" and "average" are interchangeably used to refer to this climatology.

Figure 7.19a presents the 2023 mean temperature anomalies for Africa. Above-average annual temperatures were observed over Africa except some areas in central and southern Libya, the southwestern corner of Egypt, and adjoining northwestern Sudan. Anomalies higher than +1.2°C are seen over most of northwest Africa, southwest Africa from Angola to Namibia and Botswana, and across South Sudan, central Africa, the southern half of Cameroon, and southern Nigeria (Fig. 7.19a).

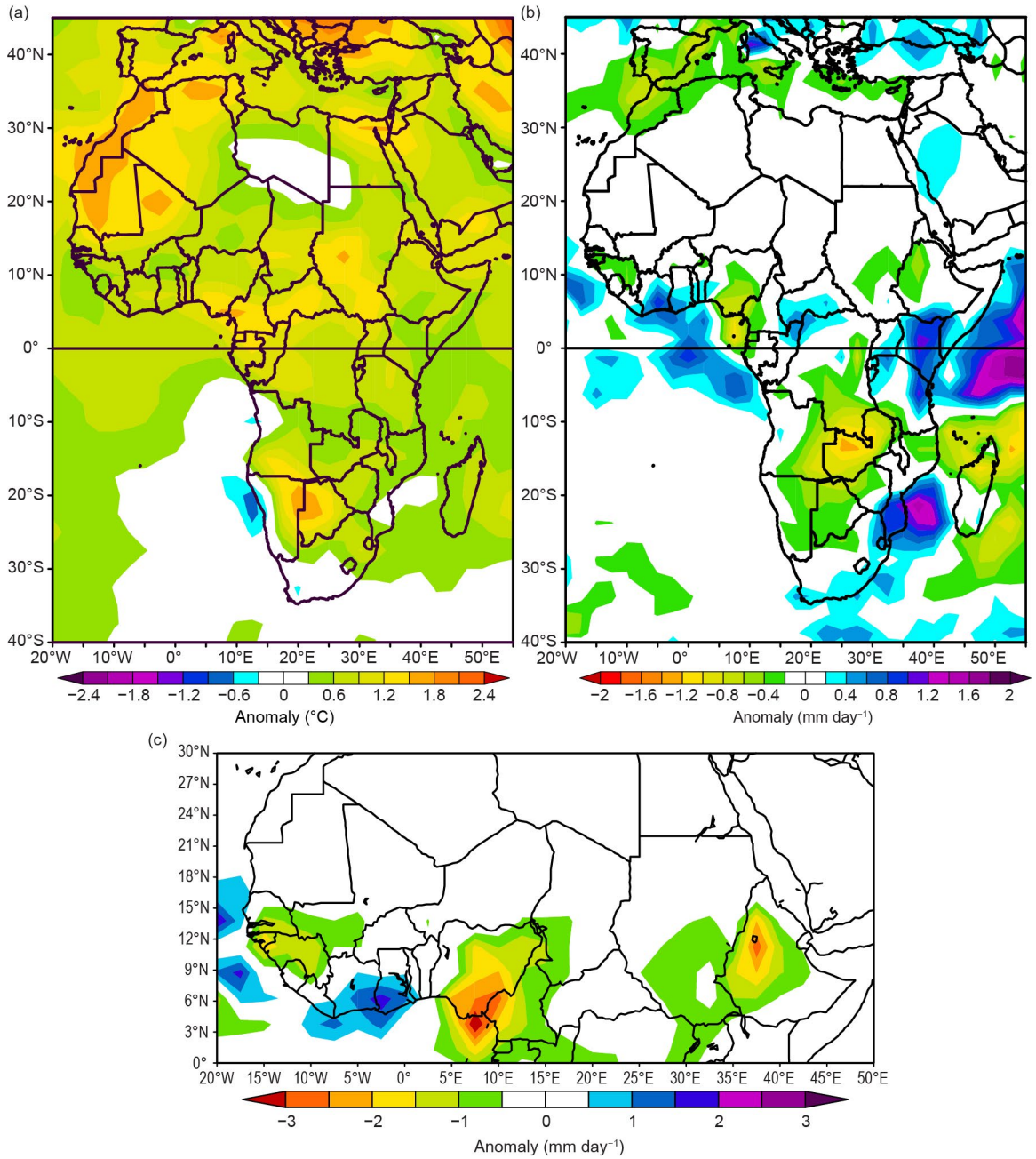

Fig. 7.19. Annual (a) temperature (°C) and (b) rainfall anomalies (mm day^{-1}) over Africa. (c) Jul–Sep rainfall anomalies (mm day^{-1}) over North Africa. Anomalies are with respect to 1991–2010 base period. Temperature is from the National Centers for Environmental Prediction's National Center for Atmospheric Research and rainfall anomalies are based on GPCP.

Above-average rainfall was observed over Kenya, Uganda, southern areas of the Central African Republic, and parts of Ghana and Cote d'Ivoire (Fig. 7.19b). Anomalies of less than −0.4 mm day^{-1} were observed in Zambia, the southeastern part of the Democratic Republic of Congo, and the southeastern corner of Angola as well as in the high rainfall zone of western Ethiopia and adjoining Sudan, southern Nigeria, and southwestern Cameroon (Fig. 7.19b). Significant below-average rainfall over these areas was also observed in 2022. The annual rainfall anomalies over most of the Sahel appears to be within the normal range (−0.2 day^{-1} to +0.2 mm day^{-1}).

The Sahel receives most of its annual rainfall during the July–September (JAS) season. In 2023, significant deficits (1.5 mm day^{-1} to >3 mm day^{-1} below normal) were observed over western Ethiopian highlands, Nigeria, Cameroon, most of Senegal, The Gambia, Guinea-Bissau, and Guinea highlands (Fig. 7.19c). Above-average JAS rainfall is seen over the southern areas of Ghana and Cote d'Ivoire.

High impact weather and climate variabilities were also reported from regions. The details of these are presented below.

1. NORTH AFRICA

—K. Kabidi, A. Sayouri, M. ElKharrim, S. Hakmi, and A. E. Mostafa

The North Africa sub-region includes Mauritania, Morocco, Algeria, Tunisia, Libya, and Egypt. Much of this region is characterized by arid and semi-arid climate, while northern parts exhibit Mediterranean climates. Precipitation over the region in 2023 was highly variable. While above-average precipitation was reported from northern Egyptian meteorological stations, droughts, along with heatwaves, were observed in northwest Africa. In September 2023, a storm and dam collapse in northern Libya caused extensive damage. In contrast, prolonged droughts (extending from past years) and above-normal temperatures were observed in Morocco.

(i) Temperature

During winter (December 2022–February 2023), both above-normal and below-normal temperatures were observed over North Africa north of 10°N (Fig. 7.20a). Anomalies of more than +1°C dominated the North African region, except for Libya. Anomalies of more than 2°C were observed in eastern Mauritania and northern and western Mali. Meteorological stations in Morocco also reported above-average minimum temperatures in January and February. Tunisian stations, on average, had temperatures up to 1.4°C above average in January and February, with anomalies from +0.3°C at Tabarka to +2.4°C at Thala. Minimum temperatures at some Tunisian stations (Mahdia, Thala, Tatouine) were up to 1.4°C above average during this period. January mean temperatures in Algeria were near normal. In northern Egypt, stations indicate above-average temperatures during December 2022 and January 2023 but below-average temperatures in February. Reports from the Egyptian Meteorology and Hydrological Services indicate that winter temperatures were impacted by the positive phase of the North Atlantic Oscillation (NAO). In contrast, the lowest minimum temperature of 0°C on 2 February was recorded at Nekhel in North Sinai, Egypt.

During spring (March–May 2023; Fig. 7.20b), anomalies of more than +2°C were observed across Morocco, western Algeria, Tunisia, and northern Mauritania, while temperatures over Libya and southwestern Egypt were below average. Northern Egypt, however, continued to see above-average temperatures. Tunisia reported monthly anomalies of +1.7°C in March and +0.8°C in May. Minimum and maximum temperatures in April were above average over Morocco, Tunisia, and Algeria. In Tunisia, maximum temperatures of 34.6°C at Bizerte and 37.8°C at Beja and Jendouba were reported.

Summer temperatures (June–August) were more than 2°C above normal over Morocco, northern Algeria, Mauritania, Tunisia, and northern and western Egypt (Fig. 7.20c). The rest of North Africa had mean temperature anomalies between +0.75°C and +2°C. On 7 June in Egypt, the station Sharm-el-sheikh reported an anomaly of +2.5°C, and Dakhla reported a maximum temperature of 48°C. Several Moroccan stations reported new local maximum temperature records during July (Smara, 49.9°C; Bouaarfa, 43.6°C; Errachidia, 44.7°C; Taourirt, 47°C) and August (Agadir, 50.4°C; Essaouira, 48.7°C; Tan-Tan, 48.2°C). Anomalies as high as +5°C were reported from Algerian stations in July, with about 95% of the stations reporting 40°C or higher.

July temperatures over Tunisia were 4°C above normal, making this the country's hottest July since records began in 1950. New records include 49.1°C at Gabes, 49.1°C at Medenine, 49°C at Tunis, 48.9°C at Kebili, and 48.3°C at Monastir. Temperatures in the country returned to near normal in August.

In Autumn (September–November), temperatures were >2°C above normal across most of North Africa, with anomalies of +0.5°C to +1.5°C observed over Libya (Fig. 7.20d). In September and November, temperature anomalies of +2.5°C to +4°C were reported from Moroccan and Algerian stations. In Tunisia, mean temperatures were 1.2°C above normal in September and 2.4°C in October.

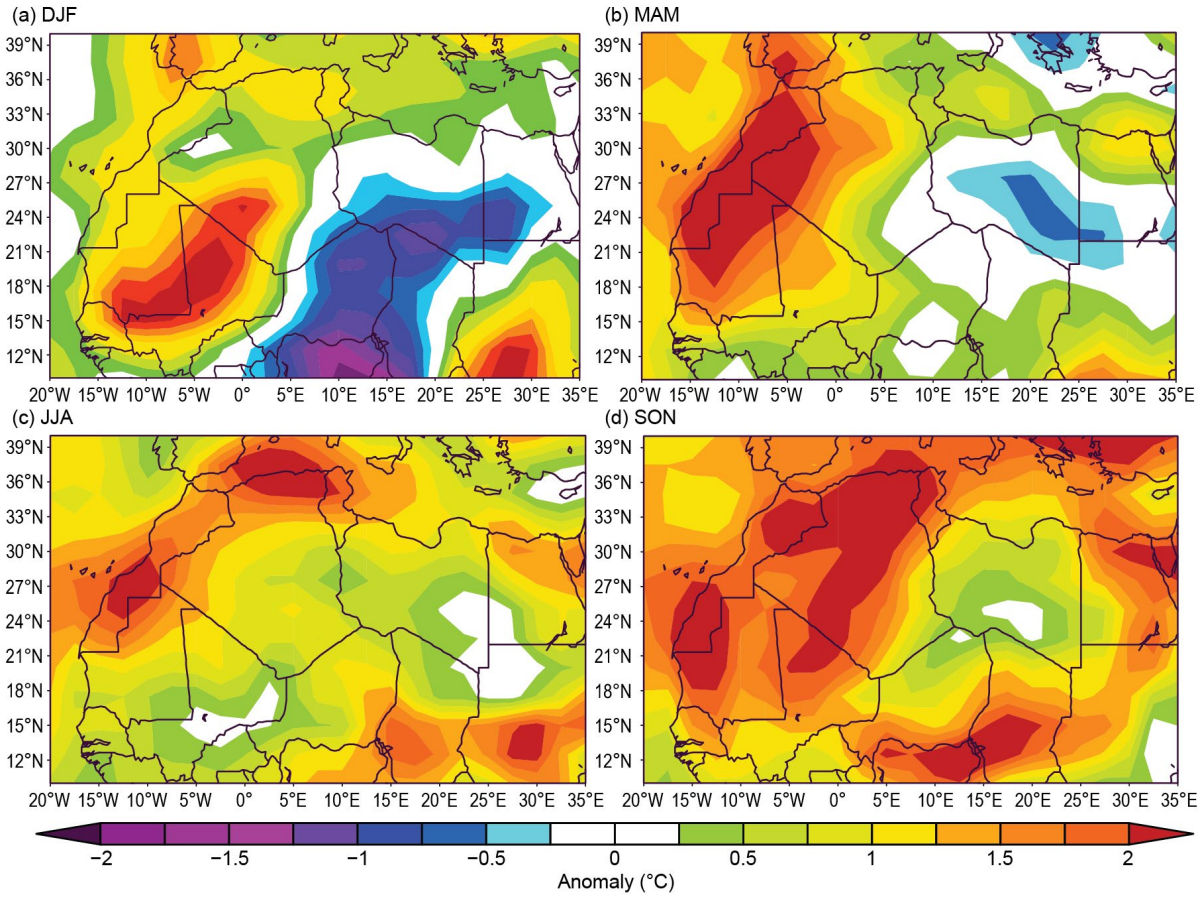

Fig. 7.20. Seasonal temperature anomalies over North Africa for (a) Dec–Feb 2022/23, (b) Mar–May 2023, (c) Jun–Aug 2023, and (d) Sep–Nov 2023. Anomalies are with respect to the 1991–2010 base period. (Source: NCEP/NCAR.)

(ii) Precipitation

Figure 7.21 shows seasonal precipitation variability in 2023. Since summer is not normally a precipitation season over the region, summer precipitation is not presented here.

Winter precipitation was between 0.2 mm day^{-1} and 1 mm day^{-1} below average over much of North Africa and as much as 0.4 mm day^{-1} below average over northeast Libya and northern Egypt (Fig. 7.21a). Moroccan stations largely report drier-than-normal conditions, with stations in the north reporting 13%–60% of their normal precipitation. Near- to above-normal precipitation was reported from Egyptian stations. Heavy rainfalls of about 35 mm were reported from Alexandria on 12 December 2023. Average annual rainfall at this station is 60 mm.

Below-normal precipitation was also observed over northwestern Algeria and northern Morocco during spring (March–May; Fig. 7.21b). In Morocco, stations reported monthly average precipitation in March, April, and May that was 93%, 62%, and 85% of normal, respectively.

Drier-than-normal conditions continued to prevail in autumn (September–November) as well (Fig. 7.21c). Precipitation was about 0.7 mm day^{-1} below normal across Morocco, Tunisia, and the northern half of Algeria. In September, stations in northern Morocco reported about 70% of normal precipitation, while southern stations saw near-normal rainfall and eastern stations above normal. Above-average precipitation was also observed over the Moroccan region

bordering the Atlantic. November and December 2023 were dry, ranging from 96% to 72% of normal. The dryness was associated with the dominance of Azores high pressure and the positive phase of the NAO that lasted several weeks. The prolonged seasonal rainfall deficit, nearly 50% of normal, was also observed over Tunisia. September and October rainfall over Tunisia was about 96% of normal.

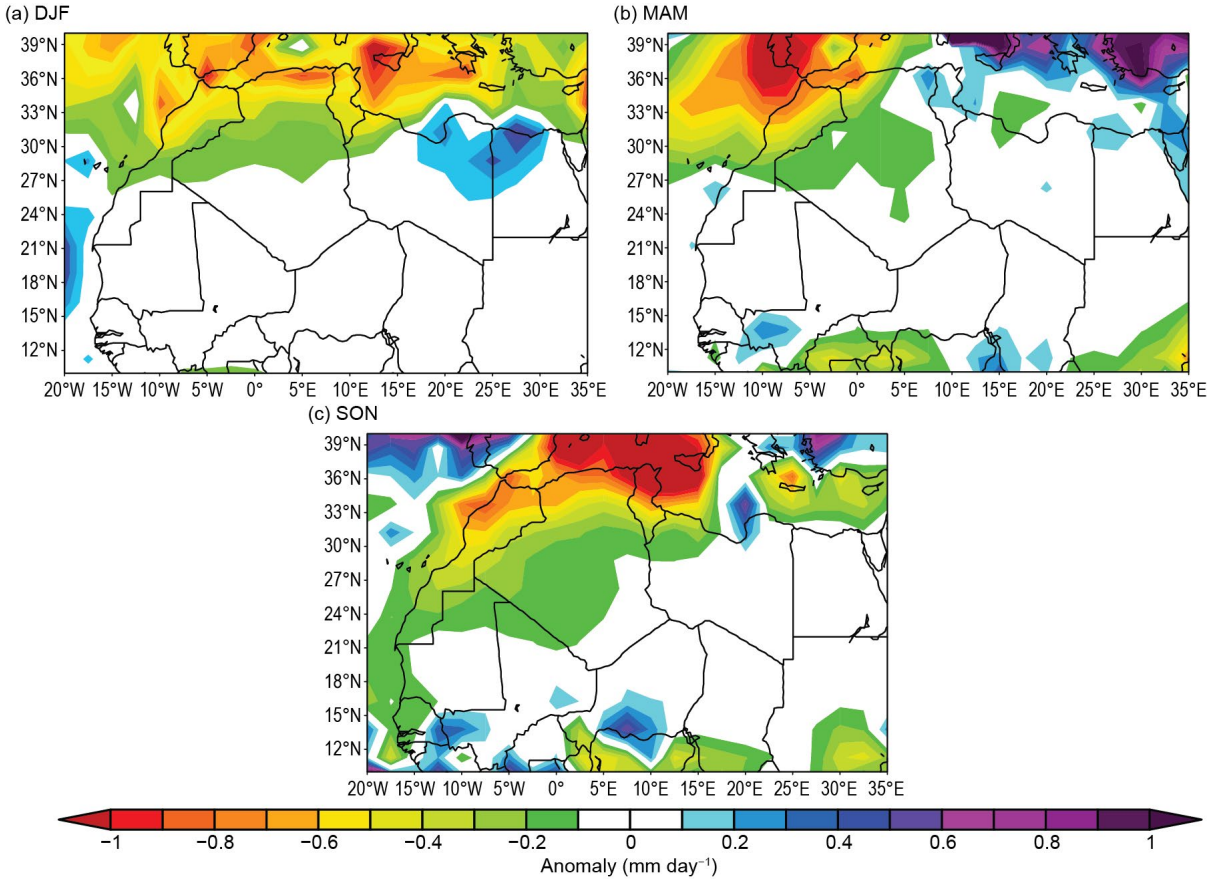

Fig. 7.21. Seasonal precipitation anomalies (mm day^{-1}) over North Africa for (a) Dec–Feb 2022/23, (b) Mar–May 2023, and (c) Sep–Nov 2023. Anomalies are with respect to the 1991–2010 base period. (Source: GPCP.)

(iii) Notable events and impacts

Record-high rainfall was observed over Libya in September, which was associated with Storm Daniel (classified as a "medicane", i.e., a tropical cyclone that forms in the Mediterranean Sea). According to the Libyan National Meteorological Center, rainfall totals ranging from 150 mm to 240 mm were recorded in the first dekad (10 days) of September. The city of Al-Bayda received a total of 414.1 mm during 10–11 September. The storm reached its peak in northeastern Libya on the 10th and brought extreme rainfall that led to devastating floods. The floods killed at least 4352 people and displaced more than 43,000, while another 8000 were missing, according to reports from the United Nations in Libya. Entire neighborhoods disappeared after waters from burst dams flooded the city of Derna.

In May, June, and September, flooding due to torrential rains caused several deaths in many parts of Algeria. During July, flash floods caused by heavy rains affected Moulay Brahim in the region of Alhouz, Morocco, causing material damages.

According to the respective government ministries, forest fires broke out in Morocco, Algeria, and Tunisia during the summer. At least 34 deaths were reported due to the fires in Algeria in July. A total of 41,000 hectares of forest was burnt in Algeria during 2023. In Morocco, 395 forest fires were reported during the year, which burnt 6420 hectares. In Tunisia, 438 forest fires burned 4800 hectares of forests.

2. WEST AFRICA

—W. Agyakwah, J. Hicks, and W. M. Thiaw

West Africa stretches from the Guinean coast to about 20°N and from the eastern Atlantic coast to Niger. It is divided into two sub-regions. The Sahel stretches from Senegal and The Gambia in the west to Niger in the east and is located between 12°N and 17°N. The Gulf of Guinea region is located to the south and runs from approximately 4°N to 10°N. This region covers the Guineas in the eastern Atlantic coast in the west to Nigeria and Cameroon in the east.

(i) Temperature

Mean annual temperatures in the Sahel region were 26°C–30°C, with the highest temperatures recorded in southern Mauritania, central and eastern Senegal, central Mali, northern Burkina Faso, southwestern and southeastern Niger, and northeastern Nigeria (Fig. 7.22). Annual mean temperature anomalies were +0.5°C to +1°C over most of the region; southern Mauritania, eastern Senegal, central Mali, and northeastern Nigeria had anomalies of +1°C to +1.5°C. Mean annual temperatures in the Gulf of Guinea region were 24°C–28°C. Anomalies of +0.5°C to +1°C were observed in many places, except southern Burkina Faso and northern Ghana, which recorded near-normal temperatures. Most of West Africa experienced mean temperatures above the 90th percentile, except for parts of Niger and Burkina Faso (Fig. 7.22).

From January to April, the monthly average temperatures were higher than usual in the far western Sahel region. Positive anomalies started spreading throughout the Sahel region from May onwards. The highest anomalies, +2°C to +3°C, were observed from September to November (SON) over southeastern Niger and northeastern Nigeria. The Gulf of Guinea experienced above-average monthly temperatures from the beginning of the year, much like the Sahel. These above-average anomalies were concentrated along the Gulf of Guinea coastal areas and spread inland over time, reaching their maximum during SON. Central Nigeria experienced the warmest temperatures with anomalies between +1.5°C and +2°C (>90th percentile).

The Sahel experienced mostly near-normal seasonal mean maximum temperatures. However, above-average temperatures dominated the Sahel region during the June–August, June–September (JAS), August–October, and SON seasons. The JAS season saw the highest positive anomalies of +2.5°C to +3°C in northeastern Nigeria (>90th percentile). The mean maximum temperatures in the Gulf of Guinea were higher during January–March (JFM), with the highest anomalies of +4.5°C to +5°C over southwestern Nigeria, which was near a record-breaking level and in the 90th to 97th percentile range.

The coldest minimum temperatures in the Sahel since 1991 occurred from January to April, with anomalies of –1.5°C to –2°C over southeastern Niger and northeastern Nigeria in February. Likewise, in the Gulf of Guinea, the lowest minimum temperatures since 1991 were observed in February, with negative anomalies of up to –3°C over southeastern Nigeria. February's coldest temperatures contributed to JFM 2023 becoming the coldest such period on record throughout both the Sahel and Gulf of Guinea regions.

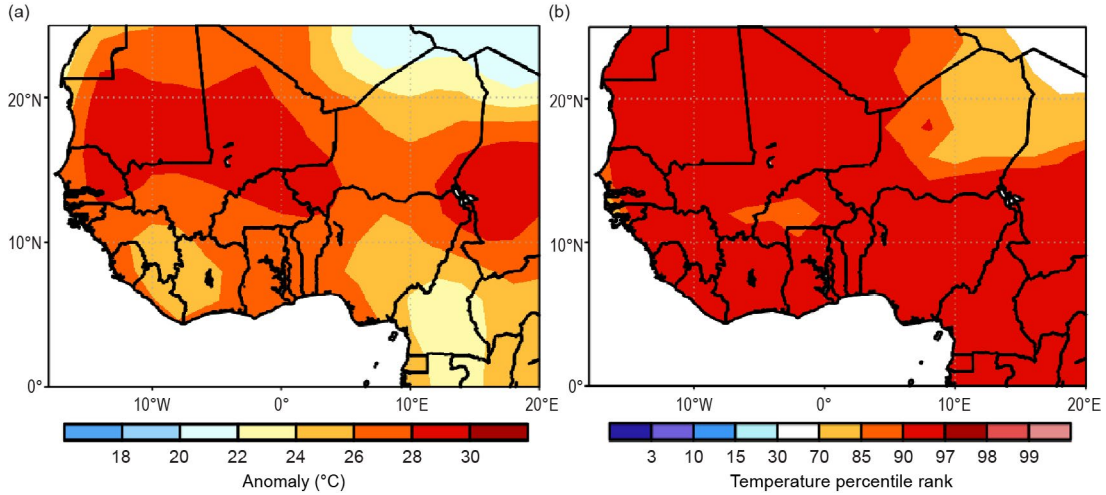

Fig. 7.22. Annual (a) mean temperature (°C; 1991–2020 base period) and (b) percentile ranking in 2023 for West Africa. (Source: NOAA National Centers for Environmental Prediction.)

(ii) Precipitation

In 2023, most of the Sahel experienced below-normal rainfall, with some areas recording deficits ranging from –50 mm to –250 mm. The Gulf of Guinea received above-average rainfall along its coastal regions, with the highest surpluses of +250 mm to +300 mm in southeastern Cote d'Ivoire and southwestern Ghana. The most significant rainfall deficits were observed in eastern Nigeria (<10th percentile).

The onset of the West African monsoon rains occurred in May and June in the southern and northern sectors of the Sahel, respectively. In May, southwestern Mali observed more rainfall than usual (10 mm–20 mm), and this trend continued in June, spreading to much of the Sahel. As the year progressed, rainfall surpluses gradually increased to between +10 mm and +100 mm in southeastern Niger and northern Nigeria. However, rainfall deficits began to appear in July and reached a peak of –100 mm in August over southern Mauritania, eastern Senegal, and southwestern Mali.

The rainy season in the Gulf of Guinea usually starts between March and May. In March, some regions, including Cote d'Ivoire and Nigeria, experienced rainfall surpluses of +10 mm to +30 mm. From April to June, there was an increase in rainfall in the Gulf of Guinea region, resulting in significant rain surpluses of +50 mm to +100 mm in southern Cote d'Ivoire and southwestern Ghana (Fig. 7.23). As the season progressed from June to September, the rain surpluses increased even further, reaching a maximum of over +100 mm in southern Cote d'Ivoire, Ghana, and Togo (Fig. 7.23). This large surplus led to 120%–200% of normal rainfall and contributed to the substantial annual rainfall surplus for those locations. Despite the abundant rainfall in the Gulf of

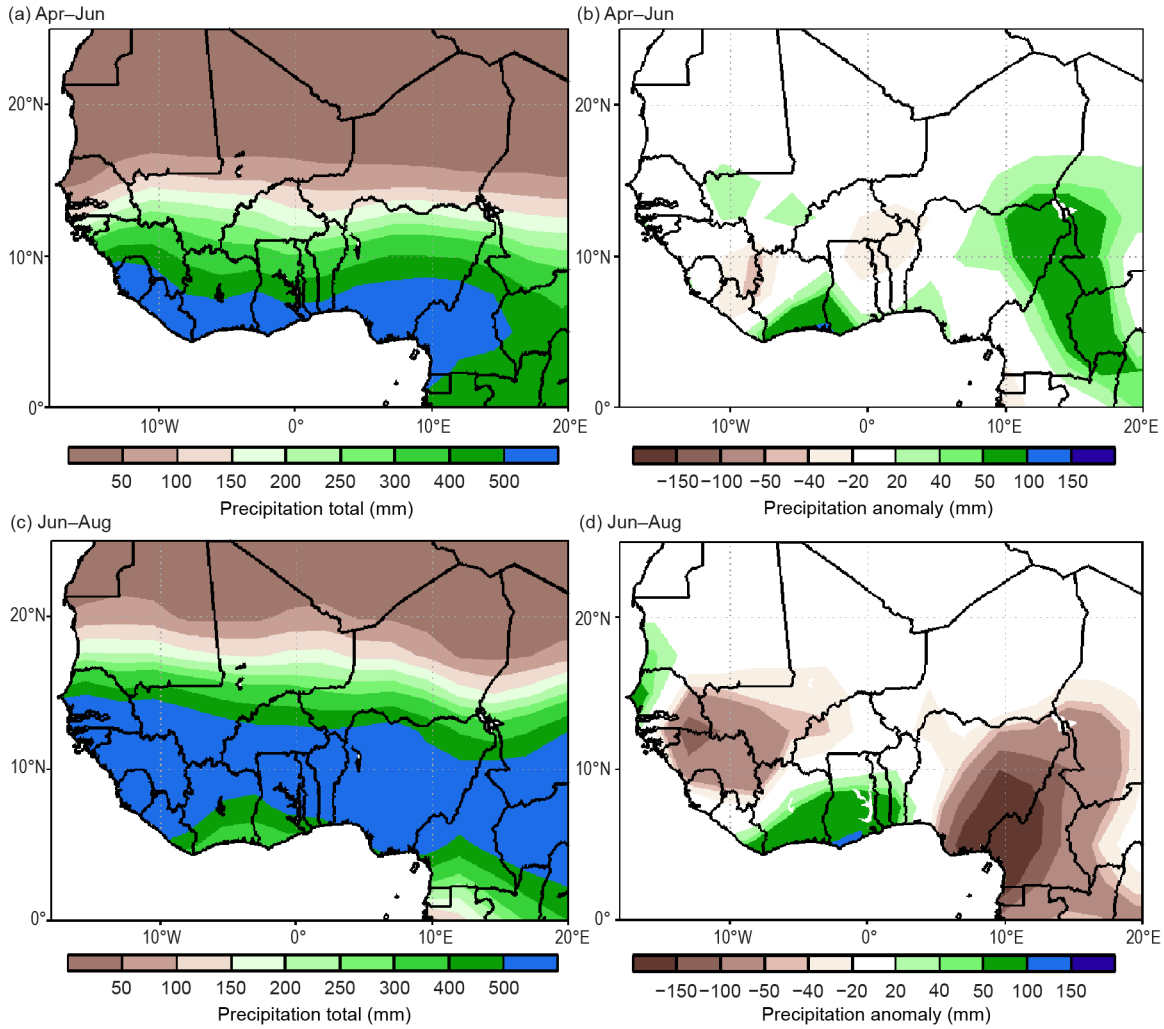

Fig. 7.23. Cumulative Apr–Jun seasonal (a) total precipitation, (b) precipitation anomalies; Jun–Aug seasonal (c) total precipitation, (d) precipitation anomalies in 2023 for West Africa (mm; 1991–2020 base period). (Source: NOAA National Centers for Environmental Prediction.)

Guinea, rainfall deficits started to increase from April (–10 mm to –50mm) and reached a maximum of –50 mm to –100 mm during August. Nigeria experienced below-average rainfall from April to May and again from July to October. Nigeria's central and eastern regions were the most affected, contributing to the annual rainfall deficit. Despite the persistent rainfall deficits, substantial surpluses ranging from +30 mm to +100 mm were recorded over Nigeria in June.

(iii) Notable events

In January, heavy rains that occurred in the previous months led to the overflowing of the Niger River at Dire in Mali, which caused flooding in the regions of Mopti and Tombouctou, according to the UN Office for the Coordination of Humanitarian Affairs. The flooding worsened the destruction already caused by the September 2022 floods in Mopti, affecting over 1000 households and damaging around 620 hectares of fields.

Heavy rainfall and storms hit Freetown on 9–10 May, causing significant damage. The National Disaster Management Agency of Sierra Leone reported seven deaths, mudslides in some parts of Freetown, and damage to the Leone Oil Facility in Kissy.

Heavy rainfall in Cote d'Ivoire on 11 June resulted in flooding, landslides, and significant building damage. Five people died in Yopougon Bel Air, and road closures in Yopougon and Songon isolated some communities.

Niger was impacted by heavy rains and floods since June, which led to 32 fatalities and dozens of injuries, and affected over 88,000 people.

On 6 and 11 August, Guinea was affected by heavy rains that caused severe flooding in Coyah, Conakry, and Siguiri. The flooding made major roads impassable for both vehicles and pedestrians.

Liberia experienced heavy rainfall during 1–4 September that caused severe flooding in the northeast. Around 15,200 people were affected, and infrastructure, houses, and facilities were swept away. Monrovia, Liberia's capital city, and surrounding areas were hardest hit, with around 12,450 people affected by five days of continuous rain beginning on 30 August.

In Ghana, heavy downpours caused flooding in March, June, and December, damaging infrastructure, crops, and homes. In September, the levels of the Lake Volta reservoir rose so high that they led to a spilling at the Akosombo Dam, displacing 30,000 people. Local officials blamed houses built in flood plains and drainage channels for the flooding.

Severe flooding in Nigeria, caused by heavy rainfall and water release from Cameroon's Lagdo Dam on 5 October, led to significant infrastructure damage in 14 of 21 Local Government Areas in Adamawa State. The flood resulted in 33 deaths and affected over 51,000 people across 214 communities, and worsened the humanitarian crisis in the region, with women and children being the most affected.

3. CENTRAL AFRICA

—J. Hicks, W. Agyakwah, and W. M. Thiaw

Central Africa features a unique climate system marked by a strong annual cycle as it spans a wide area of Africa across both the Northern and Southern Hemispheres. The region extends from the southern tip of the Democratic Republic of Congo (DRC) northward into the central areas of Chad. Longitudinally, the region extends from about 5°E to ~35°E. This analysis focuses on the sub-region encompassing Cameroon, Chad, Central Africa Republic (CAR), DRC, Congo (Republic of Congo), Gabon, Equatorial Guinea, and Sao Tome and Principe.

(i) Temperature

Annual mean temperatures were 2°C–4°C above average across much of Chad and CAR in January, with such anomalies persisting through February in southern CAR and northern DRC. During the second half of the year, a larger area of central Africa that extended from Chad to southern DRC observed mean temperatures that were 1.5°C–4°C above average, particularly from July to October. A majority of the region observed mean temperatures above their 90th percentile from May to December. Conversely, southeastern DRC experienced four months (April, May, July, and August) where mean temperatures were as much as 1.5°C below average (<15th

percentile). Monthly maximum temperatures were 4°C–5.5°C above average from southern Cameroon to northern DRC in February and in southwestern DRC during July–August. A majority of Central Africa observed maximum temperatures ranking above their 90th percentile from May to October. The July–September period ranked above the 90th percentile for much of the region outside of southeastern DRC, with maximum temperatures 5°C above average in southwestern DRC (Figs. 7.24a,b). Conversely, central DRC and southern Chad/northern CAR experienced their coldest maximum temperatures since 1991 in January and November, respectively. Despite the anomalously high maximum temperatures between July and September, southwestern DRC also observed some of their coldest minimum temperatures since 1991 during that season.

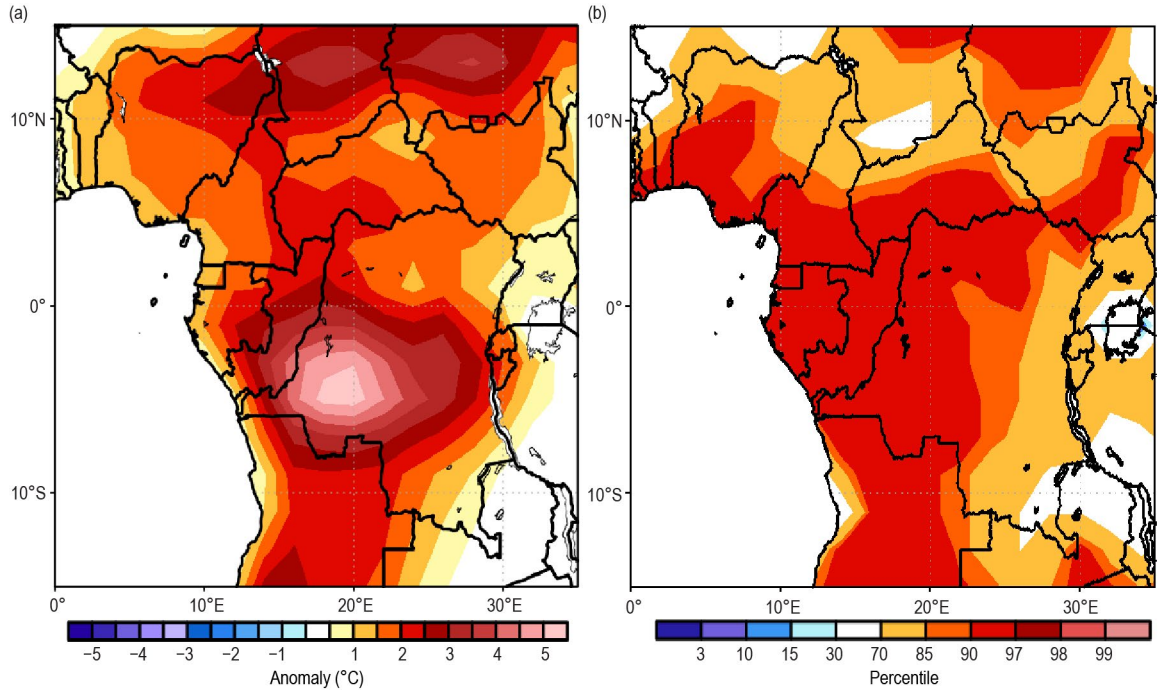

Fig. 7.24. Jul–Sep (a) maximum temperature anomalies (°C; 1991–2020 base period) and (b) maximum temperature percentile rank in 2023 for Central Africa. (Source: NOAA National Centers for Environmental Prediction.)

(ii) Precipitation

Cameroon experienced a rainy start to its wet season after observing rainfall surpluses of 50 mm–100 mm in June, which was up to two times its monthly climatology. Throughout the rest of the rainy season, Cameroon saw monthly rainfall deficits of up to –100 mm. This resulted in one of the driest three-month periods (July–September) since 1991. Monthly rainfall deficits were slightly lower in southwestern Chad over this same period (–30 to –50 mm each month), resulting in accumulations below the 15th percentile. In CAR, rainfall continued past the rainy season and into boreal autumn, resulting in accumulations that were four times higher than the climatological mean in November–December. Southern Cameroon, northern Congo, southern CAR, northern and eastern DRC, and much of Rwanda and Burundi observed rainfall surpluses of over +100 mm in November, with similar surpluses from south-central to southeastern DRC in December. Seasonal rainfall during October–December was 150 mm above the mean from southern CAR to southeastern DRC (>90th percentile; Figs. 7.25a,b). The excess November rainfall over central DRC (50 mm–100 mm) likely contributed to the below-normal maximum temperatures in the region as noted above. Towards the end of the prior wet season (January–March), abnormally dry conditions persisted in southeastern DRC. This region observed rainfall deficits of more than –100 mm in January and 50 mm–100 mm in February. This resulted in accumulations below the 10th percentile in January, while February was one of the driest on record (since 1991).

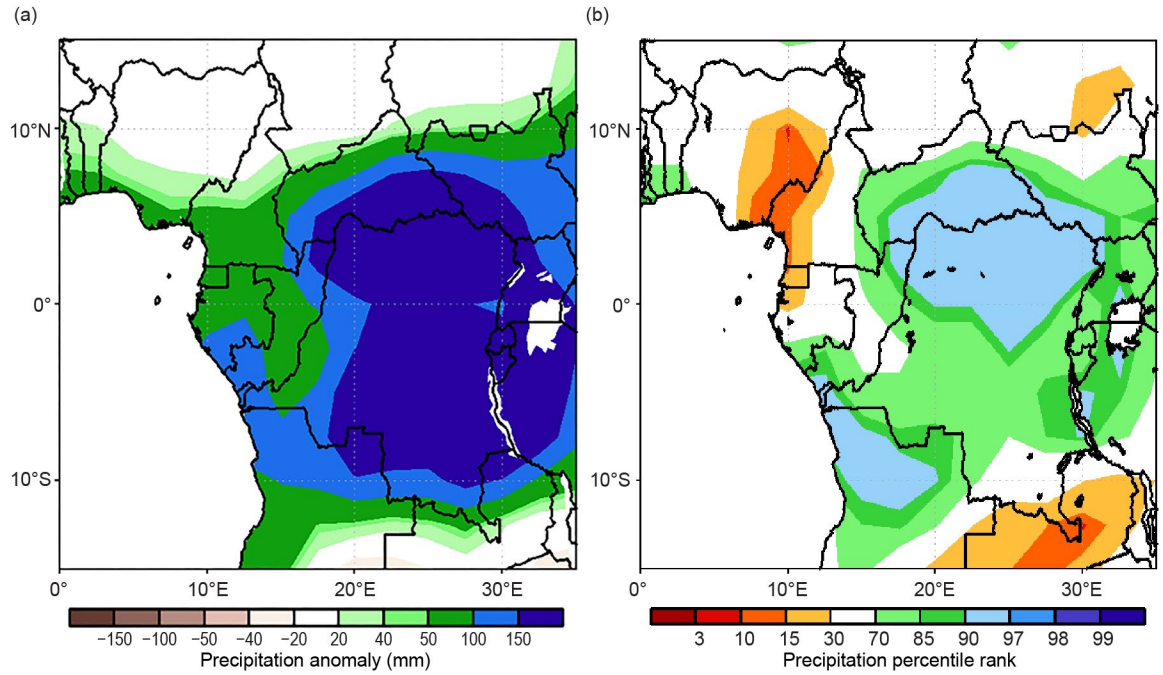

Fig. 7.25. Oct–Dec (a) precipitation accumulation anomalies (mm; 1991–2020 base period) and (b) precipitation percentile rank in 2023 for Central Africa. (Source: NOAA National Centers for Environmental Prediction.)

(iii) Notable events and impacts

Heavy rainfall and landslides during 2–4 May affected ~50,000 people in the South Kivu province of eastern DRC. Over 1500 people were displaced, more than 400 people were killed, more than 3000 houses were destroyed, and multiple health facilities and water, sanitation, and hygiene infrastructure were destroyed in the Kalehe Territory after more than 125 mm of rain fell over the area, according to the NOAA/Climate Prediction Center satellite rainfall estimates version 2 (RFE2). Heavy rainfall throughout November and December also resulted in flooding in DRC's Haut-Uele, South Kivu, and Tshopo provinces. More than 40 people were killed in and around Bukavu, the capital city of South Kivu province, after up to 100 mm of rain fell on 26 December, according to the RFE2. On the same day, 22 people were killed after heavy rainfall (>50 mm) inundated DRC's Kongo-Central province.

Flooding and mudslides in Yaoundé—the capital city of Cameroon—began on 8 October, affecting more than 700 residents, killing 30 people, and destroying 27 houses. According to the RFE2, heavy rainfall of up to 75 mm over a three-day period destroyed a water retention dam at Nkol Etam, triggering the mudslides.

Also according to the RFE2, heavy rainfall of up to 125 mm along with strong winds destroyed 200 homes and impacted 3000 people on 15 May in the Haut Ogooué province of Gabon.

On 11 August, heavy rainfall destroyed villages, houses, and agriculture in Mirvidin, Chad, after the breach of the Bongo-Gamsai dike along the Logone River. Over 2400 people were displaced. Flooding continued in southwestern Chad into September, particularly in the Logone Oriental, Mandoul, Tandjilé, and Mayo Kebbi Est provinces. Overall, during August–September, more than 1000 hectares and 2700 houses were destroyed, 5 people were killed, and over 100 people were injured.

Heavy rainfall that began in October resulted in the flooding of the Congo River, affecting more than 300,000 people in Congo by the end of December. The most impacted departments include Likouala, Sangha, Cuvette, Plateaux, Niari, Brazzaville, and Pointe-Noire. More than 360 villages were submerged, 17 people were killed, and more than 2200 hectares of farmland were flooded.

4. EASTERN AFRICA

—Z. T. Segele, E. Bekele, and W. M. Thiaw

The Greater Horn of Africa, or eastern Africa, covers 11 countries and extends 12°S–24°N and 21°E–52°E. Its northern sector comprises Sudan, South Sudan, the northern two-thirds

of Ethiopia, Eritrea, Djibouti, and northern Somalia. Southern and central Somalia, southern and southeastern Ethiopia, Kenya, northern Tanzania, Uganda, Rwanda, and Burundi are in its equatorial sector, while the southern sector encompasses central and southern Tanzania. The region has a complex terrain, with elevation ranging from about 160 m below sea level at Ethiopia's northern exit of the Rift Valley to more than 5000 m above sea level at glaciated Mount Kilimanjaro. This complex topography is further amplified by the presence of large lakes and reflects multi-faceted climate zones modulated by local and large-scale forcing such as the deep convective and moisture convergence zone, the El Niño–Southern Oscillation, the Indian Ocean dipole, the Madden Julian Oscillation, and tropical-extratropical interactions. Rainfall is bimodal in the equatorial sub-region, with two distinct rainfall seasons in March–May and October–December. Seasonal rainfall is unimodal in the northern and southern sectors, spanning November–April in the south and June–September in the north. The June–September rainfall over Ethiopia–Eritrea is locally known as "Kiremt" rains.

(i) Temperature

Annual mean temperatures in 2023 exceeded 26°C over parts of South Sudan, most of Sudan, Eritrea, and bordering regions of Ethiopia, Djibouti, Kenya, and much of Somalia (Fig. 7.26a). The highest mean annual temperatures of 30°C and above were recorded in localized areas in central Sudan, but mean temperatures above 28°C were widespread in Sudan, southern Somalia, and along the Red Sea coast. Mean annual temperature anomalies were less than +1.5°C across the region, with the largest anomalies being over South Sudan, southwestern Sudan, and along the Red Sea coast and bordering Afar regions of Ethiopia (Fig. 7.26b). Mean annual temperatures in these areas ranked between the 90th and 97th percentiles of historical records. Although anomalously warm (0.5°C to 1°C above the mean), annual mean temperatures were less than 22°C in most of central Ethiopia, southern half of Uganda, Tanzania, Burundi, Rwanda, and southwestern Kenya.

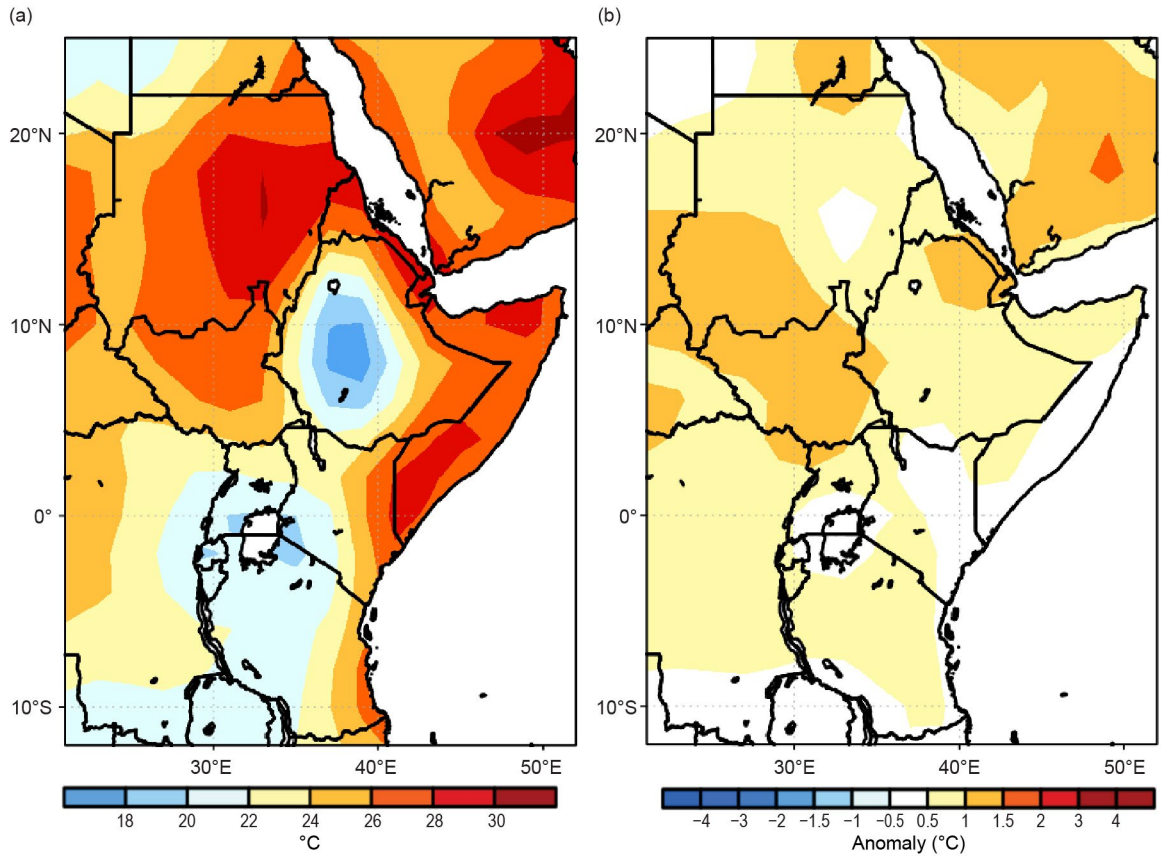

Fig. 7.26. Annual (a) mean temperature and (b) mean temperature anomalies (°C; base period 1991–2020) for eastern Africa in 2023. (Source: NOAA National Centers for Environmental Prediction.)

As the year progressed, a broad region of elevated mean monthly temperatures exceeding 30°C advanced northward from South Sudan in February and reached a peak of 36°C in northern Sudan in September. However, maximum temperatures were much higher (44°C–46°C) in northern Sudan in August and September. Areas in the Red Sea coast, including Djibouti and the Afar region of Ethiopia (northern Somalia), recorded their highest mean temperatures of 32°C–34°C (30°C–32°C) during May–June (May–September). Much of central Ethiopia registered temperatures below 22°C throughout the year. Except for southern Tanzania, which recorded mean temperatures of 24°C–26°C during September–November, most of Tanzania also had cooler temperatures through much of the year. Mean temperature anomalies were highest over South Sudan and Sudan (+3°C to +4°C) in January and over southern Sudan and eastern Ethiopia (+2°C to +3°C) in July. Mean temperatures were >90th percentile in most parts of the equatorial and northern sectors during June–September. Mean temperatures were below average by 2°C–3°C in localized areas over northern Sudan in May (lowest 15th percentile) and in cross-border regions of southeastern Ethiopia and central Somalia in November (lowest 10th percentile).

(ii) Precipitation

Annual rainfall totals in 2023 surpassed 1000 mm across western Ethiopia, South Sudan, most of Uganda, most of Rwanda, Burundi, and western and southern Tanzania (Fig. 7.27a). Western and central Uganda and western Rwanda recorded their highest annual totals in excess of 1500 mm. Most of Kenya, southern and central Ethiopia, northern South Sudan, southern Sudan, and central Tanzania received rainfall totals between 600 mm and 1000 mm. Totals were lower (50 mm–600 mm) over northern Sudan, Eritrea, Djibouti, and northeastern and eastern Ethiopia. Overall, rainfall was below normal over southeastern Sudan and over the Tigray and Wollo regions of Ethiopia, where deficits of –100 mm to –150 mm (<15th percentile) were recorded (Fig. 7.27b). The Garessa, Wajir, and Mandera counties of Kenya and southern Somalia received excessive rainfall, surpassing their normal totals by more than 300 mm (>90th percentile).

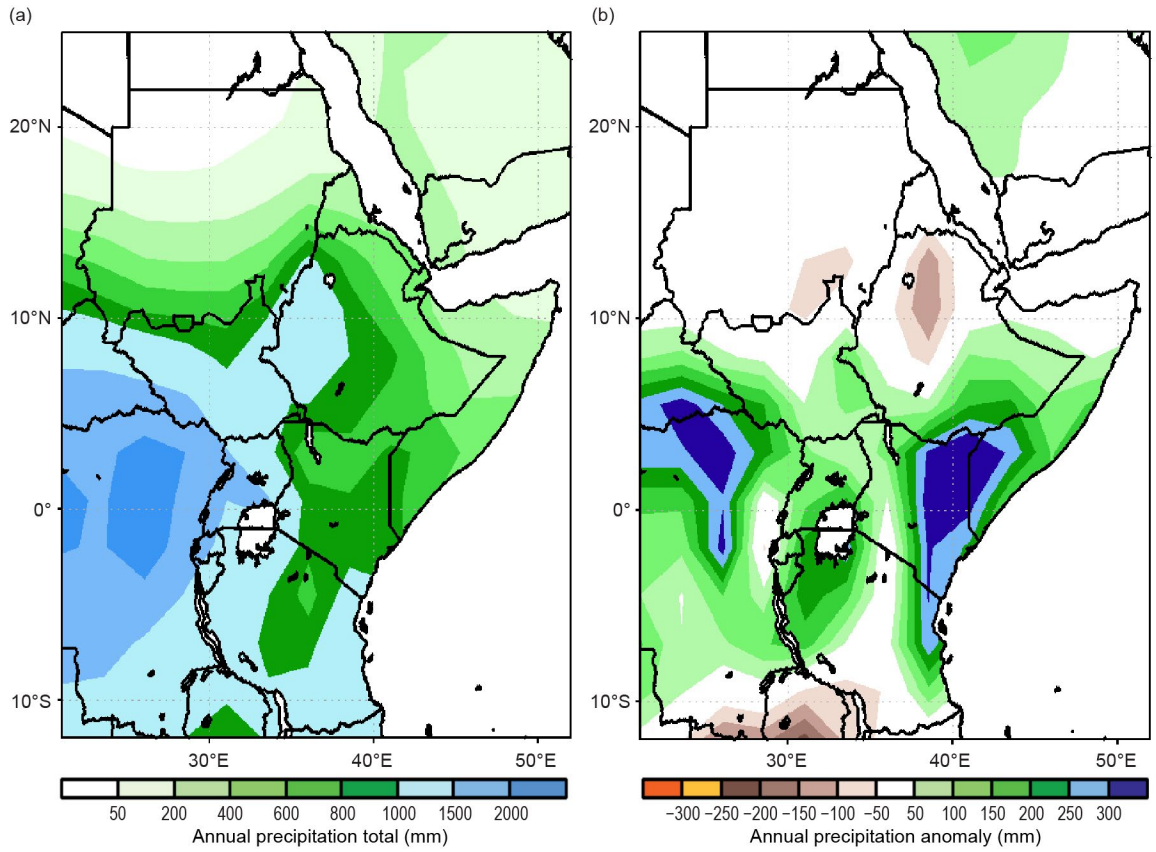

Fig. 7.27. Annual (a) total rainfall and (b) total rainfall anomalies (mm; base period 1991–2020) for eastern Africa in 2023. (Source: GPCP via NOAA National Centers for Environmental Prediction.)

Monthly rainfall totals in 2023 were widespread and in excess of 200 mm over the Lake Victoria regions and southeastern coasts of Kenya and Tanzania in April, over western and northwestern Ethiopia in July, over the equatorial sector in November, and over western Tanzania, Burundi, and Rwanda in December. The Kiremt rains highly underperformed in the northern sector in June and especially in the season's peak month of August. The Kiremt rainfall deficits in Ethiopia may be linked to the influence of anomalously warm eastern Pacific sea surface temperatures (i.e., El Niño), which is known to suppress summer rains in the region (Beltrando and Camberlin 1993). Monthly rainfall surpluses in 2023 exceeded 100 mm in the equatorial sector in March, April, and especially November, where rainfall totals were above the 90th percentiles in each month. Conversely, rainfall deficits exceeded 100 mm during the summer months, especially in August and September, across much of the northern half of Ethiopia, where recorded rainfall totals in August were below the lowest 3rd percentiles of their historical records. Overall, although 2023 rainfall totals in eastern Africa were wetter than average during March–May, October–December, and for the year, there was severe dryness during June–September that led to extensive drought conditions that remained present in Ethiopia through the end of the year.

(iii) Notable events and impacts

The transition from La Niña to El Niño helped bring relief to the prolonged drought conditions in equatorial eastern Africa during the March–May and October–December seasons. However, the 2023/24 El Niño along with positive Indian Ocean dipole conditions also led to excessive rainfall that resulted in devastating floods in many places. Exceptionally heavy rains and severe flooding over southeastern Ethiopia, Somalia, and Kenya during October–December displaced around 1.5 million people, caused human fatalities and livestock deaths, and brought significant damage to critical infrastructure, property, and crops, according to the United Nations Office for the Coordination of Humanitarian Affairs and government agencies. Heavy rains also caused devastating floods in many parts of Ethiopia, Somalia, Rwanda, Uganda, Kenya, and Tanzania during the March–May 2023 season, resulting in hundreds of fatalities, material damages, and displacements of hundreds of thousands of people. Drier-than-average conditions prevailed in the northern and western portions of eastern Africa during the June–September season.

5. SOUTHERN AFRICA

—A. C. Kruger, C. McBride, M. Robjhon, and W. M. Thiaw

Southern Africa is a region that covers a wide area in the southern portion of Africa. It extends from about 5°S to 35°S and comprises Angola, Namibia, Zambia, Botswana, Zimbabwe, Malawi, South Africa, Lesotho, Eswatini, and Mozambique. Southern Africa is characterized by two main seasons: the wet and warm season from November of the previous year to April and the dry and cold season from May to October.

(i) Temperature

Annual mean temperatures ranged from 16°C to 26°C in southern Africa, with warmer conditions in the western, part of central, and eastern sector and colder conditions across the central and southern sector of the region (Fig. 7.28a). Above-average annual mean temperatures extended from eastern Namibia, Botswana, southern and eastern Zambia, Zimbabwe, central and northeastern South Africa, Lesotho, Eswatini, and Malawi to western and northern Mozambique. The largest warm anomalies were observed over west-central Botswana, where annual mean temperatures were 1.5°C–2°C above average (Fig. 7.28b). In contrast, annual mean temperatures were below average in western Namibia.

South Africa experienced a relatively warm year, especially in the central and northern interior; in the south, temperatures were near normal. The annual mean temperature anomaly for 2023, based on the data of 20 climate stations, was on average about 0.4°C above the 1991–2020 normal, making this the eighth-warmest year on record since 1951 (Fig. 7.29). A warming trend of approximately 0.17°C per decade is indicated for the country over the period 1951–2023, statistically significant at the 5% level.

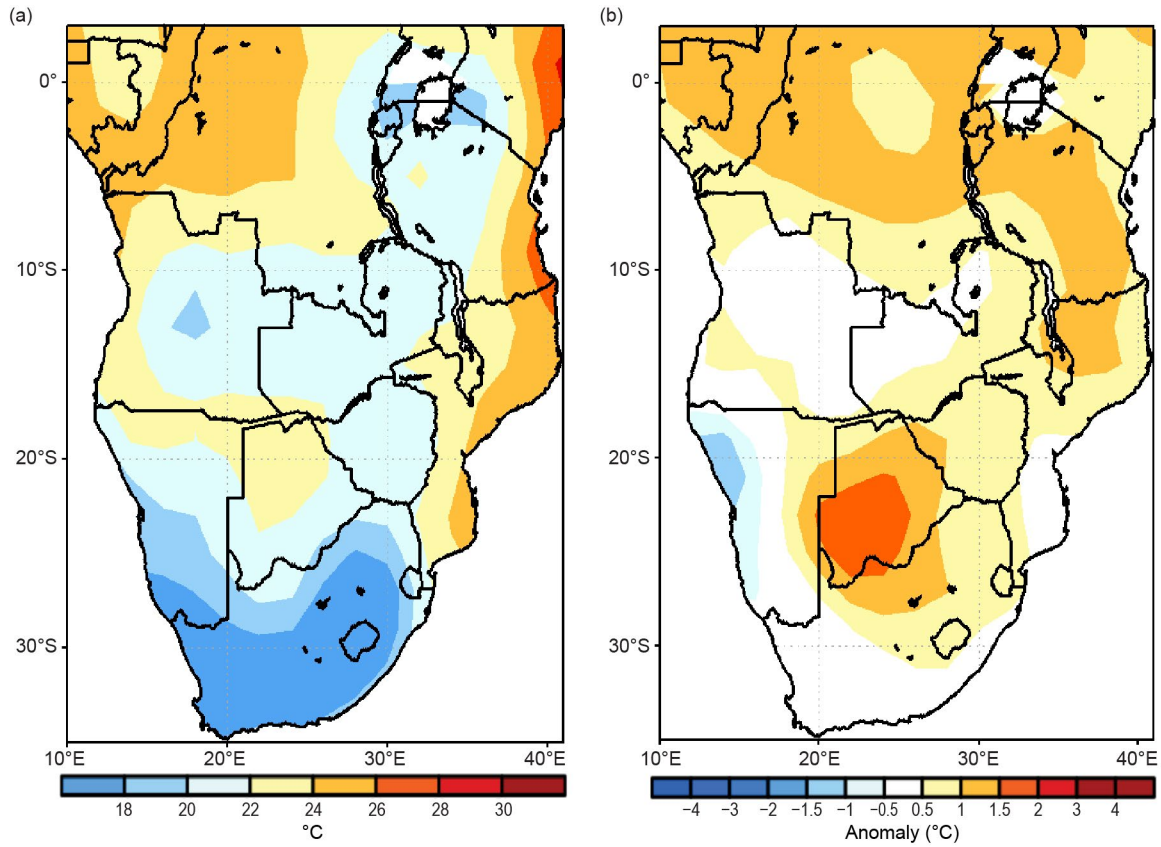

Fig. 7.28. Annual (a) mean temperatures and (b) mean temperature anomalies (°C; 1991–2020 base period) for southern Africa. (Source: NOAA National Centers for Environmental Prediction.)

Annual maximum temperatures were above average over most areas in southern Africa, with the warmest conditions in the western sector. Positive anomalies were +1.5°C to +3°C (90th–97th percentile) across Angola and eastern Namibia. Seasonally, maximum temperatures remained well above average in the western and southeastern parts of southern Africa during June–August and September–November.

Annual minimum temperatures were 1°C–3.5°C above average over the central and eastern portions of southern Africa, including Botswana, central South Africa, Zimbabwe, south-central Malawi, and western and northern Mozambique, whereas annual minimum temperatures dropped to 1°C–3°C below average in the western sector from southwestern Angola to northwestern Namibia. Minimum temperatures were well above average in Botswana during March–May, June–August, and September–November.

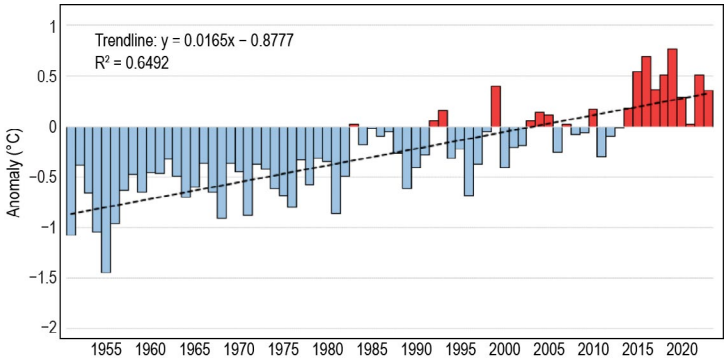

Fig. 7.29. Average surface temperature anomalies (°C; 1991–2020 base period) over South Africa based on 26 climate stations for the period 1951–2023. The linear trend is indicated by the dotted black line. (Source: South African Weather Service.)

(ii) Precipitation

Annual rainfall totals exceeded 1000 mm over the northern and eastern sectors of southern Africa, including northern Angola, northern Zambia, Malawi, the eastern two-thirds of Mozambique, and portions of eastern South Africa (Fig. 7.30a). Annual rainfall totals were below 600 mm across the central and western portions of the region from Botswana and Namibia to western South Africa. Annual rainfall was below average over central southern Africa, encompassing southeastern Angola, Zambia, eastern Namibia, Botswana, northern South Africa, and western Zimbabwe (Fig. 7.30b). The driest area was southwestern Zambia, where annual rainfall

was 200 mm–250 mm below average. Annual rainfall was above average in northern Angola, the southern and eastern tier of South Africa, Lesotho, Eswatini, and southern Mozambique, where rainfall surpluses of over 300 mm were received.

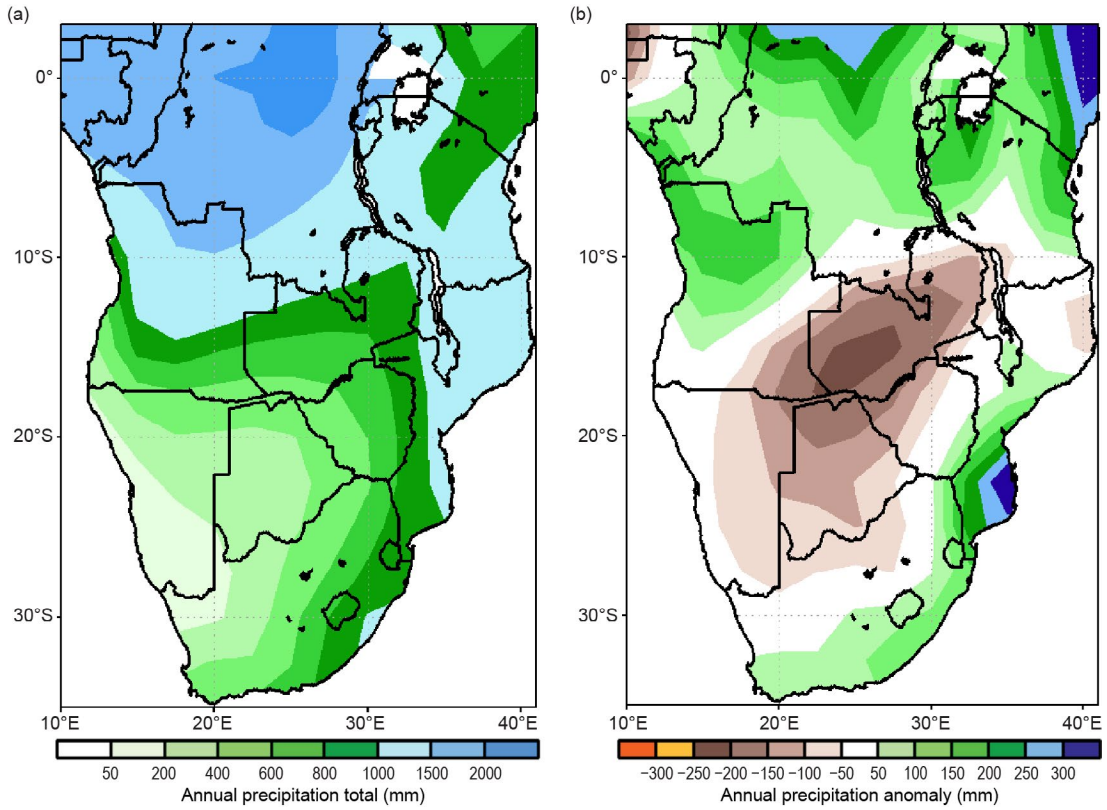

Fig. 7.30. Annual (a) rainfall totals and (b) rainfall anomalies (mm; 1991–2020 base period) for southern Africa. (Source: GPCP, NOAA National Centers for Environmental Prediction.)

In South Africa, most of the country received near-normal rainfall totals, with the exception of the northwestern interior, which received well-below-normal rainfall (Fig. 7.31). In contrast, some regions along the coast and extreme east received well-above-normal rainfall, especially in the Mpumalanga province.

While seasonal rainfall was below average across eastern Angola, Zambia, Botswana, Zimbabwe, northeastern South Africa, and southern Mozambique during December–February and March–May, drier-than-average conditions returned farther south in eastern Botswana, southwestern Zimbabwe, and parts of northern South Africa during September–November.

(iii) Notable events and impacts

During 24 February–11 March, Tropical Cyclone Freddy impacted the Niassa, Maputo, Inhambane, Gaza, Manica, Tete, Zambezia, and Sofala Provinces in Mozambique, resulting in 165 deaths, over 500 injuries, and 887,000 people affected. Rainfall totals ranged between 200 mm and 750 mm in central and southern Mozambique, according to the satellite Rainfall Estimates version 2 (RFE2). In Malawi, Cyclone Freddy triggered flooding and landslides in the

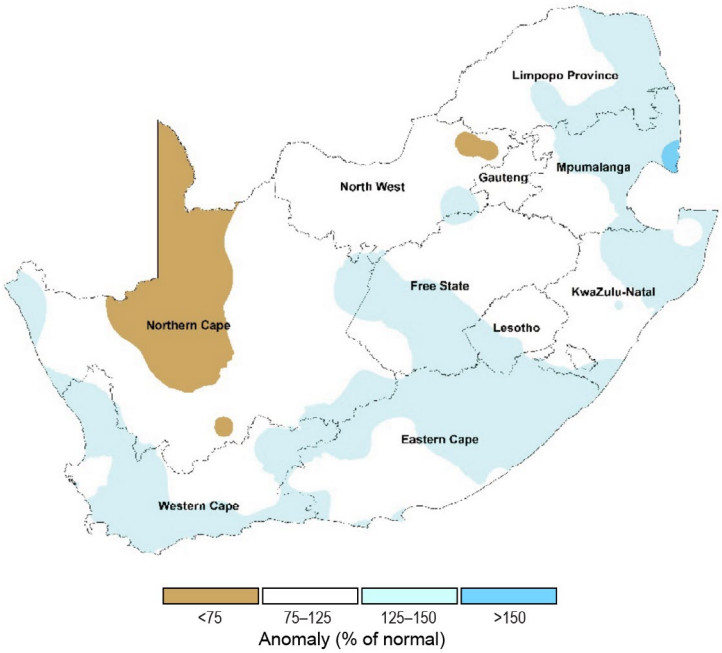

Fig. 7.31. Annual rainfall anomalies (% of normal; 1991–2020 base period) for South Africa for 2023. (Source: South African Weather Service.)

Balaka, Blantyre City, Blantyre, Chikwawa, Chiradzulu, Machinga, Mangochi, Mulanje, Neno, Nsanje, Phalombe, Thyolo, Zomba City, Zomb, and Mwanza Districts during 11–13 March, which caused 679 fatalities and 2186 injuries. See Sidebar 4.2 for details on Tropical Cyclone Freddy.

Heavy rains, with totals of 100 mm–300 mm, caused flooding in Luanda, Namibe, Lunda Norte, Lunda Sul, Malanje, Cuanza Norte, and Moxico in Angola during 1–30 April, contributing to 54 fatalities and 450 injuries, and affecting 44,450 people.

Heavy rains totaling 200 mm–750 mm led to flooding in Dar es Salaam, Kigoma, Kagera, Geita, Unguja, Arusha, and Pwani in Tanzania during 15 October–23 November. Twelve people were killed due to impacts from the rain and nearly 2,900,000 residents were affected.

During 2–6 December, heavy rains (75 mm–150 mm) triggered landslides in Katesh, Hanang District, and western Manyara Region (north) in Tanzania, which resulted in 88 fatalities, 139 injuries, and more than 5700 people affected.

In South Africa, the eastern province of KwaZulu-Natal was relatively hot at the start of 2023, and a few highest maximum and minimum temperature records were broken. In February, above-normal rainfall in the east led to several instances of flash floods, causing damage to infrastructure and loss of life. In March, the Western Cape received much above-normal rainfall, which persisted in the Cape Town metropole in April; about 130 residents and 50 shacks were flooded. In May, several major flooding events occurred in the eastern and southeastern coastal region, with more than 1200 residents evacuated from their homes in the Nelson Mandela Bay Municipality in the Eastern Cape after heavy rains on the 13th. In June, much-above-normal rainfall occurred over most of the southwestern half of South Africa; many flooding events were reported with hundreds of people left destitute and traffic disruptions in the main arterials connecting the southwest to the remainder of the country. In the far northeast, it was unusually hot and dry, and maximum temperatures of more than 30°C were reported. In September, floods were once again reported in the Western Cape. Flooding during 24–25 September led to 11 fatalities and the closure of over 200 roads, and over 80,000 people were left without electricity for an extended period. From October, floods were reported in the KwaZulu-Natal province. Several fatalities and extensive damage/destruction to infrastructure and hundreds of homes were reported. On 24 December, more than 20 people were killed in floods in Ladysmith.

6. WESTERN INDIAN OCEAN ISLAND COUNTRIES

—G. Jumaux, B. Andrade, R. Virasami, S. Dindyal, M. Robjhon, and W. M. Thiaw

The Western Indian Ocean island countries consist of Madagascar, Seychelles, Comoros, Mayotte (France), Réunion (France), Mauritius, and Rodrigues (Mauritius). There are two distinct main seasons: a warm and wet period spanning from November of the antecedent year to April and a cold and dry season lasting from May to October. Overall, above-normal temperatures in 2023 (Fig. 7.32) were associated with large-scale prevailing environmental conditions of El Niño and a positive Indian Ocean dipole. Annual rainfall was above normal in Mauritius and Seychelles and below normal in Mayotte and Réunion (Fig. 7.32).

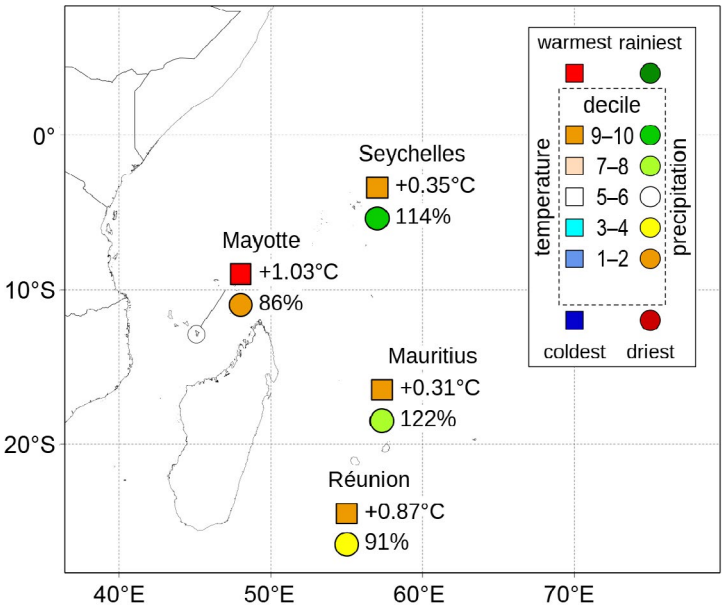

Fig. 7.32. Mean annual temperature anomalies (°C, squares), annual rainfall ratio to normal (%, circles), and their respective deciles for the western Indian Ocean island countries in 2023 (top right inset box). Base period is 1991–2020. (Sources: Météo France and meteorological services of Mauritius and Seychelles.)

(i) Temperature

In Réunion, the annual mean temperature (based on three stations) was 0.9°C above normal, the second highest since records began in 1968 (Fig. 7.33). The year started with a −0.1°C departure from normal during January–March, and then temperatures were

far above normal related to warm sea surface temperatures around the island: +1.1°C in April–June and +1.3°C in July–September (both record high), and +1.1°C in October–December (second highest).

In Mauritius, the annual mean temperature was 24.0°C, 0.3°C above normal. The highest mean temperature was in February (25.8°C) and the lowest mean temperature was in July (21.6°C; Fig. 7.34). Anomalies ranged from –1.3°C in January to +1.1°C in September. The start of the year had below-normal mean temperatures, transitioning to normal from March to June, and from July onward, with a strengthening El Nino, warm conditions were observed (+0.5°C). This warming trend persisted until the end of the year. It was the warmest September since records began in 1960.

In Mayotte (Pamandzi Airport), the annual mean temperature was the highest in the 63-year record (28.1°C, 1.0°C above normal). All months from May to December had record-high monthly mean maximum temperatures related to remarkably warm sea surface temperatures in the western Indian Ocean.

At Seychelles International Airport, the annual mean temperature anomaly for 2023 was 0.35°C above normal, the third highest since 1972. Nearly all months were above normal, except for January and February. It was the warmest December on record (anomaly of +1.0°C).

In Madagascar, annual mean temperatures were 20°C–26°C (Fig. 7.35a), with the higher temperatures observed along the west coasts and northern part of the island and lower temperatures over the central highlands. Annual mean temperatures were 0.5°C–1.0°C above average over the northern two-thirds of the country (Fig. 7.35b). These warm anomalies corresponded to the 90th–97th percentile rankings over a wide area in central and eastern Madagascar. Annual maximum temperatures were +0.5°C–1.0°C above average in central, western, eastern, and northern Madagascar. During October, the south-central region reported anomalies of +2°C to +3°C. Annual minimum temperatures also were 0.5°C–1°C above average across the northern two-thirds of the country. The warmest anomalies of +2°C to +3°C were observed in the central and eastern region during October.

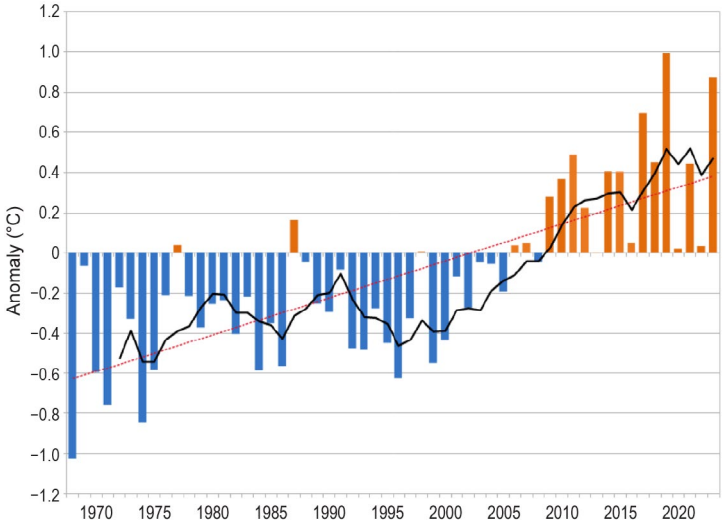

Fig. 7.33. Time series of Réunion annual mean temperature anomalies (°C; 1991–2020 base period) for the period 1968–2023. The solid black line is the five-year running mean and the dotted red line represents the linear trend. (Source: Météo-France.)

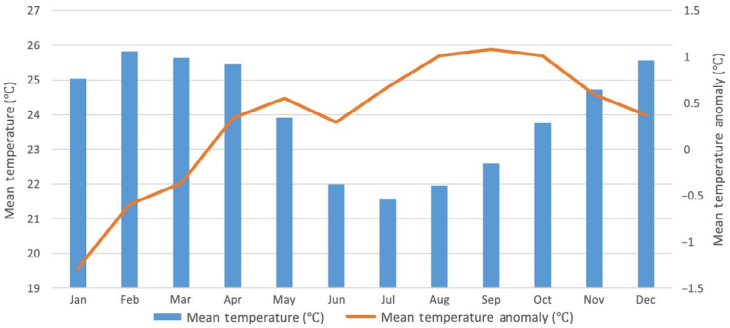

Fig. 7.34. Monthly mean temperatures for Mauritius in 2023 (blue bars, left scale) and 2023 anomalies (orange line, right scale). Base period is 1991–2020. (Source: Mauritius Meteorological Services.)

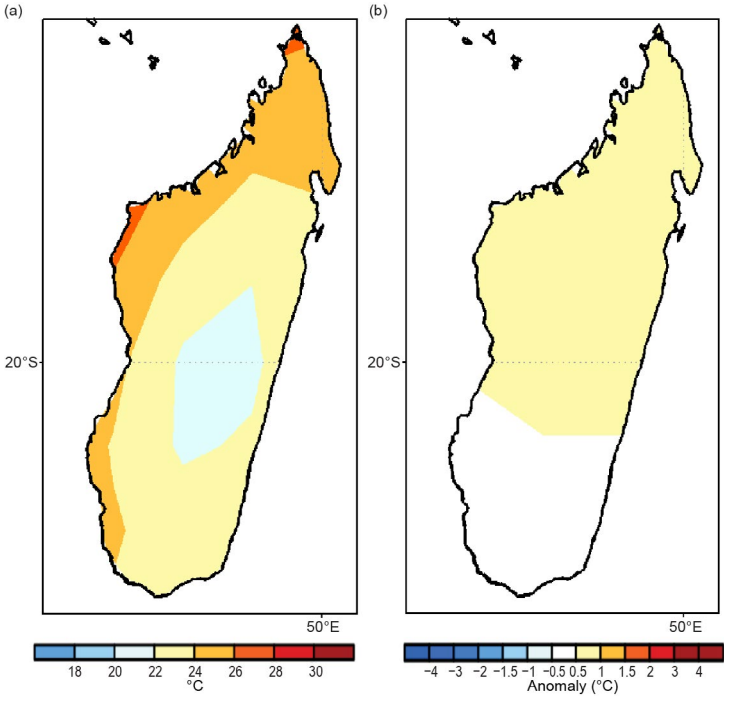

Fig. 7.35. Annual (a) mean temperatures and (b) mean temperature anomalies (°C; 1991–2020 base period) for Madagascar. (Source: NOAA National Centers for Environmental Prediction.)

(ii) Precipitation

The annual rainfall total over Réunion was 91% of normal. The rainy season (December–April) produced 71% of normal precipitation, making it the fourth-driest such period on record since records began in 1972. The dry season (May–November) was 129% of normal; this period includes the wettest November on record (289% of normal).

In Mauritius, intra-annual variability rainfall was observed throughout the year. The average cumulative annual rainfall total was 2471 mm, 122% of normal. January was wet, having seen 148% of its normal rainfall. However, February was the fifth driest on record since 1980. May was wet with 188% of rainfall, while June and July were drier than normal. August had well-above-normal rainfall, and thereafter drier conditions prevailed in September and October. November was the wettest November on record since 1905 and December had 317 mm of rainfall (192% of normal).

In Mayotte, the total annual rainfall was 86% of normal, which was the ninth-lowest on record since 1961. The rainy season (November–April) was very short, as April was the only wet month, marking the third-driest (73% of normal) such period on record. The dry season (May–October) was 67% of normal (seventh-driest). A severe drought occurred with many long-lasting water cuts. Fortunately, a wet rainy season began in December (153% of normal).

In Seychelles, the total annual rainfall (2799 mm) was 114% of normal, making 2023 the seventh-wettest year on record since 1972 (Fig. 7.36). The first half was 76% of normal (11th driest on record), and the second half was 162% of normal, the second wettest on record after 1997. The shift was related to the El Niño and the positive Indian Ocean dipole that developed in the second half of the year.

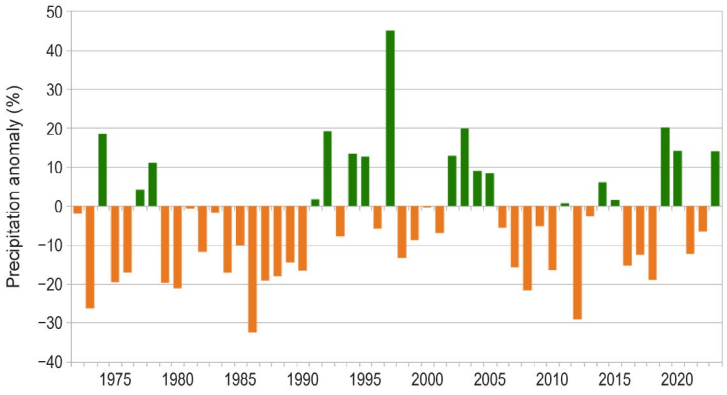

Fig. 7.36. Annual rainfall anomalies (%; 1991–2020 base period) in Seychelles for the period 1972–2023. (Source: Meteorological Services of Seychelles.)

In Madagascar, annual rainfall totals were 600 mm–2000 mm, with the highest and lowest amounts over the central highlands and southwest part of the country, respectively (Fig. 7.37a). Annual rainfall was below average in northern and southeastern Madagascar (Fig 7.37b). The driest region was near the Bay of Antongil in northeastern Madagascar, where rainfall deficits exceeded 300 mm. In contrast, annual rainfall was 50 mm–200 mm above average along the southwestern coasts of the Island.

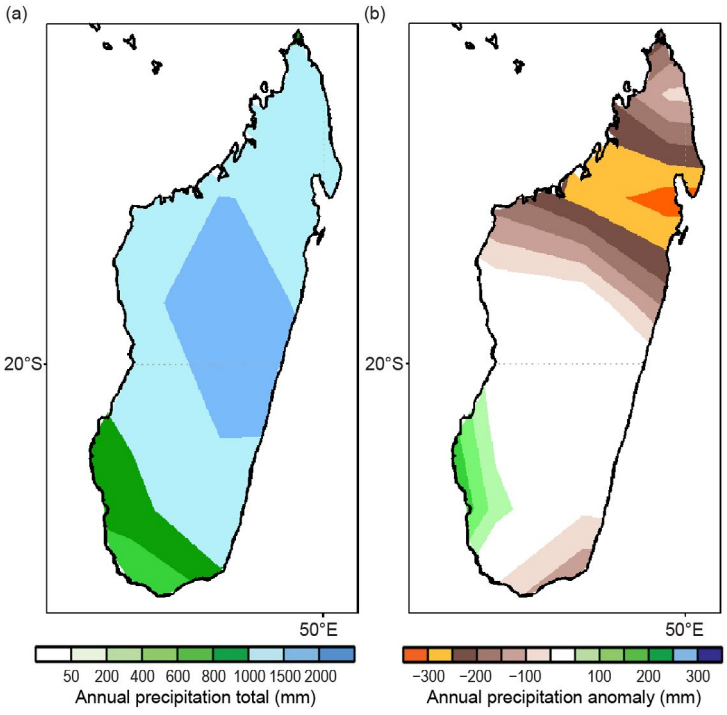

Fig. 7.37. Annual (a) rainfall totals and (b) rainfall anomalies (mm; 1991–2020 base period) for Madagascar. (Source: GPCP, NOAA National Centers for Environmental Prediction.)

(iii) Notable events and impacts

Tropical Cyclone Cheneso brought 200 mm–500 mm of rainfall, which resulted in flooding and landslides in Antalaha (Sava Region) and the Diana Region in northern Madagascar during 19–23 January, causing 53 fatalities and affecting nearly 91,000 people. During 24–25 January, Cheneso intensified and became a tropical cyclone over the Mozambique Channel but moved slowly until 26 January near the west coast of Madagascar.

In Mauritius, torrential rain was observed during 26–27 January. The most-affected regions were the central Plateau and the

eastern sector, where more than 300 mm of rainfall was recorded during 25–28 January (Fig. 7.38). The highest rainfall intensity measured was 55.1 mm h^{-1} at Wooton on the 27th.

Tropical Cyclone Freddy crossed the Indian Ocean from Australia to Mozambique during 4–24 February. Prior to landfall over Madagascar on 21 February, the center of the cyclone passed within 200 km north of Mauritius and Réunion on the 20th without causing severe damage. After entering the Mozambique Channel, the storm spent six days on land between Mozambique and Zimbabwe, then re-entered the southern Channel between 2 and 14 March. In total, Freddy hit Madagascar twice. Loss of human life and extensive material damage was reported. With winds of up to 165 km h^{-1} and rainfall totals between 100 mm and 300 mm, Freddy impacted Vatovavy, Fitovinany, Atsimo Atsinanana, Amoron'i Mania, Analamanga, Itasy, Alaotra-Mangoro, Menabe, and Atsinanana in central and eastern Madagascar during 21 February–8 March, causing 20 fatalities and affecting 299,000 people. Reports indicated one fatality and 2500 people affected in Mauritius and 25,000 people affected due to landslides in Réunion. See Sidebar 4.2 for more details on Tropical Cyclone Freddy.

In Seychelles, torrential rain in the northern part of Mahé island on 6 December caused flooding and landslides that led to power failures and three fatalities. The daily rainfall total was 360 mm at Belombre (the highest 24-hour rainfall value since records began), mainly in a five-hour period, and 310 mm at Beau Vallon.

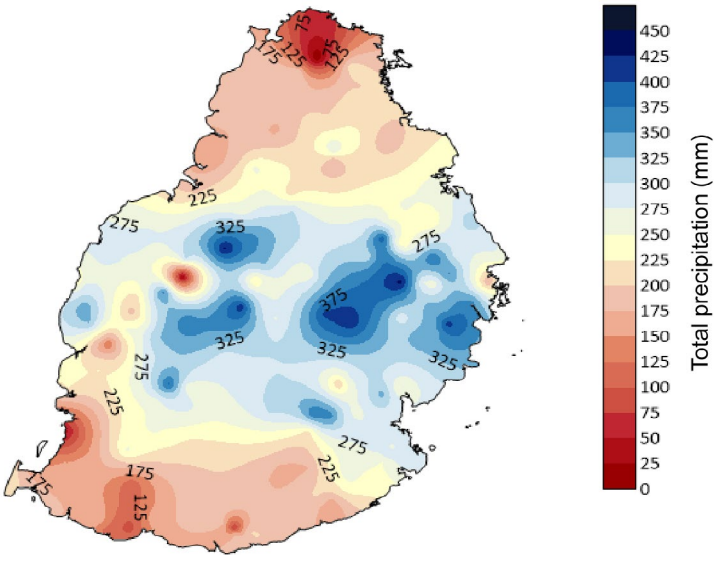

Fig. 7.38. Cumulative four-day rainfall (mm) in Mauritius during 25–28 Jan 2023. (Source: Mauritius Meteorological Services.)

f. Europe and the Middle East

—P. Bissolli (Ed.), S. Ahmadpour, C. Berne, O. Bochníček, M. Ekici, A. Gevorgyan, M. Kendon, J. Kennedy, Y. Khalatyan, V. Khan, M. Lakatos, J. Mamen, A. Orlik, A. Porat, H. Ressl, E. Rodriguez Guisado, M. Roebeling, B. Rösner, S. Sensoy, S. Spillane, K. Trachte, R. van der Linden, and G. van der Schrier

Throughout this section, 1991–2020 is the base period used for both temperature and precipitation unless otherwise specified. All seasons mentioned in this section refer to the Northern Hemisphere. More detailed information can be found in the Monthly and Annual Bulletin on the Climate in Regional Association VI (RA VI)–Europe and the Middle East, provided by the World Meteorological Organization (WMO) RA VI Regional Climate Centre on Climate Monitoring (RCC-CM; http://www.dwd.de/rcc-cm). Anomaly information has been taken from Figs. 7.40–7.43 and relevant national reports. The length of national temperature and precipitation records, annual anomalies, and rank information for each country are provided in Appendix Table 7.2. A color-coded map of the various subregions of WMO RA IV discussed in this section are shown in Fig. 7.44. Due to the high number of countries in Europe and the limited word space for each subsection, limited impact information can be provided here. More details about extreme events and impacts across Europe can be found elsewhere, e.g., https://climate.copernicus.eu/esotc/2023/key-events.

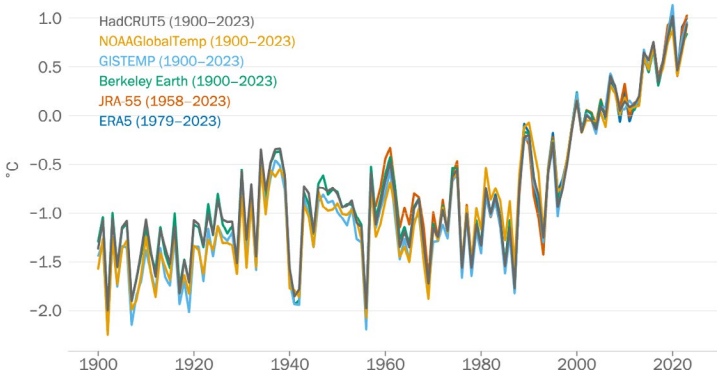

Fig. 7.39. Annual regional mean temperature for the World Meteorological Organization (WMO) Regional Association VI Europe (°C, difference from the 1991–2020 average) for the period 1900–2023. Data are from the following six datasets: Berkeley Earth, ERA5, GISTEMP, HadCRUT5, JRA-55, and NOAAGlobalTemp. (Source: WMO.)

1. OVERVIEW

Based on the WMO RA VI assessment, which utilized six datasets (Berkeley Earth, ERA5, GISTEMP, HadCRUT5, JRA-55, and NOAAGlobalTemp[1]; Fig. 7.39), the year 2023 ranked as the first or second warmest on record in Europe (here defined by the WMO RA VI Region, https://wmo.int/about-wmo/regions), depending on the dataset. The mean temperature anomaly for this year was +0.95°C (ranging from +0.84°C to +1.03°C among the six datasets).

Annual temperatures in 2023 were above average across the entire region except for some parts of the Nordic countries (Fig. 7.40). According to national data and reports, 2023 was the warmest year on record for Ireland (+1.0°C), Moldova (+1.9°C), Kazakhstan (west Kazakhstan [European part]; +1.9°C), Romania (+1.6°C), Malta (+0.7°C), Slovenia (+1.3°C), Serbia (+1.5°C), Germany (+1.3°C), Czechia (+1.4°C), Bulgaria (+1.6°C), Austria (+1.2°C), Slovakia (+1.3°C), Hungary (+1.5°C), Croatia (+1.4°C), Montenegro (+1.7°C), and the Netherlands (+1.3°C). Many other countries reported an annual temperature that was among their four highest on record.

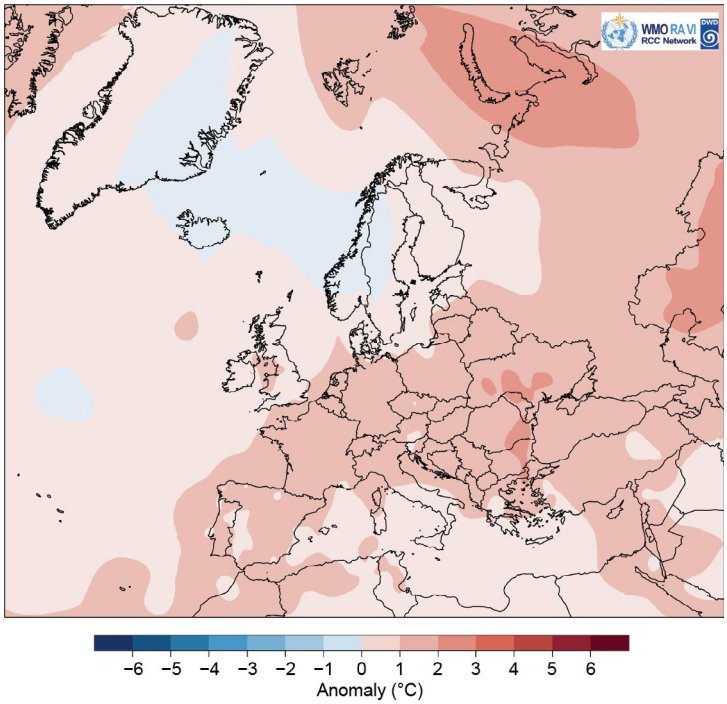

Fig. 7.40. Annual mean temperature anomalies (°C; 1991–2020 base period) for 2023. (Source: Interpolated climate station and ship data, Deutscher Wetterdienst [DWD].) The 1991–2020 anomalies were recalculated from 1981–2010 anomalies because the 1991–2020 CLIMAT data were still not available for all countries.

[1] Reference: https://jjk-code-otter.github.io/demo-dash/RegionalDashboard/wmo_ra_vi.html

According to the *European State of the Climate*—the joint report of the Copernicus Climate Change Service (C3S) and the WMO with data primarily based on the ERA5 reanalysis dataset—2023 equaled the warmest year on record, with 2020, for the WMO RA VI (Europe) domain (Copernicus and WMO 2024), with temperatures averaging 1.0°C above the 1991–2020 base period. September 2023 marked the warmest September on record, and the winter season (December 2022–February 2023) was the second warmest on record for Europe.

Based on the GHCN v4.0.1 dataset (the land component of NOAAGlobalTemp), Europe (defined here by the area 36°N–72°N, 23°W–60°E, which differs slightly from the RA VI Region) had above-average (1910–2000 base period) monthly temperatures all year, and the monthly temperature anomalies ranged between +1.05°C in May and +3.50°C in January. January and September were each the warmest on record for their respective months.

Winter 2022/23 was warmer than normal across Europe, except in Iceland and some parts of European Russia and west Kazakhstan, with positive temperature anomalies of up to +4°C. Romania (which had its warmest winter on record, with a remarkable temperature anomaly of +3.1°C) and Bulgaria were notably warmer than normal (Fig. 7.41). Armenia experienced its third-warmest winter. Spring had near-normal temperatures or was slightly cooler than normal across the region, except in the Iberian Peninsula and Eastern Europe, which were both much warmer than normal. Temperature anomalies for the season ranged from –1°C to +3°C, with the highest on the Iberian Peninsula, especially in Spain, and in European Russia and west Kazakhstan. This warmth illustrates a remarkable meridional circulation pattern in which the

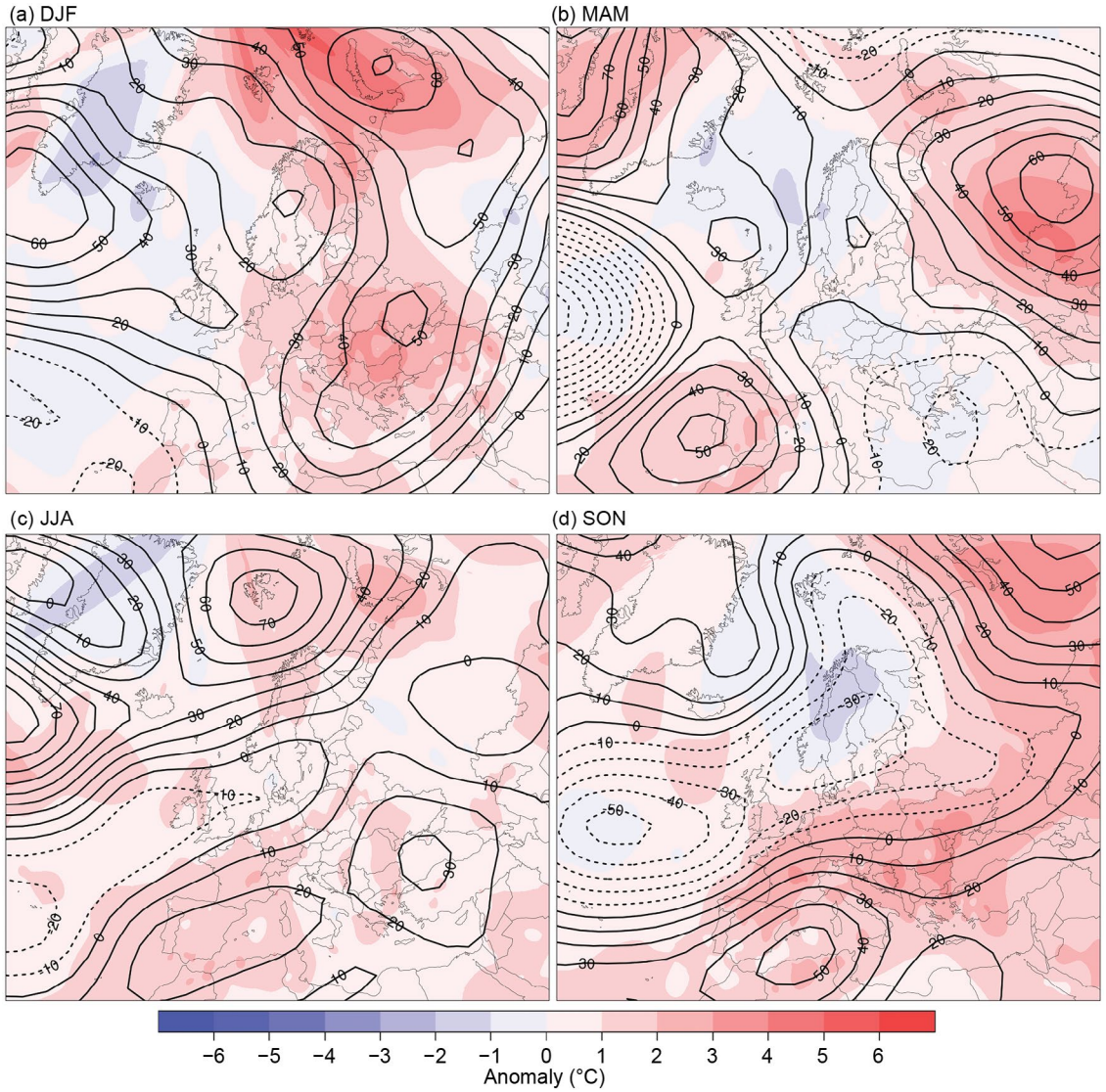

Fig. 7.41. Seasonal anomalies (1991–2020 base period) of 500-hPa geopotential height (contour; m) and surface temperature (shading; °C) using data from the NCEP/NCAR reanalysis and Deutscher Wetterdienst (DWD), respectively, for (a) Dec–Feb (DJF) 2022/23, (b) Mar–May (MAM) 2023, (c) Jun–Aug (JJA) 2023, and (d) Sep–Nov (SON) 2023.

Iberian Peninsula had anticyclonic situations while the central Mediterranean region experienced cyclonic conditions. West Kazakhstan (European part) recorded its warmest spring on record, while Ireland had its third warmest, and Portugal its second warmest. A particularly significant meridional circulation pattern was present in April, and it was warmer than normal in southwestern and northeastern parts of the region, especially in Spain, which reported its warmest April on record. In contrast, Central Europe had a cooler-than-normal April, with average anomalies of –1.0°C in Switzerland and –1.1°C in the Netherlands. May was also characterized by a strong meridional pattern, but with warmth in northwestern Europe as well. Some stations in Ireland recorded their warmest May on record. This warmth was also related to the marine heatwave in the surrounding waters (see Sidebar 3.1 for more details).

Unusually high temperatures occurred across much of Europe during summer under the influence of high pressure across much of the region, with anomalies ranging from +1°C to +2°C in large parts. The United Kingdom recorded its warmest June on record, at 2.5°C above average. The Netherlands was also record warm in June.

During autumn, except for the Nordic countries, the temperature was well above the average in the domain and was constantly influenced by a southwesterly and southerly flow of subtropical air. Parts of eastern and southeastern Europe had anomalies above +3°C. Switzerland and Denmark reported their warmest September on record at 3.8°C and +2.7°C above normal, respectively. Austria and France each reported their warmest autumn and September on record, while Italy reported its warmest autumn and October on record. Germany, Spain, Switzerland, and Poland each observed their second-warmest autumn, while Israel observed its third warmest.

Annual precipitation for 2023 was mostly near normal or wetter than normal in most parts of Europe, except for in the southern Iberian Peninsula, southern France, and Iceland, all of which were drier than normal. Precipitation totals ranged from below 60% of normal in parts of southern Europe to more than 165% of normal in various places throughout the rest of the region (Fig. 7.42). Averaged over all land areas of the RA VI Region, it was the wettest year on record according to the Global Precipitation Climatology Centre (GPCC) gridded data, but the third wettest according to ERA5 (Copernicus and WMO 2024).

Winter 2022/23 was significantly drier than normal from Iceland and western Europe to eastern Spain. In Iceland, there were large positive pressure anomalies in winter that also extended into western Europe, contributing to the dry conditions. The eastern Mediterranean region also had a dry winter. In contrast, other parts of Europe experienced a significantly wetter-than-normal winter, especially in a region extending from western Russia to the Balkans and Italy (Fig. 7.43). Spring was wetter than normal across most of Europe, with more than 125% of normal precipitation recorded in various regions, notably in parts of western Europe (southern United Kingdom and the low countries [Belgium, the Netherlands, and Luxembourg]), the central and eastern Mediterranean region, and parts of eastern Europe (Russia, Ukraine). Particularly dry were Iceland, much of the Iberian Peninsula, and a region around the Baltic Sea. The Iberian Peninsula experienced a severe drought, with areas receiving less than 40% of their spring normal (see Sidebar 7.3 for more details). Iceland was again under large high-pressure anomalies, unlike areas in southeastern parts of the domain, where low-pressure anomalies prevailed (Fig. 7.43).

Summer had mostly near-normal and wetter-than-normal precipitation in Europe. Areas with more than 125% of their normal

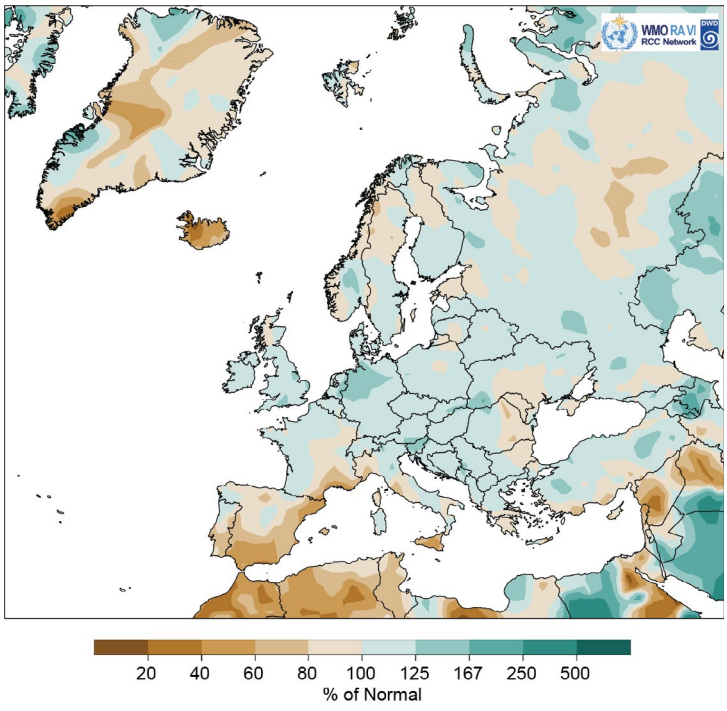

Fig. 7.42. European precipitation totals (% of 1991–2020 average) for 2023. (Source: GPCC, created by Deutscher Wetterdienst.)

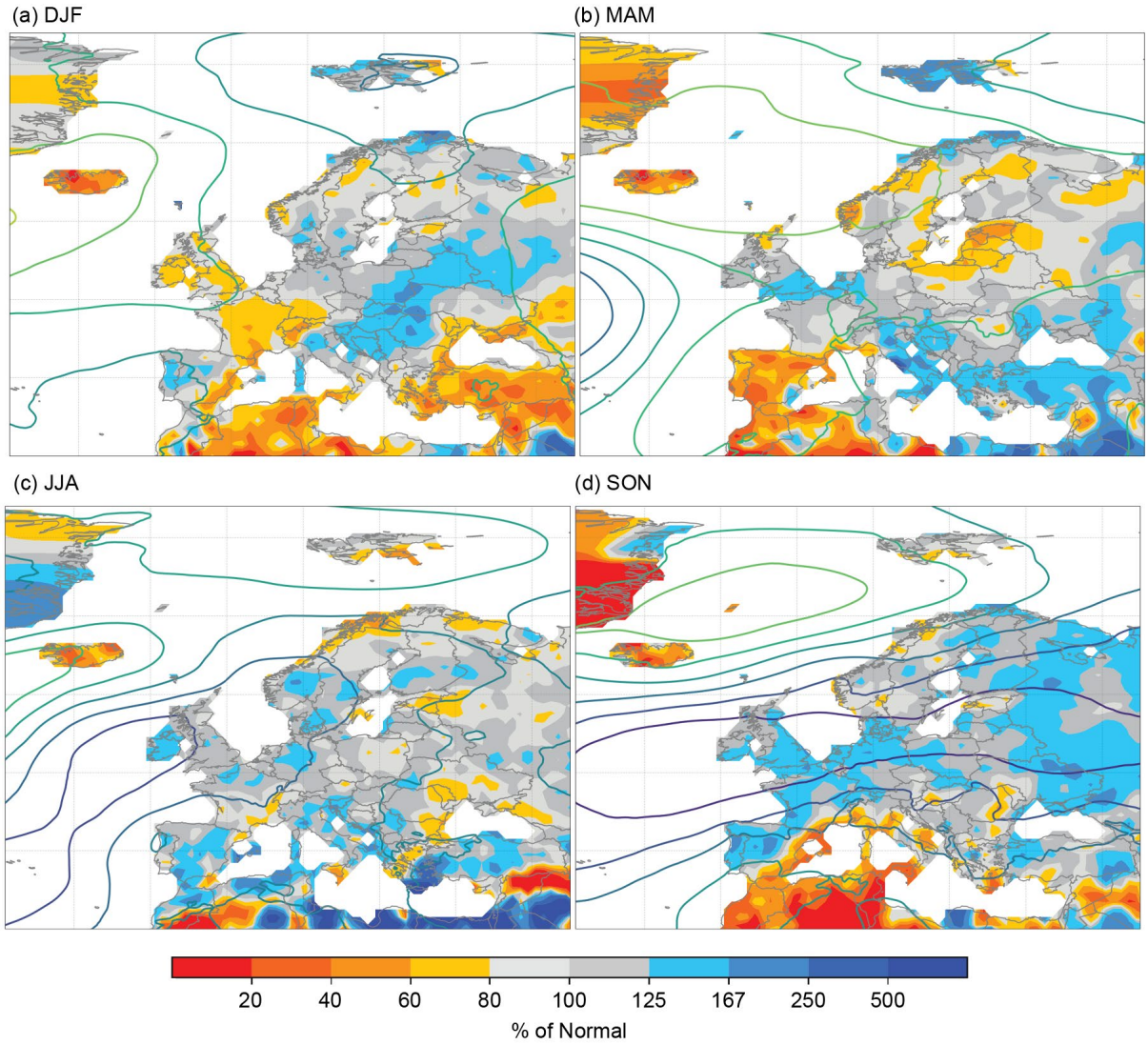

Fig. 7.43. Seasonal anomalies for 2023 (1991–2020 base period) of sea level pressure (hPa) from NCEP/NCAR reanalysis for (a) Dec–Feb (DJF) 2022/23, (b) Mar–May (MAM) 2023, (c) Jun–Aug (JJA) 2023, and (d) Sep–Nov (SON) 2023. The colored shading represents the percentage of seasonal mean precipitation for 2023 compared to 1991–2020 (Source data: GPCC, created by Deutscher Wetterdienst [DWD]).

totals were prevalent throughout the domain. Some areas in Ireland, southern Norway, northeastern Italy/Slovenia and other parts of southeastern Europe, and western Azerbaijan in the South Caucasus were particularly wet, having receiving more than 90 mm of rainfall above their respective seasonal normals. Most of the Mediterranean region had a wetter-than-normal summer, but since this part of Europe has a climatologically dry summer, anomalies were not high in absolute terms. Above-normal precipitation totals in Spain and Portugal did not compensate for the dry spring. In contrast, this season was dry again in Iceland (as the influence of high pressure continued) and in parts around the Black Sea, with seasonal totals of less than 80% of normal.

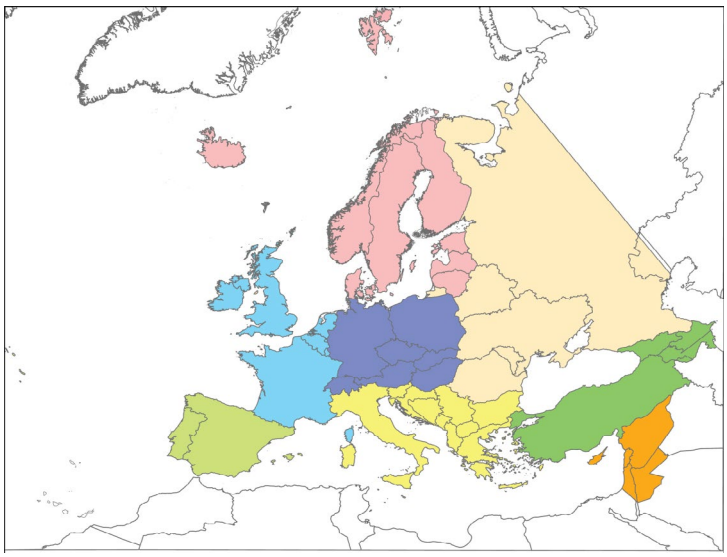

Fig. 7.44. Map of subregions in the World Meteorological Organization Regional Association VI Region of Europe

Autumn was wetter than normal across most of the region. Low-pressure systems moved over the midlatitudes from western to eastern Europe and also to the northeast and southwest. It was drier than normal again in Iceland and over the western and eastern Mediterranean basins and their coastal areas, whereas the Balkans, Greece, and Türkiye were mostly wetter than normal. However, there were large differences from month to month. In September, dry conditions prevailed over a large area of central, southeastern, and eastern Europe, but changed to a rainy period in October in central and eastern Europe and in November in southeastern Europe. In October, tropical cyclones that transitioned into midlatitude storms over the North Atlantic contributed to the wet conditions and in November, storms developed in the Black Sea region. In December 2023, some storms brought flooding in Central Europe, particularly in Germany along the Ems, Weser, and Elbe Rivers and their tributaries, while dry, cold air prevailed in northern Europe. Dryness was also prevalent in the Mediterranean region.

2. WESTERN EUROPE

This region includes Ireland, the United Kingdom, the Netherlands, Belgium, Luxembourg, and France.

(i) Temperature

In 2023, many countries in this region saw above-normal or near-normal temperatures. Ireland's mean air temperature was 1.0°C above its annual average, marking its warmest year on record. The United Kingdom recorded an annual mean temperature of 10.0°C, 0.8°C above the long-term average, marking its second-warmest year after 2022. The Netherlands experienced its warmest year since the start of its record in 1901, at 1.3°C above normal. France and Luxembourg saw their second-warmest year and Belgium its third warmest, with all three more than 1°C above normal. Across the region, all seasons experienced above-normal temperatures.

Winter 2022/23 was slightly warmer than normal in Ireland (+0.3°C anomaly) and the United Kingdom (+0.2°C). On the continent, anomalies were higher: +0.8°C in France, +0.9°C in Belgium, +1.2°C in the Netherlands, and +1.0°C in Luxembourg.

Anomalies in spring were similar to winter in the United Kingdom (+0.3°C) and higher in Ireland (+0.9°C). This was the third-warmest spring on record in Ireland; however, this overall warm period included fluctuations between colder and milder weather patterns, featuring cold spells in early March and late April. The seasonal temperature anomaly for France as a whole was +0.6°C, but up to +1°C in the west and extreme south. In contrast, spring temperatures were slightly below normal in the Netherlands (−0.2°C), Belgium (−0.3°C), and Luxembourg (−0.2°C), mainly due to a cooler April when cold air from the northeast reached the continent.

In summer, June was outstandingly warm in western Europe, while July and August were near or slightly below normal. Ireland, the United Kingdom, Belgium, and the Netherlands each experienced their warmest June on record, with anomalies of +2.5°C in Ireland and the United Kingdom, +3.2°C in the Netherlands, and +3.6°C in Belgium. Overall, the summer season was among the 10 warmest on record for all countries of western Europe except Luxembourg. Summer anomalies ranged from +0.8°C for the United Kingdom and Luxembourg to +1.4°C for France.

Anomalies in autumn were even higher than those in summer in the western European countries: Ireland (+1.0°C), the United Kingdom (+1.0°C), the Netherlands (+1.9°C), Belgium (+2.2°C), Luxembourg (+1.8°C), and France (+2.5°C). It was the warmest autumn on record in France, the second warmest in the Low countries (Netherlands, Belgium, Luxembourg), sixth warmest in the United Kingdom, and fifth warmest in Ireland. September was notable, especially for France, which saw its warmest September since the start of its record in 1900 (3.6°C above normal). The United Kingdom observed its equal warmest September in its record dating to 1884.

(ii) Precipitation

Over the year, most of western Europe received near- or above-normal precipitation. The total precipitation for the United Kingdom reached 1319 mm, which is 113% of normal. Other countries in Western Europe registered higher percentages, including Ireland (117% of normal), Belgium (121%), Luxembourg (128%), and the Netherlands (133%). The average precipitation total for France in 2023 was near normal (104%) following a very dry year in 2022. Only the southeastern

parts of France were considerably drier than normal (<60% of normal), with some parts having marked their driest year on record.

Almost all countries in western Europe received below-normal precipitation in winter 2022/23, including France (75% of normal) and Belgium (94%). The only exception was the Netherlands (102% of normal). February was extremely dry due to persistent high pressure over the area. France received only 26% of its normal monthly precipitation, marking its fourth-driest February on record since at least 1959 and the driest since 2012, while Belgium received 20% of its normal (a monthly total of just 13 mm). The Netherlands recorded 36% of its normal precipitation in February, Ireland 34%, Luxembourg 18%, and the United Kingdom 47%, its driest February since 1993.

Spring was wetter than normal across much of the region: 139% of normal in the Netherlands, 146% in Belgium, and 137% in Luxembourg. For Ireland and the United Kingdom, precipitation in spring was closer to normal (118% and 109%, respectively). France saw average rainfall across the country (102%) but below-normal precipitation in the southeast.

Summer, too, had above-normal rainfall in large parts of Western Europe. The highest national percentages were 139% of normal in Ireland and 119% in both Belgium and Luxembourg. July 2023 was the wettest July on record for Ireland, which saw 203% of its average for the month. Autumn was also wetter than normal across most of the region, with totals generally about 120%–170% of normal.

(iii) Notable events and impacts

On 17 February 2023, Storm Otto passed over western Europe. Gusts of up to 150 km h^{-1} were measured in certain regions of Scotland and northeast England.

During 21 January to 21 February (32 days), no measurable rain (>1 mm) on average fell in France, the longest such occurrence since records began in 1959 and surpassing the dry period of 17 March to 16 April 2020 (31 days).

Storm Juliette hit southern France on 26 February. In combination with cold airflow from the northeast, 5 cm–10 cm of snow fell between the Provence and Languedoc regions above 300 m altitude. In addition to the snow, the wind was strong over the south and southeast of France on 26 February, with up to 161 km h^{-1} in Cap Béar (a coastal station near the eastern Pyrenees) or 122 km h^{-1} in Avignon (Provence).

Southeastern parts of France, notably the regions close to the Mediterranean, were dry in April. Precipitation totals for the first half of April were 5 mm–20 mm on the eastern Mediterranean coast and less than 5 mm on the western Mediterranean coast.

A summer storm (Poly) impacted the Netherlands and northern Germany on 4–5 July, with heavy rainfall and strong winds, including the highest summer wind gust ever recorded in the Netherlands.

A heatwave occurred during 17–24 August across all of France. This marked the longest heatwave in the country this late in the year as well as the most intense, especially in the southern half of the country.

In late October, Storm Babet brought heavy, widespread, and persistent rain to the United Kingdom, causing serious flooding problems. The Met Office issued two red warnings for rain for eastern Scotland. November began with Storm Ciaran affecting the southern United Kingdom and western France, bringing strong winds and flooding to the region. In December, Storms Elin (Vanja), Fergus (Walter), Pia (Zoltan), Gerrit (Bodo), and Geraldine (Costa) brought strong winds, flooding, and disruption to Ireland, the United Kingdom, southern Scandinavia, the Netherlands, Belgium, and northern Germany.

3. CENTRAL EUROPE

This region includes Germany, Switzerland, Austria, Poland, Czechia, Slovakia, and Hungary.

(i) Temperature

In 2023, every country in this region reported its warmest or second-warmest year on record. Annual anomalies ranged from +1.2°C to +1.5°C.

Winter temperatures were above average, with anomalies of +2.8°C in Hungary, +2.2°C in Slovakia, +1.9°C in Czechia, +1.5°C in Germany and Austria, +2.0°C in Poland, and +1.3°C in

Switzerland. In Slovakia, 1–2 January marked the highest temperatures on record for that month. In Czechia, at the Javorník station, the maximum January temperature reached 19.6°C, the highest on record. Poland also recorded its highest January maximum temperatures.

In spring, all countries of the region had near-normal temperatures. Switzerland was the only country with a positive seasonal anomaly (+0.3°C), whereas the highest negative anomaly was in Czechia (−0.4°C). April was particularly colder than normal, with an anomaly of −2.1°C in Czechia. The average April temperatures hit record lows in Slovakia's highest mountains, notably on Lomnicky štít (−6.5°C, 1.8°C below normal), Chopek (−3.7 °C, 2.0°C below normal), and Skalnaté Pleso (−1.0°C, 2.2°C below normal).

Central European countries experienced above-normal temperatures during the summer, though in different intensity. Switzerland was 1.6°C above normal, marking its fifth-warmest summer on record. Anomalies were lower towards the north and east east of the region, and lowest in the eastern countries (Poland and Hungary: +0.8°C; Slovakia: +0.7°C). The region was affected by heatwaves originating in southwestern Europe, which weakened towards the northeast, and also by foehn effects in the Alpine region.

Autumn was the warmest or second warmest on record within Central Europe. Seasonal mean temperatures were more than 2°C above normal across almost the entire region. The highest anomaly was in Hungary at +2.6°C. September was particularly warm, with anomalies mostly between +3°C and +4°C in Central Europe and even higher locally. The anomalous warmth continued in October, particularly in the southeastern region. November had near-normal temperatures, and December 2023 was once again warmer than normal.

(ii) Precipitation

Above-average annual rainfall was observed in all parts. Germany reported 121% of its normal precipitation (especially high in the northwest), Poland 107%, Slovakia and Hungary 125%, Czechia 107%, Austria 117%, and Switzerland 112%.

During winter, the region experienced contrasting conditions. The average precipitation total for winter 2022/23 in Germany was 95% of normal, Austria received 92% of its normal, and Switzerland 69%. In contrast, winter precipitation was higher than normal in Poland (at 131%, its fourth-wettest winter on record), as it was in Slovakia (161%) and Hungary (151%), while it was near normal in Czechia (103%).

Spring precipitation was close to average or higher. Austria received 127% of its normal precipitation in spring, Germany 115%, Czechia 104%, and Slovakia 102%; Poland received 90% of its normal. April 2023 saw remarkable rainfall patterns across Austria. Precipitation was above normal in almost all regions, a phenomenon not observed since April 2017. The average precipitation total was 178% of normal, making April 2023 one of its 10 wettest April months since the mid-nineteenth century.

Summer precipitation varied across Central Europe. Switzerland was drier than normal (91% of normal). June in particular contributed to the dryness, with precipitation <61% of normal across large parts of the country and even <30% in some areas, including the Lake Constance area. Other countries experienced surpluses in summer precipitation, ranging from 103% of normal in Poland to 109% in Hungary.

Autumn was wet across the region, with rainfall totals ranging from 103% of normal in Czechia to 150% in Switzerland. Germany recorded 258.1 mm, which is 135% of its normal. Rainfall patterns varied by month. September was dry in the region, but its deficit was overcompensated by surpluses in October and November. November 2023 was the second-wettest November in Germany since the start of the record in 1881, as monthly precipitation was around 200% of normal there as well as in Czechia and Slovakia. Northern Switzerland received as much as 300% of its normal in November.

(iii) Notable events and impacts

On 4 February, a new daily average temperature record for winter was set in southern Switzerland at the Magadino/Cadenazzo station (15.1°C, measurements since 1959). Strong winds also occurred farther east in Hungary on the same day. At the Kab Mountain station in

Bakony, a gust of 129.6 km h^{-1} was measured, setting a new national daily record for maximum wind gust for 4 February.

The night of 7 February was very frosty in southern Poland after a cold front passage from the northwest; the minimum temperature dropped to –17.7°C in Zakopane. Severe frosts also occurred that same day in Slovakia, where minimum temperatures of –22°C to –23°C—the lowest temperatures of that winter—were measured in northern and central regions.

The station Rheinfelden in southwestern Germany set a new high temperature record for the first half of March, which was strongly influenced by foehn winds, with 13 March 2023 seeing 23.9°C. Several stations in Switzerland (e.g., Basel with 23.4°C) were also record warm. For the first recorded time in March, all stations below 2000-m altitude in Austria remained frost-free on the night of the 24th. The minimum temperature on 24 March was also record high in Czechia.

On 7 June, flooding in Hungary was reported due to impacts from a low-pressure system. The same system also affected southern and central Germany with up to 119 mm of precipitation falling in two hours in the Hessen region (central Germany) on 8 June. The return time for such an event is more than 100 years.

In Switzerland, new maximum temperature records for August were set at numerous measuring stations, and the 0°C level rose to a local all-time record-high altitude of 5298 meters on the night of 21 August in a balloon sounding from Payerne (measurements began in 1954). Thus, the heatwave occurred not only on the ground but also became record warm in the middle troposphere at an altitude of about 5.5 km (500-hPa level).

In early December, Storm Ciro brought snowfall across central Europe, which particularly affected southern Germany, Austria, Switzerland, Czechia, northern Italy, and Croatia and caused widespread travel disruptions in those regions. The Bavaria region (southeastern Germany) experienced its heaviest snowfall in 20 years, with approximately 50 cm accumulating in some areas.

4. IBERIAN PENINSULA

This region includes Spain and Portugal (peninsular mainland only). The reference period for Portugal is 1981–2010.

(i) Temperature

The year 2023 was the second warmest on record for Spain and Portugal, with the countries seeing anomalies of +1.3°C and +1.0°C, respectively. Spain saw above-average temperatures in winter 2022/23, marking the 10th-warmest winter since records began in 1961 and the fifth warmest in the twenty-first century. Winter was the eighth warmest in Portugal since the start of its record in 1931 (+1.1°C anomaly).

Spring 2023 was the second-warmest spring in Portugal (+1.9°C) and record warmest in Spain (+1.8°C). Spain had its third-highest summer temperature in 2023, after 2022 and 2003, at 1.3°C above normal. In Portugal, summer ranked as its sixth warmest on record, at 1.1°C above normal.

Autumn brought unusually high temperatures, with an anomaly of +1.9°C for Spain, its second-highest autumn temperature on record. In Portugal, it was the fourth-warmest autumn in the past 93 years, with an anomaly of +1.3°C. October 2023 was the second-warmest October on record in Portugal.

(ii) Precipitation

In 2023, the Iberian Peninsula had below-average rainfall. Spain recorded an average precipitation total of 536.6 mm, only 84% of its 1991–2020 normal. This marked the sixth-driest year since records commenced in 1961 and the fourth driest of the twenty-first century. Portugal recorded 735.1 mm, which was 87% of its normal.

During winter in Portugal, the total precipitation amounted to 364.2 mm (153% of normal). In mainland Spain, winter precipitation was 194.5 mm (103% of normal). Spring in Spain was drier than normal, with an average of 95.4 mm over Spain (53% of normal), its second-driest such period on record, behind 1995. Portugal observed its third-driest spring on record (99.9 mm, 49% of normal), with the driest being 2017. Throughout the season, all months saw below-normal precipitation in Portugal, particularly in April and May. April was the third driest on record.

Summer was wetter than normal, with an average precipitation total over Spain of 87.2 mm (124% of normal). This was the 16th-wettest summer on record and the third wettest of the twenty-first century, following 2010 and 2018. Summer was near normal for Portugal, receiving 54.6 mm of rain (104% of normal). June was wetter than normal, but rainfall was below average for July and August.

Autumn precipitation was above normal for both Portugal and Spain, at 410.3 mm (141% of normal) and 243 mm (121%), respectively. This marked the ninth-wettest autumn for Portugal (with a record-wet October) and the 17th wettest in mainland Spain, as well as the fifth wettest of the twenty-first century. On the Balearic Islands, however, it was the third-driest autumn since the beginning of the series, behind 1983 and 1981.

(iii) Notable events and impacts

On 28 February, Storm Juliette brought snow and wind gusts to Mallorca. The storm blocked roads, caused a power outage, and created torrents of water from melting snow.

On 11 March, Castelló de la Plana in the Valencia region of Spain set a new March record for daily maximum and minimum temperatures, reaching 30.8°C and 19.4°C, respectively. The subsequent two days were the warmest for those dates since 1950 across Spain. Record-breaking temperatures were recorded on 13 March, with Xàtiva reaching 33.1°C and Valencia Airport measuring 31.9°C. Towards the end of March, temperatures rose to over 34°C in the Murcia and Valencia regions. On 23 March, the heat triggered a large wildfire in eastern Spain, burning over 4000 hectares of land and necessitating the evacuation of more than 1800 people. The fire spread rapidly due to strong winds and dry conditions.

Three heatwaves hit Portugal's northern and central inner regions in April; 60% of the meteorological stations in the National Meteorological and Hydrological Services (NMHS) network recorded maximum air temperatures above their historical records.

Similar to other parts of Europe, northern Spain was affected by cold air in the first week of April. Several places in that region reported new local minimum temperature records as low as –8°C.

Spain saw extremely dry conditions in April. Much of the country received less than 10 mm of rainfall throughout the month, with some regions in the southeast remaining entirely dry. The monthly rainfall was less than 25% of normal in several places.

Towards the end of May, Spain received heavy rainfall following a continued spring drought, especially in the southeast. From 23 to 24 May, the areas of Andalusia, Murcia, and Valencia saw 48 hours of unprecedented rainfall that caused flash floods, which in turn forced the closure of several highways and schools.

A strong summer heatwave occurred in Spain during the final week of June, peaking at 44.4°C in El Granado (Andalusia). Extreme heat was also experienced during this time in Portugal, peaking at 42.7°C on 25 June.

On 11 July, another heatwave began and spread from southwestern Europe to the Alps. In Spain, two July maximum temperature records were broken: Albacete (air base) recorded 42.9°C, its highest since 1940, while Daroca (Zaragoza) reached 40.6°C, marking the first time that temperatures surpassed 40°C in July in over a century in this location.

August was hot, with two heatwaves occurring over the Iberian Peninsula. In Portugal, Santarém reached the highest recorded maximum temperature of 46.4°C. In several parts of mainland Spain, temperatures rose to 45.0°C and above. On 10 August, a new local all-time heat record of 46.8°C was recorded at Valencia airport, exceeding its typical August temperatures by almost 10°C.

Another heatwave occurred between 24 September and 13 October, which was the most intense heatwave in Portugal in autumn since 1941. Above-average temperatures were recorded at 26% of meteorological stations across the country.

Drought affected Portugal, with the south—particularly the Algarve and Baixo Alentejo—experiencing more severe and extreme conditions, especially from April to August.

5. THE NORDIC AND BALTIC COUNTRIES

This region includes Iceland, Norway, Denmark, Sweden, Finland, Estonia, Latvia, and Lithuania.

(i) Temperature

Annual temperatures in the northern Nordic countries were near average. Iceland and Norway had marginally below-average temperatures (−0.1°C anomaly), whereas Sweden and Finland had temperatures slightly above average (+0.2°C and +0.3°C, respectively). Anomalies were higher towards the south, with Denmark recording +0.6°C, Estonia +0.8°C, Latvia +1.0°C, and Lithuania +1.3°C. Latvia and Lithuania both experienced their third-warmest year on record.

Winter 2022/23 had above-normal temperatures across the region, particularly in its eastern parts. Finland recorded the highest anomaly at +2.1°C, whereas the other countries were mostly around 1°C warmer than normal, with Norway only 0.3°C above normal. Iceland, however, was 1°C colder than normal, marking its coldest winter since 1995. January was particularly mild in eastern parts of the region, with a monthly anomaly of +3.3°C in Lithuania and +2.0°C in Estonia.

Temperature anomalies in spring varied across the region. Normal- to below-normal temperatures occurred in the Nordic countries: Denmark saw 0.0°C, Norway −0.8°C, Finland −0.1°C, and Sweden −0.3°C. In contrast, Estonia and Latvia observed above-normal temperatures, with both recording anomalies of +0.9°C and reporting their 10th- and 11th-warmest springs, respectively. Spring in Iceland was slightly colder than normal on average due to an exceptionally cold March, which was the coldest since 1979.

Summer was warmer than normal across most of the region. It was the eighth-warmest summer on record for Norway, which had an average temperature of 1.1°C above normal. The other Nordic and Baltic countries had smaller deviations from normal, with national averages of between +0.0°C and +0.8°C. June was particularly warm (+2.5°C in Sweden, +2.6°C in Norway), as was August in the north and east of the region. July, however, was cooler than normal across the region.

Temperatures in autumn were above normal in Iceland (+0.2°C), Denmark (+0.8°C), Lithuania (+1.3°C), Estonia (+0.7°C), and Latvia (+1.1°C). Conversely, Norway, Finland, and Sweden reported below-average temperatures due to Arctic cold air outbreaks in October and November, with seasonal anomalies of −1.1°C, −0.7°C, and −0.5°C, respectively. September marked record warmth in several places, including Finland (+3.2°C anomaly), Denmark (+2.7°C), Sweden (+2.7°C), Lithuania (+3.7°C), Estonia (+3.4°C, the warmest since 1922), and Norway (+1.3°C, fifth warmest on record).

(ii) Precipitation

In 2023, precipitation varied across the region, with totals significantly above normal in most of the Nordic countries. Denmark recorded 129% of its normal precipitation, making it the wettest year on record. Sweden and Finland saw their fourth- and eighth-wettest year on record, respectively, with around 110% of normal precipitation. In Latvia, 2023 was also wetter than normal (112%). For Norway, Lithuania, and Estonia, precipitation totals were between 103% and 105% of normal, while drier-than-normal conditions occurred in Iceland (91%).

Winter 2022/23 saw mostly near-normal or above-normal precipitation across the region, except for Iceland, which received below-average amounts. Denmark experienced a significantly wetter-than-normal winter with 132% of normal precipitation, marking its eighth-wettest winter on record. January was particularly wet, with Denmark and Latvia receiving 191% and 156% of average rainfall, making it their wettest and third-wettest January on record, respectively.

Spring 2023 was mostly drier than normal across the region, particularly in the Baltic countries, which received only 72% to 78% of their normal precipitation. March was wet across most parts of the region, particularly in Finland and Latvia, which observed their second- and seventh-wettest March on record. May, in contrast, was dry. With only 28%, 31%, and 24% of normal precipitation, respectively, it was the third-driest May on record for Estonia, the second driest for Lithuania on record, and the driest on record for Latvia.

Summer was wetter than normal across most parts of the region. Denmark received 128% of its normal precipitation, mainly due to the wettest July on record for the country (215% of normal).

Norway observed its fourth-wettest August (145% of normal). In Lithuania, a wet August (168% of normal precipitation) compensated for much-drier-than-normal conditions in June and July (both 65% of normal).

Autumn was notably wet in the region, except for in Norway and Iceland. Finland experienced its fifth-wettest autumn (126% of normal), with September being its wettest on record (160% of normal precipitation). Denmark experienced its seventh-wettest autumn (132% of normal), with October seeing its fifth wettest on record (179% of normal).

(iii) Notable events and impacts

On 10 March, a high-pressure period contributed to low temperatures in the Baltic countries, with Lithuania observing a minimum of –19.4°C and Latvia experiencing its strongest frosts since December 2021. Temperatures in the interior of Estonia fell below –25°C on 10 March, with the lowest recorded at Tiirikoja (–26.3°C).

Norway experienced large snow accumulations, with some places receiving over 40 cm of snow in a single day, even in the south. Kristiansand in southern Norway recorded a remarkable snow depth increase from 3 cm to 49 cm on 17 March, marking the third-largest snowfall in March since measurements began over 100 years ago.

Another cold wave and snow storm impacted the region during 23–28 March and was most intense in Scandinavia. Tromsø in northern Norway registered a new March record for accumulated daily fresh snow depth with 179 cm, and southeastern Sweden saw significant snow accumulations, with Vattholma near Uppsala measuring 40 cm on 28 March.

Northern Norway saw snow on 1 June, with Tromsø recording –0.6°C, the first temperature below 0°C in June since 1997. Sweden and Finland also experienced some of their lowest June temperatures in decades. In early June, a countrywide cold spell hit Finland, with Saana, at an altitude of 1001 m, recording a historic low temperature of –7.7°C on 1 June, marking a new June record for the country.

A major storm passed through northern Europe on 6–8 August, bringing heavy rain, thunderstorms, and strong winds that caused floods, landslides, and casualties in Norway, Denmark, Sweden, Finland, Estonia, Latvia, and Lithuania. Record-breaking precipitation and wind speeds were reported, with significant damage to infrastructure and widespread power outages affecting thousands of households. In Estonia, a hailstorm on 7 August damaged cars, roofs, and greenhouses. The largest hailstones measured a diameter of 8 cm, the biggest on record for the country.

On 8 August, northern Europe experienced record-breaking maximum temperatures, with northern Norway reaching 30.3°C, northern Sweden observing 31.1°C in Haparanda, and Finland recording 33.2°C in Pori. On 17 August, Lithuania set a new national maximum record of 34.6°C.

In early September, northern Europe experienced a heatwave caused by an omega blocking pattern. In Norway, temperatures soared to 28.3°C in Etne, Vestland, potentially setting a new September record. Additionally, four stations in Sweden recorded new local September records (up to 27.6°C). On 12–13 September, new daily maximum temperature records were recorded at several stations in Estonia.

The nationwide average mean temperature in Denmark and Finland in September was the highest since the start of the record in 1874 and 1900, respectively; however, the period from October to December was characterized by a long cold spell in Fennoscandia, which saw below-normal temperatures during all three months. In Finland, October–December was the coldest such period since 2010. At the end of December, the sea ice extent in the Bay of Bothnia was at its largest since 2010.

6. CENTRAL MEDITERRANEAN REGION

This region includes Italy, Monaco, Malta, Slovenia, Croatia, Serbia, Montenegro, Bosnia and Herzegovina, Albania, North Macedonia, Greece, and Bulgaria.

(i) Temperature

Slovenia, Croatia, Serbia, Malta, Bulgaria, and Montenegro each experienced their warmest year on record in 2023, while Italy recorded its second warmest. All other countries in this region

experienced consistently above-average temperatures throughout the year, with many recording their highest monthly temperatures in various months.

Winter across the region was warm, with all months seeing temperatures above average. Anomalies were highest in Bulgaria (+3.0°C) and lowest in Malta (+0.3°C). Bulgaria reported its warmest winter on record, and Serbia observed its third warmest. January was particularly mild; Bulgaria's monthly average was 4.4°C above normal and Serbia's was 3.9°C above normal.

Spring saw mostly near- to below-normal temperatures across the region. Bulgaria reported its coldest May since 2005. North Macedonia, Slovenia, and Serbia recorded anomalies below normal for the season (−0.5°C, −0.05°C, and −0.3°C, respectively). Italy, Croatia, and Montenegro saw temperatures slightly above average, with anomalies ranging from +0.08°C to +0.3°C. Greece and Malta experienced above-normal temperature anomalies for spring at +1.5°C and +1.0°C, respectively, while mean temperature deviations in Bosnia and Herzegovina ranged from −0.7°C to +0.3°C.

Summer temperatures were mostly around 1°C above normal, with June and July notably warmer than average. July marked the peak of summer anomalies, with Malta and Greece reporting anomalies of +2.7°C and +3.2°C, respectively (the hottest July on record for Malta). Bulgaria experienced its third-warmest summer, at 1.2°C above normal, and its second-warmest July, with an anomaly of +2.2°C. Italy observed its third-warmest July (+2.0°C).

Italy, Malta, Slovenia, Croatia, Serbia, North Macedonia, and Bulgaria all observed their warmest autumn on record, with temperature anomalies ranging from +1.4°C to +3.3°C. September 2023 was the second warmest for Slovenia, third warmest for Italy and Serbia, and fourth warmest for Bulgaria and North Macedonia. Italy, Malta, Slovenia, and Macedonia all recorded their warmest October on record, while Serbia and Bulgaria had their second warmest. Malta reported its second-warmest November.

(ii) Precipitation

In 2023, Slovenia reported 128% of its average, making 2023 the country's third-wettest year. Other countries were closer to normal, from 96% of normal in Bulgaria and Italy to 119% of normal in Serbia.

Winter was wetter than normal in most countries. There was large variability from country to country, from 105% of normal in Slovenia to 146% in Croatia, its neighboring country. Malta received 125% of its normal precipitation. Only North Macedonia and Bulgaria received less-than-normal (85%–95%) precipitation. January was wetter than normal across almost the entire region, as was part of February. Malta observed its second-wettest February on record.

Spring also was a wet season over almost the entire region. The greatest percentages of normal were recorded in Italy (127%), Croatia (139%), and Bosnia and Herzegovina (121%). The only exception was Malta (82% of normal), which had its third-driest March on record. This contrast can be explained by the Azores High pressure zone, which expanded far into the western Mediterranean that month, while the northern Balkans were affected by midlatitude cyclonic systems.

Summer presented contrasting conditions across the region. Slovenia recorded its wettest summer on record (163% of normal precipitation), which included its second-wettest August (209%). Italy received 124% of its normal rainfall, Croatia received 141%, and Serbia 124%. Malta experienced its driest July on record, though it only saw small departures from normal for the entire season.

Autumn precipitation was below normal in Italy (77% of normal) and near normal in most of the Balkans, but with large variability from month to month. September and October were dry months, while November was much wetter than normal. Bulgaria recorded its fourth-driest October, yet its fifth-wettest November, and Serbia observed its seventh-driest October (23% of normal), yet its wettest November (162%).

(iii) Notable events and impacts

Catastrophic floods inundated several Croatian towns in May, including Obrovac, Gračac, Karlovac, Duga Resa, and Hrvatska Kostajnica, leaving numerous buildings submerged and causing contamination of drinking water, extensive damage to infrastructure such as roads

and bridges, and destruction of agricultural land and greenhouses. The floods also triggered landslides and threatened areas already flooded with additional rainfall and water waves from neighboring countries. On 15 May, 256.4 mm was measured in Gračac, which was its highest one-day total on record.

Also in May, heavy rain caused floods and landslides in northern Italy during four major events, particularly in Emilia-Romagna. The Cesena and Avellino Provinces experienced significant flooding. Within 48 hours, during 1–3 May, more than 200 mm were measured at several stations in Emilia-Romagna, marking the most intense spring precipitation event in this area since at least 1961.

On 17 June, Storm Olga's powerful winds and torrential rain caused devastation in parts of the Balkan Peninsula. Greece reported flooding, power outages, and vehicles being washed away, in addition to two fatalities. Houses in Thessaloniki flooded, and crops in western Macedonia suffered harm. Severe weather also affected Skyros Island and the Attica Region. Rivers in eastern Bosnia and Herzegovina overflowed, causing significant crop losses for farmers and prompting Tuzla to declare an emergency.

In July, central and southern Italy experienced an intense heatwave, with temperatures soaring to 8°C–10°C above average in some areas, particularly in the plains and valleys of the Alps and Apennines. Records were broken in Sardinia and Sicily, with temperatures peaking above 47°C on 24 July, reaching 48.2°C in Lotzorai and Jerzu. On 23 August, Milan saw its hottest day since 1763, with temperatures reaching 33°C.

Beginning on 19 August, a large wildfire in the Alexandroupolis municipality in Greece (the largest fire since the start of the record in 2000 in the European Union) destroyed many buildings, forced residents in 13 towns to evacuate, and killed at least 21 people. The fire burnt almost 94,000 hectares by 3 September. Overall, the total area burned in Greece in 2023 was more than four times the long-term average.

Extremely heavy precipitation during 3–6 August in Slovenia (more than 300 mm and locally more than 600 mm) led to six fatalities. The northern and central parts saw over 200 mm of rain in just 12 hours during 3–4 August. This event also caused an unprecedented flood of downstream rivers in Croatia. Koprivnica-Križevci County declared a state of natural disaster on 16 August as a result of flooding in areas including Legrand Municipality along the Drava River.

Widespread and strong thunderstorms impacted northern Italy, resulting in large hailstones 8 cm–10 cm in diameter and strong wind gusts greater than 30 m s^{-1}. On 24 July, a supercell produced record-size hail in the Friuli Venezia Giulia region; in Azzano Decimo, a 19-cm hailstone broke the European record for hail size.

In September, Greece received record rainfall from Storms Daniel and Elias, causing severe flooding in regions including Thessaly and central Greece. Zagora recorded its highest daily rainfall ever in Greece (754 mm in 21 hours, after which the station ceased reporting), resulting in significant damage to infrastructure and homes. This daily total corresponded to a normal annual total for Zagora. Heavy rains from Storm Daniel also affected southeast Bulgaria, western Türkiye, and Libya.

7. EASTERN EUROPE

This region includes Belarus, Ukraine, Moldova, Romania, the European parts of Russia, and West Kazakhstan (i.e., the country's European region).

(i) Temperature

In most places in eastern Europe, 2023 was the warmest year on record, with several individual months also recording their highest-ever temperatures. Annual temperature anomalies varied between +1.4°C in Belarus (third highest on record) and +2°C in Moldova (highest). For Romania and West Kazakhstan, it was the hottest year on record.

Except for West Kazakhstan, whose temperature was slightly below normal (–0.2°C), the region saw an overall mild winter. Romania experienced its warmest winter, with a temperature anomaly of +3.1°C. An even more notable anomaly occurred in January (+5.4°C), making it the warmest January on record in the country. The rest of the region saw seasonal temperature anomalies between +1°C and +3°C.

West Kazakhstan observed its warmest spring on record, with a temperature anomaly of +3.7°C. March was exceptionally warm (6.8°C above normal). In Belarus and Ukraine, seasonal anomalies were +0.9°C and +1.2°C, respectively. Moldova and Romania had near-normal spring temperatures. A heatwave struck many regions of European Russia in May, mainly in the east.

Summer also was warmer than normal, with anomalies of around +1°C in Belarus, Ukraine, and Romania. In Moldova, the average temperatures were 1.2°–1.7°C above normal. August was particularly warm, with maxima reaching 39.5°C and minima dropping to 10°C. Summer in European Russia started with a colder-than-normal June (≥2°C below normal in some places) and July; only August was warmer than normal.

Autumn was warmer than normal for the entire area. Romania saw its warmest autumn on record, at 2.8°C above normal. October 2023 was the country's warmest October on record, at 3.9°C above average, while September was its second-warmest September on record, at +3.4°C. Similar to Romania, Moldova saw an unusually warm autumn, with temperatures 2.8°C to 3.8°C above normal. Moldova also reported its warmest October, with temperatures 3.4°C to 5.0°C above normal. In Belarus, September was the warmest on record, with an anomaly of +3.5°C.

(ii) Precipitation

In Eastern Europe, the year as a whole had near-normal precipitation, but with locally higher annual totals. Precipitation in Belarus over the year was above average, while Moldova was characterized by below-normal precipitation, especially from August to October. Ukraine received 108% of its normal. West Kazakhstan had its sixth-wettest year, with 135% of its normal.

Winter 2022/23 was the wettest for Belarus since the start of observations in 1945, having recorded precipitation that was 152% of normal. Western Ukraine and western Romania also received above-normal precipitation, whereas winter was drier than normal around the Black Sea (Moldova, eastern Ukraine, and southwestern European Russia). Moldova received just 65% of its normal seasonal precipitation.

Spring precipitation was characterized by high spatial variability. The seasonal total in Moldova was 136% of its normal, with April 2023 being the country's wettest April on record. Its neighboring country, Romania, had a drier spring than usual, with precipitation that was 88% of its normal. May was the driest month of the season, seeing 68% of normal rainfall.

Summer was wetter than normal in Ukraine—44 mm above normal in Kyiv and 66 mm above normal in Kharkiv. West Kazakhstan received 132% of its normal precipitation for the season, as it observed its sixth-wettest July (219% of normal). Conversely, it was significantly drier than average during summer in Moldova (46% of normal); the country observed its second-driest August on record (4% of normal).

Autumn was mostly wetter than normal. Belarus experienced a rainy autumn, with a surplus of 189 mm of precipitation over the season (123% of normal). In some southern regions, totals did not exceed 5 mm, while in northern regions, 50 mm–90 mm fell (60%–100% of normal). West Kazakhstan observed its fifth-wettest autumn on record, including its second-wettest October (172% and 226% of normal, respectively).

(iii) Notable events and impacts

On 1 January, Belarus experienced its highest nationally averaged maximum January temperature on record, at 16.4°C. In the Ukraine, 1–2 January were the warmest January days since record keeping began in those countries, where several stations broke their records. Also on 1 January, Romania recorded a new monthly national high temperature of 22.5°C, surpassing its previous record set in January 2001. This "New Year warm event" occurred also in Central Europe (section 7f3). Moreover, on 19 January, the Băneasa borough of Bucharest recorded its highest daily January temperature on record (20.9°C). Average temperatures in Bulgaria, Romania, and Moldova were 15°C–17°C higher than usual.

On 13–14 June, severe weather and flooding in Krasnodar Krai, including Sochi, Russia, caused the Mzymta and Matsesta Rivers to break their banks, causing damage to four houses and dozens of roads.

On 6 July, Moldova and Ukraine experienced subtropical heat, with temperatures exceeding 38°C in Kherson and Kryvyi Rih and a daily minimum temperature of 23.4°C recorded in Odesa.

On 8 July in southern European Russia, some stations recorded daily maximum temperatures of up to 42.1°C, which was recorded at Baskuncak, close to the Kazakhstan border.

On 30 July, Russia's eastern and central regions were struck by intense rain and wind, which caused damage and at least 10 fatalities and 76 injuries. Thousands of residents in the Mari-El Region lost electricity as a result of the catastrophic weather event that happened near Lake Yalchik.

On 20 August, heavy rain (43 mm) caused flash flooding in Moscow, Russia, resulting in four fatalities.

8. MIDDLE EAST

This region includes Israel, Cyprus, Jordan, Lebanon, and Syria.

(i) Temperature

In 2023, the Middle East experienced above-normal annual temperatures. Israel and Jordan observed their third- and fifth-warmest year on record, with temperature anomalies of +1.0°C and +0.85°C, respectively. Cyprus also had its fifth-warmest year, at 1.25°C above normal.

During winter 2022/23, Israel and Cyprus experienced above-normal temperatures, with anomalies of +0.8°C and +1.2°C, respectively. In Cyprus, January was the fifth warmest on record, while February was second coldest (anomaly of −0.8°C). In February, Lebanon faced severe winter conditions, including snow in high altitudes, rain in lower regions, thunderstorms, and strong winds.

Spring was characterized by variability across the region, with temperatures having generally been slightly above normal. Israel recorded a temperature anomaly of +0.3°C, but only March was moderately warmer than normal. Cyprus recorded a spring temperature anomaly of +0.7°C, while Jordan and Syria recorded anomalies of +0.3°C and +0.4°C, respectively. Lebanon also experienced a mild spring, at 0.5°C above normal.

Jordan observed a summer temperature anomaly of +1.3°C, along with an August that was 2.4°C above normal. In Israel, summer 2023 was the fifth warmest on record, with its July and August having been second and fifth warmest, respectively. Cyprus reported a summer temperature anomaly of +0.85°C.

Autumn was notably warmer than usual across the region, with anomalies surpassing +1.0°C. In most regions, November had the highest monthly anomaly, exceeding +2°C. Israel recorded its third-warmest autumn and third-warmest September, while Cyprus had its second-warmest October, along with a September and November that were both fourth warmest. In the remaining areas of the region, November also had the highest temperature departures from normal among the autumn months.

(ii) Precipitation

Overall, precipitation totals in 2023 for most places and months were near or below normal. Israel received 521 mm of precipitation in 2023 (98% of normal). Total precipitation in Cyprus was 414 mm (82% of normal). Lebanon and Syria were also drier than normal (numbers were not available).

Winter 2022/23 was dry in the Middle East, with all regions recording below-normal rainfall. Israel and Cyprus received 75% and 64% of their seasonal averages, respectively. January was notably dry in Israel, with just 54% of average precipitation, marking its eighth-driest January on record. The total precipitation in winter was 65% of normal in Jordan, 53% in Syria, and 58% in Lebanon.

Spring was significantly wetter than normal in Israel, with 161% of normal precipitation, marking the eighth-wettest spring on record along with the fifth-wettest April. The total precipitation in Cyprus was normal (101%). Jordan experienced particularly high rainfall totals during spring, recording 289% of its normal for the season, with all months much wetter than normal. Syria received 131% of its normal spring precipitation, while Lebanon recorded slightly below-normal precipitation (96% of normal).

Summer was wetter than normal in Cyprus, with 108% of the seasonal normal precipitation. Total precipitation was 150% of normal in Syria, 204% in Lebanon, 263% in Israel, and 334% in Jordan; however, summer is the dry season in the eastern Mediterranean, and typical rainfall

amounts are low. In Israel, for example, the long-term average for June is 0.5 mm–3 mm. For July and August, it is less than 0.5 mm.

In general, the wet weather pattern continued into autumn, with September experiencing normal to above-average rainfall in the region. Most areas recorded precipitation levels above the seasonal average. Israel reported 110% of its normal precipitation, and Cyprus experienced 159% of its normal. Particularly noteworthy were Jordan and Syria, which recorded 272% and 294% of their normals, respectively.

(iii) Notable events and impacts

In January, Cyprus set a new record as the temperature at the Tepak station rose to 25.5°C due to foehn winds from the Troodos Mountains. This marked the highest temperature recorded for January in Cyprus.

In early February, Israel experienced the impact of Storm Barbara, which brought strong winds, heavy rains, and snow to the region. Wind speeds peaked at 50 km h^{-1} to 70 km h^{-1}, with gusts surpassing 100 km h^{-1}, notably reaching 119 km h^{-1} in Zefat Har Kena'an. Rainfall totals ranged from 80 mm to 150 mm in northern and central Israel. Snowfall was concentrated in the northern and central mountains, with depths exceeding 2 m on Mount Hermon and over 20 cm in the high peaks of the Golan Heights.

During 8–11 February, a massive flooding disaster occurred close to Idlib in northwest Syria. After heavy rainfall, the river's water level was high. Approximately 7000 individuals were forced to evacuate their homes as flooding submerged them.

In late March, a heatwave hit Jordan, particularly the Jordan Valley, resulting in maximum temperatures surpassing 35°C for 13 consecutive days. Ten station records were broken during this period.

During 10–12 April, heavy rain fell in the extreme south of Israel, namely in the southern Negev region. This led to river overflows and flash floods, which caused fatalities and property damage. The cities of Eilat and Paran as well as the Aravah region were the most severely hit, with at least two fatalities recorded.

On 30 May, heavy rain and hailstorms affected various parts of Jordan, causing fatalities, destruction, and flash floods. The capital city, Amman, along with Salt, Madaba, and Irbid experienced significant hailstorms that caused extensive damage.

In July, a heatwave impacted the Middle East, with Israel's Jordan Valley experiencing maximum temperatures of 43°C–46°C. It was unusual for the Middle East region to see a heatwave lasting longer than two weeks. Another noteworthy summer heatwave occurred during 12–20 August. The nights were very warm, especially in the coastal plain and the northern valleys, with an unprecedented consecutive seven to eight nights with minimum temperatures of 26°C–29°C. The Euphrates River's water level reached a historic low at Tabqa Dam in Syria, affecting nearly one million residents in the Hassakeh governorate. As a significant hydroelectric dam, it is crucial for water regulation and electricity production. The crisis impacted daily life, agriculture, and health, and increased occurrences of waterborne diseases.

A heatwave impacted Israel during 5–8 September; temperatures peaked on 8 September with 40°C recorded across the country: 40°C–42°C in the coastal plain, 42°C–44°C in the northern Negev, and 45°C–46°C in some locations of the Jordan Valley and the Arava. Several stations broke their September records, including Besor Farm (44.3°C), which surpassed its previous high of 43.6°C, and Negba (42.8°C), which exceeded its previous record of 42.4°C.

On 20 October, a warming trend began, leading to a heatwave from 21 October to 13 November. Temperatures reached 32°C–35°C in the coastal plain, northern Negev, and valleys, 35°C–39°C in the Arava, and 28°C–32°C in the mountains. Such a long heatwave that late in the year has only occurred two to three times since the early 1900s.

9. TÜRKIYE AND SOUTH CAUCASUS

This region includes Türkiye, Armenia (which has a reference period of 1961–90), Georgia, and Azerbaijan.

(i) Temperature

In Armenia, 2023 was the third-warmest year since 1935, with a temperature that was 2.2°C above the 1961–90 normal. This year was also the third warmest in Türkiye since 1971, surpassing its normal by 1.2°C.

Winter 2022/23 in Armenia was the third warmest since 1935. The average winter temperature of –3.9°C was 1.6°C above average. Türkiye's winter mean temperature was 5.5°C, 1.6°C above normal; the January mean temperature was 5.3°C, surpassing its monthly normal by 2.4°C, making it the second-warmest January for the country since 1971.

In Türkiye, the average spring temperature was 12.8°C, which was slightly above normal (+0.4°C). In Armenia, it was the second-warmest spring on record, behind only 2018. The average temperature was 7.1°C, 2.8°C above normal.

Summer 2023 in Armenia was one of the warmest on record. The average seasonal temperature reached 17.3°C, which was 1.5°C above normal. August was particularly warm, with the average monthly temperature having been 3.1°C above normal, marking the third-warmest August following 2006 and 2017. In Türkiye, the summer mean temperature was 24.7°C, 0.7°C above normal.

Autumn in Armenia was the fifth warmest since 1935. The average seasonal temperature was 9.3°C, which was 2.1°C above normal. November was the warmest on record, with the average monthly temperature 3.7°C above normal. The average autumn temperature in Türkiye was 17.4°C, which was 2.1°C above normal. November 2023 was also the warmest November on record for the country.

(ii) Precipitation

In Armenia, the total annual precipitation for 2023 was 577 mm (97% of its normal). The mean precipitation for Türkiye was 641.5 mm (112% of its normal). In Türkiye, precipitation was below average in the Marmara region, west of Ankara, Çankırı, Kırıkkale, Muğla, eastern and western parts of Antalya, Mersin, Adana, Osmaniye, Hatay, southeastern Anatolia, and eastern parts of eastern Anatolia. Total precipitation was just 40% of normal in Hatay.

During winter in Armenia, precipitation levels were 34%, 22%, and 97% of normal for December, January, and February, respectively. Türkiye also experienced below-normal precipitation throughout the winter, with all months receiving below-normal precipitation.

In Armenia, spring precipitation was near-normal, with May being the exception (81% of normal). Conversely, spring precipitation for Türkiye was above average. In March, Türkiye recorded 95.5 mm of rain (165% of normal). Additionally, precipitation totals for April and May were 151% and 127% of normal, respectively.

Summer 2023 was wet in Armenia, with seasonal precipitation reaching 169.7 mm (114% of normal). June and July had above-normal precipitation totals at 135% and 117% of normal, respectively. However, August saw a dry spell, with a monthly precipitation that was only 68% of normal. In Türkiye, June and July also had significant above-normal precipitation. The average June rainfall total was 58.1 mm (173% of normal).

The seasonal precipitation in autumn was 122.7 mm in Armenia (103% of normal). Only September had above-normal precipitation (153% of normal). Precipitation was below average in October and November, at 89% and 86% of normal, respectively. Across Türkiye, autumn precipitation exceeded the normal by 23% and by 69% compared to the previous year's autumn season.

(iii) Notable events and impacts

On 20 January, new local monthly records were set in Türkiye in high elevations at Bingol (1120 m a.s.l.; 13.8°C) and Erzurum (1800 m a.s.l.; 9.1°C), as well as in Samsun on the Black Sea coast (24.2°C) on 22 January.

On 15 August, a new national high-temperature record for Türkiye was set at 49.5°C in Eskisehir, northwestern Türkiye.

The province of Canakkale in northwest Türkiye was impacted by a wildfire on 22–23 August, which led to damage and evacuations. There were around 4080 hectares of burned land.

During 8–10 July, heavy rain in Türkiye's western and central Black Sea area resulted in flash floods and over 1000 landslides. Over 250 mm of rain fell in one day in the province of Düzce, which is near the western shore of the Black Sea.

Convective hailstorms at Ijevan station in northeastern Armenia resulted in unusually high wind gusts of up to 37 m s^{-1}. Hail diameters reached 3 cm, and rain totals of 30 mm were measured.

On 3 August, a significant landslide in a mountain resort town in northern Georgia (Kvemo Svaneti region) claimed the lives of at least 18 individuals. For many days, more than 400 firemen, helicopters, and drones were used for evacuations and the search for missing persons.

Azerbaijan recorded a temperature of 36.9°C in Baku on 30 May, making it the warmest May day in the city's measuring history.

On 4–5 June, heavy rains in many provinces in Türkiye's Black Sea region including Kastamonu, Samsun, Amasya, and Sinop caused considerable river floods and landslides.

Except for the northern and mountainous areas, most of Armenia experienced drought conditions and a dry spell toward the end of August.

Sidebar 7.3: European drought conditions in 2023

Various parts of Europe were severely impacted by dry conditions in 2023. The incidence and severity of drought varied significantly across different regions and months throughout the year, and each region faced distinct signs of drought and the ensuing effects.

The Combined Drought Indicator (CDI; Fig. SB7.5) shows severe and possibly critical European drought conditions at various times and locations. Southern and eastern Spain, southern France, most of Italy, Malta, eastern Poland, central Romania, southern Greece, Cyprus, and southern Türkiye consistently experienced warning-level drought conditions throughout most months of 2023.

Figure SB7.5a illustrates that France, the United Kingdom, and Ireland were in the warning zone in February. By April, Spain faced severe dry conditions, which were marked as a warning and alert condition (Fig. SB7.5b). This drought persisted into May for Spain, with some parts of Eastern Europe also experiencing drought conditions (Fig. SB7.5c). Drought spread across much of Europe by June, with Spain being notably dry (Fig. SB7.5d); however, July brought wetter conditions to Spain, as drought began shifting towards Central and Eastern Europe (Fig. SB7.5e). In October, Eastern and southeastern Europe, Italy, and France were all under a drought warning, while other regions did not experience drought during this time (Fig. SB7.5f).

Soil moisture indicators show that in April and May (Figs. SB7.6a,b, respectively), soil moisture anomalies in Spain were negative, indicating drier-than-normal conditions due to a combination of low precipitation and high temperatures. However, in other parts of the region, although precipitation

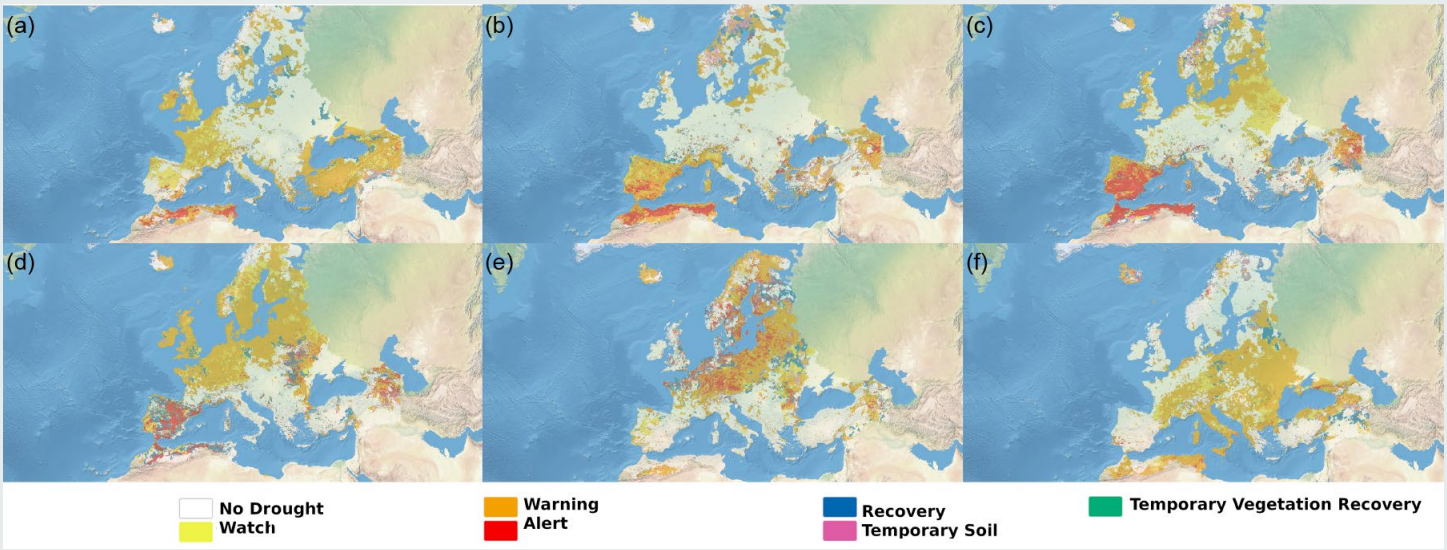

Fig. SB7.5. The Combined Drought Indicator shows drought status based on a combination of indicators of precipitation, soil moisture, and vegetation conditions for (a) mid-Feb, (b) third 10-day period of Apr, (c) third 10-day period of May, (d) mid-Jun, (e) third 10-day period of Jul, and (f) first 10-day period of Oct in 2023. (Source: European Drought Observatory of the Copernicus Emergency Management Service.)

was below normal, soil moisture anomalies remained normal or near normal. By June, the situation shifted: Spain had notably higher soil moisture anomalies, while the United Kingdom as well as Central, Eastern, and Northern Europe experienced negative, dry conditions (Fig. SB7.6c), attributed to lower precipitation in these areas and above-normal precipitation in Spain. In October, southeastern Europe in particular faced drier-than-normal soil moisture (Fig. SB7.6d). December 2023 saw near-normal or wetter-than-normal conditions across most regions except for eastern and southern Spain, which remained dry (Fig. SB7.6e), having received lower precipitation than usual for this month.

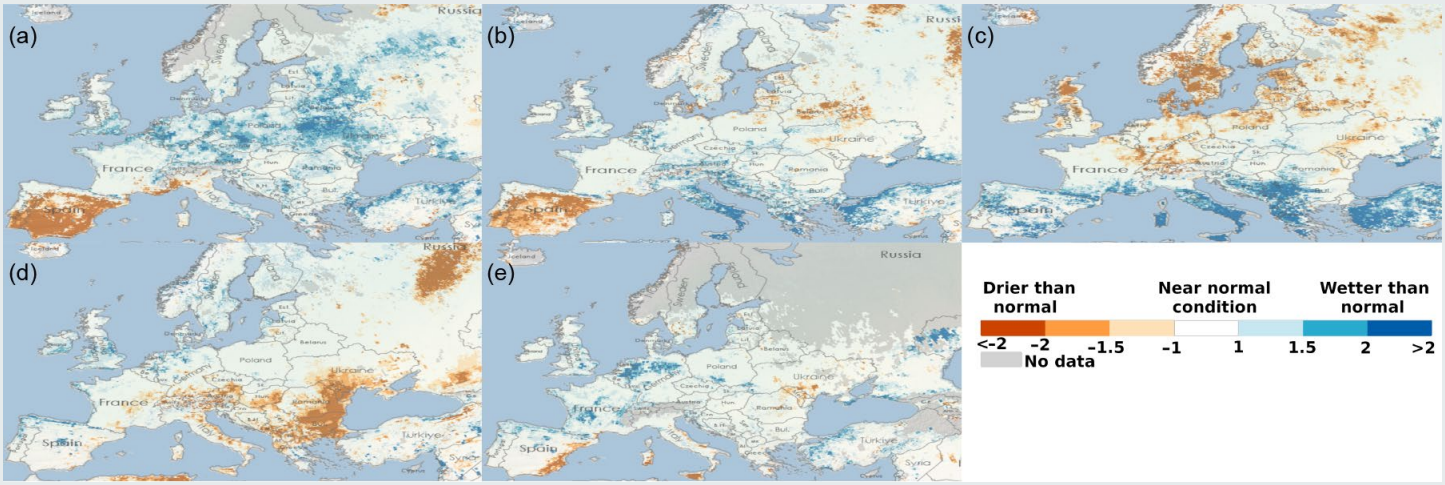

Fig. SB7.6. Soil moisture anomalies for (a) Apr, (b) May, (c) Jun, (d) Oct, and (e) Dec 2023. (Source: European Drought Observatory of the Copernicus Emergency Management Service.)

g. Asia

—Z. Zhu, Ed.

Throughout this section, the base period for the climatological normal and anomalies is 1991–2020. All seasons in this section refer to the Northern Hemisphere, with winter referring to December–February 2022/23, unless otherwise noted.

1. OVERVIEW

—Z. Zhu, P. Zhang, T.-C. Lee, R. Muharsyah, K. Takemura, A. Moise, Y. Okunaka, K. Takahashi, J. I. Seong, D. Dulamsuren, M.-V. Khiem, and H.-P. Lam

Annual mean surface air temperatures during 2023 were above normal across most of Asia and Siberia, except for northwestern South Asia and parts of Eastern Siberia, with anomalies of more than +1°C from Japan to northern China, in eastern Central Siberia, and from Western Siberia to the eastern Middle East (Fig. 7.45). In Central Asia and the Siberian plain, the anomalies were even greater than +2°C. Annual precipitation totals were above normal (>120% of normal) in central Mongolia, in western Central Asia, in and around Pakistan, and in the Arabian Peninsula, and below normal (<80% of normal) in northwestern China and from southern Central Asia to the central Middle East (Fig. 7.46).

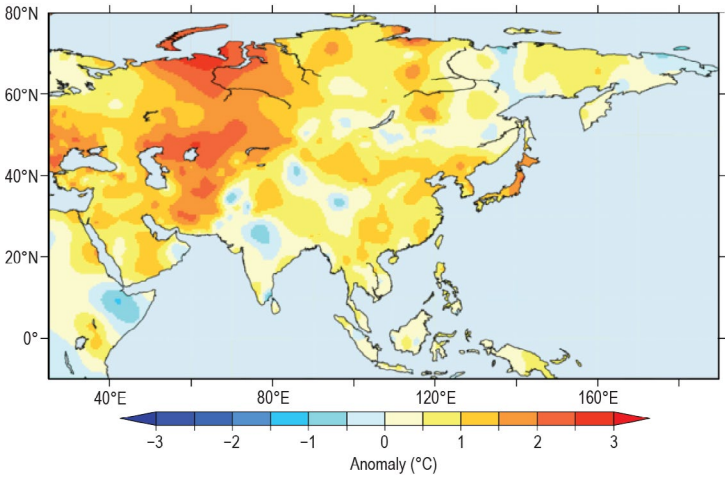

Fig. 7.45. Annual mean surface temperature anomalies (°C; 1991–2020 base period) over Asia in 2023. (Source: Japan Meteorological Agency.)

In winter, positive temperature anomalies were observed in the eastern part of Eastern Siberia, from southern Central Siberia to northern Mongolia, in northern Western Siberia, and from northwestern Southeast Asia to the southeastern Arabian Peninsula, while temperatures were below normal in and around western Eastern Siberia and from western China to southern Central Asia (Fig. 7.47a). Seasonal precipitation was above normal in northeastern Central Siberia, northwestern China, the eastern Indochina Peninsula, southern India, and the central and southern Arabian Peninsula, but below normal from the northern Indochina Peninsula to southwestern Central Asia (Fig. 7.47b).

In spring, temperatures were above normal from central East Siberia to the eastern part of East Asia and northern Western Siberia to the eastern Middle East, while temperatures were below normal in the eastern part of Eastern Siberia, from western Mongolia to western China, and from India to Pakistan (Fig. 7.47c). Seasonal precipitation was above normal in northern and western China and from southern India to Pakistan and below normal from southern China to the Indochina Peninsula, in southern Western Siberia, and from southern Central Asia to the central Middle East (Fig. 7.47d).

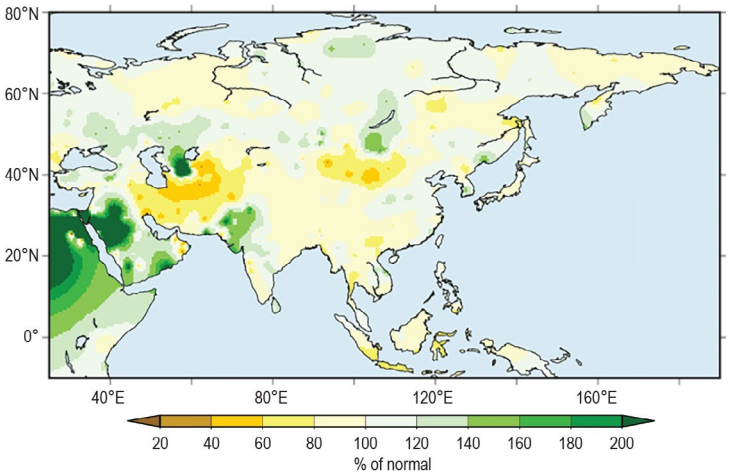

Fig. 7.46. Annual precipitation (% of normal; 1991–2020 base period) over Asia in 2023. (Source: Japan Meteorological Agency.)

In summer, positive temperature anomalies exceeding +1°C were observed from Japan to the northern Arabian Peninsula and from the western part of Eastern Siberia to northern Western Siberia, with some areas reaching +2.5°C. However, temperature anomalies were below –1°C in the northeastern part of Eastern Siberia and in and around Pakistan, with some areas below –2.5°C (Fig. 7.47e). Seasonal precipitation was above normal around Lake Baikal, from Pakistan to Turkmenistan, and in the western

Middle East, and below normal from northern to western China, in the central part of Central Asia, and in and around the eastern Arabian Peninsula (Fig. 7.47f).

In autumn, above-normal temperatures dominated in most of Asia and Siberia, with anomalies of more than +2.0°C from Central Siberia to the Middle East and from North China to Japan (Fig. 7.47g). Seasonal precipitation was much above normal from central Mongolia to western Central Asia and from the eastern to southern Middle East, and below normal in Indonesia, northwestern China, southern Japan, and the Korean Peninsula (Fig. 7.47h).

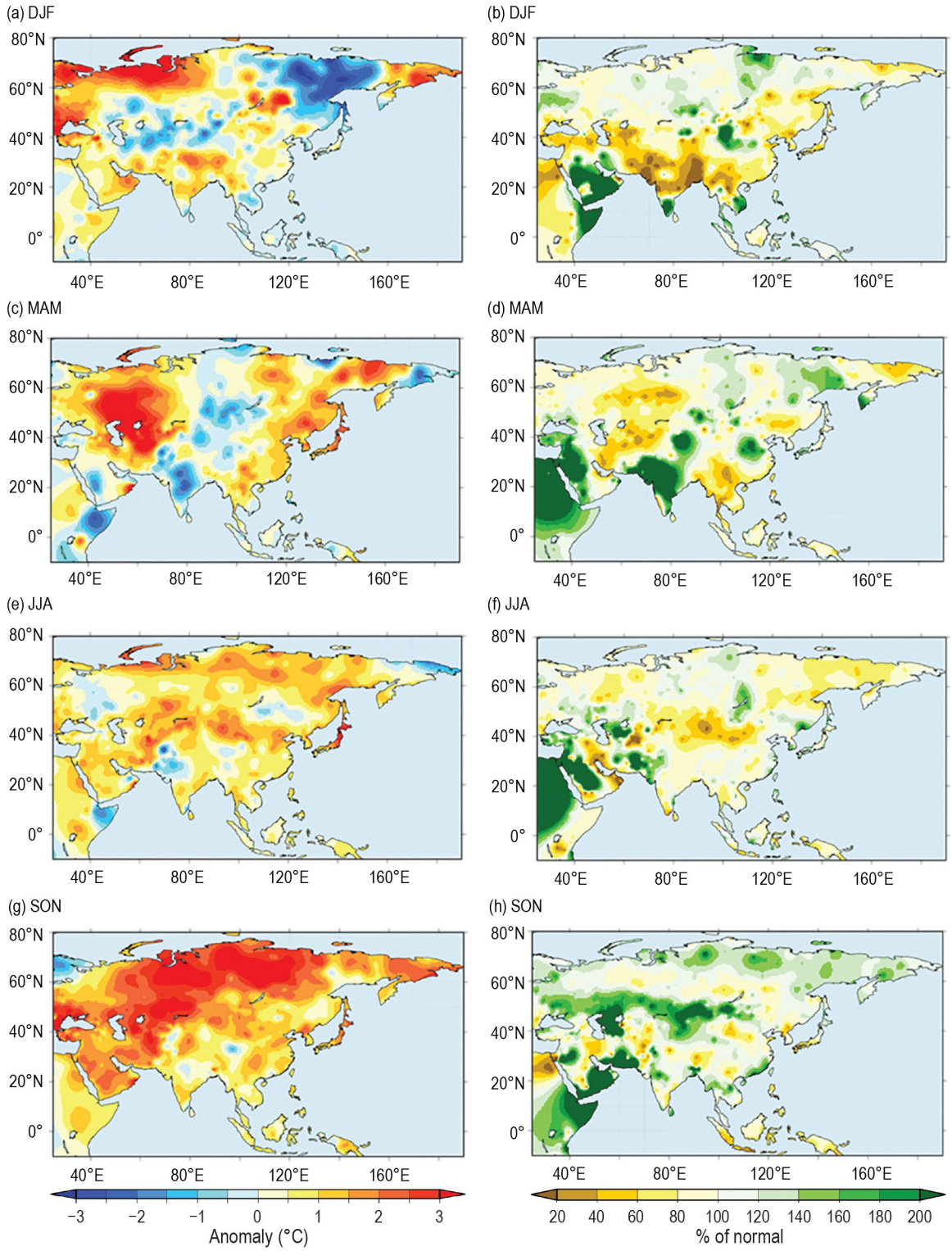

Fig. 7.47. Seasonal mean surface temperature anomalies (°C, left column) and seasonal precipitation ratios (% of normal, right column) over Asia in 2023 for (a),(b) winter, Dec–Feb (DJF); (c),(d) spring, Mar–May (MAM); (e),(f) summer, Jun–Aug (JJA); and (g),(h) autumn, Sep–Nov (SON). Anomalies and ratios are relative to 1991–2020. (Source: Japan Meteorological Agency.)

In winter, negative 500-hPa geopotential height anomalies and 850-hPa temperature anomalies were observed from Central Asia to northern East Asia, with the negative center located over eastern Siberia (Fig. 7.48a). Convective activity was enhanced near Indonesia, accompanied by 850-hPa cyclonic circulation anomalies straddling the equator from the eastern Indian Ocean to the western Pacific (Fig. 7.48b). In spring, positive 500-hPa geopotential height anomalies and 850-hPa temperature anomalies were observed over Central Asia and from the eastern part of East Asia to the midlatitude North Pacific (Fig. 7.48c). Convective activity was enhanced over India and to the east of the Philippines (Fig. 7.48d). In summer, positive 500-hPa geopotential

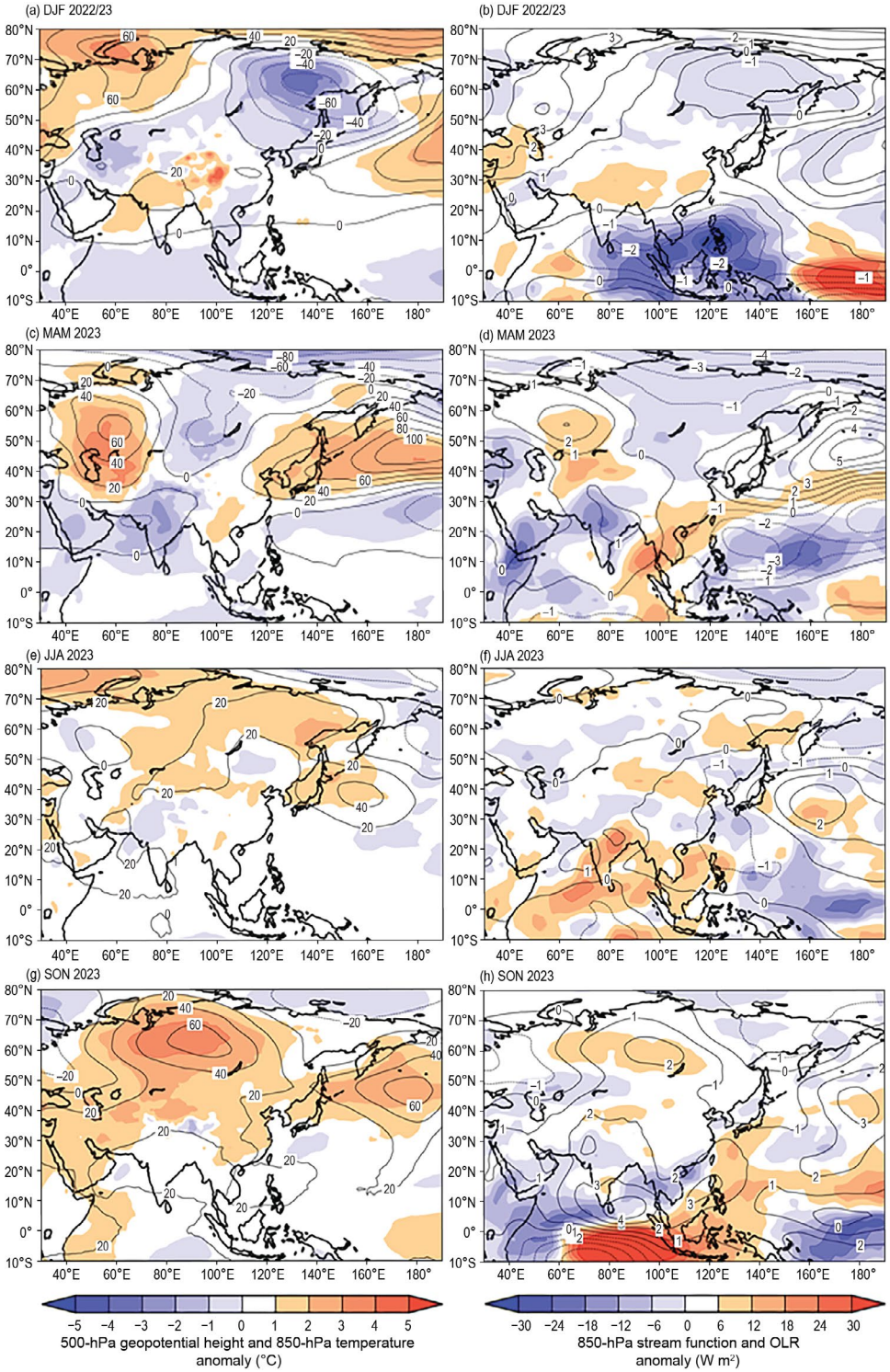

Fig. 7.48. Seasonal mean anomalies of atmospheric circulation variables in 2023 for (a),(b) winter, Dec–Feb (DJF); (c),(d) spring, Mar–May (MAM); (e),(f) summer, Jun–Aug (JJA); and (g),(h) autumn, Sep–Nov (SON). Left column: 500-hPa geopotential height (contour, gpm) and 850-hPa temperature (shading, °C). Right column: 850-hPa stream function (contour, 1 × 10^6 m^2 s^{-1}) using data from the JRA-3Q and CPC blended outgoing longwave radiation (OLR; shading, W m^{-2}) using data originally provided by NOAA. Anomalies are relative to 1991–2020. (Source: Japan Meteorological Agency.)

height anomalies accompanying positive 850-hPa temperature anomalies were observed over a wide region from Central Asia to Northeast Asia (Fig. 7.48e). Convective activity was suppressed over the northern Indian Ocean and enhanced over the tropical western and central Pacific, accompanied by 850-hPa cyclonic circulation anomalies near the Philippines (Fig. 7.48f). In autumn, positive 500-hPa geopotential height anomalies and 850-hPa temperature anomalies were dominant in the midlatitudes from Eurasia to the North Pacific, with positive geopotential height centered over the midlatitude Eurasian continent and the North Pacific Ocean (Fig. 7.48g). Convective activity was enhanced from the western Indian Ocean to South China, and suppressed from the central equatorial Indian Ocean to the Maritime Continent, accompanied by 850-hPa anticyclonic circulation anomalies straddling the equator over the Indian Ocean (Fig. 7.48h).

2. RUSSIA

—M. Yu. Bardin and N. N. Korshunova

Estimates of climate features for Russia were obtained from the hydrometeorological observations of the Roshydromet Observation Network. Anomalies are relative to the 1991–2020 base period, and national rankings and percentiles reflect the 1936–2023 period of record. Note that the temperature database was extended significantly, which in some cases changed previous ranking. The boundary between Asian Russia and European Russia is considered to be 60°E.

(i) Temperature

The year 2023 in Russia was the third warmest on record with an annual mean temperature 0.99°C above normal (Fig. 7.49a), after 2020 (+2.02°C; record warmest) and 2007 (+1.00°C; second warmest). Annual and seasonal trends are statistically significant at 1%, except for those of winter, both in Asian and European Russia. Anomalies above the 95th percentile were observed at most stations in southern European Russia, the Urals, and Western Siberia; the largest anomalies above +2°C were located around the Yenisei Bay.

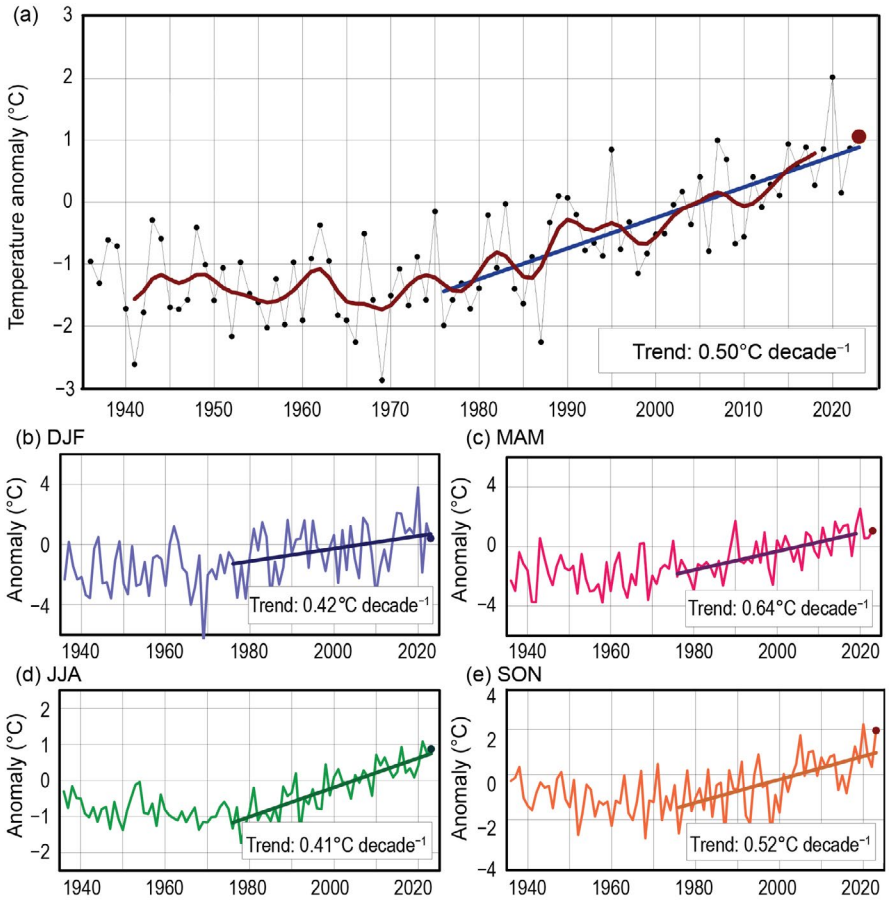

Fig. 7.49. Annual and seasonal mean temperature anomalies (°C; 1991–2020 base period) averaged over the territory of Russia for the period 1936–2023: (a) annual, (b) winter, (c) spring, (d) summer, and (e) autumn. The dark red line on the annual mean time series is an 11-point binomial filter. The linear trend (°C decade^{-1}) is calculated for the period 1976–2023.

Winter was the 23rd warmest since 1936, with a seasonal anomaly of +0.42°C (Fig. 7.49b). Negative anomalies reaching –5°C were observed across large parts of Asian Russia east of 110°E. During January, in northern Eastern Siberia and western Yakutia, an extensive cold center formed with an average monthly temperature anomaly of –8°C to –10°C (Fig. 7.50). During the second 10-day period, in the north of the Krasnoyarsk Territory, frost temperatures reached –50°C, and in Yakutia –60°C and below. At the Agata station, the second 10-day period was especially cold, as the maximum temperature was significantly lower than the normal minimum temperature. On 14 and 15 January, daily minimum air temperature records were broken. In southern Yakutia, the second 10-day period was also the coldest on record. On 15 and 18 January, the minimum air temperature dropped below –60°C, and the mean daily temperature was below the minimum normal for these days.

Spring was 1.06°C above normal, ranking 13th warmest on record (Fig. 7.49c). The European Russia spring temperature was the fourth highest, at 1.91°C above normal; all stations in southeast European Russia observed temperatures that exceeded the 95th percentile.

Summer was third warmest on record for Russia as a whole (0.87°C above normal; Fig. 7.49d), with Asian Russia record warm (1.03°C above normal). July and August were both record warm in this region, at 1.08°C and 1.40°C above normal, respectively.

Autumn was the second warmest on record, at 1.96°C above normal, following +2.24°C in 2020 (Fig. 7.49e). Asian Russia had its second warmest autumn on record (2.10°C above normal),

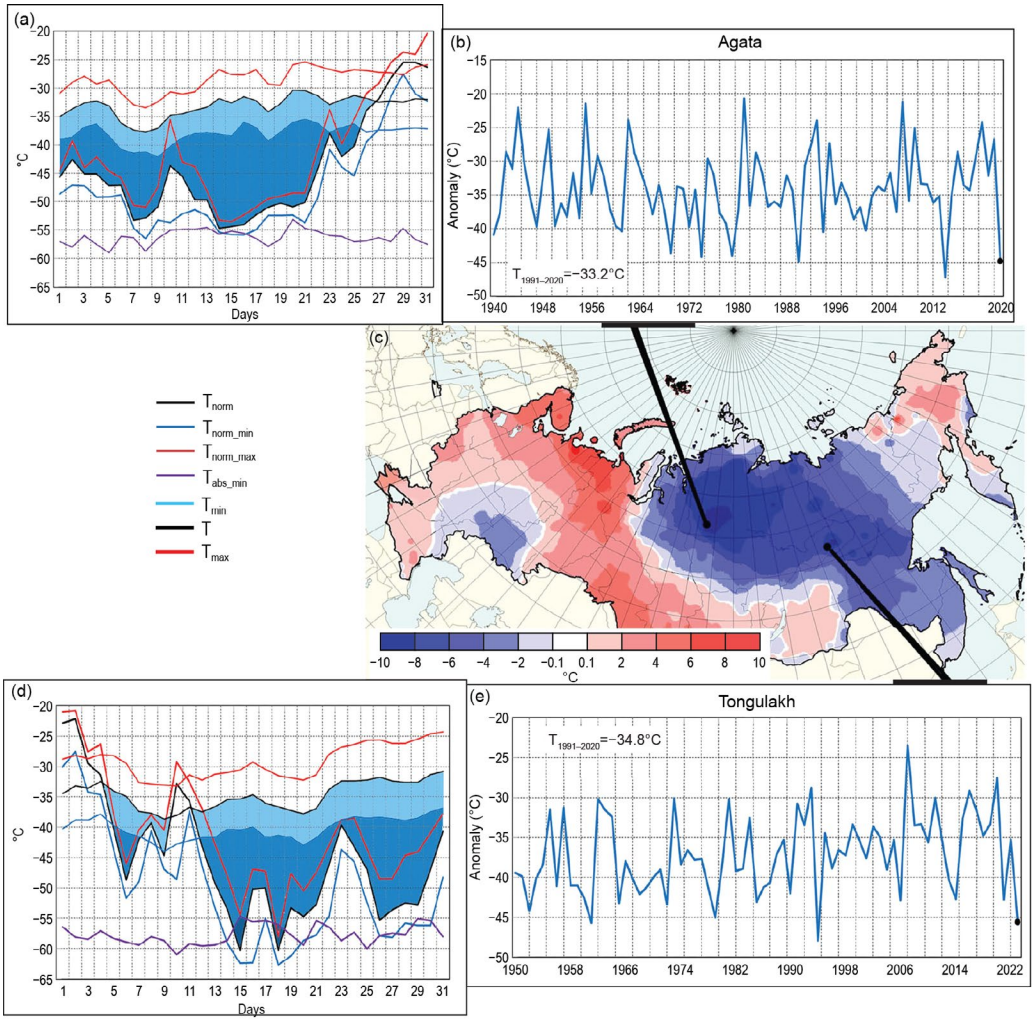

Fig. 7.50. Map of temperature anomalies across Russia (shading) in Jan 2023. Insets are of mean monthly temperature (°C) time series in Agata for the period 1940–2023 and Tongulakh for the period 1950–2023, and mean, minimum, and maximum daily temperatures (°C) in Jan 2023 at these stations. T1991-2020 on plots of monthly temperatures is the 1991–2020 mean. Plots of daily temperature show observed daily mean (T, black line), daily minimum (Tmin, blue line), and daily maximum (Tmax, red line) temperatures along with their climatological values (three uppermost curves: Tnorm, black; Tnorm_min, blue; Tnorm_max, red) and absolute minimum temperature (Tabs_min, violet). The area between the normal daily mean curve, Tnorm, and the observed daily mean curve is shaded light blue where T < Tnorm, and is shaded deep blue if T was below the normal daily minimum Tnorm_min.

and European Russia had its fourth (1.56°C above normal). September was record warm in European Russia (2.63°C above normal). October was second warmest in Asian Russia (2.81°C above normal) with temperatures above the 95th percentile at most stations between 80°E and 140°E. In European Russia, the temperature was near normal, with negative anomalies in the northwest.

(ii) Precipitation

Across Russia as a whole, the 2023 average precipitation total equaled the third highest on record, at about 106% of normal (Fig. 7.51). European Russia had 111% of normal precipitation, its fourth highest, while Asian Russia had 103% of its normal precipitation. Autumn was record wet (117% of normal) across Russia and was the second wettest for both European and Asian Russia (125% and 112%, respectively). Winter and spring were moderately wet (105% for both seasons), while summer was moderately dry (97%). Record precipitation fell in March over almost all of Russia (140% of normal), notably in Yakutia where four times the monthly normal was observed in Yakutsk. This anomalous precipitation was due in part to a vast persistent depression over the Arctic basin near the coast of Eurasia that occasionally expanded southward as far as Baikal.

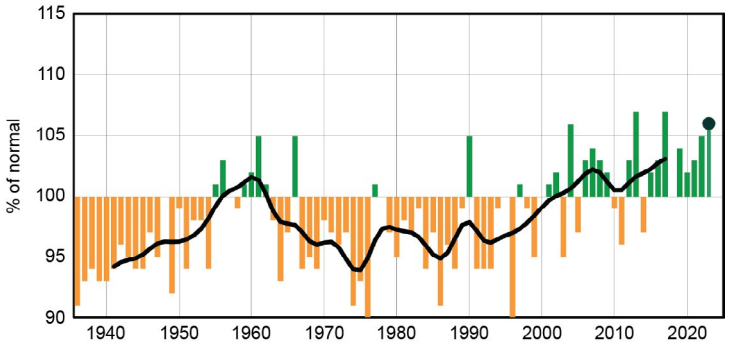

Fig. 7.51. Annual precipitation (% of normal; 1991–2020 base period) averaged over the Russian territory for the period 1936–2023. The smoothed time series (11-point binomial filter) is shown by the black line.

Precipitation in Russia has increased during the period of warming since the mid-1970s by about 1.8% per decade, mainly in spring when the rate is about 6% per decade. However, there is a vast area of decreasing precipitation in southern European Russia; the high rate of warming and increase in heatwave occurrence and duration together enhance the risk of drought in this principal grain-producing region (Fig. 7.49).

(iii) Notable events and impacts

During 6–8 February, strong northeast winds of up to 37 m s^{-1} raged in Novorossiysk and Gelendzhik. Building rooftops were damaged, shopping pavilions, fences, and bus stops were overturned, and trees, road signs, and lamp posts were toppled.

On 11–12 July, heavy rain fell in the Tuapse region of the Krasnodar Territory: Defanovka, 282.2 mm; Tuapse, 51mm; Dzhugba, 57.2 mm. In 13 settlements, 650 household plots and 39 apartment buildings were flooded, four pedestrian bridges and one road bridge were damaged, and power and water supplies were disrupted at several children's health camps. One fatality was reported, along with four missing persons.

On 10–11 August, 94 mm–190 mm of rain fell in the Primorsky Territory, which caused rivers to rise by 1 m–3.9 m (up to 5 m–8 m for the Spasovka and Razdolnaya Rivers). States of emergency were introduced in 14 municipalities. Bridges and sections of roads were destroyed, about 600 residential buildings, 1400 houses, and multi-story buildings in Ussuriysk were flooded, and dozens of settlements were cut off. More than 2000 residents were evacuated, and three fatalities were reported.

On 6 September, heavy thunderstorms accompanied by high winds of up to 32 m s^{-1} and hail with diameters between 20 mm and 23 mm impacted the Chechen Republic. More than 30 roofs were torn off or damaged, a road tunnel and nine houses were flooded, trees were knocked down, cars and power lines were damaged, and a tower crane was toppled. One fatality was reported.

On 19 November, in the Novosibirsk, Tomsk, and Kemerovo regions and the Altai Territory, a blizzard with wind speeds of up to 26 m s^{-1} (up to 37 m s^{-1} in the Altai Territory) caused significant damage to infrastructure. Four fatalities and 22 injuries were reported.

On 26 November, hurricane-force winds of up to 40 m s^{-1} were observed in the Republic of Crimea. Electricity was cut off in 273 settlements, roofs were damaged, 195 houses in the Saki district and Yevpatoria were flooded, and more than 300 people were evacuated. Seven people were injured, and one fatality was reported.

3. EAST AND SOUTHEAST ASIA

—P. Zhang, T. C. Lee, R. Muharsyah, A. Moise, K. Takemura, K. Takahashi, J. I. Seong, D. Dulamsuren, M.-V. Khiem, and H.-P. Lam

Countries considered in this section include China, Hong Kong (China), Indonesia, Japan, Republic of Korea (ROK, South Korea), Mongolia, and Vietnam. Unless otherwise noted, anomalies refer to the 1991–2020 base period.

(i) Temperature

Annual mean temperatures for 2023 across East and Southeast Asia are shown in Fig. 7.45. In 2023, the annual mean air temperature for China was 0.82°C above normal, the highest since the start of the record in 1951. In Hong Kong, 2023 was the second-warmest year since records began in 1884 with an annual mean temperature of 24.5°C, which was 1.0°C above normal.

In Japan, annual mean temperatures were above normal nationwide and significantly above normal in northern and eastern Japan. The regional average of annual mean temperature anomalies was the highest on record since 1946 in northern and eastern Japan, and tied with 1998 as the highest on record in western Japan.

The annual mean temperature for ROK was 13.7°C, 1.2°C above normal, the highest on record since 1973. March and September were 3.3°C and 2.1°C above normal, respectively, significantly contributing to the high annual mean temperature.

The annual mean temperature for Mongolia was 1.3°C above normal, its seventh-warmest year since 1940. October was record warm, with average temperatures 3.8°C above normal, and March was fourth warmest, at 3.5°C above normal.

The average temperature for Indonesia in 2023 was 27.2°C, which was 0.5°C above normal, marking the country's second-warmest year on record since 1981.

Singapore reported its fourth-warmest year, with an annual mean temperature of 28.2°C, which was 0.4°C above the long-term average. Most of the high heat stress days occurred in April, May, June, and October.

The observed annual mean temperature of Vietnam in 2023 was 1.09°C above normal. This marks the second-warmest year on record after 2019 (1.21°C above normal).

(ii) Precipitation

Annual precipitation for 2023 as a percentage of normal over East and Southeast Asia is shown in Fig.7.46. The annual mean precipitation total for China was 615.0 mm, which was 96.1% of normal and the second-lowest total of the past decade. The Meiyu over the Yangtze River basin started and ended later than normal and was six days longer than normal overall, with 364.6 mm of rainfall (14.6% above normal). The total rainfall for Hong Kong (China) in 2023 was 2774.5 mm, which was about 14% above normal.

In Japan, annual precipitation amounts were above normal on the Sea-of-Japan side of northern Japan and below normal on the Pacific side of northern and eastern Japan and in Okinawa and the Amami islands.

The annual precipitation for ROK reached 1746.0 mm, which was 131.8% of its normal of 1331.7 mm, marking the third-highest amount on record. May, July, and December experienced heavy precipitation, amounting to 188% (third wettest), 172.6% (second wettest), and 382.1% (wettest) of their respective normals.

For Indonesia, 2023 was the 10th-driest year since 1991, at 95% of normal. About 51% of the country, particularly the southern part, experienced below-normal rainfall (less than 85% of normal). The lowest rainfall total was recorded at Situbondo district, East Java, with annual rainfall of only 871 mm (67% of its normal).

Singapore's annual total rainfall averaged across the island-wide stations (2866.1 mm) was 13.1% above its long-term average of 2534.3 mm, making 2023 Singapore's seventh-wettest year since 1980. Although 2023 was generally wet, April, May, August, and October were drier than normal.

Average total annual rainfall in 2023 for Vietnam was 10%–20% below normal. However, Da Nang and Thua Thien Hue received annual rainfall 50%–60% above their normals due to a heavy rain event.

(iii) Notable events and impacts

In summer 2023, there were extreme dry and wet events that occurred in North China. From 1 June to 28 July, precipitation was 50% to 80% below normal in south-central North China and the northern Hebei province. The dryness was combined with high temperatures in the same areas. On 20 July, the area of meteorological drought above the moderate level reached its maximum area of 189,000 km^2. From 29 July to 1 August, the Beijing-Tianjin-Hebei region experienced a historically rare torrential rainfall induced by Typhoon Doksuri, with maximum rainfall of 1003 mm measured at Lincheng County in Xingtai, Hebei province.

A major and prolonged heatwave affected much of north Vietnam in May; an all-time national maximum temperature record of 44.2°C was observed at Tuong Duong on 7 May, surpassing the previous historical value of 43.4°C at Huong Khe on 20 April 2019. Heavy rain fell during 8–18 October in central Vietnam, from Nghe An to the Quang Ngai region, with total rainfall ranging from 300 mm to 600 mm; Thua Thien Hue and Da Nang received 1194 mm and 1442 mm, respectively. On 13 October, the daily rainfall in Da Nang was 409 mm, which exceeded its previous record of October rainfall (396 mm in October 2022).

Autumn precipitation was significantly below normal on the Pacific side of eastern and western Japan and in Okinawa and the Amami islands. The regional seasonal precipitation was the lowest on record for autumn since 1946 on the Pacific side of western Japan.

In the middle of the Changma season (13–18 July), a stationary front moved up and down the southern part of ROK for an extended period, dropping more than 500 mm of rain over six days. Throughout the season, approximately $560 million (U.S. dollars) in property damage was recorded and about 50 people were killed due to the intense rains.

The northern part of Lombok, West Nusa Tenggara, in Indonesia had 222 dry spell days in 2023, which was the longest dry spell on record. The drought triggered a clean water crisis for more than 13,000 people in the region.

Tropical Cyclone Koinu skirted to the south of Hong Kong (China) and brought heavy rain to the territory on 8–9 October. Rainfall on 9 October reached 369.7 mm, the highest daily rainfall on record for October.

The only typhoon that affected ROK in 2023 was Khanun. After the typhoon made landfall on the Korean Peninsula, it crossed ROK almost in a straight line from south to north. Heavy rain and strong winds resulted in $42 million (U.S. dollars) in property damage and the displacement of 15,000 people.

4. SOUTH ASIA

—O. P. Sreejith, A. K. Srivastava, and C. T. Sabeerali

Countries in this section include Bangladesh, India, Pakistan, and Sri Lanka.

(i) Temperature

In 2023, South Asia generally experienced above-normal temperatures. The annual mean land surface air temperature averaged over India was 0.65°C above the 1981–2010 average, making it the second-warmest year on record since nation-wide records commenced in 1901 (Fig. 7.52). The country-averaged seasonal mean temperatures were above normal for all seasons except the pre-monsoon season. The mean temperature anomaly was +0.83°C for winter (January–February), +0.74°C for the monsoon season (June–September), and +1.00°C for the post-monsoon season (October–December). Overall, the five warmest years on record in order are: 2016 (anomaly of +0.71°C), 2023 (+0.65°C), 2009 (+0.55°C), 2017 (+0.54°C), and 2010 (+0.54°C).

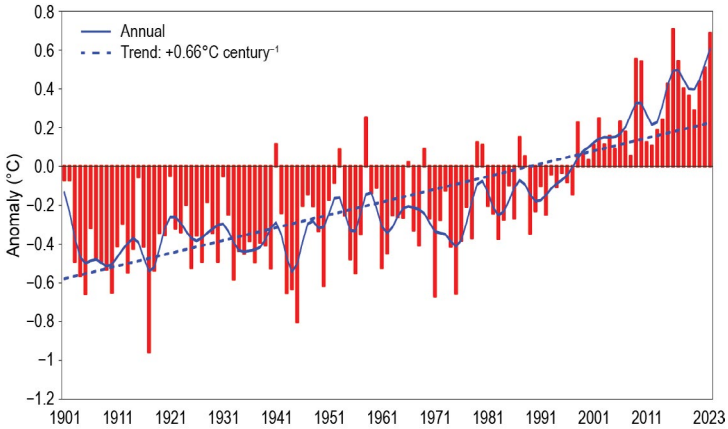

Fig. 7.52. Annual mean temperature anomalies (°C; 1981–2010 base period) averaged over India for the period 1901–2023. The smoothed time series (nine-point binomial filter) is shown as a continuous blue line, and the trend is shown by the dashed blue line.

(ii) Precipitation

The summer monsoon season (June–September) contributes about 75% of the annual precipitation over South Asia. The 2023 summer monsoon set in over Kerala (southwestern parts of peninsular India) on 8 June (the normal date is 1 June). The monsoon covered the entire country on 2 July, six days ahead of its normal date (8 July).

For India, the long-term average (LTA) value of the summer monsoon rainfall, calculated using data from 1971 to 2020, is 869 mm with a standard deviation of about ±10%. However, over smaller regions, the standard deviation is much larger (around ±19%). During 2023, the summer monsoon seasonal rainfall averaged over India was 95% of its LTA. Rainfall was fairly well distributed over the country, except over parts of the east and northeast (Fig. 7.53a). Seasonal rainfall over the homogeneous regions of northwest India, central India, South Peninsula, and east and northeast India was 101%, 100%, 92%, and 81% of their LTAs, respectively (Figs. 7.53b,c). On a monthly scale, rainfall for the country as a whole was above normal during July and September (both 113% of LTA) and below normal during June and August (91% and 64% of LTA, respectively). For August, country-wide rainfall was 162.7 mm, the lowest on record since 1901. Over the core monsoon region, the southwest monsoon was active on some days in June, July, and September, while it was significantly subdued on most days in August (Fig. 7.54).

During the winter season (January–February), rainfall over India was below normal (55% of its LTA). It was above normal (113%) during the pre-monsoon season (March–May) and below normal again (91%) during the post-monsoon season (October–December).

Pakistan, which is at the western edge of the pluvial region of the South Asian monsoon, receives 60% to 70% of its annual rainfall during the summer monsoon season (July–September). The summer monsoon sets in over eastern parts of Pakistan around 1 July with a standard deviation of five days. During 2023, the monsoon set in on 3 July. Monsoon rainfall over Pakistan was normal (104% of the LTA); however, there was large seasonal variability as July had significantly

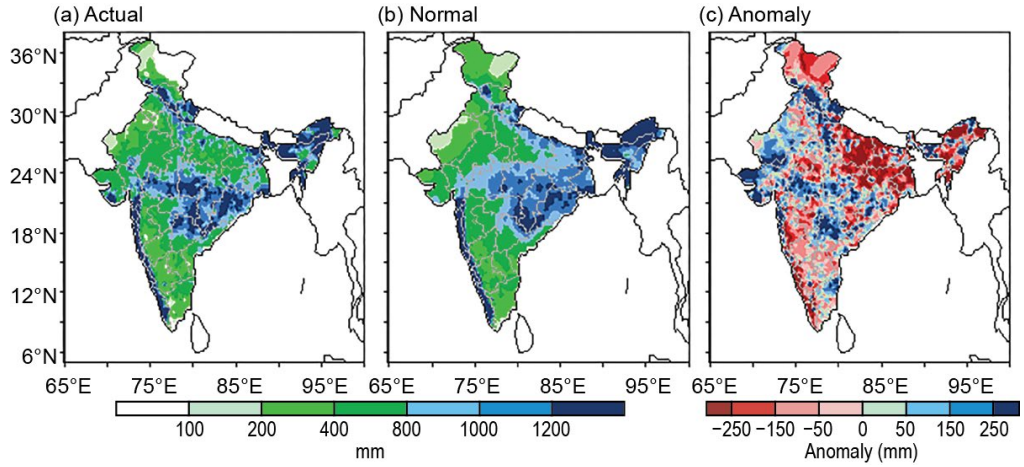

Fig. 7.53. Spatial distribution of monsoon seasonal (Jun–Sep): (a) actual, (b) normal (1971–2020 average), and (c) anomalous rainfall (mm) over India in 2023.

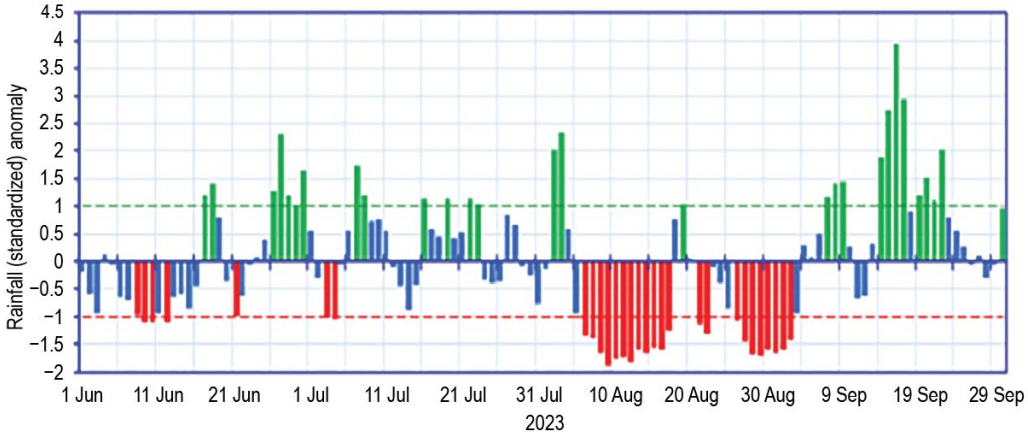

Fig. 7.54. Daily standardized rainfall anomaly time series averaged over the core monsoon zone of India for the period 1 Jun–30 Sep 2023.

above-normal (170% of the LTA) rainfall, followed by below-normal rainfall in August (34%) and near-normal rainfall in September (93%).

Bangladesh received normal rainfall during its summer monsoon season in 2023, while Sri Lanka received above-normal rainfall during its summer monsoon season (May–September).

The northeast monsoon (NEM) sets in over southern peninsular India during October and over Sri Lanka in late November. The NEM contributes 30%–50% of the annual rainfall over southern peninsular India and Sri Lanka as a whole. In 2023, the NEM set in over southern peninsular India on 21 October, and the seasonal rainfall was near normal (94%). However, many stations reported extremely heavy rain on 18 December, resulting in floods in the Thoothukudi and Tirunelveli districts of Tamil Nadu. Several stations reported more than 500 mm of precipitation: Kayalpattinam (946 mm); Tiruchendur (689 mm); Srivaikuntam (621 mm); and Kovilpatti (525 mm). Sri Lanka received above-normal rain totals during the NEM.

(iii) Notable events and impacts

Extremely Severe Cyclonic Storm Mocha, which developed in May during the pre-monsoon season, was one of the most intense cyclones ever formed over the Bay of Bengal, reaching peak 10-minute sustained winds of 115 kt (59 m s^{-1}). The storm formed on 11 May and intensified as it moved north, reaching its peak intensity early on 14 May before making landfall near the Bangladesh-Myanmar border (Fig. 7.55). There were at least five fatalities, and thousands of people were forced to seek shelter.

In recent years in India, thunderstorms accompanied by lightning strikes have been among the most common cause of fatalities. In 2023, thunderstorms and lightning claimed around 1280 lives across the country. On 4 July, approximately 43 people died due to lightning strikes associated with a severe thunderstorm that occurred in parts of Bihar, Jharkhand, Uttar Pradesh, and Madhya Pradesh.

Heavy rainfall and flood-related incidents claimed around 880 lives in different parts of India in 2023. Among these, more than 130 lives were lost in Madhya Pradesh, more than 120 in Himachal Pradesh, and more than 100 in Sikkim (mainly due to cloudburst and flooding in the Teesta basin due to a glacial lake outburst flood on 4 October). Additionally, 81 lives were lost in Uttar Pradesh, along with 75 in Uttarakhand, 71 in Maharashtra, and 56 in Rajasthan, with the remaining fatalities occurring in other states of India. A massive landslide, associated with heavy

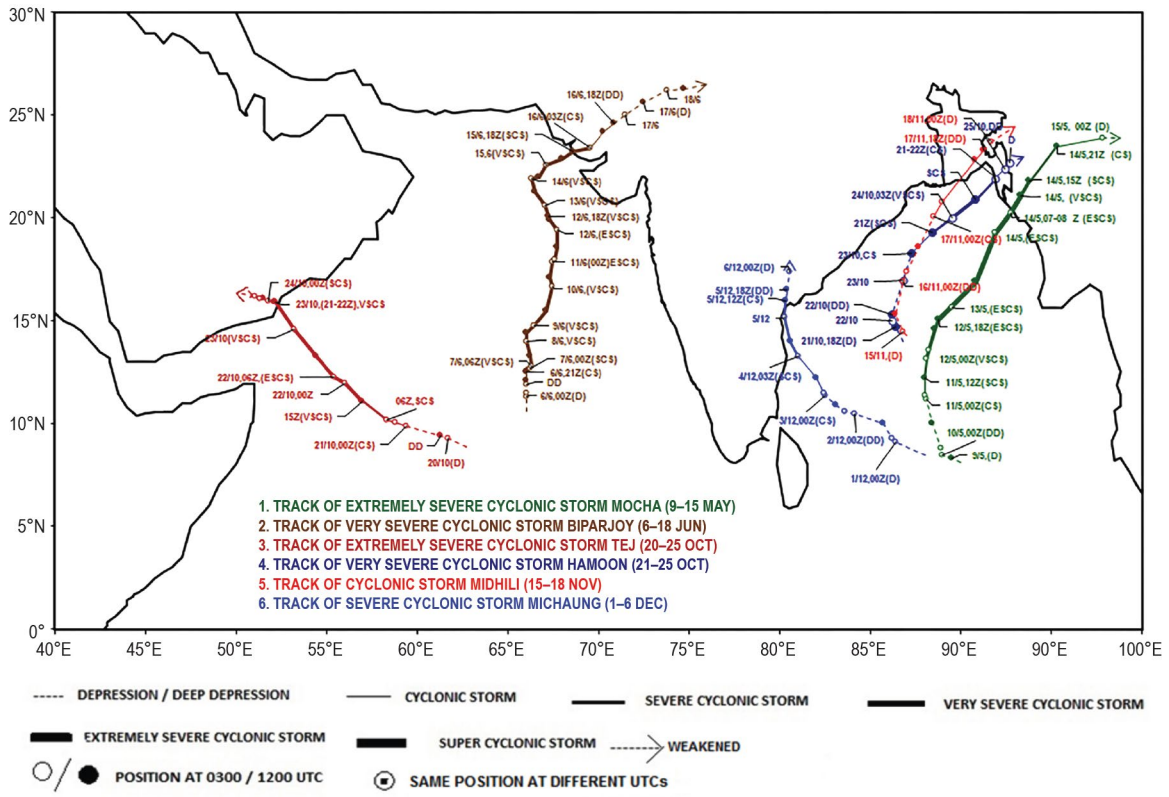

Fig. 7.55. Cyclonic storm tracks during 2023 over the North Indian Ocean.

rainfall, occurred on 19 July in the Raigad district of Maharashtra state, India, claiming 84 lives. On 14 August, a landslide in the Shimla district of Himachal Pradesh resulted in 25 fatalities.

A heatwave in June 2023 claimed more than 160 lives in various parts of India. While June is normally hot for the region, the heatwave had driven temperatures as high as 43.3°C. More than 85 lives were lost in the adversely affected state of Uttar Pradesh, along with 45 in Odisha, 25 in Jharkhand, and the remaining in Maharashtra and Chhattisgarh.

Extremely Severe Cyclonic Storm Biparjoy formed over the northeast Arabian Sea in the monsoon season during 6–19 June. Seven fatalities were reported in Rajasthan. The Bhavnagar, Banaskantha, Devbhoomi Dwarka, Gandhinagar, Jamnagar, Junagadh, and Kutch districts of Gujrat were also affected.

Severe Cyclonic Storm Michaung (1–6 December) formed in the post-monsoon season over the Bay of Bengal and crossed the south Andhra Pradesh coast close to Bapatla on 5 December as a severe cyclonic storm, claiming 24 lives in Tamil Nadu, Andhra Pradesh, and Telangana. The Malkangiri district of Odisha was also affected.

Bangladesh received very heavy rain during 5–10 August that affected 2.4 million people in four districts: Chittagong, Bandarban, Ragamati, and Cox's Bazar.

5. SOUTHWEST ASIA

—A. Vazife, A. F. Kazemi, and M. Mohammadi

This section covers the Middle East region including Iran. Unless otherwise noted, anomalies refer to the 1991–2020 base period.

(i) Temperature

Generally, 2023 was dry and warm in Iran. The data presented in Fig. 7.56 illustrate the mean surface temperature anomalies for winter, spring, summer, and autumn 2023. During winter (Fig. 7.56a), temperatures were either normal or slightly below normal in most of Iran, but notably

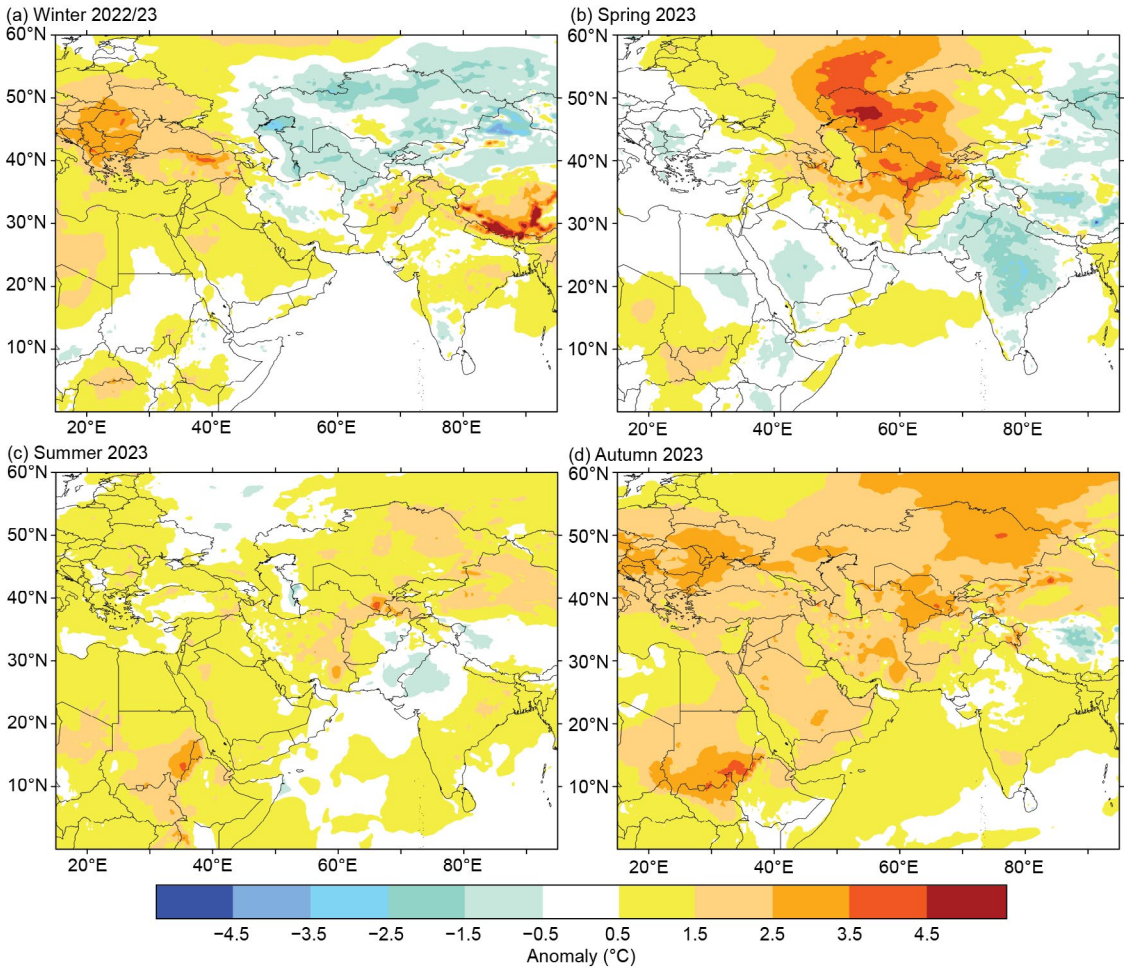

Fig. 7.56. The seasonal mean 2-m temperature anomaly (°C) in (a) winter 2022/23, (b) spring 2023, (c) summer 2023, and (d) autumn 2023.

above normal in the south. All other seasons experienced significant warmth, with spring and autumn temperatures (Figs. 7.56b,d, respectively) notably higher than usual. November 2023 was the warmest on record for the country in the past 70 years. The seasonal temperature anomalies, as depicted on the map, ranged from +0.5°C to +4.5°C.

(ii) Precipitation

Precipitation during the main rainy seasons (winter, spring, and autumn) was below normal, and severe rain deficits were observed in central, north-northwest, and northeast and east Iran.

The December 2022–February 2023 period was drier than normal in Iran. Southwest Iran received above-normal precipitation only during January. Other regions faced their third consecutive year with below-normal rain during the winter period.

Figure 7.57a shows that most of southwest Asia was drier than normal during winter, as was northern to eastern Iran and the Caspian Sea region. Moderate to severe drought occurred in vast regions of southwest Asia, including the Caspian Sea and the north and eastern half of Iran.

Spring 2023 was drier than normal (Fig. 7.57b). Eastern Saudi Arabia, eastern Iraq, and southwest Iran received above-normal rain, while vast areas of central to eastern Iran and the Caspian Sea region received normal to severely-below-normal rain during the season.

The summer season in southwest Asia typically experiences minimal rainfall; occasional thunderstorms originating from easterly monsoonal currents are the primary source of moisture. Pakistan and at times southeastern Iran also benefit from monsoonal rains through afternoon thunderstorm activity. However, there was weaker monsoonal and thunderstorm activity in summer 2023 compared to previous years, as depicted in Fig. 7.57c. This contrasts sharply with the humid conditions and above-normal monsoon activity observed in 2022, which led to significant flash floods in Iran. Autumn 2023 were also drier than normal for many parts of Iran (Fig. 7.57d).

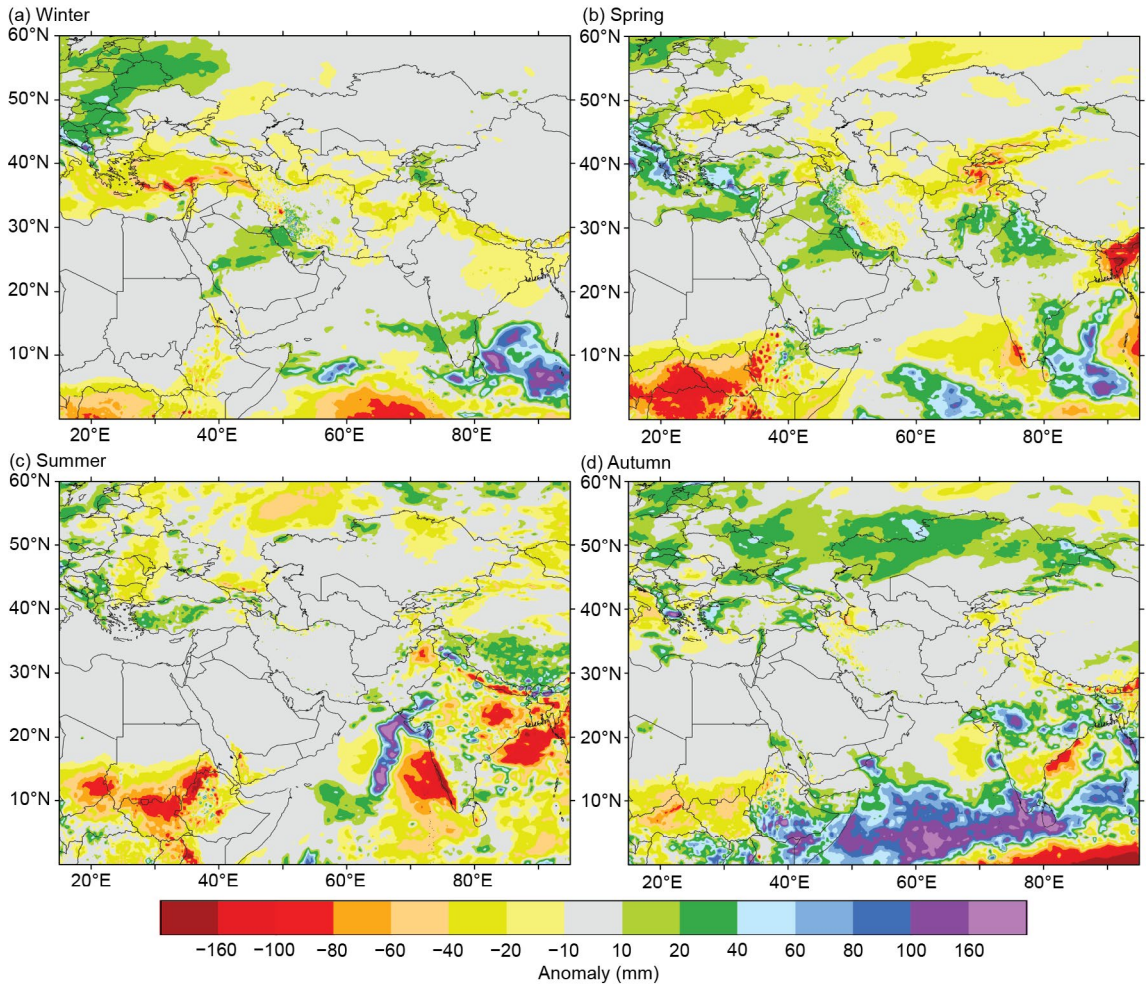

Fig. 7.57. The seasonal mean precipitation anomaly (mm) in (a) winter 2022/23, (b) spring 2023, (c) summer 2023, and (d) autumn 2023.

(iii) Notable events and impacts

The most pressing weather hazard in Iran in 2023 was persistent drought that resulted in substantial financial losses for the agricultural sector and produced severe hydrological challenges. Lake beds dried up, notably in the northwestern and eastern regions of the country. Lake Urmia in northwestern Iran nearly completely dried up, while Lake Hamoon in the east has been completely dry since 2021. The dried lake beds have become a significant source of rising dust during late spring and summer wind storms, leading to adverse health effects on the local population.

Most of Iran and the Caspian Sea region were affected by severe drought in the spring following the dry winter. Spring holds immense importance for agriculture in this region as it marks the primary growing season, with rainfall playing a pivotal role in supporting rain-fed agriculture. The dry spell that persisted through winter had a detrimental impact on crop yields, particularly affecting staple grains such as wheat, barley, and other essential rain-fed agricultural produce in the area. Summer 2023 also had below-average precipitation in most parts of southwest Asia, including Iran. The persistent dry conditions over the past three years have intensified water stress levels across many countries in the region.

6. CENTRAL ASIA

—R. Shukla and W. M. Thiaw

This section covers the Central Asia (CA) region, including the countries of Afghanistan to the south, Turkmenistan, Uzbekistan, Tajikistan, Kyrgyzstan (from west to east) in the central part of the region, and Kazakhstan to the north. Unless otherwise specified, the climatological base period is 1991–2020.

(i) Temperature

During 2023, annual mean temperatures featured a strong meridional gradient near 50°N, with temperatures ranging between 0°C and 5°C in the northern and eastern Kazakhstan regions, between 10°C and 20°C in southern and southwestern Kazakhstan, Uzbekistan, Turkmenistan, and northern, western, southern, and southeastern Afghanistan, and between 20°C and 25°C farther south in Afghanistan (Fig. 7.58a). Annual mean temperatures were lowest at around –10°C–0°C in eastern Tajikistan, southeastern Kyrgyzstan, and some parts of eastern Kazakhstan and the northeastern high-elevation region of Afghanistan (Fig. 7.58a). The magnitude of annual mean temperatures was higher (lower) than normal in many parts of Kazakhstan and western and central parts of Uzbekistan and Turkmenistan (northern and eastern Kyrgyzstan, Tajikistan,

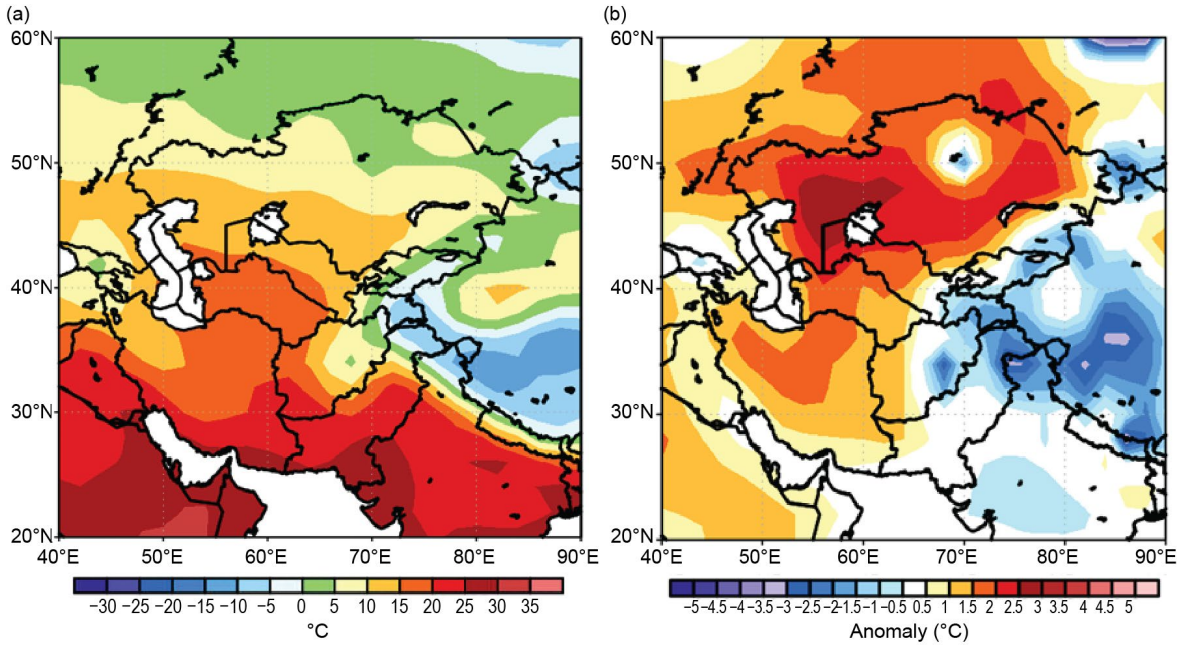

Fig. 7.58. Annual (a) mean temperature (°C) and (b) mean temperature anomalies of 2023 (°C, 1991–2020 base period) for Central Asia. (Source: NOAA National Centers for Environmental Prediction.)

and northeastern and eastern Afghanistan). Annual mean temperature anomalies were +0.5°C to +3.0°C in many parts of western, southern, central, northern, and northeastern Kazakhstan, western and central Uzbekistan, Turkmenistan, and the western and southern Afghanistan regions (Fig. 7.58b), placing 2023 in the 90th to 97th percentiles of warmest years on record in many places. The highest temperature anomalies were around +2.5°C to +3.0°C in Aktobe province in western Kazakhstan and some parts of northwestern Uzbekistan. By contrast, annual mean temperature anomalies were around –2.0°C to –0.5°C in northern, central, and eastern Kyrgyzstan, Tajikistan, northeastern, eastern, and southeastern Afghanistan, and some parts of east Kazakhstan and the country's Almaty region (Fig. 7.58b), placing 2023 in the 3rd to 10th percentiles of coldest years on record in eastern Kazakhstan.

(ii) Precipitation

Annual total precipitation for 2023 depicted a large variation across the Central Asia regions (Fig. 7.59a). The lowest precipitation totals, around 50 mm–200 mm, were received in western and southern Afghanistan, Turkmenistan, and central Uzbekistan in 2023. About 200 mm–500 mm of precipitation were received across southwestern, southern, central, and southeastern Kazakhstan, as well as Kyrgyzstan, Tajikistan, eastern and northwestern Uzbekistan, and northeastern, northern, central, southeastern, and eastern Afghanistan. Larger precipitation totals of around 500 mm–700 mm were observed in northwestern, northern, and eastern Kazakhstan (Fig. 7.59a). Seasonally, large precipitation deficits (–100 mm to –20 mm, not shown) were observed across Afghanistan, central and eastern regions of Turkmenistan, and Uzbekistan during the January–March and March–May (MAM) periods, as well as across Tajikistan and Kyrgyzstan during MAM and April–June (AMJ). The seasonal total precipitation was 20 mm–100 mm below average (lowest 3rd to 10th percentiles of driest years) across the northern, eastern, and southeastern regions of Kazakhstan during AMJ and May–July. The seasonal total precipitation was 20 mm–150 mm above average (highest 90th to 97th percentiles of wettest years) across the western, northern, central, and eastern regions of Kazakhstan during the August–October and October–December periods.

Most regions in Central Asia received maximum precipitation (rain and snowfall) during winter and spring, while northern and eastern regions of Kazakhstan received precipitation throughout the year. The annual precipitation totals were 25 mm–200 mm below normal (lowest 3rd–10th percentiles of driest years) in many parts of Afghanistan, southwestern, central,

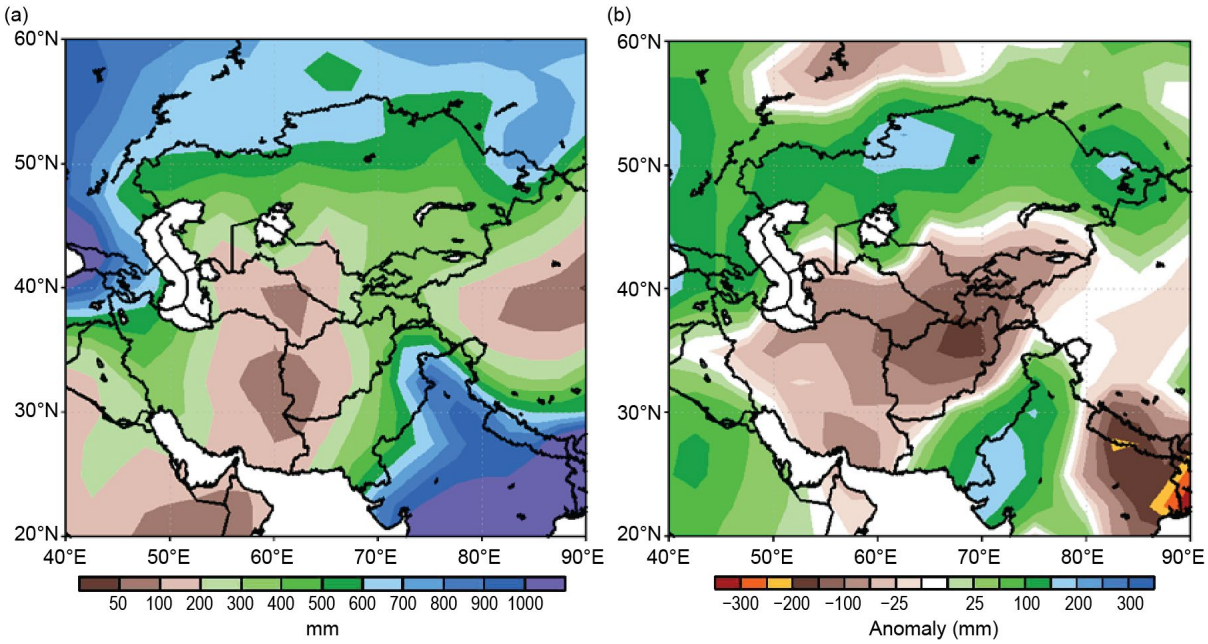

Fig. 7.59. Cumulative annual (a) precipitation (mm) and (b) precipitation anomalies (mm; 1991–2020 base period) of 2023 for Central Asia. (Source: NOAA National Centers for Environmental Prediction GPCP data.)

northern, and eastern Turkmenistan, central and eastern Uzbekistan, Kyrgyzstan, Tajikistan, and some parts of southern and southeastern Kazakhstan (Fig. 7.59b). Precipitation was below average by about 150 mm–200 mm in some parts of northern and central Afghanistan this year. By contrast, the annual total precipitation was 25 mm–200 mm above normal in many parts of western, northern, central, and eastern Kazakhstan and northwestern Uzbekistan (highest 90th–97th percentiles of wettest years in the northwestern, northern, and eastern Kazakhstan regions). About 150 mm–200 mm of above-average precipitation was observed in the Kostanay and Akmola provinces in northern Kazakhstan and some parts of the eastern Kazakhstan regions in 2023 (Fig. 7.59b).

(iii) Notable events and impacts

According to Afghanistan's minister of Disaster Management, at the start of 2023, the country experienced one of its coldest Januarys on record due to a disrupted polar vortex. Temperatures during the month reached –28°C and resulted in 162 fatalities. Based on the NOAA Climate Prediction Center Unified Gauge minimum temperature records, extreme minimum temperatures of around –35°C to –20°C were observed in many parts of Afghanistan during 9–15 January. At the end of the year, extreme minimum temperatures during 10–13 December were around –35°C to –25°C across the Zhambyl region of Kazakhstan. The state news agency Kazinform reported that the cold temperatures damaged gas pipelines in the Zhambyl region, leaving at least 1200 homes without fuel.

According to the Taliban official for Natural Disasters Management, around 10 mm–50 mm of rain fell during 20–26 March, causing flooding in 23 provinces of Afghanistan and resulting in nine fatalities, 74 injuries, and 1778 destroyed houses. According to reports from various sources including the Afghan Red Crescent Society and the Afghan National Disaster Management Authority, around 10 mm–75 mm of rain in eastern, central, southeastern, and southern Afghanistan during 21–31 July led to flash flooding and affected 6193 people across eight provinces (Kabul, Kunar, Laghman, Maidan Wardak, Nangarhar, Nuristan, Parwan, and Zabul). According to the United Nations Office for the Coordination of Humanitarian Affairs, 61 people lost their lives, 30 others were injured, 1360 houses were damaged or destroyed, and ~13,000 hectares of agricultural land were destroyed. According to Tajikistan's emergency authorities, around 10 mm–50 mm of precipitation during 26–28 August in western and eastern Tajikistan caused severe flooding and landslides across wide areas and resulted in 13 fatalities.

Sidebar 7.4: Record-breaking high temperatures over North China in October 2023

—Z. ZHU, H. HUANG, K. TAKAHASHI, AND K. TAKEMURA

During October 2023, extreme high temperatures swept through northeast Asia. Northern China was affected in a wide range of areas and set a record for its hottest October since the start of the record in 1961. Winter started more than five days late across most regions, with Shenyang marking its latest start to winter on record and Beijing marking its latest in the last decade.

The high daily maximum temperature (Tmax) anomalies in October were widespread, extending from Siberia to North China (32.5°N–54°N, 107°E–135°E), where the average temperature was 3°C higher than the 1991–2020 normal, with a northwest to southeast decline pattern (Fig. SB7.7a). The above-normal temperatures averaged over North China lasted 26 days, with a maximum anomaly of +8°C on 25 October (Fig. SB7.7b). A total of 14 extreme high-temperature days (defined as those in which daily maximum temperatures exceeded the 90th percentile) were recorded during mid- to late October. The normalized October Tmax averaged over North China (referred to as NCT hereafter) in 2023 exceeded 2.5 standard deviations, the highest since the start of the record there in 1979 (Fig. SB7.7c) and well above the second highest in 1990.

The extreme high temperatures in North China were related to a local anomalous barotropic anticyclone (i.e., heat dome). The deep high-pressure system tilted westward with height, and the center of the high-pressure anomaly at 200 hPa was

located over Lake Baikal (Fig. SB7.7d) and extended eastward to southeastern Mongolia at 500 hPa and to northeastern China at 850 hPa (Figs. SB7.7e,f). Under upper- and lower-level anomalous anticyclones, persistent descent motions and strong solar radiation from clear skies caused the high surface temperatures in North China.

The heat dome above North China was one lobe of the Rossby wave train over the Eurasian continent. As indicated by the 200-hPa wave activity flux (Fig. SB7.8a), significant wave energy propagated downstream from the North Atlantic to northeast Asia, leading to the large-scale anomalous high pressure over and around Lake Baikal. Comparing the October 2023 anomaly fields with the regression fields onto the NCT during 1979–2022, two potential universal factors for the extreme high temperatures over North China were proposed: 1) the enhanced convection anomalies over the tropical Atlantic (TAP; Fig. SB7.8b), and 2) the dipole sea surface temperature anomalies in the tropical Indian Ocean (TIS; Fig. SB7.8c). The

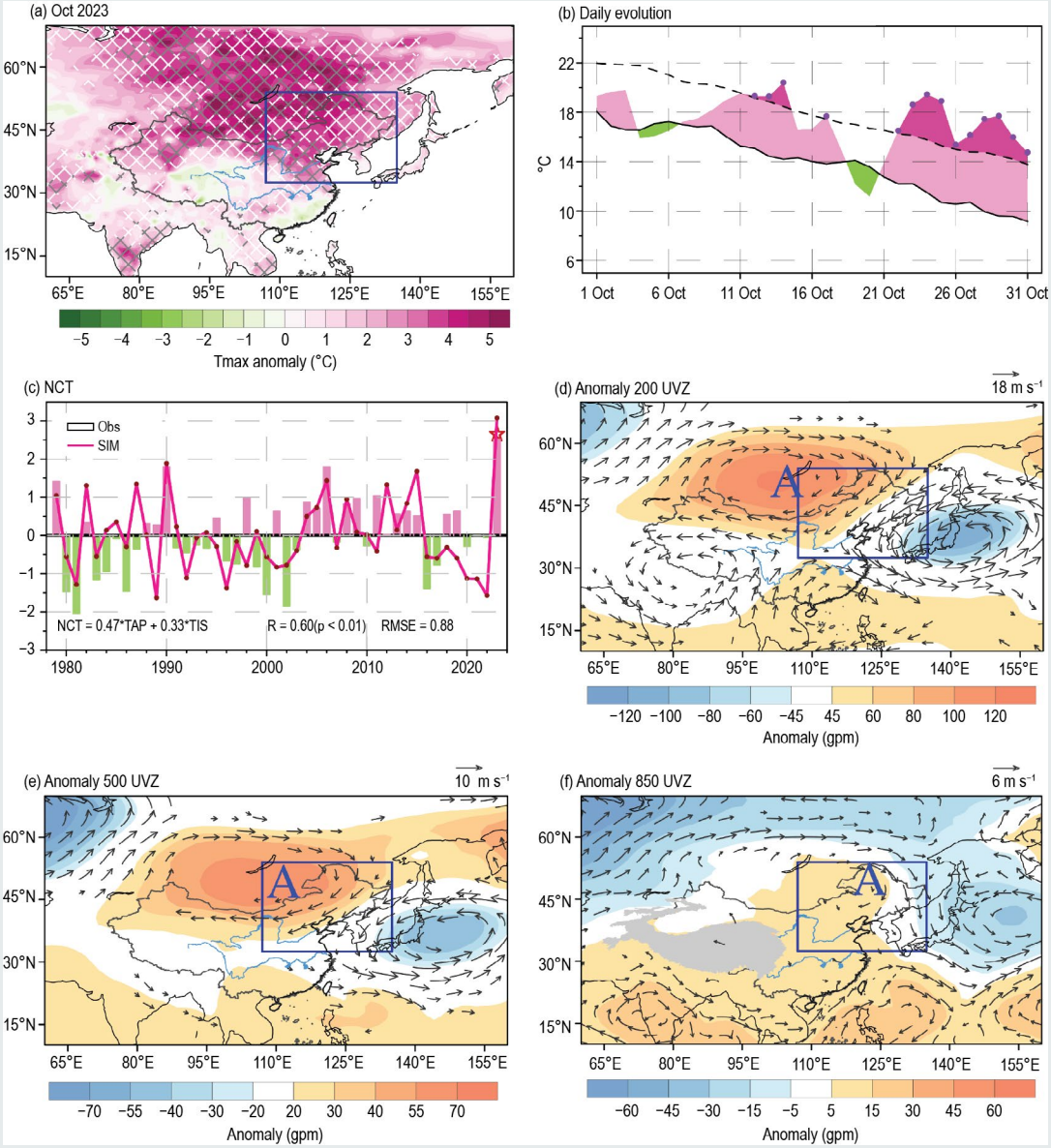

Fig. SB7.7. (a) Maximum surface temperature anomalies (Tmax, shading, °C) in Oct 2023. Areas with extreme high-temperature days (EHDs) 20% more than normal (1991–2020) are slashed with white, and areas with EHDs 30% more than normal are slashed with gray. (b) Daily evolution of Tmax averaged over North China in Oct 2023. The dashed (solid) curve represents the 90th percentile (climatological mean) of the temperature records, and the EHDs are marked with purple dots. (c) Time series of the normalized October Tmax averaged over North China (NCT) during 1979–2023 from observations (bar) and reconstructions by the multiple linear regression model (curve). The legend in the bottom left shows the linear regression equations, and the bottom right legend presents the correlation coefficients (R) and root-mean-square error (RMSE). (d) Local anomalous 200-hPa geopotential height (shading, gpm) and wind (vectors, m s^{-1}). (e),(f) As in (d) but for 500-hPa and 850-hPa, respectively. In (a) and (d)–(f), the blue frame outlines NCT and the letter "A" in (d)–(f) represents the center of the anomalous anticyclone. In (f), the Tibetan Plateau is denoted by gray shading.

diabatic heating anomaly associated with the TAP could trigger a midlatitude Rossby wave train over the Eurasian continent and end with an anomalous anticyclone over North China (Fig. SB7.8b). The TIS favored the anomalous convection in situ and excited another poleward wave train, strengthening the anomalous anticyclone over North China and increasing the local temperature (Figs. SB7.8b,c).

Using a multiple regression model, the above two factors simulate the NCT index with a correlation coefficient of 0.60 ($p<0.01$) and a root mean square error of 0.88 (Fig. SB7.7c). The model also reproduced the extremity in 2023 well, suggesting that the tropical Atlantic and Indian Oceans had significant impacts on the extreme high temperatures over North China during this period.

In addition to this high temperature record in North China, unprecedented high temperatures were also observed in northern and eastern Japan from mid-July 2023 onward. The national average temperature in Japan for summer 2023 was 1.76°C above normal, making it the warmest summer since the start of the record in 1898. From 16 July to 23 August, 106 of 915 observation stations across the country observed record-high maximum temperatures. These extreme high temperatures are associated with several factors, including tropical convection over the western North Pacific and an abnormal Pacific-Japan pattern and northward shift of the upper-level westerly jet, along with the worldwide warming tendency associated with persistent global warming.

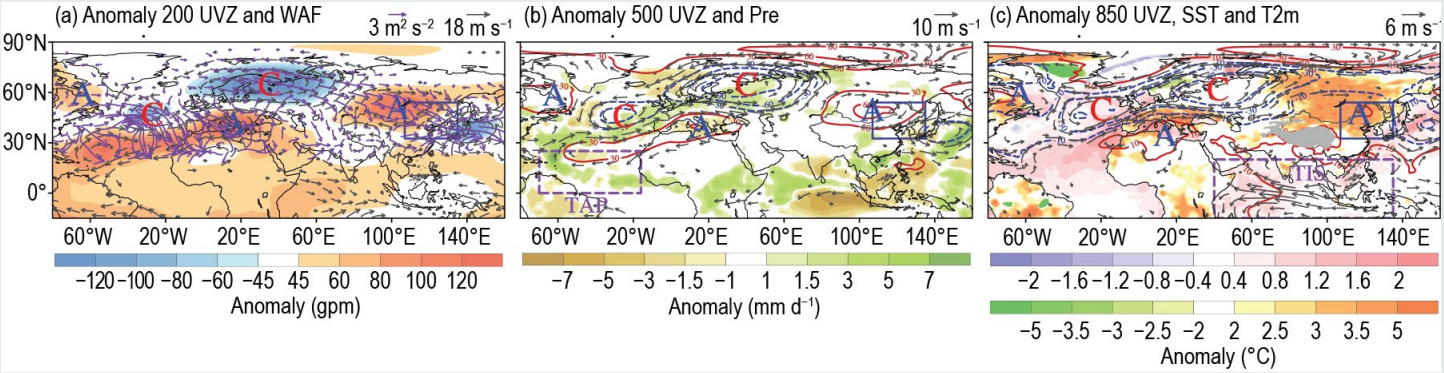

Fig. SB7.8. Oct 2023 (a) 200-hPa geopotential height (shading, gpm), wind (vectors, m s^{-1}), and wave activity flux (purple vectors, m^2 s^{-2}) anomalies, (b) 500-hPa geopotential height (contours, gpm), wind (vectors, m s^{-1}), and precipitation (shading, mm d^{-1}) anomalies, and (c) 850-hPa geopotential height (contours, gpm), wind (vectors, m s^{-1}), and sea surface temperature (SST)/maximum surface temperature (shading, °C) anomalies. The letters "A"/"C" denote the centers of anomalous anticyclones/cyclones. The blue frame outlines the domain of North China. The gray shading in (c) denotes the Tibetan Plateau. In (b),(c), the purple boxes are the domains for calculating the tropical Atlantic precipitation (TAP) and tropical Indian Ocean SST (TIS) indices.

h. Oceania

—C. Ganter, Ed.

1. OVERVIEW

—C. Ganter

The region of Oceania (Fig. 7.60) began the year affected by La Niña, which gave way to an El Niño later in the year (see section 4b for details). While the decaying La Niña provided more typical effects across the area, many regions of Oceania saw atypical effects from their usual El Niño conditions. In addition to the El Niño–Southern Oscillation (ENSO), a positive Indian Ocean dipole (IOD) also affected the region (see section 4g for details), as well as the long-term warming trend.

The year 2023 was New Zealand's second-warmest since the start of its record in 1909; Australia had its eighth-warmest year since 1910.

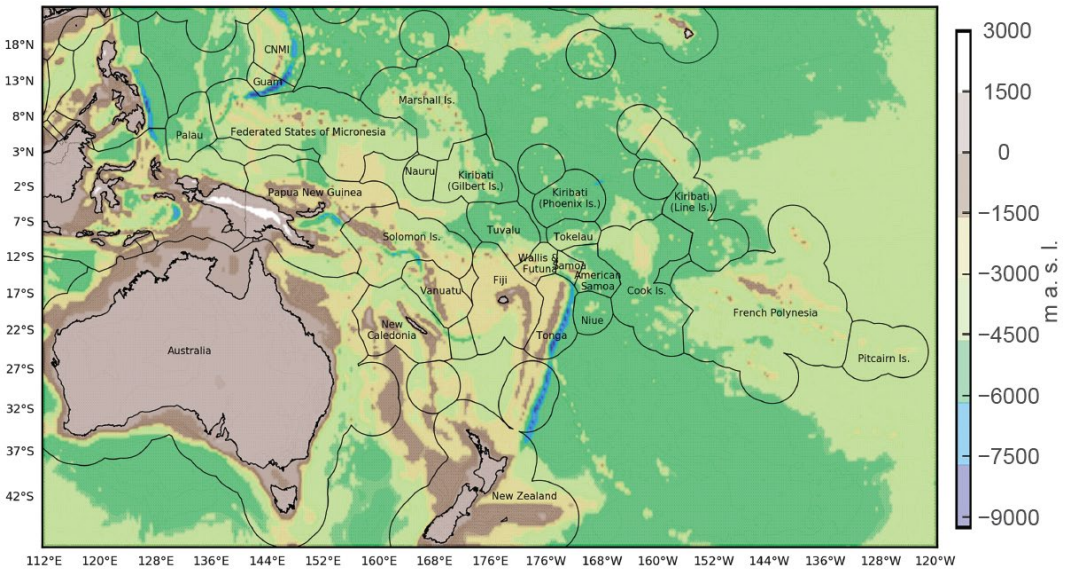

Fig. 7.60. The islands of Oceania. The colors represent topographical heights, with white and browns colors ranging from around 3000 m a.s.l to around –1500 m a.s.l. The yellow/green/blue indicates greater depths of up to 9000 m below sea level, with blue indicating the lowest depths.

2. NORTHWEST PACIFIC AND MICRONESIA

—B. Bukunt

This assessment covers the area from the dateline west to 130°E, between the equator and 20°N. It includes the U.S.-Affiliated Pacific Islands of Micronesia, but excludes the western islands of Kiribati and nearby northeastern islands of Indonesia (Fig. 7.60). The temperature analysis is based on data from ERA5 (Hersbach et al. [2020]) and scripts developed by the NWS, Alaska Region. Anomalies are calculated with respect to the 1991–2020 base period. Rainfall data is a combination of NWS station data and the MSWEP (Beck et al. [2019]) analyses as presented by the Bureau of Meteorology Pacific Climate Monitoring and the Climate And Oceans Support Program In The Pacific (COSPPac) Online Climate Outlook Forum. The base period for the precipitation station data is 1991–2020 while the maps are 1980–2021.

While the past few years followed a relatively conventional La Niña pattern that began in mid-2020, 2023 was a year of marked change as a canonical (east-based) El Niño developed during the boreal spring and summer. Meanwhile, oceanic warmth persisted at higher latitudes east of Japan and north of Hawaii, reinforcing the strongly negative Pacific Decadal Oscillation (PDO). Although the strengthening El Niño pushed the Southern Oscillation Index (SOI) into negative values by August 2023, the SOI struggled to reach negative values on par with strong El Niño events of the past (see *Notable events and impacts* for more information).

(i) Temperature

Along the equator, air temperatures were slightly (0.25°C–0.75°C) below normal to the east of the dateline during January–March (JFM). This was linked to the fading La Niña sea surface

temperature (SST) pattern. Temperatures were slightly above normal across the Republic of Palau, the western portion of the Federated States of Micronesia, Guam, and the Commonwealth of the Northern Mariana Islands (CNMI) during JFM (Fig. 7.61a). ERA5 data indicated a

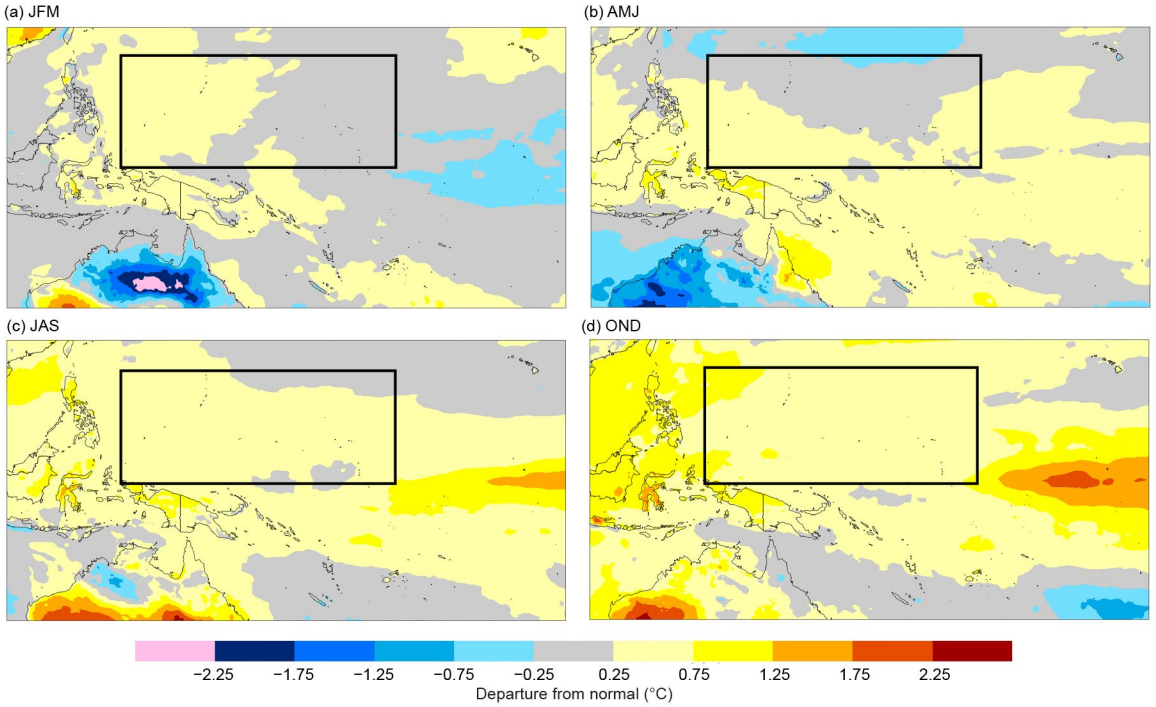

Fig. 7.61. Seasonal air temperature surface anomalies (°C) in 2023 across the west-central Pacific for (a) Jan–Mar, (b) Apr–Jun, (c) Jul–Sep, and (d) Oct–Dec. The black box defines the northwest Pacific and Micronesia region. (Source: ERA5 and Brettschneider.)

crescent-shaped region of record-high SSTs from west of Palau extending northeastward to Yap proper and waters south of Guam during the first half of 2023 (Fig. 7.62a).

The swath of slightly above-normal air temperatures across western Micronesia expanded to the rest of the region during the remainder of the year (Figs. 7.61b–d), with pockets of above-normal (0.75°C–1.25°C) air temperatures along the equator to the southeast of the Republic of the Marshall Islands (RMI) and portions of far western Micronesia (Republic of Palau [ROP] and western Yap State). Increasing air temperature anomalies to the southeast of the Marshall Islands were likely due to the growing El Niño signal. SSTs in the Niño-4 region reached record levels for the July–December period, according to ERA5 data (Fig. 7.62b). Fragments of this record-warm SST pool expanded northward to Majuro at times: Majuro tied its all-time highest minimum temperature of 28.9°C on 8 September and its highest minimum temperature in December of 28.3°C on both 2 and 22 December (records since 1946).

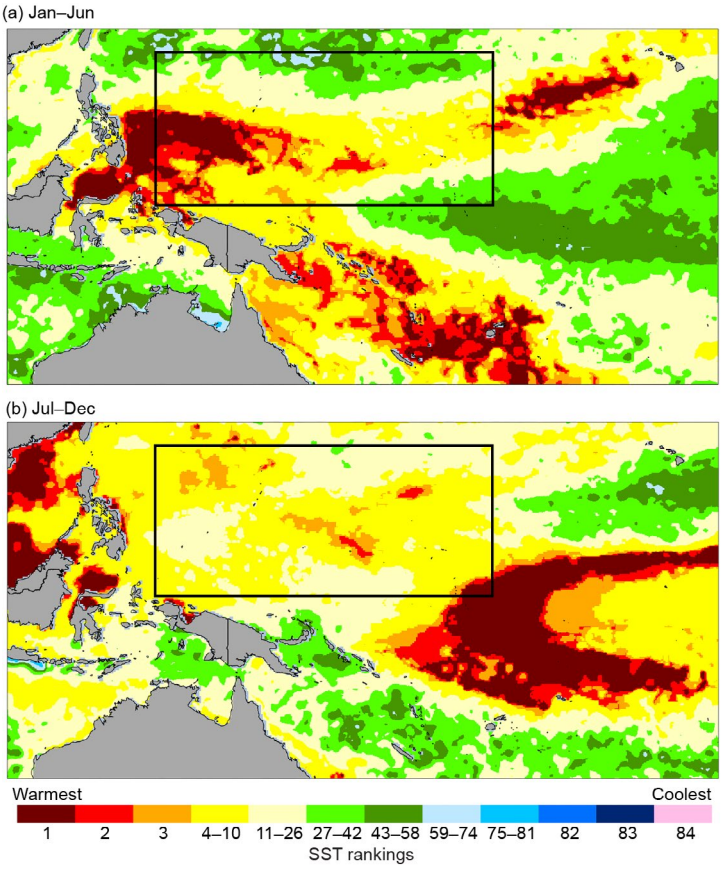

Fig. 7.62. Sea surface temperature rankings for (a) Jan–Jun and (b) Jul–Dec 2023. Ranking are based on 83 years of reanalysis data. The black box defines the northwest Pacific and Micronesia region. (Source: ERA5 and Brettschneider.)

(ii) Precipitation

Precipitation during the first half of the year followed the traditional expectations of El Niño onset with above-normal rainfall observed across Micronesia (Table 7.2; Fig. 7.63). Stations saw well-above-normal rainfall in Guam, Saipan, and Kwajalein during this time.

Patches of drier-than-normal conditions were observed during the second half of the year, particularly in portions of the central and northern Marshall Islands, far southern portions of the ROP, and the northern reaches of the CNMI (Fig. 7.63). Equatorial locations near and east of 150°E experienced very-wet conditions from July to December in response to the strengthening El Niño. Conversely, slightly drier-than-normal conditions were observed across the central and northern RMI. The dry pattern across the northern portion of the Marshall Islands can be attributed to the consolidation of tropical convection closer to the equator, as well as the absence of nascent tropical systems that have typically accompanied strong El Niño events in the past.

Guam, Pohnpei, and Kapingamarangi all experienced their second-wettest year on record, with records stretching back 75, 72, and 21 years, respectively. Saipan ended the year at fourth wettest on record. Although the above-normal rainfall statistics matched expectations of a traditional El Niño, the mechanisms for this above-normal rainfall differed significantly from other notable El Niño years, with one of the main differences this year including a retracted (westward-displaced) monsoon.

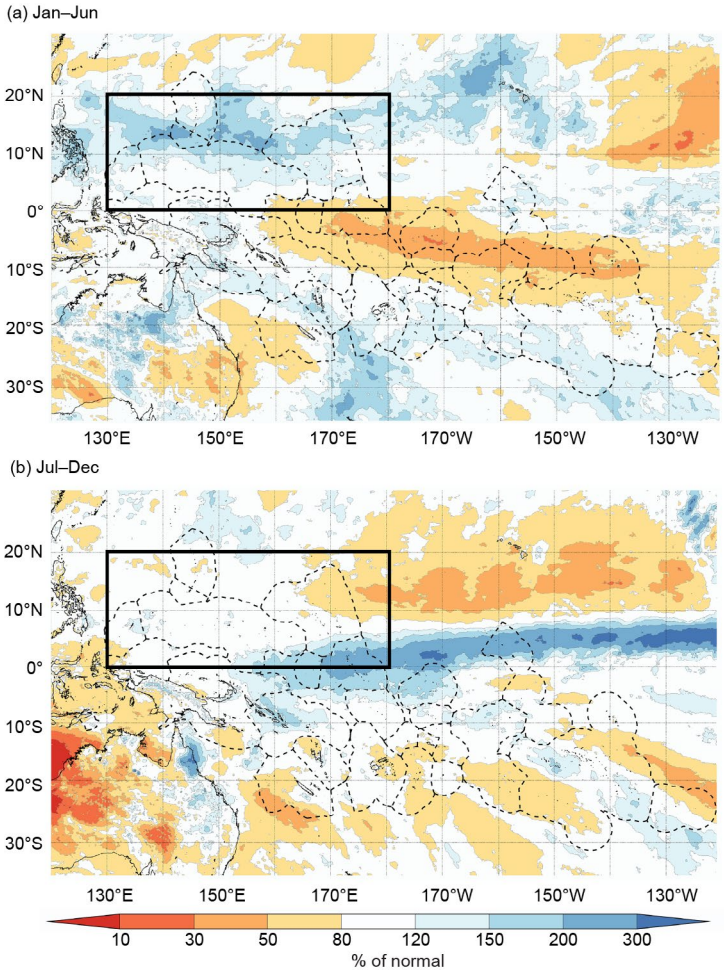

Fig. 7.63. Six-month percent of normal rainfall (%) across the central and western Pacific for (a) Jan–Jun and (b) Jul–Dec 2023. The black box defines the northwest Pacific and Micronesia region. (Source: MSWEP.)

(iii) Notable events and impacts

Typhoon Mawar was the strongest tropical cyclone (TC) to impact Guam since Super Typhoon Pongsona on 8 December 2002. Mawar gathered in Chuuk State during mid-May 2023 before curling northward and rapidly intensifying to a Category 5 super typhoon on approach to Guam. The system weakened to Category 4 and slowed its forward speed considerably as it drifted over the northern tip of Guam on 24 May. As Mawar pulled away, it underwent another period of rapid intensification that kept typhoon-force winds blowing over Guam for a total of 8–10 hours and tropical-storm force winds persisting for roughly 14 hours. Mawar dropped over 600 mm of rain in less than 24 hours, with maximum sustained winds of 210 km h^{-1} to 225 km h^{-1} across far-northern Guam. Damage estimates exceeded $4 billion U.S. dollars.

Mawar was eerily similar to Typhoon Pamela in 1976. Both 1976 and 2023 were developing El Niño years after three years of La Niña. Pamela (1976) and Mawar (2023) spawned in Chuuk State before curving northward during the month of May. Both systems delivered a hefty blow of lengthy typhoon-force winds, bringing torrential rains exceeding 600 millimeters to Guam. While the year 1976 was the wettest year on record at the Guam International Airport (3613.91 mm), 2023 became the second wettest (3556.25 mm). Nearly 20% of the annual rainfall fell in two days during both years, highlighting the importance of these infrequent but high-impact events for the island's water budget and climatology. See the NWS Guam Super Typhoon Mawar Meteorological Assessment for a more detailed examination.

Table 7.2. Average rainfall total (AVG; mm) compared to rainfall total (mm) and percent of average values (%) for select Micronesia locations in 2023 (1991–2020 base period) for Jan–Jun, Jul–Dec, and annual (Jan–Dec). Latitudes and longitudes are approximate. "Kapinga" stands for Kapingamarangi Atoll in Pohnpei State, Federated States of Micronesia. Green-filled cells with an up arrow icon (↑) indicate above-average rainfall and yellow-filled cells with a down arrow icon (↓) represent below-average rainfall. (Source: NOAA's National Weather Service.)

Location	Jan–Jun AVG Rainfall (mm)	Jan–Jun 2023 Rainfall (mm)	Jan–Jun % of Normal Rainfall	Jul–Dec AVG Rainfall (mm)	Jul–Dec 2023 Rainfall (mm)	Jul–Dec % of Normal Rainfall	Jan–Dec AVG Rainfall (mm)	Jan–Dec 2023 Rainfall (mm)	Jan–Dec % of Normal Rainfall
Saipan 15°N, 146°E	462.8	779.3 ↑	168.4 ↑	1306.1	1450.1 ↑	111.0 ↑	1768.9	2229.4 ↑	126.0 ↑
Guam 13°N, 145°E	678.7	1768.1 ↑	263.2 ↑	1813.6	1770.1 ↓	97.6 ↓	2492.3	3556.3 ↑	142.7 ↑
Palau 7°N, 134°E	1798.1	2034.3 ↑	113.1 ↑	2279.4	2256.5 ↓	99.0 ↓	4077.5	4290.8 ↑	105.2 ↑
Yap 9°N, 138°E	1191.5	1310.6 ↑	110.0 ↑	1943.4	1967.5 ↑	101.2 ↑	3134.9	3278.1 ↑	104.6 ↑
Chuuk 7°N, 152°E	1678.2	2145.5 ↑	127.8 ↑	1917.7	2100.8 ↑	109.5 ↑	3595.9	4246.4 ↑	118.1 ↑
Pohnpei 7°N, 158°E	2361.2	3024.6 ↑	128.1 ↑	2308.4	3058.2 ↑	132.5 ↑	4669.6	6082.8 ↑	130.3 ↑
Kapinga 1°N, 155°E	1880.6	2252.0 ↑	119.7 ↑	1485.1	2265.7 ↑	152.6 ↑	3365.7	4517.6 ↑	134.2 ↑
Kosrae 5°N, 163°E	2635.8	3066.5 ↑	116.3 ↑	2354.8	2548.1 ↑	108.2 ↑	4990.6	5614.7 ↑	112.5 ↑
Kwajalein 9°N, 168°E	898.4	1417.6 ↑	157.8 ↑	1553.7	1408.2 ↓	90.6 ↓	2452.1	2825.8 ↑	115.2 ↑
Majuro 7°N, 171°E	1459.0	1750.3 ↑	120.0 ↑	1875.0	1464.6 ↓	78.1 ↓	3334.0	3214.9 ↓	96.4 ↓

The biggest event of 2023 was arguably the unique El Niño that developed. There were a number of aspects that did not follow a "traditional" El Niño year for Micronesia, including westerly wind bursts (WWBs), regional TC activity, sea level heights, SST patterns, and other oscillations on longer time scales, including the PDO. Whereas strong El Niño events of the past featured flurries of WWBs and an anomalous eastward extension of the monsoon trough into far eastern Micronesia, 2023 was characterized by weaker WWBs and an abbreviated monsoon trough. Only 11 typhoons occurred in the western North Pacific basin during 2023, well below the average of 16 (see section 4g4). The number of named storms in 2023 was also extremely low (17 total), and the overall distribution was shunted west and north. While this TC activity and distribution was atypical from an El Niño standpoint, it closely followed the trends observed during the negative phase of the PDO and Pacific Meridional Mode (PMM)—both of which are linked to reduced TC activity across much of Micronesia (PDO: Scoccimarro et al. 2021; Lee et al. 2021; PMM: Zhang et al. 2016). Overall, 2023 TC statistics better matched strong post-El Niño years transitioning to La Niña (e.g., 1998 and 2010) rather than strong El Niño onset years.

Sea level heights also diverged from past strong El Niño events. While sea levels did decrease as one would anticipate during El Niño, the region of below-normal sea level heights was confined to a much smaller area, mainly south of 8°N, with lower magnitudes when compared to previous El Niño events. Sea levels at Guam and Yap typically fall below normal late in the year linked to the peak of El Niño, but tide gauges on both islands remained near or even slightly above normal.

The SOI, a measure of the atmospheric response to the ENSO, did not transition to negative values associated with El Niño until August. This was somewhat delayed compared to other prominent El Niño events. While the SOI remained negative during the second half of 2023, it was weak in magnitude. It is conceivable that the above-normal SSTs observed across much of the tropical Pacific basin during this period, along with the expansion of record SST warmth in the North Atlantic Ocean, disrupted the classic eastward El Niño shift of tropical convection into the central Pacific.

3. SOUTHWEST PACIFIC

—E. Chandler

Countries considered in this section include American Samoa, the Cook Islands, Fiji, French Polynesia, Kiribati, Nauru, New Caledonia, Niue, Papua New Guinea (PNG), Samoa, the Solomon Islands, Tokelau, Tonga, Tuvalu, Vanuatu, and Wallis and Futuna (Fig. 7.60). The temperature analysis is based on the Climate Anomaly Monitoring System (CAMS) monthly surface air temperature anomalies (https://iridl.ldeo.columbia.edu/maproom/Global/Atm_Temp/Anomaly.html). Anomalies are calculated with respect to the 1991–2020 base period. The precipitation analysis is based on the MSWEP monthly analyses as presented for the South Pacific (http://www.bom.gov.au/climate/pacific/outlooks/) and the COSPPac Online Climate Outlook Forum (https://www.pacificmet.net/products-and-services/online-climate-outlook-forum). The base period for precipitation is 1980–2021.

With the transition from La Niña at the beginning of 2023 to El Niño by mid-year, SSTs warmed quickly through the first quarter, with above-normal SSTs widespread by the second quarter across the Pacific, particularly evident in the South Pacific off-equatorial regions (see Figs. 3.2a,b). Atmospheric indicators of El Niño lagged the changes seen in the ocean, with changes to wind and cloud patterns emerging during September and October that were more typical of El Niño. These changes in the atmosphere combined with a strengthening of the warm SSTs along the equator led to a consolidation of El Niño in the Pacific through the last quarter of 2023.

In the early months of 2023, air temperatures and rainfall patterns were both typical of a La Niña event transitioning to ENSO-neutral, with atmospheric patterns more typical of El Niño becoming apparent by the last quarter of the year. Rainfall was suppressed along the equator through the first quarter of 2023, as is typical with La Niña, with the region south of 10°S and west of the Cook Islands tending to receive more rainfall than normal. The La Niña-like rainfall pattern present in early 2023 broke down during the second quarter of the year as the South Pacific transitioned into the dry season. There was a mixed rainfall pattern over the third quarter as the Pacific transitioned towards El Niño, with a more zonal South Pacific Convergence Zone (SPCZ) becoming evident towards the equator by September. Through the last quarter of 2023, enhanced rainfall was present along the equator extending the width of the Pacific. Suppressed rainfall became increasingly evident over the South Pacific from September onwards, reaching a peak in terms of magnitude and spatial extent over November and December. This pattern of rainfall across the South Pacific is often associated with El Niño.

(i) Temperature

Along the equator, air temperatures were up to 1°C below normal on and to the east of the dateline through to Kiribati during January and February, associated with warmer SSTs in the same region. A small region of below-normal air temperatures (anomalies of up to –1°C) was located near Tonga during January; however, that region weakened to near-normal levels by February, with March air temperatures having been close to normal across the Pacific (Fig. 7.64a).

Warm air temperature anomalies near the South American coast were present and extended westwards along the equator though the second quarter of the year (Fig. 7.64b), and were associated with increasing SST anomalies. Though a small region of cooler air temperatures up to 1°C below normal was located to the south of the Cook Islands during May, it warmed to near-normal by June.

During July–September (JAS), the area of +1°C to +3°C anomalies continued to expand westward along the equator in the South Pacific (Fig. 7.64c), reaching western Kiribati (Gilbert

Island group) by September with air temperature anomalies of up to +1°C. Off-equatorial air temperatures were near normal across the South Pacific.

During October–December (OND), the region of positive air temperature anomalies along the central equatorial region persisted (Fig. 7.64d). Anomalies of up to +2°C were present over much of Kiribati by December. Small regions of below-normal air temperatures were present in the off-equatorial South Pacific to the east of the dateline near Tonga and Niue during October. This region expanded during November and December eastwards to French Polynesia, with temperature anomalies reaching up to –1°C.

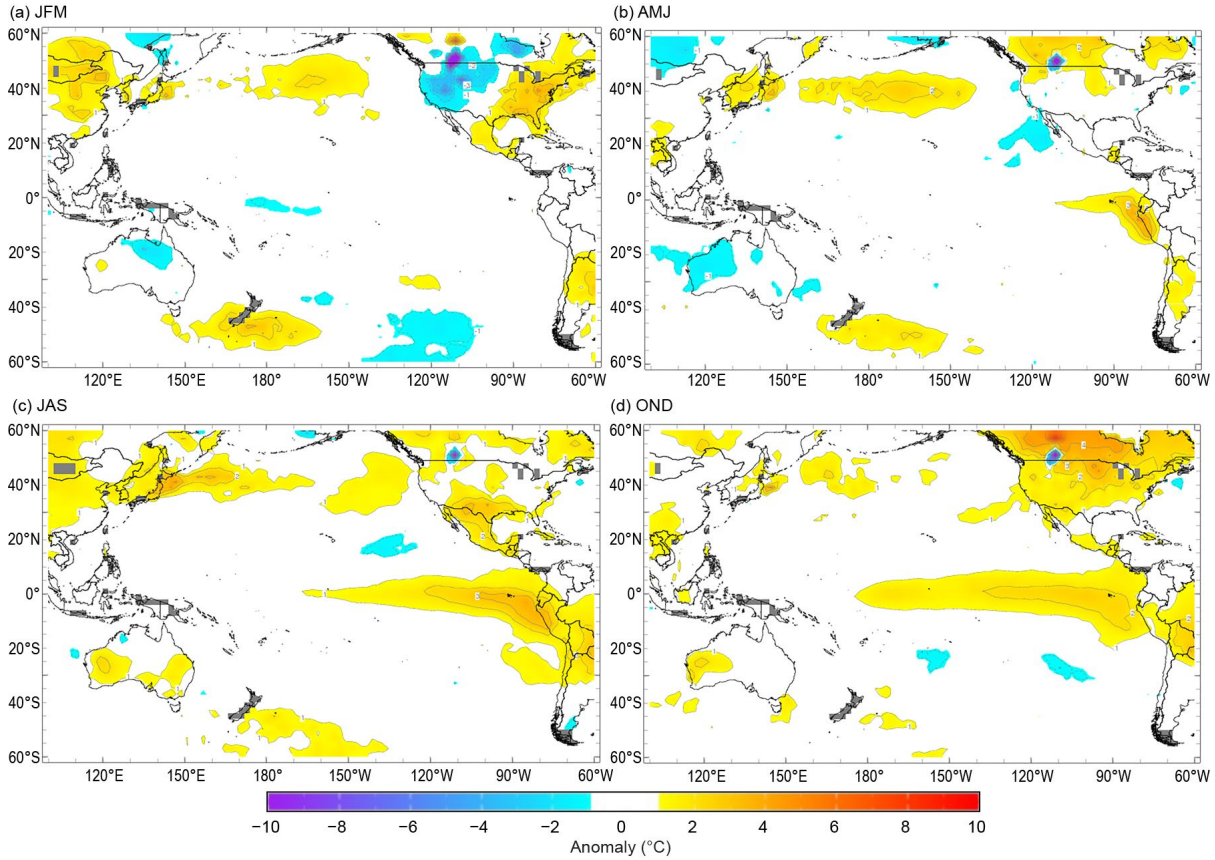

Fig. 7.64. Seasonal air temperature surface anomalies (°C) across the Pacific for (a) Jan–Mar, (b) Apr–Jun, (c) Jul–Sep, and (d) Oct–Dec. (Source: CAMS.)

(ii) Precipitation

The year began with suppressed rainfall along the equator over Kiribati, Nauru, Tuvalu, Tokelau, northern American Samoa, the northern Cook Islands, and northern French Polynesia, in a pattern typically associated with an established La Niña (Fig. 7.65a). In Tuvalu, Niulakita recorded its driest JFM on record with 358 mm (70-year climatology). The suppressed rainfall over the quarter led to several locations in Tuvalu and the northern Cook Islands receiving rainfall in their bottom 10th percentiles. The rainfall pattern south of 10°S was closer to normal with regions of enhanced rainfall. The southern Solomon Islands, Vanuatu, New Caledonia, Fiji, Wallis and Futuna, the southern Cook Islands, and southern French Polynesia experienced enhanced rainfall during January; however, through February and March, suppressed rainfall was evident over parts of the southern Solomon Islands and Fiji as rainfall patterns began to transition towards an ENSO-neutral pattern for the Pacific. Parts of Fiji recorded rainfall in their top 10th percentile during this period.

Through the second quarter of the year, the Pacific rainfall pattern was mixed as rainfall over the region continued to transition from La Niña to ENSO-neutral (Fig. 7.65b). April–June (AMJ) rainfall was near or slightly below normal over most of the region north of 10°S, although in a narrower band than during the first quarter of the year. The region of suppressed rainfall covered Kiribati (excluding the northern Line Islands), the northeastern Solomon Islands, Tuvalu and Tokelau, northern American Samoa, the northern Cook Islands, and northern French Polynesia. Another region of suppressed rainfall was present covering New Caledonia and extending to the

Australian coast. Regions of enhanced rainfall were present over most of PNG, Samoa, Tonga, Niue, the southern Cook Islands, and western and central French Polynesia. Niuatoputapu (Tonga) recorded its third-wettest AMJ on record (75 years) with 914 mm, and Faleolo (Samoa) recorded 622 mm of rainfall during AMJ, making 2023 the seventh-wettest year in its 58-year record.

Positive rainfall anomalies were present along the equator during JAS, reflecting a developing El Niño (Fig. 7.65c). The region of enhanced rainfall covered Nauru and Kiribati, causing the precipitation totals of both countries to reach their top 10th percentiles during JAS. Rainfall was also enhanced in a band from eastern PNG to Vanuatu and southern Fiji. Rainfall in this region during September was associated with an enhanced SPCZ, which was evident close to the northern Solomon Islands and in a band stretching eastward across to the northern Cook Islands. The Solomon Islands had several stations record rainfall in their top 10th percentile. Taro (Solomon Islands) and Tarawa (Kiribati) saw their second-wettest JAS on record (45- and 74-year records, respectively), with the former recording 1254 mm and the latter recording 1080 mm. In contrast, patches of suppressed rainfall covered much of the southern half of PNG and the far southern Solomon Islands into western New Caledonia. There were other isolated patches of suppressed rainfall over northern Tuvalu, the southern Phoenix Islands (Kiribati), southern Tonga, American Samoa, the central Cook Islands, and western French Polynesia.

Rainfall patterns during October–December (OND) reflected the emergence of El Niño. Rainfall was enhanced across the width of the Pacific, extending westwards over Kiribati, Nauru, and parts of PNG (Fig. 7.65d). Off the equator, rainfall was also enhanced over parts of the Solomon Islands, Nauru, northern Tuvalu, northern Tokelau, and the northern Cook Islands. Nauru recorded its wettest OND in the 80-year record with 1461 mm of rainfall, while stations across Tuvalu, Kiribati, and the Solomon Islands all recorded rainfall in their top 10th percentiles. In a typical El Niño rainfall response, rainfall across New Caledonia, Vanuatu, Fiji, Tonga, parts of Samoa and Niue, the southern Cook Islands, and southern French Polynesia was suppressed. Tonga, Fiji, and the southern Cook Islands all recorded rainfall in their lowest 10th percentiles on record, with Rarotonga (the Cook Islands) recording its second-lowest OND in its 125-year record with 209 mm.

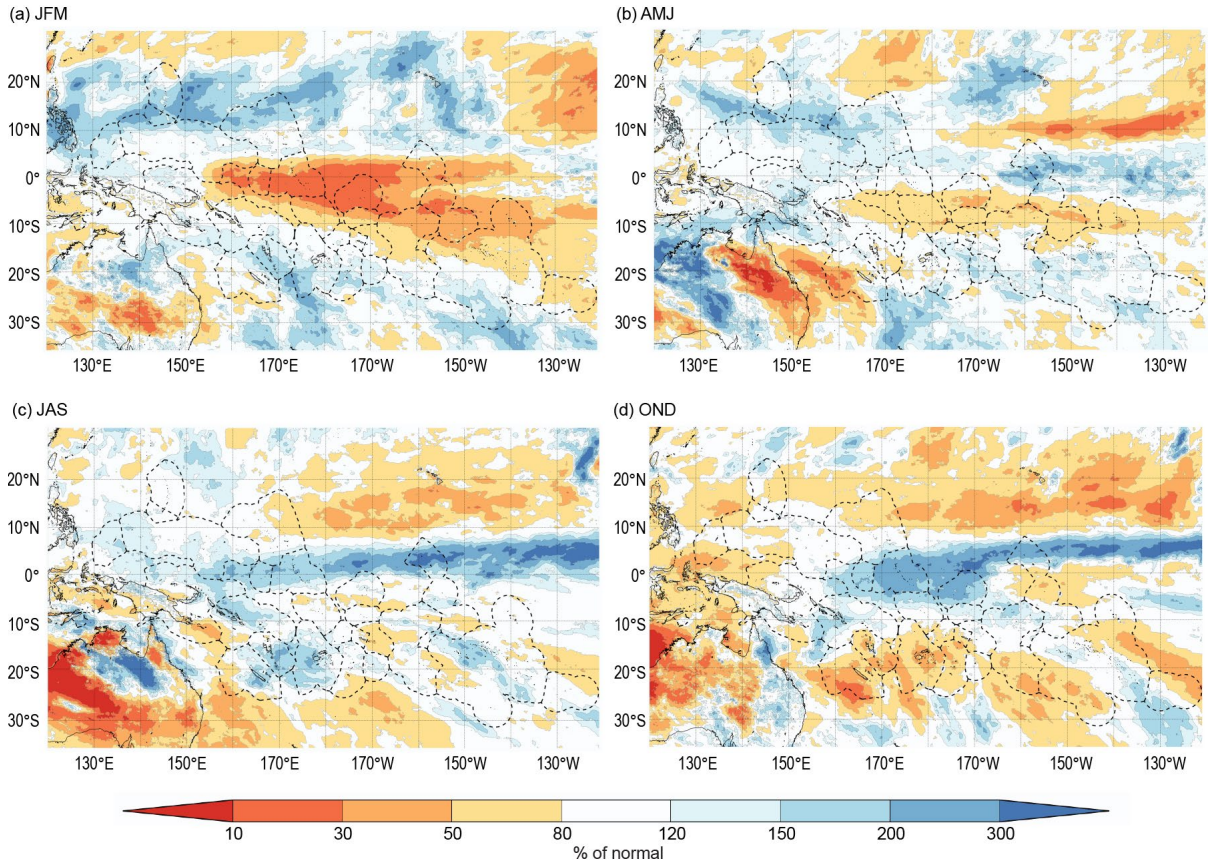

Fig. 7.65. Seasonal percentage of normal rainfall (%) across the southwest Pacific for (a) Jan–Mar, (b) Apr–Jun, (c) Jul–Sep, and (d) Oct–Dec. (Source: MSWEP.)

(iii) Notable events and impacts

The most devastating TCs to affect the South Pacific in 2023 were severe TCs Kevin and Judy, which both impacted Vanuatu within 48 hours of each other in early March. TC Judy formed north of Fiji and tracked to the west, passing to the south of the Solomon Islands in late February as the cyclone intensified. Judy then tracked southward directly over many of the central and southern islands of Vanuatu. At its peak, Judy's 10-minute sustained winds reached 175 km h^{-1} (Category 4) and a lowest central pressure of 941 hPa. Conversely, TC Kevin formed off the Australian coast in late February and tracked southeastward and, influenced by a subtropical ridge, passed over the southern islands of Vanuatu. The lowest central pressure recorded was 918 hPa, while 10-minute sustained winds peaked at 215 km h^{-1} (Category 5) as it passed away from Vanuatu.

All islands of Vanuatu were influenced by one or both cyclones over a four-day period, with approximately 80% of the population being affected by at least Category 2 winds. There were extensive interruptions to running water and power in various regions, including the capital Port Vila on 4 March, where the international airport sustained wind damage. Central Vanuatu provinces of Shefa, Tafea, Penama, and Malapa were the worst impacted in terms of damage to infrastructure and loss of communications. Fortunately, there were no reported deaths associated with either cyclone.

4. AUSTRALIA

—C. Minney

For this section, monthly area-averaged temperatures are based on the ACORN-SAT dataset (Trewin 2018), while mapped temperature analyses are based on the AWAP dataset (Jones et al. 2009), both of which begin in 1910. Area-averaged rainfall values and mapped analyses use the AGCD dataset (Evans et al. 2020), which begins in 1900. Anomalies are based on the 1991–2020 average.

(i) Temperature

The year 2023 was Australia's equal eighth-warmest year on record since 1910, with the area-averaged mean temperature having been 0.34°C above the 1991–2020 average. The area-averaged annual mean maximum temperature (Fig. 7.66) was 0.58°C above the 1991–2020 average. The area-averaged annual mean minimum temperature (Fig. 7.67) was 0.10°C above the 1991–2020 average. Maximum temperature anomalies were positive across most of Australia, excluding some areas across the tropical north and southern mainland coastal regions. Anomalies of +1°C to +2°C were recorded in Western Australia and across the Queensland–New South Wales border, extending into South Australia; anomalies of −0.5°C to −1.0°C below average were mostly observed in central parts of the Northern Territory. Minimum temperature anomalies varied across Australia; negative anomalies were recorded across much of the northern half of Australia, extending into New South Wales and eastern South Australia. Positive minimum temperature anomalies of up to +1.5°C were recorded in central Western Australia, northern South Australia, and southwest Queensland.

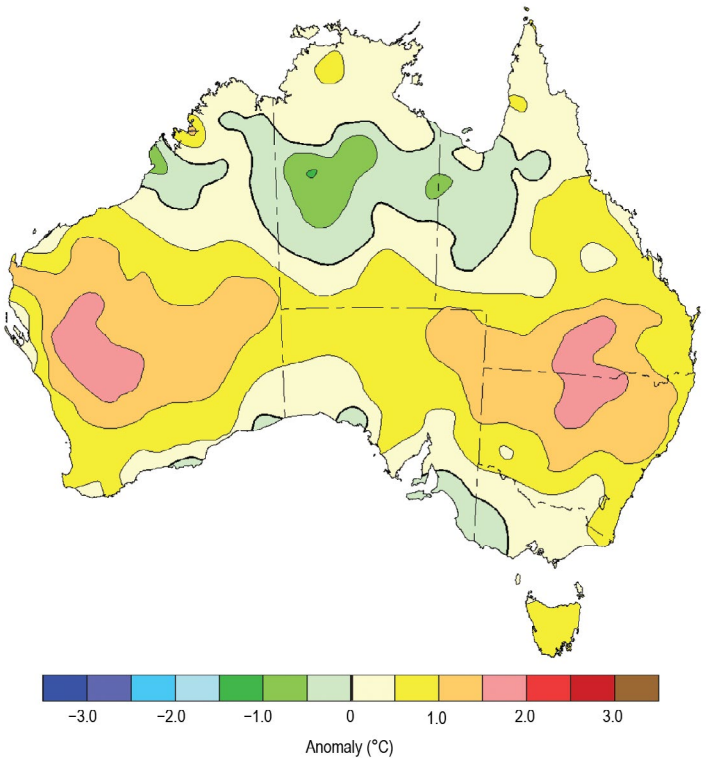

Fig. 7.66. Maximum temperature anomalies (°C) for Australia, averaged over 2023, relative to a 1991–2020 base period. Australian States/Territories are as follows, starting clockwise from the west: Western Australia, the Northern Territory, Queensland, New South Wales, Victoria, and South Australia, with the island of Tasmania in the southeast. (Source: Australian Bureau of Meteorology.)

Nationally, January was the coldest since 2002 and cool conditions continued into February for much of northern Australia, while the month was warmer for much of Western Australia. The autumn (March–May) area-averaged mean temperature was close to average.

The remainder of the year saw a shift towards warmer-than-usual temperatures. It was Australia's warmest June–November on record (since 1910). Record-high temperatures aligned with a developing El Niño and positive Indian Ocean dipole (IOD), both of which are known to increase maximum/minimum temperatures in the austral winter and spring (McKay et al. 2022). It was the warmest June on record for much of Queensland, and most of Tasmania and the eastern parts of southeast Australia had their warmest July on record. The national mean temperatures for June, July, August, September, November, and December were among their respective 10 warmest on record. The year finished up with the fourth-warmest December on record nationally.

(ii) Precipitation

Nationally, the area-averaged annual rainfall total for Australia during 2023 was 472.5 mm. This was 2.78% below the 1991–2020 average of 486.0 mm. Compared to the distribution across all years of observation from 1900 to 2023, rainfall in 2023 (Fig. 7.68) was above to very much above average across much of northern Australia and below average for much of Tasmania, northern New South Wales, southern Queensland, eastern South Australia, and western and southern Western Australia. Some small isolated areas of Cape York Peninsula in Queensland had their wettest year on record, while some localized parts of the western Australian coastline had their driest year on record.

A number of climate influences affected Australia's rainfall during 2023. These included a La Niña, which weakened and dissipated at the start of the year, and an El Niño and positive IOD that developed during the latter half of the year (Ashok et al. 2003; Hendon et al. 2007; McKay et al. 2023; see sections 4b and 4f for more details on the El Niño–Southern Oscillation and the IOD, respectively). During November and December, much of eastern Australia

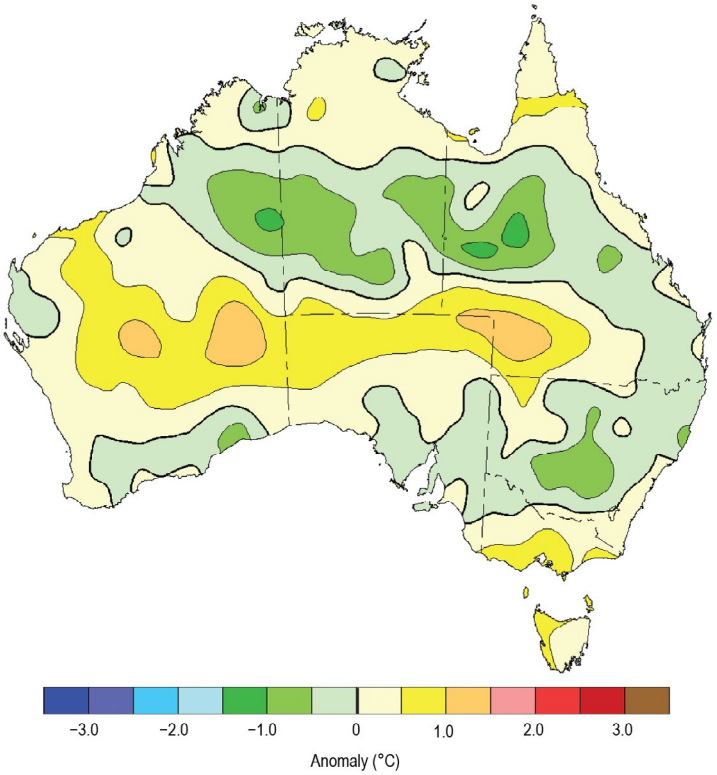

Fig. 7.67. Minimum temperature anomalies (°C) for Australia, averaged over 2023, relative to a 1991–2020 base period. (Source: Australian Bureau of Meteorology.)

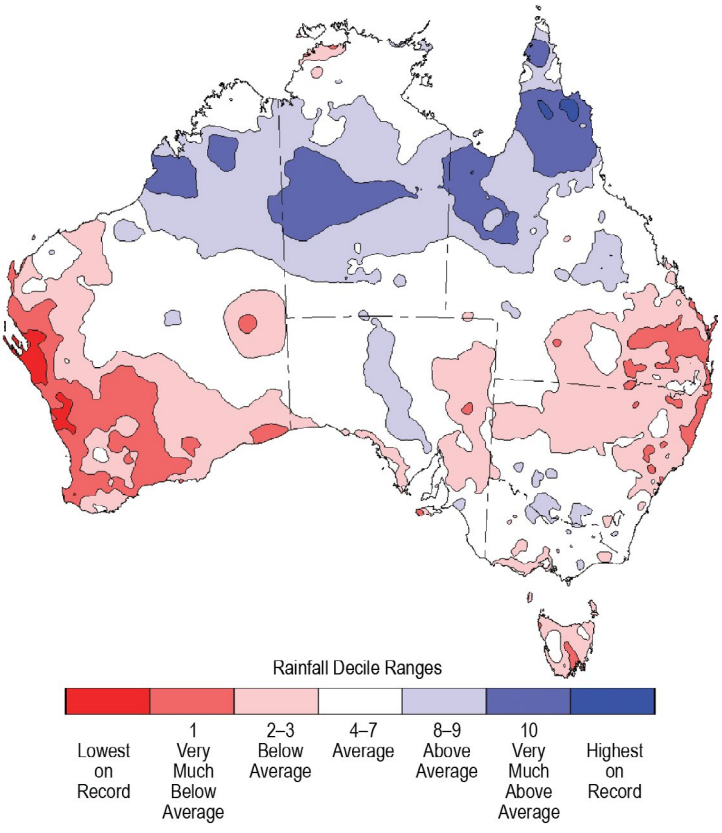

Fig. 7.68. Rainfall deciles for Australia for 2023, based on the 1900–2023 distribution. (Source: Australian Bureau of Meteorology.)

experienced widespread and at times heavy rainfall, along with isolated severe thunderstorms. A positive Southern Annular Mode (SAM) during December likely contributed to above-average rainfall over much of eastern Australia (Hendon et al. 2007). The positive SAM was influenced by a stronger-than-normal winter polar vortex (Thompson et al. 2015; see section 6b for details). Warm ocean temperatures surrounding Australia, particularly in the Tasman and Coral Seas located to the southeast and northeast of Australia, respectively, likely contributed to changes in the expected El Niño influence on rainfall patterns during November and December. The 2023 El Niño was unusual due to above-average SSTs persisting in the western Pacific. These changed SST patterns likely contributed to a delayed atmospheric Southern Oscillation Index response to SSTs and a weak response in cloudiness and wind patterns and, therefore, reduced drying impact across Australia (see http://www.bom.gov.au/climate/current/season/aus/summary.shtml).

January–April generally saw above-average rainfall across northern Australia. Rainfall was very much above average (top 10% of January–April periods) for parts of the northern Kimberley in Western Australia, which was impacted by Tropical Cyclones Ellie and Ilsa. While rainfall is typically high during the wet season in these regions, very-much-above-average rainfall for the season was also recorded in northern Queensland, which was associated with monsoonal rain and brought significant flooding to some parts. Rainfall was mostly near average farther south; however, some parts of southern Queensland, northern New South Wales, and Tasmania were below average for the four months, as was coastal western Australia, which typically receives low warm-season rainfall.

May–July mostly saw drier conditions for parts of southern and eastern Australia, with unseasonable rain events in June and July for much of the north, particularly northwestern Australia. August–October 2023 was the driest three-month period in Australia on record (since 1900), with a national area-averaged rainfall total of 22.63 mm. Most of Australia recorded below-average rainfall during this period; rainfall was the lowest on record across much of southern Queensland. Soil moisture was below to very much below average for much of southern Australia during this period.

High rainfall totals preceding 2023 meant water storages and soil moisture were high at the beginning of the year. Dry conditions during 2023 reduced overall water storages; however, storages remained high at the end of the year (74.1% accessible capacity). Rainfall deficits emerged, with May–December experiencing severe and serious deficiencies (lowest 5% and 10% of rainfall records, respectively) over much of the west of Western Australia and northern New South Wales.

(iii) Notable events and impacts

The year started with heavy rainfall, flooding, and storms across much of northern Australia. Ex-Tropical Cyclone Ellie caused significant flooding in January with the Fitzroy River in north-west Australia exceeding its major flood level and significantly impacting local communities.

Heatwaves affected many areas across Australia during February and March. Severe-intensity heatwaves affected southern Victoria and much of Western Australia during February, as well as the Pilbara district of Western Australia during March. Tropical Cyclone Ilsa made landfall as a Category 5 system on 14 April on the Pilbara Coast of Western Australia. Prior to making landfall on the Australian mainland, the highest 10-minute sustained wind speed on record across the Bureau's observation network, at 219 km h^{-1}, was recorded over Bedout Island on 13 April as Ilsa passed directly over.

Heatwaves and unusually warm conditions were experienced from September to December. Unusually warm conditions during September and October led to elevated fire risk in the Northern Territory, Queensland, and New South Wales due to the dry landscape and warm winter and spring conditions. Bushfires burned for weeks in the Northern Territory, including an estimated 1 million hectares burned by a large bushfire east of Tennant Creek, 2.8 million hectares burned in the Barkly region, and millions of hectares burned across the Tanami and central Australia (Northern Australian Fire Information 2024). Northern, central, and western Australia continued to be affected by heatwaves throughout November and December, including extreme heatwave conditions in northwest Western Australia at the end of December. Drought conditions developed along the east coast between January and October, easing with high rainfall during

November and December. Serious to record-low rainfall deficiencies also developed between May and October for much of southern Western Australia.

Significant rainfall from a series of low-pressure troughs impacted eastern Australia during the latter half of December. Severe thunderstorms impacted areas of southern and central Queensland between the 24th and 31st. Impacts included large hail, reports of a tornado between Queensland's Gold Coast and Scenic Rim, flash flooding, and damaging winds. November and December rainfall eased the rapidly developing drought conditions along most of the east coast.

Tropical Cyclone Jasper made landfall near Wajul Wajul on the Queensland north-east coast on 13 December as a Category 2 system. As the storm moved inland, it stalled over the Cape York Peninsula, bringing several days of heavy rainfall and major flooding, landslides, road closures, and damage to businesses and crops. The stalling of the system inland as well as the formation of a trough significantly contributed to the heavy rainfall totals and associated impacts.

5. AOTEAROA NEW ZEALAND

—T. Meyers

(i) Temperature

The year 2023 was New Zealand's second warmest on record, based on the mean temperature from the National Institute of Water and Atmospheric Research's (NIWA) seven-station series, which began in 1909. Annual temperatures were above average (defined as 0.51°C–1.20°C above the 1991–2020 average) or well above average (>1.20°C above average) for much of Aotearoa New Zealand (Fig. 7.69a). Small pockets of near-average temperatures (–0.50°C to +0.50°C of average) were observed around Northland, Auckland, Bay of Plenty, Gisborne, Hawke's Bay, eastern Wairarapa, southern Marlborough, Canterbury high country, and Otago.

Data from NIWA's seven-station series shows that eight months of 2023 had temperatures that were above or well above average. May and September were both the warmest on record at an astounding 1.10°C and 2.00°C above their 1991–2020 monthly averages, respectively. Meanwhile, August was relatively cool, having seen a mean temperature of –0.55°C below average and becoming the first month to have below-average national temperatures (0.51°C–1.20°C below average) since May 2017.

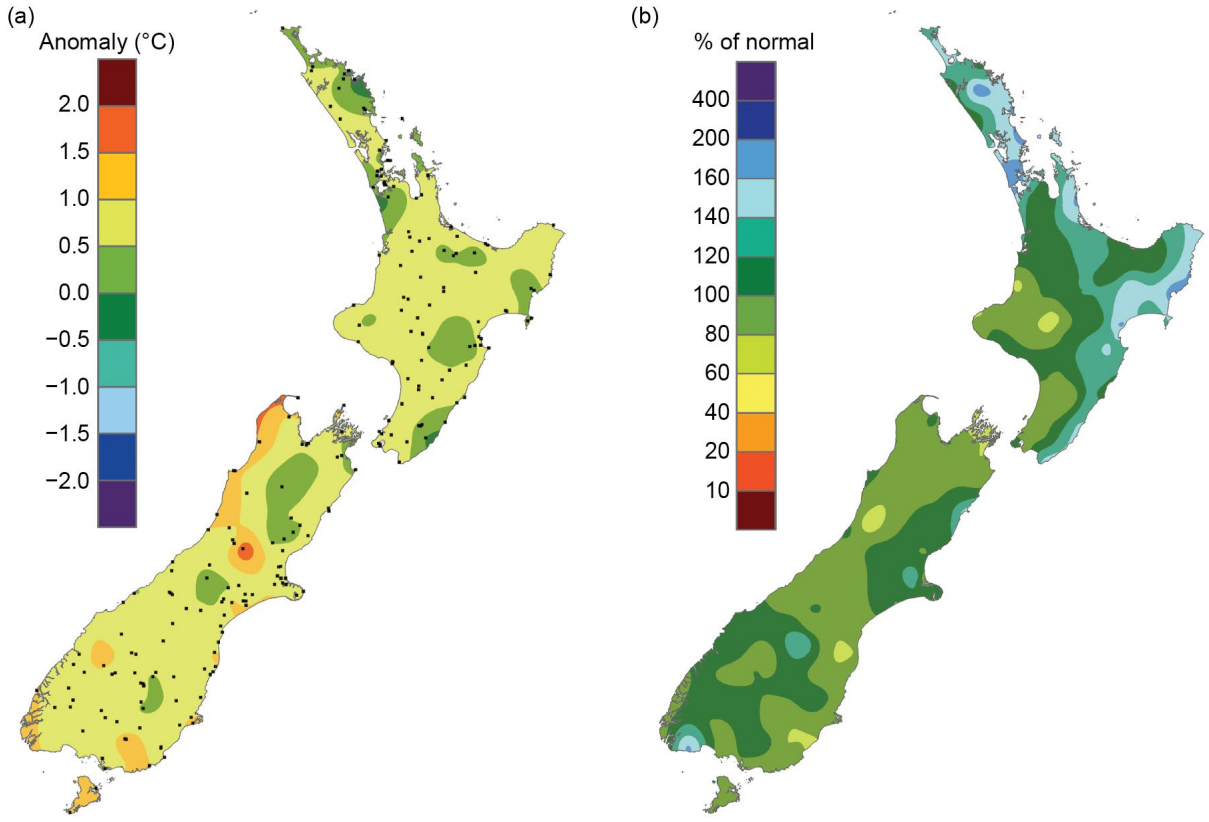

Fig. 7.69. Annual (a) average temperature anomaly (°C) and (b) total rainfall (% of normal) for 2023, relative to 1991–2020. The black dots in (a) represent the locations of climate stations used to create both the temperature and rainfall maps.

In terms of annual minimum and maximum temperatures, it was also the second-warmest year on record for both. Across the country, 58 locations observed a record or near-record annual mean temperature, 43 locations observed a record or near-record annual mean maximum temperature, and 52 locations observed a record or near-record annual mean minimum temperature. For the eighth consecutive year, no locations experienced a record or near-record cold year.

The record or near-record heat experienced around the country throughout 2023 and in recent years is consistent with expectations of a warming planet caused by anthropogenic climate change. Coastal sea surface temperatures (SSTs) also influenced terrestrial temperatures in New Zealand during 2023, with SSTs near the coasts exhibiting record or near-record warmth in all regions but the northern North Island. Coastal SSTs were average or above average nearly every month, with February ranking as the most unusually warm month as monthly SSTs off the west of the South Island peaked at 3.19°C above average, according to NOAA's OISSTv2. Averaged across 2023, SSTs were the highest on record near the eastern South Island, second highest on record near the western North Island, northern South Island, and western South Island, and third highest on record in the eastern North Island since records began in 1981.

Farther afield, SSTs around the Tasman Sea and Coral Sea were also above average for the majority of the year, and thus added to an increase in the atmospheric water vapor content around New Zealand. This in turn contributed to higher-than-average humidity, which resulted in warmer-than-average nights.

La Niña also influenced New Zealand's climate, which tends to be associated with higher-than-normal air pressure near and to the east of the country, with lower pressures to the north. This contributes to more sub-tropical, northeasterly winds than normal, which increases air temperatures, sea temperatures, and humidity. This air flow was common in the first half of the year. Meanwhile, El Niño tends to be associated with lower-than-normal air pressure to the south and southeast of the country and higher-than-normal air pressure to the north. This can lead to an increased north-to-south pressure gradient, intensifying spring-time westerly winds and fronts as they move across the county. This air flow occurred more consistently during the second half of 2023, as the ocean–atmosphere system transitioned to El Niño. However, one atypical element of the building El Niño was a persistent blocking high-pressure system to the southeast of New Zealand, which was a holdover from La Niña. This high-pressure system slowed the typical progression of weather patterns from west to east across the country and led to more northerly winds than what is usually associated with a classical El Niño circulation regime.

(ii) Precipitation

As shown in Fig. 7.69b, rainfall was well above normal (>149% of the annual normal) for parts of Northland, Auckland, Coromandel, Gisborne, and Hawke's Bay, while above-normal rainfall (120%–149% of normal) was observed throughout these same areas, as well as much of eastern Wairarapa, the eastern Tararua District, and the Bay of Plenty. Near-normal rainfall (80%–119% of normal) was observed for the rest of the country, except for small and isolated areas of below-normal rainfall (50%–79% of normal) in the Central Plateau, the West Coast, South Canterbury, and eastern Otago.

Despite the several extreme rainfall events that occurred throughout the first part of the year, 2023 was only New Zealand's 21st-wettest year on record, based on an analysis of areal-averaged rainfall anomalies from NIWA's Virtual Climate Station Network (VCSN) dating back to 1961. The nationwide rainfall anomaly in the VCSN was 104% of normal compared to the 1991–2020 normal. Of all the regularly reporting gauges, the wettest location in 2023 was Cropp River (West Coast), at 975 m a.s.l with 11,717 mm. The driest of the regularly reporting rainfall sites in 2023 was Ranfurly in the Otago region of the South Island, which reported only 359 mm.

(iii) Notable events and impacts

On 27 January, a highly localized convective weather system delivered unprecedented rainfall amounts in an event dubbed the "Auckland Anniversary Floods." Within 12 hours, over 200 mm was observed at Māngere and Auckland Airport, with hourly rainfall rates as high as 73 mm recorded. Auckland Airport was severely flooded, with floodwaters throughout the terminal buildings forcing the airport to temporarily close. Tens of thousands of travelers were impacted

by canceled and diverted flights. A state of emergency was declared in Auckland. Largely due to this event, the homogenized central Auckland rainfall series (Fowler 2021) recorded a January total of 539 mm at Albert Park, shattering the previous all-months record of 420 mm from February 1869. Rainfall data from this series began in 1853.

From 12 to 15 February, Post-Tropical Cyclone Gabrielle hit New Zealand, resulting in 11 fatalities, widespread flooding, and extensive damage to key infrastructure in the east coast of the North Island, including roads, electricity, telecommunication, and water infrastructure. A National State of Emergency was declared for only the third time in New Zealand's history. At the height of the cyclone's impact, around 225,000 homes were without power, and thousands of people were displaced as flood waters rose. In the worst-affected areas, there was significant damage to agricultural land, property, and livelihoods. Gabrielle ranks as one of the costliest natural disasters in New Zealand history, with over $16 billion New Zealand dollars ($9.5 billion U.S. dollars) of costs to the insurance industry.

Powerful winds associated with Gabrielle brought considerable damage to forestry areas in the central North Island. Nine sites recorded their strongest gust on record during 12 and 13 February, including a 124 km h^{-1} gust at Mount Ruapehu Chateau. Over 6000 hectares of pine was destroyed due to these powerful winds, possibly by a sting jet (a narrow, transient, and mesoscale airstream that descends from the mid-troposphere to the surface in some extratropical cyclones).

Exceptional flooding was seen in Hawke's Bay due to Gabrielle, particularly in Esk Valley, Hastings, where floodwater levels reached nearly to the roofs of homes and trapped dozens of people. Tareha recorded 561 mm in 24 hours on 13 February, the highest 24-hour rainfall total to be recorded in 2023 from a low-elevation station. During the event, 22 stations set new February daily rainfall records, including Whangārei (216 mm), parts of Auckland (147 mm), Napier (176 mm), and Hastings (126 mm). Entire communities were cut off due to floodwaters in Hawke's Bay and Gisborne.

Auckland, Gisborne, and Napier all experienced their wettest year on record as a result of these major rainfall events. The record for Napier is particularly noteworthy, as rainfall observations began in 1870.

Acknowledgments

Europe

Much of the information in this section is based on national climate reports kindly provided by the National Meteorological and Hydrological Services (NMHSs) of the World Meteorological Organization (WMO) Regional Association (RA) VI region. The information has been compiled at the WMO RA VI Regional Climate Centre (RCC) Node on Climate Monitoring, located at Deutscher Wetterdienst (DWD) in Germany. National contributions have been made to the cooperation between NMHSs and the RCC. https://rcccm.dwd.de/DWD-RCCCM/EN/products/reports/monthlyreports_national.html?nn=500112

Oceania

The editors wish to thank the numerous NMHSs for collecting and providing data for this report. Special thanks to all the authors in this section for their timely contributions, and the thoughtful and constructive comments from the internal and external reviewers and document editors. Data centers such as NCEP/NCAR, ECMWF-ERA, and CHIRPS are also acknowledged for making their data freely available.

The Oceania editor would like to acknowledge and thank Nava Fedaeff of the National Institute of Water and Atmospheric Research for stepping in and assisting with reviewer comments while her colleague was on leave welcoming his first child into the world.

Appendix 1: Acronyms

ANDMA	Afghanistan National Disaster Management Authority
ARCS	Afghan Red Crescent Society
C3S	Copernicus Climate Change Service
CA	Central America
CA	Central Asia
CAMS	Climate Anomaly Monitoring System
CA-NWS	Central America National Weather Service
CAR	Central African Republic
CDI	Combined Drought Indicator
CNMI	Commonwealth of the Northern Mariana Islands
CONUS	contiguous United States
DMH	Dirección de Meteorologia e Hidrologia
DRC	Democratic Republic of the Congo
DWD	Deutscher Wetterdienst
ECCC	Environment and Climate Change Canada
EHD	extreme high-temperature days
ENSO	El Niño–Southern Oscillation
FWI	Fire Weather Index
GPCC	Global Precipitation Climatology Centre
IOD	Indian Ocean dipole
LPB	Parana-La Plata basin
LTA	long-term average
LTM	long-term mean
NAO	North Atlantic Oscillation
NCEP/NCAR	National Centers for Environmental Prediction/National Center for Atmospheric Research
NCT	Tmax averaged over North China
NEM	northeast monsoon
NIWA	National Institute of Water and Atmospheric Research
NMHS	National Meteorological and Hydrological Service
NS	Nova Scotia
OCHA	Office for the Coordination of Humanitarian Affairs
OLR	outgoing longwave radiation
PM2.5	fine particulate matter
PMM	Pacific Meridional Mode
PNG	Papua New Guinea
RA VI	Regional Association VI
RCC-CM	Regional Climate Centre on Climate Monitoring
RFE2	satellite rainfall estimates version 2
RMI	Republic of the Marshall Islands
ROK	Republic of Korea
ROP	Republic of Palau
SAM	Southern Annular Mode
SOI	Southern Oscillation Index
SPCZ	South Pacific Convergence Zone
SSA	southern South America
SST	sea surface temperature

TAP	tropical Atlantic
TC	tropical cyclone
TIS	tropical Indian Ocean SST
Tm	mean temperature
Tmax	daily maximum
VCSN	Virtual Climate Station Network
WMO	World Meteorological Association
WWB	westerly wind burst

Appendix 2: Supplemental materials

Appendix Table 7.1. Maximum temperatures (TMax; °C) observed in central South America during heatwaves from August to November 2023. Long-term mean (LTM) is 1991–2020. (Sources: Peru: Servicio Nacional de Meteorología e Hidrología del Perú [SENAMHI]; Bolivia: Servicio Nacional de Meteorología e Hidrología del Bolivia [SENAMHI]; Brazil: Instituto Nacional de Meteorlogia [INMET]; Paraguay: Dirección de Meteorología e Hidrología [DMH].) A standalone dash indicates the information was not available.

August Heatwave 2023			
Location	Date	TMax	LTM
BRAZIL, Cuiabá	08/20	41.8	34.7
BRAZIL, São Paulo	08/23	32.3	24.5
BRAZIL, Rio de Janeiro	08/22	38.7	27.0
BOLIVIA, Magdalena	08/22	39.2	33.7
BOLIVIA, Guajaramirim	08/24	39.0	33.7
BOLIVIA, Ascensión de Guarayos	08/31	39.7	30.8

September Heatwave 2023			
Location	Date	TMax	LTM
BRAZIL, São Paulo	09/24	36.5	25.2
BRAZIL, São Paulo	09/23	34.8	25.2
BRAZIL, Curitiba	09/23	31.8	22.3
BRAZIL, Goiania	09/23	38.0	34.0
BRAZIL, Cuiabá	09/23	41.2	35.6
BRAZIL, Rio Branco	09/23	37.1	33.7
BRAZIL, Belém	09/23	36.3	33.2
BRAZIL, Belo Horizonte	09/25	37.5	29.9
BRAZIL, Brasília	09/25	34.8	29.1
BOLIVIA, Cobija	09/24	**39.8**	33.2
BOLIVIA, San Borja	09/24	40.4	32.8
BOLIVIA, Magdalena	09/25	**40.3**	34.1
BOLIVIA, San Joaquin	09/25	40.2	33.9
BOLIVIA, Puerto Suarez	09/26	41.3	31.9

Location	Date	TMax	LTM
BOLIVIA, San José de Chiquitos	09/26	42.7	33.7
BOLIVIA, La Paz-Laykacota	09/26	**27.5**	19.7
BOLIVIA, San Ramón	09/27	39.8	28.9
PARAGUAY, Mariscal Estigarribia	09/24	43.6	32.7
PARAGUAY, Paraguari	09/24	39.6	27.3
PARAGUAY, Villarica	09/24	38.6	27.3
PARAGUAY, Aer. Int Guarani	09/24	39.6	27.5
PARAGUAY, Caazapá	09/24	38.5	26.4
PARAGUAY, Capitan Meza	09/24	38.8	25.7
PARAGUAY, Encarnación	09/24	37.6	26.1
PARAGUAY, Pedro Juan Caballero	09/24	38.6	28.6
PARAGUAY, Puerto Casado	09/24	42.0	31.7
PERU, Papayal	09/25	35.8	28.6
PERU, Tingo de Ponaza	09/27	41.4	33.5
PERU, Chichas	09/24	28.3	–
PERU, Tabaconas	09/27	28.5	–
PERU, San Ignacio	09/28	33.4	–
PERU, Chichas	09/24	28.3	–

October Heatwave 2023

Location	Date	TMax	LTM
BRAZIL, Manaus	10/10	40.0	33.4
BRAZIL, Tarauaca	10/04	39.4	–
BRAZIL, Codajas	10/09	38.8	–
BRAZIL, Benjamin Constant	10/01	40.0	–
BRAZIL, Goiania	10/07	41.2	–
BRAZIL, Cuiaba	10/19	44.2	–
BOLIVIA, La Paz-Laykacota	10/08	**28.9**	20.5
BOLIVIA, Villamontes	10/16	46.5	34.3

Location	Date	TMax	LTM
BOLIVIA, Ascensión de Guarayos	10/19	41.5	32.7
BOLIVIA, Magdalena	10/19	**40.6**	33.8
BOLIVIA, San José de Chiquitos	10/19	**43.7**	34.7
BOLIVIA, Trinidad	10/22	41.5	33.1
PARAGUAY, Pedro Juan Caballero	10/17	38.0	29.8
PARAGUAY, Mariscal Estigarribia	10/23	43.6	35.1
PERU, Iñapari	10/24	39.0	33.2
PERU, Trujillo	10/22	27.2	21.8
PERU, Yungay	10/24	28.8	–
PERU, Rincon de la Cruz	10/28	21.6	–
PERU, Tahuaco-Yunguyo	10/11	21.0	–
PERU, Ayabaca	10/17	23.2	–

November Heatwave 2023

Location	Date	TMax	LTM
BRAZIL, Itacoatiara	11/08	39.2	–
BRAZIL, Rio de Janeiro	11/12	40.4	29.4
BRAZIL, Cuiaba	11/12	39.6	33.6
BRAZIL, Teresina	11/12	38.9	36.2
BRAZIL, Belo Horizonte	11/12	35.3	27.7
BRAZIL, Florianopolis	11/12	30.8	26.0
BRAZIL, Brasilia	11/12	32.9	26.7
BRAZIL, São Paulo	11/12	37.1	26.9
BRAZIL, Porto Murtinho	11/11	42.3	33.0
BRAZIL, Araçuaí	11/20	44.8	32.0
BRAZIL, Lavras	11/14	38.2	–
BRAZIL, Salinas	11/18	41.8	–
BOLIVIA, San Borja	11/10	41.2	32.5
BOLIVIA, Yacuiba	11/12	**44.9**	30.9

Location	Date	TMax	LTM
BOLIVIA, San Matias	11/13	42.8	34.3
BOLIVIA, Puerto Suarez	11/16	**43.5**	33.3
BOLIVIA, Cochabamba Aero	11/17	**36.2**	28.9
BOLIVIA, Santa Ana de Yacuma	11/18	39.5	32.5
BOLIVIA, Trinidad	11/18	41.3	32.3
BOLIVIA, San Ramón	11/17	39.5	32.6
BOLIVIA, San José de Chiquitos	11/08	44.1	33.7
BOLIVIA, Pto Suarez	11/16	43.5	33.3
BOLIVIA, Riberalta	11/17	39.3	32.6
BOLIVIA, San Ignacio de Moxos	11/17	38.9	32.2
PARAGUAY, Mariscal Estigarribia	11/8, 11/12	44.5	35.7
PARAGUAY, Perto Casado	11/12	42.0	32.4
PARAGUAY, Pedro Juan Caballero	11/12	39.2	29.9
PARAGUAY, Concepción	11/17	42.2	32.4
PERU, Cajatambo	11/10	20.6	–
PERU, Palca	11/14	24.6	–

Appendix Table 7.2. Temporal coverage of nationally averaged temperature and precipitation in situ observations for Europe / World Meteorological Organization (WMO) Regional Association (RA) VI region. For some countries, only one station (preferably with a long time series) has been used (name of the location in brackets). A standalone dash indicates that the information was not available.

Nation	Temperature start of record	Precipitation start of record	Source	Temperature anomaly (°C)	Rank (ordered from warmest [1] to coldest)	Precipitation anomaly (annual total in % of normal)	Rank (ordered from wettest [1] to driest)
European average	1950	1881	GHCN data (temperature), GPCC (precipitation)	+0.95	1–2	95%	91
Albania (Korce)	1963	1963	–	–	–	–	–
Andorra	1950	1950	NMHS[1]	–	–	–	–
Armenia	1935	1935	NMHS	+2.2	3	97%	49
Austria	1767	1858	NMHS	+1.2	1	117%	7
Azerbaijan (Astara)	1991	1991	–	–	–	–	–
Belarus	1881	1945	NMHS	+1.4	3	–	–
Belgium	1981	1981	NMHS	+1.1	3	174%	11
Bosnia & Herzegovina (Sarajevo)	1961	1961	NMHS	+1.3	1	116%	10
Bulgaria	1930	1930	NMHS	+1.0	1	96%	52
Croatia (Nicosia)	1961	1961	NMHS	–	1	116%	–
Cyprus	1899	1916	NMHS	+1.2	5	82%	102
Czechia	1961	1961	NMHS	+1.4	1	107%	15
Denmark	1873	1874	NMHS	+1.2	3	129%	1
Estonia	1922	1961	NMHS	+0.8	6–9	104%	20
Finland (Helsinki)	1900	1961	NMHS	+0.3	22	112%	8
France	1900	1959	NMHS	+1.4	2	104%	24
Georgia	1956	1881 (Tbilisi)	NMHS	+1.3	3	113%	11
Germany	1881	1881	NMHS	+2.4	1	169%	6
Greece	1960	1960	NMHS	+1.3	1	91%	54
Hungary	1901	1901	NMHS	+1.5	1	125%	8

Nation	Temperature start of record	Precipitation start of record	Source	Temperature anomaly (°C)	Rank (ordered from warmest [1] to coldest)	Precipitation anomaly (annual total in % of normal)	Rank (ordered from wettest [1] to driest)
Iceland	1900 (Stykkishólmur)	1921 (Reykjavik)	NMHS	–0.1	–	91%	–
Ireland	1900	1900	NMHS	+1.0	1	117%	3
Israel	1951	1935 (Deganya)	NMHS	+1.0	3	90%	34
Italy	1961	1961	NMHS	+1.1	2	96%	28
Jordan (Amman)	1923	1923	NMHS	+1.0	5	135%	20
Kazakhstan	1941	1941	NMHS	+1.9	1	85%	6
Latvia	1924	1924	NMHS	+1.0	3	112%	13
Lebanon (Beirut)	1949	1949	–	–	–	–	–
Lithuania	1961	1887 (Vilnius)	NMHS	+1.3	3	103%	20
Luxembourg (Findel)	1838	1854	NMHS	+1.0	2	234%	8
Malta (Luqa)	1923	1949	NMHS	+0.7	1	99%	97
Moldova (Chisinau)	1886	1891	NMHS	+1.9	1	78%	–
Monaco	1966	1966	NMHS	+1.2	2	55%	53
Montenegro (Podgorica)	1949	1949	NMHS	+2.34	2	109%	2
Netherlands	1901	1901	NMHS	–	1	–	–
North Macedonia	1981	1981	NMHS	+1.2	4	112%	13
Norway	1900	1900	NMHS	–0.1	37	105%	13
Poland	1951	1951	NMHS	+1.3	2	145%	17
Portugal	1931	1931	NMHS	+1.0	2	87%[5]	25
Romania	1961	1961	NMHS	+1.6	1	99%	31
Russia, European part	1936	1936	NMHS	+1.3	1	111%	4
Serbia	1951	1951	NMHS	+1.5	1	119%	6

Nation	Temperature start of record	Precipitation start of record	Source	Temperature anomaly (°C)	Rank (ordered from warmest [1] to coldest)	Precipitation anomaly (annual total in % of normal)	Rank (ordered from wettest [1] to driest)
Slovakia	1951	1961	NMHS	+1.3	2	125%	2
Slovenia	1961	1961	NMHS	+1.3	1	410%	3
Spain	1961	1961	NMHS	+1.3[3]	2	84%	57
Sweden	1860	1880	NMHS	+0.2	22	113%	4
Switzerland	1864	1864	NMHS	+1.4	2	112%	20
Syrian Arab Republic (Aleppo)	1960	1960	–	–	–	–	–
Türkiye	1971	1991	NMHS	+1.2	3	112%	–
Ukraine (Kyiv and Kharkiv)	1891	1891	NMHS	+1.8	2	108%	19
United Kingdom	1884	1836	NMHS	+0.8	2	111%	11

[1] NMHS = National Meteorological and Hydrological Service; for individual names of NMHSs see https://public.wmo.int/en/about-us/members

[2] reference period 1961–1990

[3] reference period 1981–2010

References

Alvala, R., D. F. Ribeiro, J. A. Marengo, M. E. Seluchi, D. A. Gonçalves, L. Antunes da Silva, L. A. Cuartas Pineda, S. M. Saito, 2024: Analysis of the hydrological disaster that occurred in the state of Rio Grande do Sul in September 2023: Vulnerabilities and risk management capabilities. *Int. J. Disaster Risk Reduct.*, **110**, 104645, https://doi.org/10.1016/j.ijdrr.2024.104645.

Amador, J. A., 1998: A climatic feature of the tropical Americas: The trade wind easterly jet. *Top. Meteor. Oceanogr.*, **5**, 91–102.

—— , 2008: The Intra-Americas Seas Low-Level Jet (IALLJ): Overview and future research. *Ann. N. Y. Acad. Sci.*, **1146**, 153–188, https://doi.org/10.1196/annals.1446.012.

—— , E. J. Alfaro, H. Hidalgo, and B. Calderon, 2011: Central America and the Caribbean [in "State of the Climate in 2010"]. *Bull. Amer. Meteor. Soc.*, **92** (6), S182–S183, https://doi.org/10.1175/1520-0477-92.6.S1.

—— , E. R. Rivera, A. M. Durán-Quesada, G. Mora, F. Sáenz, B. Calderón, and N. Mora, 2016a: The easternmost tropical Pacific. Part I: A climate review. *Rev. Biol. Trop.*, **64** (Suppl. 1), S1–S22, https://doi.org/10.15517/rbt.v64i1.23407.

—— , A. M. Durán-Quesada, E. R. Rivera, G. Mora, F. Sáenz, B. Calderón, and N. Mora, 2016b: The easternmost tropical Pacific. Part II: Seasonal and intraseasonal modes of atmospheric variability. *Rev. Biol. Trop.*, **64** (Suppl. 1) S23–S57, https://doi.org/10.15517/rbt.v64i1.23409.

Arias, P. A., and Coauthors, 2024: Interplay between climate change and climate variability: The 2022 drought in Central South America. *Clim. Change*, **177**, 6, https://doi.org/10.1007/s10584-023-03664-4.

Ashok, K., Z. Guan, and T. Yamagata, 2003: Influence of the Indian Ocean dipole on the Australian winter rainfall. *Geophys. Res. Lett.*, **30**, 1821, https://doi.org/10.1029/2003GL017926.

Beck, H. E., E. F. Wood, M. Pan, C. K. Fisher, D. G. Miralles, A. I. J. M. van Dijk, T. R. McVicar, and R. F. Adler, 2019: MSWEP V2 global 3-hourly 0.1° precipitation: Methodology and quantitative assessment. *Bull. Amer. Meteor. Soc.*, **100**, 473–500, https://doi.org/10.1175/BAMS-D-17-0138.1.

Beltrando, G., and P. Camberlin, 1993: Interannual variability of rainfall in the eastern Horn of Africa and indicators of atmospheric circulation. *Int. J. Climatol.*, **13**, 533–546, https://doi.org/10.1002/joc.3370130505.

CatIQ, 2024: CatIQ: Canada's loss and exposure indices provider. Accessed 29 February 2024, https://public.catiq.com/.

CCRIF SPC, 2023a: Covered area rainfall event (08/06/2023 to 13/06/2023) excess rainfall event briefing the Bahamas central. Caribbean Catastrophe Risk Insurance Facility, 14 pp., https://www.ccrif.org/sites/default/files/publications/eventreports/20230622_CCRIF_XSR_EventBriefing_BHS_C_CARE_20230608-13_Final.pdf.

—— , 2023b: Tropical cyclone Bret (AAL032023) final event briefing reportable event St. Lucia electricity services limited. Caribbean Catastrophe Risk Insurance Facility, 6 pp., https://www.ccrif.org/sites/default/files/publications/eventreports/20230703_CCRIF_FinalEventBriefing_TC_Bret_CPU_LCA_Final.pdf.

—— , 2023c: Covered area rainfall event (02/10/2023 to 05/10/2023) Dominica excess rainfall event briefing. Caribbean Catastrophe Risk Insurance Facility, 12 pp., https://www.ccrif.org/sites/default/files/publications/eventreports/20231012_CCRIF_XSR_EventBriefing_DMA_CARE_2-5October2023_Final.pdf.

—— , 2023d: Covered area rainfall event (3/10/2023 to 4/10/2023) Antigua and Barbuda excess rainfall event briefing. Caribbean Catastrophe Risk Insurance Facility, 14 pp., https://www.ccrif.org/sites/default/files/publications/eventreports/20231010_CCRIF_XSR_EventBriefing_ATG_CARE_20231010_Final.pdf.

—— , 2023e: Covered area rainfall event (16/11/2023 to 19/11/2023) excess rainfall event briefing Jamaica. Caribbean Catastrophe Risk Insurance Facility, 12 pp., https://www.ccrif.org/sites/default/files/publications/eventreports/20231128_CCRIF_XSR_EventBriefing_JAM_CARE_16Nov2023_Final.pdf.

Chen, J., K. Anderson, R. Pavlovic, M. D. Moran, P. Englefield, D. K. Thompson, R. Munoz-Alpizar, and H. Landry, 2019: The FireWork v2.0 air quality forecast system with biomass burning emissions from the Canadian Forest Fire Emissions Prediction System v2.03. *Geosci. Model Dev.*, **12**, 3283–3310, https://doi.org/10.5194/gmd-12-3283-2019.

CIFFC, 2023: Canadian Interagency Forest Fire Centre. https://ciffc.net/.

Costa, F., and J. Marengo, 2023: Statement on the 2023 Amazon drought and its unforeseen consequences. SPA Scientific-Technical Secretariat, 8 December, https://www.theamazonwewant.org/spa_publication/statement-on-the-2023-amazon-drought/.

Delforge, D., V. Wathelet, R. Below, C. L. Sofia, M. Tonnelier, J. van Loenhout, and N. Speybroeck, 2023: EM-DAT: The Emergency Events Database. https://doi.org/10.21203/rs.3.rs-3807553/v1.

DGE, 2023: Temperaturas naturales extremas (Temporada de calor 2023). Dirección General de Epidemiología, 11 pp., www.gob.mx/cms/uploads/attachment/file/847069/TNE_2023_SE30.pdf.

ECCC, 2024: Canada's top 10 weather stories of 2023. Accessed 29 February 2024, https://www.canada.ca/en/environment-climate-change/services/top-ten-weather-stories/2023.html.

EPA, 2023: Canadian wildfires prompt poor air quality alert for parts of New England on June 7, 2023. United States Environmental Protection Agency, accessed 13 February 2024, https://www.epa.gov/newsreleases/canadian-wildfires-prompt-poor-air-quality-alert-parts-new-england-june-7-2023.

Espinoza, J. C., J. C. Jimenez, J. Á. Marengo, J. Schongart, J. Ronchail, W. Lavado, and J. B. M. Ribeiro, 2024: The new record of drought and warmth in the Amazon in 2023 related to regional and global climatic features. *Sci. Rep.*, **14**, 8107, https://doi.org/10.1038/s41598-024-58782-5

Evans, A., D. Jones, R. Smalley, and S. Lellyett, 2020: An enhanced gridded rainfall analysis scheme for Australia. Bureau of Meteorology Research Rep. 41, 38 pp., http://www.bom.gov.au/research/publications/researchreports/BRR-041.pdf.

Fowler, A. M., 2021: Central Auckland rainfall, 1853-2020: Towards a homogenous record. *J. Hydrol.*, **60** (1), 25–47, https://www.hydrologynz.org.nz/journal/volume-60-2021.

Funk, C., and Coauthors, 2015: The Climate Hazards Infrared Precipitation with Stations —— A new environmental record for monitoring extremes. *Sci. Data*, **2**, 150066, https://doi.org/10.1038/sdata.2015.66.

Guardamino Soto, B., 2023: Puno: Continuo descenso del lago Titicaca y sequía del 84% de totorales causan preocupación en la region. Infobae, 26 September, https://www.infobae.com/peru/2023/09/26/puno-continuo-descenso-del-lago-titicaca-y-sequia-del-84-de-totorales-causan-preocupacion-en-la-region/.

Gutierrez, R. A., J. C. Espinoza, W. Lavado, C. Junquas, J. Molina-Carpio, T. Condom, and J. A. Marengo, 2024: The 2022-23 drought in the South American Altiplano: ENSO effects on moisture flux in the western Amazon during the prewet season. *Wea. Climate Extremes*, **45**, 100710, https://doi.org/10.1016/j.wace.2024.100710.

Hendon, H. H., D. W. Thompson, and M. C. Wheeler, 2007: Australian rainfall and surface temperature variations associated with the Southern Hemisphere annular mode. *J. Climate*, **20**, 2452–2467, https://doi.org/10.1175/JCLI4134.1.

Hersbach, H., and Coauthors, 2020: The ERA5 global reanalysis. *Quart. J. Roy. Meteor. Soc.*, **146**, 1999–2049, https://doi.org/10.1002/qj.3803.

Hidalgo, H., E. Alfaro, J. Amador, and A. Bastidas, 2019: Precursors of quasi-decadal dry-spells in the Central America Dry Corridor. *Climate Dyn.*, **53**, 1307–1322, https://doi.org/10.1007/s00382-019-04638-y.

Jain, P., and Coauthors, 2024: Canada under fire – Drivers and impacts of the record-breaking 2023 wildfire season. *ESS Open Archive*, https://doi.org/10.1038/s41467-024-51154-7.

Jones, D. A., W. Wang, and R. Fawcett, 2009: High-quality spatial climate data-sets for Australia. *Aust. Meteor. Oceanogr. J.*, **58**, 233–248, https://doi.org/10.22499/2.5804.003.

Lee, M., T. Kim, D. H. Cha, S. K. Min, D. S. R. Park, S. W. Yeh, and J. C. Chan, 2021: How does Pacific decadal oscillation affect tropical cyclone activity over far East Asia? *Geophys. Res. Lett.*, **48**, e2021GL096267, https://doi.org/10.1029/2021GL096267.

Lowe, S. R., and D. R. Garfin, 2023: Crisis in the air: The mental health implications of the 2023 Canadian wildfires. *Lancet Planet. Health*, **7**, e732–e733, https://doi.org/10.1016/S2542-5196(23)00188-2.

Mao, W., R. Shalaby, B. Agyapong, G. Obuobi-Donkor, R. Da Luz Dias, and V. I. O. Agyapong, 2024: Devastating wildfires and mental health: Major depressive disorder prevalence and associated factors among residents in Alberta and Nova Scotia, Canada. *Behav. Sci.*, **14**, 209, https://doi.org/10.3390/bs14030209.

Marengo, J. A., and Coauthors, 2024: Heavy rains and hydrogeological disasters on February 18th–19th, **2023**, in the city of São Sebastião, São Paulo, Brazil: From meteorological causes to early warnings. *Nat. Hazards*, **120**, 7997–8024, https://doi.org/10.1007/s11069-024-06558-5.

Magaña, V., J. A. Amador, and S. Medina, 1999: The mid-summer drought over México and Central America. *J. Climate*, **12**, 1577–1588, https://doi.org/10.1175/1520-0442(1999)012<1577:TMDOMA>2.0.CO;2.

Matz, C. J., M. Egyed, G. Xi, J. Racine, R. Pavlovic, R. Rittmaster, S. B. Henderson, and D. M. Stieb, 2020: Health impact analysis of $PM_{2.5}$ from wildfire smoke in Canada (2013–2015, 2017–2018). Sci. *Total Environ.*, **725**, 138506, https://doi.org/10.1016/j.scitotenv.2020.138506.

National Drought Mitigation Center, 2024: North American Drought Monitor: Maps. Accessed 10 May 2024, https://droughtmonitor.unl.edu/NADM/Maps.aspx.

NOAA/NCEI, 2024: Billion-dollar weather and climate disasters: Overview. Accessed 2 February 2024, https://www.ncei.noaa.gov/access/billions/.

Public Health Agency of Canada, 2023: Public health risk profile: Wildfires in Canada, 2023. Accessed 8 May 2024, https://www.canada.ca/en/public-health/services/emergency-preparedness-response/rapid-risk-assessments-public-health-professionals/risk-profile-wildfires-2023.html.

SENAMHI, 2023: Boletín hidrológico mensual a nivel nacional: Septiembre 2023. SENAMHI, 12 pp., https://www.senamhi.gob.pe/load/file/02609SENA-147.pdf.

McKay, R. C., J. M. Arblaster, and P. Hope, 2022: Tropical influence on heat-generating atmospheric circulation over Australia strengthens through spring. *Wea. Climate Dyn.*, **3**, 413–428, https://doi.org/10.5194/wcd-3-413-2022.

—— , and Coauthors, 2023: Can southern Australian rainfall decline be explained? *A review of possible drivers. Wiley Interdiscip. Rev.: Climate Change*, **14**, e820, https://doi.org/10.1002/wcc.820.

NAFI, 2024: Fire maps. North Australia and Rangelands Fire Information, https://firenorth.org.au/nafi3/.

Scoccimarro, E., G. Villarini, S. Gualdi, and A. Navarra, 2021: The Pacific Decadal Oscillation modulates tropical cyclone days on the interannual timescale in the North Pacific Ocean. *J. Geophys. Res. Atmos.*, **126**, e2021JD034988, https://doi.org/10.1029/2021JD034988.

Singh, D., and Coauthors, 2023: Focus on compound events. *Fifth National Climate Assessment*, A. R. Crimmins et al., Eds., U.S. Global Change Research Program, https://doi.org/10.7930/NCA5.2023.F1.

Skakun, R., G. Castilla, J. Metsaranta, E. Whitman, S. Rodrigue, J. Little, K. Groenewegen, and M. Coyle, 2022: Extending the National Burned Area Composite time series of wildfires in Canada. *Remote Sens.*, **14**, 3050, https://doi.org/10.3390/rs14133050.

Smith, A. B., 2024: 2023: A historic year of U.S. billion-dollar weather and climate disasters. NOAA/NCEI, accessed 2 February 2024, https://www.climate.gov/news-features/blogs/beyond-data/2023-historic-year-us-billion-dollar-weather-and-climate-disasters.

SPC, 2024: Tornado totals and related deaths. NOAA/National Weather Service, accessed 2 February 2024, https://www.spc.noaa.gov/climo/torn/STAMTS23.txt.

Thompson, D. W. J., M. P. Baldwin, and S. Solomon, 2005: Stratosphere–troposphere coupling in the Southern Hemisphere. *J. Atmos. Sci.*, **62**, 708–715, https://doi.org/10.1175/JAS-3321.1.

Toreti, A., and Coauthors, 2023: Drought in the Amazon basin November 2023. JRC Tech. Rep. 136439, European Commission, 28 pp., https://doi.org/10.2760/756827.

Trewin, B., 2018: The Australian Climate Observations Reference Network–Surface Air Temperature (ACORN-SAT) version 2. Bureau of Meteorology Research Rep. 032, 67 pp., http://www.bom.gov.au/research/publications/researchreports/BRR-032.pdf.

Zhang, W., G. A. Vecchi, H. Murakami, G. Villarini, and L. Jia, 2016: The Pacific meridional mode and the occurrence of tropical cyclones in the western North Pacific. *J. Climate*, **29**, 381–398, https://doi.org/10.1175/JCLI-D-15-0282.1.